SCHOLARLY PUBLICATIONS

A CURRENT AWARENESS BULLETIN
OF RESEARCH OUTPUT

@DTU

(46th Edition)

OCTOBER 2016

BY: CENTRAL LIBRARY

DELHI TECHNOLOGICAL UNIVERSITY
(FORMERLY *DELHI COLLEGE OF ENGINEERING)*
GOVT. OF N.C.T. OF DELHI
SHAHBAD DAULATPUR, MAIN BAWANA ROAD
DELHI 110042

PREFACE

This is the **Forty sixth** Issue of Current Awareness Bulletin started by Delhi Technological University, Central Library. The aim of the bulletin is to compile, preserve and disseminate information published by the faculty, students and alumni for mutual benefits. The bulletin also aims to propagate the intellectual contribution of Delhi Technological University (DTU) as a whole to the academia.

The bulletin contains information resources available in the internet in the form of articles, reports, presentations published in international journals, websites, etc. by the faculty and students of DTU. The publications of faculty and student which are not covered in this bulletin may be because of the reason that the full text either was not accessible or could not be searched by the search engine used by the library for this purpose.

The learned faculty and students are requested to provide their uncovered publications to the library either through email or in CD, etc to make the bulletin more comprehensive.

This issue contains the information published during **October 2016**. The arrangement of the contents is alphabetical. The full text of the article which is either subscribed by the university or available in the web is provided in this bulletin.

Central Library

CONTENTS

1. 3D Simulation of Flow around Different Types of Groyne Using ANSYS Fluent, ***3.Dr. Munendra Kumar*** and ***7.Aashish Malik***, Civil Engineering, DTU

2. 5G Millimeter Wave (mmWave) Communication System with Software Defined Radio (SDR), S. K. Agrawal and ***3.Dr. Kapil Sharm,*** Computer Engineering, DTU

3. Air pollution tolerance of trees in an educational institute in Delhi ***3.Deepika, 3.Parag Gour,*** and ***3.Haritash A.K.,*** Environmental Engineering, DTU

4. Ambient Polycyclic Aromatic Hydrocarbons and its Carcinogenic and Mutagenic Risk,***3.Papiya Mandal, 3.R.Sarkar*** and ***3.A.Mandal***, Civil Engineering, DTU

5. An effective web page recommender system with fuzzy c-mean clustering, ***3.Rahul Katarya*** and ***3.Om Prakash Verma,*** Computer Science & Engineering, DTU

6. An Exploration of Factors Affecting M-commerce Adoption in India, ***3.Khushbu Madan*** and ***3.Rajan Yadav,*** DSM, DTU

7. A Survey on Sentiment Analysis using Swarm Intelligenc, ***3.Akshi Kumar, 3.Renu Khorwal*** and ***3.Shweta Chaudhary***, Computer Science and Engineering, DTU

8. ANAEROBIC TREATMENT OF DAIRY EFFLUENT- A STEP FOR ENERGY SAVING & GHG MITIGATION, ***3.Rakesh Mehrotra, 3.A Trivedi*** and ***3.1 S. K. Mazumder***, Civil Engineering, DTU

9. Analyzing and modeling the performance index of ultrasonic vibration assisted EDM using graph theory and matrix approach Sanjay Kumar, Sandeep Grover and ***3.R. S. Walia***, Mechanical, Production and Industrial and Automation, DTU

10. Biofunctionalized Nanostructured Tungsten Trioxide Based Sensor for Cardiac Biomarker Detection ***3.Deepika Sandil[1], 3.Saurabh Kumar[2], 3.Kamal Arora[1], 3.Saurabh Srivastava[1], 3.B.D. Malhotra[2], 3.S.C. Sharma[1]*** and ***3.Nitin K. Puri[1]*** [1]Applied Physics, , [2]Biotechnology, DTU

11. Bismuth oxide nanorods based immunosensor for mycotoxin detection, Pratima R. Solanki***, 3.Jay Singh***[1]**,** Bharti Rupavali, Sachchidanand Tiwari and 3.***Bansi D. Malhotra***[2], [1]Applied Chemistry and Polymer Technology, [2]Biotechnology, DTU

12. Computational Analysis and Predictive Cheminformatics Modeling of Small Molecule Inhibitors of Epigenetic Modifiers, Salma Jamal, ***3.Sonam Arora*** and Vinod Scaria, DTU

13. Contact Pressure Analysis of Spur Gear using FEA, T.Veera Pratap Reddy and ***7.1 Dr. J. Govardhan***, DTU

14. Design of As2Se3 based chalcogenide ridge waveguide for generation of slow light ***3.Apurva Tewaria, 3.Ajeet Kumara, 3.Than Singh Saini*** and Ravindra Kumar Sinha, Applied Physics, DTU

15. Disposition decisions in reverse logistics by using AHP-Fuzzy TOPSIS Approach, ***3.Saurabh Agrawal[1], 3.Dr. Rajesh Kr. Singh[2]*** and Dr. Qasim Murtaza, [1]Mechanical, Production & Industrial Engineering, [2]Management, DTU

16. Effect of low pressure hydrogen environment on crystallographic properties of PdO nanoparticles, ***3.Kamal Arora, 3.Deepika Sandil, 3.Gaurav Sharma, 3.Saurabh Srivastava*** and ***3.Nitin K. Puri***, Applied Physics, DTU

17. Effect of ZnO doping on structural, dielectric, ferroelectric and piezoelectric properties of BaZr0.1Ti0.9O3 ceramics, ***3.Aditya Jain, 3.Amrish K. Panwar*** and A.K. Jha, Applied Physics, DTU

18. Electric and magnetic hotspots in the Silicon Bow-Tie nanocavity, ***3.Reena, 3.Yogita Kalra and 3.R.K. Sinha,*** Applied Physics, DTU

19. ENERGY AND EXERGY ANALYSIS OF ABSORPTION- COMPRESSION CASCADE REFRIGERATION SYSTEM, Manoj Dixit, S C Kaushik and ***3.Akhilesh Arora***, Mechanical Engineering, DTU

20. Engendering color tunable emission in calcium silicate basedphosphors via ageing of silicate source, Hyun-Joo Woo, Sakthivel Gandhi, ***3.M. Jayasimhadri***, Dong-Soo Shin, Ho Sueb Lee and Kiwan Jange, Applied Physics, DTU

21. Failure investigations of a first stage Ni based super alloy gas turbine blade, ***3.Sushila Rani, 3.Atul K Agrawal*** and ***3.Vikas Rastogi***, Mechanical, Production and Automobile Engineering, DTU

22. Gate drain-overlapped-asymmetric gate dielectric-GAA-TFET: a solution for suppressed ambipolarity and enhanced ON state behavior, ***3.Jaya Madan and 3.Rishu Chaujar***, Physics, DTU

23. Improved FPGA Implementation of Real Time Modified Mean Shift Tracking Algorithm ***3.Rajesh Rohilla*** and ***3.Rajiv Kapoor***, Electronics and Communication Engineering, DTU

24. LC-ladder filter systematic implementation by OTRA, ***3.Suman Kumari, 3.Stuti Gupta, 3.Neeta Pandey, 3.Rajeshwari Pandey*** and Rashika Anurag, ECE, DTU

25. Magnetic response of split nanotube type metamaterial at near infrared frequency ***3.Nishant Shankhwar***, Ravindra Kumar Sinha and ***3.Yogita Kalra***, Applied Physics, DTU

26. Magnetron sputtering coated optical fiber probe designs for surface plasmon resonance sensor, Rashmi A. Minz, Sudipta S. Pal, Aditi Chopra, Shivam, R.Bhatnagar***, 3.R.K Sinha***, and Samir K. Mondal, Physics, DTU

27. Multi attribute assessment of consumables for TIG welding of Aluminum Alloys, ***3.P K Baghel*** and ***3.D.S. Nagesh***, Mechanical Engineering, DTU

28. Myosin-Induced Gliding Patterns at Varied [MgATP] Unveil a Dynamic Actin Filament, Elina Bengtsson, Malin Persson, Mohammad A. Rahman, ***3.Saroj Kumar***, Hideyo Takatsuki and Alf Mansson, Biotechnology, DTU

29. New agegraphic dark energy in Brans-Dicke theory with loga- rithmic form of scalar field ***3.Pankaj Kumar*** and ***3.C. P. Singh***, Applied Mathematics, DTU

30. Numerical simulations: Toward the design of 27.6% efficient fourterminal semi-transparent perovskite/SiC passivated rear contact silicon tandem solar cell, ***3.Rahul Pandey*** and ***3.Rishu Chaujar***, Physics, DTU

31. On the application of search-based techniques for software engineering predictive modeling: A systematic review and future directions, ***3.Ruchika Malhotra***, ***3.Megha Khanna*** and Rajeev R. Raje, Software Engineering, DTU

32. Palladium Gate All Around - Hetero Dielectric - Tunnel FET based highly sensitive Hydrogen Gas Sensor, ***3.Jaya Madan and 3.Rishu Chaujar***, Physics, DTU

33. Parametric Optimization of Hybrid Electrode EDM Process***, 6.Ramakant Rana, 3.R.S. Walia,3.Qasim Murtaza*** and ***3.Mohit Tyagi***, Mechanical Engineering, DTU

34. Performance investigation of heterogeneous gate dielectric-gate metal engineered–gate all around-tunnel FET for RF applications, ***3.Jaya Madan***, R. S. Gupta and ***3.Rishu Chaujar***, Physics, DTU

35. Prominent photovoltaic response in multiferroic BFO/BTO heterostructures, ***3.Savita Sharma, 3.Nitin K. Puri***, Vinay Gupta and Monika Tomar, Applied Physics, DTU

36. REDUCTION OF FREE FATTY ACID OF JATROPHA OIL USING TAGUCHI APPROACH, ***3.Suresh Kumar Saroj, 3.Raghvendra Gautam and 3.Nikhil Shubhendu,*** DTU

37. Resource assessment for hybrid solar-biomass power plant and its thermodynamic evaluation in India ***3.U. Sahoo, 3.R. Kumar*** , P.C. Pant and ***3.R. Chaudhary***, Mechanical Engineering, DTU

38. Revised and extended calculations of level energies, M1 and E2 radiative rates for highly charged tungsten ions from W57+ to W60+, ***3.Gajendra Singh*** and ***3.Nitin K Puri***, Applied Physics, DTU

39. Stability analysis of predator–prey system with migrating prey and disease infection in both species ***3.Shashi Kant*** and ***3.Vivek Kumar***, Applied Mathematics, DTU

40. Structural Analysis and Balancing Test for Impeller Before Conducting Over Speed Test S.Rakesh and ***7.1 J.Govardhan***, DTU

41. SWOT Analysis of Ontology Driven Software Engineering, M. P. S. Bhatia, ***3.Akshi Kumar*** and Rohit Beniwal, Computer Engineering, DTU

42. Taguchi and utility based concept for determining optimal process parameters of cold sprayed coatings for multiple responses, Tarun Goyal***, 3.R. S. Walia*** and T. S. Sidhu, DTU

43. T-MQM: Testbed based Multi-metric Quality Measurement of Sensor Deployment for Precision Agriculture-A Case Study, Omprakash Kaiwartya, Abdul Hanan Abdullah, Yue Cao, Ram Shringar Raw, Sushil Kumar, D.K. Lobiyal, Ismail Fauzi Isnin, Xiulei Liu and ***7.1 Rajiv Ratn Shah,*** DTU

44. Trace detection of explosive and their derivatives in stand-off mode using time gated Raman spectroscopy ***3.Sanjay Guliaa***, Kamal K. Gulati, Vijayeta Gambhir, ***3.Rinku Sharma*** and M.N. Reddy, DTU

1. *Chancellor*
2. *Pro Vice Chancellor* — ***2.1.*** *Ex Pro Vice Chancellor*
3. *Faculty* — ***3.1.*** *Ex Faculty*
4. *Teaching-cum-Research Fellow*
5. *Alumni*
6. *Research Scholar* — ***6.1.*** *Ex Research Scholar*
7. *PG Scholar* — ***7.1.*** *Ex PG Scholar*
8. *Undergraduate Student* — ***8.1.*** *Ex Udergraduate Student*

International Conference on Recent Trends in Engineering & Science
Shree Ramchandra College of Engineering, Pune (India) ICRTES - 16
29th-30th September 2016, www.conferenceworld.in ISBN : 978-93-86171-06-1

5G Millimeter Wave (mmWave) Communication System with Software Defined Radio (SDR)

S. K. Agrawal[1],Dr. Kapil Sharma[2]

[1]*Samsung Research Institute Noida, India*

[2]*Computer Engineering Department, Delhi Technological University, India*

ABSTRACT

5G Millimeter Wave (mmWave) Communication System will provide high speed data connection with minimal latency to full-fill the upcoming user demand and need by 2020. 5G Millimeter Wave (mmWave) Communication System can provide multigigabit data rates for the several users at a time. This paper presents atmospheric attenuation control in 5G millimeter wave (mmwave) communication system for Delhi (India) based location using software defined radio (SDR). The software defined radio atmospheric attenuation is calculated for the frequencies 28 GHz, 37 GHz and 39 GHz. The atmospheric attenuation is calculated for Delhi (India) based location by considering 5G millimeter wave (mmWave) absorption due to atmospheric water vapour and atmospheric oxygen.

Keywords - Millimeter Wave (mmWave); software defined radio (SDR); Radio Frequency (RF)

I. INTRODUCTION

By 2020 demand and need for the mobile broadband will be very high and existing system will not be able to fulfill the user demand globally. 5G Millimeter Wave (mmWave) Communication System will be capable to provide low latency , high speed internet connection to the users across the Globe in an efficient manner. 5G Millimeter Wave (mmWave) Communication System can provide multi-gigabit data rates for the users across the Globe. Continuous increasing mobile internet data demand making 3 GHz spectrum overloaded. Further, there is another set of frequencies under millimeter wave (mmwave) frequency band which is under consideration for 5G millimeter wave (mmwave) communication system. The millimeter wave (mmwave) frequency spectrum is ranging from 3 GHz to 300 GHz. Research and development is in progress to identify the suitable frequency bands in millimeter wave (mmwave) frequency spectrum [1-4].

5G Millimeter Wave (mmWave) Communication System can attain multigigabit data rates for mobile broadband users. In this paper, we are discussing the mmWave 3–300 GHz spectrum along with the effect of atmospheric attenuation and its controlling along with compensation at the transmitter side. There is a requirement to provide the transmission power control in an efficient manner so that system can recognize the requirement of the transmission power. SDR based 5G Millimeter Wave (mmWave) Communication System can provide controlled transmission power in an optimum manner. 5G millimeter wave (mmwave)

ISSN (O) 2454-9665
ISSN (P) 2454-0663

communication system atmospheric attenuation is majorly caused by oxygen and water vapor gases out of various atmospheric gases [3-7].

This paper is organized as follows: Section II describe the 5G millimeter wave (mmWave) frequency spectrum communication system . Section III describe the Atmospheric Attenuation Due to Water Vapour and Oxygen in 5G Millimeter Wave (mmWave) Communication System. Further section IV describe the Software Defined Radio (SDR) for Atmospheric Attenuation Control in 5G Millimeter Wave (mmWave) Communication System .

II. 5G MILLIMETER WAVE (MMWAVE) FREQUENCY SPECTRUM

5G Millimeter Wave (mmWave) carrier frequencies allow for higher bandwidth and accordingly able to provide high speed internet data connection. 5G Millimeter Wave (mmWave) carrier frequencies have the low wavelength and leads to high attenuation and which requires signification study to decide the frequency bands. 5G Millimeter Wave (mmWave) can suffer with various type signal effects like attenuation, shadowing, Doppler effect , interference and etc. Federal Communications Commission (FCC) has recommended 5G Millimeter Wave (mmWave) carrier frequencies and bands to have research and development. The 5G Millimeter Wave (mmWave) carrier frequencies and bands are [8-11]:

- 28 GHz Band
- 37 GHz Band
- 39 GHz Band

For the above mentioned 5G Millimeter Wave (mmWave) carrier frequencies atmospheric attenuations is calculated and discussed in the following sections.

III. ATMOSPHERIC ATTENUATION DUE TO WATER VAPOUR AND OXYGEN IN 5G MILLIMETER WAVE (MMWAVE) COMMUNICATION SYSTEM

For 5G Millimeter Wave (mmWave) carrier frequencies , atmosphere gaseous losses are majorly due to the oxygen and water absorption bands. A formula for calculating predicting atmosphere gaseous absorption due to atmospheric gases oxygen and water vapor is mentioned by in ITU-R Recommendation P.618 . To calculate the gaseous attenuation due to oxygen and water vapor gases, the parameters are required for 5G millimeter wave (mmwave) communication system [3-7, 12-14]:

- 5G Millimeter Wave (mmWave) carrier frequencies
- Water vapor density for Delhi (India) based location
- Elevation angle

ISSN (O) 2454-9665
ISSN (P) 2454-0663

- Altitude (above sea level) for Delhi (India) based location and etc.

The total atmospheric attenuation for Delhi (India) based location is calculated by summing the absorption contributed by atmospheric water vapour and atmospheric oxygen . For Delhi based 5G Millimeter Wave (mmWave) Communication System water vapour density/ concentration is 10g/m3 Gaseous absorption is calculated as the sum of water vapor absorption and Oxygen absorption. The software defined radio (SDR) atmospheric attenuation calculation method is based on ITU model which is applied with 5G millimeter wave (mmwave) communication system for Delhi (India) based location [1-3, 13-17].

Figure 1 shows the effect of oxygen to millimeter wave (mmwave) propagation in different frequencies. Figure 2 shows the effect of water vapor to millimeter wave (mmwave) propagation in different frequencies. The molecules resonance of water vapour absorption takes place at approximately 22 GHz and 183 GHz, . Further absorption resonances for oxygen occurs at 60 GHz and 120 GHz. It is clear that the minimum attenuation occurs between these frequencies. It is shown in the figure that the Minimum attenuation occurs for the 28 GHz, 37 GHz and 39 GHz frequencies.

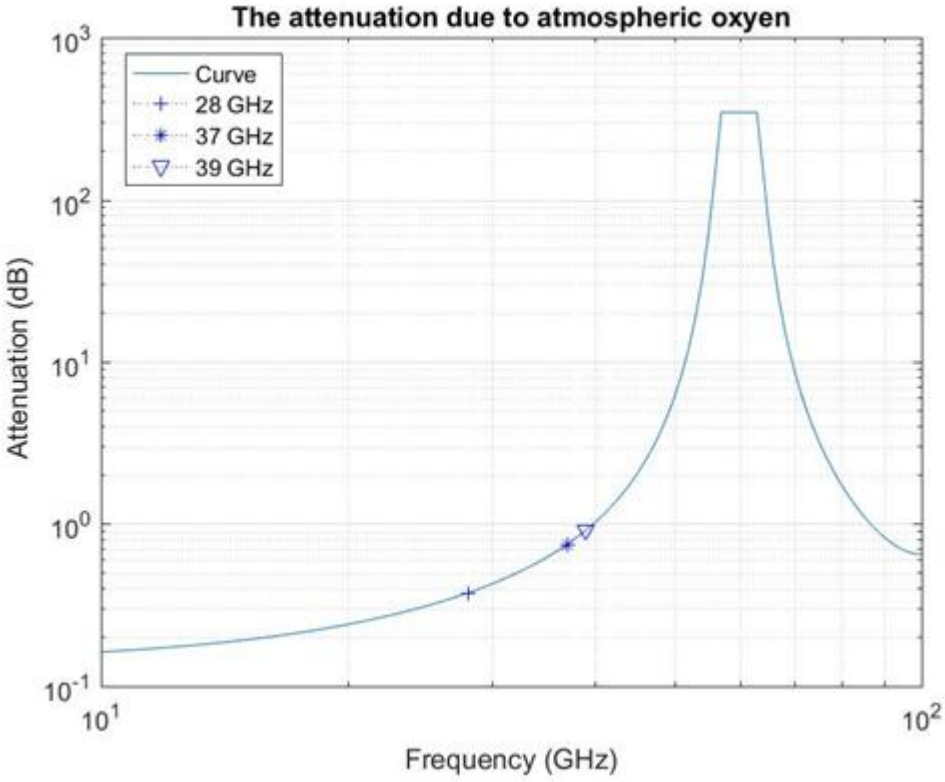


Figure 1: The attenuation due to atmospheric water vapour 5G millimeter wave (mmwave) communication system

International Journal of Innovative Research in Science and Engineering
Vol. No.2, Issue 09, September 2016
www.ijirse.com
ISSN (O) 2454-9665
ISSN (P) 2454-0663

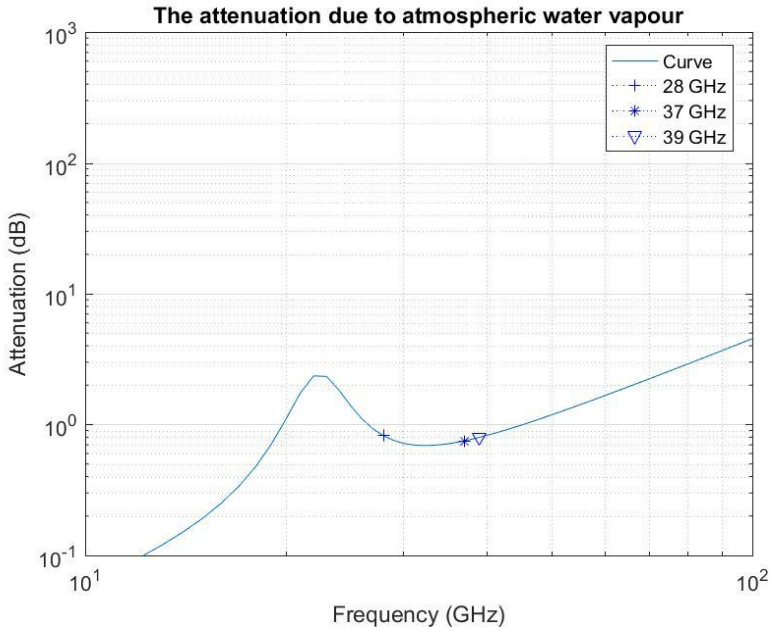


Figure 2 : The attenuation due to atmospheric oxygen 5G millimeter wave (mmwave) communication system

Figure 1 and Figure 2 show the 5G millimeter wave (mmwave) communication system atmospheric attenuation curve for the varied frequency in GHz. It is clear from the above figures that the atmospheric path loss is less for the frequencies 28 GHz, 37 GHz and 39 GHz. It also verifies the reason of having frequencies 28 GHz, 37 GHz and 39 GHz for 5G millimeter wave (mmwave) communication system.

Table 1 shows the atmospheric attenuation values due to water vapour and oxygen. The table 1 shows the attenuation values for the frequencies 28 GHz, 37 GHz and 39 GHz. The software defined radio atmospheric attenuation is calculated in real time using processors of SDR for Delhi (India) based location in 5G millimeter wave system.

Table 1: The atmospheric attenuation values for the frequencies 28 GHz, 37 GHz and 39 GHz due to water vapour and oxygen

Attenuation (dB)	Frequency 28 GHz	Frequency 37 GHz	Frequency 39 GHz
Aw *(due to atmospheric water vapour)*	0.8200	0.7500	0.7983
Ao *(due to atmospheric oxygen)*	0.3756	0.7495	0.9157

International Journal of Innovative Research in Science and Engineering
Vol. No.2, Issue 09, September 2016
www.ijirse.com
ISSN (O) 2454-9665
ISSN (P) 2454-0663

IV. SOFTWARE DEFINED RADIO (SDR) BASED ATMOSPHERIC ATTENUATION CONTROL IN 5G MILLIMETER WAVE (MMWAVE) COMMUNICATION SYSTEM

Software Defined Radio (SDR) system provides facility for parameters control at the end of the transmitters and receivers in the 5G Millimeter Wave (mmWave) Communication System . SDR can be used to implement digital signal processing (DSP) along with the below mentioned functions also [18-20]:

- Air interface
- Channel access
- Waveform synthesis
- Transmission power control and etc.

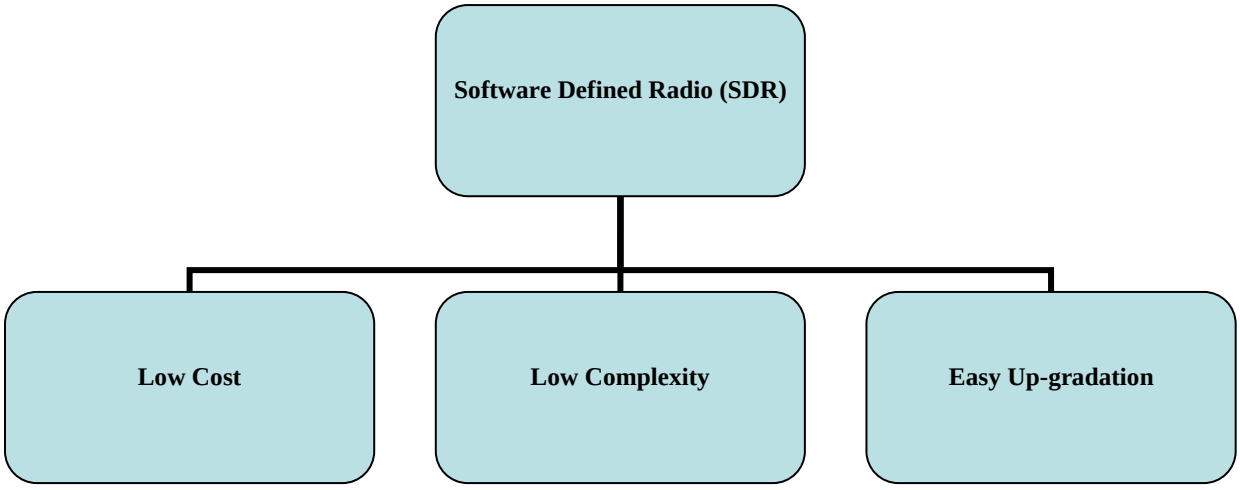


Figure 3: Features of Software Defined Radio (SDR) in 5G Millimeter Wave (mmWave) Communication System

SDRs provides optimum methods to control the transceiver as per demand and need of 5G Millimeter Wave (mmWave) Communication System . By having SDR based real-time reconfigurable processors , 5G Millimeter Wave (mmWave) Communication System can control transmission power and gain efficiently. SDRs is capable to provide variable and adaptive coding, decoding, modulation and radio access formats. It also reduces the cost, complexity and easy up-gradation as per technology update as shown in figure 3. SDR supports complex hardware functions easily in the software modules for the complicated functions like beam processing, array processing, precoding , interleaving and secure protocols and etc [18-20].

International Journal of Innovative Research in Science and Engineering
Vol. No.2, Issue 09, September 2016
www.ijirse.com
ISSN (O) 2454-9665
ISSN (P) 2454-0663

TABLE 3: The atmospheric attenuation values for the frequencies 28 GHz, 37 GHz and 39 GHz

Attenuation (dB)	Frequency 28 GHz	Frequency 37 GHz	Frequency 39 GHz
Aw *(due to atmospheric water vapour)*	0.8200	0.7500	0.7983
Ao *(due to atmospheric oxygen)*	0.3756	0.7495	0.9157
At *(Total atmospheric attenuation due to water vapour and oxygen)*	1.1956	1.4995	1.7140

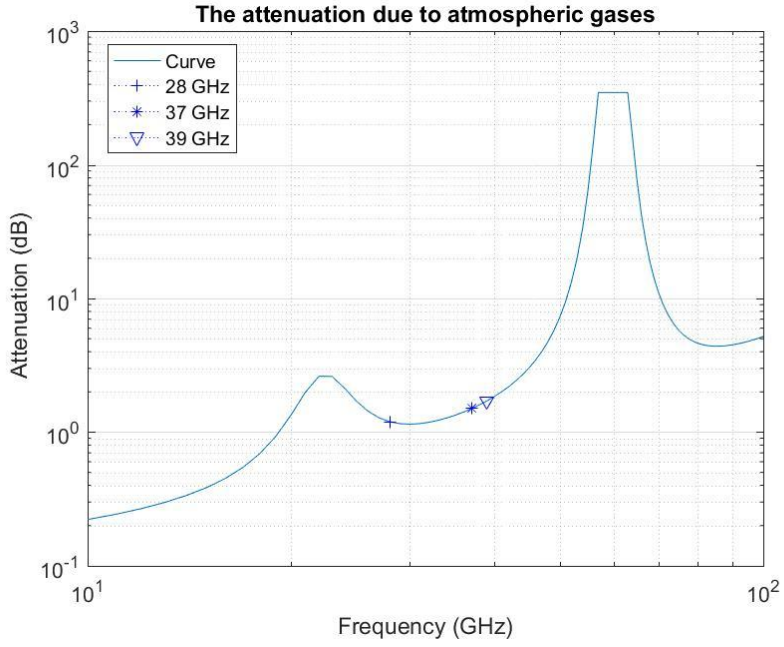


Figure 4 : The attenuation due to atmospheric gases 5G millimeter wave (mmwave) communication system

As shown in table 3 and figure 4 total atmospheric attenuation is sum of the absorption due to atmospheric water vapour and atmospheric oxygen. The table 3 along with figure 4 shows the attenuation values for the frequencies 28 GHz, 37 GHz and 39 GHz. It is clear that the atmospheric attenuation is quite less at the

ISSN (O) 2454-9665
ISSN (P) 2454-0663

frequencies 28 GHz, 37 GHz and 39 GHz. The software defined radio atmospheric total attenuation is calculated in real time using processors of SDR for Delhi (India) based location in 5G millimeter wave system.
In the context of various atmospheric conditions due to change in atmospheric water vapour and oxygen level the transceiver power must be reconfigurable to have compensated power . Software defined radio (SDR) for in 5G Millimeter Wave (mmWave) Communication System compensates the transmitted power and gain due to Atmospheric Attenuation and transmits the software controlled transmission.

V. CONCLUSION AND FUTURE WORK

This paper presented atmospheric attenuation calculation for 5G millimeter wave (mmWave) propagation absorption at the frequencies 28 GHz, 37 GHz and 39 GHz for Delhi (India) based location using software defined radio (SDR). It is shown in the paper that the atmospheric attenuation varies and depends on the millimeter wave (mmWave) frequencies. It also shows the reason of the selection of the frequencies bands 28 GHz, 37 GHz and 39 GHz for 5G Millimeter Wave (mmWave) Communication System due to low atmospheric absorption in these bands. The model in this paper allows future realistic modeling of propagation conditions for millimeter wave transmission in urban microcellular environments.
This research paper shows the importance and consideration of the atmospheric attenuation due to atmospheric water vapour and atmospheric oxygen during transmission link budget for 5G Millimeter Wave (mmWave) Communication. The paper suggest that the 5G Millimeter Wave (mmWave) Communication devices shall consider additional transmission gain to compensate for the atmospheric attenuation or path loss to provide optimum signal strength at the receiver end. Future work involves the identifying the various other causes for the atmospheric attenuation for 5G Millimeter Wave (mmWave) Communication and handling with high flexibility and high efficiency through SDR .

VI. ACKNOWLEDGMENT

This paper is specifically meant for educational purpose for completing Ph.D. degree with Delhi Technological University (DTU), Delhi India. This paper is prepared for submission to under Ph.D. progress. The authors are very much thankful to Samsung Research Institute Noida, India and Delhi Technological University (DTU) earlier recognized as Delhi-College of Engineering (DCE), New Delhi, India.

REFERENCES

[1]. Zhouye Pi et al., “An Introduction to Millimeter- Wave Mobile Broadband Systems, ” IEEE Communications Magazine, vol.49, no.6, pp.101- 107, Jun. 2011.

[2]. Andrews J.G. et al., “What Will 5G Be?, ” IEEE JSAC Special Issue On 5G Wireless Communication Systems, May 2014.

[3]. Cheol Jeong et al., “Random Access in Millimeter-Wave Beamforming Cellular Networks: Issues and Approaches, ” IEEE Communications Magazine, vol. 53, no. 1, pp.180-185, Jan. 2015.

ISSN (O) 2454-9665
ISSN (P) 2454-0663

[4]. Theodore S. Rappaport et al., "Millimeter Wave Mobile Communications for 5G Cellular: It Will Work!, " IEEE Access, vol.1, pp.335-349, May 2013.

[5]. Wonil Roh et al., "Millimeter-wave Beamforming as an Enabling Technology for 5G Cellular Communications: Theoretical Feasibility and Prototype Results, " IEEE Communications Magazine, vol. 52, no. 2, pp. 106-113, Feb. 2014.

[6]. Samsung, "5G Vision, " DMC R&D Center, Samsung Electronics Co., Ltd., Feb. 2015.

[7]. Wei L. et. al., "Key Elements to Enable Millimeter Wave Communications for 5G Wireless Systems, " IEEE Wireless Communications, vol.1, pp.136-143, Dec. 2014.

[8]. FCC, "Millimeter wave Propagation: Spectrum management Implications," office of Eng. and Tech., Bulletin no. 70, July, 1997.

[9]. FCC "Report And Order And Further Notice Of Proposed Rulemaking" , FCC 16-89, July, 2016.

[10]. Federal Communications Commission: "Evaluating compliance with FCC guidelines for human exposure to radiofrequency electromagnetic fields, " Washington, DC: FCC. Tech. Rep. Suppl. C to OET Bulletin 65, 2001.

[11]. Evaluating Compliance with FCC Guidelines for Human Exposure to Radiofrequency Electromagnetic Fields, Federal Communication Commission, OET Bulletin 65, Edition 97-01.

[12]. ITU Recommendation ITU-R RPN.618-4, 1996

[13]. International Telecommunication Union, "Water Vapour: Surface Density and Total Columnar Content," Recommendation ITU-R P.836-3, Electronic Publication, Geneva, Switzerland, November 2001.

[14]. Recommendation, "Attenuation by atmospheric gases," in ITU-R P.676-8, 10 2009.

[15]. S. K. Agrawal and P. Garg, "Calculation of Channel Capacity Considering the Effect of Different Seasons for Higher Altitude Platform System", Wireless Personal Communications, Springer, Wireless Personal Communications: vol. pp-719-729, Issue 4 2010.

[16]. S. K. Agrawal and P. Garg, "Calculation of the Channel Capacity in the Presence of Vegetation and Urban-site Environment for Higher Altitude Platform Communication System", to Wireless Personal Communications", IET Microwaves, Antenna & Propagation, IET Microw. Antennas Propag., Vol. 3, Iss. 4, pp. 703–713, 2009.

[17]. Dissanayake, A., Allnutt, J., & Haidara, F. (1997). A prediction model that combines rain attenuation and other propagation impairments along earth-satellite paths. In Proceedings of IEEE Transactions on Antenna and Propagation (Vol. 45, pp. 1546–1558), Oct. 1997.

[18]. Special issue on Software Radios, IEEE JSAC, vol. 17, no. 4, Apr. 1999, pp. 509–747.

[19]. J. Mitola. III, "Technical Challenges in the Globalization of Software Radio,'' IEEE Commun. Mag., Feb. 1999, pp. 84–89.

[20]. Yang L-L, Hanzo L. Software-defined-radio-assisted adaptive broadband frequency hopping multicarrier DSCDMA. IEEE Commun Mag 2002;40(3):174–83.

INTERNATIONAL JOURNAL OF ENVIRONMENTAL SCIENCES Volume 6, No 6, 2016

© *Copyright by the authors - Licensee IPA- Under Creative Commons license 3.0*

Research article **ISSN 0976 – 4402**

Air pollution tolerance of trees in an educational institute in Delhi

Deepika, Parag Gour, Haritash A.K.
Department of Environmental Engineering
Delhi Technological University, Bawana Road, Shahbad Daulatpur, Delhi – 110042 (India)
akharitash@dce.ac.in
doi:10.6088/ijes. 6092

ABSTRACT

The present study evaluated air pollution tolerance index (APTI) of 21 major tree species in an educational institute being classified as a sensitive area with respect to air pollution. *Magnifera indica*, *Ficus religiosa*, and *Ficus benghalensis* were classified as tolerant species having high Ascorbic acid (AA) content which helps maintain good chlorophyll levels despite lower Relative water content (RWC) values for *Ficus spp*. More than 3/4th of the species had good RWC values attributing to tolerance. It was observed that the trees with broad leaves and thick canopy had higher chlorophyll concentration compared to the trees with compound leaves and cone-type canopy. Ascorbic acid concentration chiefly governed the tolerance to air pollution. About 38% of the studied plants were classified as moderately tolerant to tolerant, and the rest as intermediate tolerant or sensitive which may be a cause concern if the concentration of pollutants of air rises. Based on APTI values, tolerant and moderately tolerant plants are recommended for green belt development and air pollution attenuation.

Keywords: Air pollution tolerance index (APTI), Air pollution, chlorophyll, Ascorbic acid (AA), Delhi

1. Introduction

Air pollution in cities has become a major problem around the globe and its health effects and environmental consequences are numerous (Kaushik et al., 2006). Continuous increase of built area, increase in number of industries and registered vehicles has resulted in loss of green cover; increased levels of SO2, NOX, SPM and hydrocarbns (Haritash and Kaushik., 2011); and an increase in local or global temperature in the form of urban heat island and global warming, respectively. The most cost effective tool to combat global warming and attenuate air pollution is to increase the forest cover. Development of green belts in industrial and urban areas, and intended social forestry programs in rural/agricultural areas can play an important role in control of air and noise pollution, reduction in soil erosion, amelioration of air quality, and enhance the aesthetic beauty of area in addition to their socio-economic and ecological benefits. Exposure to increased levels of gaseous and particulate air pollutants can affect the physical and biochemical health of plants through impingement, absorption, and accumulation of air pollutants over the plant leaves. Plants are important part of all ecosystems and these are mostly affected by air pollution. (Escobedo *et al*., 2008; Liu *et al.*, 2008; Jyothi *et al*., 2010). Air pollutants can affect plants directly via leaves or indirectly via soil acidification (Steubing *et al.*, 1989). When exposed to air pollutants, most plant experience physiological changes before exhibiting visible damage to leaves (Dohmen *et al.*, 1990).

Received on January 2016 Published on May 2016

One of the important tool to evaluate the impact of air pollution on plants is biomonitoring. Hence in the latest years increase of urban vegetation is very important not only for social reasons, but also for improving local and regional air quality. The response of plants towards air can be assessed by air pollution tolerance index (APTI) as suggested by Singh and Rao, 1983). Several authors studied usefulness of evaluating APTI for the determination of tolerance of plant species. (Agrawal *et al.,* 1997; Dwivedi *et al.,* 2007; Liu *et al.,* 2008; Dwivedi *et al.,* 2008). Ascorbic acid content (Hoque *et al.,* 1990), chlorophyll content (Flowers *et al.,* 2007), leaf extract pH (Klump *et al.,* 2000), and relative water content (Rao., 1979) are the four parameters which are used to identify tolerance levels of plant species and determination of APTI is based on all these four parameters (Singh *et al.,* 1991; Agbaire *et al.,* 2009).

The APTI provides valuable information for landscapers and greenbelt designers to select the sensitive as well as tolerant varieties of plant species for using them to identify the pollution loads of urban/industrial areas, and also to use the tolerant varieties for curbing the menace of air pollution (Jyothi *et al.,* 2010).

Since educational institutes, schools, and hospitals are classified as sensitive areas as per the standards prescribed, it is important to monitor air quality regularly besides maintaining a healthy green cover to attenuate the rising levels of air-pollutants. The present study was undertaken to evaluate APTI level of vegetation in the campus of Delhi Technological University (DTU), Delhi and identify the tolerance status of trees growing in the campus.

2. Materials and methods

2.1 Study area

The study was undertaken in Delhi Technological University located at 28.75°N latitude and 77.11°E longitude in North-West district of Delhi. The university campus is located on the outskirts of national capital territory of Delhi. The campus is surrounded by residential colonies and small and medium scale non registered industries on south-east side, and agricultural fields in North west. Bawana industrial area is located at a distance of 7-8 km on North-west side. The campus has a thick belt of vegetation and may be considered as a non-polluted to moderately polluted site with respect to air quality.

2.2 Sample analysis

Fully mature leaves in triplicates were collected in early hours of morning, taken and immediately taken to the laboratory for analysis. Utmost care was taken that the samples from each site were collected from plants growing in isoecological conditions. The fresh leaf samples were then analyzed for leaf chlorophyll, ascorbic acid, leaf extract pH, and relative water content.

2.3 Leaf extract pH

To determine the pH of leaf sap, 4.0 grams of fresh leaves was homogenized in 10ml de-ionized water. It was centrifuged at 2500 rpm for 10 minutes, and the supernatant was collected to note its pH with a digital pH-meter.

2.3 Relative water content (RWC)

Leaf RWC was determined and calculated using the formula given by Singh (1977).

$$RWC = [(FW-DW)/(TW-DW)] \times 100$$

FW - Fresh weight; DW - dry weight; and TW - turgid weight.

Fresh weight was obtained by weighing the fresh leaves. The leaves were then immersed in water over night, blotted dry and then weighed to get the turgid weight. Next, the leaves were dried overnight in an oven at 70°C and reweighed to obtain the dry weight.

2.4 Total Chlorophyll content (TCH)

Extraction and determination of chlorophyll was performed according to the method of Arnon (1949). 3.0 g of fresh leaves were blended and then extracted with 10ml of 80% acetone and left for 15min. The liquid portion was decanted into another text-tube and centrifuged at 2500 rpm for 10 min. The supernatant was collected and the absorbance was then taken at 645nm and 663nm using a spectrophotometer (Labtronics make ….). Calculations were made using formula given below:

$$\text{Cholorophyll a (mg/g)} = 12.7_{DX663} - 2.69_{DX645} \times V/1000W$$

$$\text{Cholorophyll b (mg/g)} = 22.9_{DX645} - 4.68_{DX663} \times V/1000W$$

TCh - chlorophyll a + b (mg/g); Dx - Absorbance of the extract at the wavelength Xnm; V - total volume of the extract used for chlorophyll (ml); and W = weight of the tissue (g).

2.5 Ascorbic acid (AA) content

Ascorbic acid content (expressed as mg/g) was measured using spectrometric method (Bajaj and Kaur, 1981). 1g of the sample was measured into a test-tube, 4 ml oxalic acid –EDTA extraction solution was added. Then 1ml of orthophosporic acid followed by 1ml 5% tetraoxosulphate (vi) acid. To this 2 ml ammonium molybdate was added to stand for 15min, after which the absorbance at 760nm was measured with spectrophotometer, The concentration of ascorbic acid in the samples was then extrapolated from a standard ascorbic acid curve.

2.6 APTI

The air pollution tolerance indices of common plants were determined following the method of Singh and Rao (1983). The formula of APTI is given as

$$APTI = [A(T+P) + R]/10$$

Where A - Ascorbic acid content (mg/g); T - total chlorophyll (mg/g); P - pH of leaf extract; and R - relative water content of leaf (%).

2.7 Gradation of APTIs

The spectrum of APTI was divided as four grades of air pollution tolerance referring to a previous study (Liu *et al*., 1983): tolerant (T or grade I), moderately tolerant (MT or grade II), intermediate (I or grade III), and sensitive (S). The tolerance grades were determined as follows:

(1) Tolerant: APTI> MEAN APTI+SD;

(2) Moderately tolerant: mean APTI<APTI<mean APTI+SD;

(3) Intermediate: mean APTI-SD<APTI<mean APTI;

(4) Sensitive: APTI< mean APTI-SD.

3. Results and Discussion

3.1 pH of leaf extract

pH of the leaf extract varied from 4.7 (*Neolamarckia cadamba*) to 7.2 *(Magnifera indica)* with an average of 5.9 (Table 1).The observed pH was on higher side for most of the trees indicating that the trees are moderately exposed to acidic pollutants. It is observed that with higher concentration of acidic air pollutants, the pH of cell sap decreases which might decrease the efficiency for conversion of hexose sugar to ascorbic acid. The reducing activity of ascorbic acid is observed to be more at higher pH (Agrawal 1988). Since the cell sap pH of most of the trees was on higher side except *Neolamarckia cadamba*, the vegetation may be classified as moderately tolerant to tolerant in the present study.

3.2 Relative water content

RWC is the water present in leaves relative to the full turgidity. Decreased RWC is associated with protoplasmic permeability, loss of water and dissolved nutrients, and early senescence of leaves (Agrawal and Tiwari 1997). In the present study RWC varied from 45% (*Thevetiaperuviana*) to 92.4% (*Buteamonosperma*) with an average of 67.4 %. About 24% of the studied species had low (45- 60%) RWC values, 48% had high RWC (60-75%), and 28% of the species had very high RWC indicating that most of the species are classified as tolerant with respect to RWC.

3.3 Total chlorophyll content (TCh)

Chlorophyll content of plants indicate photosynthetic activity, growth, accumulation of biomass, and health of plant. In the present study, chlorophyll content varied from 0.8mg/g (*Terminalia arjuna*) to 33mg/g (*meliaazedarach*) with an average value of 13.6mg/g. More than $2/3^{rd}$ of the studied trees had chlorophyll concentration higher than 10mg/g. Observed variations may be attributed to difference of species, age of the leaf, height of the tree, type of canopy, size and shape of leaf, and phyllotaxy. It was observed that the trees with thick and broad canopy, broad leaves, with moderate height had higher chlorophyll concentration compared to the trees with pinnately compound leaves or slender cone type canopy. The evergreen trees with high cholorophyll concentration like *Magnifera indica, Syzygium cumini, Ailanthus, Bombax, phycus spp., Azadiracta indica, Meliaazedarach,* and *Lagerstroemia indica* are observed to be tolerant species in the present study.

3.4 Ascorbic acid (AA)

The concentration of ascorbic acid is an indicator of tolerance of the plant towards air pollution, particularly SO_2. AA is an important reducing agent which facilitates conversion of SO_2 to sulphite (SO_3). Higher concentration of ascorbic acid in plants is an indicator of exposure to high concentration of SO_2, and higher tolerance of the plant. It also helps to

protect the thylakoids structure (and chlorophyll) from reactive oxygen species (ROS) formed in plants during water stress conditions. In the present study *Magnifera indica* had highest concentration of ascorbic acid (9.3mg/g) followed by *Ficus benghalensis* (8.1mg/g), *Delonix regia* (6.8mg/g), *Ficus religiosa* (6.2mg/g), *Termanalia arjuna* (5.0mg/g), *Neolalarckia cadma* (4.8mg/g), and rest of the species having comparatively lower values of ascorbic acid.

Table 1: Biochemical characteristics of the studied tree species and their tolerance gradation

S. No.	Name of the species	pH	RWC (%)	TCh (mg/g)	AA (mg/g)	APTI	Category
1	*Magnifera indica*	7.2	79.3	14.5	9.3	28.1	T
2	*Syzygium cumini*	6.2	67.6	18.3	1.6	10.7	IT
3	*Saraca asoca*	6.3	75.6	4.5	0.8	8.4	IT
4	*Ailanthus altissima*	5.9	65.4	15.5	1.6	9.9	IT
5	*Bombax ceiba*	6.4	70.0	18.6	0.8	8.9	IT
6	*Ficus religiosa*	6.4	69.1	17.4	6.2	21.7	T
7	*Dalbergia sissoo*	6.6	65.9	16.8	1.8	10.8	IT
8	*Azadirachta indica*	6.2	77.8	28.1	3.0	17.9	MT
9	*Ficus virens*	5.2	51.1	7.0	3.0	8.8	IT
10	*Ficus benghalensis*	6.1	69.2	10.0	8.1	19.9	T
11	*Neolamarckia cadamba*	4.7	83.6	10.1	4.8	15.5	MT
12	*Thevetia peruviana*	6.0	45.0	3.3	1.5	5.9	S
13	*Alstonia scholaris*	5.4	53.0	3.2	1.5	6.6	S
14	*Bauhivia variegata*	6.1	52.8	14.5	2.6	10.6	IT
15	*Eucalyptus globulus*	5.3	63.1	12.1	3.5	12.4	IT
16	*Bougainvillea glabra*	6.0	71.1	27.6	1.8	13.0	MT
17	*Butea monosperma*	6.1	92.4	7.7	3.0	13.4	MT
18	*Terminalia arjuna*	6.1	66.5	0.8	5.0	10.1	IT
19	*Melia Azedarach*	6.3	80.0	33.0	1.3	13.0	MT
20	*Lagerstroemia indica*	5.1	55.9	19.3	1.4	9.0	IT
21	*Delonix regia*	5.4	61.5	4.0	6.8	12.6	IT
Mean		5.9	67.4	13.6	3.3	12.7	
± S.D.		0.6	11.8	8.8	2.5	5.4	

T- Tolerant; MT- Moderately Tolerant; IT- Intermediate Tolerant; S-Sensitive

Bombax ceiba and *Saraca asoca* had minimum AA concentration (0.8mg/g) representing their sensitive nature with respect to ascorbic acid. An overall average of 3.3mg/L suggests that most of the plants are moderately tolerant to tolerant in the present study.

Air pollution tolerance index (APTI)

APTI is a calculated value to represent tolerant or sensitive nature of plants based on its biochemical response to air pollution. In the present study, APTI values ranged from 5.9 (*Thevetia peruviana*) to 28.1 (*Magnifera indica*) with a mean value of 12.7 (Table 1; Figure 1). Based on the classification given by Liu and Ding (2008), *Magnifera indica*, *Ficus religiosa*, *Ficus benghalensis* were found to be tolerant. About 24% of studied plants were classified as moderately tolerant (MT) and included *Azadirachta indica*, *Neolamarckia*

cadamba, *Butea monosperma*, *Bougainvillea glabra*, and *Melia azedarach*. More than 50% of the plants were classified as intermediate tolerant (IT) indicating that majority of the plants may become sensitive to air pollution if the concentration of pollutants increases. *Thevatia peruviana* and *Alstonia scholaris* were classified as sensitive plants, and their sensitivity may vary from place to place depending on the environmental conditions and levels of air pollution, particularly suspended particulate matter (Singh, 2005).

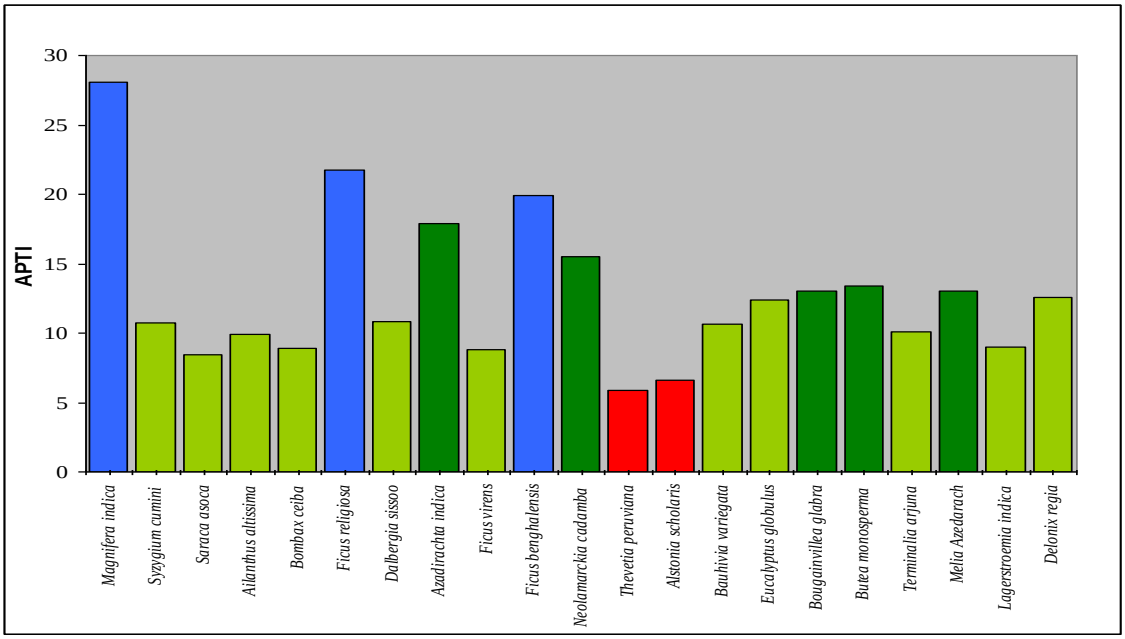


Figure1: APTI of the studied tree species

4. Conclusion

Based on the results obtained, it is observed that most of the trees in DTU campus have tolerance to air pollution. Since the area has moderate to low level of air pollution, the biochemical effects are negligible as confirmed by the values of pH of cell sap. Average pH was 5.9, which is on the higher side. The pH may drop with an increase in stress in the form of air pollution. Significantly good concentration of total chlorophyll confirmed that most of the plants are tolerant to stress. High RWC values help maintain chlorophyll concentration even under chemical stress. Apart from it, ascorbic acid safeguards the thyllakoids (and chlorophyll) during low RWC and chemical stress. In the present study, relatively good levels of ascorbic acid may be the reason for higher APTI values and tolerant behaviour of most of the species. However, more than 50% of the studied plant species were classified as intermediate tolerant which may become sensitive if the levels of air pollutants rise. It is recommended that moderately tolerant to tolerant tree species may be preferred for green belt development in the campus.

5. References

1. Agbaire, P.O., (2009), Air pollution tolerance indices (APTI) of some plants around Erhoike-kokori oil exploration site of Delta state, Nigeria, 4(6), pp 366-368.

2. Agrawal, A.L., (1988), Air pollution control studies and impact assessment of stack and fugitive emissions from CCI Akaltara Cement Factory, Project Report, Project sponsored by M/S. CCI Akaltara Cement Factory, NEERI, Nagpur.

3. Agrawal, S., and Tiwari, S.L., (1997), Susceptibility level of few plants on the basis of Air Pollutin Tolerance Index, Indian Forester, 123, pp 319-322.

4. Arnon, D.I., (1949), Copper Enzymes in isolated Choloroplasts polyphenol oxidase in Beta vulgaris, Plant Physiology, 2, pp 1-15.

5. Bajaj, K.L., and Kaur, G., (1981), Spectrophoto-metric Determination of L. Ascorbic acid in Vegetable and Fruits, Analyst, 106, pp 117-120.

6. Dohmen, G.P., Koppers, A., and Lanebarteis, C., (1990), Biochemical response of Norway spruce (*Picea abies* (L.) Karst) towards 14- month exposure to ozone and acid mist, effect on amino acid, glutathione and polyamine titers, Environmental pollution, 64, pp 375-383.

7. Dwivedi, A.K., and Tripath, B.D., (2007), Pollution tolerance and distribution pattern of plants in surrounding area of coal-fired industries, Journal of Environmental Biology, 28, pp 257-263.

8. Dwivedi, A.K., Tripath, B.D., and Shashi, (2008), Effect of ambient air sulphur-di-oxide on sulphate accumulation in plants, Journal of Environmental Biology, 29, pp 377-379.

9. Escobedo, F.J., Wagner, J.E., Nowak, D.J., (2008), Analyzing the cost effectiveness of Santiago, Chile's policy of using urban forests to improve air quality, Journal of Environmental Management, 86, pp 148-157.

10. Flowers, M.D., Fiscus, E.L., Burkey, K.O., (2007), Photosynthesis , chlorophyll fluorescence and yield of snap bean(*Phaseolus vulgaris L*) genotype differing in sensitivity to Ozone, Environ.Exp. Bot., 61, pp 190-198.

11. Haritash, A.K., and Kaushik C.P., (2011), Seasonal and spatial occurrence and distribution of respirable particulate-bound atmospheric polycyclic aromatic hydrocarbons in Hisar city and their potential health-risks. Asian Journal of Water, Environment, and Pollution, 8 (1), pp 73-80.

12. Hoque, M.A., Banu, M.N.A., and Okuma, E., (2007), Exogenous proline and glycinebetaine increase Nacl-inducedascorbate- glutathione cycle enzyme activities, and proline improves salt tolerance more than glycinebetaine in tobacco bright yellow-2 suspension- Cultured cells, Jounal of plant physiology, 164, pp 1457-1468.

13. Jyothi, J.S., and Jaya, S.D., (2010), Evaluation of air pollution tolerance index of selected plant species along roadsides in Thiruvananthapuram, Kerala, Journal of Environmental Biology, 31, pp 379-386.

14. Kaushik, C.P., Khaiwal, R., Yadav, K., Mehta, S., and Haritash, A.K., (2006), Assessment of ambient air quality in urban centres of Haryana (India) in relation to different anthropogenic activities and health risks'. Environmental Monitoring and Assessment, 122, pp 27-40.

15. Klump, G., Furlan, C.M., and Domingos, M., (2000), Response of stress indicators and growth parameters of tibouchina pulchra logn. Exposed to air and soil pollution near the industrial complex of cubatao, Brazil, Science Total Environment, 246, pp 79-91.

16. Liu, R.K., Shen, Y.W., and Liu, X.J., (1983), A study on physiological responses of plant to SO_2, Plant Physiological Communications, 4, pp 25-28.

17. Liu, Y., and Ding, H., (2008), Variation in air pollution tolerance index of plants near a steel factory: Implications for landscape for landscape-plant species selection for industrial areas, Environment Development, 4, pp 24-32.

18. Rao, D.N., (1979), Plant leaf as pollution monitoring Device, Fertilizer News, 25-28.

19. Singh, A., (1977), Practical plant physiology, Kalyan Publishers, New Delhi.

20. Singh, S.K., and Rao, D.N., (1983), Evaluation of the plants for their tolerance to air pollution, Proc symp on air pollution control held at IIT, Delhi, pp 218-224.

21. Singh, P.K., (2005), Plants as indicators of air pollution – An Indian experience. Indian Forester, 131, pp 71-80.

22. Singh, S.K., Rao, Agrawal, M., Pandey, J., and Narayan, D., (1991), Air pollution tolerance index of plants, Journal of Environmental Management, 32, pp 45-55.

23. Steubing, L., Fangmeier A, and Both, R., (1989), Effects of S02, NO2 and O3 on pollution development and morphological and physiological parameters of native herb layer species in a beech forest, Environmental pollution, 58, pp 281-302.

IARJSET
ISSN (Online) 2393-8021
ISSN (Print) 2394-1588
International Advanced Research Journal in Science, Engineering and Technology
ISO 3297:2007 Certified
Vol. 3, Issue 9, September 2016

Ambient Polycyclic Aromatic Hydrocarbons and its Carcinogenic and Mutagenic Risk – A Review

Papiya Mandal[1, 2],R. Sarkar[2], A. Mandal[2]

CSIR-National Environmental Engineering Research Institute, Zonal Laboratory, Delhi, India[1]

Department of Civil Engineering, Delhi Technological University, Delhi, India[2]

Abstract: Emission of atmospheric polycyclic aromatic hydrocarbons is gaining considerable importance in present-day scenario, as they are ubiquitous and some of them are having carcinogenic and mutagenic potency to human's health. Though PAH have few natural sources like forest fires, volcanic eruption etc. but major emission of PAHs are directly linked with urbanization, industrialization and vehicular emission. Both rural and urban environment, PAHs has significant contribution to contaminate the ambient air. Recent interest has centered to identify and quantify of PAHs in soil, water and air environment, identify their emission sources through various approaches and to evaluate their carcinogenicity and mutagenicity to human's health. The approaches distinguish anthropogenic multiple emission sources of PAHs like from petroleum combustion, diesel combustion, coal combustion industrial emission and biomass burning. This paper deals with concentrations of ambient PAHs, their emission sources and total carcinogenic and mutagenic potential risk to human's health.

Keywords: PAHs diagnostic ratios; Carcinogenicity; Mutagenicity; Air toxic.

I.INTRODUCTION

Polycyclic aromatic hydrocarbon (PAHs) are the ubiquitous pollutants in both rural and urban atmosphere, containing atleast two or more fused aromatic (benzene) rings with different arrangements and present in various environments such as soil, water, sediment and air. The term "PAH" refers to class of organic compounds consisting only carbon and hydrogen atoms.

In general PAHs are formed through pyrolysis process and subsequently recombined with other organic molecules and formed the complex compound. PAHs emissions in the atmosphere are in the form of either gaseous or particulate phases. They are highly lipophilic and mostly soluble in organic solvents. They also manifest various functions in the environment such as light sensitivity, heat resistance, conductivity, emittability, corrosion resistance, and physiological action. United States of Protection Agency (USEPA) has classified sixteen PAHs as carcinogenic. Incomplete combustion and pyrolysis of organic material influences the emission of PAHs in the gaseous form and settles on either in particulates or in soils or sediments after condensation [1&2]. Though PAH has natural and anthropogenic sources but emission of PAHs are almost anthropogenic in origin [3].

PAHs reacts with atmospheric trace gases eg., ozone, hydroxyl radicals, nitrogen dioxide and sulphur dioxide, nitro and dinitro-PAHs, and sulfonic acids [4]. The emission sources of individual PAHs are mostly from industrial emission, vehicular emission and biomass burning. The multiple emission sources of PAHs are broadly categorized into five major emission sources eg., natural, domestic, mobile, industrial and agricultural sources. The occurrence of PAHs in the atmosphere and their carcinogenicity and mutagenicity potential is of greatconcern, especially in the urban atmosphere as people are exposed to PAHs by various means. Mostly people are exposed to PAHs in both ways either inhalation of contaminated toxic air or consumption of contaminated food and water. The contaminated foods have more route of exposure of PAHs as compared to inhalation of contaminated air. Several epidemiological studies reported that complex mixture of PAHs with different molecular weights is associated with adverse health risks and potential carcinogens and mutagens [5]. It was reported by WHO, 2002, [6] reported that approximately 75% people in China, India and South East Asia, and 50–75% people in various parts of South America and Africa use solid fuels (wood, dried animal-dung-cake and crop waste) for daily cooking. Air quality guidelines for Europe country estimated that the unit risk is $9x10^{-5}$ would theoretically lead to one extra cancer case in 1 lakh exposed individuals [7].

It was estimated that Indo-Gangetic Plains alone contributes 30.21% PAHs emissions of total PAH emissions from India [8]. The annual PAHs emissions of India are estimated to be 90 Gg per year [9]. The congested traffic movement at urban areas promotes the emissions of PAHs in the urban air. Other major sources of PAH emission are from vehicle tire abrasion, asphalted surfaces and brake lining (Rogge et al. 1993a) [10].

II.FORMATION OF ATMOSPHERIC PAHs

Atmospheric PAHs are formed either due to incomplete combustion (pyrolysis) or high temperature pyrolytic process during anthropogenic activities like combustion of fossil fuels/ combustion of natural gas/ processing of coal

IARJSET
ISSN (Online) 2393-8021
ISSN (Print) 2394-1588
International Advanced Research Journal in Science, Engineering and Technology
ISO 3297:2007 Certified
Vol. 3, Issue 9, September 2016

and crude oil/ combustion of refuse material /cooking and tobacco smoking/ biomass burning etc. It may also produce as a result of natural processes such as carbonisation (pyrosynthesis). PAHs are likely to form in the atmosphere by two main mechanisms like pyrolysis and pyro-synthesis. Low hydrocarbons form PAHs by pyro-synthesis process. When temperature increased 5000C or greater than 5000C, carbon-hydrogen and carbon-carbon bonds are broken and free radicals are released in the atmosphere. These free radicals are further combined with acetylene, which condenses into aromatic ring [11]. These rings have the resistance to thermal degradation. The tendency of the hydrocarbon is to form PAH structure by the process of pyro-synthesis in the following order: aromatics > cycloolefins > Olefins >paraffins [12]. The reaction of PAHs with other atmospheric trace gases viz., NOx, SO_2, O_2 etc. may form hetero-PAHs and nitro-PAHs. benzo[a]pyrene (BaP) is recognized as most carcinogenic PAHs. Sometimes,carcinogenicity and mutagenicity of many of these hetero-PAHs compounds is greater than their parent compounds, recommended by Central Pollution Control Board [13]. Fig.1illustrates the carbonisation process of PAHs starting with ethane.

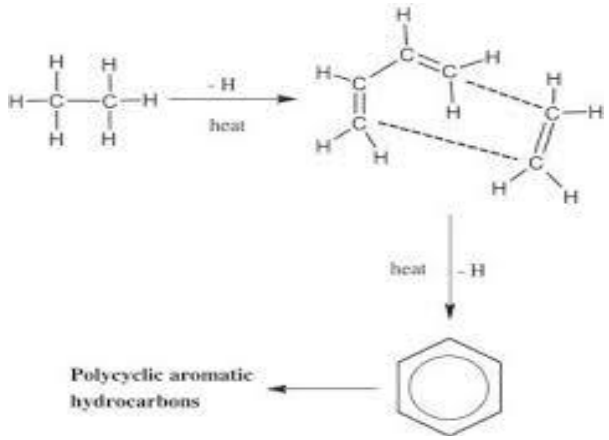


Fig. 1: Carbonisation process of PAHs starting with ethane

Atmospheric PAHs are formed during the combustion process by three possible mechanisms like slow Diels-Alder condensations, rapid radical reactions and ionic reaction mechanism [14]. For inter combustion engine, rapid radical reactions is the most favorable reaction. In this reaction process, gaseous hydrocarbon radicals are rearranged quickly to form of PAHs and lower molecular PAHs are in a state, to form higher molecular PAHs [15]. It was also reported by the researcher, that type of fuel, atmospheric temperature and presence of oxygen are also plays the significant role for formation of various types of PAHs during combustion activity [16].

III.COMMON ATMOSPHERIC PAHs & THEIR CHARACTERISTICS

The individual PAHs,physical and chemical propertiesdepend on their molecular weight. In general, PAHs have maximum melting and boiling temperature for solid, low vapor pressure, and low aqueous solubility (mg/l at 25^0C). The solubility of PAHs decreases with increasing molecular weight, but oxidation and reduction resistance increases. So, PAHs has different behavior and properties in the different environment, and they are mostly effective on biological systems. Low-molecular-weight PAHs (two and three rings) are weaker carcinogenic and mutagenic as compared to multi-ringed PAHs (four rings or more) and potential to humans health risk. Only two benzene rings are fused together inNaphthalene ($C_{10}H_8$), has the lowest molecular weight(MW=128g)among all PAHs. Whereas the maximum seven benzene rings are fused together in Coronene ($C_{24}H_{12}$), has the highest molecular weight (MW=300g) of all PAHs. The benzene rings of the environmentally significant PAHs vary from two to seven. The common atmospheric PAHs and their characteristics molecular formula, molecular weight, presence of benzene rings, water solubility, classification as per International Agency for Research on Cancer (IARC) and their phase distribution in the ambient air is shown in Table 1.

TABLE 1Common atmospheric PAHs and their characteristics

Particulate PAHs	Molecular Formula	Molecular weight (g)	Benzene Rings	Water Solubility mg/l at 25^0C	Classification as per IARC* (1983,1987)	Particle/ Gas Phase Distribution
Naphthalene (NP)	$C_{10}H_8$	128	2	31	NE	Gas Phase
Acenaphthylene (ACY)	$C_{10}H_8$	128	2	16	NE	Gas Phase
Acenaphthene (ACE)	$C_{10}H_8$	128	2	3.8	NE	Gas Phase
Phenanthrene (PHE)	$C_{14}H_{10}$	178	3	1.1	Group 3	Particle Gas Phase
Anthracene (ANT)	$C_{14}H_{10}$	178	3	0.04	Group3	Particle Gas Phase
Fluoranthene (FLA)	$C_{16}H_{10}$	202	4	0.2	Group3	Particle Gas Phase
Pyrene (PYR)	$C_{16}H_{10}$	202	4	0.13	Group3	Particle Gas Phase
Benzo(a)anthracene (BaA)	$C_{18}H_{12}$	228	4	0.011	Group2B	Particle Phase

Copyright to IARJSET

IARJSET
ISSN (Online) 2393-8021
ISSN (Print) 2394-1588
International Advanced Research Journal in Science, Engineering and Technology
ISO 3297:2007 Certified
Vol. 3, Issue 9, September 2016

Chrysene (CHR)	$C_{18}H_{12}$	228	4	0.0019	Group2B	Particle Phase
Benzo(b)fluoranthene (BbF)	$C_{20}H_{12}$	252	5	0.0015	Group2B	Particle Phase
Benzo(k)fluoranthene (BkF)	$C_{20}H_{12}$	252	5	0.0008	Group2B	Particle Phase
Benzo(j)fluoranthene (BkF)	$C_{20}H_{12}$	252	5	0.0008	Group2B	Particle Phase
Benzo(e)pyrene (BaP)	$C_{20}H_{12}$	252	5	0.0015	Group1	Particle Phase
Benzo(a)pyrene (BaP)	$C_{20}H_{12}$	252	5	0.0015	Group1	Particle Phase
Benzo(ghi)pyrelene (BghiP)	$C_{22}H_{12}$	276	6	0.00015	Group3	Particle Phase
Dibenz(ah)anthracene (DahA)	$C_{22}H_{14}$	278	5	0.0005	Group2A	Particle Phase
Indo(123-cd)pyrene (IcdP)	$C_{22}H_{12}$	276	6	0.00019	Group2B	Particle Phase
Coronene	$C_{24}H_{12}$	300	7	0.00014	Group3	Particle Phase

Group 1 Carcinogenic to humans
Group 2A Probably carcinogenic to humans
Group 2B Possibly carcinogenic to humans
Group 3 Not classifiable as its carcinogenicity to humans
Group 4 Probably not carcinogenic to humans
NE Not Evaluated
IARC*International Agency for Research on Cancer

IV.PREDOMINANT PAH SOURCE PROFILE/ MARKERS

PAHs are well-known air toxic and mostly identified as indicator for various emission sources in both rural and urban environment. They are originated from anthropogenic sources like mobile sources (e.g., cars, trucks, buses) and stationary sources (e.g., refineries, petrochemical industries, power plants, steel plants etc.), biomass burning as well as from indoor environment (e.g., cooking, smoking, construction materials, cleaning products). The natural sources include only volcanic eruptions and forest fires.

The made global emission inventory of 16 USEPA approved PAHs and estimated that total emission of PAHs is 520000 tonnes per year [9]. The annual emission of PAHs per year,only from Asian countries is 290000 tonnes, which is approximately 50% of the total global emission of ambient PAHs. The emission of PAHs in the Asian country like China and India are 144000 and 90000 tonnes per year respectively. The emission of PAHs from USA is 32000 tonnes per year, the third largest emitter of PAHs. The major source emission sources of USEPA identified PAHs in global, China, India and USA is shown in Table 2.

TABLE 2Major emission sources of USEPA identified PAHs in global, China, India and USA

Source	Global	China	India	USA
Biofuel	56.70%	66.4%	92.5%	9.1%
Wild fire	17.00%	0.0%	0.0%	3.3%
Consumer product use	6.90%	0.9%	0.6%	35.1%
Traffic oil	4.80%	2.0%	Insignificant	23.0%
Domestic coal	3.70%	10.7%	1.30%	Insignificant
Coke production	3.60%	14.4%	Insignificant	Insignificant
Petroleum refining	2.40%	1.0%	Insignificant	8.70%
Waste incineration	1.90%	Insignificant	Insignificant	9.50%
Aluminum electrolysis	1.40%	Insignificant	Insignificant	1.90%
Open straw burning	Insignificant	2.0%	3.20%	Insignificant
Gasoline distribution	Insignificant	Insignificant	Insignificant	3.00%
Aerospace industry	Insignificant	Insignificant	Insignificant	2.50%
Other	1.50%	-	2.70%	3.90%
Tonnes in thousands	**530**	**114**	**90**	**32**

Source: Zang and Tao et al.2009

IARJSET
ISSN (Online) 2393-8021
ISSN (Print) 2394-1588
International Advanced Research Journal in Science, Engineering and Technology
ISO 3297:2007 Certified
Vol. 3, Issue 9, September 2016

Benzo(a)pyrene (BaP) is considered as most carcinogenic PAHs and many countries have included BaP in their hazardous pollution list, as well in their regulatory standards. European Union Directive (EUD), 2004 has proposed average target value of BaP is one ng/m^3in PM_{10} (diameter of less than 10µg/m^3) size of particulate matter [17]. For Germany, annual average target value of BaP is 10 ng/m^3. Country like Australia, and India, annual average target value of BaP is one ng/m^3 only. Country like Belgium, and Netherland, annual average target value of BaP is reduced by 50% ie 0.5 ng/m^3. For country Croatia, France and Sweden the set target value is more stringent (0.1 ng/m^3) only.

V. IDENTIFICATION OF SOURCES OF PAHs

The emission of PAHs from a particular source depends on the processes involved for production of materials [18]. During low temperature activities like biomass burning, PAHs having low molecular weight are formed whereas PAHs having maximum molecular weight are formed in theatmosphere during high temperature activities like combustion of fuels in engines, incinerations etc. [19]. PAHs diagnostic ratios are widely used to identify anthropogenic sources of PAHs emission. The ambient PAH concentrations and their diagnostic ratios indicate the different sources of PAHs in the environment [20]. The diagnostic PAHs ratios calculated for each hypothetical source are not definitive:for example [18] reported that BaA/ (BaA+CHR)= 0.3 to 0.6 indicates the emission of PAHs from cement industry. However similar many sources like FLA/(FLA+PYR)= 0.4 to 0.5 indicates the emission of PAHs from several industries like cement, metal manufacturing, fertilizer production, diesel combustion and sometimes from road dusts also [21] BaA/(BaA+ CHR) ratio greater than 0.35 is widely accepted to indicate the contribution of biomass burning [22] and vehicular emissions [23]. The identification of ambient PAH an emission sources using diagnostic ratiois shown in Table 3.

TABLE 3Identification of ambient PAH emission sources using diagnostic ratios

Diagnostic ratio	Value range	Sources	References
FL/(FL + PYR)	<0.5	Petrol emissions	[24]
	>0.5	Diesel emissions	
FL/PYR	0.6	Vehicular emissions	[25]
FL/BeP	3.5±0.5	Automobile exhaust	[26]
ANT/(ANT+PHE)	<0.1	Petrogenic	[27]
	>0.1	Pyrogenic	
FLA/(FLA+PYR)	<0.4	Petrogenic	[28]
	0.4 - 0.5	Fossil fuel combustion	
	>0.5	Grass, wood, coal combustion	
BaA/(BaA+ CHR)	0.2 - 0.35	Coal combustion	[23]
	>0.35	Vehicular emissions	
	<0.2	Petrogenic	
BaP/(BaP + BeP)	>0.35	Combustion	[29]
	0.5	Fresh particles	
	<0.5	Photolysis (ageing of particles)	
BaP/(BaP+CHR)	0.5	Diesel emission	[30] ,[20]
IcdP/(IcdP+BghiP)	<0.2	Petrogenic	[31]
	0.2 - 0.5	Petroleum combustion	
	>0.5	Grass, wood andcoal combustion	
IcdP/BghiP	<0.4	Gasoline	[32]
BbF/BkF	>0.5	Diesel emissions	[33], [3]
BaP/BghiP	<0.6	Non-traffic emissions	[34]
	>0.6	Traffic emissions	

It was suggested that the ratio if FL/(FL+PYR) ratio is less than 0.5, indicates the petrol emission, whereas if the ratio is greater than 0.5, indicates the emission of PAHs from diesel sources[11]. Similarly the ratio of IcdP/ (IcdP+BghiP) equal to 0.62, indicates the emission of PAHs from wood combustion [35] and theratio within the range of 0.35 to 0.70, indicating diesel emission [36]. It was also indicated that if the ratio of IcdP/ (IcdP+BghiP) is less than 0.2, indicates petrogenic sources, and the ratio varies between 0.2-0.5, indicates combustion of petroleum products and if the ratio greater than 0.5 indicates combustion of biomass burning like grass wood and coal [31]. The ratios are very similar, but the researchers hadreported the different types of source [33]. If the ratio of BbF/BkF is greater than 0.5, indicates the emission from diesel source[3]. The ratio of BaP/(BaP+CHR) is equal to 0.5, indicates the diesel emission [30] and [20]. The ratio ANT/(ANT+PHE) are the indicator of

IARJSET
ISSN (Online) 2393-8021
ISSN (Print) 2394-1588
International Advanced Research Journal in Science, Engineering and Technology
ISO 3297:2007 Certified
Vol. 3, Issue 9, September 2016

petrogenic sources. If the ratio is higher than 0.10 indicates petrogenic sources with lubricant oils and fossil fuels and the ratio less than 0.10 are typically associated pyrogenic sources ie., combustion of wood, coal, coal tar etc. [27]. ANT and PHE have low molecular weight (MW= 178) and present in the atmosphere mostly in the gas phase. They are most suitable for understanding of photolysis process in the gaseous phase [23]. Similarly the ratios of few particulate PAHs like BaP and BbF, BbK and BkF are widely used to understand the influence of photo processes of the particulate phase [21]. BaP is photo degraded faster as compared to its isomer BeP and adsorbed on PM_{10} size of particulate matter was reported by [36]. The ratio of BaP/(BaP+BeP) is photosensitive, and often used as the indicator of atmospheric particle ageing and the photodegradation of gaseous and particulate PAHs [21].

During the large number of daylight hours, BaP degradation is comparatively faster in the ambient air [37] and it shows the distinct diurnal variations [38]. Sometimes, it is difficult to differentiate the individual PAHs emission sources, according to the values of diagnostics ratios of PAHs.

VI.THE SOURCE OF INDIVIDUAL AMBIENT PAHs (RELATIVE TO BaP = 1.0)

The major twelve types of ambient PAHs and their emissions from various sources like point source, near mobile source, home heating and transport source (relative to benzo[a]pyrene BaP = 1.0) was reported by WHO 1998 is shown in Table 4.

TABLE 4Thecommon source of individual ambient PAHs (Relative to BaP = 1.0)

Types of PAHs	Point source	Near mobile source	Home heating	Transport	Geometric mean
Anthracene	5.5	7.6	1	1.8	2.9
Phenanthrene	38	200	39	43	60
Fluoranthene	14	48	12	13	18
Pyrene	9.3	28	11	7.1	12
Benz[a]anthracene	1.4	0.82	1	0.78	0.97
Perylene	0.33	0.25	0.22	0.24	0.26
Benzo[e]pyrene	1.5	1.3	1.6	1.4	1.4
Benzo[g,h,i]perylene	1.4	1.5	2.4	1.3	1.6
Indeno[1,2,3-cd]pyrene	1.5	1.3	1.5	1.4	1.4
Anthanthrene	0.19	0.15	0.13	0.2	0.17
Chrysene and triphenylene	3	2.7	3.5	2.9	3
Benzofluoranthene	3.6	2.9	3.6	4.4	3.6

Source WHO, 1998

WHO report,1998 [39] suggested that from all type of selected sources, emission of phenanthrene (relative to BaP) is maximum and emission of anthanthrene (relative to BaP) is minimum in the ambient air. The other major emission sources of ambient PAHs compound relative to BaP are pyrene, followed by anthracene and benzofluoranthene.

VII. MODE OF EXPOSURE AND DAILY INHALATION OF PAHS

Humans are usually exposed to PAHs by different pathways, mostly due to inhalation of polluted air. Other pathways may be due to consumption of food, water, and dermal contact with soil and dust, CPCB, 2003 [13]. The comparative potential carcinogenic PAHs risk to non-smokers and smokers due to inhalation is shown in Table 5.

TABLE 5The comparative potential carcinogenic PAHs risk to non-smokers and smokers due to inhalation

Source of PAHs	**Inhalation of carcinogenic PAHs**			
	Non Smoker		**Smoker**	
	µg/day	**Total %**	**µg/day**	**Total %**
Food	3	9.3	3	44.6
Air	0.16	4.9	0.16	2.4
Water	0.006	0.2	0.006	<0.01
Soil (Accidental Injection)	0.06	1.9	0.06	1
Cigarette	-	-	3.5	52
Total	**3.22**	**100**	**6.72**	**100**

Copyright to IARJSET

IARJSET
ISSN (Online) 2393-8021
ISSN (Print) 2394-1588
International Advanced Research Journal in Science, Engineering and Technology
ISO 3297:2007 Certified
Vol. 3, Issue 9, September 2016

Source CPCB, 2003

People are exposed to soil contact directly at the outdoor environment, while food and water consumption are usually in the indoor environment. The exposure of PAH to humans due to inhalation may be in both gaseous and particulate form, at indoor and outdoor environment. Smokers are directly in contact with PAHs due to tobacco smoking. It is estimated that the carcinogenic PAHs potential doses due to inhalation have a wide range (0.02 to 3µg/day). The inhalation of average PAHs is approximately 0.16 µg/day. The average intake of PAH concentration through air inhalation is approximately 20 times less than food consumption and approximately 25 times more than the potential intake of drinking water [13].The table indicates that intake of carcinogenic PAHs by the smokers (6.72 µg/day) which is double as compared to the intake by non-smokers (3.22 µg/day). Smokers are directly in contact with carcinogenic PAHs about to be total 52%. Researchers estimated that inhalation of air contributes 3 to 20% of total humans exposure to PAH, which is next to PAHs exposure through food contamination. It is estimated that smokers may intake additional 1-5 µg/day of PAHs through consumption of one pack of non-filtered cigarettes.[13]. The exposure of PAHs through consumptions of food is highest (for smoker 44.6% and non-smoker 9.3%) while exposure of PAHs through consumptions of water is lowest (for smoker <0.01% and non-smoker 0.2%). The exposure of

PAH through contaminated air inhalation is highest for non-smoker (4.9%) and lowest for smoking people (2.4%).

VIII. SOURCEWISE INHALATION DAILY DOSE OF BENZO[a] PYRENE

The inhalation of potential carcinogenic PAHs in terms of BaP was estimated as per recommendation of EPA by using the individual's respiration rate.General public average inhalation rate is approximately 11.3 m^3/ day for women and 15.2m^3/day for men recommended by USEPA 1997[40]. The reported BaP concentrations at indoor environment and taking consideration of adult male inhalation rate as a worst-case scenario, the estimated daily intake dose ranged from 0.15–26 ng/day. In general, the maximum inhalation of BaP dose per day occurs in the Asian indoor environment. The cooking activity with different types of fuels like kerosene, wood, coal, cattle dung etc., the minimum inhalation of BaP per day is 93 ng/day, whereas the inhalation per day can be extended more than 25 times higher ie 2523 ng/day also. Fordomestic heating purposes, the use non-airtight stove also emits high concentrations of BaP (30–7448 ng/day). The most relevant source of exposure of BaP for individual is at the indoor environment, as people spent approximately 80–93% of their time at indoors environment. Source wise inhalation daily dose of Benzo[a]pyrene (BaP) at indoor environment is shown in Table 6.

TABLE 6Source wiseinhalation daily dose of BaP at indoor environment

Type of source	Dose of BaP (ng/day)	Comment	Reference
General	0.15–21	Homes located industrialized countries	[40]
	3–26	Asian homes	
	6–21	Indoor spaces for public in the United Kingdom and the United States	
Cooking	91–365	Chinese kitchens	[41]
	105	Cooking with kerosene as fuel	
	502	Cooking with wood as fuel	
	2523	Cooking with cattle dung as fuel	
Heating	30–7448	Indoors using non-airtight stoves	
Environmental Tobacco Smoke (ETS)	4–15	ETS-polluted indoors	[42]
	1.3–6.7	Non-ETS-polluted indoors	
	26–62	Pubs and discotheques	

Source WHO, 2010

ETS (Environmental tobacco smoke) is a complex mixture of toxic chemicals, and mostly emits due to combustion of tobacco substances like cigarettes, cigars, pipes etc. ETS is a well-known human carcinogen and has the better penetrability in terms of the airways to humans. The breathing of ETS has the serious health riskto adultsas compared to young people through diseases like, heart disease, lung cancer etc. ETS is considered as one of the major inhalation sources of PAHs in the indoor environment. At indoor environment, the daily inhalation of BaP from ETSmay range from 4 to15 ng/day, whereas Non-ETS-pollutedenvironments, BaP inhalation may vary from 1.3–6.7 ng/day only. In pubs and discotheques,24 hourly basis, the average inhalation of BaP from indoor environment can be as high as 26–62 ng/day. Children are havingpassive exposure to tobacco smoke in the indoor environmentand significantly, susceptibleto morbidity and mortality [43]. The concentrations of PAHs in the indoor

IARJSET
ISSN (Online) 2393-8021
ISSN (Print) 2394-1588
International Advanced Research Journal in Science, Engineering and Technology
ISO 3297:2007 Certified
Vol. 3, Issue 9, September 2016

environmentmay vary from 1 ng/m^{3}to 50 ng/m^3. The variation depends on types of fuel combustion like wood, coal, kerosene and other materials used for residential cooking purposes and tobacco smoke [39].

IX. CARCINOGENICITY & MUTAGENICITY

A substance that has the ability or tendency to cause cancer is known as carcinogen. It may damage the genome material (mostly DNA) of an organism or can disrupt the cellular metabolic processes. Genetics science, the definition of mutagen is a physical or chemical factor that often changes the material of genetic, mostly DNA, of aliving organism. IARC classified few substances (60 in number) which are probably or positively carcinogenic and mutagenic to humans health. These substances are classified according to agents and groups of agents, mixtures and exposure circumstances. Few PAHs are probably or positively carcinogen to humans. Among them, BaP is widely accepted as the indicator for measurement of carcinogenicity. Thus BaP-equivalent toxicity for other carcinogenic PAHs was mostly evaluated for cancer risk assessment. This approach may provide overestimation of cancer and mutagen potency of individual particulate PAH as each PAH are comparatively less carcinogen than BaP. BaP is the most carcinogenic PAHs as per the recommendation of WHO, 2010 [42]. The toxic equivalent factor (TEF) and mutagenic equivalent factor (MEF) relative to BaP are widely used for risk assessment analysis to humans.

BaP-TEQ (carcinogenic equivalents, ng/m^3) and BaP-MEQ (mutagenic equivalents, ng/m^3) are measure for sum of total 8 number of particulate PAHs (∑8PAH), having molecular weight greater than 228 gram. ∑8PAH includes benzo(a)pyrene (BaP), benz(a)anthracene (BaA), chrysene/iso-chrysene (CHR), benzo(b)fluoranthene (BbF), benzo(k)fluoranthene (BkF), indo(123-cd)pyrene (IcdP),Dibenz(a,h)anthracene(DahA),and benzo(ghi)pyrelene(BghiP). BaP-TEQ: Carcinogenic equivalents calculated from the cancer potency relative to BaP (TEF) multiplied by PAH concentration. BaP-MEQ: Mutagenic equivalents calculated from the mutagenic potency relative to BaP (MEF) multiplied by PAH concentration. TEF: toxic equivalency factors for cancer potency relative to BaP [44] and MEF: mutagenic potency factor relative to BaP [45 a,b]. The equations for measurement of BaP-TEQ and BaP-MEQ are given below.

- (BaP-TEQ)Σ8PAH = [BaA] × 0.1 + [CHR] × 0.01 + [BbF] × 0.1 + [BkF] × 0.1 + [BaP] × 1 + [IcdP] × 0.1 + [DahA] × 5 + [BghiP] × 0.01.
- (BaP-MEQ)Σ8PAH = [BaA] × 0.082 + [CHR] × 0.017 + [BbFA] × 0.25 + [BkFA] × 0.11 + [BaP] × 1 + [IcdP] × 0.31 + [DahA] × 0.29 + [BghiP] × 0.19.

TABLE 7BaP-TEQ and BaP-MEQ for children at residential indoor and outdoor air environment

	Type of PAHs	Number of samples	TEF*	BaP-TEQ (ng/m^3)	MEF*	BaP-MEQ (ng/m^3)
Residential Indoor Air Environment	Σ8PAH	255	NA	0.098–8.348	NA	0.069–19.72
	BaP	255	1	0.015–4.494	1	0.015–4.494
	BaA	255	0.1	0.002–0.132	0.082	0.001–0.108
	CHR	255	0.01	0.000–0.021	0.017	0.000–0.036
	BbF	255	0.1	0.004–0.346	0.25	0.010–0.865
	BkF	255	0.1	0.002–0.140	0.11	0.002–0.154
	IcdP	255	0.1	0.002–1.400	0.31	0.006–4.340
	DahA	255	5	0.055–1.741	0.29	0.003–0.101
	BghiP	255	0.01	0.001–0.517	0.19	0.016–9.828
Outdoor Air Environment	**Type of PAHs**	**Number of samples**	**TEF***	**BaP-TEQ (ng/m^3)**	**MEF***	**BaP-MEQ (ng/m^3)**
	Σ8PAH	82	NA	0.109–1.932	NA	0.062–2.394
	BaP	82	1	0.016–0.748	1	0.016–0.748
	BaA	82	0.1	0.001–0.059	0.082	0.001–0.048
	CHR	82	0.01	0.0003–0.008	0.017	0.001–0.013
	BbF	82	0.1	0.006–0.237	0.25	0.015–0.592
	BkF	82	0.1	0.002–0.114	0.11	0.002–0.125
	IcdP	82	0.1	0.003–0.197	0.31	0.010–0.611
	DahA	82	5	0.075–1.021	0.29	0.004–0.059
	BghiP	82	0.01	0.001–0.039	0.19	0.010–0.739

Source: Miller et al. 2010

TEF*: toxic equivalency factors for cancer potency relative to BaP (Nisbet and LaGoy et al. 1992) [44]

MEF*: mutagenic potency factor relative to BaP (Durant et al. 1996 and 1999) [45 a,b]

IARJSET
ISSN (Online) 2393-8021
ISSN (Print) 2394-1588
International Advanced Research Journal in Science, Engineering and Technology
ISO 3297:2007 Certified
Vol. 3, Issue 9, September 2016

The exposure of BaP-equivalent (BaP-TEQ and BaP-MEQ) concentrations for sum of 8 type of particulate PAHs as well as individual PAH to young children in New York City in both residential indoor and outdoor environment is presented in Table 7 [46]. The indoor (BaP-TEQ)Σ8PAH and (BaP-MEQ)Σ8PAH ranged from 0.098–8.348 ng/m^3 and 0.069–19.72 ng/m^3, respectively which were alarmingly high as compared to outdoor (BaP-TEQ)Σ8PAH (0.109–1.932 ng/m^3) and (BaP-MEQ)Σ8PAH (0.062–2.394 ng/m^3) respectively. The contributions of BaP to (BaP-TEQ)Σ8PAH and (BaP-MEQ)Σ8PAH were higher in both the residential indoor and outdoor environment as compared to other carcinogenic particulate PAHs. In the outdoor environment, the contribution of BbF to (BaP-MEQ)Σ8PAH was comparatively higher than indoor environment, might be due to traffic related emissions of PAHs. BaP is the most carcinogenic and mutagenic contributor, followed by DahA and BbF [47]. The toxicity of DahA is almost equal to BaP,though DahA is a new surrogate compound of particle phase-PAHs. Thus in present day, BaP and DahA both are considered as most air toxic, carcinogenic and mutagenic particulate PAHs in the atmospheric environment.

IX. CONCLUSION

PAHs are generated in the atmosphere due to incomplete combustion of organic compounds and toxic to air environment. The emissions of PAHs are either from pyrogenic source (natural) or petrogenic source (anthropogenic). They may present in the atmosphere either in gas phase or particulate phase or mixture of both the phases. Though there are many petrogenic sources of PAHs in the ambient air, but the in global air environment, but the maximum emission of PAHs is from biofuels (57.6%) only. India is the highest contributor of PAHs from biofuels (92.5%) followed by China (66.4%) and USA (9.1%).

PAHs are one of the major contributors of airborne inhalable particles. Hence it is necessary to understand the importance to measure the individual PAHs and identify their emission sources, so that management control plan to reduce emission of PAHs may be prepared. The emission of atmospheric PAHs occur significantlyfrom multiple emission sources like from vehicular emission, combustion of biofuels (wood, coal etc.) and industrial activities. This review article also highlighted the importance of BaP and BaP-equivalent cancer risk potential for other particulate PAHs. The particulate PAHs are more carcinogen and mutagen as compared to gaseous PAHs. Hence it is deemed necessary to control the emission of PAHs, especially the particular PAHs to reduce the carcinogenic and mutagenic risk to human's health.

ACKNOWLEDGEMENT

The authors are thankful to CPCB (Central Pollution Control Board), New Delhi for providing the relevant information about the Polycyclic Aromatic Hydrocarbons (PAHs) in air and their effects on human health. The authors are also thankful to the Director CSIR- NEERI (National Environmental Engineering Research Institute) and DTU (Delhi Technological University), for providing permission to publish this article.

REFERENCES

[1] L.C.Marr, K. Dzepina, J.L.Jimenez, F.Reisen, H.L.Bethel, J.Arey, J.S.Gaffney,N.A.Marley, & Molina, M. J. "Sources and transformation of particle–bound polycyclic aromatic hydrocarbons" Atmospheric Chemistry and Physics vol.6, pp1733-174, 2006.

[2] Douben, Peter E.T. (2003). PAHs: an ecotoxicological perspective. John Wiley & Sons (Ecological and Environmental Toxicology Series)

[3] S.S. Park, Y.J Kim, C.H.Kang, "Atmospheric polycyclic aromatic hydrocarbons in Seoul, Korea",Atmospheric Environment vol.36, pp 2917–2924, 2002.

[4] World Health organization (WHO), 2000. (Chapter5.9 Polycyclic aromatic hydrocarbons (PAHs) WHO/ Europe www. euro. who. int/__.../ AQG 2ndEd _5_9 PAH.pdf.

[5] G. Na, C. Liu, Z. Wang, L. Ge, X. Ma and Z. Yao,"Distribution and characteristic of PAHs in snow of Fildes Peninsula" Environmental Science, vol.23, pp. 1445-1451,2011.

[6] World Health organization (WHO), 2002. World Health Report 2002: Reducing Risks, Promoting Life. /http://www.who.int/whr/en/S.

[7] C.E.Bostrom, P. Gerde, A. Hanberg, B.Jerntrom, C.Johansson, T. Kyrklund, A. Rannug, M.Tornqvist, K.Victorin& R. Westerholm. "Cancer risk assessment, indicators, and guidelines for polycyclic aromatic hydrocarbons in the ambient air", Environ Health Perspect 110 (suppl), pp 451-488, 2002.

[8] D.P Singh,R. Gadi, T.K. Mandal, T. Saud, M. Saxena, S.K.Sharma "Emissions estimates of PAH from biomass fuels used in rural sector of Indo-Gangetic Plains of India",Atmospheric Environment,vol. 68, pp120-126, 2013.

[9] Y. Zhang, S. Tau.,"Global atmospheric emission inventory of polycyclic aromatic hydrocarbons (PAHs)", Atmospheric Environment vol. 43, pp 812-819, 2009.

[10] W.F. Rogge, L.M.Hildemann, M.A.Mazurek, G.R. Cass, B.R.T.Simoneit "Sources of fine organic aerosol: 2. Non-catalyst and catalyst-equipped automobiles and heavy-duty diesel trucks" Environmental Science& Technology, vol.27, pp 636–651, 1993.

[11] K.Ravindra, R.Sokhi, G. Van,"Atmospheric polycyclic aromatic hydrocarbons: source attribution, emission factors and regulation-review" Atmospheric Environment,vol. 42, pp 2895-2921, 2008a.

[12] S.E. Manahan, Environ. Chem, sixth ed. Lewis Publisher, New York, 1994.

[13] CPCB, 2003(cpcb.nic.in/.../Publication_363_Document46.pdf.)

[14] B.S.Haynes. In: Bartock, W., Sarofim, A.F. (Eds.), Fossil Fuel Combustion: a Source Book. Wiley, New York, pp. 261–326.

[15] U.E.Wiersum, "The formation of polycyclic aromatics, fullerenes and soot in combustion. The mechanism and the environmental connection. Polycyclic Aromatic Compounds, vol 11. pp 291–300, 1996.

[16] A.L.C.Lima, J.W.Farrington, C.M. Reddy" Combustion-derived polycyclic aromatic hydrocarbons in the environment—a review" Environ Forensics vol.6, pp109–131, 2005.

[17] EUD (European Union Directive), Directive 2004/107/EC of the European parliament and of the council. Official Journal of European Union L23, pp. 3–16. /http://eur-lex. europa.eu/LexUriServ/site/en/oj/2005/l_023/l_02320050126en 00030016.pdf, 2004.

[18] E. Manoli, A. Kouras, C. Samara, C."Profile analysis of ambient and source emitted particle-bound polycyclic aromatic hydrocarbons from three sites in northern Greece", Chemosphere vol.56, pp 867-878, 2004.

[19] M.M.R.Mostert, G.A.Ayoko, S.Kokot, "Application of chemometrics to analysis of soil pollutants." Trends in Analytical Chemistry vol.29,pp430-435,(2010).

[20] H. Guo, S.C. Lee, K.F.Ho, X.M.Wang, S.C. Zou."Particle-associated polycyclic aromatic hydrocarbons in urban air of Hong Kong", Atmospheric Environment, vol. 37, pp 5307–5317, 2003.
[21] M.Tobiszewski, J.Namiesnik" PAH diagnostic ratios for the identification of pollution emission sources-Review", Environmental Pollution, vol.162,pp 110-119, 2012.
[22] D.P Singh,R. Gadi, T.K. Mandal "Characterization of gaseous and particulate polycyclic aromatic hydrocarbons in ambient air of Delhi, India. Polycyclic Aromatic Compounds,vol.32, pp 556–579, 2012, DOI: 0.1080/10406638.2012.683230
[23] M. Akyüz, H. Çabuk, "Gaseparticle partitioning and seasonal variation of polycyclic aromatic hydrocarbons in the atmosphere of Zonguldak, Turkey" Scienceof the Total Environment, vol.408, pp 5550-5558, 2010.
[24] K. Ravindra, E. Wauters, R. V. Grieken, "Variation in particulate PAHs levels and their relation with the transboundary movement of the air masses" Science of the Total Environment, vol. 396, pp100-110, 2008b.
[25] A. H. Neilson," PAHs and Related Compounds", Springer, Berlin 1998.
[26] J. Oda, S, Nomura, A. Yasuhara, T. Shibamoto, "Mobile sources of atmospheric polycyclic aromatic hydrocarbons in a roadway tunnel."Atmospheric Environment, vol. 35, pp 4819–4827, 2001.
[27] C.Pies, B. Hoffmann, J. Petrowsky, Y. Yang, T.A.Ternes, T. Hofmann, "Characterization and source identification of polycyclic aromatic hydrocarbons (PAHs) in river bank soils", Chemosphere vol. 72, pp 1594-1601, 2008.
[28] R.J. Torre-Roche, W.Y.Lee, S.I. Campos-Díaz," Soil-borne polycyclic aromatic hydrocarbons in El Paso, Texas: analysis of a potential problem in the United States/Mexico border region" J. of Hazardous Materials, vol. 163,pp 946-958,2009.
[29] C. Oliveira, N. Martins, J. Tavares, C. Pio, M. Cerqueira, M. Matos, H. Silva, C. Oliveira, F. Camoes." Size distribution of polycyclic aromatic hydro-carbons in a roadway tunnel in Lisbon, Portugal" Chemosphere, 2011. doi:10.1016/ j.chemosphere.2011.01.011.
[30] N.R. Khalili,P.A. Scheff, T.M. Holsen, "PAH source fingerprints for coke ovens, diesel and gasoline engines, highway tunnels, and wood combustion emissions " Atmospheric Environment, vol. 29, pp533–542,1995.
[31] M.B.Yunker,R.W. Macdonald, R. Vingarzan, R.H. Mitchell, D. Goyette, S. Sylvestre. "PAHs in the Fraser River basin: a critical appraisal of PAH ratios as indicators of PAH source and composition" Organic Geochem, vol. 33, pp 489-515, 2002.
[32] A.M. Caricchia, S. Chiavarini, M. Pezza, "Polycyclic aromatic hydrocarbons in the urban atmospheric particulate matter in the city of Naples (Italy)"Atmospheric Environment, vol.33, pp 3731–3738,1999.
[33] P.K. Pandey, K.S.Patel, J. Lenicek, "Polycyclic aromatic hydrocarbons: need for assessment of health risks in India? Study of an urban-industrial location in India" Environmental Monitoring and Assessment.vol. 59, pp 287–319, 1999.
[34] A. Katsoyiannis, E. Terzi, Q.Y.Cai. "On the use of PAH molecular diagnostic ratios in sewage sludge for the understanding of the PAH sources. Is this use appropriate? ", Chemosphere vol. 69, pp 1337-1339, 2007.
[35] G. Grimmer, J. Jacob, K.W.Naujack, "Profile of the polycyclic aromatic compounds from crude oils—inventory by GC GC-MS. PAH in environmental materials, part 3" Fresenius Journal for Analytical Chemistry, vol. 316, pp 29–36, 1983.
[36] W. Esteve, H. Budzinski, E. Villenave, "Relative rate constants for the heterogeneous reactions of NO2 and OH radicals with polycyclic aromatic hydrocarbons adsorbed on carbonaceous particles. Part 2: PAHs adsorbed on diesel particulate exhaust SRM 1650a" Atmospheric Environment, vol.40, pp 201–211, 2006.
[37] M. del Rosario Sienra, N.G. Rosazza, M. Prendez," Polycyclic aromatic hydrocarbons and their molecular diagnostic ratios in urban atmospheric respirable particulate master", Atmospheric. Research. Vol.75, pp 267-281, 2005.
[38] Alves, C., Pio, C., Carvalho, A., Santos, C., "Atmospheric carbonaceous aerosols over grasslands of central Europe and a Boreal forest", Chemosphere vol. 63, pp 153-164, 2006.
[39] World Health organization (WHO), 1998. Selected Non-heterocyclic Polycyclic Aromatic Hydrocarbons (Environmental Health Criteria 202). Geneva.
[40] United States Environmental Protection Agency (USEPA), 1997.Washington, DC, EPA/600/P-95/002F a-c Exposure Factors Handbook (1997 Final Report)| Risk Assessment, https://cfpub.epa.gov/ncea/risk/recordisplay.cfm?deid=12464
[41] C.V.Raiyani, J.P.Jani, N.M. Desai, P.G.Shah, D.J. Parikh, S.K. Kashyap,"Assessment of indoor exposure to polycyclic aromatic hydrocarbons from urban poor using various types of cooking fuels."EnvironmentalContamination. and Toxicology, vol.50, pp 757–763,1993a
[42] World Health organization (WHO), 2010. WHO Guidelines for indoor air quality: selected pollutants www.euro.who.int/__data/assets/pdf_file/0009/128169/e94535.pdf.
[43] S.H. Hwang, J.H. Hwang, J.S. Moon & D.H. Lee, "Environmental tobacco smoke and children's health", Korean Journal of Pediatrics, vol. 55(2): pp 35–41,2012. doi: 10.3345/kjp.2012.55.2.35.
[44] Nisbet I, LaGoy P, "Toxic equivalency factors (TEFs) for polycyclic aromatic hydrocarbons (PAHs)".Regulatory Toxicology and Pharmacology,vol. 16, pp 290–300,1992.
[45] J. Durant, A. Lafleur, W. Busby, A. Lafleur, B. Penman, C. Crespi," Human cell mutagenicity of oxygenated, nitrated and unsubstituted polycyclic aromatic hydrocarbons associated with urban aerosols", Mutation Research/Genetic Toxicology and Environmental Mutagenesis, vol. 371, pp 123-157, 1996a.
[46] J. Durant, A. Lafleur, W. Busby, L. Donhoffner, B. Penman, C. Crespi,"Mutagenicity of $C_{24}H_{14}$ PAH in human cells expressing CYP1A1. Mutation Research/Genetic Toxicology and Environmental Mutagenesis, vol. 446, pp 1-14, 1999b.
[47] Durant J, Busby W, Lafleur A, Penman B, Crespi C. Human cell mutagenicity of oxygenated, nitrated and unsubstituted polycyclic aromatic hydrocarbons associated with urban aerosols. Mutation Research/Genetic Toxicology and Environmental Mutagenesis,vol.371, pp123–157, 1996.
[48] R. L. Miller, K.H. Jung, B.Yan, S.N. Chillrud, F.P. Perera, R. Whyatt, & D. Camann, "Assessment of Benzo(a)pyrene-equivalent Carcinogenicity and Mutagenicity of Residential Indoor versus Outdoor Polycyclic Aromatic Hydrocarbons Exposing Young Children in New York City", International Journal of Environmental Research & Public Health,vol. 7, pp1889–1900, 2010. doi: 10.3390/ijerph7051889
[49] M. Pufulete, J. Battershill,A. Boobis and R. Fielder."Approaches to carcinogenic risk assessment for polycyclic aromatic hydrocarbons: A UK perspective" Regulatory Toxicology and Pharmacology, vol. 40, pp 54–66, 2004.

Multimed Tools Appl
DOI 10.1007/s11042-016-4078-7

An effective web page recommender system with fuzzy c-mean clustering

Rahul Katarya [1] · **Om Prakash Verma** [1]

Received: 22 February 2016 / Revised: 4 September 2016 / Accepted: 18 October 2016
© Springer Science+Business Media New York 2016

Abstract With the exponential development of the number of users browsing the internet, an important factor that now the developer community is focussing on is the user experience. Recommender systems are the platforms that make personalized recommendations for a particular user by predicting the ratings for various items. Recommender systems majorly ignore the sequential information and rather focus on content information, but sequential information also provides much information about the behavior of the user. In this research work, we have presented a novel web-based recommender system which is based on sequential information of user's navigation on web pages. We received top-N clusters when Fuzzy C-mean (FCM) clustering is employed. We determined the similar users for the target user and also evaluated the weight for each web page. We have tried to solve that problem of recommender systems as we offered a system to forecast a user's next Web page visit. In our work, we proposed a system which generates recommendations to the users, by considering the sequential information that exists in their usage patterns of Web pages. We employed fuzzy clustering to give recommender system a sequential approach. We calculated weights for each page category considered in our system and predict top page recommendation for the target user. The real-world dataset of MNSBC is used in the experiments. The dataset consists of 5000 user entries with 6, entries per user. When we performed a comparison between the existing model with our proposed model, then it clearly showed that the accuracy of the proposed model is almost three times better than some existing systems. The accuracy of our proposed model is nearly 33 %.

Keywords Web recommender system · Clustering · Fuzzy c-mean · Accuracy

✉ Rahul Katarya
rahulkatarya@dtu.ac.in

[1] Department of Computer Science & Engineering, Delhi Technological University (Formerly Delhi College of Engineering), Shabad Daulatpur, Main, Main Bawana Road, Delhi 110042, India

Published online: 28 October 2016

1 Introduction

A collection of data in enormous amounts and affordable processing capabilities have motivated organizations to shift from the traditional world of mass production to the new world of customization. The development of e-commerce platforms has allowed companies to provide more options to the customers on a single integrated platform. The recommendation system is a decision support system which can offer the desirable information to the customers as per their needs [23, 30, 31, 61]. Recommender systems (RSs) are the platforms that make personalized recommendations for a particular user by predicting the ratings for various items [21, 28, 29, 32, 55]. The products can be recommended, by various factors such as top sellers on a site, demographics of the customer, social relation of users and past buying behavior of the client. RSs generate different recommendations to different ensemble users, thus providing customized web interface to the users. Currently, most of the e-commerce industries have enabled recommendation systems at the back end and offering personalized web recommendations to the users. Recommender systems have been developed by incorporating various disciplines such as machine learning, computational intelligence, and data mining techniques and especially heuristics and finding association patterns among the items [11, 57, 63]. Examples of popular recommender systems include Amazon.com for books, CDs and various other products, IMDB for movies and Jester system for jokes. Advancement in techniques of different domains like machine learning, pattern recognition, and statistics have made it possible to perform mining and unfold exciting as well as unknown patterns from the big data. Web data exists in several formats like URL visits, web page content, incoming and outgoing hyperlinks to the Web page. By what type of data is being analysed or mined, so web mining was broadly classified into web content, web usage and web structure mining [38, 39, 52]. Web structure mining works on the internet's hyperlink structure. Web usage mining develops innovative, implicit and valuable patterns from the usage data of users. Web page recommendation systems have quite a persistent approach to analyzing users' behavior over the internet and produce recommendations as per their preferences. It supports organizations in intelligent decision making on their customers' needs by automating the recommendations as per their preferences. While building recommender systems, the sequential characteristic of the user session is ignored. A sequential aspect of web user session has been considered by probabilistic models like Markov model while designing a web recommendation system [41]. However, the problem with the probabilistic model is that swapping probability between web categories should be known a priori, and may involve the knowledge and experience of a domain expert. In our work we have proposed a system which produces recommendations to the users, by considering the sequential information that exists in their usage patterns of web pages. We employed fuzzy c-mean clustering technique to generate soft clusters among our users and picked up top clusters for processing; that depend on the average value of cluster centers. We calculated weights for each page category that were considered in our system and predicted top page recommendation for the target user. We found out accuracy of our prediction with existing MSNBC dataset. We conducted several experiments on a large dataset of MSNBC that consisted of 5000 users with six-page visit data and predicted the seventh page. The experiment results show that our proposed model can

better utilize user's social information and outperforms the modern algorithms regarding accuracy. The leading contributions of our research work are summarized as:

- We have presented a recommender system which generates recommendations for the users, by considering the sequential information that exists in their usage patterns of web pages.
- Our proposed system considered both the content as well as the sequence of a visit during clustering to form groups of users.
- We employed fuzzy c-mean clustering techniques to generate soft clusters among our users.
- We selected top clusters for processing which depended on the average value of cluster centers.
- We calculated weights of each considered page category and predicted top page recommendation for the target user.
- We found the prediction accuracy with existing MSNBC dataset and conducted several experiments on a large dataset of MSNBC which consists of 5000 users with six-page visit data and predicted the users' seventh-page visit.
- Our proposed system was compared with state of art methods such as WRS model [41], WebPUM [24], Modified K-means [45], Multivariate [9], SemSig [20], Weighted K-means [53], Binary data clustering [16], Neuro-Fuzzy [50], XFCM [54] and C-means & COG [33].
- The experiment results showed that our proposed system performed with better results, and it can be utilized for acquiring user's social information over Web navigation based recommender system.

The remainder of this article is organized as follows: Section 2 gives a review of the background knowledge of our work. Section 3 presents our novel web page recommendation model. Section 4 describes the experiments and the performance of our proposed system, and finally, Section 5 concludes our work.

2 Related work

Various studies have been performed in improving the efficiency of recommender systems for better recommendations to the user. Recommendation systems are designed using different methods by including k-NN, decision tree, clustering, regression, heuristic approaches, neural networks and association rule mining [2, 13, 64]. Based on the kind of techniques used, recommendation systems can be categorized as content-based and collaborative based systems. The content-based approach has originated from the information retrieval and information filtering domain [5, 12]. Content-based recommender systems make recommendations based on users' past likings. The rating for any item for any individual is computed based on ratings of similar items given by the person, and primary objective is to study a function that forecasts that in which class a document fits (i.e., either adored or not liked) [6, 36]. Collaborative systems are different from content-based systems in the sense that they first found related users for target users and then make recommendations based on preferences of same users [67]. In this

methodology, recommendations are made by finding correlations among the users. The key objective of the collaborative filtering is to discover rating of the items, which are not seen by the current user and recommended the ratings to similar users. Collaborative based recommender systems can be more classified into two classes, memory based (heuristic based) and model based collaborative systems [4, 15]. Memory based systems calculate the similarity among users based on users' ratings. The algorithms of memory based systems are heuristics that make recommendations based on a whole collection of items pre-rated by the users. Model-based collaborative recommender systems generate the descriptive model of the system which are based on the users' preferences, numerous data mining, and machine learning techniques. The several methods are used such as Bayesian models, clustering models, and latent semantic models. There are various other probabilistic modeling techniques which are used for building recommender systems. Ravi et al. [46] presented a comprehensive, state-of-the-art review of the research work done on opinion mining and also examined in seven broad dimensions viz. Subjectivity classification, sentiment classification, review usefulness measurement, lexicon creation, opinion word, product aspect extraction, opinion spam detection and various applications of opinion mining. Web-page recommendation plays a significant role in smart web systems. Beneficial knowledge discovery from web usage data and adequate knowledge representation for expert web page recommendations are crucial and challenging tasks. Clustering is an essential phase in the web mining, as the data on the web is increasing in a huge way. A multitask spectral clustering model was proposed to handle the several data clustering challenges and then suggested two types of correlations such as inter-task clustering correlation, which discussed the relations among different clustering tasks and intra-task learning correlation, which permitted the procedures of learning cluster labels [60]. In the data clustering research, a clustering algorithm was proposed (discriminative nonnegative spectral clustering) that explicitly imposed an additional nonnegative constraint on the cluster indicator matrix to pursue a more interpretable resolution [59]. Nguyen et al. [43] proposed a technique to provide proficiently enhanced web page recommendation through semantic-enhancement by mixing the domain and web usage knowledge of a website. Two new models were offered to represent the domain knowledge. The first model used an ontology to represent the domain knowledge. The second model used automatically generated semantic network to represent domain terms, web-pages, and the relations between them. A solution for a cross-site cold-start product recommendation was presented, which focused on recommending goods from e-commerce portals and websites to users at social networking sites in cold-start states [66]. E-Commerce businesses have accepted web personalized procedures broadly in the form of recommender systems for prompting user behavior for customer preservation. Some studies were performed by taking three significant assistances to the body of knowledge in information systems. The first study was based on web personalization, in the second study a Utaut2 model was presented and in the third study, web personalization was dedicated on e-commerce domain [34]. An effective recommender system was proposed by handling the session data of users and presented an algorithm to divide the binary session data into a static number of groups and applied the partitioned sessions to make recommendations

[16]. Location-based social networks (LBSN) enable users to check-in at points of interests (POIs), share the information with other users on the network, and receive recommendations about new and interesting POIs in their vicinity. Schmachtenberg et al. [49] showed an approach for enhancing POI recommendations for a location-based social network by enriching it with semantic data. Social networks are playing a significant role in real-time information exchange and online human interaction such as Facebook, Twitter, LinkedIn, Amazon and Sina Weibo. The enormous volume of live information in social media stream-shave directed to the extraordinary requirement for tracking technologies. In addressing this issue, a multi-faceted brand tracking process was proposed to gather representative data from large-scale social media content [17]. In their technique, authors took benefits of the heterogeneous data of social media content. Social websites and microblogs posted on social network comprise an abundant percentage of images. Henceforth how to identify logos in images from the social network is of high value. To address this issue, a learning-based logo detection technique was suggested with social network information supporter, in which dense histogram type feature was also proposed to categorize logo and non-logo image patches [56]. Event discovery in social media has become an essential task. The foremost challenges in event detection lie in the features of social media data, such as little, informal, mixed and live. By considering all these factors, an event detection method was offered, which produced an intermediate semantic entity, named microblog clique (MC), to discover the highly correlated information among the noisy and small microblogs [18]. The Markov model is complex probabilistic model widely used for modeling sequential events. Several hybrid recommendation systems have also been developed using multiple techniques including a sequential pattern analysis. Maximum of the work related to the design of a guidance and recommended a system with subsequent data used the Markov model [25, 26]. Sequential and association pattern mining procedures have been established to find the sequential arrangements in the data. Our proposed model considers both the content as well as the sequence of a visit during clustering to form groups of users. Clustering is the approach of data mining which is adopted by various domains of web and information systems. A fuzzy diagonal co-clustering algorithm with K-means was proposed which were evaluated on synthetic and real datasets [35]. Web page recommender system has drawn attention to many researchers and industrialists as it offers attractive schemes and after regular intervals of time. So to suggest the suitable web page from the large collections of pages, a Tclus algorithm based system was presented in which authors combined the features of density based and k-means clustering algorithm by collecting the data from the website of around five months [58]. Whenever we talk about the internet based recommender system, one aspect which we will always need that is decent value of web service, but most of the web recommendations are effected with the sparsity and scalability problems. To reduce these problems, a ClucF method was offered which utilized the users and services clusters [62]. In the similar work, authors tried to the refine web recommender system in which they utilized the k-means clustering technique and compared with modified knockout refinement algorithm (MKRA) [14]. A neuro-fuzzy based system was offered in which authors tried to get patterns and browsing behavior from the web log data [50]. The neuro-fuzzy system was mixed with the neural networks and the fuzzy set theory. The browsing

behavior analysis for websites is necessary for detecting suspicious activities for online users. A news article recommender system was designed in which collaborative filtering and k-means clustering approaches were employed [8]. Authors used the WordNet-enabled k-means algorithm, which discovered the usage of word hypernyms mined from the WordNet database. In another research work for web mining, a movie recommender system was presented in which they handled the issues such as sparsity, scalability, new users and cold-start problems and they united the web mining approaches and domain specific ontologies [42]. A study was presented in which authors advised the role of agent technology in web usage mining with homomorphic encryption for e-commerce environment and they also highlighted the user's privacy and agents [51]. In the related study, the importance of the semantic web in the knowledge discovery and data mining fields were analyzed [47]. The research was accomplished in which growth of blended learning and success of education with ICT tools were taken into consideration. The blended model was mixed with a learning management system (LMS), a Web 2.0 tools and the E-learning activities recommender system (ELARS) [22]. Some authors presented a methodology to discuss the web framework which was based on observation system for earth program. Their operational tactic was composed of five technologically neutral stages to form executable business practices [48]. A personalized social document representation (PerSaDor), was presented which was based on the social media in which authors presented two ranking functions for documents which were established on their textual content and their PerSaDoR [7]. A semantic methodology was offered in which ontology was used as an arbitrated plan for the tracking data from web source's semantics. Semantic mappings among the scheme of origin and the ontology were used to transform the original data to RDF [19]. A system named as TANGO was offered which role was to study rules to abstract and fetch the information from semi-structured web pages with high precision and recall for enterprise systems. TANGO was based on an open directory of features that was characterized by resources of HTML, DOM, CSS and user-defined features [27]. A method was presented to anonymize the query logs which employed the k- anonymity and de-anonymization tools and finally regulated the possible privacy problems [44]. A study was dedicated to the dynamic features of the Kohonen procedure, which was responsible for transporting proficient incremental procedure [37]. Big data are generated from the web transactions and interactions. Unsupervised learning approaches are cooperative in separating heterogeneity of treatment effects for such actions. By taking these issues under consideration authors designed multiple imputations (MI) based fuzzy clustering and suggested a new MI-based Visualization-aided validation index (MIVOOS) in contrast to fuzzy clustering validation indexes, XB and VOS [65]. Researchers presented a method which designed the frequent page sets from weblog in the dynamic environment. They proposed T + weight tree organization and concluded by experiments that it was more competent than weighted tree method with respect to time and space [40].

3 Proposed work

Clustering of data is the process of dividing data into classes or groups so that items in the matching group are as similar as possible, and items in diverse classes are as dissimilar as

possible. Based on the nature of data and the determination for which clustering is being used, several actions of similarity may be used to place various items into classes, where the similarity measure controls how the clusters are formed. The criteria for identifying similar users is the browsing history of users. The users who have opened nearly same category of pages as our target user is likely to be in the same cluster to our target user. A pattern recognition based recommender system involves two stages; the first step is clustering followed by classification task. At the first stage, the system is provided with sufficient learning so that the classification accurateness of the system is quite significant or at the desired level. After the system learns, it generates a set of recommendations with good rankings. The new user is classified among clusters that we have taken with the help of FCM algorithm. As soon as a new user enters the system, we need to apply FCM over the whole dataset again so as to allocate each user a cluster number after that recommendation is made.

Figure 1 gives the overall flow of the model and the order of occurrence of events. First of all, in the given MSNBC dataset we employed the fuzzy c-mean clustering approach. By applying the method, we get the top-N clusters that are further used for identifying the similar users for a target user. Then we calculate the weight for each page category and finally determine the accuracy of the system.

3.1 Fuzzy c-mean clustering

In our system, we first designed clusters to obtain knowledge about web users and the classification method was used later for increase the knowledge fitness and produced recommendations. A web user may have multiple interests for which he needs to be put into multiple clusters. Hence, we have used fuzzy c-mean technique [1, 3, 10]. In fuzzy clustering or soft clustering, data elements can go to more than one cluster, and linked to each item is a set of membership levels. These specify the strength of the relationship between that data element and a particular cluster. Fuzzy clustering is a procedure of assigning these membership levels, and then using them to assign data elements to one or more clusters. The FCM algorithm efforts to partition a finite collection of n elements $X = \{X_{1,\ldots,}X_{nj}\}$ into a group of c fuzzy clusters on some given standard. Given a fixed set of data, the algorithm takes a list of c cluster centres $C = \{c_{1,\ldots,}c_c\}$.Moreover, a partition matrix W = $w_{i,j} \in$ [0, 1], i = 1,…,n, j = 1,…c, where each element w_{ij} given by Eq. 1 says the degree to which element X_i fits to cluster c_j. Like the K-means clustering, the FCM purposes to minimize an objective function.

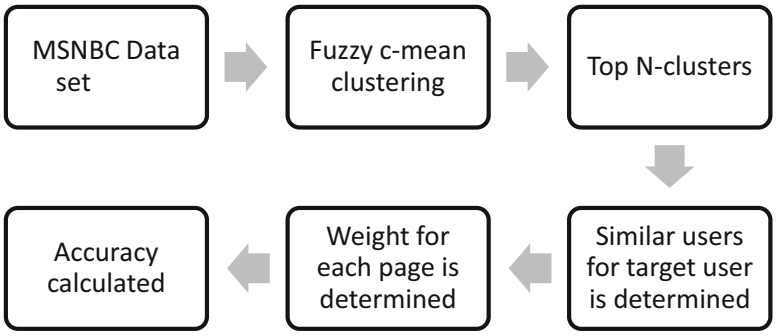


Fig. 1 Block diagram of our proposed model

$$c^{\arg min}\sum_{i=1}^{n}\sum_{j=1}^{c} w_{ij}^{m} \| \left(X_i - c_j\right) \|^2 \quad (1)$$

Where,

$$w_{ij}^{m} = {}^{1}/_{\sum_{k=1}^{c}\left[\frac{\| \left(X_i - c_j\right) \|}{\| \left(X_i - c_k\right) \|}\right]^{\frac{2}{m-1}}}$$

This alters from the k-means objective function by the addition of the membership values w_{ij} moreover, the Fusilier $m \in R$, with $m \geq 1$. The Fusilier m regulates the level of cluster fuzziness. A large m consequences in smaller memberships w_{ij} and henceforth, fuzzier clusters. In the limit $m = 1$, the memberships w_{ij} converge to 0 or 1, that suggests a crisp splitting. In the absence of experimentation or domain knowledge, m is commonly set to 2.

3.2 Selection on top 'N′ clusters

After applying fuzzy c-mean clustering, we get cluster center values for each cluster upon which processing is done instead of entire data of users present in the cluster. We are required to find out the cluster number in which each user occurs. Since we are dealing with soft clusters, we may get a number of cluster numbers for each user. That is acceptable. We are taking top 'n' clusters in our proposed work depending on the average value of cluster center values. It comes from the fact that not all but significant clusters will have a remarkable impact on recommendations.

3.3 Finding users similar to target user

We now choose our target user for whom we wish to make recommendations. After choosing target user we now need to find all users similar to target user as they would have a direct impact on user's recommendations. To find related users, we used partition matrix 'U,' that is obtained from fuzzy c-mean clustering algorithm. The similar users are found for the target user using Fuzzy c-means clustering algorithm which generates soft clusters i.e. A user can be present in more than one cluster. After that, Top N-clusters are produced for the user. We got similar users for target user which we generated through resultant matrix MAT, and which also contains all similar user entries. When a new user is encountered with having some browsing history, our system is trained to handle such cases as well. The system will first find out a similar cluster of the new user with the already existing users and after that recommendation is made for the new user as well.

3.4 Weight calculation for each page category

Since we have obtained a set of similar users, we are left with the calculation of weight for each page category. Higher the weight, higher is the probability of the page to be recommended to the user. In our proposed model we are having 17-page categories defined with ranking from 1 to 17. The data set has seventeen categories on the front page, weather, health, living, business, news, tech, local, opinion, on-air, misc., sports, summary, bbs(bulletin board service), travel, MSN-news, and MSN-sports. For the purpose of weight calculation, we maintained three matrices namely 'X,' 'Z' and 'G.'

- Matrix X contains a count of a number of times the target user has opened the specific page.
- Matrix Z contains a count of a number of times all the similar users of target user have opened the specific page.
- Matrix G contains whether a page has been opened by the target user at all or not.

Taking into consideration all these matrix values it can be understood that matrix X and matrix Z favours recommendation of a page to the user. Corresponding mathametical expressions are as follows:

$$\begin{aligned} &\text{if } (\text{msndata } (\text{user}, \text{i}) == \text{k}) \\ &\text{x(k)} = \text{x(k)} + 1; \end{aligned} \tag{2}$$

$$\begin{aligned} &\text{if}(\text{mat } (\text{i}, \text{j}) == \text{k}) \\ &\text{z(k)} = \text{z(k)} + 1; \\ &\text{if } (\text{mat } (\text{i}, \text{j}) == \text{k}) \\ &\text{if } (\text{g(k)} == 0) \end{aligned} \tag{3}$$

$$\text{g(k)} = \text{g(k)} + 1; \tag{4}$$

Where k stands for page category from 1 to 17, matrix mat contains all similar users entries of the target user, and msndata refers to dataset taken for analysis. At last, when all the above three matrix values have been calculated the final weight of each page category can be computed using the mathematical expression stated below:

$$\text{Weight (i)} = (\text{X[i]} + \text{Z[i]})/(\text{size}-\text{G[i]}) \tag{5}$$

Where i stands for page category and values used can be obtained using Eqs. 2, 3 and 4.

"size" is a number of users in the cluster of the target user obtained after applying FCM algorithm over the dataset.

3.5 Calculation of accuracy

Accuracy is the proportion of the amount of correct recommendations to the volume of whole recommendations.

Accuracy = (number of accurate recommendations) / (number of whole recommendations)

In this case, we recommend the next likely visit of the user, which is matched with the authentic next step of the user (testing). If the predicted following step is the same of the actual next state, then the event is termed as hit, else it is termed as a miss. Hence, accuracy is our case will be given as:

$$\text{Accuracy} = (\text{number of hits})/(\text{number of hits} + \text{number of miss}) \tag{6}$$

Considering the confusion matrix accuracy of the recommendation system can be defined as the ratio of significant retrieved elements to all retrieved, non-retrieved, relevant and not relevant elements. The corresponding algorithm used in the proposed work has been stated in Fig. 2.

We presented a web-based recommender system which generates recommendations of web users, by considering the sequential information that exists in their usage patterns of web pages

Input: 5000 X 6 MSNBC dataset, where a number of users are 5000, and each column contains page category number varying from 1 to 17.

1. Apply fuzzy c-mean clustering on MSNBC dataset to obtain soft clusters.
2. Select top 'N' clusters among all clusters depending on the average value of cluster centers obtained from equation 1.
3. Select the target user and find all users similar to the target user and generate matrix MAT.
4. Obtain values of matrix 'X' using the equation 2.
5. Similarly, obtain values of matrix 'Z' and 'G' using equations 3 and 4.
6. Finally, calculate a weight for each page category using equation 5, and determine values of matrix page which contain predicted page for each user.
7. Calculate accuracy of the predicted result using Equation 6.

Output: Similar users for the target user. It gives two matrices:
Center Matrix: It contains average value of columns
Partition matrix: it contains a contribution of each user in each cluster.

Fig. 2 A high-level description of the pseudocode of the proposed model

in MSNBC dataset. The proposed system considered both the content as well as the sequence of a visit during clustering to form groups of users. The fuzzy c-mean clustering procedure was employed to produce soft clusters among users and nominated limited top clusters for processing which depended on the average value of cluster centers. We computed weights of each considered web page category and predicted top page recommendation for the target user and calculated the accuracy of prediction with existing MSNBC dataset. We conducted experiments on a large dataset of MSNBC which contained 5000 users with six page visited data and predict the seventh page which has to be visited. Our proposed system was compared with state of art methods such as WRS model [41], WebPUM [24], Modified K-means [45], Multivariate [9], SemSig [20], Weighted K-means [53], Binary data clustering [16] and Neuro-Fuzzy [50]. The experiment results displayed that our proposed model performed with better results, and it can be applied for acquiring user's social information, pattern, personality and behavior over web navigation in a web-based recommender system.

4 Results and discussions

4.1 Dataset

In this paper, a real-world dataset of MNSBC is used in the experiments. The dataset consists of 5000 user entries with 6 entries per user. The dataset is distributed into two parts as follows: training data = 60 % and testing data = 40 %. The number of clusters used = 100 and number

mat | result

464x6 double

	1	2	3	4	5	6	7
1	6	9	4	10	3	10	
2	6	10	1	7	1	6	
3	6	9	1	7	1	6	
4	1	12	7	1	4	14	
5	9	10	1	8	1	9	
6	1	10	6	5	2	11	
7	1	14	1	4	7	4	

Fig. 3 Recommendation without sequential information without seventh users

of users in dataset = 5000. Entries for each user are a sequence of numbers from 1 to 17, representing browsed page history for the user. We applied our proposed model on 6 entries per user to predict the 7th page, which is to be browsed by the user. The results obtained are then checked with 7th column entry of the MSNBC dataset and accuracy is calculated by comparing values of both. For the experimental setup, we used a machine having a fourth generation Intel Core I5 processor coupled with 6GB RAM.

4.2 Results

Clearly, it can be observed from the experimentation results that our proposed model was three times efficient than WRS model [41] and also delivered proficient results when compared to other existing systems.

In Fig. 3, an input matrix for first seven users is presented without the sequential information. We need to find a 7th entry for the user. The data contains page category numbers that user browsed in the past and with the help of those, we will predict 7th-page category that user is more likely to open. In Fig. 4, output matrix for first seven users is presented with sequential information.

Table 1 shows the comparison between various existing systems. The accuracy of our proposed model is far better than the earlier proposed systems. The accuracy of our proposed model is nearly 33 % that is 1 out of every 3 predictions is correct while the accuracy of the previous system was 1 hit and 9 miss. Time should be overlooked as the proposed model provides around three times accuracy than existing method such as WRS model. We have considered a range of 20 to 32 clusters. Table 1 and Fig. 5 show the comparison among different systems with our proposed model. It clearly indicates that the accuracy of the proposed model is much better than already existing systems such as WRS model, WebPUM, Modified K-means, Multivariate, SemSig, Weighted K-means, Binary data clustering, Neuro-Fuzzy, XFCM and C-means & COG.

For the M = 20, we compared our model with other existing methods and found that WebPUM has accuracy as 22.322 as it was based on the graph partition algorithms to detect patterns of web pages. Modified K-means acquired 27.642 % of accuracy, as it was based on the fact that which computed the distances between the similar sessions of web access. In the multivariate method, the major focus was on to analyze the properties and temporal behavior of content and material of the internet pages; the accuracy percentage was retrieved as 30.274. The SemSig was based on the fact of entity linking on web pages, for M = 20 this system delivered the accuracy percentage as 29.543. We also evaluated a system which was based on the Weighted K-means, in which quality of web page recommendation was enhanced with the utilization of a combination of user profiles and mean square residue. The Weighted K-means system gave accuracy percentage as 28.285. We also evaluated a system which was based on the binary data clustering which handled the binary session and formed the fixed numbers of

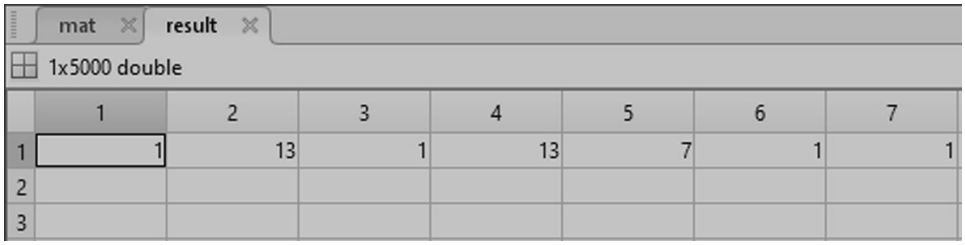


Fig. 4 Recommendation with sequential information of with the seventh user

Table 1 The comparisons with the various systems on a different number of clusters

Methods Accuracy (%) / No. of clusters(M)	M = 20	M = 21	M = 22	M = 32
WRS Model [41]	10.260	10.821	11.295	11.062
WebPUM [24]	22.322	22.872	23.364	23.964
Modified K-means [45]	27.642	27.537	27.923	28.769
Multivariate [9]	30.274	30.862	31.883	31.896
SemSig [20]	29.543	29.784	30.324	30.867
Weighted K-means [53]	28.285	28.384	28.968	29.278
Binary data clustering [16]	28.926	29.272	29.475	29.847
Neuro-Fuzzy [50]	31.537	31.496	31.865	32.245
XFCM [54]	32.672	32.837	32.973	33.154
C-means & COG [33]	31.453	31.839	32.454	32.892
Proposed Model	32.760	32.920	33.160	33.100

clusters by utilizing clustering algorithm. Binary data clustering based system provided the accuracy percentage as 28.926. A Neuro-Fuzzy based system was applied on the web recommender system which resulted in the accuracy percentage as 31.537. The exponential fuzzy clustering (XFCM) was based on clustering objective with exponential mathematical equation and delivered the accuracy percentage as 32.672 at M = 20. C-means & COG based system was evaluated and delivered the accuracy percentage as 31.453 as this system was based on the mixture of Fuzzy c-mean and center of gravity. In Table 2, we have also compared the performance of various existing systems with respect to time for the MSNBC dataset.

5 Conclusion and future work

Web recommendation has attracted much attention from both academic and industry. In this article, we have suggested a novel model to expect a user's succeeding web page visit. The experiments have been accomplished on the MSNBC dataset which is web navigation dataset.

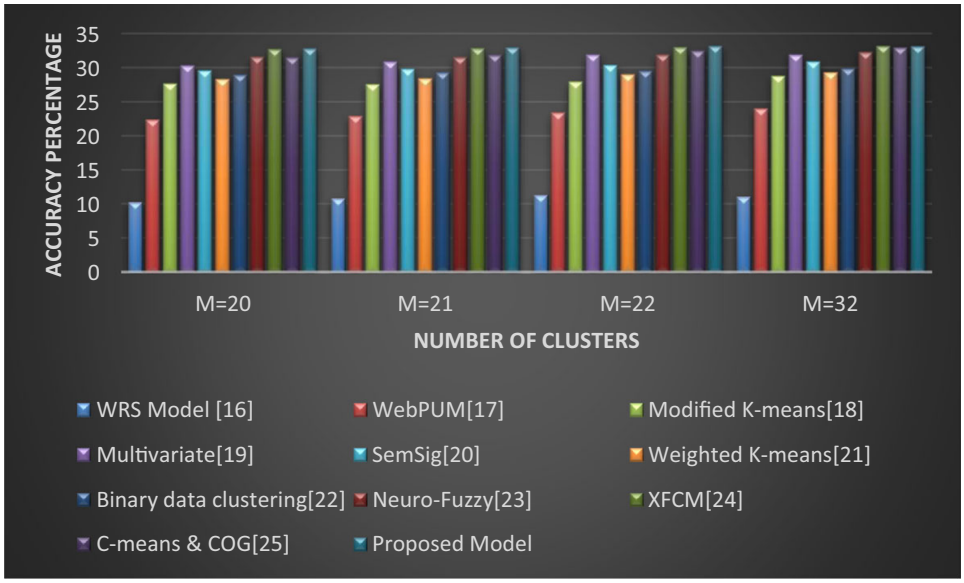


Fig. 5 Comparison with various existing systems with proposed model

Table 2 Comparision of speed for different systems for MSNBC dataset

Method/System	Time (in seconds)
WRS Model [41]	477
WebPUM [24]	498
Modified K-means [45]	277
Multivariate [9]	456
SemSig [20]	363
Weighted K-means [53]	282
Binary data clustering [16]	389
Neuro-Fuzzy [50]	410
XFCM [54]	428
C-means & COG [33]	415
Proposed Model	402

The outcomes have demonstrated the practicability of our proposed model. The subsequent visit of a user can provide useful evidence about their likes and perception. This statistics can be explored and utilized for projecting the desired category or product to the user. The probability of purchase for e-commerce companies can be enhanced, which in turn will growth the expected revenue for e-commerce organizations. The best usage of proposed system in electronic commerce (e-commerce) can be understood as follows: suppose a person wants to buy a television and search on Google but he has not checked it over any of the e-commerce websites. In that case with the help of proposed system e-commerce websites can come to know about what user is interested in buying and what should he be recommended even when the user is not explicitly looking for the product on their website also. For new websites, the proposed system is of great significance, as being new websites people will not be more likely to use them due to trust and reliability issues. However with the suggested system website owners can track that what user is going to purchase and can provide related recommendations to the user without their explicitly searching over their website. Our future work will be focused on inclusion of privacy, trust and social networks with the utilization of hybrid intelligent systems.

References

1. Baraldi A, Blonda P (1999) A survey of fuzzy clustering algorithms for pattern recognition. I. IEEE Trans Syst Man Cybern B Cybern 29:778–785
2. Barragáns-Martínez B, Costa-Montenegro E, Juncal-Martínez J (2015) Developing a recommender system in a consumer electronic device. Expert Syst Appl 42:4216–4228
3. Bezdek JC, Ehrlich R, Full W (1984) FCM: the fuzzy *c*-means clustering algorithm. Comput Geosci 10: 191–203
4. Bilge A, Gunes I, Polat H (2014) Robustness analysis of privacy-preserving model-based recommendation schemes. Expert Syst Appl 41:3671–3681
5. Bobadilla J, Ortega F, Hernando A, Gutiérrez A (2013) Recommender systems survey. Knowledge-Based Syst 46:109–132
6. Boratto L, Carta S (2014) The rating prediction task in a group recommender system that automatically detects groups: architectures, algorithms, and performance evaluation. J Intell Inf Syst:1–25

7. Bouadjenek M, Hacid H, Bouzeghoub M, Vakali A (2016) PerSaDoR: Personalized social document representation for improving web search. Inf Sci (Ny) 369:614–633. doi:10.1016/j.ins.2016.07.046
8. Bouras C, Tsogkas V (2014) Improving news articles recommendations via user clustering. Int J Mach Learn Cybern 1–15. doi:10.1007/s13042-014-0316-3
9. Calzarossa MC, Pavia FI, Tessera D (2014) Multivariate analysis of web content changes. In: 2014 IEEE/ACS 11th Int. Conf. Comput. Syst. Appl. IEEE, pp 699–706
10. Cannon RL, Dave JV, Bezdek JC (1986) Efficient implementation of the fuzzy c-means clustering algorithms. IEEE Trans Pattern Anal Mach Intell 8:248–255
11. Cao J, Li Q, Ji Y et al (2016) Detection of forwarding-based malicious URLs in online social networks. Int J Parallel Prog 44:163–180
12. Cobo MJ, Martínez MA, Gutiérrez-Salcedo M, et al. (2015) 25years at knowledge-based systems: a bibliometric analysis. Knowledge-Based Syst
13. Conforti R, de Leoni M, La Rosa M et al (2015) A recommendation system for predicting risks across multiple business process instances. Decis Support Syst 69:1–19
14. Dixit VS, Bhatia SK (2015) Refinement and evaluation of web session cluster quality. Int J Syst Assur Eng Manag 6:373–389
15. Dooms S, Audenaert P, Fostier J et al (2014) In-memory, distributed content-based recommender system. J Intell Inf Syst 42:645–669
16. Forsati R, Moayedikia A, Shamsfard M (2015) An effective web page recommender using binary data clustering. Inf Retr J 18:167–214
17. Gao Y, Wang F, Luan H, Chua T-S (2014) Brand data gathering from live social media streams. Icmr:169–176
18. Gao Y, Zhao S, Yang Y, Chua T (2015) Multimedia social event detection in microblog. In: 21st Int. Conf. MMM 2015, Sydney, Aust. January 5-7, 2015. pp 269–281
19. García MDMR, García-Nieto J, Aldana-Montes JF (2016) An ontology-based data integration approach for web analytics in e-commerce. Expert Syst Appl 63:20–34
20. Guo Z (2014) Entity linking with a unified semantic representation. In: Int. World Wide Web Conf. Committee. ACM, pp 1305–1309
21. Hasija H, Katarya R (2014) Secure code assignment to alphabets using modified ant colony optimization along with compression. Proc 2014 Int Conf Adv Comput Commun informatics, ICACCI 2014:175–181
22. Hoic-Bozic N, Holenko Dlab M, Mornar V (2015) Recommedner System and Web 2.0 Tools to Enhance Blended Learning Model. IEEE Trans Educ in press:39–44
23. Hu X, Zeng A, Shang M-S (2016) Recommendation in evolving online networks. Eur Phys J B 89:46
24. Jalali M, Mustapha N, Sulaiman MN, Mamat A (2010) WebPUM: a web-based recommendation system to predict user future movements. Expert Syst Appl 37:6201–6212
25. Javari A, Jalili M (2015) A probabilistic model to resolve diversity–accuracy challenge of recommendation systems. Knowl Inf Syst 44:609–627. doi:10.1007/s10115-014-0779-2
26. Ji K, Sun R, Shu W, Li X (2015) Next-song recommendation with temporal dynamics. Knowledge-Based Syst 88:134–143
27. Jiménez P, Corchuelo R (2016) On learning web information extraction rules with TANGO. Inf Syst 62:74–103
28. Katarya R, Jain I, Hasija H (2014) An interactive interface for instilling trust and providing diverse recommendations. In: IEEE Int. Conf. Comput. Commun. Technol. ICCCT-2014. pp 17–22. doi:10.1109/ICCCT.2014.7001463
29. Katarya R, Verma OP (2015) Restaurant recommender system based on psychographic and demographic factors in mobile environment. In: IEEE Int. Conf. Green Comput. Internet Things 2015. pp 907–912. doi:10.1109/ICGCIoT.2015.7380592
30. Katarya R, Verma OP (2016a) A collaborative recommender system enhanced with particle swarm optimization technique. Multimed Tools Appl 75:1–15
31. Katarya R, Verma OP (2016b) Recent developments in affective recommender systems. Phys A Stat Mech its Appl 461:182–190
32. Katarya R, Verma OP, Jain I (2013) User behaviour analysis in context-aware recommender system using hybrid filtering approach. Proc - 4th IEEE Int Conf Comput Commun Technol ICCCT 2013:222–227
33. Koohi H, Kiani K (2016) User based collaborative filtering using fuzzy C-means. Measurement 91:134–139
34. Krishnaraju V, Mathew SK, Sugumaran V (2015) Web personalization for user acceptance of technology: an empirical investigation of E-government services. Inf Syst Front 18:579–595
35. Laclau C, Nadif M (2016) Hard and fuzzy diagonal co-clustering for document-term partitioning. Neurocomputing 193:133–147
36. Li B, Zhu X, Li R, Zhang C (2014) Rating knowledge sharing in cross-domain collaborative filtering. IEEE Trans Cybern 45:1–15
37. Liu D, Zhang Z, Guo X (2016) Web mining based on one-dimensional Kohonen's algorithm: analysis of social media websites. Neural Comput Appl 1–5. doi:10.1007/s00521-016-2410-9

38. Lorentzen DG (2014) Webometrics benefitting from web mining? An investigation of methods and applications of two research fields. Scientometrics 99:409–445
39. Lotfy HMS, Khamis SMS, Aboghazalah MM (2015) Multi-agents and learning: implications for WebUsage mining. J Adv Res 7:285–295. doi:10.1016/j.jare.2015.06.005
40. Malarvizhi SP, Sathiyabhama B (2016) Frequent pagesets from web log by enhanced weighted association rule mining. Cluster Comput 19:269–277
41. Mishra R, Kumar P, Bhasker B (2015) A web recommendation system considering sequential information. Decis Support Syst 75:1–10
42. Moreno MN, Segrera S, López VF et al (2015) Web mining based framework for solving usual problems in recommender systems. A case study for movies' Recommendation. Neurocomputing 176:72–80
43. Nguyen TTS, Lu HY, Lu J (2014) Web-page recommendation based on web usage and domain knowledge. IEEE Trans Knowl Data Eng 26:2574–2587
44. Pàmies-Estrems D, Castellà-Roca J, Viejo A (2016) Working at the web search engine side to generate privacy-preserving user profiles. Expert Syst Appl 64:523–535
45. Poornalatha G, Raghavendra PS (2011) Web user session clustering using modified K-means algorithm. In: Adv. Comput. Commun. pp 243–252. doi:10.1007/978-3-642-22714-1_26
46. Ravi K, Ravi V (2015) A survey on opinion mining and sentiment analysis: tasks, approaches and applications. Knowledge-Based Syst 89:14–46. doi:10.1016/j.knosys.2015.06.015
47. Ristoski P, Paulheim H (2016) Semantic web in data mining and knowledge discovery: a comprehensive survey. Web Semant Sci Serv Agents World Wide Web 36:1–22
48. Santoro M, Nativi S, Mazzetti P (2016) Contributing to the GEO model web implementation: a brokering service for business processes. Environ Model Softw 84:18–34
49. Schmachtenberg M, Strufe T, Paulheim H (2014) Enhancing a location-based recommendation system by enrichment with structured data from the web. In: Proc. 4th Int. Conf. Web Intell. Min. Semant. - WIMS '14. pp 1–12. doi:10.1145/2611040.2611080
50. Shivaprasad G, Reddy NVS, Acharya UD, Aithal PK (2015) Neuro-fuzzy based hybrid model for web usage mining. Procedia Comput Sci 54:327–334
51. Sobitha Ahila S, Shunmuganathan KL (2016) Role of agent Technology in Web Usage Mining: homomorphic encryption based recommendation for E-commerce applications. Wirel Pers Commun 87:499–512
52. Thanh T, Nguyen S, Lu HY, Lu J (2014) Web-page recommendation based on web usage and domain knowledge. IEEE Trans Knowl Data Eng 26:2574–2587
53. Thiyagarajan R, Thangavel K, Rathipriya R (2014) Recommendation of web pages using weighted K-means clustering. Int J Comput Appl 86:44–48
54. Treerattanapitak K, Jaruskulchai C (2012) Exponential fuzzy C-means for collaborative filtering. J Comput Sci Technol 27:567–576
55. Verma OP, Katarya R, Bhargava V, Maheshwari N (2011) Use of semantic web in enabling desktop based knowledge management. ICECT 2011–2011 3rd Int Conf Electron Comput Technol 5:190–193
56. Wang F, Qi S, Gao G et al (2016) Logo information recognition in large-scale social media data. Multimed Syst 22:63–73
57. Wu X, Zhu X, Wu G-Q, Ding W (2014) Data mining with big data. IEEE Trans Knowl Data Eng 26:97–107
58. Xie X, Wang B (2016) Web page recommendation via twofold clustering: considering user behavior and topic relation. Neural Comput Appl 1–9. doi:10.1007/s00521-016-2444-z
59. Yang Y, Yang Y, Shen HT et al (2013) Discriminative nonnegative spectral clustering with out-of-sample extension. IEEE Trans Knowl Data Eng 25:1760–1771
60. Yang Y, Ma Z, Yang Y et al (2015) Multitask spectral clustering by exploring intertask correlation. IEEE Trans Cybern 45:1069–1080
61. Yera R, Castro J, Martínez L (2016) A fuzzy model for managing natural noise in recommender systems. Appl Soft Comput 40:187–198
62. Yu C, Huang L (2016) CluCF: a clustering CF algorithm to address data sparsity problem. Serv Oriented Comput Appl 1–13. doi:10.1007/s11761-016-0191-8
63. Yu X, Liu Y, Huang X, An A (2012) Mining online reviews for predicting sales performance: a case study in the movie domain. IEEE Trans Knowl Data Eng 24:720–734
64. Zhang H-R, Min F (2016) Three-way recommender systems based on random forests. Knowledge-Based Syst 91:275–286
65. Zhang Z, Fang H, Wang H (2016) A new MI-based visualization aided validation index for mining big longitudinal web trial data. IEEE Access 4:2272–2280. doi:10.1109/ACCESS.2016.2569074
66. Zhao WX, Li S, He Y et al (2016) Connecting social media to E-commerce: cold-start product recommendation using microblogging information. IEEE Trans Knowl Data Eng 28:1147–1159
67. Zhu K, Wu R, Ying L, Srikant R (2014) Collaborative filtering with information-rich and information-sparse entities. Mach Learn:177–203



Rahul Katarya is working as an Assistant Professor in Department of Computer Science & Engineering in Delhi Technological University, Delhi India. His research interests include Big Data & prediction, Web Mining Social Networks Recommender systems Personalization, Knowledge discovery, Computational intelligence, Multimedia, Human behaviour, and business intelligence.



Dr. Om Prakash Verma is HOD and Professor in Department of Computer Science & Engineering in Delhi Technological University, Delhi India. His research interests include signal processing image processing soft computing evolutionary computing nature inspired swarm algorithm.

Advances in Economics and Business Management (AEBM)
p-ISSN: 2394-1545; e-ISSN: 2394-1553; Volume 3, Issue 1; January-March, 2016, pp. 1-6
© Krishi Sanskriti Publications
http://www.krishisanskriti.org/Publication.html

An Exploration of Factors Affecting M-commerce Adoption in India

Khushbu Madan[1] and Rajan Yadav[2]

[1,2]Delhi School of Management, Delhi Technological University
E-mail: [1]khushbu.madan@gmail.com, [2]rajan.yadav.dsm@gmail.com

Abstract
Purpose: *The increasing penetration of mobile phones along with the changing lifestyle of people has given mobile phone the status of a lifestyle device from being a mere tool to connect. This has led to development of numerous mobile applications enabling consumers to transact over mobile devices, giving rise to a new market of mobile commerce popularly known as m-commerce. However, m-commerce is still in its initial stage. Various studies have been conducted around the world to determine the factors that inhibit m-commerce adoption by consumers in different countries but not much has been done in the Indian context. The purpose of this study is to determine and examine the impact of various factors that affect m-commerce adoption intention of Indian consumers.*

Methodology*: Research model was developed borrowing constructs from the technology acceptance model and TAM2 along with two additional constructs based on review of available literature. An online survey was administered on 170 Indian respondents. Multiple Regression & Factor analysis were then applied to analyze the data.*

Findings*: The results indicates that m-commerce Adoption Intention by Indian consumers is affected by Perceived Usefulness (p value=.000), Perceived Risk (p value=0.000), Social Influence (p value=0.000) and Variety of Services (p value=0.004), whereas, Perceived Ease of Use (p value=0.905) is found to be statistically insignificant.*

Implications*: The results will provide service providers & marketers of m-commerce services, a better ground for developing suitable marketing strategies.*

Keywords*: M-commerce, Perceived Usefulness, Perceived Ease of Use, Perceived Risk, Social Influence and Variety of Services.*

1. INTRODUCTION:

The increase in overall penetration of mobile phones along with the changing preferences of people has given mobile phone the status of a lifestyle device from being a mere tool to connect. This has led marketers to develop numerous mobile based applications enabling consumers to enter into transactions using their mobile devices, giving rise to a new market of mobile commerce popularly known as m-commerce. The advancement in the internet technologies (2G, 3G) as well as the mobile communication industry has further increased its scope. The functionality of mobile phones has gone far beyond the function of merely connecting people to a host of other functions such as internet surfing, entertainment, online shopping and the like [22]. M-commerce includes all such activities that precede and follow the actual commercial transaction. [1,18]

The term “m-commerce” was defined for the first time in 1997 by Kevin Duffey as "the delivery of electronic commerce capabilities directly into the consumer’s hand, anywhere, via wireless technology". Since then numerous researchers have defined m-commerce in many ways. Most researchers explained it as any monetary transaction conducted via a mobile telecommunications network. [14, 10, 20]

M-commerce involves a new set of services, business models and related technologies that are quite different from those involved in traditional e-commerce. It may be considered as a step ahead of e-commerce. E-commerce may be described as exchange of good, services, information or any payment made using electronic medium over telecommunication networks. [1, 18] M-commerce offers an additional advantage of mobility in combination with the advantages offered by e-commerce. It provides mobile devices such as smart phones, tablets, laptops and PDAs, the ability to transact i.e. to buy and sell goods online. [3]

The unprecedented growth in the mobile technology and increasing inclination of consumers towards high end mobile devices such as smart phones, has given marketers an entirely new arena to exploit in the form of m-commerce market. Due to easy availability of mobile phones ranging from high priced to low priced models, along with affordable prices of mobile internet connections; m-commerce has the ability to tap the potential of market that was earlier unreached through the existing chains of e-commerce. However, m- commerce is still in its early stage. Numerous studies show that so far m-commerce services have failed in appealing to the hearts and minds of its potential users. Moreover, the development of m-commerce in different countries is significantly different. This difference may be attributed to various social, infrastructural & cultural factors such as varying range of m-commerce services offered, mobile telecommunication infrastructure,

social influence and cultural environment of m-commerce consumers as well as the marketing strategies utilised by service providers.

Previous studies have indicated fair success of m-commerce in developing economies like china, Malaysia, Kenya & Philippines as compared to the developed nations. This may be attributed to the fact that in developing nations mobile phones are more widely penetrated in comparison to financial services such as banking, insurance as well as trading services. India being a developing nation and having mobile phone penetration of almost 76% (tele-density of 76.36 percent, TRAI Data, August 2014), has a great potential for m-commerce services. In order to support m-commerce in India, The Reserve Bank of India has also issued guidelines for mobile banking transactions in October, 2008. However actual adoption is still low. This shows that there exist certain factors hindering its adoption by Indian consumers. The purpose of this study is to identify such factors and examine their impact on the overall m-commerce adoption intention.

This study is conducted in two parts. The first part deals with the identification of important factors affecting m-commerce adoption through reviewing literature available on research related to m-commerce adoption and adoption intention of similar technologies conducted in different parts of the world. The second part includes an empirical study conducted to analyse the impact of the factors identified on the overall m-commerce Adoption Intention (AI) of Indian consumers by applying statistical techniques such as Multiple Regression and Factor Analysis on the data collected. The findings can help marketers and service providers in designing marketing interventions as well as appropriate mobile applications incorporating the aspects of factors affecting adoption intention of their prospective consumers, thereby, increasing their inclination towards adoption and usage of new mobile based services. The results are further helpful to managers in predicting factors that might affect adoption intention of some new related technology introduced in future.

2. LITERATURE REVIEW:

2.1 M-commerce

The term “m-commerce” was used for the first time in 1997, since then numerous researchers have defined m-commerce in many ways. Most researchers define m-commerce to be any monetary transaction (i.e. buying and selling of goods and services) conducted using mobile devices over mobile telecommunication network. [14, 10, 16, 8] Another definition of m-commerce similar to this is ‘‘Any transaction, involving the transfer of ownership or rights to use goods and services, which is initiated and/or completed by using mobiles access to computer-mediated networks with the help of mobile devices’’[20].

M-commerce from a broader viewpoint can be defined as a wide range of business activities that precede and follow the actual transaction of sale. [1, 18] It includes all such activities related to a potential commercial transaction conducted over a wireless network via some mobile handheld device such as smart phone, laptop, palmtop or tablet. [19] It involves an emerging set of services and applications accessible by people from their internet enabled mobile devices. [17]

Another view which considers m-commerce to be an extension or a step forward of e-commerce defines m-commerce as “an e-commerce for users on the move” [24]. The real value of m-commerce arises from its ability to enable internet usage on any time and any where basis [24]. M-commerce can be distinguished from e-commerce on the basis of two main dimensions “mobility” and “locatability” on which it has an advantage over e-commerce. [10]

M-Commerce and e-commerce share common fundamental principles of business transaction i.e. transacting via electronic medium. However, the difference exists in the mode of communication (wired Local Area Network in case of E-Commerce & wireless Network in case of M-commerce), the types of Internet access devices (wired devices in case of e-commerce such as desktops, laptops, etc. & wireless devices in case of m-commerce such as mobile phones, PDAs, etc.) the development languages and communication protocols (HTML in case of e-commerce & WML or cHTML in case of m-commerce), as well as technologies supporting each environment. [5]

2. 2 Theoretical background and Research Model:

Numerous researchers have developed various models to explain technology adoption intention of consumers from time to time. Technology Adoption Model (TAM) [9] is one of the most widely accepted model. The two major dimensions of this model are Perceived usefulness (PU) and Perceived Ease of Use (PEOU). Many researchers have adapted this model to explain adoption intention of similar technologies. [4, 29, 6, 30, 7] Extension of this model, TAM2 included Social Influence (SI) as an important construct along with PU and PEOU [23]. The Unified Theory of Acceptance and Use of Technology (UTAUT) is another model which explains employee behaviour towards acceptance of organisation information system. [25] From the review of such existing models, few of the most popularly accepted and investigated factors are identified for the purpose of this study.

2.2.1 Perceived usefulness (PU):

It refers to the extent to which a user considers that using a new product or new technology is useful in performing tasks in their daily life. PU is another construct in the Technology Adoption Model [9]. PU is defined as the degree to which a person believes that using a particular system would enhance his or her job performance. [9] Extended models such as TAM2 [23] as well as, TAM3 [26], also consider this factor. PU is also considered by the UTAUT model as a significant factor affecting adoption intention [25]. Other than these

models, various researchers have also considered the positive role of this factor in influencing consumer's adoption intention for m-commerce. [4, 6, 22] Hence, this study hypothesizes that:

H1: Perceived Usefulness (PU) has a positive influence on consumer's M-commerce Adoption Intention (AI)

2.2.2 Perceived ease of use (PEOU):

PEOU refers to the extent to which a new product should be useful and is easy enough to use for consumers to intend to use the product. It is one of the two constructs given in Technology Acceptance Model (TAM) [9]. PEOU is defined as the degree to which a person believes that using a particular system would be free of effort. It is also included in TAM2 model, an extension of TAM [23] as well as TAM3 [26]. The UTAUT model for organisation information system, also consider PEOU as an important factor to be considered. [25] Since 1989 till today numerous researchers have considered PEOU as an important factor having a positive influence on m-commerce adoption intention of the consumers in different countries. [13, 6, 22] Hence, his study hypothesizes that:

H2: Perceived Ease of Use (PEOU) has a positive influence on consumer's M-commerce Adoption Intention (AI).

2.2.3 Perceived risk (PR):

Perceived risk refers to financial, social, physical, psychological, time risk and product associated risks, consumers undertake while making transactions online. [28] Important personal information is usually stored on users' mobile phones, and therefore security and privacy risks involved in m-commerce transactions can be quite high. [7] M-commerce involves undertaking financial transaction over mobile devices, which is perceived to be risky by the users. Numerous researchers such have considered this factor to be significant in explaining m-commerce adoption rate. [13, 12, 30, 22, 6]

The degree of trust consumers have on m-commerce application providers with respect to their reputation, security, and privacy policies followed by them, also influences m-commerce adoption intention. [7] Moreover, lack of face-to face interactions, clear regulations, and reliable information that can be accessed by the vendors, makes it difficult for users to trust m-commerce sufficiently to subscribe to it. [21, 6] Trust was considered to be a major factor in determining m-commerce adoption intention by other researchers as well. [6, 30, 7] Since Perceived Risk and Trust are closely related to each other, hence for the purpose of this study, Trust factor has also been included while measuring Perceived Risk. The study hypothesizes that:

H3: Perceived Risk (PR) has a negative influence on consumer's M-commerce Adoption Intention (AI).

2.2.4 Variety of services (VOS):

Although m-commerce have many applications, but the variety of services offered by it might not be comparable to services offered by e-commerce websites. [6] Many previous researchers were of the opinion that the variety of m-commerce services available also affects m-commerce adoption intention. [2, 7] It was found that consumers' interest in services related to m-mailing and routine banking services was remarkably high as compared to other variety of services. [2] and the variety of services offered to the consumers do affect m-commerce adoption in a positive manner. [7] Hence, this study hypothesizes that:

H4: Variety of Services (VOS) has a positive influence on consumer's M-commerce Adoption Intention (AI).

2.2.5 Social influence (SI):

Social influence was defined as the degree to which an individual perceives how important others believe that he or she should use the new system. [25] It relates to the extent to which decision to use a product or service is influenced by the opinions of family, relatives, or friends. [15] This construct has been widely considered by various researchers to determine usage intention of similar technologies related to internet, e-commerce, mobile banking and the like. [13; 27] People exploit online banking is because they are encouraged by people surrounding them to accept and utilize online banking. [22] Existing models explaining usage intention of similar technologies such as TAM2 [23] and UTAUT model also include Social Influence as an important construct of the model. Other researchers have also acknowledged SI to be an important factor having a positive influence in on m-commerce adoption. [11;6] Hence, this study hypothesizes that:

H5: Social Influence (SI) has a positive influence on consumer's M-commerce Adoption Intention *(AI)*

3. PROPOSED RESEARCH MODEL:

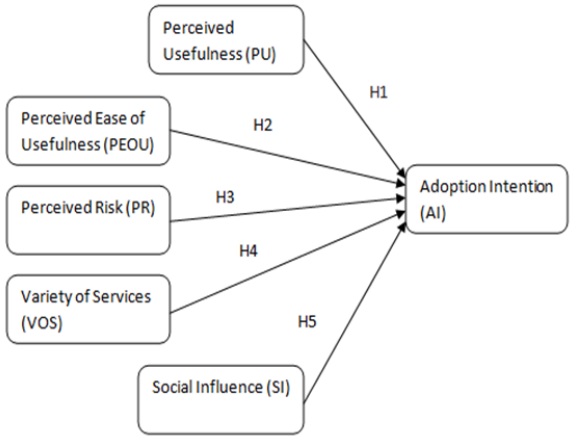


Fig. 1: Proposed Model

4. RESEARCH METHODOLOGY:

4.1. Measures of the construct:

For the purpose of this study a questionnaire was developed comprising of 5 major constructs namely Perceived Usefulness, Perceived Ease of Use, Perceived Risk, Variety of Services and Social Influence. Items selected for each of the constructs were adapted from previous studies to ensure content validity. All the questions related to independent and dependent variables, were surveyed on a Likert Scale ranging from 1 (as strongly disagree) to 5 (as strongly agree).

4.2. Data Collection and Sampling:

A sample of 170 Indian respondents was collected with the help of the developed questionnaire. Questionnaire was circulated online among students as well as working professionals. The demographics of the sample collected may be summarised as follows:

In the sample of 170 respondents almost 71% (120) were less than 30 years of age, 21% (36) were between 30 years to 45 years and the remaining 8%(14) respondents were above the age of 45 years. Almost 79%(134) of them were males and 21%(36) were females. 34%(58) of them were having a family income of less than Rs. 75,000, 30%(51) had a family income ranging from Rs. 75,001 to Rs. 1,50,000 and 36%(61) were having family income above Rs. 1,50,000.

4.3 Data Analysis and Results:

Multiple Regression Techniques were applied on the data collected in order to test the hypothesis proposed in this study. Perceived Usefulness (PU), Perceived Ease of Use (PEOU), Perceived Risk (PR), Variety of Services (VOS) and Social Influence (SI) were considered to be independent factors affecting the dependent factor which is Adoption Intention (AI) in this case.

The following tables were generated:

Table 1: Mean and Standard Deviation of PU, PEOU, PR, VOS & SI Descriptive Statistics

	Mean	Std. Deviation	N
What is your intention to adopt Mobile Commerce?	3.66	.986	170
PEOUavg	4.02	.800	170
PUavg	3.75	.897	170
PRavg	3.53	.960	170
VOSavg	3.71	.895	170
SIavg	2.75	1.138	170

Table 2: R square & Adjusted R square Values
Model Summary

Model	R	R Square	Adjusted R Square	Std. Error of the Estimate
1	.784a	.614	.603	.621
a. Predictors: (Constant), SIavg, PEOUavg, PRavg, PUavg, VOSavg				

The coefficient of R2 is 0.614 in the above table, which indicates that all the independent variables i.e. PU, PEOU, PR, VOS & SI account for 61.4% of the variance in m-commerce Adoption Intention (AI).

Table 3: ANOVAa

Model		Sum of Squares	Df	Mean Square	F	Sig.
1	Regression	100.898	5	20.180	52.270	.000b
	Residual	63.314	164	.386		
	Total	164.212	169			
a. Dependent Variable: What is your intention to adopt Mobile Commerce?						
b. Predictors: (Constant), SIavg, PEOUavg, PRavg, PUavg, VOSavg						

Table 4: p-values for PU, PEOU, PR, VOS & SI Coefficientsa

Model		Unstandardized Coefficients		Standardized Coefficients	t	Sig.	Collinearity Statistics	
		B	Std. Error	Beta			Tolerance	VIF
1	(Constant)	.044	.264		.166	.868		
	PEOU	-.009	.080	-.008	-.119	.905	.562	1.780
	PU	.314	.076	.286	4.159	.000	.497	2.012
	PR	.304	.068	.296	4.484	.000	.539	1.855
	VOS	.244	.084	.222	2.892	.004	.401	2.497
	SI	.180	.045	.208	4.012	.000	.874	1.144
a. Dependent Variable: What is your intention to adopt Mobile Commerce?								

By observing the values of VIF from the above table we can conclude that there is no evidence of multicollinearity because the VIFs are within acceptable levels. Moreover, by observing the p-values of each factor in the sig. column, we can conclude that Perceived Usefulness (PU), Perceived Risk (PR), Variety of Services (VOS) as well as Social Influence (SI) are significant in explaining dependent variable i.e. Adoption Intention (AI) since p-value for these factors is less than 0.05.

This result supports hypothesis H2, H3, H4 & H5. The above table also shows that the p-value for Perceived Ease of Use (PEOU) is greater than 0.05, suggesting that PEOU is insignificant in explaining m-commerce Adoption Intention (AI) ruling out hypothesis H1.

5. DISCUSSIONS AND IMPLICATIONS:

The study indicates that factors such as Perceived Usefulness (PU) (p-value- 0.000), Variety of Services (VOS) (p-value-0.004) and Social Influence (SI) (p-value-0.000) have a positive influence on the m-commerce Adoption Intention of Indian consumers. Whereas, Perceived Risk (PR) (p-value-0.000) has a negative influence on the Adoption Intention and Perceived Ease of Use (PEOU) (p-value- 0.905) is found to be insignificant. The above findings can help marketers and service providers in designing marketing interventions as well as appropriate mobile applications incorporating the aspects of these factors affecting adoption intention of their prospective consumers. Hence, providing marketers with a way by which they can increase their consumer's inclination towards adoption and usage of new mobile based services. The study can be further extended by future researchers to include other important factors to the model used in this study and can be adapted to study adoption intention of other related technologies as well. Marketers can use the results as a basis for predicting factors that might influence adoption intention of some new future technology and can plan their entry strategies accordingly.

REFERENCES

[1] Adam, N. R., Dogramaci, O., Gangopadhyay, A., & Yesha, Y. (1998).*Electronic commerce: technical, business, and legal issues*. Prentice-Hall, Inc..

[2] Anckar, B. (2002). Motivators for adoption of mobile commerce: Findings from a national consumer survey. In *Proceedings of the International Conference on Decision Making and Decision Support in the Internet Age (DSIage 2002)* (pp. 4-7).

[3] Antovski, L., & Gusev, M. (2008). M-Commerce services. *Retrieved January*.

[4] Bax, S., & McGill, T. J. (2003). Predicting web page development success: An exploratory study.

[5] Coursaris, C., & Hassanein, K. (2002). Understanding m-commerce: a consumer-centric model. *Quarterly journal of electronic commerce*, *3*, 247-272.

[6] Chong, A. Y. L., Chan, F. T., & Ooi, K. B. (2012). Predicting consumer decisions to adopt mobile commerce: Cross country empirical examination between China and Malaysia. *Decision Support Systems*, *53*(1), 34-43.

[7] Chong, A. Y. L. (2013). A two-staged SEM-neural network approach for understanding and predicting the determinants of m-commerce adoption.*Expert Systems with Applications*, *40*(4), 1240-1247.

[8] Chong, A. Y. L. (2013). Predicting m-commerce adoption determinants: A neural network approach. *Expert Systems with Applications*, *40*(2), 523-530.

[9] Davis, F. D. (1989). Perceived usefulness, perceived ease of use, and user acceptance of information technology. *MIS quarterly*, 319-340.

[10] Dholakia, N., & Rask, M. (2002). Dynamic elements of emerging mobile portal strategies M-Commerce is all about personalization, permission and specification.

[11] Harris, P., Rettie, R., & Cheung, C. K. (2005). Adoption and usage of m-commerce: A cross-cultural comparison of Hong Kong and the United Kingdom. *Journal of Electronic Commerce Research*, *6*(3), 210-224.

[12] Islam, M. A., Khan, M. A., Ramayah, T., & Hossain, M. M. (2011). The adoption of mobile commerce service among employed mobile phone users in Bangladesh: self-efficacy as a moderator. *International Business Research*, *4*(2), p80.

[13] Kleijnen, M., De Ruyter, K., & Wetzels, M. (2004). Consumer adoption of wireless services: discovering the rules, while playing the game. *Journal of interactive marketing*, *18*(2), 51-61.

[14] Müller-Veerse, F. (1999). Mobile commerce report. *Durlacher Research Ltd*.

[15] Riquelme, H. E., & Rios, R. E. (2010). The moderating effect of gender in the adoption of mobile banking. *International Journal of Bank Marketing*, *28*(5), 328-341.

[16] Shuster, T. (2001). Pocket Internet and M-Commerce-(How) Will it Fly?.*February*, *1*, 2001.

[17] Sadeh, N. (2003). *M-commerce: technologies, services, and business models*. John Wiley & Sons.

[18] Turban,E., Lee,J., King,D., & Chung,HM. (2000). Electronic commerce: a managerial perspective. *Upper Saddle River, NJ: Prentice Hall*.

[19] Tarasewich, P., Nickerson, R. C., & Warkentin, M. (2002). Issues in mobile e-commerce. *Communications of the association for information systems*,*8*(1), 3.

[20] Tiwari, R., & Buse, S. (2007). The mobile commerce prospects: a strategic analysis of opportunities in the banking sector. *Hamburg: Hamburg University Press.*33.

[21] Tsu Wei, T., Marthandan, G., Yee-Loong Chong, A., Ooi, K. B., & Arumugam, S. (2009). What drives Malaysian m-commerce adoption? An empirical analysis. *Industrial Management & Data Systems*, *109*(3), 370-388.

[22] Thakur, R., & Srivastava, M. (2013). Customer usage intention of mobile commerce in India: an empirical study. *Journal of Indian Business Research*,*5*(1), 52-72.

[23] Venkatesh, V., & Davis, F. D. (2000). A 1theoretical extension of the technology acceptance model: Four longitudinal field studies. *Management science*, *46*(2), 186-204.

[24] Vittet-Philippe, P., & Navarro, J. M. (2000). Mobile e-business (m-commerce): State of play and implications for European enterprise policy.*European Commission Enterprise Directorate-General E-Business Report*,*3*(6).

[25] Venkatesh, V., Morris, M. G., Davis, G. B., & Davis, F. D. (2003). User acceptance of information technology: Toward a unified view. *MIS quarterly*, 425-478.

[26] Venkatesh, V., & Bala, H. (2008). Technology acceptance model 3 and a research agenda on interventions. *Decision sciences*, *39*(2), 273-315.

[27] Venkatesh, V., Thong, J., & Xu, X. (2012), "Consumer acceptance and use of information technology: Extending the unified theory of acceptance and use of technology", *MIS Quarterly*, Vol. 36, pp. 157–178.

[28] Wu, J. H., & Wang, S. C. (2005). What drives mobile commerce?: An empirical evaluation of the revised technology acceptance model.*Information & management*, *42*(5), 719-729.

[29] Yang, H., Liu, H., & Zhou, L. (2010). Predicting Chinese young consumers' acceptance of mobile advertising: a structural equation modeling approach.*Chinese Journal of Communication*, *3*(4), 435-452.

[30] Zhang, L., Zhu, J., & Liu, Q. (2012). A meta-analysis of mobile commerce adoption and the moderating effect of culture. *Computers in Human Behavior*, *28*(5), 1902-1911.

International Journal of Engineering Applied Sciences and Technology, 2016
Vol. 1, Issue 10, ISSN No. 2455-2143, Pages 5-8
Published Online August - September 2016 in IJEAST (http://www.ijeast.com)



ANAEROBIC TREATMENT OF DAIRY EFFLUENT- A STEP FOR ENERGY SAVING & GHG MITIGATION

Rakesh Mehrotra, A Trivedi
Dept. Of Civil Engineering,
Delhi Technological University,
Delhi-42

S. K. Mazumder
Former Professor,
Delhi College of Engineering,
Delhi

I. INTRODUCTION

India has emerged as one of the world's largest producer and fastest growing markets for milk and milk products with an annual growth of over 4-5%. As per FAO report (June 2016), India produced 146.3million tonnes of milk in 2014-15 fiscal, which comprised about 18-19% of global production. It is estimated that 148.15 million tonnes of milk will be produced in 2015-16 and a production of 155.2 million tonnes of milk in expected in 2016-17.India has a unique pattern of production, processing and marketing/consumption of milk, which is not comparable with any large milk producing country. Only a small part of milk produced in India is processed. The organized sector (large scale dairy plants) processes about 25-28 million tonnes annually, which is 18-20 per cent of the total production.(140)/ 3,800 LLPD of milk. According to NDDB and Crisil Research estimates, the country produces around **3,800 LLPD** of milk, accounting for a fifth of the global output. About 40 per cent of this is retained by producers (farmers) for household consumption; another 41 per cent share is with the unorganised segment. **Only 19 per cent** is procured, processed and sold through by organised dairies currently. **Organised sector is expected to grow to 25% of total production in** 2018-1050 LLPD of milk from 730 LLPD of milk.

(www.thehindubusinessline.com, 27 oct / 21 Dec 2015)
In the organized sector, there are over 1000 dairy plants in the cooperative, public and private sectors, registered with the Government of India and the State Governments. These plants are projected to process nearly 100 million litres of milk per day. (one single organization with brand AMUL has presently an aggregate national processing capacity of 28.0 million litres per day & expected to be 32 million litres per day by 2017). Most of the plants are in the co-operative or private sector. The processing capacity is expected to grow many fold through external investments in the future to cater to a large market in the Indian cities
The effluent is generated in dairy plant, from washing of cans/tankers, cleaning in place of process equipment(such as pasteurizers, separators, pipelines, chillers, vats, storage tank and silos, sachet filling machines),floor washings, spillages/leakages of milk/milk products, boiler blow down, softener regeneration water & bleed from the condenser etc.[1]
The volume and strength of the effluent generated in a dairy vary from plant to plant. The characteristics depend on the products and production level. Average characteristics as observed during the CPCB survey (1992)[2] are presented in the table 1

Table 1: combined wastewater characteristics of dairies.

Parameter	Milk Processing	Integrated Dairy
BOD_5	657-1,016	1,634-4,953
COD	1,341-2,195	3,800-8,631
SS	538-657	89-4,953
Nitrogen	50.25-126.2	96.32
pH	6.6-6.9	5.6-6.8
Oil and grease	-	280-2,207

- Note: all units are mg/l except pH.

It is estimated that the quantum of milk washed into the drain amounts to almost 2% of milk handled and the volume of wastewater generated is nearly 2 to 5 times of milk processed. Hence, Indian Dairies produce an aggregate 200-500 million litres of wastewater per day.

International Journal of Engineering Applied Sciences and Technology, 2016
Vol. 1, Issue 10, ISSN No. 2455-2143, Pages 5-8
Published Online August - September 2016 in IJEAST (http://www.ijeast.com)



The dairy plant waste water consists of highly biodegradable organic matter. Aerobic technologies of dairy waste treatment are the most commonly employed methods of treatment in India.[1]

It has been realized recently that anaerobic treatment offers several advantages over aerobic system in terms of energy, chemicals and sludge handling costs. High rate anaerobic systems are capable of removing 60-90% COD and have the advantage of capturing 80-90% of biochemical energy of organic matter in the form of biogas[4].

Energy being a scarce resource in India, therefore the energy analysis of waste water treatment system assumes great importance. In this study, comparisons have been made between aerobic & anaerobic treatment with a view to project the energy saving effected by adopting anaerobic process technology for treatment of dairy waste water in India & the resultant benefits in terms of GWP.

Due to high organic composition, dairy effluents are readily treated by biological process. The treatment process is determined by flow rate, waste strength and stream conditions. Methods used for treatment of dairy effluent include Physico-chemical treatment, Aerobic biological treatment such as Aerated lagoon, Conventional Activated Sludge Process, Extended Aeration, Trickling Filter, Oxidation Pond, Flocculating Algae-Bacterial System etc. ASP is the most common form of biological treatment employed for dairy effluent with COD removal efficiency of 90%. In aerobic systems the provision of oxygen for biochemical oxidation renders the system highly energy intensive.

Rapid advances in bioscience and recent developments in biochemical process engineering are having a substantial impact on the application of anaerobic biotechnology to waste treatment and energy production[5]. Anaerobic treatment units of following configurations have been successfully employed for treatment of dairy waste:

A. Anaerobic contact process

1. Upflow Anaerobic Sludge Blanket Process
2. Anaerobic Activated Sludge Process.
3. Anaerobic digester.

B. Submerged Media Anaerobic Bacteria

1. Anaerobic fixed film Bio-reactors (anaerobic filter)
2. Anaerobic Attached Film Expanded-Bed/ Fluidised-Bed Reactors.
3. Anaerobic Rotating Biological Contactor.

Anaerobic treatment alone does not suffice to reduce the BOD/COD to permissible levels. Therefore, additional Aerobic polishing is required before final disposal.

Table 2: Performance of Anaerobic attached growth bio-reactors on dairy waste

Type of Reactor	OLR Kg.COD/m^3d	Total COD removal, %	Waste strength g COD L^{-1}	Temp	Ref.
Anaerobic Attached Bed Bioreactors	<1.19	80	0.8-3.5	Ambient	6
Anaerobic Packed Bed Upflow Filter	1.348	88	1.203	35	7

Energy Considerations in Dairy wastewater treatment

Aerobic process are inherently energy intensive processes, whereas anaerobic processes are not only requiring lesser energy input but are capable of producing energy by way of biogas. Aerobic process for sewage treatment consume 12-15 kWh/person/year for Activated sludge process, 16-19 kWh/person/year for Oxidation ditch and 7-11 kWh/person/year for Trickling filter. Anaerobic process such as Anaerobic filter and Upflow Anaerobic Sludge Blanket Reactor require only 0.05 kWh/person/year.[8]

*There are however some practical aspect associated with Anaerobic treatment systems: COD removed as sludge- upto 30%, Gas recovery- > 23% COD and Methane remaining in the effluent- .028 M^3/ M^3 waste water.

Mathematical equations to predict the energy consumption in Anaerobic filter and Up-flow sludge blanket reactor are given.[9]

Energy input kWh/year:

Anaerobic Filter =1657.Q.H (i)

UASB = 1657.7Q $(S_s-1)(1-f_e)H_s$ (ii)

Assuming, pump efficiency = 0.8,

Efficiency of motor = 0.75

h = Head lost in Anaerobic filter in m.

H_s = height of sludge blanket in m.

f_e = Porosity of sludge blanket, Dimension less.

S_s = Specific gravity of sludge blanket, Dimension less.

Further the anaerobic waste treatment system have the advantage of capturing the biochemical energy of organic matter in the form of biogas (0.415 m^3 biogas/kg COD removed). The biogas thus produced can be utilized as a fuel for heating or it could be used effectively as a primary fuel source for reciprocating engines and gas turbines. The engine power can be applied to drive electric generator, compressor, pump etc. Gas can be also used to run dual-fuel engines and gas turbine for generating electricity for supplementary implant needs or for sale.

International Journal of Engineering Applied Sciences and Technology, 2016
Vol. 1, Issue 10, ISSN No. 2455-2143, Pages 5-8
Published Online August - September 2016 in IJEAST (http://www.ijeast.com)



II. CASE STUDY

In this case study, it is intended to find the energy budgeting of effluent treatment for the whole of the **organized Indian dairy industry**. Comparisons have been made between (i) proposed Anaerobic pre-treatment followed by Aerobic polishing and (ii) currently popular Extended Aeration-Activated Sludge process.

1. Study Basis:

Total Number of Dairies in India = appx 1000
Total capacity of Dairy plants = 100 MLD (in terms of volume of milk processed)
Assuming the volume of wastewater generated from the dairy processing plants is '2.404' times of volume of milk processed.
Wastewater generated from the plants = 240.415 MLD
Chemical Oxygen Demand of a typical dairy = 1500mg/l
Consider 80% of COD being consumed/ utilised for biochemical reactions to be accomplished in an anaerobic process.

Therefore, COD removed = 1200 mg/l
Total COD removed/day
= 240.415 MLD × 1200 × 10^{-6}
= 288.498 × 10^3 kg COD.

It is reported that one kg of COD is capable of producing 0.415 m^3 of biogas.
Therefore, quantity of biogas generated per day = 288.498 × 10^3 × 0.415 = **119727 m^3**
Calorific value of 1m^3 biogas = 6000 kcal. (The energy equivalent of biogas = 6.978 kWh)

2. Energy saving and cost benefits:

(I) Saving due to recovery of Biogas as a bye product in Anaerobic treatment and its utilisation.

Thus, the total energy available from biogas = 11,9727 × 6.978
= **8.355 lakh kWh/d**

(a) The thermal energy can be transferred by a heat exchanger @ 75% efficiency = 8.355 × 0.75
= 6.266 lac kWh/d

Thermal energy is required for various heating requirements in Dairy plants, so it can act as a light diesel oil (LDO) substitute (calorific value of LDO = 10,700 kcal)
Fuel equivalent in terms of LDO = 67136.64kg
Cost of LDO @ Rs.40/-kg = Rs. 2685465.6/-
Alternatively, if the biogas produced is used for the generation of electricity in a duel- fuel engine:

(b) Electrical energy generated by a duel fuel engine operating @34% efficiency = 8.355 × 0.34
= 2.841 lac kWh/d

(II) Energy demand for treatment of effluent:

It is roughly estimated that energy demand for option :

A. With Anaerobic –Aerobic process = 17hp(EM)/MLD of waste being treated.
B. With Aerobic treatment process = 100 hp(EM)/MLD of waste being treated

Therefore, saving due to implementation of proposed Anaerobic-Aerobic treatment process = 83hp(EM)/ MLD
Therefore, energy saving in treating total waste generated by Indian milk processing industry (B-A) = 240.415 × 83
= 19955 hp(EM)/d
= 359180 kWh/d
= 3.59 lac kWh/d
Therefore, the aggregate energy saving in all 1000 Indian dairies by Anaerobic- Aerobic processs is **3.59 lac kWh/d**
If electricity price @ Rs 6/- per unit
Saving in electricity bill = **Rs.21,54,000/d**
Hence the total conservation of electrical energy by adopting Anaerobic treatment of dairy waste = 3.59+2.841
= **6.431 lac kWh/d**
Considering the price of electricity @ Rs.6/-per unit (kWh) and the contribution of fuel to the total cost of electicity generation taken as 50% of the total generation cost.
Therefore, contribution of bye product biogas for electricity generation
= **Rs.8, 52,300/- per day**
= Rs. 311 million/yr.
Annual O&M cost (assumed) = Annual cost of electricity × 1.2
For (A) 17hp×0.75×240.415×24×365×1.2×6 = Appx. **Rs. 53.77 million**
(B)100hp×0.75×240.415×24×365×1.2×6 = Appx. **Rs. 316.3 million**
Difference in Annual O&M = **Rs. 262.43 million**

3. Annualised cost:

Capital cost
(A) Anaerobic- Aerobic Process = **Rs.8789.2 million**
(B) Aerobic process = **Rs.6358.8 million**
Difference in capital cost = Rs. 2430.4 million
Assuming an interest rate @ 12% & inflation rate @ 6% for design period of 20 yrs & taking 5% salvage on replacement.
Annualised capital cost = Cap. Cost×crf (6%-20yrs) – (0.05) cap.cost×sfdf (6%-20yrs)
(Note : crf = capital-recovery factor, sfdf= sinking-fund deposit factor)
Therefore, annualized capital cost
(A) Rs 755 million
(B) Rs 549 million
Total annual cost (without considering energy recovery from biogas) = Annualised capital cost + Annualised O&M cost
(A) 755**million** + 53 million **= Rs.808.8 million**
(B) 546 **million** + 316.3 million **= Rs.862.3million**

International Journal of Engineering Applied Sciences and Technology, 2016
Vol. 1, Issue 10, ISSN No. 2455-2143, Pages 5-8
Published Online August - September 2016 in IJEAST (http://www.ijeast.com)



Therefore, annual gain by adopting(A) compared to (B)- **Rs 53.5 million & Option A is a better economic choice.**

Diff. in cost on O&M+ electricity generation/yr(from recovered Biogas) for A = Rs. **262.43 million+ 311 million**= Rs. 573.43 million

Therefore, by an extra capital expenditure of Rs. 2430.4 million on Anaerobic-Aerobic technology, we get an additional saving of Rs.573.43 million annually on recurring cost. Therefore, pay back on investment can be achieved in 4.3 years only.

III. CONCLUSIONS

The following conclusions are drawn from the above case study:

1. Saving on energy demand in comparison with activated sludge process = **3.59 lac kWh/d**
2. Energy gain due to recovery of Biogas as a bye product = 8.355 lac kWh/d equivalent as calorific value. Biogas can be directly used for raising steam/ heating required in the Dairy plant , thus saving fossil fuel.
3. Total conservation of energy in Indian Dairy Processing Industry = (**3.59 + 6.266) lac kWh/d** = 9.856 **lac kWh/d.**

It is found that by adopting combined Anaerobic-Aerobic treatment at additional capital investment of Rs. 2430.4 million yields annual cost benefits of Rs. 573.43 million./yr and pay back on investment can be achieved in a short span of 4.3yrs. Implementation of such treatment process with gas recovery, while controlling pollution can result in energy conservation for the nation.

IV. REFERENCES

1. CII, (2009). *Indian Dairying: Challenges and Opportunities.* Background Paper.Conference on "Indian Dairy Industry" organized by Confederation of Indian Industries at N.D.R.I., Karnal on 22nd Oct., 2009.
2. Arvanitoyannis I.S(2008) waste management for the food industry, Elsevier academic press, Amsterdam
3. Comprehensive Industry Document Dairy Industry, Central Pollution Control Board ,Delhi. Sept.1993.
4. Owen, William.F.,(1982) Energy in Wastewater Treatment, Prentice-Hall, Inc., Englewood Cliffs, New Jersey, pp. 199-240, 259-263.
5. Switzenbaum, S., Scott C.Dankin,(1981) Anaerobic Expanded Bed Treatment of Whey, Proceedings of 36th Purdue Industrial Waste conference, Purdue University, pp. 414-424.
6. Sammaiah,P., Sastry, C.A. and Murthy, D.V.S.,(1991a). Dairy Waste Water Treatment using Anaerobic contact Filter, Indian Journal of Environmental Protection, Vol-11, No.6, pp418-424.
7. Taori, K.B., Dhabadgonkar, K. and Raman, V.,(1983) Dairy waste treatment by Anaerobic Packed Bed Upflow filter. IAWPC Tech. Annual, X, pp.21-29
8. Arceivala, S. J. and Asolekar, S. R. (2006)" Wastewater Treatment for Pollution Control" (3rd Edition), McGraw Hill Education (India) Pvt. Ltd., New Delhi
9. Anaerobic Technology for Domestic Waste water Treatment, Ch.7, pp.4-5, ISTE Summer School, June 1991, Deptt. Of Civil Engg., MNR Engg. College, Allahabad.
10. Amritkar, S.R., Introduction of Anaerobic Pretreatment in Treating dairy Effluents- A positive Step towards Conservation and Co-Generation of energy, 3rd International conference-Appropriate Waste Management technologies for developing countries, Nagpur, Feb. 1995 vol.1 pp. 127-132

Int J Interact Des Manuf
DOI 10.1007/s12008-016-0355-y

TECHNICAL PAPER

Analyzing and modeling the performance index of ultrasonic vibration assisted EDM using graph theory and matrix approach

Sanjay Kumar[1] · **Sandeep Grover**[1] · **R. S. Walia**[2]

Received: 19 September 2016 / Accepted: 3 October 2016
© Springer-Verlag France 2016

Abstract This paper is an endeavor to comprehend an interactive learning process of ultrasonic vibration assisted Electrical Discharge Machining (USEDM) process performance index. The factors influencing the USEDM process are identified and analyzed, through a logical and systematic framework of graph theory and matrix approach. The interdependency of factors are distinguished and examined. A systematic model of USEDM performance index is proposed to utilize graph theoretic approach (GTA). The performance index for USEDM is obtained so from the matrix model and digraphs to comprehend the power of subjective factors affecting. Factors and sub-factors impacting the performance are perceived and collected into five essential groups e.g. flushing, cavitation, abnormal discharge, dimensional accuracy and surface morphology. GTA framework reveals that the flushing, surface morphology and dimensional accuracy impact the basically ascertains, however cavitation effect can in like manner be unequivocal variables for USEDM performance index regard.

Keywords Flushing · Cavitation · Dimensional accuracy · Surface morphology · Performance · Diagraph · Matrix

✉ Sanjay Kumar
sanjaykpec@yahoo.co.in

Sandeep Grover
groversandeep@hotmail.com

R. S. Walia
waliaravinder@yahoo.com

[1] Department of Mechanical Engineering, YMCA University of Science and Technology, Faridabad, Haryana 121006, India

[2] Department of Mechanical, Production and Industrial and Automation, Delhi Technological University, Delhi 110042, India

1 Introduction

Electrical discharge machining (EDM) is a fascinating advance manufacturing technology for machining of aerospace, automotive industry and surgical components [1]. But machine of advance materials for high accuracy and high surface quality deteriorate its performance index. Researchers have been consistently working on traditional EDM with an aim to accomplish better dissemination of dielectric liquid and stable discharge conditions [2] that outcomes enhanced MRR [4], thin recast layer [3], better process stability [5], high aspect ratio [6], and vitality productive arcing and short circuit [7].

In literature, researchers are encountering difficulties in selecting the most appropriate objective and attribute for USEDM process index. The usual criteria considered for the USEDM performance index evaluation include mode of vibration, flushing, cavitation, abnormal discharge, dimensional accuracy and surface morphology, etc. Depending on the domain of traditional EDM, USEDM is a multiple objective and multi-attribute decision making problem. A schematic diagram for USEDM to workpiece is shown in Fig. 1. Shabgard et al. [9] presented the formulation and solution of a multiple objective optimization problem using fuzzy-based algorithm for prediction of material removal rate (MRR), tool wear ratio (TWR), and surface roughness (Rz, Rk) for traditional EDM and ultrasonic-assisted EDM (US/EDM) processes for tungsten carbide (WC–10%Co). Jangra et al. [10] proposed grey relation analysis to optimize multiple machining characteristics in traditional wire EDM. Jangra et al. [11] builds a flexible and comprehensive model to evaluate the carbide compacting die performance process with wire EDM by identifying the various attribute through literature review using graph theory approach (GTA). Rao and Gandhi [12] developed a

Published online: 17 October 2016

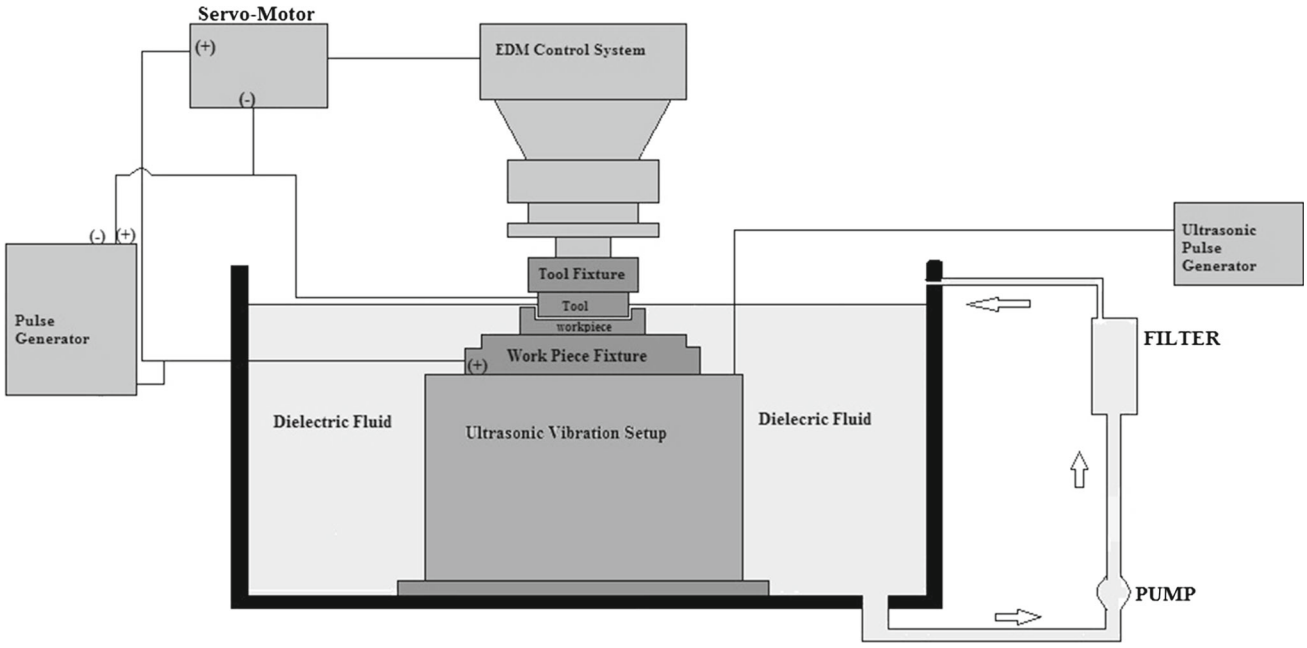


Fig. 1 Schematic diagram of ultrasonic assisted EDM to workpiece [8]

universal machinability model for work material using GTA. Tzeng and Chen [13] used Taguchi fuzzy-based approach for modeling and optimization of high-speed EDM process for machining of SKD11 tool steel in EDM process. The selection decisions of objective and attribute are complex in USEDM, as the technological challenges involved in it. Necessary conditions for achieving higher performance index consist in understanding the current and upcoming objective functions and attributes influencing the USEDM environment. Authors have identified some qualitative as well as quantitative parameters through literature, affecting USEDM performance, such as flushing (evacuation of debris, pumping effect and stirring effect) and abnormal discharge (arcing and short circuit, discharge wave distribution) etc as shown in Table 1. It requires a simple, systematic and logical methods or mathematical tools to guide researchers for considering selection attributes/objectives and their interrelations. To meet these technological challenges, authors have select interactive graph theory approach with an objective to compare attributes, and likewise obtain the most appropriate combination of attributes. Interactive designing and manufacturing approach through FE analysis allow researchers to monitor the simulation of such a complex USEDM process, and helps in interrupting USEDM process performance through changes in the factors one at a time. It allow for interactive enhancement of knowledge of ultrasonic vibration assisted EDM, and to test USEDM process by FE analysis and simulation. Graph theory approach is a logical and systematical approach useful for modeling and analyzing various kinds of science and technological problems [14]. An endeavor has been made through this present work to know the nature and therefore assessed the relative interdependency and legacy of various dependent and driver variables, which in past have been speculatively analyzed with likelihood instead of assurance without considering USEDM as whole system. The principle objectives of this study are:

- To identify and categorize the various decisive factors and sub-factors affecting the performance UEDM under process.
- To establish interdependency among these qualitative/quantitative factors by quantitatively analyzing their inheriting strength using the Graph-Theoretic Approach (GTA).
- To achieve a range and coefficient of variation of performance index value through a structural GTA methodology.

Literature has been reviewed to identification and categorization of the various factors sub-factors. The range of USEDM process performance index that has been achieved and intensity of factors affecting are calculated quantitatively. The major findings and implications of this research are discussed in conclusions.

2 Literature review

Electrical discharge machining (EDM) is set to meet the unending needs of the manufacturing ventures for advance

Table 1 Factors and sub-factors affecting the USEDM process performance

Factors	Sub-factors	References
1. Flushing	1. Suction and exhaust of dielectric due to pumping action	[17,19,21,55,57]
	2. Debris and gas bubble debris evacuation	[17,18,22,24,57]
	3. Frequency of pumping action	[18]
	4. Stirring effect	[5,20]
2. Cavitation	1. Ultrasonic field force	[23,58]
	2. Acoustic pressure	[17,23,57]
	3. Dielectric fluid density	[5,54]
	4. Sound velocity in dielectric	[5]
	5. Vibration amplitude	[5,47]
3. Abnormal discharge	1. Arcing and short circuit	[16,29]
	2. Debris concentration	[27,51]
	3. Discharge wave distribution	[2,30]
4. Dimensional accuracy	1. Aspect ratio	[1,32,37]
	2. Tool wear	[33,34]
	3. Wetting effect	[27,38]
	4. Traverse direction of UV	[31,51]
	5. Tool geometry	[33]
5. Surface morphology	1. Thickness of recast and heat effect layer	[24,40,50]
	2. Size of micro holes and cracks	[8]
	3. Residual stress	[17]
	4. Micro-hardness	[8,49]

and difficult to machine materials. This machining process has colossal potential for development. USEDM is one of the magnificent ideas as of now picking up consideration with the target to increase the value of customary EDM process. On the premise of literature surveys, the main factors and sub-factors affecting USEDM process execution are recognized and gathered in Table 1. Most of researchers in USEDM literature are concerned with the experimental quantitatively analysis approach. Their goal was to develop a concise and comprehensive characterization of variables affecting the performance index of USEDM in the form of a mathematical model to analyze its behavior under a changing environment. But the technological challenge such as discharge gap monitoring, evacuation of debris from discharge gap, cavitation effect, arcing, short circuit, debris concentration forced to opt for other alternative approaches for solution. Also a huge cost is involved in these scientific experimental approaches. Interactive designing and manufacturing approach allow authors to monitor the simulation and helps in interrupting the changes in the parameters of USEDM for interactive enhancement of knowledge of ultrasonic vibration assisted EDM through FE analysis. The interactive design and manufacturing approach provides approximate solution in a reasonable time frame and cost, and with reasonable effort.

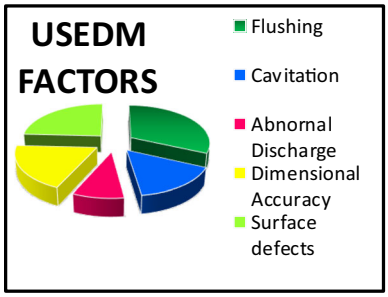
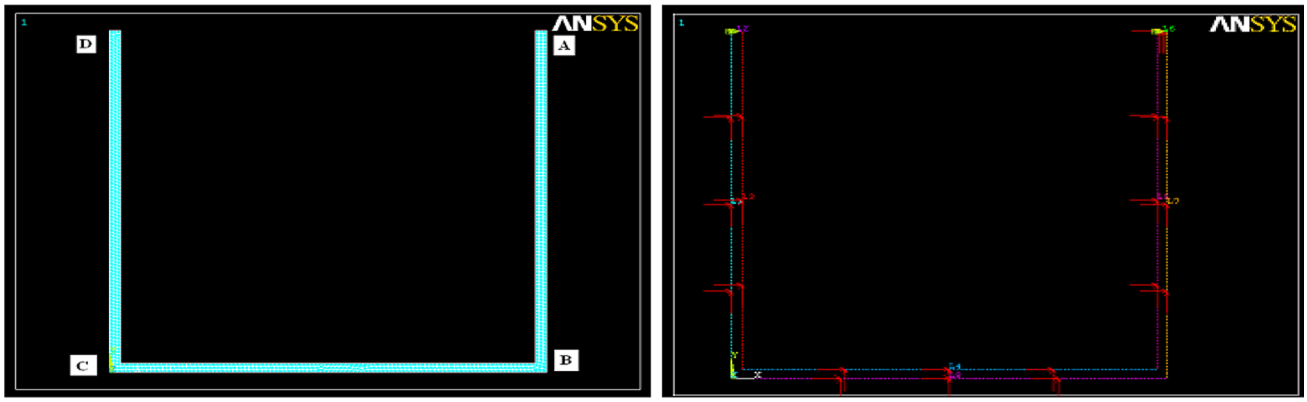


Fig. 2 Contribution of various factors in USEDM performance considered by researchers

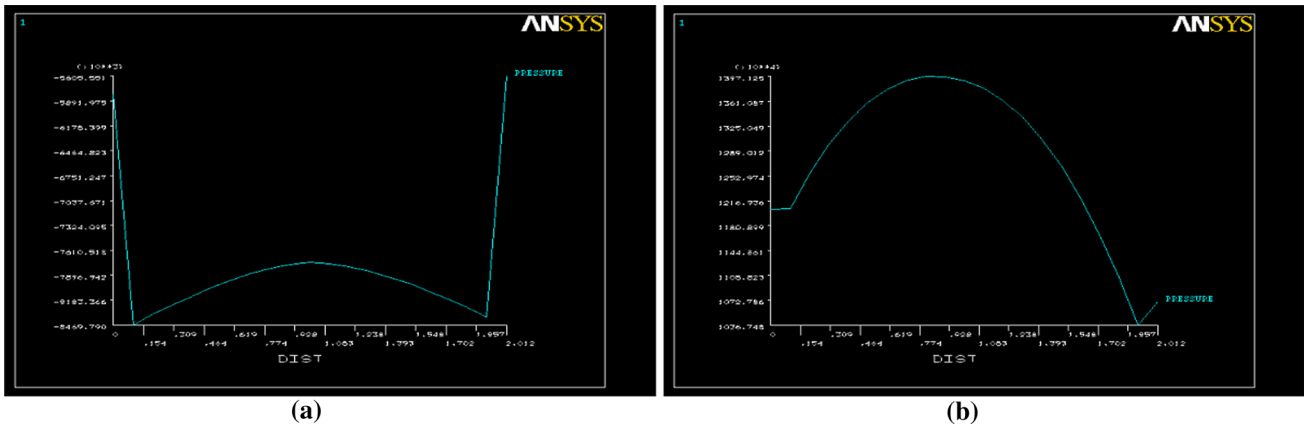
2.1 Identification and categorization of factors

Form literature survey, It has been found that the ultrasonic vibration in traditional EDM process is a convoluted undertaking. There are sure attributes which contribute for USEDM process performance index grouped here in this study and discussed in next paragraphs. It is found that researchers have less explored the influence of factors such as cavitation, abnormal discharge, where as flushing of contaminated dielectric fluid, dimensional accuracy and surface morphology are the most frequently considered factors significantly affecting the performance of USEDM process as shown in Fig. 2.



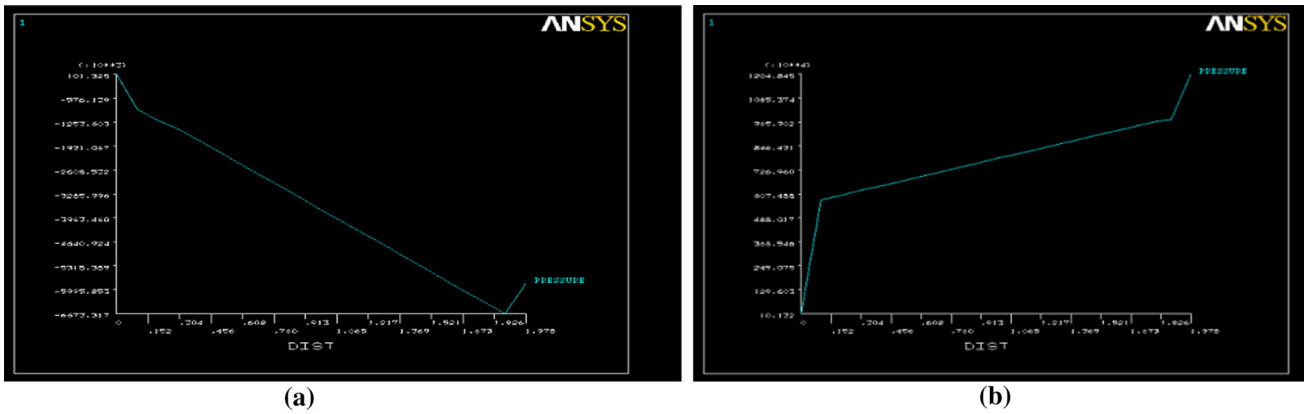
(a) (b)

Fig. 3 UEDM process; **a** domain and finite element mesh; **b** boundary conditions [55]



(a) (b)

Fig. 4 Graphical variation of pressure v/s distance along the path BC for; **a** downward; **b** upward motion of workpiece [55]



(a) (b)

Fig. 5 Graphical variation of pressure v/s distance along the path AB for; **a** downward; **b** upward motion of workpiece [55]

2.1.1 Flushing (H_1)

Flushing is characterized as the right flow of dielectric liquid between the tool and the work piece [15]. Generally the flushing is accomplished by infusion, suction, side flushing and pumping activity [16]. The hammering action of tool electrode splashes contaminated dielectric fluid and allows the fresh to move into the gap [17]. The high frequency pumping action of the tool tip, pump the debris away and suck fresh dielectric into machining region, increase discharge efficiency and metal removing rate (MRR) [18]. The mechanical vibration influences the frontal discharge gap due to two major effects. One of which is vibration of dielectric medium and other is working gap width through periodic

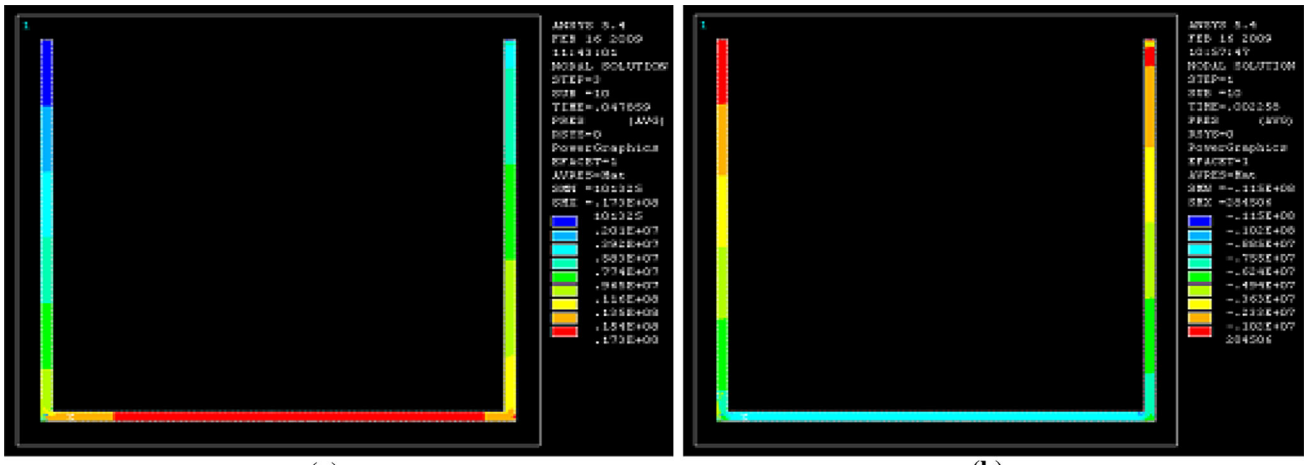


Fig. 6 Pressure variation of dielectric during; **a** upward motion; **b** downward motion [55]

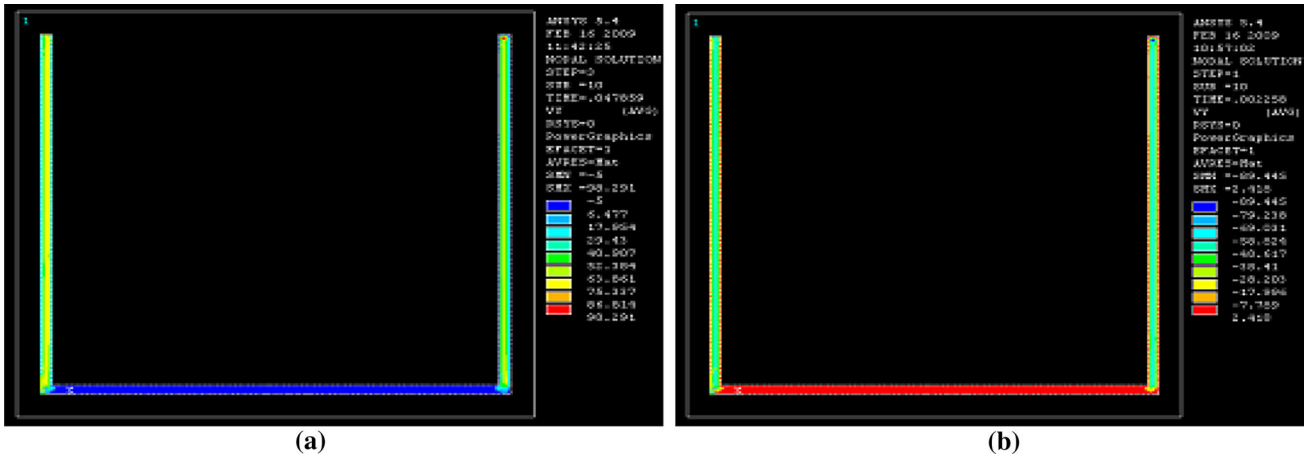


Fig. 7 Velocity variation along the y-axis during **a** downward motion; **b** upward motion of work piece [55]

feed-retraction-movements of the vibrating parts [19]. The strong stirring effect caused by UV action, which results in excellent flushing in micro EDM process that increased the machining efficiency more than 60 times [20]. Stirring effect is helpful to uniformly distribute the carbon nano-fibers in the dielectric fluid [5]. The ultrasonic waves propagates as elastic wave through tool electrode and results in alternative compression and rarefaction of dielectric medium to workpiece [21]. The mechanical vibration cause relative motion of tool to the workpiece imparts the kinetic energy to the discharged debris. This cause the debris and gas bubbles to remove easily and results fewer shot circuits occurred in discharging [22]. Singh et al. [55] developed FEA model using ANSYS 5.4 software for the analysis pressure variation. A two dimensional FEA model has been proposed by authors for workpiece vibration. Figure 3a, b shows the domain and boundary condition. The pumping action has been taken for the present analysis. For the FLOTRAN CFD elements, the velocity are obtained from the conservation of momentum principle and the pressure is obtained from the conservation of mass principle. EDM dielectric is pumped out while workpiece upward motion similar to the pumping action of the reciprocating pumps. And during the downward motion of the workpiece dielectric is sucked inside shown in Figs. 4 and 5 graphical variation of pressure v/s distance along horizontal (BC) and vertical (AB) directions, respectively. They concluded form their results of pressure variation of dielectric medium as shown in Fig. 6a, b that pumping action of workpiece vibration is similar to that of reciprocating pump. The results of velocity variation along y-axis during downward and upward motion as shown in Fig. 7a, b causes better flushing than traditional EDM.

2.1.2 Cavitation (H_2)

Murthi and Philip [23] identified cavitation (nucleation, growth, and burst of gaseous bubbles), ultrasonic field forces (radiation force, Stoke's force, Bernoulli's attraction), and acoustic streaming as the factors having significant effects in ultrasonic assisted EDM. This phenomenon is strongly

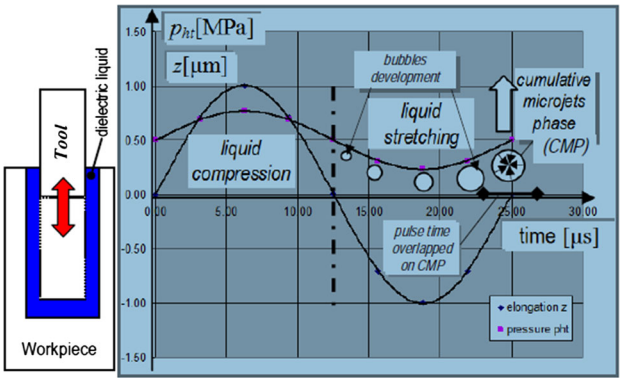


Fig. 8 Ultrasonically induced cavitation phenomenon in the gap of µEDM + US (frequency 40 kHz, amplitude 1 µm and density of liquid = 840 kg/m^3) [58]

related to acoustic pressure, oscillations frequency, and dielectric fluid density, sound velocity in dielectric and vibration amplitude [5]. This alternating pressure variation which leads to increased hydrostatic pressure variation [24]. Compression cycles exert a positive pressure and push the liquid molecules together, while expansion cycles increase a critical size of bubble until it violent collapse in the liquid [25]. The violent collapse of bubbles in the gap, generate shock waves parallel to machined surface, are responsible of roughness decrease [26]. Pressure variation causes more molten metal to be removed from the carter, causing debris a strong drift [16]. Ghiculescu et al. [57,58] proposed FEM model of metal removing mechanism of ultrasonic tool vibration assisted micro EDM. They considered thermal and cavitational effects of UV using cosmol multiphysics and time dependent heat transfer in solids. The ultrasonic oscillation period consists of semiperiod of dielectric compression from the gap and a stretching semiperiod shown in Fig. 8.

FEA results for comparative volume removal by signal discharge shown in Fig. 9 proves that EDM system when overlapped with the cumulative micro jet phase increase the volumetric metal removal of traditional EDM. The bubbles so produced become non-spherical and drive high speed jets of liquid into the electrode surfaces, and create shockwaves.

This can generate a wide range of pits and produce newly exposed highly heated surfaces that may be responsible for the erosion of the tool and workpiece materials [40]. The cavitation occurs more easily when the homogeneity of the liquid is disturbed by external particles. The debris within the discharge gap created during the EDM enhances the cavitation effect.

2.1.3 Abnormal discharge (H_3)

In EDM metal removing is due to thermal phenomenon caused by local temperature in the region of 8000–12,000 °C [15]. A layer of metal melted and ejected due to electric discharge as a result of ionization of dielectric medium, and tiny particles from the workpiece surface evacuated called debris. However, when debris remains between the electrode and the workpiece surface, the electric discharge occurs not between the electrode and the workpiece surface but between the debris and the electrode [27].

The accumulation of debris in discharge gap that restrict the further machining is called a state of abnormal discharge. The performance of EDM process depends on the discharge energy, where as higher discharge energy lead to poor surface finish. The control system reduce the current or energy and smaller the gap. This makes control task more complex and accumulation debris may build a bridge between the electrode and workpiece, allowing arcing to occur that lead to short and open circuit [16].

Nishiwaki et al. [51] measured the discharge gap and depth of hole by using the pulse echo technique during EDM process. Elastic waves generated during electrical discharge in gap, these wave passes through workpiece and variation of the received elastic waves are detected by ultrasonic transducer. Figure 10 show the variation of discharge gap with machining time, Fig. 10a shows condition of normal discharge, electric discharge generates when the electrode approaches workpiece surface at once. Elastic waves are caused at electric discharge points cannot be detected because the elastic waves become a noise. When debris concentration becomes high an abnormal electric discharge state occurs. Then, the workpiece cannot be machined further. In order to control the abnormal discharge state flushing of these highly concentrated debris discharge gap is must. As shown in Fig. 10b, the electric discharge is hardly generated and the discharge gap, δ, becomes larger than that of the normal discharge state.

The total duration of arcing is reduced by the application vibration and decreases with increasing frequency. The numbers of arc discharge increases with frequency and results in significant reduction of machining time [28]. Adhesion occurs when the molten metal of the workpiece become attached to the tool electrode, causing the abnormal discharge as a result of short-circuiting between the workpiece and tool electrode, and inhibiting recovery of EDM machining. Ultrasonic vibration is used to remove adhesion and hence arcing and short circuit that increase metal removing rate [29].

Yu et al. [27] observed that the machining speed slowed down when the hole was drilled deeply in normal microhole drilling by EDM. The planetary movement of an electrode provided an uneven gap through which the bubbles and debris escaped from the working area easily to avoid blocking the dielectric flow into working area occurred in normal micro-hole drilling. In ultrasonic vibration assistance, the tool electrode feed rate increased significantly because the ultrasonic vibration enhanced the wetting effect in discharge gap as shown in Fig. 11.

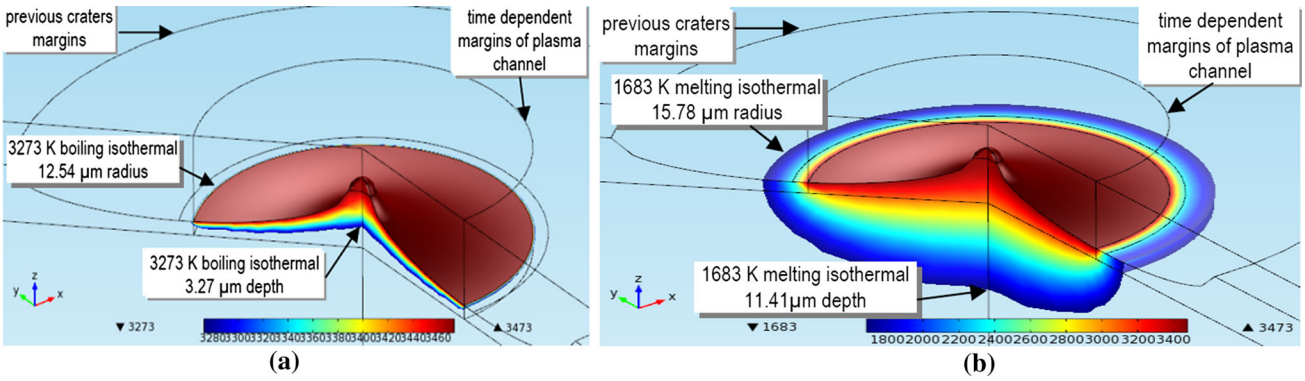


Fig. 9 Comparative volume removal by signal discharge at **a** micro-EDM; **b** US-EDM

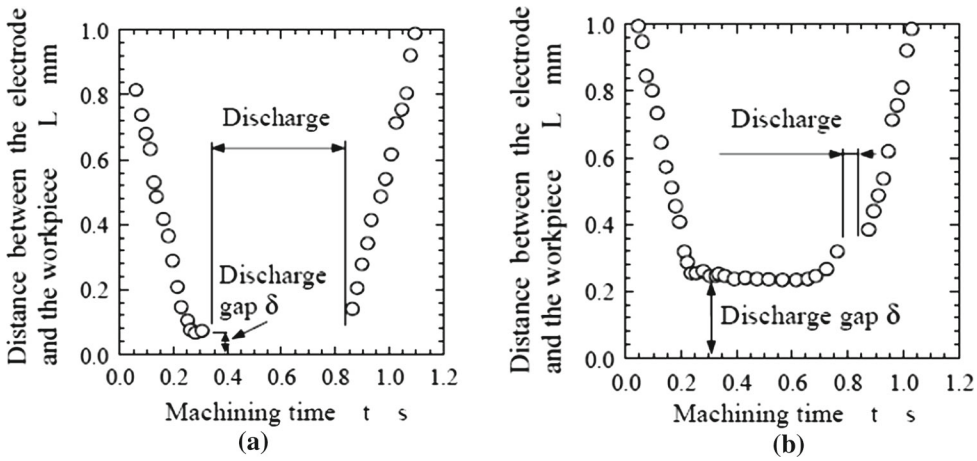


Fig. 10 Discharge gap vs machining time [51]. **a** Normal discharge state. **b** Abnormal discharge state

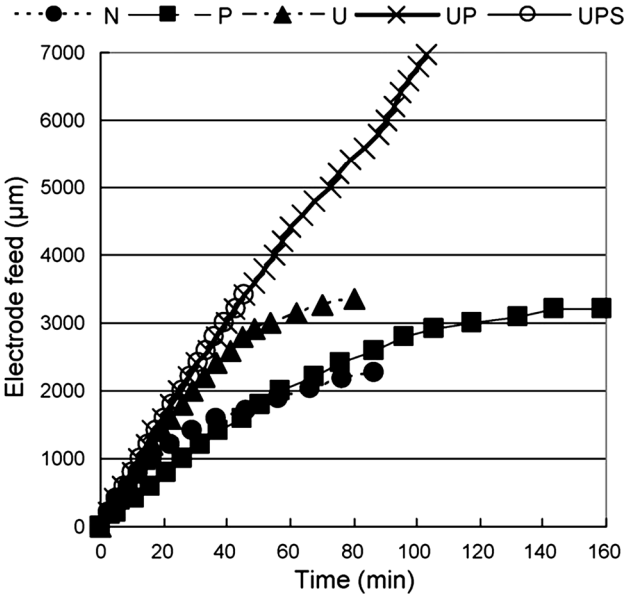


Fig. 11 Electrode feed vs. time; N for normal EDM; P for planetary; UP; ultrasonic vibration with planetary [27]

The high-frequency ultrasonic vibration shifts the discharge points and makes the discharge wave distribution more uniform and form discharge channels [2]. The debris produced from the melted metal can accumulate in the discharge gap and cluster with carbon element and tar produced from the pyrolysis of kerosene, thus making the discharge condition abnormal and leading to arcing. The ignition delay reduces due to discharge wave form that improves the bridging effect to facilitate the normal discharge [30]. A comparative discharge waveforms using traditional EDM and combination process of EDM with USM are shown in Fig. 12a, b.

A higher discharge frequency and regular discharge wave profile obtained by ultrasonic vibration increase machining efficiency compare to without vibration [31].

2.1.4 Dimensional accuracy (H_4)

The machining of holes with high aspect ratio and depth faces dimensional inaccurate, the inaccuracy increases with complex geometry. The tapered hole and overcut are resultant of critical frontal tool wears [1,32]. Dimensional accuracy is a function of tool geometry (shape and size) and its path [33]. Tool wear is affected by the precipitation of carbon from the hydrocarbon dielectric onto the electrode surface during sparking. They also argued that the rapid wear on the electrode edge was due to the failure of carbon to precipitate at difficult-to-reach regions of the electrode [34]. In addition,

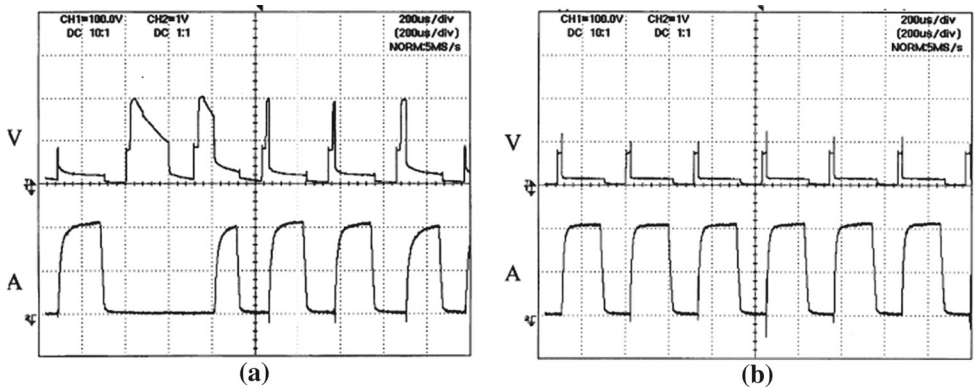


Fig. 12 **a** Typical discharge waveforms using conventional EDM (condition: Ip.12 A, tp.200 ms); **b** typical discharge waveforms using combination process of EDM with USM (condition: Ip.12 A, tp.200 ms) [30]

the worn electrode reduces the machining accuracy because the generated feature is the result of a combination of the tool electrode shape and its tool path [33]. Ultrasonic vibration assistance of workpiece slightly decreases the tool wear ratio (TWR) on finishing regime, the exception is found at pulse-on time 50 μs as shown in Fig. 13 [35]. When the debris traverses longer distance before to be expelled completely, these can generate more sparks between tool and the workpiece walls and result higher overcut [36]. The adhesion of the oil-decomposed carbon to the electrode surface is the cause electrode wear rate and it is higher when complex direction of prorogation of vibration is imparted [31]. High aspect ratio restrict the debris evacuation because of the turned over edges of the craters, secondary discharge occurs easily at hole internal surface that cause taper dimensional inaccuracy [37]. Wetting effect of ultrasonic vibration weakens the boundary between bubble and dielectric that cause reduction of viscous resistance and the bubbles are broken easily and consequently higher aspect ratio can be achieved [27,38].

Srivastava et al. [39] and Abdullah et al. [1] applied the ultrasonic vibration causes slight increase in the tool wear as the amount of recast layer deposited on the tool reduces.

2.1.5 Surface morphology (H_5)

A typical cross-section of work surface after traditional EDM process exhibits a thin layer of molten metal and has no fixed thickness usually very hard below this. The molten metal region of workpiece layer in extremely hot region vaporized and expelled away by high pressure wave generate due to dielectric turbulence from the electric discharge, while material underneath remain solid. This cause stress concentration, pinholes and micro-cracks and eventually leading poor strength of the workpiece [41]. According to Lin et al. [30], the possible reason for thin recast layer in the combination EDM/USM process is the completely remove of molten metal for the gap as shown in Fig. 14.

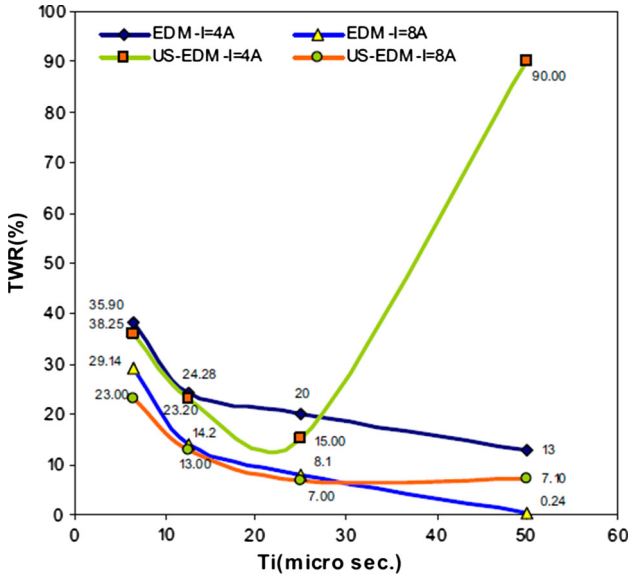


Fig. 13 Tool wear ratio against pulse-on time with and without ultrasonic employment [35]

In USEDM process the recast layer is more regular and continuous, it is sometime slightly thicker. The residual stresses set up to a certain depth only, no significant effect is observed at the surface, residual stresses having the same value without or with vibrations [17]. Lin et al. [49] find that softening layer adjoining hardness layer improves the hardness of machined surface significantly. Singh et al. [8] conducted experimentation with continues and discontinues UV action of workpiecce and found that ultrasonic vibration decrease the size and numbers of micro-cracks on work surface.

3 Methodology

A definitive objective of GTA is to demonstrating and analyzing target factors through scientifically substances to assess dependency or independency and communications

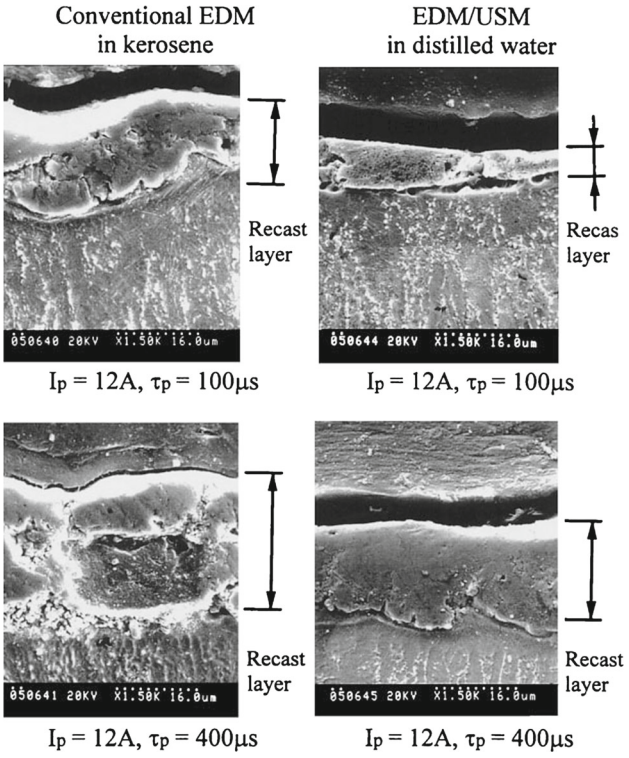


Fig. 14 Typical SEM micrographs of the recast layer [30]

exist among qualitative/quantitative variables of a framework [56]. In this study, a modified framework is developed shown in Fig. 15. The step by step approach is explained in next paragraphs. Various researchers have used GTA methodology to evaluate the performance in manufacturing technology. Rao et al. [53] proposed digraph and matrix strategy to assess machinability of wokpiece and failure cause examination of machine tool. Gandhi and Agarwal [44] exhibited GTA strategy for framework wear investigation. The USEDM performance index elements distinguished and gathered in this paper with likelihood rather than assurance.

The GTA approach gives a precise normal for the USEDM performance, albeit new for advance manufacturing technology, to abstain from speculating and instinct in touching base at conclusions. A network showing factors and their interactions has been proposed to model the USEDM process through graph representation.

If interactions are not direction dependent, the environment is represented by an undirected graph; if direction dependent, it is called a digraph representation [45]. The five major factors and their corresponding sub-factors are utilized to assess the degree of the performance index as indicated in Eq. 1.

$$\text{USEDM Performance Index} = f\{(H_1)^{a}, (H_2)^{b}, (H_3)^{c}, (H_4)^{d} \,\&\, (H_5)^{e}\} \quad (1)$$

where H_1, H_2, H_3, H_4 & H_5 represent the inheritance value of factors affecting the USEDM performance Index; and intensity of dependency value a, b, c, d and e are the extend of individual factors affecting the objective function.

The endeavor here is to co-relate these five critical elements, their quantification of inheritance value based on sub-elements and interdependencies of these critical elements, dependency value of individual factors obtained through digraph correlation representation [46].

3.1 Digraph representation for USEDM process performance

A digraph is utilized to speak to the restrictive variables of USEDM process index and their interdependency as far as hubs and edges. In an undirected diagram, no bearing is allocated to the edges in the graph, while coordinated diagrams or digraphs have directional edges [43]. A USEDM process performance digraph speaks to the procedure steadiness measure of attributes or elements ($H_i's$) through its hubs and the edges compare to the reliance of components ($h_{ij}'s$). "h_{ij}" demonstrates the level of reliance of the ith component on the jth variable. In the digraph "h_{ij}" is spoken to as a guided edge from hub i to hub j. The digraph licenses us to imagine the USEDM elements and gives sentiment complex associations among components.

3.1.1 Digraph generation at system level for USEDM factors

The five broad factors identified in the previous section from literature review i.e flushing (H_1), cavitation (H_2), abnormal discharge (H_3), dimensional accuracy (H_4) and surface morphology (H_5) are directed edges in the performance digraph represent the dependence of one factor on another shown in Fig. 16.

The cavitation (H_2) is shown affecting all other factors. Flushing (H_1) affects other three factors, i.e. a directed edge from (H_1) to abnormal discharge H_3, dimensional accuracy (H_4) and surface morphology (H_5); researchers have attempted some innovative ideas to achieve this by injection, suction, side flushing and pumping action and through addition assistances [52]. Abnormal discharge factors (H_3) affects H_4 and H_5. Surface Morphology (H_5) is affected by all the factors. It may be noted that the Surface Morphology cannot affect flushing, cavitations and other factors (thus no directed edge from H_5 to other factors).

3.1.2 Digraph generation at sub-system level for USEDM Sub-factors

The interdependency of sub-factor at sub-system levels are visualized through digraphs as shown in Figs. 17, 18, 19,

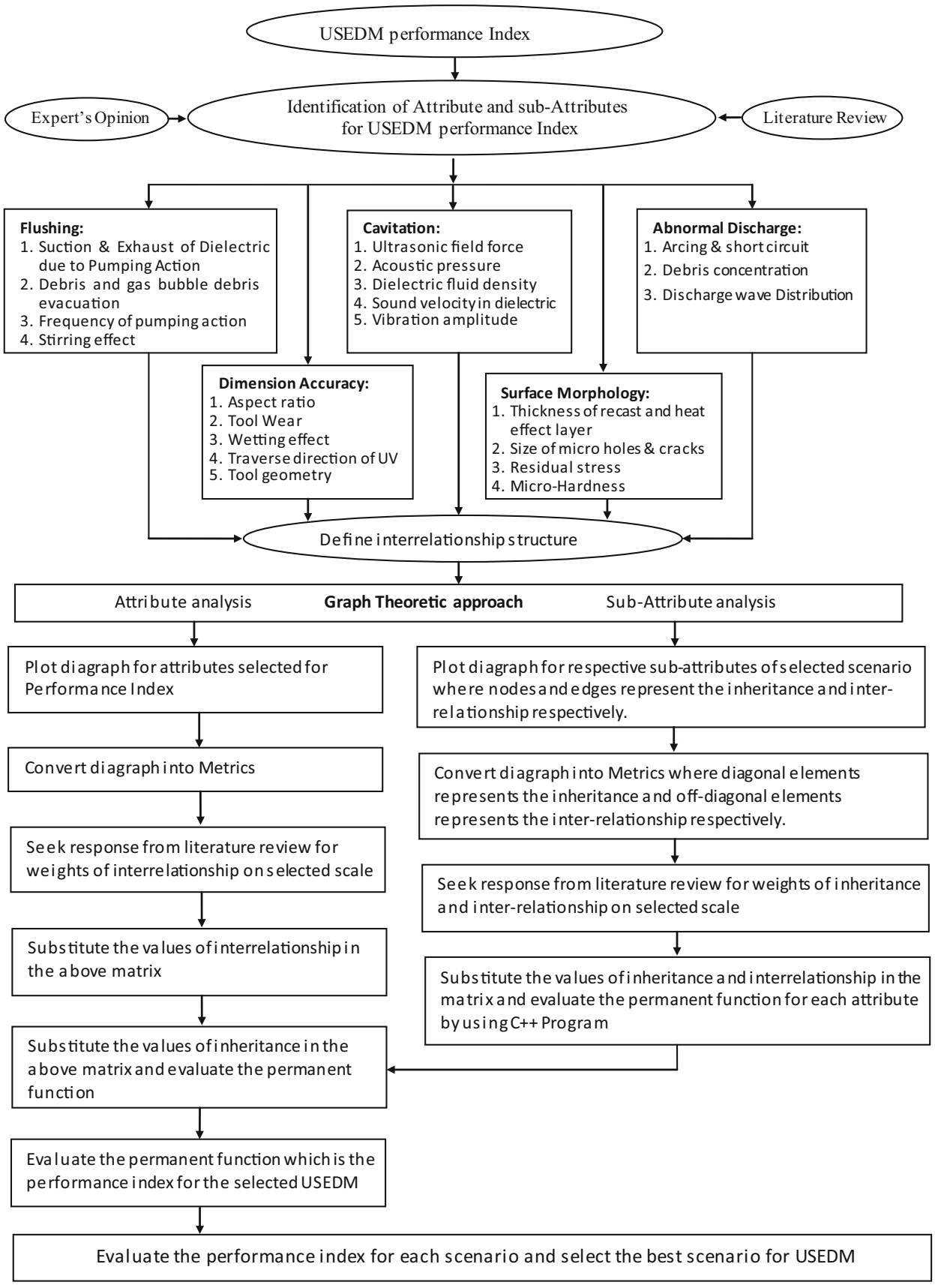


Fig. 15 Modified Framework for USEDM performance Index Evaluation [42]

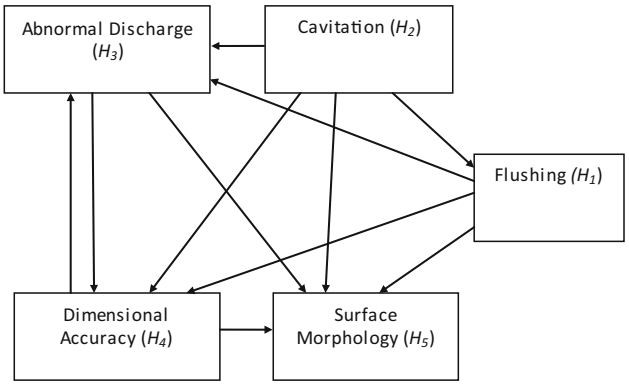
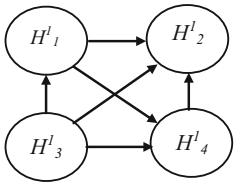


Fig. 16 USEDM process performance evaluation digraph. Nodes: *1.* flushing (H_1); *2.* cavitation (H_2); *3.* abnormal discharge (H_3); *4.* (H_4); *5.* surface morphology (H_5)

Fig. 17 The digraph representation for flushing



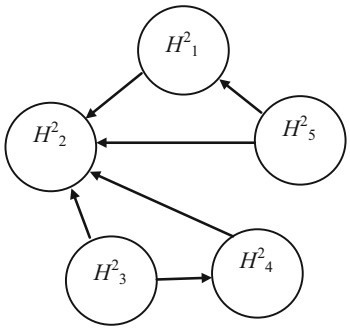
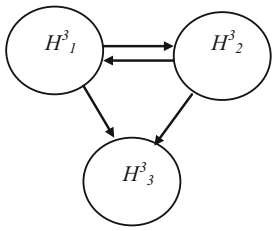


Fig. 18 The digraph representation for cavitation

Fig. 19 The digraph representation for abnormal discharge



20 and 21. Superscript denotes the subsystem and subscript indicate the sub-factor affecting the subsystem.

3.2 USEDM process performance matrix representation [USEDM]

Since a digraph is a visual representation, it helps in analysis to a limited extent only [46]. To establish an expression for USEDM performance index, the digraph is represented in matrix form, which is convenient in computer processing also. A digraph of five factors leading to a fifth order

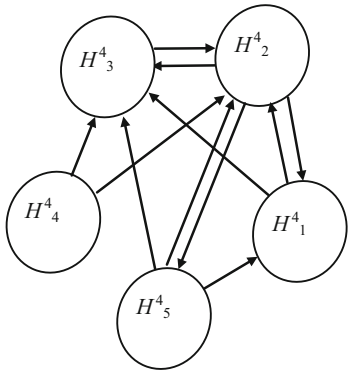
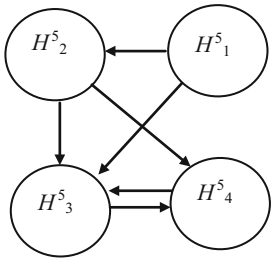


Fig. 20 The digraph representation for dimensional accuracy

Fig. 21 The digraph representation for surface morphology



symmetric (0, 1) matrix $[A] = [h_{ij}]$. The rows and columns in the matrix represent interactions among factors, i.e. h_{ij} represents the interaction of the 'ith' factor with the 'jth' factor;

$$h_{ij} = 1; \text{ if factor '}i\text{' is connected to factor '}j\text{'}$$
$$= 0, \text{ otherwise:}$$

Generally $h_{ij} \neq h_{ji}$ as USEDM performance factors are directional and $h_{ii} = 0$, as a factor is not interacting with itself. The USEDM process performance matrix is square and non-symmetric and is analogous to the adjacency matrix in graph theory. The USEDM matrix '$[A]$' representing the digraph shown in Fig. 16 is written as Eq. 2;

$$[A] = \begin{array}{c} Factors \\ H_1 \\ H_2 \\ H_3 \\ H_4 \\ H_5 \end{array} \begin{array}{c} \begin{array}{ccccc} H_1 & H_2 & H_3 & H_4 & H_5 \end{array} \\ \begin{bmatrix} 1 & 0 & 0 & 0 & 0 \\ 0 & 1 & 0 & 0 & 0 \\ 0 & 0 & 1 & 0 & 0 \\ 0 & 0 & 0 & 1 & 0 \\ 0 & 0 & 0 & 0 & 1 \end{bmatrix} \end{array} \tag{2}$$

Off-diagonal elements with value 0 or 1 represent the interdependency of USEDM performance factors. The diagonal elements are 0 since the effect/inheritance of USEDM performance factors is not taken into consideration. To consider this, another USEDM characteristic matrix is defined.

3.2.1 USEDM process performance characteristic matrix [CM-USEDM]

Let 'H' as the variable representing USEDM process performance factors. The characteristic matrix already used to characterize USEDM process performance elements. The USEDM characteristic matrix '$[B]$' as shown in Eq. 3, for the digraph shown in Fig. 7, may be expressed as $[H\ I - A]$, where '$[A]$' is the matrix represented in Eq. 2 and consider '$[I]$', an identity matrix.

$$[B] = \begin{array}{c} Factors \\ H_1 \\ H_2 \\ H_3 \\ H_4 \\ H_5 \end{array} \begin{array}{c} \begin{array}{ccccc} H_1 & H_2 & H_3 & H_4 & H_5 \end{array} \\ \begin{bmatrix} H & 0 & -1 & -1 & -1 \\ -1 & H & -1 & -1 & -1 \\ 0 & 0 & H & -1 & -1 \\ 0 & 0 & -1 & H & -1 \\ 0 & 0 & 0 & 0 & H \end{bmatrix} \end{array} \tag{3}$$

In the $[B]$ matrix the value of all diagonal elements is the same, i.e. all USEDM performance factors have been assigned the same value which is not true in practice, since all USEDM process performance factors have different values depending on various sub-factors affecting them. Moreover interdependencies have been assigned values of 0 and 1 depending on whether it is there or not. To consider this, another matrix, the USEDM process performance variable characteristic matrix is considered.

3.2.2 USEDM process performance variable characteristic matrix [VCM-USEDM]

The USEDM process performance variable characteristic matrix takes into consideration the effect of different factors and their interactions. The digraph in Fig. 7 is considered for defining [VCM-USEDM]. As stated earlier the 'H_i's and 'h_{ij}'s represent nodes and edges, respectively, in the digraph. Consider a matrix '$[C]$' with off-diagonal elements 'h_{ij}' representing interactions between USEDM factors, i.e. instead of 1 (as in Eq. 3).

Another matrix '$[D]$' is taken with diagonal elements 'H_i', i = 1, 2, 3, 4, 5 where the 'H_i' represent the effect of various factors, i.e. instead of 'H' only (as in Eq. 3). Considering matrices '$[C]$' and '$[D]$', VCM-USEDM is expressed as: $[E] = [D - C]$

$$[E] = \begin{array}{c} Factors \\ H_1 \\ H_2 \\ H_3 \\ H_4 \\ H_5 \end{array} \begin{array}{c} \begin{array}{ccccc} H_1 & H_2 & H_3 & H_4 & H_5 \end{array} \\ \begin{bmatrix} H_1 & 0 & -h_{13} & -h_{14} & -h_{15} \\ -h_{21} & H_2 & -h_{23} & -h_{24} & -h_{25} \\ 0 & 0 & H_3 & -h_{34} & -h_{35} \\ 0 & 0 & -h_{43} & H_4 & -h_{45} \\ 0 & 0 & 0 & 0 & H_5 \end{bmatrix} \end{array} \tag{4}$$

The matrix provides a powerful tool through its determinant, called the variable characteristic USEDM performance multinomial [VC-USEDM]. This is a characteristic of the USEDM process and represents the USEDM performance of the process, considering the effect of USEDM process elements and their interactions. Due to consideration of selective interaction of USEDM process performance factors (as per Fig. 7), some of the diagonal elements in the matrix in Eq. 4 are zero. The determinant of the matrix in Eq. 4, i.e. the variable characteristic USEDM multinomial, carries positive and negative signs with some of its coefficients. Hence complete information in the USEDM performance will not be obtained as some will be lost due to addition and subtraction of numerical values of diagonal and off diagonal elements (i.e. 'H_i's and 'h_{ij}'s). Thus the determinant of the variable characteristic matrix, i.e. the matrix in Eq. 4, does not provide complete information concerning the USEDM process performance. For this, another USEDM process performance variable permanent matrix, [VPM-USEDM], is introduced.

3.2.3 USEDM process performance variable permanent matrix [VPM-USEDM]

The performance in USEDM process enabled when the effect of all the factors is maximum. Since total quantitative value is not obtained in [VCM-USEDM], the USEDM process performance variable permanent matrix is defined for the process in general (assuming interactions among all factors) as $[H] = [D+C]$, where $[D]$ and $[C]$ have the same meaning as stated earlier.

$$[H] = \begin{array}{c} Factors \\ H_1 \\ H_2 \\ H_3 \\ H_4 \\ H_5 \end{array} \begin{array}{c} \begin{array}{ccccc} H_1 & H_2 & H_3 & H_4 & H_5 \end{array} \\ \begin{bmatrix} H_1 & h_{12} & h_{13} & h_{14} & h_{15} \\ h_{21} & H_2 & h_{23} & h_{24} & h_{25} \\ h_{31} & h_{32} & H_3 & h_{34} & h_{35} \\ h_{41} & h_{42} & h_{43} & H_4 & h_{45} \\ h_{51} & h_{52} & h_{53} & h_{54} & H_5 \end{bmatrix} \end{array} \tag{5}$$

Thus, the variable permanent USEDM process performance matrix [VPM-USEDM] corresponding to the five-critical factors of USEDM performance digraph (Fig. 16) is given by

$$VPM - USEDM = \left[H^*\right] = \begin{array}{c} Factors \\ H_1 \\ H_2 \\ H_3 \\ H_4 \\ H_5 \end{array} \begin{array}{c} \begin{array}{ccccc} H_1 & H_2 & H_3 & H_4 & H_5 \end{array} \\ \begin{bmatrix} H_1 & 0 & h_{13} & h_{14} & h_{15} \\ h_{21} & H_2 & h_{23} & h_{24} & h_{25} \\ 0 & 0 & H_3 & h_{34} & h_{35} \\ 0 & 0 & h_{43} & H_4 & h_{45} \\ 0 & 0 & 0 & 0 & H_5 \end{bmatrix} \end{array} \tag{6}$$

The diagonal elements H_1, H_2, H_3, H_4 and H_5 represent the contribution of the five critical factors in creating the USEDM

process performance and the off-diagonal elements represent interdependencies of each element in the matrix. The contribution can be expressed quantitatively and is explained later in this paper.

3.3 Permanent representation for USEDM performance function

Both digraph and matrix representations are not unique as these change by changing the labeling of nodes. To develop a unique representation, independent of labeling, a permanent function of the matrix variable permanent matrix-USEDM (VPM-USEDM) is proposed for this purpose. Permanent is a standard matrix function and is used in combinatorial mathematics [48]. The permanent function is obtained in a similar manner as its determinant. A negative sign appears in the calculation of determinant while in the permanent, i.e. the variable permanent function, positive signs reduce these negative signs. These computation processes result in a multinomial (Eq. 6) that's every term has a physical significance related to the environment. This multinomial representation includes all the information regarding critical elements including human aspects and strategic policies and interactions amongst them. Quantitative USEDM evaluation of an organization is obtained from VPF-USEDM by substituting numerical values of the 'H_i's and 'h_{ij}'s which are obtained analytically or by comparing to ideal cases. This single numerical index is the representation of a typical USEDM environment in quantitative terms. The variable permanent USEDM function (VPF-USEDM), being the characteristic of the USEDM environment of an organization is a powerful tool for its analysis. The VPF-USEDM expression corresponds to the five-factor digraph/VPM-USEDM and is given by;

$$[\text{VPF-USEDM}] = per[H^*]$$

tors and all of the possible interdependency and inheritance between the various factors. The terms are the sets of distinct diagonal elements (i.e., 'H_i's) and loops of off-diagonal elements of different sizes (i.e., $h_{ij}h_{ji}$, $h_{ij}h_{jk}h_{ki}$, etc.).

The permanent of the matrix (i.e. Eq. 7) is a mathematical expression in symbolic form. It ensures an estimate of the USEDM process performance. Equation 7 contains M! terms. Each term is useful for USEDM experts as each term serves as a test for the interdependency. Equation 7 contains terms arranged in M + 1 group, where M is the number of factors, which in this case is 5. The physical significance of various grouping is explained as follows.

- The first term (grouping) represents a set of M unconnected USEDM performance factors, i.e. $H_1H_2H_3\ldots H_m$
- The second grouping is absent in the absence of self-loops.
- Each term of the third grouping represents a set of two-element USEDM loops (i.e. $h_{ij}h_{ji}$) and is the resultant USEDM interdependency and inheritance of characteristics 'i' and 'j' and the USEDM measure of the remaining M-2 unconnected elements.
- Each term of the fourth grouping represents a set of three-element USEDM loops ($h_{ij}h_{jk}h_{ki}$ or its pair $h_{ik}h_{kj}h_{ji}$) and the USEDM performance measure of the remaining M-3 unconnected elements.
- The fifth grouping contains two subgroups. The terms of the first sub grouping consist of two-element USEDM loops (i.e. $h_{ij}h_{ji}$ and $h_{kl}h_{lk}$) and USEDM component (H_m). The terms of the second grouping are a product of four-element USEDM loops (i.e. $h_{ij}h_{jk}h_{kl}h_{li}$) or its pair (i.e. $h_{il}h_{lk}h_{kj}h_{ji}$) and USEDM performance components (i.e. H_m).
- The terms of the sixth grouping are also arranged in two sub-groupings. The terms of the first sub-grouping are a product of a two-element USEDM performance loop (i.e. $h_{ij}h_{ji}$) and a three-element USEDM loop (i.e. $h_{kl}h_{lm}h_{mk}$) or its pair (i.e. $h_{km}h_{ml}h_{lk}$). The second sub-

$$\begin{aligned} per\left[H^*\right] = &\left[\prod_{i=1}^{m} H_i\right] + \left[\sum_i \sum_j \sum_k \sum_l \sum_m \sum_n (h_{ij}h_{ji})H_kH_lH_m\right] \\ &+ \left[\sum_i \sum_j \sum_k \sum_l \sum_m (h_{ij}h_{jk}h_{ki} + h_{ik}h_{kj}h_{ji})H_lH_m\right] \\ &+ \left[\begin{array}{l}\sum_i \sum_j \sum_k \sum_l \sum_m (h_{ij}h_{ji})(h_{kl}h_{lk})H_m \\ +\sum_i \sum_j \sum_k \sum_l \sum_m (h_{ij}h_{jk}h_{kl}h_{li} + h_{il}h_{lk}h_{kj}h_{ji})H_m\end{array}\right] \\ &+ \left[\begin{array}{l}\sum_i \sum_j \sum_k \sum_l \sum_m (h_{ij}h_{ji})(h_{kl}h_{lm}h_{mk} + h_{km}h_{ml}h_{lk}) \\ +\sum_i \sum_j \sum_k \sum_l \sum_m (h_{ij}h_{jk}h_{kl}h_{lm}h_{mi} + h_{im}h_{ml}h_{lk}h_{kj}h_{ji})\end{array}\right] \end{aligned} \tag{7}$$

grouping consists of a five-component USEDM loop (i.e. $h_{ij}h_{jk}h_{kl}h_{lm}h_{mi}$) or its pair ($h_{im}h_{ml}h_{lk}h_{kj}h_{ji}$).

Similarly other terms of the expression are defined. Thus, the USEDM performance Index function characterizes a mode of vibration for the considered machining operation as it contains all possible structural components of the factors and their interdependency and inheritance.

3.4 Quantification of 'H_i 's and 'h_{ij} 's

Quantification of the 'H_i's and 'h_{ij}'s (i.e. the diagonal and off-diagonal elements of permanent matrix of USEDM performance index) is required for evaluation of USEDM performance. The qualitative measure of the factors (i.e. the 'H_i's) is evaluated considering each 'H_i's as a subsystem and the graph theoretic approach is applied in each system. The USEDM performance index is a measure of the ease with which a material can satisfactorily be machined in a given machining operation. The USEDM performance function defined above i.e., Eq. 7 is used for evaluation of the performance index as it contains the presence of factors and their inherent interdependency. The numerical value of the USEDM performance function is called the performance index. As the USEDM performance function contains only positive terms, therefore higher values of 'H_i's and 'h_{ij}'s will result in an increased value of the USEDM performance index. To calculate this index, the required information from literature review and expert opinion are the values of 'H_i's and 'h_{ij}'s. The value of 'H_i' is obtained from a standard or specified test. If a quantitative value is not available, then a ranked value judgement on a scale, e.g., from 0 to 10, is adopted.

The value of of H_i and h_{ij} are evaluated with the Table 2 is suggested, which represents the performance attributes on a qualitative scale.

Table 2 Value of USEDM performance factors (H_i)

Qualitative measure of factors	Assigned value of importance of factors (H_i)
Extremely low	1
Very low	2
Low	3
Below average	4
Average	5
Above average	6
High	7
Very high	8
Extremely high	9

Table 3 Quantification measure of interdependency of diagonal elements 'h_{ij}'

S. no	Class description	Qualitative measure of interdependencies of 'h_{ij}'s
1	Very strongly dependent	5
2	Strongly dependent	4
3	Medium dependent	3
4	Weakly dependent	2
5	Very weakly dependent	1

It is workable for a given process some of the H_i qualities will be subjective and the rest quantitative. Also, these quantitative qualities will have diverse units. It is in this way attractive to change over or standardize the quantitative estimation of the H_i on the same scale as the subjective quality, i.e., 0–10.

The interdependency between two characteristics (i.e., h_{ij}) for a given USEDM operation is likewise appointed a quality on the scale 0–5 from Table 3 and is masterminded into six classes. The relative interdependency suggests that a property "i" is contrasted and another trait "j" as far as its interdependency for the given USEDM process.

4 Illustration of USEDM performance index

As discussed, the UEDM performance is a function of five elements and their interdependence. Although it is very difficult (and not common) to talk about USEDM performance in quantitative terms, the variable permanent function USEDM performance (i.e. Eq. 6) is a useful tool and estimate of the USEDM process.

4.1 Matrix permanent function generation at system Level

It is a function of various USEDM elements, their interdependencies and complexities. Hence the USEDM performance index USEDM process is given as:

$$\begin{aligned}&\text{USEDM performance index} = \text{per}[H^*]\\&= \text{Permanent value of [VPM-USEDM]};\\&VPM\text{-}USEDM = per[H^*]\\&= \begin{array}{c} Factors \\ H_1 \\ H_2 \\ H_3 \\ H_4 \\ H_5 \end{array} \begin{array}{c} \begin{array}{ccccc} H_1 & H_2 & H_3 & H_4 & H_5 \end{array} \\ \begin{bmatrix} H_1 & 0 & 5 & 5 & 4 \\ 4 & H_2 & 3 & 3 & 4 \\ 0 & 0 & H_3 & 4 & 3 \\ 0 & 0 & 3 & H_4 & 2 \\ 0 & 0 & 0 & 0 & H_5 \end{bmatrix} \end{array}\end{aligned} \tag{8}$$

4.2 Matrix and variable permanent function generation at sub-system level

Using generalized equation the variable permanent matrix (VPM) for each sub-system digraph (Figs. 8, 9, 10, 11 and 12) is written in Eqs. (9, 10, 11, 12, 13). The interdependency between sub-factors are assigned using table below, while the inheritance is assigned in next step.

$$VPM \text{ for flushing} = per[H^1]$$

$$= \begin{array}{c} sub\,factors \\ H_1^1 \\ H_2^1 \\ H_3^1 \\ H_4^1 \end{array} \begin{array}{c} \begin{array}{cccc} H_1^1 & H_2^1 & H_3^1 & H_4^1 \end{array} \\ \begin{bmatrix} H_1^1 & 5 & 0 & 3 \\ 0 & H_2^1 & 0 & 0 \\ 5 & 4 & H_3^1 & 4 \\ 0 & 4 & 0 & H_4^1 \end{bmatrix} \end{array} \tag{9}$$

$$VPM \text{ for cavitation} = per[H^2]$$

$$= \begin{array}{c} sub\,factors \\ H_1^2 \\ H_2^2 \\ H_3^2 \\ H_4^2 \\ H_5^2 \end{array} \begin{array}{c} \begin{array}{ccccc} H_1^2 & H_2^2 & H_3^2 & H_4^2 & H_5^2 \end{array} \\ \begin{bmatrix} H_1^2 & 4 & 0 & 0 & 0 \\ 0 & H_2^2 & 0 & 0 & 0 \\ 0 & 4 & H_3^2 & 4 & 0 \\ 0 & 5 & 0 & H_4^2 & 0 \\ 3 & 5 & 0 & 0 & H_5^2 \end{bmatrix} \end{array} \tag{10}$$

$$VPM \text{ for abnormal discharge} = per[H^3]$$

$$= \begin{array}{c} sub\,factors \\ H_1^3 \\ H_2^3 \\ H_3^3 \end{array} \begin{array}{c} \begin{array}{ccc} H_1^3 & H_2^3 & H_3^3 \end{array} \\ \begin{bmatrix} H_1^3 & 2 & 2 \\ 5 & H_2^3 & 5 \\ 3 & 0 & H_3^3 \end{bmatrix} \end{array} \tag{11}$$

$$VPM \text{ for dim.accuracy} = per[H^4]$$

$$= \begin{array}{c} subfactors \\ H_1^4 \\ H_2^4 \\ H_3^4 \\ H_4^4 \\ H_5^4 \end{array} \begin{array}{c} \begin{array}{ccccc} H_1^4 & H_2^4 & H_3^4 & H_4^4 & H_5^4 \end{array} \\ \begin{bmatrix} H_1^4 & 4 & 3 & 0 & 0 \\ 4 & H_2^4 & 3 & 0 & 5 \\ 4 & 0 & H_2^4 & 0 & 0 \\ 0 & 3 & 3 & H_4^4 & 0 \\ 4 & 4 & 4 & 0 & H_5^4 \end{bmatrix} \end{array} \tag{12}$$

$$VPM \text{ for surface morphology} = per\left[H^5\right]$$

$$= \begin{array}{c} sub\,factors \\ H_1^5 \\ H_2^5 \\ H_3^5 \\ H_4^5 \end{array} \begin{array}{c} \begin{array}{cccc} H_1^5 & H_2^5 & H_3^5 & H_4^5 \end{array} \\ \begin{bmatrix} H_1^5 & 3 & 4 & 3 \\ 0 & H_2^5 & 2 & 2 \\ 0 & 0 & H_3^5 & 4 \\ 0 & 0 & 3 & H_4^5 \end{bmatrix} \end{array} \tag{13}$$

4.3 Quantification of 'H_i 's and 'h_{ij} 's for USEDM sub-system level

The values of these factors and their interdependence for diagonal elements are found on the basis of the data available in the literature and the experience of manufacturing personnel. If a quantitative value is not available, then a ranked value judgment on a scale (*e.g.*, from 1 to 10) is adopted form Table 2, suggested for this purpose. To assign numerical values to the interdependence of barrier 'h_{ij} off diagonal elements the opinions of manufacturing experts can be recorded. But this interdependence of factors cannot be measured directly and, hence, qualitative values may be adopted. These qualitative values of the interdependence of enablers are also assigned form Table 3 on a scale (*e.g.*, 1–5), as suggested in Tables 4, 5, 6, 7 and 8.

Table 4 Quantification of flushing sub-factors

Factors	Flushing (H_1)			
Sub-factors	H_1^1	H_2^1	H_3^1	H_4^1
Quantitative value	8	9	7	6

Table 5 Quantification of cavitation sub-factors

Factors	Cavitation (H_2)				
Sub-factors	H_1^2	H_2^2	H_3^2	H_4^2	H_5^2
Quantitative value	2	9	8	7	7

Table 6 Quantification of abnormal discharge sub-factors

Factors	Abnormal discharge (H_3)		
Sub-factors	H_1^3	H_2^3	H_3^3
Quantitative value	9	8	7

Table 7 Quantification of dimensional accuracy sub-factors

Factors	Dimensional accuracy (H_4)				
Sub-Factors	H_1^4	H_2^4	H_3^4	H_4^4	H_5^4
Quantitative value	7	9	7	6	8

4.4 Calculation of permanent function for USEDM system and subsystem Level

The value of permanent function of each system and subsystem is evaluated by generalized Eq. 7. A computer program in MATLAB has been developed for it. Values of diagonal elements to sub-system have been provided in Tables (4, 5, 6, 7 and 8) using Table 4. These values are selected based on the previously published research, pervious experiments and FEA analysis carried by authors. Permanent function or index values of each sub-system are obtained

Table 8 Quantification of surface morphology sub-factors

Factors	Surface morphology (H_5)			
Sub-factors	H_1^5	H_2^5	H_3^5	H_4^5
Quantitative value	8	8	7	7

under different conditions of sub-factors.

$$VPM\ H_1 = per[H^1]$$

$$= \begin{array}{c} sub\ factors \\ H_1^1 \\ H_2^1 \\ H_3^1 \\ H_4^1 \end{array} \begin{array}{c} \begin{array}{cccc} H_1^1 & H_2^1 & H_3^1 & H_4^1 \end{array} \\ \begin{bmatrix} 8 & 5 & 0 & 3 \\ 0 & 9 & 0 & 0 \\ 5 & 4 & 7 & 4 \\ 0 & 4 & 0 & 6 \end{bmatrix} \end{array} = 3024$$

$$VPM\ H_2 = per[H^2]$$

$$= \begin{array}{c} sub\ factors \\ H_1^2 \\ H_2^2 \\ H_3^2 \\ H_4^2 \\ H_5^2 \end{array} \begin{array}{c} \begin{array}{ccccc} H_1^2 & H_2^2 & H_3^2 & H_4^2 & H_5^2 \end{array} \\ \begin{bmatrix} 2 & 4 & 0 & 0 & 0 \\ 0 & 9 & 0 & 0 & 0 \\ 0 & 4 & 8 & 4 & 0 \\ 0 & 5 & 0 & 7 & 0 \\ 3 & 5 & 0 & 0 & 7 \end{bmatrix} \end{array} = 7056$$

$$VPM\ H_3 = per[H^3]$$

$$= \begin{array}{c} sub\ factors \\ H_1^3 \\ H_2^3 \\ H_3^3 \end{array} \begin{array}{c} \begin{array}{ccc} H_1^3 & H_2^3 & H_3^3 \end{array} \\ \begin{bmatrix} 9 & 2 & 2 \\ 5 & 8 & 5 \\ 3 & 0 & 7 \end{bmatrix} \end{array} = 652$$

$$VPM\ H_4 = per[H^4]$$

$$= \begin{array}{c} sub\ factors \\ H_1^4 \\ H_2^4 \\ H_3^4 \\ H_4^4 \\ H_5^4 \end{array} \begin{array}{c} \begin{array}{ccccc} H_1^4 & H_2^4 & H_3^4 & H_4^4 & H_5^4 \end{array} \\ \begin{bmatrix} 7 & 4 & 3 & 0 & 0 \\ 4 & 9 & 3 & 0 & 5 \\ 4 & 0 & 7 & 0 & 0 \\ 0 & 3 & 3 & 6 & 0 \\ 4 & 4 & 4 & 0 & 8 \end{bmatrix} \end{array} = 46{,}632$$

$$VPM\ H_5 = per[H^5]$$

$$= \begin{array}{c} sub\ factors \\ H_1^5 \\ H_2^5 \\ H_3^5 \\ H_4^5 \end{array} \begin{array}{c} \begin{array}{cccc} H_1^5 & H_2^5 & H_3^5 & H_4^5 \end{array} \\ \begin{bmatrix} 8 & 3 & 4 & 3 \\ 0 & 8 & 2 & 2 \\ 0 & 0 & 7 & 4 \\ 0 & 0 & 3 & 7 \end{bmatrix} \end{array} = 3904$$

$$VPM\ USEDM = per[H^*]$$

$$= \begin{array}{c} Factors \\ H_1 \\ H_2 \\ H_3 \\ H_4 \\ H_5 \end{array} \begin{array}{c} \begin{array}{ccccc} H_1 & H_2 & H_3 & H_4 & H_5 \end{array} \\ \begin{bmatrix} 3024 & 0 & 5 & 5 & 4 \\ 4 & 7056 & 3 & 3 & 4 \\ 0 & 0 & 652 & 4 & 3 \\ 0 & 0 & 3 & 46{,}632 & 2 \\ 0 & 0 & 0 & 0 & 3904 \end{bmatrix} \end{array}$$

$$= 3.28647 \times 10^{18}$$

4.5 Coefficient of variation of USEDM performance index for system and sub-system level

The coefficient of variation for USEDM performance index can be evaluated by assuming the hypothetical extreme values of the USEDM sub-factors matrix diagonal elements. The index value is maximum or minimum when all the factors are affecting extremely high (9) or extremely low (1) as in Table 2, to the diagonal elements of the permanent function matrix correspondingly from Table 5. Hence, the USEDM performance index value can be calculate at these extreme values of sub-factors index (Table 9).

5 Conclusions

The exceptional commitment of the present work is to measure the impacts of different attributes in the execution ultrasonic vibration in traditional EDM process. The interdependency of the component/sub-variables signifies the importance of that specific attribute/sub-attributes with other element/sub-elements under thought. It has been observed in this study that, other than flushing and dimensional accuracy, cavitation likewise has a critical contribution. As cavitation is being viewed as essentially, one can't disregard the cavitation part of ultrasonic vibration usage and its repercussions.

The scientific model proposed in this paper can be utilized to add to a suitable speculation for the execution of ultrasonic vibration in traditional EDM process in view of the legacy and interdependency of various proposed component/sub-variables. This would help in controlling and upgrading process of customary EDM. Be that as it may, this methodology is to some degree new thinking in the space of USEDM. Portions of the outcome might significant commitment of this study are;

- The enormous numerical estimation of the performance index. For instance, 3.28647×10^{18} might seem to be an odd figure for down to earth purposes. But coefficient of variable utilized to round it off may indicate the significance.
- As the coefficient of variable for the USEDM is high that demonstrates the noteworthiness of the variables considered for USEDM performance Index.
- The coefficient of variable for surface morphology and flushing is underneath 20 % that show that ultrasonic vibration conferred to USEDM clearly enhance the flushing, surface morphology and dimensional accuracy.
- Cavitation and abnormal discharge's coefficient of variable is high and these attributes are less investigated by the researchers in literature, yet influence the USEDM performance index fundamentally.
- The digraph representation shows complex interdependency of variables and sub elements, cavitation influences every other component and corresponding coefficient of variable for this is high it deciphers very noteworthy element in USEDM process. In any case, the specialized impediments restrain its appropriateness in USEDM process.

Table 9 The coefficient of variation of index values of the permanent function

Permanent function	Performance index value	Maximum performance index	Minimum performance index	Coefficient of variation of index
Per(H^1)	3024	6561	6	7.90
Per(H^2)	7056	59,049	1	76.10
Per(H^3)	652	903	47	37.26
Per(H^4)	46,632	109,449	737	15.36
Per(H^5)	3904	7533	13	3.47
Per(H^*)	3.28647×10^{18}	2.88436×10^{20}	2.70278×10^{6}	99.84

References

1. Ho, K.H., Newman, S.T.: State of the art electrical discharge machining (EDM). Int. J. Mach. Tools Manuf. **43**, 1287–1300 (2003)
2. Guo, Z.N., Lee, T.C., Yue, T.M., Lau, W.S.: Study on the machining mechanism of WEDM with ultrasonic vibration of the wire. J. Mater. Process. Technol. **69**, 212–221 (1997)
3. Murali, M.S., Ganesh, B.P., Kamlakar, P.R.: A study on process parameters of ultrasonic assisted micro EDM based on Taguchi method. J. Mater. Eng. Perform. **17**, 210–215 (2007)
4. Changshui, G., Zhengxun, L.: A study of ultrasonically aided micro-electrical-discharge machining by the application of workpiece vibration. J. Mater. Process. Technol. **139**, 226–228 (2003)
5. Liew, P.J., Yan, J., Kuriyagawaa, T.: Fabrication of deep microholes in reaction-bonded SiC by ultrasonic cavitation assisted micro-EDM. Int. J. Mach. Tools Manuf. **76**, 13–20 (2014)
6. Egashira, K., Masuzawa, T.: Micro ultrasonic machining by the application of work piece vibration. CIRP Ann. Manuf. Technol. **48**, 131–134 (1999)
7. Praneetpongrung, C., Fukuzawa, Y., Nagasawa, S., Yamashita, K.: Effects of the EDM combined ultrasonic vibration on the machining properties of Si_3N_4. Mater. Transact. **51**(11), 2113–2120 (2010)
8. Singh, J., Walia, R.S., Satsangi, P.S., Singh, V.P.: Hybrid electric discharge machining process with continuous and discontinuous ultrasonic vibrations on workpiece. Int. J. Mech. Syst. Eng. **2**(1), 22–33 (2012)
9. Shabgard, M.R., Badamchizadeh, M.A., Ranjbary, G., Amin, K.: Fuzzy approach to select machining parameters in electrical discharge machining (EDM) and ultrasonic-assisted EDM processes. J. Manuf. Syst. **32**, 32–39 (2013)
10. Jangra, K., Jain, A., Grover, S.: Optimization of Multiple-machining characteristics in wire electrical discharge machining of punch die using gray relational analysis. J. Sci. Ind. Res. **69**, 606–612 (2010)
11. Jangra, K., Grover, S., Aggarwal, A.: Digraph and matrix method for the performance evaluation of carbide compacting die manufactured by wire EDM. Int. J. Adv. Manuf. Technol. **54**, 579–591 (2010)
12. Rao, R.V., Gandhi, O.P.: Digraph and Matrix methods for the machinability evaluation of work materials. Int. J. Mach. Tools Manuf. **42**, 321–330 (2002)
13. Tzeng, Y.F., Chen, F.C.: Multi-objective optimisation of high-speed electrical discharge machining process using a Taguchi fuzzy-based approach. J. Mater. Process. Technol. **28**, 1159–1168 (2007)
14. Gandhi, O.P., Agrawal, V.P.: FMEA—a digraph and matrix approach. Reliab. Eng. Syst. Saf. **35**, 147–158 (1992)
15. Pandey, P.C., Shan, H.S.: Modern Machining Process. Tata McGraw Hill publishing Company, New Delhi (2009)
16. Ghoreishi, M., Atkinson, J.: A comparative experimental study of machining characteristics in vibratory, rotary and vibro-rotary electro-discharge machining. J. Mater. Process. Technol. **120**, 374–384 (2002)
17. Kremer, D., Lebrun, J.L., Hosari, B., Moisan, A.: Effects of ultrasonic vibrations on the performances in EDM. Ann. CLRP **38**(1), 199–202 (1989)
18. Lee, T.C., Zhang, J.H., Lau, W.S.: Machining of engineering ceramics by ultrasonic vibration assisted EDM method. Mater. Manuf. Processes **13**(1), 133–146 (1998)
19. Schubert, A., Zeidler, H., Oschätzchen, M.H., Schneider, J., Hahn, M.: Enhancing micro-EDM using ultrasonic vibration and approaches for machining of nonconducting ceramics. J. Mech. Eng. **59**(3), 156–164 (2013)
20. Huang, H., Zhang, H., Zhou, L., Zheng, H.Y.: Ultrasonic vibration assisted electro-discharge machining of microholes in nitinol. J. Micromech. Microeng. **13**, 693–700 (2003)
21. Zhixin, J., Zhang, J., Xing, A.: Ultrasonic vibration pulse electro-discharge machining of holes in engineering ceramic. J. Mater. Process. Technol. **53**, 811–816 (1995)
22. Kim, D.J., Yi, S.M., Lee, Y.S., Chu, C.N.: Straight hole micro EDM with a cylindrical tool using a variable capacitance method accompanied by ultrasonic vibration. J. Micromech. Microeng. **16**, 1092–1097 (2006)
23. Murthi, V.S.R., Philip, P.K.: A comparative analysis of machining characteristics in ultrasonic assisted EDM by response surface methodology. Int. J. Prod. Res. **25**(2), 259–272 (1987)
24. Kremer, D., Lhiaubet, C., Moisan, A.: Study of the effect of synchronizing ultrasonic vibrations with pulses in EDM. Ann. CIRP **40**, 211–214 (1991)
25. Pang, Y.L., Abdullah, A.Z., Bhatia, S.: Review on sonochemical methods in the presence of catalysts and chemical additives for treatment of organic pollutants in wastewater. Desalination **277**, 1–14 (2011)
26. Marinescu, N.I., Ghiculescu, D., Jitianu, G.: Solutions for technological performance increasing at ultrasonic aided electro discharge machining. Int. J. Mater. Form. **2**(1), 681–684 (2009)
27. Yu, Z.Y., Zhang, Y., Li, J., Luan, J., Zhao, F., Guo, D.: High aspect ratio micro-hole drilling aided with ultrasonic vibration and planetary movement of electrode by micro-EDM. CIRP Ann. Manuf. Technol. **58**, 213–216 (2009)
28. Garn, R., Schubert, A., Zeidler, H.: Analysis of the effect of vibrations on the micro-EDM process at the workpiece surface. Precis. Eng. **35**, 364–368 (2011)
29. Mahardika, M., Prihandana, G.S., Endo, T., Tsujimoto, T., Matsumoto, N., Arifvianto, B., Mitsui, K.: The parameters evaluation and optimization of polycrystalline diamond micro-electro discharge machining assisted by electrode tool vibration. Int. J. Adv. Manuf. Technol. **60**, 985–993 (2012)

30. Lin, Y.C., Yan, B.H., Chang, Y.S.: Machining characteristics of titanium alloy (Ti-6Al-4V) using a combination process of EDM with USM. J. Mater. Process. Technol. **104**, 171–177 (2000)
31. Iwai, M., Ninomiya, S., Suzuki, K.: Improvement of EDM properties of PCD with electrode vibrated by ultrasonic transducer. In: The 17th CIRP Conference on Electro Physical and Chemical Machining (ISEM) Procedia CIRP **6**, 146–150 (2013)
32. Prihandana, G.S., Mahardika, M., Hamdi, M., Wong, Y.S., Mitsui, K.: Effect of micro-powder suspension and ultrasonic vibration of dielectric fluid in micro-EDM processes—Taguchi approach. Int. J. Mach. Tools Manuf. **49**, 1035–1041 (2009)
33. Narasimhan, J., Yu, Z., Rajurkar, K.P.: Tool wear compensation and path generation in micro and macro EDM. J. Manuf. Processes **7**(10), 76–82 (2005)
34. Mohri, N., Saito, N., Higash, M.: A new process of finish machining on free surface by EDM methods. Ann. CIRP **40**(1), 207–210 (1991)
35. Shabgard, M.R., Sadizadeh, B., Kakoulvand, H.: The effect of ultrasonic vibration of work-piece in electrical discharge machining of AISIH13 tool steel. World Acad. Sci. Eng. Technol. **52**, 392–396 (2009)
36. Teimouri, R., Baseri, H.: Experimental study of rotary magnetic field-assisted dry EDM with ultrasonic vibration of workpiece. Int. J. Adv. Eng. Technol. **67**, 1371–1384 (2012)
37. Wansheng, Z., Zhenlong, W., Shichun, D., Guanxin, C., Hongyu, W.: Ultrasonic and electric discharge machining of deep hole titanium alloy. J. Mater. Process. Technol. **120**, 101–106 (2002)
38. Kwan, K.M., Benatar, A.: Modeling of ultrasonic forced wetting process by dimensional analysis. In: Proceedings of 59th Society of Plastics Engineers Annual Conference, pp 1239–1243 (2001)
39. Srivastava, V., Pandey, P.M.: Effect of process parameters on the performance of EDM process with ultrasonic assisted cryogenically cooled electrode. J. Manuf. Processes **14**, 393–402 (2012)
40. Abdullah, A., Shabgard, M.R., Ivanov, A., Mohammad, T., Shervanyi, T.: Effect of ultrasonic assisted EDM on the surface integrity of cemented tungsten carbide (WC-Co). Int. J. Adv. Manuf. Technol. **41**, 268–280 (2009)
41. Guu, Y.H., Hocheng, H.: Effect of workpiece rotation on machinability during electric discharge machining. Mater. Manuf. Processes **16**(1), 91–101 (2001)
42. Agrawal, S., Singh, R.K., Murtaza, Q.: Outsourcing decisions in reverse logistics: sustainable balanced scorecard and graph theoretic approach. Resour. Conserv. Recycl. **108**, 41–53 (2016)
43. Deo, N.: Graph theory with application to engineering and computer science. Prentice Hall, New Delhi (2000)
44. Gandhi, O.P., Agrawal, V.P.: A digraph approach to system wear evaluation and analysis. Trans. ASME **116**, 268–274 (1994)
45. Grover, S., Agrawal, V.P., Khan, I.A.: A digraph approach to TQM evaluation in an industry. Int. J. Prod. Res. **42**(19), 4031–4053 (2004)
46. Grover, S., Agrawal, V.P., Khan, I.A.: Role of human factors in TQM: a graph theoretic approach. Bench. Mark. Int. J. **13**(4), 447–468 (2006)
47. Hitoshi, O., Hamada, S., Aoyama, T.: Ultrasonic cavitation assisted EDM of CFRP. Electr. Mach. Technol. **36**(112), 21–26 (2012)
48. Jurkat, W.B., Ryser, H.J.: Matrix factorization of determinants and permanents. J. Algebra **3**, 1–27 (1966)
49. Lin, Y.C., Yan, B.H., Huang, Y.F.: Surface modification of Al-Zn-Mg aluminum alloy using EDM with USM. J. Mater. Process. Technol. **115**, 359–366 (2001)
50. Mesee, J., Fukuzawa, Y., Shigeru, N., Daiki, H., Muttamara, A.: Surface modification using EDM combined ultrasonic vibration. Jpn. Soc. Precis. Eng. **P32**, 1213–1214 (2014)
51. Nishiwaki, N., Hori, S., Natsu, W.: Detection of electric discharge machining state by using ultrasonic technique. In: 17th World Conference on Nondestructive Testing, Shanghai, China, pp 25–28 (2008)
52. Pandey, A., Singh, S.: Current research trends in variants of electrical discharge machining: a review. Int. J. Eng. Sci. Technol. **2**(6), 2172–2191 (2010)
53. Rao, R.V., Gandhi, O.P.: Failure cause analysis of machine tools using digraph and matrix methods. Int. J. Mach. Tools Manuf. **42**, 521–528 (2002)
54. Shabgard, M.H., Alenabi, H.: Ultrasonic assisted electrical discharge machining of Ti-6Al-4V alloy. Mater. Manuf. Processes **30**, 991–1000 (2015)
55. Singh, J., Walia, R.S., Satsangi, P.S., Singh, V.P.: FEM modeling of ultrasonic vibration assisted workpiece in EDM process. Int. J. Mech. Syst. Eng. **1**(1), 8–16 (2012)
56. Wani, M.F., Gandhi, O.P.: Development of maintainability index for mechanical systems. Reliab. Eng. Syst. Saf. **65**(3), 259–270 (1999)
57. Ghiculescu, D., Marinescu, N.I., Nanu, S.: Innovative solution for performance increase at micro electrical discharge machining aided by ultrasonic. Nonconventional Technologies Review Romania, pp 15–20 (2014)
58. Ghiculescu, D., Marinescu, N.I., Nanu, S., Ghiculescu, D.: Multiphysics 3D finite element modelling of Micro-electrodischarge machining Aided by Ultrasonic. Nonconventional Technologies Review Romania, pp 72–77 (2012)

Author's Accepted Manuscript



www.elsevier.com

Biofunctionalized Nanostructured Tungsten Trioxide Based Sensor for Cardiac Biomarker Detection

Deepika Sandil, Saurabh Kumar, Kamal Arora, Saurabh Srivastava, B.D. Malhotra, S.C. Sharma, Nitin K. Puri

PII: S0167-577X(16)31567-1
DOI: http://dx.doi.org/10.1016/j.matlet.2016.09.107
Reference: MLBLUE21545

To appear in: *Materials Letters*

Received date: 20 June 2016
Revised date: 29 August 2016
Accepted date: 26 September 2016

Cite this article as: Deepika Sandil, Saurabh Kumar, Kamal Arora, Saurabh Srivastava, B.D. Malhotra, S.C. Sharma and Nitin K. Puri, Biofunctionalized Nanostructured Tungsten Trioxide Based Sensor for Cardiac Biomarker Detection, *Materials Letters,* http://dx.doi.org/10.1016/j.matlet.2016.09.107

This is a PDF file of an unedited manuscript that has been accepted for publication. As a service to our customers we are providing this early version of the manuscript. The manuscript will undergo copyediting, typesetting, and review of the resulting galley proof before it is published in its final citable form. Please note that during the production process errors may be discovered which could affect the content, and all legal disclaimers that apply to the journal pertain.

ACCEPTED MANUSCRIPT

Biofunctionalized Nanostructured Tungsten Trioxide Based Sensor for Cardiac Biomarker Detection

Deepika Sandil[1], Saurabh Kumar[2], Kamal Arora[1], Saurabh Srivastava[1], B.D. Malhotra[2], S.C. Sharma[1], Nitin K. Puri[1*]

[1] *Advanced Sensor Laboratory, Department of Applied Physics, Delhi Technological University, Delhi-110042, India*
[2] *Department of Biotechnology, Delhi Technological University, Main Bawana Road, Delhi-110042, India*

Accepted manuscript

Abstract

We report results of the studies relating to the technological development of 3-aminopropyl tri-ethoxy saline (APTES) conjugated tungsten trioxide nanoparticles (APTES/n-WO_3) based sensor for cardiac Troponin I (cTnI) detection. The APTES/n-WO_3 nanoparticles were deposited onto indium tin oxide (ITO) coated glass electrode via electrophoretic deposition technique and were subsequently functionalized with troponin antibodies (anti-cTnI). The n-WO_3/ITO and anti-cTnI/APTES/n-WO_3/ITO electrodes were characterized using X-ray diffraction (XRD), UV-vis spectroscopy, Fourier transform infrared (FT-IR) spectroscopy, atomic force microscopy (AFM) and electrochemical impedance spectroscopy (EIS) respectively. This immunosensor exhibited a wider linear detection range (1-250 ng mL^{-1}) with good sensitivity (26.56 Ω $ng^{-1}mL\ cm^{-2}$).

KEYWORDS: Nanostructured tungsten trioxide, Troponin, Immunosensor, Electrophoretic deposition.

***Corresponding Authors Email:** nitin.phy@dce.edu, saurabhnpl@gmail.com, bansi.malhotra@gmail.com

ACCEPTED MANUSCRIPT

1. Introduction

The fusion of biological molecules and nano-structured metal oxides is known to play an important role towards the development of nano-scale devices in clinical diagnostics and electronic applications[1]. Among the various nanostructured metal oxides, nanostructured tungsten trioxide (n-WO_3) has been found to have interesting physical and chemical properties[2]. n-WO_3 exhibits good electrical conductivity and catalytic behavior, that may perhaps make them suitable for application as "electronic wires" to enhance electron transfer between redox centers in proteins and electrode surfaces [3]. Besides this, the high surface-to-volume ratio and electrical properties of n-WO_3 can be used as labels or tracers for electrochemical analysis. The n-WO_3 has been predicted to have biosensing applications. Hariharan et.al employed WO_3 based biosensor for L- dopa detection with high selectivity and sensitivity[4]. Sun et.al utilized WO_3 for the glucose detection with high efficiency; thus, holding great promises for applications in bioelectronics[5]. There is thus a good scope to explore WO_3 for the efficient detection of other important bio-analytes.

Acute myocardial infarction (AMI) is a major cause of death caused by necrosis of myocardial tissue due to ischemia. Among the various biomarkers, cardiac Troponin I (cTnI) has been recognized as a principle biomarker with high specificity and great selectivity for the cardio vascular diseases. The level of cTnI in normal subjects is around 1 ng mL^{-1} that may increase to 550 ng mL^{-1} in AMI patients[6]. Hence rapid and sensitive detection of cTnI with good detection range is urgently required for the early treatment of AMI. In the present work, we demonstrate the development of a simple and label-free immunosensor to detect myocardial symptomatic biomarker Troponin-I using nanostructured tungsten trioxide. The proposed detection strategy is simple, economical and is based on direct immobilization of an antibody over 3–aminopropyl triethoxy saline (APTES) functionalized n-WO_3/ITO electrode. The results of the present studies exhibit good sensitivity, broad detection range and high storage stability.

2. Experimental

All chemicals of analytical grade were purchased from Sigma-Aldrich. The XRD (Bruker D-8 Advance), FT-IR (Nicolet 380) and AFM (Park system XE-100) were used for

Accepted manuscript

ACCEPTED MANUSCRIPT

characterization of material and electrodes. The electrochemical studies were carried out on an Autolab Potentiostat/Galvanostat (Metrohm, Netherlands) using a three- electrode system. De-ionized water (18.2 MΩ) was used for preparation of solutions.

The details of synthesis of nanostructured tungsten trioxide (n-WO_3) and its Functionalization with APTES have been given in the Supplementary Information sheet. [12] Thin film of APTES functionalized n-WO_3 over ITO (APTES/n-WO_3/ITO) electrode was prepared by electrophoretic deposition (EPD) technique. The anti-cTnI antibodies were immobilized over APTES/n-WO_3/ITO electrode. The fabrication of APTES/n-WO_3/ITO electrode and anti-cTnI/APTES/n-WO_3/ITO bioelectrode has been given in the Supplementary Information sheet [12]. The Schematic of fabrication of immunoelectrode has been demonstrated in Scheme 1.

3. Results and discussion

The XRD studies were carried out to investigate the crystallinity and phase of n-WO_3 powder and shown in figure 1(i). The presence of intense characteristic peak at 24.22^0 and other diffraction peaks at 28.56^0, 33.99^0, 41.39^0, 50.09^0, 55.6^0 and 61.58^0 are well indexed to (200), (112), (220), (222), (114), (420) and (134) planes, respectively (JCPDS 71-0131) and reveal the presence of orthogonal phase in WO_3 with good crystalline structure. The average crystallite size *D* of WO_3 nanoparticles was estimated to be 20 nm using Debye-Scherer equation.

$$\boldsymbol{D = \frac{0.9\,\lambda}{\beta\, Cos\theta}} \qquad (1)$$

Fig. 1(ii) shows Fourier transform infrared spectra (FT-IR) of the (a) n-WO_3, (b) APTES/n-WO_3, (c) anti-cTnI/APTES/n-WO_3. The band seen at 1410 cm^{-1} [Fig. 1(ii, a)] represents stretching vibration of ν (W–O) whereas broad band at 770 cm^{-1} corresponds to ν (W–O_{inter}–W) stretching vibration of the bridging O_2[7].In figure 1(ii, b), band seen at 3421 cm^{-1} is due to asymmetric (N–H) stretching vibration of NH_2 whereas peaks at 1614 cm^{-1} and 1422 cm^{-1} corresponds to δ(–NH_2) and δ (Si–CH_2) respectively present in APTES[8-10].The peak at 2932 cm^{-1} is attributed to methylene group (–CH_2) indicating that silane agent was grafted onto the surface successfully and the peak at 1122 cm^{-1} is due to stretching mode of Si–O–Si[9].

ACCEPTED MANUSCRIPT

These results suggest that APTES is successfully anchored on the WO_3 surface. In the FT-IR spectra of antibody immobilized APTES/n-WO_3 /ITO electrode (Fig.1 ii c), the bands seen at 3462 cm^{-1}, 1636 cm^{-1} and 733 cm^{-1} can be attributed to the amide B, amide I and amide IV respectively indicating successful immobilization of the antibody on the electrode. Whereas bands observed at 2927 cm^{-1} ($–CH_2$) and at 1101 cm^{-1} (Si–O–Si) were found to be shifted after antibody immobilization.

Topography and surface roughness of the electrode are known to play an important role in determining the conformation of the adsorbed protein layer[10]. Figure 2 represents the topographical image of 3-D height plots for the electrodes. It can be seen that the average surface roughness of n-WO_3/ITO electrode (0.307 nm; Fig. 2a) decreased to 0.120 nm (Fig. 2b) after modification with APTES suggesting the formation of a uniform layer due to intermolecular interaction between APTES and n-WO_3/ITO surfaces. Finally after immobilization of anti-cTnI on APTES/n-WO_3/ITO electrode surface (Fig. 2c), average roughness increased to 5.9 nm indicating attachment of the antibody molecules.

Electrochemical impedance spectroscopy (EIS) technique was utilized to determine the interfacial properties between the electrode–electrolyte boundaries. Fig. 3(a) shows the Nyquist plot obtained for bare ITO electrode, APTES/n-WO_3/ITO and anti-cTnI/APTES/nWO_3/ITO electrodes in the PBS (pH 7.0) containing 5mM $[Fe(CN)_6]^{4-/3-}$ in the frequency range 10^7 to 10^{-2} Hz at a biasing potential of 10 mV. The charge transfer process in these electrodes was investigated by measuring charge transfer resistance (R_{ct}) at the electrode/electrolyte interface. It was observed that magnitude of R_{ct} for ITO electrode (434.07 Ω) increased to 543.15 Ω for APTES/n-WO_3/ITO electrode indicating modification of the ITO electrode with APTES modified WO_3 nanoparticles. And after the antibody immobilization, R_{ct} of anti-cTnI/APTES/n-WO_3/ITO electrode further increased to 589.36 Ω indicating the insulating nature of the antibody molecules.

Electrochemical response studies of the anti-cTnI/APTES/n-WO_3/ITO immunoelectrode were conducted as a function of cTnI concentration (1-250 ng mL^{-1} using EIS technique (Fig. 3b). R_{ct} was evaluated from the diameter of the Nyquist plot while fitting the curve under Randles circuit. It was found that R_{ct} of the immunoelectrode (anti-cTnI/APTES/n-WO_3/ITO) increased linearly as a function of cTnI concentration (1-250 ng mL^{-1}). This could

Accepted manuscript

ACCEPTED MANUSCRIPT

perhaps be due to the formation of electrically insulating antigen–antibody complexes produced from the specific interaction of the cTnI and antibody that may block the electron transfer via $[Fe(CN)_6]^{3-/4-}$[11]. The linear variation of the R_{ct} value obtained from the calibration plot (Fig. 3c) obeys Eq. (3)

R_{ct} (Ω) = 618.70 (Ω) + 6.64 (Ω ng $^{-1}$ mL) * [concentration (ng mL^{-1})] (3)

with regression coefficient (R^2) = 0.99.

The APTES/n-WO_3/ITO based immunosensor exhibits high sensitivity of 26.56 Ω $ng^{-1}mL\ cm^{-2}$ in the linear detection range of 1-250 ng mL^{-1}. Furthermore, a control experiment was performed to investigate the electrochemical response of APTES/n-WO_3/ITO electrode towards cTnI without using anti-cTnI. We did not observe any significant change in magnitude of R_{ct} with respect to different concentration of cTnI. This result indicated that the sensor response was due to the immunoreactions between anti-cTnI and cTnI molecules only. Figure S2 compares R_{ct} response of anti-cTnI/APTES/n-WO_3/ITO immunoelectrode in presence of serum sample (containing 100 ng mL^{-1} cTnI) and standard sample (100 ng mL^{-1} cTnI) [12]. The estimated low RSD value (2.65%) indicated that the anti-cTnI/APTES/n-WO_3/ITO immunoelectrode could be utilized for real sample analysis. The storage stability of the anti-cTnI/APTES/n-WO_3/ITO immunoelectrode was investigated by observing the EIS response and measuring the R_{ct} value at a regular interval of five days up to 40 days in presence of 50 ng mL^{-1} cTnI concentration (Fig. 3d). The R_{ct} value was found to be 92% of its initial response for up to 30 days, thereafter it further decreased to 80% at the end of 40 days. This indicated the storage stability of the fabricated biosensor as 30 days. The reproducibility and selectivity studies of the fabricated biosensor has been demonstrated in the Supplementary Information sheet [12] Table I shows the characteristics of the fabricated biosensor along with some those reported in the literature for cTnI detection [see Supplementary Information sheet] [12]. The APTES/n-WO_3/ITO based biosensor exhibits a much higher sensitivity (26.56 Ω $ng^{-1}mL\ cm^{-2}$), good stability (30 days), and an extended linearity (1-250 ng mL^{-1}) than some of the other sensors reported in the literature.

4. Conclusion

In summary, we have successfully synthesized and functionalized nanostructured tungsten trioxide (n-WO_3). Thin films of APTES/n-WO_3/ITO have been fabricated via

ACCEPTED MANUSCRIPT

electrophoretic deposition technique and followed by covalent immobilization of antibody of cTnI for the detection of cTnI using EIS technique. In comparison with other reported Troponin biomarker detection methods including biosensors, the proposed biosensor is simple and label free. It exhibits a wider detection range as 1-250 ng mL^{-1}, sensitivity as 26.56 Ω $ng^{-1}mL\ cm^{-2}$, storage stability as 30 days and detection limit as16 ng mL^{-1}. This may be attributed to high antibody loading properties and rapid electron transfer kinetics of n-WO_3. This superior sensing performance of the n-WO_3 based immunosensor reveals its potential for electrochemical biosensing applications. Further efforts should be made to further improve the detection limit of this proposed biosensor.

Acknowledgements

The authors thank Prof. Yogesh Singh, Vice chancellor, Delhi Technology University, Delhi, India for providing the research facilities. The financial supports received from IUAC sponsored project (Grant No. IUAC/XIII.7/UFR-56324) and Department of Science and Technology, India (Grant No. DST/INSPIRE/04/2014/002540) are gratefully acknowledged.

References

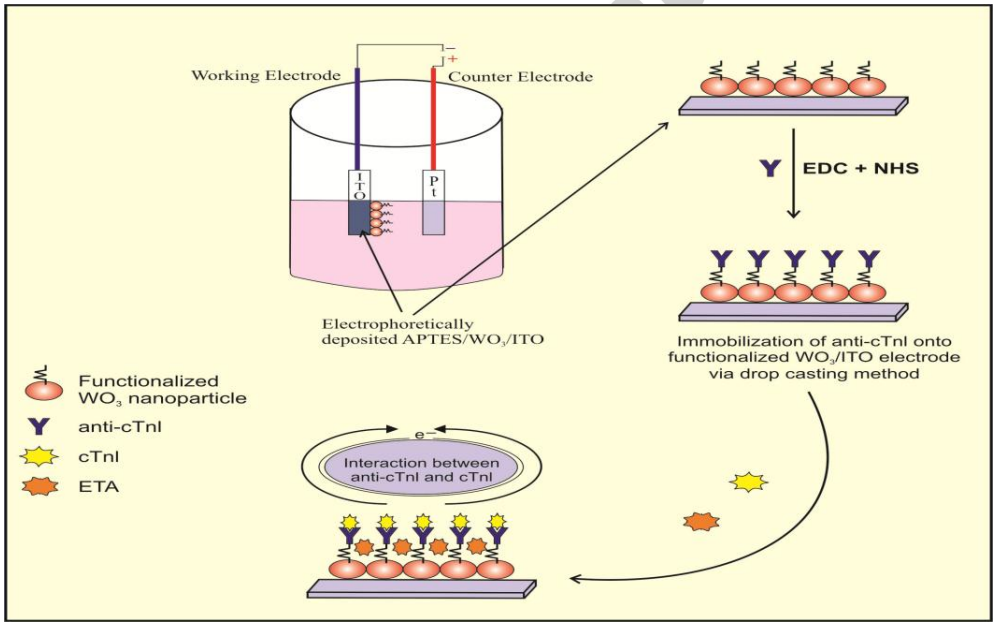
[1] P.R. Solanki, A. Kaushik, V.V. Agrawal, B.D. Malhotra, Nanostructured metal oxide-based biosensors, NPG Asia Materials 3(1) (2011) 17-24.
[2] H. Zheng, J.Z. Ou, M.S. Strano, R.B. Kaner, A. Mitchell, K. Kalantar- zadeh, Nanostructured tungsten oxide–properties, synthesis, and applications, Advanced Functional Materials 21(12) (2011) 2175-2196.
[3] Z. Deng, Y. Gong, Y. Luo, Y. Tian, WO 3 nanostructures facilitate electron transfer of enzyme: application to detection of H 2 O 2 with high selectivity, Biosensors and Bioelectronics 24(8) (2009) 2465-2469.
[4] V. Hariharan, S. Radhakrishnan, M. Parthibavarman, R. Dhilipkumar, C. Sekar, Synthesis of polyethylene glycol (PEG) assisted tungsten oxide (WO 3) nanoparticles for l-dopa bio-sensing applications, Talanta 85(4) (2011) 2166-2174.
[5] Q.-Q. Sun, M. Xu, S.-J. Bao, C.M. Li, pH-controllable synthesis of unique nanostructured tungsten oxide aerogel and its sensitive glucose biosensor, Nanotechnology 26(11) (2015) 115602.
[6] A. Periyakaruppan, R.P. Gandhiraman, M. Meyyappan, J.E. Koehne, Label-free detection of cardiac troponin-i using carbon nanofiber based nanoelectrode arrays, Analytical chemistry 85(8) (2013) 3858-3863.
[7] M. Tong, G. Dai, Y. Wu, X. He, D. Gao, WO3 thin film prepared by PECVD technique and its gas sensing properties to NO2, Journal of Materials Science 36(10) (2001) 2535-2538.

Accepted manuscript

ACCEPTED MANUSCRIPT

[8] N. Majoul, S. Aouida, B. Bessaïs, Progress of porous silicon APTES-functionalization by FTIR investigations, Applied Surface Science 331 (2015) 388-391.
[9] M. Ata, Y. Liu, I. Zhitomirsky, A review of new methods of surface chemical modification, dispersion and electrophoretic deposition of metal oxide particles, RSC Advances 4(43) (2014) 22716-22732.
[10] K.K. Jagadeesan, S. Kumar, G. Sumana, Application of conducting paper for selective detection of troponin, Electrochemistry Communications 20 (2012) 71-74.
[11] S. Srivastava, V. Kumar, M.A. Ali, P.R. Solanki, A. Srivastava, G. Sumana, P.S. Saxena, A.G. Joshi, B. Malhotra, Electrophoretically deposited reduced graphene oxide platform for food toxin detection, Nanoscale 5(7) (2013) 3043-3051.
[12] See Supplementary Information sheet for the preparation of n-WO3, its functionalization, fabrication of bioelectrode, UV-Vis, real sample analysis, reproducibility, selectivity studies and comparison table.

Scheme 1



ACCEPTED MANUSCRIPT

Figure 1

Fig. 1.(i)

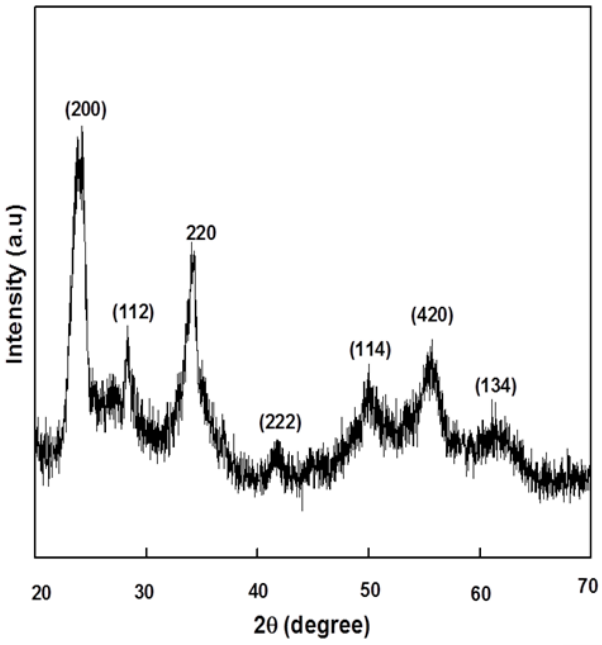
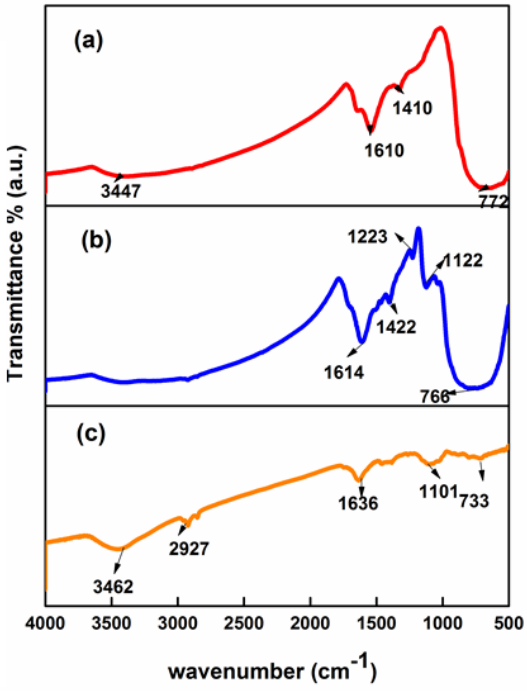
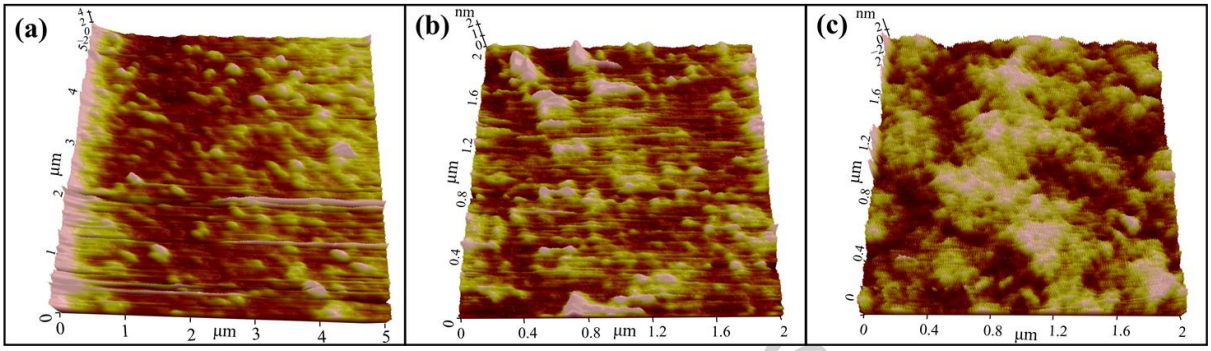


Fig. 1.(ii)



ACCEPTED MANUSCRIPT

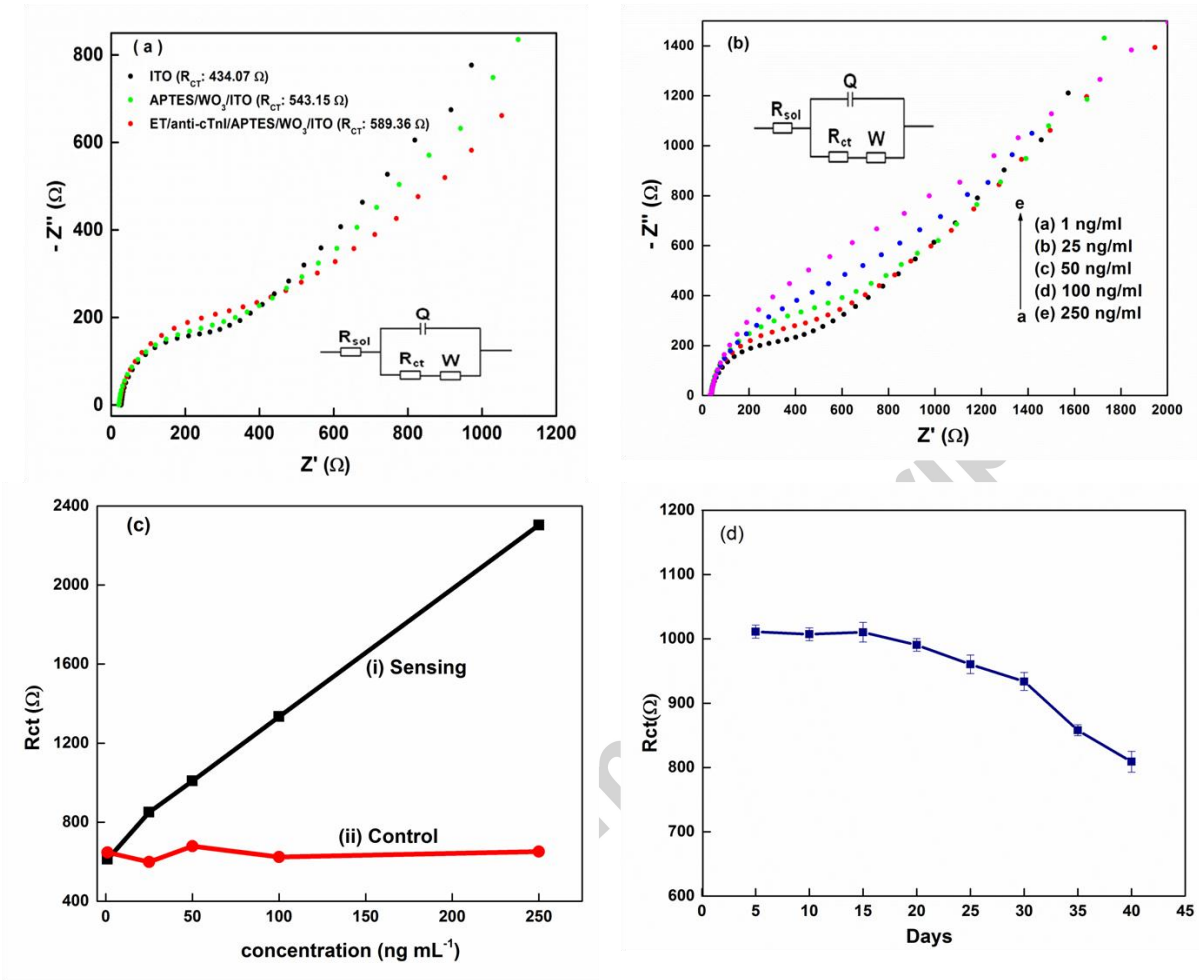
Figure 2



Accepted manus

ACCEPTED MANUSCRIPT

Figure 3



ACCEPTED MANUSCRIPT

Figure legends:

Scheme 1: Schematic of fabrication of the anti-cTnI/APTES/n-WO_3/ITO bioelectrode for Troponin-I detection.

Fig. 1(i): X-ray diffraction pattern obtained for the WO_3 nanoparticles

Fig. 1(ii): FT-IR spectra of **(a)** n-WO_3, **(b)** APTES/n-WO_3 and **(c)** anti-cTnI/APTES/n-WO_3.

Fig. 2: AFM image of a**)** n-WO_3/ITO electrode, **(b)** APTES/n-WO_3/ITO electrode and **(c)** anti-cTnI/APTES/n-WO_3/ITO bioelectrodes.

Fig. 3: (a) shows results of the electrochemical impedance spectroscopy (EIS) studies of the various fabricated electrodes (ITO, APTES/n-WO_3/ITO and anti-cTnI/APTES/n-WO_3/ITO) **(b)** Response studies of the anti-cTnI/APTES/n-WO_3/ITO immunoelectrode as a function of cTnI concentration (1- 250ng/mL) using EIS technique **(c)** Calibration plot obtained between R_{ct} and cTnI concentration with control studies **(d)** Stability studies of the anti-cTnI/APTES/n-WO_3/ITO immunoelectrode.

Highlights

- Thin film of APTES conjugated n-WO_3 was electrophoretically fabricated
- APTES/n-WO_3 was biofunctionalized for impedemetric detection of cardiac Troponin-I
- The immunosensor reveals high selectivity, reproducibility and long term stability
- It displays high sensitivity (26.56 Ω $ng^{-1}mLcm^{-2}$) and linearity (1-250 ng mL^{-1})
- The proposed immunosensor holds great promises in the biomedical field

Accepted manuscript

Materials Science and Engineering C 70 (2017) 564–571

Contents lists available at ScienceDirect

Materials Science and Engineering C

journal homepage: www.elsevier.com/locate/msec

Bismuth oxide nanorods based immunosensor for mycotoxin detection

Pratima R. Solanki [a,b,*], Jay Singh [a,c], Bharti Rupavali [a], Sachchidanand Tiwari [b], Bansi D. Malhotra [a,d,*]

[a] DST Centre for Biomolecular Electronics, CSIR-National Physical Laboratory, K.S. Krishnan Marg, New Delhi, India
[b] Special Centre for Nano Sciences, Jawaharlal Nehru University, New Delhi 110067, India
[c] Department of Applied Chemistry and Polymer Technology, Delhi Technological University, Shahbad Daulatpur, Main Bawana Road, Delhi 110042, India
[d] Department of Biotechnology, Delhi Technological University, Shahbad Daulatpur, Main Bawana Road, Delhi 110042, India

ARTICLE INFO

Article history:
Received 15 June 2016
Received in revised form 19 August 2016
Accepted 12 September 2016
Available online 13 September 2016

Keywords:
Bismuth oxide nanorods (nBi_2O_3)
Aflatoxin B1
Immunosensor
Electrochemical studies

ABSTRACT

We report results of the studies relating to fabrication of an efficient immunosensor based on bismuth oxide nanorods (nBi_2O_3), electrophoretically deposited onto indium-tin-oxide (ITO) coated glass substrate. This immunosensor was fabricated by immobilization of anti-aflatoxin monoclonal antibodies (Ab-AFB1) and bovine serum albumin (BSA) for aflatoxin B1 detection. The structural and morphological studies of n-Bi_2O_3 have been carried out by XRD, UV–vis spectrophotometer; SEM, AFM and FTIR. It was found that the nBi_2O_3 provided improved sensing characteristics to the electrode interface in terms of electroactive surface area, diffusion coefficient, charge transfer rate constant and electron transfer kinetics. The results of electrochemical response studies of this BSA/Ab-AFB1/nBi_2O_3/ITO immunosensor revealed good linearity in the range of 1–70 ng dL^{-1} with low detection limit of 8.715 ng/dL, improved sensitivity of 1.132 μA/(ng/dL cm^{-2}), regression coefficient R^2 of 0.918 and reproducibility of >11 times. The association constant for the BSA/Ab-AFB1/nBi_2O_3/ITO immunosensor was determined as 7.318 ng/dL.

© 2016 Elsevier B.V. All rights reserved.

1. Introduction

The nanostructured metal oxides have recently aroused much attention of researchers actively engaged in different scientific disciplines including materials science, bioscience and nanotechnology due to their interesting properties and potential applications [1,2]. In the past decade, several researches on the synthesis of low-dimensional nanostructures are underway [3,4]. Their attractive properties and a wide range of applications have been attributed to their interesting structures. Bismuth and its compounds are fascinating to scientists due to their unique structures and properties [5] such as highly anisotropic Fermi surface, high refractive index, dielectric permittivity and low carrier densities [6,7]. Therefore, it has been widely used for the development of solid oxide fuel cells, gas sensors, photoelectric materials, high temperature superconductor materials, catalysts, functional ceramics [8–11]. Recently, 1D metal oxides have been found to display high surface basicity, fast oxygen ion mobility, efficient charge transfer ability and interesting catalytic properties [12,13]. These properties have been predicted to be useful for investigating the effect of both dimensionality and size on physical properties, and also for application in nanodevices [3]. Bismuth oxide (Bi_2O_3) based compounds are known to be better solid electrolytes than those of zirconia since the face-centred cubic (fcc) Bi_2O_3 has been found to exhibit the highest ion conductivity of all oxide ion conductors.

Bi_2O_3 is one of the important metal oxides since it plays a significant role in modern solid-state technology due to its peculiar properties such as wide band gap, high refractive index, high dielectric permittivity, high oxygen conductivity, resistivity, photoconductivity and photoluminescence, etc. Its excellent properties have been found to have a variety of applications such as catalysts, optical coatings [14], photovoltaic cells, microwave integrated circuits, fuel cells [15], nanoenergetic gas generator [16] and in the fabrication of sensors [17,18]. Moreover, they have been predicted to provide a favorable environment for the biomolecules adsorption, nontoxicity, chemical inertness, biocompatibility, greater surface free energy, and good electrochemical stability, etc. [19,20]. Recently, Bi_2O_3 film has been utilized for the detection of phenolic compounds using amperometric biosensors [21]. A composite of Bi_2O_3 with chitosan has been used for the fabrication of an electrochemical DNA biosensor [18]. Ding et al. have fabricated a nano-Bi_2Ox electrode for glucose detection by amperometric technique [19]. A nanocomposite of Bi_2O_3-multi walled carbon nanotubes (MWCNTs) onto glassy carbon electrode (GCE) has utilized for hydrogen peroxide detection [20]. A lithium doped bismuth oxide - MWCNTs modified GCE has found application in monitoring electrocatalytical behavior of ascorbic acid [22,23].

The contamination of food by mycotoxins is currently a matter of great concern, as these are responsible for many diseases [24,25]. Worldwide, about 25% of crops are annually affected by toxigenic fungi. Thus, mycotoxins have become a part of the food chain. High levels of mycotoxins in the diet can cause adverse acute and chronic effects on humans and animals. These may particularly affect liver, kidney,

* Corresponding authors at: DST Centre for Biomolecular Electronics, CSIR-National Physical Laboratory, K.S. Krishnan Marg, New Delhi, India.
E-mail addresses: pratimarsolanki@gmail.com (P.R. Solanki), bansi.malhotra@gmail.com (B.D. Malhotra).

http://dx.doi.org/10.1016/j.msec.2016.09.027
0928-4931/© 2016 Elsevier B.V. All rights reserved.

nervous system, endocrine and immune systems [26]. Aflatoxin B1 (AFB1) is one of the most potent toxic substances as compared to other types of aflatoxins i.e. B_2, B_3, G_1 and G_2 that occur naturally. AFB1 is known to be carcinogenic, mutagenic, immunosuppressive agents that are a group of closely related mycotoxins produced by fungi *Aspergillus flavus* and *A. parasites* in fruit, vegetable and food product [27]. The aflatoxins may cause contamination of nuts (almonds, walnuts), cereals (rice, wheat, maize) and oilseeds (soybean and peanuts). Some of the conventional methods currently being used for mycotoxins detection include thin layer chromatography liquid chromatography, high-performance liquid chromatography, immune-chromatography, enzyme-linked immunosorbent assay [28,29]. These techniques are time consuming, expensive, and require high skilled manpower, sometimes may give unreliable results for food and biological samples due to the difficulty in obtaining a clear solution for analysis. Thus, there is an urgent need for the development of reliable, rapid, quick and sensitive method for detection of aflatoxins. Kalita et al. have fabricated ring like nickel nanoparticles (RnNi) NPs of 10–20 nm through pulsed laser ablation method for an electrochemical immunosensor for AFB1 detection. This bioelectrode shows the linearity as 5–100 ng dL^{-1}, sensitivity of 0.59 μA/ng dL^{-1} with detection limit of 32.7 ng dL^{-1} [30]. Singh et al. used samarium oxide nanorods modified ITO electrode for the co-immobilization of Ab-AFB1. This fabricated immunoelectrode (BSA/Ab-AFB_1/n-Sm_2O_3/ITO) showed the detection of AFB1 in a range of 10–700 pg mL^{-1} with sensitivity and detection limit of 48.39 μA pg^{-1} mL^{-1} cm^{-2} and 57.82 pg mL^{-1} cm^{-1}, respectively [31]. The microelectrode was fabricated using 2-aminoethane thiol (AET) on Au electrode and used for fabrication of immunosensor by self assembling of horseradish peroxidase (HRP) and AFB1 antibody molecules for AFB1 detection [32]. The linear range was found to be from 0.5 to 10 ng mL^{-1} with a relatively low detection limit of 0.1 ng mL^{-1}. Glassy carbon electrode (GCE) consisting of chitosan/Au nanoparticle/anti-AFB_1, and a Fe_3O_4 magnetic core with a gold shell functionalized with 3-((2-mercaptoethylimino) methyl) benzene-1,2-diol for the detection of AFB1 [33]. This immunoelectrode revealed the detect range of 0.6–110 ng mL^{-1} with a detection limit of 0.2 ng mL^{-1} for AFB1. Polythionine (PTH)/AuNP modified GCE based electrochemical immunosensor exhibited a linear range of 0.6–2.4 ng mL^{-1} AFB1 and a limit of detection of 0.07 ng mL^{-1} AFB1 for the determination of aflatoxin B1 [34].

We report results of studies relating to the preparation of Bi_2O_3 nanorods *via* sol-gel method for development of an immunosensor for aflatoxin AFB1 detection. It is shown that the Ab-AFB1/nBi_2O_3/ITO bioelectrode exhibits improved sensitivity, low detection limit and wide detection range (Table 1).

2. Materials and methods

2.1. Materials

Bismuth nitrate [$Bi(NO_3)_3 \cdot 5H_2O$], polyethylene glycol (PEG), nitric acid (HNO_3) were purchased from MERCK (New Delhi, India). Aflatoxin B1 (AFB1), anti-aflatoxin B1 mouse monoclonal antibodies (Ab-AFB1) and bovine serum albumin (BSA, 98%) were procured from Sigma-Aldrich (USA). All other chemicals were of analytical grade and used without further purification. The indium-tin-oxide (ITO) coated glass (Balzers) sheet of resistance 15 W/cm was used as substrate for deposition of the desired nanocomposite that worked as the working electrode. All solutions in these studies were prepared using deionized water of resistivity of not less than 18 MΩ taken from a Milli-Q water purification system (Milli-Q, USA).

2.2. Preparation of antibody aflatoxin B1 (Ab-AFB1) and bovine serum albumin (BSA) solutions

The stock solution of AFB1 was freshly prepared in phosphate buffer (50 mM, pH 7.0) with 10% methanol and aliquoted in different working concentrations (1–70 ng dL^{-1}). Ab-AFB1 was prepared in phosphate buffer (50 mM, pH 7.0) prior to being used. 0.15 M sodium azide (NaN_3) was added into both these solutions as a preservative and stored at −20 °C when not in use. The bovine serum albumin (BSA, 98%) was freshly prepared (2 mg mL^{-1}) in phosphate buffer (50 mM, pH 7.0) and used as blocking agent for non-specific binding sites.

2.3. Synthesis of Bi_2O_3 nanorods

In a typical procedure, 0.05 mol $Bi(NO_3)_3$ was dissolved into 30 mL of 0.05 mol/L HNO_3 to get transparent Bi^{3+} acidic solution. 20 mL polyethylene glycol (PEG-600) was added drop wise as a dispersant to the above solution and magnetically stirred for 2 h at room temperature. 50 mL of NaOH (4 mol) aqueous solutions was quickly poured into it under vigorous stirring resulting in a yellow solution. The resultant yellow solution was stirred at 90 °C for 2 h. Then it was filtered and washed with deionized water and ethanol for 5–10 times. The precipitation was dried at 70 °C for 12 h in vacuum drier to obtain faint yellow Bi_2O_3 nanorods.

2.4. Preparation of nBi_2O_3 films by electrophoretic deposition

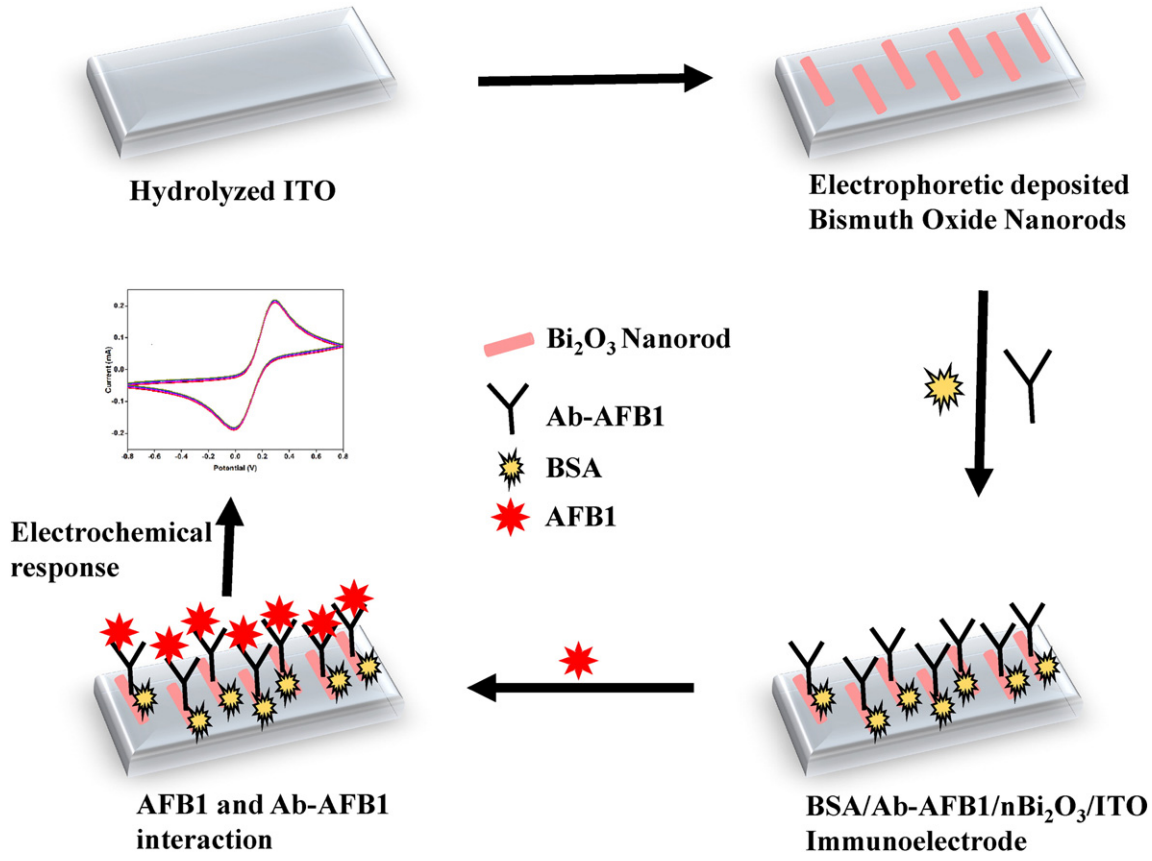
Electrophoretic deposition (EPD) was carried out by using a DC battery (BioRad, Model 200/2.0). Prior to deposition of nBi_2O_3 onto ITO substrate, uniform suspension of known amount of nBi_2O_3 (10 mg) was prepared in de-ionized water (1 mg mL^{-1}) through vigorous stirring followed by sonication for about 1 h. During EPD, a platinum foil (1 cm × 2 cm) was used as the anode and a hydrolyzed ITO coated glass plate as cathode. The two electrodes, placed parallel to each other with separation of 1 cm, were dipped in the nBi_2O_3 colloidal suspension. The colloidal suspension solution consisted of positively charged nBi_2O_3 nanoparticles. Since ITO plates were hydrolyzed, OH group were present on its surface. The optimized condition for EPD of Bi_2O_3 nanorods onto ITO plates was obtained as 10 V for 20 s as the nBi_2O_3 film exhibits maximum amperometric current at this condition. During the process positively charged Bi_2O_3 nanorods were attracted with OH group present on ITO surface *via* electrostatic interaction. Thus nBi_2O_3 (0.25 cm^2) was deposited onto ITO plate. This nBi_2O_3/ITO electrode was washed with deionized water followed by ethanol to remove any unbound particles and dried at room temperature (25 °C) for 12 h.

2.5. Fabrication of immunoelectrode

The optimal amount of freshly prepared solution (10 μL) of Ab-AFB1 was uniformly spread onto the desired nBi_2O_3/ITO electrode surface and

Table 1
Characteristics of the BSA/Ab-AFB1/nBi_2O_3/ITO immunoelectrode along with those reported in the literature for aflatoxin B1 detection, with their important parameters.

Bioelectrode	Detection method	Sensitivity	Limit of detection	Detection range	Stability (days)	Ref.
RnNi-film/ITO	Electrochemical	0.59 μA/ng dL^{-1}	32.7 ng dL^{-1}	5–100 ng dL^{-1}	60	[30]
BSA/anti-AFB1/MWCNTs/ITO	Electrochemical	95.2 mA ng/mL cm^{-2}	0.08 ng mL^{-1}	0.25–1.375 ng mL^{-1}	45	[31]
BSA-anti-AFB1/Au NPs	Conductometric	–	10.1 ng mL^{-1}	0.5–10 ng mL^{-1}	12	[32]
GCE/chitosan/AuNP/aAFB1	Electrochemical	–	0.2 ng mL^{-1}	0.6–110 ng mL^{-1}	–	[33]
PTH/AuNP/GCE	Electrochemical	–	0.07 ng mL^{-1}	0.6–2.4 ng mL^{-1}	–	[34]
BSA/Ab-AFB1/nBi_2 O_3/ITO	Electrochemical	1.132 μA ng/dL cm^{-2}	8.72 ng dL^{-1}	1–70 ng dL^{-1}	15	Present work



Scheme 1. Schematic representation of fabrication of the Ab-AFB1/nBi_2O_3/ITO immunosensor.

kept undisturbed in a humid chamber for about 12 h at 25 °C. The Ab-AFB1/nBi_2O_3/ITO bioelectrode was washed thoroughly with phosphate buffer (50 mM, pH 7.0) to remove any unbound antibodies followed by drying at room temperature (25 °C). The non-specific binding sites of the modified Ab-AFB1/nBi_2O_3/ITO bioelectrode were blocked by using bovine serum albumin (BSA, 98%). 10 μL freshly prepared BSA solution (1 mg mL^{-1}) was uniformly spread over Ab-AFB1/nBi_2O_3/ITO bioelectrode and kept overnight in a humid chamber at room temperature (25 °C) followed by washing with phosphate buffer (50 mM, pH 7.0) to remove any unbound biomolecules. The optimal amount of Ab-AFB1 (10 μL) and BSA (10 μL) to obtain the maximum magnitude of current response in PBS (50 mM, pH 6.0, 0.9% NaCl) containing $[Fe(CN)_6]^{3-/4-}$ (5 mM) at 20 mV/s scan rate using CV technique. This fabricated Ab-AFB1/nBi_2O_3/ITO bioelectrode was dried and was further used for characterization and AFB1 detection.

Scheme 1 shows the stepwise fabrication of the Ab-AFB1/nBi_2O_3/ITO bioelectrode along with the interaction between AFB1 and Ab-AFB1 on the nBi_2O_3/ITO electrode surface. The nBi_2O_3 carries positive charge and Fac part (COO^- group) of Ab-AFB1 is negative charge which could bind electrostatically onto nBi_2O_3/ITO surface. The adsorption of Ab-AFB1 on the nBi_2O_3/ITO retains their bioactivity due to their biocompatibility.

2.6. Characterizations techniques

The structure, shape and crystallite size of synthesized nBi_2O_3 nanoparticles were investigated using X-ray diffraction (XRD), Rigaku D/Max 2200 diffractometer with CuKα radiation 10 at λ = 1.5406 Å. FT-IR spectra of the electrode was recorded with FTIR spectrophotometer (PerkinElmer, Spectrum BX II). Transmission electron microscopy (TEM) studies were carried with JEOL JEM-2200 FS (Japan). The surface morphological studies of Ab-AFB1/nBi_2O_3/ITO bioelectrode and BSA/Ab-AFB1/nBi_2O_3/ITO immunosensor were investigated using atomic force microscopy (AFM, Model Vicco 440, Nanoscope) and Scanning Electron Microscopy (SEM, Zeiss, EVO, 40). The cyclic voltammetry (CV), differential pulse voltammetry (DPV) and electrochemical impedance spectroscopy (EIS) measurements were recorded on an Autolab Potentiostat/Galvanostat (Eco Chemie, The Netherlands). The electrochemical measurements were conducted on a three-electrode system with BSA/Ab-AFB1/nBi_2O_3/ITO immunoelectrode as the working electrode, a platinum (Pt) wire as the counter electrode, and saturated Ag/AgCl electrode as a reference electrode in phosphate buffer saline (PBS, 50 mM, pH 6.0, 0.9% NaCl) containing 5 mM $[Fe(CN)_6]^{3-/4-}$ as a mediator.

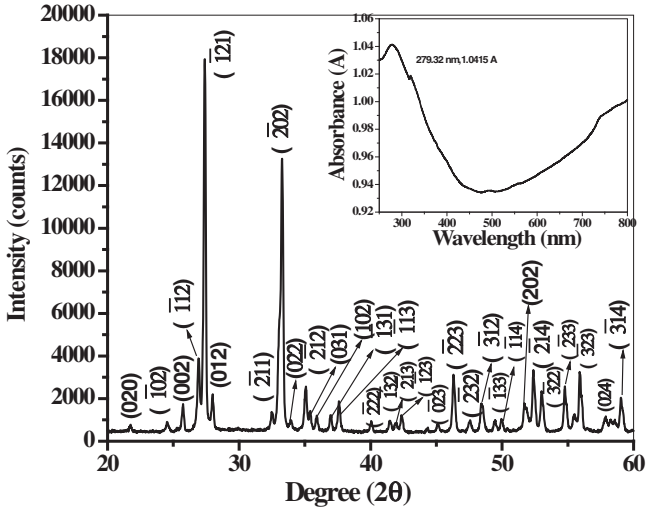
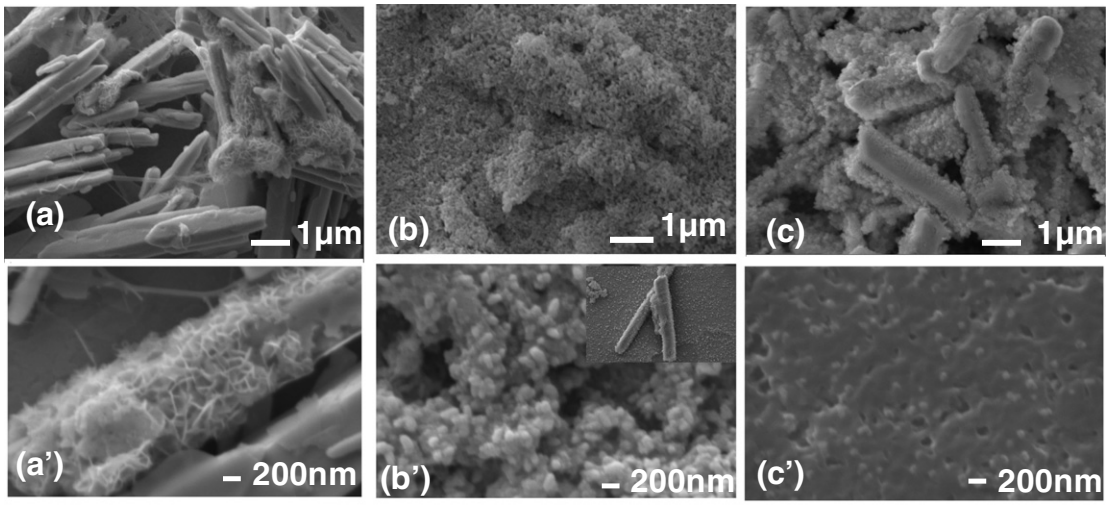


Fig. 1. X-ray diffraction pattern of nanostructured Bi_2O_3. Inset shows UV–vis spectrum of Bi_2O_3 nanoparticles.

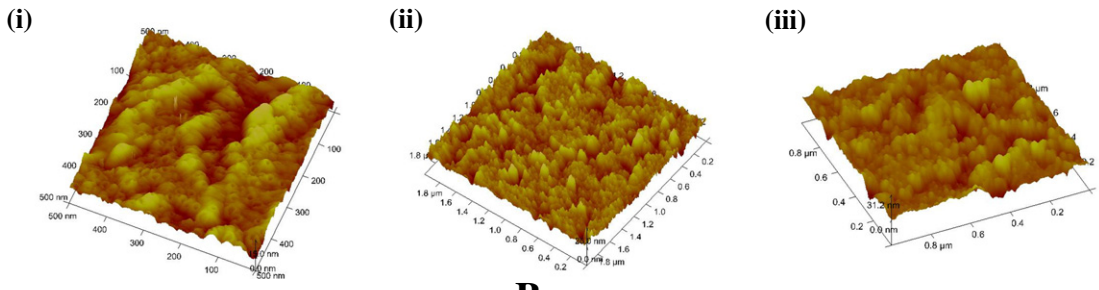
3. Results and discussions

3.1. Structural and morphological studies

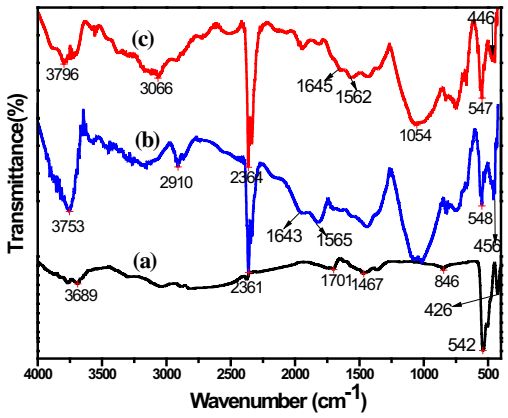
The X-ray diffraction pattern obtained for the synthesized product is shown in Fig. 1. All the diffraction peaks could be indexed to single phase of monoclinic Bi_2O_3 (α-Bi_2O_3). The calculated lattice constants (a = 5.849 Å, b = 8.169 Å, and c = 7.511 Å) are in good agreement with the standard values of a = 5.848 Å, b = 8.166 Å, and c = 7.510 Å (JCPDS 27-0053) that confirm the formation of crystalline structure. The XRD pattern shows reflection planes in (002), (−112), (−202), (−212), (−232), (−214), (−323) and (400). No peak



A



B



C

Fig. 2. (A): SEM image of (a) nBi_2O_3/ITO electrode, (a′) extended image of (a); (b) Ab-AFB1/nBi_2O_3/ITO bioelectrode, (b) extended image of (b), (c) BSA/Ab-AFB1/nBi_2O_3/ITO immunoelectrode (c′) extended image of (c). (B): AFM image of (i) nBi_2O_3/ITO, (ii) Ab-AFB1/nBi_2O_3/ITO bioelectrode, (iii) BSA/Ab-AFB1/nBi_2O_3/ITO immunoelectrode. (C): FTIR spectra of (a) nBi_2O_3/ITO electrode, (b) Ab-AFB1/nBi_2O_3/ITO bioelectrode (c) BSA/Ab-AFB1/nBi_2O_3/ITO immunoelectrode.

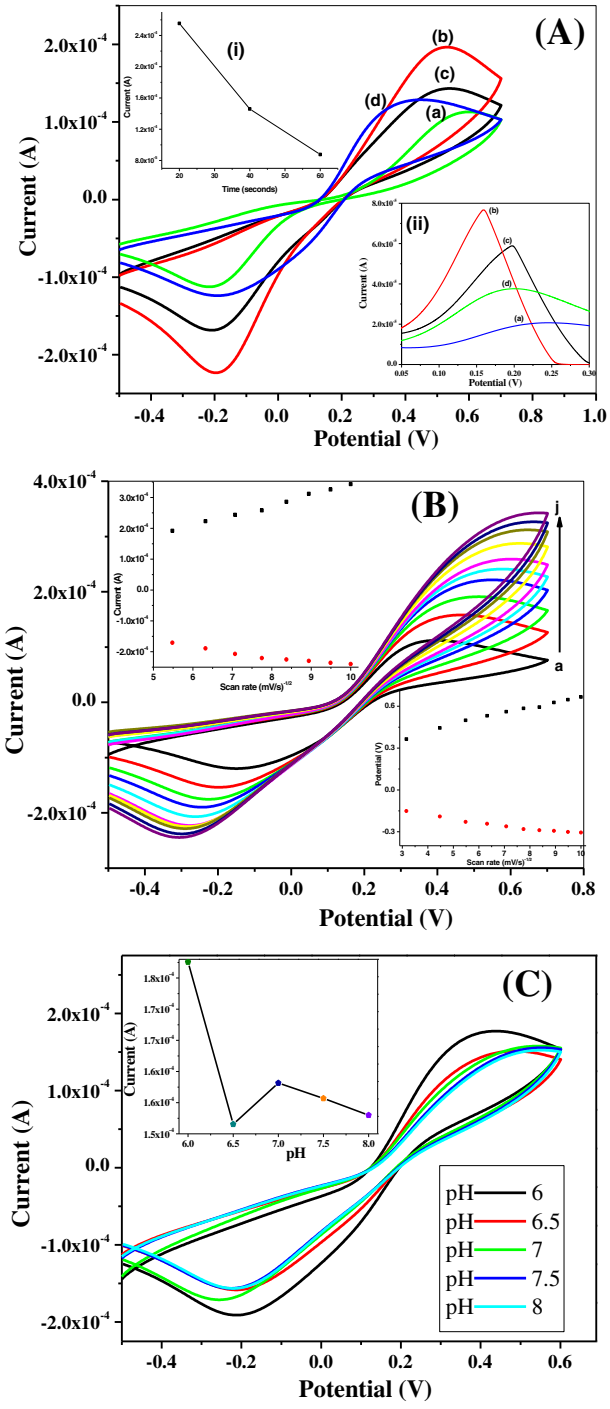


Fig. 3. (A): Cyclic voltammogram (CV) obtained for (a) bare ITO electrode (b) nBi_2O_3/ITO electrode (c) Ab-AFB1/nBi_2O_3/ITO bioelectrode (d) BSA/Ab-AFB1/nBi_2O_3/ITO immunoelectrode. Inset (i) shows the optimization of time for nBi_2O_3 film deposited onto ITO surface. Inset (ii) shows the DPV of (a) bare ITO electrode, (b) nBi_2O_3/ITO electrode, (c) Ab-AFB1/nBi_2O_3/ITO bioelectrode, (d) BSA/Ab-AFB1/nBi_2O_3/ITO immunoelectrode. (B): CV of BSA/Ab-AFB1/nBi_2O_3/ITO immunoelectrode as a function of scan rate. The inset shows the linearity of the oxidation and reduction peak currents. (C): CV of BSA/Ab-AFB1/nBi_2O_3/ITO immunoelectrode as a function of pH varies from 6.0–8.0. Inset shows the plot between oxidation current and pH valve.

corresponding to any impurity was detected, suggesting single crystalline nature of Bi_2O_3. The average crystallite size found to be as ~55 nm was calculated by the Scherrer formula as shown below (Eq. (1)).

$$D = \frac{0.9\lambda}{\beta \cos\theta} \quad (1)$$

where, D is the crystallite size in Å, β is the full width at half maxima (FWHM) of the diffraction peaks, θ is the glancing angle and (λ = 1.54060 Å) is the wavelength of X-ray.

The UV–visible spectrum shows a strong absorption peak at 279 nm which corresponds to the Bi^{3+} in Bi_2O_3 as compared to bulk (~320) nm [35] (inset Fig. 1). This result shows a blue shift ~41 nm indicating the formation of the nanostructured Bi_2O_3. The absorption of a photon, leading to excitation of an electron from the valence band to the conduction band in the semiconductor, is referred to as band gap energy (Eg). Compared to polycrystalline material, the nanoparticles often show a shift of the band gap energy (Eg) towards higher value due to decrease in the size of the particle. The blue shift of 24–26 nm of the absorption band is observed in the absorption spectra. This is due to the fact that the nanostructures are laterally quantum confined and occupy energy levels that are different from the traditional continuum of energy levels or bands found in a bulk material.

The surface morphological studies of nBi_2O_3/ITO film, Ab-AFB1/nBi_2O_3/ITO bioelectrode and BSA/Ab-AFB1/nBi_2O_3/ITO immunosensor investigated using SEM are shown in Fig. 2A(a–c; a′–c′), respectively. SEM image (a) of nBi_2O_3/ITO clearly reveals uniform distribution of 1D nanostructure (nanorods ID) that provides a fibrous morphology due to electrophoretic deposition of nBi_2O_3 on ITO plates. The bundles of nanorods observed with different size provide rough provide high surface-to-volume ratio resulting in enhanced loading of antibodies. Image (a′) shows that the single nanorods have a fibrous morphology. The image (b) exhibits that the antibodies Ab-AFB1 are fully covered with the nanorods in the form of small granular structure that confirms the immobilization of antibodies onto the nBi_2O_3/ITO electrodes. The image (b′) clearly shows that the individual nanorod can be used to load higher amount of Ab-AFB1. However, after the immobilization of BSA onto the Ab-AFB1/nBi_2O_3/ITO bioelectrode [image (c, c′)] results in the increased granules size of the Ab-AFB1 immobilized nanorods indicating blocking of the non-specific sites. This confirms the immobilization of BSA onto Ab-AFB1/nBi_2O_3/ITO bioelectrode.

The morphological studies of nBi_2O_3/ITO film, Ab-AFB1/nBi_2O_3/ITO bioelectrode and BSA/Ab-AFB1/nBi_2O_3/ITO immunosensor were investigated using atomic force microscopy (AFM), respectively [Fig. 2B]. The AFM image of nBi_2O_3/ITO revealed that the nanorods were open on the top surface indicating nanoporous morphology [image (a)]. After the immobilization of antibodies Ab-AFB1 onto the nBi_2O_3/ITO films, the nanoporous morphology changed to granular form [image (b)] indicating immobilization of Ab-AFB1 onto the nBi_2O_3/ITO electrodes. This could be assigned to electrostatic interaction between the positive charge of matrix nBi_2O_3/ITO electrode and the negative charge of carboxyl group of antibody AFB1. The AFM image (c) showed that the surface morphology of Ab-AFB1/nBi_2O_3/ITO bioelectrode changed after the immobilization of BSA. As compared to the nBi_2O_3 film, the average peak height (Rpm) decreased after immobilization of Ab-AFB1 (4.59 nm) onto nBi_2O_3/ITO surface (7.28 nm) and increased after the immobilization of BSA (4.94 nm). The variation of the peak-to-valley height (R_{max}) measured as 61.3 nm for nBi_2O_3/ITO electrode decreased to 36.7 nm for Ab-AFB1/nBi_2O_3/ITO bioelectrode, then further decreased to 31.8 nm for the BSA/Ab-AFB1/nBi_2O_3/ITO immunosensor.

The FTIR spectrum obtained for the synthesized Bi_2O_3 nanorods in the range of 400–4000 cm^{-1} is shown in Fig. 2C (a). Four characteristic bands can be clearly seen from Fig. 2C (a), in which the broad band at 3689 cm^{-1} corresponds to the stretching vibration of OH, while the band appearing at 1701 cm^{-1} and 1467 cm^{-1} represents the stretching mode of absorbed H_2O. In addition, the band located at 1350 cm^{-1} can be ascribed to the bending vibration of NO_3^-, this suggests that the as-synthesized BiOx contains a large amount of NO_3^- groups that are crucial for further surface functionalization and coating by any other functional groups. The band 846 cm^{-1} is due to Bi—O—Bi and band at 542 and 426 cm^{-1} are attributed to the stretching mode of Bi—O metal oxide bond. The additional bands at 2365 and 1014 cm^{-1} for nBi_2O_3/ITO

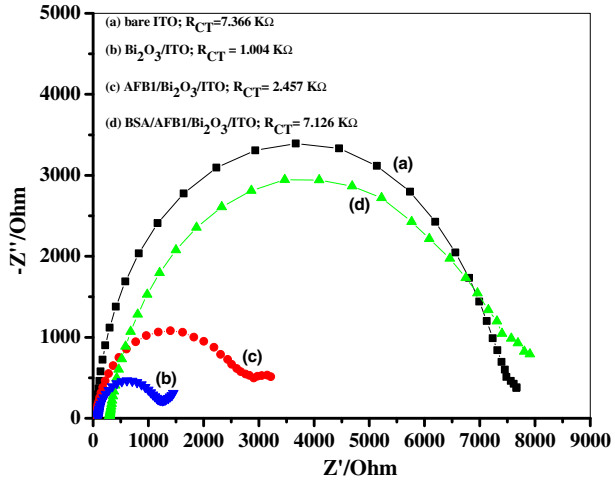


Fig. 4. EIS of (a) bare ITO electrode, (b) nBi_2O_3/ITO electrode, (c) Ab-AFB1/nBi_2O_3/ITO bioelectrode, (d) BSA/Ab-AFB1/nBi_2O_3/ITO immunoelectrode.

film were attributed to the carbonate and sulphate impurity present during the film formation. The antibody Ab-AFB1 conjugated in nBi_2O_3/ITO electrode Fig. 2C (b) resulted in the increase in carbonyl absorption at 1643 cm^{-1} and the broad strong band observed at 3753 cm^{-1}. However, after immobilization of antibodies, the characteristic peaks containing NH_3^+ of amide I band appeared at 1643 cm^{-1} and NH bending of amide II band at 1565 cm^{-1} indicating immobilization of antibodies onto Bi_2O_3/ITO film. The metal band (M-O) stretching of Ab-AFB1/Bi_2O_3/ITO immunoelectrode increased in comparison to nBi_2O_3/ITO film indicating the presence of electrostatic interaction. The spectra of BSA/Ab-AFB1/nBi_2O_3/ITO immunoelectrode [Fig. 2C (c)] shows lowering of wave number value in compression to that of Ab-AFB1/nBi_2O_3/ITO immunoelectrode due to deactivation at the binding sites of Ab-AFB1.

3.2. Electrochemical studies

The cyclic voltammograms (CV) obtained for various nBi_2O_3 based electrodes in phosphate buffer (50 mM, pH 6.0, 0.9% NaCl) containing $[Fe(CN)_6]^{3-/4-}$ at a scan rate of 20 mV/s are shown in Fig. 3A. It can be seen that the anodic potential (Fig. 4) shifted towards the higher current and the cathodic peak potential shifts in the reverse direction. In case of the nBi_2O_3/ITO electrode (curve b), the magnitude of peak current is increased as compare to ITO electrode (curve a). This suggests that electrophoretically deposited nBi_2O_3/ITO electrode promotes fast electron transfer due to the formation of a continuous array of Bi_2O_3 nanoparticles throughout the electrophoretic network at the electrode. Moreover, the value of the peak current is decreased after the immobilization of Ab-AFB1 onto the nBi_2O_3/ITO electrode (curve c). This may be attributed to the available non-binding sites onto Ab-AFB1 and nBi_2O_3/ITO electrode that play an important role in deaccelerating electron transfer between Ab-AFB1 and the nBi_2O_3/ITO electrode. Further, the magnitude of current is decreased after the immobilization of BSA (curve d) revealing that the blocking of non-binding sites of Ab-AFB1 hinders electron transfer between medium and electrode, indicating the immobilization of BSA onto the Ab-AFB1/nBi_2O_3/ITO bioelectrode. The optimization time for film deposition [inset Fig. 3A(i)] was found to be as 20 s indicating that Bi_2O_3 was highly charged and it moved faster towards ITO electrode.

The differential pulse voltammograms (DPV) obtained for the ITO electrode (curve a), nBi_2O_3/ITO electrode (curve b), Ab-AFB1/nBi_2O_3/ITO bioelectrode (curve c), BSA/Ab-AFB1/nBi_2O_3/ITO immunosensor (curve d) are shown in Fig. 3A [inset (ii)]. The DPV studies showed similar response as those of the CV studies. The magnitude of anodic peak current of ITO was the lowest (curve a). It increased after nBi_2O_3 was electrophoretically deposited onto ITO surface (curve b). The anodic peak current decreased after immobilization of Ab-AFB1 onto nBi_2O_3/ITO electrode (curve c). It decreased further on immobilization of BSA onto Ab-AFB1/nBi_2O_3/ITO bioelectrode (curve d).

The CV of the BSA/Ab-AFB1/nBi_2O_3/ITO immunosensor obtained as a function of scan rate varying from 10 to 100 mV/s is shown in Fig. 3B. It was found that the potential and the magnitude of currents were dependent on scan rate. The magnitudes of both anodic (Epa) and cathodic (Epc) peak currents and potential peak shift ($\Delta Ep = Epa - Epc$) increased linearly with the scan rate suggesting that the electrode reaction was a diffusion controlled process. It was also observed that the peak height varied directly with the sweep rate (with linear regression coefficient 0.918), indicating improved electrocatalytic behavior. Thus this nBi_2O_3/ITO can be used for the immobilization of Ab-AFB1 providing sufficient accessibility to electrons to shuttle between the antibody and the electrode. The surface concentration of the BSA/Ab-AFB1/nBi_2O_3/ITO immunosensor was estimated from the plot of current versus potential (CV) using Brown-Anson model that is based on the following equation:

$$Ip = \frac{n^2 F^2 I^* AV}{4RT} \quad (2)$$

where n is the number of electrons transferred (1), F is the Faraday constant (96,485 C/mol), I^* is the surface concentration of the BSA/Ab-AFB1/nBi_2O_3/ITO immunosensor (mol cm^{-2}), A is the surface area of the electrode (0.25 cm^2), V is the scan rate (20 mV/s), R is the gas constant (8.314 J mol^{-1} K^{-1}) and T is the room temperature (300 K). The surface concentration of nBi_2O_3/ITO was calculated as 4.22×10^{-11} mol/cm^2 which decreases to 3.08×10^{-11} mol/cm^2 for Ab-AFB1/nBi_2O_3/ITO bioelectrode and further decreased to 2.77×10^{-11} mol/cm^2 for BSA/Ab-AFB1/nBi_2O_3/ITO immunosensor.

3.3. Effect of pH

The effect of pH value on the performance of the biosensor is of great importance, because the activity of the immobilized antibody is pH dependent. The effect of pH (ranging from 6 to 8) onto BSA/Ab-AFB1/nBi_2O_3/ITO immunosensor was investigated using CV technique in PBS (50 mM 0.9% NaCl) containing $[Fe(CN)_6]^{3-/4-}$ at scan rate of 20 mV/s (Fig. 3C). It was found that magnitude of the peak current decreased and the peak potential shifted towards higher potential on increasing the pH. This could be due to decrease in the concentration of positively charged moieties present onto nBi_2O_3 matrix as pH of PBS approaches towards its isoelectric point resulting in decreased interaction between redox ions $[Fe(CN)_6^{3-/4-}]$ onto nBi_2O_3 surface. This resulted in increased hindrance in electron transport between the medium and electrode leading to decreased value of electrochemical signal at elevated pH. In the case of BSA/Ab-AFB1/nBi_2O_3/ITO immunosensor, magnitude of change in current response was higher at pH 6 and decreased from 6.0 to 6.5 (Fig. 3C). This result suggested that BSA/Ab-AFB1/nBi_2O_3/ITO immunosensor could be used at pH 6.0 for aflatoxin B1 detection. Moreover, it appeared that higher pH was responsible for desorption of the biomolecule, and the current response decreased by ~19% at pH < 8.0. Thus all the experiments were conducted at pH 6.0. The results of electrochemical measurements conducted in triplet sets under identical conditions revealed good reproducibility. Thus pH 6.0 was selected for the subsequent experiments.

3.4. Electrochemical impedance spectra

The EIS of bare ITO electrode, nBi_2O_3/ITO electrode, Ab-AFB1/nBi_2O_3/ITO bioelectrodes and BSA/Ab-AFB1/nBi_2O_3/ITO immunosensor in PBS

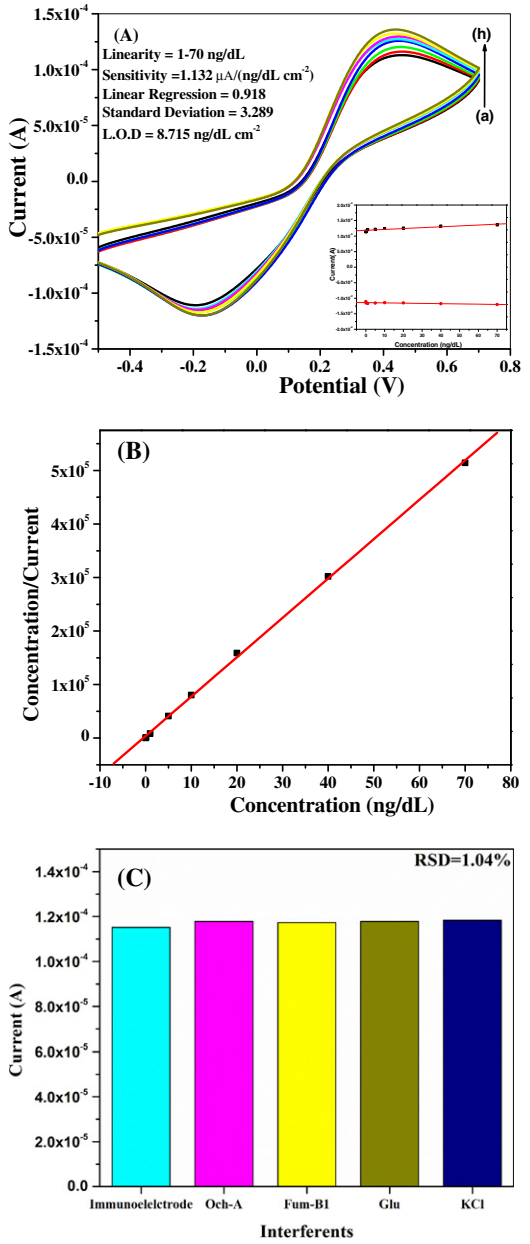


Fig. 5. (A): Electrochemical response studies of the BSA/Ab-AFB1/nBi_2O_3/ITO immunoelectrode as a function of aflatoxin B1 concentration using CV. Inset shows the linear fit curve of sensitivity of BSA/Ab-AFB1/nBi_2O_3/ITO immunoelectrode. (B): Hanes plot between the substrate concentration and substrate concentration/current obtain from previous figure [Fig. 5A]. (C): Selectivity studies of BSA/Ab-AFB1/nBi_2O_3/ITO immunoelectrode.

containing $[Fe(CN)_6]^{3-/4-}$ in the frequency range, 0.00–10^7 Hz was studied by monitoring charge transfer resistance (R_{CT}) at the electrode and electrolyte interface (Fig. 4). In the EIS, the semicircle part corresponds to electron-transfer limited process and its diameter is equal to the electron transfer resistance, R_{CT} that controls electron transfer kinetics of the redox probe at the electrode interface [36]. It can be seen from the Nyquist plots that semicircle of the nBi_2O_3/ITO electrode (R_{CT} = 1.005 KΩ; curve b) is smaller than that of the bare ITO electrode (R_{CT} = 7.366 KΩ; curve a). This suggested that nBi_2O_3 resulted in improved conductivity of the electrode. Further, the R_{CT} value increased after the immobilization of Ab-AFB1 onto the nBi_2O_3/ITO electrode (curve c) indicating that non-binding sites on Ab-AFB1 perhaps facilitated electron transfer between the Ab-AFB1/nBi_2O_3/ITO bioelectrode and electrolyte. Moreover, R_{CT} increased after immobilization of BSA onto the Ab-AFB1/nBi_2O_3/ITO bioelectrode (curve d), revealing hindrance in electron communication between the BSA/Ab-AFB1/nBi_2O_3/ITO immunosensor and electrode. Thus, R_{CT} value was obtained in the sequence: R_{CT} (curve b) < R_{CT} (curve c) < R_{CT} (curve d) < R_{CT} (curve a). The value of R_{CT} is dependent on electrochemical reaction time constant, τ (τ = $1/2\pi f_{max}$ = Rp·CdL, where f_{max} is the frequency at which maximum Z'' is obtained, Rp is the polarization resistance and CdL is the double layer capacitance).

3.5. Electrochemical response studies

The electrochemical response of the BSA/Ab-AFB1/nBi_2O_3/ITO immunosensor was investigated as a function of aflatoxin B1 concentration (0.125–70 ng dL^{-1}) using the CV techniques [Fig. 5A]. The magnitude of current was found to increase on addition of aflatoxin B1. This was attributed to the formation of an antigen-antibody complex between aflatoxin B1 and Ab-AFB1 on the electrode surface that acted as an electron transfer accelerating layer for transfer of electrons. The BSA/Ab-AFB1/nBi_2O_3/ITO immunosensor exhibited good linearity in the range of 1–70 ng dL^{-1} with low detection limit of 8.715 ng/dL cm^{-2}, linear regression coefficient R^2 of 0.918 and reproducibility of >11 times. The sensitivity of the BSA/Ab-AFB1/nBi_2O_3/ITO immunosensor calculated from the slope of curve was found to be 1.132 μA/(ng dL^{-1} cm^{-2}). The standard deviation from the linear regression analysis for the bioelectrode was found to be 3.289 μA. Fig. 5B shows the Hanes plot between the substrate concentration and substrate concentration/current obtained from Fig. 5A. The association constant (K_a) for the BSA/Ab-AFB1/nBi_2O_3/ITO immunosensor, estimated by Hanes plot i.e. graph between [substrate concentration] and [substrate concentration/current] [Fig. 5B] was found to be as 7.318 ng dL^{-1}. The value of K_a is known to depend on various factors such as matrix and the method of immobilization of antibodies that could bring different conformational changes in the antibody structure. The small K_a value indicates that increased affinity of BSA/Ab-AFB1/nBi_2O_3/ITO immunosensor can be attributed to favorable conformation of Ab-AFB1 and higher loading onto nBi_2O_3/ITO electrode surface.

The reproducibility of the proposed BSA/Ab-AFB1/nBi_2O_3/ITO immunosensor was estimated by repetitive measurement of current response with 25 ng dL^{-1} standard AFB1 solutions in PBS. The results obtained in five repeated measurements show an RSD of 2–3%, indicating that the obtained data are reproducible.

The selectivity test of BSA/Ab-AFB1/nBi_2O_3/ITO immunoelectrode was performed with the mycotoxins [Ochratoxin A (Och A), Fumonisin B1 (Fum B1)], glucose (Glu) and potassium chloride (KCl), which are generally present in milk. The interferent solutions were of normal concentrations: Och A (7 mg mL^{-1}); Fum B1 (8.38 mM); Glu (1 ng mL^{-1}) and KCl (100 pg mL^{-1}) was used [Fig. 5C]. The electrochemical behavior of BSA/Ab-AFB1/nBi_2O_3/ITO immunoelectrode was monitored in the presence of these interferents under similar condition using CV technique. It was found that there was not much change in magnitude of current in the presence of these interferents. We observed a low relative standard deviation (RSD) of 1.04%, indicating negligible interferents with other analytes, indicating that the fabricated BSA/Ab-AFB1/nBi_2O_3/ITO immunoelectrode was highly selective for aflatoxin B1 detection.

The storage stability of this BSA/Ab-AFB1/nBi_2O_3/ITO immunoelectrode was investigated by observing the current response at a regular interval of 5 days for 45 days with 25 ng mL^{-1} concentration of AFB1. The results of these studies revealed no significant decrease in the current (within 5%) after 45 days, indicating excellent storage stability.

4. Conclusions

The electrophoretically derived nanostructured nBi_2O_3 film has been used to fabricate an Ab-AFB1 based immunosensors for aflatoxin B1detection. It has been shown that the presence of nBi_2O_3 results in a

favorable environment with increased electroactive surface. The fabricated BSA/Ab-AFB1/nBi_2O_3/ITO immunoelectrode shows remarkably enhanced sensitivity and selectivity for aflatoxin B1. This immunosensor shows relatively rapid response (15 s), high sensitivity 1.132 μA/(ng/dL cm^{-2}), broad linear range (1–70 ng/dL), low detection limit (8.715 ng/dL), linear regression coefficient 0.918, good reproducibility and long term stability. The wide detection range and high sensitivity has been assigned to the amplification of the magnitude of current response since Bi_2O_3 nanoparticles with good biocompatibility maintain the biological activity of the antibody and improve the electron transfer between analyte (aflatoxin B1) and BSA/Ab-AFB1/nBi_2O_3/ITO immunoelectrode surface. The low value of association constant (K_a) of 0.234 nM indicates high antibody affinity of Ab-AFB1 to aflatoxin B1. The results clearly suggest that nBi_2O_3/ITO electrode provides an attractive matrix for effective immobilization of antibodies for fabricating of third generation biosensors and bioelectronics devices. The unique properties of nBi_2O_3 and the ease of nBi_2O_3 nanostructure fabrication make this material extremely interesting for biosensor applications.

Acknowledgements

We thank Director, CSIR-National Physical Laboratory, New Delhi for providing the facilities. PRS is grateful to the Department of Science and Technology (DST), India for Young Scientist Award. JS acknowledges Department of Science and Technology, New Delhi, India for the INSPIRE Faculty award [IFA-13-CH-105].

References

[1] P.R. Solanki, A. Kaushik, V.V. Agrawal, B.D. Malhotra, NPG Asia Mater. 3 (2011) 17–24.
[2] A.P.F. Turner, Chem. Soc. Rev. 42 (2013) 3184–3196.
[3] P.R. Solanki, M.A. Ali., V.V. Agrawal, A.K. Srivastava, R.K. Kotnala, B.D. Malhotra, RSC Adv. 3 (2013) 16060–16067.
[4] Y.T. Chen, R. Gong, W. Zhang, X.Q. Xu, Y.Q. Fan, W.S. Liu, Mater. Lett. 59 (2005) 909–911.
[5] W.G. Lu, Y. Ding, Y.X. Chen, Z.L. Wang, J.Y. Fang, J. Am. Chem. Soc. 127 (2005) 10112–10116.
[6] Y.M. Lin, S.B. Cronin, J.Y. Ying, M.S. Dresselhaus, J.P. Heremans, Appl. Phys. Lett. 76 (2000) 3944.
[7] L. Leontie, M. Caraman, M. Delibas, G.I. Rusu, Mater. Res. Bull. 36 (2001) 1629–1637.
[8] M. Gotic, S. Popovic, S. Music, Mater. Lett. 61 (2007) 709–714.
[9] N.V. Skorodumova, A.K. Jonsson, M. Herranen, M. Stromme, G.A. Niklasson, B. Johansson, S.I. Simak, Appl. Phys. Lett. 86 (2005) 241910.
[10] L.S. Zhang, W.Z. Wang, J. Yang, Z.G. Chen, W.Q. Zhang, L. Zhou, S.W. Liu, Appl. Catal. A Gen. 308 (2006) 105–110.
[11] T.P. Gujar, V.R. Shinde, C.D. Lokhande, S.H. Han, J. Power Sources 161 (2006) 1479–1485.
[12] Y.B. He, G.R. Li, Z.L. Wang, C.Y. Su, Y.X. Tong, Energy Environ. Sci. 4 (2011) 1288–1292.
[13] N. Soltanzadeh, A. Morsali, Ultrason. Sonochem. 17 (2010) 139–144.
[14] M. Schuisky, A. Hdrsta, Chem. Vap. Depos. 2 (9) (1996) 235–238.
[15] N. Jiang, E.D. Wachsman, J. Am. Ceram. Soc. 82 (11) (1999) 3057–3064.
[16] K.S. Martirosyan, L. Wang, A. Vicent, D. Luss, Nanotechnology 20 (2009) 405609.
[17] M. Khairy, R.O. Kadara, D.K. Kampouris, C.E. Banks, Electroanalysis 22 (2010) 1455–1459.
[18] S. Taufik, N.A. Yusof, T.W. Tee, Ramli, Int. J. Electrochem. Sci. 6 (2011) 1880–1891.
[19] S.N. Ding, D. Shan, H.G. Xue, S. Cosnier, Bioelectrochemistry 79 (2010) 218–222.
[20] A.P. Periasamy, S. Yang, S.M. Chen, Talanta 87 (2011) 15–23.
[21] D. Shan, J. Zhang, H.G. Xue, Y.C. Zhang, S. Cosnier, S.N. Ding, Biosens. Bioelectron. 24 (2009) 3671–3676.
[22] M. Zidan, T.W. Tee, A.H. Abdullah, Z. Zainal, G.J. Kheng, Int. J. Electrochem. Sci. 6 (2011) 279–288.
[23] R. Liman, Chemosphere 93 (2) (2013) 269–273.
[24] J.L. Richard, Int. J. Food Microbiol. 119 (1) (2007) 3–10.
[25] B.D. Malhotra, S. Srivastava, M.A. Ali, C. Singh, Appl. Biochem. Biotechnol. 174 (3) (2014) 880–896.
[26] K.I. Cigic, H. Prosen, Int. J. Mol. Sci. 10 (1) (2009) 62–115.
[27] S.J. Daly, G.J. Keating, P.P. Dillon, B.M. Manning, R. O'Kennedy, H.A. Lee, M.R.A. Morgan, J. Agric, Food Chem. 48 (2000) 5097–5104.
[28] C.M. Maragos, V.S. Thompson, Nat. Toxins 7 (1999) 371–376.
[29] P.R. Solanki, A. Kaushik, T. Manaka, M.K. Pandey, M. Iwamoto, V.V. Agrawal, B.D. Malhotra, Nanoscale 2 (2010) 2811–2817.
[30] P. Kalita, J. Singh, M.K. Singh, P.R. Solanki, G. Sumana, B.D. Malhotra, Appl. Phys. Lett. 100 (2012) 093702.
[31] J. Singh, A. Roychoudhury, M. Srivastava, P.R. Solanki, D.W. Lee, S.H. Lee, B.D. Malhotra, J. Mater. Chem. B 1 (2013) 4493–4503.
[32] Y. Liu, Z. Qin, X. Wu, H. Jiang, Biochem. Eng. J. 32 (2006) 211–217.
[33] L. Masoomi, O. Sadeghi, M.H. Banitaba, A. Shahrjerdi, S.S.H. Davarani, Sensors Actuators B 177 (2013) 1122–1127.
[34] J.H.O. Owino, O.A. Arotiba, N. Hendricks, E.A. Songa, N. Jahed, T.T. Waryo, et al., Sensors 8 (2008) 8262–8274.
[35] M. Peng, L. Wondraczek, J. Mater. Chem. 19 (2009) 627–630.
[36] M.A. Ali, S. Srivastava, P.R. Solanki, V. Reddy, V.V. Agrawal, C.G. Kim, R. John, B.D. Malhotra, Sci. Rep. 3 (2013) 2661.

Comparative Analysis of Block Key Encryption Algorithms

Mukta Sharma
Research Scholar
Teerthanker Mahaveer
University, Moradabad

R. B. Garg, PhD
Ex-Professor
University of Delhi
Delhi

ABSTRACT
Humankind has grown phenomenally from Stone Age to information technology age. Information technology is deeply treasured; mainly because of the Internet. The internet has brought great changes in almost every domain of life. Besides a computer, laptop, Desktop, even a Mobile Phones, I-Pad, IPod have the facility to use the Internet. With the Internet, life has become easier to get things done at a great speed and effortlessly. Such as searching for some information, retrieving maps, images, bookings for air tickets, movie tickets, sports or concerts tickets, hotel reservations, grocery, vegetables, and fruits, paying bills online, transferring money without going to the bank, etc. and the list is endless. It is a well-known phrase "Each coin has two sides"; similarly, with the benefits of using the internet, there are many threats or flaws. The Internet has given easy access to attack our personal information, financial transactions, etc. by hackers, pedophiles, net extortion, and salami attacks and so on. There are numerous attacks, and the researchers are trying to figure out some solution for them. One of the most popular ways to ensure security is using cryptography.

This research paper is written with intent to explore symmetric key encryption algorithms. The research paper will focus on numerous symmetric key algorithms which have been ensuring security while transacting funds online. A study on block cipher algorithms gave a horizon to do a comparative analysis based on its working, real-time implementation, architecture, performance/scalability, flaws, etc.

General Terms
Block Ciphers, Cryptography, Symmetric Key Algorithm, etc.

Keywords
Advanced encryption Standard (AES), Asymmetric Key, Blowfish, Cryptography, Data Encryption Standard (DES), IDEA, Symmetric Key, Triple Data Encryption Standard (3DES)

1. INTRODUCTION
According to NIST, Computer Security Handbook [NIST95] defines the term computer security as "The protection afforded to an automated information system in order to attain the applicable objectives of preserving the integrity, availability, and confidentiality of information system resources (includes hardware, software, firmware, information / data, and telecommunications)"[4].Security is one of the most significant topics of research and discussions. Following objectives have been briefly explained regarding requirements and the definition of a loss of security:-

• Confidentiality: focus on two important traits one is data confidentiality, and the other is Privacy. Data confidentiality assures that information is confidential and is accessed by authorized users only. Whereas, Privacy ensures individuals to control the rights of collecting, storing, and disclosing their personal information to only those whom they wish to share [9] [26].

In short, confidentiality can be defined as preserving authorized restrictions on accessing and revealing the information (it may be personal or proprietary information). A loss of confidentiality is the unauthorized disclosure of information.

• Integrity: highlights two traits data integrity and system integrity. Data integrity: Promises that information and programs are consistent, trustworthy and reliable. System integrity: Should guarantee that a system performs is working in a proper manner, which means it should not allow unauthorized manipulation of the system [9] [26].

In Brief, Integrity is protecting against improper information modification or destruction and inaccessibility by unauthorized users. Loss of integrity allows any unauthorized modification or destruction of information [26].

• Availability is the assurance of giving the desired, correct information timely to the authentic user.

In short, Availability is an agreement of accessing accurate information to the authorized user. A loss of availability is the disruption of access to information or an information system [9] [26].

Cryptology is the study of reading, writing and breaking of codes. It comprises of cryptography (secret writing) and cryptanalysis (breaking code) as shown in figure 1. Symmetric cryptographic algorithms; which are used to hide messages have been the focus of research. Cryptography has given a platform which can ensure not only confidentiality but also integrity, availability, and non-repudiation of messages/ information.

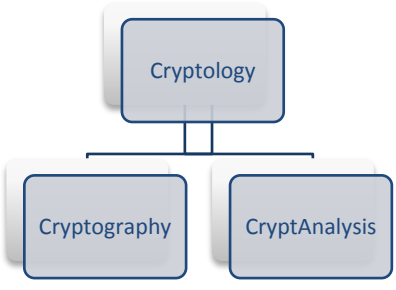


Fig. 1: Classification of Cryptology

Two Greek words Crypt (Secret) and graphics (Writing) makes Cryptography, means secret writing. It is one of the most important techniques to deal with security, especially in transacting information online [22]. Encryption and Decryption are two processes used to perform a cryptographic algorithm. Encryption will scramble the plain text or message

or information; into Ciphertext (scrambled text). Decryption is the reverse process used to retrieve the plain text from the cipher (scrambled text) [26]. Symmetric Key Encryption Algorithm, Asymmetric Key Encryption Algorithms, and Protocols are the way of implementing Cryptography as shown in figure 2. Symmetric Key (the same key is shared for communication by both sender and receiver to encipher and decipher the text). Unlike Symmetric Key, Asymmetric Key uses a set of keys (one public key-globally announced and another private key used to decrypt the message). Stream Cipher and Block Ciphers are two separate ways of classifying Symmetric Key. Stream Cipher as the name specifies a single stream of data or information is encrypted and then decrypted at a time. Block Cipher works with block or chunks of data or message instead of a single stream, character, or byte. This paper has focused primarily on block ciphers [24]. Block ciphers can build strong or secure algorithm by using Claude Shannon two atomic operations multiple times, two services are:-

- Confusion- Is mapping of one value to another, Obscuring (hiding) relationship between Plain Text and Cipher Text. Substitution is a good example of Confusion (Substitution Table, Lookup Table, S-Boxes, etc.) [24].
- Diffusion- The influence of one each plain text bit is spread over many cipher text. Reordering of bit position for each of the inputs. Example- Permutation

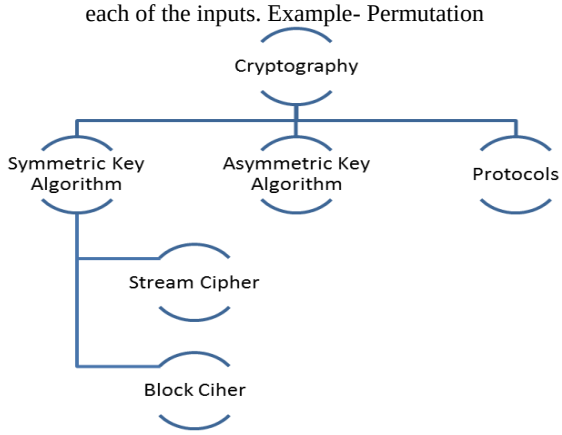


Fig. 2: Organization of Cryptography

2. CLASSIFICATION OF BLOCK CIPHER ALGORITHMS

In the market there are various block cipher algorithms, out of which some are patented, some algorithms were used extensively earlier, and few are widely acceptable even now. This paper will shed light on the following algorithms depicted in figure 3.

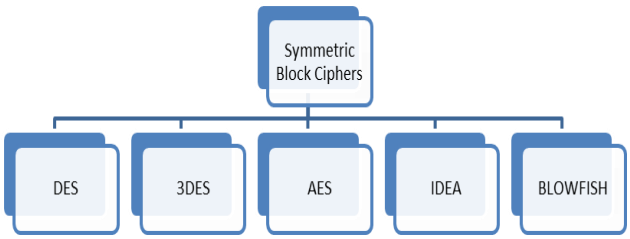


Fig. 3: Symmetric Key Block Ciphers

3. COMPARATIVE ANALYSIS

For ensuring security Cryptography is considered to be apt especially Symmetric Key Block Cipher algorithms are highly recommended. The paper focuses on the key aspects, factors, and varied parameters for analyzing the algorithms. They can be categorized as depicted in figure 4 [3] [5] [18] [19].

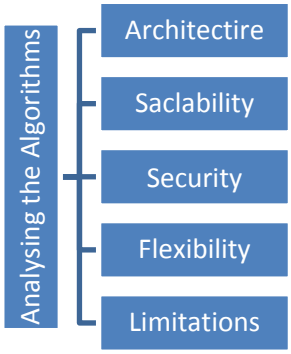


Fig. 4: Testing Parameters for Algorithms

1. **Architecture** –The basic structure involves its characteristics like whether it is a symmetric key algorithm or asymmetric key algorithm. The architecture deals with the specifications like key size, network type (Feistel network or substitution-permutation network), functions or operations it can perform and how they are implemented, how many rounds, etc. In short, architecture means the basic structure and layout of the algorithm [3] [5] [18] [19].
2. **Scalability –** It is one of the key element on which encryption algorithms can be analyzed. It is used to analyze the performance of the algorithm based on certain parameters such as Memory Consumption, Encryption rate, Software-Hardware performance; Computational efficiency, Mode, Data File type, speed, throughput, etc. [3] [5] [18] [19].
3. **Security-** It is one of the most significant parts of a cryptography algorithm which resists an attack. Key Length plays a pivotal role in context to Security. The greater the key length, difficult it becomes to crack. If an algorithm use Confusion and Diffusion it becomes little safer. A number of rounds enhance the security, if an algorithm uses Confusion, Diffusion multiple times, it can ensure better security, therefore, it is said to be more secure with number of rounds. But an increasing number of rounds makes the process very slow [22] [24].
4. **Flexibility**-This determines whether the algorithm can endure minor modifications according to the requirements
5. **Limitations (Known Attacks) –** This defines how excellent the algorithm works by using the computer resources available to it. Further, how often it is vulnerable to different types of attacks.

4. WORKING AND IMPLEMENTATION

1) **DES** stands for Data Encryption Standard designed by IBM in 1972 and was later adopted as a standard by US government in 1974 published by NIST [7] [17] [21] [29].

DES works on Feistel network. 64 bit Plain Text is given as an input and 64 bit Cipher Text comes as an output. Initially, Key is of 64 bits; parity bits (8, 16, 24, 32, 40, 48, 56, and 64) are removed. Later computation is carried on 56 bits key. PC-1 is used just once and PC-2 is used every time to compute a new sub key of **48 bits, instead of 56 bits**. 16 rounds are executed, Left Circular Shift is also based on the rounds like 1, 2, 9 and 16 move 1left bit and rest all rounds (3, 4, 5, 7, 8, 10, 11, 12, 13, 14 and 15) move 2 bits which finally makes 28bit (4*1+ 12*2= 28 bits)

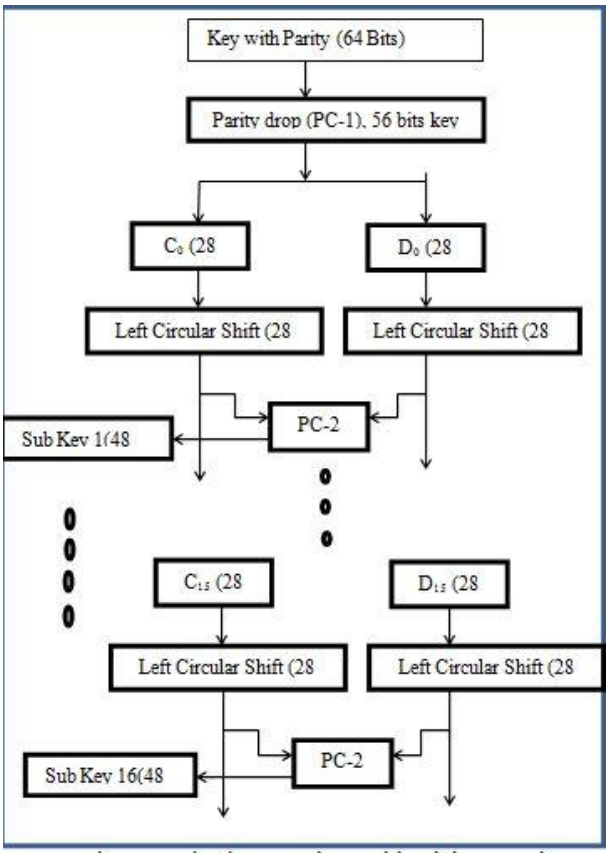


Fig. 5 Sub Key Generation

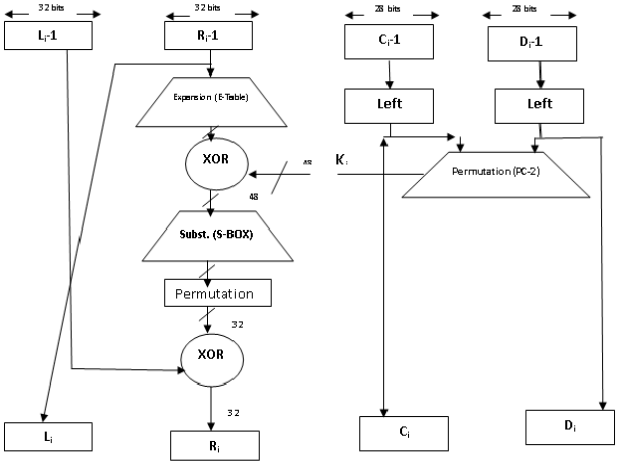


Fig. 6 DES Rounds

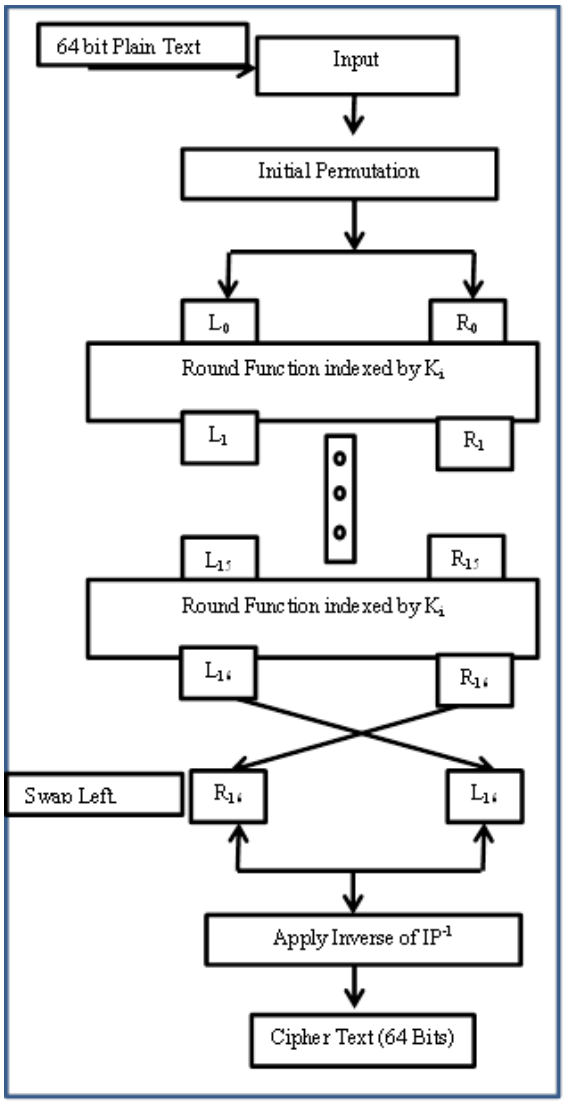


Fig. 7 DES Working

- **Rounds-** Initially, R is 32 bits, and it needs to be expanded to 48 bits so that XOR can be performed. Initially, the R is 4*8=32, and Expansion Matrix needs to expand it to 6*8=48. For the expansion, one previous bit is concatenated as the first bit, and one next bit is added as the last bit like 1234 will be expanded as 32(previous bit)1234 and 5(next bit)

Table 1: Expansion Permutation Table

1	2	3	4	5	6	7	8	Remark
1234							29303132	4*8=32
3212345							**28**29303132**1**	6*8=64

- XOR is also known as Modulo 2.
- S-Box substitutes 48-bit input to 32bit output. Eight blocks of 6 bits (i.e. 48 bits). Each S-Box (Total 8 S-Boxes) will generate a 4-bit output (4*8=32). First and last bit of a block are used for the row. Middle 4 values of a block are used to represent

column and then using S-Box table can take the value and convert it to a hexadecimal value.

Actual working of DES

- 64 bits are given as an input
- Initial permutation is carried on 64 bit block.
- Split into two halves of 32 bits each (L_0,R_0)
- R (L_i, R_i) passed to 16 rounds. Rounds are identical.
- After last round L_{16} & R_{16} are swapped to create pre output
- Inverse permutation is performed. Plain Text is finally converted to Cipher Text.

2) **Need for any other Algorithm**- After more than 20 years of successful journey of DES. The exhaustive key search started causing its discomfort. In Dec 1988 Deep Crack; special purpose DES hardware cracker was made for $2, 50, 000. In 1990 two Israeli researchers with the help of Differential Cryptanalysis were able to break using Known Plain Text attack. In the year 1993, one Japanese scientist worked on Linear Cryptanalysis. Later in the year 2007 software named COPACOBAMA was introduced for just $70,000 to break DES. **Triple DES or 3DES**- In November, 1998 to ensure security 3DES was introduced as an enhancement of Data Encryption Standard. It was not feasible regarding money & popularity and usage of DES to completely abandon DES. DES was widely adopted by large security architectures. Therefore, the manner was changed instead of running DES just once; it was decided to run it three times for better security. It led to the modified schemes of Triple DES (sometimes known as 3DES) [29].

This method is similar to the original DES, but it is applied three times (performs three iterations) to increase the security. 3DES uses 64-bit block size as an input and give 64 bit as an output, 16*3=48 rounds; and a key length of 168 bits (56*3). The 3DES encryption algorithm works in a sequence Encrypt-Decrypt-Encrypt (EDE). The decryption process is just reverse of Encryption process (Decrypt- Encrypt-Decrypt). 3DES is more complicated and designed to protect data against different attacks. 3DES has the advantage of the reliability and a longer key length that eliminates many attacks like brute force. 3DES higher security was approved by the U.S. Government. Triple DES has one significant limitation; it is much slower than other block encryption methods.

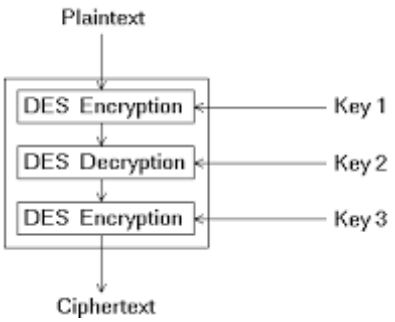


Fig. 8 3DES

- **The encryption algorithm is:**

Ciphertext = EK3(DK2(EK1(Plaintext)))

As the display in figure 8, the plain text is encrypted with DES along with Key, K1 then the ciphertext of the first round will be decrypted with Key, K2 and lastly the result of round 2; the plain text will be encrypted with Key, K3 to get the final Ciphertext.

- **The decryption algorithm is:**

Plaintext = DK1(EK2(DK3(Ciphertext)))

Decryption works in a reverse direction. In this, the Ciphertext decrypt with key, K3 to generate a plain text which will then be encrypted with Key, K2 to get cipher text and then finally cipher text will be decrypted with Key, K1 to get the final plain text.

The standards define three keying options:

- Keying option 1-All three keys are different. Keying option 1 is the strongest, with 3 × 56 = 168 independent key bits. Secure but time-consuming.
- Keying option 2- K1 and K2 are independent, and K3 = K1. It is less secure with 2*56=112 independent key bits.
- Keying Option 3- All three keys are identical, i.e. K1 = K2 = K3. It is equivalent to DES, with only 56 bits. Not recommended by NIST.

3) **IDEA-** (International Data Encryption Algorithm) is a symmetric key block cipher algorithm, developed at ETH in Zurich, Switzerland. IDEA was designed by Xuejia Lai and James Massey. It was published in 1991 and was initially named as Improved Proposed Encryption Standard (IPES) as it was the modified version of Proposed Encryption Algorithm. The name was changed in 1992 to International Data Encryption Algorithm. It is based on substitution-permutation structure. It is a block cipher that uses a 64-bit plain text, divided equally into 16bits each (16*4=64); with eight rounds and a Key Length of 128-bits. For each round 6 sub keys are required four before the round and two within the round (8*6= 48 sub keys+ 4 sub keys are used after the last or eighth round that makes total 52 sub- keys). IDEA does not use S-boxes. IDEA uses the same algorithm in reverse order for decryption [1] [28].

- **Keys**

A 128-bit key is split into 16 bits sub-keys from K1 to K8. Then the bits are shifted to the left 25 bits, ensuring that repetition does not occur in the sub keys. The resulting 128-bit string is split into eight 16-bit blocks that become the next eight sub keys. The shifting and splitting process is repeated until 52 sub keys are generated.

- **Actual Working of IDEA**
  - The 64 bit plaintext is divided into four blocks (A, B, C, and D)
  - 128 bit key is divided into 52 sub-keys (K1..K52)
  - 8 rounds with 6 sub keys= 4 keys before the round and 2 keys in the round
- Round 1 (there are 8 round and they are identical)
  - Multiply A by K1, Add K2 to B, Add K3 to C, Multiply D by K4.
  - Compute E=A XOR C and F= B XOR D.

- Multiply E by K5. Add the new value of E to F.
- Now multiply F by K6. Add the result of F, to E.
- Then XOR F with A and with C and XOR E with B and D separately.
- Swap B and C.
- Repeat this entire seven more times, using K7 through K48. After the eighth round do not swap B and C.
- Last step would be multiplying A by K49. Add K50 to B. Add K51 to C. Multiply D by K52.

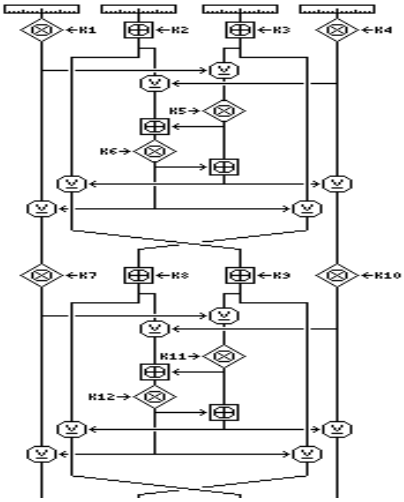


Fig. 9: IDEA

4) **AES-** In the year 1998, NIST conducted a competition open for all, where they accepted many algorithms, out of which they selected 15 algorithms. After analysis by the cryptographic research community five best cryptography algorithms (MARS, RC6, Rijndael, Serpent, and Twofish) were shortlisted. In 2000, NIST declared Rijndael as a new Advanced Encryption Standard and on May 26, 2002, it became effective as a federal government standard. Rijndael was proposed by Joan Daemen and Vincent Rijmen. AES is also a symmetric key algorithm based on the substitution–permutation Network [2] [8] [12] [32].

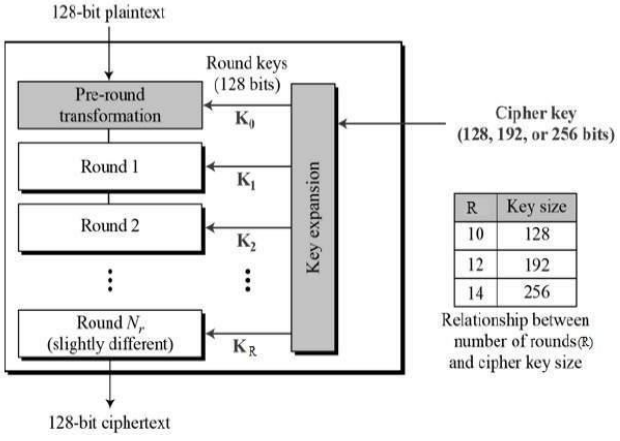


Fig. 10 AES

As depicted in Fig. 10, AES use a 128-bit block as plain text, which is organized as 4*4 bytes array also called as State and is processed in several rounds. It has variable Key length 128, 192 or 256-bit keys. Rounds are variable 10, 12, or 14 depends on the key length (Default # of Rounds = key length/32 + 6). For 128 bit key, a number of rounds are 10; 192 bit key, 12 rounds and for 256 bit key, 14 rounds. It only contains a single S- box (which takes 8 bits input, and give 8 bits output) which consecutively work 16 times. Originally the cipher text block was also variable, but later it was fixed to 128 bits.

The Encryption and decryption process consists of 4 different transformations applied consecutively over the block data bits, in a fixed number of iterations, called rounds. The four different changes are described in detail below:

- Sub Bytes function performs a non-linear substitution of bytes that operates independently on each byte of the State using a substitution table (S-box). 4*4 matrixes are used for substitution. There are 16 parallel S-boxes each with eight inputs and eight outputs. S-boxes are based on two mathematical properties Multiplication and Affine Transformation. This S-box which is invertible is constructed by first taking the multiplicative inverse in the finite field GF (28) with irreducible polynomial m(x) = x8 + x4+ x3 + x + 1. The element {00} is mapped to itself. Then affine transformation is applied (over GF (2)).
- Shift Rows function performs byte-wise circular shifts on last three rows of the state. In this function, first row is not shifted, the second row is shifted 1 byte left the position, the third row is shifted left by two positions and in the fourth row, 3 bytes are shifted leftward.
- Mix Columns function operates on each State column-by-column, treating each column as a four-term polynomial. The columns are considered as polynomials over GF (28) and multiplied by modulo x4 + 1 with a fixed polynomial a(x) = {03} x3+ {01} x2+ {02} x.
- Add Round Key is the final function; in this, a 16 byte Key is simply XOR with the 16-byte state. Each Key is obtained from Key expansion algorithm.
- Key Expansion: The purpose is to calculate round key for each round, based on the original key. This function comprises of three sub-functions:-
  a. Sub Word takes a four-byte input and applies S-box to each of four bytes to produce an output word.
  b. Rot Word takes a word, performs cyclic permutation, and returns the word.
  c. Round Const function contains a round constant array that performs a bitwise XOR function. Round constant array contains values given by ½xi_1; f00g; f00g; f00g_ with xi_1 being powers of x (x is denoted as {02}) in the field GF (28).

The decryption process is the direct inverse of the encryption process. Hence the last round values of both the data and key are first round inputs for the decryption process and follows in decreasing order.

AES is extremely fast and compact cipher. For implementers its symmetric and parallel structure provides excellent and an active resistance against cryptanalytic attacks. The larger block size prevents birthday attacks, and large key size prevents brute force attacks

5) BlowFish

Blowfish is a symmetric block cipher, designed in 1993 by Bruce Schneier. It works on of 64-bit block size. Key length is variable from 32 bits to 448 bits. It has16 rounds and is based on Feistel network. It has a simple structure, and it's easy to implement. It encrypts data on 32-bit microprocessors at a rate of 18 clock cycles per byte so much faster than AES, DES, and IDEA. Since the key size is large, it is complex to break the code in the blowfish algorithm. It is vulnerable to all the attacks except the weak key class attack. It is unpatented and royalty-free. It requires less than 5K of memory to run Blowfish [23] [30].

- **Sub-Key**

Blowfish uses a large number of sub-keys. Subkeys must be pre-computed before any data encryption or decryption. The sub-keys are calculated using the Blowfish algorithm:

1. Initialize first the P-array and then the four S-boxes, in order, with a fixed string. This string consists of the hexadecimal digits of pi (less than initial 3): P1 = 0x243f6a88, P2 = 0x85a308d3, P3 = 0x13198a2e, P4 = 0x03707344, etc.
2. XOR P1 with the first 32 bits of the key, XOR P2 with the second 32-bits of the key, and so on for all bits of the key (possibly up to P14). Repeatedly cycle through the key bits until the entire P-array has been XOR with key bits. (For every short key, there is at least one equivalent longer key; for example, if A is a 64-bit key, then AA, AAA, etc., are equivalent keys.)
3. Encrypt the all-zero string with the Blowfish algorithm, using the sub-keys described in steps (1) and (2).
4. Replace P1 and P2 with the output of step (3).
5. Encrypt the output of step (3) using the Blowfish algorithm with the modified sub keys.
6. Replace P3 and P4 with the output of step (5).

Continue the process, replacing all entries of the P array, and then all four S-boxes in order, with the output of the continuously changing Blowfish algorithm.

In total, 521 iterations are required to generate all required sub-keys. Applications can store the sub keys rather than execute this derivation process multiple times.

- **Data encryption:**
  - The input is a 64-bit data element, X.
  - Split X into two halves of 32-bits each: XL, XR.
  - Then, for i = 1 to 16
    - XL = XL XOR Pi
    - XR = F(XL) XOR XR
    - Swap XL and XR
  - After the sixteenth round, swap XL and XR again to undo the last swap.
  - Then, XR = XR XOR P17 and XL = XL XOR P18.
  - Finally, recombine XL and XR to get the Ciphertext.

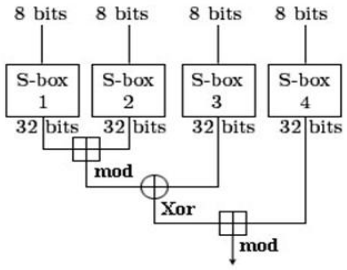


Fig. 11: Round function of Blowfish Algorithm

1. Architecture

Table 2: Architecture [9] [22] [26]

Factors	DES	3DES	IDEA	AES	Blowfish
Developed in year	1974	1998	1991	2000	1993
Developed By	IBM	IBM	Xuejia Lai, James Massey	Rijmen, Daemen	Bruce Schneier
Key length (bits)	56	112, 168	128	128, 192 or 256	32 to 448
Cipher Type	Symmetric Key Algorithm				
Block Size (bits)	64	64	64	128	64
Rounds	16	48	8	10,12,14	16
Used Functions	IP, IP-1, E, P, S-Box(8), PC-1, PC-2	IP, IP-1, E, P, S-Box(8), PC-1, PC-2	N.A	S-Box (1), GF(2^8)	S-Box (4)
Used Operations	XOR, <<<, >>>	XOR, <<<, >>>	XOR, Addition modulo 2^{16}, Multiplication modulo 2^{16+1}	XOR, <<<, >>>	+, XOR, <<<, >>>
Structure of Algorithms	Feistel Network	Feistel Network	Lai-Massey Scheme	Substitution-Permutation Network	Feistel Network
Real World Examples	Digital right management	Blackberry Enterprise server	PGP (Pretty Good Privacy)	Smart Card	SSL

SCALABILITY/ PE

2. Scalability/ Performance

A system is scalable if its performance remains stable even under the critical scenario. The performance of any system can be evaluated on specific criteria. Such criteria's, factors or parameters are known as performance metrics. [6] [11] [15] [27] [31]

Any algorithm can be evaluated on the basis of time and space complexity. To evaluate the performance of encryption and decryption algorithm following criteria's should be considered:-

1. Encryption Time- It can be defined as the time taken to convert a plaintext to a ciphertext
2. Decryption Time- The time Taken for Decryption process. Means time taken for converting cipher text to plain text.
3. Throughput Time- The throughput of the encryption process can be calculated as the total plaintext in bytes encrypted divided by the encryption time.

Total plain text bytes/Total encryption time

4. CPU Utilization & Memory Usage/ Consumption- Total memory used during encryption/ decryption process.
5. Key Length- Total Key length or key size of an algorithm
6. Tunability- It is very popular to define encrypted parts and the encryption parameters used for different applications and requirements.
7. Number of Rounds- Number of iterations in an algorithm.
8. Block Size- The size of each chunk of Plain Text.
9. Number of Functions used- The total number of Functions used for substitution transformation. For example number of S-boxes, Permutation metrics, etc.
10. Number of Operations used – Number of operators like +,*, XOR, <<<, >> etc.
11. Avalanche Effect- It is a required property of cryptographic hashing algorithm. It means that a small change in the input (say one bit) can bring a big change in the output [24] [22].

Avalanche Effect= Number of flipped bits in ciphered text/ Number of bits in ciphered text

- First Order Sac- Change in 1-bit Plain text effect can flip many bits of output
- Higher Order Sac- Change many bits in Plain Text and more than half bits should flip in the output.

1. Robustness against statistical attacks - Statistical analysis is the practice of detecting hidden information by applying statistical tests. Most of the algorithms leave a mark that can be easily detected through statistical analysis. To be able to pass by an eavesdropper without being detected, an algorithm must not leave such a mark in the encrypted file as be statistically significant [9].
2. Robustness against manipulation - In the secure communication, the file may undergo changes by an attacker to remove hidden and encrypted information. It is preferable for the algorithms to be robust against either malicious or unintentional changes [9].
3. Independent of file type - File type and File size also play an important role. There are so many different file types used for communication. The most powerful algorithms thus possess the ability to encrypt any type of information in any type of file [9].

3. Security

Cryptographic security defines whether encryption scheme is secure against Brute Force & different plain - cipher text attacks. A cipher is used to provide protection from undesirable disclosure of plain text. Any cryptanalyst or hacker breaks the cipher with an aim to recover the plaintext. If a secret key is recovered by the hacker, then he can read all messages after that as quickly as the legitimate user. Security is always said relative to threats. Assuming, the attackers have access to everything across the insecure channel is Internet, the security of a cipher can be assessed after considering the computational capability of hacker [10] [13] [14] [16] [20].

Kerckhoff's assumption: The cryptanalyst knows the complete process of encryption and decryption except for the value of the secret key. It implies that the security of a secret-key cipher system rests entirely on the secret key. Following are the few attacks:

- Cipher text-only - Here, the attacker is assumed to have a part of cipher text, and he tries to obtain the associated key to further decrypt the plain text [26].
- Known-plaintext attack – In this we assume the hacker to have few sample of a pair of plain text and cipher text. Using this hacker tries to obtain relative secret key [26].

Table 3: Scalability Criteria's [6] [11] [15] [27] [31]

	DES	3DES	IDEA	AES	Blowfish
Encryption Time	High	High	Low	High	High
Decryption Time	Medium	Medium	High	High	Low

Resource Consumption	Requires more CPU cycles and Memory	Requires effective resource consumption	Lower Power Consumption	Consumes resources when data and block size is big	Requires pre-Processing
Computational Speed	Fast	Moderate	Fast	Fast	Very Fast
Throughput	Medium	Low	High	High	Very High
Avalanche effect	Resists	Resists	Resists	Resists	Resists
Tunability	No	No	No	No	No
Independent of file Type	No	No	No	No	No

Table 4: Security Factors [10][13][14][16][20]

	DES	3DES	IDEA	AES	Blowfish
Plaintext/Ciphertext pairs (Differential Cryptanalysis 2^Block Size)	2^64	2^64	2^128	2^64	2^64
Processing complexity(2^KeySize)	7.2 x 10^16 (2^56)	5.1 x 10^33 (2^112) to 3.74 x 10^50 (2^168)	3.4 x 10^38 (2^ 128) to 1.15 x 10^77(2^256)	3.4 x 10^38 (2^128)	4.29 x 10^9 (2^32) to 7.26 x 10^134 (2^448)
Cryptanalysis Resistance	Vulnerable to Linear and Differential Cryptanalysis, Brute Force	Vulnerable to differential brute force. Attackers can analyze Plain Text, Vulnerable to Chosen plain text, Known plain text	Vulnerable to weak keys(key-schedule attacks and related-key differential timing attacks)	Strong against truncated differential, linear interpolation and square attacks, Vulnerable to Chosen plain text, Known plain text	Vulnerable to differential brute force Attack, Dictionary attack
Security	Inadequate	Vulnerable	High	High	High
Robustness against statistical attacks	Medium	High	High	High	High

- Chosen-plaintext attack – It is an associate attack model. The arbitrary plain text is chosen to be encrypted for the corresponding cipher.4. Chosen-cipher text attack –The cryptologist gathers data, a minimum of partially, by selecting a cipher-text and getting its decipherment beneath an unknown key.
- Chosen-text attack - A chosen text attack is a combination of wanting plain-text and chosen cipher-text attack [9].
- Brute-force attack - This type of attack is a passive attack. This attack performs an exhaustive search for cracking the key. Exhaustive search means calculating every possible combination that could make up a password and test it to see if the password is correct.
- Dictionary attack – In a nutshell, a dictionary attack is a kind of brute force attack where the attacker can rate keys in order of most probable, least likely, compile a list of the most likely (the dictionary), and test them in that order [9].
- Timing attack Timing attacks is a side channel attack which enables an attacker to extract secrets maintained in a security system by observing the time it takes the system to respond to various queries.

- Man-in-the-middle attack - This is the type of active attack. It is a form of eavesdropping in which the attacker controls the entire conversation. Here the attacker secretly relays and possibly alters the communication between two parties who believe they are directly communicating with each other.

4. Flexibility

Table 5: Flexibility [9][26]

	DES	**3DES**	**IDEA**	**AES**	**Blowfish**
Flexibility	No	Yes	No	Yes	Yes
Remarks	No modification is allowed	3 times iteration	No modification is allowed	Structure was flexible to the multiples of 64.	key length must be multiples of 32 bits

5. Limitations (Known Attacks)

Table 6: Limitations [9][22][26]

DES	3DES	IDEA	AES	Blowfish
Highly vulnerable to Linear Cryptanalysis, Weak keys and Brute force. Only 2^56 combinations are required to break the key. It was designed for Hardware so works slow for software.	Exposed to differential and related key attacks. Also susceptible to certain variation of meet-in the middle attack.	Susceptible to different classes of weak keys and are highly exposed to key attacks such as Key Schedule & Related key differential timing attacks. First three rounds of IDEA algorithm is observed for related-key differential timing attacks and Key- schedule attacks.	No serious weakness; Some initial rounds of AES are observed unprotected i.e. initial round can break by square method.	Vulnerable to weak keys, 4 rounds are exposed to 2nd order differential attacks.

5. CONCLUSION

Comparative analysis of few significant block ciphers on different parameters like Security, flexibility, etc. has been done. The architecture and working of all the algorithms have been discussed in the paper. The overall generalized observation being made is that Blowfish algorithm is remarkably better on throughput, power consumption, and processing time as compared to other algorithms. No attack yet has been able to

break Blowfish, and it has better performance and efficiency. Another algorithm AES with its variable key length and a varying number of rounds make it an excellent choice to rely on security as well as the flexibility. 3DES is still considered secure besides the only limitation of being extremely slow.

6. REFERENCES

[1] Daemen, J., Govaerts, R. and Vandewalle, J. (1998).*Weak Keys for IDEA*, Springer-Verlag.

[2] Daemen, J., Rijmen, V.(AES Proposal: Rijndael. Retrieved From: http://csrc.nist.gov/encryption/aes/rijndael/Rijndael.pdf

[3] Deep, T.V. & Reddy, V. S. R. (2015). Comparative Analysis of AES finalist algorithms and low power methodology for RC6 block cipher - A Review. International Journal For Technological Research In Engineering, Vol. 2(6)

[4] Denning, D. E. R. (1982). Cryptography and data Security. Addison-Wesley Publishing Company. Menlo Park, California

[5] Ebrahim, M, et al. (2013). *Symmetric Algorithm Survey: A Comparative Analysis*. International Journal of Computer Applications, Vol. 61(20)

[6] Elminaam, A., Abdual, D. S., Kader, H.M., and Hadhoud, M.M. (2010).*Evaluating The Performance of Symmetric Encryption Algorithms*. International Journal of Network Security, Vol.10(*3), PP.213 -219*

[7] Engelfriet, A.(2012). The DES encryption algorithm,‖ Available at www.iusmentis.com/technology/encryption/des/,.

[8] FIPS 197 (2001). Announcing the ADVANCED ENCRYPTION STANDARD (AES). Retrieved From: http://csrc.nist.gov/publications/fips/fips197/fips-197.pdf

[9] Forouzan, B. A., "Data Communications & Networking", Fourth Edition, 2008, New York: Tata McGraw- Hill.

[10] Jeeva, A.L., Palanisamy, V. & Kanagaram, K.(2012). *Comparative Analysis of Performance Efficiency and Security Measures of Some Encryption Algorithms.* International Journal of Engineering Research and Applications, Vol. 2(3)

[11] Johnson, N. F., Jajodia, S. (1998). Steganalysis of imges created using current steganography software. In IHW'98 -Proceedings of the International Information hiding workshop.

[12] Kak, A. (2015). Computer and Network Security- AES: The Advanced Encryption Standard [pdf file].Retrieved from https://engineering.purdue.edu/kak/compsec/NewLectures/Lecture8.pdf

[13] Kaur, M. Kaur(2016), K. *A Comparative Review on Data Security Challenges in Cloud Computing*. International Research Journal of Engineering and Technology, Vol. 03(1)

[14] LAI, X. (1992). *On the Design and Security of Block Ciphers*, ETH-9752, Zurich

[15] Mehdi, H. (2013). *Checking EABC Performance in Comparison Others Cryptography Algorithms*. International journal of Computer Science & Network Solutions, Vol. 1(1).

[16] Mushtaque, A, M. (2014). Comparative Analysis on Different parameters of Encryption Algorithms for Information Security. International Journal of Computer Sciences and Engineering Vol.-2(4), pp (76-82)

[17] National Bureau of Standards, "Data Encryption Standard," FIPS Publication 46, 1977.

[18] Nema, P., &.Rizvi, M.A. (2015).Critical Analysis of Various Symmetric Key Cryptographic Algorithms. International Journal on Recent and Innovation Trends in Computing and Communication, Vol.3(6)

[19] Pandav, R.M., & Verma, V.K (2015). *Data Security using Various Cryptography Techniques: A recent Survey*. International Journal for Research in Engineering Application & Management, Vol. 01**(09).**

[20] Rayan, A.M., Abdel-Hafez, A.A., Hafez, I.M. (2016). *Provably Secure Encryption Algorithm based on Feistel Structure*. International Journal of Computer Applications, Vol. 139(1)

[21] Rouse, M. (2006). Data Enryption Standards (DES). Available at http://searchsecurity.techtarget.com/definition/Data-Encryption-Standard.

[22] Schneier B., "Applied Cryptography", John Wiley& Sons Publication, New York, 1994.

[23] Schneier, B. (1994).Description of a New Variable-Length Key, 64-Bit Block Cipher (Blowfish),‖ *Fast Software Encryption, Cambridge Security Workshop Proceedings, Springer-Verlag*, 1994, Available at http://www.schneier.com/paper-blowfish-fse.html

[24] Shannon, Claude, Communications theory of Secrecy Systems, Bell systems Technical Journal. 28 (4): 656 - 715.

[25] Sharma, S. & Bhatt, S.(2015). Comparative Analysis - Performance, Efficiency and Security Measures of Block Cipher Algorithms. IJEDR, Vol. 3(3).

[26] Stallings William, "Cryptography and Network Security Principles and Practice", Fifth Edition, Pearson Education, Prentice Hall, 2011.

[27] Tamimi, A.A. "Performance Analysis of Data Encryption Algorithms. Retrieved October 1, 2008 from http://www.cs.wustl.edu/~jain/cse567-06/ftp/encryption_perf/ index.html

[28] Thaduri, M., Yoo, S. and Gaede, R. " An Efficient Implementation of IDEA encryption algorithm using VHDL", Elsevier, **(2004)**.

[29] Tropical Software, Triple DES Encryption, Available at http://www.tropsoft.com/strongenc/des3.htm,

[30] Gatliff, B. (2003). Encrypting data with the Blowfish algorithm. Available at http://www.design-reuse.com/articles/5922/ encrypting-data-with-the-blowfish-algorithm.

[31] Verma, O.P, Agarwal, R., Dafouti, D. & Tyagi, S.(2011). *Performance Analysis of Data Encryption Algorithms.* IEEE- Delhi Technological University India, 2011.

[32] Wagner, R. N. The Laws of Cryptography Retrieved From http://www.cs.utsa.edu/~wagner/laws/

PLOS ONE

RESEARCH ARTICLE

Computational Analysis and Predictive Cheminformatics Modeling of Small Molecule Inhibitors of Epigenetic Modifiers

Salma Jamal[1] ‡, **Sonam Arora**[2] ‡, **Vinod Scaria**[3]*

1 CSIR Open Source Drug Discovery Unit (CSIR-OSDD), Anusandhan Bhawan, Delhi, India, **2** Delhi Technological University, Delhi, India, **3** GN Ramachandran Knowledge Center for Genome Informatics, CSIR Institute of Genomics and Integrative Biology (CSIR-IGIB), Delhi, India

These authors contributed equally to this work.
‡ These authors are joint first authors on this work.
* vinods@igib.in

CrossMark
click for updates

OPEN ACCESS

Citation: Jamal S, Arora S, Scaria V (2016) Computational Analysis and Predictive Cheminformatics Modeling of Small Molecule Inhibitors of Epigenetic Modifiers. PLoS ONE 11(9): e0083032. doi:10.1371/journal.pone.0083032

Editor: Wei Yan, University of Nevada School of Medicine, UNITED STATES

Received: June 10, 2013

Accepted: October 30, 2013

Published: September 13, 2016

Copyright: © 2016 Jamal et al. This is an open access article distributed under the terms of the Creative Commons Attribution License, which permits unrestricted use, distribution, and reproduction in any medium, provided the original author and source are credited.

Funding: SJ acknowledges a Project Fellowship from CSIR-OSDD. This work was funded by the Council of Scientific and Industrial Research (CSIR), India through Grant BSC0122 (CARDIOMED). The funders had no role in study design, data collection and analysis, decision to publish, or preparation of the manuscript.

Competing Interests: The authors have declared that no competing interests exist.

Abstract

Background

The dynamic and differential regulation and expression of genes is majorly governed by the complex interactions of a subset of biomolecules in the cell operating at multiple levels starting from genome organisation to protein post-translational regulation. The regulatory layer contributed by the epigenetic layer has been one of the favourite areas of interest recently. This layer of regulation as we know today largely comprises of DNA modifications, histone modifications and noncoding RNA regulation and the interplay between each of these major components. Epigenetic regulation has been recently shown to be central to development of a number of disease processes. The availability of datasets of high-throughput screens for molecules for biological properties offer a new opportunity to develop computational methodologies which would enable in-silico screening of large molecular libraries.

Methods

In the present study, we have used data from high throughput screens for the inhibitors of epigenetic modifiers. Computational predictive models were constructed based on the molecular descriptors. Machine learning algorithms for supervised training, Naive Bayes and Random Forest, were used to generate predictive models for the small molecule inhibitors of histone methyl-transferases and demethylases. Random forest, with the accuracy of 80%, was identified as the most accurate classifier. Further we complemented the study with substructure search approach filtering out the probable pharmacophores from the active molecules leading to drug molecules.

Results

We show that effective use of appropriate computational algorithms could be used to learn molecular and structural correlates of biological activities of small molecules. The

computational models developed could be potentially used to screen and identify potential new biological activities of molecules from large molecular libraries and prioritise them for in-depth biological assays. To the best of our knowledge, this is the first and most comprehensive computational analysis towards understanding activities of small molecules inhibitors of epigenetic modifiers.

Introduction

Though all cells in an organism inherit the same genomic template, the dynamic expression of the genome provides for the cell-type and tissue specific organisation and functional organisation of multi-cellular organisms [1]. This dynamic regulation is largely dependent on the regulatory layer of interactions between multiple biomolecules, operating at the chromatin organisation, transcriptional and post-transcriptional levels [2]. The regulatory layer contributed by the Epigenetic layer has been one of the favourite areas of interest recently [3]. The epigenetic layer of regulation comprises largely of DNA modifications, histone modifications and noncoding RNA regulation and the interplay between each of these major components. The understanding of this epigenetic layer of gene regulation has largely been fuelled by large-scale genome-wide maps of both DNA modifications and histone modifications [4], thanks to the availability of high-throughput sequencing based assays to qualify epigenetic marks across the genome. Epigenetic modifications and their dysregulation has been implicated in the pathophysiology of a wide spectrum of diseases [3].Though present understanding of the role of epigenetic dysregulation contributing to the pathophysiology of diseases is rudimentary, a number of diseases including cancers [5] neuropsychiatric disorders [6], metabolic disorders [7] have been shown to have a strong association with epigenetic dysregulation.

Histone organization and post-transcriptional modification of histones contribute a major and well studied class of epigenetic marks. Histone proteins are integral components of the nucleosome and post-transcriptional modification of histones and their interplay with DNA base modifications largely regulate the transcription of genes. These post-transcriptional modifications of histones are modulated by proteins popularly known as histone modifiers, which dynamically regulate the pattern of modifications across the genome through a concerted, but poorly understood mechanism. Ample evidence in the recent years have shown that DNA methylation and histone modifications could modulate gene expression [8], mark gene boundaries [9] and potentially differentiate between protein-coding and noncoding gene promoters in the genome [10,11]. Histone modifiers or Epigenetic modifiers are largely categorised into three groups [12]. The first group of proteins largely post-translationally 'write' marks on the histone tail. Well studied examples of such proteins include histone Methyltransferases or acetyltransferases. The second group of proteins largely 'erase' existing marks on the histone, and include well characterized proteins like demethylases and deacetylases. The third and potentially poorly understood class of proteins recognise specific epigenetic marks and bind to the histone complex modulating their regulatory effect.

Epigenetic modifiers have been recently studied in detail as they could be attractive drug targets for diseases where epigenetic dysregulation play an important role, as in the case of some cancers [13]. This has been complemented by the availability of high throughput screening methodologies and assays for many of these proteins [14, 15]. The availability of these large-scale screening datasets in public domain also provide an immense opportunity to model the activities based on physicochemical and/or structural properties of molecules. These models

would be immensely useful in drug discovery applications to significantly reduce the time and effort by prioritising molecules with desirable activities for in-depth screening and biological validation. Such approaches have been extensively used by our group previously towards modelling activities [16–19].

In the present study, we employed four datasets of high-throughput screens for inhibitors of epigenetic modifiers. We used machine learning approaches using chemical descriptors to create accurate predictive models for the activities. We also use an independent substructure based approach to identify commonly enriched substructures associated with the activities. To the best of our knowledge, this is the first report of computational modelling of biological activities of small molecule inhibitors of epigenetic modifiers.

Methodology

Dataset source

The data for the potential inhibitors of Histone methyltransferases and demethylases was downloaded from PubChem repository of chemical compounds. The datasets were downloaded corresponding to AID 504332, AID 504339, AID 2147 and AID 540317.

Bioassay AID 504332. The qHTS was based on an assay developed for the inhibitors of G9a (Histone Lysine Methyltransferase) and included 30,875 active and 2, 67,000 inactive compounds. G9a is a histone methyltransferase which belongs to SET-domain containing family and specifically catalyzes methylation of Lys9 of histone H3 (H3K9) in mammalian euchromatic regions repressing the transcription [20, 21]. The knockdown of G9a results in transcriptional activation and inhibits cancer cells growth [22].

Bioassay AID 504339. The dataset contains inhibitors of JMJD2A-Tudor Domain JMJD2A, which is a jumonji-domain-containing histone demethylase (Lysine-specific demethylase 4A). JMJD2A binds to trimethylated H3K4 and H4K20 via the tudor domains and causes demethylation which may result in both, transcriptional repression and activation [23, 24]. Binding of JmjD2A to histone results in positioning of the enzymes for methylating adjacent regions causing rapid methylation over large area of chromatin [25, 26]. Targeting of the JMJD2A-tudor domain interaction with the methylation marks on lysine residues of histone, H3 and H4, tails may lead to selective demethylation of a given methyllysine locus based on the methylation state of adjacent histone marks. The demethylase activity follows radical attack mechanism using Fe (II) and α-ketoglutarate as co-factors. The substrate (mono, di or tri-methylated lysine) to be demethylated is determined by the association of enzymes with cofactors. The data contain 16,919 active compounds and 3, 38,945 inactive compounds.

Bioassay AID 2147. The dataset contains small molecule inhibitors of Human Jumonji Domain Containing 2E (JMJD2E). JMJD2E is a histone modifier enzyme and functions as a histone demethylase. Histone lysine demethylases catalyze the demethylation of methylated lysine side-chains on histones H3 and H4, thus acts to reverse the methylation reactions catalyzed by histone lysine methyltransferases. The high throughput data contained a total of 3,523 active and 1, 88,950 inactive compounds.

Bioassay AID 540317. The assay was developed to identify the first inhibitors of protein methyltransferases. The dataset contained 2,142 active and 3, 67,962 inactive compounds screened for potential inhibitors of HP1-beta chromodomain interactions with Methylated Histone Tails HP1 (Heterochromatin protein). The N- terminal chromodomain containing HP1 proteins bind to the methylated histones and further results in gene repression and heterochromatin formation. The interaction harbors an N- terminal chromodomain that binds to the tri-methylated lysine 9 of histone H3, H3K9me3, and a C-terminal chromoshadow domain. Compounds in PubChem are characterized based on Activity Score calculated using AC50.

AC50 is the concentration at which 50% of the activity is observed. Compounds having AC50 values less than or equal to 20 micromolar with corresponding activity score between 40–100 were considered as active compounds. Compounds having AC50 value greater than the highest concentration tested (for example 20 micromolar) and activity score 0 were considered as inactive compounds. The rest compounds with activity score between 1–39 were considered as inconclusive compounds.

All the datasets were obtained through the confirmatory bioassay screens conducted by NCGC, NIH Molecular Libraries Probe Production Network. The Amplified Luminescent Proximity Homogeneous Assay (AlphaScreen) from PerkinElmer was used for identification of these inhibitors. It is a homogeneous assay technology used for screening of different classes of targets and analytes. Donor and acceptor beads coated with a layer of hydrogel are utilized. The beads are conjugated with biological molecules. With excitation, ambient oxygen is converted to reactive singlet oxygen in the donor bead. The singlet oxygen species reacts with thioxene compounds in the acceptor bead to generate a chemiluminescent signal that emits at 370 nm. Streptavidin-coated and anti-IgG antibody-coated beads were employed for detecting the methylation state of biotinylated-histone peptide.

Pre-processing of data

The files obtained from PubChem in the Structure Data Format (SDF) were used to generate 2D molecular descriptors using PowerMV [27], a popular toolkit for computing chemical descriptors. PowerMV generated a total of 179 molecular descriptors describing the physicochemical properties of the molecule (like hydrogen bond donors, acceptors, number of rotatable bonds, charge, polarizability, aromaticity etc.). The descriptor file generated was saved in comma separated (CSV) format. The attributes having same bit string descriptor values throughout the dataset (all 0's or all 1's) were filtered out. The list of the descriptors generated and used is available as S1 Table.

Processing data and model building

The files saved in CSV format were then converted to ARFF (Attribute Relation File Format) compatible with Weka. The models were built using different classifications viz. Naive Bayes and Random Forest as described previously [16, 17, 18, 19]. For each base model we have used cost sensitive classifier in order to reduce the false negative rate. This was imperative as the datasets were highly imbalanced with a large inactive set compared to the active set. The misclassification cost is incremented on false negatives until the false positive rate reduces to 20%. Assignment of the cost is random irrespective of the base classifier used. Cost sensitive classification is based on cost-proportionate weighting of the training examples, which can be realized either by applying weights to the classification algorithm, or by resampling of instances according to costs. We used Weka 3.6 (Waikato Environment for Knowledge Analysis) [28] which is a toolbox for data mining and machine learning algorithms. Weka provides a simple GUI supporting data from various sources and in different file formats. It has multiple algorithms (including that of regression, association rule mining, clustering, classification etc.) and preprocessing tools that allow comparison of different methods. The workbench is used for both supervised as well as unsupervised algorithms. The data visualization facilities help in easy access and analysis of results. The dataset was then further randomly split into training and test sets. The training data comprising maximum part of complete data (80%) was used to train the model using different algorithms and the test set (20%) was to evaluate each of the models. All computation was performed on CDAC-Garuda supercomputing facility using the OSDD-Garuda web interface.

Cross validation

K-fold cross validation is one of the most popularly sued methods of cross-validation of the accuracy of a model. In k-fold cross validation, the entire data is divided into k subsets (folds) of equal sizes and training is done for (k-1) sets and testing is done on one set. The process is repeated k number of times so that each set is tested at least once. The average error rate is computed for all tests. We have used (k = 5) or a 5-fold cross validation here since the dataset was large.

Model performance evaluation

The 2X2 confusion matrix used by Weka contains the following values:

- True positives (TP): class members classified as class members.
- True negatives (TN): class non-members classified as non-members.
- False positives (FP): class non-members classified as class members.
- False negatives (FN): class members classified as class non-members.

We additionally used the following measures for the statistical evaluation of the models:

- **Sensitivity** is the proportion of actual positives which are predicted positive, i.e.TP / (TP + FN).
- **Specificity** is the proportion of actual negatives which are predicted negatives, i.e. TN / (TN + FP).
- **ROC** is receiver operating characteristic curve which is a 2D curve parameterized by one parameter of the classification algorithm, e.g. some threshold in the true positive rate /false positive rate.
- The **Matthews correlation coefficient** is a measure of correlation between the observed and predicted binary classifications and quality of the classifier. The values range between −1 and +1.
- **Balanced Classification Rate (BCR)** introduces a balance in the classification calculated as 1⁄2. (Sensitivity + Specificity).
- **Accuracy** is the efficiency of the classifier to predict true values, i.e. TP+TN) / (TP+TN+FP +FN) * 100).

Substructure search

Aligning structures on a key structural framework help chemists to interpret the influence of substituents on the template as initial point towards understanding structure-activity information. With the aim of finding molecules which have similar properties to act as a drug, similarity search of compounds was done. Library MCS, a tool from ChemAxon [29], based on hierarchical clustering algorithm was used to cluster the molecules and find the potential bioactive substructures. Hierarchical clustering only requires a measure of similarity between groups of data points. Maximal Common Substructure Search (MCS) is the process of finding the largest structure that is a substructure or part of all the molecules in a given set. Initial structures are found at the bottom of the hierarchy. The next level contains the maximum common structures of clusters of initial molecules; subsequent levels provide larger clusters of smaller common substructures.

Minimal MCS size refers to the smallest size of the maximum common substructure searched for by the algorithm. For different datasets different values were considered owing to

the number of top level clusters found and the level count. For AID 504332 and 540317, minimal MCS size was taken 9 and for AID 504339 and 2147 it was 10 and 11 respectively. After the clusters were formed using LibMCS, we got the molecular scaffolds in the form of sdf and SMILES file. The active and inactive 3D structure files were then used to search the similar substructures with the smiles generated. This was done using the jcsearch algorithm of ChemAxon [30]. The similarity is calculated on the basis of the molecular descriptor or fingerprint of the chemical structures to compare. The Substructures were evaluated for enrichment using chi-square test. The p-values were computed to evaluate the significance of enrichment. The substructures which had at least 1% matches among the active dataset entries, p-value less than 0.01 and enrichment factor more than 5 were considered significant.

Results

The datasets obtained from PubChem were processed to generate 2D molecular descriptors using PowerMV. The descriptors were finally culled to 155 from 179 descriptors after removing values which were either null or the same for the entire dataset and could not contribute to the classification (S1 Table). The complete data after splitting into train and test sets was loaded in Weka-3.6 to build different classifier models for the evaluation of compounds. Initially standard classification of the data was performed. However, since the datasets were skewed, cost sensitive classification was introduced. The misclassification cost was applied on false negatives and incremented until the rate of false positives reached 20%. The costs applied in different datasets for different models are shown in Table 1. Naive bayes used minimum cost for the classification of the objects.

Evaluation of models included various statistical parameters. The accuracy of Random forest was predicted to be the highest for all the datasets. A comparison between the sensitivity of both the classification models amongst different datasets was made depicting the sensitivity of Random forest more than the Naive Bayes in all cases. Recent studies on comparison of classifiers performance have reported that Random forest outperforms Naïve bayes in terms of accuracy of prediction [31]. Random forest uses multiple decision trees to place an instance into a particular class and the output is the average of the individual trees output whereas Naïve bayes is a probabilistic approach which calculates the probability of a compound being in a particular class on the basis of presence of certain independent features [32]. It has also been shown that the assembly of trees gives much accurate prediction than single one [33]. Our group has also previously shown that the Random forest has outperformed Naïve bayes in similar cheminformatics analyses [16–19] on bioassay datasets. Fig 1 shows the plot between sensitivity of Naive Bayes and Random Forest amongst AID 504332, 504339, 2147 and 540317. Similarly the specificity was compared where Naive Bayes outperforms in AID 504339 and 2147. In case of AID 540317 specificity of both was comparable and Random Forest showed higher specificity in AID 504332. Fig 2 is the comparative graph between the specificity of both classification models amongst all four datasets.

Table 1. Misclassification costs used for False Negatives (FN).

PubChem Assay ID	*Naive Bayes*	*Random Forest*
AID 504332	2	50
AID 504339	10	1000
AID 2147	45	3000
AID 540317	30	25000

doi:10.1371/journal.pone.0083032.t001

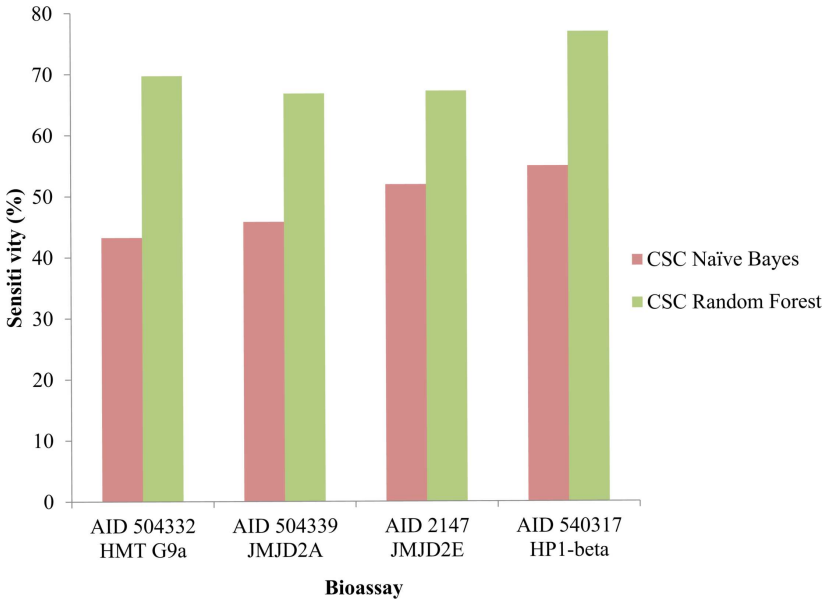


Fig 1. Graph between sensitivity of Naive Bayes and Random Forest amongst AID 504332, 504339, 2147 and 540317.

doi:10.1371/journal.pone.0083032.g001

The sensitivity and specificity were used to calculate the balanced classification rate for each model. Random forest showed the most balanced classification out of both. As a measure of quality, Matthews's correlation coefficient (MCC) was calculated. The Matthews correlation coefficient (MCC) also known as the phi coefficient is a measure of correlation between the actual and predicted classifications. Table 2 shows the classification results of all the datasets along with the statistical evaluation. The summary of the parameters are summarised in Table 3.

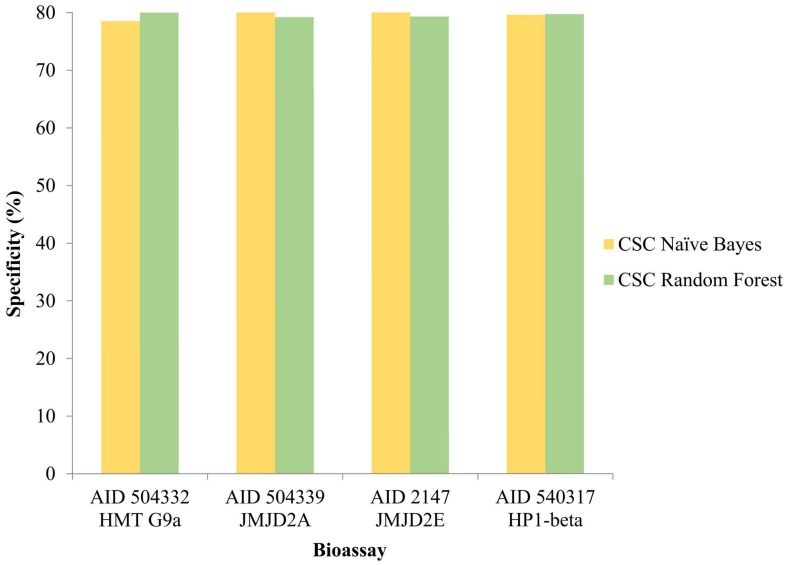


Fig 2. Comparative graph between the specificity of both classification models amongst all four datasets.

doi:10.1371/journal.pone.0083032.g002

Table 2. Overall summary of the performance of the models.

PubChem Assay ID	Classifer	TP Rate	FP Rate	ROC	Accuracy	MCC	BCR
AID 504332	CSCNB	43.2	21.5	66.5	74.84	0.15	60.89
	CSCRF	69.7	19.5	82.1	79.39	0.35	75.11
AID 504339	CSCNB	45.8	19.6	68.5	79.43	0.10	63.08
	CSCRF	66.8	20.8	79.4	78.88	0.17	72.99
AID 2147	CSCNB	51.9	20.0	72.4	79.58	0.09	65.97
	CSCRF	67.2	20.7	80.1	79.12	0.14	73.24
AID 540317	CSCNB	54.9	20.4	74.2	79.45	0.06	67.25
	CSCRF	76.9	20.3	85.8	79.67	0.10	78.28

doi:10.1371/journal.pone.0083032.t002

A perfect test would have 100% sensitivity and specificity, but in realistic scenarios, however this is seldom achieved and a balance between sensitivity and specificity is desirable. For that, a relation of sensitivity and specificity on a graph, called a "Receiver-Operator-Characteristic (ROC) curve" was plotted. Fig 3 summarises the ROC plot for Random Forest classification model for the four datasets. The Area under the curve for the ROC-plots was 0.82, 0.68, 0.80 and 0.67 for the AID 504332, AID 504339, AID 2147 and AID 540317 respectively.

Evaluation of significantly enriched scaffolds

In the process of drug discovery the local similarity between the structures proved to be useful in designing of new chemical compounds as potential drugs. We used JChem module, LibMCS and clustered the active compounds of all the datasets. In the present study, we have also evaluated enriched substructures, rather than substructures which are exclusive for the actives. Conceptually this would mean that the feature/substructure in consideration alone would not have necessary predictive ability to define activity, but rather has a larger probability to be found among the actives. It is believed that the compounds having similar structures often have similar properties and biological activities [34].Our analysis shows a subset of the substructures are significantly enriched in the actives compared to inactives by a few folds. The presence of the feature/substructure alone would not have necessary predictive ability to define activity, but rather has a larger probability to be found among the actives.

Clustering analysis of AID 504332

The 30875 active compounds clustered into a total of 5,150 clusters of which the 726 top level cluster compounds were considered. The compounds were clustered upto level 6 out of which 258 singletons were removed. The enrichment and its significance, was analyzed by chi-square test. Analysis revealed 19 significantly enriched scaffolds which had p-value less than 0.01 and an enrichment factor > 5.

Table 3. Shows the details of the LibMCS cluster report for different data sets studied.

LibMCS parameters	AID 504332	AID 504339	AID 2147	AID 540317
MCS size	9	10	11	9
Level Count	6	6	5	6
Top level cluster count	726	1026	702	216
Total Cluster Count	5150	7113	3791	1437
Singletons	258	416	365	93
Significant substructures	19	9	9	8

doi:10.1371/journal.pone.0083032.t003

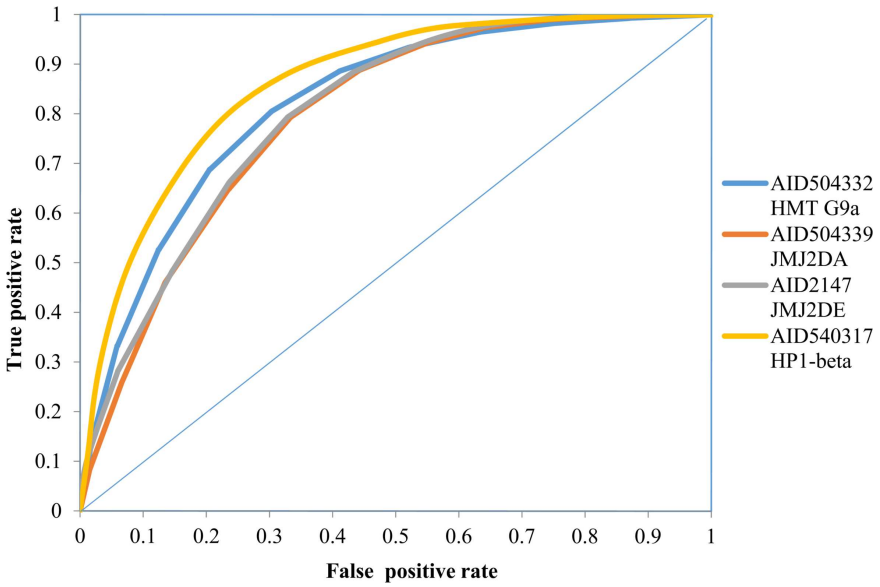


Fig 3. ROC plot for Random Forest classification model for the four datasets.

doi:10.1371/journal.pone.0083032.g003

Clustering analysis of AID 504339

A total of 16919 active compounds were clustered upto 6 levels at MCS size 10. 416 singletons were removed and 1026 compounds obtained at top level were taken for further analysis. We obtained 9 substructures prioritized by p-value (less than 0.01) and enrichment factor > 5.

Clustering analysis of AID 2147

The 3523 compounds were clustered keeping MCS size as 11, we obtained 3791 total clusters. A total of 702 compounds were obtained at level 5 out of which 365 singletons were removed. The final prioritization was done keeping p value less than 0.01 and enrichment factor > 5, the analysis resulted in 9 substructures.

Clustering analysis of AID 540317

The 2142 active compounds were clustered upto 6 levels keeping MCS size as 9. We obtained 216 compounds at top level after removing 93 singletons. Analysis revealed 8 significantly enriched scaffolds which had p-value less than 0.01 and an enrichment factor > 5.

The results for the clustering approach used and the enriched scaffold for each of the datasets considered have been summarised in tables (S2–S5 Tables).

Discussion

Understanding the function and regulation of epigenetic modifier proteins have been recently an actively pursued area of research [35]. This has been more so, with the increasingly understood mechanisms of epigenetic regulation in the pathophysiology of a number of diseases. The role of epigenetic modifiers has been extensively studied in a variety of neoplasms [36, 37, 38, 39, 40]. It has also been discussed that molecules that could target epigenetic modifiers could be a potential new avenue for drug development [41]. In fact, targeting epigenetic modifiers as potential drug targets have been extensively discussed and pursued [42, 43]. The cornerstone of any rational drug discovery process starts from systematic screening of molecular

libraries against target proteins, and assaying them for their biological outputs or phenotypes. Testing large libraries of molecules for specific biological activities are usually time consuming and extremely costly. Computational methods for pre-selecting molecules from large libraries would offer a plausible time and cost-effective alternative [41]. It has been suggested that accurate methodologies to pre-select molecules for in-depth biological assays would accelerate the process of drug discovery. A number of methodologies including molecular docking [44, 45] and other cheminformatics methods [46, 47, 48] have been extensively used to prioritise molecules in drug discovery process. Machine learning approaches have been used extensively now for building predictive models for pre-selecting molecules form large molecular databases [16–19]. The availability of datasets of high-throughput screens on large molecular libraries of small molecules which are quite diverse offers an enormous opportunity to learn molecular and structural properties of molecules and their association or correlation with phenotypic or biological outcomes.

The present manuscript discusses how computational methods could be used to mine potential actives based on chemical descriptors. We propose a computational pre-screening would improve the chance of finding an active from a given dataset, which could potentially imply savings in cost and resources. In real-life situations, chemists synthesize molecules based on scaffolds which are largely associated with activity. We have additionally used a substructure enrichment analysis to understand substructures which are largely associated with activity, nevertheless does not imply activity. This would allow chemists to suitably modify molecules or be able to synthesize molecules of a particular variety or based on a particular scaffold, so as to potentially improve the hit rate. We do find a significant large number, albeit a significant small number by proportion due to the very fact that there are a far higher number of molecules in the inactive set compared to that of actives.

We show that machine learning based approaches can provide computational models which are highly accurate which could be potentially used to screen large molecular libraries. The study is not without caveats, the first being the paucity of data sets in public domain encompassing inhibitors for a large number of epigenetic modifiers precludes us from creating a comprehensive suite of predictive models, which could be eventually possible with more data sets being available in public domain. In the future, many such computational models could be integrated to provide for desirable set of properties or biological activities and has the potential to be integrated into drug discovery pipelines, with significant gains in the cost and timespan associated with a conventional drug discovery process [49]. The present study also provides the first comprehensive overview and cheminformatics analysis of small molecule modulators of epigenetic modifiers.

Supporting Information

S1 Table. List of the molecular descriptors used from PowerMV.
(DOCX)

S2 Table. Depicts significantly enriched scaffolds found in AID 504332.
(DOCX)

S3 Table. Shows the significant substructures found in AID 504339 along with their p-value and chi-square statistics.
(DOCX)

S4 Table. Shows the enriched substructures in AID 2147 with a threshold of 5 for enrichment factor and p-value less than 0.01.
(DOCX)

S5 Table. Shows significantly enriched substructures in AID 540317.
(DOCX)

Acknowledgments

The authors thank Dr. Chetana Sachidanandan and Dr. Shantanu Sengupta for reviewing the manuscript. The authors are also thankful for discussions with members of the Open Source Drug Discovery (OSDD) Programme. SJ acknowledges a Project Fellowship from CSIR-OSDD. The authors acknowledge the support from National Knowledge Network (NKN) and CDAC-Garuda for computing. The authors acknowledge technical help and support from the CDAC-Garuda team, especially Ms. Janaki Chintalapati, Ms. Mangala N and Dr. Subrata Chattopadhyay.

Author Contributions

Conceived and designed the experiments: SJ VS.

Performed the experiments: SA SJ.

Analyzed the data: SA SJ.

Contributed reagents/materials/analysis tools: VS.

Wrote the paper: SA SJ VS.

References

1. Alberts B, Johnson A, Lewis J (2002) The Molecular Genetic Mechanisms That Create Specialized Cell Types. Molecular Biology of the Cell. 4th edition. New York: Garland Science.
2. Blake WJ (2003) Noise in eukaryotic gene expression. Nature 422: 633–637. PMID: 12687005
3. Miller-Jensen K (2011) Varying virulence: epigenetic control of expression noise and disease processes. Trends in Biotechnol. 29: 517–525.
4. Bird A (2007) Perceptions of epigenetics. Nature 447 (7143): 396–8. PMID: 17522671
5. Momparler RL (2003) Cancer epigenetics. Oncogene 22: 6479–6483. PMID: 14528271
6. Graff J, Kim D, Dobbin MM, Tsai LH (2011) Epigenetic Regulation of Gene Expression in Physiological and Pathological Brain Processes. Physiol Rev. 2011 91(2): 603–49. doi: 10.1152/physrev.00012.2010 PMID: 21527733
7. Volkmar M, Dedeurwaerder S, Cunha DA, Ndlovu MN, Defrance M, et al. (2012) DNA methylation profiling identifies epigenetic dysregulation in pancreatic islets from type 2 diabetic patients. EMBO J. 31 (6): 1405–26. doi: 10.1038/emboj.2011.503 PMID: 22293752
8. Handy DE, Castro R, Loscalzo J (2011) Epigenetic modifications: basic mechanisms and role in cardiovascular disease. Circulation. 123(19): 2145–56. doi: 10.1161/CIRCULATIONAHA.110.956839 PMID: 21576679
9. Bird A (2002) DNA methylation patterns and epigenetic memory. Genes and Dev. 16: 6–21. PMID: 11782440
10. Sati S, Ghosh S, Jain V, Scaria V, Sengupta S (2012) Genome-wide analysis reveals distinct patterns of epigenetic features in long non-coding RNA loci. Nucleic Acids Research 40(20): 10018–31. doi: 10.1093/nar/gks776 PMID: 22923516
11. Wang XQ, Crutchley JL, Dostie J (2011) Shaping the Genome with Non-Coding RNAs. Curr Genomics 12(5): 307–321. doi: 10.2174/138920211796429772 PMID: 21874119
12. Aiese CR, Sanseverino W, Cremona G, et al. (2013) Genome-wide analysis of histone modifiers in tomato: gaining an insight into their developmental roles. BMC Genomics 14:57. doi: 10.1186/1471-2164-14-57 PMID: 23356725
13. Arrowsmith CH, Bountra C, Fish PV, Lee K, Schapira M (2012) Epigenetic protein families: a new frontier for drug discovery. Nature Reviews Drug Discovery 11: 384–400. doi: 10.1038/nrd3674 PMID: 22498752

14. Quinn AM, Simeonov A (2011) Methods for Activity Analysis of the Proteins that Regulate Histone Methylation. Current Chemical Genomics 5: 95–105. doi: 10.2174/1875397301005010095 PMID: 21966349
15. Falk H, Connor T, Yang H, Loft KJ, Alcindor JL, et al. (2011) An efficient high-throughput screening method for MYST family acetyltransferases, a new class of epigenetic drug targets. J Biomol Screen. 16(10): 1196–205. doi: 10.1177/1087057111421631 PMID: 22086725
16. Periwal V, Rajappan JK, Jaleel AU, Scaria V (2011) Predictive models for antitubercular molecules using machine learning on high-throughput biological screening datasets. BMC Res Notes 4: 504. doi: 10.1186/1756-0500-4-504 PMID: 22099929
17. Periwal V, Kishtapuram S, Scaria V (2012) Computational models for in-vitro antitubercular activity of molecules based on high-throughput chemical biology screening datasets. *BMC Pharmacol*. 12:1. doi: 10.1186/1471-2210-12-1 PMID: 22463123
18. Jamal S, Periwal V, Consortium O, Scaria V (2012) Computational analysis and predictive modeling of small molecule modulators of microRNA. J Cheminform. 4:16. doi: 10.1186/1758-2946-4-16 PMID: 22889302
19. Jamal S, Periwal V, Open Source Drug Discovery Consortium, Scaria V (2013) Predictive modeling of antimalarial molecules inhibiting apicoplast formation. BMC Bioinformatics 14(1):55.
20. Shinkai Y, Tachibana M (2011) H3K9 methyltransferase G9a and the related molecule GLP. Genes & Dev. 25:781–788.
21. Tachibana M, Sugimoto K, Nozaki M, Ueda J, Ohta T, et al. (2002) G9a histone methyltransferase plays a dominant role in euchromatic histone H3 lysine 9 methylation and is essential for early embryogenesis. Genes & Dev. 16:1779–1791.
22. Kondo Y, Shen L, Ahmed S, Boumber Y, Sekido Y. Downregulation of Histone H3 Lysine 9 Methyltransferase G9a Induces Centrosome Disruption and Chromosome Instability in Cancer Cells. PLoS ONE. 3(4): e2037. doi: 10.1371/journal.pone.0002037 PMID: 18446223
23. Ozboyaci M, Gursoy A, Erman B, Keskin O (2011) Molecular Recognition of H3/H4 Histone Tails by the Tudor Domains of JMJD2A: A Comparative Molecular Dynamics Simulations Study. PLoS ONE 6(3): e14765. doi: 10.1371/journal.pone.0014765 PMID: 21464980
24. Cloos PA, Christensen J, Agger K, Helin K (2008) Erasing the methyl mark: histone demethylases at the center of cellular differentiation and disease. Genes Dev. 22:1115–1140. doi: 10.1101/gad.1652908 PMID: 18451103
25. Vermeulen M, Timmers HT (2010) Grasping trimethylation of histone H3 at lysine 4. Epigenomics 2 (3):395–406. doi: 10.2217/epi.10.11 PMID: 22121900
26. Musselman CA, Lalonde ME, Cote J, Kutateladze TG (2012) Perceiving the epigenetic landscape through histone readers. Nat Struct Mol Biol. 19(12):1218–27. doi: 10.1038/nsmb.2436 PMID: 23211769
27. Liu K, Feng J, Young SS (2005) PowerMV: a software environment for molecular viewing, descriptor generation, data analysis and hit evaluation. J Chem Inf Model 45:515–522. PMID: 15807517
28. Bouckaert RR, Frank E, Hall MA, Holmes G, Pfahringer B, et al. (2010) Weka -Experiences with a Java Open-Source Project. Journal of Machine Learning Research 2533–2541.
29. Budapest H. Chemaxon: Library MCS, version 0.7; 2008.
30. Budapest H. Chemaxon: Jcsearch, version 5.8.2.
31. Caruana R, Niculescu-Mizil A (2006) An empirical comparison of supervised learning algorithm. In Proceedings of the 23rd International Conference on Machine Learning, Pittsburg, PA. ACM: New York.
32. Bin C, Robert PS, Viktor H, Johannes HV (2012) Comparison of Random Forest and Pipeline Pilot Naive Bayes in Prospective QSAR Predictions. J. Chem. Inf. Model 52, 792–803. doi: 10.1021/ci200615h PMID: 22360769
33. Svetnick V, Wang T, Tong C, Liaw A, Sheridan RP (2005) Boosting: an ensemble learning tool for compound classification and QSAR modeling. J. Chem. Inf. Model 45, 786–799. PMID: 15921468
34. Johnson M, Maggiora G (1990) Concepts and Applications of Molecular Similarity. New York: Wiley.
35. Piekarz RL, Bates SE (2009) Epigenetic Modifiers: Basic Understanding and Clinical Development. Clin Cancer Res. 15:3918–26. doi: 10.1158/1078-0432.CCR-08-2788 PMID: 19509169
36. Shu XS, Geng H, Li L, Ying J, Ma C, et al. (2011) The epigenetic modifier PRDM5 functions as a tumor suppressor through modulating WNT/β-catenin signaling and is frequently silenced in multiple tumors. PLoS One. 6(11):e27346. doi: 10.1371/journal.pone.0027346 PMID: 22087297
37. Kaneda A, Feinberg AP (2005) Loss of imprinting of IGF2: a common epigenetic modifier of intestinal tumor risk. Cancer Res. 65(24):11236–40. PMID: 16357124

38. Mund C, Lyko F (2010) Epigenetic cancer therapy: Proof of concept and remaining challenges. Bioessays 32(11): 949–57. doi: 10.1002/bies.201000061 PMID: 21154865

39. Vlerken LE, Kiefer CM, Morehouse C, Li Y, Groves C (2013) EZH2 is required for breast and pancreatic cancer stem cell maintenance and can be used as a functional cancer stem cell reporter. Stem Cells Transl Med. 2(1):43–52. doi: 10.5966/sctm.2012-0036 PMID: 23283488

40. Leong HS, Chen K, Hu Y, Lee S, Blewitt ME (2013) Epigenetic regulator Smchd1 functions as a tumor suppressor. Cancer Res. 73(5):1591–9. doi: 10.1158/0008-5472.CAN-12-3019 PMID: 23269277

41. Unoki M (2011) Current and potential anticancer drugs targeting members of the UHRF1 complex including epigenetic modifiers. Recent Pat Anticancer Drug Discov. 6(1):116. PMID: 21110828

42. Xu J, Hagler A (2002) Chemoinformatics and Drug Discovery. Molecules 7:566–600.

43. Kumar N, Hendriks BS, Janes KA, de Graaf D, Lauffenburger DA (2006) Applying Computational modeling to drug discovery and development. Drug Discov Today. 11(17–18): 806–11. PMID: 16935748

44. Huang SY, Zou X (2010) Advances and challenges in protein-ligand docking. Int J Mol Sci. 11 (8):3016–34. doi: 10.3390/ijms11083016 PMID: 21152288

45. Diller DJ, Merz KM Jr (2001) High throughput docking for library design and library prioritization. Proteins 43(2):113–24. PMID: 11276081

46. Lv S, Xu Y, Wang Q, Li X, Su B (2012) Prioritizing cancer therapeutic small molecules by integrating multiple OMICS datasets. OMICS. 16(10):552–9. doi: 10.1089/omi.2012.0005 PMID: 22917481

47. Rabinowitz JR, Goldsmith MR, Little SB, Pasquinelli MA (2008) Computational molecular modeling for evaluating the toxicity of environmental chemicals: prioritizing bioassay requirements. Environ Health Perspect. 116(5):573–7. doi: 10.1289/ehp.11077 PMID: 18470285

48. Sean E, Binghe W (2006) Computer Applications in Pharmaceutical Research and Development. Wiley Series in Drug Discovery and Development. 1st Edition.

49. Ekins S, Freundlich JS (2013) Computational Models for Tuberculosis Drug Discovery. Methods Mol Biol. 993: 245–62. doi: 10.1007/978-1-62703-342-8_16 PMID: 23568475

International Journal of Electrical Electronics Computers & Mechanical Engineering (IJEECM)
ISSN: 2278-2808
www.ijeecm.org Volume 3 Issue8 ǁ Aug. 2016

IJEECM journal of Mechanical Engineering (ijeecm-jme)

Contact Pressure Analysis of Spur Gear using FEA

T.Veera Pratap Reddy [1], J.Govardhan [2]
[1,2] *Mechanical Engineering Department,*
[1,2] AVN Institute of Engineering and Technology, Koheda Road, Ibrahimpatnam, Ranga Reddy Dist., T.S(India)

***Abstract*— This paper is Gear is one of the most critical components in a mechanical power transmission system, and most industrial rotating machinery. Spur gear has teeth cut in parallel to each other and imposes radial loads on shafts. Contact stresses are one of the factors which effects performance of gears transmission.**

This project work made an attempt to summarize about contact stresses developed in a mating spur gear which has involute teeth. A pair of spur gears are taken from a lathe gear box and proceeded forward to calculate contact stresses on their teeth. Contact failure in gears is currently predicted by comparing the calculated Hertz contact stress to experimentally determined allowable values for the given material. The method of calculating gear contact stress by Hertz's equation originally derived for contact between two cylinders. Analytically these contact stresses are calculated for different module, and these results are compared with the results obtained in modeling analysis in ANSYS. As there involves many iterations in calculating contact stresses analytically a simplified approach is made in VISUAL BASIC for different parameters like module, power, speed. Etc.

A model of mating spur gears is generated in PRO/ENGINEER and this model is imported to ANSYS 14.5 Package. The imported model is analyzed in ANSYS workbench for calculating contact pressure for different module of spur gear. These results are compared with analytical results and thus conclusions are made on observing the results. A result advises that with increase in module, Contact Pressure decreases for a pair of spur gears. Results help us to give better performance and future scope in the power transmission field.

Keywords: **Spur gear, Contact stress, Involute, Pro/Engineer, ANSYS 14.5.**

I. INTRODUCTION

A gear is a rotating machine part having cut teeth, or cogs, which mesh with another toothed part in order to transmit torque. Two or more gears working in tandem are called a transmission and can produce a mechanical advantage through a gear ratio and thus may be considered a simple machine. Geared devices can change the speed, magnitude, and direction of a power source. The most common situation is for a gear to mesh with another gear, however a gear can also mesh a non-rotating toothed part, called a rack, thereby producing translation instead of rotation[3].

The cut teeth are also called 'cogs'. Gears are one of the most important parts of any machine or a mechanism [4].Some of the sectors in which gears play a vital role are:

- Turbine plant
- Hot and Cold Rolling
- Construction machinery
- Elevator industry

GEAR TOOTH TERMINOLOGY

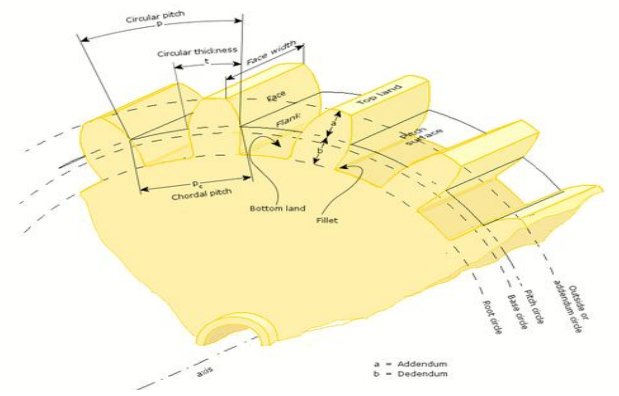


Figure1 Standard system of Gear Teeth

In a gear drive, two types of curves, the cycloidal and the involute, are generally used. In a gear drive, the shape of the tooth depends upon the pressure angle. Gears of involute profile with 14.5°, 20° full-depth and 20° stub pressure angles are most commonly used in industries. A 20° pressure angle full-depth involute gear tooth has various advantages over the other pressure angles. BIS has recommended the use of 20° pressure angle full depth involute gear tooth.[4]

Pitch point: The point of tangency of the pitch circles of a pair of mating gears. [2]
Common tangent: The line tangent to the pitch circle at the pitch point. [2]
Line of action: A line normal to a pair of mating tooth profiles at their point of contact. [2]

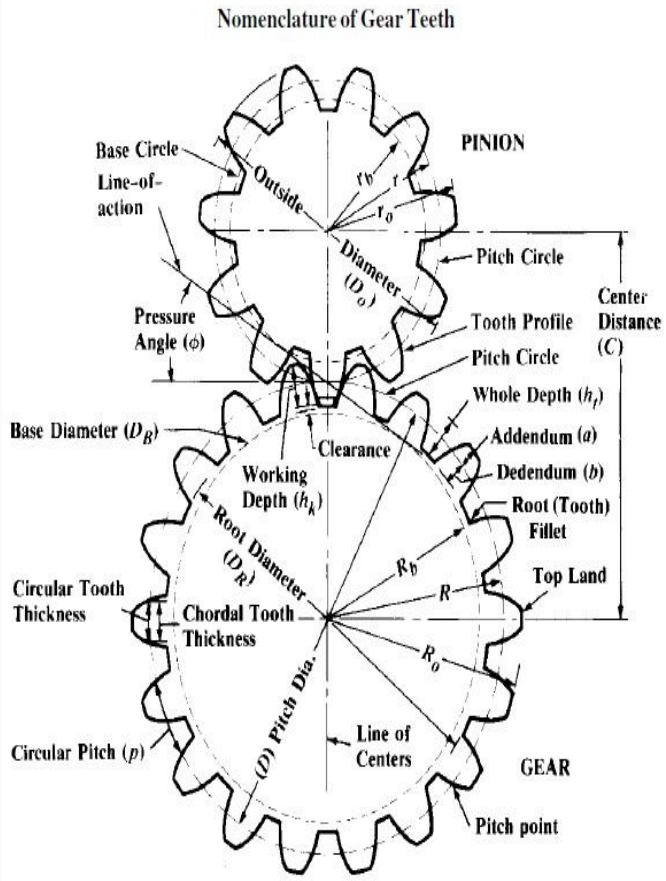


Figure2 Nomenclature of Gear Teeth

Path of contact: The path traced by the contact point of a pair of tooth profiles. The angle between the common normal at the point of tooth contact and the common tangent to the pitch circles. Pressure angle is also the angle between the line of action and the common tangent.[2]

Crowning:
Grinding of tooth edges to prevent edge loading is known as crowning.[2]



Figure3Spur Gear

INTRODUCTION TO SPUR GEARS

Spur gears are the most common type of gears. They have straight teeth, and are mounted on parallel shafts. Sometimes, many spur gears are used at once to create very large gear reductions.[7]

Spur gears are the simplest form of Gears available. They are also the most commonly used gears in the market. Spur Gears are found generally in the form of a cylinder or disk. These gears are applied for varying the force and speed of a rotating axle. These gears have a straight teeth.[7]

Conjugate action

Mating gear teeth against each other to produce rotary motion are similar to cams. When the tooth profiles are designed so as to produce a constant angular-velocity ratio during meshing, they are said to have conjugate action. A geometric relationship can be derived for the form of tooth profiles to provide conjugate action which is summarized as Law of Gearing as follows: "A common normal to the tooth profiles at their point of contact must, in all positions of the contacting teeth, pass through a fixed point on the line-of-centers called the pitch point. Any two curves or profiles engaging each other and satisfying the law of gearing are Conjugate curves.[9]

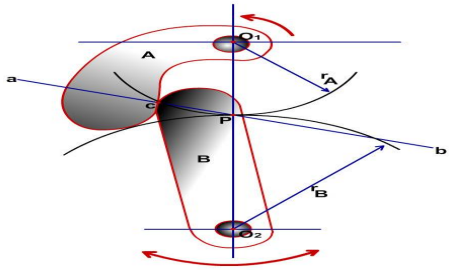


Figure4 conjugate Curves

When one curved surface pushes against another, the point of contact occurs where the two surfaces are tangent to each other (point c), and the forces at any instant are directed along the common normal ab to the two curves. [9]

TOOTH PROFILE

CYCLOIDAL:

The cycloid gear profile is a form of toothed gear used in mechanical clocks. The gear tooth profile is based on the epicycloids and hypocycloid curves, which are the curves generated by a circle rolling around the outside and inside of another circle, respectively.[8]

An advantage of the cycloid teeth over the involutes one is that wear of Cycloid tooth is not as fast as with involutes tooth. For this reason, gears transmitting very large amount of power are sometimes cut with cycloid teeth. [8]

1. Since the cycloid teeth have wider flanks, therefore the cycloid gears are stronger than the involutes gears, for the same pitch. These are preferred for cast teeth. [8]
2. In cycloid gears, the contact takes place between a convex flank and concave surface, where as in involutes gears, the convex surface are in contact. This condition results in less wear in cycloid wear and however the difference in wear is negligible. [8]
3. The interference in cycloid gears does not occur at all. Though there advantages of cycloid gears they are outweighed by the greater simplicity and flexibility of the involutes gears.[8]

INVOLUTE

The involutes gear profile is the most normally used system for gearing. In an involutes gear, the profiles of the teeth are involutes of a circle. The involutes of a circle are the spiraling curve traced by the end of an imaginary taut string unwinding itself from that stationary circle called the base circle. In involutes gear design, contact between a pair of teeth occurs at a single instantaneous point. Rotation of the gears causes the location of this contact point to move across the respective tooth surfaces.[8]

MATERIALS OF SPUR GEARS

While coming to manufacturing materials for Spur gears[8] Different materials used for gear manufacturing are:

1. Steel
2. Nylon
3. Aluminum
4. Bronze
5. Cast iron
6. Phenolic
7. Bakelite
8. Plastics

SPUR GEAR DESIGN

Single spur gears usually have a ratio range between 1:1 and 1:6. Pitch line velocity can be up to 25 m/s. The spur gear shows an excellent operating efficiency that is between 98-99%. The pinion of the spur gear is always made from a harder material as compared to wheels. An ideal Spur Gear pair is the one that has the highest number of teeth that is totally consistent with factors in strength and wear [10]. Suitable number of teeth on Spur gear is a follows:

12 13 14 15 16 18 20 22 24 25 28 30 32 34 38 40 45 50 54 60 64 70 72 75 80 84 90 96 100 120 140 150 180 200 220 250 In the case of spur gears, design for Gears are made by taking into account the specific velocity ratio and the distance between central shafts which is represented by the following equations, the distance calculated between the center of two shafts is given by:

$$x=(d1+d2)/2 \quad [10]$$

The speed or velocity ratio is calculated by:

N1/N2=d2/d1=T2/T1

Where,

X = the distance between the center of the two shafts

N1 = the speed of the driver

T1 = Number of teeth found on the driver

d1 = Driver's Pitch circle diameter

N2 = Speed of the follower

T2 = Number of teeth of the follower

d2 = Pitch circle diameter of the follower

Pc = Circular pitch

From the above equations, calculations of d1 and d2 (or T1 and T2) and circular pitch (Pc) are made. It is to be noted here that, the values obtained of T1 and T2, can be a whole number or sometimes may not be whole number. But in gear design, as the number of teeth is invariably a whole number, there is a need to for a slight change in the values of x, d1, and d2. This is to ensure that the number of teeth in the gear design always comes as a complete number.[10]

ADVANTAGES OF PRO/ENGINEER

- It is much faster and more accurate. Once a design is completed. 2D and 3D views are readily obtainable.
- The ability to incorporate changes in the design process is possible.
- It provides a very accurate representation of model specifying all other dimensions hidden geometry etc.
- It provides a greater flexibility for change. For example if we like to change the dimensions of our model, all the related dimensions in design assembly, manufacturing etc. will automatically change.
- It provides clear 3D models, which are easy to visualize and understand.
- Pro/E provides easy assembly of the individual parts or models created it also decreases the time required for the assembly to a large extent.

3D MOULDING

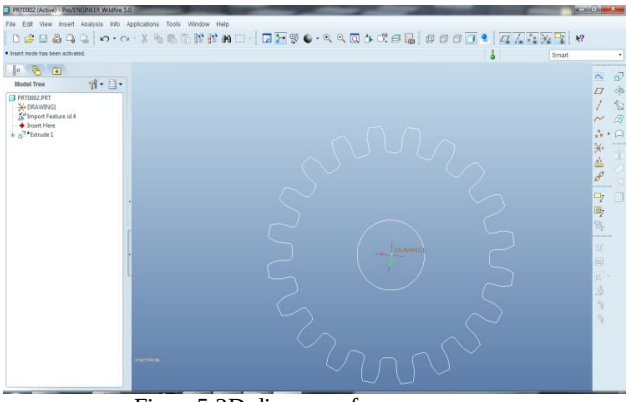


Figure5 2D diagram of super gear

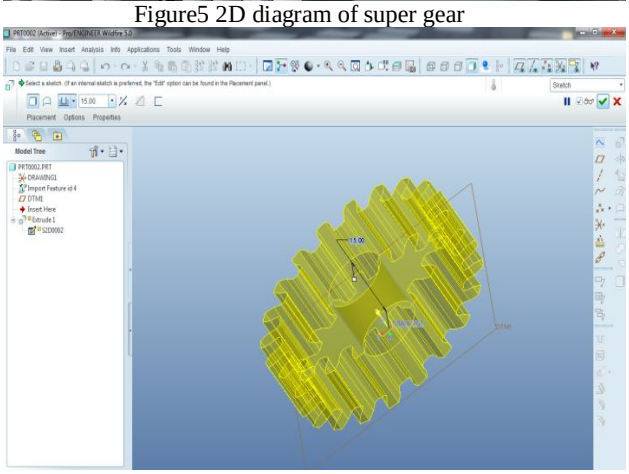


Figure6 Extrude the spur gear

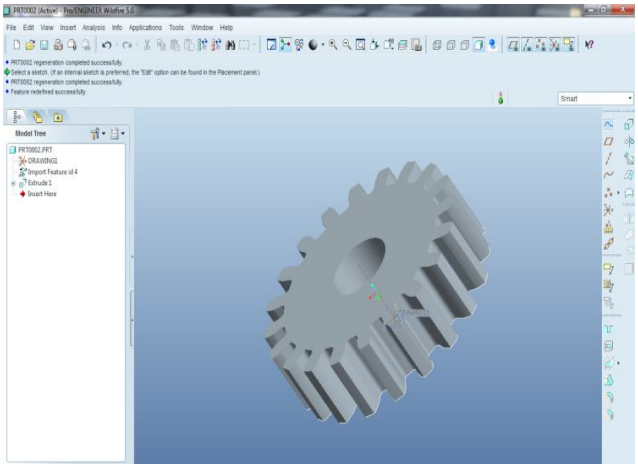


Figure7 3D Moulding

2D DESIGN

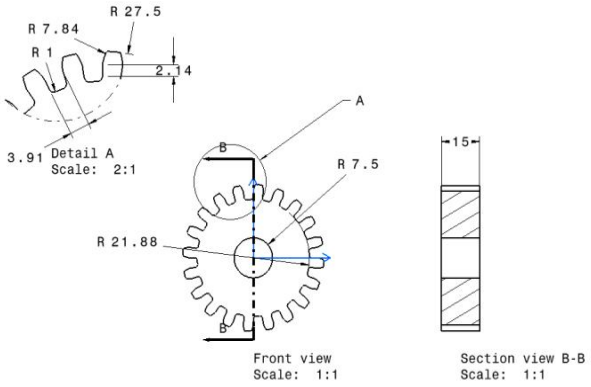


Figure8 2D DESIGN

INTRODUCTION TO FEA

The Basic concept in FEA is that the body or structure may be divided into smaller elements of finite dimensions called “Finite Elements”. The original body or the structure is then considered as an assemblage of these elements connected at a finite number of joints called “Nodes” or “Nodal Points”. Simple functions are chosen to approximate the displacements over each finite element. Such assumed functions are called “shape functions”. This will represent the displacement within the element in terms of the displacement at the nodes of the element.[5]

Nowadays, even the most simple of products rely on the finite element method for design evaluation. This is because contemporary design problems usually cannot be solved as accurately & cheaply using any other method that is currently available. Physical testing was the norm in the years gone by, but now it is simply too expensive and time consuming also.[5]

TYPES OF ENGINEERING ANALYSIS

Structural Analysis

It consists of linear and non-linear models. Linear models use simple parameters and assume that the material is not plastically deformed. Non-linear models consist of stressing the material past its elastic capabilities. The stresses in the material then vary with the amount of deformation as in. [6]

Vibrational Analysis

It is used to test a material against random vibrations, shock, and impact. Each of these incidences may act on the natural vibration frequency of the material which, in turn, may cause resonance and subsequent failure. [6]

FatigueAnalysis

It helps designers to predict the life of a material or structure by showing the effects of cyclic loading on the specimen. Such analysis can show the areas where crack propagation is most likely to occur. Failure due to fatigue may also show the damage tolerance of the material. [6]

Heat Transfer

It analysis models the conductivity or thermal fluid dynamics of the material or structure. This may consist of a steady-state or transient transfer. Steady-state transfer refers to constant thermo properties in the material that yield linear heat diffusion. [6]

RESULTS OF FINITE ELEMENT ANALYSIS

Preprocessing

The user constructs a model of the part to be analyzed in which the geometry is divided into a number of discrete sub regions, or elements," connected at discrete points called nodes." Certain of these nodes will have fixed displacements, and others will have prescribed loads. These models can be extremely time consuming to prepare, and commercial codes vie with one another to have the most user-friendly graphical “preprocessor" to assist in this rather tedious chore. Some of these preprocessors can overlay a mesh on a preexisting CAD file, so that finite element analysis can be done conveniently as part of the computerized drafting-and-design process.[5]

Postprocessing

In the earlier days of finite element analysis, the user would pore through reams of numbers generated by the code, listing displacements and stresses at discrete positions within the model. It is easy to miss important trends and hot spots this way, and modern codes use graphical displays to assist in visualizing the results. A typical postprocessor display overlays colored contours representing stress levels on the model, showing a full field picture similar to that of photo elastic or moiré experimental results.[5]

ANALYSIS RESULTS
A-36

Imported model in to Ansys

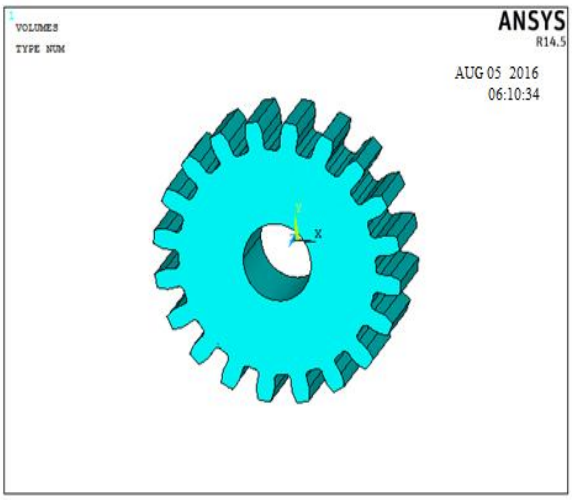


Figure9 Imported model in to Ansys

Element Type: solid 20 nodes 95

Material Properties:

Youngs Modulus (EX) : 200 GPA

Poisson's Ratio (PRXY): 0.26

Density : $7.85e^{-6}$

MESHEDMODEL

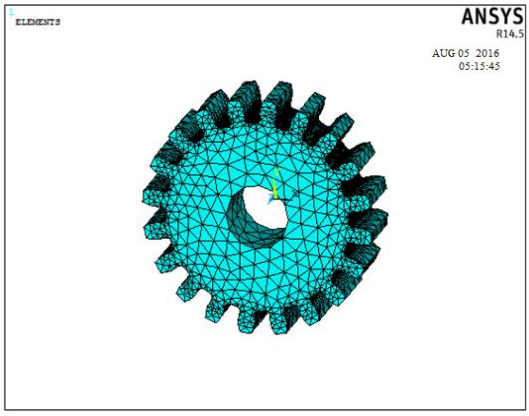


Figure10 Meshed Model

LoadsPressure – 20.325 MPA

Displacement

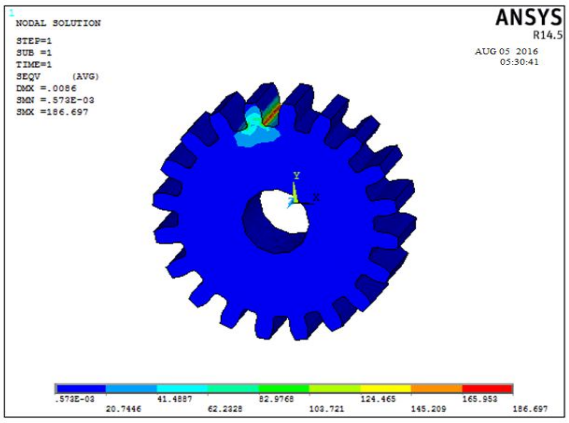


Figure11 Displacement

Solution

Solution – Solve – Current LS – ok

Post Processor

General Post Processor – Plot Results – Contour Plot - Nodal Solution – DOF Solution – Displacement Vector Sum

STRESS

General Post Processor – Plot Results – Contour Plot – Nodal Solution – Stress – Von Mises Stress

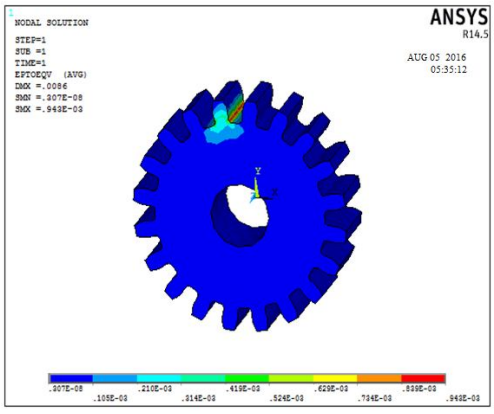


Figure12Stress

General Post Processor – Plot Results – Contour Plot – Nodal Solution –strain- totalVon Mises **strain**

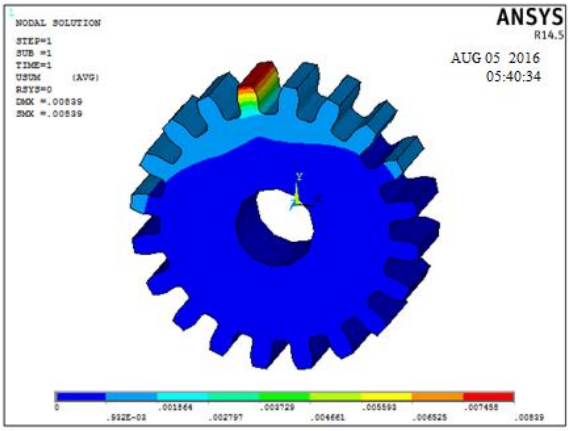


Figure13 Von Mises strain

ALUMINUM 514
MATERIAL PROPERTIES
Element Type: solid 20 nodes 95
Material Properties:
Youngs Modulus (EX) : 205 GPA
Poisson's Ratio (PRXY) : 0.29
Density : $7.85e^{-6}$
Load Pressure – 20.325 MPA
Displacement

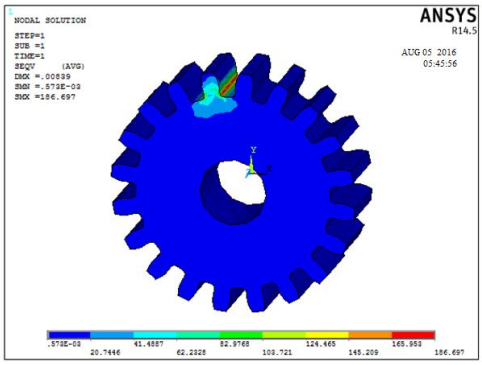


Figure14Displacement Solution

Solution – Solve – Current LS – ok
Post Processor
General Post Processor – Plot Results – Contour Plot - Nodal Solution – DOF Solution – Displacement Vector Sum

STRESS

General Post Processor – Plot Results – Contour Plot – Nodal Solution – Stress – Von Mises Stress

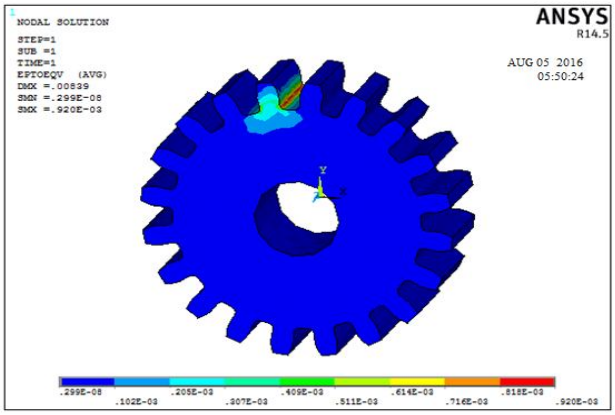


Figure15 Stress

STRAIN
General Post Processor – Plot Results – Contour Plot – Nodal Solution –strain- totalVon Mises **strain**

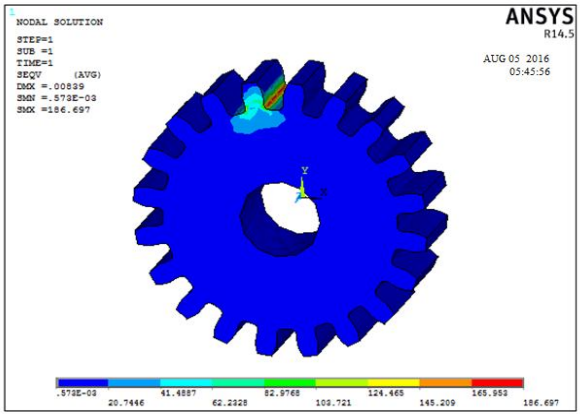


Figure16 Von Mises strain

ALLUMINIUM 4337
MATERIAL PROPERTIES
Element Type: solid 20 nodes 95
Material Properties:
Young's Modulus (EX) : 209 GPA
Poisson's Ratio (PRXY): 0.30
Density : $7.75e^{-6}$
Load :Pressure – 20.325 MPA

Displacement

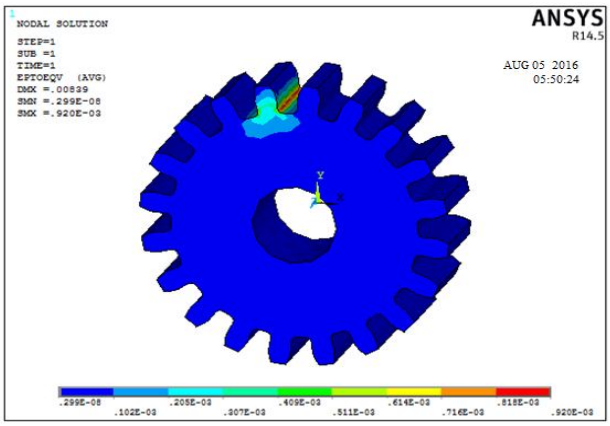


Figure17 Displacement

Solution
Solution – Solve – Current LS – ok
Post Processor
General Post Processor – Plot Results – Contour Plot - Nodal Solution – DOF Solution – Displacement Vector Sum

STRESS

General Post Processor – Plot Results – Contour Plot – Nodal Solution – Stress – Von Mises Stress

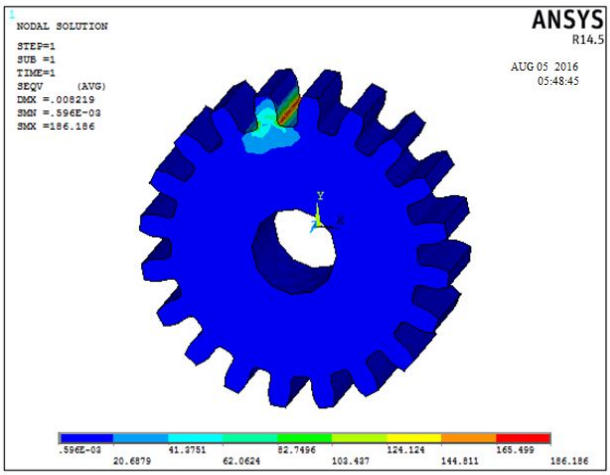


Figure18 Von Mises Stress

STRAIN

General Post Processor – Plot Results – Contour Plot – Nodal Solution –strain- totalVon Mises **strain**

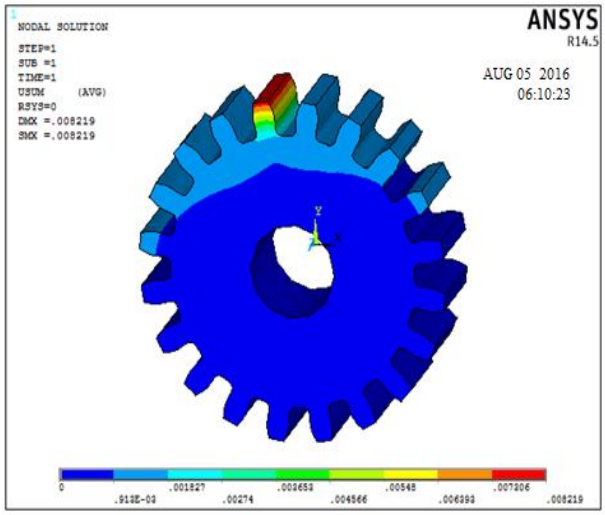


Figure19 Von Mises strain

TUNGSTEN CARBIDE

Imported model in to Ansys

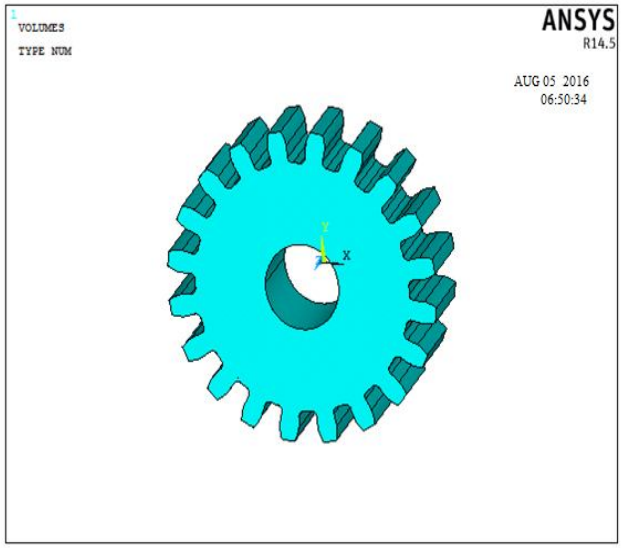


Figure20 Imported model in to Ansys

Element Type: solid 20 nodes 95
Material Properties:
Youngs Modulus (EX) : 572 GPA
Poisson's Ratio (PRXY): 0.23
Density : 7.75 e^{-6}

MESHED MODEL

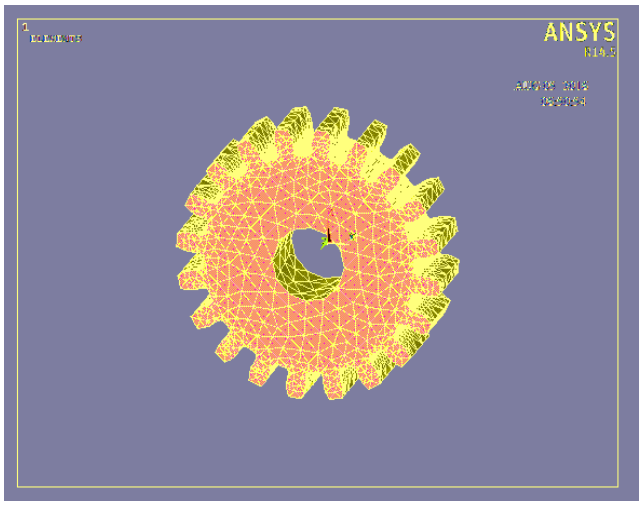


Figure21 Meshed Model

Load Pressure – 20.325 MPA

Displacement

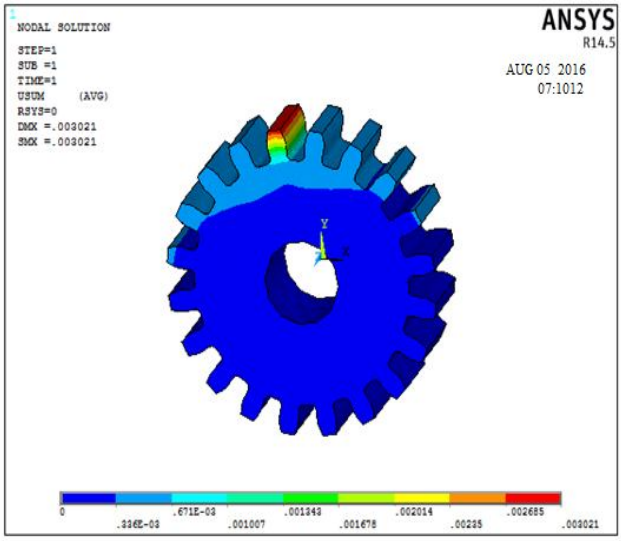


Figure22 Displacement

Solution

Solution – Solve – Current LS – ok

Post Processor

General Post Processor – Plot Results – Contour Plot - Nodal Solution – DOF Solution – Displacement Vector Sum

STRESS

General Post Processor – Plot Results – Contour Plot – Nodal Solution – Stress – Von Mises

Stress

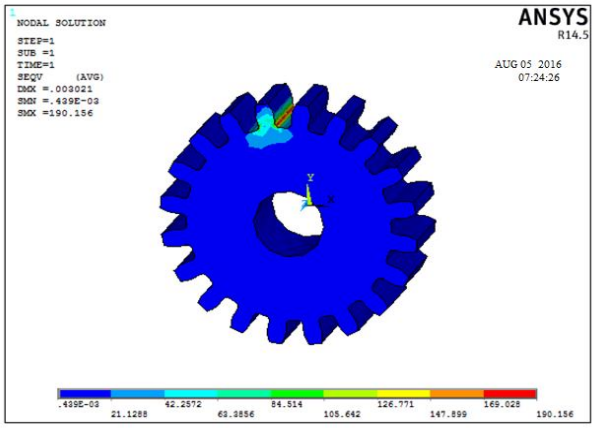


Figure23 Von Mises Stress

STRAIN

General Post Processor – Plot Results – Contour Plot – Nodal Solution –strain- totalvon Mises

strain

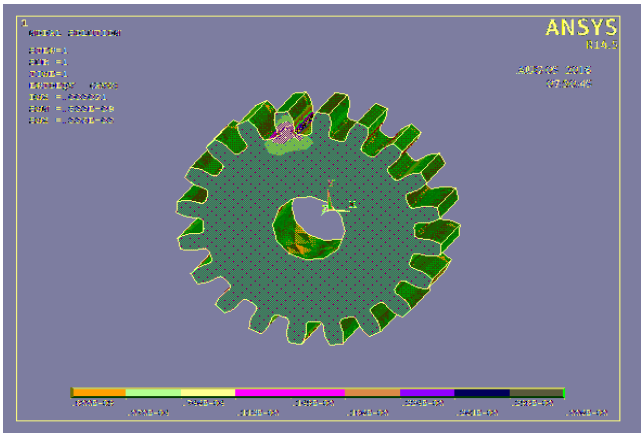


Figure24 Von Mises strain

RESULTS TABLES

Structural Analysis

NAME OF THE MATERIAL	DISPLACEMENT mm	STRESS N/mm^2	STRAIN
A-36	0.0086	186.697	0.943E^{-6}
Aluminum 514	0.00839	186.697	0.929E^{-6}
Alluminium 4337	0.008219	186.186	.900E^{-03}
Tungsten Carbide	0.003021	190.156	0.336E^{-6}

CONCLUSION

The projects dealt with contact stress, considering contact ratio, approach angle, recess angle, contact and length of contact. The stress was more than the correct value of contact stress obtaining from approximating tools. This search was certainly not easy and cannot be carried out without the use of finite element analysis. To apply finite element method in contact stress a special technique was used rather the regular elements, to distinguish between the contact regions which were in two parts. One was the first body named target region and the other body was named contact region. For target region, target elements were used and in contact region contact elements were used. ANSYS software presents a significant technique for this purpose which was used here. A computer program was developed to plot one pair of teeth in contact at different positions of contact depending on the formulation as shown in section 5. The selected angular interval value was 3°, the progress of contact was studied at each 3° interval, which means that there were 10 cases of contact under consideration. These 10 cases were used to build 10 finite element contact models and contact finite element analysis was done under the load and material conditions were named. The maximum stress result obtained from AGMA stress calculation method was 587MPa while the maximum contact stress obtained from the finite element contact analysis was 595MPa (case five) under the same conditions, it is clear that the agreement is good. The ultimate stress of steel (C45) is 630-710MPa and the yield stress is 360MPa, therefore, the analysis is at elastic–plastic range, but by considering the very small area of contact region, it will be very natural to obtain high contact stress, which will be for very limited period of time. The results shows a high value of contact stress in the beginning of the contact, and then it starts to reduce until it reaches the location of single tooth contact, here it increased to the maximum value of the contact, but exactly after exceeding this single contact region it was reduced. At the end of the contact, the stress increased suddenly to a high value almost close to the maximum value, at this stage a sliding was occurred in the contact region at the maximum stress points as shown in Fig.

ACKNOWLEDGEMENT

The authors are Grateful to the Management of AVN institute of Engineering and Technology, Koheda, R.R Dist., Telangana India, for providing the facilities for the execution of this project of Department of Mechanical Engineering

REFERENCES

1) ANSYS (2012), Release 14.5, SAS IP, ANSYS Inc. U.S.A., (www.ansys.com).

2) Gearing by ChristopherJ.McCauleyFrom Machinery's Handbook pocket companion, (http://www.globalspec.com/reference/68260/203279/gearing)
3) Gears, From Wikipedia, (https://en.wikipedia.org/wiki/Gear)
4) Design and Manufacture of gears, from Wikipedia, (http://en.wikipedia.org/wiki/Design_and_Manufacture_of_gears)
5) The Finite Element Method In Engineering by S. S. Rao, Fourth Edition, Butterworth-Heinemann Linacre House, Barcelona, Spain
6) Understanding Overall EquipmentEffectiveness, Reliability And Maintainability by D.H. Stamatis, The OEE Primer, CRC press, Taylor & Francis Group, New York)
7) Maitra G.M. (1996), 'Hand Book of Gear Design', Tata McGraw-Hill Publishing Company Limited, New Delhi, 2nd edition.
8) Gear Materials, Properties, and Manufacture, Edited by Joseph R. Davis, ASM International, Materials Park, OH 44073-0002
9) Shigley J.E. and Charles R.M. (2003), 'Mechanical Engineering Design', Tata McGraw-Hill, New Delhi, 6th edition.
10) SpurGear And Its Types, (http://www.classle.net/#!/classle/book/spur-gear-and-its-types/)



a) Dr. J. Govardhan, M.E (DU), Ph.D.

Dr. J. Govardhan holds Ph.D. in Mechanical Engineering from Osmania University, Hyderabad. He obtained his Masters degree from Delhi College of Engineering, Delhi University and bachelors from Institute of Engineers (India).

He served defence for 20 years. Also has 16 years of teaching experience in various positions at Padmasri BV Raju Institute of Engineering and Technology, Narsapur, DVR College of Engineering and Technology, Kandi and PRRM College of Engineering and Technology, Shabad. He is presently Principal of AVN Institute of Engineering and Technology at Hyderabad.



T. Veera Pratap Reddy, PG Scholar, Dept. of AMS, AVN Institute of Engineering and Technology, Ranga Reddy(Dt) Telangana, India, E-mail: veerapratapreddy1990@gmail.com

He worked at The Indian Hume Pipe Company Limited for 2 years after completion of the graduation as Engineer in Production Department.

Optik 127 (2016) 11816–11822

Contents lists available at ScienceDirect

Optik

journal homepage: www.elsevier.de/ijleo

Original research article

Design of As_2Se_3 based chalcogenide ridge waveguide for generation of slow light

Apurva Tewari [a], Ajeet Kumar [a,*], Than Singh Saini [a], Ravindra Kumar Sinha [b]

[a] Advanced Photonics Simulation Research Laboratory, Department of Applied Physics, Delhi Technological University (Formerly Delhi College of Engineering), Delhi 110042, India
[b] CSIR-Central Scientific Instruments Organisation, Sector 30C, Chandigarh 160030, India

ARTICLE INFO

Article history:
Received 27 May 2016
Accepted 30 September 2016

Keywords:
Slow light
Nonlinear optics
Chalcogenide ridge waveguide
Stimulated brillouin scattering

ABSTRACT

A theoretical investigation of the design of a ridge waveguide in highly nonlinear As_2Se_3 chalcogenide glass has been carried out for the generation of stimulated Brillouin scattering (SBS) based slow light. The effective-mode-area and confinement loss of the waveguide structure has been obtained for single-mode operation and their variation with the geometrical parameters. Maximum allowable pump power and the time delay experienced by the pulse propagating in the ridge waveguide operating at a wavelength of 1.56 μm have been calculated. A maximum delay of ~249 ns has been achieved for a 10 cm long ridge waveguide at a pump power of 390 mW. It is observed that time delay can be tuned with input pump power and length of the proposed ridge waveguide. Such tunable features of the slow light can have potential applications in realization of an all-optical network.
© 2016 Elsevier GmbH. All rights reserved.

1. Introduction

Slow light means the possibility to reduce the velocity of optical signal and thus able to control it. It is basically reducing the group velocity of light, not the phase velocity [1]. It has become a topic of increasing interest in the recent years, because of its huge practical potential, along with the fundamental physical interests. It has numerous potential applications in optical information processing, such as optical data storage, quantum computing, optical memories, optical communication systems, data synchronization and optical buffering [2–4]. On-chip all-optical processing of signals with less wasted heat is possible by storing the light and enhancing the nonlinearity.

Many mechanisms have been proposed to achieve slow-light. These methods for slowing down light are divided into two groups; those based on material resonance and others on material structure. Stimulated Brillouin scattering (SBS) [5–9], Stimulated Raman scattering (SRS) [10], coherent population oscillation [11], and optical parametric amplification [12] are some of the techniques to slow down light. Among all different mechanisms, Stimulated Brillouin scattering (SBS) is one of the most promising methods to achieve slow light. It is because it operates at room temperature, can work with very low pump powers, for almost any wavelength and has higher efficiency. SBS is a process in which there is a large amplification of optical pulse in a very narrow spectral region. It causes increase in the group index of the medium, thus increasing the transit time. Increase in the transit time of the light propagating in the medium causes it to slow down significantly.

* Corresponding author.
E-mail address: ajeetdph@gmail.com (A. Kumar).

http://dx.doi.org/10.1016/j.ijleo.2016.09.106
0030-4026/© 2016 Elsevier GmbH. All rights reserved.

A lot of work has been done in observation of slow light in optical fibers. Initially, silica-based fibers were used for generation of slow light, but to obtain suitable delay in these fibers long length of fibers (in order of kilometres) was required. Scheinder et al. employed a silica-based fiber for generation of millimetre waves [13]. Later, to reduce the fiber length and to lower power requirements, materials having large Brillouin gain (g_B) were obtained. Tellurite and chalcogenide are two such materials having high non-linearity and high refractive index [14–16]. Abedin et al. observed strong Stimulated Brillouin scattering in single-mode As_2Se_3 chalcogenide fiber [17] and in single-mode Tellurite fiber [18]. Song et al. reported very efficient slow light generation in As_2Se_3 chalcogenide fiber [19]. Abedin et al. reported generation of slow light in single mode Er-doped Tellurite fiber [20]. Recently, Saini et al. showed slow light generation in single-mode tellurite fibers [21]. Photonic crystal fibers have shown to be an excellent medium in slowing down light. *Yang* et al. reported large delay slow light based on Stimulated Brillouin scattering in a short length of small-core pure silica photonic crystal fiber [22]. Recently, tunable slow light generation in photonic crystal fiber structure is reported by Sinha et. al [23].

Realisation of slow light in optical fibers is known to have several applications and a lot of work is being done in this area. However on-chip realisation of SBS slow light is still very less explored. Pant et al. reported for the first time the maximum delay of ~23 ns for a 7 cm long chalcogenide rib waveguide [24]. It is difficult to observe slow light effect in an optical waveguide because to achieve a significant delay (ΔT_g) in a small length (L), we require a large group refractive index change (Δn_g) since $\Delta T_g = L\Delta n_g/c$. In this work, we have attempted to improve the time delay of the SBS based slow light and study other features of slow light in optical waveguides. We have designed an As_2Se_3 based chalcogenide glass ridge waveguide for the generation of SBS based slow-light. The modal analysis of the proposed structure has been performed using commercially available software 'COMSOL Multiphysics' based on finite element method. We have solved two non-linear coupled SBS equations for the chalcogenide ridge waveguide structure using the optical properties of As_2Se_3 based chalcogenide glass [25]. Effective-mode-area and confinement loss have been calculated using the imaginary part of the effective index of the propagating mode at the pump wavelength. The time-delay of the output pulse in ridge waveguide is calculated for the operation at 1.56 μm wavelength. Its variation with pump power, Brillouin gain and length of the waveguide is obtained by developing MATLAB codes, thus tunable feature of slow light is observed.

2. Slow light using SBS

SBS is a nonlinear process in which the light incident to an optical waveguide scatters in the backward direction. This backward scattering can be used for amplification of the signal travelling in the direction opposite to the pump. The high intense pump wave is made to interact with the counter propagating weak signal wave resulting in the generation of slow travelling intensity wave which causes travelling density variations (variations in the refractive index) in the medium. This wave is called the acoustic wave. This occurs when the travelling intensity wave has the frequency equal to the difference between the frequencies of the pump wave and signal wave. The travelling refractive index grating can cause coupling of power between pump and signal waves at phase matching condition. The grating diffracts the light from the higher frequency pump wave to the weak signal wave, which as a result, experiences a gain.

Let ω_P and ω_S are the frequencies of pump wave and signal wave, respectively and I_p and I_s their intensities. Phase matching condition states that the difference in their frequencies should be equal to the brillouin frequency shift (Ω_B), i.e., $\omega_P - \omega_S = \Omega_B$. The signal frequency is much smaller than pump frequency.

The coupled nonlinear differential equations for the pump and the signal waves are given by the equations below [26].

$$\frac{dI_P}{dZ} = -g_B I_P I_S - \alpha_P I_p \tag{1}$$

$$-\frac{dI_s}{dZ} = +g_B I_P I_S - \alpha_S I_s \tag{2}$$

where, g_B is the Brillouin gain coefficient, α_P and α_S are material losses at pump and signal frequencies, respectively. If we assume that the pump wave is undepleted, then $\alpha_P = \alpha_S = \alpha$, thus the solution to the above equations is given by

$$I_s(0) = I_s(L)\exp\left(\frac{g_B P_p L_{eff}}{A_{eff}} - \alpha L\right) \tag{3}$$

Here, P_p is the input pump power, A_{eff} is the effective-mode-area of the propagating mode, α is the attenuation constant of the waveguide, L is the real length of waveguide and L_{eff} is the effective length of waveguide which is given by the Eq. (4).

$$L_{eff} = \frac{[1 - \exp(-\alpha L)]}{\alpha} \tag{4}$$

Effective-mode-area, A_{eff} is defined as

$$A_{eff} = \frac{\left(\iint_{-\infty}^{\infty} |E|^2 dxdy\right)^2}{\left(\iint_{-\infty}^{\infty} |E|^4 dxdy\right)} \tag{5}$$

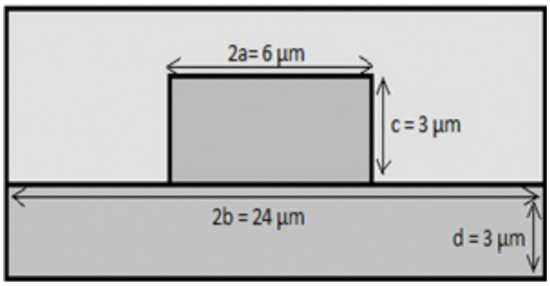


Fig. 1. Cross-sectional view of the As_2Se_3 based chalcogenide ridge waveguide structure.

where, E denotes electric field distribution in the waveguide. The Brillouin gain coefficient is defined a

$$g_B\left(\Omega\right) = \frac{g_p\left(\frac{\tau_B}{2}\right)^2}{\left(\Omega - \Omega_B\right)^2 + \left(\frac{\tau_B}{2}\right)^2} \tag{6}$$

Here, g_p is the maximum value of the gain at $\Omega = \Omega_B$ and is given by

$$g_p = \frac{2\pi n^7 {p_{12}}^2}{c{\lambda_P}^2 \nu_A \Delta\nu_B} \tag{7}$$

where, n is the refractive index of the material used in waveguide, p_{12} is the longitudinal elasto-optic coefficient, c is the velocity of light in free space, λ_P is wavelength of the pump wave, ν_A is the acoustic velocity, and $\Delta\nu_B$ is the Brillouin gain bandwidth. We require a minimum pump power to initiate the SBS effect. It is when the brillouin gain is larger than the losses of the waveguide, and is given by

$$P_{min} = \frac{\alpha A_{eff} L}{K g_B L_{eff}} \tag{8}$$

Also, there is a maximum power above which the output signal gets distorted. When the pump power reaches this maximum allowable power, the backscattered waves are generated from the background noises in the waveguide which leads to output signal distortion. It is given by the following relation [20]

$$P_{max} = 21\frac{A_{eff}}{K g_B L_{eff}} \tag{9}$$

where, K is the polarization factor, the polarisation properties of the waveguide decides its value. If the polarization is maintained, its value is 1, and it is 0 if not maintained. It is shown from some results that $K = 0.667$ is an appropriate value for low birefringence waveguide with high polarization beat length [20,27]. The time-delay per unit length per unit pump power induced due to SBS effect in the slow light devices is expressed as [5,20]

$$\frac{\Delta t_d}{P_p L_{eff}} = \frac{g_B K}{\tau_B} \tag{10}$$

Here, τ_B is the Brillouin line width ($\tau_B = 2\pi\Delta\nu_B$, where $\Delta\nu_B$ is the Brillouin gain bandwidth as mentioned above) [28]. Brillouin gain is an another parameter which depends on the input pump power and it is expressed as [29]

$$\text{Gain}\,[\text{dB}] = 10\log(\exp\left(g_B K\left(\frac{P_p}{A_{eff}}\right)L_{eff}\right) - \alpha L \tag{11}$$

Theoretical value of the gain is given by

$$G_{th} = 4.34\left(\frac{g_B K \times 1\text{mW} \times L_{eff}}{A_{eff}}\right) \tag{12}$$

Another important parameter that defines the suitability of waveguide to be used as a slow light medium is figure of merit (FOM). It is defined as [19]

$$FOM = \frac{Gain\,[dB]}{P_p L_{eff} n} = 4.34\left(\frac{g_B K L_{eff}}{A_{eff} n L}\right) \tag{13}$$

3. Design of the proposed ridge waveguide

We have proposed an As_2Se_3 based chalcogenide ridge waveguide for single-mode operation for the generation of slow-light based on stimulated Brillouin scattering. The cross-sectional view of the proposed ridge waveguide is shown in Fig. 1. The

Table 1
Optical properties of As_2Se_3 based chalcogenide glass at 1.56 μm.

Parameters	Chalcogenide (As_2Se_3)
Refractive index, n	2.815
Brillouin gain coefficient, g_B(m/W)	6.75×10^{-9}
Brillouin gain bandwidth, $\Delta\nu_B$ (MHz)	13.2
Loss (dB/m)	0.90

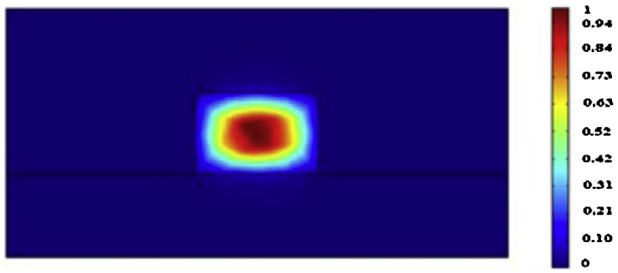


Fig. 2. Normalized electric field distribution of fundamental mode in proposed ridge waveguide at pump wavelength.

substrate material used is silica ($n = 1.44$). The material used in the ridge is As_2Se_3 based chalcogenide glass. Chalcogenide has a refractive index of 2.815 for operation at the wavelength of 1.56 μm. The optical properties of As_2Se_3 based chalcogenide material are taken from the Ref. [25] and represented in the Table 1.

The ridge width '*a*' and height '*c*' are the parameters that are varied to calculate the effective-mode-area 'A_{eff}' and confinement loss of the fundamental mode of the waveguide. Further, the time-delay is observed and its variation with the pump power, gain and length of the waveguide are shown. The length of the waveguide is taken to be 10 cm.

4. Results and discussions

For optimum single-mode operation with low loss we have taken the ridge half width (*i.e.* '*a*') as 3 μm and trench height (*i.e.*'*c*') as 3 μm. The normalized electric field distribution of the fundamental mode of the proposed structure is shown in Fig. 2 at pump wavelength. It can be observed that the mode is well confined within the ridge. It ensures low confinement loss for this mode since most of the light is confined inside the ridge.

The effective-mode-area of an optical waveguide enhances its nonlinear effect. Nonlinearity of the waveguide is inversely proportional to the effective-mode-area. Thus it is considered a very important parameter in the study of slow light in ridge waveguide. The effect of the variations in ridge width on effective-mode-area is shown in Fig. 3(a). It is shown that effective-mode-area increases on increasing the width of the waveguide since the core size increases. At a = 2 μm, the value of the A_{eff} is found to be 5.64 μm^2 and increases for higher values of core half width. Since for optimum single mode operation with low loss, we have taken core half width as 3 μm, at this core width, the effective mode area of the propagating mode is 8.42 μm^2.

Confinement loss of the waveguide is another important parameter of the optical waveguide. At core half width of 3 μm, the confinement loss of the propagating mode is found to be as low as 4×10^{-4} dB/m. It is a very desirable result as it ensures very low-loss operation of the waveguide at the optimized dimensions. The effect of changing the core width on confinement loss is shown in Fig. 3(b). It shows that the confinement loss decreases on increasing the core width. It so happens because

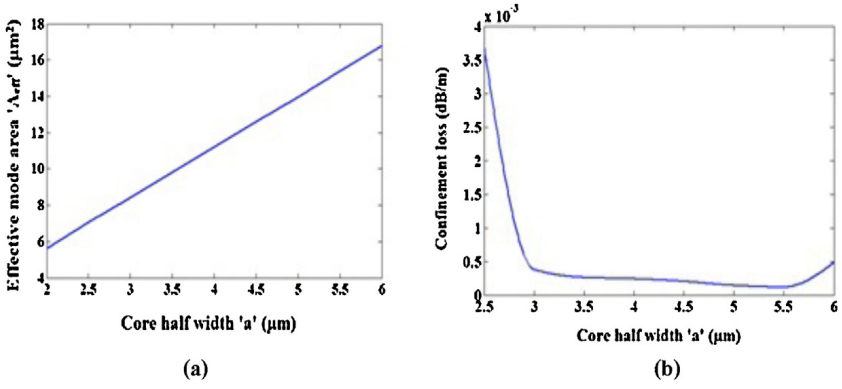


Fig. 3. (a) Variation of effective mode area with half width of the ridge waveguide. (b) Variation of the confinement loss with half width of the ridge waveguide.

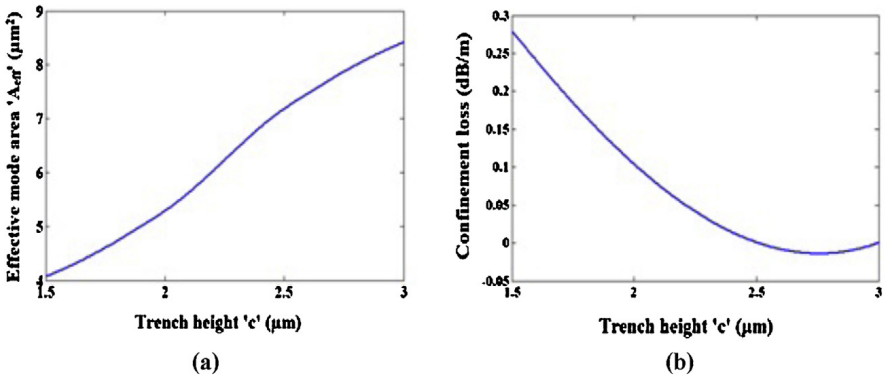


Fig. 4. (a) Variation of the effective mode area with trench height of the ridge waveguide. (b) Variation of the confinement loss with trench height of the ridge waveguide.

as the core width increases, the core-cladding refractive index difference increases. This causes the electric field to be more confined in the core of the waveguide, thus higher confinement of light in core and lower confinement loss.

The effect of changing the trench height of the ridge waveguide on the effective-mode-area and confinement loss of the waveguide is also observed. The effective-mode-area increases on increasing the trench height '*c*' and the effect is shown

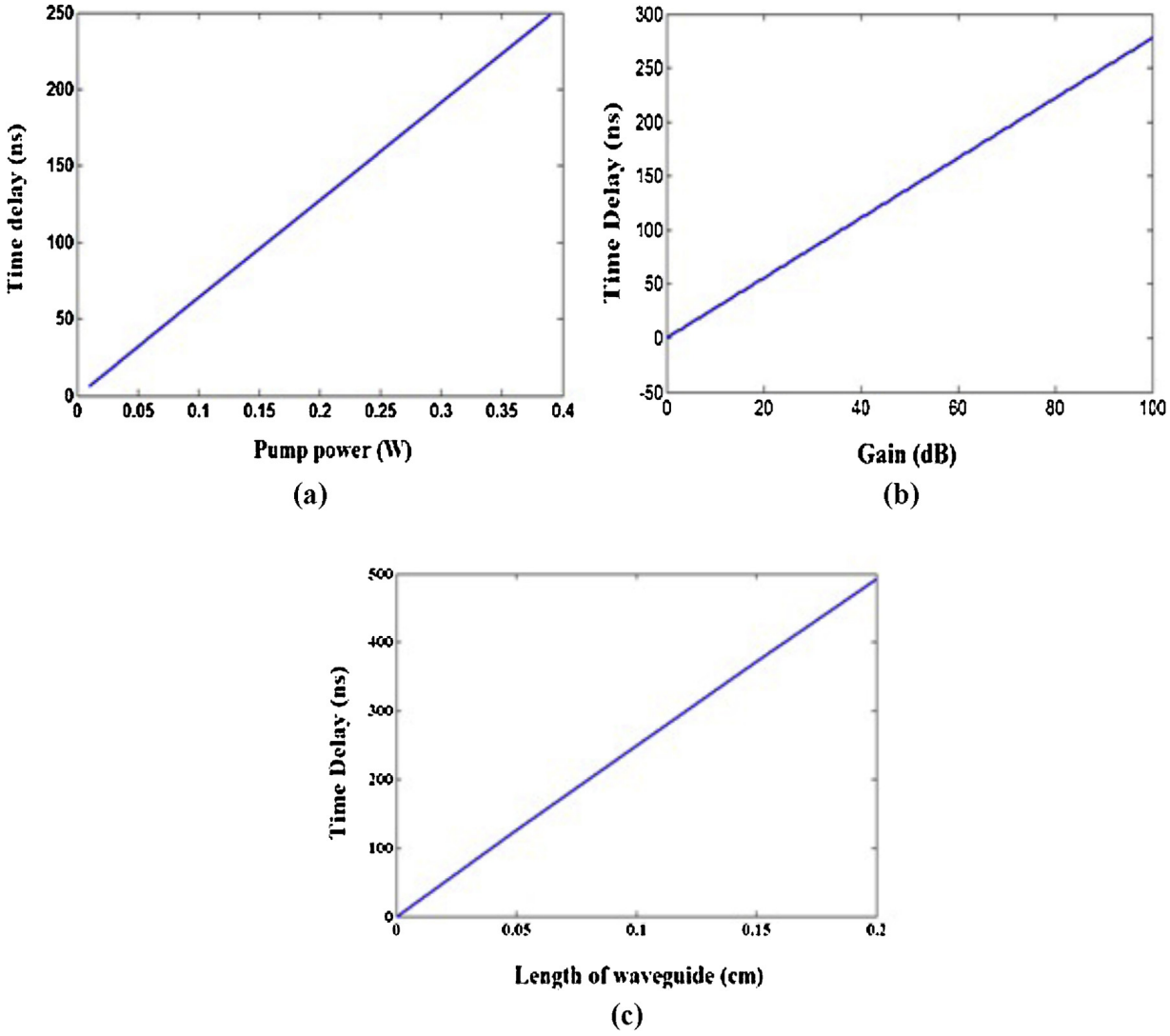


Fig. 5. Time delay as a function of (a) pump power. (b) Brillouin gain. (c) length of the ridge waveguide.

in Fig. 4(a). As the height increases, effective refractive index difference also increases. Hence similar to the variation of confinement loss with '*a*', confinement loss also decreases with increase in height as shown in Fig. 4(b).

The effective length of 10 cm long waveguide is calculated using Eq. (4) and it comes out to be 9.9 cm. Taking these values of L_{eff} and A_{eff} for single-mode operation and considering the optical properties of As_2Se_3, we have calculated maximum and minimum power using the Eqs. (8) and (9) mentioned above. We get P_{max} = 396 mw and P_{min} = 0.3 mW. In our simulation, we have taken the pump power (P_p) as 390 mW to avoid distorted output for SBS based slow light operation. From the previous results [20,27], the value of polarization factor K is taken to be 0.667.

Finally, the time-delay in output pulse is calculated. We have achieved a maximum delay of ~249 ns for a waveguide of length 10 cm and input power of 390 mW. The time-delay is varied for different values of P_p ranging from 0.5 to 390 mW. The linearly increasing variation time delay with pump power is shown in Fig. 5(a). At higher input powers, the optical field substantially contribute to the phonon population. This simulated effect is the reason for linear increase of time-delay with pump power. Similarly, variation of the time-delay with Brillouin gain and with length of the waveguide is shown in Fig. 5(b) and (c), respectively. The time-delay linearly increases with maximum delay reaching to 249 ns at 90 dB. The maximum time-delay of 493 ns is achieved for 20 cm long waveguide. Thus we can get the required time-delay by tuning the pump power, Brillouin gain and length of the waveguide.

The theoretical gain (G_{th}) and figure of merit (FOM) of the waveguide is also calculated to check the suitability of the waveguide for slow-light operation. We obtained the theoretical gain of 0.229 and FOM equal to 815.9 for the proposed structure.

5. Conclusion

We have designed an As_2Se_3 based chalcogenide ridge waveguide and analysed for the generation of SBS based tunable slow-light. The effective-mode-area and confinement loss of the proposed waveguide has been studied for its various structural parameters and calculated for optimum single-mode operation. For the proposed waveguide parameters, we have obtained the effective-mode-area of 8.42 μm^2 and confinement loss as low as 4×10^{-4} dB/m. The minimum and maximum power for undistorted output pulse has been calculated. The maximum time-delay up to ~249 ns has been achieved for a waveguide of length 10 cm pumped with 390 mW power. The variation of time delay with pump power, Brillouin gain and length of the proposed waveguide has been observed. The proposed ridge waveguide is able to provide a much larger time-delay in optical waveguides as compared to the previously reported work [24]. The simulated results also indicate that the slow-light can be obtained with tunable features by tuning the time-delay of the output pulse with pump power and other structural parameters of the waveguide. Finally we obtained a theoretical gain equal to 0.229 and FOM of the waveguide to be 816. Thus it can be concluded that with high gain and FOM, the proposed ridge waveguide is suitable for SBS based slow-light applications with tunable features and have potential applications in compact slow light based photonic devices.

Acknowledgement

The authors gratefully acknowledge the TUN-IND bilateral research project, Department of science and Technology, Govt. of India.

References

[1] T. Baba, Slow light in photonic crystals, Nat. Photon. 2 (2008) 465–473.
[2] J.T. Mok, B.J. Eggleton, Expect more delays, Nature 433 (2005) 811–812.
[3] M. Santagiustina, G. Eisenstein, L. Thevenaz, J. Capmany, J. Mork, J.P. Reithmaier, A.D. Rossi, S. Sales, K. Yvind, S. Combrie, J. Bourderionnet, Slow light devices and their applications to microwaves and photonics, IEEE Photonics Soc. Newsl. (2012) 5–12.
[4] S. Rawal, R.K. Sinha, R.M. De La Rue, Silicon-on-insulator photonic crystal miniature devices with slow light enhanced third-order nonlinearities, J. Nanophotonics 6 (2012) 063504.
[5] K.Y. Song, M. Gonzalez Herraez, L. Thevenaz, Observation of pulse delaying and advancement in optical fibers using stimulated Brillouin scattering, Opt. Exp. 13 (2005) 82–88.
[6] L.Y. Ren, Y. Tomita, Transient and nonlinear analysis of slow-light pulse propagation in an optical fiber via stimulated Brillouin scattering, J. Opt. Soc. Am. B 26 (2009) 1281–1288.
[7] S.H. Wang, L.Y. Ren, Y. Liu, Y. Tomita, Zero-broadening SBS slow light propagation in an optical fiber using two broadband pump beams, Opt. Exp. 16 (2008) 8067–8076.
[8] E.P. Ippen, R.H. Stolen, Stimulated Brillouin scattering in optical fibers, Appl. Phys. Lett. 21 (1972) 539–540.
[9] A. Kobyakov, M. Sauer, D. Chowdhury, Stimulated Brillouin scattering in optical fibers, Adv. Opt. Photon. 2 (2010) 1–59.
[10] J. Sharping, Y. Okawachi, A. Gaeta, Wide bandwidth slow light using a Raman fiber amplifier, Opt. Exp. 13 (2005) 6092–6098.
[11] M.S. Bigelow, N.N. Lepeshkin, R.W. Boyd, Superluminal and slow-light propagation in a room-temperature solid, Science 301 (2003) 200–202.
[12] D. Dahan, G. Eisenstien, Tunable all optical delay via slow and fast light propagation in a Raman assisted fiber optical parametric amplifier: a route to all optical buffering, Opt. Exp. 13 (2005) 6234–6248.
[13] T. Schneider, D. Hannover, M. Junker, Investigation of Brillouin scattering in optical fibers for the generation of millimeter waves, J. Lightwave Technol. 24 (2006) 295–304.
[14] V. Shiryaev, M. Churbanov, Trends and prospects for development of chalcogenide fibers for mid-infrared transmission, J. Non-Cryst. Solids 377 (2013) 225–230.
[15] B.J. Eggleton, B.L. Davies, K. Richardson, Chalcogenide photonics, Nat. Photonics 5 (2011) 141–148.
[16] T.S. Saini, A. Kumar, R.K. Sinha, Broadband mid-infrared supercontinuum spectra spanning 2–15 μm using As2Se3 chalcogenide glass triangular-core graded-index photonic crystal fiber, J. Lightwave Technol. 33 (18) (2015) 3914–3920.
[17] K.S. Abedin, Observation of strong stimulated Brillouin scattering in single-mode As_2Se_3 chalcogenide fiber, Opt. Exp. 13 (2005) 10266–10271.

[18] K.S. Abedin, Stimulated Brillouin scattering in single-mode tellurite glass fiber, Opt. Exp. 14 (24) (2006) 11766–11772.
[19] K.Y. Song, K.S. Abedin, K. Hotate, M.G. Herraez, L. Thevenaz, Highly efficient brillouin slow and fast light using As_2Se_3 chalcogenide fiber, Opt. Exp. 14 (2006) 5860–5865.
[20] K.S. Abedin, G.W. Lu, T. Miyazaki, Slow light generation in single mode Er-doped tellurite fiber, Electron. Lett. 44 (1) (2008) U16–U21.
[21] T.S. Saini, A. Kumar, R.K. Sinha, Slow light generation in single mode tellurite fibers, J. Mod. Optics 62 (7) (2015) 508–513.
[22] S. Yang, H. Chen, C. Qiu, M. Chen, M. Chen, S. Xie, J. Li, W. Chen, Slow-light delay enhancement in small core pure silica photonic crystal fiber based on Brillouin scattering, Opt. Lett. 33 (2008) 95–97.
[23] R.K. Sinha, A. Kumar, T.S. Saini, Analysis and design of single-Mode As_2Se_3-Chalcogenide photonic crystal fiber for generation of slow light with tunable features, IEEE J. Selected Top. Quantum Electr. 22 (2) (2016) 4900706.
[24] R. Pant, A. Byrnes, C.G. Poulton, E. Li, D.Y. Choi, S. Madden, B.L. Davies, B.J. Eggleton, Photonic-chip-based tunable slow and fast light via stimulated Brillouin scattering, Opt. Lett. 37 (5) (2012) 969–971.
[25] C. Florea, M. Bashkanshy, Z. Dutton, J. Sanghera, P. Pureza, I. Aggarwal, Stimulated Brillouin scattering in single-mode As_2S_3 and As_2Se_3 chalcogenide fibers, Opt. Exp. 14 (2006) 12063–12070.
[26] G.P. Agrawal, Nonlinear Fiber Optics, 5th ed., Academic, San Diego, CA, 2013, pp. 355–388.
[27] M.O. Van Deventer, A.J. Deventer, Polarization properties of stimulated Brillouin scattering in single-mode fibers, J. Lightwave Technol. 12 (4) (1994) 585–590.
[28] G.M. Gehring, R.W. Boyd, A.L. Gaeta, D.J. Gauthier, A.E. Willner, Fiber-based slow-light technologies, J. Lightwave Technol. 26 (23) (2008) 3752–3762.
[29] G. Qin, H. Sotobayashi, M. Tsuchiya, A. Mori, T. Suzuki, Y. Ohishi, Stimulated Brillouin scattering in a single mode tellurite fiber for amplification, lasing and slow light generation, J. Lightwave Technol. 26 (2008) 492–498.

Disposition decisions in reverse logistics by using AHP-Fuzzy TOPSIS Approach

1. Introduction

Growing concern for the environment, legislations, and corporate social responsibility has increased the interest of researchers and practitioners in reverse flows in last two decades (Fleischmann *et al.*, 1997). The importance of well-managed reverse flows is being recognized by practitioners and academicians from widespread research areas including green logistics (Dekker *et al.*, 2012; Knemeyer *et al.*, 2002), green marketing (Carter and Rogers, 2008; Shamah, 2012), and sustainability (Carter and Easton, 2011; Markley and Davis, 2007). Some of the organizations like HP, Phillips, and Dell have implemented reverse logistics to gain a socio-economic advantage over competitors. Similarly other leading manufacturers such as Canon and Xerox have also attained remanufacturing rates of nearly ninety percent for the used equipments. Reverse logistics has been studied by researchers across the industries from the beverage containers (Jayaraman *et al.*, 2003), publishing industry (Wu and Cheng, 2006), electronics industry (Janes *et al.*, 2009), cell phone industry (Agrawal *et al.,* 2014) to the pharmaceuticals industry (Narayana *et al.*, 2014) and so on. Reverse logistics programs for reducing, reusing, and recycling wastes may produce tangible and intangible value (Kopicki *et al.*, 1993). A well-managed reverse logistics may result in important cost savings in procurement, inventory and transportation costs (Kannan *et al.*, 2009).

Reverse logistics is "the process of planning, implementing, and controlling the efficient, cost effective flow of raw materials, in-process inventory, finished goods, and related information from the point of consumption to the point of origin for the purpose of recapturing or creating value or proper disposal" (Rogers and Tibben-Lembke, 1999). Returned products are collected from the customer through product acquisition, and are inspected and sorted out into different categories. The next step is to take disposition decision for further processing. Reuse; repair; refurbish, remanufacture; recycle; and disposal are the common disposition alternatives discussed by authors frequently in the literature (Thierry *et al.*, 1995, Blackburn *et al.*, 2004; Carter and Ellram, 1998; Krikke *et al.*, 2003). Very little attention has been given to the disposition decisions in reverse logistics. No comprehensive study was found exploring various disposition alternatives and approach for selecting appropriate disposition alternative.

© Emerald Group Publishing Limited
This is a pre-print of a paper and is subject to change before publication. This pre-print is made available with the understanding that it will not be reproduced or stored in a retrieval system without the permission of Emerald Group Publishing Limited.

This paper aims at developing a framework for selection of best reverse logistic disposition alternative. A combination of Analytical Hierarchy Process (AHP) and Technique for Order Preference by Similarity to Ideal Solution (TOPSIS) under fuzzy environment is utilized for selecting the best disposition alternative. The criteria were selected based on literature review and discussion with the experts, and their weights were determined by using the AHP approach. The Fuzzy TOPSIS approach is proposed for the selection of the best disposition alternative. Triangular fuzzy numbers were used because of their ability to handle the uncertainty and vagueness of the data. A combination of AHP and fuzzy TOPSIS approach is utilized because of its appropriateness in providing the solutions in a multi-criteria decision environment. Also, this approach is first time being utilized for such type of disposition problem. The approach has been used previously by many authors in providing solutions to the various MCDM problems (Onut and Soner, 2008; Gumus, 2009; Prascevic and Prascevic, 2013; Kumar and Singh, 2012; Senthil *et al.*, 2014).

The remainder of this paper is structured as follows: Section 2 explores the literature on reverse logistics processes, and disposition decisions including criteria for selection of best disposition alternative. Step by step AHP, and fuzzy-TOPSIS approach is enumerated in section 3. A numerical example of Indian electronic firm along with results and discussion is analyzed and summarized in Section 4. Finally, Section 5 concludes the study along with future outlook and limitations of this research.

2. Literature Review

An extensive literature review was carried out to understand the reverse logistics processes, to explore the previous research on disposition in reverse logistics, and to study the multi-criteria decision making approach i.e. AHP and Fuzzy-TOPSIS. The literature review is described in following section.

2.1 Reverse logistics processes

Major reverse logistic processes are product acquisition/gate keeping, collection, inspection /sorting, disposition, and redistribution. These reverse logistics processes are shown in figure 1. Figure shows the basic flows of returned products from their acquisition to their disposition and redistribution, and is described in following section.

© Emerald Group Publishing Limited
This is a pre-print of a paper and is subject to change before publication. This pre-print is made available with the understanding that it will not be reproduced or stored in a retrieval system without the permission of Emerald Group Publishing Limited.

[Insert figure 1 here]

2.1.1 Product Acquisition and Gate Keeping

Product acquisition is the process of acquisition of used products from the end users for further processing. Gate keeping is a set of practices performed usually by retailers to identify the products which are allowed into the system or given back to the user or disposed by retailers.

2.1.2 Collection

Products after acquisition are collected and delivered to the facilities for inspection, sorting, and the disposition. Collection is the process in which a firm gains the possession of returned products (Fleischmann *et al.*, 2003). Typically, there are three collection methods identified as manufacturers directly collect from customers, manufacturers collect via retailers or manufactures collect through third party logistics (Kumar and Putnam, 2008). Selection of collection process depends on the quantity and cost of the collection (Atasu *et al.,* 2013). For operating prospective reverse logistics efficiently, designing reverse logistics must involve decisions of collection centres and related parameters having sufficient success potentials (Pochampally and Gupta, 2004).

2.1.3 Inspection and Sorting

Returned products are uncertain in terms of quantity, time of returns, and condition or quality of products. The quality or condition of returned products may differ greatly unlike forward flow in which quality of products is ascertained before distribution. So a separate inspection of each item is required for sorting the products into different categories.

2.1.4 Disposition

Once the products are inspected and sorted out, next step is to take decision for their disposition. Reuse; repair; refurbish, remanufacture; recycle; and disposal are the common disposition alternatives discussed by authors frequently in the literature (Thierry *et al.*, 1995, Blackburn *et al.*, 2004; Carter and Ellram, 1998; Krikke *et al.*, 2003).

© Emerald Group Publishing Limited
This is a pre-print of a paper and is subject to change before publication. This pre-print is made available with the understanding that it will not be reproduced or stored in a retrieval system without the permission of Emerald Group Publishing Limited.

Recycling is generally concerned with the material recovery from the products of low value (Blackburn *et al.*, 2004). Recycling alternative is also selected when the original product materials can be utilized for another product or assembly or subassembly (Skinner, 2008). In most of the cases, recovery value is low in recycling and at the same time it requires high investments in equipments. Therefore, higher processing volumes are required to make it economically viable (Fleischmann *et al.*, 2000). Remanufacturing is generally concerned with material recovery from the products having high value (Blackburn *et al.*, 2004). Uncertainty in terms of quality, quantity and timing of product returns are the critical factors for the success of remanufacturing (Rogers and Tibben-Lembke, 1999). Since this is intermediary between the collection and redistribution, it requires a lot of efforts because of having complex supply chain structure (Fleischmann *et al.*, 1997). Reusing alternatives require only minor inspection, cleaning, and minor maintenance, and requires less efforts because of having a rather flat supply chain structure (Fleischmann *et al.*, 2000). Repairing is concerned with repairing and servicing of products and retuning those products to the customers (Fleishmann *et al.*, 2000). Generally a decentralized repairing center close to customer is preferred (Fleischmann *et al.*, 2000). The last disposition alternative is disposal. If the products cannot be sold or reused at the point of return location, and the product return is not economically feasible because of low volume and high transportation costs then products are preferred to be destroyed (Skinner, 2008).

2.1.5 Redistribution

Products after refurbishment or remanufacturing are redistributed into the potential market for resale to the users. Reusable products need to be sold into the proper market through redistribution. These products may be sold with the new product or may be sold in the secondary markets.

2.2. Disposition decisions

As shown in figure 1, products are returned by the users and diagnostic tests are performed on them to decide the further action for recapturing maximum value from the returned products. Disposition decisions depend upon proposition of the product sold to the customer such as quality, selling price, and logistics cost, and demand of the product in the market. If the product has sufficiently high value and the quality of returned product is good enough for recapturing

© Emerald Group Publishing Limited
This is a pre-print of a paper and is subject to change before publication. This pre-print is made available with the understanding that it will not be reproduced or stored in a retrieval system without the permission of Emerald Group Publishing Limited.

value then product can be remanufactured because of higher re-sale value (Stock, 2001). In a study, Tan and Kumar (2006) found that the part replacements from suppliers must be preferred over refurbishment of computer being more profitable. So the firm may adopt the disposition strategy of parts replacement rather than refurbishment. Skinner *et al.* (2008) found that choose to destroy the product must be preferred in case of resource scarcity because other disposition alternatives like recycling or remanufacturing may need higher investment for recapturing value, although, there may be legal restrictions on destroying some products in many countries. Gobbi (2011) reported that if time is not relevant then recycling is preferred; and reprocessing is preferred if time is primarily relevant. Guide *et al.* (2008) developed a model for the returned products considering the time of the return, the quality of the product and the clogging effect at the remanufacturing facility. Karamouzian *et al.* (2014) developed a queuing theory based optimal disposition model which utilizes an acquisition policy by grading the return products to maximize the product recovery value. Some of the multi-criteria decision making models have also been used for the disposition decision making. Wadhwa *et al.* (2009) developed a flexible decision model for the selection of best alternative of disposition strategy. Senthil *et al.* (2012) utilized the combination of AHP and TOPSIS approach for the selection of appropriate channel to carry out reverse logistics operations either by manufacturer or third party or formation of joint consortium. Hazen (2011) analyzed the strategic factors to provide a summary of these factors for the betterment of a firm's reverse logistics functions. Different firms in different industries have been using potential disposition alternatives (reuse, recycle, remanufacture, and repair or disposal) in practice but no model or methodology or approach was found for selecting the best disposition alternative in reverse logistics system.

2.3 Criteria for the selection of best disposition alternative

After literature review and discussion with experts, major criteria identified for selection of disposition alternatives are economic benefits, environmental benefits, corporate social responsibility, stake holder's needs, and reverse logistics resources. These criteria for the selection of the disposition alternatives are shown in figure 3. The overall objective, disposition alternative selection is shown at the top and criteria are shown at secondary level. The criteria are described in the following sections:

© Emerald Group Publishing Limited
This is a pre-print of a paper and is subject to change before publication. This pre-print is made available with the understanding that it will not be reproduced or stored in a retrieval system without the permission of Emerald Group Publishing Limited.

i) Economic benefits

Economics is seen as the major driver to all the recovery options, where the firm may gain both direct as well as indirect economic benefits through recapturing value from returned products (Ravi *et al.*, 2005). The recovery of the products for remanufacturing, repair, reconfiguration, or recycling through proper disposition can lead to profitable business opportunities (Andel, 1997). Guide and Wassenhove (2003) gave an example of the US firm ReCellular, which by refurbishing the cell phones gained a significant economic advantage.

ii) Environmental benefits

Environmental concerns are the significant force shaping the economy as well as one of the most important issues faced by businesses (Murphy and Poist, 2003). Many companies have focused on reverse logistics operations because of environmental reasons (Rogers and Tibben-Lembke, 1999). Disposition decisions are greatly affected by the environmental policy of an organization. Sometimes a firm recycles the products rather than disposal even if it is costlier.

iii) Corporate social responsibility

Corporate social responsibility involves actions not only by few countries like India but also the self driven in many countries for the goodness of society. Corporate social responsibility provide guidelines to outline firm approach, strategies and associations with stakeholders while addressing ethical values, legal fulfillment, and economic progress (Sarkis *et al.*, 2010). Corporate social responsibility may greatly influence the reverse logistics disposition decision depending on the policy of an organization. According to Sarkis *et al.* (2010), reverse logistics can make significant contribution to the sustainability and hence corporate social responsibility efforts of an organization.

iv) Stake holder's needs

The stakeholders of large firms have also become more concerned about customer attitudes and are more conscious of environmental issues and want to be socially responsible themselves (Bowen *et al.*, 2001). Because of pressures from consumers, manufacturers are asking their suppliers to adopt the environmental friendly practices (Lamming and Hampson, 1996). Similarly, stake holders in the distribution system are pressuring their suppliers to be more environmentally responsible (Hall, 2001). Stake holders may also influence the disposition

© Emerald Group Publishing Limited
This is a pre-print of a paper and is subject to change before publication. This pre-print is made available with the understanding that it will not be reproduced or stored in a retrieval system without the permission of Emerald Group Publishing Limited.

decisions in an organization because of their growing awareness and concerns. Disposition decisions must be taken by keeping in mind the stake holder's need.

v) Reverse logistics resources

Availability and effective utilization of resources is essential for fully exploring the true value potential of reverse logistics. Dowlatshahi (2005) stated that the overall success of reverse supply chain system depends on the effective use of available resources. Disposition decisions depend on the availability of resources in an organization. For example, if recycling facilities are not available then products may be disposition to the third party for recycling.

3. Research Methodology

Multiple criteria decision making (MCDM) are the approaches in which decision makers assess the variety of alternatives under given set of criteria and then select the best one using a MCDM. The responses of the decision makers are represented in the form of decision matrix which consists of three main parts including alternatives, criteria, and the weights of relative importance. In this paper, a combination of AHP and Fuzzy-TOPSIS approach has been applied because of their inherent advantages. The proposed approach is described in the following section.

3.1 Analytic Hierarchy Process (AHP)

One of the multi-criteria decision techniques for decision making problems is the Analytic Hierarchy Process (AHP). Saaty (1980, 2000) developed AHP approach which segregates the decision making problem into the level of hierarchies of objectives, criteria, and alternatives. An AHP hierarchy may be structured into the number of levels required to fully characterize a particular decision situation. Functional characteristics of AHP including the capability to handle decision problems involving prejudiced judgments, number of decision makers, and the evaluation of preference consistency make the AHP a very constructive approach (Triantaphyllou, 2000). Also, AHP can handle both tangible and non tangible characteristics efficiently especially when the subjective decisions of individuals comprise an imperative element of the decision system. AHP approach has been utilized by many authors in previous research for solving variety of multi-criteria decision making problems (Bhatti *et al.*, 2010;

© Emerald Group Publishing Limited
This is a pre-print of a paper and is subject to change before publication. This pre-print is made available with the understanding that it will not be reproduced or stored in a retrieval system without the permission of Emerald Group Publishing Limited.

Barker and Zabinsky, 2011; Garg *et al.*, 2012; Subramanian, 2014). The step by step approach of AHP by using the geometric mean method is described in following section:

Step 1: Establish the objectives and their evaluation criteria and sub-criteria. As discussed above, develop a hierarchical structure with the objective at the top level, the criteria and sub-criteria at the lower levels and the alternatives at the end.

Step 2: Determine the relative importance of criteria with respect to the top level objective. Prepare a pair wise comparison matrix using the relative importance of criteria on a specified or selected scale. The pair wise comparison of criteria indicates the relative importance of one criterion over other in the perception of decision maker. The judgments of decision makers are entered using the basic scale of the AHP (Saaty 1980, 2000). The scale used in AHP for the preparation of the pair wise comparison matrix is a discrete scale from ranging from 1 to 9 as shown in table 1.

[Insert Table 1 here]

Step 3: After the pair wise comparison of sub-criteria with respect to the element in a higher level criteria, the weight of each criteria is calculated by taking geometric mean of the all elements of the row and their normalization in pair wise comparison matrix. In order to check the consistency, the largest eigen value (λ_{max}) should be roughly equal to the number of elements in the comparison matrix (n). The deviation of λ_{max} from the number of elements (n) is a measure of consistency of the judgment of decision makers. The consistency index (CI) may be calculated by using following relationship:

$$CI = (\lambda_{max} - n)/(n-1)$$

Step 4: Now obtain the random index (*RI*) by using the table 2, the consistency ratio may be estimated by using the relation given below.

© Emerald Group Publishing Limited
This is a pre-print of a paper and is subject to change before publication. This pre-print is made available with the understanding that it will not be reproduced or stored in a retrieval system without the permission of Emerald Group Publishing Limited.

[Insert Table 2 here]

$$CR = CI/RI$$

If the consistency ratio is 0.1 or less, it is considered as acceptable for the matrix of the order of M> 4. If the consistency ratio is more than 0.1 (the acceptable value), the inconsistency may occur, and the judgments are not considered as trustworthy. In this situation, the assessment process is required to be improved. Consistency ratio helps in ensuring the reliability of decision maker in obtaining the preferences for the criteria.

3.2 Fuzzy TOPSIS Approach

The TOPSIS method was developed by Hwang and Yoon (1981) to provide solutions to the Multi-criteria Decision Making problems. This method is based on the concept that the chosen alternative should have the shortest Euclidean distance from the ideal solution, and the farthest from the negative ideal solution. According to Kim *et al.* (1997), the advantages of TOPSIS include

(i) a logic that represents the justification of individual choice;
(ii) a scalar value that reports for both the best and worst alternatives concurrently;
(iii) a simple step by step approach that can easily be formulated into a spreadsheet; and
(iv) the performance measures of all alternatives on attributes can be visualized on a polyhedron, at least for any two dimensions.

In this method, the best selected alternative should have the minimum distance to the positive ideal solution and maximum distance from the negative ideal solution. The traditional TOPSIS method assumes rankings and weights of the criteria in crisp numbers. However, crisp data are not adequate to capture real situation because human judgments may be vague and cannot be estimated accurately. One of the alternatives in these situations is use of the fuzzy set theory to handle the uncertainty of human judgments. Zadeh (1965) introduced fuzzy set theory first time into the TOPSIS for effectively handling the vagueness and ambiguity of the human judgments. In fuzzy TOPSIS, linguistic variables are used for the ratings and weights of criteria, sub-criteria and alternatives. The following steps, introduced by Chen (1997) are used for the proposed research.

© Emerald Group Publishing Limited
This is a pre-print of a paper and is subject to change before publication. This pre-print is made available with the understanding that it will not be reproduced or stored in a retrieval system without the permission of Emerald Group Publishing Limited.

Step 1: Respondents must be asked to choose the best alternative among the linguistics terms for a given question. A 5-point scale having the linguistic terms low, fairly low, medium, fairly high, and high, as shown in Figure 2 are selected for the proposed study. This figure helps in determining the fuzzy number for the linguistic terms of 5-point scale.

[Insert figure 2 here]

The fuzzy number of each linguistic term is determined with the help of the figure 2. Fuzzy numbers for each of the selected linguistic terms are presented in table 3.

[Insert Table 3 here]

Step 2: The TOPSIS method evaluates the following fuzzy decision matrix

$$D = \begin{bmatrix} x_{11} & x_{12} & \cdots & x_{13} & \cdots & x_{1n} \\ x_{21} & x_{22} & \cdots & x_{23} & \cdots & x_{2n} \\ \cdots & \cdots & \cdots & \cdots & \cdots & \cdots \\ \cdots & \cdots & \cdots & \cdots & \cdots & \cdots \\ \cdots & \cdots & \cdots & \cdots & \cdots & \cdots \\ x_{m1} & x_{m2} & \cdots & x_{m3} & \cdots & x_{mn} \end{bmatrix} \quad \textbf{(1)}$$

Where $x_{ij}(= (a_{ij}, b_{ij}, c_{ij}))$ is a fuzzy number corresponding to the linguistic term assigned for the ith Alternative (DM) to the jth factor. $i = 1,2, \ldots \ldots \ldots, m$ are the number of alternatives and $j = 1,2, \ldots \ldots \ldots, n$ are the number of criteria.

Step 3: This step involves neutralizing the weights of the decision matrix and generating fuzzy un-weighted matrix (R).

To generate R, following relationship can be applied.

$$R = [r_{ij}]_{mXn}\ , r_{ij} = \left(\frac{a_{ij}}{c_j^*}, \frac{b_{ij}}{c_j^*}, \frac{c_{ij}}{c_j^*}\right) \quad (2)$$

© Emerald Group Publishing Limited
This is a pre-print of a paper and is subject to change before publication. This pre-print is made available with the understanding that it will not be reproduced or stored in a retrieval system without the permission of Emerald Group Publishing Limited.

Where $c_j^* = \max_i c$

Step 4: Calculate the weighted normalized decision matrix.

$$V = [v_{ij}]_{mXn};\ i = 1,2,\ldots\ldots\ m;\ j = 1,2,\ldots\ldots\ n \tag{3}$$

The weighted normalized value v_{ij} is calculated as

$$v_{ij} = r_{ij} * w_j; \tag{4}$$

where $w_j\ (j\ \epsilon\ n)$ is the weight of jth criteria as calculated in first part of approach by using AHP.

Step 5: Determine the ideal and negative ideal solution.

$$A^* = \{v_1^*, v_2^*, \ldots\ldots v_n^*\} \tag{5.1}$$

$$A^- = \{v_1^-, v_2^-, \ldots\ldots v_n^-\} \tag{5.2}$$

Since the positive and negative ideals are used for the research, the following terms are used for ideal and negative ideal solution.

$$v_j^* = (1,1,1) \tag{6.1}$$

$$v_j^- = (0,0,0) \tag{6.2}$$

Step 6: Calculate the sum of distances from positive and negative ideal solution for each factor.

$$D_j^* = \sum_{i=1}^{m} d(v_{ij} - v_i^*) \quad j = 1,2,\ldots\ldots n \tag{7.1}$$

$d(v_{ij} - v_i^*)$ is the distance between two fuzzy numbers which can be calculated by using the vector algebra. For example distance between two numbers $A1(a_1, b_1, c_1)\ and\ A2(a_2, b_2, c_2)$ can be calculated as

$$d(A1 - A2) = \sqrt{\frac{1}{3}[(a_2 - a_1)^2 + (b_2 - b_1)^2 + (c_2 - c_1)^2]}$$

© Emerald Group Publishing Limited
This is a pre-print of a paper and is subject to change before publication. This pre-print is made available with the understanding that it will not be reproduced or stored in a retrieval system without the permission of Emerald Group Publishing Limited.

Similarly, the separation from the negative ideal solution is given as

$$D_j^- = \sum_{i=1}^{m} d(v_{ij} - v_i^-), \quad j = 1,2,.....n \tag{7.2}$$

Step 7: Calculate the relative closeness to the ideal solution. The relative closeness with respect to A* is defined as

$$C_j = D_j^* / (D_j^* + D_j^-), \; j = 1,2,.....n \tag{8}$$

Step 8: Rank the preference order based on the order of the values of C_j

4. Case Illustration

AHP-Fuzzy TOPSIS approach is applied to a real life problem in an electronic firm, ABC Limited located in the NCR of Delhi, India. The Firm is among leading cell phone manufacturers in India and willing to put into practice the reverse logistics operations. The firm has nationwide network of more than 1700 dealers and 400 distributors, 18 branch offices and 110 customer care centers. The data for the selection criteria were collected through direct questions. The following steps were followed to develop a disposition decision making model for the firm.

4.1 Model the Problem as a hierarchy

The problem is structured into the three levels of the hierarchy as shown in figure 3. The objective of the problem is shown at the top most level of the hierarchy. The second level defines the criteria in reference to the top level. The third level of the hierarchy represents the alternatives. Top level "disposition alternative selection" represents the overall objective or goal of the problem. The second level indicates the criteria (economic benefits, environmental benefits, corporate social responsibility, stake holder's needs, reverse logistics resources) on which top level goal is to be decided. These criteria were identified through the discussion with the experts and past literature review as discussed above. The bottom level denotes the number of alternatives including recycling, reuse, remanufacturing, repairing, and disposal.

© Emerald Group Publishing Limited
This is a pre-print of a paper and is subject to change before publication. This pre-print is made available with the understanding that it will not be reproduced or stored in a retrieval system without the permission of Emerald Group Publishing Limited.

[Insert figure 3 here]

4.2 Construct a pair wise comparison matrix

After the construction of level of hierarchy, the pair wise comparison matrix is formed for each level of criteria. A panel of five experts, having substantial industry experience was formed to compare the criteria for pair wise comparison. Experts were asked to compare each of the criteria with other criteria and rate them on a 9-point scale shown in table 1 and discussed in section 3.1. Subsequent AHP approach steps were followed and the weights for all the criteria were calculated and are shown in table 4. Economic benefits have maximum weight (0.494) among all selected criteria which means the firm is more inclined towards financial benefits in comparison to other criteria. Environmental benefits and corporate social responsibility are next two higher weight criteria. Stake holder's need has lower weight comparatively. Reverse logistics resources has minimum weight which indicates the insufficiency of reverse logistics resources in the firm.

[Insert Table 4 here]

4.3 Test the Consistency by calculating the Eigen Vectors

Random Index was determined and with the help of RI, Consistency Index was determined. Since the Consistency Ratio obtained is less than 0.1, the matrix is accepted. The weights are consistent and they are used in the selection process.

λ_{max}	6.51
CI	0.087
RI	1.11
CR	0.0784

4. 4 Decide the order of preference using Fuzzy-TOPSIS

© Emerald Group Publishing Limited
This is a pre-print of a paper and is subject to change before publication. This pre-print is made available with the understanding that it will not be reproduced or stored in a retrieval system without the permission of Emerald Group Publishing Limited.

Experts were asked to compare the five disposition alternative on a 5-point scale shown in table 3. Responses were obtained from the experts in linguistic terms as discussed in step 1 in section 3.2. These responses were converted into the fuzzy numbers by using table 3. The responses obtained from the decision makers are represented in fuzzy evaluation matrix, table 5. The weights for criteria, obtained from the AHP method are also shown in fuzzy evaluation matrix.

[Insert Table 5 here]

Weighted fuzzy evaluation matrix is obtained by using fuzzy evaluation matrix, equation 2, equation 3 and equation 4 as discussed in step 2, 3 and 4 of the fuzzy TOPSIS approach. Weighted fuzzy evaluation matrix is shown in table 6.

[Insert Table 6 here]

Subsequent steps of fuzzy-TOPSIS approach were followed and orders of preferences for various disposition alternatives were determined as shown in table 7. The equation 5.1, 5.2 and equation 6.1, 6.2 were used for determining the distance from positive ideal solution and from negative ideal solution and are shown in table 7. The values of C_j were obtained by using equation 7 and final ranking is done based on these values.

[Insert Table 7 here]

The value of closeness coefficient indicates the rank. The higher value represents the better ranking. Hence the alternatives are ranked in the order of Repairing (0.874) > Reuse (0.870) > Recycling (0.864) > Disposal (0.844) > Remanufacturing (0.837). The firm should disposition the returned mobile phones for repairing or reuse if possible, in current business scenario of the firm. Otherwise the firm may prefer recycle them rather than disposal or remanufacturing. Manager of the firm may gain information about disposition in reverse logistics for mobile phones. It is evident from the results that remanufacturing is not viable option for the firm. The

© Emerald Group Publishing Limited
This is a pre-print of a paper and is subject to change before publication. This pre-print is made available with the understanding that it will not be reproduced or stored in a retrieval system without the permission of Emerald Group Publishing Limited.

study may be used by the managers to relook into the remanufacturing as disposition option for returned mobile phones.

5. Conclusion

Globalization, fast depletion of resources, environmental concern, and government regulation results in both pressure and drivers for the companies to implement reverse logistics. Reverse logistics is the process of collection, inspection and sorting, disposition, reusing, remanufacturing recycling, or disposal of returned / used products from the end user to the manufacturer for the purpose of economic, environmental, and social benefits. Disposition of returned products appropriately is important for gaining these benefits from reverse logistics. Since economical criteria are also involved in the study, the disposition strategy may be important task for any industry. The question is that which disposition alternative, the industries will be able to adopt for the returned product and process them efficiently. There is no study found answering this challenging question. A combination of AHP and Fuzzy-TOPSIS approach is proposed for the selection of best disposition alternative. The problem has been defined as a MCDM approach under uncertainty dealing with imprecise judgments from decision makers. A numerical example of an Indian electronic firm is utilized for the purpose of demonstration of the approach. Five criteria economic benefits, environmental benefits, corporate social responsibility, stake holder's needs, reverse logistics resources were considered for the selection of best disposition alternative among recycling, reuse, remanufacturing, repairing, disposal. A combination of AHP and fuzzy-TOPSIS was applied in which repairing is found to be first disposition preference for the given case. The second alternative, suggested is reuse, if possible. Recycling must be preferred over remanufacturing even if low recapturing value. Recycling is preferred because remanufacturing is not cost effective and resale of used mobile phones is also not encouraging for the firm. Disposal is preferred over remanufacturing but environmental concerns are there. The disposition decision will help the firm in improving the overall reverse logistic performance. The study may help the managers in disposition decision making by utilizing the proposed approach for the selection of best disposition alternative. Although, findings from the study cannot be generalized as it is just illustration of an approach. Further study may be carried out based on survey based data and more case studies to validate the findings. In future, research may be also carried out by combining AHP with other MCDM

© Emerald Group Publishing Limited
This is a pre-print of a paper and is subject to change before publication. This pre-print is made available with the understanding that it will not be reproduced or stored in a retrieval system without the permission of Emerald Group Publishing Limited.

approach to confirm the robustness of model. Also, Cost benefit analysis along with other factors discussed above may be carried out further strengthening the outcome of the study.

Acknowledgements

We would like to express our special gratitude and thanks to industry persons for giving us such attention and time.

References

1. Agrawal, S., Singh, R.K. and Murtaza, Q. (2014), "Forecasting product returns for recycling in Indian electronics industry", *Journal of Advances in Management Research,* Vol. 11 No. 1, pp. 102-114.
2. Andel, T. (1997), "Reverse logistics: A second chance to profit", *Transportation and Distribution,* Vol. 38 No. 7, pp. 61–64.
3. Atasu, A., Toktay, L.B. and Van Wassenhove, L.N. (2013), "How collection cost structure drives a manufacturer's reverse channel choice", *Production and Operations Management,* Vol. 22 No. 5, pp. 1089-1102.
4. Barker, T.J. and Zabinsky, Z.B. (2011), "A multi criteria decision making model for reverse logistics using analytical hierarchy process", *Omega,* Vol. 39 No. 5, pp. 558-573.
5. Bhatti, R.S., Kumar, P. and Kumar, D. (2010), "Analytical modeling of third party service provider selection in lead logistics provider environments", Journal of Modelling in Management, Vol. 5 No. 3, pp. 275-286.
6. Blackburn, J.D., Guide, Jr. V.D.R., Souza, G.C. and Wassenhove, L.N.W. (2004), "Reverse supply chains for commercial returns"' *California Management Review,* Vol. 46 No. 2, pp. 6-22.
7. Bowen, F.E., Cousins, P.D., Lamming, R.C. and Faruk, A.C. (2001), "The role of supply chain management capabilities in green supply", *Production and Operations Management,* Vol. 10 No. 2, pp. 174-89.
8. Carter, C.R. and Easton, P.L. (2011), "Sustainable supply chain management: evolution and future directions", *International Journal of Physical Distribution and Logistics Management,* Vol. 41 No. 1, 46-62.

© Emerald Group Publishing Limited
This is a pre-print of a paper and is subject to change before publication. This pre-print is made available with the understanding that it will not be reproduced or stored in a retrieval system without the permission of Emerald Group Publishing Limited.

9. Carter, C.R. and Ellram, L.M. (1998), "Reverse logistics: a review of the literature and framework for future investigation", *Journal of Business Logistics,* Vol. 19 No. 1, pp. 85-102.
10. Carter, C.R. and Rogers, D.S. (2008), "A framework of sustainable supply chain management: moving toward new theory", *International Journal of Physical Distribution and Logistics Management,* Vol. 28 No. 5, pp. 360-87.
11. Chen, C.T. (1997), "Extensions of the TOPSIS for group decision-making under fuzzy environment", *Fuzzy Sets and Systems,* Vol. 114, pp. 1-9.
12. Dekker, R., Bloemhof, J. and Mallidis, I. (2012), "Operations Research for green logistics – An overview of aspects, issues, contributions and challenges", *European Journal of Operational Research,* Vol. 219 No. 3, pp. 671-679.
13. Dowlatshahi S. (2005), "A strategic framework for the design and implementation of remanufacturing operations in reverse logistics", *International Journal of Production Research,* Vol. 43 No. 16, pp. 3455-80.
14. Fleischmann, M. *et al.* (1997), "Quantitative models for reverse logistics: a review", *European Journal of Operational research,* Vol. 103 No. 1, pp. 1-17.
15. Fleischmann, M., *et al.* (2000), "A characterization of logistics networks for product recovery", *Omega,* Vol. 28 No. 6, pp. 653-666.
16. Fleischmann, M., Van Nunen, J.A.E.E. and Grave, B. (2003), "Integrating closed-loop supply chains and spare parts management at IBM", *Interfaces,* Vol. 33 No. 6, pp. 44-56.
17. Garg, R. Rahman, Z., Qureshi, M.N. and Kumar, I. (2012) "Identifying and ranking critical success factors of customer experience in banks: An analytic hierarchy process (AHP) approach", *Journal of Modelling in Management,* Vol. 7 No. 2, pp. 201-220.
18. Gobbi, C. (2011), "Designing the Reverse Supply Chain: the impact of the product residual value", *International Journal of Physical Distribution and Logistics Management,* Vol. 41 No. 8, pp. 768-796.
19. Guide, V. D. R. and Wassenhove, L. N. (2003), *Full cycle supply chains,* Carnegie Mellon Press, Pittsburgh, PA.
20. Guide, Jr. V.D.R., Gunes, E.D., Souza, G.C. and VanWassenhove L.N. (2008), "The optimal disposition decision for product returns", *Operations Management Research,* Vol. 1 No. 1, pp. 6-14.

© Emerald Group Publishing Limited
This is a pre-print of a paper and is subject to change before publication. This pre-print is made available with the understanding that it will not be reproduced or stored in a retrieval system without the permission of Emerald Group Publishing Limited.

21. Gumus, A. T. (2009), "Evaluation of hazardous waste transportation firms by using a two step fuzzy-AHP and TOPSIS methodology", *Expert Systems with Applications,* Vol. 36, pp. 4067-4074.
22. Hall, J. (2001), "Environmental supply chain innovation", *Greener Management International,* No. 35, pp. 105-119.
23. Hazen, B. T. (2011), "Strategic reverse logistics disposition decisions: from theory to practice", *International Journal of Logistics Systems and Management,* Vol. 10 No. 10, pp. 275-292.
24. Hwang C.L. and Yoon K. (1981), *Multiple attribute decision making: methods and applications*, Springer, Verlag, Berlin.
25. Janes, B., Schuur, P. and Brito, De, M.P. (2009), "A reverse logistics diagnostic tool: the case of the consumer electronics industry", *The International Journal of Advanced Manufacturing Technology,* Vol. 47, pp. 495-513.
26. Jayaraman, V., Patterson, R.A. and Rolland, E. (2003), "The design of reverse distribution networks: Models and solution procedures", *European Journal of Operational Research,* Vol. 150, pp. 128-149.
27. Kannan, G., Pokharel, S. and Sasikumar, P. (2009), "A hybrid approach using ISM and fuzzy TOPSIS for the selection of reverse logistics provider", *Resources, Conservation and Recycling,* Vol. 54 No. 1, pp. 28-36.
28. Karamouzian, A., Jalali-Naini, S.G.H. and Mahdavi-Mazdeh, M. (2014), "Management of returned products to a remanufacturing facility considering arrival uncertainty and priority processing", *International Journal of Operational Research,* Vol. 20, pp. 331-340.
29. Kim, G., Park, C.S. and Yoon, K.P. (1997), "Identifying investment opportunities for advanced manufacturing systems with comparative-integrated performance measurement", *International Journal of Production Economics,* Vol. 50 No. 1, pp. 23-33.
30. Knemeyer, A.M., Ponzurick, T.G. and Logar, C.M. (2002), "A qualitative examination of factors affecting reverse logistics systems for end-of-life computers", *International Journal of Physical Distribution and Logistics Management,* Vol. 32 No. 6, pp. 455-79.
31. Kopicki, R., Berg, M., Legg, L., Dasappa, V. and Maggioni, C. (1993), *Reuse and recycling: Reverse logistics opportunities*, Oak Brook: Council of Logistics Management.

© Emerald Group Publishing Limited
This is a pre-print of a paper and is subject to change before publication. This pre-print is made available with the understanding that it will not be reproduced or stored in a retrieval system without the permission of Emerald Group Publishing Limited.

32. Krikke, H.R., Bloemhof-Ruwaard, J. and Van Wassenhove, L.N. (2003), "Concurrent product and closed-loop supply chain design with an application to refrigerators", *International Journal of Production Research,* Vol. 41 No. 16, pp. 3689-3719.
33. Kumar, S. and Putnam, V. (2008), "Cradle to cradle: Reverse logistics strategies and opportunities across three industry sectors", *International Journal Production Economics,* Vol. 115, pp. 305-315.
34. Prascevic, Z. and Prascevic, N. (2013), "One modification of fuzzy TOPSIS method", *Journal of Modelling in Management,* Vol. 8 No. 1, pp. 81-102.
35. Kumar, P. and Singh, R.K. (2012), "A fuzzy AHP and TOPSIS methodology to evaluate 3PL in a supply chain", *Journal of Modelling in Management,* Vol. 7 No. 3, pp. 287-303.
36. Lamming, R. and Hampson, J. (1996), "The environment as a supply chain management issue", *British Journal of Management,* Vol. 7 (Special issue), S45-S62.
37. Markley, M.J. and Davis, L. (2007), "Exploring future competitive advantage through sustainable supply chains", *International Journal of Physical Distribution and Logistics Management,* Vol. 37 No. 9, pp. 763-74.
38. Murphy, P. and Poist, R. (2003), "Green perspectives and practices: a comparative logistics study", Supply Chain Management: An International Journal, Vol. 8 No. 2, pp. 122-131.
39. Narayana, S.A., Elias, A.A. and Pati, R.K. (2014), "Reverse logistics in the pharmaceuticals industry: a systemic analysis", *The International Journal of Logistics Management,* Vol. 25 No. 2, pp. 379-398.
40. Onut, S., and Soner, S. (2008), "Transshipment site selection using the AHP and TOPSIS approaches under fuzzy environment", *Waste Management,* Vol. 28, pp. 1552-1559.
41. Pochampally, K. and Gupta S.M. (2004), "A business mapping approach to multi-criteria group selection of collection centers and recovery facilities", *Proceedings of the 2004 IEEE International Symposium on Electronics and the Environment*, pp. 249-254.
42. Ravi, V., Shankar, R. and Tiwari, M.K. (2005), "Productivity improvement of a computer hardware supply chain", *International Journal of Productivity and Performance Management,* Vol. 54 No. 4, pp. 239-255.
43. Rogers, D.S. and Tibben-Lembke, R. (1999), *Going backwards: reverse logistics trends and practices,* Reno, NV: Reverse Logistics Executive Council.

© Emerald Group Publishing Limited
This is a pre-print of a paper and is subject to change before publication. This pre-print is made available with the understanding that it will not be reproduced or stored in a retrieval system without the permission of Emerald Group Publishing Limited.

44. Saaty T.L. (2000), *Fundamentals of decision making and Priority Theory,* 2nd ed. Pittsburgh PA: RWS Publications.
45. Saaty, T.L. (1980), *The Analytical Hierarchy Process,* McGraw-Hill, New York, NY.
46. Shamah, Rania AM. (2012), "Innovation within green service supply chains for a value creation", *Journal of Modelling in Management*, Vol. 7 No. 3, pp. 357-374.
47. Sarkis, J., Helms, M.M., Hervani, A.A. (2010), "Reverse logistics and social sustainability", *Corporate Social Responsibility and Environmental Management*, Vol. 17 No. 6, pp. 337-354.
48. Senthil, S., Srirangacharyulu, B. and Ramesh, A. (2012), "A decision making methodology for the selection of reverse logistics operating cshannels", *Procedia Engineering,* Vol. 38, pp. 418-428.
49. Senthil, S., Srirangacharyulu, B. and Ramesh, A. (2014), "A robust hybrid multi-criteria decision making methodology for contractor evaluation and selection in third-party reverse logistics", *Expert Systems with Applications,* Vol. 41 No. 1, pp. 50-58.
50. Skinner, L.R., Bryant, P.T. and Richey, R.G. (2008), "Examining the impact of reverse logistics disposition strategies", *International Journal of Physical Distribution and Logistics Management,* Vol. 38 No. 7, pp. 518-539.
51. Stock, J.R., (2001), "The 7 deadly sins of reverse logistics", *Material Handling Management,* Vol. 56 No. 3, pp. 5-11.
52. Subramanian, N., Gunasekaran, A., Abdulrahman, A. and Liu, C. (2014), "Factors for implementing end-of-life product reverse logistics in the Chinese manufacturing sector", *International Journal of Sustainable Development and World Ecology,* Vol. 21 No. 3, pp. 235-245.
53. Tan, A.W.K. and Kumar, A. (2006), "A decision-making model for reverse logistics in the computer industry", *The International Journal of Logistics Management,* Vol. 17 No. 3, pp. 331-354.
54. Thierry, M., *et al.* (1995), "Strategic issues in product recovery management", *California Management Review,* Vol. 37 No. 2, pp. 114-135.
55. Triantaphyllou, E. (2000), *Multi-criteria decision making methods: a comparative study*, Kluwer Academic Publishers, Dordrecht.

© Emerald Group Publishing Limited
This is a pre-print of a paper and is subject to change before publication. This pre-print is made available with the understanding that it will not be reproduced or stored in a retrieval system without the permission of Emerald Group Publishing Limited.

56. Wadhwa, S., Madaan, J. and Chan, F.T.S. (2009), "Flexible decision modeling of reverse logistics system: a value adding MCDM approach for alternative selection", *Robotics and Computer-Integrated manufacturing,* Vol. 25 No. 2, pp. 460-469.
57. Wu, C.J. and Cheng, W.P. (2006), "Reverse logistics in the publishing industry: China, Hong Kong, and Taiwan", *International Journal of Physical Distribution and Logistics Management,* Vol. 36 No. 7, pp. 507-523.
58. Zadeh, L.A. (1965), "Fuzzy sets", *Information and Control,* Vol. 8, pp. 338-353.

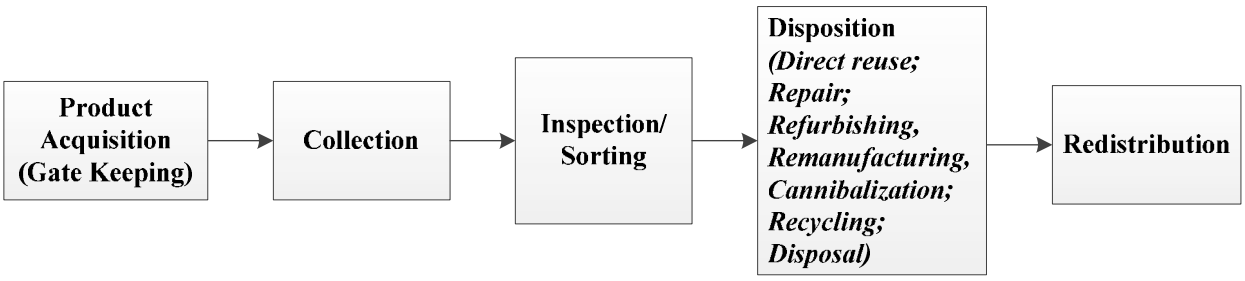


Figure 1: Basic flows of reverse supply chain

© Emerald Group Publishing Limited
This is a pre-print of a paper and is subject to change before publication. This pre-print is made available with the understanding that it will not be reproduced or stored in a retrieval system without the permission of Emerald Group Publishing Limited.

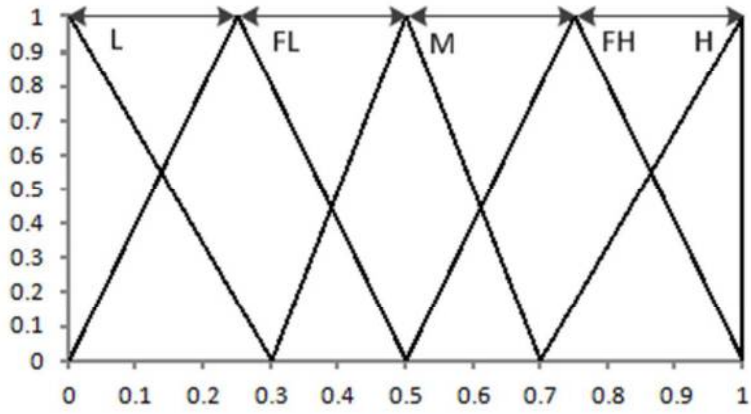


Figure 2: Linguistics scales and triangular fuzzy numbers

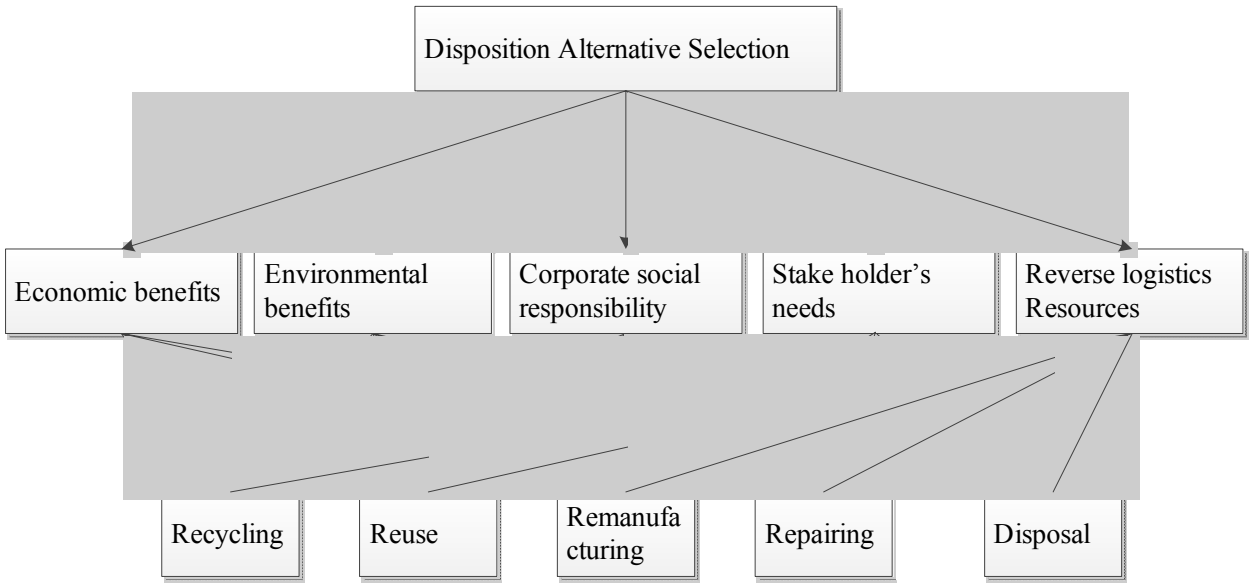


Figure 3. Level of hierarchy for the selection of reverse logistics disposition alternatives

About the Authors

© Emerald Group Publishing Limited
This is a pre-print of a paper and is subject to change before publication. This pre-print is made available with the understanding that it will not be reproduced or stored in a retrieval system without the permission of Emerald Group Publishing Limited.

Saurabh Agrawal is an Assistant Professor in Mechanical, Production & Industrial Engineering Department at Delhi Technological University, Delhi, India. He has vast experience of academics, research and the industry both in India and in USA. His research focus is in the areas of supply chain management, reverse logistics, sustainability and e-waste management. He received his Master of Business Administration (MBA) from Oregon State University, USA; Master in Technology (M.Tech) from Indian Institute of Technology (IIT), Delhi, India; Bachelor of Engineering (B.E.) from Indian Institute of Technology (IIT), Roorkee, India. Saurabh Agrawal is the corresponding author and can be contacted at: agrawals.iit@gmail.com

Dr. Rajesh Kr. Singh is Professor in Operations area at Management Development Institute, Gurgaon, India. Before moving to MDI, Gurgaon, he has also worked at Delhi Technological University, Delhi. His areas of interest include Supply Chain Management, Small Business Management and Quality Management. He has published around 125 research papers in reputed international/national journals and conferences. His papers have appeared in journals such as Production Planning and Control, Journal of Industrial and Production Engg, Industrial management and Data Systems, Singapore Management Review, International Journal of Productivity and Performance Management, Benchmarking: An International Journal, Journal of Modelling in Management, Competitiveness Review, Global Journal of Flexible Systems and Management, Journal of Advances in Management Research, International Journals of Productivity and Quality Management, International Journal of Services and Operations Management, Management Research Review, IIMB Management Review etc.

Dr. Qasim Murtaza received his doctorate in Manufacturing Engineering from Dublin City University, Dublin, Ireland and is presently working as Associate Professor (Production Engg) with Delhi Technological University (formerly Delhi College of Engineering), Delhi India.. He has published his research work in reputed journals and attended several international conferences.

© Emerald Group Publishing Limited
This is a pre-print of a paper and is subject to change before publication. This pre-print is made available with the understanding that it will not be reproduced or stored in a retrieval system without the permission of Emerald Group Publishing Limited.

Table 1. Scale of Preference (Source: Saaty, 1980)

Preference weights	Definition	Explanation
1	Equally important	Two attributes make equal contribution
3	Moderate	one activity is slightly favored over another activity
5	Strong	one activity is strongly favored over another activity
7	Very Strong	one activity is very strongly favored over another activity
9	Extreme	The verification favoring one activity over another is of the maximum possible order of confirmation
2,4,6,8	Intermediate Values	When conciliation is needed
Reciprocals	Reciprocals for opposite evaluation	

Table 2. Average value of Random Index

Attributes	1	2	3	4	5	6	7	8	9	10
Random Index (RI)	0	0	0.52	0.39	1.11	1.25	1.35	1.40	1.45	1.49

Table 3. Linguistic terms and fuzzy numbers

Linguistic term	Fuzzy Number
Low	(0.0,0.1,0.3)
Fairly Low	(0.1,0.3,0.5)
Medium	(0.3,0.5,0.7)
Fairly High	(0.5,0.7,0.9)
High	(0.7,0.9,1.0)

© Emerald Group Publishing Limited
This is a pre-print of a paper and is subject to change before publication. This pre-print is made available with the understanding that it will not be reproduced or stored in a retrieval system without the permission of Emerald Group Publishing Limited.

Table 4. Pair wise comparison of all criteria

Criteria	C 1	C 2	C 3	C 4	C 5	Weight
Economic benefits (C 1)	1	6	5	3	7	0.494
Environmental benefits (C 2)	1/6	1	1/4	2	2	0.118
Corporate social responsibility (C 3)	1/5	4	1	2	5	0.224
Stake holder's needs (C 4)	1/3	1/2	1/2	1	2	0.108
Reverse logistics Resources (C 5)	1/7	1/2	1/5	1/2	1	0.056

Table 5. Fuzzy evaluation matrix

	C1	C2	C3	C4	C5
Recycling	FH (0.5,0.7,0.9)	FH (0.5,0.7,0.9)	M (0.3,0.5,0.7)	H (0.7,0.9,1.0)	M (0.3,0.5,0.7)
Reuse	FH (0.5,0.7,0.9)	FH (0.5,0.7,0.9)	M (0.3,0.5,0.7)	M (0.3,0.5,0.7)	FH (0.5,0.7,0.9)
Remanufacturin	H (0.7,0.9,1.0)	H (0.7,0.9,1.0)	H (0.7,0.9,1.0)	M (0.3,0.5,0.7)	M (0.3,0.5,0.7)
Repairing	FH (0.5,0.7,0.9)	M (0.3,0.5,0.7)	M (0.3,0.5,0.7)	M (0.3,0.5,0.7)	M (0.3,0.5,0.7)
Disposal	H (0.7,0.9,1.0)	FH (0.5,0.7,0.9)	H (0.7,0.9,1.0)	H (0.7,0.9,1.0)	H (0.7,0.9,1.0)
Weight	0.494	0.118	0.224	0.108	0.056

Table 6. Weighted fuzzy evaluation matrix

	C1	C2	C3	C4	C5
Recycling	(0.247,0.346,0.445)	(0.059,0.083,0.106)	(0.067,0.112,0.157)	(0.076,0.097,0.108)	(0.017,0.028,0.039)
Reuse	(0.247,0.346,0.445)	(0.059,0.083,0.106)	(0.067,0.112,0.157)	(0.032,0.054,0.076)	(0.028,0.039,0.050)
Remanufacturing	(0.346,0.445,0.494)	(0.083,0.106,0.118)	(0.157,0.202,0.224)	(0.032,0.054,0.076)	(0.017,0.028,0.039)
Repairing	(0.247,0.346,0.445)	(0.035,0.059,0.106)	(0.067,0.112,0.157)	(0.032,0.054,0.076)	(0.017,0.028,0.039)
Disposal	(0.346,0.445,0.494)	(0.059,0.083,0.106)	(0.157,0.202,0.224)	(0.076,0.097,0.108)	(0.039,0.050,056)

Table 7. Distances to ideal solution and overall value

Alternatives	D_j^*	D_j^*	C_j	Ranking
Recycling	4.344	0.682	0.864	3
Reuse	4.372	0.655	0.870	2
Remanufacturing	4.197	0.819	0.837	5
Repairing	4.400	0.632	0.874	1
Disposal	4.237	0.783	0.844	4

© Emerald Group Publishing Limited
This is a pre-print of a paper and is subject to change before publication. This pre-print is made available with the understanding that it will not be reproduced or stored in a retrieval system without the permission of Emerald Group Publishing Limited.

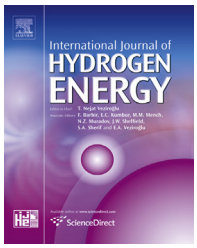
INTERNATIONAL JOURNAL OF HYDROGEN ENERGY XXX (2016) 1–7



Available online at www.sciencedirect.com

ScienceDirect

journal homepage: www.elsevier.com/locate/he



Effect of low pressure hydrogen environment on crystallographic properties of PdO nanoparticles

*Kamal Arora, Deepika Sandil, Gaurav Sharma, Saurabh Srivastava, Nitin K. Puri**

Advanced Sensor Laboratory, Department of Applied Physics, Delhi Technological University, Main Bawana Road, Shahbad Daulatpur, Delhi, 110042, India

ARTICLE INFO

Article history:
Received 16 June 2016
Received in revised form
6 September 2016
Accepted 7 September 2016
Available online xxx

Keywords:
In-situ X-ray
Palladium oxide
Palladium hydride
Low pressure
Hydrogen sensing

ABSTRACT

Palladium oxide (PdO) nanoparticles (~20–130 nm) are synthesized using sol–gel method. The crystal structure of PdO is determined using X-ray diffraction (XRD) whereas surface morphology, shape and size of PdO nanoparticles are analyzed using scanning electron microscopy and transmission electron microscopy. The optical band gap is estimated as 1.8 eV using UV–Vis spectroscopy. The effect of hydrogen gas at low pressure (25, 50, 75 and 100 mbar) on palladium oxide nanoparticle is studied using In-situ X-ray diffraction at room temperature. It is found that face centered cubic (fcc) palladium hydride (PdH_x) crystal structure is formed and the intensity of peaks representing tetragonal PdO (t-PdO) crystal structure almost vanished as the pressure increased to 100 mbar. Also, it is found that the value of lattice constant increased significantly, when the pressure becomes equivalent to 100 mbar due to phase transition (α-β) in PdH_x lattice. It shows that PdO nanoparticles can be used for storage and sensing of hydrogen gas at ambient atmosphere.

© 2016 Hydrogen Energy Publications LLC. Published by Elsevier Ltd. All rights reserved.

Introduction

Hydrogen gas is the lightest, odorless and colorless gas having calorific value three times greater than that of carbon based fuel [1]. These properties makes it best candidate to be used as fuel or energy source in various applications. At present, hydrogen is being used in nuclear reactors, fuel cells and space industries. It is difficult to store hydrogen as it can permeate through materials easily; Furthermore, hydrogen gas becomes flammable and explosive if its concentration becomes greater than 4 percent within the atmosphere [2]. Thus, monitoring and sensing of hydrogen gas in the area of its application is of prime importance.

Detection of hydrogen gas leak through human sensory organs is not possible because it is colorless and odorless in nature. There are various types of sensors on the basis of sensing mechanism. Metal oxide resistive type sensor has gained wide importance over others due to their high stability, selectivity, sensitivity and long life. A good amount of research work has been conducted over years on hydrogen sensing with various nanostructure metal oxides such as Tin oxide (SnO_2), Zinc oxide (ZnO), Tungsten oxide (WO_3), Nickel oxide (NiO), Vanadium oxide (VO_2), Copper oxide (CuO), Titanium oxide (TiO_2), Niobium oxide (Nb_2O_5) and Magnesium oxide (MgO) [3–11]. Nanostructures of these metal oxides show efficient hydrogen sensing characteristics than their bulk counterparts because they have high area to volume ratio, lower working temperature and doping of these metal oxides with suitable catalyst such as palladium (Pd), platinum (Pt) increased their sensitivity towards hydrogen [12]. Palladium doped metal oxide has been extensively explored for hydrogen sensing due

* *Corresponding author.*
E-mail address: nitin.phy@dce.edu (N.K. Puri).

http://dx.doi.org/10.1016/j.ijhydene.2016.09.040
0360-3199/© 2016 Hydrogen Energy Publications LLC. Published by Elsevier Ltd. All rights reserved.

Please cite this article in press as: Arora K, et al., Effect of low pressure hydrogen environment on crystallographic properties of PdO nanoparticles, International Journal of Hydrogen Energy (2016), http://dx.doi.org/10.1016/j.ijhydene.2016.09.040

to their high selectivity, low activation barrier, high diffusion coefficient & high adsorption coefficient for hydrogen gas [13].

Effects of hydrogen environment on pure Pd nanoparticles and nanoclusters have been studied extensively. It has been reported that Pd forms Palladium hydride (PdH_x) instantly due to high affinity of Pd towards hydrogen. When the hydrogen concentration (x) is low, $0.1 < x < 0.7$, a solid Pd–H solution known as α-phase PdH_x is formed, whereas for $x > 0.7$, hydride phase, known as β-phase comes into existence. Adsorption of hydrogen is maximum in α-phase as compared to hydrogen rich β-phase. There is a phase transition (α-β), as the hydrogen pressure increases which results in lattice expansion of PdH_x crystal structure. The storage of hydrogen in interstitial sites takes place at grain boundaries into subsurface region (0.7–1.1 nm) from surface and within the lattice depending on the concentration of hydrogen [14,15]. Pd readily reacts with hydrogen to form palladium hydride which results in an expansion of 6% in system lattice. The lattice coefficient increases linearly until the H/Pd ratio becomes equal to 0.7 and becomes constant thereafter [16]. In Pd–H system, hydrogen gets stored into octahedral interstitial voids within face centered cubic lattice of Pd [17]. Suleiman et al. showed that lattice expansion in β-phase PdH_x depends strongly on size of their nanostructures. The large Pd nanoclusters shows high lattice expansion in contrast to smaller nanoclusters which do not experience any expansion in their crystal structure and this data is in complete accordance with other types of Pd nanostructures too. Additionally, as the hydrogen pressure is increased from 18 mbar to 100 mbar, there is an abrupt lattice expansion from 3 Å to 4 Å at 100 mbar in large nanoclusters [18]. The difference between the lattice constant of α and β PdH_x crystal structure decreases as the Pd particle size decreases, i.e. lattice expansion reduces in smaller Pd nanoparticles [19]. Okazaki et al. showed that the annealed Pd crystal nanostructures have higher hydrogen adsorption permittivity in comparison to unannealed structures [20]. Baldi et al. studied the phase transition of individual Pd nanocrystals using Insitu electron energy loss spectroscopy and find it in good accordance with literature reported observations for group of Pd nanocrystals [21].

However, at low temperature and high hydrogen pressure, pure Pd gets damaged by hydrogen due to a phenomenon known as hydrogen embrittlement. Also, pure Pd gets irreversibly poisoned due to the poisoning by deposition of sulfur from sulfur containing gases present in the atmosphere [22]. On the other hand, PdO nanoparticles are less prone to these contaminations as they have high operating temperatures and are covered with the protective oxide layer [23]. Thus, palladium oxide (PdO) nanoparticles would be more favorable for sensing and storage of hydrogen than pure Pd.

Few research works has been reported regarding hydrogen sensing mechanism of PdO nanostructures thin film but PdO nanostructures has not been studied for its hydrogen storage characteristics. The first work is reported in 2010 by Lee et al. who studied PdO thin film grown by sol–gel method for hydrogen sensing application via resistive sensing mechanism and observed that it showed good efficiency for sensing 2% hydrogen gas at room temperature [24]. Chiang et al. investigated hydrogen gas sensing study of PdO nanoflakes thin film at temperatures below 250 °C, it is found that thin film showed good sensing behavior at temperature above 200 °C which accords with oxygen vacancy model [25].

Palladium oxide (PdO) converts irreversibly into Pd on reduction and can be used as active catalyst in various applications. The band gap of PdO is experimentally found to be equal to 1.5 eV using electrical conductivity measurements [26].

To the best of our knowledge, the effect of hydrogen environment on tetragonal palladium oxide (t-PdO) nanoparticles has not been explored before. We report the effect of low pressure (25, 50, 75 & 100 mbar) hydrogen gas on crystal structure and lattice constants of palladium oxide nanoparticles using In-situ X-ray diffraction study. Palladium oxide (PdO) nanoparticles are synthesized using simple and cost effective sol–gel method.

Experimental details

Sol–gel synthesis of PdO nanoparticles

All the procured chemicals belong to AR grade with purity of ~99.9%. 1.56 g of palladium chloride ($PdCl_2$) powder (procured from Fisher) is dissolved in 90 ml solution containing 40 ml Hydrochloric acid (HCl) and 50 ml Ethanol (C_2H_5OH) (procured from Sigma Aldrich). The molarity of final solution is calculated to be equal to 0.1 M. Initially, $PdCl_2$ is added to C_2H_5OH directly, but the powder could not dissolve in the solution. However, on addition of HCl, a clear brown solution is obtained. The following chemical formulas could be the possible explanation of complete reaction.

$$PdCl_2 + HCl \rightarrow PdCl_4 + HCl$$

$$PdCl_4 + C_2H_5OH \rightarrow Pd(OH)_2 + C_2H_5Cl + HCl$$

$$Pd(OH)_2 \rightarrow PdO$$

The final solution is kept for 24 h to complete the total reaction as a part of ageing process. The resultant brown colored solution is kept in oven at 80 °C for 24 h to obtain brown powder particles. The powder is divided into three samples 'a', 'b' & 'c', each annealed respectively at three different temperatures 600 °C, 800 °C & 1000 °C in tubular furnace. All three samples are analyzed to study their crystal structure, surface morphology, optical band gap and crystallographic changes in presence of hydrogen gas by characterizing them through X-ray diffraction experiment, scanning electron microscopy (SEM), Transmission electron microscopy (TEM), UV–Vis spectroscopy and In-situ X-ray diffraction experiment.

X-ray diffraction experiment (XRD)

Fig. 1(i–iii) shows XRD spectra of sample 'a', 'b' & 'c' respectively. On comparison of the intensity peaks with the published data (CAS number: 88-2434 & 88-2335), the corresponding peaks belongs to (002), (110), (112), (103), (200) and (202) planes, indicating the formation of tetragonal palladium oxide crystal structure (t-PdO). It can be seen that peaks

Please cite this article in press as: Arora K, et al., Effect of low pressure hydrogen environment on crystallographic properties of PdO nanoparticles, International Journal of Hydrogen Energy (2016), http://dx.doi.org/10.1016/j.ijhydene.2016.09.040

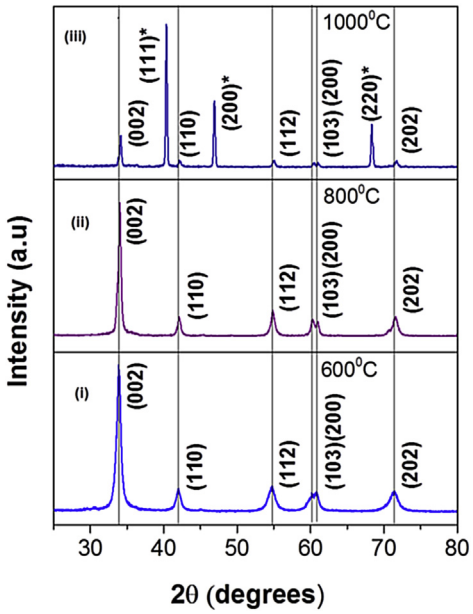


Fig. 1 – XRD spectra comparison of (i) sample 'a', (ii) sample 'b' & (iii) sample 'c'.

becomes narrower and shifted towards right side as temperature increased due to the increase in lattice parameters as a result of temperature induced strain. In Fig. 1(ii), the peaks are less broad and peak splitting is clearly visible in comparison to Fig. 1(i), which defines the good crystalline nature of sample b. Whereas in Fig. 1(iii), three additional peaks come into existence along with regular t-PdO characteristic peaks. Intense peak seen at 40° along with two new peaks arising at 46° and 68° defines (111)*, (200)* and (220)* planes respectively of face centered cubic (fcc) Pd crystal. Thus, t-PdO lattice starts to decompose into fcc Pd lattice as the temperature is raised from 800 °C to 1000 °C. Annealing at high temperature results in the formation of PdO crystal phase as the rate of formation of PdO is compatible with its rate of decomposition into Pd crystal [27]. The results obtained from XRD analysis are found to be in accord with the reported literature [20].

Using Debye Scherrer formula (Eq. (1)) [28], the crystallite size of tetragonal crystal structure was found to be equal to 24.02 nm.

$$D = \frac{0.9\lambda}{\beta \cos \theta} \quad (1)$$

where, D represent crystallite size, λ is wavelength, β is the FWHM (Full width half maxima) and θ is the angle having maximum intensity.

Scanning electron microscopy

Fig. 2(i–iii) represents the scanning electron micrographs of samples 'a', 'b' and 'c'. In Fig. 2(i), no defined particle boundaries can be seen in SEM images of sample 'a' due to agglomeration. In Fig. 2(ii) of sample 'b', particles with more defined particle boundaries are visible. Also, some voids on the surface can be observed in this image. Whereas, rod like crystalline pattern could be observed in SEM image of sample 'c' (Fig. 2(iii)), boundaries and individual particles are non-visible in this image. Thus, it is visible from SEM images, that sample 'a' has particles in nanometer range but no surface uniformity can be observed, whereas sample 'c' comprises non-uniform rod like structure on the surface. Comparatively, sample 'b' has better surface uniformity and distinguishable particle geometry.

UV–Vis spectroscopy

Fig. 3(i) denotes the UV–Vis transmission spectra of sample 'b', there is a strong absorption at 186 nm and gradually, transmission curve becomes constant and decays steadily with wavelength. Sample 'b' has a direct band gap of 1.84 eV, as visible in Fig. 3(ii) containing Tauc plot based on UV–Vis spectral analysis. Several research papers reported direct band gap of PdO to be equivalent to 2 eV [26]. Thus, our study fits the reported data approximately.

Transmission electron microscopy

Fig. 4 represents the Transmission electron microscopy (TEM) and Selected area electron diffraction (SAED) images of samples 'a', 'b', and 'c'. The SAED images show the various Bragg reflection planes of tetragonal palladium oxide which is calculated using relation of reciprocal lattice with interplanar spacing [29]. It can be seen in Fig. 4(i.a) that sample 'a' contains small particles which are grouped together to form clusters of size (20–50 nm). Fig. 4(ii.a) (SAED) shows amorphous nature of sample 'a', with a fainted ring formation due to reflection from highly Bragg reflection favored (101) plane. Fig. 4(i.b) denotes particle size in the range of 10–125 nm, but the respective SAED pattern (Fig. 4(ii.b)) reflects the pure crystalline nature of sample 'b' which is annealed at 800 °C and presence of t-PdO phase can be observed in this sample. The SAED image contains the ordered continuous ring as well as dot patterns due to the presence of single and poly-crystals respectively.

The presence of characteristics (101) plane of tetragonal PdO crystals complements the XRD spectra of the sample 'b'. Sample 'c' contains purely single crystal structure which can be observed in the SAED image (Fig. 4(ii.c)) that contains sporadic ring like structure formed by various dots. Also, it shows the additional peaks (200) & (220) of fcc Pd crystal structure along with (100) peak of t-PdO crystal, thus confirming the presence of both Pd and PdO nanoparticles in sample 'c'. The TEM image in Fig 4(i.c) shows the presence of agglomerated particles which are difficult to distinguish from one another and their size ranges from 20 to 50 nm. TEM also confirms the highly ordered and nano structured formation in sample 'b' along with the presence of interstitial sites which may aid in the adsorption of other atoms, thus sample 'b' would be more favorable for In-situ XRD studies due to its well defined surface morphology, composition as well as crystal structure among other samples.

Results and discussions

In-situ XRD measurements

PdO nanoparticles annealed at 800 °C (sample 'b') are introduced into In-situ XRD spectroscopy vacuum chamber in form of a

Please cite this article in press as: Arora K, et al., Effect of low pressure hydrogen environment on crystallographic properties of PdO nanoparticles, International Journal of Hydrogen Energy (2016), http://dx.doi.org/10.1016/j.ijhydene.2016.09.040

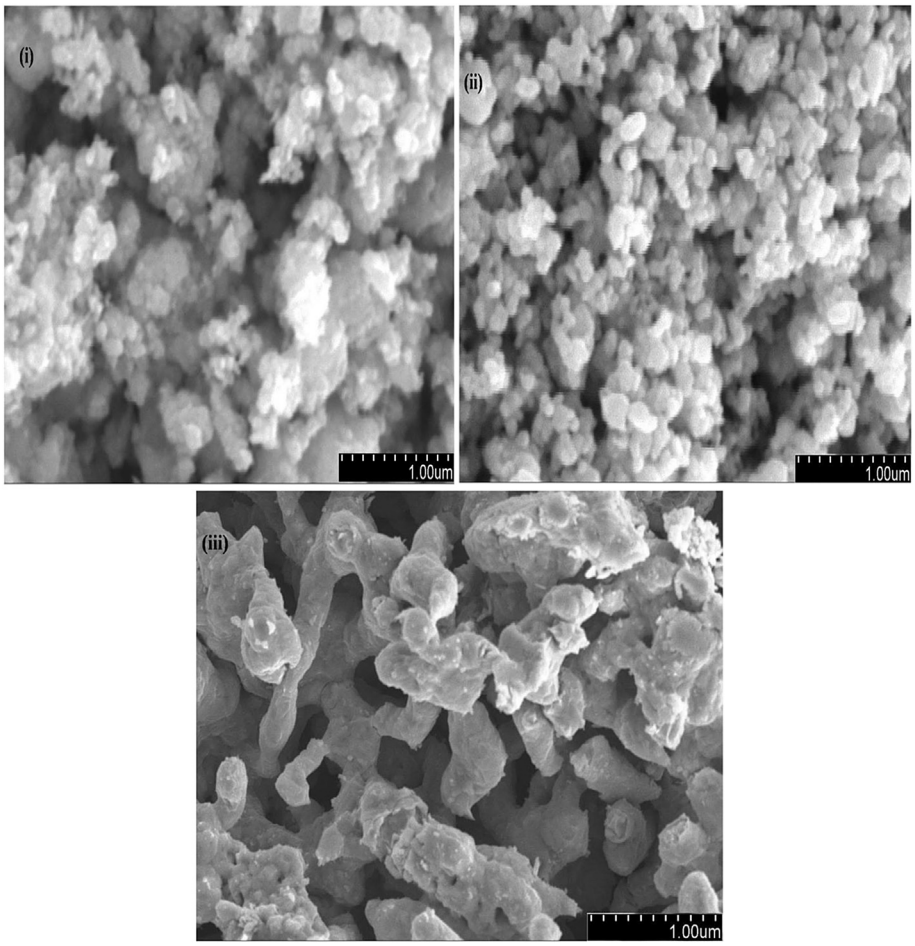


Fig. 2 – SEM images of (i) sample 'a', (ii) sample 'b', (iii) sample 'c'.

pellet. Hydrogen gas is introduced into the chamber at different pressures. When the hydrogen gas comes into contact with surface of PdO, the oxygen atoms are detached from the surface and form water molecules resulting in vacant sites for adsorption. These vacant sites are filled with hydrogen atoms. PdO has high affinity toward hydrogen as compared to water, thus hydrogen react with Pd on the surface to form Palladium hydride (PdH_x). As, the pressure increases, hydrogen gas absorbs inside the pellet and gets stored into the interstitial sites of PdO nanoparticles [30]. Fig. 5 represent In-situ XRD spectroscopy studies of sample 'b' with variable hydrogen gas environmental pressure (25, 50, 75, 100 mbar). In Fig. 5(i), the peaks present in this spectra correspond to same planes [(100), (002), (110), (112), (103), (200) & (202)], as observed in XRD spectra in presence of air, hence confirming the tetragonal crystal structure of sample 'b'. Fig. 5(ii) denotes the XRD spectra of sample 'b' in presence of

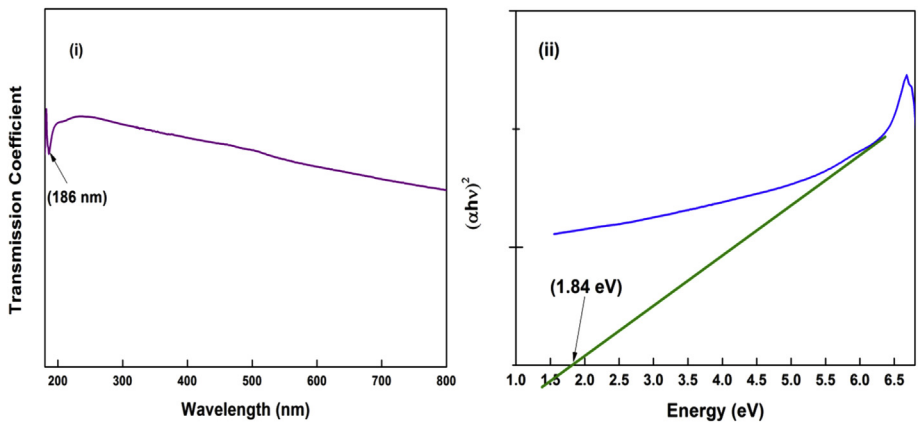


Fig. 3 – (i) UV–Vis transmission spectra and (ii) Band gap estimated from Tauc plot.

Please cite this article in press as: Arora K, et al., Effect of low pressure hydrogen environment on crystallographic properties of PdO nanoparticles, International Journal of Hydrogen Energy (2016), http://dx.doi.org/10.1016/j.ijhydene.2016.09.040

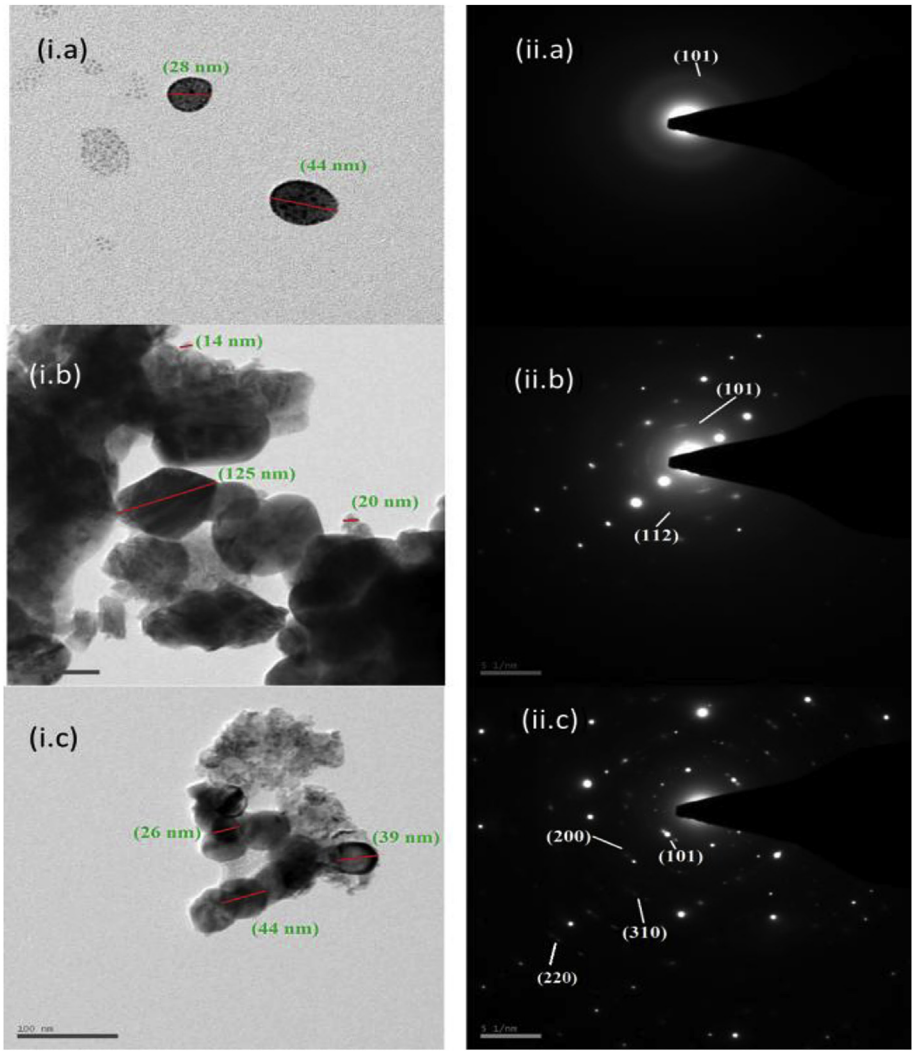


Fig. 4 – (i) TEM images, (ii) SAED images of Sample 'a', Sample 'b' and Sample 'c'.

hydrogen gas at 25 mbar pressure, new planes such as (111)*, (101)*, (110*), (200)* and (211)* along with palladium oxide crystal planes have been formed, describing the formation of face centered cubic (fcc) palladium hydride crystal structure along with tetragonal palladium oxide crystal structure. Whereas, at 50 mbar hydrogen pressure (Fig. 5(ii)), mixed planes of palladium oxide as well palladium hydrides are observed, but the intensity of peaks belonging to palladium oxide tetragonal structure planes has reduced significantly. On the other hand, intensity of peaks representing fcc palladium hydride structure planes has risen comprehensively.

As the pressure escalates from 50 mbar to 100 mbar, all the peaks corresponding t-PdO disappears, except (002) plane revealing that sample mainly consist of fcc PdH_x crystal structure.

Effect of H_2 pressure on lattice constants

In Fig. 6, the lattice parameters for t-PdO ($x = y \neq z$) lattice is calculated for different pressures, where x, y and z are longitudinal and transverse axis respectively [20]. It is observed that at 0 mbar pressure, the transverse axis (z) lattice constant is calculated to be approx. (4.01 ± 0.002) Å, while for longitudinal (x, y) is (3.06 ± 0.0005) Å. As pressure increased gradually from 25 to 100 mbar the value of x, y decreases slightly from (3.06 ± 0.0005) Å to (3.03 ± 0.0009) Å, but increased sharply to (4.06 ± 0.004) Å as approaches 100 mbar, while z remains constant. This slight decrement in lattice constant (3.06 ± 0.0005 Å to 3.03 ± 0.0009 Å) may be attributed to contraction of lattice on being surrounded by hydrogen atoms, but as the pressure reaches 100 mbar, there is a phase transition from α-PdH_x to hydrogen rich β-PdH_x, which results in expansion of lattice in the crystal structure. The result obtained is in good accordance with the work done on Pd nanoparticles [18]. The t-PdO nanoparticles behave similar to Pd nanoparticles in the presence of hydrogen and presence of oxide layer does not hamper its hydrogen absorption characteristics. Gurlo et al. reported that substitution of the hydrogen atoms in the gaps present in between the Pd nanoparticles, result in decrease of its electrical resistance which is the working principle of Pd based highly sensitive hydrogen gas sensing devices [14]. However, in case of Pd

Please cite this article in press as: Arora K, et al., Effect of low pressure hydrogen environment on crystallographic properties of PdO nanoparticles, International Journal of Hydrogen Energy (2016), http://dx.doi.org/10.1016/j.ijhydene.2016.09.040

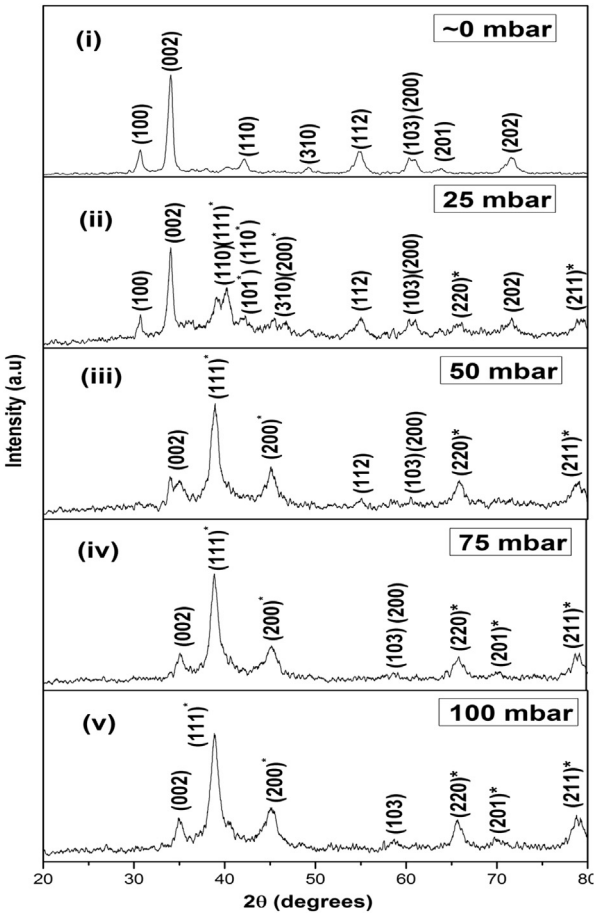


Fig. 5 – XRD spectra of sample b at (i) 0 mbar (ii) 25 mbar (iii) 50 mbar (iv) 75 mbar (v) 100 mbar hydrogen pressure.

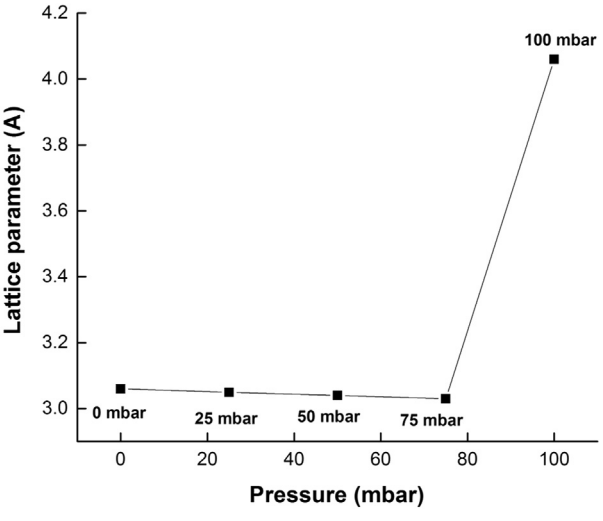


Fig. 6 – Effect of hydrogen gas environment pressure on lattice constants.

nanoclusters, both volume expansion along with resistivity change contributes towards sensing mechanism. The fabricated sensor exhibits good transient response and more efficiency as compared to other sensing devices [30].The lattice expansion due to the phase transition to hydrogen rich β-PdH_x (Fig. 6) implies that the synthesized t-PdO has high affinity towards hydrogen which makes it an efficient candidate for hydrogen storage applications.

Conclusion

PdO nanoparticles of dimension ~20 nm have been grown using sol–gel chemical method, the synthesized samples is annealed at three different temperatures. It is observed that PdO crystal structure starts decomposing to Pd crystal structure at 1000 °C.These samples are characterized with XRD, SEM, UV–Vis, TEM to determine their crystal structure, surface morphology, particle size, and band gap. It is found that PdO nanoparticles annealed at 800 °C shows the best characteristics out of others and hence is subjected to In-situ XRD study in presence of hydrogen gas at low environmental pressure. It is observed that PdO crystal structure has transformed into PdH_x crystal structure gradually with increase in the pressure. There is a phase transition (α-β) in PdH_x crystal structure as hydrogen pressure reached 100 mbar resulting in significant lattice expansion. The PdO nanoparticles demonstrate similar characteristics compared to Pd nanoparticles in the presence of hydrogen gas at low pressure.

Results of the study indicate that the PdO nanoparticles annealed at 800 °C can be used efficiently in hydrogen gas sensors and storage devices. The efforts will be made to utilize this sample for hydrogen gas sensing and solid state hydrogen gas storage at ambient condition.

Acknowledgement

The authors thank Prof. Yogesh Singh, Vice Chancellor, Delhi Technological University, Delhi, India for providing the research facilities. We are grateful to Inter-University Accelerator center (IUAC), and University of Delhi, Delhi, India for providing X-ray diffractometer and transmission electron microscope respectively to carry out necessary studies during this research experiment. The financial supports received from IUAC sponsored project (Grant No. IUAC/XIII.7/UFR-56324) and Department of Science and Technology, India (Grant No. DST/INSPIRE/04/2014/002540) are gratefully acknowledged.

REFERENCES

[1] Broom D. Hydrogen storage materials, green energy and technology. London: Springer-Verlag; 2011.
[2] Khanuja M, Kala S, Mehta B, Kruis F. Concentration-specific hydrogen sensing behavior in monosized Pd nanoparticle layers. Nanotechnology 2008;20(1):015502.
[3] Shen Y, Yamazaki T, Liu Z, Meng D, Kikuta T, Nakatani N, et al. Microstructure and H_2 gas sensing properties of

undoped and Pd-doped SnO_2 nanowires. Sens Actuators B Chem 2009;135(2):524–9.
[4] Kashif M, Ali M, Ali SMU, Hashim U. Sol–gel synthesis of Pd doped ZnO nanorods for room temperature hydrogen sensing applications. Ceram Int 2013;39(6):6461–6.
[5] Boudiba A, Roussel P, Zhang C, Olivier M-G, Snyders R, Debliquy M. Sensing mechanism of hydrogen sensors based on palladium-loaded tungsten oxide (Pd–WO_3). Sens Actuators B Chem 2013;187:84–93.
[6] Fasaki I, Giannoudakos A, Stamataki M, Kompitsas M, György E, Mihailescu I, et al. Nickel oxide thin films synthesized by reactive pulsed laser deposition: characterization and application to hydrogen sensing. Appl Phys A 2008;91(3):487–92.
[7] Baik JM, Kim MH, Larson C, Yavuz CT, Stucky GD, Wodtke AM, et al. Pd-Sensitized single vanadium oxide nanowires: highly responsive hydrogen sensing based on the metal – insulator transition. Nano Lett 2009;9(12):3980–4.
[8] Hoa ND, Van Quy N, Jung H, Kim D, Kim H, Hong S-K. Synthesis of porous CuO nanowires and its application to hydrogen detection. Sens Actuators B Chem 2010;146(1):266–72.
[9] Wen Z, Tian-mo L. Hydrogen sensing characteristics and mechanism of nanosize TiO 2 dope with metallic ions. Phys B Condens Matter 2010;405(2):564–8.
[10] Wang Z, Hu Y, Wang W, Zhang X, Wang B, Tian H, et al. Fast and highly-sensitive hydrogen sensing of Nb_2O_5 nanowires at room temperature. Int J Hydrogen Energy 2012;37(5):4526–32.
[11] Callini E, Pasquini L, Piscopiello E, Montone A, Antisari MV, Bonetti E. Hydrogen sorption in Pd-decorated Mg–MgO core-shell nanoparticles. Appl Phys Lett 2009;94(22):221905.
[12] Hübert T, Boon-Brett L, Black G, Banach U. Hydrogen sensors–a review. Sens Actuators B Chem 2011;157(2):329–52.
[13] Khanuja M, Mehta B, Agar P, Kulriya P, Avasthi D. Hydrogen induced lattice expansion and crystallinity degradation in palladium nanoparticles: effect of hydrogen concentration, pressure, and temperature. J Appl Phys 2009;106(9):093515.
[14] Gurlo A, Clarke DR. High-sensitivity hydrogen detection: hydrogen-induced swelling of multiple cracked palladium films on compliant substrates. Angew Chem Int Ed 2011;50(43):10130–2.
[15] Yamauchi M, Ikeda R, Kitagawa H, Takata M. Nanosize effects on hydrogen storage in palladium. J Phys Chem C 2008;112(9):3294–9.
[16] Fukai Y, Ōkuma N. Formation of superabundant vacancies in Pd hydride under high hydrogen pressures. Phys Rev Lett 1994;73(12):1640.
[17] Narehood D, Kishore S, Goto H, Adair J, Nelson J, Gutierrez H, et al. X-ray diffraction and H-storage in ultra-small palladium particles. Int J Hydrogen Energy 2009;34(2):952–60.
[18] Suleiman M, Jisrawi N, Dankert O, Reetz M, Bähtz C, Kirchheim R, et al. Phase transition and lattice expansion during hydrogen loading of nanometer sized palladium clusters. J Alloys Compd 2003;356:644–8.
[19] Akiba H, Kofu M, Kobayashi H, Kitagawa H, Ikeda K, Otomo T, et al. Nanometer-size effect on hydrogen sites in palladium lattice. J Am Chem Soc 2016;138(32):10238–43.
[20] Okazaki J, Ikeda T, Tanaka DAP, Suzuki TM, Mizukami F. In situ high-temperature X-ray diffraction study of thin palladium/α-alumina composite membranes and their hydrogen permeation properties. J Membr Sci 2009;335(1):126–32.
[21] Baldi A, Narayan TC, Koh AL, Dionne JA. In situ detection of hydrogen-induced phase transitions in individual palladium nanocrystals. Nat Mater 2014;13(12):1143–8.
[22] Khanuja M, Mehta B, Shivaprasad S. Two approaches for enhancing the hydrogenation properties of palladium: metal nanoparticle and thin film over layers. J Chem Sci 2008;120(6):573–8.
[23] Penner S, Wang D, Jenewein B, Gabasch H, Klötzer B, Knop-Gericke A, et al. Growth and decomposition of aligned and ordered PdO nanoparticles. J Chem Phys 2006;125(9):094703.
[24] Lee YT, Lee JM, Kim YJ, Joe JH, Lee W. Hydrogen gas sensing properties of PdO thin films with nano-sized cracks. Nanotechnology 2010;21(16):165503.
[25] Chiang Y-J, Li K-C, Lin Y-C, Pan F-M. A mechanistic study of hydrogen gas sensing by PdO nanoflake thin films at temperatures below 250°C. Phys Chem Chem Phys 2015;17(5):3039–49.
[26] Nilsson P. Optical properties of PdO in the range of 0.5–5.4 eV. J Phys C Solid State Phys 1979;12(7):1423.
[27] Gabasch H, Unterberger W, Hayek K, Klötzer B, Kleimenov E, Teschner D, et al. In situ XPS study of Pd (111) oxidation at elevated pressure, Part 2: palladium oxidation in the 10–1 mbar range. Surf Sci 2006;600(15):2980–9.
[28] Cullity BD, Weymouth JW. Elements of X-ray diffraction. Am J Phys 1957;25(6):394–5.
[29] Wahab MA. Solid state physics: structure and properties of materials. Alpha Science Int'l Ltd; 2005.
[30] Gupta D, Dutta D, Kumar M, Barman P, Sarkar C, Basu S, et al. A low temperature hydrogen sensor based on palladium nanoparticles. Sens Actuators B Chem 2014;196:215–22.

Please cite this article in press as: Arora K, et al., Effect of low pressure hydrogen environment on crystallographic properties of PdO nanoparticles, International Journal of Hydrogen Energy (2016), http://dx.doi.org/10.1016/j.ijhydene.2016.09.040

ARTICLE IN PRESS

Ceramics International #vol# (xxxx) xxxx–xxxx

Contents lists available at ScienceDirect

Ceramics International

journal homepage: www.elsevier.com/locate/ceramint

Effect of ZnO doping on structural, dielectric, ferroelectric and piezoelectric properties of $BaZr_{0.1}Ti_{0.9}O_3$ ceramics

Aditya Jain[a], Amrish K. Panwar[a,*], A.K. Jha[b]

[a] Department of Applied Physics, Delhi Technological University (Formerly Delhi College of Engineering), Bawana Road, Delhi 110042, India
[b] Department of Applied Science, A.I.A.C.T.R. Geeta Colony, Delhi 110031, India

ARTICLE INFO

Keywords:
Ceramics
Electron microscopy
Crystal structure
Dielectric properties
Piezoelectricity

ABSTRACT

This study provides a fundamental understanding of structural, dielectric, ferroelectric and piezoelectric properties of bare and ZnO-doped $BaZr_{0.1}Ti_{0.9}O_3$ (BZT) solid solutions synthesized using mechanochemical activation technique. Structural investigation has been carried out using XRD patterns of the synthesized compositions by Rietveld refinement method. It confirms the formation of tetragonal phase with *P4mm* space group for ZnO doping up to 2.5 wt%, while in 5.0 wt% ZnO-doped sample, BZT and ZnO are distributed as individual phases of tetragonal (*P4mm*) and hexagonal ($P6_3mc$), respectively. Microstructural analysis shows that average grain size increases quite rapidly with the increase of ZnO content. Detailed analysis of dielectric constant as a function of temperature for the prepared samples shows that the frequency independent dielectric constant maximum shifts to lower temperature with increase in ZnO doping. The ferroelectric ordering is confirmed using P-E loop measurements. The piezoelectric constant of the synthesized specimens were found to decrease with increasing ZnO content.

1. Introduction

Barium titanate is known to be most common ferroelectric material in ABO_3 perovskite family. The most studied materials based on this family are barium strontium titanate, barium hafnate titanate and barium zirconate titanate. Generally, $BaTiO_3$ based materials have high dielectric constant and low dielectric loss, in order to further reduce the dielectric loss at low frequencies, Zr^{4+} is substituted into barium titanate to form barium zirconate titanate (BZT) [1]. BZT has attracted a lot of attention for its potential application for random access memory, multi-layered ceramic capacitors, piezoelectric actuators, microwave technology, etc. [2–7]. Barium titanate and barium zirconate titanate form fully miscible solid solution and a stable perovskite crystal structure. BZT is an important member of $BaTiO_3$ based ferroelectric materials family and it is an alternative to $Ba_{1-x}Sr_xTiO_3$ solid solution for ceramic capacitors and microwave tunable applications. Also, BZT possesses small leakage current, which may be due to better chemical stability of Zr^{4+} than Ti^{4+} and thus, it stands out as a potential material for ceramic capacitors. In ceramics, the permanent polarization starts to disappear above Curie temperature and so for practical applications, the control of T_c is of great importance. In electrical and electronics engineering, high permittivity and low loss ceramics are required for a broad range of applications, such as high energy density storage capacitors, semiconductor manufacturing, noise filters, etc.

The diffuse phase transition behavior in BZT based materials is beneficial in achieving superior piezoelectric and electrocaloric properties [8,9]. It has been observed that the partial occupancy of Zr^{4+} at Ti^{4+} site not only lowers the Curie temperature but also helps in stabilizing the BZT lattice [10]. The temperature stability of ceramics depends on chemical substitution and the presence of core-shell grains. The basic structure of core-shell type materials comprises of a microstructure made up of biphasic grains [11,12]. This type of granular structure has two regions, the core and the surrounding shell. The core is made up of pure $BaTiO_3$ while the shell is $BaTiO_3$ modified by cations, which occupy A or B sites in the perovskite structure. A microstructure composed of such core-shell grains results in suppression of permittivity maxima and spontaneous polarization, which characterizes the ferroelectric properties of ceramics [4,9,13,14]. It has been reported that addition of non-ferroelectric materials results in the decrease of dielectric constant as well as the dielectric loss [15–20]. In this work, various amount (1.0, 2.5, 5.0 wt%) of non-ferroelectric material ZnO were added to $BaZr_{0.1}Ti_{0.9}O_3$ (BZT) to synthesize BZT-ZnO ceramic composite. It is to be noted that at B-site of BZT, Ti/Zr ratio has been chosen to be 0.9/0.1, which is due to overall better properties as compared to other combinations of Ti and Zr.

* Corresponding author.
E-mail address: panwaramar@gmail.com (A.K. Panwar).

http://dx.doi.org/10.1016/j.ceramint.2016.10.157
Received 12 September 2016; Received in revised form 18 October 2016; Accepted 24 October 2016
Available online xxxx
0272-8842/ © 2016 Elsevier Ltd and Techna Group S.r.l. All rights reserved.

Please cite this article as: Jain, A., Ceramics International (2016), http://dx.doi.org/10.1016/j.ceramint.2016.10.157

Till date there are modest numbers of reports on Zr substituted $BaTiO_3$ solid solutions and thin films. A comprehensive literature survey reveals that there are not many reports on extensive study of ZnO doped BZT, which prompted the authors to synthesize the present composition. In the present study, structural, dielectric, ferroelectric and piezoelectric properties of ZnO doped BZT have been investigated and have been reported here.

2. Experimental

$BaZr_{0.1}Ti_{0.9}O_3$ powder was prepared using mechanochemical activation technique. The starting raw chemicals were $BaCO_3$ (99.9%), ZrO_2 (99.9%) and TiO_2 (99.8%) of *Sigma-Aldrich* make. All precursor materials were taken in the stoichiometric ratio and milled in air atmosphere at 450 rpm for effective 30 h. Ball milling was carried out using a *Retsch PM100* planetary ball mill. A Zirconia vial with the diameter of 45 mm and 30 Zirconia balls with the diameter of 10 mm were used as milling medium. The milled powders were calcined at 1100 °C for 4 h to form the desired phase. Then various amount of ZnO (prepared by wet chemical method) were added to the BZT powder. The composite materials were re-milled for 5 h under the same condition and then dried at 50 °C. Then these obtained solid solutions were subsequently mixed with polyvinyl alcohol and compacted into disk-shaped pellets with approximately 10 mm diameter and 1 mm thickness at a pressure of 120 kN. The pellets were then sintered at 1250 °C for 4 h.

The phase and crystallographic structure of as-prepared samples were examined by *Bruker make D8 Advance* X-ray diffractometer using $CuK_{\alpha 1}$ radiation having a wavelength of 1.540 Å. The microstructural features and surface morphology of sintered pellets were analyzed using *Hitachi* make *S-3700N* scanning electron microscope. The sintered pellets were polished to 1 mm thickness and then silver paste was applied on both sides of pellets to form electrodes, the pellets were then cured at 150 °C for 30 min. Further, these pellets were used to perform dielectric measurement by *Agilent* make *4284A* LCR meter at 1 kHz, 10 kHz, 100 kHz and 1 MHz frequencies. Temperature dependent dielectric measurement was carried out within the temperature range of 27–250 °C. The hysteresis loops of the samples were recorded by *M/s Marine India, Delhi* make P-E loop tracer. DC conductivity and I-V measurement were performed using *Keithley 6517A* electrometer.

3. Results and discussion

3.1. X-ray diffraction (XRD)

The crystalline structure of bare and ZnO doped BZT have been investigated. In order to understand the structural modification by the addition of ZnO in barium zirconate titanate, the structural refinement was carried out by Rietveld method using *X'Pert Highscore Plus* software. Fig. 1(a)–(d) shows the Rietveld refined X-ray diffraction patterns of $BaZr_{0.1}Ti_{0.9}O_3$-*x*ZnO for *x*=0.0, 1.0, 2.5 and 5.0 wt%. Here, the samples are abbreviated as BZT for *x*=0.0 wt%, BZT1 for *x*=1.0 wt %, BZT2.5 for *x*=2.5 wt% and BZT5 for *x*=5 wt%. Barium titanate (JCPDS no. 01-074-1957) and zinc oxide (JCPDS no. 00-001-1136) were taken as the reference patterns and the peaks were refined using the Pseudo-Voigt function. A well-recognized tetragonal phase with *P4mm* space group is observed for BZT-*x*ZnO up to *x*=2.5 wt%, however, as the ZnO content increases to *x*=5.0 wt%, ZnO peaks began to appear. It is apparent that in BZT5 sample; $BaZr_{0.1}Ti_{0.9}O_3$ and ZnO are distributed as individual phases of tetragonal (*P4mm* space group) and hexagonal ($P_{63}mc$ space group), respectively. Table 1 shows the detailed structural parameters obtained after Rietveld refinement analysis. The lattice parameter '*a*' is found to increase with ZnO doping, however, the lattice parameter '*c*' and cell volume of the *P4mm* unit cell of BZT phase is found to decrease with ZnO doping.

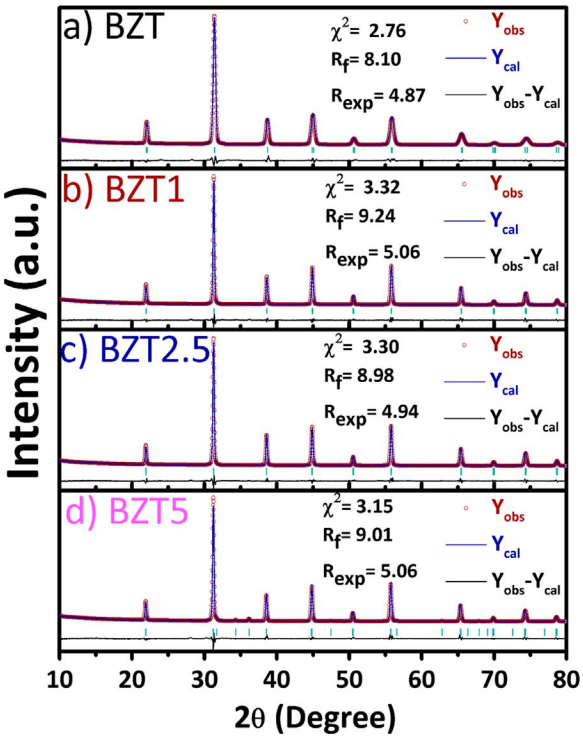


Fig. 1. Rietveld refined X-ray diffraction (XRD) patterns of BZT-*x*ZnO samples at room temperature, namely (a) BZT, (b) BZT1, (c) BZT2.5 and (d) BZT5.

The slight change in lattice parameters and consequently in c/a ratio may be attributed to addition of different crystal structure ZnO (hexagonal) in BZT (tetragonal). This addition of ZnO may be introducing some distortion in the parent perovskite material and therefore resulting in increase of '*a*' and decrease in '*c*'. The solubility of a dopant in BZT depends not only on the ionic charge but also on the ionic radii of the dopant [21,22]. Although, the charge of the Zn^{2+} ion is the same as that of Ba^{2+} ion, the ionic radii of the Zn^{2+}(0.074 nm, 6 CN) ion is close to that of the Ti^{4+}/Zr^{4+} ions (0.0605/0.072 nm, 6 CN) [23]. Hence, there is more possibility for Zn ions to go on to Ti/Zr site compared to Ba site. This may be understood by assuming that Zn^{2+} is replacing Ti^{4+}/Zr^{4+} ions and Zn acts as acceptor ion BZT lattice, the solution of BZT-*x*ZnO can be expressed by the following relation:

$$Zn \xrightarrow{BaZr_xTi_{1-x}O_3} Zn''_{Ti/Zr} + V_o^{\cdot\cdot} \quad (1)$$

Above equation describes the presence of oxygen vacancies by doping of Zn. With the increase in Zn content in BZT lattice, oxygen vacancies get increased. In the tetragonal phase of BZT, TiO_6/ZrO_6 octahedra form only corner sharing layers and when Ti^{4+}/Zr^{4+} is doped by acceptor dopant, oxygen vacancies are created.

3.2. Microstructural studies

The effect of ZnO doping on $BaZr_{0.1}Ti_{0.9}O_3$ is correlated with their densification, microstructural development and grain growth behavior. Fig. 2(a)–(d) shows the SEM micrograph of pure $BaZr_{0.1}Ti_{0.9}O_3$ ceramic and ZnO-doped $BaZr_{0.1}Ti_{0.9}O_3$ ceramics. All the samples show dense and relatively homogeneous microstructure with well faceted close-packed grains. ZnO-doping has a significant effect on the grain size of BZT ceramics. The average grain size of samples BZT, BZT1, BZT2.5 and BZT5 is observed to be 0.265, 1.95, 3.10 and 3.87 μm, respectively. It is clear that average grain size of specimens increases with ZnO-doping. Even at low dopant concentration of ZnO (i.e. at 1.0 wt%) the grain size is influenced significantly, which suggests that addition of ZnO has promoted grain growth. The dominant mechanism for grain growth during sintering process is diffusion and so increase in

Table 1
Rietveld refined XRD parameters for BZT, BZT1, BZT2.5 and BZT5.

Sample		Space group	Crystal structure	Lattice parameters (Å)	Cell volume (Å^3)	χ^2	R_{exp}	R_f	R_{Bragg}
BZT		P4*mm*	Tetragonal	a=4.0178 c=4.0353	65.1432	2.76	4.87	8.10	1.69
BZT1		P4*mm*	Tetragonal	a=4.0205 c=4.0279	65.1105	3.32	5.06	9.24	1.33
BZT2.5		P4*mm*	Tetragonal	a=4.0208 c=4.0272	65.1104	3.30	4.94	8.98	1.81
BZT5	**BZT phase**	P4*mm*	Tetragonal	a=4.0230 c=4.0307	64.2348				3.63
						3.15	5.06	9.01	
	ZnO phase	P6$_3$*mc*	Hexagonal	a=3.2428 c=5.1971	47.3305				1.82

grain size may be attributed to the diffusion of larger ionic radii Zn^{2+} ions onto the B-site [24]. Another reason for increase in grain size may be the enhancement in mass transport caused by ZnO addition which led to increased grain boundary diffusion and consequently resulting in grain growth of the ceramics [25,26]. It is a well-known fact that the grain size of ceramics is dependent on its sintering temperature and soaking duration at the peak temperature [27–29]. These two factors do have a major effect on the microstructure of the final sintered specimen and hence, they do affect the dielectric and ferroelectric properties of the ceramics.

3.3. Dielectric studies

Fig. 3(a)–(d) shows the temperature dependence of dielectric constant and loss of the pure and ZnO-doped BZT ceramics. The dielectric properties were measured in the frequency range of 0.5–100 kHz. It is seen that the Curie temperature, T_c of pure and ZnO-doped BZT ceramics of BZT, BZT1, BZT2.5 and BZT5, corresponding to the maximum permittivity is 67.5 °C, 65 °C, 63.5 °C and 61.5 °C, respectively. It is clear that the addition of ZnO causes a little decrement in the Curie temperature. The Curie temperature of perovskite materials sensitively depends on the kind of acceptor ion on A or B sites. The Curie temperature shift in these specimens is determined by the ionic radius, the valance state and the ground state of the acceptor ion [30,31]. The shift of ferroelectric transition temperature is attributed to tilting of BO_6 octahedra and so ionic radii of B-site atom does play a crucial role in determining the Curie temperature. Further, the acceptor ion and the presence of oxygen vacancies both contribute in diminishing tetragonal symmetry and the ferroelectric state and thus lead to decrease of the Curie temperature [32,33]. It is observed that the value of dielectric constant is maximum at lower frequency, which may be due to the maximum contribution of space charge polarization at lower frequencies. The dielectric constant values of all the ceramic samples increases with the increase in temperature and near Curie temperature, it shows strong anomalies in the dielectric values. This behavior near T_c can be explained on the basis of increase in domain wall mobility with the rise in temperature. Also in perovskite materials, the phase transition usually occurs due to

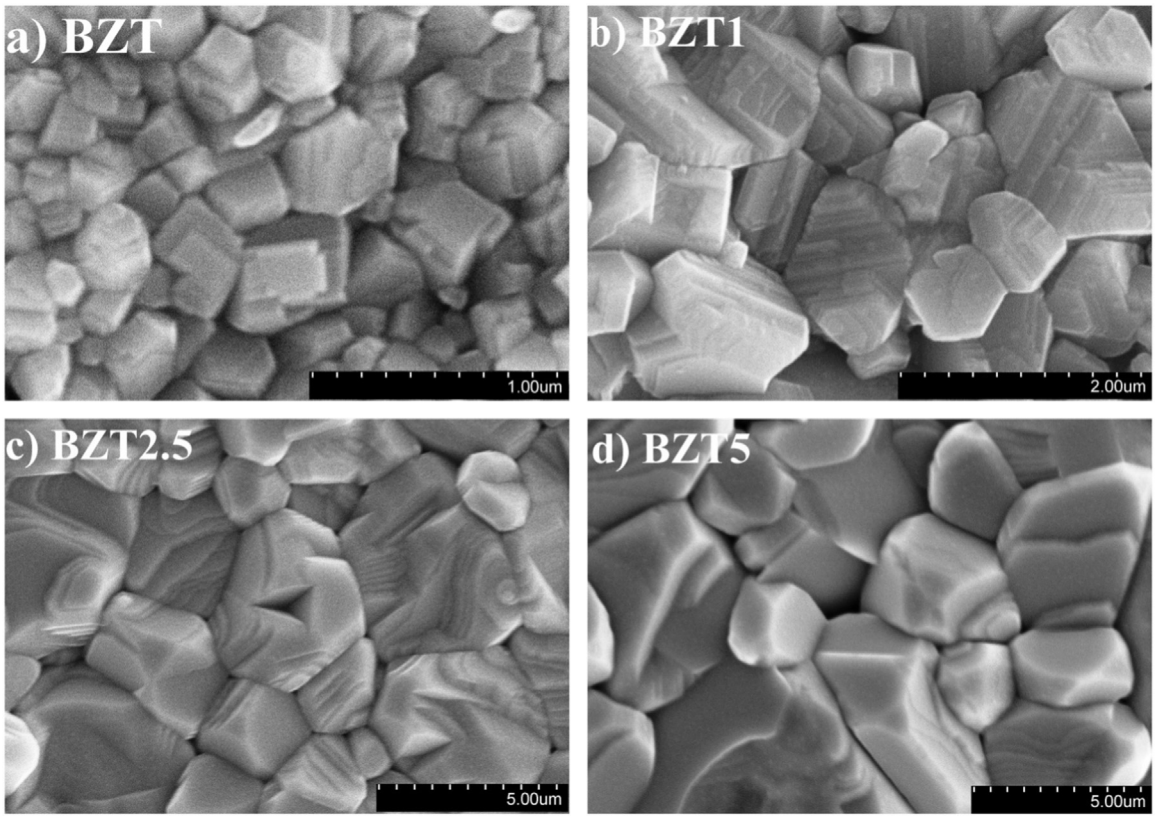


Fig. 2. SEM micrograph of sintered pellets for BZT-*x*ZnO samples: (a) BZT, (b) BZT1, (c) BZT2.5 and (d) BZT5.

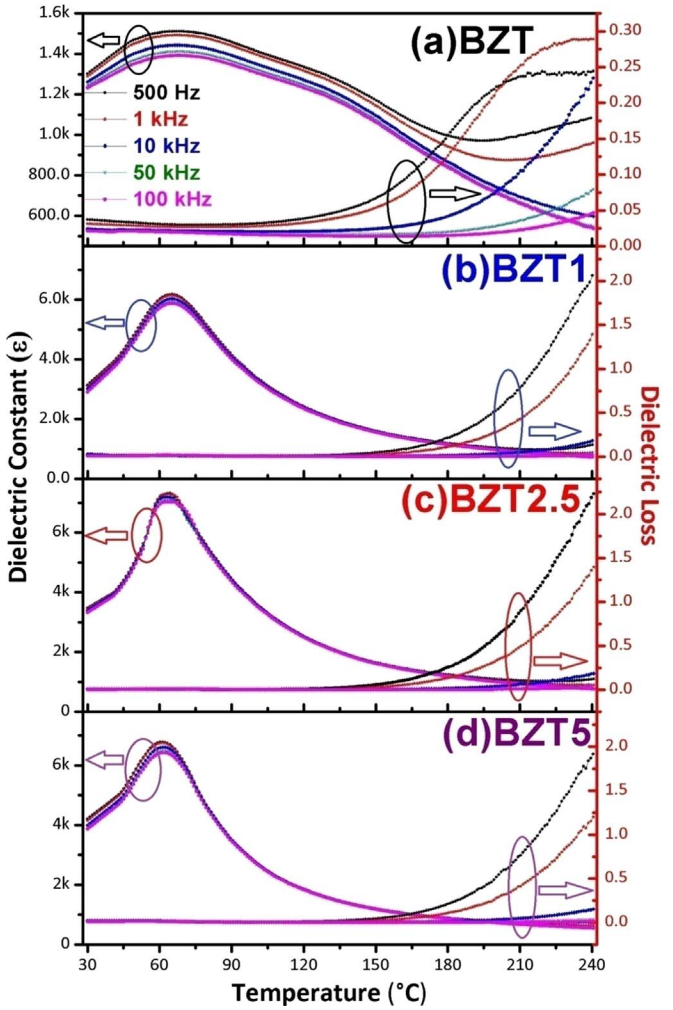


Fig. 3. Dielectric constant and dielectric loss as a function of temperature for the BZT-*x*ZnO samples: (a) BZT, (b) BZT1, (c) BZT2.5 and (d) BZT5.

fluctuation of temperature dependent low frequency optical soft mode [34].

The dielectric constant of these compositions is influenced by many factors such as grain size, crystallinity, phase and so on. The dielectric constant value of the samples BZT, BZT1, BZT2.5 and BZT5 at 500 Hz were found to be 1515, 6197, 7341 and 6796, respectively. When ZnO is doped in $BaZr_{0.1}Ti_{0.9}O_3$, the larger grain size of ZnO doped BZT ceramics leads to the higher dielectric constant. However, when ZnO content is 5.0 wt%, the dielectric constant of the ceramics decreases slightly, which may be due to the presence of non-ferroelectric secondary phase that can lead to low dielectric constant [1]. Higher addition of ZnO results in two-phase microstructure, and hence, the dielectric constant of the ceramics decreases on increasing ZnO doping above 2.5 wt%. When the ZnO content is more than 2.5 wt%, the changes in crystallinity induced by Zn^{2+} ion has greater effect on the dielectric constant than that of the grain size. Therefore, the sample BZT2.5 with higher crystallinity, larger grain size and absence of non-ferroelectric secondary phase has the highest dielectric constant. The character of ferroelectric phase transition at Curie temperature, T_c has changed strongly with the ZnO content. At higher ZnO contents, BZT-*x*ZnO ceramics show a narrow dielectric constant-temperature curve compared to pure BZT. The reason for broad dielectric curve in pure BZT may be due to mechanical stress and inhomogeneous distribution of Zr^{4+} ions on Ti^{4+} sites and so it can be inferred that ZnO doping leads to decrease in mechanical stress and stabilizes the distribution of Zr^{4+} ions on Ti^{4+} site. The T_c of the BZT-*x*ZnO ceramics shift to lower temperature when x changes from 0.0 to 5.0 wt%. This decrease in Curie temperature is possibly caused by the appearance of greater ion disorder in BZT lattice. Ion disorder affects long-range interactions inside the material, resulting in the decrease of transition temperatures.

It is observed that dielectric loss of ZnO-doped BZT specimens is lower than that of the pure BZT specimen between 30 and 130 °C. Above 130 °C, ZnO containing samples have shown an abrupt rise in dielectric loss and increases with further increase in temperature. The increase in dielectric loss may be attributed to increase in leakage current that depends on the crystal structure impurities like vacancies, dislocation and ionic charge imbalance. Another reason for the increase in dielectric loss may be the shallow contribution by the thermally activated charge carriers in the material which would result in decrease of dipolar polarization. The higher conductivity of ZnO-doped ceramics also results in the occurrence of electrical conduction through the dielectric and leads to higher loss. It can also be seen that the dielectric constant and dielectric loss curves for all the four samples show no frequency dispersion.

Normal ferroelectrics in the paraelectric state, i.e. above Curie temperature T_c follow Curie-Weiss law described by

$$\varepsilon = \frac{C}{T - T_c} (T > T_C), \tag{2}$$

where, T_c represents the Curie-Weiss temperature and C is the Curie constant. A diffuse phase in ferroelectric material is generally characterized by three factors such as a deviation from Curie-Weiss law in the vicinity of Curie point, broadening of the dielectric constant maxima at the Curie temperature and a separation between the maximum of dielectric constant and dielectric loss [35]. Curie-Weiss law is modified for diffuse phase transition and is described by [36,37]:

$$\frac{1}{\varepsilon} - \frac{1}{\varepsilon_m} = \frac{(T - T_c)^\gamma}{C'} \tag{3}$$

where, γ represents diffuseness parameter and C' denotes the Curie constant. The parameter γ provides information on phase transition behavior of any material. 0The value, γ=1 corresponds to normal ferroelectric behavior and $1 < \gamma < 2$ correspond to a diffuse phase transition [38,39]. Fig. 4 shows a relation between $\ln(T - T_c)$ and $\ln(1/\varepsilon - 1/\varepsilon_m)$. It is well-known fact that in disordered structure the broadening of the phase transition is very common. In such cases, the dielectric properties of materials are extremely non-linear close to Curie temperature. Considering these non-linear effects, a modified Landau's theory of Gibbs free energy [40] that includes an additional term in the form of stress can provide an appropriate explanation. Also, it is observed that the disordered states evolved as a result of the local strain induced by Zr doping in BTO and further with ZnO doping will

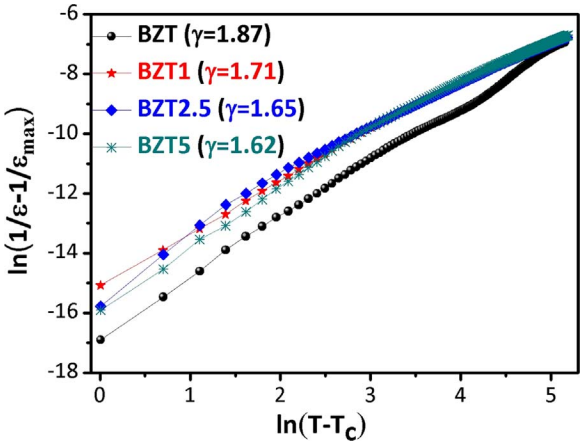


Fig. 4. The plot of $\ln(1/\varepsilon - 1/\varepsilon_m)$ as a function of $\ln(T - T_c)$ for pure and ZnO-doped $BaZr_{0.1}Ti_{0.9}O_3$ ceramic samples at 100 kHz.

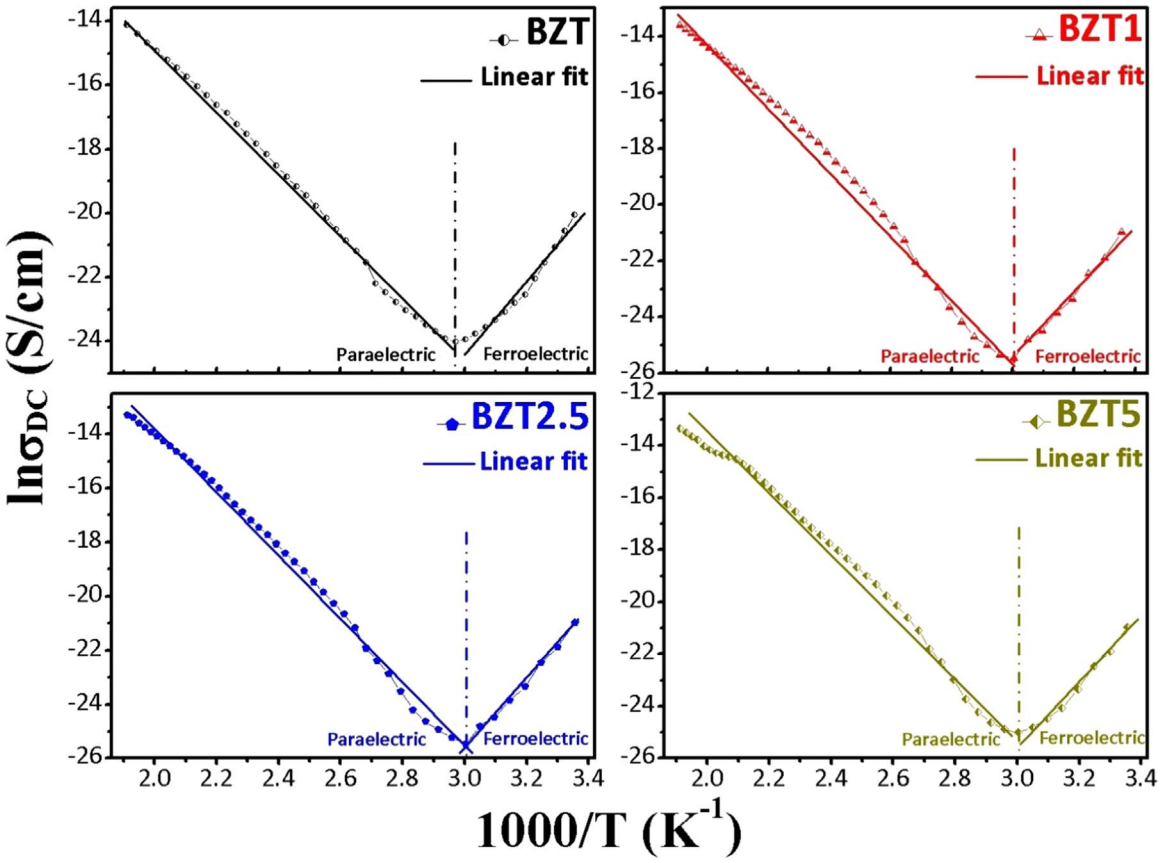


Fig. 5. Variation of DC electrical conductivity, σ with temperature for BZT, BZT1, BZT2.5 and BZT5.

continue above T_c. Thus, in all the samples the transition is of diffused nature and hence γ is found to deviate significantly from the normal ferroelectric value of the exponent, i.e., γ=1.

3.4. Conductivity studies

The effect of temperature on DC electrical conductivity for bare and ZnO-doped BZT ceramic was investigated. Fig. 5 illustrates an Arrhenius plot, in which $\ln(\sigma_{DC})$ is plotted against the reciprocal of absolute temperature, the slope of which yields the apparent activation energy for the synthesized ceramic samples. The Arrhenius equation in its functional form for DC electrical conductivity can be expressed as:

$$\sigma_{dc}=\sigma_o \exp\frac{-E_a}{K_B T} \tag{4}$$

where K_B is the Boltzmann constant, E_a represents the activation energy and T is the absolute temperature. In ceramic materials, the temperature dependent conductivity is affected by hopping of electrons and charge transfer through the excited state. It has been observed that there is a change in slope around Curie temperature which corresponds to a change in activation energy E_a. This anomaly around T_c explains that different conduction mechanism is in play in ferroelectric and paraelectric state. In the low-temperature region, the extrinsic defects are amenable for the conduction, whereas, in high-temperature region, the thermally active oxygen vacancies contribute prominently to conduction mechanism [41]. Activation energies derived from the slopes of Arrhenius plots are found to decrease with ZnO doping in the synthesized specimens. The activation energies of pure and ZnO-doped BZT ceramics are listed in Table 2.

3.5. Ferroelectric studies

Fig. 6 shows the *P-E* loops of the studied specimens at room temperature by varying the electric field up to ~ 30 kV/cm at an operating frequency of 50 Hz. The saturated P-E hysteresis loops confirm the ferroelectric nature of BZT-*x*ZnO ceramics. The saturation polarization ($2P_s$), remnant polarization ($2P_r$) and coercive field ($2E_c$) values for the studied samples are listed in Table 2. The shapes of hysteresis *P-E* loop are associated with the crystalline structure of the materials. The reason being that, in a crystalline material the dipole moments line up with each other to form domains that ranges in size from a few unit cells to the entire crystal [42]. However, in non-crystalline materials, the dipoles get aligned in random direction resulting a decrease in net dipole moment. This decrease in dipole moment leads to change in remnant polarization and coercive field consequently affecting the shape of P-E hysteresis loop [43]. The ferroelectric loops of BZT1, BZT2.5 and BZT5 confirm the relaxor behavior of these ceramics as the slim saturated loops having small remanence and coercivity with higher saturation polarization are a characteristic of relaxor ferroelectrics [44,45]. It is observed that the remnant polarization ($2P_r$) and coercive field ($2E_c$) decreases as ZnO content increases, which may be due to oxygen vacancies present in the sample. These oxygen vacancies affect the domain wall motion by screening off the polarization charge. Also they create an energy barrier against the domain walls and leads to domain wall pinning [46]. Moreover, with the addition of ZnO content, the TiO_6/ZrO_6 octahedral void would become narrow. This would cause the Ti^{4+}/Zr^{4+} in the centers of octahedra difficult to move, which results in a lower contribution to polarization. Low coercive field ($2E_c$) of the samples indicates that the ZnO doped BZT samples are ferroelectrically soft and very low electric field is sufficient to cause the switching of domains. Moreover, the better crystallinity of BZT as compared to ZnO-doped samples may benefit to its better remnant polarization and superior ferroelectric properties. Due to higher conductivity of ZnO, there may be a decrease in the resistance of BZT-*x*ZnO samples, which subsequently lead to a reduction in polarization for the ZnO-doped samples

Table 2
Saturation polarization (P_s), remnant polarization ($2P_r$), coercive field ($2E_c$), Discharged energy density (J), material resistance, piezoelectric constant (d_{33}) and activation energy (E_a) for BZT, BZT1, BZT2.5 and BZT5.

Sample	$2P_s$ (μC/cm^2)	$2P_r$ (μC/cm^2)	$2E_c$ (kV/cm)	J (J/cm^3)	R (MΩ)	d_{33} (pC/N)	E_a (eV)	
							Ferroelectric region	Paraelectric region
BZT	21.40	10.02	16.44	0.046	23.20	265	0.95 ± 0.005	0.76 ± 0.005
BZT1	30.31	3.96	4.10	0.122	19.68	192	0.91 ± 0.005	0.74 ± 0.005
BZT2.5	34.02	3.32	2.22	0.115	7.52	134	0.89 ± 0.005	0.72 ± 0.005
BZT5	25.16	2.54	1.44	0.095	3.72	92	0.83 ± 0.005	0.69 ± 0.005

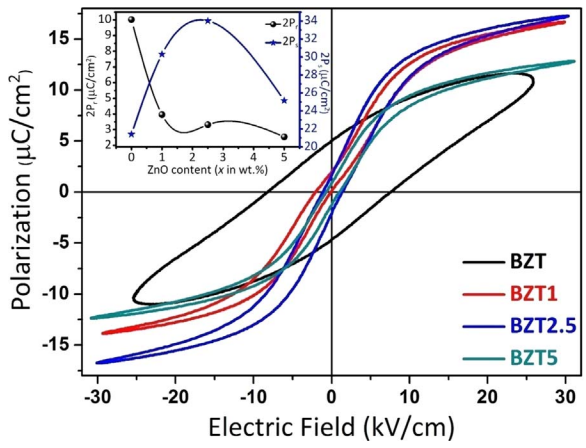


Fig. 6. Ferroelectric hysteresis loops of Pure and ZnO doped BZT ceramic samples at room temperature and inset shows the variation of remnant polarization ($2P_r$) and saturation polarization with ZnO content (x in wt%).

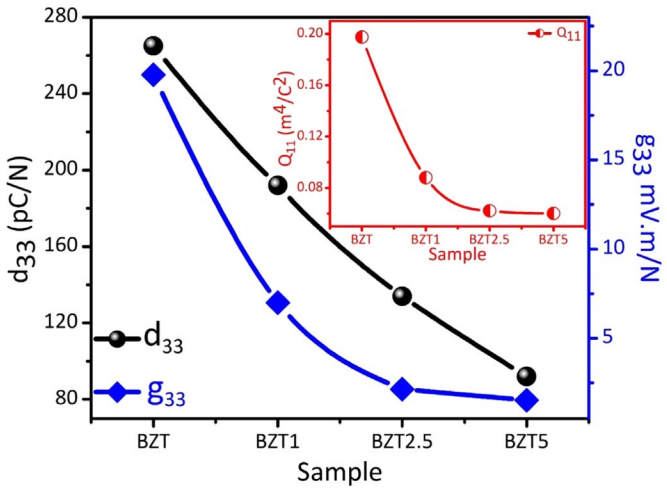


Fig. 7. Variation of piezoelectric constant (d_{33}), piezoelectric voltage coefficient (g_{33}) and electrostrictive coefficient (Q_{11}) (inset) as a function of ZnO doping.

compared to pure BZT.

It is a well-known fact that ferroelectric characteristics of ceramics are affected by their composition, crystal phase, microstructure, lattice defects and imperfections like oxygen vacancies [47]. Another way of determining the stability of ferroelectric phase is by structural transition with additional factors like the incorporation of dopants or foreign atoms. It is observed that remnant polarization of ZnO doped BZT compositions are lower compared to that of pure BZT. This is possibly due to the fact that the pure BZT is in tetragonal phase with space group P4*mm* and it exhibits non-centrosymmetric crystal structure, which favors ferroelectricity. However, in doped compositions, there is development of additional hexagonal phase of ZnO i.e. P6$_3$*mc*, which is centrosymmetric in nature and a centrosymmetric structure does not favor ferroelectricity due to zero or negligible electric dipole moment. Therefore, it is reasonable to conclude that the decrease of ferroelectricity in ZnO doped BZT is likely due to following two factors: one is the formation of oxygen vacancies and the other is the occurrence of additional hexagonal phase by ZnO doping.

The energy storage density of linear and non-linear dielectric materials can be obtained from the discharged energy density under the applied electric field, being represented by the integral function:

$$J = \int EdP \tag{5}$$

where, J is the energy density, E is the applied electric field and P is the polarization or displacement charge. Eq. (5) has been used to calculate the discharged energy density of the studied specimens and is listed in Table 2. Discharge energy density of all the samples were obtained under ~30 kV/cm. The slim ferroelectric loop with lower remnant polarization and coercive field is highly desirable for high energy storage density [48,49]. It is observed that pure BZT sample possesses the lowest discharged energy density which may be due to higher remnant polarization and coercive field as compared to ZnO doped samples.

3.6. Piezoelectric studies

Poling plays a key role in determining the piezoelectric properties of polycrystalline piezoelectric materials. In the process of electrical poling on the application of an external electric field materials with arbitrary distributed ferroelectric domains become polarized with net polarization developed in the direction of the applied electric field. Optimized electrical poling conditions such as, poling time, proper poling temperature and poling voltage are needed for enhanced piezoelectric properties. Fig. 7 shows the variation of piezoelectric constant (d_{33}), piezoelectric voltage coefficient (g_{33}) and electrostrictive coefficient (Q_{11}) as a function of ZnO doping. In the present study, the samples were poled for 2 h at an applied electric field of E ~1.5 kV/mm and poling temperature of T_P ~60 °C, exhibited an optimum piezoelectric behavior. According to thermodynamic theory of ferroelectricity [50], the piezoelectric constant is directly related to the dielectric constant (ε') and remnant polarization (P_r) of the material and can be expressed by the relation as:

$$d_{33} = 2P_r \varepsilon_{33} Q_{11} \tag{6}$$

where, ε_{33} is the dielectric permittivity and Q_{11} denotes the electrostrictive coefficient of the system. The pure BZT sintered at 1250 °C with a grain size of 265 nm shows the highest d_{33} value of 312 pC/N. It is observed that with ZnO addition, the d_{33} value decreases abruptly. Some previous reports [51,52] on piezoceramics have demonstrated that smaller sized grains tend to have smaller domain sizes which result in higher value of d_{33}, the reason being that the domain walls having small areas will respond more actively to external electrical or stress signals. Moreover, it may happen that doped ZnO may have precipitated at the grain boundaries, resulting in the accumulation of space charges and thus limited the movement of domains inside the material [53]. Piezoelectric voltage coefficient (g_{33}) and electrostrictive coefficient was measured for all the four samples. It is observed that both g_{33} and Q_{11} decreases with ZnO doping similar to piezoelectric

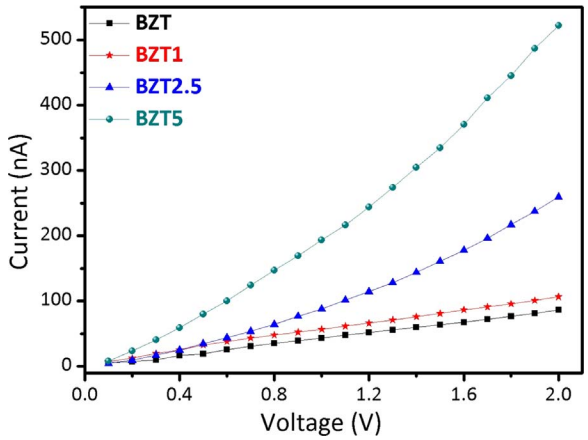


Fig. 8. I-V characteristics of bare and ZnO doped BZT ceramic samples measured at room temperature.

constant. On the basis of above measurements, it can be concluded that ZnO doping on BZT have resulted in worsening of piezoelectric properties.

3.7. I-V characteristics

The DC I-V characteristics of pure and ZnO doped BZT samples, measured at room temperature in the voltage range of 0–2 V are shown in Fig. 8. Here, it can be observed that pure BZT and ZnO doped BZT samples shows a linear dependence of the current in 0–2 V range. In $BaTiO_3$ based ceramic materials, the charging current flows through the material during polarization, such current results from the flow of free charges from the inside of the material, changes in domain configuration and charges coming out from the electrodes [54]. The distinctly seen section of I-V characteristics where Ohm's law is satisfied is used to evaluate the material resistance.

When the applied voltage is small, a comparatively weak electric field appears at the grain boundaries, and also, non-linear effects occurring in the material are weak, which results in lower value of current. Moreover, when the concentration of equilibrium charges inside the material is more than injected ones, we observe a linear relation between voltage and current. The electric field that disturbs the charges inside the grain is small because it is additionally lowered by the depolarizing field of material [4,28,55]. The resistance value of all the samples calculated from the linear portion of I-V characteristics is listed in Table 2. It is observed that the pure BZT sample has the highest ohmic resistance which decreases with increasing ZnO content. These results are in good agreement with the results obtained from conductivity studies, where also the activation energy was found to decrease with increasing ZnO doping.

4. Conclusion

Solid solutions of BZT-*x*ZnO were synthesized with different ZnO content using a standard high temperature and low-cost mechanochemical activation technique. Detailed X-ray structural analysis followed by Rietveld refinement confirms the formation of tetragonal crystal structure with P4*mm* space group for BZT, BZT1 and BZT2.5. However, in BZT5 sample, $BaZr_{0.1}Ti_{0.9}O_3$ and ZnO are distributed as individual phases of tetragonal (P4*mm* space group) and hexagonal ($P6_3mc$ space group), respectively. The microstructural analysis reveals that the shape, size and distribution of BZT has got modified on the addition of ZnO in it. A decrease in diffuse phase transition accompanied with a decrease in Curie temperature towards room temperature is observed with the ZnO doping on BZT system. P-E loop measurements demonstrate the well saturated ferroelectric loops. However, ZnO doping results in a remarkable decrease in remnant polarization and coercive field of the systems, which suggests that the ZnO doped samples are ferroelectrically soft. The activation energy of the samples were found to decrease with ZnO doping which is in good agreement with results obtained from I-V measurement. Combining all these properties, BZT-*x*ZnO can have potential application in energy storage devices as they require a ferroelectric material with low remnant polarization (P_r), high spontaneous polarization and high breakdown strength.

Acknowledgements

Authors are thankful for the support of DST-SERB (Grant no. PS/039/2011), India to carry out this research work.

References

[1] W. Cai, J. Gao, C. Fu, L. Tang, Dielectric properties, microstructure and diffuse transition of Ni-doped $Ba(Zr_{0.2}Ti_{0.8})O_3$ ceramics, J. Alloy. Compd. 487 (2009) 668–674.
[2] J.F. Ihlefeld, W.J. Borland, J.-P. Maria, Dielectric and microstructural properties of barium titanate hafnate thin films, Thin Solid Films 516 (2008) 3162–3166.
[3] P.A. Jha, A. Jha, Effect of sintering temperature on the grain growth and electrical properties of barium zirconate titanate ferroelectric ceramics, J. Mater. Sci. – Mater. Electron. 24 (2013) 1511–1518.
[4] G. Liu, R.D. Roseman, Effect of BaO and SiO2 addition on PTCR $BaTiO_3$ ceramics, J. Mater. Sci., vol. 34, pp. 4439–4445.
[5] T. Li, X. Long, Piezo-/dielectric properties of perovskite-structure high-temperature relaxor ferroelectrics: The $Pb(Lu_{1/2}Nb_{1/2})O_3$–$Pb(Zn_{1/3}Nb_{2/3})$ O_3–$PbTiO_3$ ternary ceramics, Mater. Res. Bull. 51 (2014) 251–257.
[6] M.M. Hoque, A. Dutta, S. Kumar, T.P. Sinha, Dielectric relaxation and conductivity of $Ba(Mg_{1/3}Ta_{2/3})O_3$ and $Ba(Zn_{1/3}Ta_{2/3})O_3$, J. Mater. Sci. Technol. 30 (2014) 311–320.
[7] X. Zeng, S. Yu, R. Sun, R. Du, Microstructure, thermal and dielectric properties of homogeneous bismaleimide-triazine/barium titanate nanocomposite films, Mater. Chem. Phys. 131 (2011) 387–392.
[8] J.P. Praveen, K. Kumar, A. James, T. Karthik, S. Asthana, D. Das, Large piezoelectric strain observed in sol–gel derived BZT–BCT ceramics, Curr. Appl. Phys. 14 (2014) 396–402.
[9] I. Norezan, A.K. Yahya, M.K. Talari, Effect of $(Ba_{0.6}Sr_{0.4})TiO_3$ (BST) doping on dielectric properties of $CaCu_3Ti_4O_{12}$ (CCTO), J. Mater. Sci. Technol. 28 (2012) 1137–1144.
[10] R. Rani, S. Singh, J. Juneja, K. Raina, C. Prakash, Dielectric properties of Zr substituted BST ceramics, Ceram. Int. 37 (2011) 3755–3758.
[11] W. Heywang, Structural engineering of ferroelectrics, Ferroelectrics 49 (1983) 3–14.
[12] H. Saito, H. Chazono, H. Kishi, N. Yamaoka, X7R multilayer ceramic capacitors with nickel electrodes, Jpn. J. Appl. Phys. 30 (1991) 2307.
[13] K. Watanabe, H. Ohsato, H. Kishi, Y. Okino, N. Kohzu, Y. Iguchi, T. Okuda, Solubility of La–Mg and La–Al in $BaTiO_3$, Solid State Ion. 108 (1998) 129–135.
[14] T. Takeuchi, E. Bétourné, M. Tabuchi, H. Kageyama, Y. Kobayashi, A. Coats, F. Morrison, D.C. Sinclair, A.R. West, Dielectric properties of spark-plasma-sintered $BaTiO_3$, J. Mater. Sci., vol. 34, pp. 917–924.
[15] J. Zhai, D. Hu, X. Yao, Z. Xu, H. Chen, Preparation and tunability properties of $Ba(Zr_xTi_{1-x})O_3$ thin films grown by a sol–gel process, J. Eur. Ceram. Soc. 26 (2006) 1917–1920.
[16] Y. Chen, X.-L. Dong, R.-H. Liang, J.-T. Li, Y.-L. Wang, Dielectric properties of $Ba_{0.6}Sr_{0.4}TiO_3/Mg_2SiO_4$/MgO composite ceramics, J. Appl. Phys. 98 (2005) 4107.
[17] N. Maikhuri, A.K. Panwar, A. Jha, Investigation of A-and B-site Fe substituted $BaTiO_3$ ceramics, J. Appl. Phys. 113 (2013) 17D915.
[18] J. Echigoya, S. Hayashi, Y. Obi, Directional solidification and interface structure of $BaTiO_3$-$CoFe_2O_4$ eutectic, J. Mater. Sci., vol. 35, pp. 5587–5591.
[19] J. Rani, K.L. Yadav, S. Prakash, Dielectric and magnetic properties of $xCoFe_2O_4$–$(1-x)[0.5Ba(Zr_{0.2}Ti_{0.8})O_3$–$0.5(Ba_{0.7}Ca_{0.3})TiO_3]$ composites, Mater. Res. Bull. 60 (2014) 367–375.
[20] T. Sundararajan, S. Balasivanandha Prabu, Spark plasma sintering of microwave processed nanocrystalline barium titanate and their characterisations, Mater. Chem. Phys. 139 (2013) 465–470.
[21] S. Das, R. Mishra, B. Roul, Magnetic and ferroelectric properties of Ni doped $BaTiO_3$, Solid State Commun. 191 (2014) 19–24.
[22] D.-J. Shin, J. Kim, S.-J. Jeong, J.-H. Koh, Piezoelectric and ferroelectric properties in $Ba(Zr,Ti)O_3$ and CuO-$Ba(Zr,Ti)O_3$ ceramics, Mater. Res. Bull. (2016).
[23] Rt Shannon, Revised effective ionic radii and systematic studies of interatomic distances in halides and chalcogenides, Acta Crystallogr. Sect. A: Found. Crystallogr. 32 (1976) 751–767.
[24] S.-W. Zhang, H. Zhang, B.-P. Zhang, G. Zhao, Dielectric and piezoelectric properties of $(Ba_{0.95}Ca_{0.05})(Ti_{0.88}Zr_{0.12})O_3$ ceramics sintered in a protective atmosphere, J. Eur. Ceram. Soc. 29 (2009) 3235–3242.
[25] F. Rubio-Marcos, J.J. Romero, M.G. Navarro-Rojero, J.F. Fernandez, Effect of ZnO on the structure, microstructure and electrical properties of KNN-modified piezoceramics, J. Eur. Ceram. Soc. 29 (2009) 3045–3052.
[26] M. Promsawat, A. Watcharapasorn, S. Jiansirisomboon, Effects of ZnO nanopar-

ticulate addition on the properties of PMNT ceramics, Nanoscale Res. Lett. 7 (2012) 65.
[27] A. Herabut, A. Safari, Processing and electromechanical properties of $(Bi_{0.5}Na_{0.5})_{(1-1.5x)}La_xTiO_3$ ceramics, J. Am. Ceram. Soc. 80 (1997) 2954–2958.
[28] S. Sarraute, O.T. Sørensen, B.F. Sørensen, E.R. Hansen, Microstructure dependent thermophysical properties of Ni–Zn ferrite–$BaTiO_3$ functionally graded ceramics, J. Mater. Sci., vol. 34, pp. 99–104.
[29] L.-J. Gao, X.-L. Liu, J.-Q. Zhang, S.-Q. Wang, J.-F. Chen, Grain-controlled barium titanate ceramics prepared from high-gravity reactive precipitation process powder, Mater. Chem. Phys. 88 (2004) 27–31.
[30] H. Kishi, N. Kohzu, Y. Iguchi, J. Sugino, M. Kato, H. Ohsato, T. Okuda, Occupational sites and dielectric properties of rare-earth and Mn substituted $BaTiO_3$, J. Eur. Ceram. Soc. 21 (2001) 1643–1647.
[31] H.-I. Hsiang, K.-Y. Lin, F.-S. Yen, C.-Y. Hwang, Effects of particle size of $BaTiO_3$ powder on the dielectric properties of $BaTiO_3$/polyvinylidene fluoride composites, J. Mater. Sci., vol. 36, pp. 3809–3815.
[32] P. Hansen, D. Hennings, H. Schreinemacher, Dielectric properties of acceptor-doped (Ba,Ca)(Ti,Zr)O_3 ceramics, J. Electroceram. 2 (1998) 85–94.
[33] C. Muralidhar, P.K.C. Pillai, Dielectric behaviour of barium titanate-polyvinylidene fluoride composites, J. Mater. Sci., vol. 23, pp. 1071–1076.
[34] P. Mishra, P. Kumar, Enhanced dielectric and piezoelectric properties of BZT–BCT system near MPB, Ceram. Int. 40 (2014) 14149–14157.
[35] X. Tang, K.-H. Chew, H. Chan, Diffuse phase transition and dielectric tunability of $Ba(Zr_yTi_{1-y})O_3$ relaxor ferroelectric ceramics, Acta Mater. 52 (2004) 5177–5183.
[36] K. Uchino, S. Nomura, Critical exponents of the dielectric constants in diffused-phase-transition crystals, Ferroelectrics 44 (1982) 55–61.
[37] H. Chen, C. Yang, C. Fu, J. Shi, J. Zhang, W. Leng, Microstructure and dielectric properties of $BaZr_xTi_{1-x}O_3$ ceramics, J. Mater. Sci. – Mater. Electron. 19 (2008) 379–382.
[38] Z. Xiao-Li, C. Xiang-Ming, Ferroelectric transition and curie—weiss behavior in some filled tungsten bronze ceramics, Chin. Phys. Lett. 31 (2014) 015201.
[39] Y. Mao, S. Mao, Z.-G. Ye, Z. Xie, L. Zheng, Solvothermal synthesis and Curie temperature of monodispersed barium titanate nanoparticles, Mater. Chem. Phys. 124 (2010) 1232–1238.
[40] S. Rajan, P.M. Gazzali, G. Chandrasekaran, Electrical and magnetic phase transition studies of Fe and Mn co-doped $BaTiO_3$, J. Alloy. Compd. 656 (2016) 98–109.
[41] N. Kumar, P. Tirupathi, B. Kumar, M. Pastor, A. Pandey, R. Choudhary, Observation of dielectric relaxor behavior in $Pb_{0.95}Sr_{0.05}(Zr_{0.5}Ti_{0.5})O_3$ ceramics, Adv. Mater. Lett. (2015).
[42] D.M. Fanning, Structure Property Relations in Ferroelectric Materials, University of Illinois Urbana-Champaign, United States of America, 2000.
[43] P. Radaelli, D. Cox, M. Marezio, S.-W. Cheong, P. Schiffer, A. Ramirez, Simultaneous structural, magnetic, and electronic transitions in $La_{1-x}Ca_xMnO_3$ with x= 0.25 and 0.50, Phys. Rev. Lett. 75 (1995) 4488.
[44] S. Patel, A. Chauhan, R. Vaish, Enhancing electrical energy storage density in anti-ferroelectric ceramics using ferroelastic domain switching, Mater. Res. Exp. 1 (2014) 045502.
[45] L.E. CROSS, Dielectric, piezoelectric, and ferroelectric components, Piezoelectricity (1992) 284.
[46] S.M. Moussa, B.J. Kennedy, B.A. Hunter, C.J. Howard, T. Vogt, Low temperature structural studies on $PrAlO_3$, J. Phys.: Condens. Matter 13 (2001) L203.
[47] Z. Zhao, V. Buscaglia, M. Viviani, M.T. Buscaglia, L. Mitoseriu, A. Testino, M. Nygren, M. Johnsson, P. Nanni, Grain-size effects on the ferroelectric behavior of dense nanocrystalline $BaTiO_3$ ceramics, Phys. Rev. B: Condens. Matter 70 (2004) 024107.
[48] T. Wang, L. Jin, Y. Tian, L. Shu, Q. Hu, X. Wei, Microstructure and ferroelectric properties of Nb_2O_5-modified $BiFeO_3$-$BaTiO_3$ lead-free ceramics for energy storage, Mater. Lett. 137 (2014) 79–81.
[49] P. Wawrzała, J. Korzekwa, Charge-discharge properties of PLZT x/90/10 ceramics, Ferroelectrics 446 (2013) 91–101.
[50] H. Baerwald, Thermodynamic theory of ferroelectric ceramics, Phys. Rev. 105 (1957) 480.
[51] S. Shao, J. Zhang, Z. Zhang, P. Zheng, M. Zhao, J. Li, C. Wang, High piezoelectric properties and domain configuration in $BaTiO_3$ ceramics obtained through the solid-state reaction route, J. Phys. D: Appl. Phys. 41 (2008) 125408.
[52] H. Takahashi, Y. Numamoto, J. Tani, S. Tsurekawa, Piezoelectric properties of $BaTiO_3$ ceramics with high performance fabricated by microwave sintering, Jpn. J. Appl. Phys. 45 (2006) 7405.
[53] M. Zhu, L. Liu, Y. Hou, H. Wang, H. Yan, Microstructure and electrical properties of MnO-doped $(Na_{0.5}Bi_{0.5})_{0.92}Ba_{0.08}TiO_3$ lead-free piezoceramics, J. Am. Ceram. Soc. 90 (2007) 120–124.
[54] A. Dedyk, A. Kanareykin, E. Nenasheva, J.V. Pavlova, S. Karmanenko, IV and CV characteristics of ceramic materials based on barium strontium titanate, Tech. Phys. 51 (2006) 1168–1173.
[55] W. Osak, K. Tkacz, Investigation of IV characteristics in polycrystalline $BaTiO_3$, J. Phys. D: Appl. Phys 22 (1989) 1746.

Electric and magnetic hotspots in the Silicon Bow-Tie nanocavity

Reena,[1] Yogita Kalra,[1] and R.K. Sinha[1,2]

[1]TIFAC-center of Relevance and Excellence in Fiber Optics and Optical Communication, Department of Applied Physics, Delhi Technological University (Formerly Delhi College of Engineering, University of Delhi), Bawana Road, Delhi-110042, India
[2] CSIR-Central Scientific Instruments Organisation, Sector 30 C, Chandigarh-160 030, India
Email: dr_rk_sinha@yahoo.com

Abstract: We report enhancement of electric and magnetic fields in the silicon bow-tie nanocavity at visible wavelength. For our design, electric and magnetic resonances have been optically induced at the wavelength of 620 nm.
OCIS codes: (040.6040) Silicon; (260.5740) Resonance; (290.0290) Scattering

1. Introduction

Resonant behavior of electric and magnetic fields have been studied to engineer the control of light at the nanometer scale due to its enormous applications in the field of nanophotonics such as sensors [1], nanoantennas [2] and low threshold lasers [3]. High permittivity dielectrics which are lossless as compared to metals have been used for this purpose to enhance the quality of the nanostructures. The magnetic resonance in the Silicon nanoparticles has been demonstrated experimentally in the paper [4 -5]. Recently, electric and magnetic hotspots have been observed between the nanodimers of two cylinders [6]. In this paper, we have proposed a nanocavity consisting of two tip to tip triangles, where electric field enhancement takes place between the two triangles at the wavelength of electric and magnetic resonance.

2. Design

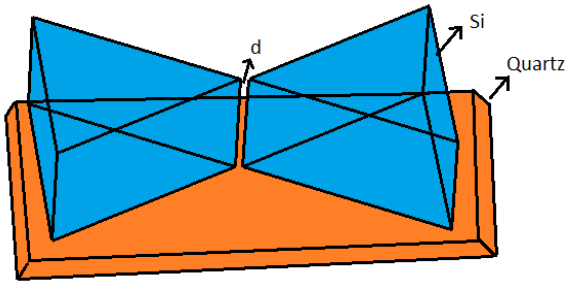


Fig. 1. Schematic diagram of bow-tie Si nanocavity on the quartz substrate with distance d between the two tip to tip triangles of bow-tie.

The nano cavity is designed based on the two silicon (Si) tip to tip triangles situated on the quartz substrate, as shown in figure 1, where d is the gap between the two triangles. Height and length of the triangles have been taken to be 200 nm. The gap between the two triangles has been varied from 4nm to 16 nm to observe the effect of variation in the gap between two triangles.

3. Results and discussion

The variation of normalized scattering cross section (σ_{norm}) with wavelength has been analyzed using finite element method as shown in figure 2. Peaks in the scattering cross section one at the wavelength of 635 nm (with blue curve) corresponds to the electric dipole (ED) and another at the wavelength of 630 nm (with green curve) corresponds to the magnetic dipole. Electric and magnetic resonances interfere at the wavelength of 620 nm as shown in figure 2. Red curve shows the total scattering cross section.

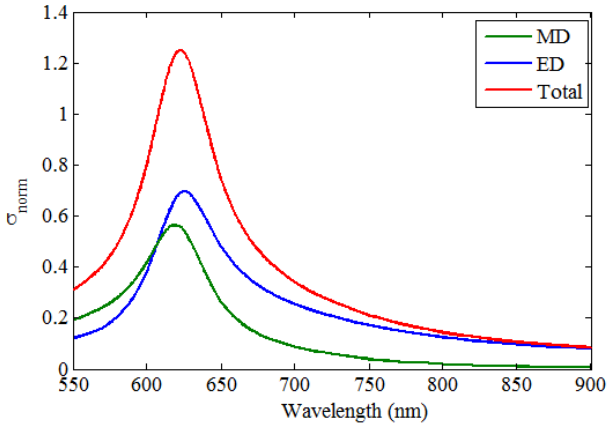


Fig. 2. Variation of normalized scattering cross section with wavelength showing peaks of electric dipole (ED) and magnetic dipole (MD).

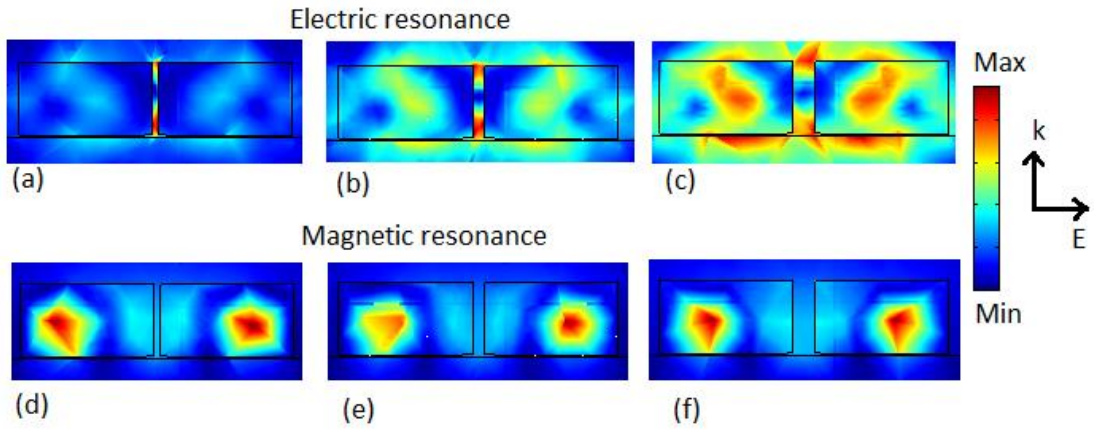


Fig. 3. (a) - (c) Enhancement of electric field between the two triangles of Bow-Tie nanocavity for the gaps of (a) 4 nm (b) 8 nm and (c) 16 nm. (d) – (f) Enhancement of the magnetic field in the triangles of the nanocavity for the gaps of (a) 4 nm (b) 8 nm and (c) 16 nm at the wavelength 620 nm.

Figures 3 (a) – (c) shows the electric and magnetic resonances at the wavelength of 620 nm. From the figure, it is clear that at this wavelength electric field is confined between the two triangles and as we increase the gap between the two triangles from 4 nm to 16 nm, confinement of the electric field decreases. Figure 3 (d) – (f) show the confinement of the magnetic field in the triangles of the bow-tie structure. There is no significant change in the confinement of the magnetic field by changing the gap between the triangles.

4. Conclusion

It has been concluded that electric field has been confined in the nanocavity of the two triangles of the nanostructure and magnetic field in the triangles of the bow-tie at the resonant wavelength. This indicates the formation of hotspots in the silicon nanocavity, which have a large number of applications in the field of sensors, cavity quantum electrodynamics and low threshold lasers.

5. References

[1] F. Vollmer and S. Arnold, "Whispering-gallery-modes biosensing: label free detection down to single molecules," Nat. Methods **5,** 591-596 (2008).
[2] G. Boudarham, R. Abdeddaim and N. Bonod, "Enhancing the magnetic field intensity with a dielectric gap aantenna," App. Phys. Letters **104**, 021117 (2014).
[3] S. M. Spillane, T. J. Kippenberg and K. J. Vahala, "Ultralow-threshold Raman laser using a spherical dielectric microcavity," Nature **415,** 621-623 (2002).
[4] A. I. Kuznetsov, A. E. Miroshnichenko, Y. H. Fu, J. B. Jhang and B. Luk'yanchuk, " Magnetic light" Sci. Rep. **2**, 492 (2012).
[5] Y. H. Fu, A. I. Kuznetsov, A. E. Miroshnichinko, Y. F. Yu and B. Luk'yanchuk, " Directional visible light scattering by silicon nanoparticles" Nat. Commun. **4**, 1527 (2013).
[6] R. M. Bakker, D. Peryakov, Y. F. Yu, D. Markovich, R. P. Domínguez, L. Gonzaga, A. Samusev, Y. Kivshar, B. Luk'yanchuk and A. I. Kuznetsov, " Magnetic and electric hotspots with silicon nanodimers" **15**, 2137-2142 (2015).

Research Article – JTEN – 2015 – 150

Journal of Thermal Engineering
Yildiz Technical University Press, Istanbul, Turkey
Vol. 2, No. 6, Special Issue 5, pp. 995-1006, December, 2016.

http://eds.yildiz.edu.tr/journal-of-thermal-engineering/Articles
Manuscript Received October 27, 2015; Accepted December 06, 2015

This paper was recommended for publication in revised form by Regional Editor Hafiz Muhammad Ali

ENERGY AND EXERGY ANALYSIS OF ABSORPTION- COMPRESSION CASCADE REFRIGERATION SYSTEM

***Manoj Dixit**
Centre for Energy Studies,
Indian Institute of Technology Delhi
New Delhi, Delhi, India

S C Kaushik
Centre for Energy Studies,
Indian Institute of Technology Delhi
New Delhi, Delhi, India

Akhilesh Arora
Department of Mechanical Engineering, Delhi Technological University
Delhi, Delhi, India

Keywords: absorption, compression, COP, exergy destruction, exergetic efficiency
** Corresponding author: Phone:* 91-9540660289
E-mail address: mandix@ces.iitd.ac.in

ABSTRACT

In this study, an Absorption- Compression Cascade Refrigeration, comprising of a VCR system in low temperature stage and a VAR system at the high temperature stage, is analyzed. CO_2, NH_3 and R134a have been considered as refrigerants in the compression stage and the H_2O-LiBr refrigerant absorbent pair in the absorption stage. The analysis has been realized by means of a mathematical model of the refrigeration system. The study presents the results obtained regarding the performance of the refrigeration system based on energy and exergy analysis. The comparative study helps to find out the best refrigerant and appropriate operation parameters. It is found in the study that cascade condenser, compressor and refrigerant throttle valve are the major source of exergy destruction.

INTRODUCTION

There are various applications which require temperature in the range of - 30°C to - 100°C. It includes food preservation, rapid freezing, ice production, storage of medical products, drugs and so on. It is not economical to obtain temperature below -40°C, using single stage vapour compression refrigeration (VCR) system or single stage vapour absorption refrigeration (VAR) system [1]. Therefore, in order to obtain such low temperatures cascade refrigeration system is the best choice. The conventionally employed two stage cascade compression refrigeration systems consume a lot of electricity. About 56% of total electricity generation in India is done through fossil fuel burning [2] which causes emission of harmful gases like carbon dioxide and oxides of sulphur and nitrogen. Also, the refrigerants used in these conventional VCR systems are the major cause of ozone depletion and global warming. Therefore such a cooling technology is needed which can at least reduce the electricity consumption, if it cannot eliminate high grade energy consumption completely.

Vapour absorption refrigeration systems cascaded with vapour compression systems are capable of reducing electricity consumption together with maintaining high coefficient of performance (COP). This refrigeration system would decrease the electricity consumption compared to the two stages compression systems, since it is only required to operate the compression system at the low stage, whereas the absorption system is driven by heat. The heat driven VAR systems are of different configurations which can be operated by heat sources of temperature varying from 60°C to 200°C [3]. Generally, single effect VAR cycle is employed in cascade system and it requires generator temperature between 80-120°C. However, if heat is available at lower temperature then half effect configuration [4] can be used as it requires generator temperature between 60-80°C [5] and if heat is available at higher temperature then double effect [6], triple effect [7] and GAX [8] absorption refrigeration cycles can be used. The presence of flexibility of choosing the suitable configuration of VAR depending upon the temperature of available heat allows sustainable utilization of energy resources.

Fernández-Seara et al. [9] carried out a study on compression-absorption cascade system. Ammonia-water was the working substance in absorption refrigeration cycle whereas carbon dioxide was used as a refrigerant in compression cycle. The COP of 0.253 was reported by them. Kairouani and Nehdi [10] proposed a geothermal energy driven absorption-compression cascade refrigeration system and reported the COP of 5.4-6.2 (excluding pump work and generator heat load). Garimella et al. [11] developed a computational model of a waste heat driven single effect LiBr/H_2O absorption-subcritical CO_2 compression cycle for megawatt scale low temperature (-40℃) cooling for high heat flux electronic application. They reported that this novel cascade cooling system consumed 31% less electricity than the equivalent VCR system. Cimsit and Ozturk [12] used different refrigerants and working pairs for the analysis of compression-absorption cascade systems. Ammonia, R134a, R-410A were used in compression section while NH_3/H_2O and LiBr/H_2O were used as working substances in absorption section of cascade cycle. It was concluded that electricity consumption in cascade systems is 48-51% lower than conventional VCR systems. They also reported that LiBr/H_2O based cascade system outperformed NH_3/H_2O based cascade refrigeration system by registering 33% higher COP. Wang et al. [13] studied the solar assisted R134a compression-LiBr/H_2O absorption cascade refrigeration system. Electric power consumption was reported to be lower by 50% in comparison with VCR system. Jain et al. [2] performed the first law and second law based thermodynamic analysis of cascaded vapour compression-absorption system (CVCAS) which consists of single effect VAR system coupled with VCR system. The electric power consumption in CVCAS was 61% lower than that in VCR system for same operating conditions. Colorado and Velazquez [14] carried out exergy based thermodynamic analysis of compression-absorption refrigeration cycle using NH_3, CO_2 and R134a in VCR section and H_2O-LiBr in VAR section so as to find out best working substance and suitable operating parameters. It was shown that highest irreversibility occurs in cascade condenser, accounting for around 19.96%, 19.31% and 13.28% of the total irreversibilities using NH_3, CO_2 and R134a respectively. A thermodynamic analysis of compression-absorption cascade refrigeration system using modified Gouy-Stodola equation was carried out by Jain et al. [15]. In their study they obtained the optimum temperature of cascade condenser which corresponds to minimum irreversibility and maximum COP of the system. Further, a comparative study of compression-absorption cascade refrigeration system and two stage vapour compression refrigeration system (TSVCS) reveals that primary energy consumption of compression absorption cascade system is 60.6% less and electrical COP is 153.6% more than that of TSVCS.

It is obvious from the literature review that though a lot of work on energy based analysis is reported, yet the exergy based thermodynamic analysis of absorption-compression cascade refrigeration system is limited. In this study attention is focussed on the components which are the major sites of exergy destruction. It is also endeavoured to find out the effects of various operating and design parameters on exergy destruction in different components, COP and exergetic efficiency.

SYSTEM DESCRIPTION

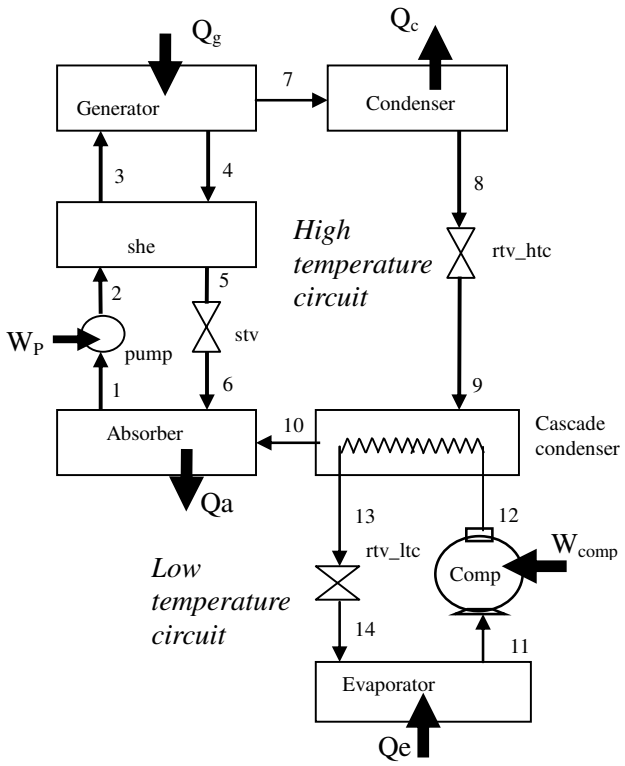


Figure 1. Absorption-compression cascade refrigeration system

A cascade refrigeration system in general comprises of a low temperature circuit (LTC) and a high temperature circuit (HTC). Actual cooling load is supplied to LTC while its heat of condensation acts as a cooling load to HTC which ultimately rejects heat to the surroundings. Thus LTC and HTC are coupled through a common heat exchanger referred to as cascade condenser, which acts as condenser for LTC refrigeration cycle and evaporator for HTC refrigeration cycle. In case of absorption-compression cascade refrigeration system, VAR cycle is utilized in HTC and VCR cycle is employed in LTC. In this study single effect LiBr-H_2O vapor absorption refrigeration cycle is used in HTC and R134a, CO_2 and NH_3 have been considered as refrigerants in the compression stage as shown in Fig.1. The compression system comprises of the evaporator, compressor, condenser and an expansion device. The major components of single effect VAR system are the absorber, generator, condenser, evaporator, solution heat

exchanger, pump, solution throttle valve and a refrigerant throttle valve. The single effect absorption cycle is separately described by authors [16].

THERMODYNAMIC ANALYSIS

Assumptions

(a) The system operates under steady state conditions.

(b) Cascade condenser is perfectly isolated.

(c) Heat losses and pressure drops in connecting lines and various components are neglected.

(d) The subcooling and superheating in discharge and suction lines are neglected.

(e) The expansion process is isenthalpic.

(f) The solutions at the exit of generator and absorber are saturated in equilibrium at their respective concentrations and temperatures.

(g) Reference environmental temperature and pressure are 25°C and 101.3 kPa respectively.

The thermodynamic analysis of compression absorption system involves the principles of mass conservation, energy conservation and exergy balance.

Mass Balance

The mass flow rate through each component of low temperature circuit is $\dot{m}_{r,ltc}$. It is calculated using eqn. (1).

$$\dot{Q}_{evap} = \dot{m}_{r,ltc}\left(h_{11} - h_{14}\right) \tag{1}$$

Mass balance at absorber or generator

$$\dot{m}_s = \dot{m}_r + \dot{m}_w \tag{2}$$

Here, $\dot{m}_r$ is mass flow rate of refrigerant through condenser and evaporator.

Energy Balance

$$\dot{Q}_{abs} = \dot{m}_{10}h_{10} + \dot{m}_6 h_6 - \dot{m}_1 h_1 \tag{3}$$

$$\dot{Q}_{gen} = \dot{m}_7 h_7 + \dot{m}_4 h_4 - \dot{m}_3 h_3 \tag{4}$$

$$\dot{Q}_{cond} = \dot{m}_7\left(h_7 - h_8\right) \tag{5}$$

$$\dot{Q}_{she} = \dot{m}_3\left(h_3 - h_2\right) = \dot{m}_4\left(h_4 - h_5\right) \tag{6}$$

$$\dot{W}_{pump} = \dot{m}_2\left(h_2 - h_1\right) \tag{7}$$

$$\dot{W}_{comp} = \dot{m}_{r,ltc}\left(h_{12} - h_{11}\right) \tag{8}$$

Exergy Balance

By the application of second law of thermodynamics, exergy destruction in each component of the absorption-compression cascade refrigeration system is obtained and furnished below:

$$\dot{E}D_{abs} = \dot{m}_{10}\left(h_{10} - T_0 s_{10}\right) + \dot{m}_6\left(h_6 - T_0 s_6\right) - \dot{m}_1\left(h_1 - T_0 s_1\right) \tag{9}$$

$$\dot{E}D_{gen} = \dot{m}_3\left(h_3 - T_0 s_3\right) - \dot{m}_4\left(h_4 - T_0 s_4\right) - \dot{m}_7\left(h_7 - T_0 s_7\right) + \dot{Q}_{gen}\left(1 - T_0 / T_{gen}\right) \tag{10}$$

$$\dot{E}D_{cond} = \dot{m}_7\left(h_7 - T_0 s_7\right) - \dot{m}_8\left(h_8 - T_0 s_8\right) \tag{11}$$

$$\dot{E}D_{cc} = \dot{m}_r\left((h_9 - h_{10}) - T_0(s_9 - s_{10})\right) + \dot{m}_{r,ltc}\left((h_{12} - h_{13}) - T_0(s_{12} - s_{13})\right) \tag{12}$$

$$\dot{E}D_{she} = \dot{m}_s\left((h_2 - h_3) - T_0(s_2 - s_3)\right) + \dot{m}_w\left((h_4 - h_5) - T_0(s_4 - s_5)\right) \tag{13}$$

$$\dot{E}D_{rtv,htc} = \dot{m}_r T_0\left(s_9 - s_8\right) \tag{14}$$

$$\dot{E}D_{stv} = \dot{m}_w T_0\left(s_6 - s_5\right) \tag{15}$$

$$\dot{E}D_{comp} = \dot{m}_{r,ltc} T_0\left(s_{12} - s_{11}\right) \tag{16}$$

$$\dot{E}D_{evap} = \dot{m}_{r,ltc}\left((h_{14} - h_{11}) - T_0(s_{14} - s_{11}) + \dot{Q}_{evap}\left(1 - T_0 / T_{evap}\right)\right) \tag{17}$$

$$\dot{E}D_{rtv,ltc} = \dot{m}_{r,ltc} T_0\left(s_{14} - s_{13}\right) \tag{18}$$

$$\dot{E}D_{total} = \dot{E}D_{abs} + \dot{E}D_{gen} + \dot{E}D_{cond} + \dot{E}D_{cc} + \dot{E}D_{she} + \dot{E}D_{rtv,htc} + \dot{E}D_{stv} + \dot{E}D_{comp} + \dot{E}D_{evap} + \dot{E}D_{rtv,ltc} \tag{19}$$

Performance indices

$$COP = \frac{\dot{Q}_{evap}}{\dot{Q}_{gen} + \dot{W}_{pump} + \dot{W}_{comp}} \quad (20)$$

Exergetic efficiency

$$\eta_{ex} = \frac{\dot{Q}_{evap}\left|1 - T_0/T_r\right|}{\dot{Q}_{gen}\left(1 - T_0/T_{gen}\right) + \dot{W}_{pump} + \dot{W}_{comp}} \quad (21)$$

Exergy destruction ratio

In order to identify and compare the sites of thermodynamic inefficiencies from the point of view of exergy analysis, the exergy destruction ratio $(Y_{d,k})$ for each component is calculated. It is defined as the ratio of exergy destruction rate in a component to the total exergy destruction rate of the system [17] and it is expressed as:

$$Y_{d,k} = \dot{E}D_k / \dot{E}D_{total} \quad (22)$$

where 'k' denotes any component.

Initial/operating parameters

The parameters assumed for computation of results are mentioned in Table 1.

Table 1. Parameters for the analysis

S. No.	Parameters	Value
1.	Cooling capacity ($\dot{Q}_{evap}$)	100 kW
2.	Isentropic efficiency of compressor (η_{comp})	60-80 %
3.	Evaporator temperature (T_{evap})	-35 to -55 °C
4.	Cascade condenser temperature (T_{cc})	2 to 16 °C
5.	Generator temperature (T_{gen})	80 to 110 °C
6.	Absorber temperature (T_{abs})	35 to 45 °C
7.	Condenser temperature (T_{cond})	35 to 45 °C
8.	Effectiveness of solution heat exchanger (ε_{she})	0.6-0.9
9.	Approach in cascade condenser (OT)	0 to10 °C
10.	Difference between evaporator and space temperature (DT)	7 °C

Model validation

A simple steady state simulation model based on sequential modular approach has been developed and implemented in a computer program using EES software [18]. The model equations are formulated from species, mass, energy and exergy balances. The thermodynamic model of absorption-compression cascade refrigeration system developed in this work is validated by the numerical data of Cimsit and Ozturk [12]. R134a and LiBr-H_2O are considered as working substances in VCR and VAR cycles for validation.

Table 2 clearly indicates that there exist good agreements between the present data and those provided by Cimsit and Ozturk [12]. The maximum error is $\pm$ 2.03%, which may be attributed to the usage of different correlations for the calculation of thermophysical properties of LiBr-H_2O.

Table 2. Comparison of performance data of present model with that of Cimsit and Ozturk [12]

Parameters	Present model	Cimsit and Ozturk [12]	Difference (%)	Operating Parameters
$\dot{Q}_{abs}$ (kW)	74.27	72.76	2.03	T_{cond} = 40°C
$\dot{Q}_{gen}$ (kW)	77.98	76.45	1.96	T_{gen} = 90°C
$\dot{Q}_{cond}$ (kW)	62.09	61.06	1.66	T_{cc} = 10°C
$\dot{W}_{comp}$ (kW)	8.39	8.25	1.67	T_{evap} = -10°C
COP	0.579	0.590	-1.90	ε_{she} = 0.6
				η_{comp} =0.72
				$\dot{Q}_{evap}$ = 50 kW

RESULTS AND DISCUSSION

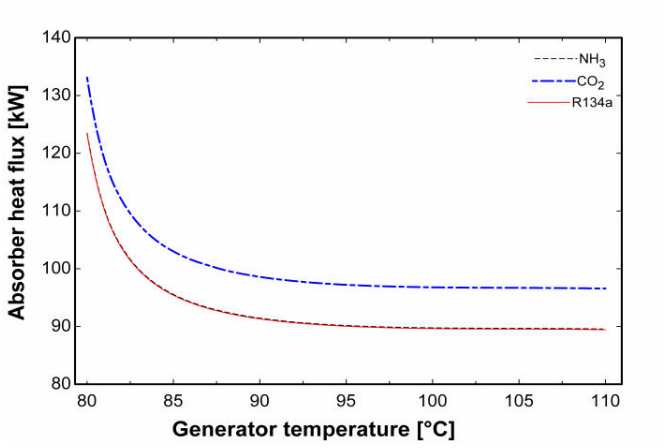
For the base case the operating parameters considered are as follows: generator, condenser, evaporator, cascade condenser temperatures are 85°C, 40°C, -45°C and 7°C. The absorber temperature is same as the condenser temperature. The approach in cascade condenser is 7°C, Isentropic efficiency of compressor is 0.8 and effectiveness of solution heat exchanger is 0.7. In order to perform the parametric analysis one parameter is varied within the given limits while others are kept constant.

First law analyses

Figures 2(a), (b) and (c) respectively show the variation of COP, generator heat load and absorber heat load with the generator temperature. It is clear from Fig. 2(a) that absorption-compression cascade refrigeration system achieves maximum COP at a particular generator temperature. The maximum values of COP for NH_3, CO_2 and R134a are 0.4307,

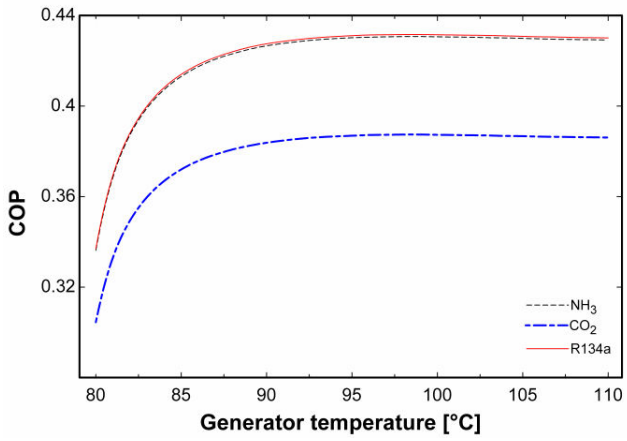
0.3874 and 0.4316 respectively and the corresponding generator temperature is 98°C. The COP of the system operating with R134a is approximately 10% higher than that obtained with CO_2. The COP of NH_3 system is marginally lower than that of R134a based system. The variation of COP with generator temperature depends inversely on the variation of generator heat load for constant cooling capacity system. It is obvious from Fig 2(b) that there exists a generator temperature corresponding to which generator heat load is minimum. The value of generator temperature corresponding to minimum generator heat load is equal to that corresponding to maximum COP. Considering the absorber heat load, shown in Fig. 2(c), it can be stated that highest amount is delivered in case of CO_2 whereas lowest in case of R134a.

Fig. 3(a) shows the COP of absorption-compression cascade refrigeration system as a function of evaporator temperature. As evaporator temperature is increased from -55°C to -35°C, increase in COP is registered.

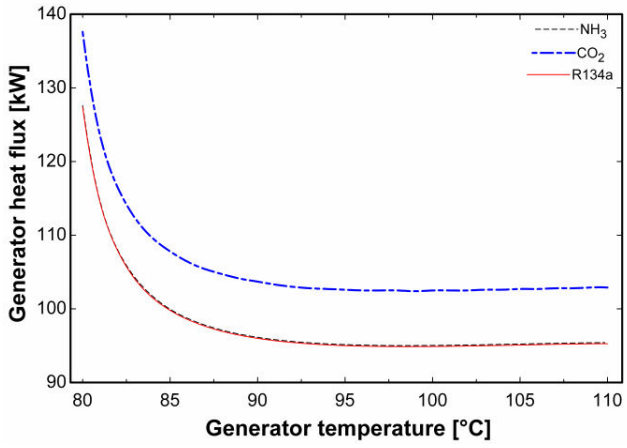


(c)

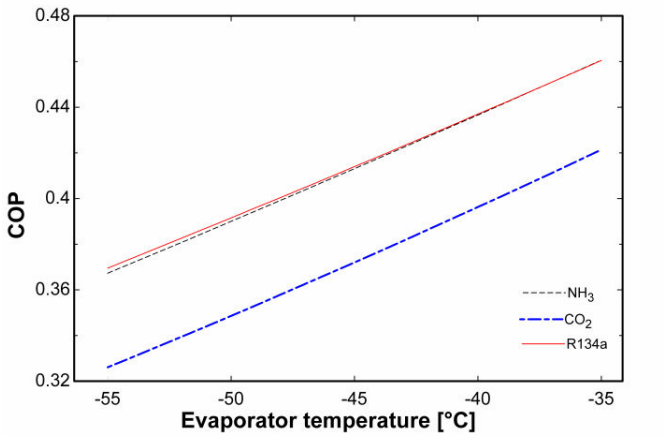
Figure 2. (a) COP, (b) generator heat load and (c) absorber heat load against generator temperature



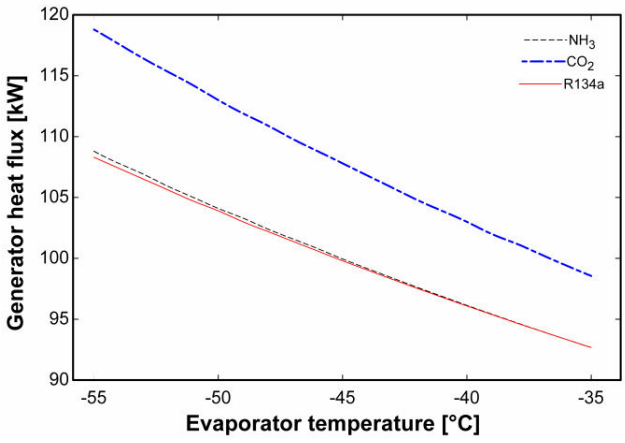
(a)



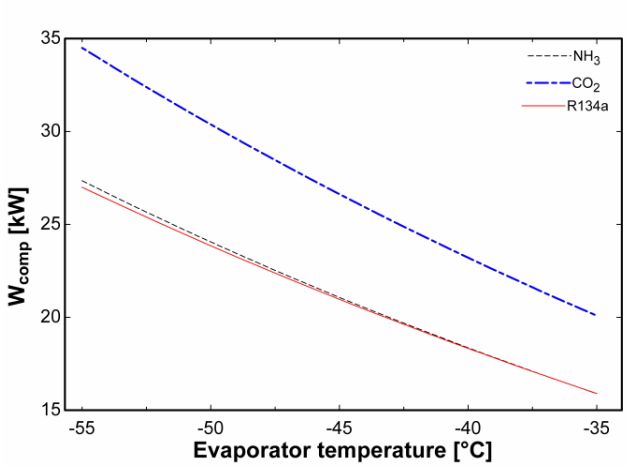
(b)



(a)



(b)



(c)

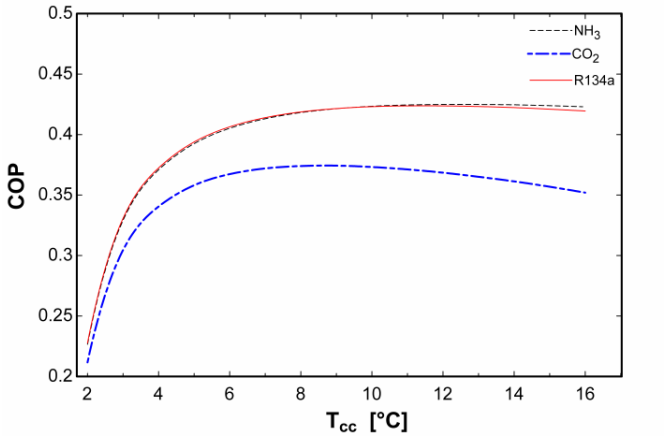
Figure 3. (a) COP, (b) generator load and (c) work of compression against evaporator temperature

The COP of R134a based system increases from 0.3695 to 0.4605 whereas the COP of CO_2 based system increases from 0.3261 to 0.4214. The COP of NH_3 based system is lower but closer to R134a based system. In Fig. 3(b) it can be seen that as evaporator temperature decreases from -35°C to -55°C, heat required in generator increases from 92 to 108 kW, 98 to 119 kW and 102 to 109 kW respectively for R134a, CO_2 and NH_3 based systems. The decrease in compressor work of absorption-compression cascade refrigeration system with increase in evaporator temperature is shown in Fig. 3(c). As evaporator temperature increases from -55°C to -35°C, compressor work decreases by almost 40% for all the refrigerants. It means rise in evaporator temperature by 1°C can reduce the electricity consumption by 2%. Carbon dioxide based system requires highest electrical input (20-35 kW) in the form of compressor work while R134a based system needs minimum electrical energy (16-27 kW).

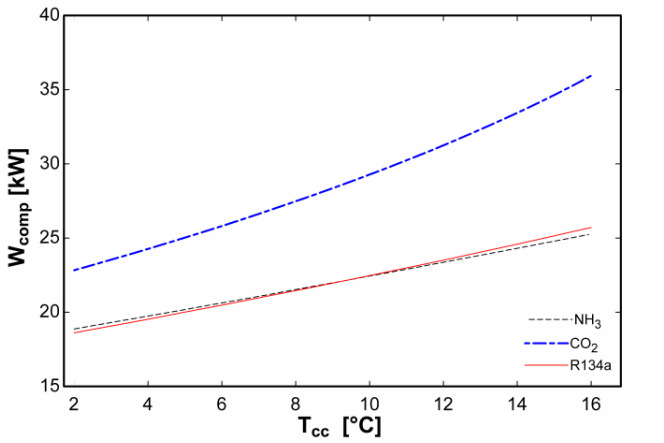
The cascade condenser temperature is one of the most important design parameters as it has intense effect on the performance of the absorption-compression cascade refrigeration system. Its lowest value is restricted to be above 0°C when LiBr-H_2O is the working substance in VAR subsystem because it depends on the freezing point of water. From Fig. 4(a) it can be seen that with the increase in cascade condenser temperature from 2 to 16°C, COP first increases, achieves a maximum and then reduces. The increase in cascade condenser temperature causes increase in absorber pressure, increase in pressure ratio across the compressor and increase in mass flow rate in VCR subsystem. The first two factors account for increase in compressor power as shown in Fig. 4(b) while the last factor i.e. increase in absorber pressure accounts for decrease in strong solution concentration (X_s). The weak solution concentration (X_w) remains constant. Hence, solution circulation ratio (=X_w/ (X_w-X_s)) decreases. The reduction in solution circulation ratio decreases the heat required in the generator as shown in Fig. 4(c). Thus, COP of cascade refrigeration system may increase or decrease depending upon the increase in compressor power requirement and reduction in generator heat duty.

It is clear from Figs. 4(a), (b) and (c) that maximum values of COP occur at different cascade condenser temperature for different refrigerants. In case of NH_3, maximum COP is 0.4249 and it occurs at 12.47°C whereas for R134a and CO_2 the maximum COP values are 0.4237 and 0.3743, occurring at 11.45°C and 8.64°C respectively.

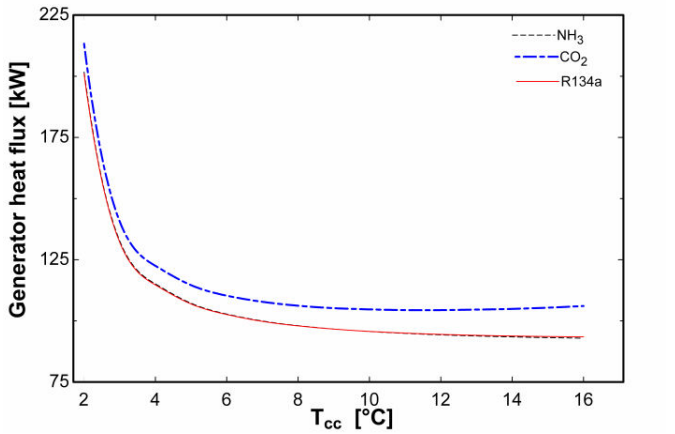
For all values of cascade condenser temperature, the performance of CO_2 based system is inferior to the performance of the other two systems. However, the NH_3 based system and R134a based system perform differently at different cascade condenser temperature, though the difference is marginal. It can be observed that NH_3 based system outperforms R134a based system at higher cascade condenser temperature, particularly above 10°C for the conditions considered in this study.



(a)



(b)



(c)

Figure 4. (a) COP, (b) generator load and (c) work of compression against cascade condenser temperature

Second law analyses

Fig. 5 shows the exergetic efficiency and exergy destruction rates of R134a, ammonia and carbon dioxide based systems versus generator temperature at design conditions. It indicates a maximum value of exergetic efficiency ($\eta_{ex,max}$) and a minimum value of exergy destruction rate as T_{gen} increases from 80°C to 110°C.The variation of exergetic efficiency with generator temperature can be explained in similar way as variation of COP with T_{gen}. However, temperature of the heat source is additional factor which govern the exergetic efficiency, resulting in higher slope of exergetic efficiency as compared to corresponding COP. The maximum values of exergetic efficiency for NH_3, CO_2 and R134a based absorption-compression cascade refrigeration system are 35.43%, 29.99% and 35.56% respectively, occurring at same generator temperature of 85°C. The corresponding minimum values of exergy destruction rates are 24.43 kW, 31.29 kW and 24.30 kW for NH_3, CO_2 and R134a based cascade systems.

The comparison of Fig. 5 and Fig. 2(a) reveals that maximum exergetic efficiency and maximum COP occur at different generator temperatures. Also, an increase of 11.70%, 10.66% and 11.72% in the second law efficiency of NH_3, CO_2 and R134a based systems is observed as generator temperature is increased from 80°C to 85°C.

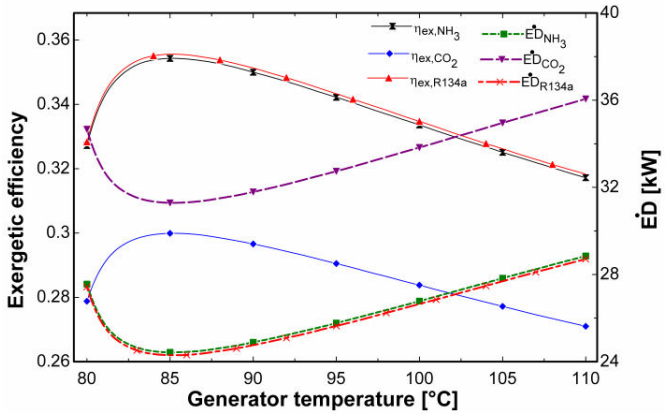
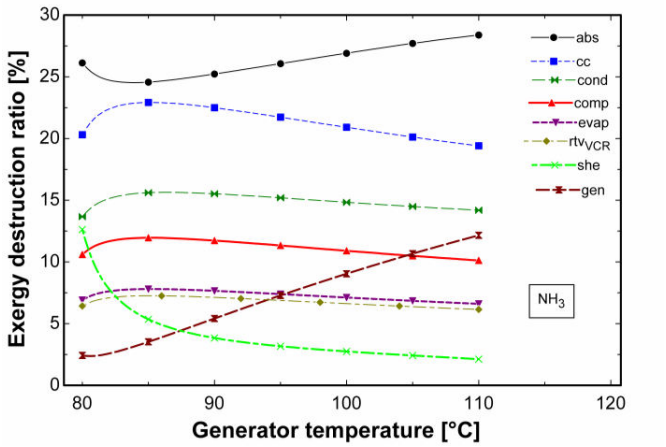
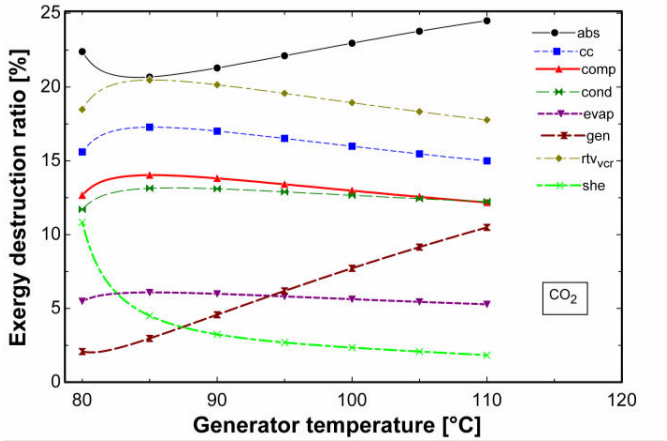


Figure 5. Exergetic efficiency and total exergy destruction rate against generator temperature

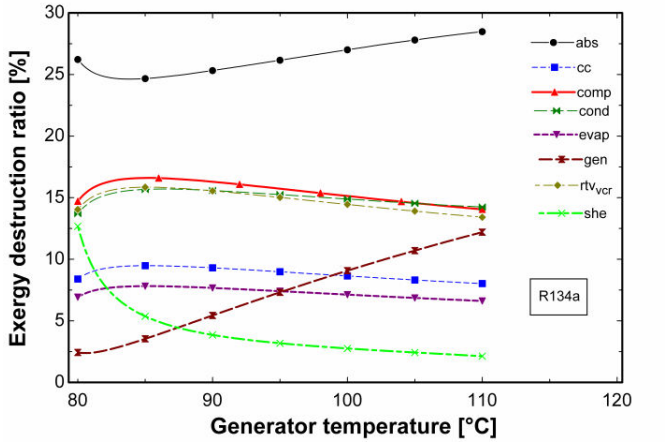
Figs. 6(a), (b) and (c) respectively show the variation of exergy destruction ratio of the main components of NH_3-LiBr/H_2O, CO_2- LiBr/H_2O and R134a- LiBr/H_2O absorption-compression cascade refrigeration systems with generator temperature. At the generator temperature corresponding to maximum exergetic efficiency, the sites of major irreversibilities are different for different working substances. The absorber, the cascade condenser and the condenser are the major contributors of exergy destruction for NH_3-LiBr/H_2O system with exergy destruction ratio of 24.57%, 22.92% and 15.61% respectively. In case of CO_2- LiBr/H_2O system the



(a)



(b)



(c)

Figure 6. Exergy destruction ratio of main components against generator temperature for (a) Ammonia (b) Carbon dioxide and (c) R134a refrigerants

major sources of exergy destruction are absorber (20.68%), RTV_{vcr} (20.47%) and cascade condenser (17.28%) whereas for R134a- LiBr/H_2O cascade system absorber (24.63%), compressor (16.56%) and RTV_{vcr} (15.82%) are the prominent locations of exergy destruction.

Fig. 7 shows exergetic efficiency as a function of cascade condenser temperature. As cascade condenser temperature increases from 2°C to 16°C, exergetic efficiency attains a maximum value at a particular value. The NH_3-LiBr/H_2O cascade system attains maximum exergetic efficiency (35.43%) at cascade condenser temperature of 7°C whereas CO_2- LiBr/H_2O and R134a- LiBr/H_2O systems attain maximum exergetic efficiencies at cascade temperature of 5°C and 6°C respectively. The corresponding maximum exergetic efficiencies of CO_2- LiBr/H_2O and R134a- LiBr/H_2O systems are 30.30% and 35.58%. Thus it can be said that exergetic efficiency attains maximum value at different cascade condenser temperatures, depending on the working substance considered. Furthermore, it is seen from the figure that the poorest exergetic performance is exhibited by CO_2- LiBr/H_2O, whereas the best performance may be shown by either of NH_3-LiBr/H_2O and R134a- LiBr/H_2O system depending upon the value of cascade condenser temperature. At higher values of cascade condenser temperature NH_3-LiBr/H_2O outperform R134a- LiBr/H_2O cascade system.

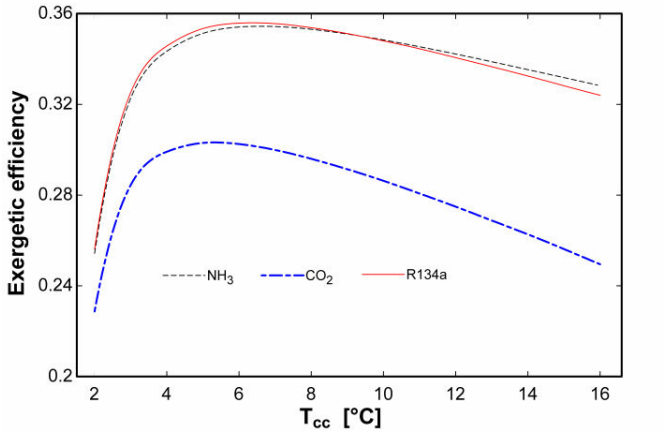
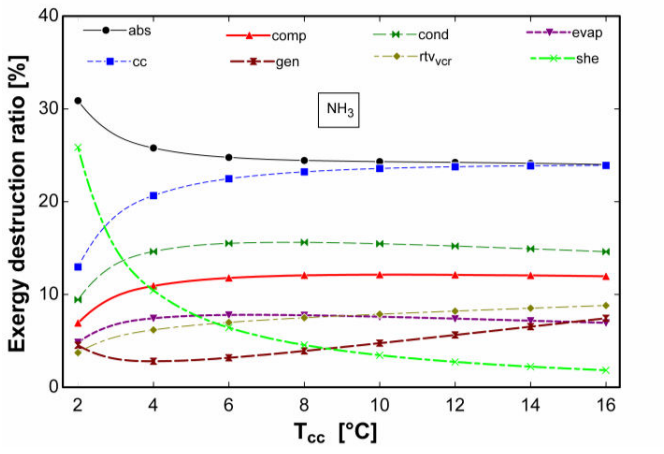


Figure 7. Exergetic efficiency against cascade condenser temperature

Figs. 8(a), (b) and (c) show the exergy destruction ratio of various components as a function of cascade condenser temperature. At cascade condenser temperature of 7°C (corresponding to maximum exergetic efficiency for NH_3-LiBr/H_2O system), absorber accounts for maximum exergy destruction followed by cascade condenser, condenser and compressor. For CO_2-LiBr/H_2O system, at cascade condenser temperature of 5°C (corresponding to maximum exergetic efficiency), the major sources of exergy destruction are identified as absorber, RTVvcr and cascade condenser. In case of R134- LiBr/H_2O system the main sites of exergy destruction are found to be absorber, compressor and condenser.



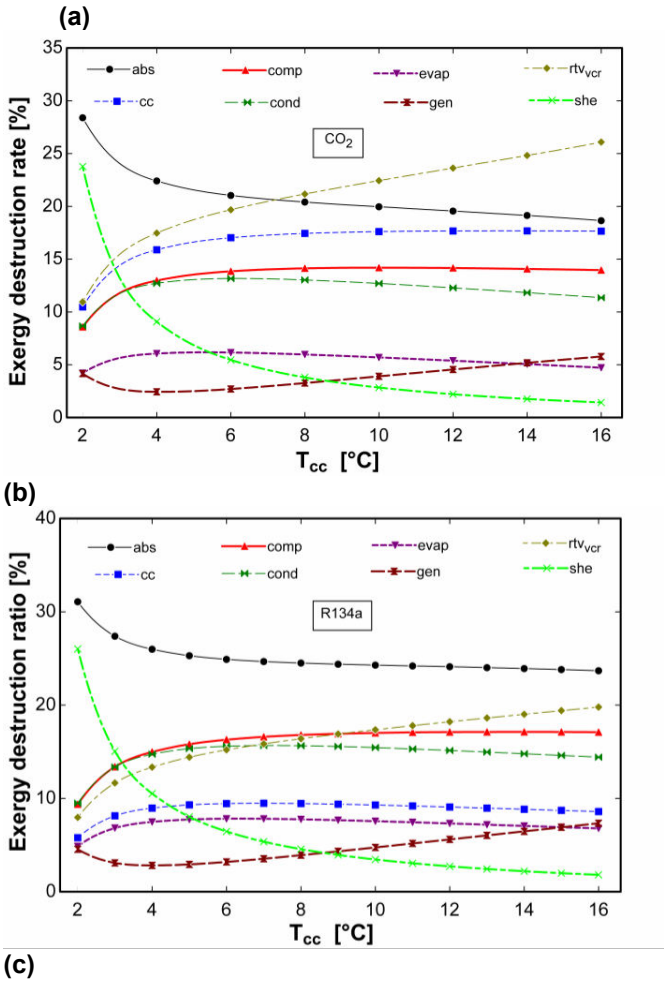


Figure 8. Exergy destruction ratio of main components against cascade condenser temperature for (a) Ammonia (b) Carbon dioxide and (c) R134a refrigerants

Fig. 9 reveals the variation of exergetic efficiency with evaporator temperature. It is observed that with the increase in evaporator temperature the rate of decrease in exergetic efficiencies of NH_3-LiBr/H_2O and R134a-LiBr/H_2O are respectively 3.26% and 4.23%, whereas for CO_2-LiBr/H_2O cascade system it is 1.5% only.

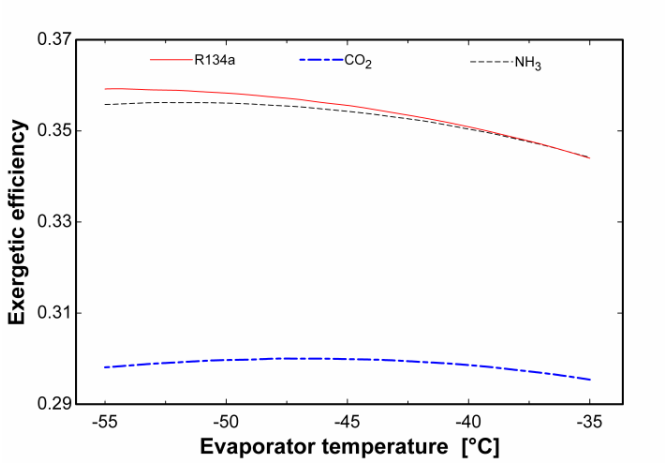
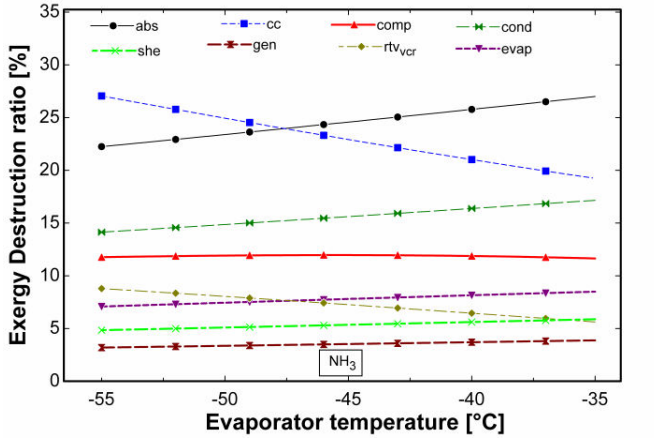


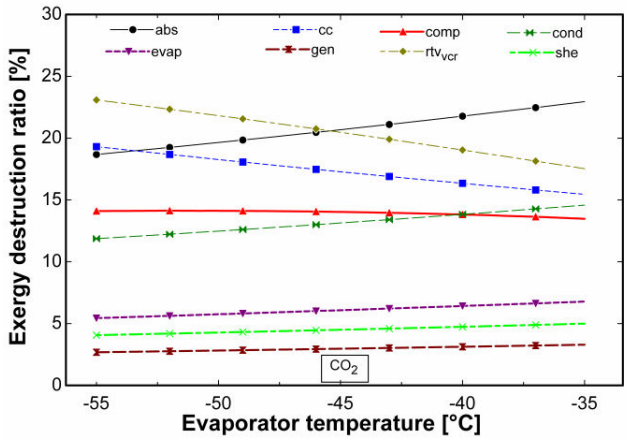
Figure 9. Exergetic efficiency against evaporator temperature

Figs. 10(a), (b) and (c) respectively show exergy destruction ratio of various components of NH_3, CO_2 and R134a based refrigeration systems as a function of evaporator temperature. As evaporator temperature increases from -55°C to -35°C, the exergy destruction ratio of absorber, condenser, generator, evaporator and solution heat exchanger increases while that of refrigerant throttle valve of VCR subsystem decreases for all the three refrigerants. However, the variation in exergy destruction ratio is of varying degree. In case of cascade condenser and compressor, the trends are quite diverse and depend on the refrigerant used. Exergy destruction ratio of cascade condenser decreases for NH_3 and CO_2 based systems whereas for R134a based system it first attains a minimum value and then begins to rise. Similarly, exergy destruction ratio of compressor first attains a maximum value and then falls for NH_3 and CO_2 based systems while it reduces continuously for R134a based system.

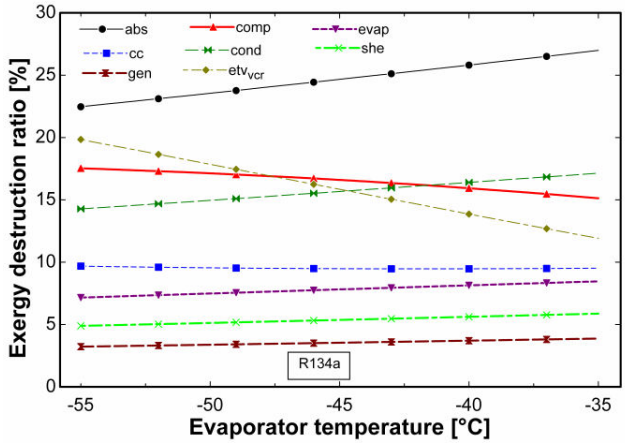
Exergy destruction ratio of various components for NH_3-LiBr/H_2O is shown in Fig. 10(a). It is observed that at low evaporator temperatures cascade condenser is the major source of irreversibility while at higher values of evaporator temperature it is absorber in which maximum exergy destruction takes place. Fig. 10(b) shows that refrigerant throttle valve of VCR and absorber are the main sites of irreversibilities at evaporator temperature of -55°C and -35°C respectively. Absorber remains the major source of exergy destruction throughout the evaporator change for R134a-LiBr/H_2O cascade refrigeration system.



(a)



(b)



(c)

Figure 10. Exergy destruction ratio of main components against evaporator temperature for (a) Ammonia (b) Carbon dioxide and (c) R134a refrigerants

Fig. 11 shows the variation of exergetic efficiency with compressor isentropic efficiency. As expected, both the COP and the exergetic efficiency improves with the increase in compressor isentropic efficiency. With the increase in compressor isentropic efficiency from 0.6 to 0.9, the COP (not shown in figure) of NH_3, CO_2 and R134a based systems increase from 0.3625 to 0.4333, from 0.3210 to 0.3928 and from 0.3634 to 0.4341 respectively. Correspondingly, exergetic efficiencies increase from 28.82% to 38.38% for NH_3, from 24.08% to 32.66% for CO_2 and from 28.93% to 38.50% for R134a systems as shown in Fig. 11. Thus, it is clear that effect of compressor isentropic efficiency on the performance of absorption-compression cascade system is quite significant.

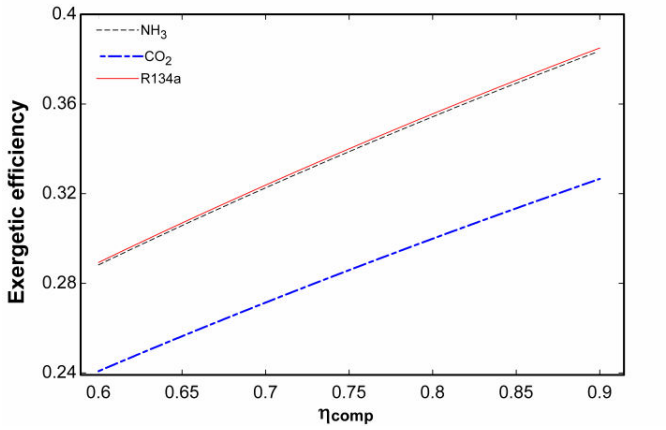
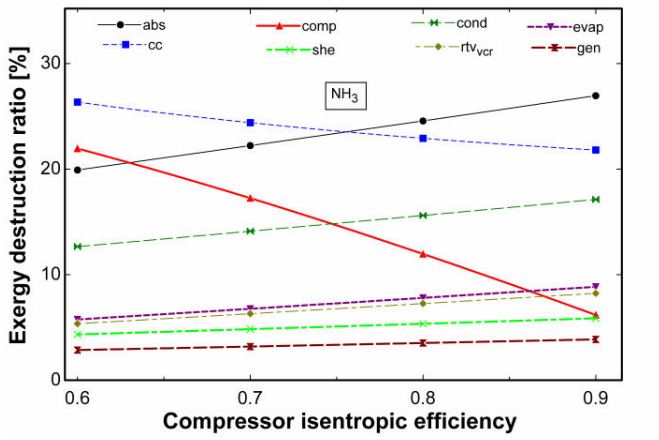
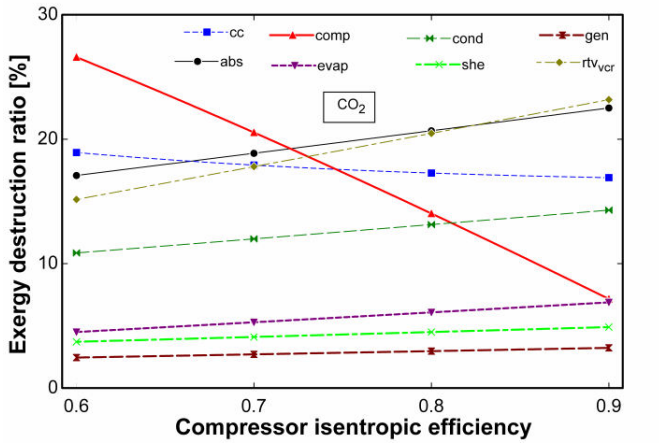


Figure 11. Exergetic efficiency versus compressor isentropic efficiency

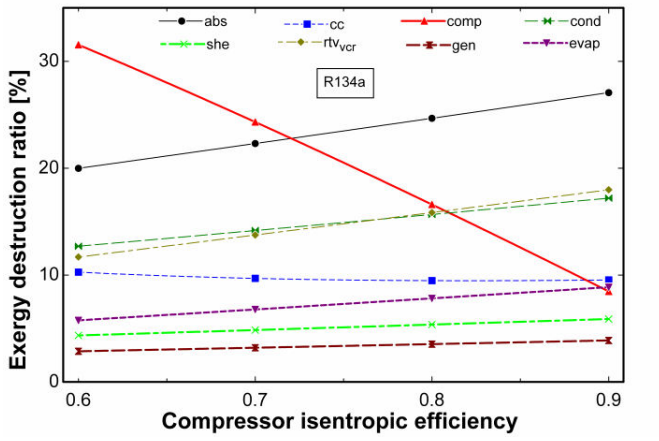
Fig. 12(a), (b) and (c) respectively show the variation of exergy destruction ratio of various components of NH_3-LiBr/H_2O, CO_2--LiBr/H_2O and R134a--LiBr/H_2O cascade systems with compressor isentropic efficiency. It is found in the study that as isentropic efficiency of the compressor drops from 0.9 to 0.6 exergy destruction rate of compressor in particular and the exergy destruction rate of the absorption-compression cascade refrigeration system as a whole y increase substantially. For NH_3-LiBr/H_2O system, compressor irreversibility increases from 1.331 kW to 7.267 kW while total irreversibility increases from 21.53 kW to 33.11 kW. For CO_2--LiBr/H_2O system, compressor and total irreversibilities increase from 1.978 kW to 11.24 kW and 27.63 kW to 42.26 kW respectively. Similarly, in case of R134a--LiBr/H_2O cascade system, exergy destruction rate of the compressor increases from 1.814 kW to 10.39 kW and total exergy destruction rate increases from 21.42 kW to 32.93 kW as isentropic efficiency of compressor reduces to 0.6 from 0.9.



(a)



(b)



(c)

Figure 12. Exergy destruction ratio of main components against compressor isentropic efficiency for (a) Ammonia (b) Carbon dioxide and (c) R134a refrigerants

CONCLUSIONS

The following conclusions are drawn from the present study:

(a) The maximum value of COP and exergetic efficiency occur corresponding to different generator temperatures. The maximum exergetic efficiency occurs at a temperature lower than the generator temperature corresponding to maximum COP.

(b) The generator temperature has greater impact on COP while exergetic efficiency is comparatively less affected by it. An increase of around 28% in COP is found with the increase in generator temperature whereas the corresponding increase in exergetic efficiency is about 11%.

(c) Maximum COP and maximum exergetic efficiency occur at different cascade condenser temperature for different refrigerants in VCR subsystem. Maximum COP occurs at higher cascade condenser temperature than at which maximum exergetic efficiency is obtained.

(d) The sites of highest irreversibilities are different for different refrigerants. For NH_3-LiBr/H_2O system it is cascade condenser, for CO_2-LiBr/H_2O system it is refrigerant throttle valve of VCR subsystem and in case of R134a-LiBr/H_2O system it is compressor.

(e) At design point, R134a-LiBr/H_2O absorption-compression cascade refrigeration system is the best performer from the view point of both first law and second law of thermodynamics.

NOMENCLATURE

COP	Coefficient of performance
$\dot{E}D$	Exergy destruction rate (kW)
h	Specific enthalpy (kJ.kg^{-1})
HTC	High temperature circuit
LTC	Low temperature circuit
$\dot{m}$	Mass flow rate (kg.s^{-1})
$\dot{Q}$	Heat transfer rate (kW)
s	Specific entropy(kJ.kg^{-1}.K^{-1})
T	Temperature ($^{\circ}C$ or K)
VAR	Vapour absorption refrigeration
VCR	Vapour compression refrigeration
Y_d	Exergy destruction ratio
$\dot{W}$	work transfer rate (kW)
Greek letters	
ϵ	Effectiveness of heat exchanger
η	efficiency
η_{ex}	Exergetic efficiency
Subscripts	
0	Reference state
1, 2…	State points
a, abs	absorber
c,cond	Condenser

cc	Cascade condenser
comp	Compressor
e, evap	Evaporator
g, gen	Generator
htc	High temperature circuit
ltc	Low temperature circuit
p	pump
r	Refrigerant, room
rtv	Refrigerant throttle valve
s	Strong solution
she	Solution heat exchanger
stv	Solution throttle valve
w	Weak solution

ACKNOWLEDGMENTS

The support of Ministry of New and Renewable Energy (MNRE), government of India is duly acknowledged.

REFERENCES

[1] Chakravarthy, V.S., Shah, R.K., Venkatarathnam, G., 2011. A Review of Refrigeration Methods in the Temperature Range 4–300 K. J. Therm. Sci. Eng. Appl. 3, 020801. doi:10.1115/1.4003701

[2] Jain, V., Kachhwaha, S.S., Sachdeva, G., 2013. Thermodynamic performance analysis of a vapor compression–absorption cascaded refrigeration system. Energy Convers. Manag. 75, 685–700. doi:10.1016/j.enconman.2013.08.024

[3] Dixit, M., Arora, A., Kaushik, S.C., 2016. Energy and exergy analysis of a waste heat driven cycle for triple effect refrigeration. Journal of Thermal Engineering 2(5), 954-961

[4] Arora, A, Dixit, M., Kaushik, S.C., 2016. Computation of optimum parameters of a half effect water-lithium bromide vapour refrigeration system. Journal of Thermal Engineering 2(2), 683-692

[5] Herold, K.E., Radermacher, R., Klein, S.A., 1996. Absorption chillers and heat pumps. CRC press, USA.

[6] Kaushik, S.C., Arora, A., 2009. Energy and exergy analysis of single effect and series flow double effect water–lithium bromide absorption refrigeration systems. Int. J. Refrig. 32, 1247–1258. doi:10.1016/j.ijrefrig.2009.01.017

[7] Kaita, Y.T., 2002. Simulation results of triple-effect absorption cycles. Int. J. Refrig. 25, 999–1007

[8] Dixit, M., Arora, A., Kaushik, S.C., 2015. Thermodynamic analysis of GAX and hybrid GAX aqua-ammonia vapor absorption refrigeration systems. International Journal of Hydrogen Energy 40, 16256-16265

[9] Fernández-Seara, J., Sieres, J., Vázquez, M., 2006. Compression-absorption cascade refrigeration system. Appl. Therm. Eng. 26, 502–512. doi:10.1016/j.applthermaleng.2005.07.015

[10] Kairouani, L., Nehdi, E., 2006. Cooling performance and energy saving of a compression-absorption refrigeration system assisted by geothermal energy. Appl. Therm. Eng. 26, 288–294. doi:10.1016/j.applthermaleng.2005.05.001

[11] Garimella, S., Brown, A.M., Nagavarapu, A.K., 2011. Waste heat driven absorption/vapor-compression cascade refrigeration system for megawatt scale, high-flux, low-temperature cooling. Int. J. Refrig. 34, 1776–1785. doi:10.1016/j.ijrefrig.2011.05.017

[12] Cimsit, C., Ozturk, I.T., 2012. Analysis of compression-absorption cascade refrigeration cycles. Appl. Therm. Eng. 40, 311–317. doi:10.1016/j.applthermaleng.2012.02.035

[13] Wang, L., Ma, A., Tan, Y., Cui, X., Cui, H., 2012. Study on solar assisted cascade refrigeration system. Energy Procedia, 16, 1503–1509

[14] Colorado, D., Velazquez, V.M., 2013. Exergy analysis of a compression-absorption cascade system for refrigeration. Int. J. Energy Res; 37, 1851-65

[15] Jain, V., Sachdeva, G., Kachhwaha, S.S., 2015. Thermodynamic modelling and parametric study of a low temperature vapour compression-absorption system based on modified Gouy-Stodola equation. Energy 79, 407–418. doi:10.1016/j.energy.2014.11.027

[16] Arora, A., Kaushik, S.C., 2009. Theoretical analysis of LiBr/H 2 O absorption refrigeration systems. Int. J. Energy Res. 33, 1321–1340. doi:10.1002/er.1542

[17] Bejan, A., Tsatsaronis, G., Moran, M., 1996.Thermal design and optimization. New York: John Wiley & Sons, Inc.

[18] Klein S.A., Alvarado F., 2005. Engineering Equation Solver, Version 7.441, F-Chart software, Middleton, WI

Sensors and Actuators B xxx (2016) xxx–xxx

Contents lists available at ScienceDirect

Sensors and Actuators B: Chemical

journal homepage: www.elsevier.com/locate/snb

Engendering color tunable emission in calcium silicate based phosphors *via* ageing of silicate source

Hyun-Joo Woo[a], Sakthivel Gandhi[b], M. Jayasimhadri[c], Dong-Soo Shin[d], Ho Sueb Lee[e], Kiwan Jang[e,*]

[a] Research Institute of Basic Sciences, Changwon National University, Changwon 51140, Republic of Korea
[b] Centre for Nanotecnology & Advanced Biomaterials, SASTRA University, Thanjavur 613401, India
[c] Department of Applied Physics, Delhi Technological University, Delhi, 110042, India
[d] Department of Chemistry, Changwon National University, Changwon 51140, Republic of Korea
[e] Department of Physics, Changwon National University, Changwon 51140, Republic of Korea

ARTICLE INFO

Article history:
Received 4 July 2016
Received in revised form
29 September 2016
Accepted 6 October 2016
Available online xxx

Keywords:
Warm white LED
Ca_2SiO_4
Orthosilicate
Emission spectrum
Optical properties
Sol-gel synthesis

ABSTRACT

In this work, an artificially tunable luminescence emitting Ca_2SiO_4 based Eu^{2+} ions doped phosphor was successfully developed using differently aged propylene glycol modified silane (PGMS) as the silica source. The powder XRD patterns of all the prepared samples confirm the presence of three different crystal phases namely α_L', β & γ, which afford for the variable site accommodation of Eu^{2+} dopant in the host. Prototype phosphor converted LEDs (pc-LEDs) have also been fabricated using all the prepared phosphors. Photoluminescent and electroluminescent properties were investigated for the synthesized phosphors and prototype pc-LEDs, respectively. Colorimetric properties such as CIE coordinates, CCT and CRI values calculated to compare the effects of differently aged PGMS on the Eu^{2+} doped Ca_2SiO_4 phosphor, which confirmed the ability to produce color tuning with ageing of silicate source. The results indicate that these phosphors are potential candidates to use in solid state lighting applications.

© 2016 Elsevier B.V. All rights reserved.

1. Introduction

In recent years, there is a growing importance in generating energy saving and environmental friendly white light emitting sources, which emit light with less power consumption and without releasing any harmful gases [1–5]. Among those sources, the fabricating phosphor converted warm white LED that closely mimics the light spectrum of the sun received much more attention due to its low cost, ease of preparation and high energy efficiency [6–10]. Normally, the method of tuning emission wavelength or emissive color of light can be obtained by altering the phosphors. This alteration is possible within the phosphor by changing the host lattice, synthetic approaches, the dopant and its concentration as well [11–14]. The structural and luminescence properties of few rare earth ions activated alkaline earth orthosilicate M_2SiO_4 ($M:Ca^{2+}/Sr^{2+}/Ba^{2+}$) phosphors have been investigated and reported elsewhere [3,15–19]. Especially, there are various emission colors reported for Eu^{2+} or Ce^{3+} doped Ca_2SiO_4 phosphors by changing the concertation or synthesizing different methods. This colour variation is mainly possible due to the existence of several crystal phases namely blue emitting β-Ca_2SiO_4:Ce^{3+}, yellow emitting γ-Ca_2SiO_4:Ce^{3+}, green emitting β-Ca_2SiO_4:Eu^{2+} and red emitting α_L'-Ca_2SiO_4:Eu^{2+}. Our previous studies reported the tunable emission from the single host by changing the concentration of dopant or using crystal phase stabilizers [20]. There are also few studies that show the tunable emission from a single host by introducing co-dopants where the tunable emission is possible by altering the dopant/co-dopant ratio across the single host [21,22]. However, the unique attempt has been successfully implemented for the first time in this paper to synthesize a single host phosphor to obtain an emission color tunability by ageing of silicate source (PGMS) to alter the crystal site engineering.

In this study, we report a novel method to achieve the artificial tunable emission from a single host using PGMS as a silicate source *via* sol-gel technique. As a new input, the differently aged PGMS was employed to synthesize Ca_2SiO_4:Eu^{2+} phosphors. The silicate source PGMS was prepared and divided into four parts in which the first part was utilized on the day of preparation to make phosphor. The other parts were utilized in the consecutive days 2–4 to syn-

* Corresponding author at: Department of Physics, Changwon National University, 9, Sarim-dong, Changwon, GN, 51140, Republic of Korea.
E-mail address: kwjang@changwon.ac.kr (K. Jang).

http://dx.doi.org/10.1016/j.snb.2016.10.027
0925-4005/© 2016 Elsevier B.V. All rights reserved.

Please cite this article in press as: H.-J. Woo, et al., Engendering color tunable emission in calcium silicate based phosphors *via* ageing of silicate source, Sens. Actuators B: Chem. (2016), http://dx.doi.org/10.1016/j.snb.2016.10.027

thesize the same phosphor with the same stoichiometric ratio. The structural and luminescence properties of all the phosphors were studied thoroughly. To the best of our knowledge, this is the first report to synthesize tunable color emitting orthosilicate phosphor using a differently aged silicate source (PGMS).

2. Materials and methods

The $Ca_{2-x}SiO_4:xEu^{2+}$ phosphors were prepared *via* a sol-gel synthesis method, using $Ca(NO_3)_2{\cdot}6H_2O$, $Eu(NO_3)_3{\cdot}6H_2O$ and citric acid powders as starting materials. Initially, PGMS solution was prepared as reported in our previous paper [20]. Briefly, 22.3 mL of TEOS and 22.3 mL of propylene glycol were mixed in a round-bottomed flask and stirred for 48 h at 80 °C to get a turbid bilayered liquid. Exactly, 15 mL of distilled water was mixed with 5 mL of turbid bilayered liquid (TEOS + propylene glycol) solution. To the above mixture, 0.1 mL of concentrated hydrochloric acid was added slowly and stirred well to get a transparent PGMS solution. The prepared PGMS was used as silicate source to prepare phosphors.

The phosphor was prepared using differently aged PGMS solutions (PGMS-1 day, PGMS-2days, PGMS-3 days and PGMS-4days). The particular solution was taken in a beaker along with the aqueous solution containing the mixture of $Ca(NO_3)_2{\cdot}6H_2O$ and an appropriate amount of $Eu(NO_3)_3{\cdot}6H_2O$ and citric acid. This mixture was initially stirred at 80 °C for 2 h to get a homogeneous solution. The 2.28 mL of propylene glycol was added to it under stirring for another 24 h at 120 °C to obtain the polymerized gel and then subjected to thermal treatment in ambient atmosphere at 1300 °C for 6 h to decompose the organic compound in the polymerized gel sample. Finally the $Ca_{2-x}SiO_4:xEu^{2+}$ powders were made at 1100 °C for 4 h in reduced atmospheric (5% H_2 + 95% N_2) condition.

The structural properties of all the phosphors were investigated by employing a Philips X'pert, MPD 3040 X-ray diffractometer with CuKα radiation (λ = 1.5406Å) at 40 kV and 30 mA. The photoluminescence spectra were measured using the PL spectroscopy (FP – 8500, JASCO, Japan) with a 150 W Xe lamp as the excitation source.

The prototype white LEDs were constructed using 400 nm chip along with differently aged PGMS assisted phosphors. The phosphor was initially mixed with silicone gel and kept a drop on 400 nm LED chip. The chip was then kept under vacuum for 2 h and heated at 80 °C for overnight. The CIE color coordinates, CRI and CCT of all the proto-type white LEDs were measured using ocean optics detector (HR4000). The proto-type LED was operated with ~3.2 V by Agilent (E3633A) at room temperature.

3. Results and discussion

3.1. X-ray diffraction studies of sol-gel synthesized $Ca_2SiO_4:Eu^{2+}$

The influence of differently aged PGMS on the crystal structure of sol-gel synthesized europium doped Ca_2SiO_4 phosphors have been examined using X-ray diffractometer. The XRD patterns of differently aged PGMS assisted $Ca_{1.95}Eu_{0.05}SiO_4$ phosphors showed several crystal phases which include the γ-Ca_2SiO_4, α_L'-$Ca\alpha_2SiO_4$ and β-Ca_2SiO_4. Their corresponding phases are thermodynamically stable orthorhombic, thermally stable orthorhombic and metastable monoclinic phases. The standard database patterns of all the α_L', β & γ phases are shown in Fig. 1 for comparison and denoted with different symbols for the similar patterns.

The cell parameters of α_L' type with *Pna21* space are noticed as a = 20.53, b = 9.5, c = 5.6 Å & V = 1089.6 while the values of β type with *P121*/n1 space are found to be a = 5.51, b = 6.76, c = 9.32 Å & V = 346.1. The space group *Pbnm*, γ type Ca_2SiO_4 includes the cell parameters of a = 5.07, b = 11.21, c = 6.76 Å and V = 384.7. The PGMS assisted $Ca_{1.95}Eu_{0.05}SiO_4$ phosphor synthesized with one day aged

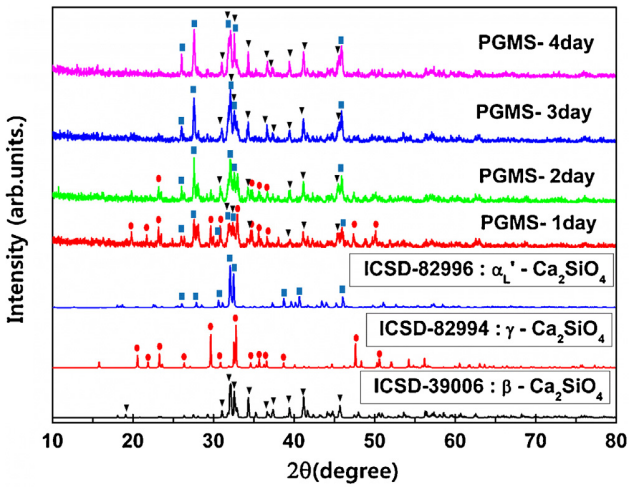


Fig 1. Powder XRD patterns of differently aged PGMS assisted $Ca_{1.95}Eu_{0.05}SiO_4$ phosphors synthesized *via* sol-gel process along with standard diffraction patterns.

PGMS source consists mixed phase of α_L', β and γ phases. For the other samples synthesized with 2–4 days aged PGMS, γ phase reduced with the ageing and finally became negligible. At the same time, α_L' phase remains unchanged and β phase increased with the increase in aging of PGMS. Although the introduction of dopant makes no change in the crystal structure, the ageing of PGMS source exhibits a significant change in the crystal structure, which in turn produce variation in the photoluminescence properties.

The change in the ratio of crystal phases may be due to the ageing of PGMS source. Briefly to explain, the ageing of PGMS induces the production of SiO_2 polymers in it. The amount of SiO_2 in the PGMS solution decides the formation of crystal phase. For example, only less number of SiO_2 polymers available in the first day of PGMS that helps to form the Ca_2SiO_4 crystal with approximately equal number of α_L', β and γ phases. As the number of days increase, the formation of SiO_2 polymers in PGMS increases with ageing time and this may contribute to increasing in β and simultaneously reducing in γ phases.

3.2. The photoluminescence (PL) studies of $Ca_2SiO_4:Eu^{2+}$ phosphors

The excitation and emission spectra of all the differently aged PGMS assisted $Ca_{1.95}Eu_{0.05}SiO_4$ phosphors were analyzed and shown in Fig. 2. The excitation spectra have been recorded by monitoring at the emission wavelength of 630 nm (Fig. 2(c)), which exhibit a broadband consists of several splits within the range of 200 and 550 nm. This may be due to the different excitation energy levels at different environments in the crystal. The XRD patterns show multiple crystal structures namely α_L', β & γ which result with the excitation of different energy levels. The emission spectra of all the samples were recorded at an excitation wavelength of 400 & 450 nm (Fig. 2(b) (a)), which correspond to most of the commercial LEDs wavelengths. A broad emission band has been noticed along with a maximum intensity peak at 630 nm for all the samples under 450 nm excitation wavelengths. But, the samples excited at 400 nm exhibit different patterns of emissions where the maximum emission peak at 630 nm was observed only for the sample synthesized with 1 day aged PGMS source. The increase in the age of PGMS shifts the emission from red to green region. All the phosphors revealed with two major peaks, one at shorter wavelength 525 nm and the other one at longer wavelength 630 nm. The intensity of shorter wavelength peak increases with the increase in the age of PGMS. At the same time, a decrease in intensity of longer wave-

Please cite this article in press as: H.-J. Woo, et al., Engendering color tunable emission in calcium silicate based phosphors *via* ageing of silicate source, Sens. Actuators B: Chem. (2016), http://dx.doi.org/10.1016/j.snb.2016.10.027

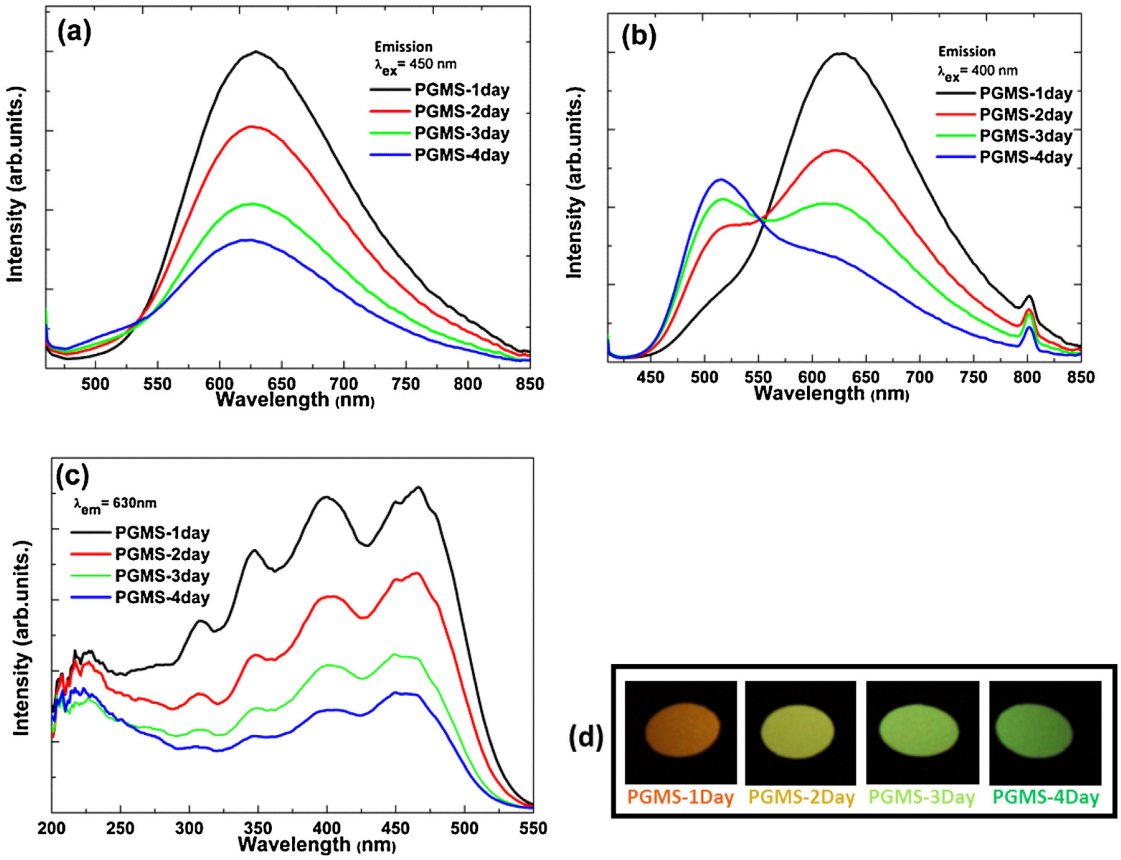


Fig. 2. Photoluminescence characteristics of differently aged PGMS assisted $Ca_{1.95}Eu_{0.05}SiO_4$ phosphors. Emission spectra under the excitation maximum of 450 (a) & 400 nm (b) and excitation spectra under the emission maximum of 630 (c). Digital images of all the differently aged PGMS assisted $Ca_{1.95}Eu_{0.05}SiO_4$ phosphors illuminated under 365 nm of UV lamp (d).

length peak was also observed. This can be well understood by the XRD analysis where, we have noticed a direct correlation between the increase in β-Ca_2SiO_4 phase and reduce in γ phase with the increase in PGMS ageing. Hence, the blue shift has been observed while the ageing of PGMS source increases which promotes the more β-type Ca_2SiO_4 crystal. Hence, a color tunable emission has been achieved finally by adjusting the emission in the phosphor *via* differently aged PGMS sources. This change in the emission color can be directly related to the change of crystal phase ratio in the phosphor with the ageing of PGMS source.

The corresponding emission color area of all the PGMS assisted $Ca_{1.95}Eu_{0.05}SiO_4$ phosphors are marked in the CIE diagram (Fig. 3(e)). The corresponding points are marked in CIE diagram as P1–P4 which represent the color point of differently aged PGMS assisted $Ca_{1.95}Eu_{0.05}SiO_4$ phosphors namely reddish yellow (x = 0.53, y = 0.43), yellow (x = 0.46, y = 0.45), greenish-yellow (x = 0.41, y = 0.47) and green (x = 0.36, y = 0.48), respectively. The similar changes in color have been also observed in Fig. 2(d) while illuminating the samples under 365 nm UV lamp. Meanwhile the color point of the conventional SiO_2-assisted $Ca_{1.95}Eu_{0.05}SiO_4$ and commercial YAG:Ce^{3+} phosphors are mentioned as y & x, respectively in the same CIE diagram.

3.3. Proto-type warm white LED

All the PGMS assisted $Ca_{1.95}Eu_{0.05}SiO_4$ phosphors were utilized for the fabrication of the prototype warm white emitting LEDs under the near ultraviolet light emitting chips (400 nm) to understand its efficiency. Emission spectra of the constructed prototype LEDs are shown in Fig. 3(a–d). The spectrum of LED that was fabricated with $Ca_{1.95}Eu_{0.05}SiO_4$ phosphor synthesized by using one day aged PGMS source, showed a warm white light along with the color values of (0.34, 0.34), CCT = 5400 K & CRI = 93. The emission behavior little bit shifts to the cold white light from warm region when the same phosphor synthesized with 2–4 days aged PGMS sources. The corresponding color spots of the entire prototype LEDs are marked in the CIE diagram. The points in CIE diagram z1–4 correspond to the color point of prototype LEDs constructed with differently aged PGMS assisted $Ca_{1.95}Eu_{0.05}SiO_4$ phosphors. The CIE coordinates, CCT and CRI values are found to be (z1: x = 0.34, y = 0.34), 5400 K and 93; (z2: x = 0.35, y = 0.35), 5600 K and 94, (z3: x = 0.33,y = 0.33), 5700 K and 94; and (z4: x = 0.33,y = 0.33), 5800 K and 95 for $Ca_{1.95}Eu_{0.05}SiO_4$ phosphors synthesized using 1–4 days aged PGMS sources, respectively. The color point of prototype LED constructed with commercial YAG:Ce^{3+} phosphor is also marked in the same diagram as (z5: x = 0.29, y = 0.3).

4. Conclusions

To summarize, a color tunable silicate based phosphor has been developed *via* sol-gel process by altering the crystal phase ratios *via* using differently aged PGMS as silica source in the whole crystal system. The crystal phase ratios in this crystal host can be varied with a new approach called the ageing of silicate source.

The luminescence characteristics of differently aged PGMS assisted $Ca_{1.95}Eu_{0.05}SiO_4$ phosphors could be well tuned from reddish yellow to green. The fabricated prototype LEDs by using these phosphors generated a warm white light by $Ca_{1.95}Eu_{0.05}SiO_4$ phos-

Please cite this article in press as: H.-J. Woo, et al., Engendering color tunable emission in calcium silicate based phosphors *via* ageing of silicate source, Sens. Actuators B: Chem. (2016), http://dx.doi.org/10.1016/j.snb.2016.10.027

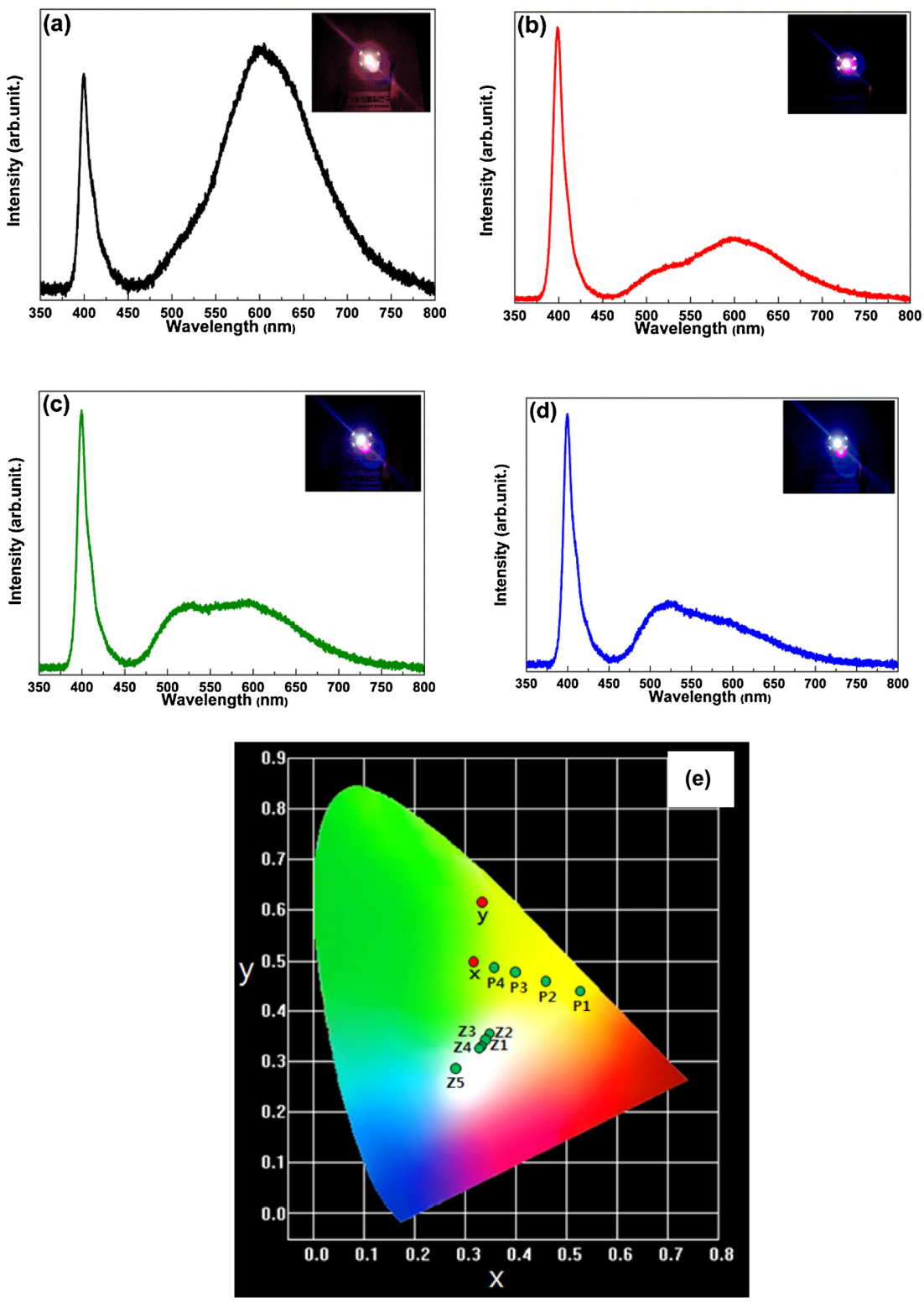


Fig. 3. Prototype LEDs. The electroluminescence of 400 nm LEDs which are fabricated with one (a), two (b), three (c) & four days (d) aged PGMS assisted $Ca_{1.95}Eu_{0.05}SiO_4$ phosphors. The insets are the digital images of illuminating prototype LEDs. The CIE color coordinates (e) show the color points of all the phosphors and prototype LEDs. The point P1–P4 are related to the color area of 1–4 days aged PGMS assisted $Ca_{1.95}Eu_{0.05}SiO_4$ phosphors while the points z1–z4 are representing the color area corresponding to the prototype LEDs. The points x & y are belong to the conventional SiO_2 assisted Ca_2SiO_4: Eu^{2+} & commercial YAG:Ce^{3+} phosphors and z5 represents the color of prototype LED fabricated with commercial YAG:Ce^{3+} phosphor [17].

Please cite this article in press as: H.-J. Woo, et al., Engendering color tunable emission in calcium silicate based phosphors *via* ageing of silicate source, Sens. Actuators B: Chem. (2016), http://dx.doi.org/10.1016/j.snb.2016.10.027

phor made with 1 day aged PGMS whereas the 2–4 days aged PGMS assisted $Ca_{1.95}Eu_{0.05}SiO_4$ phosphors shifted the color of light towards cold white light, respectively. So, this research work provides valuable information in making tunable luminescence system by controlling the α_L', β & γ crystal phases of Ca_2SiO_4 using differently aged silicate sources and also very useful information for making a color tunable LED based light source which is suitable for creating the various lighting environment by using a single host.

Acknowledgments

This work was supported by the Priority Research Centers Program through the National Research Foundation of Korea funded by the Ministry of Education, Science and Technology (NRF–2010–0029634) and was also partially supported by the Korean government (NRF–2015–056886).

References

[1] E.F. Schubert, J.K. Kim, H. Luo, Q. Xi, Solid-state lighting–a benevolent technology, Rep. Prog. Phys. 69 (2006) 3069–3099.
[2] S. Ye, F. Xiao, Y.X. Pan, Y.Y. Ma, Q.Y. Zhang, Phosphors in phosphor-converted white light-emitting diodes: recent advances in materials, techniques and properties, Mater. Sci. Eng. R 71 (2010) 1–34.
[3] E.F. Schubert, J.K. Kim, Solid-state lighting sources getting smart, Science 308 (2005) 1274–1278.
[4] A. Zukauskas, M.S. Shur, R. Caska, Introduction to Solid-State Lighting, John Wiley & Sons Inc, New York, 2012.
[5] S. Nakamura, G. Fasol, The Blue Laser Diode, Springer-Verlag, Berlin, 1997.
[6] J.M. Phillips, M.E. Coltrin, M.H. Crawford, A.J. Fischer, M.R. Krames, R. Mueller-Mach, G.O. Mueller, Y. Ohno, L.E.S. Rohwer, J.A. Simmons, J.Y. Tsao, Research challenges to ultra-efficient inorganic solid-state lighting, Laser Photon. Rev. 1 (2007) 307–333.
[7] M. Yamada, Y. Narukawa, H. Tamaki, Y. Murazaki, T. Mukai, A methodological study of the best solution for generating white light using nitride-based light-emitting diodes, IEICE Trans. Electron. E88-C (2005) 1860–1871.
[8] M.S. Shur, A. Zukauskas, Solid-state lighting: toward superior illumination, Proc. IEEE. 93 (2005) 1691–1703.
[9] S. Pimputkar, J.S. Speck, S.P. DenBaars, S. Nakamura, Prospect for LED lighting, Nat. Photonics 3 (2009) 180–182.
[10] M.R. Krames, O.B. Shchekin, R. Mueller-Mach, G.O. Mueller, L. Zhou, G. Harbers, M.G. Craford, Status and future of high-power light-emitting diodes for solid-state lighting, J. Disp. Technol. 3 (2007) 160–175.
[11] T. Taguchi, Present status of energy saving technologies and future prospect in white LED lighting, IEEJ Trans. 3 (2008) 21–26.
[12] P. Dorenbos, Energy of the first $4f^7 \rightarrow 4f^6 5d$ transition of Eu^{2+} in inorganic compounds, J. Lumin. 104 (2003) 239–260.
[13] P. Dorenbos, Relating the energy of the $[Xe]5d^1$ configuration of Ce^{3+} in inorganic compounds with anion polarizability and cation electronegativity, Phys. Rev. B: Condens. Matter Mater. Phys. B65 (2002) 235110.
[14] S. Ye, F. Xiao, Y.X. Pan, Y.Y. Ma, Q.Y. Zhang, Phosphors in phosphor-converted white light-emitting diodes: recent advances in materials, techniques and properties, Mater. Sci. Eng. R 71 (2010) 1–34.
[15] K.C. Mishra, M.E. Hannah, A. Piquette, V. Eyert, P.C. Schmidt, K.H. Johnson, First-principles investigation of the luminescence mechanism of Eu^{2+} in $M_2SiO_4:Eu^{2+}$ (M = Ba, Sr), ECS J. Solid State Sci. Techol. 1 (2012), R87–R81.
[16] S. Gandhi, K. Sakthivel, B.J. Kwon, H.J. Woo, H.S. Lee, D.S. Shin, K. Jang, A novel efficient mesoporous silica assisted green emitting phosphors-an exotic remote phosphor with high quantum yield, RSC Adv. 5 (2015) 44192–44197.
[17] S. Gandhi, K. Thandavan, B.J. Kwon, H.J. Woo, D.S. Shin, K. Jang, Solvothermal synthesis of red and green emitting $Ca_{1.65}Sr_{0.35}SiO_4:Eu^{3+}$ and $Ca_{1.65}Sr_{0.35}SiO_4:Eu^{2+}$ phosphors for solid-state lighting applications, Ceram. Int. 40 (2014) 5245–5254.
[18] H. Liu, Y. Hao, H. Wang, J. Zhao, P. Huang, B. Xua, Luminescent properties of R+ doped $Sr_2SiO_4:Eu^{3+}$ (R+ = Li+, Na+ and K+) red-emitting phosphors for white LEDs, J. Lumin. 131 (2011) 2422–2426.
[19] J.S. Lee, Y.J. Kim, Effects of barium on luminescent properties of $Sr_{2-x}Ba_xSiO_4:Eu^{2+}$ nanoparticles, Ceram. Int. 39 (2013) S555–558.
[20] H.J. Woo, S. Gandhi, B.J. Kwon, D.S. Shin, S.S. Yi, J.H. Jeong, K. Jang, Soluble silica assisted synthesis and luminescent characteristics of yellow emitting $CaSrSiO_4:Eu^{2+}$ phosphors for warm white light production, Ceram. Int. 41 (2015) 5547–5553.
[21] Y. Sato, H. Kato, M. Kobayashi, T. Masaki, D.H. Yoon, M. Kakihana, Tailoring of deep-red luminescence in $Ca_2SiO_4:Eu^{2+}$, Angew. Chem. Int. 53 (2014) 7756–7759.
[22] Z. Mao, Z. Lu, J. Chen, B.D. Fahlman, D. Wang, Tunable luminescent Eu^{2+}-doped dicalcium silicate polymorphs regulated by crystal engineering, J. Mater. Chem. C 3 (2015) 9454–9460.

Biographies



Dr. Hyun-Joo, Woo received her Ph.D. degree in physics from Changwon National University, South Korea in 2015. Presently she is working as a Post-doctoral researcher in Research Institute of Basic Sciences, Changwon National University, South Korea and concentrating on the optical & structural properties of phosphor by employing some new kind of silicate sources such as water soluble silica (propylene glycol, TEOS mixture) and inorganic mesoporous silica.



Dr. Sakthivel Gandhi obtained his doctorate in nanotechnology from SASTRA University, Thanjavur, India and Master's degree in applied chemistry from National Institute of Technology, Trichy, India. His research areas of interest include materials chemistry particularly in the synthesis of nano materials and their application in various field like MRI, *etc.*



Dr. M. Jayasimhadri is currently working as an Assistant Professor in Applied Physics Department at Delhi Technological University, Delhi, India. He received his doctoral degree from S.V. University Tirupati, India in 2006. He has also earlier worked as a Post-doctoral fellow and Research Professor at POSTECH and Changwon National University, South Korea. His research interests include optical/fluorescence spectroscopy of rare earth doped materials, nanotechnology and thermoelectric materials.



Dr. Dong-Soo Shin is a professor in Department of Chemistry at Changwon National University, South Korea. He received his Ph.D degree in Chemistry from SungKyunKwan University, South Korea in 1987. His research fields include the optical properties of hybrid organic materials.



Dr. Ho Sueb Lee is a professor in Department of Physics at Changwon National University, South Korea. He received his Ph.D degree in Applied Physics from Busan National University, South Korea in 1990. His research fields include the Optical Properties of materials.



Dr. Kiwan Jang is a professor in Department of Physics at Changwon National University, South Korea. He received his Ph.D degree in Physics and Astronomy from The University of Georgia, USA (United State of America) in 1994. His research fields of interest include optical functional materials including phosphor materials.

Please cite this article in press as: H.-J. Woo, et al., Engendering color tunable emission in calcium silicate based phosphors *via* ageing of silicate source, Sens. Actuators B: Chem. (2016), http://dx.doi.org/10.1016/j.snb.2016.10.027

Available online at www.sciencedirect.com

ScienceDirect

Materials Today: Proceedings XX (2016) XXX–XXX

materialstoday: PROCEEDINGS

www.materialstoday.com/proceedings

PMME 2016

Failure investigations of a first stage Ni based super alloy gas turbine blade

Sushila Rani[a]*, Atul K Agrawal[b], Vikas Rastogi[c]

[a]*Assistant Professor-Department of Mechanical, Production and Automobile Engineering, Delhi Technological University, Delhi-110042, India*

[b]*Assistant Professor-Department of Mechanical, Production, and Automobile Engineering, Delhi Technological University, Delhi-110042, India*

[c]*Professor -Department of Mechanical, Production, Industrial and Automobile Engineering, Delhi Technological University, Delhi-110042, India*

Abstract

This paper deals with the failure investigations of the first stage gas turbine blade of 30MW gas turbine. This blade is manufacture with of nickel based super alloy IN738. The main focus of the paper is to found the causes of failure of the blade. The investigations included the visual inspection, SEM fractrography, chemical analysis, microstructure analysis, X-ray diffraction and stress evaluation by using Finite Element Software ANSYS. By these investigations, it is found that the blade failure takes place due to the combined effect of erosion, oxidation, overheating, and hot corrosion.
© 2016 Elsevier Ltd. All rights reserved.
Selection and Peer-review under responsibility of International Conference on Processing of Materials, Minerals and Energy (July 29th – 30th) 2016, Ongole, Andhra Pradesh, India.

Keywords: First stage gas turbine blade; Nickel based IN738LC alloy; SEM; overheating; hot corrosion.

1. Introduction

Turbine blade failure cause sudden stop of turbine which results in economic loss. In order to increase the reliability, efficiency of the turbine and to rectify the blade failure problems from the root it is necessary to perform the detailed failure analysis of turbine blade [1].The common failures found in gas turbine blade includes overheating [1], corrosion [2,3,4], oxidation [5,6], erosion [2], degradation of coating of turbine blade [3,5,7], creep [2,3] and fatigue [8, 9]. The failure of gas turbine blade is due to the combination of aforesaid failure mechanisms.

* Corresponding author. Tel.: 09873575460
E-mail address: sranidtu@gmail.com

2214-7853 © 2016 Elsevier Ltd. All rights reserved.
Selection and Peer-review under responsibility of International Conference on Processing of Materials, Minerals and Energy (July 29th – 30th) 2016, Ongole, Andhra Pradesh, India.

This paper presents failure investigations of a first stage gas turbine blade. Gas Turbine blade material composition analysis, visual inspection, SEM fractrography, chemical analysis, microstructure analysis, X-ray diffraction and stress evaluation by using Finite Element Software ANSYS were performed.

2. Background

A first stage gas turbine blade of 30 MW gas turbine with operating temperature 1100^0C having service exposure of 1,30,000 hrs was investigated (Fig. 1). The blade is manufactured with nickel-base super alloy Inconel 738LC by means of investment casting process, containing directional solidified grain structure. The blade has aluminide coating (Pt–Al_2) provided by means of diffusion process. Different views of gas turbine blade are shown in (Fig. 2).

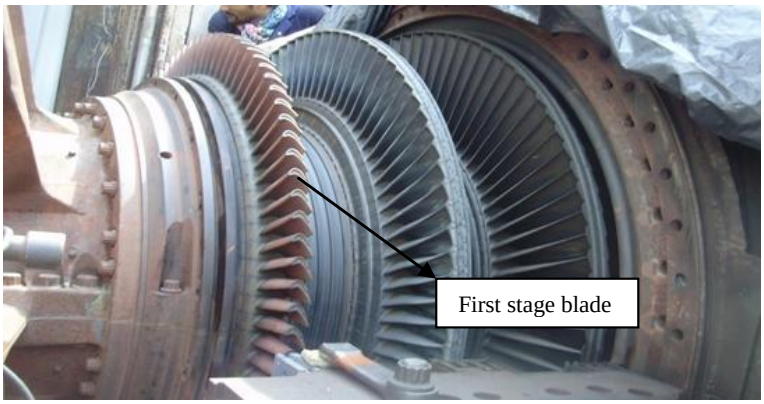


Fig. 1: General view of Gas turbine showing position of first stage blade



Fig. 2: Views of failed gas turbine blade (a) front view, (b) Rear view & (c) side view

3. Experimental details

The failed gas turbine blade is collected from Indraprastha Gas Power Plant, located in India. The blade has tip crack on both leading edge and trailing edge [4]. Two specimens about 15x10x5 mm^3 from the cracked tip of trailing edge and three specimens called as reference samples about 10x10x5 mm^3 from the bottom of trailing edge were cut by means of wire cutting process. Next, these specimens are polished using standard metallographic techniques and etched with acetone [5]. The scanning electronic microscope (SEM), Hitachi S-3700N equipped with an X-ray energy dispersive spectrometer (EDS) as shown in Fig. 3 were used to observe surface morphology, chemical compositions and microstructure of these specimens [4]. The stress analysis of a gas turbine blade was carried out using finite element software ANSYS [9].

4. Results and discussions

4.1. Visual examination

From the visual examination it is found that the failed gas turbine blade has crack on the tip of leading edge as well as on the tip of trailing edge. Both the leading edge and the trailing edge are found eroded along with the oxide scale formation in the airfoil region on both concave and convex sides.

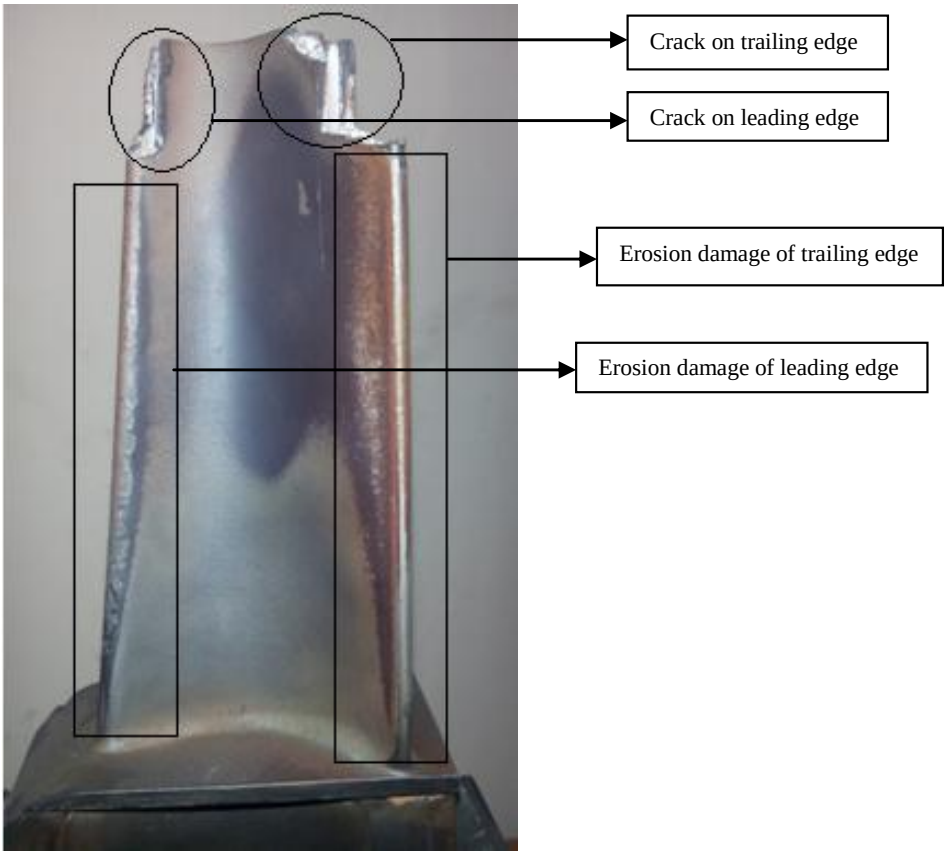


Fig. 3: Crack and Erosion damage found on leading and trailing edge of the first stage IN738 gas turbine blade

4.2 Chemical Analysis

From spectroscopy analysis, the composition (% wt) of blade material is given in Table 1 by using Optical Emission Analyzer spectrometer model- 49 DV4. The chemical analysis results shows that the blade material is in accordance with nickel based super alloy IN738 [12].

Table 1: *The Chemical composition of Inconel 738LC superalloy (wt%)*

Alloy	Cr	Co	Al	W	Ti	Ta	Mo	Ni
Std. IN738LC	16	8.3	3.4	2.6	3.38	1.75	1.7	Remaining
Failed turbine blade	14.63	10.49	2.83	3.54	4.65	0.31	1.11	62.28

4.3 Microstructure Evaluation

The microstructure investigation of the crack tip at the trailing edge was carried out. Two samples were cut by means of wire cutting operation over the trailing edge as shown in Fig. 4. For evaluating microstructure, a sample was prepared from the root region of the failed blade.

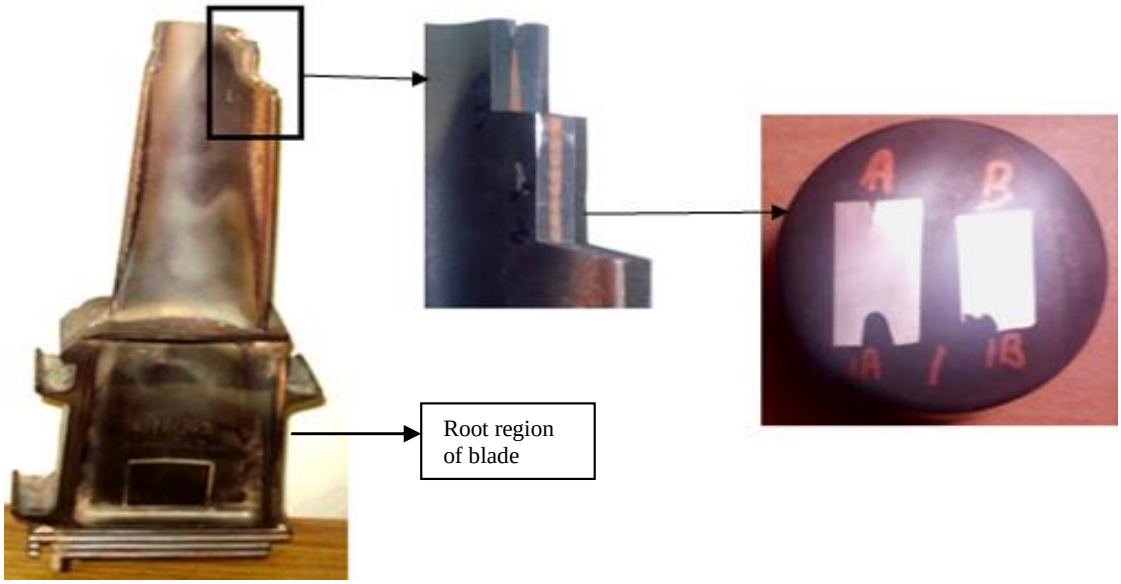


Fig. 4: Specimens cut from failed turbine blade

Fig. 5 shows the microstructure of the reference sample. It consists of carbides of MC precipitated on grain boundaries, grain interior and matrix. An EDS spectrum of turbine blade material is shown in Fig. 6.
Fig. 7 shows X-ray diffraction pattern of reference sample of turbine blade [13].

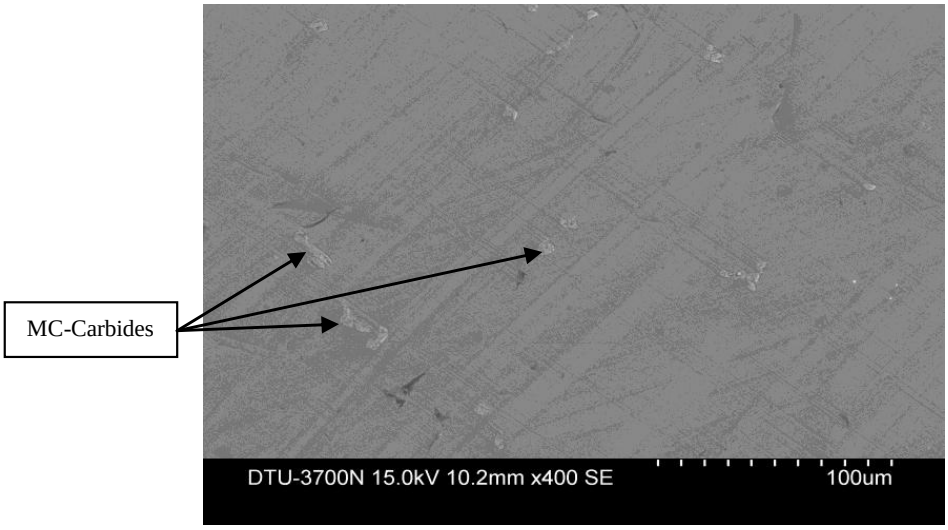


Fig. 5 : MC-carbides precipitated on grain boundaries and matrix

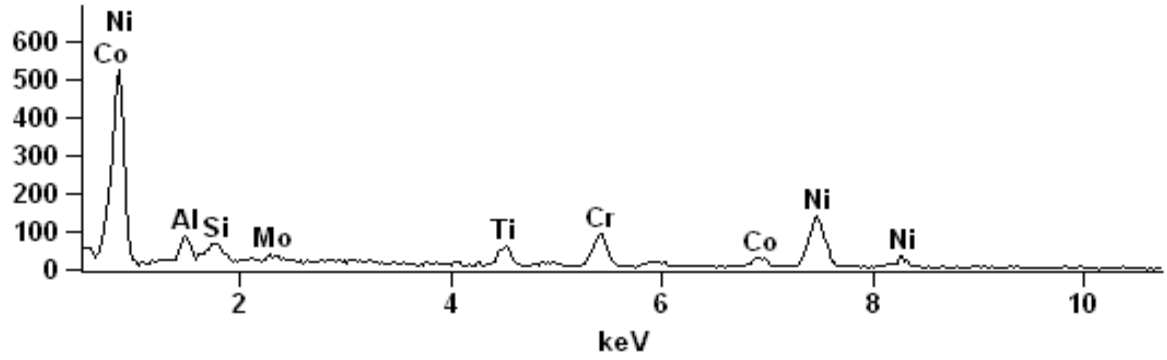


Fig. 6: An EDS spectrum of reference sample of turbine blade

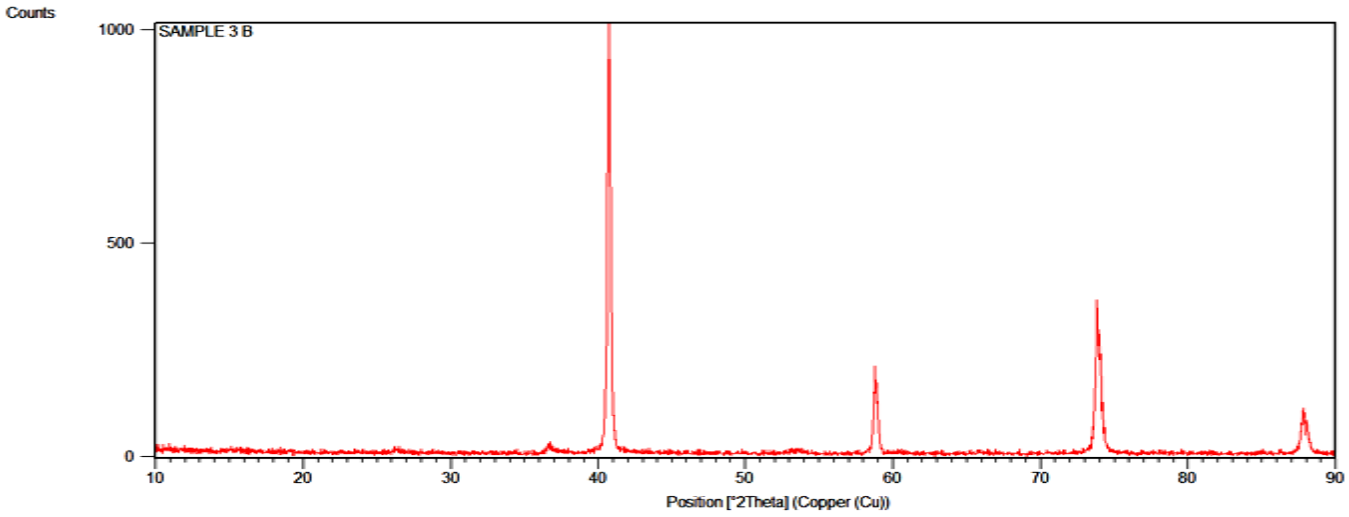


Fig. 7: X-ray diffraction pattern of reference sample of turbine blade

At high temperature working of turbine blade for long period results in the formation of topologically closed packed (TCP) phases as shown in Fig. 8. The mechanical properties of the blade material are degraded due to structure instability of the alloy which further results in decrease of turbine life.

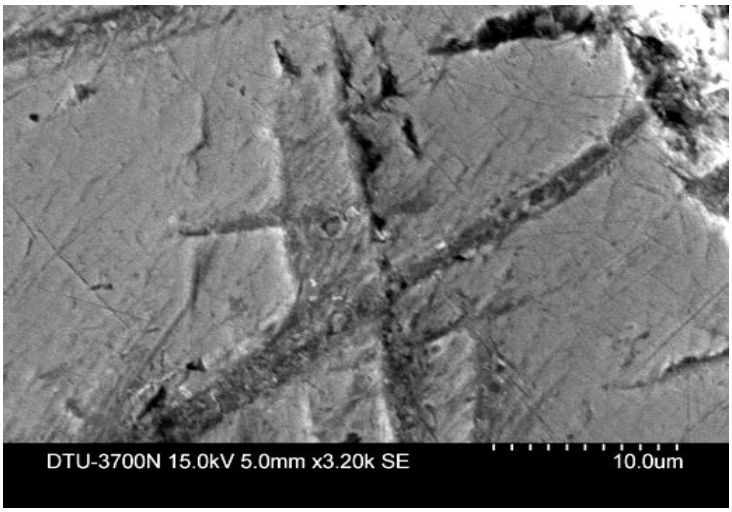


Fig. 8: Topologically Closed Packed (TCP) phase of the first stage IN738 gas turbine blade after service of 1,30,000 hrs

4.4 Crack evaluation

Fig. 9 shows rapid oxidation at high temperature in the presence of sodium sulfate which form by the combination of sulphur, oxygen and sodium. Sodium sulfate combine with chromium to form a mixture of salts and sulphur which is released due to the reduction of sodium sulphate. This released sulphur penetrates inward and react with chromium to form chromium sulfide in the substrate. Further, sulfides are converted to complex unstable metal oxides as corrosion proceeds and sulphur which is released penetrates deeply to form more sulfides into the substrate. An EDS spectrum confirmed the presence of corrosion products shown in Fig. 10. Fig. 11 shows X-ray diffraction pattern of sample collected from failed blade [13].

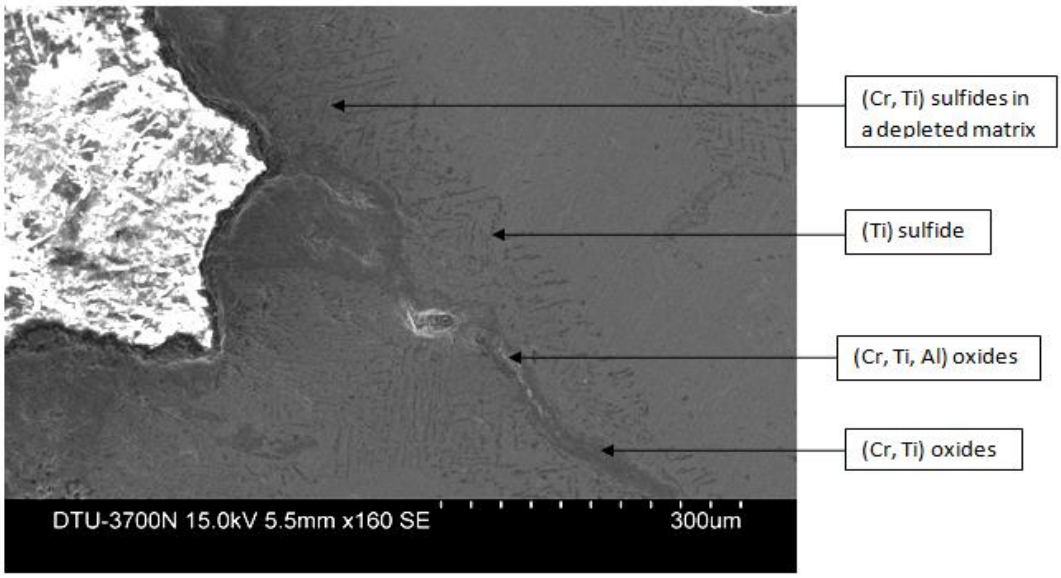


Fig. 9: Hot corrosion: subscale oxides and sulfides are visible in the substrate

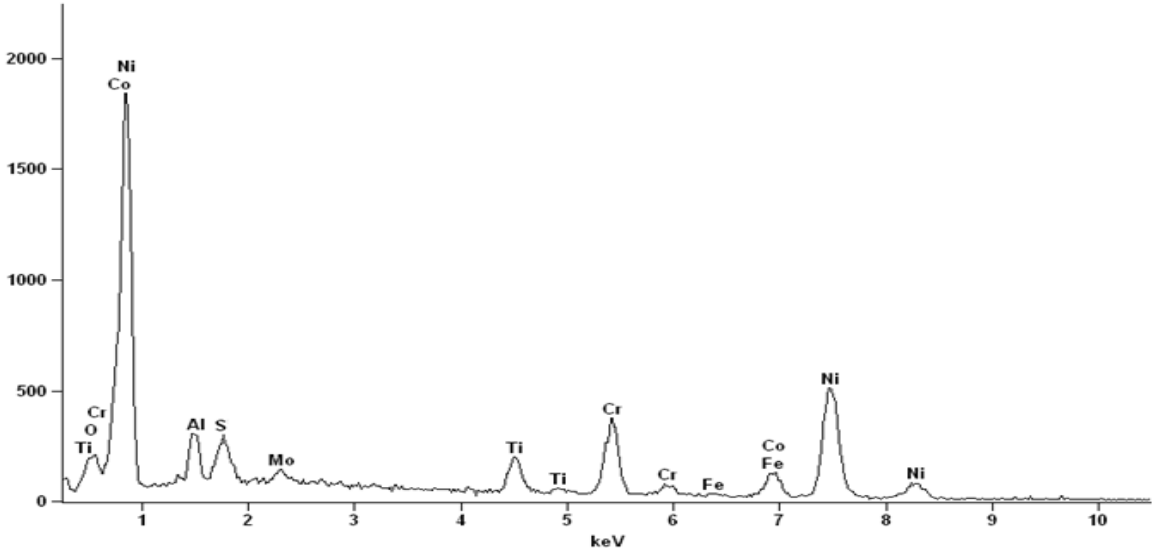


Fig. 10: The EDS spectrum of corrosion products confirm hot corrosion

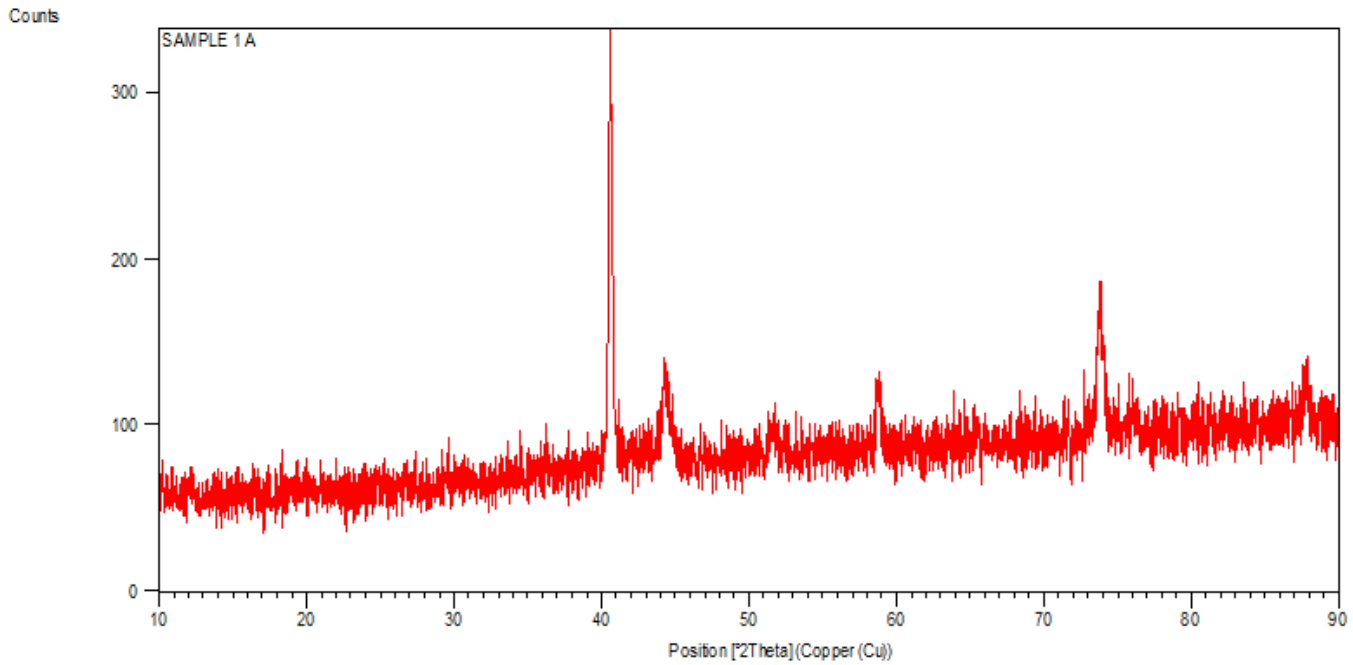


Fig. 11: X-ray diffraction pattern of failed blade

4.5 Stress Evaluation

The stress of first stage IN738 gas turbine blade is evaluated by performing static structural analysis of gas turbine blade on finite element software ANSYS [10]. The maximum tensile stress found approximately 393 MPa as shown in Fig. 12.

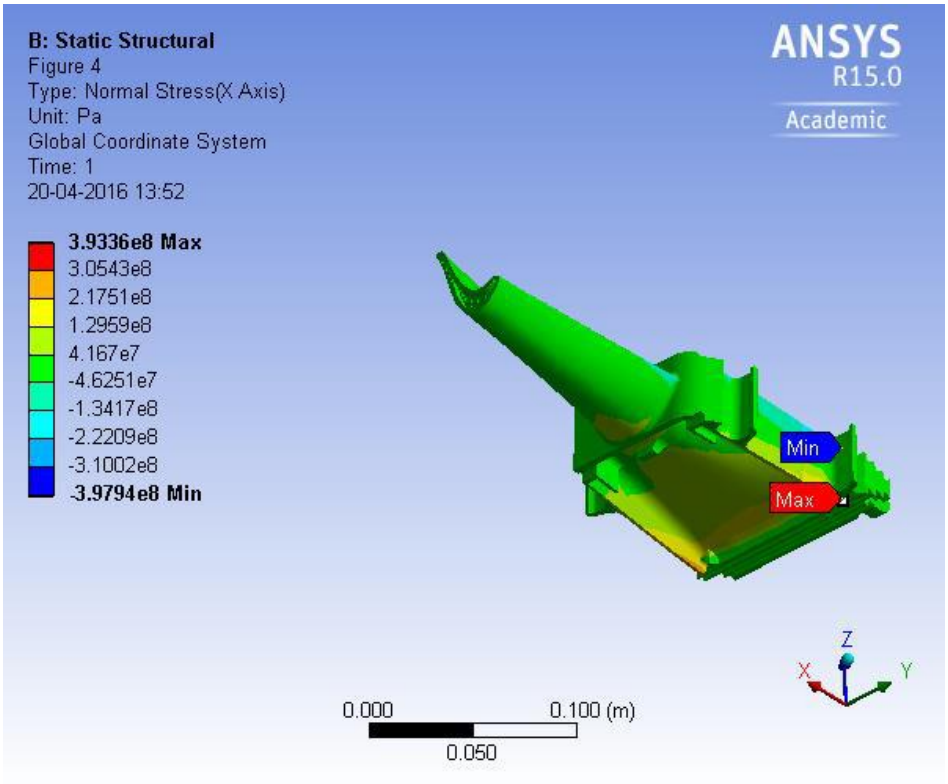


Fig. 12: Normal stress of the first stage gas turbine blade

Fig. 13(a) and 13(b) shows a very good agreement between crack location at the tip of trailing edge and leading edge of the failed first stage gas turbine blade and FEM results [10].



Fig. 13(a): Failed first stage gas turbine blade

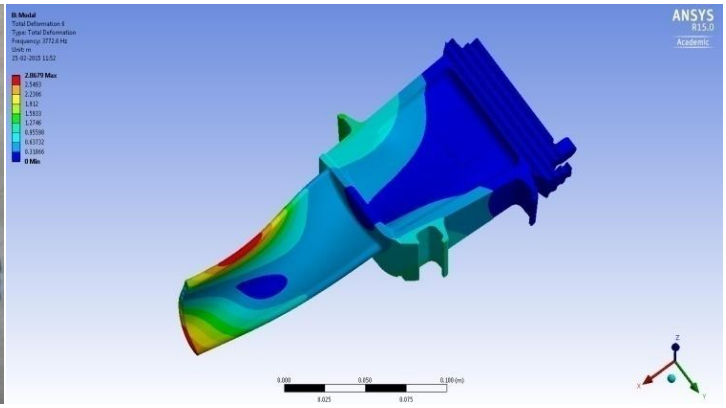


Fig. 13(b): Total deformation of the first stage gas turbine blade

5. Discussions:

The reddish color of blade surface is due to presence of aluminum oxide (Al_2O_3), which results due to oxidation of Al-Pt coating. The inclusions that flow in the hot gas stream are responsible for erosion of blade surface. These inclusions form oxides and impinge on the blade surface.

The alloy composition (% wt) of blade material obtained by using Optical Emission Analyzer spectrometer shows that the material of gas turbine blade has similar chemical composition as of the nickel based super alloy IN738. From the chemical composition, microstructure evolution and stress evaluation it is clear that blade was not failed due to material defects [11].

At high temperature operation of gas turbine blade carbides of MC type transforms to carbides of $M_{23}C_6$ type.

SEM images obtained by Hitachi S-3700N scanning electronic microscope shows the presence of sulfides and oxides in the substrate which are the by products of hot corrosion, and Topologically Closed Packed (TCP) phase of the first stage IN738 gas turbine blade which results due to overheating. The EDX spectrum confirms hot corrosion and overheating. X-ray diffraction patterns of samples collected from failed turbine blade are also shown. There x-ray patterns are similar to IN-738 nickel based alloy found in literature.

Therefore, the ultimate failure of gas turbine blade takes place due to the combined effect of erosion, oxidation, overheating and hot corrosion.

6. Conclusions:

1. Based upon the chemical composition, microstructure evolution and stress evaluation, it is clear that the blade was not failed due to material defect.
2. The surface metal of the blade degraded due to erosion and oxidation. The coating is heavily oxidized and offers no protection to base metal.
3. Formation of Topologically Closed Packed (TCP) phase results due to overheating.
4. Presence of sulfides and oxides in the substrate results due to hot corrosion.
5. The combination of erosion, oxidation, overheating and hot corrosion is responsible factors for ultimate failure of gas turbine blade.

Acknowledgements

The first stage failed gas turbine blade is collected from Indraprastha Gas Power Plant. The authors would be thankful to physics department of Delhi Technological University for help in conducting experiments in physics laboratory.

References:

1. Tawancy, H.M., Hadhrami, L.M., "Degradation of turbine blades and vanes by overheating in a power plant", Engineering Failure Analysis, vol. 16, 2009, pp-273-280.
2. Xie, Y., Wang, M., Zhang, G., "Analysis of super alloy turbine blade tip cracking during service", Engineering Failure Analysis, vol. 13, 2006, pp-1429-1436.
3. Khajavi, M.R., Shariat, M.H., "Failure of first stage turbine blades", Engineering Failure Analysis, vol. 11, 2004, pp-589-597.
4. Eliaz, N., Shemesh, G., Latanision, R.M., "Hot corrosion in gas turbine component", Engineering Failure Analysis, vol. 9, 2002, pp-31-43.
5. Mazur, Z., Ramirez, A., Amezcua, C.A., "Failure analysis of a gas turbine blade made of Inconel 738LC alloy", Engineering Failure Analysis, vol. 12, 2005, pp-474-486.
6. Vardar, N., Ekerim A., "Failure analysis of gas turbine blade in a thermal power plant", Engineering Failure Analysis vol. 14, 2007, pp-743-749.
7. Rybhinov,A.I., Gestov, L.B., Mozhaiskaya, N.V., " Operation experience with cast rotor blades made of Russian alloys in stationary gas turbines", Thermal Engineering, 2012, Vol. 59, No. 3, pp. 242–249. © Pleiades Publishing, Inc., 2012.
8. Kim, H., "Crack evaluation of the fourth stage blade in a low – pressure steam turbine", Engineering Failure Analysis, vol. 18, pp-907-913, 2011.Naeem, M.T., Jazayeri, S.A., Rezamahdi, N., "Failure analysis of gas turbine blades", Proceedings of The 2008 IAJC-IJME International Conference, paper 120,ENG 108.
9. Dowson,P., Dowson, D., " Selection of material and material related processes for FCC power recovery turbines" , Thirty eight turbo machinery symposium,2009, pp 187-212.
10. Naeem, M.T., Jazayeri, S.A., Rezamahdi, N., "Failure analysis of gas turbine blades", Proceedings of The 2008 IAJC-IJME International Conference, paper 120, ENG 108.
11. Bhagi, L., Rastogi, V., Gupta, P., "Fractographic investigations of the failure of L-1 low pressure steam turbine blade", case studies in Engineering Failure Analysis, vol. 1, 2013, pp-72-78.
12. Alloy IN738 technical data, Inco the international nickel company, Inc. One New York plaza, New York, N.Y. 10004.
13. Shishkovsky, I. V., Nazarov, A.P., "Comparison of Additive Technologies for Gradient Aerospace Part Fabrication from Nickel-Based Superalloys", Intech open science, chapter-10, 2015, pp-211-245.

Appl. Phys. A (2016)122:973
DOI 10.1007/s00339-016-0510-0

Applied Physics A
Materials Science & Processing

Gate drain-overlapped-asymmetric gate dielectric-GAA-TFET: a solution for suppressed ambipolarity and enhanced ON state behavior

Jaya Madan[1] · **Rishu Chaujar**[1]

Received: 11 September 2016 / Accepted: 14 October 2016
© Springer-Verlag Berlin Heidelberg 2016

Abstract The goal of this work is to overcome the major impediments of tunnel FET such as the inherent ambipolar current (I_{AMB}) and the lower ON current (I_{ON}). To suppress the I_{AMB}, gate drain overlap (GDO) engineering scheme has been incorporated over the cylindrical gate all around TFET (GAA-TFET). However, to enhance the I_{ON}, heterogate dielectrics (HD) are used in the gate oxide region. Results indicate that an appreciably reduced I_{AMB} and significantly enhanced I_{ON} has been obtained with the amalgamation of GDO and HD, respectively, onto GAA-TFET. Further, the effect of GDO length (L_{ov}) has also been studied. Quantitative analysis of ambipolarity factor "α" reveals that at large L_{ov}, "α" improves. It is found that GDO degrades the high-frequency (HF) performance such as cutoff frequency (f_T) of the device, because of the enhanced parasitic capacitances. To surpass the deterioration at HF caused by GDO, the dielectric over GDO region has been altered, and it has been analyzed that by inserting a material of low-dielectric constant ($k = 1$) and parasitic capacitances of the device reduces, resulting into enhancement in f_T. Moreover, the low-k dielectric inserted over L_{ov} reduces the I_{AMB} supplementary, along with enhanced f_T. Suppressed I_{AMB} and enhanced f_T of GDO–HD–GAA-TFET with low-k dielectric over L_{ov} make it adequate for application in HF and digital circuitry.

✉ Rishu Chaujar
rishu.phy@dce.edu

Jaya Madan
jayamadan.2012@gmail.com

[1] Microelectronics Research Lab, Department of Engineering Physics, Delhi Technological University, Bawana Road, Delhi 110042, India

1 Introduction

Lower subthreshold swing, lower OFF current, and immunity against short channel effects (SCEs) of tunnel field effect transistor (TFET) have marked it as one of the possible substitute devices for low-power applications. TFET uses different current conduction mechanisms (other than MOSFET), i.e., band-to-band tunneling (BTBT) of electrons from valence band of source to conduction band of channel other than thermionic emission of carriers over the barrier as in case of MOSFET. The presence of higher tunneling barrier width at the source channel junction (tunneling junction) for low gate bias results into lower I_{OFF}. Moreover, the intrinsic BTBT mechanism of electrons provides immunity against SCEs. The absence of thermionic emission delimits the TFET from thermal limit of 60 mV/decade on subthreshold swing (SS) (fundamental limit of MOSFET) [1–4]. In spite of these advantages, TFET has few shortcomings such as lower I_{ON} (caused by lower tunneling rate of electronics) and ambipolar behavior making it unsuitable for practical applications. Various techniques has been already proposed for enhancing the I_{ON} [5, 6], and for reducing the I_{AMB} [7, 8].

Ambipolarity is an intrinsic behavior of TFET that refers to the conduction for both positive and negative gate biases at a constant drain bias. In ambipolar region, conduction of holes (electrons) dominates for p-type (n-type) behavior of TFET. Ambipolarity is a serious issue for TFET. Although the ambipolar effect has been used for sensing application in [9], the ambipolar effect of the device limits its application for digital inverters. Schottky barrier (SB) transistors also suffer from the ambipolar conduction. But the solution to reduce ambipolarity for SB transistors is comparatively simple as to choose the appropriate contacts for source and drain [10]. In case of TFET, the ambipolarity is due to the

Published online: 21 October 2016

lowering of barrier width at the drain channel junction for negative gate bias. Various engineering schemes has been reported up to now to suppress the ambipolar current of TFET up to now such as: (a) heterogate dielectric [5, 11], (b) gate drain underlap or short gate [6], (c) heterojunction TFET [8], (d) asymmetric source/drain doping [7, 12], and (e) gate drain-overlapped TFET [13, 14].

In this work, cylindrical gate all around (GAA) architecture has been used that offers better device performance over their planar equivalents. GAA architecture with circular geometry provides confined volume body and excellent electrostatic control over channel and consequently boosts the tunneling probability that leads to improved I_{ON} [15]. In addition, gate drain overlap (GDO), asymmetric source/drain doping, and heterogate dielectric engineering scheme (HD) have been amalgamated onto GAA-TFET. GDO and asymmetric source/drain doping reduces the ambipolar current and HD enhances ON current of the device.

This paper is organized as follows: Sect. 2 demonstrates the device structure, simulation models, and calibration results. Section 3 consists of results and discussion, and Sect. 4 summarizes the result. Section 3 is composed of three subsections, i.e., 3.1 that shows the comparative analysis of GAA-TFET, GDO–GAA-TFET, HD–GAA-TFET, and GDO–HD–GAA-TFET, 3.2 that shows the effect of L_{ov} of GDO–HD–GAA-TFET, and 3.3 showing the improvement in HF parameters of GDO–HD–GAA-TFET has been analyzed.

2 Device structure and simulation models

The schematic cross-sectional view of the entire device architectures [i.e., GDO–HD–GAA-TFET (a), GAA-TFET (b), GDO–GAA-TFET (c), and HD–GAA-TFET (d)] considered in this work are shown in Fig. 1a–d. The device structure parameters and their values are stated in Table 1. Drain is intentionally lesser doped than source to reduce the tunneling at drain channel junction for negative gate bias and thus the ambipolarity effect [16]. All simulations have been performed using the ATLAS device simulator [17]. The models activated during simulation are: concentration- and field-dependent mobility model, Shockley–Read–Hall for carrier recombination, non-local BTBT, band gap narrowing, and Fermi–Dirac statistics. The reason of choosing the non-local band-to-band tunneling model (instead of local model) is to incorporate the effect of electric field at each point in the tunneling path. As in local models such as Kane's model, the electric field is constant at the entire tunneling path because of the triangular barrier approximation of energy bands. But non-local BTBT models have non-uniform electric field that changes at each point in the tunneling path, thus being more accurate [18]. To calibrate the non-local BTBT model, the tunneling masses were tuned from their default values, i.e., me.tunnel $= 0.322m_o$ and mh.tunnel $= 0.549m_o$ to make it best fit with the experimental data [19], where m_o is the rest mass of electron. In simulation, the value of effective tunneling mass has been set on the material statement for silicon material used in source, channel, and drain. The adjusted value of me.tunnel $= 0.22m_o$ and mh.tunnel $= 0.52m_o$.

The tuning of the effective tunneling masses is attributed to the fact that tunneling probability depends exponentially on electron and hole tunneling masses. Moreover, reduced electron tunneling mass enhances the tunneling probability and thus the drain current. The calibration of simulation models with experimental data for transfer characteristics shows close proximity as evident from Fig. 1b and thereby validates the choice of model parameters. In addition, the experimental realization of GDO–HD–GAA-TFET can be done by integration of various previously reported process

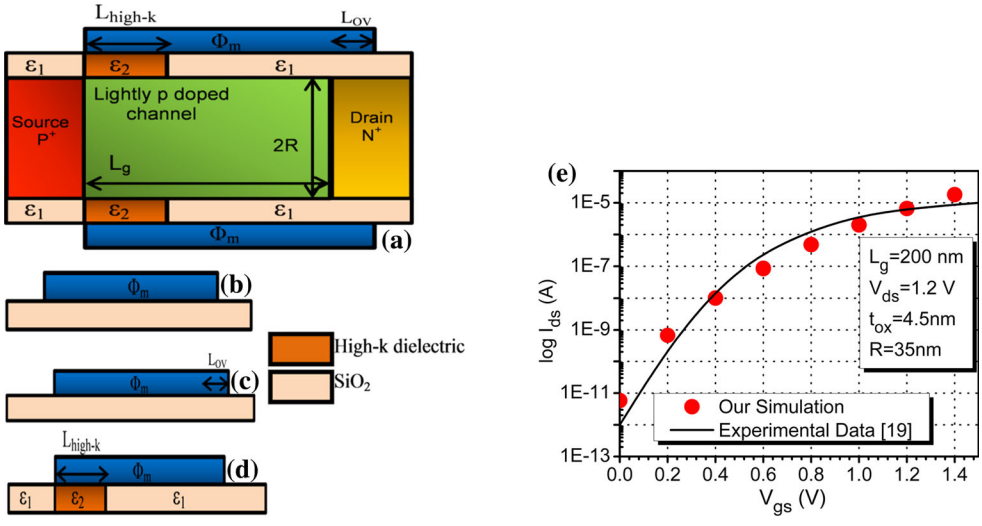


Fig. 1 Schematic structure of **a** gate drain-overlapped heterogate dielectric gate all around tunnel FET (GDO–HD–GAA-TFET) **b** GAA-TFET, **c** GDO-GAA-TFET, **d** HD-GAA-TFET **e** Calibration with the published result, I_{ds}–V_{gs} characteristics of 200-nm gate length SiNW-TFET at $V_{ds} = 1.2$ V, $T_{ox} = 4.5$ nm, Diameter $= 70$ nm

Table 1 Device parameters and values

Parameter	Value
Channel length L_g	50 nm
Channel radius R	10 nm
Gate oxide thickness T_{ox}	2 nm
Metal work function	4.3 eV
High-k dielectric ε_2	HfO_2k = 21
ε_1	SiO_2k = 3.9
Length of high-k dielectric $L_{high\text{-}k}$	10 nm
Source doping (p^+)	1×10^{20} cm^{-3}
Channel doping (lightly p-type)	1×10^{16} cm^{-3}
Drain doping (n^+)	1×10^{18} cm^{-3}

flow. The HD dielectrics can be formed by etching SiO_2 followed by the deposition of high-k material [5]. Thereafter, for processing of GDO, the electron beam lithography can be used for patterning of gate metal and then the electron beam evaporation can be used for gate metallization [20].

3 Results and discussion

3.1 Impact of GDO and HD engineering scheme

In this subsection, the effect of GDO and HD architectures on GAA-TFET is examined in terms of transfer characteristics, ambipolar conduction, threshold voltage (V_{th}), subthreshold swing (SS), transconductance (g_m), parasitic capacitances, cutoff frequency (f_T), and intrinsic delay (τ).

First and foremost, a comparative analysis of all the devices mentioned in Table 1 in terms of transfer characteristics is done as shown in Fig. 2a. Results thus obtained shows that GAA-TFET suffers from low I_{ON} along with large I_{AMB}. The low I_{ON} of GAA-TFET is due to the wide barrier width that reduces the tunneling rate and thus the I_{ON}. Both lower I_{ON} and large I_{AMB} limits GAA-TFET for practical applications. With incorporation of GDO architecture on GAA-TFET, i.e., for GDO-GAA-TFET, I_{AMB} reduces from an order of 10^{-13} to 10^{-15} A. The suppressed I_{AMB} for GDO-GAA-TFET is a consequence of the broadened barrier width at the drain–channel junction due to the overlapped gate over the drain. However, with application of GDO, the drain current is unaltered for positive V_{gs}. The unaltered I_{ds} for positive V_{gs} in case of GDO–GAA-TFET is due to the fact that barrier width at the tunneling junction remains unaltered with GDO architecture. The transfer characteristics of HD–GAA-TFET plotted in Fig. 2a shows a significantly large improvement in I_{ON} from an order of 10^{-10} to 10^{-5} A, without any change in I_{AMB}. The enhanced I_{ON} of HD–GAA-TFET is attributed to the steeper band bending caused by the presence of high-k material over the tunneling junction in HD engineering scheme [21, 22].

However, the drain channel junction is immune to the effects of high-k material being present over the source channel junction, thereby resulting in an unaltered I_{AMB} for HD-GAA-TFET. Consequently, for the case of GDO–HD–GAA-TFET, both I_{ON} (enhanced) and the I_{AMB} (reduced) have been improved. The I_{ON} and I_{AMB} of all the devices under considerations are plotted in Fig. 2b. The I_{AMB} is defined as the drain current at $V_{gs} = -1.0$ V and $V_{ds} = 1.0$ V. Consistent with above explanations, I_{AMB} is considerably suppressed for GDO–GAA-TFET and GDO–HD–GAA-TFET. Moreover, I_{ON} of HD–GAA-TFET and GDO–HD–GAA-TFET are appreciably improved. Thus, the GDO–HD–GAA-TFET has overcome the major obstacles of TFET such as lower I_{ON} and higher ambipolar current.

The threshold voltage (V_{th}) and subthreshold swing (SS) of aforementioned devices are illustrated in Fig. 3a, b, respectively. The consequence of large tunneling barrier width and lower tunneling rate of electrons for GAA-TFET and GDO–GAA-TFET results in higher V_{th} of these device architectures which is evident from Fig. 3a.

Further, the incorporation of HD scheme on GAA-TFET enhances the band bending at the tunneling junction that lowers the barrier width and thereby allows more electrons

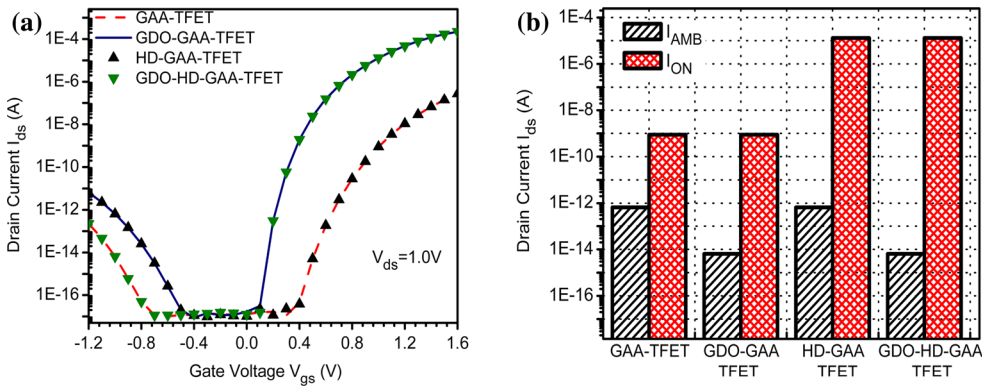


Fig. 2 **a** Transfer characteristics of GAA-TFET, HD-GAA-TFET, GDO-GAA-TFET and GDO–HD–GAA-TFET at constant drain bias $V_{ds} = 1.0$ V **b** Ambipolar current (I_{AMB}) and ON current (I_{ON}) of all the devices. For GDO architecture, $L_{ov} = 5$ nm; for HD scheme, HfO_2 is used as high-k gate dielectric $\varepsilon_2 = 21$

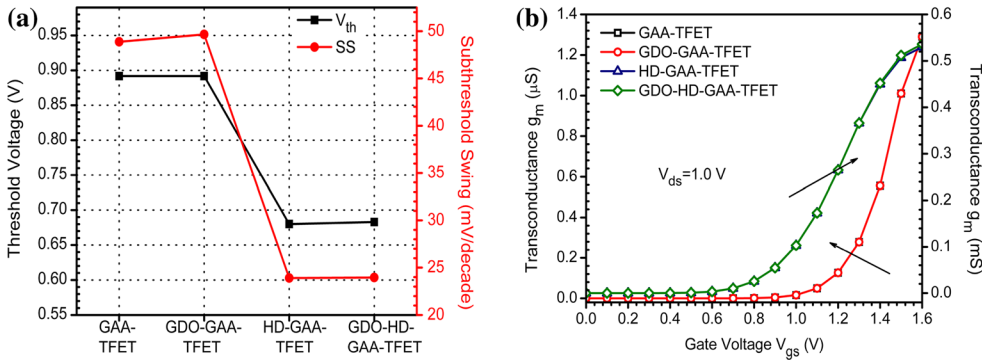


Fig. 3 **a** Threshold voltage (V_{th}) and Subthreshold swing (SS), **b** transconductance of GAA-TFET, HD-GAA-TFET, GDO-GAA-TFET, and GDO–HD–GAA-TFET. For GDO architecture, $L_{ov} = 5$ nm; for HD scheme, HfO_2 $\varepsilon_2 = 21$ is used as high-k gate dielectric

to tunnel through the source channel junction. Subsequently, the V_{th} of HD–GAA-TFET and GDO–HD–GAA-TFET reduces considerably in comparison with that of GAA-TFET and GDO–GAA-TFET as shown in Fig. 3a. Consistent with the above results, the lower I_{ON} of GAA-TFET and GDO–GAA-TFET results in large SS. However, the high-k material incorporated in HD engineering scheme, i.e., HD–GAA-TFET and GDO–HD–GAA-TFET, enhances the I_{ON} without any negotiation in I_{OFF}, contributing to lower SS. In TFETs, the gate voltage controls the drain current, and thus, the ratio of I_{ds} to the V_{gs} at constant drain bias defined as the transconductance or the mutual conductance g_m becomes an important performance parameter for TFET. For acquiring a high gain or large driving capability, the g_m should be high. The g_m of all the device architectures under consideration is shown in Fig. 3b. Significant improvement in g_m is achieved with incorporation of HD engineering scheme onto GAA-TFET as shown in Fig. 3b. In addition to this, the analogous profile of GAA-TFET/GDO–GAA-TFET and HD–GAA-TFET/GDO–HD–GAA-TFET is attributed to the similar transfer characteristics (in positive V_{gs} regime) of these architectures as explained for Fig. 2a.

The switching speed of device is affected by the parasitic capacitances. Further, in this work, the HD engineering scheme is incorporated to enhance the I_{ON} of TFET, and thus it is requisite to analyze the impact of both HD and GDO engineering on the parasitic capacitances. The parasitic capacitances of all the device architectures are analyzed in terms of gate-to-source capacitance C_{gs} and the total gate capacitance C_{gg} and are shown in Fig. 4. It must be noted that C_{gs} is significantly smaller than C_{gg} for all the device architectures.

The larger C_{gg} in each case is due to the fact of major contribution of C_{gd} to C_{gg} in case of TFET [23]. Results reveal degradation in C_{gg} and C_{gs} with the incorporation of HD architecture. Thus, there is a need to trade-off between the ON current and the parasitic capacitance of TFET, as per the application. The similar profile of C_{gs} for the case of GAA-TFET/GDO–GAA-TFET and HD–GAA-TFET/

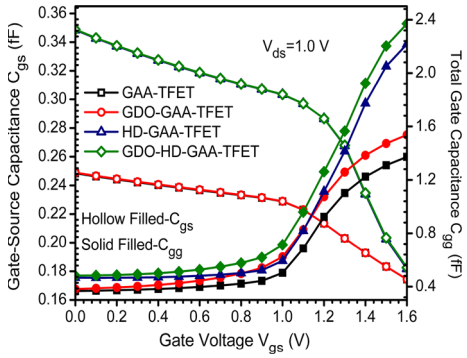


Fig. 4 Gate to source capacitance C_{gs} and total gate capacitance C_{gg} of all the devices at constant drain bias $V_{ds} = 1.0$ V. For GDO architecture, $L_{ov} = 5$ nm; for HD scheme, HfO_2 $\varepsilon_2 = 21$ is used as high-k gate dielectric

GDO–HD–GAA-TFET is due to the fact that GDO architecture (incorporated for reducing the I_{AMB}), is at the drain channel junction, and it thus does not affect the gate source capacitance.

In order to analyze the high-frequency HF performance, the cutoff frequency of all the devices is studied. Cutoff frequency f_T is defined as the frequency at which the short-circuit current gain drops to 0 dB, and mathematically it is expressed as:

$$f_T = \frac{g_m}{2\pi(C_{gs} + C_{gd})} \tag{1}$$

where g_m is the transconductance, C_{gs} and C_{gd} are gate-to-source and gate-to-drain capacitances. As evident from Eq. 1, f_T depends directly on g_m and inversely on the parasitic capacitances. It is clearly evident from Fig. 5a that the degradation in C_{gg} has been overcome by the g_m. Thus, the dominated g_m results into superior f_T for GDO–HD–GAA-TFET and HD–GAA-TFET. The peak value of f_T, increases from 0.15 GHz to 38 GHz, with the amalgamation of HD engineering scheme. Another vital performance parameter for evaluation of the switching speed is the intrinsic delay τ, defined as:

$$\tau = \frac{C_{gg} V_{dd}}{I_{ON}} \tag{2}$$

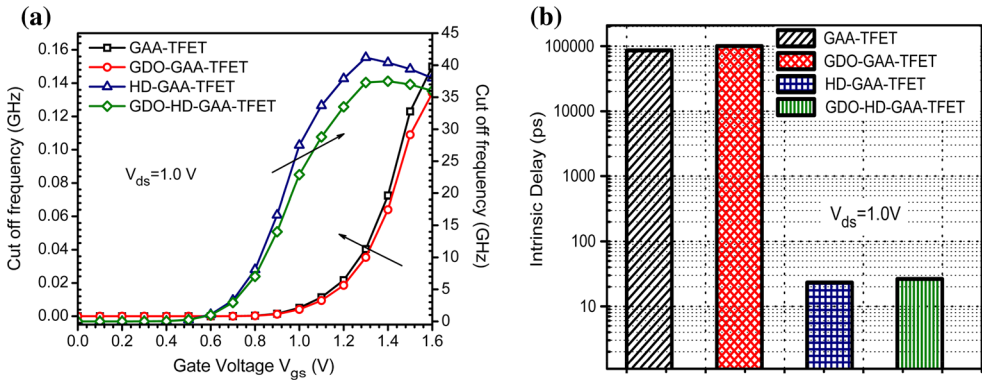


Fig. 5 **a** Cutoff frequency f_T, **b** intrinsic delay τ of GAA-TFET, HD-GAA-TFET, GDO-GAA-TFET and GDO–HD–GAA-TFET. For GDO architecture, $L_{ov} = 5$ nm; for HD scheme, HfO_2 $\varepsilon_2 = 21$ is used as high-k gate dielectric

Figure 5b shows the comparison of all the device architectures in terms of intrinsic delay. As is evident from the figure, there is a tremendous reduction in τ, with the incorporation of HD engineering scheme. The reduced τ for HD-GAA-TFET and GDO–HD–GAA-TFET is due to the presence of high-k that enhances I_{ON}.

It is analyzed that the enhanced I_{ON} dominates over the degraded parasitic capacitance, thereby improving the τ of HD–GAA-TFET and GDO–HD–GAA-TFET. Quantitatively, τ of HD–GAA-TFET and GDO–HD–GAA-TFET reduce to an order of 20 ps in comparison with τ of GAA-TFET and GDO-GAA-TFET for which τ is of order of 100 ns.

3.2 Impact of L_{ov} on GDO-GAA-TFET

After comparing GAA-TFET with HD–GAA-TFET, GDO–GAA-TFET, and GDO–HD–GAA-TFET, the effect of L_{ov} of GDO–HD–GAA-TFET has also been analyzed. The performance of GDO–HD–GAA-TFET for various L_{OV} is examined in terms of transfer characteristics, ambipolar current, ambipolarity factor α, energy band diagrams, electric field, band-to-band tunneling rate of electrons, parasitic capacitances, and cutoff frequency (f_T).

Figure 6a shows the transfer characteristics of GDO–HD–GAA-TFET for various overlapped lengths $L_{OV} = 0$, 5, 6, 7 and 8 nm. As clearly evident from the graph the ON state characteristic is immune to the variations of L_{OV} as explained previously.

The main advantage of variation of L_{OV} is for negative gate bias, i.e., reduction in the ambipolar current. It is clearly evident from Fig. 6a that ambipolar current reduces with increase in L_{OV}. The reduction in I_{AMB} with increase in L_{OV} is mainly attributed to the enhanced effective control over the barrier width at drain channel junction for negative gate biases for higher L_{OV}. Also for $L_{OV} = 0$ nm, i.e., when no gate drain overlapping is there, the ambipolar current is considerably large $\sim 10^{-11}$ A and is basically due to narrowing of barrier width at the drain channel junction for negative gate bias. Furthermore, to quantify the efficiency of GDO–HD–GAA-TFET, ambipolarity factor (α) is studied and is defined as [24].

$$\alpha = \log\left(\frac{I_{AMB}}{I_{OFF}}\right) \tag{3}$$

Figure 6b shows the ambipolar current and the ambipolarity factor of GDO–HD–GAA-TFET. Reduction in I_{AMB} from an order of 10^{-12} to 10^{-17} A has been found with an increase in L_{OV} from 0 nm to 8 nm as evident from Fig. 6b. Negative (or less value) of α illustrates minimized ambipolar conduction. As clearly illustrated in Fig. 6b, considerable reduction in α has been obtained with increase

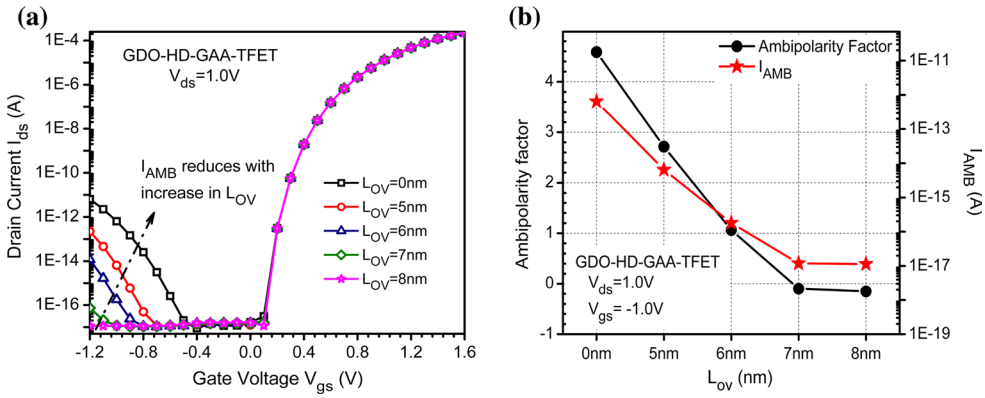


Fig. 6 **a** Transfer characteristics of GDO–HD–GAA-TFET at constant drain bias $V_{ds} = 1.0$ V for various $L_{OV} = 0$, 5, 6, 7 and 8 nm **b** Ambipolar current and ambipolarity factor for all the cases

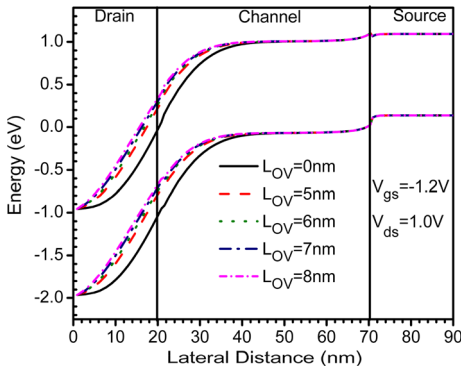


Fig. 7 Energy band diagram along the channel length of GDO–HD–GAA-TFET at constant $V_{ds} = 1.0$ V and $V_{gs} = -1.2$ V for various $L_{OV} = 0$, 5, 6, 7 and 8 nm

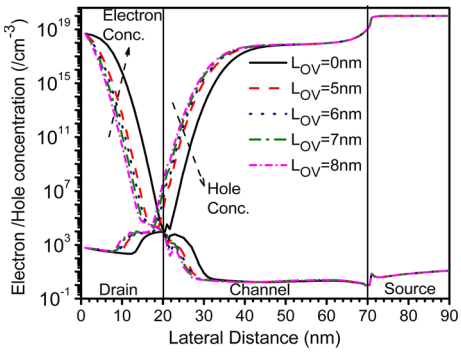


Fig. 9 Electron and hole concentration along the channel length of GDO–HD–GAA-TFET at $V_{ds} = 1.0$ V and $V_{gs} = -1.2$ V for various $L_{OV} = 0$, 5, 6, 7 and 8 nm

in L_{OV}. Furthermore, for $L_{OV} = 7$ nm and 8 nm, α becomes negative signifying that there is no effect of ambipolar conduction in the analog performance.

The reduction in I_{amb} with increase in L_{OV} can be better understood by studying the energy band diagram of GDO–HD–GAA-TFET at $V_{gs} = -1.2$ V and $V_{ds} = 1.0$ V as shown in Fig. 7. It should be noted that the effect of L_{OV} on energy bands are only at the drain channel junction and unaffected at the tunneling junction. For negative gate bias, the bands near the drain are moved upwards with an increase in L_{OV}, resulting into broadening of tunneling barrier width at the drain channel junction. This broadened barrier width at the drain channel junction reduces the probability of tunneling of electrons at the drain channel junction and thus reduces the ambipolar current as shown in Fig. 6a.

The plot of electric field at a constant $V_{gs} = -1.2$ V and $V_{ds} = 1.0$ V has also been studied and is shown in Fig. 8a. Because of the negative gate bias, the peak value at the drain channel junction is much higher than at the tunneling junction. Moreover, at the drain channel junction, the electric field is maximum for the case when no gate drain overlapping has been done or $L_{OV} = 0$ nm. Progressive reduction in peak value of electric field at the drain channel junction has been obtained with gradual increase in L_{OV}.

This reduced electric field at the drain channel junction is mainly responsible for the reduction in band-to-band tunneling BTBT of electrons at the drain channel junction as shown in Fig. 8b. Thus, the ambipolar current is reduced by increasing L_{OV}. The electron and hole concentration at a constant $V_{gs} = -1.2$ V and $V_{ds} = 1.0$ V is shown in Fig. 9. As for negative gate bias, the holes are majority carriers (as if TFET is working as a p-TFET for ambipolar conduction) in the channel region. With an increase in L_{OV}, the electric field near drain channel junction decreases resulting into increase (decrease) in hole (electron) concentration as evident from Fig. 9.

The circuit performance of TFET is appreciably affected by the parasitic capacitance that limits the upper switching speed of the device. The effect of parasitic capacitances cannot be ignored at HF operating regime. In addition to this, as gate is being overlapped over drain in GDO engineering scheme, and thus there is a need to examine the effect of drain-overlapped capacitance (C_{dov}) over the gate drain capacitance (C_{gd}) and thus the total gate capacitance (C_{gg}).

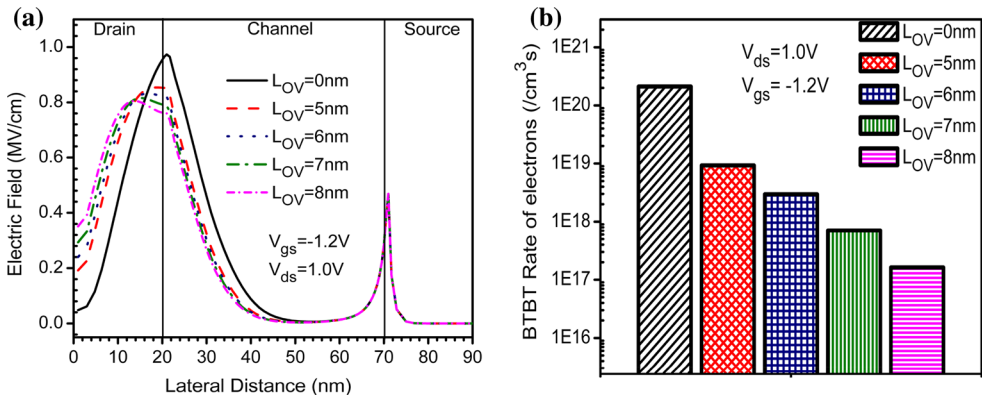


Fig. 8 **a** Electric field along the channel length of GDO–HD–GAA-TFET at $V_{ds} = 1.0$ V and $V_{gs} = -1.2$ V for various $L_{OV} = 0$, 5, 6, 7 and 8 nm **b** BTBT rate of electrons at the drain channel junction for all the cases

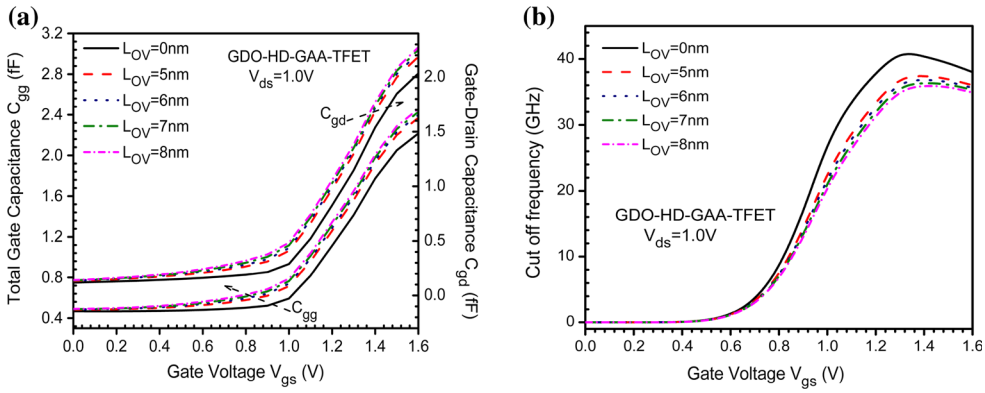


Fig. 10 **a** Total gate capacitance, gate drain capacitance and **b** Cutoff frequency of GDO–HD–GAA-TFET at $V_{ds} = 1.0$ V for various $L_{OV} = 0$, 5, 6, 7 and 8 nm

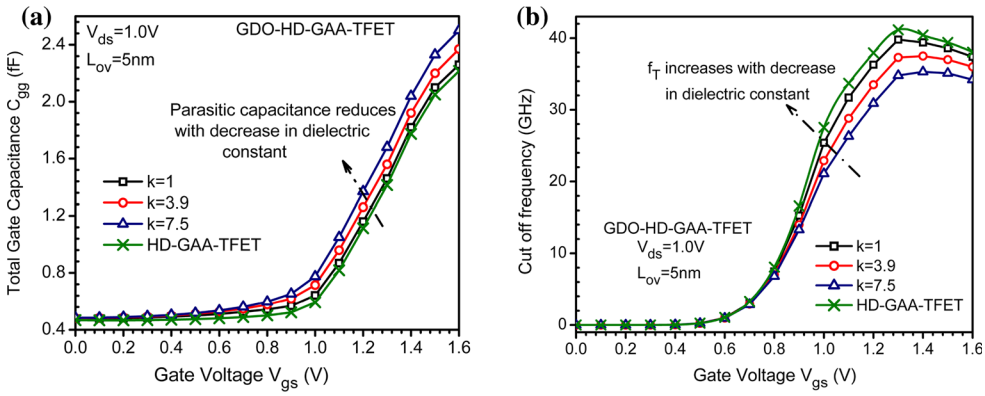


Fig. 11 **a** Total gate capacitance and **b** Cutoff frequency of GDO–HD–GAA-TFET at $V_{ds} = 1.0$ V for $L_{OV} = 5$ nm and various dielectric materials

$$C_{gd} = C_{of} + C_{dif} + C_{sif} + C_{dov} + C_{gd,inv} \quad (4)$$

where C_{of} is the outer fringing capacitance, C_{dif} and C_{sif} are the inner fringing capacitances at drain and source sides, respectively.Also another vital parameter for appraising the HF performance of the device is the cutoff frequency f_T. Thus, the effect of GDO on the parasitic capacitances and f_T has also been investigated. Effect of L_{ov} on C_{gg} and C_{gd} is shown in Fig. 10a for GDO–HD–GAA-TFET. The same profile and magnitude of both C_{gg} and C_{gd} is mainly attributed to the fact that for TFET large fraction of C_{gg} is contributed by C_{gd} as compared to C_{gs} [25]. Further, as the L_{ov} increases, the parasitic capacitances increases, thus resulting in decrease in cutoff frequency (f_T) of the device as shown in Fig. 10a,b. However, the decrease in f_T is only of 9 % and 12 % for $L_{ov} = 5$ nm and 8 nm, respectively.

3.3 Improving the HF performance of GDO–HD–GAA-TFET

To surpass the degradation on f_T caused by GDO, the dielectric over GDO region has been altered from SiO_2 to Si_3N_4 ($k = 7.5$) and vacuum dielectric ($k = 1$). Results thus obtained for total gate capacitance are shown in Fig. 11a. It is clearly evident from Fig. 11a that dielectric (inserted over L_{OV}) with higher dielectric constant enhances the C_{gg} and vice versa. Moreover, the insertion of vacuum dielectric over L_{ov} region reduces the parasitic capacitance. Thus, the degradation caused by GDO is replenished by inserting a vacuum dielectric over L_{OV}. In addition, the C_{gg} of GDO–HD–GAA-TFET with high-k over L_{OV} is also compared with that of HD-GAA-TFET. It is obtained that the integration of GDO scheme increases the C_{gg} insignificantly. However, this degradation in parasitic capacitances can be overlooked in comparison with the decrease in ambipolar conduction that blocks the application of TFET in digital circuitry. The effect of inserted dielectric over L_{OV} on f_T is shown in Fig. 11b. The f_T being inversely proportional to C_{gg} is thus enhanced due to the presence of vacuum dielectric over L_{OV} as shown in Fig. 11b. Peak value of f_T increases by 6.2 % in the presence of vacuum dielectric over L_{OV} in comparison with SiO_2. Moreover, to realize the effect of GDO more clearly, f_T of HD–GAA-TFET is also studied, and results thus obtained show marginal degradation in f_T with the integration of GDO architecture. This degradation in f_T with integration of GDO is attributed to the enhanced parasitic capacitances for GDO (as shown in Fig. 11a).

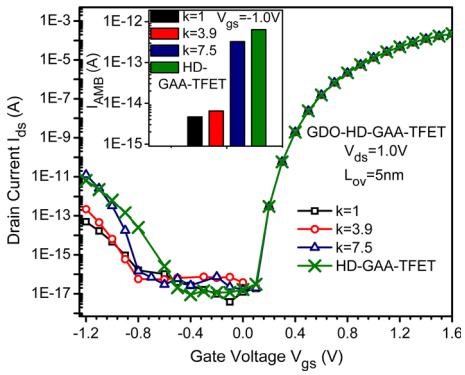


Fig. 12 Transfer characteristics of GDO–HD–GAA-TFET at $V_{ds} = 1.0$ V for $L_{OV} = 5$ nm and various dielectric materials

To determine the effect of inserted dielectric constant over L_{ov} region on the ambipolar characteristics, the transfer characteristics of GDO–HD–GAA-TFET with various dielectric constants over L_{ov} region is studied as shown in Fig. 12. It is clearly evident from Fig. 12 that for Si_3N_4 the ambipolar current is increased by 50.18 times and for the insertion of vacuum over L_{ov}, the ambipolar current is reduced by 1.39 times (in comparison with SiO_2). Moreover, to investigate the impact of GDO, the drain current of HD–GAA-TFET is also examined. It is analyzed that for HD–GAA-TFET the ambipolar conduction and thus the I_{AMB} are considerably enhanced in comparison with GDO–HD–GAA-TFET. The reduction in I_{AMB} is also shown in the inset of Fig. 12. It is evident from the inset that the I_{AMB} of HD-GAA-TFET is remarkably higher in comparison with GDO–GAA-TFET. Suppressed I_{AMB} and enhanced f_T of GDO–HD–GAA–TFET with low-k dielectric over L_{ov} make it eligible for application of digital circuitry.

4 Conclusion

This study proposed a device structure which overcomes the major shortcomings of tunnel FET. With the help of GDO architecture, the ambipolar behavior has been controlled and by amalgamation of HD scheme, the ON current of the device is enhanced. Reduced I_{AMB} and higher I_{ON} thus make it suitable for digital circuitry applications. It is revealed from the results that GDO improves the ambipolar characteristics, but it simultaneously degrades the HF performance of the device. Thus, to overcome the degradation caused by GDO, vacuum gate dielectric is inserted over the region of L_{OV}. The vacuum dielectric inserted over L_{OV} reduces the parasitic capacitances and the ambipolar current and enhances the cutoff frequency of the device, thereby resulting in an overall device improvement (analog and HF performance). Therefore, GDO–HD–GAA-TFET with vacuum dielectric over L_{ov} can be used for the development of better analog/low-power RF circuits.

Acknowledgments Authors would like to thank to Microelectronics Research Lab, Department of Engineering Physics Delhi Technological University, for carrying out this work. One of the authors (Jaya Madan) would like to thank University Grants Commission, Govt. of India, for providing the necessary financial assistance during the course of this research work.

References

1. J. Goldberger, A.I. Hochbaum, R. Fan, P. Yang, Silicon vertically integrated nanowire field effect transistors. Nano Lett. **6**, 973–977 (2006)
2. J. Madan, R. Chaujar, Interfacial Charge Analysis of Heterogeneous Gate Dielectric-Gate All Around-Tunnel FET for Improved Device Reliability. IEEE Trans. Device Mater. Reliab. **16**, 227–234 (2016)
3. K. Mao, T. Mizutani, A. Kumar, T. Saraya, T. Hiramoto, Suppression of within-device variability in intrinsic channel tri-gate silicon nanowire metal–oxide–semiconductor field-effect transistors. Jpn. J. Appl. Phys. **51**, 02BC06 (2012)
4. N. Singh, A. Agarwal, L. Bera, T. Liow, R. Yang, S. Rustagi, C. Tung, R. Kumar, G. Lo, N. Balasubramanian, High-performance fully depleted silicon nanowire (diameter $\leq$ 5 nm) gate-all-around CMOS devices. IEEE Electron Device Lett. **27**, 383–386 (2006)
5. W.Y. Choi, W. Lee, Hetero-gate-dielectric tunneling field-effect transistors. IEEE Trans. Electron Devices **57**, 2317–2319 (2010)
6. A.S. Verhulst, W.G. Vandenberghe, K. Maex, G. Groeseneken, Tunnel field-effect transistor without gate-drain overlap. Appl. Phys. Lett. **91**, 053102 (2007)
7. K. Boucart, A.M. Ionescu, Double-gate tunnel FET with high-gate dielectric, (2007)
8. S. Cho, M.-C. Sun, G. Kim, T.I. Kamins, B.-G. Park, J.S. Harris Jr., Design optimization of a type-I heterojunction tunneling field-effect transistor (I-HTFET) for high performance logic technology. J. Semiconductor Technology and Science **11**, 182–189 (2011)
9. A. Gao, N. Lu, Y. Wang, T. Li, Robust ultrasensitive tunneling-FET biosensor for point-of-care diagnostics, Scientific reports, 6 (2016)
10. H.-C. Lin, M.-F. Wang, C.-Y. Lu, T.-Y. Huang, Ambipolar Schottky barrier silicon-on-insulator metal–oxide–semiconductor transistors. Solid-State Electronics **47**, 247–251 (2003)
11. J. Madan, R. Chaujar, Palladium gate all around-Hetero dielectric-tunnel FET based highly sensitive hydrogen gas sensor, Superlattices and Microstructures, (2016)
12. J. Madan, R. Gupta, R. Chaujar, Performance investigation of heterogeneous gate dielectric-gate metal engineered–gate all around-tunnel FET for RF applications, Microsystem Technologies, (2016) 1–10
13. A. Mallik, A. Chattopadhyay, S. Guin, A. Karmakar, Impact of a spacer–drain overlap on the characteristics of a silicon tunnel field-effect transistor based on vertical tunneling. IEEE Trans. Electron Devices **60**, 935–943 (2013)
14. A. Naderi, P. Keshavarzi, The effects of source/drain and gate overlap on the performance of carbon nanotube field effect transistors. Superlattices Microstruct. **52**, 962–976 (2012)
15. R. Gandhi, Z. Chen, N. Singh, K. Banerjee, S. Lee, CMOS-Compatible Vertical-Silicon-Nanowire Gate-All-Around p-Type

Tunneling FETs With-mV/decade Subthreshold Swing. IEEE Electron Device Lett. **32**, 1504–1506 (2011)
16. P.-F. Wang, K. Hilsenbeck, T. Nirschl, M. Oswald, C. Stepper, M. Weis, D. Schmitt-Landsiedel, W. Hansch, Complementary tunneling transistor for low power application. Solid-State Electronics **48**, 2281–2286 (2004)
17. A.U.S. Manual, Silvaco, Santa Clara, CA, (2010)
18. A. Biswas, S.S. Dan, C. Le Royer, W. Grabinski, A.M. Ionescu, TCAD simulation of SOI TFETs and calibration of non-local band-to-band tunneling model. Microelectron. Eng. **98**, 334–337 (2012)
19. Z. Chen, H. Yu, N. Singh, N. Shen, R. Sayanthan, G. Lo, D.-L. Kwong, Demonstration of tunneling FETs based on highly scalable vertical silicon nanowires. IEEE Electron Device Lett. **30**, 754–756 (2009)
20. Y.-S. Choi, T.-P. Rhee, K.-D. Yoo, T. Won, A new submicron MOSFET technology with Gate Overlap on Twin Oxide (GOTO) LDD structure. Microelectron. Eng. **15**, 253–256 (1991)
21. J. Madan, R. Gupta, R. Chaujar, Analytical drain current formulation for gate dielectric engineered dual material gate-gate all around-tunneling field effect transistor. Jpn. J. Appl. Phys. **54**, 094202 (2015)
22. J. Madan, R. Gupta, R. Chaujar, Mathematical modeling insight of hetero gate dielectric-dual material gate-GAA-tunnel FET for VLSI/analog applications, Microsystem Technologies, (2016) 1–8
23. Y. Yang, X. Tong, L.-T. Yang, P.-F. Guo, L. Fan, Y.-C. Yeo, Tunneling field-effect transistor: capacitance components and modeling. IEEE Electron Device Lett. **31**, 752–754 (2010)
24. A. Shaker, M. Ossaimee, A. Zekry, M. Abouelatta, Influence of gate overlap engineering on ambipolar and high frequency characteristics of tunnel-CNTFET. Superlattices Microstruct. **86**, 518–530 (2015)
25. S. Mookerjea, R. Krishnan, S. Datta, V. Narayanan, On enhanced Miller capacitance effect in interband tunnel transistors. IEEE Electron Device Lett. **30**, 1102–1104 (2009)

Engineering Science and Technology, an International Journal xxx (2016) xxx–xxx

HOSTED BY

ELSEVIER

Contents lists available at ScienceDirect

Engineering Science and Technology, an International Journal

journal homepage: www.elsevier.com/locate/jestch



Full Length Article

LC-ladder filter systematic implementation by OTRA

Suman Kumari [a], Stuti Gupta [a], Neeta Pandey [a,*], Rajeshwari Pandey [a], Rashika Anurag [b]

[a] Dept. of Electronics and Communication Engineering, Delhi Technological University, Delhi, India
[b] Dept. of Electronics and Communication Engineering, JSS Academy of Technical Education, Noida, India

ARTICLE INFO

Article history:
Received 14 May 2016
Revised 4 October 2016
Accepted 5 October 2016
Available online xxxx

Keywords:
LC-ladder
Operational simulation
Leap frog method
OTRA

ABSTRACT

In this paper Operational Trans Resistance Amplifier (OTRA) based LC-ladder filter implementation is presented. The proposed realization uses leap frog method which is a systematic approach for LC-ladder design. The OTRA is a current mode active block with low impedance at both input and output terminals. This active element is therefore a suitable choice for realizing voltage output filter. The proposed structure uses all grounded passive components that make it attractive from integration viewpoint. The validity of this approach is demonstrated by PSPICE simulations using CFOA (IC AD844) realization of OTRA. The simulated results are found in close agreement to proposed theory.

© 2016 Karabuk University. Publishing services by Elsevier B.V. This is an open access article under the CC BY-NC-ND license (http://creativecommons.org/licenses/by-nc-nd/4.0/).

1. Introduction

Continuous time (CT) filter are extensively used in applications pertaining to communication, instrumentation and measurements. In some applications these filters have advantages over discrete-time counterparts as these do not produce sampling noise, consume less power and are much simpler to implement. This has led researchers to continue exploring the design and development of CT filters.

The primary filter design approach consists of (i) selection of order of the filter using design specifications for a given application (ii) determining the appropriate transfer function and (iii) circuit synthesis and implementation of the obtained transfer function. The transfer functions can be implemented either entirely out of passive components or using discrete/ integrated active circuits.

Higher order CT filters are synthesized using two dominant approaches namely cascaded biquads and lossless doubly terminated LC ladder realization. Generally lossless doubly terminated LC ladder method is preferred as suggested in vast literature [1,2], since this method leads to component variation-tolerant filter realizations, much better dynamic range of performance and improved passband magnitude response accuracy than cascaded biquads. The only disadvantage of this method is the use of inductor as it's realization in an integrated circuit (IC) form is not feasible in terms of space utilization, cost and tunability [1]. This shortcoming may be overcome either by using element replacement method or by leap frog method. In element replacement method inductors are replaced by gyrators. This method is suitable for grounded inductor based designs only as realizing high quality floating inductors proves to be challenging. Use of frequency dependent negative resistance (FDNR) is another method of element replacement however it is suitable for designing low pass filters. In leap frog method signal flow graph (SFG) approach is used to emulate the relationship between various passive elements. These SFGs are then physically realized using lossy and lossless active integrators [2]. The filter realizations so obtained are called active LC-ladder filters.

Few leap frog method based active LC-ladder filters [3–23] of varying order, using different approximation functions have been presented in literature. The structures use variants of second generation current conveyors (CCII) namely multiple output CCII (MOCCII)[4], dual/multiple output current controlled CCII (DOCCCII/MOCCCII) [5–7], differential voltage CC (DVCC) [8], differential voltage current controlled CCII (DVCCC) and differential voltage current controlled Current Feedback Operational amplifier (DVCCCFOA) [9], current feedback operational amplifier (CFOA) [10], current feedback amplifier (CFA) [11]; current differencing buffer amplifier [12–14], current controlled current differencing buffer amplifier (CCCDBA) [15], current differencing transconductance amplifier (CDTA) [16–17], operational transconductance amplifier [18–20], current backward transconductance amplifier [21], CMOS based differential integrators [3], CMOS based lossy and lossless integrators [22–23]. These available structures provide voltage [9,10,15,18–20] and current [3–8,11–14,16,17,21–23]

* Corresponding author.
E-mail address: n66pandey@rediffmail.com (N. Pandey).
Peer review under responsibility of Karabuk University.

http://dx.doi.org/10.1016/j.jestch.2016.10.003
2215-0986/© 2016 Karabuk University. Publishing services by Elsevier B.V.
This is an open access article under the CC BY-NC-ND license (http://creativecommons.org/licenses/by-nc-nd/4.0/).

Please cite this article in press as: S. Kumari et al., LC-ladder filter systematic implementation by OTRA, Eng. Sci. Tech., Int. J. (2016), http://dx.doi.org/10.1016/j.jestch.2016.10.003

outputs respectively. However, the structures [7–9,11–14,18–20] do not provide output at appropriate impedance level therefore additional active blocks may be needed to access the output. Further [7] is active only structure which uses parasitic pole of operational amplifier making it's tuning difficult. It is also observed that the active blocks used in available LC-ladder filters [3–23] employ large number (sixteen or more) of MOS/bipolar transistors per block for its realization. This number will considerably increase further if current sources used for biasing purpose are realized through MOS/bipolar transistors. A detailed comparison of salient features of these structures is given in Table 1. It is clear from Table 1 that a limited literature is available on structures providing voltage output [9–11,15,18–20]. Furthermore these structures do not provide output at low impedance except for those presented in [10,15].

The Operational Trans Resistance Amplifier (OTRA) [24–29] is a current input voltage output active block which is neither slew limited nor does its gain bandwidth product is fixed unlike conventional voltage mode opamp. Additionally the effect of parasitic capacitances at the input can be eliminated due to internally grounded input terminals. These features make OTRA a suitable choice for realizing voltage output leapfrog filter. Therefore, the present work focuses on developing OTRA based LC-ladder filter with the systematic approach using leapfrog structure. Comparing the proposed structure with available literature on voltage mode LC-ladder filter with low output impedance [10] [15] reveals following:

- The proposed topology uses six OTRAs to provide 6th order response whereas [10] and [15] provide 5th and 3rd order responses respectively with same number of active blocks.
- The 5th order CFOA based structure [10] uses eight resistors out of which six are floating.
- The 3rd order CCCDBA based structure [15] uses fourteen resistors out of which seven are floating.
- The proposed structure uses sixteen resistors for providing 6th order response. All the resistances have one terminal connected at either of input ports of OTRA which are internally grounded. Thus the proposed structure is benefitted from integration viewpoint.
- The CMOS based realization of CFOA [10] employs eighteen resistors and two current sources while CCCDBA [15] uses twenty four resistors and floating current source. Both these active blocks would be requiring additional transistors to realize current sources. The OTRA realization uses only fourteen transistors thus will occupy smaller chip area.

Rest of the paper is organised in the following manner. Section 2 elaborates on the concept of nth order LC-ladder filter realization using leapfrog method. Section 3 elucidates on the employment of OTRA for this application. In Section 4, the simulation results for a sixth order Chebyshev low pass filter prototype are shown and Section 5 concludes the paper.

2. LC-ladder filter realization using leap frog method

In this section the leapfrog realization of doubly terminated LC-ladder is elucidated. An nth order doubly terminated LC-ladder having only inductors in series arm and capacitors in shunt arm is depicted in Fig. 1.

The current in shunt arm and voltage across shunt arm are represented respectively as

Table 1
Summary of features of available LC-ladder filters based on leap frog method.

Ref. No.	Active blocks	Output	Output Impedance	Need of additional active block	Filter order, approximation and type	Inbuilt Tunability
[3]	CMOS based integrator	Current	High	No	5th order, Butterworth, low pass filter	Yes
[4]	MOCC	Current	High	No	3rd order, elliptic, low pass filter	No
[5]	MCCCII	Current	High	No	5th order, Butterworth, low pass filter 6th order, Chebyshev, band pass filter	Yes
[6]	DO-CCCII	Current	High	No	8th – order elliptic band pass filter	Yes
[7]	OA + CCCII	Current	Low	Yes	3rd order, Butterworth, low-pass filter 6th order Chebyshev bandpass filter	Yes
[8]	DVCC	Current	Low	Yes	5th order, Butterworth, low-pass filter 6th order, Chebyshev, band-pass filter	No
[9]	DVCCFOA + DVCCCII	Voltage	High	Yes	3rd order, Butterworth, low-pass filter	Yes
[10]	CFOA	Voltage	Low	No	5th order, – , low-pass filter 5th order, – , high-pass filter	No
[11]	CFA	Current	Low	Yes	6th order, Chebyshev, band-pass filter 3rd order, Chebyshev, band-reject filter 3rd –order, Chebyshev, high-pass notch	No
		Voltage	High	Yes	3rd order, elliptic, low-pass filter	
[12]	CDBA	Current	Low	Yes	5th order, Butterworth, low-pass filter 6th order, Chebyshev, band-pass filter	No
[13]	CDBA	Current	Low	Yes	3rd order, Butterworth, low-pass filter	No
[14]	CDBA	Current	Low	Yes	3rd order, Butterworth, low-pass filter 6th order, Chebyshev, band-pass filter	No
[15]	CCCDBA	Voltage	Low	No	3rd order, – , low-pass filter 3rd order, – , high-pass filter	Yes
[16]	CDTA	Current	High	No	7th order, elliptic, low-pass filter	Yes
[17]	CDTA	Current	High	No	6th order, Butterworth, low-pass filter	Yes
[18]	OTA	Voltage	High	Yes	–	Yes
[19]	OTA	Voltage	High	Yes	7th order, Chebyshev, low-pass filter	Yes
[20]	OTA	Voltage	High	Yes	3rd – order, Elliptic, low-pass filter	Yes
[21]	CBTA	Current	High	No	5th order, Butterworth, low-pass filter	Yes
[22]	CMOS	Current	High	No	5th order, Chebyshev, low-pass filter	Yes
[23]	CMOS	Current	High	No	3rd order, Chebyshev low-pass filter	Yes

Please cite this article in press as: S. Kumari et al., LC-ladder filter systematic implementation by OTRA, Eng. Sci. Tech., Int. J. (2016), http://dx.doi.org/10.1016/j.jestch.2016.10.003

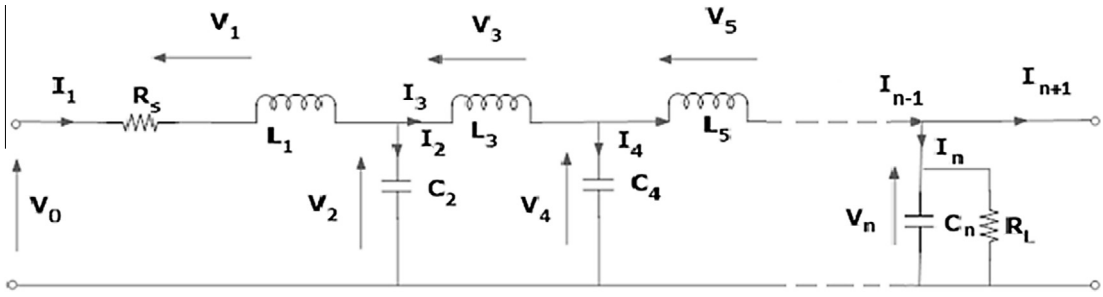


Fig. 1. An nth order doubly terminated LC-ladder.

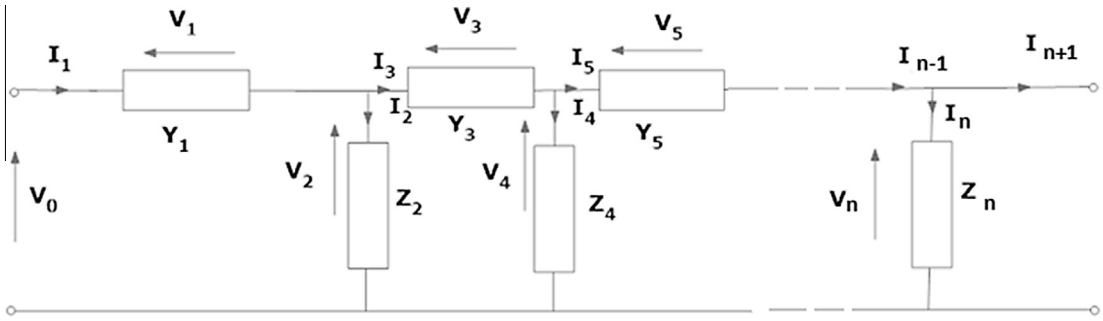


Fig. 2. An nth order doubly terminated LC-ladder with general immittances.

$$I_j = I_{j-1} - I_{j+1} \quad (j = 2,4,6,\ldots\ldots,n-2) \tag{1}$$

and

$$V_j = V_{j-1} - V_{j+1} \quad (j = 1,3,5,\ldots\ldots,n-1) \tag{2}$$

Since, $I_{n+1} = 0$ so $I_n = I_{n-1}$.

Voltage at different nodes are given as

$$V_j = \frac{I_j}{sC_j} \quad (j = 2,4,6,\ldots\ldots,n-2)$$
$$V_n = \frac{I_n}{sC_n + G_L} \tag{3}$$

where $G_L = 1/R_L$.

The currents in series arm are given by

$$I_{j-1} = \frac{V_{j-1}}{sL_{j-1}} \quad (j = 4,6,\ldots\ldots,n) \tag{4}$$

$$I_1 = \frac{V_1}{sL_1 + R_S} \tag{5}$$

Representing the elements in series arm as admittances and those in shunt arm as impedances Fig. 1 modifies to Fig. 2.

The series arm current is related to node voltages by

$$I_j = Y_j\,(V_{j-1} - V_{j+1}) \quad (j = 1,3,5,\ldots\ldots,n-1) \tag{6}$$

The correspondence between node voltage and series arm currents is given by

$$V_j = Z_j\,(I_{j-1} - I_{j+1}) \quad (j = 2,4,6,\ldots\ldots,n-2) \tag{7}$$

$$V_n = Z_n I_{n-1} \tag{8}$$

The active realizations of the above equations will depend on terminal characteristics of the constituent active block. As this work uses OTRA as active block that processes current difference and provides voltage output, some changes are necessary for performing voltage differencing operation. The following section elaborates on it.

3. OTRA based implementation

The OTRA is a three terminal current mode active device shown symbolically in the Fig. 3 and is characterised by following terminal equation

$$V_0 = R_m(I_+ - I_-) \tag{9}$$

where R_m is transresistance gain of OTRA. For ideal operation, R_m approaches infinity forcing the input currents to be equal and therefore this active block should be used in negative feedback configuration. The input terminals of OTRA are virtually grounded and hence are low impedance terminals. This property of OTRA leads to cancellation of parasitic effects at input thus making it a suitable for high frequency applications.

The OTRA provides voltage as output therefore direct realization of Eq. (8) is not possible. Eq. (8) is multiplied by scaling resistor R_{SC} to convert current into voltage. Eq. (6) modifies to

$$\mathbf{R_{SC}I_j} = \mathbf{R_{SC}Y_j(V_{j-1} - V_{j+1})} \;\rightarrow\; \boldsymbol{V_{Ij} = t_{Yj}[V_{j-1} - V_{j+1}]}$$
$$(\mathbf{j} = 1,3,5,\ldots\ldots,\mathbf{n}-1) \tag{10}$$

$$\text{where, } \boldsymbol{Y_1} = \frac{1}{\boldsymbol{sL_1 + R_S}}, \mathbf{Y_j} = \frac{1}{\boldsymbol{sL_j}}, \boldsymbol{t_{Yj}} = \mathbf{R_{SC}Y_j},$$
$$(j = 3,5,\ldots\ldots,n-1) \tag{11}$$

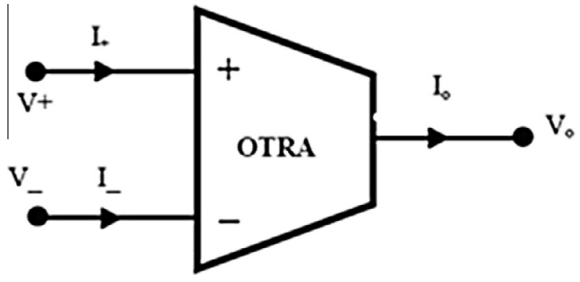


Fig. 3. OTRA Circuit Symbol.

Please cite this article in press as: S. Kumari et al., LC-ladder filter systematic implementation by OTRA, Eng. Sci. Tech., Int. J. (2016), http://dx.doi.org/10.1016/j.jestch.2016.10.003

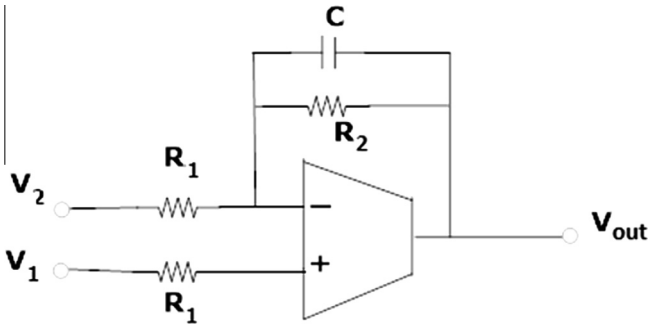


Fig. 4. OTRA based Differencing Lossy Integrator.

Using Eqs. (10), node voltages represented in Eqs. (7) and (8) are modified to Eqs. (12) and (13) respectively.

$$j = \frac{\mathbf{Z_j}}{\mathbf{R_{SC}}}(\mathbf{R_{SC}I_{j-1}} - \mathbf{R_{SC}I_{j+1}}) \rightarrow \boldsymbol{V_j} = \boldsymbol{t_{Zj}}[\boldsymbol{V_{I(j-1)}} - \boldsymbol{V_{I(j+1)}}] \quad (\mathbf{j} = 2, 4, 6, \ldots\ldots \mathbf{n} - 2) \tag{12}$$

$$\mathbf{V}_n = \frac{\mathbf{Z}_n}{\mathbf{R_{SC}}}\mathbf{R_{SC}I_{n-1}} \quad \rightarrow \quad \boldsymbol{v}_n = \boldsymbol{t}_{Zn}\boldsymbol{v}_{I(n-1)} \tag{13}$$

$$\text{where, } \mathbf{Z_j} = \frac{1}{\mathbf{sC_j}}\mathbf{Z_n} = \frac{1}{\mathbf{sC_n} + \mathbf{G_L}}, \boldsymbol{t}_{Zj} = \frac{\mathbf{Z_j}}{\mathbf{R_{SC}}}, \quad (j = 2, 4, 6, \ldots\ldots, n - 2) \tag{14}$$

It may be observed that active realization of Eqs. (10)–(14) is possible through differencing lossy and lossless integrator. The OTRA based differencing lossy integrator is given in Fig.4. The output voltage V_{out} is expressed in terms of V_1 and V_2 as:

$$\mathbf{V_{out}} = \frac{1}{\mathbf{sC} + \mathbf{G}_2}\left(\frac{\mathbf{V}_1}{\mathbf{R}_1} - \frac{\mathbf{V}_2}{\mathbf{R}_1}\right) \tag{15}$$

A differencing lossless integrator can also be realized using Fig. 4 if R_2 is chosen to be infinity. Using these differencing lossy and lossless integrators, a complete OTRA based n^{th} order LC-ladder as given in Fig. 5 can be realized.

4. Non-ideality analysis

Ideally the transresistance gain of OTRA approaches infinity and forces the two input currents to be equal. However, practically the transresistance gain R_m is finite and frequency dependent therefore its effects on the behavior of realized LC-ladder should be considered.

Considering a single pole model, the transresistance gain R_m can be expressed as

$$R_m(s) = \left(\frac{R_0}{1 + (\boldsymbol{s}/\boldsymbol{\omega}_0)}\right) \tag{16}$$

For high frequencies, the transresistance gain $R_m(s)$ reduced to:

$$R_m(s) = \left(\frac{1}{\boldsymbol{sC_p}}\right) \tag{17}$$

Here R_0 is DC open loop transresistance gain, ω_0 is the transresistance cut-off frequency and $C_p = 1/R_0\omega_0$ is the parasitic capacitance. Considering finite transresistance gain the output voltage V_0 of Fig. 4 is recomputed as

$$V_{out} = \frac{1}{s(C + Cp) + G_2}\left(\frac{V_1}{R_1} - \frac{V_2}{R_1}\right) \tag{18}$$

Eq. (18) clearly indicates that V_{out} modifies in presence of C_p. However, the effect can be accommodated through self-compensation i.e. by pre adjusting the value of capacitor C or by connecting a capacitor of value C_p between ' + ' and output terminal of OTRA.

5. Simulation Results

The theoretical proposition is functionally verified by taking a prototype sixth order Chebyshev low pass filter with 0.1 dB ripple in passband which may be obtained by considering n = 6 in Fig. 1. The normalized values of various passive elements [2] are $L_1 = 1.1681$, $C_2 = 1.4040$, $L_3 = 2.0562$, $C_4 = 1.5171$, $L_5 = 1.9028$, $C_6 = 0.8618$ and $R_{Load} = 0.7378$. Considering the passband bandwidth of 340krad/s, source resistor $\mathbf{R_s} = 1.2$ kΩ and assuming $C_1 = C_2 = C_3 = C_4 = C_5 = C_6 = C = 0.5$ nF the values of the resistors for proposed OTRA based low-pass LC-ladder circuit are calculated as $R_S = 6.9$ kΩ., $R_1 = 2$ kΩ, $R_2 = 33$ kΩ, $R_3 = 3.6$ kΩ, $R_4 = 30$ kΩ,

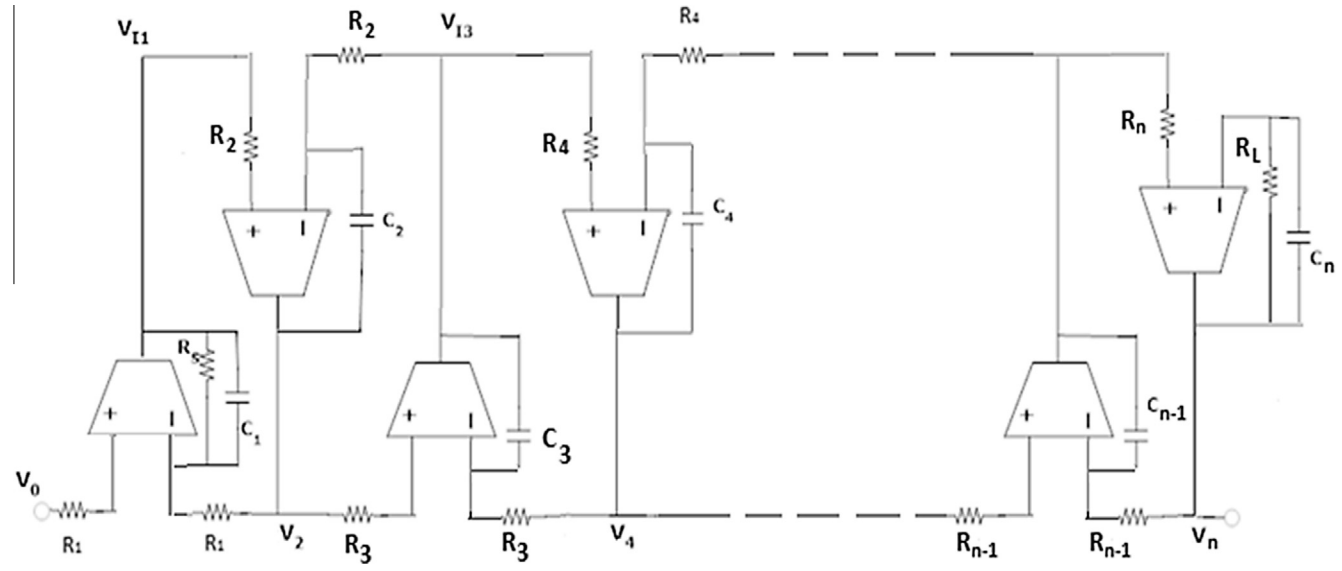


Fig. 5. Proposed OTRA based n^{th} order doubly terminated LC-ladder.

Please cite this article in press as: S. Kumari et al., LC-ladder filter systematic implementation by OTRA, Eng. Sci. Tech., Int. J. (2016), http://dx.doi.org/10.1016/j.jestch.2016.10.003

R_5 = 3.3 kΩ, R_6 = 17 kΩ, R_L = 3.9 kΩ. For verification purpose, CFOA BASED realization of OTRA [30] is used.

Fig. 6 shows the simulated and theoretical frequency responses for proposed OTRA based low-pass LC-ladder. The simulated passband bandwidth is observed to be 54 kHz which is in close agreement to the theoretical value. To study the response in time domain of the designed low pass filter an input comprising of three sinusoidal frequency components, 1 kHz, 54 kHz and 100 kHz is applied. The input time domain waveform and its corresponding frequency spectrum are depicted in Fig. 7 whereas those of output are depicted in Fig. 8. It is observed that the frequency components around f_0 are slightly attenuated and frequency components greater than f_0 are negligible.

It is well known that higher order filters based on LC ladder show very low sensitivity to component variation. To illustrate this fact the passband bandwidth is measured through Monte Carlo simulation with 10% tolerance in (i) only capacitors, (ii) only resistors and (iii) both resistors and capacitors. The histograms

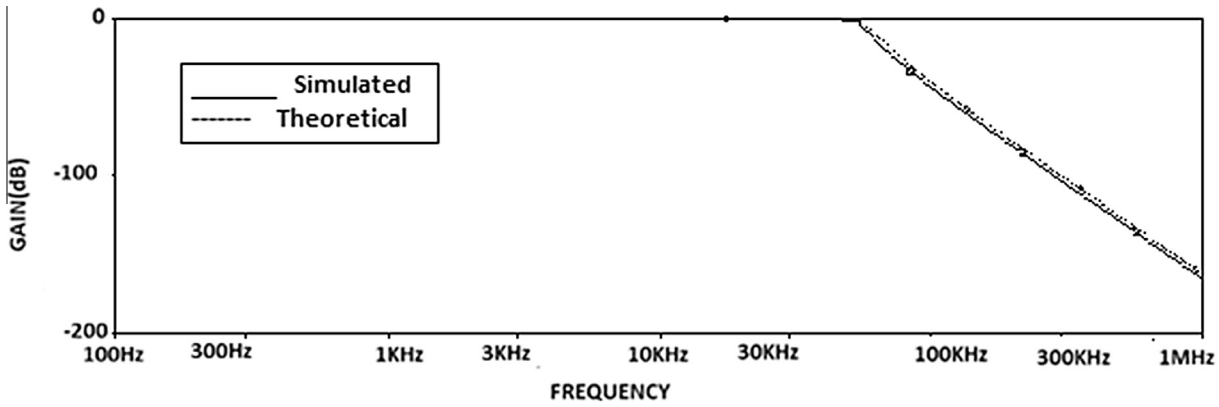


Fig. 6. Simulated and theoretical frequency responses of the OTRA based low-pass LC-ladder.

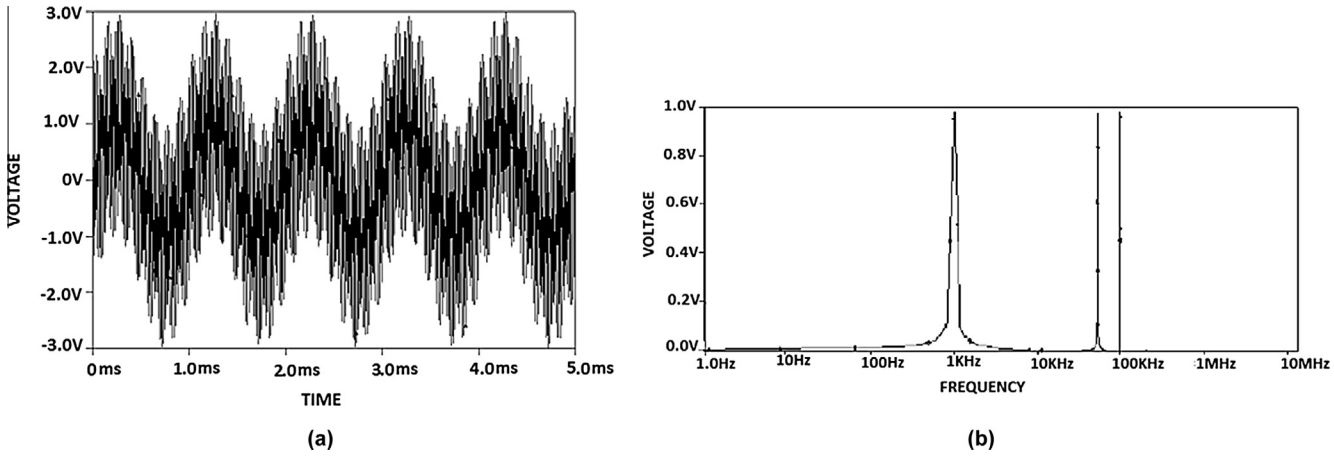


Fig. 7. (a) Input Signal (a) Time domain waveform (b) Frequency spectrum.

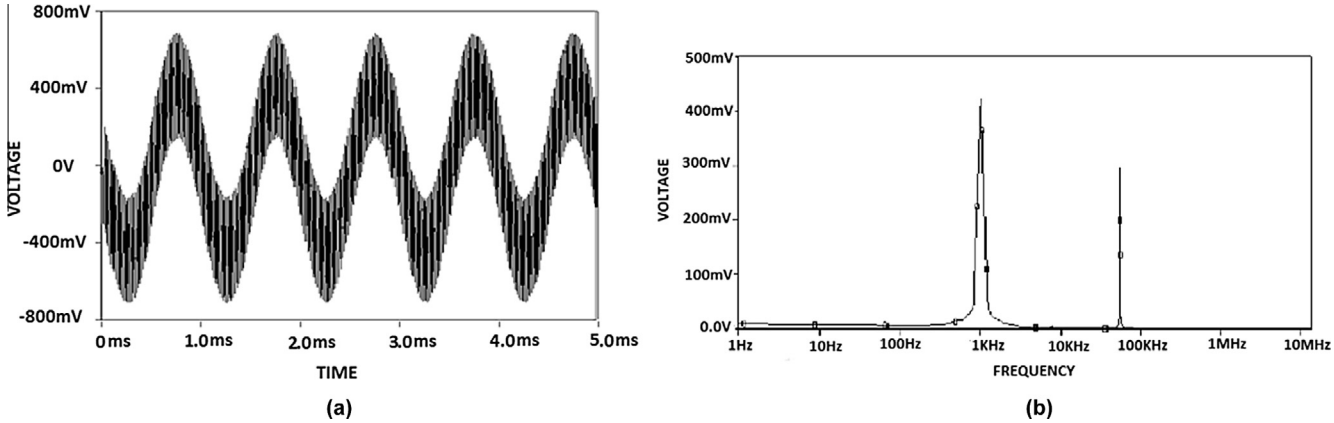


Fig. 8. Output signal (a) Transient Response (b) Frequency spectrum.

Please cite this article in press as: S. Kumari et al., LC-ladder filter systematic implementation by OTRA, Eng. Sci. Tech., Int. J. (2016), http://dx.doi.org/10.1016/j.jestch.2016.10.003

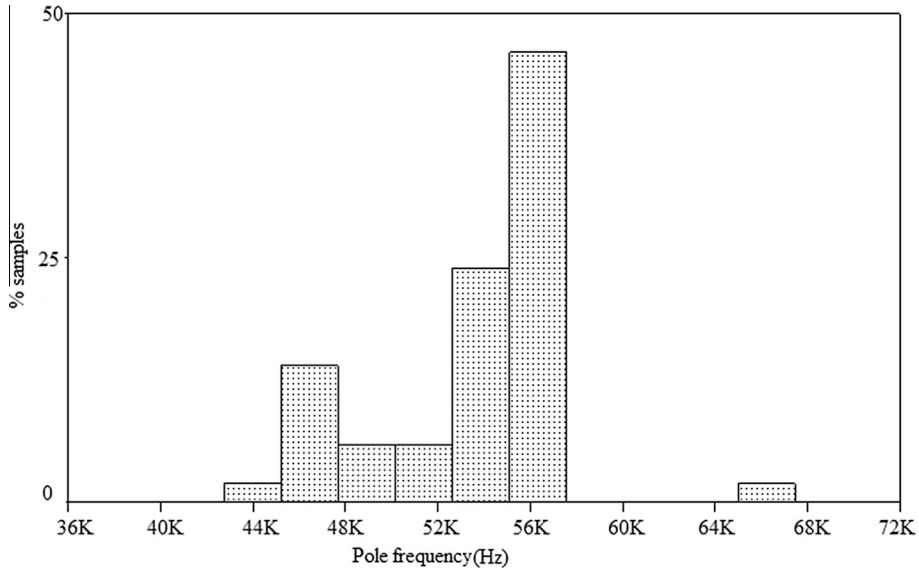


Fig. 9. Monte Carlo analysis with 10% tolerance in capacitance values.

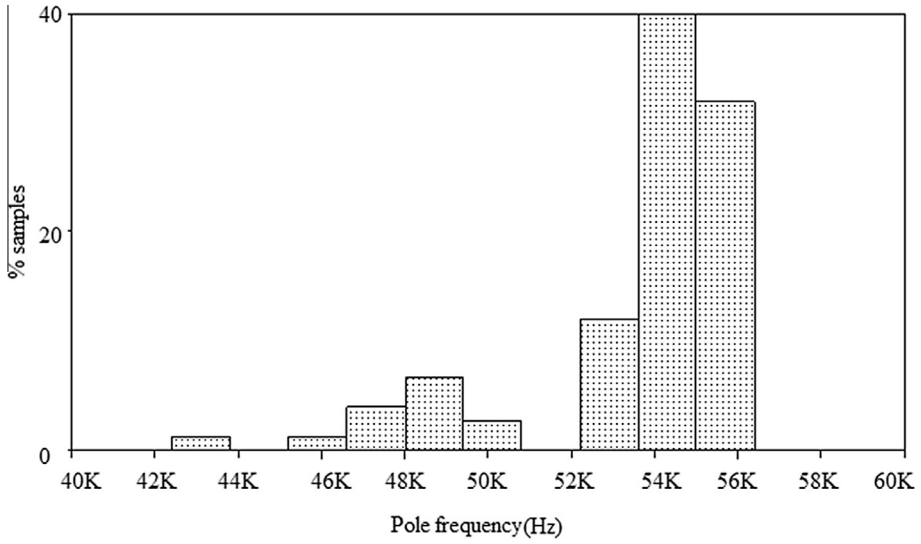


Fig. 10. Monte Carlo analysis with 10% tolerance in resistance values.

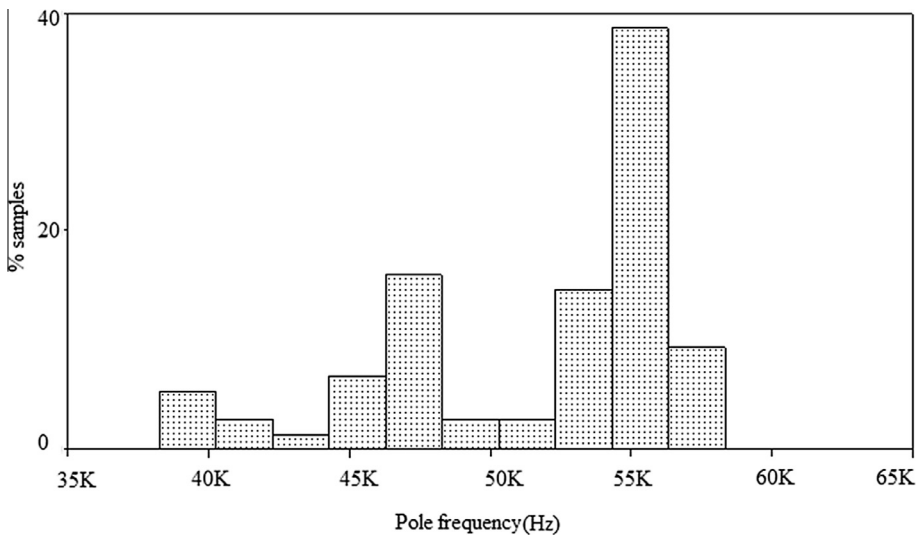


Fig. 11. Monte Carlo analysis with 10% tolerance in resistance and capacitance values.

Please cite this article in press as: S. Kumari et al., LC-ladder filter systematic implementation by OTRA, Eng. Sci. Tech., Int. J. (2016), http://dx.doi.org/10.1016/j.jestch.2016.10.003

obtained through simulations for cases (i)–(iii) are shown in Figs. 9–11 respectively. It is found that 75% of the samples are within ±3% of designed passband value.

6. Conclusion

A systematic development of OTRA based voltage-mode LC-ladder filter based on the leapfrog method is presented. A sixth order Chebyshev low pass filter prototype is developed for illustration of the proposed theory which used six OTRAs, six capacitors and fourteen resistors. All passive components are grounded in the realization which makes the proposition suitable from integration viewpoint. The designed structure is verified using PSPICE simulation where OTRA is emulated using two CFOAs. A close agreement is observed between the theoretical formulation and simulation results.

References

[1] A. Thanachayanont, A. Payne, CMOS floating active inductor and its application to bandpass filter and oscillator designs, IEE Proc. Circuits Device Syst. 147 (2000) 42–48.
[2] R. Shaumann, M.E. Van Valkenburg, Design of Analog Filters, Oxford University Press, Oxford (UK), 2001.
[3] S. Sa-ad, D. Chaythong, A high frequency current mode ladder filter using multiple output lossless integrator, in: ISPACS2008 International Symposium in Intelligent Signal Processing and Communication systems, 2008, pp. 1–4.
[4] J. Wu, E. El-Masry, Current-mode ladder filters using multiple output current conveyors, IEE Proc. Circuits Devices Syst. 143 (4) (1996) 218–222.
[5] A. Jiraseree-Amornkunt, N. Fujii', W. Surakampontorn, Realisation of electronically tunable ladder filters using multi-output current controlled conveyors, in: ISCAS 2003 Proceedings of the 2003 International Symposium on Circuits and Systems, IEEE, 2003, pp. I-541–I-544.
[6] A. Campeanu, J. Gal, Systematic implementation method of LC-ladder filter by MO-CCCII circuits, ELECO2007, in: 5th International Congress and Exhibition of Electrical and Electronic Engineering, 2007.
[7] X. Yanhui, H. Peng, Realisation of low pass and band-pass leapfrog filters using OAs and CCCIIs, MAAS 2009, in: Proceedings of International conference Management and Service Science, IEEE, 2009, pp. 1–4, http://dx.doi.org/10.1109/ICMSS.2009.5303743.
[8] Y.-H. Xi, X. Li, Active Simulation of passive Leapfrog Ladder Filters Using DVCCs, ICIT 2008, in: IEEE International Conference on Industrial Technology, IEEE, 2008, pp. 1–5.
[9] C. Laoudias, C. Psychalinos, Comparative study of resistorless filters using differential voltage current controlled current feedback operational amplifiers and differential voltage current controlled current conveyors, ISRN Electron. 2013 (2013) 7–11. Article ID 910170.
[10] P.K. Sinha, A. Saini, P. Kumar, S. Mishra, CFOA based low pass and high pass ladder filter—a new configuration, Circuits Syst. 5 (2014) 293–300.
[11] T.S. Rathore, U.P. Khot, CFA-based grounded-capacitor operational simulation of ladder filters, Int. J. Circuit Theor. Appl. 36 (2008) 697–716.
[12] W. Tangsrirat, N. Fujii, W. Surakampontorn, Current-mode leapfrog ladder filters using CDBAs, ISCAS 2002, in: IEEE International Symposium on Circuits and Systems, IEEE, 2002, pp. V57–V60.
[13] W. Tangsrirat, W. Surakampontorn, N. Fujii, Realization of leapfrog filters using current differential buffered amplifiers, IEICE Trans. Fundam. E86-A (2) (2003) 318–326.
[14] W. Tangsrirat, K. Klahan, T. Dumawipata, W. Surakampontorn, Low-voltage NMOS-based current differencing buffered amplifier and its application to current-mode ladder filter design, Int. J. Electron. 93 (11) (2006) 777–791.
[15] V. Ramola, S. Mishra, R.K. Singh, D.S. Chauhan, CCCDBA based implementation of voltage mode third order filter, Advances in Communication, Network, and Computing, Springer, 2012. pp. 185–192.
[16] A. Uygur, H. Kuntman, Seventh-order elliptic video filter with 0.1 dB pass band ripple employing CMOS CDTAs, Int. J. Electron. Commun. (AEU) 61 (2007) 320–328.
[17] J. Xu, C. Wang, The Current Difference Transconductance Amplifier (CDTA), <www.edn.com/Pdf/ViewPdf?contentItemId=4405810>.
[18] Y. Sun, Synthesis of leap-frog multiple-loop feedback OTA-C filters, IEEE Trans. Circuits Syst. II: Express Briefs 53 (9) (2006) 961–965.
[19] H.W. Su, Y. Sun, A CMOS 100 MHz continuos-time seventh order 0.05o equiripple linear phase leapfrog multiple loop feedback Gm-C filter, IEEE Int. Symp. Circuits Syst. II (2002) 17–20. Phoenix, AZ.
[20] C. Feng, The design of OTA-C filter based on the prototype of ladder LC-filter, J. Theor. Appl. Inf. Technol. 49 (1) (2013) 144–148.
[21] U.E. Ayten, M. Sagba, H. Sedef, Sedef current mode leap frog ladder filters using a new active block, Int. J. Electron. Commun. (AEU) 64 (2010) 503–511.
[22] P. Prommee, N. Wongprommoon, Tunable CMOS-based current mode fifth-order ladder low-pass Filter, TSP 2013, in: 36th International Conference on Telecommunications and Signal processing, IEEE, 2013, pp. 397–401.
[23] T. Kunto, P. Prommee, M.T. Abuelma'atti, Electronically tunable current-mode high-order ladder low-pass filters based on CMOS technology, Radioengineering 24 (4) (2015) 974–987.
[24] K.N. Salama, A.M. Soliman, CMOS operational transresistance amplifier for analog signal processing, Microelectron. J. 30 (3) (1999) 235–245.
[25] R. Pandey, N. Pandey, M. Bothra, S.K. Paul, Operational transresistance amplifier based multiphase sinusoidal oscillator, J. Electric. Comput. Eng. 2011 (2011) 1–8.
[26] C.L. Hou, H.C. Chien, Y.K. Lo, Square wave generators employing OTRAs, IEE Proc. Circuits Devices Syst. 152 (6) (2005) 718–722.
[27] Y.K. Lo, H.C. Chien, H.G. Chiu, Switch controllable OTRA based bistable multivibrators, IET Circuits Devices Syst. 2 (4) (2008) 373–382.
[28] A. Gupta, R. Senani, D.R. Bhaskar, A.K. Singh, OTRA-based grounded-FDNR and grounded-inductance simulators and their applications, Circuits Syst. Signal Process. 31 (2) (2012) 489–499.
[29] A. Gokcen, S. Kilinc, U. Cam, Fully integrated universal biquads using operational transresistance amplifier with MOS-C realisation, Turk. J. Electric. Eng. Comput. Sci. 19 (3) (2011) 363–372.
[30] Y.K. Lo, H.C. Chien, H.G. Chiu, Switch controllable OTRA based bistable multivibrator, IET Circuit Devices Syst. 2 (4) (2008) 373–382.

Please cite this article in press as: S. Kumari et al., LC-ladder filter systematic implementation by OTRA, Eng. Sci. Tech., Int. J. (2016), http://dx.doi.org/10.1016/j.jestch.2016.10.003

Magnetic response of split nanotube type metamaterial at near infrared frequency

Nishant Shankhwar[1], **Ravindra Kumar Sinha**[2] **and Yogita Kalra**[1]

[1] *Department of Applied Physics, Delhi Technological University, New Delhi, INDIA*

[2] *Central Scientific Instruments Organization (CSIO), Chandigarh, INDIA*

Abstract: In this paper we present the design of a split nanotube type metamaterial which shows strong magnetic resonance at infrared frequency. Its operation is similar to that of split ring resonator (SRR) but is easier to fabricate at nanoscale.

OCIS codes: 160.3918.

1. Introduction

The ability of Split Ring Resonator (SRR) to provide artificial negative permeability is well known. It has successfully shown strong magnetic resonance at microwave frequencies [1, 2]. But due to fabrication difficulties, SRR has not been able to provide negative magnetism at optical frequencies. Though other designs have been developed to match SRRs, they all have shown only a weak magnetic response with small values of negative permeability [3, 4]. We propose a design of metamaterial structure whose operation is similar to that of an SRR, but its nanoscale fabrication is easier.

2. Design and Analysis

The proposed design consists of long split nanotubes made up of silver. The inner region of each nanotube is filled with Sodium Fluoride NaF (n = 1.32) and the surrounding medium is air. Figure 1 shows schematic diagram of cross-section of the split nanotube in which all the dimensional parameters have been mentioned.

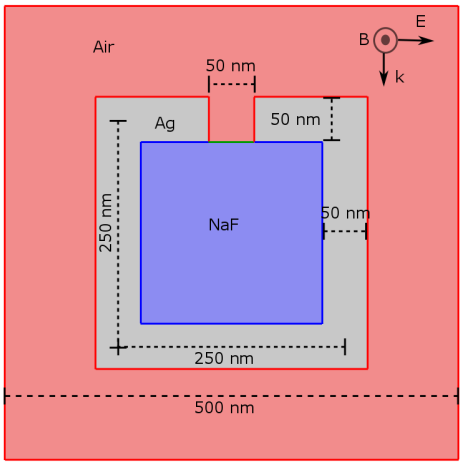


Fig. 1. Schematic diagram of a cross section of split nanotube with all the dimentional and material parameters

The permittivity of silver has been calculated according to Drude's model as $\varepsilon(\omega) = 1 - \omega_p^2/(\omega^2 + i\omega\omega_c)$ where ω is the frequency of the incident wave, $\omega_p = 14 \times 10^{15}$ rad/s is the plasma frequency and $\omega_c = 0.032 \times 10^{15}$ rad/s is the collision frequency of silver [5]. Frequency domain analysis has been performed in COMSOL® Multiphysics and s-parameters have been obtained.

3. Results and Conclusion

The effective material parameters have been calculated from s-parameters using Kramer-Kronig's relation based parameter retrieval technique [6]. Figure 2 shows effective material parameters, viz., refractive index, magnetic permeability & electric permittivity and reflection, transmission & absorption coeffcients.

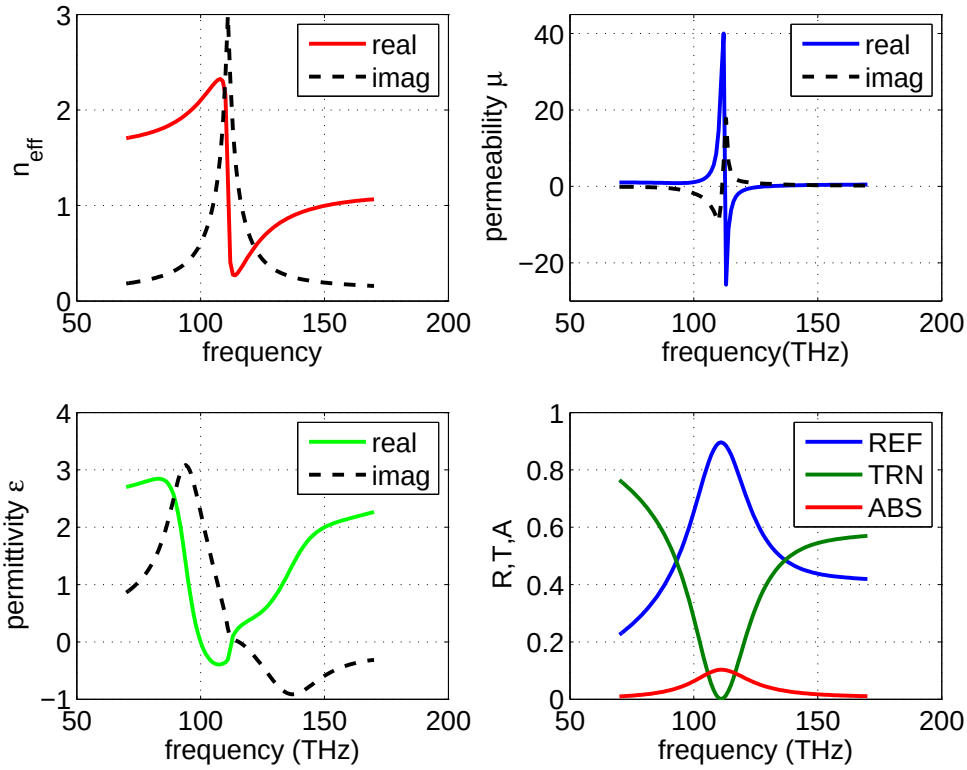


Fig. 2. Variation of the effective parameters of the proposed metamaterial structure with respect to frequency. A strong magnetic resonance is observed at 112 THz.

It can be concluded from figure 2 that the proposed metamaterial structure shows strong magnetic resonance at 112 THz ($= 2.65\ \mu m$, near infrared) . The electric resonance observed at 95 THz ($= 3.16\ \mu m$) is due to electric dipole formed across 50 nm gap of the split.

References

1. J. B. Pendry, A. J. Holden, D. Robbins, and W. Stewart, "Magnetism from conductors and enhanced nonlinear phenomena," Microwave Theory and Techniques, IEEE Transactions on **47**, 2075–2084 (1999).
2. D. R. Smith, W. J. Padilla, D. Vier, S. C. Nemat-Nasser, and S. Schultz, "Composite medium with simultaneously negative permeability and permittivity," Physical review letters **84**, 4184 (2000).
3. T.-J. Yen, W. Padilla, N. Fang, D. Vier, D. Smith, J. Pendry, D. Basov, and X. Zhang, "Terahertz magnetic response from artificial materials," Science **303**, 1494–1496 (2004).
4. S. Linden, C. Enkrich, M. Wegener, J. Zhou, T. Koschny, and C. M. Soukoulis, "Magnetic response of metamaterials at 100 terahertz," Science **306**, 1351–1353 (2004).
5. W. Cai and V. M. Shalaev, *Optical metamaterials*, vol. 10 (Springer, 2010).
6. Z. Szabo, G.-H. Park, R. Hedge, and E.-P. Li, "A unique extraction of metamaterial parameters based on kramers–kronig relationship," Microwave Theory and Techniques, IEEE Transactions on **58**, 2646–2653 (2010).

This article has been accepted for publication in a future issue of this journal, but has not been fully edited. Content may change prior to final publication. Citation information: DOI 10.1109/JSTQE.2016.2613859, IEEE Journal of Selected Topics in Quantum Electronics

Magnetron sputtering coated optical fiber probe designs for surface plasmon resonance sensor

Rashmi A. Minz, Sudipta S. Pal, Aditi Chopra, Shivam, R.Bhatnagar, R.K Sinha, and Samir K. Mondal

***Abstract*—In this work we have reported the design of the Surface Plasmon Resonance probes prepared from partially etched polymer optical probe and specially tapered single-mode fiber tip probe which are gold coated in Magnetron-sputtering (MS) unit. The coating parameters and conditions are discussed in details to achieve sensitive SPR probes. The sensor probes work in transmission modes. The gold coated etched in-line polymer fiber probe demonstrates high sensitivity, ~2459 nm/RIU and working range includes visible to infra red wavelength. The fiber tip probe with very small interaction area demonstrates sensitivity, ~166 nm/RIU. The in-line fiber probe could be used for large volume sample and the pointed fiber tip could be used for small volume samples.**

***Index Terms*—Evanescent Wave (EW), Magnetron Sputtering (MS), Refractive Index (R.I), Surface Plasmon Resonance (SPR)**

I. INTRODUCTION

Surface Plasmon resonance (SPR) phenomenon has emerged as an attractive spectroscopic analytical technique used in chemistry, physics, and bio-science advanced research [1]–[3].The Plasmonic based sensor is a promising field of research since the inception of the Surface Plasmon. The SPR is associated with collective oscillation of free electrons at the surface of metal-dielectric nano-structure under certain conditions[4]. Depending upon the nature of nano-material structure, the Plasmonic sensors are categorized into localized SPR (LSPR) sensor[5] and SPR sensor[6]. An LSPR usually needs monolayer coating of nano-particles on the source of evanescent wave where scattering from nano-particles contributes in the LSPR [7]–[9]. In case of SPR it is propagating surface wave which is supported at the interface between a bulk metal film and a dielectric[10]. The resonance is a result of the interaction between electromagnetic vectors in the incident light and free electrons available on the surface of specific Plasmonic coating[11].The excitation of surface Plasmon requires phase matching between the natural oscillation frequencies of the electron clouds present in the metal and the electromagnetic wave [12].

Manuscript received 27TH May 2016; revised August XXX; accepted XXXXX.
*Rashmi A.Minz is with AcSIR (Academy of scientific and innovative Research) CSIO, S. Sarkar Pal,Aditi Chopra,shivam,R.Bhatnagar,R.K Sinha and S. K. Mondal, are with the department of Advanced Materials and Sensors,CSIO—Central Scientific Instruments Organisation, Chandigarh 160 030, India (e-mail: rashmiachla@gmail.com , sudipta.sarkar12@gmail, chopra.aditi1410@gmail.com , shivam.bargujar102@gmail.com, rbh5@rediffmail.com, dr_rk_sinha@yahoo.com and samirmondal01@gmail.com).

Usually, such matching occurs when the nano material structure is excited with evanescent waves involving TM mode. SPR arises as a result of coupling between the incident light propagation constant K_d, and surface Plasmon's propagation constant, K_{SP}, of the conducting film at a resonance angle for kretchman configuration or resonance wavelength for waveguides such as optical fiber. The surface Plasmon propagation constant can be expressed by

$$K_{SP} = \frac{2\pi}{\lambda}\left(\frac{\varepsilon_m \varepsilon_s}{\varepsilon_m + \varepsilon_s}\right)^{1/2} \quad (1)$$

where ε_m the real is part of the metal dielectric constant and ε_s is the dielectric constant of the sensing layer.

The light propagation constant K_d is the lateral component of the wave vector of the incident light in the dielectric medium and is given by

$$K_{\mathrm{d}} = \frac{2\pi}{\lambda}\sqrt{\varepsilon_d}\,\sin\theta \quad (2)$$

where 'θ' is the incident angle through the light coupling medium such as prism, waveguide or optical fiber. ε_d is the dielectric constant of the dielectric medium, λ is the wavelength of the incident light. Momentum matching and energy conservation condition, $K_{SP} = K_{\mathrm{d}}$ determines the value of θ as

$$\theta = \sin^{-1}\left[\frac{\left(\frac{\varepsilon_m \varepsilon_s}{\varepsilon_m + \varepsilon_s}\right)}{\varepsilon_d}\right]^{1/2} \quad (3)$$

The angle can be related to the critical angle θ_{cr} for total internal reflection. As the propagation constant of the surface Plasmon and the incident light matches to each other at the dielectric-metal interface, the SPR occurs leading to sharp dip in the intensity of the transmitted light due to energy transfer. Field intensity of Surface Plasmon wave (SPW) decays exponentially away from the interface. Any perturbation of refractive index within the SPW zone brings characteristic change in the SPR spectra. However, optimization of light confining structure is one of the key topics in this area[13][14].The optical fiber based SPR sensor structure is becoming a popular [15] option due to the fact that optical fiber is immune from several factors such as electromagnetic

1077-260X (c) 2016 IEEE. Personal use is permitted, but republication/redistribution requires IEEE permission. See http://www.ieee.org/publications_standards/publications/rights/index.html for more information.

This article has been accepted for publication in a future issue of this journal, but has not been fully edited. Content may change prior to final publication. Citation information: DOI 10.1109/JSTQE.2016.2613859, IEEE Journal of Selected Topics in Quantum Electronics

interference. It is also easier to generate evanescent wave, necessary for exciting surface Plasmon, in optical fiber. This can also be considered as miniaturisation of the sensor probe compared to bulky Kretchman configuration used in bio sensing applications[16]–[18].The fiber optic SPR sensor has different Plasmonic response and sensitivity depending upon the design parameters such as tapering [19]or bending[20] of the fiber, and coating materials including the thickness. It is to be mentioned that the multimode fiber is preferred for in-line fiber based SPR probe due to lower value of critical angle given by

$$\theta_{cr} = \sin^{-1}\left(\frac{n_{cl}}{n_c}\right) \quad (4)$$

where n_{cl} and n_c are refractive index of cladding and core respectively. The low angle allows more light to response the Plasmonic resonance [21]. It should also be mentioned that the light incident angle θ at the fiber core-cladding boundary should be equal to the critical angle to generate evanescent wave which satisfies the boundary conditions for SPR.

In this work we have reported gold coated chemically etched in-line multimode polymer optical fiber and specially tapered pointed single-mode optical fiber tip based SPR sensors probes. The coating is done using Magnetron sputtering technique in a customized Magnetron sputtering unit. The in-line-fiber sensor can be used for large volume of sample sensing while pointed tip can be used for small volume of sample sensing. The work has been presented below in the order of SPR probes fabrication, sensing experiments, Results and discussions and finally the conclusion.

II. SPR PROBE PREPARATION

A. In-Line Fiber Probe Preparation:

The Plastic clad silica multimode optical fiber 400EMT (low OH content) of diameter 400 um is used in our experiment. The sensing region is prepared by burning the Tefzel jacket (buffer) by flame (hobby and torch method) and is cleaned with acetone to remove the cladding in the desired sensing region. The exposed fiber core is etched in 48% HF in order to reduce the core diameter to ~150μm. The etched polymer fiber can generate more evanescent wave enhancing SPR with the metallic film. The MS unit has been modified to accommodate optical fiber with rotational option for uniform coating around the etched part. The deposition pressure for the sputtering unit chamber is maintained at 2.1×10^{-2} Torr. Before gold coating, the sample is given thin chromium coating which helps adhering gold film. The chromium is coated at 21.6 W and gold coating is done at power of 4 W. No. of Rotations are varied while keeping all other parameters fixed. The sensing length of the fiber is kept ~ 1.5 cm as sensing length beyond this doesn't show any improvement [22][23].To standardize the coating thickness with rotation, we have primarily chosen a planer structure placed on rotating platform. The coated film is characterized using AFM which is shown in Fig. 1.

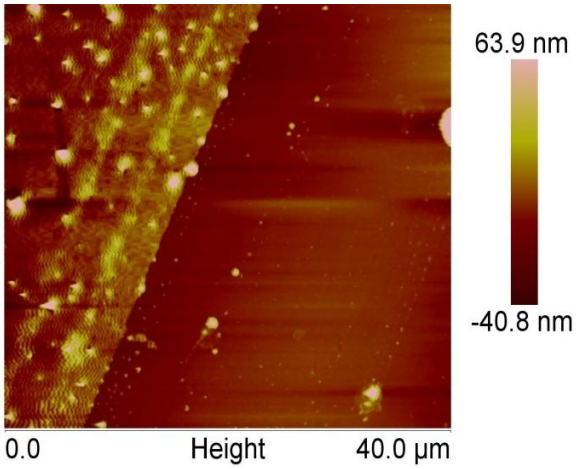


Fig. 1. AFM images characterizing the thickness of the gold coating film.

The details about rotations of samples and sensitivity can be found in Table 1.

B. Pointed Fiber Tip Based Probe Preparation

The in-line optical fiber sensor as SPR probe in transmission mode with large interaction area works for large volume of samples. However, there are many instances where one has to measure very small volume of sample. For such experiments, tapered optical fiber tip based SPR probe is ideal one[24]. A novel optical fiber tip is proposed for the pointed fiber tip SPR probe. The tip is prepared from photosensitive single-mode optical fiber of diameter 125μm by chemical etching guided by capillary action [25].The tapered optical fiber tip with cavity and a protruded pointed probe is further coated with thin film of chromium and gold in the same sputtering unit. In this case the tip is oriented towards the target so that rotation of the sample is not required. The sputtering condition is similar to etched polymer fiber coating. However, instead of rotation the fiber tip is exposed 10 seconds for chromium coating followed by 3 minutes for gold coating inside the chamber. This is equivalent to coating thickness of ~ 40 nm.

Fig. 2 is the SEM image of a typical chromium-gold coated pointed fiber tip used in our experiment. The thickly coated optical fiber tip contains a protruded antenna like structure within the cavity. The unique optical fiber tip enhances the evanescent wave significantly at the tip end due to the tapered structure which enhances SPR response. It is to be mentioned that similar type of fiber tip has been reported for attenuation based sensor[26]. However, the design we have considered takes the advantage of novel tip, the Magnetron sputtering coating and its SPR response.

1077-260X (c) 2016 IEEE. Personal use is permitted, but republication/redistribution requires IEEE permission. See http://www.ieee.org/publications_standards/publications/rights/index.html for more information.

This article has been accepted for publication in a future issue of this journal, but has not been fully edited. Content may change prior to final publication. Citation information: DOI 10.1109/JSTQE.2016.2613859, IEEE Journal of Selected Topics in Quantum Electronics

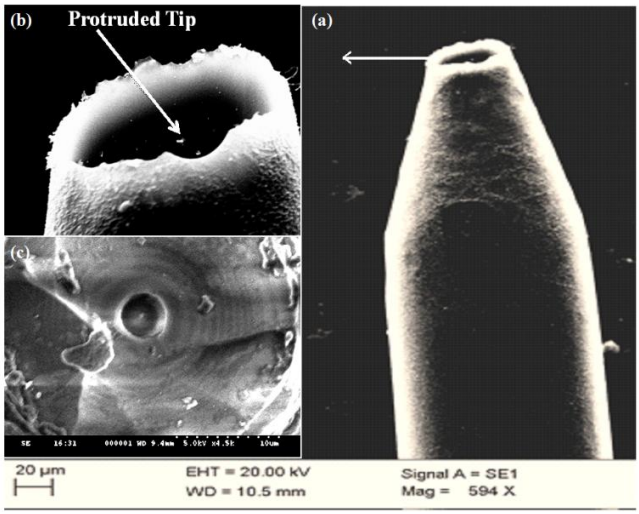


Fig. 2. (a) SEM image of gold coated optical fiber tip. (b) Side view of the zoomed tip. (c) Top view of FESEM image of a similar protruded uncoated tip, scale bar 10µm.

III. Sensing Experimentation

A. *In-Line fiber SPR Sensor Probe Experimentation*

Fig.3 is the schematic of the experimental setup used in the sensing experimentation. SPR condition and resolution depend upon the properties of optical system and the transuding medium [27]. For the wavelength interrogation of optical fiber probe a white light source is coupled to the fiber and spectrometer records the intensity of the transmitted light. Tungsten halogen lamp HL2000FHSA and USB4000 spectrophotometer from ocean optics have been used in our experiment. SMA connectors with universal fiber terminator connect the fiber with light source and spectrometer.

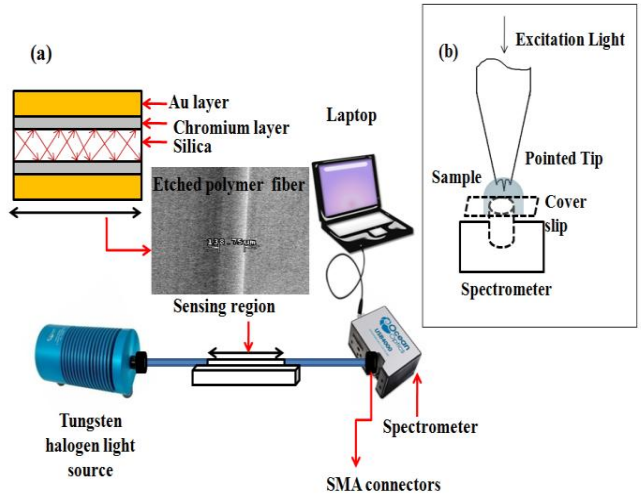


Fig. 3. Schematic of the experimental setup (a) for in-line sensor probe (b) pointed tip fiber probe. The fiber tip is placed vertically in a stable translation stage to move it in the samples on the thin cover slip which is placed on the opening path to the spectrometer.

The glycerol samples are prepared with water solution and the refractive indexes of solutions are checked in AtagoRx-7000i refractometer. The optical fiber sensor probe is inserted into a flow cell where glycerol and distilled water solutions ranging from RI 1.338 to 1.398 were successively fed into the sensing region. For different concentration of glycerol the recorded refractive index values obtained are 1.338, 1.343, 1.351, 1.356, 1.360, 1.370, 1.374, 1.376, 1.390 and 1.398 for concentration of 5%, 10%, 15%, 20%, 25%, 30%, 35%, 40%, 45% and 50% respectively. The spectrometer acquires data using the following principle.

A reference spectrum and dark spectrum need to be recorded. The reference spectrum is acquired with bare fiber probe; the dark spectrum is obtained by blocking the light path in front of the tungsten halogen light source. A sample spectrum is recorded with the metallic film coated fiber for different solutions. The measured sample transmission Spectra $M(\lambda)$ of the fiber sensor probe is obtained by the following equation

$$\mathrm{M}(\lambda) = \frac{(\lambda_s - \lambda_d)}{(\lambda_r - \lambda_d)} \times 100 \qquad (5)$$

where λ_s, λ_d and λ_r represent sample wavelength, dark signal and Reference Wavelength respectively. The data obtained is recorded using Spectra suite software. The scan average value is set at 50 times in order to get better SPR curve and high signal to noise ratio. The data is further processed using origin software for the analysis.

IV. Result and Discussion

A. *In-Line-Fiber SPR Probe Results*

As the white light source is coupled with the probe input, the etched part of the fiber with coating interacts with the entire spectra of the Tungsten source. It interacts strongly over certain wavelength domain which matches criteria for surface Plasmon supported by the dielectric and metal structure. The characteristics of light-matter interaction are reflected in the transmission spectra obtained in the spectrometer. The transmission spectra experiences loss over the wavelength range due to transfer of energy to surface Plasmon causing a dip in the spectra. The surface Plasmon propagating on the surface of the optical fiber is perturbed due to change in medium of the fiber's surroundings resulting in shift of the position of the dip. This change in position of the dip is used for sensing the refractive index change. The spectral characteristics of SPR response are presented in Fig. 4. for different glycerol and water concentration giving different RI values. The spectra show both the change in intensity and in the position of the dip, namely red shift of the absorbance wavelength with the increase in surrounding RI. It may be pointed out that intensity based pointed optical fiber tip sensor has already been explored [24]. Though change in intensity could be a sensing parameter, in our study we have considered change in dip in the spectra due to SPR as the sensing parameter. Spectrum data processing is same as it is mentioned in section III since pointed tip sensor also works in the transmission mode.

1077-260X (c) 2016 IEEE. Personal use is permitted, but republication/redistribution requires IEEE permission. See http://www.ieee.org/publications_standards/publications/rights/index.html for more information.

This article has been accepted for publication in a future issue of this journal, but has not been fully edited. Content may change prior to final publication. Citation information: DOI 10.1109/JSTQE.2016.2613859, IEEE Journal of Selected Topics in Quantum Electronics

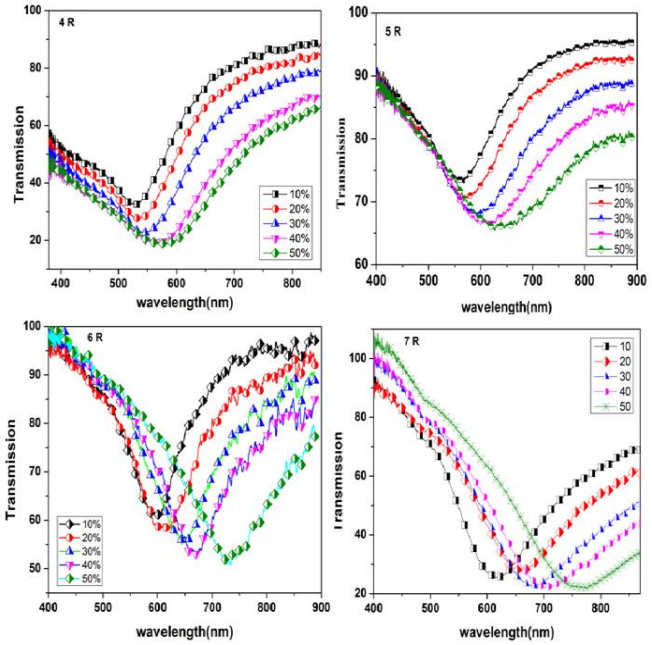


Fig. 4. Transmission Spectra of Surface Plasmon resonance sensor for varied Rotation with different R.I solution

Fig. 4. represents the response of the probe with different coating thickness which is approximately determined by the number of rotations. With the more number of rotations and the increased thickness the SPR curve is shifting from visible to infra red regime. Sensing response of SPR probe, the relative wavelength shift as a function of refractive index, is plotted for different rotation and for various concentrations as mentioned in section III A. For the clarity of the figures, we have plotted SPR response for few selective concentrations. However, in Fig. 5. we have considered all the concentrations used in the experiments. As the no of rotation varies from 4 to 7 the sensing response has increased significantly. One rotation is equivalent to 36 seconds. For the 8th rotation we have achieved sensitivity of ~2459 nm/RIU, although the sensitivity is nearly saturated for thickness corresponding to 6 rotations, ~2232 nm/RIU. The overall range of shifting is from ~520 nm to ~850 nm.

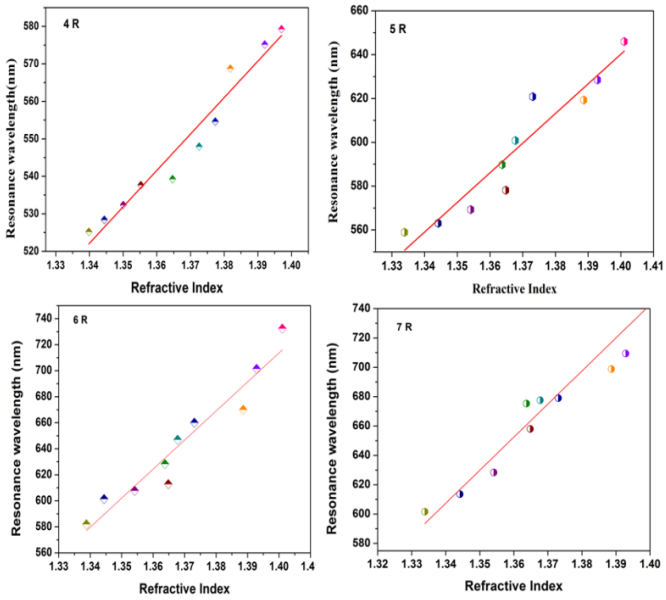


Fig. 5. Sensitivity characteristic of the SPR response for different rotations (R)

The probe has been tested for concentrations starting from 5% to 50% and the sensitivity results are plotted in Fig. 5.The results demonstrate the repeatability of the sensor probe. TABLE I indicates the quantitive relations among the number of rotations and the sensitivity.

TABLE I
SHOWS RELATION BETWEEN NUMBER OF ROTATIONS AND SENSITIVITY

Sl. No.	Deposition Time (Rotation)	Sensitivity (nm/RIU)
1	3	612.97
2	4	997.66
3	5	1352.75
4	6	2232.23
5	7	2253.06
6	8	2458.88.

Fig. 6. shows the trend of shifting of the dip towards near-infra red region. From rotation 2 to rotation 7, the coating thickness increases in step of ~(5 to 6) nm to the thickness ~40 nm. It is to be noted that increasing the thickness of gold coating leads to shift of the dip from visible to near Infra region [28] and the resonance curve becomes more sensitive leading to increase in sensitivity [29][30] of the probe. It can also be mentioned that gold thin film of thickness 45 nm to 50nm corresponds to the best surface Plasmon response[31].

1077-260X (c) 2016 IEEE. Personal use is permitted, but republication/redistribution requires IEEE permission. See http://www.ieee.org/publications_standards/publications/rights/index.html for more information.

This article has been accepted for publication in a future issue of this journal, but has not been fully edited. Content may change prior to final publication. Citation information: DOI 10.1109/JSTQE.2016.2613859, IEEE Journal of Selected Topics in Quantum Electronics

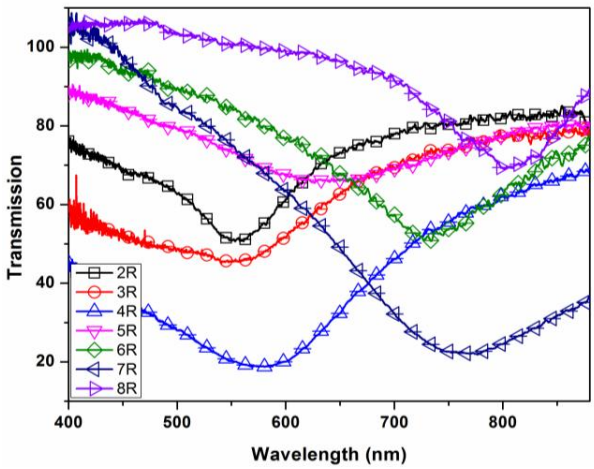


Fig. 6. Response curve of SPR for different rotations for glycerol concentration 50%

B. Pointed Fiber tip SPR Probe Results

The experimental arrangement for pointed fiber tip based sensor is similar to the in-line fiber SPR probe experimentation in transmission mode. In this arrangement, the tip is vertically placed on the spectrometer entrance with cover slip[24].The samples are placed on the cover slip such that the tip enters into the sample. The spectrometer scan the transmission spectrum transmitted through the fiber tip. Enhanced evanescent waves at the tip interact with the sample through surface Plasmon which has been used in other type of applications [32][33] as well. As the probe is dipped into solution of liquid like water, acetone and methanol, we observe a dip in the transmitted light. In this experiment we have avoided glycerol like solution due to its sticky nature. The transmission spectra of the pointed gold coated optical fiber probe are presented in Fig. 7.

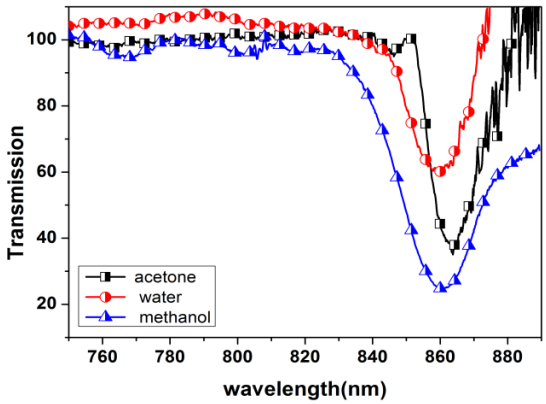


Fig. 7. Transmission spectra of gold coated pointed plasmonic fiber tip in presence of various chemicals

The dips for acetone, water and methanol are observed at 864 nm, 859 nm and 860 nm respectively. It is to be mentioned that water (1.33) and methanol (1.329) have nearly same value of refractive index which may be the reason the position of dips are nearly same. However, methanol experiences higher transmission loss. Considering the refractive index of the acetone, 1.36, and the shift compared to the water, the sensitivity of the tip obtained is166.4 nm/RIU for ~40 nm coating thickness. The sensitivity is less due to lesser area of interaction. However, such fiber tip sensor probe has the advantage of sensing small volume samples. In this case we have presented proof of the concept with coating thickness ~45 nm which results in near saturated SPR response as observed in-line sensor probe. However, a detail study can be done separately.

V. CONCLUSION

In conclusion, we have reported Magnetron sputtering based gold coating to develop sensitive SPR based sensor. A partially etched polymer fiber and a pointed optical fiber tip are considered for SPR sensor probes. The sensor probes are gold coated using customized Magnetron sputtering unit with an option of sample rotation. The response of the probe significantly depends upon the coating thickness which is varied with the rotation of the samples during sputtering. The in-line polymer fiber sensor with coating thickness ~40 nm shows high sensitivity, ~2459 nm/RIU. In case of specially pointed fiber tip with coating thickness ~40 nm, we observe sensitivity ~166 nm/RIU. The in-line fiber probe can be used for large sample volume detection whereas the pointed fiber probe could be useful for small volume of sample, ~µl, sensing.

ACKNOWLEDGEMENT

The authors acknowledge staff members of Advanced Materials and Sensors division for their support during the work. The authors also acknowledge Dr. Akash Deep and Sanjeev Bhardwaj for helping with FESEM characterization.

REFERENCES

[1] S. Srivastava and B. Gupta, "Fiber Optic Plasmonic Sensors: Past, Present and Future," *Open Opt. J.*, vol. 7, no. 1902, pp. 58–83, 2013.

[2] P. K. Jain, X. Huang, I. H. El-Sayed, and M. A. El-Sayed, "Noble metals on the nanoscale: Optical and photothermal properties and some applications in imaging, sensing, biology, and medicine," *Acc. Chem. Res.*, vol. 41, no. 12, pp. 1578–1586, 2008.

[3] P. Singh, "SPR Biosensors: Historical Perspectives and Current Challenges," *Sensors Actuators, B Chem.*, vol. 229, pp. 110–130, 2016.

[4] A. G. Brolo, "Plasmonics for future biosensors," *Nat. Photonics*, vol. 6, pp. 709–713, 2012.

[5] K. A. Willets, R. Van Duyne, and R. P. Van Duyne, "Localized Surface Plasmon Resonance Spectroscopy and Sensing," *Annu. Rev. Phys. Chem.*, vol. 58, no. 1, pp. 267–297, 2007.

[6] M. E. Stewart, C. R. Anderton, L. B. Thompson, J. Maria, S. K. Gray, J. A. Rogers, and R. G. Nuzzo, "Nanostructured plasmonic sensors," *Chem. Rev.*, vol. 108, no. 2, pp. 494–521, 2008.

[7] E. Hutter and J. H. Fendler, "Exploitation of Localized Surface Plasmon Resonance," *Adv. Mater.*, vol. 16, no. 19, pp. 1685–1706, 2004.

[8] A. K. Sharma and B. D. Gupta, "Fiber optic sensor based on surface plasmon resonance with nanoparticle films," *Photonics Nanostructures - Fundam. Appl.*, vol. 3, no. 1, pp. 30–37, 2005.

[9] R. . A. Minz, S. S. Pal, R. K. Sinha, and S. K. Mondal, "Plasmonic Coating on Chemically Treated Optical Fiber Probe in the Presence of Evanescent Wave: a Novel Approach for Designing Sensitive Plasmonic Sensor," *Plasmonics*, vol. 11, no. 2, pp. 653–658, 2016.

[10] J. Homola, S. S. Yee, and G. Gauglitz, "Surface plasmon resonance sensors: review," *Sensors Actuators, B Chem.*, vol. 54, no. 1, pp. 3–15, 1999.

[11] A. V. Zayats, I. I. Smolyaninov, and A. a. Maradudin, "Nano-optics of surface plasmon polaritons," *Phys. Rep.*, vol. 408, no. 3–4, pp.

1077-260X (c) 2016 IEEE. Personal use is permitted, but republication/redistribution requires IEEE permission. See http://www.ieee.org/publications_standards/publications/rights/index.html for more information.

This article has been accepted for publication in a future issue of this journal, but has not been fully edited. Content may change prior to final publication. Citation information: DOI 10.1109/JSTQE.2016.2613859, IEEE Journal of Selected Topics in Quantum Electronics

131–314, 2005.
[12] Y. Yuan and L. Ding, "Theoretical investigation for excitation light and fluorescence signal of fiber optical sensor using tapered fiber tip.," *Opt. Express*, vol. 19, no. 22, pp. 21515–23, 2011.
[13] B. D. Gupta and R. K. Verma, "Surface Plasmon Resonance-Based Fiber Optic Sensors: Principle, Probe Designs, and Some Applications," *J. Sensors*, vol. 2009, pp. 979761–1–979761–12, 2009.
[14] L. Yin, V. K. Vlasko-Vlasov, J. Pearson, J. M. Hiller, J. Hua, U. Welp, D. E. Brown, and C. W. Kimball, "Subwavelength focusing and guiding of surface plasmons," *Nano Lett.*, vol. 5, no. 7, pp. 1399–1402, 2005.
[15] A. K. Sharma, R. Jha, and B. D. Gupta, "Fiber-Optic Sensors Based on Surface Plasmon Resonance : A Comprehensive Review," *IEEE Sensors*, vol. 7, no. 8, pp. 1118–1129, 2007.
[16] Y. Shevchenko, N. U. Ahamad, A. Ianoul, and J. Albert, "In situ monitoring of the formation of nanoscale polyelectrolyte coatings on optical fibers using Surface Plasmon Resonances.," *Opt. Express*, vol. 18, no. 19, pp. 20409–20421, 2010.
[17] J. Satija, N. S. Punjabi, V. V. R. Sai, and S. Mukherji, "Optimal Design for U-bent Fiber-optic LSPR Sensor Probes," *Plasmonics*, vol. 9, no. 2, pp. 251–260, 2014.
[18] A. Leung, P. M. Shankar, and R. Mutharasan, "A review of fiber-optic biosensors," *Sensors Actuators, B Chem.*, vol. 125, no. 2, pp. 688–703, 2007.
[19] S. Kumar, G. Sharma, and V. Singh, "Sensitivity of tapered optical fiber surface plasmon resonance sensors," *Opt. Fiber Technol.*, vol. 20, no. 4, pp. 333–335, 2014.
[20] M. Napiorkowski and W. Urbanczyk, "Effect of bending on surface plasmon resonance spectrum in microstructured optical fibers," *Opt. Express*, vol. 21, no. 19, pp. 22762–22772, 2013.
[21] N. Cennamo, D. Massarotti, R. Galatus, L. Conte, and L. Zeni, "Performance comparison of two sensors based on surface plasmon resonance in a plastic optical fiber," *Sensors (Basel).*, vol. 13, no. 1, pp. 721–35, 2013.
[22] P. Hlubina, M. Kadulova, D. Ciprian, and J. Sobota, "Reflection-based fibre-optic refractive index sensor using surface plasmon resonance," *J. Eur. Opt. Soc. Rapid Publ.*, vol. 9, p. 14033, 2014.
[23] Yogendra S. Dwivedi & Anuj K. Sharma & B. D. Gupta, "Influence of Design Parameters on the Performance of a Surface Plasmon Sensor Based Fiber Optic Sensor," *Plasmonics*, vol. 3, no. 2, pp. 79–86, 2008.
[24] Y.-H. Tai and P.-K. Wei, "Sensitive liquid refractive index sensors using tapered optical fiber tips.," *Opt. Lett.*, vol. 35, no. 7, pp. 944–6, 2010.
[25] S. S. Pal, S. K. Mondal, P. P. Bajpai, and P. Kapur, "Optical fiber tip for field-enhanced second harmonic generation," *Opt. Lett.*, vol. 37, no. 19, p. 4017, 2012.
[26] O. Esteban, N. Díaz-Herrera, M.-C. Navarrete, and A. González-Cano, "Surface plasmon resonance sensors based on uniform-waist tapered fibers in a reflective configuration.," *Appl. Opt.*, vol. 45, no. 28, pp. 7294–7298, 2006.
[27] M. Piliarik and J. Homola, "Surface plasmon resonance (SPR) sensors: approaching their limits?," *Opt. Express*, vol. 17, no. 19, pp. 16505–16517, 2009.
[28] W. Knoll, "Influence of Metal Film Thickness on the Sensitivity of Surface Plasmon Resonance Biosensors," *Appl. Spectrosc.*, vol. 59, no. 5, pp. 661–667, 2005.
[29] Y. Yuan, L. Ding, and Z. Guo, "Numerical investigation for SPR-based optical fiber sensor," *Sensors Actuators B Chem.*, vol. 157, no. 1, pp. 240–245, 2011.
[30] H. Moayyed, I. T. Leite, L. Coelho, J. L. Santos, and D. Viegas, "Theoretical Study of Phase-Interrogated Surface Plasmon Resonance Based on Optical Fiber Sensors with Metallic and Oxide Layers," *Plasmonics*, vol. 10, no. 4, pp. 979–987, 2015.
[31] A. A. Rifat, G. A. Mahdiraji, Y. M. Sua, R. Ahmed, Y. G. Shee, and F. R. M. Adikan, "Highly sensitive multi-core flat fiber surface plasmon resonance refractive index sensor," *Opt. Express*, vol. 24, no. 3, p. 2485, 2016.
[32] Y. Chang, Y. Chen, and H. Kuo, "Nanofiber optic sensor based on the excitation of surface plasmon wave near fiber tip," *Biomed. Opt. Express*, vol. 11, no. 2006, pp. 014032–014035, 2006.
[33] P. Uebel, S. T. Bauerschmidt, M. A. Schmidt, and P. St.j. Russell, "A gold-nanotip optical fiber for plasmon-enhanced near-field detection," *Appl. Phys. Lett.*, vol. 103, no. 2, pp. 2–6, 2013.



Rashmi A Minz received her B.Tech degree in Electronics and Instrumentation with honors from Dr. M.G.R University Chennai, India.She received her M.Tech with distinction in Advanced Instrumentation engineering from Academy of scientific and innovative research, CSIO in 2014. Currently she is Trainee Scientist and pursuing her PhD in Photonics group at CSIO (central scientific and instruments organisation), Chandigarh India. She is a member of SPIE. Her current research interests include Plasmonic sensors, optical biosensors, and near field instruments designing.



Sudipta Sarkar Pal received her B.Sc from Bethune College, Kolkata and M.Sc from Calcutta University. She received her Phd from Saha Institute of Nuclear Physics, Kolkata,West Bengal,India (2006). She was Visiting Research Fellow at Max-Planck-Institut für Metallforschung, Stuttgart,Germany, Post Doctoral Fellow at Katholieke Universiteit Leuven, Belgium (2006-2008), Visiting Scientist at Materials Science Division, Indira Gandhi Centre for Atomic Research (IGCAR), Kalpakkam, Tamil Nadu, India (2008-2009), Guest Lecturer at Department of Nanoscience and Nanotechnology, Panjab University, Chandigarh, India (2009-2010) and Fellow Scientist, CSIR-Central Scientific Instruments Organization (CSIR-CSIO), Chandigarh, India (2010-June 2012). Currenlty she is a Senior Scientist in Advanced materials and sensors CSIO,Chandigarh.Her ongoing research interest is in the field of Nanophotonics and Plasmonics.



Aditi Chopra received the B.Tech degree in Biomedical Engineering and M.Tech in Nanoscience and Technology from Punjab Technical University, Jalandhar in 2010 and 2014 respectively. She's currently working as a Senior Project Fellow in CSIO. Her research interest includes nanomaterials and nanomedicine**.**

1077-260X (c) 2016 IEEE. Personal use is permitted, but republication/redistribution requires IEEE permission. See http://www.ieee.org/publications_standards/publications/rights/index.html for more information.

This article has been accepted for publication in a future issue of this journal, but has not been fully edited. Content may change prior to final publication. Citation information: DOI 10.1109/JSTQE.2016.2613859, IEEE Journal of Selected Topics in Quantum Electronics



Shivam received B.E degree in Mechanical engineering from Chandigarh College of engineering and technology, India in 2014. Currently he is working as project fellow in CSIO Chandigarh. His research interests are mechanical designing and its applications.



Randhir Bhatnagar has received M.Tech in Opto electronics from IIT Delhi. He is currently chief scientist and head of the department of advanced materials and sensors divison, CSIO, Chandigarh. He is specialized in design of optoelectronics system and instrumentation. His research interests are gas sensing, Plasmonic sensor and PH sensing.



R. K. Sinha received M. Sc. degree in Physics from the Indian Institute of Technology (IIT), Kharagpur, India, in 1984, and Ph.D. degree in the area of Fiber Optics and Optical Communication Technology from the IIT, Delhi, India, in 1990. He had held various research and academic positions at Indian Institute of Science (IISc), Bangalore during 1991, Birla Institute of Technology and Science (BITS), Pilani during 1992-1994, REC (now NIT), Hamirpur during 1994-1998 and at Delhi College of Engineering-DCE (now Delhi Technological University-DTU),University of Delhi during December 31, 1998 to July 01, 2015. Prof. Sinha is a Fulbright Scholar – recipient of Fulbright-Nehru Fellowship to acquire first hand knowledge of Higher Education Systems and Practices of USA covering over a dozen US universities and higher educational institutions as an International Educational Administrator in 2013**.** He has been awarded-The Institution of Electronics and Telecommunication Engineers (IETE) Biman-Behari Sen Memorial Award for outstanding research in the area of Telecom Grade Optical Fibers and Optoelectronic Devices Optics in 2012 (ii) Emerging Optoelectronics Technology Award [(CEOT-IETE, India)]-2006 for outstanding research work in the area of Nano-photonics, (iii) S. K. Mitra Memorial Award for Best Research Paper in IETE Technical Review 2002 on Nanostructure Electron Waveguides and Devices and (iv) his coauthored research paper has won several Best Research Paper Awards which include Swarna Jayanti Puraskar (Gold Medal) from the National Academy of Sciences in the area of Nano-scale Optical Devices for the year 2001, Reliance Technology Awards 2010, SPIE 2014 best research presentation award and OSI-2014 second best poster presentation award. He is Fellow of SPIE- The International Society of Optical Engineering, Fellow of the IETE, and a Fellow of Optical Society of India, a Member of The Optical Society (OSA, USA), a Member of IEEE and a Member of The Photonics Society of IEEE**.**He is currently the Director of CSIR-Central Scientific Instruments Organisation (CSIO), Chandigarh with effect from July 02, 2015. His research areas are photonic crystal fiber sensors, metamaterials and plasmonics.



Dr.Samir K Mondal has received M.Sc degree in Physics and PhD degree in Fiber and Integrated Optics from University of Calcutta. He has postdoctoral research experience from the University of California, Irvine, USA and University of Minnesota, Minneapolis, USA. Later on he had joined Tyndall National Institute, Ireland as Research Scientist. Dr. Mondal has research collaborations with research teams from France, China and Russia. At present he is working as a Principal Scientist in the department of Advanced Material and Sensors, CSIR-CSIO (central scientific and instruments organisation), Chandigarh. Besides serving as Associate Editor Members in couple international journals, he regularly reviews manuscripts from reputed journals in the area of photonics and optics. His research interests are Optical nanoantenna and nanophotonics, Optical nano-tweezer, Near field optics, Surface Plasmon sensor and Optical coherence tomography imaging.

1077-260X (c) 2016 IEEE. Personal use is permitted, but republication/redistribution requires IEEE permission. See http://www.ieee.org/publications_standards/publications/rights/index.html for more information.

Multi attribute assessment of consumables for TIG welding of Aluminum Alloys

P K Baghel* and D.S. Nagesh

Department of Mechanical Engineering, Delhi Technological University, Bawana Road, New Delhi 110042, India

*Corresponding author: E-mail address: pushpbaghel.pb@gmail.com:

Tel: +91 9968738431

Abstract

Consumable materials for welding processes such as Filler Alloy, Electrode, and Shielding Gas have major implications in welding technology. Selecting the appropriate set of consumable materials for welding Aluminium alloys from various available alternates, gives rise to a significant decision making problem. This study proposes a strategic justification tool based on integrated analytical hierarchy process – Technique for Order preference by similarity to ideal solution (AHP-TOPSIS) to screen and select the best possible combination of filler alloy, electrode and shielding gas for TIG welding. Based on qualitative analysis of available alternates, ER 5356 filler alloys and 0.8 % zirconiated electrode are selected as suitable consumable in combination with pure argon as shielding gas. The proposed result is experimentally validated using mechanical property testing.

Key words: Pulse TIG, AHP-TOPSIS, filler alloy, electrode, shielding gas

1. Introduction

Dissimilar aluminum alloys combinations are widely used in aerospace and automobile applications such as inner body panel, heat shields, structural components, ladders, space frames etc. [1]. Several welding processes such as Friction Stir Welding (FSW) and laser welding are gaining popularity for welding aluminum but TIG welding is still most widely used process for joining aluminum because of its heat control ability (narrow heat affected zone) and eco-friendly nature (no spatter and smoke). Although Friction Stir Welding has several advantages like no voids and cracking, no distortion of workpiece, no need of filler material, no shielding gas required, clean and environment friendly process because there are no harmful effects like arc formation, radiation, release of toxic gas etc. However as compared to TIG welding process some

disadvantages of the friction stir welding process has been identified as well like exit hole is left when the tool is withdrawn. This limitation is serious when pressure vessels and cargo oil tanks are manufactured. Heavy-duty clamping is required to hold the plates to combat large downward force. In addition to this it is less flexible i.e difficult to weld when thickness varies.

The ideal weld joint should have tensile strength close to base metal and must be free from hot cracks and residual stress. Consumable materials namely filler alloy, electrode and shielding gas play a vital role in deciding the manufacturing quality and cost of weld joint [2].

When multiple choices are present, choosing the optimum material of desired properties from large number of available materials is a tedious task. It is essential to base the final decision using well structured selection methodology in consideration with all possible relevant attributes or properties. Multi Attribute Decision Making (MADM) Models are generally used to provide an encompassing analysis of all involved multiple attributes.

In an unstructured decision problem in welding processes, such models have recently been used by many researchers. Khorshidi et al. [3] used TOPSIS for selecting the optimal refinement condition to achieve maximum tensile property in Al-15%Mg_2Si composite whereas Mirhedayatian et al. [4] employed TOPSIS approach and integrated fuzzy data envelopment analysis in welding process selection for repairing nodular cast iron engine block.

The selection of consumable materials is of prime importance to accomplish the joint of desired specifications however there are not enough investigations in this direction. Therefore there is a need for an extensive selection framework before undertaking the manufacturing process.

In present research, Technique for order preference by similarity to ideal solution (TOPSIS) integrated with Analytical hierarchy process (AHP), is employed to select an optimal combination of consumable materials for welding dissimilar aluminum alloys.

2. Materials and Methodology

Consumable in welding processes comprise of filler alloy, electrode material and shielding gas. The filler alloy determines the transverse and longitudinal strength of the

weld joint. Therefore the filler material should have attributes like high tensile properties, impact toughness and low cost. There are mainly five filler alloy that are used listed in Table 1.

Table 1 List of attributes and alternates for filler alloy [1]

Properties	ER5356	ER5556	ER5183	ER5654	ER5554
1. Yield Strength (MPa)	240	158.579	275	220.63	124.10
2. Tensile Strength (MPa)	268.89	317.15	296.47	227.52	186
3. Elongation 2%	17	14	17	17	8
4. Brinell Hardness (HB) (@load 500 Kg: thickness 10:ohm)	105	65	99	83	39
5. Cost ($)	13.5	16	15.5	17.2	13
6. Longitudinal Shear Strength (MPa)	117.21	137.89	127.55	82.73	79.289
7. Transverse Shear Strength (MPa)	179.26	206.84	193.05	124.10	103.42
8. Impact Strength (J)	18.2	15.7	16	13	10

Table 2 presents the alternates and attributes of Electrode used in Pulse TIG welding of Aluminum alloys

Table 2 List of attributes and alternates for electrode [2]

Properties	Pure Tungsten	2%Thoriated	2%Ceriated	1.5% Lanthanated	0.8%Zirconiated
1. Electrode Oxide Work Function (eV)	0.01	2.6	3.2	2.5	0.3
2. Density (g/cm^3)	19.25	11.72	6.65	5.7	6.49
3. Volume% of 2% weight of electrode	6	3.8	5.2	5.7	6.9
4. Melting Point (°C)	3410	1750	795	826	1852
5. Electron negativity (according to pauling)	1.7	1.3	1.0	1.1	1.2
6. Cost ($)	23.99	14.99	18.4	23.99	20.3
7. Particle Size (Nm)	30	50	40	20	30

. Tungsten electrode used in TIG welding is a consumable. It merely serves as the terminal for the electric arc which produces the heat needed to join the base metal being welded. The shape of the tungsten electrode tip is an important process variable in GTA welding. Tungsten electrode geometry has an effect on the arc shape (thereby affecting

the weld bead size and shape), the weld penetration, and point longevity of the electrode. In addition to the arc shape, different tungsten material pose different characteristics which influences arc start ability, electrode life, and contamination resistance.

Selection of right shielding gas composition is significantly affect metallurgical structure, properties, soundness and heat treated response of weld. The desired characteristics with suitable alternates are listed in Table 3.

Table 3 List of attributes and alternates for shielding gas [5, 6]

Properties	Pure Argon	Pure Helium	25%Argon+75%Helium	75%Argon+25%Helium	50%Argon+50%Helium
1. Thermal Conductivity W/mK at (1.013 bar at 0°C)	0.016	0.1513	0.1174	0.0498	0.0836
2. Gas density (lb/wft) at 0°C, 1 atm	0.1114	0.0111	0.0361	0.0863	0.0612
3. Specific gravity (g/cm³) Air=1	1.38	0.1368	0.4476	1.0692	0.7584
4. Ionization potential (eV)	15.7	24.5	22.3	17.9	20.1
5. Cost (per100g) ($)	0.5	5.2	4.025	1.675	4.15
6. Specific Heat capacity at (kJ/(Kg.K C_p (1.013 bar and 25°C)	0.520	5.19	4.0225	1.6875	2.855

TOPSIS method is employed to evaluate and find the best suitable alternative in the present work. It was first proposed in 1981 [7].

The methodology involves the evaluation of Euclidean distance from the positive and the negative ideal solution for the given alternate. The best possible alternative will be closest to the positive ideal solution and far away from negative ideal solution.

TOPSIS is a suitable choice for material selection as it is a relatively more systematic process. It provides both qualitative and quantitative analysis of the available data. The TOPSIS method involves a tool for evaluation of weights of each attribute/ criterion. In this study, this task is performed using AHP method. The relative weights hence generated are used in TOPSIS process to find the final priority ranking of available alternatives.

It was developed by Satty [8] to handle complex problems based on multiple criteria. The flexibility and intuitiveness of AHP method provide edge over other methods. It facilitate group decision making by finding the geometric mean of the individual pair wise comparisons.

Fig 1 depicts (AHP-TOPSIS) MADM methodology for welding process consumables selection

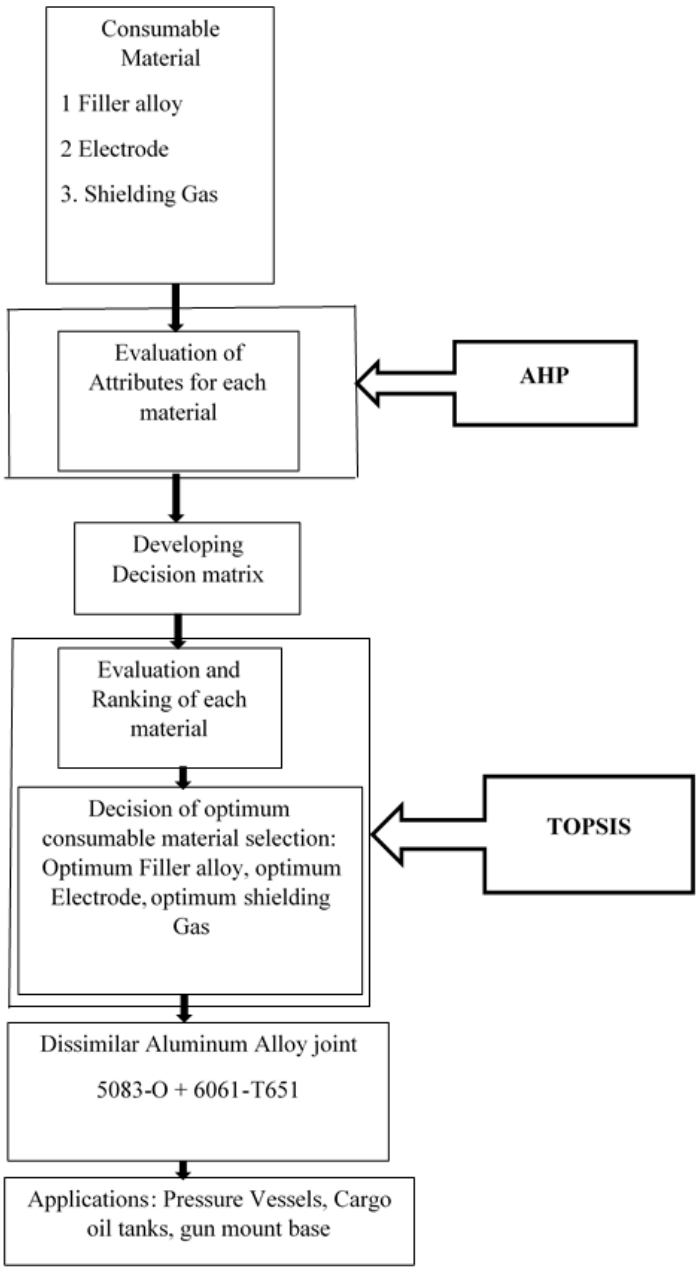


Fig 1 Flow chart depicting Integrated AHP-TOPSIS methodology for consumable materials selection

The AHP method

To determine the relative importance of different attributes with respective to the objective following steps are followed.

The multiple pair-wise comparisons are based on a standardized comparison scale of nine levels (Table 4)

Table 4 Nine point intensity of importance scale

Relative importance (a_{ij})	**Description (i over j)**
1	Equal importance
3	Moderate importance
5	Strong importance
7	Very strong importance
9	Absolute importance
2, 4, 6, 8	Intermediate values

Let C = {Cj|j = 1, 2, . . . , n} be the set of criteria.

The result of the pair-wise comparison on n criteria can be summarized in an (n × n) evaluation matrix A. The every element a_{ij} (i,j = 1, 2, . . . , n) denotes the relative importance of factor i with respect to factor j. A criteria compared with itself is always assigned the value 1 so the main diagonal entries of the pair-wise comparison matrix are all 1.

Square matrix A containing every element a_{ij} is shown in Eq. (1).

$$A=\begin{pmatrix} 1 & a_{12} & \dots & a_{1m} \\ a_{21} & 1 & \dots & a_{2m} \\ \dots & \dots & \dots & \dots \\ a_{m1} & a_{m2} & \dots & 1 \end{pmatrix},\ a_{ij}=1/a_{ji}, a_{ji\neq 0} \tag{1}$$

- The relative normalized weight (W_i) of each factor is evaluated by finding the geometric mean of *i*th row and normalizing the geometric means of rows in the comparison matrix.

$$GM_i=\left\{a_{i1}\times a_{i2}\times a_{i3}\times\dots\times a_{ij}\right\}^{1/n}$$

and

$$W_i = GM_i \Big/ \sum_{j=1}^{j=n} GM_i$$

Matrix X is obtained to denote an n-dimensional column vector. The sum of the weighted values is computed for the importance degrees of alternatives, then X=*A*W*, where:

$$W = [W_1, W_2, W_3, ..., W_n]^T$$

$$X = A * W = \begin{bmatrix} 1 & a_{12} & ... & a_{1n} \\ a_{21} & 1 & ... & a_{2n} \\ ... & ... & ... & ... \\ a_{n1} & a_{n2} & ... & 1 \end{bmatrix} \begin{bmatrix} W_1 \\ W_2 \\ ... \\ W_n \end{bmatrix} = \begin{bmatrix} C_1 \\ C_2 \\ ... \\ C_n \end{bmatrix} \quad (2)$$

- The consistency values (*CV*) are calculated for the cluster of alternatives represented by the vector.

$$CV_i = \frac{C_i}{W_i}$$

- The largest eigenvalue λ_{max} is obtained which is the mean of the consistency values.
- The consistency index (*CI*) is calculated by

$$CI = \frac{\lambda_{max} - n}{n-1}$$

The AHP output quality is strictly related to the consistency of the pair wise comparison judgements.

- The random index (*RI*) is obtained for the number of factors being used in decision making (Table 5)

Table 5 Random index (*RI*) values

Criteria	RI	Criteria	RI
3	0.52	7	1.35
4	0.89	8	1.40
5	1.11	9	1.45
6	1.25	10	1.49

- The final consistency ratio (*CR*) is calculated as the ratio of the *CI* and *CR*

$$CR = \frac{CI}{RI} \tag{3}$$

The acceptable upper limit for *CR* is 0.1. The evaluation process has to be repeated to improve the consistency, if the final consistency ratio exceeds this value. This consistency check is essential to establish the validity of the pair wise comparison matrix evaluation.

TOPSIS method consists of following steps

Step 1: Construction of the normalized decision matrix

The Euclidean length of a vector, the element r_{ij} of the normalized decision matrix R is evaluated using the following transformation

$$r_{ij} = \frac{X_{ij}}{\sqrt{\sum_{i=1}^{m} (X_{ij})^2}}$$
$$j = 1, 2, ..., n; \quad i = 1, 2, ..., m; \tag{4}$$

Here, r_{ij} is the normalized preference measure of the *i*th alternative. 'm' is the number of alternatives, 'n' is the number of criteria

Step 2: Construction of the weighted normalized decision matrix
Multiply the columns of the normalized decision matrix with the set of weights obtained by AHP

W = (w_1,w_2, $w_{3,.....,}w_n$) to obtain weighted normalized decision matrix:

$$V = RW = \begin{pmatrix} w_1 \cdot r_{11} & w_2 \cdot r_{12} & \dots & w_n \cdot r_{1n} \\ w_1 \cdot r_{21} & w_2 \cdot r_{22} & \dots & w_n \cdot r_{2n} \\ . & . & & . \\ . & . & & . \\ w_1 \cdot r_{m1} & w_2 \cdot r_{m2} & \dots & w_n \cdot r_{mn} \end{pmatrix} \tag{5}$$

Step 3: Determination of the ideal and negative- ideal solutions. The ideal solution and negative ideal solution value sets are determined, respectively as follows:

$$\left\{V_1^+, V_2^+, ..., V_n^+\right\} = \left\{\left(\underset{i}{Max} V_{ij} \middle| J \in K\right), \left(\underset{i}{Min} V_{ij} \middle| J \in K'\right) | i = 1, 2, ..., m\right\} \quad (6)$$

$$\left\{V_1^-, V_2^-, ..., V_n^-\right\} = \left\{\left(\underset{i}{Min} V_{ij} \middle| J \in K\right), \left(\underset{i}{Max} V_{ij} \middle| J \in K'\right) | i = 1, 2, ..., m\right\} \quad (7)$$

Where,

$K = \{j = 1, 2, 3, ..., n$ and j is associated with benefit criteria$\}$

$K' = \{j = 1, 2, 3, ..., n$ and j is associated with cost criteria$\}$

Step 4: Measurement of separation distances from ideal and negative ideal solutions. Euclidean distances for each alternative are, respectively calculated as:

$$S_i^+ = \left\{\sum_{j=1}^{n} \left(V_{ij} - V_j^+\right)^2\right\}^{1/2}; i = 1, 2, ..., m \quad (8)$$

$$S_i^- = \left\{\sum_{j=1}^{n} \left(V_{ij} - V_j^-\right)^2\right\}^{1/2}; i = 1, 2, ..., m \quad (9)$$

Step 5: Calculation of the relative closeness to the idea solution. The relative closeness to the ideal solution can be defined as:

$$C_i = \frac{S_i^-}{S_i^+ + S_i^-}; i = 1, 2, ..., m; \; 0 \le C_i \le 1 \quad (10)$$

The higher the closeness means better the rank.

Step 6: Ranking of the preference order

The preference order is ranked on the basis of the order of C_i. Hence, the optimum alternative is the one which is nearer to the ideal solution and farther to the negative ideal solution.

3. Result and Discussion

3.1 Computational Results

The normalized decision matrix for filler alloy, electrode, shielding gas is calculated using Equation (4) as shown in matrices (11), (12) and (13) respectively

$$\begin{bmatrix} 0.5351 & 0.4262 & 0.5064 & 0.5740 & 0.3994 & 0.4702 & 0.4821 & 0.5401 \\ 0.3156 & 0.5632 & 0.4170 & 0.3553 & 0.4734 & 0.5531 & 0.5562 & 0.4659 \\ 0.5900 & 0.4884 & 0.5064 & 0.5412 & 0.4586 & 0.5116 & 0.5191 & 0.4748 \\ 0.4528 & 0.3918 & 0.5064 & 0.4538 & 0.5089 & 0.3318 & 0.3337 & 0.3858 \\ 0.2470 & 0.3303 & 0.2383 & 0.2132 & 0.3846 & 0.3180 & 0.2781 & 0.2967 \end{bmatrix} \quad (11)$$

$$\begin{bmatrix} 0.0021 & 0.7691 & 0.4781 & 0.7735 & 0.5927 & 0.5203 & 0.3780 & 0.5401 \\ 0.5383 & 0.4682 & 0.3028 & 0.3970 & 0.4533 & 0.3251 & 0.6300 & 0.4659 \\ 0.6625 & 0.2657 & 0.4143 & 0.1803 & 0.3487 & 0.3990 & 0.5040 & 0.4748 \\ 0.5176 & 0.2277 & 0.4542 & 0.1874 & 0.3835 & 0.5203 & 0.2520 & 0.3858 \\ 0.0621 & 0.2593 & 0.5498 & 0.4201 & 0.4184 & 0.4403 & 0.3780 & 0.2967 \end{bmatrix} \quad (12)$$

$$\begin{bmatrix} 0.0743 & 0.7042 & 0.7041 & 0.3452 & 0.0705 & 0.0627 \\ 0.7024 & 0.0702 & 0.0698 & 0.5387 & 0.7038 & 0.6525 \\ 0.5450 & 0.2282 & 0.2284 & 0.4903 & 0.5455 & 0.5050 \\ 0.2312 & 0.5455 & 0.5455 & 0.3936 & 0.2288 & 0.2102 \\ 0.3881 & 0.3869 & 0.3869 & 0.4420 & 0.3871 & 0.5207 \end{bmatrix} \quad (13)$$

These weights of all attributes of respective consumables are evaluated using AHP method and the results are presented in Table. 6

Table 6 Weights of the attributes from AHP method

Attributes	Filler Alloy Weights	Electrode Weights	Shielding Gas Weights
A_1	0.0326	0.0311	0.0428
A_2	0.0235	0.0447	0.1006
A_3	0.0476	0.1586	0.1595
A_4	0.1059	0.1036	0.0640
A_5	0.3313	0.2399	0.2504
A_6	0.1572	0.3542	0.3824
A_7	0.2306	0.0675	
A_8	0.0709		

A weighted normalized decision matrix for filler alloy, electrode, shielding gas is presented in matrices (14), (15) and (16)

$$\begin{bmatrix} 0.0174 & 0.0100 & 0.0241 & 0.0608 & 0.1323 & 0.0739 & 0.1112 & 0.0427 \\ 0.0103 & 0.0132 & 0.0199 & 0.0376 & 0.1568 & 0.0869 & 0.1283 & 0.0368 \\ 0.0192 & 0.0115 & 0.0241 & 0.0573 & 0.1519 & 0.0804 & 0.1197 & 0.0375 \\ 0.0148 & 0.0092 & 0.0241 & 0.0481 & 0.1686 & 0.0522 & 0.0770 & 0.0305 \\ 0.0081 & 0.0078 & 0.0113 & 0.0226 & 0.1274 & 0.0500 & 0.0641 & 0.0234 \end{bmatrix} \quad (14)$$

$$\begin{bmatrix} 0.0001 & 0.0344 & 0.0755 & 0.0797 & 0.1417 & 0.1842 & 0.0255 & 0.0427 \\ 0.0167 & 0.0209 & 0.0478 & 0.0409 & 0.1083 & 0.1151 & 0.0425 & 0.0368 \\ 0.0206 & 0.0119 & 0.0655 & 0.0186 & 0.0833 & 0.1413 & 0.0340 & 0.0375 \\ 0.0161 & 0.0102 & 0.0718 & 0.0193 & 0.0917 & 0.1842 & 0.0170 & 0.0305 \\ 0.0019 & 0.0116 & 0.0869 & 0.0433 & 0.1000 & 0.1558 & 0.0255 & 0.0234 \end{bmatrix} \quad (15)$$

$$\begin{bmatrix} 0.0032 & 0.0708 & 0.1123 & 0.0221 & 0.0177 & 0.0240 \\ 0.0301 & 0.0071 & 0.0111 & 0.0345 & 0.1762 & 0.2495 \\ 0.0233 & 0.0230 & 0.0364 & 0.0314 & 0.1366 & 0.1931 \\ 0.0099 & 0.0549 & 0.0870 & 0.0252 & 0.0573 & 0.0804 \\ 0.0166 & 0.0389 & 0.0617 & 0.0283 & 0.0969 & 0.1991 \end{bmatrix} \quad (16)$$

3.2 Ranking Results

The relative closeness to the ideal solution hence can be found using equation (10). The ranks are assigned based on their ‘C’ values and are given in Table 7. The larger the value of closeness the better is the rank.

Table 7 TOPSIS analysis result

Filler Alloy			Electrode			Shielding gas		
Alternates	C_i	Rank	Alternates	C_i	Rank	Alternates	C_i	Rank
ER 5356 (C_1)	0.8358	1	Pure Tungsten (C_1)	0.4084	4	Pure Argon (C_1)	0.7149	1
ER 5556 (C_2)	0.6184	3	2% Thoriated (C_2)	0.5789	2	Pure Helium (C_2)	0.2850	4
ER 5183 (C_3)	0.7205	2	2% Ceriated (C_3)	0.4745	3	25%Argon+75%Helium(C_3)	0.3280	3
ER 5654 (C_4)	0.3142	5	1.5% Lanthanated (C_4)	0.2835	5	75%Argon+25%Helium(C_4)	0.6719	2
ER 5554 (C_5)	0.3516	4	0.8% Zirconiated (C_5)	0.5869	1	50%Argon+50%Helium(C_5)	0.2363	5

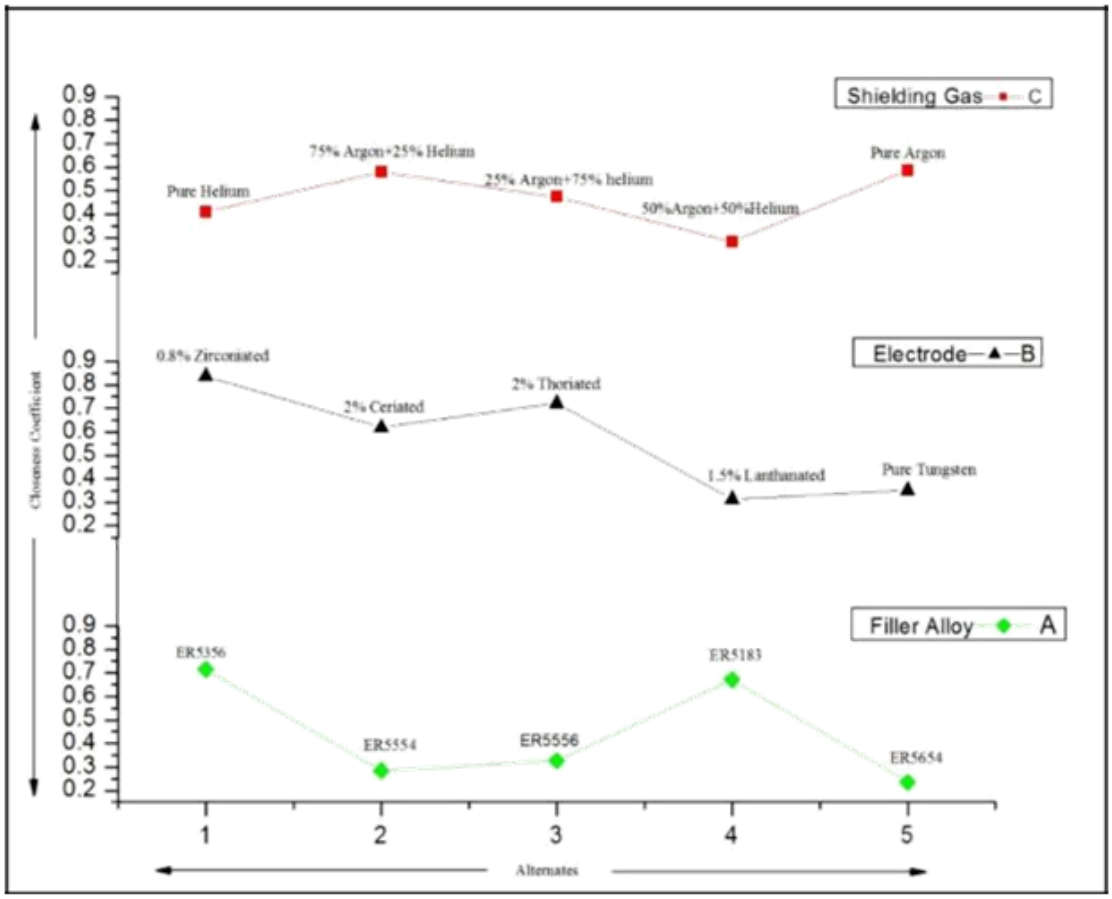


Fig. 2 Block diagram for material selection application

It can be concluded from Table 7, filler alloy; ER5356 has the highest ranking followed by ER 5183 while ER 5654 is the least ranked material. In arc electrode selection problem the optimum arc electrode is 0.8 % Zirconiated electrode is best alternate as it has slightly higher "C" value than 2% thoriated electrode. Shielding gas analysis results indicate pure Argon as the optimum consumable component closely followed by Ar-He gas blend as second best alternative.

3.3 Welding Experimentation

The butt welding of Aluminum alloy of 5083-O and 6061-T651 using Pulse TIG welding (Triton 220 AC/DC) is performed to establish the applicability and validity of the selection model.

The chemical composition of filler alloys used has been depicted in Table 8.

Table 8 : Chemical composition of filler alloys used

Composition	Si	Mg	Fe	Cu	Mn	Cr	Zn	Ti	Al
ER 5356	0.23	5.0	0.40	0.05	0.12	0.9	0.10	0.13	Balance
ER 5556	0.25	5.1	0.40	0.10	0.75	0.13	0.25	0.13	Balance
ER 5183	0.40	4.8	0.40	0.10	0.75	0.15	0.25	0.15	Balance
ER 5654	0.22	3.5	0.23	0.05	0.01	0.25	0.20	0.10	Balance
ER 5554	0.25	2.7	0.40	0.10	0.75	0.13	0.25	0.13	Balance

Experimental validation has been conducted using highest ranking materials namely, ER5356 as filler alloy, 0.8% zirconiated electrode and pure Argon shielding gas as shown in Figure 3

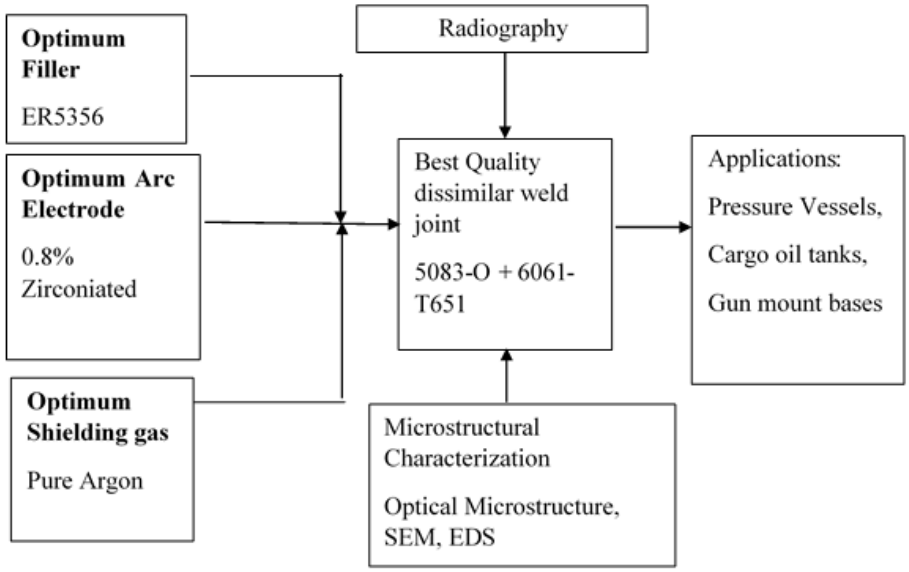


Fig. 3 Flow diagram depicting applications of 5083-O and 6061-T651

3.3.1 Radiography Examination

Welding was examined using radiography to check lack of penetration as shown in Fig. 4. No visual defects is observed in radiography film indicate proper fusion in weld joint leading to successful welding. 10 ×12 cm is the scale bar used

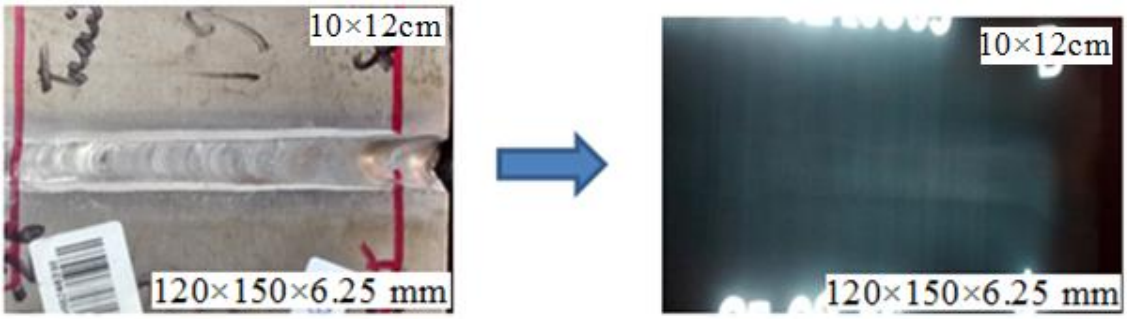


Fig. 4 a) Weld joint 5083-O + 6061 T-651 b) Radiography

3.3.2 Microstructure Characterizations

Microstructural characterization is important since various characteristics of phase particles especially mechanical properties, corrosion resistance are dependent on form of Mg_2Si in which it exists in a particular material.

Microstructural characterization using optical microscope and SEM (Scanning electron microscope) images (3700N Hitachi) to check grain refining and formation of brittle phase shown in fig 5.

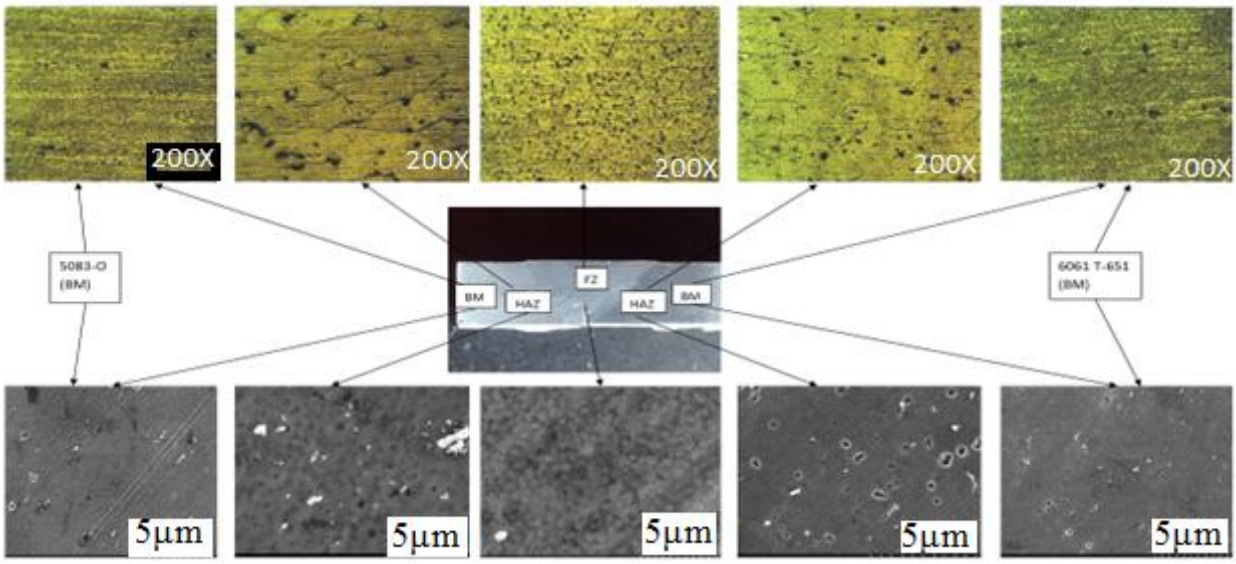


Fig. 5 Microstructure (200X) and SEM (5µm) images of Base metal, Heat affected Zone, Fusion zone at both sides

Microstructure shows three different regions i.e Base metal, Heat affected zone, Fusion zone on either side of weld. Fig 6.shows Fusion zone (FZ) region, fine equiaxed grains

of aluminum solid solution containing soluble phase consisting of Mg_2Si particles shows proper grain refinement. Hence improved weld quality is accomplished

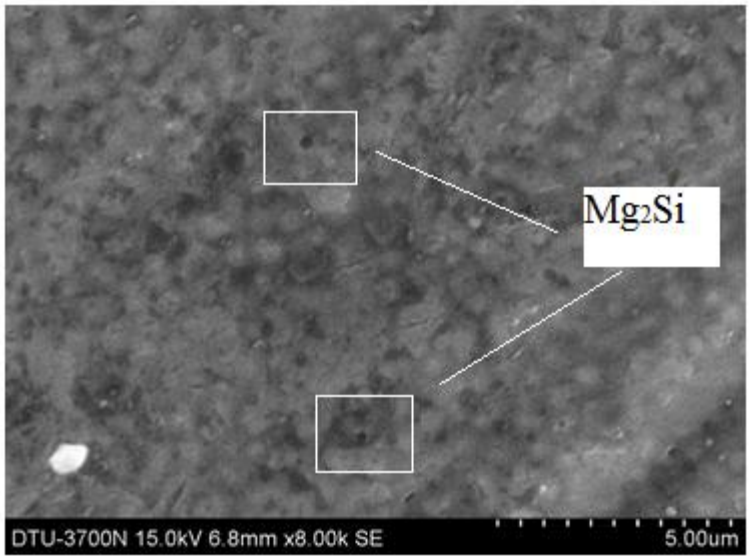


Fig 6 SEM image of Mg_2Si particle

4. Conclusion

Selection of welding process consumables are important tasks of decision making in engineering design. There is a requirement to study the correlation between available material alternates and their attributes to produce a robust welding of Aluminum alloys at the lowest overall cost. AHP-TOPSIS based MADM model makes it possible to provide both qualitative and quantitative study of intangible factors in welding process.

The relevance of such decision support tool lies in enabling welding/design engineers to improvise the process management with minimum available data.

In future research the approach can be used for selection of dissimilar metal alloys for common extrusion applications.

References

1. Mutombo, K.(2011) *Corrosion of fatigue behaviour of 5083-H111 and 6061-T651 Aluminium alloy welds.*Unpublished PhD Thesis. University of Pretoria, South Africa

2. Scott Funderburk, R. (1998). Key Concepts in Welding Engineering–Post Weld Heat Treatment. Welding Innovation. 15(2)
3. Khorshidi, R., Hassani, A., Rauof, A.H., Emamy, M. (2013). Selection of an optimal refinement condition to achieve maximum tensile properties of Al– 15%Mg2Si composite based on TOPSIS method. *Materials & Design* ,46, 442– 450. DOI10.1016/j.matdes.2012.09.050
4. Mirhedayatian, S.M., Vahdat, S.E., Jelodar, M.J., Saen, R.F.(2013). Welding process selection for repairing nodular cast iron engine block by integrated fuzzy data envelopment analysis and TOPSIS approaches. *Materials and Design*, 43, 272–282. DOI10.1016/j.matdes.2012.07.010
5. Huang, H.Y.(2009). Effects of shielding gas composition and activating flux on GTAW weldments. *Materials and Design* ,30, 2404–2409. DOI: 10.1016/j.matdes.2008.10.024.

6. Huang, H.Y.(2010). Argon-hydrogen shielding gas mixtures for activating flux-assisted gas tungsten arc welding. Metallurgical and Materials Transactions A: *Physical Metallurgy and Materials Science* , 41, 2829–2835. DOI: 10.1007/s11661-010-0361-9
7. Hwang, C and yoon, K (1981). Multiple attribute decision making methods and application survey. Springer Berlin
8. Satty, T L (2008). Decision making with the analytic hierarchy process. *Int. J. Services sciences*, 1,83-98 **DOI**: http://dx.doi.org/10.1504/IJSSci.2008.01759

Biophysical Journal
Article

Biophysical Society

Myosin-Induced Gliding Patterns at Varied [MgATP] Unveil a Dynamic Actin Filament

Elina Bengtsson,[1] Malin Persson,[1] Mohammad A. Rahman,[1] Saroj Kumar,[1] Hideyo Takatsuki,[1] and Alf Månsson[1,*]

[1]Department of Chemistry and Biomedical Sciences, Faculty of Health and Life Sciences, Linnaeus University, Kalmar, Sweden

ABSTRACT Actin filaments have key roles in cell motility but are generally claimed to be passive interaction partners in actin-myosin-based motion generation. Here, we present evidence against this static view based on an altered myosin-induced actin filament gliding pattern in an in vitro motility assay at varied [MgATP]. The statistics that characterize the degree of meandering of the actin filament paths suggest that for [MgATP] $\geq$ 0.25 mM, the flexural rigidity of heavy meromyosin (HMM)-propelled actin filaments is similar (without phalloidin) or slightly lower (with phalloidin) than that of HMM-free filaments observed in solution without surface tethering. When [MgATP] was reduced to $\leq$0.1 mM, the actin filament paths in the in vitro motility assay became appreciably more winding in both the presence and absence of phalloidin. This effect of lowered [MgATP] was qualitatively different from that seen when HMM was mixed with ATP-insensitive, N-ethylmaleimide-treated HMM (NEM-HMM; 25–30%). In particular, the addition of NEM-HMM increased a non-Gaussian tail in the path curvature distribution as well as the number of events in which different parts of an actin filament followed different paths. These effects were the opposite of those observed with reduced [MgATP]. Theoretical modeling suggests a 30–40% lowered flexural rigidity of the actin filaments at [MgATP] $\leq$ 0.1 mM and local bending of the filament front upon each myosin head attachment. Overall, the results fit with appreciable structural changes in the actin filament during actomyosin-based motion generation, and modulation of the actin filament mechanical properties by the dominating chemomechanical actomyosin state.

INTRODUCTION

Actin is one of the most abundant eukaryotic proteins (1) and plays key roles in intracellular transport, cell signaling, cellular shape changes, and cell motility (2). These processes involve controlled actin polymerization and depolymerization, as well as actin-myosin interactions (3). Force and motion generation involving different isoforms of myosin II motors and actin filaments (F-actin) is central in all cells and the basis for muscle contraction. In this process, the actin filaments are often viewed as rope-like passive interaction partners (4) despite evidence from spectroscopy, ultrastructural studies, and myosin-binding data indicating that the actin filament structure is dependent on myosin head attachment and the state of the attached myosin motor domains (1,3,5–18).

One way to detect changes in the actin filament state is to monitor the filament flexural rigidity, EI, because E (the Young's modulus) and I (the second moment of inertia of the filament cross section) reflect the intermonomer interaction strength and filament geometry, respectively (18). The flexural rigidity is a measure of the resistance to bending and is often quantified using the persistence length, L_P^f. This is a characteristic correlation length for thermal bending fluctuations along the filament that is related to the flexural rigidity as L_P^f = EI/kT (where k is the Boltzmann constant and T is the absolute temperature). For example, two different flexibility states of actin filaments have been found with different nucleotides bound to the actin subunits in the presence and absence of phalloidin or with and without binding of myosin (5,6,9,10,19–21). Recently, evidence was presented for what seems to be a third flexibility state with even higher flexibility (lower Lp^f), e.g., after cofilin binding (22) or after tethering of the filaments to a surface via proteins that bind along the actin filament side (23). This is consistent with ideas of a strongly dynamic actin filament (1,7,8,24). However, these ideas are not unequivocally supported (25,26) (discussion in (1)), and no marked difference in filament flexibility

Submitted January 11, 2016, and accepted for publication August 22, 2016.

*Correspondence: alf.mansson@lnu.se

Malin Persson's present address is Department of Kinesiology and Physical Education, Karolinska Institutet, Stockholm, Sweden and Department of Kinesiology, McGill University, Montreal, Canada.

Saroj Kumar's present address is Department of Biotechnology, Delhi Technological University, Delhi-42, India.

Editor: Kazuhiro Oiwa.

http://dx.doi.org/10.1016/j.bpj.2016.08.025

© 2016 Biophysical Society.

This is an open access article under the CC BY-NC-ND license (http://creativecommons.org/licenses/by-nc-nd/4.0/).

between different conditions of myosin-induced actin motility has been observed previously.

In an in vitro motility assay (IVMA), fluorescence-labeled actin filaments are propelled by surface-adsorbed myosin molecules (27,28), or rather, myosin motor fragments such as heavy meromyosin (HMM). A convenient way to describe the statistics of the winding filament paths is to use the path persistence length (Lp^p) (5,29,30), which is the sliding distance after which the memory of the initial tangent angle of the path is effectively lost. Recent results (5,31–33) provide strong evidence that the Lp^p corresponds directly to the Lp^f, i.e., it is determined by the flexural rigidity of the actin filaments. On this basis, we concluded that the flexural rigidity of phalloidin-stabilized actin filaments is reduced to the level of phalloidin-free filaments when the former are propelled by HMM at ionic strengths of <100 mM, but not at a higher ionic strength (130 mM) (5). We hypothesized that this discrepancy is due to the failure of myosin-induced structural changes to propagate along the actin filaments at high ionic strength (5). If this is indeed the case, increased density of active myosin heads along the actin filament would be expected to make Lp^p more similar for phalloidin-free and phalloidin-stabilized filaments.

In conflict with the notion that the actin filament paths in an IVMA are fully determined by thermal fluctuations that reflect Lp^f, a recent study (34) suggested that nonthermal fluctuations due to motor-induced forces are important. These forces were largely attributed to motors temporarily acting as cross-linkers between the filament and the surfaces, e.g., as would be expected for cross-bridges in postpowerstroke states. Therefore, a change in the fraction of such motors may be expected to modify the filament paths.

Experiments using lowered MgATP concentrations allowed us to test the above ideas. This intervention reduces the rate of myosin head detachment from actin without changing the attachment rate constant (35), causing an increased density of the attached myosin heads (cf. Fig. 2 in (35)) with the leading head being closer to the filament front. This would facilitate the propagation of myosin-induced structural changes to the free leading end. Furthermore, lowered [MgATP] would increase the fraction of myosin heads in the postpowerstroke state, which is expected to influence nonthermal contributions to the filament trajectories (34). As an alternative approach to increase the fraction of such braking cross-bridges, we mixed functional HMM with HMM that had been made ATP insensitive and noncycling by treatment with N-ethylmaleimide (hereafter termed NEM-HMM).

Unexpectedly, we found a substantial reduction in $L_P{}^p$ by lowering [MgATP] from 1 to 0.05 mM. The observed effect was considerably greater than would be expected according to the hypothesis of improved propagation of structural changes. Together with the effects of HMM and phalloidin on Lp^f, this finding is consistent with three mechanically distinct actin filament states. Among these states, the one with the lowest flexural rigidity (at low [MgATP]) has not, to the best of our knowledge, been observed previously for HMM-propelled filaments. Additionally, our results are consistent with local structural changes occurring in the actin filament upon each myosin head attachment. Finally, we found evidence for a substantially reduced frequency of bursts with an anomalous nonthermal influence (34) on the filament paths at low [MgATP]. This was in contrast to the increase of such an influence after addition of NEM-HMM at 1 mM MgATP. The results are consistent with the idea that reduced Lp^p at lowered [MgATP] to a substantial degree reflects reduced Lp^f, whereas a nonthermal influence relies on the presence of a fraction of noncycling myosin heads. Overall, the results are consistent with a dynamic actin filament whose global and local structure is affected by actin-myosin interaction kinetics. We discuss the mechanisms that promote the formation of a high-flexibility state at low [MgATP] and also consider the properties of this state in relation to key cellular functions and adaptations.

MATERIALS AND METHODS

Ethics statement

All experiments using animal material were approved by the Regional Ethics Committee for Animal Experiments in Linköping, Sweden (reference numbers 58-08, 96-11, and 73-14), and performed in accordance with national and European Union legislations.

Protein preparations and IVMAs

HMM was obtained from fast skeletal muscle myosin, and actin was prepared from acetone powder from skeletal muscle (28,36). Actin filaments were formed by addition of KCl (50 mM) and $MgCl_2$ (2 mM), and in some cases MgATP (3 mM), with no apparent difference in the results. The filaments were treated with tetramethylrhodamine isothiocyanate phalloidin (TRITC-Ph) at molar excess or were fluorescence labeled using N-hydroxysuccinimide rhodamine (NHS-Rh) without phalloidin (5). NEM-HMM was obtained as described previously (37–39). Briefly, HMM (~500 μg/mL) was dialyzed against imidazole-EDTA buffer (10 mM imidazole, 50 mM KCl, 10 mM EDTA, pH 7.0) using a centrifugal concentrator (Vivaspin 2, 28-9322-47; GE Healthcare, Little Chalfont, UK), and treated with NEM (1 mM final concentration; E1271; Sigma-Aldrich, St. Louis, MO) dissolved in ethanol and diluted with the imidazole-EDTA buffer. After incubation for 1 h at 25°C, the NEM-HMM was dialyzed against imidazole-EDTA buffer for removal of excess NEM. The concentration of NEM-HMM was measured using a Bradford assay. The proteins were stored at −80°C until use. The method that we generally use for HMM preparation yields submicromolar concentrations. For some experiments, the HMM concentration was increased to 3–5 μM by a procedure in which HMM (~0.5 μM) was centrifuged at 14,000 × g for 29 min at 4°C using 30 kD cutoff membranes (Nanosep Centrifugal Devices; Pall, Port Washington, NY). The concentrated HMM had similar actin-propelling properties (velocity and fraction of motile filaments) as before the concentration procedure, as tested in separate experiments.

For the IVMAs, glass coverslips functionalized with trimethylchlorosilane (TMCS) (40) were assembled into flow cells that were incubated with HMM (for 2 min), followed by a number of rinsing and blocking steps before addition of 2–10 nM fluorescently labeled actin filaments (30 s). Subsequently, an assay solution containing 0.01–3 mM MgATP, 2.5 mM creatine phosphate, 56 U mL^{-1} creatine kinase, 0.64% methylcellulose, and 115 mM KCl was added. The flow-cell temperature varied between 25.2°C and 29.1°C between different assays. The IVMA conditions were similar to those previously described as important for unbiased studies of path persistence lengths (30). Motility assays with 25% and 30% NEM-HMM out of the total amount of HMM were performed in the presence of 1 mM MgATP, and other experimental conditions were similar to those employed in standard IVMAs.

The image sequences were recorded using an EM-CCD camera (C9100; Hamamatsu Photonics, Hamamatsu, Japan) with a pixel magnification of 0.165 × 0.165 μm^2 per pixel, or a cooled CCD camera (Orca-ER, C4742-95; Hamamatsu Photonics) with a pixel magnification of 0.198 × 0.198 μm^2 per pixel, at frame rates of 5–10 s^{-1} as appropriate. See Supporting Materials and Methods in the Supporting Material for details.

Persistence lengths of actin filament paths and actin filaments in solution

The path persistence length (L_P) of the actin filaments in the IVMA was obtained (5,30) on the basis of the cosine correlation function (CCF), $<\cos(\theta(s) - \theta(0))>$ (where $\theta(s)$ is the instantaneous sliding direction), plotted against the distance (s) along the filament path. An algorithm developed in MATLAB (The MathWorks, Natick, MA) was used to manually track the filaments to obtain $\theta(s)$ and s. Filaments stuck on dead rigor-like HMM heads or filaments undergoing abrupt direction changes (defined by a cutoff value set to 1.5 radians) were excluded before the CCF was fitted (30). The L_P value was obtained from fits of the following equation to the data:

$$\langle \cos(\theta(s)\text{-}\theta(0)) \rangle = \exp(-s/[2 * Lp]). \quad (1)$$

A similar principle was used to obtain the persistence length of actin filaments in solution, aside from using the instantaneous tangent angle at positions s along the filament instead of the tangent angle along the path. For these measurements, actin was diluted to a concentration of 5–40 nM in an assay buffer-based solution but without methylcellulose and MgATP. To create a flow cell of <5 μm thickness, 3–5 μL of the actin sample was sandwiched between a small coverslip (18 × 18 mm^2) and a glass slide. The surfaces were soaked in bovine serum albumin and dried before use. For measurements in the presence of HMM, polyethylene glycol (PEG)-derivatized surfaces (Supporting Materials and Methods) (41) were used to prevent HMM adsorption to the surfaces. In this case, 1–5 μL of the actin+HMM+MgATP sample was sandwiched between the two PEG-coated glass slides (20 × 20 mm^2). In all cases, the flow cells were sealed with nail polish before measurements were obtained at room temperature (20–23°C), and images were recorded with a 0.05 s exposure time.

Statistical analysis, including nonlinear regression

For nonlinear regression and statistical analyses, GraphPad Prism (v. 6.05; GraphPad Software, San Diego, CA) was used. The same program was used to calculate the 95% confidence interval (CI) for a proportion using the modified Wald method. The mean values, without considering the experimental variation at each s-value, were used for nonlinear regression fits to the CCF. This procedure was used due to the decreasing number of data points at increasing values of s and hence an increased uncertainty at higher s-values. If not otherwise stated, the data are given as the mean ± 95% CI.

RESULTS

Evidence suggesting different actin filament flexibility states

Numerical values of Lp^f and Lp^p were obtained at 130 mM ionic strength from exponential fits to the CCF (Eq. 1; Fig. S1). For derivation of Lp^f (Fig. S1 *A*), the CCF was obtained by observing a large number of filaments floating in solution between two closely spaced coverslips. For derivation of Lp^p (Fig. S1 *B*), the CCF was obtained from the paths (Fig. 1) of filaments propelled by HMM in the IVMA (5). In most of the IVMA experiments, the HMM incubation concentration was 120 μg/mL, which is expected to give an isotropic HMM density in the range of 5000–7000 μm^{-2} on TMCS-derivatized surfaces (42–44). Inclusion of methylcellulose in IVMAs has no effect on Lp^p (5). Furthermore, since Lp^f values are similar regardless of whether 1 mM MgATP is present or not (5), MgATP was not included in measurements of Lp^f.

In qualitative agreement with previous results (5), phalloidin-free actin filaments exhibited lower Lp^f and Lp^p values than phalloidin-stabilized filaments (Fig. 2). Furthermore, as was observed previously (5), the Lp^p of phalloidin-labeled filaments at 1 mM MgATP was lower than the Lp^f. For phalloidin-free filaments, on the other hand, the Lp^p and Lp^f were similar (~10 μm). The simplest explanation for these results is that the Lp^p is fully determined by the flexural rigidity of the actin filaments (5,30,33), and that the flexural rigidity of phalloidin-free filaments is unchanged, whereas that of phalloidin-stabilized filaments is reduced upon binding to HMM in an IVMA (5).

When [MgATP] was reduced from 1 mM to 0.05 mM, the velocity decreased 5- to 10-fold (Table S1) but the fraction of motile filaments increased from 60% to 80% (in the absence of blocking actin or other methods for removing dead rigor-like heads) at 1 mM MgATP to almost 100% at 0.05 mM MgATP. Furthermore, the fraction of very short filaments (<<1 μm) increased at low MgATP (Fig. 1 *C*) due to motility-induced fragmentation. It is clear from Fig. 1 that the very short filaments (<<1 μm; *white arrowheads* in Fig. 1) follow distinctly more winding paths than the longer filaments (Movies S1 and S2). We attribute this finding to repeated pivoting of the very short filaments around temporary single surface attachment points via one myosin head (31). Importantly, however, also if filaments shorter than 1 μm were excluded from the analysis, the paths were noticeably more winding on average at low than at high [MgATP] (Fig. 1 *E*; Movies S1 and S2). This is quantitatively reflected in a markedly reduced path persistence length (Figs. 2 and S1 *B*). Thus, Lp^p values at 0.05 mM MgATP, in both the presence and absence of phalloidin,

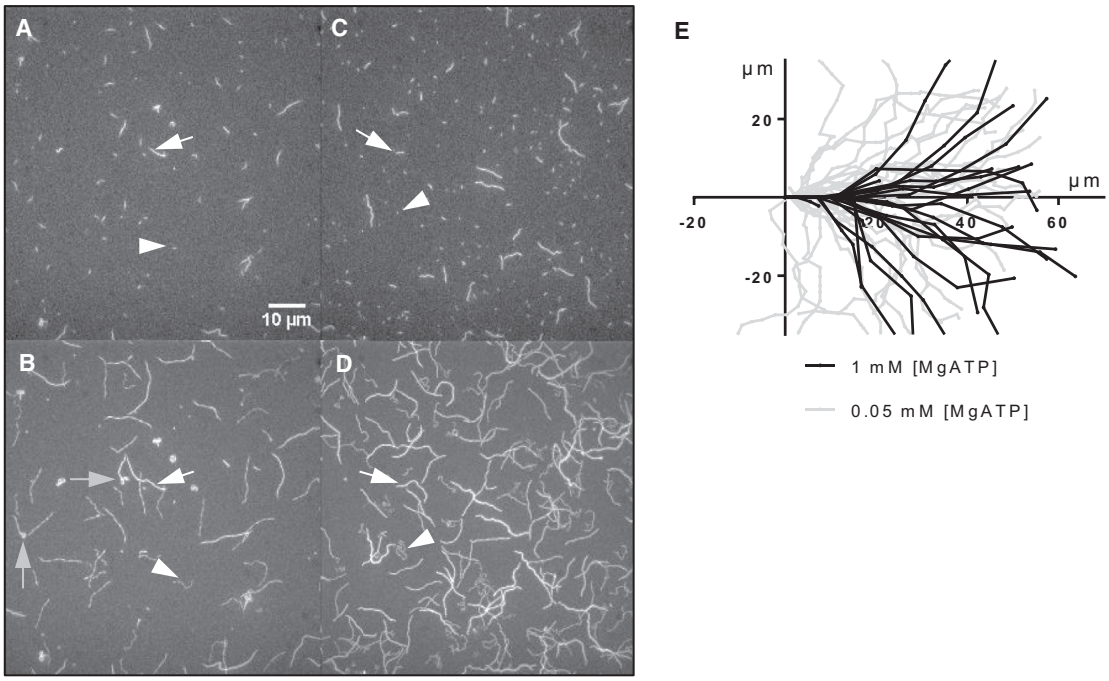


FIGURE 1 Actin filaments propelled by HMM in the IVMA at 1 and 0.05 mM MgATP. (*A*) Fluorescence micrograph (0.2 s) illustrating the starting point of filaments (1 mM MgATP) whose trajectories are illustrated in (*B*). The white arrow and white arrowhead point to typical filaments >1 μm and <1 μm long, respectively. (*B*) Trajectories of filaments at 1 mM MgATP obtained by overlaying five subsequent image frames in a sequence starting with that in (*A*). The white arrow and white arrowhead point to trajectories of corresponding filaments in (*A*). Gray arrows indicate trajectories with abrupt changes in sliding direction toward the end of the observed path due to pinning of filaments on rigor-like dead heads. Such rare trajectories were excluded from the analysis (see text). (*C*) Snapshot as in (*A*) but illustrating the starting point of trajectories in (*D*) (0.05 mM MgATP; arrow and arrowhead as described in *A*). (*D*) Trajectories of filaments at 0.05 mM MgATP obtained by overlaying 20 subsequent image frames in a sequence starting with that in (*C*). A larger number of frames were used to compensate for the lower velocity compared with that obtained at 1 mM MgATP (arrow and arrowhead as described in *B*). (*E*) Trajectories of long (>1 μm) filaments (excluding those with abrupt changes in sliding direction) from (*A*)–(*D*), replotted based on manual tracking in MATLAB. Trajectories at 1 mM MgATP and 0.05 mM MgATP are shown in black and gray, respectively, with the starting point translated to the origin after rotation for the initial sliding direction to be along the horizontal axis. Note that there are more winding paths on average at 0.05 mM MgATP. No methods were used in these experiments to remove or block dead rigor-like heads, e.g., precentrifugation of HMM with ATP and actin or inclusion of blocking actin. All grayscale images were similarly enhanced for contrast and brightness by histogram stretching using ImageJ (71).

were appreciably lower than any value we have previously observed. The filament length distributions were, however, very similar at low and high [MgATP] for filaments included in the quantitative analysis (Fig. S2).

Buckling or related phenomena do not explain low Lp^p at low [MgATP]

The paths of HMM-propelled filaments in the IVMA were governed by the path of the filament front at 0.05 mM MgATP, as was found previously at 1 mM MgATP and also predicted theoretically ((5,31); however, see (34)). This is consistent with the thin appearance of the filament trajectories in Fig. 1 *D*, suggesting that all parts of a filament trace out a similar path. Quantitative evidence is presented in Fig. S3, which shows a <16 nm average lateral deviation from the path of the leading end per micrometer of filament sliding. This magnitude of deviation can be fully explained by thermal fluctuations of the actin filament segments between subsequent myosin-binding sites (cf. equations in (20)) together with uncertainty in the estimates of the filament axis position by Gaussian fits to microscopy images. The results in Fig. S3 were obtained using the long filaments in Fig. 1, *C* and *D*, which were selected for highly curved trajectories to maximize the risk of deviations from a single path. The very small lateral deviations found are in accord with the idea (5,31) that fluctuations of the free leading filament end are the major determinant of the filament paths and therefore of the Lp^p. The findings shown in Figs. 1 *D* and S3 thus argue against appreciable bursts of a nonthermal influence on the filament paths (34). Such bursts would include buckling events, i.e., the emergence of unstable mechanical states of the actin filament with lateral bending into a sinusoidal form of unpredictable amplitude (45) at compressive forces above certain critical values (see below and Supporting Materials and Methods). More generally, the results in Fig. S3 argue against substantial local distortions, independent of origin, that would cause different filament segments to follow different paths (46).

Because myosin heads are in a nucleotide-free, strongly bound, postpowerstroke state for a larger fraction of their actin-attached time when [MgATP] is lowered, we tested

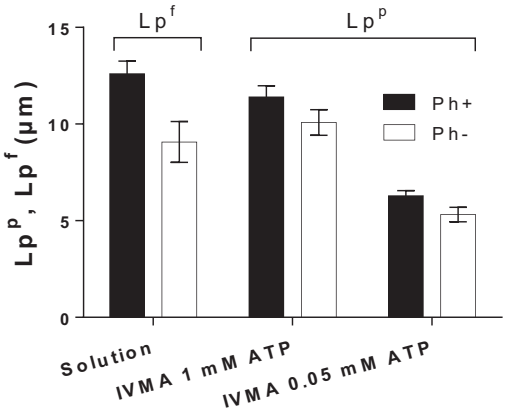


FIGURE 2 Persistence lengths of filaments in solution (Lp^f) and path persistence lengths (Lp^p) with (*black bars*, Ph+) and without (*open bars*, Ph−) phalloidin. Comparison of persistence lengths under different conditions obtained from fits such as those shown in Fig. S1, *A* and *B*. Data (mean ± 95% CI) from at least 200 independent filaments (Lp^f) or filament paths (Lp^p). Only filaments longer than 1 μm were included in the analysis of Lp^p. Other analysis criteria as in (30).

how statically bound heads in a similar state would affect motility and sliding paths. For this purpose, we mixed ordinary HMM with NEM-HMM, which is known (38) to act as a strongly bound, noncycling myosin analog that is not dissociated by MgATP. When motility assays at 1 mM MgATP were performed in the presence of NEM-HMM (added as 30% of total [HMM]), the motility behavior was qualitatively very different from that observed at low [MgATP]. In the latter case, the sliding velocity was substantially reduced compared with that obtained at 1 mM MgATP, but the fraction of motile filaments was increased (see above). In contrast, the inclusion of 30% NEM-HMM caused a smaller reduction in the maximum velocity than in the fraction of motile filaments. Thus, whereas the velocity was reduced by 45% from 7.56 ± 0.30 μm/s to 4.12 ± 0.63 μm/s (n = 30 filaments), the fraction of motile filaments was reduced by 79% from 0.65 ± 0.3 to 0.14 ±0.08 (n = 5 image frames). Very similar results were obtained with 25% NEM-HMM. In further contrast to the effect of lowered [MgATP], different parts of a filament frequently traced out different trajectories in the presence of 25–30% NEM-HMM. These deviations from a single path are readily resolved in standard fluorescence micrographs (Fig. S4) without the need for a detailed analysis as in Fig. S3. Interestingly, similar deviations were present in the supporting movies in a recent study (34), in which the behavior was interpreted as local and random injections of energy by interactions of cycling myosin motors with the actin filament. Here, we attribute the deviations in the presence of noncycling NEM-HMM to buckling events caused by MgATP-insensitive myosin heads that did not detach before exerting large resistive forces. This translates into local compressive forces that are above the critical force of buckling for filaments with a rather large average distance between neighboring actin-attached heads, as expected at high [MgATP]. This explanation is similar to that proposed for nonthermal fluctuations by Weber et al. (34). However, the difference is that we attribute the deviations from one single path (related to a non-Gaussian curvature of the filament) to noncycling cross-bridges, whereas Weber et al. (34) attributed them to cycling cross-bridges that are temporarily cross-linked to the actin filament, e.g., as would be expected for postpowerstroke myosin heads. The latter idea is not immediately consistent with our findings. Whereas we saw a limited number of events with different paths of different filament segments (and non-Gaussian curvature) at 1 mM MgATP, we did not detect such events at 0.05 mM MgATP (Figs. 1 *D* and S3), where the time spent by myosin heads in the postpowerstroke state was appreciably increased.

The above results suggest that the free leading end of the actin filament at low [MgATP] determines the HMM-propelled filament paths. However, for practical reasons, a detailed analysis of filament paths (Fig. S3) could only be applied to a small fraction of all filaments. Therefore, further analysis is required to more definitively rule out the possibility that subtle effects related to buckling or similar events in a large population of filaments contribute to low Lp^p at low [MgATP]. As pointed out above, large angular changes due to buckling are readily identified (e.g., paths with *red arrows* in Figs. 1 *A* and S4) and excluded during either tracking or analysis. In the analysis phase, filaments are excluded if they exhibit angular changes above a certain cutoff value (see Materials and Methods) (30). However, buckling events that cause angular changes below the cutoff are not eliminated. This may distort the distribution of angular updates away from a single Gaussian expected from thermal fluctuations of the leading filament end and increase the width of the distribution (cf. (34)). Therefore, we analyzed several thousands of angular updates (Fig. 3). If occasional buckling events contributed to low Lp^p at 0.05 mM MgATP, there would be an increased number of large and abrupt angular changes between tracking points if no cutoff were used to remove them. Furthermore, one would expect an increased deviation from a single Gaussian of the distribution of angular updates (a non-Gaussian path curvature distribution). In contrast, we found a better single Gaussian fit (Fig. 3, *B* and *C*) at 0.05 mM than at 1 mM MgATP. The lack of systematic deviations from a Gaussian at 0.05 mM MgATP is clear from normally distributed vertical residuals (Fig. 3 *C*) between the fitted curve and experimental data (d'Agostino-Pearson normality test; p = 0.0718) and with the mean value of the residuals indistinguishable from zero (t-test; p = 0.4402). In contrast, at 1 mM MgATP the residuals were nonnormal (p = 0.0033), with an average value different from zero (p = 0.0063), suggesting systematic deviations. Further, the number of large update events in the ranges of [−2.5, −1.5] and [1.5, 2.5] rad in Fig. 3 corresponded to

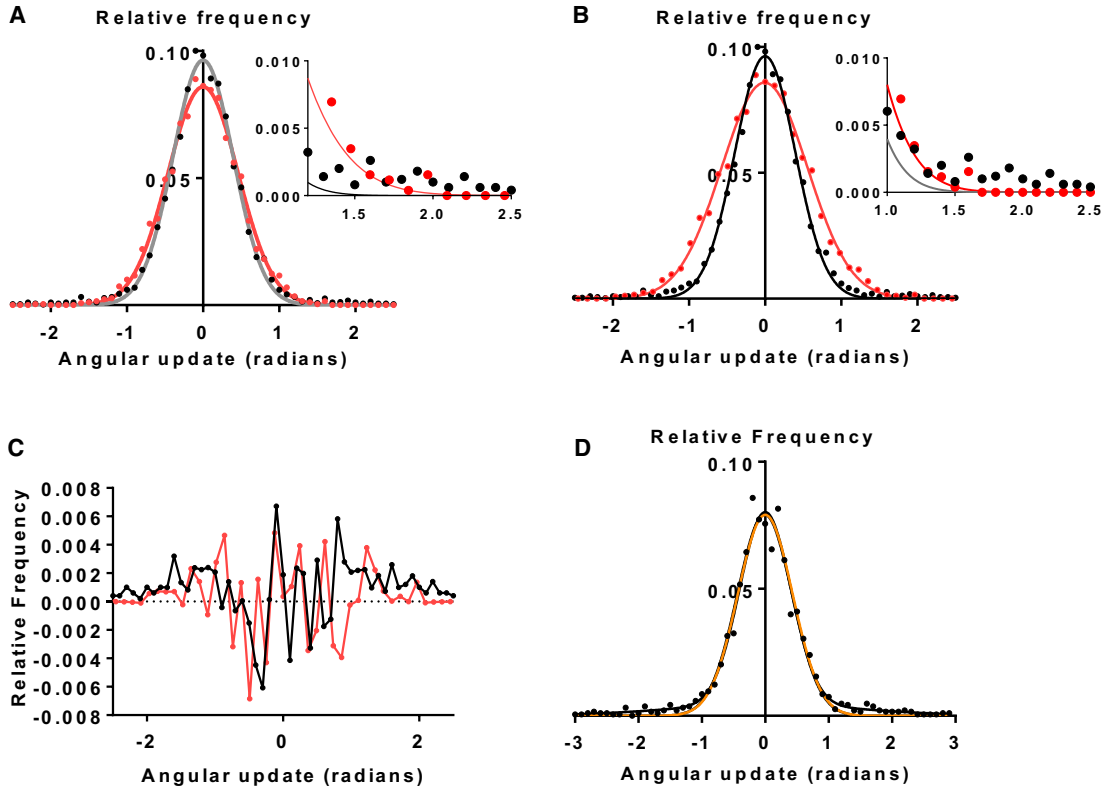


FIGURE 3 Relative frequency distributions for angular updates in the sliding direction between image frames for phalloidin-stabilized actin filaments. (*A*) Data uncorrected for different velocities and interframe times. Black, 1 mM MgATP (time between frames: 0.2 s; sliding velocity 11.73 μm s^{-1}); brighter line and symbols, 0.05 mM MgATP (time between frames: 0.8 s; sliding velocity 1.94 μm s^{-1}). Curves represent Gaussian fits to the data. Total number of events (angular updates): 4970 at [MgATP] = 1 mM and 2588 at [MgATP] = 0.05 mM. Inset: upper tails of distributions shown at higher resolution. (*B*) Data in (*A*) at 0.05 mM [MgATP] were multiplied by $1.2 = \sqrt{11.73x0.2}/1.94x0.8$ to correct for the shorter distance moved between tracking points compared with 1 mM [MgATP] (correction only for the width of the Gaussian, not for the total area under curve). The HMM incubation concentration is 120 μg/mL in (*A*) and (*B*). Note the higher number of large, abrupt changes in the sliding direction (tails of distribution) at high [MgATP] (*black*) compared with low [MgATP] (*brighter line* and *symbols*). (*C*) Vertical residuals (connected by lines for clarity) between data for 1 mM MgATP (*black*) or 0.05 mM MgATP (*bright*) and Gaussian curves in (*B*). Note the larger systematic deviations between the data and Gaussian fit at 1 mM than at 0.05 mM MgATP, particularly for large angular updates (<-1.5 rad and >1.5 rad). For a statistical analysis of residuals, see text. (*D*) Distribution as in (*A*) but for actin filaments propelled by HMM at 1 mM MgATP in the presence of 25–30% NEM-HMM after removal of stationary filaments (Fig. S5, *A* and *B*). Average velocity: 3.87 μm/s. Time between updates: 0.4 s. Bright curve: single Gaussian fit. Black curve: sum of two Gaussians assuming that the mean of each Gaussian component is constant and equal to 0 rad. To see this figure in color, go online.

only 0.35% ± 0.25% (mean ± 95% CI; $n = 2588$) of all events at 0.05 mM MgATP, compared with 2.17% ± 0.41% ($n = 4970$) at 1 mM MgATP. The good fit to a single Gaussian at low [MgATP] is what one would expect for angular updates due to thermal fluctuations of the filament leading end. This is in contrast to what we observed when NEM-HMM (25–30%) was mixed with normal HMM (Fig. 3 *D*). In that case, we found that the sum of two Gaussians gave an appreciably better fit to the data than a single Gaussian. According to the Akaike information criterion (taking into account differences in the sum of squared residuals and applying a penalty for more parameter values in a model), the double Gaussian model was 54 times more likely to fit the data than the single Gaussian. Furthermore, 4.2% ± 0.96% ($n = 1715$) of all update events were in the ranges of [−2.5, 1.5] and [1.5, 2.5] rad, which is significantly higher than in the absence of NEM-HMM (see above). The improved fit with a double compared with a single Gaussian in the presence of NEM-HMM is also evident from the more symmetrical residuals obtained with a double Gaussian (Fig. S5, *C* and *D*). This suggests a non-Gaussian curvature distribution of the actin filament paths as well as a non-Gaussian curvature distribution of the filament itself (34) associated with different paths of different filament segments (Fig. S4).

As a final test to determine whether occasional buckling effects contribute to low Lp^p values at low [MgATP], we performed experiments in which the distance between neighboring myosin heads along the actin filament was varied at 0.05 mM MgATP. This was achieved by lowering the HMM incubation concentration from 120 μg/mL to either 40 μg/mL or 20 μg/mL. These changes reduced the HMM surface density by >35% (40 μg/mL) and >65% (20 μg/mL) (Fig. S6; *dashed lines*), causing an increased

average distance ($<L_f>$; Eq. S4) between attached myosin heads by at least 1.5 and 2.9 times, respectively. The critical buckling force, $F_c \approx \pi^2 Lp^f$ kT/$<L_f>^2$ (Supporting Materials and Methods) is inversely proportional to $<L_f>^2$ ((45,47,48)) and may be estimated to 76 pN and 13 pN at an HMM incubation concentration of 120 and 20 μg/mL, respectively, compared with a maximum force of ~10 pN per myosin head. One would therefore expect an increased risk of buckling and a reduced Lp^p value upon a reduction in the HMM incubation concentration if buckling effects influence Lp^p. In contrast, we found no significant effect (Fig. 4) of the HMM incubation concentration on Lp^p.

We conclude that buckling, as defined above, is extremely rare and has no effect on Lp^p at 0.05 mM MgATP. The buckling frequency is higher at 1 mM MgATP and even higher in the presence of NEM-HMM, but is still uncommon. Below (see Fig. 6), we also consider the possibility that there are random bending effects (other than buckling) close to the leading filament end associated with each myosin head attachment. Such effects may be due to off-axis forces by myosin motors, local conformational changes upon myosin attachment, and bulging of the filament segment between the two leading myosin heads attached to actin. For a detailed account of these possibilities, see Supporting Materials and Methods.

Detailed relationship between Lp^p and [MgATP]

In view of the above results, we felt confident in considering the possibility that actin filament structural states with a lower flexural rigidity dominate during acto-myosin motility at low versus high [MgATP]. If so, one would expect a switch from high to low Lp^p values at critical [MgATP], with fairly constant values above and below this critical concentration. Studies of Lp^p over a range of MgATP concentrations (0.01–3 mM; Fig. 5 *A*), corresponding to a 30-fold variation in sliding velocity (Fig. 5 *B*), were in reasonable agreement with this idea, with an average Lp^p value almost twofold higher at [MgATP] $\geq$ 0.25 mM than at [MgATP] $\leq$ 0.1 mM (*horizontal solid lines* in Fig. 5 *A*). However, the data (Fig. 5 *A*) suggest that the stepwise [MgATP] dependence is superimposed on a graded increase of Lp^p between 0.01 and 1 mM MgATP. Importantly, in a previous study (5), no change in Lp^p was seen when the sliding velocity was reduced from 6 to 3 μm/s by lowering the temperature. This suggests that the effect is specific to reduced [MgATP] and is not a result of reduced velocity per se.

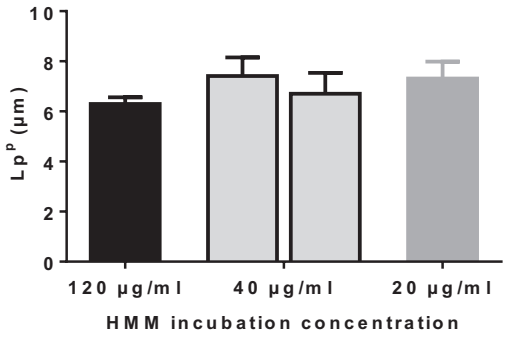


FIGURE 4 Lp^p at 0.05 mM MgATP and different HMM incubation concentrations. One actin preparation was tested at all HMM incubation concentrations and another was tested at 40 μg/mL. Each experimental point (mean $\pm$ 95% CI) was obtained by fitting Eq. 1 to the CCF for >200 independent filament paths. See also Fig. S2.

When [MgATP] approaches zero, the fraction of the actin-attached myosin heads in the nucleotide-free AM state (rigor) approaches one (49), as also captured by modeling (Fig. S7). If the Lp^p value (<5 μm) at the lowest tested [MgATP] is simply due to binding of myosin heads in the absence of nucleotide, one would expect a similar very low persistence length, Lp^f, for actin filaments in solution upon addition of HMM in the absence of MgATP. However, Lp^f was only reduced from 12.67 $\pm$ 0.50 μm in the absence of HMM to 9.21 $\pm$ 1.39 μm (Fig. 5, *A* and *C*) upon equimolar binding of HMM to actin filaments that were floating in solution between closely spaced coverslips. The effect of HMM binding on Lp^f in solution depended on the HMM/actin molar ratio, with the regression coefficient for Lp^f versus HMM concentration (Fig. 5 *C*) being significantly below zero ($p = 0.0078$). We also estimated the Lp^f of actin filaments in solution upon mixing with 0.5 μM HMM and 0.01 mM MgATP, and found that the Lp^f was similar to that obtained for bare actin filaments (Fig. 5 *C*). Increasing the HMM concentration to 4 μM in the presence of MgATP had complex effects (Fig. S8; Movies S4, S5, S6, and S7; see also (6,10))) that precluded reliable estimates of Lp^f. The effects included occasional high-amplitude bending events, presumably due to actin-myosin interactions. These events were associated with filament fragmentation, an effect that was more pronounced at 1 mM than at 0.05 mM MgATP. Additionally, calculations suggested low myosin head labeling of the actin filament (Table S3). Finally, there was evidence for the presence of a fraction of dead (rigor-like) myosin heads (which are likely to always exist in HMM preparations; Fig. S8 *C*; cf. Fig. 1).

Modeling of Lp^p at different [MgATP] and HMM incubation concentrations

As indicated by the data in Fig. 5, the stepwise decrease in Lp^p is superimposed on a continuous decrease with lowered [MgATP]. One possible basis for this continuous effect is local structural changes, e.g., stochastic bending or local conformational changes of the actin filament that occur upon each myosin head attachment (Fig. S9). Such an effect is expected to increase with reduced [MgATP] because the reduced velocity, without a reduction in the myosin head attachment rate, causes more myosin head attachments for a given sliding distance.

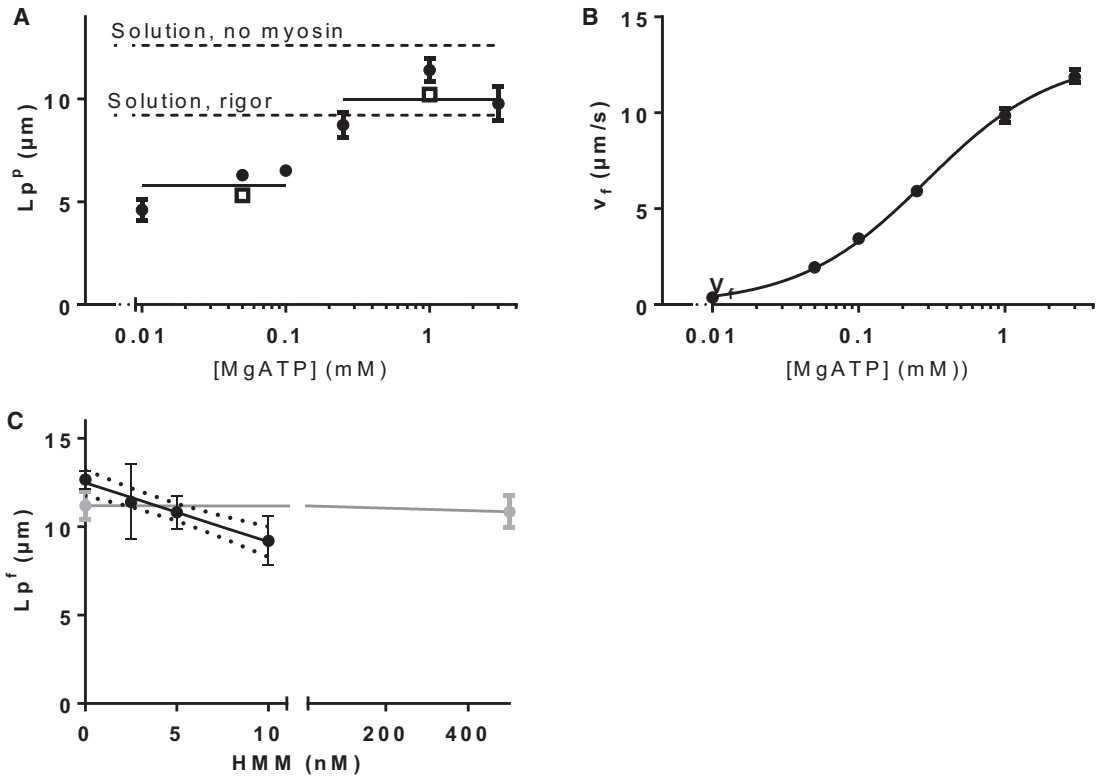


FIGURE 5 Effects of varied [MgATP]. (*A*) Lp^p plotted against [MgATP] on a logarithmic scale obtained after HMM incubation at 120 μg/mL. Each experimental point (mean ± 95% CI) was obtained by fitting Eq. 1 to the CCF for >200 independent filament paths. Solid symbols: phalloidin-stabilized filaments. Open symbols: phalloidin-free filaments. Solid lines: mean Lp^p values for [MgATP] $\leq$ 0.1 mM and [MgATP] $\geq$ 0.25 mM, respectively. Upper and lower dashed lines: Lp^f for phalloidin-stabilized filaments in solution before and after full labeling with HMM in the absence of MgATP. (*B*) Average velocities for phalloidin-stabilized filaments in (*A*) plotted against [MgATP]. (*C*) Effect of HMM binding on Lp^f with actin filaments floating in solution between closely spaced (<5 μm) coverslips (see Materials and Methods). Black symbols and lines: no MgATP. Number of filaments: 0 nM, 809; 2.5 nM, 75; 5 nM, 132; 10 nM, 85. Actin monomer concentration: 10 nM. The regression line (*solid black line*) is shown with the 95% CI (*dotted lines*). Slope: -0.33 ± 0.13 μm nM^{-1}, significantly below zero ($p = 0.0078$). The slope was significantly ($p = 0.0452$) below zero even if the point on the vertical axis was omitted from the linear regression analysis. Gray symbols and line: experiment with ($n = 341$ filaments) and without ($n = 231$ filaments) addition of HMM at 0.5 μM to actin filaments in solution (20 nM) in the presence of 0.01 mM MgATP.

We modeled the mechanism underlying this phenomenon by assuming that each myosin head attachment adds a random angular change, with variance V_{xb}, to that attributed to thermal motion. Under these conditions the apparent persistence length, Lp^{app} (corresponding to Lp^p), would vary with the average distance, $<x>_1$, between subsequent myosin head attachments at the filament front, according to a hyperbolic relationship (Eq. S9):

$$\mathrm{Lp^{app}} = Lp^f \frac{\langle x \rangle_1}{\langle x \rangle_1 + Lp^f V_{xb}}. \qquad (2)$$

Here, $<x>_1$ is approximated from experimental data using $<x>_1 = v_f <t>_1$, where v_f is the average sliding velocity and $<t>_1$ is the average time between subsequent myosin head attachments at the filament front (Eq. S2). The quantity $<x>_1$ is correlated with the average steady-state distance, $<L_f>$ (see above) between myosin heads along the actin filament (excluding filament ends; cf. (50)), but the latter value (Eq. S4) is higher. Whereas there are experimental uncertainties in both v_f and $<t>_1$, the changes in $<t>_1$ upon an altered HMM incubation concentration depend primarily on the myosin head density, which is quite reproducible between experiments for TMCS-derivatized surfaces (Fig. S6).

Plots of Lp^p versus $<x>_1$ for all [MgATP] and HMM incubation concentrations are depicted in Fig. 6. The solid horizontal straight lines in Fig. 6 *A* correspond to fits obtained under the assumptions that $V_{xb} = 0$ (i.e., no structural effect of individual head attachments) with one actin filament state at [MgATP] $\leq$ 0.1 mM and another state at [MgATP] $\geq$ 0.25 mM (cf. Fig. 5). Clearly, the fit is poor, with each line being outside the 95% CIs of several individual data points. We also attempted to fit the data assuming the same values of both Lp^f and V_{xb} ($V_{xb} > 0$) at high and low [MgATP] (*gray lines* in Fig. 6 *A*), but the fit was also rather poor in this case (see details below). The results are better reproduced by two mechanisms operating simultaneously: 1) a stepwise decrease in Lp^f when [MgATP] is reduced to <0.25 mM superimposed

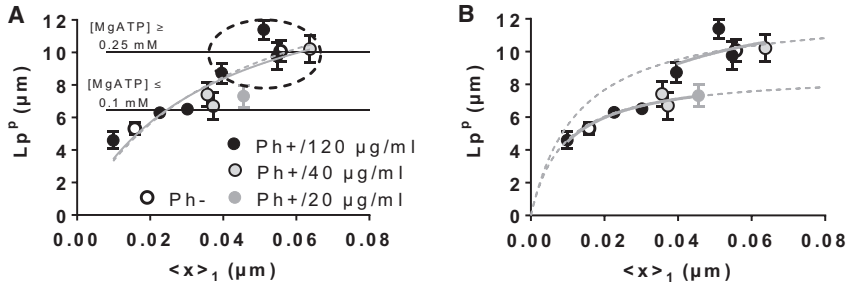


FIGURE 6 Experimental path persistence lengths versus the calculated average sliding distance $<x>_1$ between subsequent myosin head attachments. Solid symbols: with phalloidin (Ph+). Open clear symbols: without phalloidin (Ph−). (*A*) Assumptions that $V_{xb} = 0$ (*black horizontal lines*) or that there is one value of both V_{xb} and Lp^f that is independent of [MgATP] (*gray curved lines*). Black horizontal lines represent the mean value ($Lp^p = Lp^f$ in Eq. 2) of data points at [MgATP] $\geq$ 0.25 mM (data within *dashed ellipse*) and [MgATP] $\leq$ 0.1 mM, respectively. Gray lines represent fits to all data using one value of both V_{xb} and Lp^f, either including the data without phalloidin (*dashed line*) or not (*solid line*). (*B*) Fits of Eq. 2 to the same data as in (*A*) under the assumption that the Lp^f values are different at [MgATP] $\geq$ 0.25 mM and [MgATP] $\leq$ 0.1 mM (*dashed and solid gray lines*). Dashed gray lines represent fits limited to experiments in the presence of phalloidin (Ph+), with the numerical value of V_{xb} obtained from the fit at [MgATP] $\leq$ 0.1 (*lower curve*) and then fixed at this value when fitting Eq. 2 for [MgATP] $\geq$ 0.25 mM (*upper curve*). Solid gray lines represent fits to Ph− and Ph+ data obtained with both Lp^f and V_{xb} varied at [MgATP] $\leq$ 0.1 mM and [MgATP] $\geq$ 0.25. Each experimental point (mean $\pm$ 95% CI) was obtained by fitting Eq. 1 to the CCF for >200 independent filament paths. HMM incubation concentration: 120 μg/mL (*black*), 40 μg/mL (*light gray in black circles*), or 20 μg/mL (*dark gray*). For details on the fits, see text and Table S2.

on 2) an additional reduction of Lp^p with reduced [MgATP] due to more myosin head attachments per sliding distance ($V_{xb} > 0$). Based on these assumptions, we first fitted Eq. 2 to all of the data obtained at [MgATP] $\leq$ 0.1 mM, including all HMM incubation concentrations (20–120 μg/mL; cf. Fig. 4). The resulting fit (Fig. 6 *B*) was excellent, giving $Lp^f = 8.69 \pm 1.33$ μm (mean $\pm$ 95% CI) and $V_{xb} = 0.0010 \pm 0.0005$. Also, the data point obtained in the absence of phalloidin fell on the line even though it was not included in the fitting procedure. If we then fixed the value of V_{xb} at 0.0010, assuming that this parameter is independent of [MgATP], we obtained a good fit at [MgATP] $\geq$ 0.25 mM with $Lp^f = 12.7 \pm 1.7$ μm. When we instead allowed V_{xb} to vary in the fitting procedure, also at high [MgATP] and including the data point in the absence of phalloidin, we obtained the following parameter values at [MgATP] $\geq$ 0.25 mM (*solid gray lines* in Fig. 6 *B*): $Lp^f = 13.9 \pm 16.4$ μm $V_{xb} = 0.0014 \pm 0.0045$. Whereas these values have appreciable uncertainties, the similarity of the mean V_{xb} value to that obtained at low [MgATP] is consistent with the idea that the numerical value of V_{xb} is independent of $<x>_1$. One may relate the numerical value to real structural changes by realizing that $V_{xb} = 0.001$ corresponds to a standard deviation of 0.03 rad, i.e., a root mean-square change in filament angular direction of 1.8° per myosin head attachment.

Based on the Akaike criterion (see above), two different models at [MgATP] $\geq$ 0.25 mM and [MgATP] $\leq$ 0.1 mM (Fig. 6 *B*) are 13 times more likely to be correct than one given model at different [MgATP] (*gray line* in Fig. 6 *A*). This is in agreement with the overlap of the 95% CIs of 10 out of 12 of the individual data points with the lines representing two models (Fig. 6 *B*), but an overlap with the gray line (one model) in Fig. 6 *A* in only six out of 12 cases. Additionally, the variances of the vertical deviations between the data and the one-model (*gray*, Fig. 6 *A*) and two-model (*blue*, Fig. 6 *B*) fits were 1.15 and 0.753, respectively, i.e., appreciably lower for the two-model case (see Table S2).

As illustrated in Fig. 2 (see also (5,21)), phalloidin increases the flexural rigidity of actin filaments observed floating in solution between two narrowly spaced (<5 μm) coverslips. However, the differences between path persistence lengths in the presence and absence of phalloidin under otherwise similar conditions are considerably smaller (Fig. 1) (5). Therefore, data obtained in the presence and absence of phalloidin fit into the same general picture when a range of conditions are considered as in Fig. 6.

We also attempted to account for the data in Fig. 6 by assuming that the [MgATP] dependence is solely due to the [MgATP] dependence of V_{xb}, i.e. assuming that Lp^f is independent of [MgATP]. However, we obtained poorer fits to the experimental data regardless of whether we assumed a stepwise change of V_{xb} as a function of [MgATP] or a continuous change as a function of $<x>_1$ (Fig. S10).

To summarize, the analyses in Figs. 6 and S10 suggest that 1) different Lp^f values at [MgATP] $\leq$ 0.1 mM (low Lp^f) and [MgATP] $\geq$ 0.25 mM (high Lp^f), and 2) [MgATP]-independent bending of the actin filament upon each myosin head attachment.

DISCUSSION

Key findings in relation to previous work

A central finding of this work was the substantial reduction of Lp^p upon a decrease of [MgATP] to $\leq$0.1 mM. This effect was considerably greater than the decrease in the flexural rigidity (Lp^f) of phalloidin-stabilized actin filaments upon HMM binding in solution. The effect of reduced [MgATP] on Lp^p is not attributed to nonthermal contributions of a type considered recently (34,46). The results we obtained with NEM-HMM instead suggest that such contributions with anomalous filament curvatures (34) are associated with an inhomogeneous HMM population with a high

ratio of statically noncycling to cycling myosin heads. This idea is consistent with the virtual disappearance of anomalous curvatures at low [MgATP]. Under these conditions, the number of cycling myosin heads attached at each given point in time is increased (35) compared with the situation at high [MgATP], whereas the number of dead, rigor-like, nonfunctional heads is not. This increased fraction of cycling heads also explains the larger fraction of motile filaments at low [MgATP].

After considering recently raised issues (34,46) and experimental complications (Figs. 1, 3, 4, and S2–S6), we focused on mechanisms that seem to provide the simplest explanations for the low Lp^p at low [MgATP]. First, the results in Fig. 6 are consistent with two different structural states of the actin filament in the IVMA, with a switch between these states occurring between 0.1 and 0.25 mM MgATP, possibly due to global, cooperative changes in the entire actin filament structure. This is in agreement with previous evidence for different actin filament structural states (7,12,13,24) with cooperative switching between them (1,24,51). Superimposed on the stepwise transition between 0.1 and 0.25 mM MgATP, there was a graded reduction in Lp^p with reduced [MgATP]. The latter effect was correlated with the number of myosin head attachments per sliding distance at the actin filament front (Fig. 6), as well as to the average density of the myosin heads along the filament. One possible basis for this effect is local structural changes (7), e.g., local stochastic bending or local conformational changes in F-actin structure, associated with each myosin head binding independently of the MgATP concentration (Fig. S8). This idea is consistent with the good fits of Eq. 2 to the data obtained by assuming two different Lp^f values but one given value of V_{xb} (Fig. 6 *B*). We also tested alternative models (Fig. 6) that did not involve a change in Lp^f upon reduced [MgATP]. However, none of these models gave as good fit to the data as that obtained with two different Lp^f values at high and low [MgATP].

The results accord with three different structural states of the actin filaments (Fig. S10). These states are characterized by low (8–9 μm), intermediate (~10 μm), or high (>~12 μm) persistence lengths. The state with the highest rigidity exists only in the presence of phalloidin and the absence of myosin binding (Fig. 2; see (5) for details), whereas the state with the lowest flexural rigidity is observed at low [MgATP] in the IVMA and with HMM in solution in the absence of MgATP. The possibility that the state is mechanically similar to that observed upon cofilin binding (22) and strong binding of a number of side-attached actin-binding proteins on a surface (23) needs further consideration.

Possible role of two myosin heads during HMM-induced sliding at low [MgATP]

One may consider the idea that both heads of a given HMM molecule bind sequentially during in vitro sliding at low [MgATP], possibly associated with bending of the filament to accommodate the two heads sterically. Such bending would contribute to the low Lp^p value at low [MgATP]. However, there is previous evidence against two-headed binding under these conditions, based on perfect hyperbolic fits of velocity-[MgATP] data (35). Nor do the data presented here suggest that two-headed binding plays a role. If such binding appreciably contributes to a lowered path persistence length in the motility assay at low [MgATP], one would expect a progressive increase of the effect when [MgATP] is reduced from 0.1 to 0.01 mM. Under these conditions, there would thus be one effect due to the increased number of two-headed attachments and another effect due to the increased number of attachments per sliding distance. We found that the latter effect is sufficient to explain the change in Lp^p in the range of [MgATP] from 0.01 to 0.1 mM (*lower curve* in Fig. 6 *B*). Further, if two-headed binding is important, it would occur only in a fraction of the binding events. As such, it would be expected to cause a double-Gaussian distribution of angular updates in the sliding direction, as observed in the presence of NEM-HMM but not at low [MgATP].

Mechanisms underlying the [MgATP] dependence of Lp^f

Changes in the dominant myosin state (7,12,13) or changes in filament tension alone (52–54) may modify the actin filament structure and affect the flexural rigidity. Therefore, we sought to determine how the predominant chemomechanical actin-myosin states in the IVMA differed at [MgATP] $\leq$ 0.1 mM and [MgATP] $\geq$ 0.25 mM. To that end, we used a recent cross-bridge model (35) that accounts well for a range of experimental findings. Both versions of this model, with linear and nonlinear cross-bridge elasticity, predict that the total fraction of attached myosin heads exhibits an accelerated increase below 0.25 mM MgATP. Furthermore, the fraction of heads in the nucleotide-free state (the AM-state) is predicted to increase above ~50% in the range of 0.1–0.25 mM MgATP. In this context, it is of interest to note that the actin-attacked myosin heads in the model (35) exhibit a wide range of strains, causing local forces on the actin filament (Fig. S9 *C*). This leads us to hypothesize that nucleotide-free AM states exerting a spectrum of forces on the filament, including compressive forces, are mechanistically important for the high-flexibility state at low [MgATP]. However, importantly, as argued above, this effect is not a complication attributed to buckling effects. Instead (see also (5,31,33)), we believe that structural changes at the myosin-binding region of actin allosterically affect nearby filament segments, including the myosin-free and tension-free leading end, reducing the flexural rigidity of this segment.

The idea that compressive forces due to myosin heads in the AM state are important for reducing Lp^f is consistent

with the finding that HMM binding to actin filaments in solution (with some interhead strain) in the absence of MgATP reduces Lp^f, whereas binding of myosin subfragment 1 (one-headed) (10) does not. The idea also fits with the similarity of the Lp^f value at low [MgATP] in the IVMA (from the analysis in Fig. 6) to the Lp^f value of actin filaments floating in solution in the presence of HMM without MgATP (Fig. 5 *C*). In both cases, the AM state dominates and there are compressive forces due either to interhead strain (in solution) or strain due to myosin heads in the postpowerstroke state that counteract propulsive forces by other heads.

Large-amplitude bending events, as observed by us and others (6,10) in the presence of HMM and MgATP in solution, occur with very sparse myosin head binding (cf. Table S3), and various other complexities affect the interpretation (see above and (10)). Nevertheless, one may argue that similar bending events are important in the IVMA. However, given the large amplitude of the bending events in solution and the considerably higher myosin head density in the motility assay, one would then expect the Lp^p to be appreciably lower than the Lp^f. This is in direct conflict with what we observed for phalloidin-free filaments (Fig. 2).

Functional significance and relevance for nanotechnological applications

MgATP concentrations of $\leq$0.1 mM are unlikely to be relevant in cells even under severely fatiguing conditions or hypoxia (55), arguing against adaptive values of the increased flexibility of actin filaments at low [MgATP]. However, one possibility that deserves to be tested in future studies is that this property has been retained during evolution (56) from nonmuscle to muscle actin isoforms. In this context, it is of interest to note that nonmuscle myosin II exhibits low physiological velocities ($<$1 μm/s) and slow detachment kinetics similar to those of fast skeletal myosin II at low [MgATP] (57). Furthermore, in the same context, it is of interest to note that actin filament disassembly (3) due to interaction with nonmuscle myosin II at the trailing end of nonmuscle cells seems to be important for normal motility of nonmuscle cells. Such disassembly would be facilitated by a reduced filament flexural rigidity, as was recently noted in the presence of cofilin (58). Disassembly is actually also observed (59) in the IVMA when actin filaments are propelled by fast skeletal muscle HMM at [MgATP] $\leq$ 0.1 mM (see also Fig. 1).

The data presented here extend our knowledge (5,60) about how experimental conditions (e.g., filament length, [MgATP], dead myosin heads, and [HMM]; cf. Figs. 1, 2, 3, 4, and 5) affect the path persistence length and path curvature of HMM-propelled filaments. This is important for nanotechnological applications of actin and myosin, such as biosensing (61,62) and parallel computation (63), due to the central role of Lp^p in determining how effectively myosin-propelled actin filaments are guided through nanofabricated networks (32,46,61,64).

CONCLUSIONS

We have further validated a recently developed approach (5,30,31,33) to obtain the actin filament flexural rigidity from the path persistence length, and demonstrated that it provides access to conditions that may not be readily probed otherwise. Using this approach, we have provided evidence for three different actin filament flexibility states, the most flexible of which becomes significantly populated during myosin-induced actin filament sliding at low [MgATP]. The results are in accordance with the idea that actin filaments dynamically switch between a range of structural states depending on, e.g., the imposed tension and binding of myosin heads in the different states. Furthermore, the effect of altered distance between subsequent myosin attachment points suggests that long-range cooperative structural changes are superimposed on short-range changes associated with the attachment of each myosin head. The results also shed light on recently studied phenomena that suggest nonthermal contributions to the filament paths (34). Finally, the data relate to important physiological phenomena and are of value for nanotechnological applications using actin and myosin.

SUPPORTING MATERIAL

Supporting Materials and Methods, ten figures, three tables, and seven movies are available at http://www.biophysj.org/biophysj/supplemental/S0006-3495(16)30747-0.

AUTHOR CONTRIBUTIONS

A.M. designed and conceived the study. E.B., M.P., H.T., M.A.R., and S.K. performed experiments. E.B., M.A.R., and A.M. analyzed data. A.M., E.B., M.P., H.T., M.A.R., and S.K. wrote the manuscript.

ACKNOWLEDGMENTS

We thank Professor S. Tågerud, Dr. M. Bergström, and Dr. S. Karlsson (Linnaeus University) for valuable comments and suggestions, particularly pertaining to methodological issues but also to other aspects of this work. We also thank Dr. T. Korten (Technische Universität Dresden) for advice on surface functionalization.

This work was funded by the Swedish Research Council (projects Nos. 621-2010-5146 and 2015-05290), the Carl Trygger Foundation, the Crafoord Foundation, the faculties of Natural Sciences and Engineering and Health and Life Sciences at Linnaeus University, and the European Union, Future and Emerging Technologies Program within the Seventh Framework Program, grant agreement number 613044 (ABACUS). A.M. is a cofounder, co-owner, and CEO of the startup company ActoSense Biotech AB (Kalmar, Sweden), which aims to develop diagnostic devices based on the aggregation of cytoskeletal elements, particularly actin filaments. A.M. also holds two Swedish patents, one U.S. patent (U.S. 8658 381), and one European Union patent (EP 2 092 343) in this field.

SUPPORTING CITATIONS

References (65–70) appear in the Supporting Material.

REFERENCES

1. Galkin, V. E., A. Orlova, and E. H. Egelman. 2012. Actin filaments as tension sensors. *Curr. Biol.* 22:R96–R101.
2. Pollard, T. D., and J. A. Cooper. 2009. Actin, a central player in cell shape and movement. *Science.* 326:1208–1212.
3. Wilson, C. A., M. A. Tsuchida, …, J. A. Theriot. 2010. Myosin II contributes to cell-scale actin network treadmilling through network disassembly. *Nature.* 465:373–377.
4. Geeves, M. A., and K. C. Holmes. 2005. The molecular mechanism of muscle contraction. *Adv. Protein Chem.* 71:161–193.
5. Vikhorev, P. G., N. N. Vikhoreva, and A. Månsson. 2008. Bending flexibility of actin filaments during motor-induced sliding. *Biophys. J.* 95:5809–5819.
6. Yanagida, T., M. Nakase, …, F. Oosawa. 1984. Direct observation of motion of single F-actin filaments in the presence of myosin. *Nature.* 307:58–60.
7. Prochniewicz, E., T. F. Walseth, and D. D. Thomas. 2004. Structural dynamics of actin during active interaction with myosin: different effects of weakly and strongly bound myosin heads. *Biochemistry.* 43:10642–10652.
8. Kozuka, J., H. Yokota, …, T. Yanagida. 2006. Dynamic polymorphism of single actin molecules in the actin filament. *Nat. Chem. Biol.* 2:83–86.
9. Orlova, A., and E. H. Egelman. 1993. A conformational change in the actin subunit can change the flexibility of the actin filament. *J. Mol. Biol.* 232:334–341.
10. Le Goff, L., F. Amblard, and E. M. Furst. 2002. Motor-driven dynamics in actin-myosin networks. *Phys. Rev. Lett.* 88:018101.
11. Tsaturyan, A. K., N. Koubassova, …, S. Y. Bershitsky. 2005. Strong binding of myosin heads stretches and twists the actin helix. *Biophys. J.* 88:1902–1910.
12. Prochniewicz, E., H. F. Chin, …, E. M. De La Cruz. 2010. Myosin isoform determines the conformational dynamics and cooperativity of actin filaments in the strongly bound actomyosin complex. *J. Mol. Biol.* 396:501–509.
13. Tokuraku, K., R. Kurogi, …, T. Q. Uyeda. 2009. Novel mode of cooperative binding between myosin and Mg2+ -actin filaments in the presence of low concentrations of ATP. *J. Mol. Biol.* 386:149–162.
14. Diensthuber, R. P., M. Müller, …, D. J. Manstein. 2011. Phalloidin perturbs the interaction of human non-muscle myosin isoforms 2A and 2C1 with F-actin. *FEBS Lett.* 585:767–771.
15. Drummond, D. R., M. Peckham, …, D. C. White. 1990. Alteration in crossbridge kinetics caused by mutations in actin. *Nature.* 348:440–442.
16. Yanagida, T., and F. Oosawa. 1975. Effect of myosin on conformational changes of F-actin in thin filament in vivo induced by calcium ions. *Eur. J. Biochem.* 56:547–556.
17. Miki, M., P. Wahl, and J. C. Auchet. 1982. Fluorescence anisotropy of labeled F-actin: influence of divalent cations on the interaction between F-actin and myosin heads. *Biochemistry.* 21:3661–3665.
18. Oosawa, F., and S. Asakura. 1975. Thermodynamics of the Polymerization of Protein. Academic Press, New York.
19. Bugyi, B., G. Papp, …, M. Nyitrai. 2006. Formins regulate actin filament flexibility through long range allosteric interactions. *J. Biol. Chem.* 281:10727–10736.
20. Gittes, F., B. Mickey, …, J. Howard. 1993. Flexural rigidity of microtubules and actin filaments measured from thermal fluctuations in shape. *J. Cell Biol.* 120:923–934.
21. Isambert, H., P. Venier, …, M. F. Carlier. 1995. Flexibility of actin filaments derived from thermal fluctuations. Effect of bound nucleotide, phalloidin, and muscle regulatory proteins. *J. Biol. Chem.* 270:11437–11444.
22. McCullough, B. R., L. Blanchoin, …, E. M. De la Cruz. 2008. Cofilin increases the bending flexibility of actin filaments: implications for severing and cell mechanics. *J. Mol. Biol.* 381:550–558.
23. Crevenna, A. H., M. Arciniega, …, D. C. Lamb. 2015. Side-binding proteins modulate actin filament dynamics. *eLife.* 4:4.
24. Galkin, V. E., A. Orlova, …, E. H. Egelman. 2010. Structural polymorphism in F-actin. *Nat. Struct. Mol. Biol.* 17:1318–1323.
25. Behrmann, E., M. Müller, …, S. Raunser. 2012. Structure of the rigor actin-tropomyosin-myosin complex. *Cell.* 150:327–338.
26. Fujii, T., A. H. Iwane, …, K. Namba. 2010. Direct visualization of secondary structures of F-actin by electron cryomicroscopy. *Nature.* 467:724–728.
27. Kron, S. J., and J. A. Spudich. 1986. Fluorescent actin filaments move on myosin fixed to a glass surface. *Proc. Natl. Acad. Sci. USA.* 83:6272–6276.
28. Kron, S. J., Y. Y. Toyoshima, …, J. A. Spudich. 1991. Assays for actin sliding movement over myosin-coated surfaces. *Methods Enzymol.* 196:399–416.
29. Nitta, T., A. Tanahashi, …, H. Hess. 2006. Simulating molecular shuttle movements: towards computer-aided design of nanoscale transport systems. *Lab Chip.* 6:881–885.
30. Bengtsson, E., M. Persson, and A. Månsson. 2013. Analysis of flexural rigidity of actin filaments propelled by surface adsorbed myosin motors. *Cytoskeleton (Hoboken).* 70:718–728.
31. Duke, T., T. E. Holy, and S. Leibler. 1995. "Gliding assays" for motor proteins: a theoretical analysis. *Phys. Rev. Lett.* 74:330–333.
32. Nitta, T., A. Tanahashi, …, H. Hess. 2008. Comparing guiding track requirements for myosin- and kinesin-powered molecular shuttles. *Nano Lett.* 8:2305–2309.
33. Takatsuki, H., E. Bengtsson, and A. Månsson. 2014. Persistence length of fascin-cross-linked actin filament bundles in solution and the in vitro motility assay. *Biochim. Biophys. Acta.* 1840:1933–1942.
34. Weber, C. A., R. Suzuki, …, E. Frey. 2015. Random bursts determine dynamics of active filaments. *Proc. Natl. Acad. Sci. USA.* 112:10703–10707.
35. Persson, M., E. Bengtsson, …, A. Månsson. 2013. Nonlinear cross-bridge elasticity and post-power-stroke events in fast skeletal muscle actomyosin. *Biophys. J.* 105:1871–1881.
36. Pardee, J. D., and J. A. Spudich. 1982. Purification of muscle actin. *Methods Enzymol.* 85:164–181.
37. Williams, D. L., Jr., L. E. Greene, and E. Eisenberg. 1988. Cooperative turning on of myosin subfragment 1 adenosinetriphosphatase activity by the troponin-tropomyosin-actin complex. *Biochemistry.* 27:6987–6993.
38. Swartz, D. R., and R. L. Moss. 1992. Influence of a strong-binding myosin analogue on calcium-sensitive mechanical properties of skinned skeletal muscle fibers. *J. Biol. Chem.* 267:20497–20506.
39. Kuhn, J. R., and T. D. Pollard. 2005. Real-time measurements of actin filament polymerization by total internal reflection fluorescence microscopy. *Biophys. J.* 88:1387–1402.
40. Sundberg, M., J. P. Rosengren, …, A. Månsson. 2003. Silanized surfaces for in vitro studies of actomyosin function and nanotechnology applications. *Anal. Biochem.* 323:127–138.
41. Papra, A., N. Gadegaard, and N. B. Larsen. 2001. Characterization of ultrathin poly(ethylene glycol) monolayers on silicon substrates. *Langmuir.* 17:1457–1460.
42. Persson, M., N. Albet-Torres, …, M. Balaz. 2010. Heavy meromyosin molecules extending more than 50 nm above adsorbing electronegative surfaces. *Langmuir.* 26:9927–9936.

43. Balaz, M., M. Sundberg, …, A. Månsson. 2007. Effects of surface adsorption on catalytic activity of heavy meromyosin studied using a fluorescent ATP analogue. *Biochemistry.* 46:7233–7251.

44. Sundberg, M., M. Balaz, …, A. Månsson. 2006. Selective spatial localization of actomyosin motor function by chemical surface patterning. *Langmuir.* 22:7302–7312.

45. Howard, J. 2001. Mechanics of Motor Proteins and the Cytoskeleton. Sinauer Associates, Sunderland, MA.

46. Ishigure, Y., and T. Nitta. 2015. Simulating an actomyosin in vitro motility assay: toward the rational design of actomyosin-based microtransporters. *IEEE Trans. Nanobioscience.* 14:641–648.

47. Timoshenko, S. P., and J. M. Gere. 1961. Theory of Elastic Stability, 2nd ed. McGraw-Hill, New York.

48. Brangwynne, C. P., F. C. MacKintosh, …, D. A. Weitz. 2006. Microtubules can bear enhanced compressive loads in living cells because of lateral reinforcement. *J. Cell Biol.* 173:733–741.

49. Cooke, R., and K. Franks. 1980. All myosin heads form bonds with actin in rigor rabbit skeletal muscle. *Biochemistry.* 19:2265–2269.

50. Uyeda, T. Q., S. J. Kron, and J. A. Spudich. 1990. Myosin step size. Estimation from slow sliding movement of actin over low densities of heavy meromyosin. *J. Mol. Biol.* 214:699–710.

51. Prochniewicz, E., Q. Zhang, …, D. D. Thomas. 1996. Cooperativity in F-actin: binding of gelsolin at the barbed end affects structure and dynamics of the whole filament. *J. Mol. Biol.* 260:756–766.

52. Uyeda, T. Q., Y. Iwadate, …, S. Yumura. 2011. Stretching actin filaments within cells enhances their affinity for the myosin II motor domain. *PLoS One.* 6:e26200.

53. Hayakawa, K., H. Tatsumi, and M. Sokabe. 2011. Actin filaments function as a tension sensor by tension-dependent binding of cofilin to the filament. *J. Cell Biol.* 195:721–727.

54. Greene, G. W., T. H. Anderson, …, J. N. Israelachvili. 2009. Force amplification response of actin filaments under confined compression. *Proc. Natl. Acad. Sci. USA.* 106:445–449.

55. Allen, D. G., and C. H. Orchard. 1987. Myocardial contractile function during ischemia and hypoxia. *Circ. Res.* 60:153–168.

56. Mounier, N., and J. C. Sparrow. 1997. Structural comparisons of muscle and nonmuscle actins give insights into the evolution of their functional differences. *J. Mol. Evol.* 44:89–97.

57. Yengo, C. M., Y. Takagi, and J. R. Sellers. 2012. Temperature dependent measurements reveal similarities between muscle and non-muscle myosin motility. *J. Muscle Res. Cell Motil.* 33:385–394.

58. McCullough, B. R., E. E. Grintsevich, …, E. M. De La Cruz. 2011. Cofilin-linked changes in actin filament flexibility promote severing. *Biophys. J.* 101:151–159.

59. Hooft, A. M., E. J. Maki, …, J. E. Baker. 2007. An accelerated state of myosin-based actin motility. *Biochemistry.* 46:3513–3520.

60. Takatsuki, H., E. Bengtsson, and A. Månsson. 2013. Flexural rigidity of actin bundles propelled by heavy meromyosin. *Biophys. J.* 104:649a.

61. Lard, M., L. Ten Siethoff, …, A. Månsson. 2013. Ultrafast molecular motor driven nanoseparation and biosensing. *Biosens. Bioelectron.* 48:145–152.

62. Korten, T., A. Månsson, and S. Diez. 2010. Towards the application of cytoskeletal motor proteins in molecular detection and diagnostic devices. *Curr. Opin. Biotechnol.* 21:477–488.

63. Nicolau, D. V., Jr., M. Lard, …, D. V. Nicolau. 2016. Parallel computation with molecular-motor-propelled agents in nanofabricated networks. *Proc. Natl. Acad. Sci. USA.* 113:2591–2596.

64. Nitta, T., and H. Hess. 2012. Effect of path persistence length of molecular shuttles on two-stage analyte capture in biosensors. *Cell. Mol. Bioeng.* 6:109–115.

65. Klinth, J., A. Arner, and A. Månsson. 2003. Cardiotonic bipyridine amrinone slows myosin-induced actin filament sliding at saturating [MgATP]. *J. Muscle Res. Cell Motil.* 24:15–32.

66. Gillespie, D. 1976. A general method for numerically simulating the stochastic time evolution of coupled chemical reactions. *J. Comput. Phys.* 22:403–434.

67. Woledge, R. C., N. A. Curtin, and E. Homsher. 1985. Energetic Aspects of Muscle Contraction. Academic Press, London.

68. Välimaa, L., K. Pettersson, …, T. Lövgren. 2004. Quantification of streptavidin adsorption in microtitration wells. *Anal. Biochem.* 331:376–384.

69. Nyitrai, M., R. Rossi, …, M. A. Geeves. 2006. What limits the velocity of fast-skeletal muscle contraction in mammals? *J. Mol. Biol.* 355:432–442.

70. Kojima, H., A. Ishijima, and T. Yanagida. 1994. Direct measurement of stiffness of single actin filaments with and without tropomyosin by in vitro nanomanipulation. *Proc. Natl. Acad. Sci. USA.* 91:12962–12966.

71. Schneider, C. A., W. S. Rasband, and K. W. Eliceiri. 2012. NIH Image to ImageJ: 25 years of image analysis. *Nat. Methods.* 9:671–675.

New agegraphic dark energy in Brans-Dicke theory with logarithmic form of scalar field

Pankaj Kumar [2], **C. P. Singh** [1]

[1,2]Department of Applied Mathematics,
Delhi Technological University
Bawana Road, Delhi-110 042, India.
[1]cpsphd@rediffmail.com
[2]pankaj.11dtu@gmail.com

arXiv:1609.02751v1 [gr-qc] 9 Sep 2016

Abstract Recently, the current authors (arXiv:gr-qc/1609.01477) have proposed and analyzed in detail the logarithmic form of Brans-Dicke scalar field ϕ as $\phi \propto ln(\alpha+\beta a)$, where α and β are positive constants, to alleviate the problems of interacting holographic dark energy models in Brans-Dicke theory. In this paper, the cosmological evolution of a new agegraphic dark energy (NADE) model within the framework of Friedmann-Robertson-Walker Universe is analyzed with the same form of scalar field in Brans-Dicke theory. We derive the equation of state parameter w_D and deceleration parameter q of NADE model. It is observed that $w_D \to -1$ when $a \to \infty$, i.e., the NADE mimics cosmological constant in the late time evolution. Indeed, due to the assumption of logarithmic form of Brans-Dicke scalar field the NADE in Brans-Dicke theory behaves like NADE in general relativity in the late time evolution. The NADE model shows a phase transition from matter dominated phase in early time to accelerated phase in late time. We further extend NADE model by including the interaction between dark matter and NADE. In this case, w_D definitely crosses the phantom divide line ($w_D = -1$) in the late time evolution. The phase transition from matter dominated to NADE dominated phase may be achieved at early stage in interacting model. Further, we show that the interacting NADE model resolves the cosmic coincidence problem as the energy density ratio may evolve sufficiently slow at present.

Keywords- New agegraphic dark energy, Brans-Dicke theory, Coincidence problem.

[1]Corresponding author

1 Introduction

The cosmological observations like type Ia supernovae [1, 2] have provided the convincing evidence that our Universe is dominated by two dark components containing dark matter (DM) and dark energy (DE). The nature of DM and DE is one of the most important issues today in modern cosmology. The dark matter plays a role in explaining galactic curves and large scale structure where as dark energy explains the present cosmic accelerated expansion of the Universe. In the literature, the accelerating cosmologies have been described by two ways : dark energy content and modified gravity. In DE models, the accelerated expansion has been explained by modifying the right-hand side of the Einstein equations, i.e., by modifying the energy-momentum tensor. The modified gravity theory corresponds to modifying the left-hand side of Einstein equations, i.e., by modifying the geometric part. We refer [3, 4] for detail study of DE models and modified gravity.

However, we are still far from a compelling theory which could explain not only the recent accelerated expansion but also the primordial cosmology, structure formation, dark matter problem etc. without facing any problem. Whatever the way we choose to explain these problems, the quantum effects should be incorporated to come up with an accurate theory of gravity. The gravity theory which incorporates the principles of quantum mechanics, known as quantum theory of gravity. Although, the quantum gravity is not a well established theory, there are some concepts which have been proposed based on the principles of quantum gravity. In this context, the holographic dark energy (HDE) and agegraphic dark energy (ADE), which contain some significant properties of the quantum gravity, have been proposed as a candidate of DE to explain the recent accelerated expansion of the Universe. These DE models are able to present a unified model of the Universe and explain some other problems of the modern cosmology like coincidence problem [5].

The HDE models are based on the holographic principle [6] and have been studied extensively in the literature [7, 8, 9, 10, 11, 12, 13, 14] . On the other hand, the ADE models are based on the quantum fluctuations of the space-time. Using the concept of quantum fluctuations of space-time, Károlyházy and his collaborators [15, 16, 17] have observed that the distance t in Minkowaski space-time can not be known to a better accuracy than

$$\delta t = \gamma\, t_p^{2/3}\, t^{1/3}, \tag{1}$$

where t_p denotes reduced Planck time and γ is a dimensionless constant of order unity. We assume $\hbar = k_b = c = 1$ throughout in this paper. Maziashvili [18, 19] has argued that the quantum energy density of the metric fluctuations of Minkowaski space-time can be estimated using the relation (1) with the time-energy uncertainty relation. Maziashvili [18, 19] and Sasakura [20] have independently obtained the energy density of metric fluctuations of Minkowaski space-time which is given by

$$\rho_D \sim \frac{1}{t_p^2 t^2} \sim \frac{M_p^2}{t^2}, \tag{2}$$

where $M_p^2 = (8\pi G)^{-1}$ represents the reduced Planck mass. This energy density can be viewed as the density of DE, i.e., the ADE. Following the line of the relations (1) and (2), Cai [21] proposed the original ADE model in which the energy density of the ADE has the form

$$\rho_D = \frac{3n^2 {M_p}^2}{T^2}, \tag{3}$$

where T is age of the Universe. The numerical factor $3n^2$ has been introduced to parameterize some uncertainties like the species of quantum fields in the Universe, the effects of curved space-time, etc. A number of papers on ADE models are available which deal with various aspects of the evolution of the Universe [22, 23, 24, 25, 26]. Wei and Cai [27] have proposed

a new version of this model referred as "new agegraphic dark energy" model, abbreviated as NADE by replacing the cosmic age T with the cosmic conformal age η for the time scale in (3). Thus, in this model, the dark energy density is of the form

$$\rho_D = 3n^2 M_p^2 \, \eta^{-2}, \tag{4}$$

where the conformal time η is defined as

$$\eta = \int_0^t \frac{dt}{a} = \int_0^a \frac{da}{Ha^2}, \tag{5}$$

where a is the scale factor of the Universe and $H = \dot{a}/a$ is the Hubble parameter. Here, an overdot denotes derivative with respect to the cosmic time t. The most attractive merit of the NADE is that it has been proven to fit the data well. The cosmological constraints and other aspects of NADE models have been studied in the literature [28, 29, 30, 31].

The Brans-Dicke (BD) theory [32], which is a natural alternative and simple generalization of general relativity, provides a suitable framework for dynamical DE models. In this theory, the gravitational constant G is replaced with the inverse of a time-dependent BD scalar field ϕ, namely, $\phi = (8\pi G)^{-1}$ which couples to gravity with a coupling parameter w. One important property of BD theory is that it gives simple expanding solutions for scalar field and scale factor which are compatible with the solar system observations. The BD theory explains the recent accelerated expansion of the Universe and accommodates the observational data as well [33, 34, 35].

In the BD theory, the NADE models have been studied to discuss the recent accelerated expansion of the Universe [36, 37, 38, 39]. To the best of our knowledge in all the papers available in the literature on HDE, ADE and NADE models in the framework of BD theory, it has been assumed that the BD scalar field evolves as a power law of scale factor, $\phi \propto a^m$, m is a constant. In our previous paper [40], we have discussed the drawback of this relation of BD scalar field in BD theory. One can observe that this relation would always give the constant deceleration parameter (DP) irrespective of the matter content. This means that the phase transition of the Universe can not be obtained with the power-law form of BD scalar field. Therefore, to over come from this problem we have proposed a new relation between BD scalar field and scale factor, namely, a logarithmic form $\phi \propto ln(\alpha + \beta a)$ which is free from this problem. In the paper we have demonstrated that the logarithmic form of BD scalar field is not only suitable to explain the phase transition of the Universe but also it resolves the cosmic coincidence problem in an effective way.

As the logarithmic form of BD scalar field presents some interesting results in HDE model, therefore, it is worthwhile to discuss the evolution of the NADE model with this form. In this paper, we extend our previous work to analyze the evolution of the Universe in the NADE model in BD theory with the logarithmic form of BD scalar field. We derive the equation of state (EoS) parameter w_D and DP q of NADE model to discuss the evolution of the Universe. We further extend NADE model by including the interaction between dark matter and NADE in BD theory. We show that the interacting NADE model resolves the cosmic coincidence problem as the energy density ratio may evolve sufficiently slow at present.

The paper is organized as follows: In section 2, we present the equations of motion of NADE model in the framework of BD theory. Further, section 2 is divided into two subsections 2.1 and 2.2. In subsection 2.1, we discuss the non-interacting NADE model. Subsection 2.2 is devoted to interacting NADE model. The summary of our findings is presented in section 3.

2 NADE in BD theory with logarithmic scalar field

The action for the BD theory in the Jordan frame is given by

$$S = \int d^4x\sqrt{-g}\left[\frac{1}{2}(-\phi R + \frac{\omega}{\phi} g^{\mu\nu}\partial_\mu\phi \, \partial_\nu\phi) + \mathcal{L}_m\right], \tag{6}$$

where R, g and $\mathcal{L}_m$ represent the Ricci scalar curvature, determinant of the metric tensor $g_{\mu\nu}$ and the matter Lagrangian density, respectively. Here, ϕ and ω denote BD scalar field and BD coupling parameter, respectively. In this theory, the Newtonian constant G is replaced with a time dependent scalar field ϕ such that $\phi = (8\pi G)^{-1}$. The dimensionless parameter ω is introduced to represent a coupling between scalar field and gravity. In Jordan frame, the scalar field and matter field do not interact and matter minimally couples to the metric.

We assume a homogeneous and isotropic FRW space-time to discuss the evolution of the Universe. The FRW line element is given by

$$ds^2 = dt^2 - a^2(t)\left[\frac{dr^2}{1-kr^2} + r^2(d\theta^2 + \sin^2\theta\, d\phi^2)\right], \tag{7}$$

where a is the cosmic scale factor and k is curvature parameter. The curvature parameter has three possible values $k = -1, 0, 1$ which represent to open, flat and closed geometry of the Universe, respectively. We assume that the Universe is filled with pressureless dark matter (DM) and NADE. We exclude baryonic matter and radiation due to their negligible contribution to total energy budget in the late time evolution.

The variation of the action (6) with respect to the metric tensor, $g_{\mu\nu}$ for the line element (7) yield the following field equations.

$$H^2 + \frac{k}{a^2} + H\frac{\dot{\phi}}{\phi} - \frac{\omega}{6}\frac{\dot{\phi}^{\,2}}{\phi^{\,2}} = \frac{\rho_m + \rho_D}{3\phi}, \tag{8}$$

$$2\frac{\ddot{a}}{a} + H^2 + \frac{k}{a^2} + 2H\frac{\dot{\phi}}{\phi} + \frac{\omega}{2}\frac{\dot{\phi}^{\,2}}{\phi^{\,2}} + \frac{\ddot{\phi}}{\phi} = -\frac{p_D}{\phi}, \tag{9}$$

$$\ddot{\phi} + 3H\dot{\phi} = \frac{\rho_m + \rho_D - 3p_D}{2\omega + 3}, \tag{10}$$

where ρ_m and ρ_D denote the energy density of DM and NADE respectively, and p_D is the pressure of NADE. The Eq. (10) is known as the wave equation of the BD scalar field.

Let us assume the relation between BD scalar field and scale factor as [40]

$$\phi = \phi_0\, ln(\alpha + \beta a), \tag{11}$$

where ϕ_0, $\alpha > 1$ and $\beta > 0$ are constants. Substituting (11) into (8) we find

$$H^2\left(1 + \frac{k}{a^2} + \frac{\beta a}{(\alpha+\beta a)\, ln(\alpha+\beta a)} - \frac{w}{6}\frac{\beta^2 a^2}{(\alpha+\beta a)^2\, \{ln(\alpha+\beta a)\}^2}\right) = \frac{\rho_m + \rho_D}{3\phi}. \tag{12}$$

It is easy to observe from the Friedmann equation (12) in BD theory that the standard cosmology of GR will be recovered in the limit of $\beta \to 0$.

In BD theory, the BD scalar field is taken as $\phi = (8\pi G)^{-1}$ which implies $\phi = M_p^2$. Therefore, in this theory the energy density of NADE in (4) is now becomes

$$\rho_D = 3n^2\phi\, \eta^{-2}. \tag{13}$$

The critical energy density ρ_{cr} and energy density of the curvature ρ_k can be defined as follows

$$\rho_{cr} = 3\phi H^2, \qquad \rho_k = 3k\phi a^{-2}. \tag{14}$$

It has been observed that the representation of quantities and equations in the terms of fractional energy densities are useful from the point of view of calculation as well as from the point of view of physical interpretation of the results. The fractional energy densities can be defined in their usual forms as

$$\Omega_m = \frac{\rho_m}{\rho_{cr}} = \frac{\rho_m}{3\phi H^2}, \tag{15}$$

$$\Omega_D = \frac{\rho_D}{\rho_{cr}} = \frac{n^2}{\eta^2 H^2}, \tag{16}$$

$$\Omega_k = \frac{\rho_k}{\rho_{cr}} = \frac{k}{a^2 H^2}. \tag{17}$$

In what follows, we consider the non-interacting and interacting NADE models, and discuss their physical behaviors.

2.1 Non-interacting NADE model

Let us assume that DM and NADE do not interact and their energy densities follow the conservation equations

$$\dot{\rho}_m + 3H\rho_m = 0, \tag{18}$$

$$\dot{\rho}_D + 3H(1 + w_D)\rho_D = 0, \tag{19}$$

where $w_D = p_D/\rho_D$ denotes the equation of state (EoS) parameter of NADE. Using (11), (13) and (16) in the conservation equation (19), one can find the value of w_D as

$$w_D = -1 - \frac{\beta a}{3(\alpha + \beta a)\, ln(\alpha + \beta a)} + \frac{2}{3na}\sqrt{\Omega_D}. \tag{20}$$

It is to be noted that the EoS parameter w_D of NADE given by (20) reduces to its respective form in GR [22] for $\beta = 0$, that is,

$$w_D = -1 + \frac{2}{3na}\sqrt{\Omega_D}. \tag{21}$$

From (21) we observe that the w_D does not cross the phantom divide line $w_D = -1$ in the framework of GR.

Let us examine the behavior of the term $\frac{\beta a}{(\alpha+\beta a)\, ln(\alpha+\beta a)}$ present in (20) to discuss the behavior of w_D. We observe that the term $\frac{\beta a}{(\alpha+\beta a)\, ln(\alpha+\beta a)}$ is zero at $a = 0$, achieves its maximum value during the evolution, and converges to zero as $a \to \infty$ in the late time evolution . The maximum value of the term $\frac{\beta a}{(\alpha+\beta a)\, ln(\alpha+\beta a)}$ lies in the interval]0, 1[depending on the value of α. We observe that $\max\{\frac{\beta a}{(\alpha+\beta a) ln(\alpha+\beta a)}\} \to 1$ as $\alpha \to 1$ and for large value of α we get a small maximum value of the term. It is to be noted that the maximum value does not depend on the value of β. The time when the term will attain its maximum value depends on the values of α and β. For a large value of α, it occurs in the late time and for a large value of β, it will occur in the early time, and vice-versa.

Now, from (20) we observe that $w_D \to -1$ in the late time as the last two terms converge to zero, i.e., the NADE mimics the cosmological constant in the late time evolution. Wei and Cai [22] have also observed in GR that NADE mimics cosmological constant in the late time evolution. Indeed, the NADE with logarithmic form of BD scalar field in the BD theory behaves like NADE in GR in the late time evolution due to the term $\frac{\beta a}{(\alpha+\beta a) ln(\alpha+\beta a)}$ which converses to zero as $a \to \infty$. However, in the power law form of BD scalar field the NADE crosses the phantom divide line in the late time evolution because the second term is a constant $\frac{2m}{3}$ for power-law form $\phi \propto a^m$ [36]. It is also interesting to note that w_D may cross the phantom divide line if $\sqrt{\Omega_D} < [\frac{\beta n a^2}{2(\alpha+\beta a)\, ln(\alpha+\beta a)}]$ during the evolution but ultimately it will mimic the cosmological constant in the late time evolution. However, for a sufficiently large value of α and a sufficiently small value of n the phantom divide line crossing is not possible. If α has a small value ($\alpha \to 1$) and n a large value then the value of β is crucial to observe the phantom divide crossing and therefore for sufficiently small value of β the possibility of $w_D < -1$ may be observed.

Let us discuss the evolution of the Universe using the deceleration parameter which is

defined by $q = -\frac{a\ddot{a}}{\dot{a}^2}$. Using (11), (13), (16) and (17) in (9), the deceleration parameter q can be obtained as

$$q = \frac{1 + 3w_D\Omega_D + \Omega_k - \frac{\beta^2 a^2}{(\alpha+\beta a)^2\, ln(\alpha+\beta a)} + \frac{2\beta a}{(\alpha+\beta a)\, ln(\alpha+\beta a)} + \frac{\omega\beta^2 a^2}{2(\alpha+\beta a)^2\, \{ln(\alpha+\beta a)\}^2}}{2 + \frac{\beta a}{(\alpha+\beta a)\, ln(\alpha+\beta a)}}. \tag{22}$$

The value of BD parameter ω plays an important role in the value of q. The solar system experiment Cassini gave a very stringent high bound result on w as $|\omega| > 40000$ [41, 42]. However, the cosmological observations put relatively lower bounds on ω [43, 44, 45]. The term $\frac{\beta^2 a^2}{(\alpha+\beta a)^2\, ln(\alpha+\beta a)}$ present in (22) is zero at $a = 0$ which achieves its maximum value during the evolution and converges to zero in the late time evolution like the term $\frac{\beta a}{(\alpha+\beta a)\, ln(\alpha+\beta a)}$. The maximum value of this term lies in the interval $]0,\ 0.41[$ depending on the value of α. Due to a large value of ω suggested by the observations, the last term of the numerator in (22) containing ω will dominate in the early phase of the evolution of the Universe. Thus, we observe a positive value of q, i.e., the Universe evolves under the decelerated rate of the expansion. It means that the matter dominates the early phase of the expansion of the Universe. Thus, the NADE model with logarithmic form $\phi \propto ln(\alpha + \beta a)$ explains the matter dominated phase of the Universe. Since, in the late time evolution $w_D \to -1$, and last three terms of numerator and last term of denominator of (22) converge to zero, therefore, we obtain the late time value of q as

$$q \approx \frac{1 - 3\Omega_D + \Omega_k}{2}. \tag{23}$$

It is expected that $\Omega_D \to 1$ in the late time evolution. There are three possibilities for Ω_k: (i) $\Omega_k > 0$ for close Universe ($k > 0$), (ii) $\Omega_k = 0$ for flat Universe ($k = 0$), and (iii) $\Omega_k < 0$ for open Universe ($k < 0$). However, the observations suggest that our Universe is almost flat ($k \approx 0$) at present time. Therefore, if we take $k = 0$, i.e., $\Omega_k = 0$ for late time evolution then we have $q \approx \frac{1-3\Omega_D}{2}$. Thus, we may obtain an accelerated expansion for $\Omega_D > 1/3$. If we take present value $\Omega_D = 0.70$ obtained by resent observations then we get $q = -0.55$ which shows the accelerated expansion. One can observe that the accelerated expansion occurs more easily if we consider the open geometry of the Universe ($\Omega_k < 0$). In the case of close Universe ($\Omega_k > 0$), the accelerated expansion is possible but a relatively large value of Ω_D is required, i.e, a large value of n^2 is required to achieve it.

So far, we have obtained decelerated expansion in the early phase of the evolution which explains the matter dominated phase and accelerated expansion in the late time evolution which explains the NADE dominated phase. Thus, the present model successfully explains the recent phase transition of the Universe from decelerated expansion to accelerated expansion. The time of phase transition depends on the values of the parameters of the model α, β, n^2 and ω. It may be observed from (22) that if phase transition occurs at time t_1 for value ω_1 then it will happen at time t_2 for ω_2 where $t_1 < t_2$ and $\omega_1 < \omega_2$. For a large value of n^2 it occurs at earlier stage. In the similar way, one can see the effects of α and β depending on their effects on the terms $\frac{\beta a}{(\alpha+\beta a)\, ln(\alpha+\beta a)}$ and $\frac{\beta^2 a^2}{(\alpha+\beta a)^2\, ln(\alpha+\beta a)}$ as discussed above.

The logarithmic form in NADE model is free from the constant deceleration parameter problem of the power-law form and explains the phase transition of the Universe in the framework of the BD theory. Thus, this form serves our propose well.

Let us discuss the cosmic coincidence problem which has not been addressed for NADE models in the framework of BD theory. Steinhardt [46] addressed first time the coincidence problem- why are the matter and DE densities comparable at present time? In the conventional ΛCDM model very specific conditions of very early Universe are required to observe the matter and DE densities of the same order today. There are two ways to resolve the coincidence problem. In one of the ways, we should observe the energy density ratio $r_0 \sim \mathcal{O}(1)$ for a wide range of the initial conditions. In the other way, either r should converse to a constant value or evolve very slowly in the late time evolution(including present time) such that $r_0 \sim \mathcal{O}(1)$.

In the ΛCDM model, the energy density ratio r evolves as $|\frac{\dot{r}}{r}|_0 = 3H_0$. Here and throughout the paper, the zero subscript denotes the present value of the quantity. Using (18) and (19) one can obtain the evolution of r as

$$\dot{r} = 3rHw_D. \tag{24}$$

As we have observed that NADE mimics cosmological constant in the late time when $a \to \infty$. Therefore, if we take $w_{D0} = -1$, we get $|\frac{\dot{r}}{r}|_0 = 3H_0$ which is same as in the ΛCDM model. Thus, there is no reduction in the acuteness of coincidence problem. However, we have a time-dependent w_D, therefore, it is possible to have a less acute coincidence problem if we have $w_{D0} > -1$. The quintessence like EoS ($w_D > -1$) may be achieved for $\sqrt{\Omega_D} > \frac{\beta n a^2}{2(\alpha+\beta a)\ ln(\alpha+\beta a)}$ as can be observed from (20). It is to be noted that Eq. (20) has a time-dependent second term which converses to zero in the late time whereas the second term is a constant in case of power-law form. Therefore, the quintessence like EoS may be achieved more easily with logarithmic form in comparison to the power-law form of BD scalar field in the present time. Thus, the logarithmic form is more suitable to achieve a less acute coincidence problem. The observations also suggest quintessence like EoS of NADE [28]. Let us assume $w_{D0} = -2/3$, we obtain $|\frac{\dot{r}}{r}|_0 = 2H_0$ which is less acute coincidence problem in comparison to the ΛCDM model. On the other hand, the problem is more acute if w_D has phantom like EoS ($w_D < -1$). In this case, the coincidence problem becomes more worse than the ΛCDM model.

In conclusion, the coincidence problem may not be resolved significantly for non-interacting NADE model in the framework of BD theory, however, there are possibilities to achieve a less acute problem. The logarithmic form of BD scalar field is more suitable to have a less acute coincidence problem than power-law form.

2.2 Interacting NADE model

A number of authors [47, 48, 49, 50, 51] have studied the interaction between DM and DE and recent cosmological observations [52, 53, 54, 55] also support it. The interacting DE models have also been studied as a possible candidate to resolve the coincidence problem [56, 57, 58]. Therefore, in this subsection we extend the NADE model by considering the interaction between DM and NADE.

Assuming that the DM and NADE exchange energy through the interaction Q, the continuity equations become

$$\dot{\rho}_m + 3H\rho_m = Q, \tag{25}$$

$$\dot{\rho}_D + 3(1 + w_D)H\rho_D = -Q. \tag{26}$$

The sign of interaction term Q is crucial and defines the direction of the energy transfer, i.e., for $Q > 0$, there is an energy transfer from NADE to DM, and for $Q < 0$, there is an energy transfer from DM to NADE. The interaction between DM and NADE is a quantum scale phenomenon, therefore, the interaction term Q should be defined by the theory of quantum gravity. We do not have a satisfactory theory of quantum gravity, therefore, the dimension of the conservation equation has been used to choose a suitable form of Q in the literature. The conservation equations of DM and NADE imply that the interaction term should has the units of energy density $\times$ $(time)^{-1}$. Therefore, we may have the interaction term of the following forms: (i) $Q \propto H\rho_D$, (ii) $Q \propto H\rho_m$ or (iii) $Q \propto H(\rho_m + \rho_D)$. In this paper, we use the last assumption which is more general than first two. This form can be rewritten as

$$Q = 3b^2H(\rho_m + \rho_D), \tag{27}$$

where b^2 is a coupling constant. Using (11), (13), (16) and (27) in (26), we get

$$w_D = -1 - b^2(1 + r) - \frac{\beta a}{3(\alpha + \beta a)\ ln(\alpha + \beta a)} + \frac{2}{3na}\sqrt{\Omega_D}. \tag{28}$$

It is easy to observe that the EoS parameter of NADE achieves its respective form in GR for $\beta = 0$. We observe that w_D contains the third term as time-dependent whereas it is constant term in this place in power-law form of BD scalar field. Therefore, the evolution of w_D in our model will be different from that of power-law form. As discussed in section 2.1, analyzing the terms in w_D in (28), one can observe that w_D will definitely cross the phantom divide in the late time evolution, where $w_D \to -1 - b^2(1+r)$ as $a \to \infty$. The interaction between DM and NADE is the deriving force behind the phantom crossing in the late time. The late time value of w_D depends on the values of coupling constant b^2 and density ratio r. It means that it depends on how DM and NADE interact and what is the ratio of their densities. In the interacting NADE model, we observe that w_D may cross the phantom divide line more easily and earlier in the framework of BD theory than GR.

The expression of q remains same as in the case of non-interacting NADE which is given by (22). However, the evolution of q is different due to different value of w_D for interacting NADE given by (28). From (20) and (28), we observe that the EoS parameter of interacting NADE has an extra term $b^2(1+r)$ with negative sign than non-interacting NADE. Therefore, it is easy to observe from (22) that the recent phase transition of the Universe from matter dominated phase to NADE dominated phase is more easily achieved and we may achieve it at earlier stage in the interacting case. Thus, the interacting NADE model explains the recent phase transition of evolution of the Universe in the framework BD theory with logarithmic form of BD scalar field.

Let us study the evolution of r to check whether the interaction between DM and NADE is able to alleviate the coincidence problem or not. Using (25), (26) and (27), the evolution of r can be obtained as

$$\dot{r} = 3rH\left[w_D + b^2\frac{(1+r)^2}{r}\right]. \tag{29}$$

Here, we have the sum of the terms w_D and $b^2\frac{(1+r)^2}{r}$ which have negative and positive value respectively. Thus, the resultant value of terms within bracket will be less than $|w_D|$. Moreover, for a suitable value of b^2, we may achieve $|w_D + b^2\frac{(1+r)^2}{r}| << |w_D|$. Now, it is evident from (24) and (29) that the energy density ratio r may evolve more slowly in interacting NADE model than the ΛCDM model and non-interacting NADE model. Therefore, the interaction between dark components of the Universe may play an important role in the explanation of the coincidence problem. To achieve a soft coincidence we should observe $|\frac{\dot{r}}{r}|_0 \leq H_0$ [59]. The condition of soft coincidence may be easily achieved in our model if b^2 satisfies the condition, $b^2 \leq \frac{(1-3w_{D0})r_0}{3(1+r_0)^2}$. If we use the present observational values $r_0 \simeq 3/7$ and $w_{D0} \simeq -1$, we obtain the constraint $b^2 \leq 7/25$ to achieve soft coincidence problem. Even for a suitably small values of b^2, r may evolve more slowly at present which may resolve the coincidence problem more effectively. For example, if we take $b^2 = \frac{1}{5}$ and $w_{D0} = -1$ then we obtain $|\frac{\dot{r}}{r}|_0 \leq \frac{H_0}{7}$ which shows significantly slow variation of r compare to conventional ΛCDM model and condition mentioned above for soft coincidence.

Feng et al. [60] found that a small coupling constant b^2 is compatible with observation and also required to alleviate the coincidence problem. It also required to satisfy the second law of thermodynamics (also, see references within [60]). We also observe that the coupling constant b^2 should be a small quantity to avoid the coincidence problem which shows the compatibility with the observations. Thus, the interaction between DM and NADE in the framework of BD theory with logarithmic BD scalar field may resolve the coincidence problem effectively.

3 Conclusion

In this paper, we have investigated how the NADE model evolves in BD theory by assuming the logarithmic form of BD scalar field. The motive is that the existing power-law form of BD scalar field, $\phi = \phi_0\, a^m$ gives a constant value of DP whatever may be the energy content.

Therefore, it can not describe the phase transition of the Universe. However, many authors have found time-dependent DP by using the same power-law form which shows a contradiction. To overcome from this problem we have recently proposed and analyzed the logarithmic form of BD scalar field, $\phi = \phi_0\, ln(\alpha+\beta a)$ in HDE model (see, Ref.[40]). This form of BD scalar field is free from the above described problem and plays an important role in explaining the evolution of the Universe. It also resolves the cosmic coincidence problem. Therefore, analyzing the importance of this form, we have extended our work to NADE model within the framework of FRW line element in BD theory. We have discussed the dynamics of non-interacting and interacting NADE models by EoS parameter w_D and DP q. We have also discussed the cosmic coincidence problem. The results of these two models are summarized as follows:

In non-interacting NADE model, we have observed that the NADE model successfully explains the recent phase transition from matter dominated to NADE dominated phase. In this model the NADE mimics cosmological constant in the late time whereas it achieves phantom like behavior for power-law form [36]. It has also been observed that w_D may cross the phantom divide line under certain constraint but ultimately it will mimic the cosmological constant in late time evolution. Further, we have shown that a less acute coincidence problem than conventional ΛCDM model may be achieved, however, it is not able to alleviate the problem effectively. The logarithmic form of BD scalar field is more suitable to achieve a less acute coincidence problem than power-law form.

In interacting NADE model, the recent phase transition from decelerated phase to accelerated phase has also been achieved. However, the accelerated expansion may be achieved earlier in this model than non-interacting model. In the late time evolution, it has been analyzed that w_D definitely crosses the phantom divide line. We have shown that the energy density ratio r may evolve sufficiently slow in the present time which resolves the coincidence problem. Thus, the interacting NADE model may be able to alleviate the coincidence problem effectively.

In conclusion, we can say that the logarithmic form of BD scalar field is suitable to explain the recent accelerated expansion of the Universe in NADE model. This model shows the phase transition of the evolution of the Universe as we get the time dependent DP. It also resolves the cosmic coincidence problem effectively. Also, in the limit $\beta \to 0$, the NADE model in general relativity is recovered.

References

[1] A.G. Riess et al., Astron. J. **116**, 1009 (1998)

[2] S. Perlmutter et al., Astrophys. J. **517**, 565 (1999)

[3] E.J. Copeland, M. Sami, S. Tsujikawa, Int. J. Mod. Phys. D **15**, 1753 (2006)

[4] K. Bamba et al., Astrophys. Space Sci., 342, 155 (2012), arXiv:gr-qc/1205.3421

[5] S. Nojiri, S.D. Odintsov, Gen. Rel. Grav. **38**, 1285 (2006), arXiv:hep-th/0506212

[6] G. 't Hooft, arXiv:gr-qc/9310026 (1993)

[7] M. Li, Phys. Lett. B **603**, 1 (2004)

[8] D. Pavón, W. Zimdahl, Phys. Lett. B **628**, 206 (2005)

[9] M.R. Setare, Phys. Lett. B **644**, 99 (2007)

[10] N. Banerjee, D. Pavón, Phys. Lett. B **647**, 477 (2007)

[11] L. Xu, W. Li, J. Lu, Eur. Phys. J. C **60**, 135 (2009)

[12] A. Sheykhi, Phys. Lett. B **681**, 205 (2009)

[13] M. Li et al., J. Cosmol. Astropart. Phys. **09**, 021 (2013)

[14] S. Ghaffari, M.H. Dehghani, A. Sheykhi, Phys. Rev. D **89**, 123009 (2014)

[15] F. Károlyházy, Nuovo. Cim. A**42**, 390 (1966)

[16] F. Károlyházy, A. Frenkel, B. Lukács, In Physics as Natural Philosophy (Eds. A. Shimony, H. Feschbach, MIT Press, Cambridge, MA, 1982)

[17] F. Károlyházy, A. Frenkel, B. Lukács, In Quantum Concepts in Space and Time (Eds. R. Penrose, C.J. Isham, Clarendon Press, Oxford, 1986)

[18] M. Maziashvili, Phys. Lett. B **652**, 165 (2007)

[19] M. Maziashvili, Int. J. Mod. Phys. D **75**, 1531 (2007)

[20] N. Sasakura, Prog. Theor. Phys. **102**, 169 (1999)

[21] R.G. Cai, Phys. Lett. B **657**, 228 (2007)

[22] H. Wei, R.G. Cai, Phys. Lett. B **665**, 1 (2007)

[23] K.Y. Kim, H. W. Lee, Y.S. Myung, Phys. Lett. B **660**, 118 (2008)

[24] I.P. Neupane, Phys. Lett. B **673**, 111 (2009)

[25] H. Wei, R.G. Cai, Eur. Phys. J. C **59**, 99 (2009)

[26] O.A. Lemets, D.A. Yerokhin, L.G. Zazunov, J. Cosmol. Astropart. Phys. **01**, 007 (2011)

[27] H. Wei, R.G. Cai, Phys. Lett. B **660**, 113 (2008)

[28] H. Wei, R.G. Cai, Phys. Lett. B **663**, 1 (2008)

[29] M.R. Setare, Astrophys. Space Sci. **326**, 27 (2010)

[30] K. Saaidi, H. Sheikhahmadi, A.H. Mohammadi, Astrophys. Space Sci. **338**, 355 (2012)

[31] J.F. Zhang, Y.H. Lee, X. Zhang, Eur. Phys. J. C **73**, 2280 (2013)

[32] C. Brans, R.H. Dicke, Phys. Rev. **124**, 925 (1961)

[33] O. Bertolami, P.J. Martins, Phys. Rev. D **61**, 064007 (2000)

[34] H. Kim, Mon. Not. R. Astron. Soc. Lett. **364**, 813 (2005)

[35] T. Clifton, J.D. Barrow, Phys. Rev. D **73**, 104022 (2006)

[36] A. Sheykhi, Phys. Rev. D **81**, 023525 (2010)

[37] A. Sheykhi, M. Jamil, Phys. Lett. B **694**, 284 (2011)

[38] A. Pasqua, S. Chattopadhyay, Astrophys. Space Sci. **348**, 284 (2013)

[39] V. Fayaz, Astrophys. Space Sci. **361**, 86 (2016)

[40] C.P.Singh, Pankaj Kumar, arXiv:1609.01477[gr-qc]

[41] B. Bertotti, L. Iess, P. Tortora, Nature **426**, 374 (2003)

[42] C. Will, Living Rev. Relativity **9**, 3 (2006)

[43] V. Acquaviva et al., Phys. Rev. D **71**, 104025 (2005)

[44] F.Q. Wu, X. Chen, Phys. Rev. D **82**, 083003 (2010)

[45] Y.C. Li, F.Q. Wu, X. Chen, Phys. Rev. D **88**, 084053 (2013)

[46] P. Steinhardt, in Critical Problems in Physics, edited by V.L. Fitch, D.R. Marlow (Princeton University Press, Princeton, NJ, 1997)

[47] L. Amendola, C. Quercellini, Phys. Rev. D **68**, 023514 (2003)

[48] W. Zimdahl, D. Pavón, Gen. Relativ. Gravit. **35**, 413 (2003)

[49] G. Farrar, P.J.E. Peebles, Astriohys. J. **604**, 1 (2004)

[50] B. Gumjudpai et al., J. cosmol. Astropart. Phys. **06**, 007 (2005)

[51] C. Skordis, A. Pourtsidou, E.J. Copeland, Phys. Rev. D **91**, 083537 (2015)

[52] G. Olivares, F. Atrio, D. Pavón, Phys. Rev. D **71**, 063523 (2005)

[53] C. Feng et al., J. Cosmol. Astropart. Phys. **09**, 005 (2007)

[54] S. Cao, N. Liang, Z.H. Zhu, Mon. Not. R. Astron. Soc. **416**, 1099 (2011)

[55] A.A. Costa et al., Phys. Rev. D **89**, 103531 (2014)

[56] M.S. Berger, H. Shojaei, Phys. Rev. D **73**, 083528 (2006)

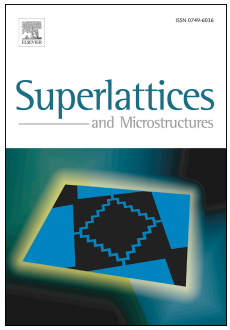
[57] S. del Campo et al., Phys. Rev. D **74**, 023501 (2006)

[58] S. del Campo, R. Herrera, D. Pavón, J. Cosmol. Astropart. Phys. **01**, 020 (2009)

[59] S. del Campo, R. Herrera, D. Pavón, Phys. Rev. D **78**, 021302 (2008)

[60] C. Feng et al., Phys. Lett B **665**, 111 (2008)

Accepted Manuscript



Numerical simulations: Toward the design of 27.6% efficient four-terminal semi-transparent perovskite/SiC passivated rear contact silicon tandem solar cell

Rahul Pandey, Rishu Chaujar

PII: S0749-6036(16)31164-8

DOI: 10.1016/j.spmi.2016.10.033

Reference: YSPMI 4578

To appear in: *Superlattices and Microstructures*

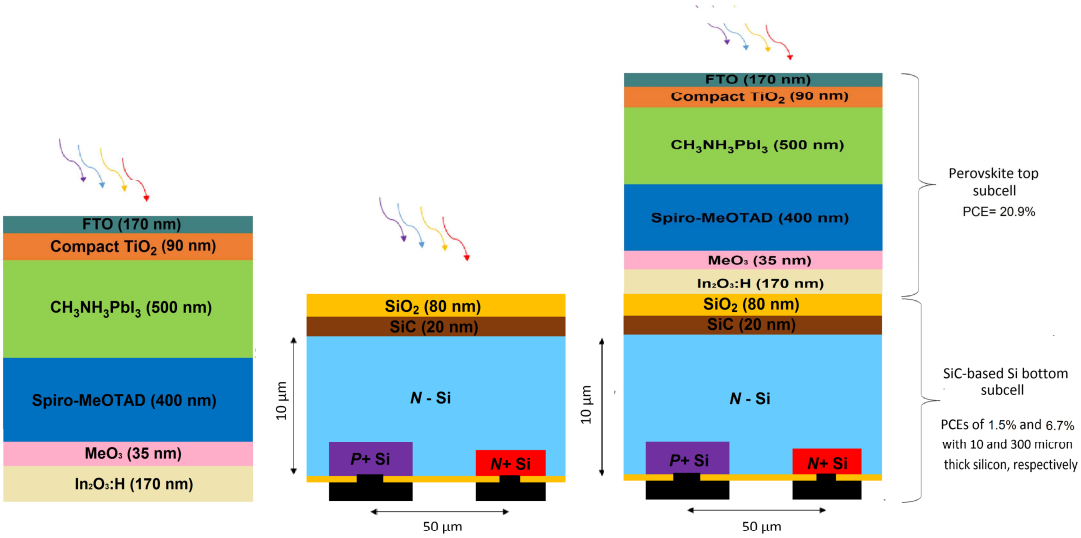
Received Date: 6 October 2016

Accepted Date: 12 October 2016

Please cite this article as: R. Pandey, R. Chaujar, Numerical simulations: Toward the design of 27.6% efficient four-terminal semi-transparent perovskite/SiC passivated rear contact silicon tandem solar cell, *Superlattices and Microstructures* (2016), doi: 10.1016/j.spmi.2016.10.033.

This is a PDF file of an unedited manuscript that has been accepted for publication. As a service to our customers we are providing this early version of the manuscript. The manuscript will undergo copyediting, typesetting, and review of the resulting proof before it is published in its final form. Please note that during the production process errors may be discovered which could affect the content, and all legal disclaimers that apply to the journal pertain.

ACCEPTED MANUSCRIPT



PCE= 20.9%

PCE= 15.3% with 10µm thick Si

PCE= 21.4% with 300µm thick Si

ACCEPTED MANUSCRIPT

Numerical simulations: Toward the design of 27.6% efficient four-terminal semi-transparent perovskite/SiC passivated rear contact silicon tandem solar cell

Rahul Pandey and Rishu Chaujar *

Department of Engineering Physics, Delhi Technological University, New Delhi, India
Shahbad Daulatpur, Main Bawana Road, New Delhi, Delhi 110042
E-mail: Rishu.phy@dce.edu*

Abstract- In this work, a novel four-terminal perovskite / SiC-based rear contact silicon tandem solar cell device has been proposed and simulated to achieve 27.6 % power conversion efficiency (PCE) under single AM1.5 illumination. 20.9% efficient semitransparent perovskite top subcell has been used for perovskite/silicon tandem architecture. The tandem structure of perovskite-silicon solar cells is a promising method to achieve efficient solar energy conversion at low cost. In the four-terminal tandem configuration, the cells are connected independently and hence avoids the need for current matching between top and bottom subcell, thus giving greater design flexibility. The simulation analysis shows, PCE of 27.6 % and 22.4 % with 300 µm and 10 µm thick rear contact Si bottom subcell, respectively. This is a substantial improvement comparing to transparent perovskite solar cell and c-Si solar cell operated individually. The impact of perovskite layer thickness, monomolecular, bimolecular, and trimolecular recombination have also been obtained on the performance of perovskite top subcell. Reported PCEs of 27.6% and 22.4% are 1.25 times and 1.42 times higher as compared to experimentally available efficiencies of 22.1% and 15.7% in 300 µm and 10 µm thick stand-alone silicon solar cell devices, respectively. The presence of SiC significantly suppressed the interface recombination in bottom silicon subcell. Detailed realistic technology computer aided design **(**TCAD) analysis has been performed to predict the behaviour of the device.

Keywords — Perovskite; organic-inorganic halide; silicon; simulation; solar cell; tandem.

1. Introduction

Refining the performance of the photovoltaic (PV) device is crucial to surge their competitiveness with a conventional source of electricity. Crystalline silicon solar cell have dominated the PV market for decades, with 90% current market share. The efficiency of the crystalline silicon solar cell has only marginally improved during the last 15 years, wafer size efficiency as high as 25.6% has been reported, which is close to the theoretical maximum efficiency of 29.4% [1, 2]. However, to make photovoltaic fully competitive with the conventional energy source, further cost effective energy efficient module is required. Therefore, to obtain the higher efficiency at lower cost Si-based tandem approaches have been proposed, which combine a silicon cell with a low-cost cell with wide-bandgap (1.6-1.9 eV) absorber material to form a tandem cell. Commonly, III-V semiconductors

have been used on the top of silicon to make a tandem cell; however, their large area production is costly and challenging [3]. The emergence of organic-inorganic halide perovskite solar cell drastically changes the situation. The methylammonium-lead-halide, $CH_3NH_3PbX_3$ (X=Br, I) perovskite has a tunable band gap, ranging from 1.6 to 2.3 eV depending on halide composition. The solar cell based on organometal halides represents an emerging photovoltaic (PV) technology. Optical absorption of methylammonium-lead-halide on nanocrystalline TiO_2 surface produces the power conversion efficiency of 3-4%, in a liquid based dye-sensitized solar cell (DSSC), as first discovered in 2009. Further by optimizing the perovskite coating condition the PCE has been doubled after 2 years. However, owing to stability issue liquid based perovskite receives little attention. In 2012, a long-term stable perovskite solar cell was developed with PCE of 10%, by substituting the solid hole conductor with liquid electrolytes. The outstanding improvement in PCE achieved in the past few years suggest that it is a capable candidate for the next-generation PV technology [4]. In the year 2015, the certified efficiency has reached 20.1% [5]. Recently, record PCEs of 20.8 % and 21.1 % have been achieved in perovskite solar cells [6, 7]. Further, in tandem based approach, 13.7% efficient 2-terminal perovskite/silicon multijunction solar cell enabled by a silicon tunnel junction has been reported [8]. Moreover, 21.2% and 19.2% efficient monolithic perovskite/silicon tandem solar cell with a cell of 0.17 cm^2 and 1.22 cm^2 respectively, have been proposed in the literature [9] and previous research work shows perovskite-based cell is a good candidate to be used in tandem configuration with silicon cell to produce an efficient cell under illumination. Moreover, this work proposes a new 4-terminal perovskite/silicon-based tandem device for energy efficient applications. The $CH_3NH_3PbI_3$ based perovskite solar cell has been used for the top subcell, and SiC passivated all back contact Si solar cell has been used for the bottom subcell. The SiC has been used to prevent the interface recombination in silicon-based bottom subcell. Tandem device investigated in this work achieves PCE of 27.6 % with 300 µm thick Si subcell and PCE of 22.4% with 10 µm thick Si subcell which is 1.25 times and 1.42 times higher as compared to experimentally available efficiencies of 22.1% and 15.7% in 300 µm and 10 µm thick stand-alone silicon solar cell devices, respectively [10, 11].

2. Device structure, models, and methods

The carrier dynamics in perovskite device can be quantitatively described by the following equation according to different recombination mechanisms:

$$\frac{dn(t)}{dt} = -Cn^3 - Bn^2 - An \qquad (1)$$

Where n (t) is the charge carrier density and *A*, *B* and *C* denotes the monomolecular, bimolecular and trimolecular recombination rate constants. Literature reports, monomolecular, bimolecular, and trimolecular recombination rate constant as SRH recombination, radiative recombination, and auger recombination coefficients, respectively [12]. With the rapid progress in perovskite-based solar cell device performance, critical studies i.e. device simulation considering the impact of the various recombination mechanisms on photovoltaic device parameters are lagging. In present work, technological computer aided design (TCAD) analysis has been done with the help of Silvaco ATLAS device simulator to study the performance of $CH_3NH_3PbI_3$ based perovskite solar cell. The parameters for each model have been calibrated according to experimentally available data as reported in [12, 13]. This results in 20.9% efficient perovskite solar cell. Fig. 1(a-c) shows the simulated device structure. Fluorine doped tin oxide has been used as a front contact for perovskite solar cell. The Compact TiO_2 is *N*-type, with doping density of 5×10^{19} cm^{-3}, whereas $CH_3NH_3PbI_3$

and Spiro-MeOTAD are *P*-type with doping density of 2.14×10^{17} cm^{-3} and 3×10^{18} cm^{-3} respectively. In a four-terminal configuration, the perovskite top subcell requires two transparent contacts. Therefore, hydrogenated indium oxide (In_2O_3: H) based rear transparent electrode has been used for perovskite solar cell as reported in [14]. For bottom silicon subcell, dimensions (46µm-wide *P*+, and 30-µm-wide *N*+) was used. The substrate was *N*-type, with doping density (3×10^{15} cm^{-3}). *P*+ region was doped with boron (4×10^{20} cm^{-3}, depth of 300 nm). *N*+ region was doped with phosphorous (1×10^{20} cm^{-3}, depth of 100 nm). The Poisson equation (2) is solved along with electron and hole continuity equation (3-4) to obtain the current density- voltage (J-V) curve. The last term in equation 3 and 4 known as recombination term R_n, R_p

$$\frac{d}{dx}\left(-\varepsilon(x)\frac{d\Psi}{dx}\right) = -q\left[\begin{matrix} n(x) - p(x) + N_a^-(x) - N_d^+(x) + \\ n_t(x) - p_t(x) \end{matrix}\right] \quad (2)$$

$$\frac{dn_p}{dt} = D_n\frac{d^2n_p}{dx^2} + n_p\mu_n\frac{d\xi}{dx} + \mu_n\xi\frac{dn_p}{dx} + G_n - \frac{n_p - n_{p0}}{\tau_n} \quad (3)$$

$$\frac{dp_n}{dt} = D_p\frac{d^2p_n}{dx^2} - p_n\mu_p\frac{d\xi}{dx} - \mu_p\xi\frac{dp_n}{dx} + G_p - \frac{p_n - p_{n0}}{\tau_p} \quad (4)$$

Where q the electron charge, D the diffusion coefficient, ε is the permittivity and G the generation rate. The $n_s, n_t p_s$ and p_t are the free electron, trapped electron, free hole, and trapped hole, respectively. ψ is the electrostatic potential. N_a^- the ionized acceptor-like doping concentration and N_d^+ are the ionized donor-like doping concentration. ξ is the electric field and τ_n, τ_p are the carrier lifetimes. Further, when models are enabled, the SRH, auger, and radiative recombination rate are included in the recombination terms in the carrier continuity equations (3-4). Perovskite cell is simulated, based on the recombination dynamics in $CH_3NH_3PbI_3$ with the help of SRH, Auger, and radiative recombination models to account monomolecular, bimolecular and trimolecular recombinations in the perovskite top subcell. Whereas concentration dependent SRH, Auger, concentration dependent mobility, and bandgap narrowing models have been used for the bottom silicon solar cell [15]. The radiative recombination model is omitted for silicon solar cell since it is an indirect bandgap semiconductor. The input parameters for perovskite cell used in simulation has been obtained from already published results [16] and shown in Table 1. The optical properties of all the materials used in the simulation are shown in Fig. 2(a-f).

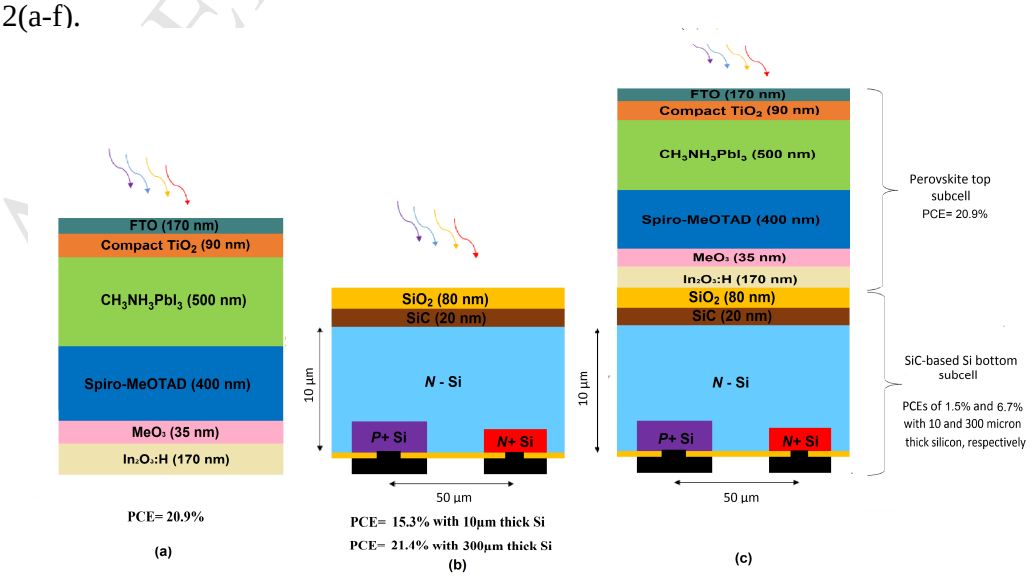


Figure 1. The device structures used in simulation: (a) perovskite top subcell with indium oxide (In_2O_3: H) as transparent rear electrode, (b) SiC-based silicon bottom subcell and (c) mechanically stacked perovskite/silicon tandem cell.

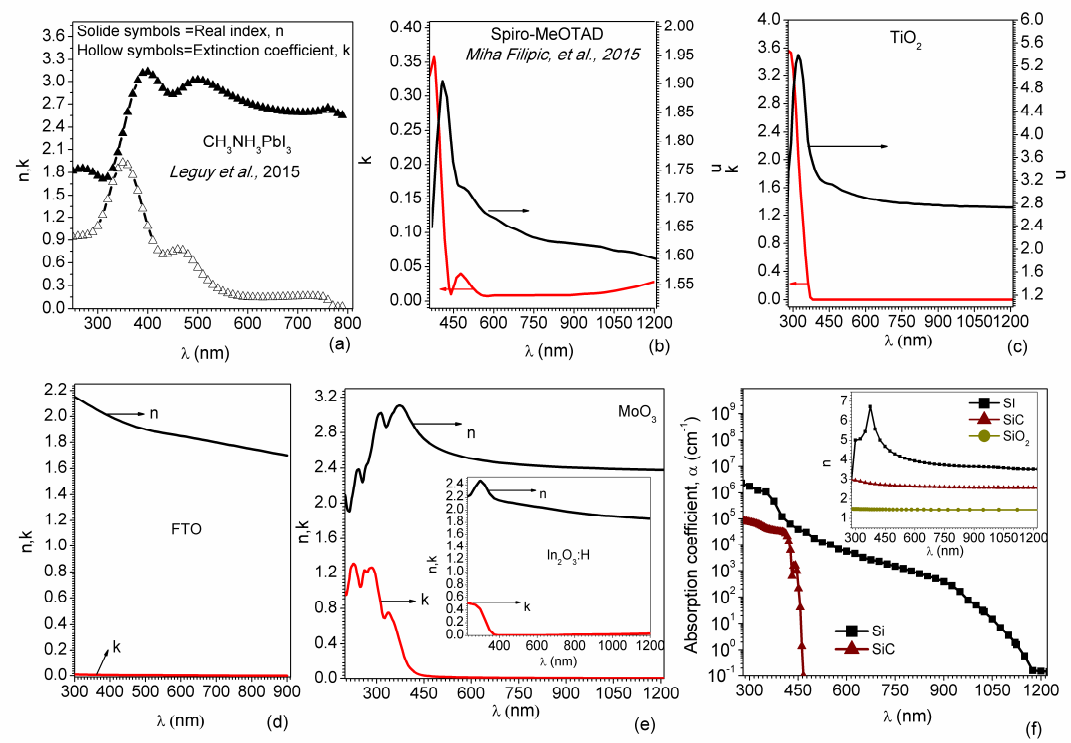


Figure 2. The optical properties used in simulation: (a) n, k of $CH_3NH_3PbI_3$ obtained from *Leguy et al., 2015 [32]*, (b) n, k of Spiro-MeOTAD obtained from *Filipic et al., 2015 [33]*, (c) n,k of TiO_2, (d) n,k of FTO, (e) n,k of MoO_3. Inset shows the n,k of In_2O_3:H and (f) absorption coefficient of silicon and SiC. Inset shows real index of Si, SiC, and SiO_2 respectively.

2.1 Recombination models

2.1.1 Shockley-Read-Hall (SRH) recombination.

The basic SRH recombination is modelled as follows:

$$R_{SRH} = \frac{pn - n_{ie}^2}{\tau_{n0}\left[p + n_{ie}\exp\left(\frac{E_i - E_t}{k_b T}\right)\right] + \tau_{p0}\left[n + n_{ie}\exp\left(\frac{E_t - E_i}{k_b T}\right)\right]} \quad (5)$$

The n_{ie} is the effective intrinsic carrier concentration and its value for perovskite and silicon are $1.97\times10^7\,cm^{-3}$ an $5.21\times10^9\,cm^{-3}$, respectively. K_b is Boltzmann's constant and E_i and E_t are the intrinsic fermi level and trap energy level, respectively. T is the lattice temperature in degree Kalvin. n and p are the electron and hole concentrations. Basic for the SRH model are the assumptions of one trap level in the forbidden band i.e. $E_t = E_i$ and corresponds to the most efficient recombination center. τ_{n0} and τ_{p0} are the electron and holes lifetimes. Also, the constant carrier lifetimes that are used in the SRH recombination model above can be made a function of doping concentration and results in concentration dependent SRH model where τ_{n0} and τ_{p0} will be replaced by τ_n and τ_p [17].

$$\tau_n = \frac{\tau_{n0}}{1 + N/N_{SRHN}},\ \tau_p = \frac{\tau_{p0}}{1 + N/N_{SRHP}} \quad (6)$$

N is the doping concentration in silicon and $N_{SRHN} = N_{SRHP} = 5\times10^{16}\,cm^{-3}$. The bulk lifetime 10^{-3} s and 10^{-5} s has been used for 300 µm and 10µm thick bottom silicon cell respectively, whereas 10^{-6} s has been used for perovskite film and the impact of a lifetime has also been obtained in the result section.

2.1.2 *Auger recombination*

Auger recombination occurs through a three particle transition whereby a mobile carrier is either captured or emitted. The underlying physics of such processes is unclear, and normally a more qualitative understanding is sufficient. Auger recombination has been modeled using the following expression:

$$R_{AUGER} = C_n\left(pn^2 - n_0 n_{ie}^2\right) + C_p\left(np^2 - p_0 n_{ie}^2\right) \qquad (7)$$

The auger coefficients, C_p=9.9x10^{-32} cm^6.s^{-1} and C_n=2.8x10^{-31} cm^6.s^{-1} have been used for *p*-type and *n*-type silicon, respectively, at 300K temperature [18]. Whereas, auger coefficient for the perovskite film has been obtained from experimental data [12, 13] and shown in Table 2. n_o, p_o are the concentration of electron and holes at equilibrium.

2.1.3 Radiative recombination

In radiative recombination, an electron loses energy on order of the band gap and moves from the conduction band to the valence band. This effect is necessary for narrow gap semiconductors and semiconductors whose specific band structure allows direct transitions. By assuming a capture rate C_c^{OPT} the partially involved process can be written as:

$$R_{np}^{OPT} = C_c^{OPT} np, \qquad (8)$$

These rates must be equal in thermal equilibrium so that

$$C_{np}^{OPT} = C_c^{OPT} n_{ie}^2 \qquad (9)$$

The total band to band recombination is the difference of the partial rates i.e.

$$R_{np}^{OPT} = C_c^{OPT}\left(np - n_{ie}^2\right) \qquad (10)$$

The radiative rate coefficient for perovskite film has been obtained from experimental data [12, 13] and shown in Table 2

2.1.4 Surface recombination

The standard method is to model interface recombination in a similar manner as the bulk generation-recombination rate. The recombination rate is an extension of the SRH model by introducing the surface recombination velocities for electrons and holes (S_{n0} or S_{p0}).

$$R_{surface} = \frac{pn - n_{ie}^2}{\tau_n^{eff}\left[p + n_{ie}\exp\left(\frac{E_i - E_t}{k_b T}\right)\right] + \tau_p^{eff}\left[n + n_{ie}\exp\left(\frac{E_t - E_i}{k_b T}\right)\right]} \qquad (11)$$

Here:

$$\frac{1}{\tau_n^{eff}} = \frac{1}{\tau_n^i} + \frac{d_i}{A_i} S_{n0} \text{ and } \frac{1}{\tau_p^{eff}} = \frac{1}{\tau_p^i} + \frac{d_i}{A_i} S_{p0} \quad (12)$$

With

$$S_{p0} = \sigma_p \nu_{th} \mathrm{N}_{st} \text{ and } S_{n0} = \sigma_n \nu_{th} \mathrm{N}_{st} \quad (13)$$

Where, A_i and d_i are the area and the length of the interface node i and τ_n^i is the bulk lifetime calculated at a node i along the interface. S_{p0}, S_{n0}, σ_p and σ_n are the surface recombination velocities parameters and capture cross section for holes and electrons respectively. N_{st} is the surface states per unit area and ν_{th} is the thermal velocity of the charge carrier (~ 10^7 cm.s^{-1} in Si at 300 K). The surface recombination effect incorporated in the bottom silicon solar cell using interface statement in ATLAS software and $S_{p0} = S_{n0}$ =100 cm.s^{-1} have been used.

Table 1 Material parameters used in simulation

Material		Compact TiO_2	$CH_3NH_3PbI_3$	Spiro-MeOTAD	Silicon	SiC
Dielectric Constant		100	30	3	11.8	9.72
Band Gap (eV)		3.2	1.5	2.91	1.12	2.2
Electron Affinity (eV)		4	3.93	2.2	4.17	4.2
Thickness (µm)		0.09	0.5	0.4	10, 300	0.02
Electron, Hole mobility (cm2/V·s)		0.006, 0.006	50, 50	0.0001, 0.0001	1417, 470	1000, 50
Effective conduction band (DOS) (cm^{-3})		1×10^{21}	2.5×10^{20}	2.5×10^{20}	2.76×10^{19}	6.49×10^{18}
Effective valence band (DOS) (cm^{-3})		2×10^{20}	2.5×10^{20}	2.5×10^{20}	1.02×10^{19}	1.66×10^{18}
Conduction tail states	$N^{c\text{-}tail}$ A (cm^{-3})	10^{14}	10^{14}	10^{14}	n/a	n/a
	$E^{c\text{-}tail}$ A (eV)	0.01	0.015	0.01	n/a	n/a
Valence tail states	$N^{v\text{-}tail}$ D (cm^{-3})	10^{14}	10^{14}	10^{14}	n/a	n/a
	$E^{v\text{-}tail}$ D (eV)	0.01	0.015	0.01	n/a	n/a
Acceptor-like (A) dangling bond states	N^{db} A (cm^{-3})	10^{17}	10^{14}	10^{16}	n/a	n/a
	E^{db} A (eV)	1.1	1.2	1.1	n/a	n/a
	σ^{db} A (eV)	0.1	0.1	0.1	n/a	n/a
Donor-like (D) dangling bond states	N^{db} D (cm^{-3})	10^{17}	10^{14}	10^{16}	n/a	n/a
	E^{db} D (eV)	1.1	1.2	1.1	n/a	n/a
	σ^{db} D (eV)	0.1	0.1	0.1	n/a	n/a

3. Results

3.1 Analysis of perovskite top subcell

In this section, the analysis of perovskite top subcell has been performed, where the impact of $CH_3NH_3PbI_3$ thickness on photovoltaic parameters has been obtained. The spectrum response i.e. external quantum efficiency (EQE) of the device is presented in Fig. 3 and the J-V curve is shown in Fig. 3b, respectively. The result shows that the performance of the device increases with increasing the thickness of perovskite layer. Perovskite layers with < 400nm thickness are not proficient to absorb the photons of visible spectrum region efficiently as shown in Fig. 3a. Significant improvement is observed in the thickness range of 50-400 nm. Therefore, substantial improvement in current density is also observed as shown in Fig. 3b, however, the open circuit voltage (V_{OC}) decreases slightly. Indicating increased carrier recombination in a thicker film. Further, increasing the thickness from 400 to 1000 nm does not provide any substantial improvement. The simulation results are in agreement with the fact that increasing the thickness of perovskite, results in higher PCE [19-21].

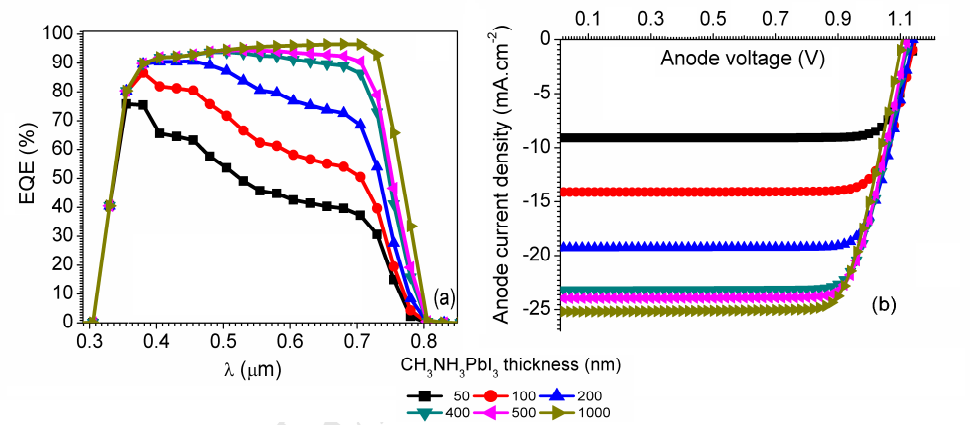


Figure 3. Impact of perovskite layer thickness on perovskite top subcell: (a) EQE, and (b) J-V curve.

The efficiency limit for $CH_3NH_3PbI_3$ solar cell having a perfect mirror at the rear side has been predicted by a detailed balance model, which shows short circuit current density (J_{SC}), V_{OC}, fill factor (FF), and PCE of 25.97 mA.cm^{-2}, 1.315 V, 91%, and 30.0%, respectively in 500 nm thick perovskite solar cell [22]. Whereas the device (which do not include perfect mirror at rear side) simulated in this work, shows J_{SC}, V_{OC}, FF, and PCE of 24.1 mA.cm^{-2}, 1.3 V, 82%, and 25.9%, respectively, as shown in Fig. 4a. The J-V curve presented in Fig. 4a has been obtained by eliminating the recombination models such as Auger, and radiative recombination. This has been done to perceive the impact of these recombination dynamics on the performance of perovskite solar cell. Further, recombination dynamics has been included in the simulation and three J-V curves are obtained with different second and third order recombination rate constants i.e. *B* and *C*. The constants *B* and *C* have been obtained from recent experimental data as reported by (*Yang et al.*, 2015 and *Wehrenfennig et al*., 2014) [12, 13]**.** The carrier lifetime 10^{-6}s has been used for SRH recombination model. Fig. 4b shows significant degradation when recombination dynamics is incorporated in the $CH_3NH_3PbI_3$ layer. The square and circle symbol based J-V curve are based on the constants reported by (*Wehrenfennig et al*., 2014) and (*yang et al.*, 2015), respectively. Triangular symbol based J-V curve is also obtained for optimum performance by selecting the smaller values of the constants as shown in Fig. 4b. The PCEs of 19.7%, 20.9%, and 21.0% have been obtained, and the same has been reported in Table 2.

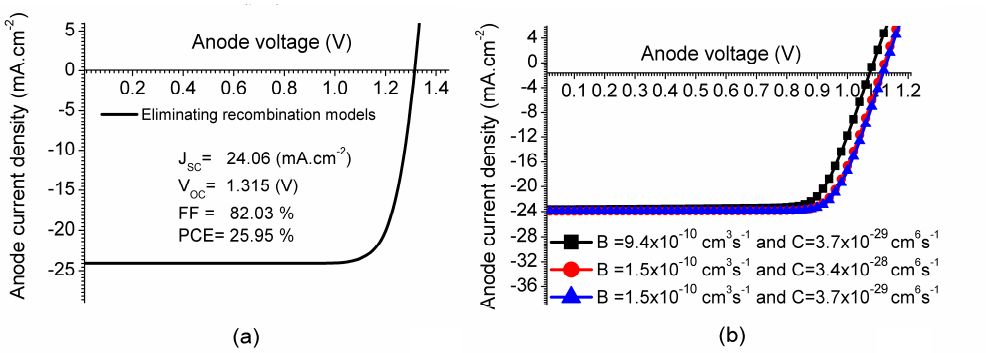


Figure 4. (a) The J-V curve of the perovskite top subcell, by eliminating the recombination models and (d) J-V curve of the perovskite top cell with different bimolecular and trimolecular carrier recombination coefficient as reported in [12, 13]

Table 2. Photovoltaic parameters of perovskite solar cell: charge carrier decay constant has been obtained from experimentally available data from [12, 13].

Charge Carrier Decay Constants		**Photovoltaic Parameters**			
2nd order, B ($cm^3\ s^{-1}$)	3rd order, C ($cm^6\ s^{-1}$)	J_{SC} ($mA.cm^{-2}$)	V_{OC} (V)	FF (%)	PCE (%)
9.4×10^{-10}	3.7×10^{-29}	23.70	1.08	76.7	19.7
1.5×10^{-10}	3.4×10^{-28}	23.95	1.12	77.8	20.9
1.5×10^{-10}	3.7×10^{-29}	23.96	1.13	77.8	21.0

Moreover, the use of SRH model gives the freedom to obtain the impact of material quality on the performance of the device. SRH recombination is defect-limited and proportional to the defect density. Literature reports, first order recombination lifetime range from 10 to 10^3 ns [23-25]. Therefore, the impact of material quality on photovoltaic parameters has been obtained by changing the carrier lifetime from 10 to $5x10^3$ ns and presented in Fig. 5 (a-d). Fig. 5 shows as the carrier lifetime changes from $5x10^{-6}$ s to $5x10^{-8}$ s the change in J_{SC}, V_{OC}, FF, and PCE are 23.98 to 23.40 $mA.cm^{-2}$, 1.12 to 1.09 V, 78.2 % to 74.8 %, and 21.0% to 19.1%, respectively. This results in 2.4%, 2.6%, 4.3%, and 9.0% decrease in J_{SC}, V_{OC}, FF, and PCE, respectively. However as the lifetime of the carriers changes from $5x10^{-6}$ s to 10^{-8} s, the decrease in J_{SC}, V_{OC}, FF, and PCE is 5.3%, 4.6%, 4.6%, and 14.1%, respectively as shown in Fig. 5(a-d). The photovoltaic parameters of 10^{-6} s lifetime based perovskite device simulated in this work is almost equivalent to high performance mixed cation perovskite solar cells with record power conversion efficiencies of 20.8% and 21.1% reported in [6-7], whereas, the performance of low carrier lifetime based perovskite device is also in close approximation with the experimentally available data [26]. Furthermore, fundamental recombination dynamics inside the perovskite region has also been obtained and shown in Fig. 6(a-d). Fig. 4b and Fig. 6 shows that the impact of trimolecular recombination is lower compared to bimolecular recombination, on the photovoltaic parameters, since perovskite material has a direct bandgap. Therefore, Auger recombination is sufficiently suppressed, and this has been verified by experimental results [27]. The effect of trimolecular recombination, however, is not ignorable at high charge carrier density.

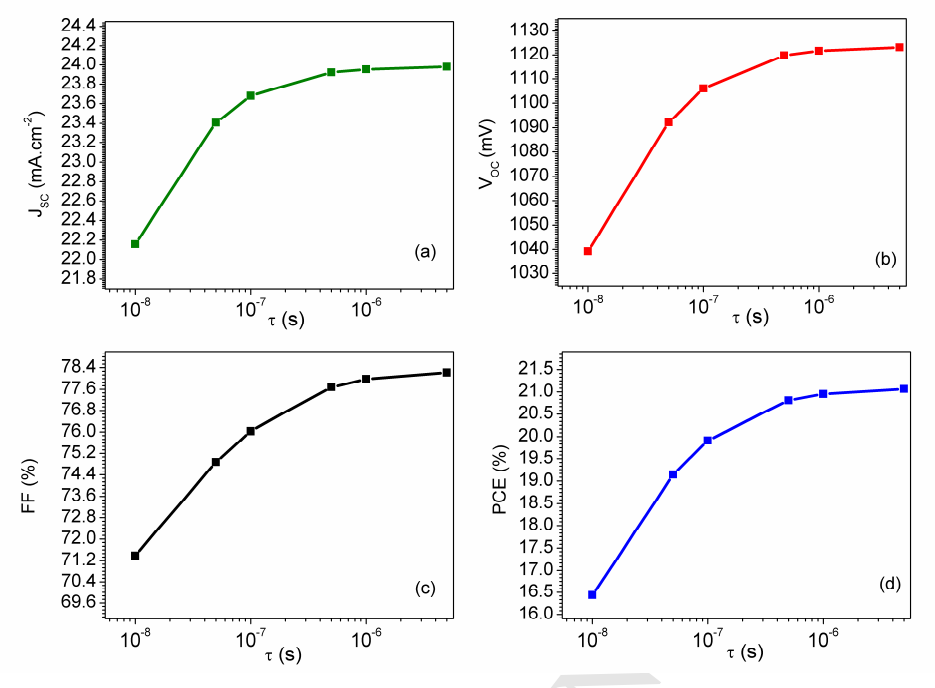


Figure 5. The impact of first order recombination lifetime on the device photovoltaic parameters for perovskite top subcell: (a) J_{SC}, (b) V_{OC}, (c) FF, and (d) PCE

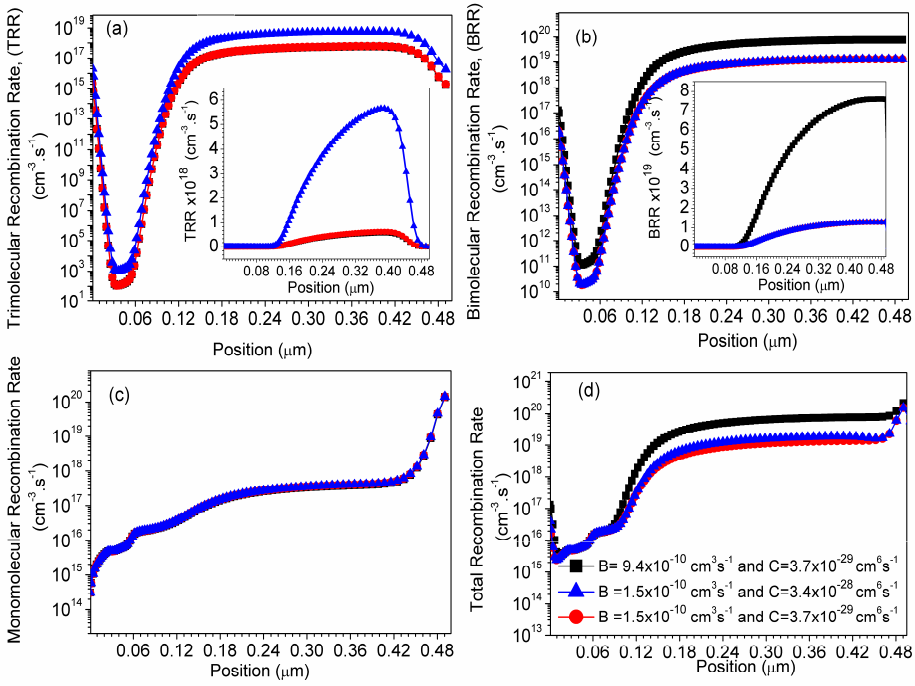


Figure 6. The carrier recombination rate inside the perovskite region with different bimolecular and trimolecular carrier recombination coefficient as reported in [9, 10]. Inset shows the recombination rate on linear scale. Analysis has been done under short circuit condition with standard AM1.5 illumination. Also, fixed first order recombination lifetime 10^{-6} s has been used during simulation

3.2 Analysis of SiC-based silicon bottom subcell and 4-terminal perovskite/SiC-based silicon tandem solar cell

This section demonstrates four-terminal stacked tandem device based on perovskite as top cell and SiC-based silicon cell as bottom subcell, as schematically shown in Fig. 1c. The efficiency of each subcell is evaluated, and the sum of the two gives the overall efficiency in a tandem configuration. Two different thickness i.e. 10 and 300-micron thick silicon wafer-based devices have been used for bottom subcell silicon solar cell. The performance of bottom silicon subcell is measured with perovskite device (Fig. 1a) as a filter under standard AM1.5 illumination. The motivation to design SiC-based silicon cell is to suppress the interface recombination and improvement of V_{OC}, in rear contact architecture-based silicon solar cell. Initially, we have analyzed the SiC-based rear contact silicon solar cell. The contour representation of recombination rate has been shown in Fig. 7(a-b), the analysis reveals that recombination rate near the SiC/*N*-Si interface is small compared to the bulk region (*N*-Si) of the device. The presence of SiC creates a positive electric field at the interface and direction are directed from SiC to Si, rendering it energetically unfavorable for hole transport to SiC/*N*-Si interface, resulting in a low concentration of holes at the passivating interface [28-30]. In surface recombination process, an electron from conduction band recombines with the hole in the valence band via a defect level within the bandgap. If the concentration of one comrade electrons or holes is drastically reduced, then recombination rate reduces strongly [31]. Therefore, sinking the hole concentration at the interface will produce higher concentration difference between electrons and holes, and thus results in lower surface recombination rate, as shown in Fig. 7(a-b). EQEs of perovskite top subcell and silicon bottom subcell in the tandem configuration are shown in Fig. 8(a). The result shows the 10 microns thick Si-based bottom subcell device is not capable of absorbing high energy photon compared to 300-micron thick device. Since photon absorbance is directly related to the absorption coefficient and the thickness of the material used. This leads to superior photovoltaic performance of 300 microns thick Si bottom subcell based tandem device, as shown in Table 3. Further, the performance of Si cell without perovskite filter has also been presented in Fig. 8(b), for comparison. In a stand-alone configuration, the J_{SC} of 28.08 mA.cm^{-2} and 37.64 mA.cm^{-2} have been obtained in 10 microns and 300-micron thick wafer based rear contact solar cells, respectively as shown in Fig. 8(b). After adding the perovskite top cell, the J_{SC} of bottom Si cell decreases to 3.06 mA.cm^{-2} and 12.61 mA.cm^{-2} for 10 and 300 micron thick devices respectively due to reduced light intensity. The decrease in FF and V_{OC} are only marginally, resulting in 1.5% and 6.7% efficient two Si-based bottom subcell, shown in Table 3. Therefore, together with the 20.9% efficiency of perovskite top subcell, this results in 22.4% and 27.6% efficient tandem devices with 10 and 300-micron thick silicon-based bottom subcells, respectively. This is a substantial improvement comparing to transparent perovskite solar cell and c-Si solar cell operated individually.

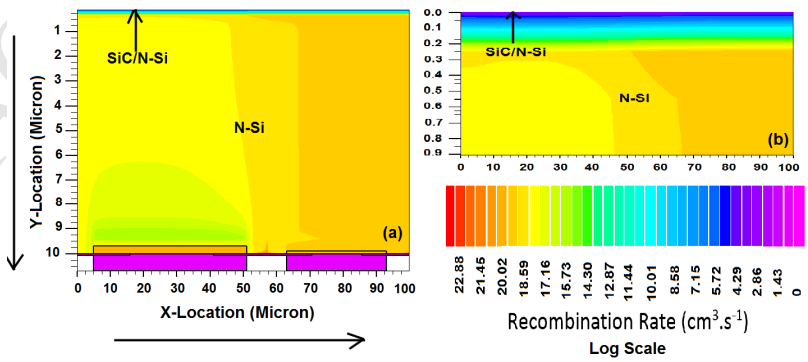


Figure 7. (a) The contour representation of recombination rate in SiC-based bottom silicon subcell, (b) magnified view near SiC/n-Si interface.

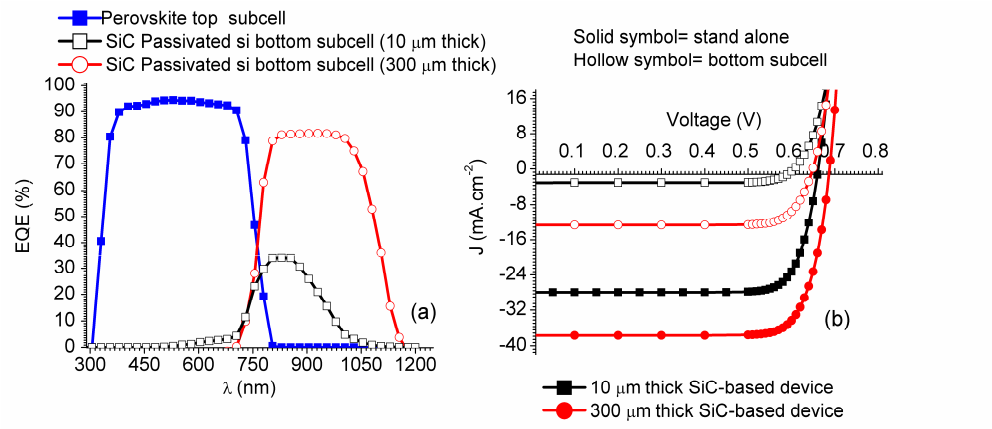


Figure 8. (a) EQE of perovskite top subcell and SiC based silicon bottom subcell in tandem configuration, and (b) J-V curve of silicon cell in stand-alone and bottom subcell configuration.

Table 3 Photovoltaic parameters of the 4 terminal perovskite / SiC-based silicon tandem solar cell

Solar cells	J_{SC} (mA.cm^{-2})	V_{OC} (mV)	FF (%)	PCE (%)
Perovskite top subcell	23.95	1121	77.8	20.9
Si bottom cell 10 micron in stand-alone, subcell	28.08, 3.06	662, 606	82.3, 81.8	15.3, 1.5
Si bottom cell 300 micron in stand-alone, subcell	37.64, 12.61	688, 649	82.9, 82.3	21.4, 6.7
4-terminal using 10 micron thick Si bottom subcell				20.9+1.5=22.4
4-terminal using 300 micron thick Si bottom subcell				20.9+6.7=27.6

Moreover, the impact of carrier lifetime has been studied to obtain the effect of material quality on the performance of bottom subcell, and the results are presented in Fig. 9(a-d). The 10µm thick device is thin compared to conventional ~300µm thick silicon solar cells and hence, the device can be fabricated with inexpensive, less pure material. Also, the charge carriers need to diffuse shorter length whereas, in 300 µm thick device, a long carrier lifetime is required to collect the carrier. Therefore, the photovoltaic performance of thinner device shows the negligible impact of material quality, whereas significant degradation has been observed in the thicker device. Results shows for lower carrier lifetime (10^{-5} s) the performance of 300 micron thick is lower compared to 10-micron thick device, due to higher bulk recombination of the carrier in the thicker device, since lifetime is small. The desired material quality and the device can be selected from Fig. 9 depending upon the application. Total efficiency in tandem configuration can be obtained by adding the efficiencies of bottom subcell and perovskite top cell.

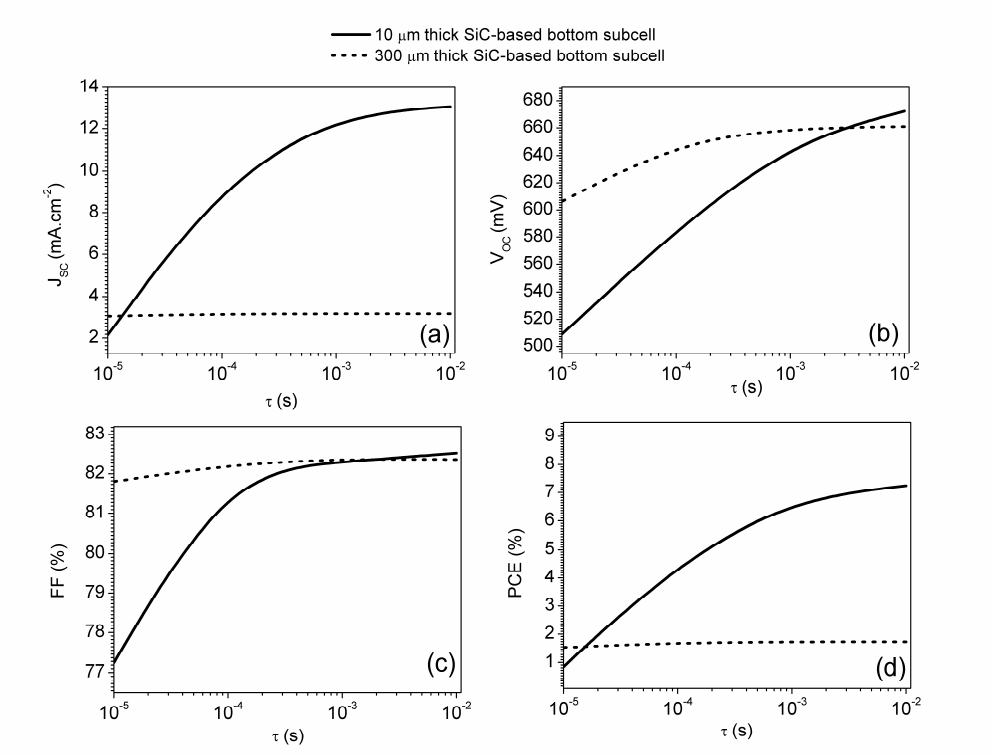


Figure 9. Impact of carrier lifetime on the performance of bottom silicon subcell under tandem configuration: (a) J_{SC}, (b) V_{OC}, (c) FF, and (d) PCE

4. Conclusions

This work presents TCAD analysis of 27.6% efficient 4-terminal perovskite/SiC-based silicon tandem solar cell for energy efficient applications. This is a substantial improvement comparing to transparent perovskite solar cell and c-Si solar cell operated individually. The motivation to design SiC-based silicon bottom subcell is to suppress the interface recombination by preventing the minority carrier to reach the passivating interface. The 21.4% efficient individually operated SiC-based rear contact silicon solar cell is combined in four terminal tandem configuration with 20.9% efficient perovskite cell. The perovskite device has been used as top subcell whereas silicon rear contact device has been used as bottom subcell. The efficiency of bottom si subcell went down 6.7% compared to 21.4% when operated stand-alone due to reduced light intensity. The influence of silicon material quality on the performance of bottom silicon subcell has also been obtained. Detailed analysis of perovskite top subcell has been done. The impact of perovskite layer thickness, perovskite material quality has been obtained on the performance of perovskite top subcell. The nature of all fundamental recombination i.e. monomolecular, bimolecular, and trimolecular recombination have been obtained inside the perovskite region, to understand the device physics of perovskite top subcell.

Acknowledgement

The authors would like to thank Microelectronics Research Lab, Department of Engineering Physics, Delhi Technological University to carry out this work. Rahul Pandey (JRF) acknowledge UGC, Govt. of India for providing fellowship.

References

[1] P. Loper, B. Niesen, S.J. Moon, S. Martin De Nicolas, J. Holovsky, Z. Remes, M. Ledinsky, F.J. Haug, J.H. Yum, S. De Wolf, C. Ballif, Organic-inorganic halide perovskites: Perspectives for silicon-based tandem solar cells, IEEE Journal of Photovoltaics 4 (2014) 1545-1551.

[2] A. Richter, M. Hermle, S.W. Glunz, Reassessment of the Limiting Efficiency for Crystalline Silicon Solar Cells, IEEE Journal of Photovoltaics 3 (2013) 1184-1191.

[3] C.D. Bailie, M.D. McGehee, High-efficiency tandem perovskite solar cells, MRS Bulletin 40 (2015) 681-686.

[4] N.-G. Park, Perovskite solar cells: an emerging photovoltaic technology, Materials Today 18(2) (2015) 65-72.

[5] W.S. Yang, J.H. Noh, N.J. Jeon, Y.C. Kim, S. Ryu, J. Seo, S.I. Seok, High-performance photovoltaic perovskite layers fabricated through intramolecular exchange, Science. (2015) science.aaa9272.

[6] D. Bi, W. Tress, M.I. Dar, P. Gao, J. Luo, C. Renevier, K. Schenk, A. Abate, F. Giordano, J.-P. Correa Baena, J.-D. Decoppet, S.M. Zakeeruddin, M.K. Nazeeruddin, M. Grätzel, A. Hagfeldt, Efficient luminescent solar cells based on tailored mixed-cation perovskites, (2016).

[7] M. Saliba et al., Cesium-containing triple cation perovskite solar cells: improved stability, reproducibility and high efficiency, Energy Environ. Sci. 9 (2016) 1989-1997.

[8] J.P. Mailoa, C.D. Bailie, E.C. Johlin, E.T. Hoke, A.J. Akey, W.H. Nguyen, M.D. McGehee, T. Buonassisi, A 2-terminal perovskite/silicon multijunction solar cell enabled by a silicon tunnel junction, Applied Physics Letters 106 (2015).

[9] J. Werner, C.-H. Weng, A. Walter, L. Fesquet, J.P. Seif, S. De Wolf, B. Niesen, C. Ballif, Efficient Monolithic Perovskite/Silicon Tandem Solar Cell With Cell Area > 1 cm 2, The Journal of Physical Chemistry Letters 7 (2015) acs.jpclett.5b02686.

[10] M.S. Branham, W.-C. Hsu, S. Yerci, J. Loomis, S.V. Boriskina, B.R. Hoard, S.E. Han, G. Chen, 15.7% Efficient 10-μm-Thick Crystalline Silicon Solar Cells Using Periodic Nanostructures., Advanced materials (Deerfield Beach, Fla.) (2015) 2182-2188.

[11] H. Savin, P. Repo, G. von Gastrow, P. Ortega, E. Calle, M. Garín, R. Alcubilla, Black silicon solar cells with interdigitated back-contacts achieve 22.1% efficiency., Nature nanotechnology 10 (2015) 1-6.

[12] Y. Yang, M. Yang, Z. Li, R. Crisp, K. Zhu, M.C. Beard, Comparison of Recombination Dynamics in $CH_3NH_3PbBr_3$ and $CH_3NH_3PbI_3$ Perovskite Films: Influence of Exciton Binding Energy, The Journal of Physical Chemistry Letters 6 (2015) acs.jpclett.5b02290.

[13] C. Wehrenfennig, G.E. Eperon, M.B. Johnston, H.J. Snaith, L.M. Herz, High Charge Carrier Mobilities and Lifetimes in Organolead Trihalide Perovskites, Advanced Materials 26 (2014) 1584-1589.

[14] F. Fu, T. Feurer, T. Jäger, E. Avancini, B. Bissig, S. Yoon, S. Buecheler, A.N. Tiwari, Low-temperature-processed efficient semi-transparent planar perovskite solar cells for bifacial and tandem applications, Nature Communications 6 (2015) 8932.

[15] D.S. Software, ATLAS User ' s Manual, (2013) 567-1000.

[16] F. Liu, J. Zhu, J. Wei, Y. Li, M. Lv, S. Yang, B. Zhang, J. Yao, S. Dai, Numerical simulation: Toward the design of high-efficiency planar perovskite solar cells, Applied Physics Letters 104 (2014) 253508.

[17] M.E. Law, E. Solley, M. Liang, D.E. Burk, Self-consistent model of minority-carrier lifetime, diffusion length, and mobility, IEEE Electron Device Letters 12 (1991) 401-403.

[18] J. Dziewior, W. Schmid, Auger coefficients for highly doped and highly excited silicon, Applied Physics Letters 31 (1977) 346.

[19] W.A. Laban, L. Etgar, Depleted hole conductor-free lead halide iodide heterojunction solar cells, Energy & Environmental Science 6 (2013) 3249.

[20] L. Etgar, P. Gao, Z. Xue, Q. Peng, A.K. Chandiran, B. Liu, M.K. Nazeeruddin, M. Grätzel, Mesoscopic $CH_3NH_3PbI_3/TiO_2$ heterojunction solar cells., Journal of the American Chemical Society 134 (2012) 17396-9.

[21] S. Sun, T. Salim, N. Mathews, M. Duchamp, C. Boothroyd, G. Xing, T.C. Sum, Y.M. Lam, The origin of high efficiency in low-temperature solution-processable bilayer organometal halide hybrid solar cells, Energy & Environmental Science 7 (2014) 399.

[22] W.E.I. Sha, X. Ren, L. Chen, W.C.H. Choy, The efficiency limit of $CH_3NH_3PbI_3$ perovskite solar cells, Applied Physics Letters 106 (2015) 221104.

[23] H. Zhu, Y. Fu, F. Meng, X. Wu, Z. Gong, Q. Ding, M.V. Gustafsson, M.T. Trinh, S. Jin, X.-Y. Zhu, Lead halide perovskite nanowire lasers with low lasing thresholds and high quality factors., Nature materials 14 (2015) 636-42.

[24] C. Wehrenfennig, M. Liu, H.J. Snaith, M.B. Johnston, L.M. Herz, Homogeneous emission line broadening in the organo lead halide perovskite $CH_3NH_3PbI_{3-x}Cl_x$, Journal of Physical Chemistry Letters 5 (2014) 1300-1306.

ACCEPTED MANUSCRIPT

[25] D. Shi, V. Adinolfi, R. Comin, M. Yuan, E. Alarousu, A. Buin, Y. Chen, S. Hoogland, A. Rothenberger, K. Katsiev, Y. Losovyj, X. Zhang, P.A. Dowben, O.F. Mohammed, E.H. Sargent, O.M. Bakr, Low trap-state density and long carrier diffusion in organolead trihalide perovskite single crystals, Science 347 (2015) 519-522.
[26] M. Liu, M.B. Johnston, H.J. Snaith, Efficient planar heterojunction perovskite solar cells by vapour deposition, Nature 501 (2013) 395-398.
[27] G. Xing, N. Mathews, S.S. Lim, N. Yantara, X. Liu, D. Sabba, M. Grätzel, S. Mhaisalkar, T.C. Sum, Low-temperature solution-processed wavelength-tunable perovskites for lasing., Nature materials 13 (2014) 476-80.
[28] R. Pandey, R. Chaujar, Rear contact SiGe solar cell with SiC passivated front surface for >90-percent external quantum efficiency and improved power conversion efficiency, Solar Energy 135 (2016) 242-252.
[29] R. Pandey, R. Chaujar, Numerical simulation of rear contact silicon solar cell with a novel front surface design for the suppression of interface recombination and improved absorption, Current Applied Physics (2016), doi: 10.1016/j.cap.2016.09.002
[30] R. Pandey, R. Chaujar, Front Surface Passivation Scheme for Back-Contact Back-Junction (BC-BJ) Silicon Solar Cell, Advance Science Letters 22 (2016) 815-820.
[31] A.G. Aberle, Surface passivation of crystalline silicon solar cells: a review, Progress in Photovoltaics: Research and Applications 8 (2000) 473-487.
[32] M.A. Leguy, Y. Hu, M. Campoy-quiles, M.I. Alonso, O.J. Weber, P. Azarhoosh, M.V. Schilfgaarde, M.T. Weller, T. Bein, J. Nelson, P. Docampo, P.R.F. Barnes, Reversible Hydration of $CH_3NH_3PbI_3$ in Films, Single Crystals, and Solar Cells, (2015).
[33] M. Filipič, P. Löper, B. Niesen, S. De Wolf, J. Krč, C. Ballif, M. Topič, $CH_3NH_3PbI_3$ perovskite / silicon tandem solar cells: characterization based optical simulations., Opt. Express 23 (2015) A263-78.

ACCEPTED MANUSCRIPT

ACCEPTED MANUSCRIPT

Highlights

- Innovative perovskite/silicon based 4-terminal tandem cell has been proposed and simulated.
- Perovskite top subcell shows 20.9% power conversion efficiency (PCE).
- PCEs of 27.6% and 22.4% have been achieved with 300 μm and 10 μm thick silicon bottom subcells
- Fundamental recombination dynamics are obtained inside the device.
- Impact of material quality on the performance of tandem device has been obtained.
- Result shows, proposed design, can be a good candidate to obtained ultra-high efficiencies

ACCEPTED MANUSCRIPT

Swarm and Evolutionary Computation xx (xxxx) xxxx–xxxx

Contents lists available at ScienceDirect

Swarm and Evolutionary Computation

journal homepage: www.elsevier.com/locate/swevo

Survey Paper

On the application of search-based techniques for software engineering predictive modeling: A systematic review and future directions

Ruchika Malhotra[a,*], Megha Khanna[b,c], Rajeev R. Raje[d]

[a] Department of Software Engineering, Delhi Technological University, India
[b] Delhi Technological University, India
[c] Sri Guru Gobind Singh College of Commerce, University of Delhi, India
[d] Department of Computer and Information Science, Indiana University-Purdue University Indianapolis, Indiana, IN, USA

ARTICLE INFO

Keywords:
Search-based techniques
Change prediction
Defect prediction
Effort estimation
Maintainability prediction
Software quality

ABSTRACT

Software engineering predictive modeling involves construction of models, with the help of software metrics, for estimating quality attributes. Recently, the use of search-based techniques have gained importance as they help the developers and project-managers in the identification of optimal solutions for developing effective prediction models. In this paper, we perform a systematic review of 78 primary studies from January 1992 to December 2015 which analyze the predictive capability of search-based techniques for ascertaining four predominant software quality attributes, i.e., *effort, defect proneness, maintainability* and *change proneness*. The review analyses the effective use and application of search-based techniques by evaluating appropriate specifications of fitness functions, parameter settings, validation methods, accounting for their stochastic natures and the evaluation of developmental models with the use of well-known statistical tests. Furthermore, we compare the effectiveness of different models, developed using the various search-based techniques amongst themselves, and also with the prevalent machine learning techniques used in literature. Although there are very few studies which use search-based techniques for predicting maintainability and change proneness, we found that the results of the application of search-based techniques for effort estimation and defect prediction are encouraging. Hence, this comprehensive study and the associated results will provide guidelines to practitioners and researchers and will enable them to make proper choices for applying the search-based techniques to their specific situations.

1. Introduction

Software engineering predictive modeling (SEPM) helps software professionals in optimizing resources and thus, in producing high quality, efficient, and maintainable software products at low costs. For instance, an efficient predictive model, which suggests the occurrence of defects in a particular class in the forthcoming release of the software, will enable the practitioners to closely evaluate that class by allocating more resources to its testing than the other classes. Such an allocation may help in reducing the errors in the next release of the software. In order to develop an efficient predictor, a classifier needs to be trained with the help of available historical data. The trained classifier can then be used to predict various quality attributes of future software products. Software metrics, which represent various characteristics of a software product, are used for developing and validating these predictive models. Examples of such metrics include Chidamber and Kemerer metrics suite [1], and the Quality Model for Object-Oriented Design metrics suite [2]. These metrics represent various properties of software such as coupling, cohesion, inheritance levels, and size.

A lot of research has been carried out in the field of SEPM, which uses statistical and Machine Learning (ML) techniques for developing predictive models. However, recently a new class of prediction methods, called Search-based techniques, has gained importance in SEPM tasks. A number of studies have established the applicability of the search-based techniques in various software engineering tasks such as requirement analysis, reverse engineering, software product line engineering, software testing, software test case generation, and software project management [3–12]. However, only few studies ascertain the usefulness of the search-based techniques for predicting software development effort, defects, software maintenance effort (maintainability) and maintenance-based changes.

Search-based techniques are meta-heuristic procedures, which are capable of identifying an optimized solution from a large search space

* Corresponding author.
E-mail addresses: ruchikamalhotra2004@yahoo.com (R. Malhotra), meghakhanna86@gmail.com (M. Khanna), rraje@cs.iupui.edu (R.R. Raje).

http://dx.doi.org/10.1016/j.swevo.2016.10.002
Received 24 February 2016; Received in revised form 1 August 2016; Accepted 14 October 2016
Available online xxxx
2210-6502/ © 2016 Elsevier B.V. All rights reserved.

Please cite this article as: Malhotra, R., Swarm and Evolutionary Computation (2016), http://dx.doi.org/10.1016/j.swevo.2016.10.002

consisting of potential solutions. They have been successfully used for a number of tasks such as optimal design of FIR filters [13–15], impulse response system identification [16], cloud computing resource scheduling [17] and load forecasting [18]. The search process in a search-based technique is guided by a fitness evaluator which ascertains the appropriateness of a specific solution [11]. The application of search-based techniques for predictive modeling has been advocated by Harman and Jones [19] and Harman [20], as these techniques are efficient in balancing constraints and conflicts. Moreover, they are also efficient in handling noisy, partially inaccurate and incomplete data sets. Other advantages of search-based techniques include their simple problem solving approach and robustness [20,21]. These techniques avoid getting trapped in local optima and conduct the global search efficiently. Harman and Clark [22] have argued that the performance metrics, such as the classification accuracy, can be used by search-based techniques as fitness functions and hence, can be used to create software engineering predictive models.

Given the newly identified relationship between the search-based techniques and predictive modeling, it is necessary to systematically study empirical evidences reported in literature about the use of search-based techniques for the development of software engineering predictive models. There have been a few efforts in that direction in the recent past. For example, a study by Afzal and Torkar [23] focused on a specific search-based technique (Genetic Programming) for estimation and prediction tasks in software engineering. Wen et al. [24] conducted a review of ML techniques for estimating software development effort. Similarly, a study by Ferrucci et al. [12] provides an overview of the application of search-based techniques to the various issues of the software project management. A position paper by Malhotra [25], briefly provides an overview of search-based techniques for defect prediction. Unlike these earlier efforts, this paper presents an extensive analysis about the use of search-based techniques for SEPM, with a specific focus on: (1) software development effort estimation, (2) defect prediction, (3) maintainability prediction, and (4) change prediction. These four attributes are important to estimate in order to effectively allocate resources while developing and maintaining a software product. Moreover, the appropriate prediction of these attributes in the early phases of software development lifecycle helps practitioners to build timely and cost-effective products, while increasing their commitment towards developing a good quality product. We evaluate search-based techniques reported in the literature, covering a time period from January 1992 to December 2015, used for the SEPM tasks. Moreover, this study also explores the effective experimental setups and methods followed in literature for using search-based techniques for SEPM tasks. The four quality attributes evaluated by this study are as follows:

- Software Development Effort/ Effort Estimation: This quality attribute estimates the effort required to develop a specific software product [24]. Effort estimation is important as software project managers require important information from past projects to plan and analyze the effort required for project development [26]. Such knowledge is critical in efficient allocation of human resources so that products can be delivered on time and within the planned budget.
- Defect Prediction: This quality attribute predicts whether a specific module/class of a software will contain defects in the forthcoming releases of the product. Identification of defect prone classes, as indicated earlier, is important as the cost of correcting defects increases exponentially in later phases of the software development cycle [27]. Thus, it is important for researchers to eliminate defects as early as possible to ensure customer satisfaction making the defect proneness prediction an important software quality attribute.
- Maintenance Effort/ Maintainability Prediction: This quality attribute measures the ease with which a software module/class can be modified. It represents the effort required to evolve a particular software module/class. Since, the maintenance phase absorbs 60–70% of the total project resources [27], it is essential for software managers to estimate maintenance effort in the early phases so that proper planning and allocation can be done.
- Change Prediction: This quality attribute predicts whether a specific module/class of software will evolve, i.e., require changes after the software product goes into its operational phase. The determination of change-prone nature of a class helps practitioners in efficient resource allocation as these classes need more attention in the early phases of development so that minimal changes get carried to the next stage. Such steps would ensure an efficient maintainable software product.

It is worth noting that defect prediction and change prediction are binary in nature, i.e., are classification problems. On the other hand, software development effort estimation and maintainability prediction are regression problems.

This paper analyses studies carried out between January 1992 and December 2015. It summarizes and assesses empirical evidences associated with these studies regarding: (1) the use of search-based techniques for software development effort estimation, defect prediction, maintainability prediction and change prediction models; (2) the validation techniques, number of runs to account for the stochastic nature, tools used and performance metrics used for SEPM using search-based techniques; (3) the use of different fitness functions for SEPM; (4) the performance capabilities of the search-based techniques for SEPM; (5) the comparative predictive capabilities of the search-based techniques and the ML techniques; (6) the use of different tests to statistically validate the comparative performance of various techniques, and (7) the advantages and disadvantages of the search-based techniques.

It should be noted that this study is a significant enhancement of author's earlier published article [28], where a limited number of Research Questions (RQs) were evaluated. In this study, we extend the previous work by adding three new research questions (RQ2, RQ3 and RQ6 - see the next section). These questions address the details of the experimental setup (validation method, number of runs, simulation tools and performance metrics) required for SEPM using search-based techniques. We also examine different fitness functions used by search-based techniques to develop effective software engineering predictive models and different statistical tests used in literature to perform comparative evaluation of search-based techniques for SEPM. In addition to the previous quality attributes addressed in [28], we also add a new quality attribute, i.e., maintainability prediction. Moreover, this study also significantly elaborates the discussion of the previous research questions reported in [28].

The rest of the paper is organized as follows: Section 2 presents the method used in conducting the review. Section 3 states the results of the review. Section 4 describes the threats to validity of the review. Section 5 discusses the results of various research questions. Finally, Section 6 presents conclusions of this study and mentions future directions.

2. Method

Kitchenham [29] identified three basic stages in any systematic review - namely, Planning, Conducting and Reporting. Planning is concerned with the establishment of the need of the review and the review protocol. A review protocol, created in the planning stage, clearly defines the research questions to be addressed by the review. A research question for a review study is the aim with which we investigate and review the literature in order to assess its current state. These research questions should be generated with clear objectives in a researcher's mind so as to guide the research methodology and the investigation process. Research questions are based on the intent with which we explore the studies for analyzing a specific topic

or phenomenon. Furthermore, the review protocol also encompasses the search strategy for extracting appropriate studies for the review, the criteria for an unbiased selection of candidate studies, the procedure for quality analysis of the candidate studies and the procedure for data collection and synthesis from the selected primary studies to appropriately answer the research questions. The conducting stage of a review involves an execution of the strategies decided in the review protocol to collect, extract, monitor and synthesize the studies of the review. Finally, the reporting stage reports the findings of the analysis. This stage involves stating clear answers to the research questions. In our study, three reviewers analyzed the collected studies independently. In case of inconsistent opinions, the majority opinion was followed after consulting an outside expert. In this section, we describe the details of these three stages as they relate to our task of analyzing various studies reported in the literature.

2.1. Research questions

As indicated earlier, the aim of this review is to examine the use of different search-based techniques for SEPM. Thus, as a first step, we identify studies which have used search-based techniques for developing effort estimation, defect prediction, maintainability prediction, and change prediction (change proneness) models. To assist in achieving this first step, we formulated the following research questions in the review (see Table 1).

2.2. Search strategy and study selection

In order to develop and formulate a search strategy, for selecting relevant studies reported in literature, we constructed and designed our search terms using the following steps.

- Divide the research questions into respective logical units.
- Identify the search terms from relevant paper titles, abstracts and keywords.
- Determine the synonyms and equivalent terms for all the studies.
- Use Boolean OR to join and compile equivalent terms and synonyms together.
- Use of Boolean AND to join and compile major distinguishable search terms.

Based on these steps, the following search string was used to identify the set of relevant studies available in five prominent databases, namely, IEEEXplore, ACM Digital Library, SpringerLink, ScienceDirect and Wiley Online Library. Also, as Xanthakis et al. [30] first used a search-based technique for a software engineering application (software testing), the period of the search was chosen from January 1992 to December 2015.

("software" OR "application" OR "project" OR "open source project" OR "product") AND ("Effort" OR "Defect" OR "Fault" OR "Error" OR "Cost" OR "Maintainability" OR "Maintenance Effort" OR "Change" OR "Size") AND ("proneness" OR "prone" OR "prediction" OR "probability" OR "classification" OR "estimation") AND ("Search based" OR "Evolutionary" OR "Meta-heuristic" OR "heuristic" OR "Multi-objective") AND ("Genetic Programming" OR "Gene Programming" OR "Genetic Algorithm" OR "Particle Swarm Optimization" OR "Ant Colony Optimization" OR "Classifier System" OR "Simulated Annealing" OR "Tabu Search" OR "Cuckoo Search" OR "Artificial Bee Colony" OR "Evolutionary Programming" OR "Memetic Algorithm" OR "Neuroevolution" OR "Artificial Immune System (AIS) OR "Differential Evolution" OR "Harmony Search" OR "Teaching-learning-based Optimization").

In addition, to perform an exhaustive search, we also manually searched various prominent Search Based Software Engineering (SBSE) venues such as the proceedings of the Genetic and

Table 1
Research Questions.

RQ#	Research Question	Description
RQ1	What are the commonly used search-based techniques for SEPM?	This question focuses on the categorization of different search-based techniques and also identifies commonly used techniques reported in the literature for developing effort estimation, defect prediction, maintainability prediction and change prediction models.
RQ2	What experimental settings are used for SEPM using search-based techniques?	This question investigates various experimental settings used by studies reported in literature for software engineering predictive model development using search-based techniques.
RQ2.1	Which type of validation is performed for SEPM using search-based techniques?	This question identifies the various validation methods reported in literature for SEPM using the search-based techniques.
RQ2.2	How many runs/executions have been performed in the experiment to account for the stochastic nature of search-based techniques for SEPM?	As it is essential to perform multiple runs in order to account for the stochastic nature of search-based techniques, this question attempts to identify the most frequently used number of runs reported in literature for SEPM using search-based techniques.
RQ2.3	Which tools have been used for aiding the application of search-based techniques to SEPM?	This question identifies commonly used standard tools reported in literature which aid in the use of search-based techniques for SEPM.
RQ2.4	Which performance metrics are used by experiments for analyzing the developed software engineering predictive model?	This question identifies the performance metrics used in literature for assessing a specific software engineering predictive model.
RQ3	Which fitness functions have been used by search-based techniques for SEPM?	This question explores the different fitness functions used by search-based techniques for effective SEPM in order to search for an optimal solution amongst a number of solutions.
RQ4	What is the predictive performance of a specific search-based technique for SEPM tasks?	This question estimates the predictive performance of different search-based techniques for various predictive modeling tasks (e.g., effort estimation/ defect prediction/ maintainability prediction/ change prediction).
RQ5	What is the comparative performance of the models predicted using search-based techniques and models predicted using ML techniques for SEPM?	This question aims to perform a comparative analysis of the predictive capability of different search-based techniques when compared amongst themselves or with different ML techniques.
RQ6	Which statistical tests have been used to compare the predictive ability of different search-based techniques for SEPM?	This question explores the various statistical tests used in literature which are used for validating the comparative performance of different search-based techniques.
RQ7	What are advantages and disadvantages of search-based techniques for SEPM?	This question evaluates both the strengths as well as the weaknesses of a specific technique, which should be known before employing it for SEPM tasks.

Evolutionary Computation Conference (GECCO) and the symposium on Search-based Software Engineering (SSBSE), and the search-based repository (http://crestweb.cs.ucl.ac.uk/resources/sbse_repository/repository.html). These auto and manual efforts resulted in a set of candidate studies, whose reference lists were also further scanned in order to extract more relevant studies. Although we used useful insights from review studies [12,23,24] and extracted reference lists from them, they were not a part of the systematic review process as they did not yield empirical results. As a result of this comprehensive effort, we identified 139 relevant studies. These studies were then subjected to the inclusion and exclusion criteria, as indicated in Appendix A.1, for identification of the candidate studies. The excluded studies from the review are mentioned in Appendix A.7. These papers were excluded on the basis of title and abstract. After applying the inclusion and exclusion criteria, 92 studies were selected for further quality assessment.

2.3. Quality analysis

It is important to analyze the significance and contribution of each selected study in answering the various research questions. Thus, we formulated a questionnaire as suggested by Wen et al. [24] to systematically evaluate the significance of a specific study and assigned a quality score to each study. We evaluated all the 92 candidate studies [26,31–121] according to 18 quality questions as described in Appendix A.2. Each study was assessed and graded on all the 18 specified questions. The grade given to a specific study for a particular quality question could be 1 (in case the study satisfactorily answers the question as “Yes”), 0.5 (in case the study does not completely address the question and the question was “Partly” answered) or 0 (in case the study does not answer the question at all and it is a “No”). The quality score of a study, is obtained by aggregating the grades allocated to each quality question for that specific study. It signifies how well the study has been conducted and its relevance to the research questions and its strength. A study could attain a maximum quality score of 18 and a minimum score of 0. A study with a higher quality score is more significant and a good example of proper use of search-based techniques to SEPM than a study with a low score. In order to perform an unbiased quality evaluation, the evaluation of the studies was done by at least two authors of this review independently. Any disagreements were discussed and a consensus was reached. The average of the aggregated scores provided by the authors was assigned to each study.

All the 92 studies were divided according to the scores allotted to them. We accepted only those studies as primary studies, which obtained an acceptable quality score, i.e., greater than or equal to 50% of the perfect quality score, which is 9. These resulted in 78 selected studies, which were termed as the primary studies in this review and were used to answers the research questions indicated above. Appendix A.2 indicates the percentage of all candidate studies which were evaluated as “Yes”, “Partly” or “No” for each of the 18 quality questions. It should be noted that 14 studies [108–121] were rejected on the basis of the quality analysis.

2.4. Data extraction and synthesis

In order to answer the various RQs, we needed to extract data from the selected 78 studies. This was manually done with the aid of a data extraction card which summarized all the details of a study, including its title, author name, publishing details, search-based techniques used, performance metrics analyzed, experimental settings, and fitness functions. The data extraction card also reports the RQ's addressed by a specific study. In order to conduct an unbiased analysis, we independently collected data from each study and cross checked their extracted information in order avoid errors or omissions.

After the data extraction, it is essential to synthesize all the collected data in order to provide appropriate answers to all the research questions. Although, a single study may provide answers to the research questions, the main aim of this step is to provide a collective answer which can form an important evidence in the literature to establish strong and conclusive results. Thus, we analyzed both the quantitative data such as the performance of a specific technique on a specific data set, as well as the qualitative data, such as different validation methods used, the usage of statistical tests and the types of search-based techniques.

3. Results

This section presents answers to all the research questions described in Section 2.1. A brief overview of all the 78 selected primary studies is presented at the beginning and is followed by specific answers to each research question.

3.1. Overview of primary studies

This section provides an overview of the 78 selected primary studies. All these primary studies analyze the applicability of search-based techniques for SEPM.

3.1.1. Publication score

The majority of primary studies (54%) were published in the proceedings of various conferences or symposiums, while only 42% of the primary studies were published in peer reviewed journals. Three primary studies were published as chapters. A number of journal studies were published in Information and Software Technology Journal (8%) and the Journal of Systems and Software (6%). Amongst conferences, the ACM Symposium on Applied Computing contained 6% of the studies, GECCO published 5% of the studies, while SSBSE published 4% of the studies. Appendix A.3 indicates the venues in which most number of publications were published.

3.1.2. Quality assessment of primary studies

Of the 78 primary studies, 38 studies used search-based techniques for effort estimation. However, only 29 primary studies used search-based techniques for defect prediction and 3 primary studies for maintainability prediction. Also, it was found that there were 11 primary studies which aimed at change prediction. It should be noted that a study by Tsakonas and Dounias [46] developed both the effort estimation and defect prediction models. Similarly, two other studies [70,71], , developed models for both defect prediction as well as change prediction. Thus, these three studies were counted under both the categories for which models were predicted.

Table 2 shows the unique identifiers assigned to all the primary studies and is sorted by the quality score allotted to each study. It should be noted that the higher the quality score, the more is the significance of a specific study in Table 2, the effort estimation studies are prefixed with ES, the defect prediction studies with DS, the maintainability prediction studies with MS and the change prediction studies were prefixed with CS. The highest quality score of 17.5 was achieved by DS13, followed by 3 studies (ES24, ES30 and ES33), each of which achieved a score of 17. The top four studies, according to average citation count per year, were ES16, ES19, ES4, DS10 and ES13. It should be noted that two of these five most cited studies were published in the Journal of Systems and Software. Also, the top scoring study (DS13) was published in the Journal of Systems and Software. Other high ranking studies, i.e., ES24, ES30 and ES33, were published in the Information and Software Technology Journal, the ACM Symposium of Applied Computing and the Empirical Software Engineering Journal respectively.

3.1.3. Distribution of primary studies according to publication year

The year-wise (1992–2015) distribution of all the primary studies with respect to effort estimation, defect prediction, maintainability

Table 2
Primary studies.

S. No.	Name	Score	S. No.	Name	Score	S. No.	Name	Score
DS13	Carvalho [79]	17.5	ES11	Huang [40]	14.5	ES28	Chavoya [57]	13
ES24	Oliveira [53]	17	ES13	Chiu [42]	14.5	DS17	Chiu [83]	13
ES30	Sarro [59]	17	ES16	Huang [45]	14.5	ES9	Regolin [26]	12.5
ES33	Corazza [62]	17	ES26	Sheta [55]	14.5	ES12	Sheta [41]	12.5
ES34	Minku [63]	16.5	ES31	Bardsiri [60]	14.5	ES29	Araujo [58]	12.5
ES37	Bardsiri [66]	16.5	DS2	Hochman [69]	14.5	DS5	Liu [72]	12.5
ES2	Dolado [32]	16	DS4, CS2	Khoshgoftaar [71]	14.5	DS14	Jin [80]	12.5
ES4	Burgess [34]	16	DS12	Afzal [78]	14.5	DS24	Abaei [90]	12.5
ES32	Barros [61]	16	DS25	Harman [91]	14.5	CS11	Malhotra [107]	12.5
DS7	Carvalho [73]	16	CS9	Malhotra [105]	14.5	ES17, DS6	Tsakonas [46]	12
DS10	Catal [76]	16	CS5	Azar [100]	14.5	ES18	Li [47]	12
DS29	Jin [95]	16	ES6	Kirsopp [36]	14	DS8	Tsakonas [74]	12
ES7	Shan [37]	15.5	ES19	Li [48]	14	DS11	Singh [77]	12
ES10	Lokan [39]	15.5	DS9	Vandercruys [75]	14	MS3	Kumar [98]	12
DS15	Liu [81]	15.5	DS19	Yu [85]	14	DS16	Pendharkar [82]	11.5
DS23	Canfora [89]	15.5	DS20	Rodriguez [86]	14	DS26	Kewen [92]	11.5
DS28	Arar [94]	15.5	DS27	Malhotra [93]	14	CS6	Balogh [102]	11
ES3	Shukla [33]	15	CS4	Azar [101]	14	MS1	Baqais [96]	11
ES8	Lefley [38]	15	ES1	Dolado [31]	13.5	ES14	Faheem [43]	10.5
ES15	Braga [44]	15	ES5	Dolado [35]	13.5	ES25	Sheta [54]	10.5
ES21	Ferrucci [50]	15	ES23	Ferrucci [52]	13.5	ES36	Dan [65]	10.5
ES22	Ferrucci [51]	15	ES27	Aljahdali [56]	13.5	DS1	Hochman [68]	10.5
ES35	Minku [64]	15	DS3, CS1	Liu [70]	13.5	CS3	Vivanco [99]	10.5
DS21	Sarro [87]	15	DS18	Martino [84]	13.5	MS2	Malhotra [97]	10.5
CS7	Basgalupp [103]	15	CS10	Malhotra [106]	13.5	ES38	Azzeh [67]	9.5
CS8	Basgalupp [104]	15	ES20	Tsakonas [49]	13	DS22	Can [88]	9

prediction and change prediction is shown in Fig. 1. It should be noted that the most number (18%) of the effort estimation and defect prediction studies were published in the year 2010. The first studies for effort estimation, defect prediction, maintainability prediction and change prediction were published in the year 1998, 1996, 2012 and 2001 respectively. Harman and Jones [19] coined the term Search-Based Software Engineering (SBSE) in 2001, leading to a rise in the number of studies after 2001 (Fig. 1). According to Fig. 1, it can be seen that 79% of the primary studies were published between the years 2008–2015. This trend could be due to the commencement of the annual SSBSE symposium in the year 2009, which aims at assessing the current state of SBSE research, discusses and identifies challenges faced by the SBSE researchers and evaluates the impact of SBSE on present state of software engineering research.

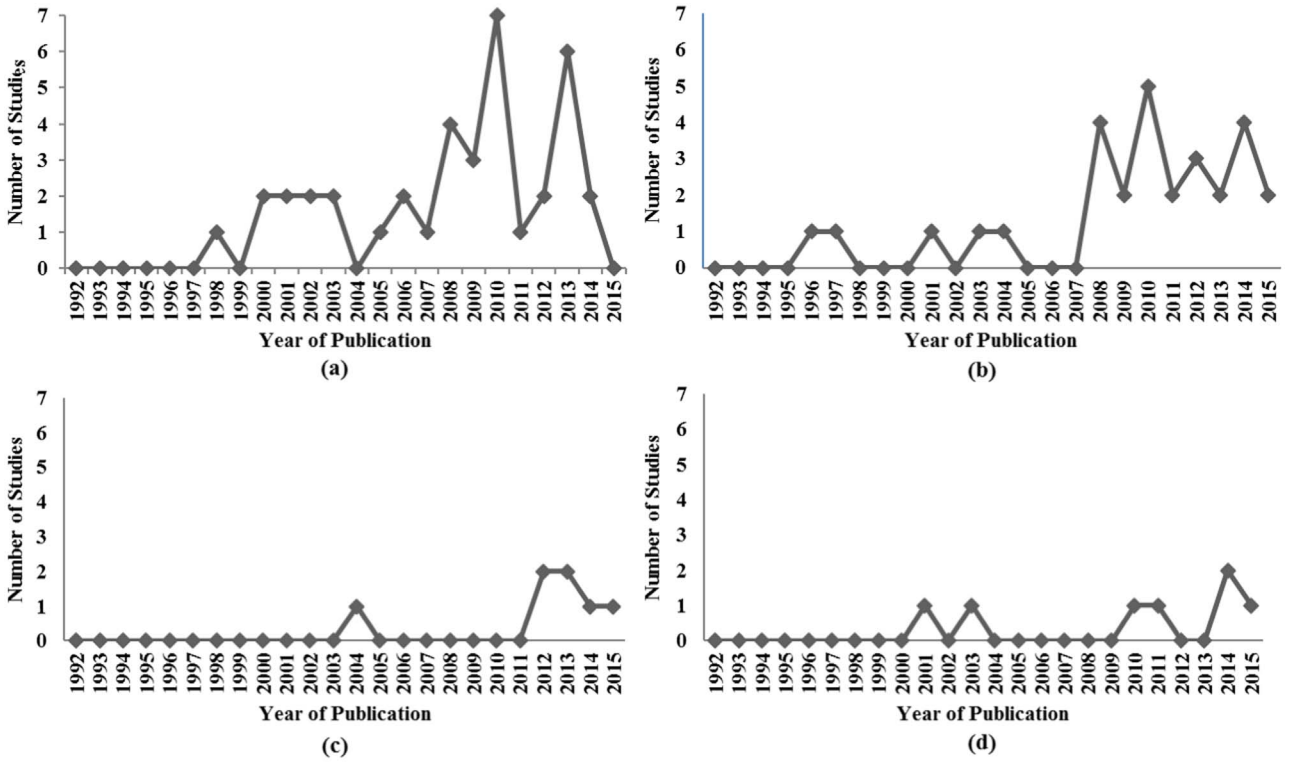


Fig. 1. Distribution of Studies across different years (a) Effort Estimation (b) Defect Prediction (c) Maintainability Prediction (d) Change Prediction.

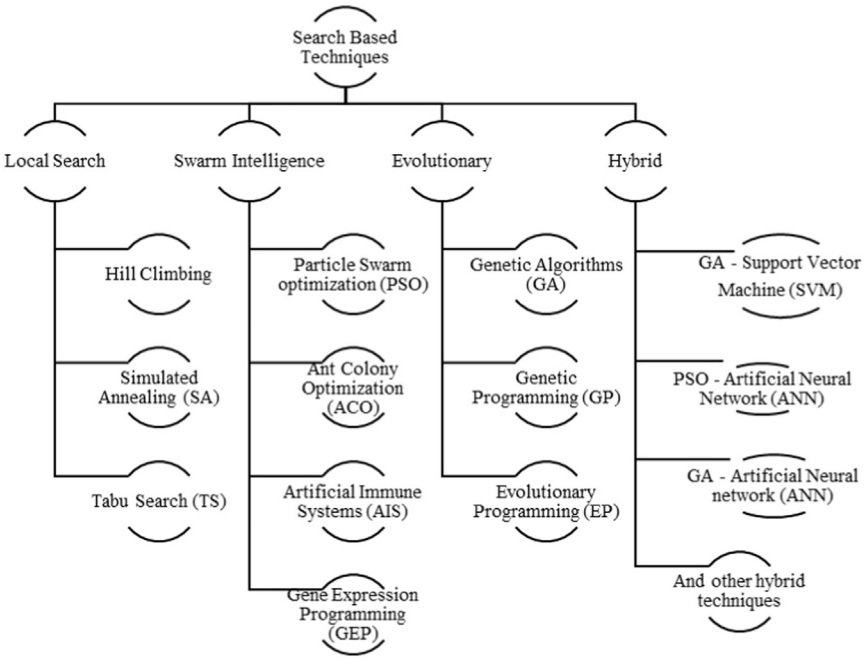


Fig. 2. Categorization of Search-based techniques (from [28]).

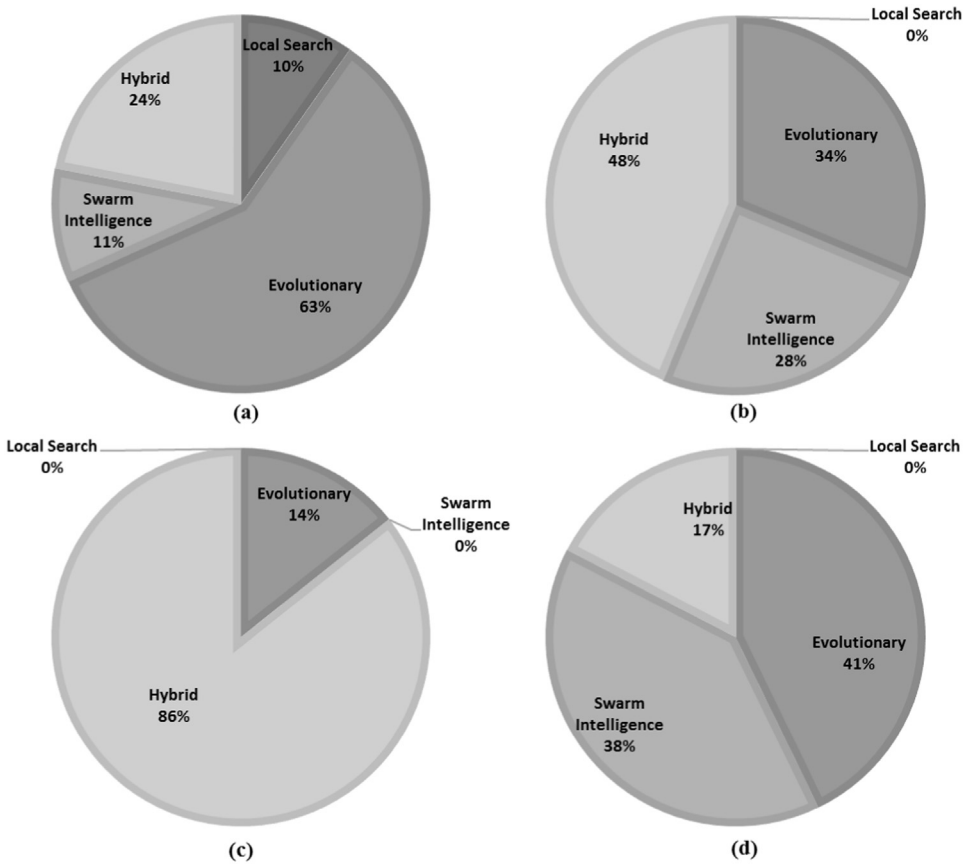


Fig. 3. Distribution of studies based on search-based techniques categorization (a) Effort estimation (b) Defect prediction (c) Maintainability prediction (d) Change prediction.

3.2. Categories of search-based techniques (RQ1)

Different search-based techniques which are used for SEPM are classified into four categories: Local Search, Swarm Intelligence, Evolutionary and Hybrid [28]. Fig. 2 presents this categorization in detail.

Fig. 3 depicts the percentage of studies which used a specific category of search-based technique for effort estimation, defect prediction, maintainability prediction and change prediction. As indicated in Fig. 3 below, we summarize the following trends for each quality attribute:

Effort Estimation: A majority of effort estimation studies (63%) used the evolutionary techniques followed by the hybrid techniques (24%). The most commonly used evolutionary technique was Genetic Programming (GP), which was employed in the 39% of effort estimation studies. This was closely followed by Genetic Algorithms (GA), which was used in 16% of the effort estimation studies. Other prominent search-based techniques used for effort estimation are: Particle Swarm Optimization (PSO), Genetic Algorithm- Artificial Neural Network (GA-ANN), Tabu Search (TS), Evolutionary Programming (EP), Genetic Algorithm- Support Vector Machine (GA-SVM) with a linear kernel function, GA-SVM with a radial basis kernel function, and Particle Swarm Optimization- Artificial Neural Networks (PSO-ANN) amongst others.

Defect Prediction: The most commonly used category for defect prediction was the hybrid search-based techniques (48%). These techniques include choices such as GA-SVM, and SA-PNN (Simulated Annealing Probabilistic Neural Network). In addition, Swarm intelligence techniques were used in 28% of defect prediction studies. This swarm intelligence category consists of a number of Artificial Immune Systems (AIS) algorithms such as the AIRS1 (Artificial Immune Recognition System), AIRS2, AIRS2Parallel (AIRS2P), CLONALG (CLG), Clonal Selection Classifier Algorithm (CSCA), IMMUNOS1 (IM1), IMMUNOS2 (IM2), IMMUNOS99 (IM99), PSO algorithm and its variants (MOPSO (Multi-objective PSO), ADMPSO (Adaptive Dynamical and Median PSO)), Ant Colony Optimization (ACO) and Gene Expression Programming (GEP)). Evolutionary algorithms (mainly GP) were explored in 34% of the defect prediction studies. However, local search algorithms were not evaluated by any defect prediction study.

Maintainability Prediction: All the maintainability prediction studies used the hybrid search-based techniques. These techniques include the GA-ANN, evolutionary fuzzy rule learning techniques and evolutionary fuzzy symbolic regression techniques.

Change Prediction: A majority of change prediction studies (45%) evaluated the use evolutionary techniques such as GP and GA. Only 27% of the studies used swarm intelligence techniques for developing models. These techniques included GEP, Constricted Particle Swarm Optimization (CPSO) and ACO. However, 28% of the studies used hybrid techniques which include alternatives such as the GP-DT (GP based decision trees), and NNEP (Neural Net Evolutionary Programming), Evolutionary decision tree (LEGAL Tree), HEAD-DT (Hyper-heuristic Evolutionary Algorithm- Decision Tree) amongst others. No change prediction study, out of the 11 primary studies, used a local search technique.

From the above statistics, it can be seen that the most popular search-based techniques, for various prediction tasks, are Hybrid techniques. These techniques are popular as they are capable of incorporating the advantages of both statistical and search-based techniques or ML and search-based techniques in a single approach. They provide global optimized solutions, which are characteristics of search-based techniques, combined with faster convergence which are characteristics of ML techniques [122]. The evolutionary techniques, specifically GA and GP, are the next popular search-based techniques for SEPM. Their advantages include simplicity, flexibility, and the ease with which they can adapt to changing circumstances [122]. The GP technique is commonly used for developing effort estimation models, as it does not make pre-assumptions about the distribution of underlying data and can efficiently operate on a small portion of training set to generate effective rules [32,34,54]. Also, GP can take into account whether the source of data is internal to an organization or outside the organization by using appropriate multipliers, thus, building effective prediction models [38]. However, evolutionary techniques take large running times to find optimal solutions. Swarm intelligence techniques are efficient, as they are based on collective behaviour and are easy to implement. However, they have not been extensively explored for SEPM. These trends also show restricted use of local search techniques for SEPM. The reasons for such restrictive use are: a) local search techniques require a suitable "starting point", which is a major hindrance as the search of a suitable starting point may take several days, b) these techniques require extensive programming effort, and c) it is impractical to evaluate the goal functions for local search-based techniques with large number of variables.

Table 3
Validation methods for SEPM using search-based techniques.

Validation Technique	Description	Study Identifier
Leave-one-out Cross Validation (LOOCV)	This validation method involves N iterations for a data set with N data points. Each iteration uses (N −1) data points for training and only one data point for model validation. The process is performed in such a way that each data point is used exactly once for the model validation.	ES6, ES29, ES33, ES38 DS6 CS3
K-Fold Cross Validation	The K-fold cross validation involves partitioning of the original data into K equal sized sets. In order to validate the model, only one of the K sets is retained, while the other (K−1) sets are used for training the model. This process is repeated K times and it is ensured that each set is used only once for model validation. The frequently used values for K are 10 and 3.	ES3, ES11, ES13, ES14, ES16, ES17, ES18, ES19, ES20, ES22, ES23, ES24, ES30, ES31, ES32, ES33, ES37 DS6, DS7, DS8, DS10, DS12, DS13, DS14, DS18, DS22, DS23, DS24, DS25, DS27, DS28 MS3 CS4, CS5, CS6, CS7, CS8, CS9, CS10, CS11
Hold-out Validation	Hold-out validation involves partitioning the original data into two sets, one for training the model and the other for validating the model. The most commonly used partitioning scheme uses 75% of the data for training purposes and the other 25% for validation.	ES1, ES2, ES4, ES7, ES8, ES9, ES12, ES15, ES21, ES22, ES25, ES26, ES27, ES28, ES34, ES35 DS1, DS2, DS3, DS4, DS5, DS9, DS11, DS15, DS16, DS18, DS19, DS20, DS21, DS29 MS2 CS1, CS2

3.3. Experimental settings for SEPM using search-based techniques (RQ2)

In order to effectively develop a software engineering predictive model, it is important to analyze and explore various experimental settings such as validation techniques, the number of runs to address the stochastic nature of search-based techniques, the tools used for simulation and the performance metrics used to assess the developed software engineering predictive models. The research question (RQ3) explores the most commonly used experimental settings described in the literature for the SEPM using search-based techniques.

3.3.1. Validation methods for SEPM using search-based techniques

In order to develop a predictive model and assess its effectiveness, it is crucial to use an efficient validation method. Table 3 provides a description of various validation methods used for SEPM using search-based techniques. Table 3 also states a brief description of the validation methods along with the identifiers of the studies which use a specific validation method. The three most common validation methods used in the selected 78 studies were the Leave-one-out Cross Validation (LOOCV) method, the K-fold cross validation method and the hold-out validation method. The K-fold cross validation is the

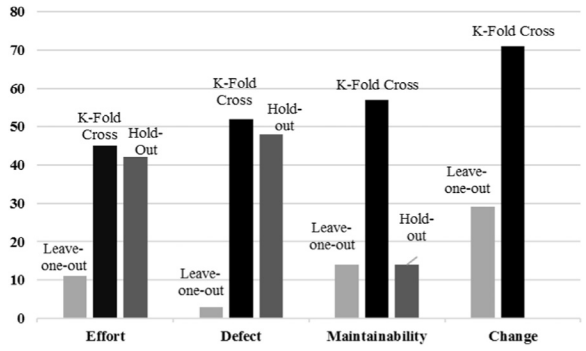


Fig. 4. Distribution of studies according to different validation methods for various quality attributes.

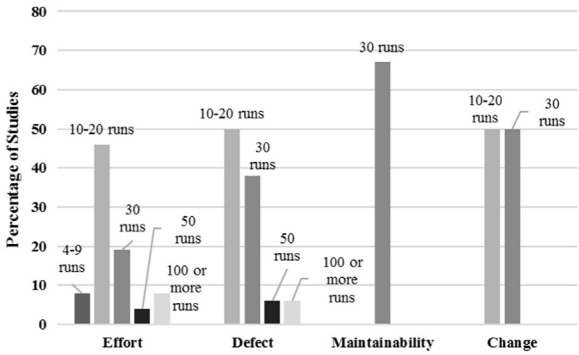


Fig. 5. Distribution of studies according to number of runs for various quality attributes.

most frequently used method, which was used in about 51% of primary studies.

Fig. 4 depicts the distribution of the primary studies using different validation methods, according to a specific quality attribute. These attributes are described below:

Effort Estimation: The hold-out validation method was used in 42% of the effort estimation studies, while the LOOCV method was used by 11% of the effort estimation studies. Around 45% of the effort estimation studies used the K-fold cross validation. Out of these 45% of effort estimation studies, 53% of the studies used 3-fold cross validation (K=3) techniques, while the other 47% used 10-fold cross validation technique (K=10).

Defect Prediction: As shown in Fig. 4, 48% of defect prediction studies used K-fold cross validation method. Also, 48% of defect prediction studies use hold-out validation. The K value was taken as 10 in all the defect prediction studies except DS17 (K=3). Only one study used the LOOCV method.

Maintainability Prediction: Around 33% of maintainability prediction studies used the ten-fold cross validation method and LOOCV methods respectively. One maintainability prediction study did not mention its validation method.

Change Prediction: The majority (81%) of the change prediction studies used ten-fold cross validation technique (K=10). Two change prediction studies used hold-out validation while only one change prediction study used LOOCV method.

In certain studies, such as DS4, DS9, and DS11, the size of data sets used is large enough in order to use hold-out validation to minimize overfitting. Although, the hold-out validation technique is used in a large number of studies (42% of effort estimation studies and 48% of defect prediction studies), the most commonly used technique according to Table 3 is ten-fold cross-validation. This is because the hold-out validation technique exhibits higher variance in results. For example, if we have a single hold-out set with 25% of data for testing and 75% for training, the test set is relatively small and would lead to a lot of variations in results due to different partitions of data for training and test sets. Since ten-fold cross validation averages the results obtained over ten partitions, it reduces variance and the data is not sensitive to partitioning. This gives an accurate estimate of performance. However, a better scenario would be to perform repeated ten-fold cross validation where the data is re-partitioned for every round to increase the number of estimates, before an average is obtained. The next section discusses the number of runs performed by different primary studies to increase the validity of results.

3.3.2. Number of runs to account for Stochastic nature of search-based techniques for SEPM

All the search-based techniques are stochastic in nature. According to Ali et al. [3], it is essential to perform 10 or more runs in order to effectively address the stochastic nature of the search-based techniques. Out of 78 primary studies, 63% of the studies explicitly mentioned that they performed multiple runs for accounting for the stochastic nature of the search-based techniques. Appendix A.4 provides the details of the number of runs performed by each primary study to account for the stochastic nature of the search-based techniques.

Fig. 5 shows the percentage distribution of primary studies using different number of runs to account for the stochastic nature of search-based techniques for the effort estimation, defect prediction, maintainability prediction and change prediction. A detailed description of the usage of different number of runs is as follows:

Effort Estimation: Around 68% of the effort estimation studies mentioned that they accounted for the stochastic nature of search-based techniques by performing multiple runs. Out of these 68% studies, a majority (46%) of the studies performed 10–20 runs and 19% of these studies performed 30 runs. Only one effort estimation study performed 50 runs. 8% of the effort estimation studies, which try and account for the stochastic nature of search-based techniques, used only 4–9 runs and another 8% of these studies used 100 or more runs.

Defect Prediction: 41% of defect prediction studies mentioned that they performed multiple runs to account for the stochastic nature of search based techniques. Of these, 41% of the studies, 38% of the studies used 30 runs and 50% of the studies used 10–20 runs. Finally, 50 runs and 100 or more runs were performed by one defect prediction study each.

Maintainability Prediction: Only one maintainability prediction study mentioned that it accounted for the stochastic nature of search-based techniques by performing multiple runs. However, it did not mention the number of runs it performed.

Change Prediction: Only 55% of change prediction studies reported that they performed multiple runs. Out of these studies, 33% of the studies conducted 10–20 runs, and the remaining 67% conducted 30 runs.

It should be noted that 37% of the primary studies do not explicitly mention whether they performed multiple runs to account for the stochastic nature of search-based techniques or not.

3.3.3. Tools for effective use of search-based techniques for predictive modeling

An existence of tools which effectively simulate search-based techniques aids the development of software engineering predictive models using search-based techniques. However, only 45% of primary studies used and mentioned the use of tools for simulating search-based techniques. Table 4 shows the most commonly used tools along with the identifiers of the studies which use these tools. These tools are useful and effective for developing predictive models and the use of such tools considerably decreases the developer's efforts. Furthermore, with the aid of such tools studies can be easily replicated.

It may be noted that since a large number of studies do not provide details of the simulation tools used, it is difficult to repeat their efforts on their specific data sets.

Table 4
Tools for simulating Search-based Techniques.

Name of the tool	Study identifier
Software of the New-Castle Symbolic optimization Research Group	ES1, ES2, ES5
ArchAngel CBR Tool	ES6, ES18
LIL-GP Tool	ES9, ES23, ES26, DS3, DS4, DS5, DS15, CS1, CS2
DCTG-GP Tool	ES10
Various Toolboxes in MATLAB (PSO Toolbox, GP Toolbox, Global Optimization Toolbox, Genetic Algorithm Optimization Toolbox)	ES25, ES27, DS12, DS23, DS26, DS29, MS3
Waikato Environment for Knowledge Analysis (WEKA) Tool	DS7, DS10, DS13, DS24, CS6
DTREG Tool	DS11, DS27, MS1, CS10
Orange Data Mining Tool	DS20
Knowledge Extraction based on Evolutionary Learning (KEEL) Tool	MS6, CS9, CS11

3.3.4. Performance metrics for evaluating models for SEPM

The performance and estimation accuracy of different search-based techniques can be evaluated with the help of various performance metrics, which are used to assess the effectiveness of the software engineering predictive models developed by these techniques. Fig. 6 shows the most frequently used performance measures in effort estimation, defect prediction, maintainability prediction and change prediction studies along with the percentage use of these measures. Appendix A5 indicates the description of most commonly used performance metrics along with the study identifiers which use them. A detailed description of the usage of different performance measures for each quality attribute is as follows:

Effort Estimation: Most of the effort estimation studies (87%) used the Mean Magnitude of Relative Error (MMRE) as a performance evaluator for effort estimation models. Around 68% of effort estimation studies used Pred (25) for assessing the performance of the developed effort estimation models. Other commonly used performance evaluators were the Median Magnitude of Relative Error (MdMRE), Magnitude of Relative Error (MRE), Mean Square Error (MSE) and coefficient of regression (R^2). Around 61% of the effort estimation studies also used other miscellaneous performance evaluators such as the Adjusted Mean Square Error (AMSE), Balanced Mean Magnitude of Error (BMMRE), Root Relative Square Error (RRSE), Magnitude of Relative Error Relative to the Estimate (EMRE), and Variance Accounted For (VAF) amongst others. All these performance metrics were used in very few studies and were thus clubbed into the miscellaneous category.

Defect Prediction: The most commonly used performance evaluators in defect prediction studies were sensitivity and accuracy, used in 62% and 59% of the studies respectively. Precision and Area Under the Receiver Operating Characteristic (ROC) Curve (AUC) performance metrics were used in 34% of the studies each. Type I and Type II errors, misclassification rate, specificity, F-measure, and PF (probability of false alarm) were other commonly used performance metrics in defect prediction studies. Some other performance metrics grouped under the miscellaneous category were G-mean, weighted accuracy, support, coverage, balance, and Normalized Expected Cost of Misclassification (NECM) amongst others.

Maintainability Prediction: As there are only three maintainability prediction studies, it is difficult to find the most commonly used performance metrics. Some of the used performance metrics are MRE, MMRE, Pred(25), Mean Absolute Relative Error (MARE), Root mean Square Error (RMSE) and Mean Absolute Error (MAE). Pred(30) and Standard Error of the Mean (SEM) were grouped under the miscellaneous category performance evaluators.

Change Prediction: Accuracy was the most commonly used performance evaluator in change prediction studies (73%). Other frequently performance metrics were sensitivity, Type I and Type II error rates, misclassification rate, precision, F-measure and AUC. The G-measure, tree size, j-index and specificity were grouped under the miscellaneous category of performance evaluators for change prediction models.

It can be seen that as effort estimation and maintainability

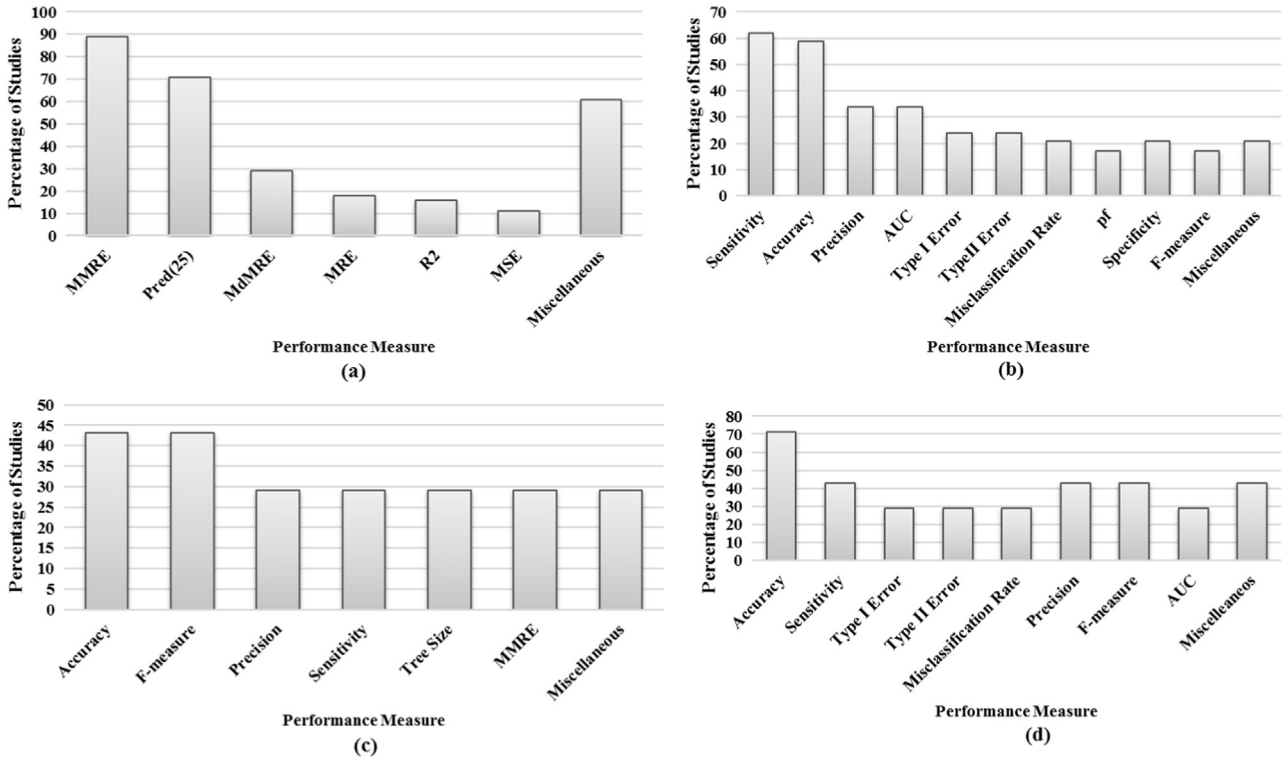


Fig. 6. Performance Metrics for (a) Effort Estimation (b) Defect Prediction (c) Maintainability Prediction (d) Change Prediction.

prediction are regression problems, they use a number of common performance metrics such as MMRE and Pred(25). However, effort estimation models have been evaluated using other performance metrics such as MRE, MSE, R^2, AMSE, BMMRE, RRSE, EMRE and VAF amongst many others. Studies, which use search-based techniques for maintainability prediction should evaluate the developed models using these performance metrics too in order to analyze the overall capability of the developed maintainability prediction models.

Also, it may be noted that Accuracy is a traditional performance metric used by defect prediction as well as change prediction studies. It is easy to compute using a confusion matrix. As defect prediction and change prediction are classification problems, they use common performance metrics namely accuracy, sensitivity, Type I error, Type II error, AUC, precision, misclassification rate, specificity and F-measure. Apart from accuracy, certain other performance metrics such as sensitivity, precision, F-measure, specificity and pf can also be computed using a confusion matrix. Also, as indicated by certain studies, while evaluating models which predict a binary variable (e.g., defect proneness or change proneness), models which exhibit low sensitivity values are not very useful and are worse than models which exhibit low precision values as it is primarily important to identify classes/modules which are defect prone or change prone in nature [87,91]. However, the use of accuracy and precision has been discouraged in the recent literature since, while evaluating a binary variable as the class imbalance problem needs to be considered. A data set is said to be imbalanced if there is a large occurrence of instances of a particular type. For example, if a data with 1000 instances contains 50 defect prone instances and 950 non defect prone instances, it is highly imbalanced. Using such a data set to build quality models would lead to biased results. Thus, the use of traditional performance metrics such as the accuracy, sensitivity or precision is not appropriate in such cases [124–126]. Recent studies advocate the use of stable performance measures such as the AUC, and the G-mean for evaluating models trained by imbalanced data sets [25,91,129].

3.4. Fitness functions of search-based techniques for SEPM (RQ3)

Search-based techniques evaluate the goodness of a number of solutions in order to search for an optimal or near optimal solution. The fitness function is used to evaluate the efficiency of a specific solution. Different studies use different fitness functions for evaluation that are generally based on performance measures (See Section 3.3.4). This section gives a brief description of the most commonly used fitness functions for effort estimation, defect prediction, maintainability prediction and change prediction studies. 80% of primary studies explicitly stated the fitness functions used for evaluating the goodness of a solution. Appendix A.6 lists the commonly used fitness functions by the effort estimation and defect prediction studies.

Effort Estimation: Fig. 7(a) depicts the percentage of effort estimation studies using a specific fitness function. According to the Figure, MSE and MMRE were the most commonly used fitness functions –29% each - in the primary studies. Other fitness functions used were the MdMRE, VAF, Least Absolute Deviation (LAD) and certain combinations of MMRE and Pred (25). A few studies used multi-objective fitness functions to evaluate a solution. For example, Logarithmic Standard Deviation (LSD), MMRE and Pred (25) were also used collectively to evaluate the fitness of a solution. Some studies used other miscellaneous functions, such as Pred (25) (ES12, ES18) and MAE (ES37) amongst others.

Defect Prediction: Fig. 7(b) shows the percentage of studies using a particular fitness function for defect prediction. According to the Figure, 21% of defect prediction studies use accuracy and its variants as fitness functions. The misclassification cost and its variants are also used for ascertaining the goodness of a defect prediction model in 28% of the studies. The F-measure, the multi-objective function of specificity and sensitivity, and the product of specificity and sensitivity were

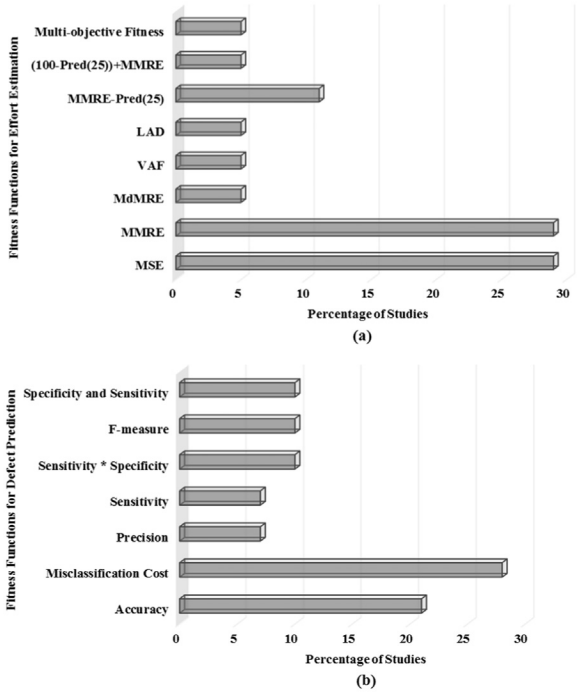


Fig. 7. Fitness Functions for a) Effort Estimation b) Defect Prediction Models.

each used by 10% of defect prediction studies. Other fitness functions used for defect prediction studies were precision and sensitivity. A number of defect prediction studies (31%) also used other miscellaneous fitness functions such as the G-mean, the mean absolute percentage error, and the lift.

Maintainability Prediction: Only one maintainability study (MS3) specified its fitness function which was the inverse of Root Mean Square Error (RMSE).

Change Prediction: Nine change prediction studies (81%) clearly stated the fitness functions used by them while developing change prediction models. CS1 used the misclassification costs for fitness purpose, while the CS2 used a multi-objective fitness function which includes the tree size along with the misclassification cost for evaluation. CS4 used Accuracy, J-index and average number of rules per rule set as fitness criteria. The CS5 study used a function which reported the proportion of correct predictions to incorrect predictions, while the CS9 used accuracy with penalty as a fitness evaluator. Other used fitness functions in change prediction studies were accuracy (CS3, CS8) and F-measure (CS6, CS7) which were used by 18% of change prediction studies each.

It can be seen from the above discussion that a wide variety of performance metrics have been employed as fitness functions for developing various software quality models. However, a researcher should explore a number of different performance evaluators as fitness functions as a change in fitness function may lead to significant change in results [51]. Moreover, only 8% of primary studies used multi-objective fitness functions; the use of multi-objective fitness functions should be explored as it helps in creating balanced and stable models by optimizing several constraints simultaneously.

3.5. Predictive capability of search-based techniques for SEPM (RQ4)

It is essential to evaluate and assess the predictive capability of different search-based techniques in order to ascertain their usefulness for developing various predictive models. This section evaluates the predictive performance of search-based techniques by reporting the values of different performance metrics (stated in Section 3.3.4).

In order to generalize the results, we report the results of only those

techniques which have been evaluated on at least three different data sets and have been used by at least two primary studies. This is required to prevent the bias due to an exceptional performance of a technique in a specific study or on specific data sets. The statistics reported are obtained by analyzing the results data set-wise. However, it may be noted that the results of a specific technique may vary in accordance with the data set on which it is applied. To reduce this effect, we remove the outlier values for a specific technique obtained for a particular data set. Moreover, we report the median values obtained by a specific technique. We use the following rule for extracting data values of various performance metrics. The rules are chosen in such a manner that the optimum values are taken. This is because the performance of search-based techniques may vary a lot due to parameter settings and we tend to explore the best possible value which can be obtained by application of various search-based techniques.

- If the same study evaluates a particular data set more than once with different experimental settings, we take the best value (optimal) for a specific performance metric.

- If more than one study uses a particular data set with the same technique, we use the best value of the performance metric values reported in the studies.

Effort Estimation: As discussed in Section 3.3.4, MMRE and Pred (25) are the most commonly used performance evaluators for assessing effort estimation models. A good effort estimation model will have low MMRE values and high Pred (25) values. In order to analyze the predictive performance of different search-based techniques, we extracted the values of MMRE and Pred (25) on different data sets used in different effort estimation studies. Some of the most commonly used effort estimation data sets were academic projects by Dolado (ES1, ES2, ES5, ES8), Desharnais data set (ES4, ES15, ES17, ES18, ES19, ES22, ES23, ES24, ES29, ES30, ES32, ES38), Finnish data set (ES6, ES8, ES30), NASA software projects (ES12, ES15, ES17, ES23, ES24, ES25, ES26, ES32, ES35, ES36, ES38), ISBSG data set (ES7, ES9, ES10, ES11, ES14, ES31, ES34, ES35, ES37), COCOMO data set (ES1, ES3, ES16, ES20, ES24, ES29, ES32, ES36, ES37, ES38) and IBM DP data set (ES5, ES9, ES13, ES18) amongst many others. Fig. 8 illustrates the outliers, associated with these two performance evaluators, for different search-based methods when applied on different data sets. According to the figure, the GP technique obtained very high MMRE values on the ISBSG and COCOMO data sets and GA-ANN technique obtained a very high MMRE value on the IBM DP data set. These outliers were removed before further analysis.

Table 5 describes the minimum (Min.), maximum (Max.), mean, median and standard deviation (S.D.) values of the MMRE and Pred (25) performance evaluators, after removing the outliers in order to reduce bias. According to the Table, the GA-ANN technique gave the best average MMRE value of 0.23, while the GA-SVM (RBF) gave the best Pred (25) value of 79.11. The GP technique gave the worst MMRE average score of 0.54, while the TS technique gave the worst Pred (25) value of 39. It may also be noted that, the mean MMRE values of all the reported techniques range between 0.23 and 0.54. Also the mean Pred (25) values of the techniques, apart from the TS technique, range between 50–80%. The poor results of the TS technique could be due to its local nature. Thus, the use of search-based techniques is encouraging as the reported ranges are close to the acceptable level (Pred (25) > =75% and MMRE < =0.25) for effort estimation models as stated by Conte et al. [123].

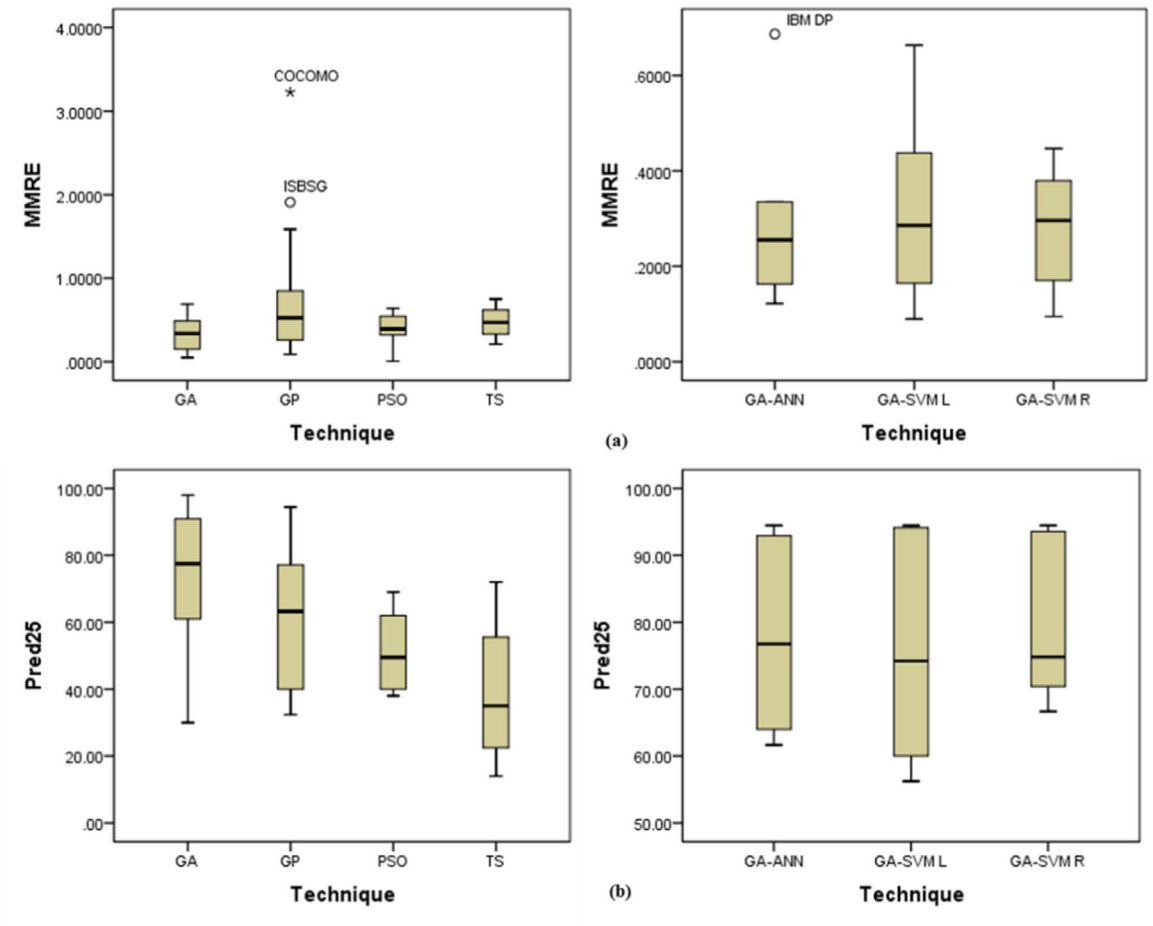


Fig. 8. Outliers for Effort Estimation Models according to Data Sets (a) MMRE (b) Pred (25).

Table 5
Results of Search-based Techniques for Effort Estimation Models.

Technique	Count	Performance measure	Min.	Max.	Mean	Median	S.D.
TS	4	MMRE	0.21	0.75	0.48	0.47	0.22
	4	Pred (25)	14.00	72.00	39.00	35.00	24.34
PSO	7	MMRE	0.01	0.64	0.40	0.39	0.22
	6	Pred (25)	38.00	69.00	51.33	49.50	12.19
GA	10	MMRE	0.05	0.69	0.34	0.33	0.22
	10	Pred (25)	30.00	98.00	73.53	77.50	22.66
GP	10	MMRE	0.09	1.58	0.54	0.48	0.38
	16	Pred (25)	32.40	94.40	60.57	63.25	22.95
GA-SVM (Linear)	6	MMRE	0.09	0.66	0.32	0.29	0.21
	6	Pred (25)	56.25	94.44	75.53	74.21	16.93
GA-SVM (RBF)	6	MMRE	0.09	0.45	0.28	0.30	0.14
	6	Pred (25)	66.67	94.44	79.11	74.80	11.92
GA-ANN	5	MMRE	0.12	0.33	0.23	0.19	0.09
	6	Pred (25)	61.67	94.44	77.75	76.74	14.14

Defect Prediction: As mentioned in Section 3.3.4, the accuracy and sensitivity are the most commonly used performance metrics for defect prediction studies. However, we also use the AUC as it is a stable performance metric for evaluating models developed using imbalanced data sets, as mentioned in Section 3.3.4.

A number of data sets were used for developing defect prediction models which included the telecommunication data set (DS1, DS2, DS5, DS12), NASA data sets (CM1, PC1, PC2, PC3, PC4, KC1 with modules, KC1 with classes, KC2, JM1, KC3, MW1) which are publicly available in the PROMISE repository used by DS6, DS7, DS8, DS9, DS13, DS14, DS15, DS16, DS17, DS19, DS20, DS22, DS24, and DS26 and various open source data sets such as Lucene, Ant, Camel, Tomcat, Jedit etc. (DS11, DS18, DS21, DS23). Fig. 9 presents the outliers of different search-based techniques, when reported on different data sets. As seen in the figure, the MOPSO, IM1 and GP had one outlier each according to accuracy values, and the CLG and IM1 techniques also had one outliers each according to AUC values. The Telecommunication data set was an outlier for AIRS1 and GP technique according to sensitivity values.

A good defect prediction model exhibits higher values of accuracy, sensitivity or AUC metrics. Table 6 presents comparative results of the defect prediction models using the selected performance evaluators, after removing the outliers. It reports the minimum (Min.), maximum (Max.), mean, median and standard deviation (S.D.) values. According to the Table 6, the GEP, GA-SVM and the MOPSO techniques gave the best results using to the mean accuracy (85.84%), the mean sensitivity (71.31%) and the mean AUC values (0.78) respectively. The most of the search-based techniques (except IM1 and GA-SVM) gave good performance scores for the accuracy metric in the range 70–85%. However, it can be noted that only the performance of the models developed by the MOPSO and the GEP techniques gave an acceptable value for the AUC metric in the range 0.7–0.8. Since MOPSO uses a multi-objective fitness function, it provides effective results for developing efficient defect prediction models [7,68].

Maintainability Prediction: *Different search-based techniques, such as the GA-ANN, NNEP and other evolutionary fuzzy rule learning and evolutionary symbolic regression techniques were used in different maintainability studies. Thus, we could not report the cumulative statistics for each technique. The MMRE values, for maintainability prediction models developed using search-based techniques, ranged between 0.25–0.39; while their Pred (25) values ranged up to 60%. These values indicate an acceptable performance of the search-based techniques for developing maintainability prediction models.*

Change Prediction: *For change prediction studies, different studies used different search-based techniques, such as the GA-LDA, HEAD-DT, NNEP, GA, GP and the GP-DT amongst others. Hence, the statistics for a single technique could not be reported. However, according to the primary studies, the reported accuracy performance metric of the models predicted using search-based techniques for change prediction ranged between 60–85% for a number of techniques on different data sets such as Jedit, Simutrans, Eclipse amongst others (CS4, CS5, CS7, CS8, CS9, CS10, CS11). Also, the F-measure values for various search-based techniques, used in change prediction studies, ranged between 63–75% (CS6, CS7).*

It can be seen that the results obtained using different performance metrics of a number of search-based techniques are encouraging for their use in SEPM tasks. However, researchers should evaluate various characteristics, such as its intrinsic characteristics, its advantages and disadvantages, and the comprehensibility of the developed models, of a search-based technique to determine an overall capability and suitability of search-based techniques in specific scenarios for SEPM tasks.

3.6. Comparative performance of search-based techniques for SEPM (RQ5)

This section compares the performance of different search-based techniques amongst themselves and with other ML techniques used for developing effort estimation, defect prediction, maintainability prediction and change prediction models. It should be noted that while comparing the performance of search-based techniques, we analyzed the results data set-wise and followed the same rules as discussed in Section 3.5. We also performed the Wilcoxon sign rank test with α=0.05 to statistically evaluate the comparison results.

3.6.1. Comparative Performance of search-based techniques for effort estimation

We analyzed the performance of six search-based techniques, namely, PSO, GA, GP, GA-SVM (Linear), GA-SVM (RBF) and GA-ANN amongst themselves, and six other ML techniques (Artificial Neural Networks (ANN), Classification and Regression Trees (CART), Case Based Reasoning (CBR), Support Vector Machine with Linear kernel (SVM-Lin), Support Vector Machine with RBF Kernel (SVM-RBF) and Bagging (BG)) for developing effort estimation models, according to the MMRE values. These techniques were selected as they are commonly used in literature and sufficient data could be collected for comparison purposes for these techniques with other search-based techniques (i.e., used by at least two primary studies and on three data sets). Table 7 reports the results of the Wilcoxon sign rank test when different techniques are compared amongst each other. The symbol "↑*" represents significantly better (α=0.05) results of the technique stated in the row when compared with the technique stated in the column, while "↓*" represents significantly worse results. However, the symbols "↑" and "↓" represents better or worse results respectively, but these results were not found statistically significant. The symbol "=" represents the equal performance of the two compared methods, while the symbol

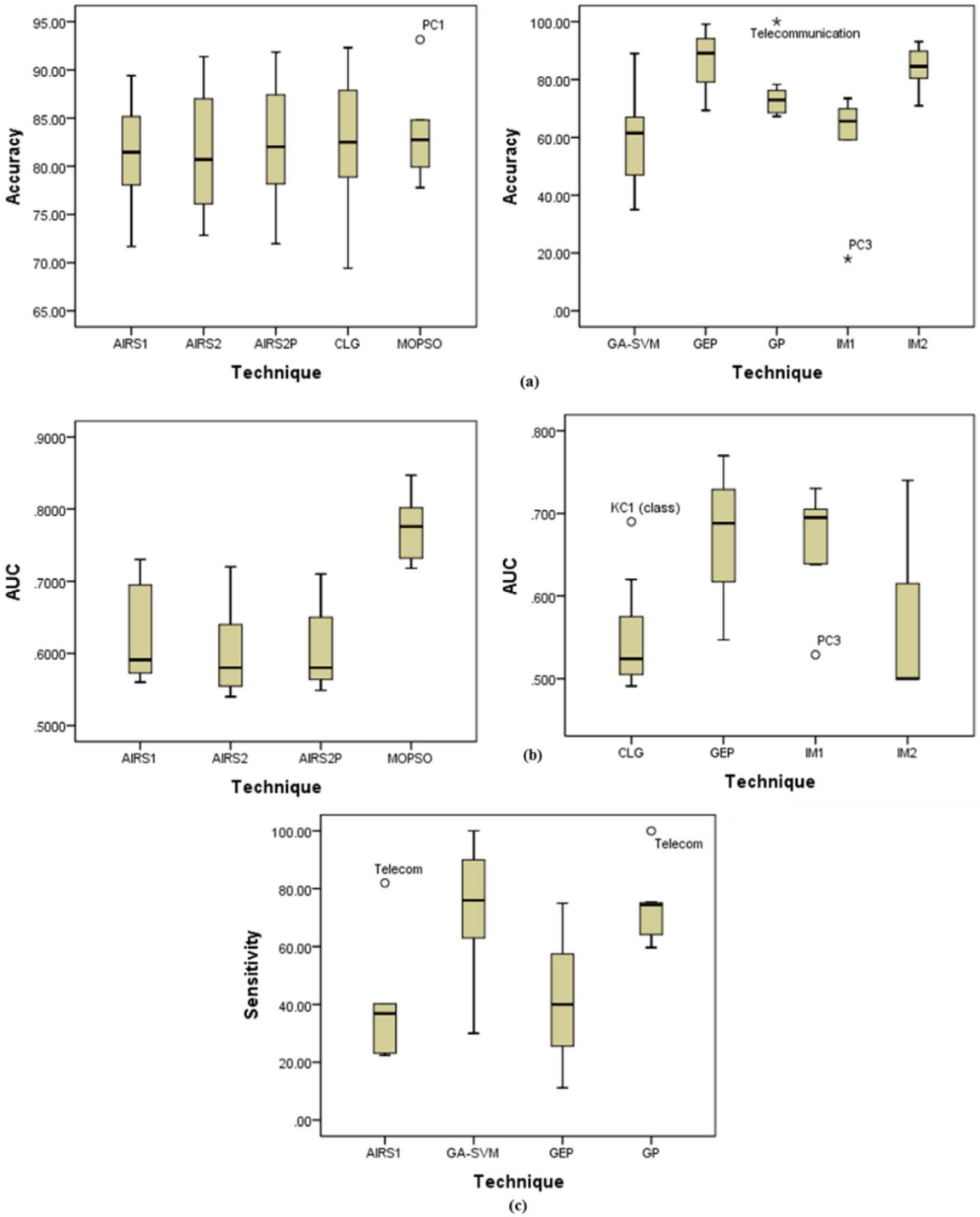


Fig. 9. Outliers for Defect Prediction Models according to Data Sets (a) accuracy (b) AUC (c) sensitivity.

"NC" represents that, we could not find sufficient data in literature to compare the corresponding two techniques.

It can be seen from the above Table 7, that the PSO technique performed better than ANN, CART and SVM-Lin techniques but not significantly. It was found equivalent to the GP technique. Similarly, the GA technique is significantly better than only the CART technique, although it performed better than GA-SVM (LIN), GA-SVM (RBF), GA-ANN, CBR, SVM-Lin and BG. However, it was found to be equivalent to the ANN technique.

Fig. 10 summarizes the comparison results stated in Table 7. According to the Figure, the GP technique, performed worse than all the techniques except two (ANN and CART). The GA technique performed better than 7 other techniques. However, the results were significant in only one case. Similarly, the PSO technique performed better than two other compared techniques. The results show good performance of the GA search-based technique for developing effort estimation models as it was found better than most of the other compared techniques. This could be due to strengths of GA technique which include no assumptions about the underlying data, does not get trapped in local minima and performs a simplified automatic search [40–42,53,68]. The PSO technique is also effective, because as compared to GA it has less number of parameters which need adjustment. Similarly, the results of other search-based techniques were also encouraging.

Table 6
Results of Search-based Techniques for Defect Prediction Models.

Technique	Count	Performance measure	Min.	Max.	Mean	Median	S.D.
MOPSO	5	Accuracy	77.79	84.81	81.60	80.90	3.05
	6	AUC	0.72	0.85	0.78	0.78	0.05
AIRS1	6	Accuracy	71.67	89.40	81.20	81.46	6.36
	4	Sensitivity	22.40	40.20	30.63	29.95	9.20
	8	AUC	0.56	0.73	0.62	0.59	0.07
AIRS2	7	Accuracy	72.93	91.37	81.58	80.70	7.25
	7	AUC	0.54	0.72	0.60	0.58	0.06
Airs2P	7	Accuracy	71.98	91.86	82.42	82.02	7.27
	7	AUC	0.54	0.71	0.61	0.58	0.06
CLG	7	Accuracy	69.42	92.31	82.53	82.50	7.71
	6	AUC	0.49	0.62	0.53	0.52	0.05
IM1	5	Accuracy	59.17	69.74	64.41	64.82	4.23
	7	AUC	0.64	0.73	0.69	0.70	0.03
IM2	7	Accuracy	70.91	93.06	84.15	84.55	7.61
	7	AUC	0.50	0.74	0.57	0.50	0.11
GP	6	Accuracy	67.26	78.30	71.59	71.31	4.34
	6	Sensitivity	59.67	75.44	68.79	69.30	6.10
GEP	3	Accuracy	69.30	99.11	85.84	89.10	15.17
	3	Sensitivity	11.11	75	42.03	40.00	31.99
	3	AUC	0.55	0.77	0.67	0.69	0.11
GA-SVM	9	Accuracy	35.00	89.00	59.93	61.50	16.52
	9	Sensitivity	30.00	100.00	71.31	76.00	25.46

Table 7
Wilcoxon Test Results of Search-based Techniques comparison on MMRE.

Technique	PSO	GA	GP	GA-SVM (Linear)	GA-SVM (RBF)	GA-ANN	ANN	CART	CBR	SVM-LIN	SVM-RBF	BG
PSO	–	NC	=	NC	NC	NC	↑	↑	NC	↑	NC	NC
GA	NC	–	↑	↑	↑	↑	=	↑*	↑	↑	NC	↑
GP	=	↓	–	↓	↓	↓	↑	↑	=	↓	↓	↓
GA-SVM (LIN)	NC	↓	↑	–	↓	↓	↓	NC	NC	NC	NC	↓
GA-SVM (RBF)	NC	↓	↑	↑	–	↓	↓	NC	NC	NC	NC	↓
GA-ANN	NC	↓	↑	↑	↑	–	↓	NC	NC	NC	NC	↓

3.6.2. Comparative performance of search-based techniques for defect prediction

We analyzed the performance of nine search-based techniques (MOPSO, AIRS1, AIRS2, Airs2P, CLG, IM1, IM2, GP and GA-SVM) amongst themselves and with nine other ML techniques (Bayesian Networks (BN), Naïve Bayes (NB), Random Forests (RF), ANN, J48, Repeated Incremental Pruning to Produce Error Reduction, a rule learning algorithm (RIPPER), Decision tree C4.5, SVM, and Nearest Neighbor Algorithm with Non-nested Generalized Exemplars (NNGE)) for developing defect prediction models. Again, these techniques were chosen as they were evaluated by at least two primary studies on three data sets. We compared the defect prediction models based on the accuracy and AUC values. The sensitivity values were not considered as very few techniques (only three) could be compared using the sensitivity values. Tables 8 and 9 report the Wilcoxon sign rank test comparison results of different techniques using the accuracy and AUC values respectively. The symbolic notation of Tables 8 and 9 are the same as followed in Table 7.

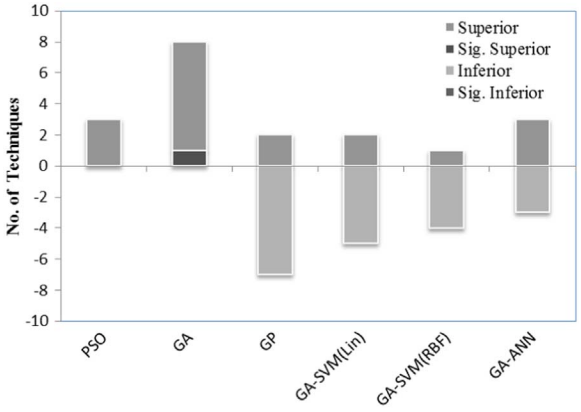


Fig. 10. Wilcoxon test results of Search-based techniques comparison based on MMRE values.

It can be seen from Table 8, that the GP technique performed significantly worse than all other compared techniques except IM1. However, the MOPSO technique performed better than all the other compared search-based techniques using the accuracy values. A similar trend was seen with the MOPSO technique, when it was compared using the AUC values (Table 9). The GA-SVM technique, though compared by less number of techniques, performed significantly better than C4.5, NB and ANN techniques, when compared using accuracy values.

Fig. 11 summarizes the comparison results stated in Tables 8 and 9. As seen in this Figure, the IM1 and GP were the worst search-based techniques according to the accuracy values. On the other hand, the IM2 and CLG were the worst search-based techniques according to the AUC values. Our results are in accordance with [65] where Immunos algorithms were not found effective for large data sets. Since the use of accuracy has been criticized in the literature due to the imbalanced nature of the data sets [127,128], we advocate the results obtained using the AUC technique. Thus, the MOPSO technique is the best search-based technique mentioned in literature for developing defect prediction models, when evaluated using AUC values. It may also be noted that the performance of several AIS algorithms (AIRS1, AIRS2, AIRS2P, CLG and IM1) was poorer than the most other search-based techniques and ML techniques. However, more studies should be conducted to yield conclusive results, as the performance metrics of

Table 8
Wilcoxon test results of search-based techniques comparison based on accuracy.

	MOPSO	AIRS1	AIRS2	AIRS2P	CLG	IM1	IM2	GP	GA-SVM	BN	NB	RF	ANN	J48	RIPPER	C4.5	SVM	NNGE
MOPSO	–	↑	↑	↑	↑	↑*	↑	↑*	NC	↑	↓	↓	↓	↓	↓	↓	↓	↑
AIRS1	↓	–	↓*	↓*	↓*	↑*	↓*	↑*	NC	↓	↓*	↓*	↓*	↓*	↓*	↓*	↓	↓
AIRS2	↓	↑*	–	↓*	↓	↑*	↓*	↑*	NC	↑	↑	↓*	↓*	↓*	↓*	↓*	↓	↓
AIRS2P	↓	↓*	↑	–	↓	↑*	↓	↑*	NC	↑	↑	↓*	↓*	↓*	↓*	↓	↓	↓
CLG	↓	↑*	↑*	↑	–	↑*	↓*	↑*	NC	↑	↑	↓*	↓*	↓*	↓*	↓	↑	↑
IM1	↓*	↓*	↓*	↓*	↓*	–	↓*	↓*	NC	↓*	↓*	↓*	↓*	↓*	↓*	↓*	↓*	↓*
IM2	↓	↑*	↑*	↑	↑*	↑*	–	↑*	NC	↑	↑	↓	↓	↑	↓	↓	↑	↑
GP	↓*	↓*	↓*	↓*	↓*	↑*	↓*	–	NC	↓*	↓*	↓*	↓*	↓*	↓*	↓*	↓*	↓*
GA-SVM	NC	NC	NC	NC	NC	NC	NC	NC	–	NC	↑*	↑	↑*	NC	NC	↑*	↑	NC

Table 9
Wilcoxon test results of search-based techniques comparison based on AUC.

	MOPSO	AIRS1	AIRS2	AIRS2P	CLG	IM1	IM2	BN	NB	RF	ANN	J48	RIPPER	C4.5	SVM	NNGE
MOPSO	–	↑*	↑*	↑*	↑*	↑*	↑*	↑	↑*	↑	↑*	↑*	↑*	↑*	↑*	↑*
AIRS1	↓*	–	↑	↓	↑*	↓	↑	↓*	↓*	↓*	↓	↓*	↑	↓*	↑	=
AIRS2	↓*	↓	–	↓	↑*	↓	↑	↓*	↓*	↓*	↓*	↓*	↑	↓	↑	=
AIRS2P	↓	↓	↑	–	↑*	↓	↑	↓	↓*	↓*	↓	↓	↑	↓	↑	=
CLG	↓*	↓*	↓*	↓*	–	↓*	↑	↓*	↓*	↓*	↓*	↓*	↓*	↓	↓	↓
IM1	↓*	↑	↓	↑	↑*	–	↑*	↓*	↓*	↓*	↓	↓	↑*	↓	↑*	↑
IM2	↓*	↓*	↓	↓*	↓	↓*	–	↓*	↓*	↓*	↓*	↓*	↓	↓	↓	↓

the models developed by these techniques were reported in very few studies.

3.6.3. Comparative performance of search-based techniques for maintainability prediction and change prediction

As there are very few studies for maintainability prediction and change prediction studies, we did not have sufficient data to statistically compare the results of different techniques. However, certain studies (MS2, MS3, CS2, CS4, CS5, CS7, CS8, CS9, CS11) did report a comparative analysis of different search-based techniques amongst themselves or with other ML techniques.

MS2 compared two evolutionary fuzzy algorithms with a number of decision tree, neural network and support vector algorithms and found the evolutionary fuzzy algorithms to be significantly better than most of the compared techniques. The study MS3 compared the neuro-genetic approach with the BN, ANN, regression tree and many other ML techniques and was found showing promising results.

The CS2 study compared a standard GP approach with GP-based decision trees for developing change prediction models and found that the GP-based decision trees are better. However, the study did not perform any statistical comparison. Study CS4 compared the GA technique with the C4.5 techniques to develop change prediction models and evaluated it on both balanced and unbalanced data sets. Their results indicate that the GA technique outperformed the C4.5 technique. The study CS5 statistically compared the ACO technique with the C4.5 technique for the change prediction and concluded that the ACO technique provided significantly better results. The studies CS7 and CS8 compared the performance of LEGAL Tree and HEAD-DT with other techniques such as the CART and J48 and concluded that the LEGAL Tree and the HEAD-DT outperform other techniques for the change prediction. The study CS9 compared the performance of seven search-based techniques (Hierarchical Decision Rules (HIDER), NNEP, Constricted Particle Swarm Optimization (CPSO), Supervised Classifier System (SUCS), Genetic Learning Adaboost (GL-AB), Genetic Algorithm-based classifier system with Intervalar Rules (GA-Int) and Fuzzy Hybrid Genetics-Based Machine Learning (FH-GBML)) with three ML techniques namely, C4.5, ANN and SVM. According to the results of that study, the SUCS technique, an evolutionary technique, gave the best change prediction model with a mean accuracy value of 78%, when compared with all the other search-based and ML techniques. The results were also supported by a statistical test. Study CS11 again compared six search-based techniques, i.e., CPSO, HIDER, SUCS, NNEP, Memetic Pittsburgh Learning Classifier System (MPLCS) and Fuzzy Learning based on Genetic Programming Grammar Operators and Simulated Annealing (GFS_SP) with a number of ML techniques, such as ANN, BG, and Random Forests, using the Friedman test. Although, the best performing technique was BG, the search-based techniques showed efficient capability and promising results in developing change prediction models.

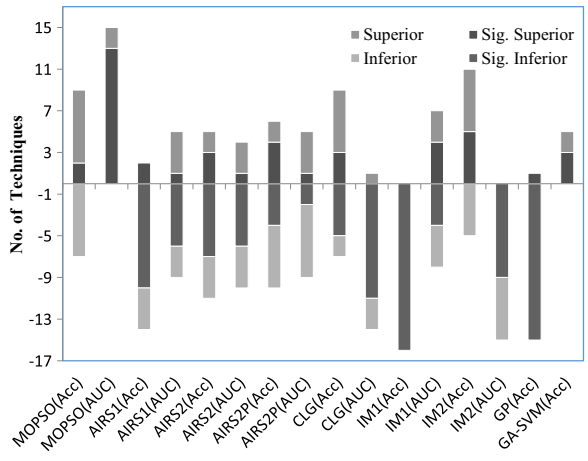


Fig. 11. Wilcoxon test results of Search-based techniques comparison based on accuracy and AUC values.

3.7. Statistical tests as used in primary studies (RQ6)

It is important to statistically validate the comparative results of different techniques in order to provide an effective support to the reported conclusions [130]. Only 38% of the primary studies used statistical tests for comparison among different techniques. Appendix A.7 indicates the statistical tests used by different primary studies along with their identifiers. Fig. 12 shows primary studies that have used various statistical tests according to different quality attributes (effort, defect, maintainability and change).

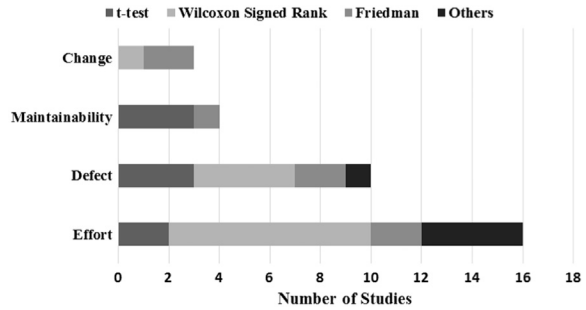


Fig. 12. Distribution of studies according to different statistical tests used.

A brief description of the use of different statistical tests is as follows:

Effort Estimation: Around 42% of effort estimation studies used a statistical test for a comparison among various techniques. The majority of the effort estimation studies used the Wilcoxon signed rank test followed by the *t*-test and the Friedman test. Some other tests used for statistical comparison in effort estimation studies were ANOVA, the Mann-Whitney *U* test and the post-hoc Nemenyi test.

Defect Prediction: 40% of defect prediction studies used statistical validation for a comparison among different techniques. Four defect prediction studies used the Wilcoxon signed rank test, 4 studies used the *t*-test and only one defect prediction study used the Friedman test for statistical comparative analysis. The study DS17 used the McNemar's test.

Maintainability Prediction: Only one maintainability prediction study used a statistical test (*t*-test) for effective comparison of different techniques.

Change Prediction: 45% of change prediction studies used statistical tests for a comparative analysis amongst different techniques. Two change prediction studies each used the *t*-test and the Friedman test. One change prediction study used the Wilcoxon signed rank test.

It may be noted that the majority of the studies use non-parametric statistical tests such as the Wilcoxon signed rank test, Friedman test, Mann-Whitney *U* test and Nemenyi test as compared to parametric tests (e.g., *t*-test, ANOVA test, and McNemar's test). This is because parametric tests require complete information about the population and require specific assumptions, such as the data normality to be true before the application of these tests. Although, these properties make parametric tests more powerful, they are difficult to use as compared to the non-parametric tests which do not require any assumptions with respect to the population and are simple and easy to understand. The trends, reported in the primary studies, also show that the *t*-test and the Wilcoxon signed rank test are the most commonly used tests in literature, i.e., most of the studies try and evaluate pairwise comparisons amongst different techniques. However, as the *t*-test requires large sample sizes and normal distribution, most studies use the Wilcoxon test for pairwise statistical comparisons if the differences amongst pairs is non-normal. It should also be noted that the Wilcoxon test can be used as a post-hoc test after the application of the Friedman test which increases the number of studies choosing it for statistical analysis.

3.8. Advantages and disadvantages of search-based techniques (RQ7)

This section describes different advantages and disadvantages of various search-based techniques as stated by the primary studies. Table 10 states various identifiers of the studies which support the specific characteristic of a particular technique. However, it may be noted that the reported properties of various search-based techniques may be valid only in the context of the study which states it. Therefore, it is difficult to conclude the scenarios which encourage the application of a specific search-based technique. However, in order to reduce study bias, we only report those properties which are advocated by at least two studies.

Table 10
Advantages and disadvantages of search-based techniques.

Technique	Advantages	Studies
GP	Helps in generating symbolic equations to model underlying data relationships. It produces comprehensible models.	ES1, ES2, ES4, ES9, ES17, ES26, DS4, DS5, CS2.
	Helps in identifying nonlinearities of underlying data and can operate on only a small portion of data for extracting rules.	ES1, ES2, ES10, ES26
	It is non-parametric in nature. Hence, does not make any assumptions about the underlying data.	ES1, ES2, ES5, ES8, ES10, ES26, DS5, DS8
	It is appropriate for high dimensional problems and vast space of cost functions due to its parallel nature, directed search process by recombination operators and fitness functions.	ES3, ES5, ES9, ES10, DS10, DS15
	It helps in finding unusual relationships by discovering data trends. It is adaptive in nature.	ES1, ES2, ES4, ES10, ES26, DS4, DS8, CS2
	It is robust in nature as it can handle noisy data well.	ES8
	It is a global search technique which does not get trapped in the local optima.	ES26, DS4, CS2
	It can automatically eliminate unrelated attributes and extract important attributes.	ES10, ES26
	It is capable of automatically extracting a solution from the training data.	DS3, DS4, DS5, CS1, CS2
GA	It does not make any assumptions about the underlying data distribution.	ES11, ES13, ES15, DS1
	It can easily perform simplified and automatic search in complex and multimodal search spaces.	DS1, DS2
	It does not return to the local minima.	ES12, ES24, DS1, DS2
PSO	It is a fast converging technique.	ES31, ES37, DS29
MOPSO	It can handle numerical as well as discrete attributes.	ES38, DS7, DS13
	It allows rules to be expressed as different objectives which can then be found in a single unique run.	DS7, DS13
LEGAL Tree	It produces comprehensible models with a small tree size.	CS7, CS8
GP_DT	It is flexible and provides a practical solution to optimize conflicting objectives.	DS4, CS2
Disadvantages		
GP	It requires a large set up time and running effort.	ES4, ES10
GA	It requires a large number of runs so that they are not trapped in local optima.	ES10, MS1

4. Threats to validity

Our review is conducted using the assumption that the primary studies are unbiased. However, if this is not the case, there is a threat to the validity to our review results [23]. Also, our review does not include any unpublished results [128].

Quality assessment was performed by the authors independently to avoid bias. This procedure strengthens the conclusion validity of the results. In order to compare different techniques, we extracted performance metrics data from various studies. However, these studies use varied experimental designs (parameter settings, validation techniques, fitness functions, etc.). This may be a possible threat to the results of the review. However, we performed the outlier analysis and also reported the median values to reduce this threat.

The advantages and disadvantages of different search-based techniques, which are inferred from primary studies, may be a representation of only the author's opinion [24]. However, these characteristics are extracted from studies with acceptable quality standards after performing a rigorous quality analysis. Moreover, we state only those properties which are advocated by at least two studies. Thus, this threat is reduced.

5. Discussions of results and future guidelines to researchers

This section discusses the various results specific to each research question and also states various recommendations for future researchers who intend to use search-based techniques for SEPM tasks.

5.1. Discussions of Results

After analyzing the 78 primary studies, we conclude that search-based techniques can be used in three ways for SEPM: a) for performing feature selection, b) for deciding the weights, structure or parameters of other techniques, or c) for developing predictive models. We first provide discussions specific to each research question:

- (RQ1) Different search-based techniques were broadly categorized into four categories, namely, Local Search techniques, Swarm Intelligence techniques, Evolutionary techniques, and Hybrid search-based techniques. According to the studies that we analyzed, the evolutionary techniques were the most commonly used techniques for effort estimation. However, the hybrid search-based techniques were the most commonly used techniques for the defect prediction and maintainability prediction tasks. A majority of change prediction studies used the swarm intelligence techniques. These trends indicate a limited use of local search techniques for SEPM, which could be because the local search techniques require considerable programming expertise, large set up time, and are not appropriate for goals involving a large number of variables.
- (RQ2) The most commonly used validation method, for SEPM using search-based techniques, was the K-fold cross validation with a value of K=10. This method produces accurate estimates of a model's performance with low variance in results. A number of studies, which accounted for the stochastic nature of search-based techniques by performing multiple runs, performed the number of runs between 10 and 20. Very few studies used well-established tools for simulating search-based techniques. This trend indicates shortage of such tools for simulating various search-based techniques. The most commonly used tool was the LIL-GP tool as GP was used for predictive modeling in a large number of studies.
- MMRE and Pred (25) are the most frequently evaluated performance metrics for effort estimation models, while the accuracy, the sensitivity, and the AUC performance metrics are analyzed by the most number of defect prediction studies. Some of the used performance metrics for maintainability prediction were MRE, MMRE, Pred(25), Mean Absolute Relative Error (MARE), Root mean Square Error (RMSE) and Mean Absolute Error (MAE). A majority of change prediction studies used the accuracy as a performance metric. In general, the most commonly evaluated and traditional performance metric for the quality attributes which are binary in nature is accuracy. However, there is a shift towards other stable performance metrics such as the AUC, and the G-mean. For variables which are continuous in nature, it is common to use estimates of errors such as the MMRE, and the Pred (25) for evaluating the performance of the developed model.
- (RQ3) The MSE and MMRE were the most commonly used fitness functions in effort estimation studies. Similarly, the accuracy and its variants as well as various combinations of Type I and Type II errors were the most commonly used fitness functions in defect prediction studies. Maintainability prediction study used inverse of RMSE fitness evaluation. However, different change prediction studies used different fitness functions for developing change prediction models, the most commonly being accuracy and f-measure. It is important for researchers to appropriately select a fitness function for achieving optimum results. This can be done by performing repeated studies which optimize different fitness functions for developing effective software engineering predictive models and comparing their results in order to choose an optimum fitness function. Also, the use of multi-objective fitness functions should be explored as they help to balance out various constraints. This is possible by maximizing or minimizing more than one objective while developing software engineering predictive models.
- (RQ4) For effort estimation tasks, a majority of search-based techniques show an acceptable level of predictive capabilities with the MMRE values ranging between 0.23 - 0.54 and Pred (25) values ranging between 50 and 80. The predictive capability of search-based techniques, such as MOPSO, is good for defect prediction with accuracy values ranging between 70–85% and the AUC values ranging between 0.7 and 0.8. The MMRE values, for maintainability prediction models developed using search-based techniques, were in the range of 0.25–0.39 and the Pred(25) values were up to 60%. Search-based techniques exhibited an acceptable performance for change prediction models as their accuracy values ranged between 60–85% and F-measure values ranged between 63–75%.
- (RQ5) The results of the Wilcoxon test indicate that the GA technique outperforms a majority of other techniques when used on the most data sets for effort estimation tasks. Thus, this technique has been used by the most of the effort estimation studies. However, for the defect prediction tasks, the MOPSO technique works well. The GA technique has not been used much for developing defect prediction models. Also, the MOPSO technique outperformed the most of the other search-based techniques and the ML techniques when used with a majority of the data sets for defect prediction. Certain studies compared search-based techniques with other techniques for developing maintainability prediction and change prediction models. The results of these studies support the use of search-based techniques, as they performed better than the other compared techniques for developing these models in majority of the studies. These results encourage the use of search-based techniques as they are robust, provide global optimum results and easily adapt to changing circumstances.
- (RQ6) Statistical tests were used by only few (38%) studies for the comparison amongst different techniques. The most frequently used test for comparing software engineering predictive models using search-based techniques was the Wilcoxon signed rank test due to its non-parametric nature. It does not require any assumptions for the investigated data to follow a normal distribution.
- (RQ7) The characteristics, advantages and disadvantages of a specific search-based techniques are unique. Thus, it is essential for the research community and the software practitioners to analyze the techniques carefully before using them for a specific predictive modeling task. However, as only few studies discuss the properties of search-based techniques, it is difficult to generalize the scenario which makes the application of a specific search-based technique suitable.

5.2. Future guidelines to researchers

Based on the results of the study, studies in future should incorporate the following guidelines for using search-based techniques for developing software engineering predictive models:

- As indicated in the results, only 5% of the total primary studies analyzed the predictive capability of Local search-based techniques for developing software engineering predictive models. Therefore, there an urgent need for future studies to evaluate the effectiveness

of these techniques for SEPM.

- According to the quality analysis, only 63% of the studies completely stated the parameter settings used for developing models using search-based techniques. Although validation methods were clearly specified in majority of the studies, but there were certain studies (20%) which did not describe the experimental settings used for the model development. The specification of parameters and validation methods are very important to perform repeated and replicated studies. Thus, future studies should clearly describe the experimental settings in order to enable effective repeated application of the work.
- According to the results, 50% of the studies do not specify whether they performed multiple runs to account for the stochastic nature of search-based techniques. Future studies should account for the randomness of search-based techniques by performing appropriate number of runs in order to produce accurate and repeatable results.
- It is seen that majority of studies which predict continuous variables such as effort and maintainability use MMRE or Pred (25) and those which predict binary variables such as defect-proneness and change-proneness use accuracy and sensitivity. However, recent studies also advocate the use of other effective performance evaluators like MdMRE and Pred (50) for continuous variables and AUC, G-mean, G-measure, etc. for binary variables. Moreover, AUC and G-mean are termed as stable performance measures as they are efficient when imbalanced software quality data is available. Thus, future studies should incorporate multiple and stable performance evaluators for developed models.
- According to the results, 20% of the studies did not clearly specify the fitness functions evaluated in the study. A change in fitness functions leads to variation in results. Thus, proper specification of fitness functions is important for researchers to perform repeated studies. Future studies should evaluate different fitness functions and especially explore multi-objective fitness functions to determine their suitability and achieve optimum results.
- According to the results, 21% of the studies do not compare the capabilities of search-based techniques with ML techniques and other search-based techniques. However, there is an urgent need for more studies to assess and evaluate the performance of search-based techniques amongst each other and with well-established ML techniques. Although, our results advocate the use of search-based techniques for SEPM, comparative analysis is important to establish generalized results about their effectiveness.
- It can be seen from the results that majority (62%) of the studies did not use any statistical test for comparative analysis. Hence, future studies should statistically evaluate the significance of their results.
- It is important for researchers and practitioners to evaluate the characteristics, advantages as well as disadvantages of search-based techniques, before selecting it for model development, feature selection or parameter optimization tasks, which aid in SEPM. Thus, it is essential for researchers to perform an in-depth analysis of a search-based technique before using it.

6. Conclusions and future work

This study performed an extensive and systematic literature review to analyze and explore the use of different search-based techniques for SEPM tasks (effort estimation, defect prediction, maintainability prediction and change prediction). We selected 78 primary studies to effectively answer the above mentioned seven research questions pertaining to different categories of search-based techniques used in literature for SEPM. Out of the selected 78 primary studies, 38 studies explored the use of the search-based techniques for effort estimation models, 29 studies explored the use of search-based techniques for defect prediction models, 3 studies evaluated search-based techniques for maintainability prediction models and 11 study for change prediction models. The results of the study advocate the use of search-based techniques for SEPM tasks. After taking into account the discussions specific to each RQ (Section 5.1), we propose the following future work for researchers who intend to use search-based techniques for SEPM:

- Future work should explore and assess search-based techniques for developing software effort estimation, defect prediction and especially maintainability prediction and change prediction models as we found only limited studies which use search-based techniques for SEPM. However, as the results of the review encourage the use of search-based techniques, a large number of studies should be carried out for ascertaining the capability of search-based techniques.
- Apart from prediction accuracy, future work should focus on other aspects for evaluation of search-based techniques. These aspects may include the cost effectiveness of the developed models, their comprehensibility, and their generalization capability. These evaluators would help in an effective and thorough evaluation of the capabilities of any search-based technique. Future work should focus on developing intuitive models for predicting various software quality attributes using search-based techniques.
- Future work should evaluate the run-time consumed by search-based techniques for SEPM tasks and explore alternatives for reducing it. Recent studies [131,132] propose the use of parallel or cloud-based search-based software engineering for effective implementation of search-based techniques. These implementations may lead to significant reduction in the running time for the model development. Thus, active exploration and evaluation of such alternatives which will overcome the shortcomings of search-based techniques can aid in their efficient application to SEPM tasks.
- In future, researchers and practitioners should develop and establish a number of tools which ease the application of search-based techniques to SEPM tasks since the results of the review reveal that majority of studies (55%), do not use any well-established tools for simulating search-based techniques as there is shortage of tools which reliably simulate of search-based techniques. These tools should provide an easy, reliable and flexible interface to interested users for effective use of search-based techniques.
- Future work should incorporate a number of other validation techniques such as inter-release validation, cross-project validation or temporal validation, which reduce validation bias and evaluates the developed models in real and practical scenarios. Also, studies in future should use varied data sets using a number of other programming languages apart from C, C++ and Java for developing SEPM using search-based techniques.
- Future work should focus on careful design of experiments which use search-based techniques for SEPM tasks by taking into account the various threats to validity to the results of the study. These threats include conclusion, internal, construct and external validity threats. Such a practice would lead to effective application of search-based techniques for predictive modeling tasks and would yield practical and reliable results which can be used by the software industry.

Acknowledgement

R. Malhotra was supported, while performing this research, by the Grant received from the University Grants Commission of India under the Raman Fellowship for Post-Doctoral Research.

Appendix

A.1 Inclusion and exclusion criteria

The inclusion and exclusion criteria used in the study are listed below:

Inclusion Criteria:

- Empirical studies which use search-based techniques for effort prediction, defect prediction, maintainability prediction and change prediction.
- Empirical studies which use search-based techniques for developing software engineering predictive models.
- Empirical studies which use search-based techniques for the feature selection before the model development or the parameter optimization of a ML technique before developing a software engineering predictive model.
- Empirical studies which compare search-based techniques with ML techniques for SEPM.
- Empirical studies which compare two or more search-based techniques for SEPM.
- Exclusion Criteria:
- Empirical studies which are based on other dependent variables such as the reliability prediction, and defect count [e.g., Costa and Pozo 2006; Afzal et al. 2008 etc.].
- Empirical studies which are similar, i.e., those studies which have been published in a conference proceeding and an extended version of which has been published in a journal [e.g., Catal et al. 2007; Liu et al. 2007; Sheta et al. 2008; Rodriguez et al. 2009; etc.].
- Empirical studies which do not use search-based techniques [e.g., Kpodjedo et al. 2011].
- Review studies [e.g., Harman 2012; Ferrucci et al. 2014 etc.].
- Empirical studies which focus on clustering [e.g., Wang et al. 2004; Hari et al. 2011 etc.].
- Poster papers, PhD Dissertations and studies with no empirical validation were excluded, as we wanted to account for published work which presented adequate details of empirical analysis [e.g., Harman 2010b; Ferrucci et al. 2011; Sarro 2011; Jiang 2006 etc.].

A.2 Quality assessment questionnaire

We evaluated all the 92 candidate studies according to the 18 quality questions described in Table 11. The table reports the percentage of studies which answered a specific quality question as “Yes”, “Partly” or “No” for the 92 candidate studies..

A.3 Summary of top venues for publication

Table 12 indicates the number publications that appeared in a specific journal or a conference.

A.4 Number of runs for SEPM using search-based techniques

Table 13 shows the study identifiers along with the number of runs performed by a specific study. As shown in Table 13, certain studies mentioned that they performed multiple runs however, they did not

Table 11
Quality Assessment questionnaire.

Q#.	Quality Questions	Yes	Partly	No
Q1	Does the study state its objectives or research questions in a clear and concise manner?	93%	7%	0%
Q2	Does the study clearly define and reports its independent variables?	66%	24%	10%
Q3	Does the study use a suitable number of data sets analyzed by it? Is the size of data sets used appropriate?	70%	29%	1%
Q4	Does the study clearly define and state its data sources and data collection procedure?	66%	25%	9%
Q5	Does the study appropriately justify the use or selection of a search-based technique for predictive modeling tasks?	44%	39%	17%
Q6	Does the study clearly characterize, define and describe the various search-based techniques used by it?	75%	21%	4%
Q7	Does the study use appropriate validation technique for model evaluation?	86%	2%	12%
Q8	Is the fitness function clearly stated?	80%	3%	17%
Q9	Does the study state the parameter settings of the search-based techniques used?	63%	20%	17%
Q10	Does the study perform appropriate number of runs to account for the stochastic nature of search-based techniques?	50%	7%	43%
Q11	Does the study clearly state the performance metrics used by it?	79%	11%	10%
Q12	Does the study analyze or state the advantages and disadvantages of the search-based techniques?	27%	30%	43%
Q13	Does the study perform ant comparative analysis of the models predicted using different techniques (statistical vs search-based technique, ML vs search-based technique or amongst search based-techniques)?	78%	1%	21%
Q14	Does the study demonstrate the statistical comparison amongst two techniques with the help of statistical tests?	38%	0%	62%
Q15	Does the study report its limitations or threats to validity of its results?	20%	0%	80%
Q16	Is the research methodology used by the study repeatable?	47%	42%	11%
Q17	Does the study clearly report its findings? Do the findings relate to the aims of the research?	82%	17%	1%
Q18	Is the study adequately cited in literature (citation count per year)?	84%	1%	15%

Table 12
Summary of Publications.

Publication Name	Type	No. of studies	Percentage of studies
Information and Software Technology	Journal	6	8%
ACM Symposium on Applied Computing	Conference	5	6%
Journal of Systems and Software	Journal	4	5%
GECCO	Conference	4	5%
Information Sciences	Journal	3	4%
Applied Soft Computing	Journal	3	4%
SSBSE	Conference	3	4%
IEEE Transactions on Software Engineering	Journal	2	3%
Expert Systems with Applications	Journal	2	3%
Empirical Software Engineering	Journal	2	3%
Software Quality Journal	Journal	1	1%

Table 13
Number of runs for SEPM using search-based techniques.

Number of runs	Study identifier
100 and more runs	ES5, ES6 DS15
50 runs	ES28 DS14
30 runs	ES10, ES31, ES34, ES35, ES37 DS2, DS7, DS13, DS23, DS25, DS29 CS4, CS5, CS7, CS8
10–20 runs	ES2, ES3, ES4, ES8, ES15, ES21, ES22, ES23, ES24, ES30, ES32, ES33 DS1, DS3, DS4, DS5, DS10, DS21, DS24, DS28 CS1, CS2
4–9 runs	ES7, ES25.
Multiple runs (not specific)	ES1, ES9, ES14, ES26 MS1

specify the exact number of runs..

A.5 Performance metrics for effort estimation and defect prediction

Tables 14 and 15 mention the descriptions of some of the commonly used and important performance metrics for effort estimation and defect prediction studies, along with the identifiers of the studies which use them..

A.6 Fitness functions for effort estimation and defect prediction

Tables 16 and 17 indicate various fitness functions used in the effort estimation and defect prediction studies along with the study identifiers of the studies using the fitness function.

A.7 Statistical tests used for comparative analysis

Table 18 shows the various statistical tests used by different primary studies along with their study identifiers.

A.8 Candidate Studies Removed after Applying Exclusion Criteria

M. Evett, T. M. Khoshgoftar, P-D. Chien, E. Allen. GP-based software quality prediction. In *Proceedings of the 3rd Annual Conference Genetic Programming* (1998), 60–65.

R. Sitte. A framework for quantifying error-proneness, *In Proceedings of 1st Asia-Pacific conference on Quality Software* (2000), 63–68.

M. Reformat, W. Pedrycz, N. J. Pizzi. Software quality analysis with the use of computational intelligence, *Information and Software Technology*, 45, 7(2003), 405–417.

Y. Liu, T. M. Khoshgoftaar. Building decision tree software quality classification models using genetic programming, *In Proceedings of Genetic and Evolutionary Computation* (2003), 1808–1809.

Q. Wang, B. Xu, J. Zhu. Extract quality rules from software quality prediction model based on neural network, *In Proceedings of 16th IEEE International Conference on Tools with Artificial Intelligence* (2004), 191–195.

T. M. Khoshgoftaar, Y. Liu and N. Seliya. A mulitobjective module-order model for software quality enhancement, *IEEE Transactions on Evolutionary computation*, 8, 6(2004), 593–608.

T. M. Khoshgoftaar, Y. Xiao, K. Gao. Multi-Objective Optimization by CBR GA-Optimizer for Module-Order Modeling, *In Proceedings of SEKE* (2004), 220–225.

H. Jiang. Can the genetic algorithm be a good tool for software engineering searching problem? In Proceedings of 30th International Computer Software and Applications Conference (2006), 362–366.

S. Bouktif, H. Sahraoui, Giuliano. Simulated annealing for improving software quality, In Proceedings of Conference on Genetic and Evolutionary Computation (2006), 1893–1900.

E. O. Costa, A. Pozo, A (μ + λ) – GP algorithm and its use for regression problems, 18th International Conference on tools with

Table 14
Performance metrics for effort estimation models.

Performance metric	Description	Study identifier
Magnitude of Relative Error (MRE)	|Estimated Effort − Actual Effort|/Actual Effort	ES14, ES16, ES28, ES31, ES36, ES37
Mean Magnitude of Relative Error (MMRE)	$\frac{1}{N}\sum_{i=1}^{N}\frac{\lvert Estimated\ \ Effort - ActualEffort\rvert}{Actual\ \ Effort}$; N represents the total number of observations.	ES1, ES2, ES4, ES5, ES7, ES8, ES9, ES10, ES11, ES13, ES14, ES15, ES16, ES17, ES18, ES19, ES20, ES21, ES22, ES23, ES24, ES25, ES26, ES27, ES28, ES29, ES30, ES31, ES32, ES34, ES35, ES36, ES37
Pred(25)	It represents the percentage of predictions which fall within the 25% rage of the actual value.	ES1, ES2, ES4, ES5, ES7, ES8, ES9, ES10, ES11, ES13, ES15, ES16, ES17, ES18, ES19, ES20, ES21, ES22, ES23, ES24, ES29, ES30, ES31, ES34, ES35, ES36
Median Magnitude of Relative Error (MdMRE)	It measures the median values among all MRE's.	ES11, ES13, ES18, ES19, ES21, ES22, ES23, ES30, ES34, ES35
Mean Square Error (MSE)	$\frac{1}{N}\sum_{i=1}^{N}(Estimated\ \ Effort - Actual\ \ Effort)^2$; N represents the total number of observations.	ES1, ES3, ES10, ES24
Coefficient of Regression (R^2)	It is the coefficient of regression	ES1, ES3, ES4, ES7, ES8, ES10, ES35.
Variance Accounted For (VAF)	$[1 - \frac{\mathrm{var}(Actual\ \ Effort - Estimated\ \ Effort)}{\mathrm{var}(Actual\ \ Effort)}]*100\%$	ES26, ES27

Table 15
Performance metrics for defect prediction models.

Performance Metric	Description	Study Identifier
Sensitivity (Recall)	It measures the percentage of correctly predicted defect prone classes by the model.	DS6, DS8, DS9, DS11, DS12, DS13, DS17, DS18, DS19, DS20, DS21, DS23, DS24, DS25, DS26, DS27, DS28, DS29
Accuracy	Accuracy is defined as the percentage of total correct predictions (defect prone and not defect prone) by a prediction model.	DS6, DS8, DS9, DS10, DS11, DS13, DS14, DS16, DS17, DS18, DS19, DS20, DS21, DS22, DS24, DS26, DS27, DS28
Precision	It is a measure of percentage of correctly predicted defect prone classes out of total defect prone predictions.	DS6, DS8, DS13, DS17, DS18, DS20, DS21, DS23, DS26, DS27
Specificity	It measures the percentage of correctly predicted not defect prone classes by the model.	DS9, DS11, DS17, DS19, DS20, DS27, DS29
Area Under the Receiver Operating Characteristic (ROC) Curve (AUC)	An ROC is a plot with sensitivity values on the horizontal axis and 1-specificity values on the vertical axis.	DS7, DS10, DS11, DS12, DS13, DS19, DS24, DS27, DS28, DS29
Type I Error	Type I error occurs when a non-defect prone module is incorrectly classified as defect prone.	DS1, DS2, DS3, DS4, DS5, DS15
Type II Error	Type II error occurs when a defect prone module is incorrectly classified as non-defect prone.	DS1, DS2, DS3, DS4, DS5, DS15
Misclassification Rate	It is defined as various combinations of Type I and Type II error to analyze the cost of misclassification.	DS1, DS2, DS3, DS4, DS15
Pf (Probability of False Alarm)	It is defined as the ratio of incorrectly predicted defect prone classes.	DS6, DS8, DS12, DS24, DS28
F-measure	It is defined as the harmonic mean of precision and sensitivity.	DS13, DS17, DS18, DS21, DS26

Artificial Intelligence (2006), 10–17.

Y. Liu, T. M. Khoshgoftaar, J. F. Yao. Developing an effective validation strategy for genetic programming models based on multiple datasets, *In Proceedings of International Conference on Information reuse and Integration* (2006), 232–237.

C. Catal, B. Diri. Software fault prediction with object-oriented metrics based artificial immune recognition system, *Product-focused Software Process Improvement,* Springer Berlin Heidelberg (2007), 300–314.

D. Azar, D. Precup. An Adaptive Approach to Optimize Software Component Quality Predictive Models: Case of Stability, In Proceedings of New Technologies, Mobility and Security (2007), 297–310. Springer Netherlands.

M. Mohd, Rosli, N. H. I. Teo, N. S. M. Yusop, N. S. Mohammad. The design of a software fault prone application using evolutionary algorithm, *In Proceedings of IEEE Conference on Open Systems* (2007), 338–343.

T. M. Khoshgoftaar, Y. Liu. A multi-objective software quality classification model using genetic programming, *IEEE Transactions on Reliability*, 56, 2(2007), 237–245.

Y. Liu, T. M. Khoshgoftaar, J. F. Yao. Building a novel GP-based software quality classifier using multiple validation datasets, *In Proceedings of IEEE International Conference on Information reuse and Integration* (2007), 644–650.

Table 16
Fitness functions for effort estimation models.

Fitness Function	Study identifier
MSE	ES1, ES2, ES3, ES5, ES6, ES7, ES8, ES10, ES20, ES29, ES32
MMRE	ES4, ES9, ES10, ES14, ES16, ES17, ES19, ES21, ES22, ES23, ES30
MdMRE	ES21, ES22
VAF	ES12, ES26
LAD	ES10, ES28
MMRE-Pred(25)	ES11, ES13, ES31, ES37
(100-Pred(25))+MMRE	ES15, ES24
Multi-objective Fitness Function	ES34, ES35
Miscellaneous	ES10, ES18, ES22, ES33, ES38

Table 17
Fitness functions for defect prediction models.

Fitness Function	Study Identifier
Accuracy	DS11, DS16, DS17, DS18, DS20, DS27
Precision	DS18, DS20
Sensitivity (Recall)	DS18, DS20
Sensitivity * Specificity	DS6, DS8, DS14
Multi-objective: specificity and sensitivity	DS7, DS13, DS19
F-measure	DS18, DS20, DS21
Misclassification cost	DS1, DS2, DS3, DS4, DS5, DS15, DS28, DS29
Miscellaneous	DS9, DS12, DS17, DS20, DS22, DS23, DS24, DS25, DS26

Table 18
Statistical Tests used for Comparison of Search-based Techniques.

Statistical test	Study identifier
t-test	ES2, ES3
	DS2, DS12, DS15, DS19
	MS2
	CS7, CS8
Wilcoxon signed rank test	ES21, ES22, ES23, ES30, ES33, ES34, ES35, ES37
	DS7, DS13, DS23, DS25
	CS5
Friedman test	ES32, ES35
	DS9, DS28
	CS9, CS11
ANOVA test	ES10, ES28
Mann-Whitney *U* test	ES24
Nemenyi test	ES32
McNemar's test	DS17

Sheta, A. D. Rine, A. Ayesh. Development of software effort and schedule estimation models using soft computing techniques. *In Proceedings of IEEE World Congress on Computational Intelligence and Evolutionary Computation* (2008), 1283–1289.

R. Vivanco, D. Jin. Enhancing predictive models using principal component analysis and search-based metric selection: a comparative study, In Proceedings of the 2nd International Symposium on Empirical Software Engineering and Measurement (2008), 273–275.

W. Afzal, R. Torkar and R. Feldt. Prediction of fault count data using genetic programming, *In Proceedings of IEEE Multitopic Conference* (2008), 349–356.

W. Afzal, R. Torkar. A comparative evaluation of using genetic programming for predicting fault count data, *In Proceedings of 3rd International conference on Software Engineering Advances* (2008a), 407–414.

D. Azar, H. Harmanani, R. Korkamaz. A hybrid heuristic approach to optimize rule-based software quality estimation models, *Information and Software Technology*, 51, 9(2009), 1365–1376.

X. Bin., Z. Li, Y. Na, L. Jing. A genetic algorithm based method of fault maintenance in software-intensive system, In Proceedings of 1st International workshop on Software Technology and Computer Science (2009), 1056–1059.

D. Rodríguez, J. C. Riquelme, R. Ruiz, J. S. Aguilar-Ruiz. Searching for Rules to find Defective Modules in Unbalanced Data Sets. In Proceedings of 1st International *Search Based Software Engineering* (2009), 89–92.

W. Afzal, R. Torkar, R. Feldt. Search-based prediction of fault count data, In *Proceedings of 1st International Symposium on Search-based Software Engineering* (2009), 35–38.

J. Tang, Q. Cai, and Y. Liu. Gear fault diagnosis with neural network based on niche genetic algorithm. *In Proceedings of International Conference on Machine Vision and Human-Machine Interface* (2010), 596–599.

F. G. De Freitas, J. T. de Souza. Ten years of search based software

engineering: A bibliometric analysis, In *Search Based Software Engineering* (2011), 18–32.

F. Ferrucci, C. Gravino, F. Sarro. How multi-objective genetic programming is effective for software development effort estimation? *In proceedings of Search Based Software Engineering* (2011), 274–275.

C.M.V.K. Hari, T. S. Sethi, B. S. S. Kaushal, A. Sharma. CPN-a hybrid model for software cost estimation. In Proceedings of *Recent Advances in Intelligent Computational Systems* (2011), 902–906.

S. Kpodjedo, F. Ricca, P. Galinier, Y. G. Guéhéneuc, G. Antoniol. Design evolution metrics for defect prediction in object oriented systems, *Empirical Software Engineering,* 16, 1(2011), 141–175.

F. Sarro. Search-based approaches for software development effort estimation, In Proceedings of 12th International Conference on Product Focused Software Development and Process Improvement (2011), 38–43.

B. H. Wu. An evolutionary approach to evaluate the quality of software systems, In Proceedings of 4th International workshop on Advanced Computational Intelligence (2011), 381–386.

I. Thamarai, S. Murugavalli. Using differential evolution in the prediction of software effort, In *Proceedings of Fourth International Conference on Advanced Computing* (2012), 1–3.

M. Harman, S. A. Mansouri, and Y. Zhang. Search-based software engineering: Trends, techniques and applications. *ACM Comput. Surv.* 45, 1, Article 11 (2012), 61 pages.

R. Ligeiro. Monitoring applications: An immune inspired algorithm for software-fault detection. *Applied Soft Computing*, 24 (2014), 1095–1104.

C. Marinescu. How good is genetic programming at predicting changes and defects? *International Symposium on Symbolic and Numeric Algorithms for Scientific Computing* (2014), 544–548.

J. Moyersoms, E. J. de Fortuny, K. Dejager, B. Baesens, D. Martens. Comprehensible software fault and effort prediction: A data mining approach. *Journal of Systems and Software*, 100(2015), 80–90.

D. Ceke, B. Milasinovic. Early effort estimation in web application environment. *Journal of Systems and Software*, 103(2015), 219–237.

Y. Abdi, S. Parsa, Y. Seyfari. A hybrid one-class rule learning approach based on swarm intelligence for software fault prediction. *Innovations in System Software Engineering*, 11(2015), 289–301.

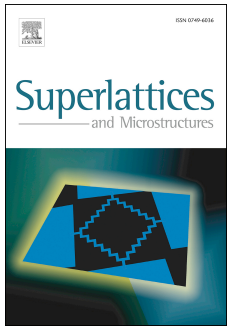
References

[1] S.R. Chidamber, C.F. Kemerer, A metric suite for object-oriented design, IEEE Trans. Softw. Eng. 20 (6) (1994) 476–493.
[2] J. Bansiya, C.G. Davis, A hierarchical model for object-oriented design quality assessment, IEEE Trans. Softw. Eng. 28 (1) (2002) 4–17.
[3] S. Ali, L.C. Briand, H. Hemmati, R.K. Panesar-Walawege, A systematic review of the application and empirical investigation of search-based test case generation, IEEE Trans. Softw. Eng. 36 (6) (2010) 742–762.
[4] M. Harman, Y. Jia, J. Krinke, W. B. Langdon, J. Petke, Y. Zhang. Search based software engineering for software product line engineering: A survey and directions for future work, in: Proceedings of the 18th International Software Product Line- Vol. 1, 2014a, pp. 5–18.
[5] M. Harman, W.B. Langdon, Westley Weimer. Genetic programming for reverse engineering. In Proceedings of the 20th Working Conference on Reverse Engineering, 2013, pp. 1–10.
[6] M. Harman, Yue Jia, Yuanyuan Zhang, Achievements, open problems and challenges for search based software testing, in: Proceedings of the 8th International Conference on Software Testing, Verification and Validation, 2015, pp. 1–12.
[7] J. Clarke, J.J. Dolado, M. Harman, R. Hierons, B. Jones, M. Lumkin, B. Mitchell, S. Mancoridis, K. Rees, M. Roper, M. Shepperrd, Reformulating software engineering as a search problem, IEE Proc. Softw. 150 (3) (2003) 161–175.
[8] P. McMinn, Search-based software test data generation: a survey, Softw. Test. Verif. Reliab. 14 (2) (2004) 105–156.
[9] W. Afzal, Search-based Prediction of Software Quality: Evaluations and Comparisons (Ph.D thesis), 2011.
[10] J. Clarke, M. Harman, R. Hierons, B. Jones, M. Lumkin, K. Rees, M. Roper, M. Shepperd. The application of metaheuristic search techniques to problems in software engineering, Software Engineering using Metaheuristic Innovative Algorithms) Technical Report. SEMINAL-TR-01-2000
[11] M. Harman, P. McMinn, J.T. De Souza, S. Yoo. Search based software engineering: techniques, taxonomy and tutorial. In Lecture Notes in Empirical Software Engineering and Verification, Vol. 7007. Springer-Verlag Berlin, Heidelberg, 2012, pp. 1–59.
[12] F. Ferrucci, M. Harman, F. Sarro, Search-based software project management, in: Gunther Ruhe, Claes Wholin (Eds.), Software Project Management in a Changing World, Springe, 2014, pp. 373–379.
[13] A. Aggarwal, M. Kumar, T.K. Rawat, D.K. Upadhyay, Optimal design of 2D FIR filters with quadrantally symmetric properties using fractional derivative constraints, Circuits Syst. Signal Process. 35 (6) (2016) 2213–2257.
[14] M. Kumar, T.,K. Rawat, Optimal fractional delay-IIR filter design using cuckoo search algorithm, ISA Trans. 59 (2015) 39–54.
[15] M. Kumar, T.,K. Rawat, Optimal design of FIR fractional order differentiator using cuckoo search algorithm, Expert Syst. Appl. 42 (7) (2015) 3433–3449.
[16] M. Kumar, A. Aggarwal, T.K. Rawat, Bat algorithm: application to adaptive infinite impulse response system identification, Arab. J. Sci. Eng. (2016) 1–18.
[17] H-H. Li, F. Yu-Wen, Z. Zhi-Hui, L. Jing-Jing. Renumber strategy enhanced particle swarm optimization for cloud computing resource scheduling, in: Proceedings of the 2015 IEEE Congress on Evolutionary Computation, 2015, pp. 870–876.
[18] M.B. Abdul Hamid, T.K. Abdul Rahman. Short term load forecasting using an artificial neural network trained by artificial immune system learning algorithm, in: Proceedings of Computer Modelling and Simulation, 2010, pp. 408–413
[19] M. Harman, B.F. Jones, search based software engineering, Inf. Softw. Technol. 43 (14) (2001) 833–839.
[20] M. Harman, The relationship between search based software engineering and predictive modeling, In Proceedings of 6th International conference on Predictive Models in Software Engineering. 2010, 1.
[21] Mark Harman, Why the virtual nature of software makes it ideal for search based optimization, in: Proceedings of the 13th International Conference on Fundamental Approaches to Software Engineering, Heidelberg, 2010b, pp. 1–12.
[22] M. Harman, J. Clark. Metrics are fitness functions too, in: Proceedings of 10th IEEE International Symposium on Software Metrics. USA, 2004, pp. 58–69.
[23] W. Afzal, R. Torkar, On the application of genetic programming for software engineering predictive modeling: a systematic review, Expert Syst. Appl. 38 (9) (2011) 11984–11997.
[24] J. Wen, S. Li, Z. Lin, Y. Hu, C. Huang, Systematic literature review of machine learning based software development effort estimation models, Inf. Softw. Technol. 54 (1) (2012) 41–59.
[25] R. Malhotra. Search based techniques for software fault prediction: current trends and future directions, in: Proceedings of the 7th International Workshop on Search-based Software Testing, 2014, New York, pp. 35–37
[26] E.N. Regolin, G.A. De Souza, A. RT Pozo, S.R. Vergilio, Exploring machine learning techniques for software size estimation, Proc. Chil. Comput. Sci. Soc. (2003) 130–136.
[27] Y. Singh, R. Malhotra, Object-Oriented Software Engineering, PHI Learning, New Delhi, India, 2012.
[28] R. Malhotra, M. Khanna, Software engineering predictive modeling using search-based techniques- Sytematic review and future directions, in: Proceedings of the 1st North American Search Based Software Engineering Symposium, 2015, Michigan, pp. 1–16
[29] B.A. Kitchenham, Guidelines for performing systematic literature review in software engineering, Technical report EBSE-2007-001, UK.
[30] S. Xanthakis, C. Ellis, C. Skourlas, A.L. Gall, S. Katsikas, K. Karapoulis, K. Application of genetic algorithms to software testing, in: Proceedings of the 5th International conference on Software Engineering and its Applications, Toulouse, 1992, pp. 625–636.
[31] J. Dolado, L. Fernandez, Genetic programming, neural networks and linear regression in software project estimation, in: Proceedings of International Conference on Software Process Improvement, Research, Education and Training. London, 1998, pp. 157–170.
[32] J. Dolado, A validation of component based method for software size estimation, IEEE Trans. Softw. Eng. 26 (10) (2000) 1006–1021.
[33] K.K. Shukla, Neuro-genetic prediction of software development effort, Inf. Softw. Technol. 42 (10) (2000) 701–713.
[34] C.J. Burgess, M. Lefley, Can genetic programming improve software effort estimation? A comparative evaluation, Inf. Softw. Technol. 43 (14) (2001) 863–873.
[35] J. Dolado, On the problem of the software cost function, Inf. Softw. Technol. 43 (1) (2001) 61–72.
[36] C. Kirsopp, M.J. Shepperd, J. Hart. Search Heuristics, Case-based reasoning and software project effort prediction, in: Proceedings of the Genetic and Evolutionary Computation Conference, San Francisco, CA, USA, 2002, pp. 1367–1374.
[37] Y. Shan, R. I. Mckay, C. J. Lokan, D. L. Essam. Software project effort estimation using genetic programming, In Proceedings of International Conference on Communications, Circuits and Systems and West Sino Expositions, 2002, pp. 1108–1112.
[38] M. Lefley, M.J. Shepperd. Using genetic programming to improve software effort estimation based on general data sets, in: Proceedings of the 2003 international conference on Genetic and evolutionary computation, Berlin, Heidelberg, 2477–2487.
[39] C. Lokan. What should you optimize when building an estimation model?, In Proceedings of 11th IEEE International software metrics symposium, Como, 34, 2005.
[40] S.-J. Huang, N.-H. Chiu, Optimization of analogy weights by genetic algorithm for software effort estimation, Inf. Softw. Technol. 48 (11) (2006) 1034–1045.
[41] A.E. Sheta, Estimation of the COCOMO model parameters using genetic algorithms for NASA software projects, J. Comput. Sci. 2 (2) (2006) 118.

[42] N.-H. Chiu, S.-J. Huang, The adjusted analogy-based software effort estimation based on similarity distances, J. Syst. Softw. 80 (4) (2007) 628–640.
[43] A. Faheem, S. Bouktif, A. Serhani, I. Khalil. Integrating function point project information for improving the accuracy of effort estimation, in: Proceedings of 2nd International Conference on Advanced Engineering Computing and Applications in Sciences, 2008, pp. 193–198.
[44] P.L. Braga, A.L.I. Oliveira, S.R.L. Meira, A GA-based feature selection and parameters optimization for support vector regression applied to software effort estimation, in: Proceedings of the 2008 ACM Symposium on Applied Computing, ACM, New York, NY, USA, 2008, pp. 1788–1792
[45] S.-J. Huang, N.-H. Chiu, Li-Wei Chen, Integration of the grey relational analysis with genetic algorithm for software effort estimation, Eur. J. Oper. Res. 188 (3) (2008) 898–909.
[46] A. Tsakonas, G. Dounias. Application of Genetic Programming in Software Engineering Empirical Data Modeling, in: Proceedings of the 3rd International Conference on Software and Data Technologies, 2008, pp. 295–300.
[47] Y.F. Li, M. Xie, T.N. Goh, A study of mutual information based feature selection for case based reasoning in software cost estimation, Expert Syst. Appl. 36 (3) (2009) 5921–5931.
[48] Y.F. Li, M. Xie, T.N. Goh, A study of project selection and feature weighting for analogy based software cost estimation, J. Syst. Softw. 82 (2) (2009) 241–252.
[49] A. Tsakonas, G. Dounias. Deriving models for software project effort estimation by means of genetic programming, in: Proceedings of the 1st Conference on Knowledge Discovery and Information Retrieval, Madeira, 2009.
[50] F. Ferrucci, C. Gravino, R. Oliveto, F. Sarro, E. Mendes. Investigating tabu search for web effort estimation, in: Proceedings of the 36th EUROMICRO Conference on Software Engineering and Advanced Application, Lille, 2010, pp. 350–357.
[51] F. Ferrucci, C. Gravino, R. Oliveto, F. Sarro. Genetic programming for effort estimation: an analysis of the impact of different fitness functions, in: Proceedings of the 2nd International Symposium on Search Based Software Engineering, Benevento, 2010, pp. 89–98.
[52] F. Ferrucci, C. Gravino, R. Oliveto, F. Sarro. Estimating software development using tabu search, in: Proceedings of 12th International conference on Enterprise Information Systems, Madeira, 2010, pp. 236–241.
[53] A.L.I. Oliveira, P.L. Braga, R.M.F. Lima, M.L. Cornélio, GA-based method for feature selection and parameters optimization for machine learning regression applied to software effort estimation, Inf. Softw. Technol. 52 (11) (2010) 1155–1166.
[54] Alaa F. Sheta, Aladdin Ayesh, David Rine, Evaluating software cost estimation models using particle swarm optimisation and fuzzy logic for NASA projects: a comparative study, Int. J. Bio-Inspired Comput. 2 (6) (2010) 365–373.
[55] F. Sheta, Alaa, Alaa Al-Afeef, A GP effort estimation model utilizing line of code and methodology for NASA software projects, in: Proceedings of the 10th International Conference on Intelligent Systems Design and Applications, 2010b, pp. 290–295.
[56] S. Aljahdali, Alaa F. Sheta, Software effort estimation by tuning COOCMO model parameters using differential evolution, in: Proceedings of ACS/IEEE International Conference on Computer Systems and Applications-AICCSA (2010), 2010, pp. 1–6.
[57] A. Chavoya, C. Lopez-Martin, M.E. Meda-Campa, Applying genetic programming for estimating software development effort of short-scale projects, in: Proceedings of the 8th International Conference on Information Technology: New Generations International Conference, 2011, pp. 174–179.
[58] R. De, A. AraúJo, Adriano L.I. Oliveira, Sergio Soares, Silvio Meira, An evolutionary morphological approach for software development cost estimation, Neural Netw. 32 (2012) 285–291.
[59] F. Sarro, F. Ferrucci, C. Gravino. Single and Multi Objective Genetic Programming for software development effort estimation, in: Proceedings of the 27th Annual ACM Symposium on Applied Computing, ACM, New York, NY, USA, 2012, pp. 1221–1226.
[60] V.K. Bardsiri, D.N. Jawawi, S.Z. Hashim, E. Khatibi, A. PSO-based, Model to increase the accuracy of software development effort estimation, Softw. Qual. J. 21 (3) (2013) 501–526.
[61] R.C. Barros, M.P. Basgalupp, R. Cerri, T.S. Da Silva, A.C.P.L.F. De Carvalho, A grammatical evolution approach for software effort estimation.In Proceedings of the 15th annual conference on Genetic and evolutionary computation, 2013, New York, NY, USA, pp. 1413–1420.
[62] Anna Corazza, Sergio Di Martino, Filomena Ferrucci, Carmine Gravino, Federica Sarro, Emilia Mendes, Using tabu search to configure support vector regression for effort estimation, Empir. Softw. Eng. 18 (3) (2013) 506–546.
[63] L.L. Minku, X. Yao, Software effort estimation as a multiobjective learning problem, ACM Trans. Softw. Eng. Method. 22 (4) (2013) 32.
[64] L. L. Minku, X. Yao. An analysis of multi-objective evolutionary algorithms for traversing ensemble models based on different performance measures in software effort estimation, in: Proceedings of the 9th International Conference on Predictive Models in Software Engineering, Maryland, 2013b, 8.
[65] Z. Dan. Improving the accuracy in software effort estimation: using artificial neural network model based on particle swarm optimization, in: Proceedings of IEEE International Conference on Service Operations and Logistics, and Informatics, Dongguan, 2013, ppp. 180–185.
[66] V.K. Bardsiri, D.N. Jawawi, S.Z. Hashim, E. Khatibi, A flexible method to estimate the software development effort based on the classification of projects and localization of comparisons, Empir. Softw. Eng. 19 (4) (2014) 857–884.
[67] M. Azzeh, A.B. Nassif, S. Banitaan. A better case adaptation method for case-based effort estimation using multi-objective optimization, in: Proceedings of IEEE International Conference on Machine Learning and Applications, Detroit, 2014, pp. 409–414.
[68] R. Hochman, T.M. Khoshgoftaar, E.B. Allen, J.P. Hudepohl, Using the genetic algorithm to build optimal neural networks for fault-prone module detection, in: Proceedings of the 7th International Symposium on Software Reliability Engineering, 1996, pp. 152–162.
[69] R. Hochman, T.M. Khoshgoftaar, E.B. Allen, J.P. Hudepohl. Evolutionary neural networks: a robust approach to software reliability problems, In Proceedings of 8th IEEE International Symposium on Software Reliability Engineering, 1997, pp. 13–26.
[70] T.M. Khoshgoftaar, Y. Liu. Genetic programming model for software quality classification, in: Proceedings of the 6th International symposium on High Assurance Systems Engineering, 2001, pp. 127–136.
[71] T. M. Khoshgoftaar, N. Seliya, Y. Liu. Genetic programming-based decision trees for software quality classification, in: Proceedings of the 15th IEEE International Conference on Tools with Artificial Intelligence, 2003, pp. 374–383.
[72] Y. Liu, T.M. Khoshgoftaar. Reducing overfitting in genetic programming models for software quality classification, in: Proceedings of the 9th IEEE International Symposium on High-Assurance Systems Engineering, 2004, pp. 56–65.
[73] A. B. De Carvalho, A. Pozo, S. R. V. Carvalho, A. Lenz. Predicting fault proneness of classes though a multiobjective particle swarm optimization algorithm, in: Proceedings of the 20th IEEE International Conference on Tools with Artificial Intelligence, Dayton, 2008, pp. 387–394.
[74] A. Tsakonas, G. Dounias, Predicting defects in software using grammar-guided genetic programming, Artif. Intell.: Theor. Models Appl. 5138 (2008) 413–418.
[75] O. Vandercruys, D. Martens, B. Baesens, C. Mues, M. De Backer, R. Haesen, Mining software repositories for comprehensible software fault prediction models, J. Syst. Softw. 81 (5) (2008) 823–839.
[76] C. Catal, B. Diri, Investigating the effect of dataset size, metrics sets, and feature selection techniques on software fault prediction problem, Inf. Sci. 179 (8) (2009) 1040–1058.
[77] Y. Singh, A. Kaur, R. Malhotra, Prediction of software quality model using gene expression programming, Product-Focus. Softw. Process Improv. 32 (2009) 43–58.
[78] W. Afzal. Using faults-slip-through metric as a predictor of fault-proneness, in: Proceedings of the 17th Asia Pacific Software Engineering Conference, Sydney, 2010, pp. 414–422.
[79] A.B. De Carvalho, A. Pozo, S.R. Vergilio, A symbolic fault-prediction model based on multiobjective particle swarm optimization, J. Syst. Softw. 83 (2010) 868–882.
[80] C. Jin, E-M Dong, L-Na. Software fault prediction model based on adaptive dynamical and median particle swarm optimization, in: Proceedings of the 2nd International Conference on Multimedia and Information Technology, Kaifeng, 2010, pp. 44–47.
[81] Y. Liu, T.M. Khoshgoftaar, N. Seliya, Evolutionary optimization of software quality modeling with multiple repositories, IEEE Trans. Softw. Eng. 36 (6) (2010) 852–864.
[82] P.C. Pendharkar, Exhaustive and heuristic search approaches for learning a software defect prediction model, Eng. Appl. Artif. Intell. 23 (2010) 34–40.
[83] N.-H. Chiu, Combining techniques for software quality classification: an integrated decision network approach, Expert Syst. Appl. 38 (4) (2011) 4618–4625.
[84] S. Di Martino, F. Ferrucci, C. Gravino, F. Sarro, A genetic algorithm to configure support vector machines for predicting fault-prone components, Product-Focus. Softw. Process Improv. 6759 (2011) 247–261.
[85] L. Yu, An evolutionary programming based asymmetric weighted least squares support vector machine ensemble learning methodology for software repository mining, Inf. Sci. 191 (2012) 31–46.
[86] D. Rodriguez, R. Ruiz, J.C. Riquelme, J.S. Aguluir-Ruiz, Searching for rules to detect defective modules: a subgroup discovery approach, Inf. Sci. 191 (2012) 14–30.
[87] F. Sarro, S. Di Martino, F. Ferrucci, C. Gravino. A further analysis on the use of genetic algorithm to configure support vector machine for inter release fault prediction, in: Proceedings of the 27th Annual ACM Symposium on Applied Computing, Riva Del Garda, 2012b, pp. 1215–1220.
[88] H. Can, X. Jianchum, Z. Ruide, L. Juelong, Y. Qiliang and X. Liqiang, A new model for software defect prediction using particle swarm optimization and support vector machine, in: Proceedings of the 25th Chinese Control and Decision Conference, Guiyang, 2013, pp. 4106-4110.
[89] G. Canfora, A. De Lucia, M. Di Penta, R. Oliveto, A. Panichella, S. Panichella. Multi-objective cross-project defect prediction, In Proceedings of 6th International Conference on Software Testing, Verification and Validation, Luxembourg, 2013, pp. 252–261.
[90] G. Abaei, A. Selamat, A survey of software fault detection based on different prediction approaches, Vietnam J. Comput. Sci. 1 (2014) 79–95.
[91] M. Harman, S. Islam, Y Jia, Leandro L. Minku, F. Sarro, K. Sirivisut, Less is more: temporal fault predictive performance over multiple hadoop releases, in: Proceedings of the 6th International Symposium on Search Based Software Engineering, Fortaleza, 2014b, 240–246.
[92] L. Kewen, C. Chenxi, L. Wenying, F. Xianghua, L. Qinghua, Software defect prediction using fuzzy integral fusion based on GA-FM, Wuhan. Univ. Nat. Sci. 19 (5) (2014) 405–408.
[93] R. Malhotra, Comparative analysis of statistical and machine learning methods for predicting faulty modules, Appl. Soft Comput. 21 (2014) 286–297.
[94] O.F. Arar, K. Ayan, Software defect prediction using cost sensitive neural network, Appl. Soft Comput. 33 (2015) 263–277.
[95] C. Jin, S.-W. Jin, Prediction approach of software fault-proneness based on hybrid artificial neural network on quantum particle swarm optimization, Appl. Soft Comput. 35 (2015) 717–725.

[96] A.A.B. Baqais, M. Alshayeb, Z.A. Baig. Hybrid intelligent model for software maintenance prediction, in: Proceedings of World Congress on Engineering, London, 2013, pp. 358–362.
[97] R. Malhotra, A. Chugh. Application of evolutionary algorithms for software maintainability prediction using object-oriented metrics, in: Proceedings of the 8th Bio-inspired Information and Communication Technology, 2014d, pp. 348–351.
[98] L. Kumar. D.K. Naik, S. K. Rath. Validating the effectiveness of object-oriented metrics for predicting maintainability, in: Proceedings of the 3rd International Conference on Recent Trends in Computing, 2015, pp. 798–806.
[99] V. Rodrigo, N. Pizzi. Finding effective software metrics to classify maintainability using a parallel genetic algorithm, In Proceedings of Conference on Genetic and Evolutionary Computation, Seattle, 2004, pp. 1388–1399.
[100] D. Azar, A genetic algorithm for improving accuracy of software quality predictive models: a search-based software engineering approach, Int. J. Comput. Intell. Appl. 9 (2) (2010) 125–136.
[101] D. Azar, J. Vybihal, An ant colony optimization algorithm to improve software quality prediction models: case of class stability, Inf. Softw. Technol. 53 (4) (2011) 388–393.
[102] G. Balogh, A.Z. Vegh, A. Beszedes. Prediction of software development modification effort enhanced by a genetic algorithm, in: Proceedings of the 4th International Symposium on Search Based Software Engineering, 2012, Trento, Italy
[103] M.P. Basgalupp, R.C. Barros, D.D. Ruiz. Predicting software maintenance through evolutionary-based decision trees, in: Proceedings of the 27th Annual ACM Symposium on Applied Computing, Riva Del Garda, 2012, pp. 1209–1214.
[104] M.P. Basgalupp, R.C. Barros, T.C. Da Silva, A. De Carvalho. Software effort prediction: a hyper-heuristic decision-tree based approach, in: Proceedings of the 28th Annual ACM Symposium on Applied Computing, Coimbra, 2013, pp. 1109–1116.
[105] R. Malhotra, M. Khanna, The ability of search-based algorithms to predict change-prone classes, Softw. Qual. Prof. 17 (1) (2014) 17–31.
[106] R. Malhotra, M. Khanna. A new metric for predicting software change using gene expression programming, in: Proceedings of the 5th international Workshop on Emerging Trends in Software Metrics, 2014f, pp. 8–14.
[107] R. Malhotra, M. Khanna, Mining the impact of object oriented metrics for change prediction using machine learning and search-based techniques, in: Proceedings of Advances in Computing, Communications and Informatics, Kochi, 2015, pp. 228–234.
[108] M. Evett, T. M. Khoshgoftaar, Using genetic programming to determine software quality, in: Proceedings of the Twelfth International Florida Artificial Intelligence Research Society Conference, 1999, pp. 113–117.
[109] J.S. Aguilar-Ruiz, I. Ramos, J.C. Riquelme, M. Toro, An evolutionary approach to estimating software development projects, Inf. Softw. Technol. 43 (14) (2001) 875–882.
[110] K. Kaminsky, G. Boetticher. How to predict more with less, defect prediction using machine learners in an implicitly starved domain, in: Proceedings of the 8th World Multi-conference on Systems, Cybernetics and Informatics, Orlando, 2004.
[111] K. Kaminsky, G. Boetticher. Building a genetically engineerable evolvable program (GEEP) using breadth-based explicit knowledge for predicting software defects, in: Proceedings of Annual Meeting of the Fuzzy Information Processing, Alberta, 2004a, pp. 10–15.
[112] S.S. Dahiya, J.K. Chhabra, S. Kumar. Use of genetic algorithm for software maintainability metrics conditioning, in: Proceedings of the International Conference on Advanced Computing and Communications, 2007, pp. 87–92
[113] R. Vivanco, Y. Kamei, A. Monden, K.I. Matsumoto, D. Jin. Using search-based metric selection and oversampling to predict fault prone modules, in: Proceedings of the 23rd Canadian Conference on Electrical and Computer Engineering, Canada, 2010, pp. 1–6.
[114] L. Zhenyou, Intelligently predict project effort by reduced models based on multiple regressions and genetic algorithms with neural networks, in: Proceedings of International Conference on E-Business and E-Commerce, Guangzhou, 2010, pp. 1536–1542.
[115] J-C Lin, C-T Chang, S-Y Huang. Research on software effort estimation combined with genetic algorithm and support vector regression, in: Proceedings of International Symposium on Computer Science and Society, 2011, pp. 349–352.
[116] T.K. Sharma, M. Pant. Halton based initial distribution in artificial bee colony algorithm and its application in software effort estimation, in: Proceedings of the 6th International conference on Bio-Inspired Computing: Theories and Applications, Penang, 2011, 80–84.
[117] B. Dhanalaxmi, G. Apparao Naidu, K. Anuradha. Adaptive PSO based association rule mining technique for software defect classification using ANN, in: Proceedings of International Conference on Information and Communication Technologies, 2014, Kochi, pp. 432–442.
[118] F. Soleimanian, R. Rezaii, B. Arasteh. A new approach by using tabu search and genetic algorithms in software cost estimation, in: Proceedings of International Conference on Application of Information and Communication Technologies, Rostov-on-don, 2015, pp. 113–117.
[119] A.D. Bakar, A.B. Sultan, H. Zulzalil, J. Din. Applying evolution programming Search Based Software Engineering (SBSE) in selecting the best open source software maintainability metrics, in: Proceedings of IEEE Symposium on Computer Applications and Industrial Electronics, 2012, pp. 70–73
[120] R. Malhotra, A. Jain, Fault prediction using statistical and machine learning methods for improving software quality, J. Inf. Process. Syst. 8 (2) (2012) 241–262.
[121] Ye Fei, X. Zhu, Y. Wang. A new software maintainability evaluation model based on multiple classifiers combination. in: Proceedings of International Conference on Quality, Reliability, Risk, Maintenance, and Safety Engineering 2013, pp. 1588–1591.
[122] C. Grosan, A. Abraham, Hybrid evolutionary algorithms: methodologies, architectures, and reviews, Stud. Comput. Intell. 75 (2007) 1–17.
[123] S.D. Conte, H.E. Dunsmore, V.Y. Shen, Software Engineering Metrics and Models, Benjamin-Cummings Publ. Co., Redwood City, CA, USA, 1986.
[124] H. Zhang, X. Zhang, Comments on 'data mining static code attributes to learn defect predictors', IEEE Trans. Softw. Eng. 33 (9) (2007) 635–636.
[125] H. He, E.A. Garcia, Learning from imbalanced data, IEEE Trans. Knowl. Data Eng. 21 (9) (2009) 1263–1284.
[126] T. Menzies, A. Dekhtyar, J. Distefano, J. Greenwald, Problems with precision: a response to comments on 'data mining static code attributes to learn defect predictors', IEEE Trans. Softw. Eng. 33 (9) (2007) 637–640.
[127] S. Lessmann, B. Baesans, C. Mues, S. Pietsch, Benchmarking classification models for software defect prediction: a proposed framework and novel findings, IEEE Trans. Softw. Eng. 34 (4) (2008) 485–496.
[128] R. Malhotra, A systematic review of machine learning techniques for software fault prediction, Appl. Soft Comput. 27 (2015) 504–518.
[129] T. Menzies, J. Greenwald, Data mining static code attributes to learn defect predictors, IEEE Trans. Softw. Eng. 33 (1) (2007) 2–13.
[130] A. Arcuri, L.C. Briand, A practical guide for using statistical tests to assess randomized algorithms, In: Proceedings of International Conference on Software Engineering, Honolulu, 2011, pp. 1–10.
[131] L. Di Geronimo, F. Ferrucci, A. Murolo, F. Sarro. 2012. A parallel genetic algorithm based on hadoop mapreduce for the automatic generation of junit test suites, in: Proceedings of the 5th International Conference on Software Testing, Verification and Validation, 2012, pp. 785–793.
[132] D.R. White. Cloud computing and SBSE., in: Proceedings of 5th International Symposium on Search-based Software Engineering, St. Petersburg, 2013, pp. 16–18

Accepted Manuscript



Palladium gate all around - Hetero dielectric -tunnel FET based highly sensitive hydrogen gas sensor

Jaya Madan, Rishu Chaujar

PII: S0749-6036(16)30526-2

DOI: 10.1016/j.spmi.2016.09.050

Reference: YSPMI 4540

To appear in: *Superlattices and Microstructures*

Received Date: 21 July 2016

Accepted Date: 28 September 2016

Please cite this article as: J. Madan, R. Chaujar, Palladium gate all around - Hetero dielectric -tunnel FET based highly sensitive hydrogen gas sensor, *Superlattices and Microstructures* (2016), doi: 10.1016/j.spmi.2016.09.050.

This is a PDF file of an unedited manuscript that has been accepted for publication. As a service to our customers we are providing this early version of the manuscript. The manuscript will undergo copyediting, typesetting, and review of the resulting proof before it is published in its final form. Please note that during the production process errors may be discovered which could affect the content, and all legal disclaimers that apply to the journal pertain.

ACCEPTED MANUSCRIPT

Palladium Gate All Around - Hetero Dielectric - Tunnel FET based highly sensitive Hydrogen Gas Sensor

Jaya Madan[1] and Rishu Chaujar[2]

Microelectronics Research Lab, Department of Engineering Physics, Delhi Technological University, Bawana Road, Delhi-110042, India

jayamadan@dtu.ac.in[1] and rishu.phy@dce.edu[2]

***Abstract*—The paper presents a novel highly sensitive Hetero-Dielectric-Gate All Around Tunneling FET (HD-GAA-TFET) based Hydrogen Gas Sensor, incorporating the advantages of band to band tunneling (BTBT) mechanism. Here, the Palladium supported silicon dioxide is used as a sensing media and sensing relies on the interaction of hydrogen with Palladium-SiO_2-Si. The high surface to volume ratio in the case of cylindrical GAA structure enhances the fortuities for surface reactions between H_2 gas and Pd, and thus improves the sensitivity and stability of the sensor. Behaviour of the sensor in presence of hydrogen and at elevated temperatures is discussed. The conduction path of the sensor which is dependent on sensors radius has also been varied for the optimized sensitivity and static performance analysis of the sensor where the proposed design exhibits a superior performance in terms of threshold voltage, subthreshold slope, and band to band tunnelling rate. Stability of the sensor with respect to temperature affectability has also been studied, and it is found that the device is reasonably stable and highly sensitive over the bearable temperature range. The successful utilization of HD-GAA-TFET in gas sensors may open a new door for the development of novel nanostructure gas sensing devices.**

***Index Terms*—Gas sensor, Gas adsorption, hetero gate dielectric, tunnel FET.**

I. INTRODUCTION

Hydrogen gas (H_2) participates as a clean energy in fuel cells and energy carrier and thus acts as a strong candidate to replace fossil fuels that are at the edge of exhaustion. But the smaller size of H-atoms attributes to the risk of leakage and thus creates a need for the detection of H_2 gas for fuel monitoring. Moreover, H_2 is an extremely flammable gas as it can burn at a concentration of 4% in air and have a large window (4-75% v/v H_2) of flammability in comparison with methane, ethane, natural gas, etc. Thus, H_2 gas sensors have perpetual demand for automotive, environmental monitoring, petroleum refining process, and medical industries [1, 2]. These gas sensors mainly work as transducer devices that detect the presence of H_2 gas, measure its concentration, and produce an electrical signal that is further calibrated with the magnitude of H_2 gas concentration. Out of various gas sensors such as catalytic sensors, semiconductor sensors, electrochemical sensors and infrared sensors; semiconductor sensors have numerous benefits and can be used for an extensive range of gases including toxic, combustible, etc. Further, the low cost, high sensitivity, stability, fast response time, wide operation temperature range and reliability make it highly applicative for detection of variety of gases. [3-5]

Palladium (Pd) has a very high selectivity towards H_2 gas. Pd based gas sensor rely on the fact that after absorption of H_2 gas, a chemical species called palladium hydride is formed, which has a comparatively high electrical resistance. Apart from high selectivity, out of several catalytic metals, the sensitivity of Pd for hydrogen is highly appreciable because of the sites located at Pd-SiO_2 interface (in case of MOS architecture based FETs such as MOSFET and TFETs) along with the surface reactions, participating in the catalytic reactions. It is also reported that at room temperature and atmospheric pressure, Pd can absorb up to 900 times its volume of hydrogen [6, 7]. When H_2 molecules interact with Pd surface, the H_2 molecules dissociate on the surface of metal to form atomic hydrogen and some of the dissociated H-atoms diffuse through the Pd surface. The probability of dissociation of H_2 on Pd is almost unity, or H_2 dissociates very meritoriously on Pd. Within few nanoseconds, the diffused H-atoms reaches to the interface of Pd and SiO_2 or the H-atoms gets adsorbed at the SiO_2-Pd interface. The H-atoms reaching the metal-insulator interface gets polarised and forms surface dipole layer. This dipole layer in turns modulates the work function, conductivity, etc. and thus affects the device electrical properties. The high sensitivity of Pd for H_2 is mainly attributed to the great polarisation of H-atoms at the Pd-SiO_2 interface rather than the large diffusion of H-

atoms through Pd [8, 9].

The key focus of earlier research work had been to enhance sensitivity and selectively (for a particular gas) and is done by either exploring suitable sensitive films or by various device design engineering schemes. For high sensitivity and selectivity, numerous films such as metal compounds [10-12], polymers [13], organic compounds [14], hydrated salts [15] and catalytic metals [16-18] were used. In the novel device design, dual gate MOSFET; nanowire MOSFET, conventional TFET, etc. has already been taken into consideration. Till now in order to fulfill the requirement of sensing H_2 gas, silicon nanowire based H_2 gas sensor was proposed by Cao A et al. [2]. Further, to obtain appreciable sensitivity, the surface of SiNW FET sensor was functionalised with catalytic layers of Pd nanoparticles by Bongsik Choi et al. [19], for enhancing the selectivity and thus the sensitivity. Moreover, various gas sensors using metal oxide nanowires such as SnO_2, ZnO and In_2O_3 have been reported previously. A lot of work in the field of semiconductor gas sensors has been carried out with MOSFETs. But there is a need to investigate TFET as a gas sensor, as TFET is highly suitable for low power digital CMOS applications. The novel properties of TFET such as low leakage current, lower subthreshold swing (lower than 60mV/decade); immunity against short channel effects makes it an outstanding candidate for low power devices in the semiconductor industry [20-23]. Apart from these remarkable features, TFET suffers from few shortcomings such as low I_{ON}, ambipolar current and high threshold voltage. So to overcome these drawbacks, various engineering schemes were introduced such as hetero gate dielectric engineering, gate metal work function engineering, heterojunction devices, gate drain underlap/ overlap TFETs, etc. In heterogate-dielectric (HD) scheme, a high-k material has been locally inserted (near the source side) in the gate dielectric to enhance the ON-current [24]. The presence of high-k dielectric results into a higher band bending due to increasing surface potential (at a constant gate bias) [25-27]. This boosted band bending leads to reduction in tunneling barrier width, which further increases the generation rate and hence, on-current. In this work, the concept of palladium gate based Tunnel FET for H_2 gas sensing applications has been proposed. In addition, hetero gate dielectric engineering scheme and gate all around architecture has also been incorporated to further enhance the sensitivity of the hydrogen gas sensor.

II. Structural Descriptions And Simulation Methodology

Table 1 indicates the structural parameters of all four devices based gas sensor which are compared for the improved sensitivity. For GAA-TFET and HD-GAA-TFET, cylindrical geometry is considered. In the case of HD-GAA-TFET, the channel consists of two regions; region 1 (near the source L_1 =20nm) and region 2 (near the drain L_2=30nm). Region 1 consists of high-k dielectric (optimized value is 21 corresponds to HfO_2) and region 2 is of low-k dielectric (SiO_2, k= 3.9) whereas, in the case of GAA TFET, the entire channel consists SiO_2. In both the cases, radius (R) is 10nm. To reduce ambipolarity effect, source and drain are doped asymmetrically in the case of TFET. Uniform doping profile has been considered in each case. The source and drain junctions are abruptly doped for an effective BTBT and the interface of high-k and SiO_2 is taken as abrupt.

Table 1: - Default structural parameters for all the devices based gas sensors.

Parameters / Device	Channel Length (nm)	Source doping (cm^{-3})	Drain doping (cm^{-3})	Channel/Substrate doping (cm^{-3})
Conventional MOSFET	50	n^+ -10^{19}	n^+ -10^{19}	p -10^{16}
Conventional TFET		p^+ -10^{20}	n^+ -5×10^{18}	p -10^{16}
GAA TFET		p^+ -10^{20}	n^+ -5×10^{18}	p -10^{16}
HD-GAA-TFET	50=20+30 $L=L_1+L_2$	p^+ -10^{20}	n^+ -5×10^{18}	p -10^{16}

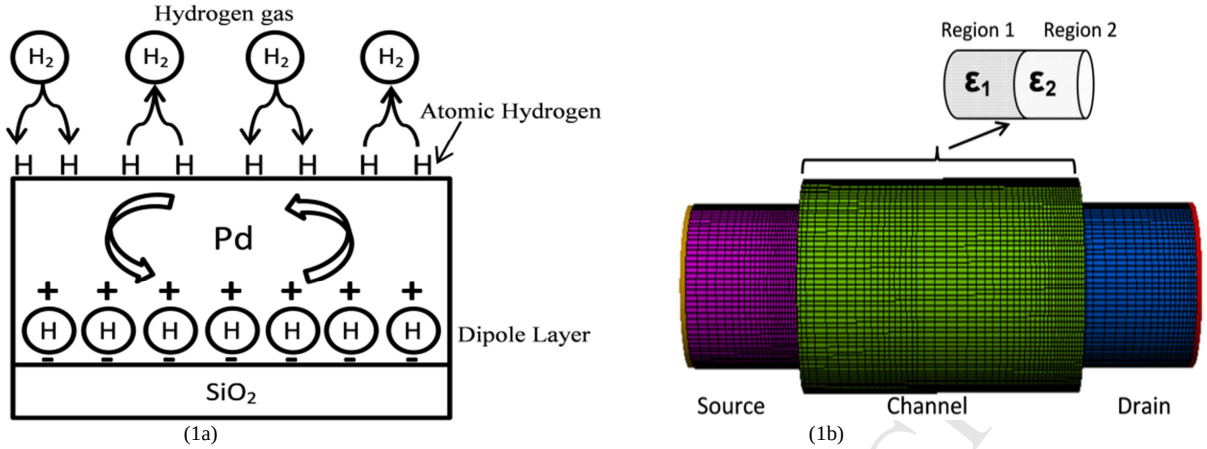
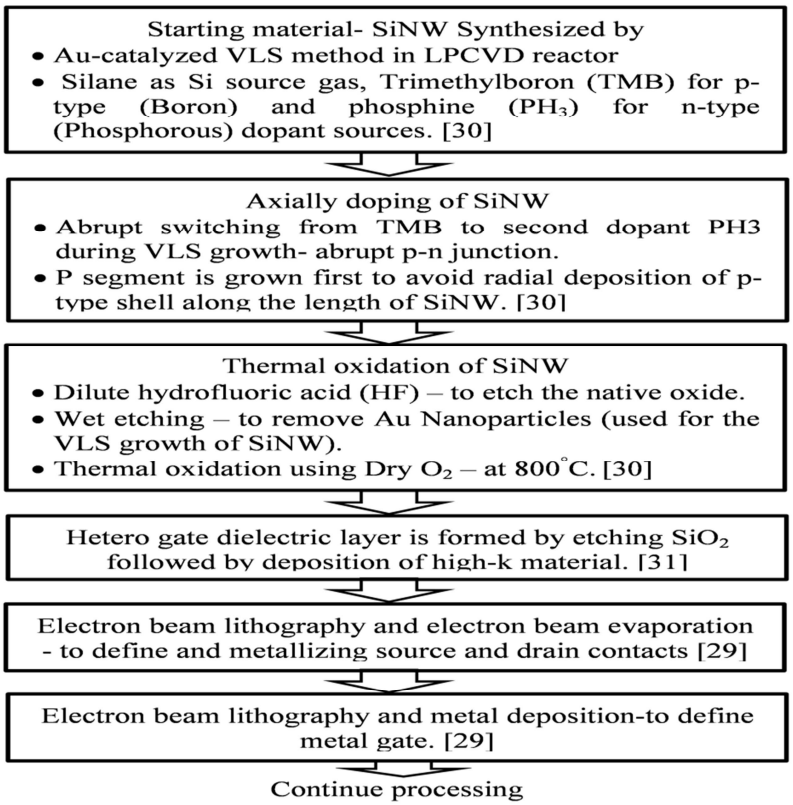
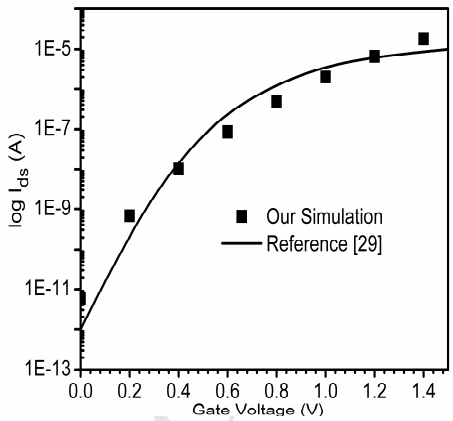


Fig. 1. (a) Schematic of adsorption of H_2 gas molecules, diffused through Pd films and formation of dipoles at the Pd-SiO_2 interface. (b) Meshed structure of HD-GAA-TFET gas sensor.

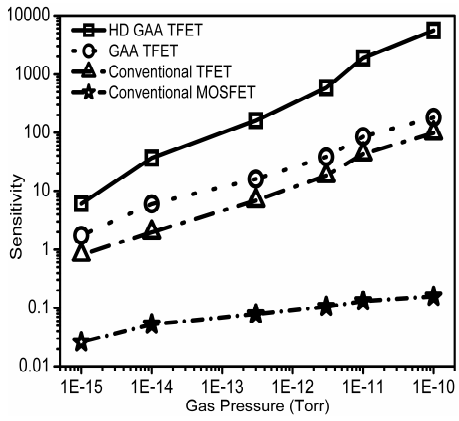
All simulations have been performed using ATLAS device simulator. The models activated during simulation of TFET Gas Sensor are as follows: concentration and field dependent mobility model, Shockley-Read-Hall for carrier recombination, non-local BTBT, band gap narrowing and Fermi-Dirac statistics. For conventional MOSFET based gas sensor, models invoked for simulation are: - Shockley-Read-Hall for carrier recombination, Lombardi CVT mobility model, concentration and field dependent mobility model and boltzmann transport statistics. The most important model for Tunnel FET simulations is the band-to-band tunneling (BTBT) model. A non-local model is chosen in this work instead of local model, to incorporate the effect of electric field at each point in the tunneling path. In local models such as Kane's model the triangular barrier approximation of energy bands results into constant electric field at the entire tunneling path. But the non-local BTBT model have a more physical basis as the field changes at each point in the tunneling path. Both the numerical methods- Gummel (decoupled) together with Newton's (Fully coupled) have been incorporated to solve mathematically the carrier transport equation [28]. Pd with work function 5.1eV is used as the catalytic metal gate and gate oxide thickness is 2nm for all the cases. The entire analysis has been performed at room temperature. For TFET, the calibration of non-local BTBT model is done with the experimental data [29]. The tunneling masses were tuned from their default values i.e. me.tunnel=0.322m_o and mh.tunnel=0.549m_o to make it best fit with the experimental data. Where; mo is the rest mass of electron. The adjusted value of me.tunnel=0.22m_o and mh.tunnel=0.52 m_o. The calibrated results are shown in Fig. 2(a). The fabrication feasibility of proposed gas sensor i.e. HD-GAA-TFET gas sensor is shown in the Table 2. To add further, the gate all around TFET has already been fabricated by various researchers such as Chen et al, [29] fabricated vertical silicon_nanowire TFET, Gandhi et al, [32, 33] fabricated both vertical Si-nanowire n-type and p-type TFET. Therefore the proposed gas sensor can be fabricated using the above device design schemes, in which the advantages of hetero gate dielectric architecture has been incorporated onto GAA TFET for attaining higher sensitivity. In addition, the work function of the gate metal has been altered to incorporate the corresponding effect of change in hydrogen gas pressure as reported in [34].

Table II.
Summary of Process Flow for HD-GAA-TFET Implementaion.





(2a)



(2b)

Fig. 2: (a) Calibration with the published result, transfer characteristics of 200 nm gate length SiNW-TFET at V_{ds}=1.2V, t_{ox}=4.5nm, Diameter=70nm. (b) Sensitivity comparison of conventional MOSFET, conventional TFET, GAA-TFET and HD-GAA-TFET as a function of gas pressure.

III. SENSITIVITY ANALYSIS OF PROPOSED GAS SENSOR

Sensitivity (S) is defined as;

$$S = \frac{I_{After\ gas\ adsorption} - I_{Before\ gas\ adsorption}}{I_{Before\ gas\ adsorption}}$$

Where; $I_{before\ gas\ adsorption}$ and $I_{after\ gas\ adsorption}$ are the drain current before the gas adsorption and the drain current after gas adsorption. In Fig. 2(b), sensitivity is plotted as a function of gas pressure for conventional MOSFET, conventional TFET, GAA-TFET, and HD-GAA-TFET. It is observed that the sensitivity of either of the TFET is higher in comparison with to conventional MOSFET over the entire pressure range.

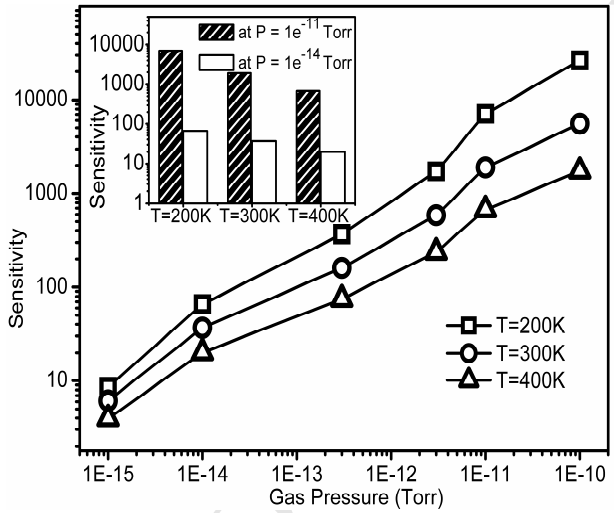


Fig. 3: Sensitivity comparison of HD-GAA-TFET as a function of gas pressure at various temperatures. Inset: - Sensitivity at constant pressures values at temperature= 200K, 300K and 400K for HD-GAA-TFET.

The improved sensitivity in case of TFET is mainly attributed to the fact that TFET overcomes the limitation of subthreshold swing, which is limited to 60mV/decade in MOSFET. This limited SS of MOSFET bounds the sensitivity of the device as is clearly evident from Fig. 2. At a pressure of 1×10^{-10} Torr, the sensitivity of conventional TFET is 626 times greater with respect to conventional MOSFET. With the application of GAA structure, the sensitivity is further enhanced by almost three times in comparison to conventional TFET. It is due to the enhanced gate controllability of cylindrical GAA geometry. Further, it is observed that at a pressure of $1e^{-10}$ Torr, the sensitivity of HD-GAA-TFET is 3.5 X 10^4 times, 56 times and 30 times enhanced in comparison to the conventional MOSFET, conventional TFET, and GAA-TFET respectively. In addition, the amalgamation of HD scheme onto GAA architecture further improves the sensitivity. Enhanced sensitivity with the application of hetero gate dielectric scheme is mainly due to the higher band bending at the tunneling junction, and thus enhancement in the BTBT rate of electrons and drain current of the device is achieved. The reason for enhanced sensitivity from conventional TFET to GAA-TFET is due to higher surface to volume ratio of cylindrical architecture that enhances the probability of diffusion of H-atoms (which are dissociated) through the Pd, and hence increases the number of dipoles formed at the Pd-SiO_2 interface, thereby enhancing sensitivity of the design as a sensor.

A. Impact of temperature

In addition to the properties of the semiconductor, surface reactions between gas and catalytic metal are also dependent on temperature. So there is a need to study the effect of temperature in order to investigate the stability of the gas sensor. The results are studied only for HD-GAA-TFET as it is highly sensitive as evident from Fig. 2. Moreover, for stable operation of a sensor, the sensor should be least affected by the temperature. It is clear from Fig. 3 that at low pressure, the sensitivity is least affected by temperature but by an increase in pressure, the effect of temperature is comparatively large. Overall, the sensor has an endurable stable response to H_2 gas over an extensive

temperature range. With an increase in temperature, the H_2 coverage over the catalytic metal (Pd) will decrease, and thus leads to a reduction in sensitivity. Moreover, the effect of temperature at constant pressure is plotted in the inset of Fig. 3, which illustrates that at low pressure, the sensitivity is less dependent of temperature.

B. Impact of radius

As the conduction path of the device in case of a cylindrical GAA MOSFET/TFET is mainly affected by the radius of the channel, there is a need to study the effect of radius on the sensitivity of proposed gas sensor. The effect of the radius of silicon pillar has been analyzed by taking three different radii such as 5nm, 10nm and 15nm as shown in Fig. 4. As we reduce the radius from 10nm to 5nm, the sensitivity of the sensor reduces considerably by many orders. The reduction in sensitivity is mainly attributed to the reduced probability of surface reactions at the palladium surface (because of the reduction in surface area) with the hydrogen gas molecules. Moreover, the increase in channel radius from 10nm to 15nm does not enhance the sensitivity of the proposed sensor considerably. It is because the higher radius of the sensor enhances the surface area but on the other side, it reduces the gate controllability over the channel. So the results at 10nm radius can be measured as optimized for a gas sensor with superior sensitivity.

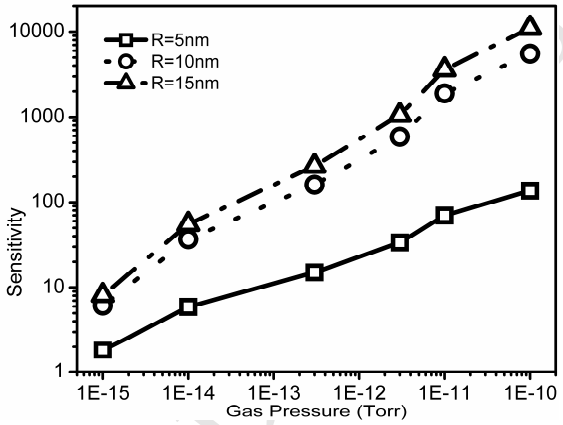


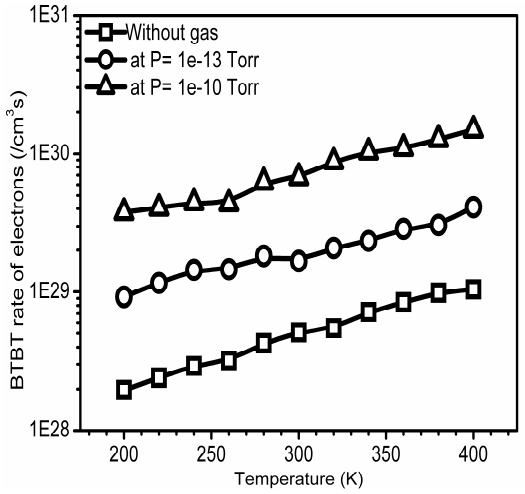
Fig. 4: Sensitivity comparison of HD-GAA-TFET as a function of gas pressure at a different radius.

IV. STATIC PERFORMANCE ANALYSIS FOR PROPOSED GAS SENSOR

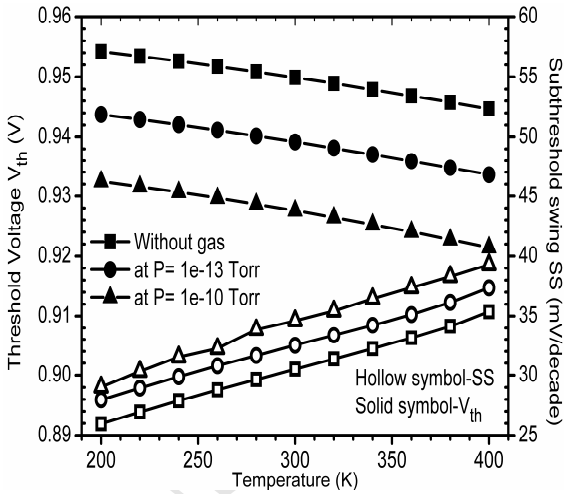
A. Impact of temperature

After investigating the sensitivity of the sensor, the effect of temperature on basic static performance parameters of sensor such as BTBT of electrons, threshold voltage and subthreshold swing is evaluated. Figs. 5(a-b) show the BTBT rate of electrons, threshold voltage and subthreshold swing of the H_2 sensor. It is clearly shown in Fig. 5(a), that the BTBT rate is higher when gas is present, in comparison to the case when no gas molecules are there. In addition, for low pressure, less number of hydrogen-atoms are diffused through the Pd-gate, resulting in a lesser number of dipoles formations at the Pd-SiO_2 interface. Thus, comparatively less band bending will take place in the channel, and more tunneling barrier width is obtained, resulting in lowering of BTBT rate. Further, as the gas pressure increases, more number of H-atoms are diffused through the Pd surface and hence, enhances the number of dipoles formed at the Pd-SiO_2, thereby lowering the barrier width at the tunneling junction and resulting in enhanced BTBT rate. Further, as the temperature increases, the BTBT rate of electrons increases, because increase in temperature changes the properties of the semiconductor as well as the reaction rate between the gas and catalytic metal. Fig. 5(b) shows the effect of temperature on the threshold voltage and subthreshold swing of HD-GAA-TFET gas sensor. When no H_2 gas molecules are present, or the dipoles at the Pd-SiO_2 interface are not formed, the threshold voltage of the sensor is comparatively large. It is because of the lower BTBT rate of electrons when the gas is absent, as shown in Fig. 5(a). Further, as the pressure of the gas increases, the threshold voltage of the sensor decreases, because of the aforementioned reason. Lastly, the effect of temperature and gas pressure is studied on the SS of HD-GAA-TFET H_2 gas sensor. It must be noted that the SS of HD-GAA-TFET gas sensor has overcome the fundamental limit of the MOSFET, i.e. limitation of 60mV/decade, for entire temperature range and at any gas pressure. The SS increases with an increase in gas pressure which can be understood by the previously mentioned

reasons. Moreover, with an increase in temperature, the SS of the sensor increases. Thus, there is a trade-off between improved sensitivity and improved static performance at high temperatures.



(5a)



(5b)

Fig. 5: Effect of temperature variations on (a) BTBT rate of electrons, (b) threshold voltage and subthreshold swing of HD-GAA-TFET gas sensor with radius R=10nm at constant gas pressures.

B. Impact of radius

After studying the effect of temperature, effect of channel radius of cylindrical GAA structure at constant gas pressures has been studied on the static performance of H_2-gas sensor. Effect of channel radius on BTBT rate of electrons for three cases can be seen in Fig. 6(a). It is clearly shown that with reduction in channel radius, the BTBT rate enhances significantly. This rise in BTBT rate of electrons is mainly attributed to higher band bending at lower channel radius, which enhances the probability of tunneling of electrons from the valence band of the source to conduction band of the channel, and thus the BTBT rate of electrons. Moreover, it is illustrated that an increase in gas pressure results in remarkable enhancement in BTBT. As the pressure of the gas increases, more band bending occurs at the tunneling junction and thus results into an increase of BTBT rate of electrons at different radii. The effect of gas pressure and channel radius on the threshold voltage and subthreshold swing has also been plotted in Fig. 6(b). The increase in BTBT rate of electrons with pressure reduces the threshold voltage of the sensor, as higher BTBT rate of electrons turns the device ON at lower gate voltage. Further, the threshold voltage is higher for higher channel radius at any gas pressure. There is an increase (decrease) in SS with an increase in gas pressure (channel radius) respectively, because of the aforementioned reasons.

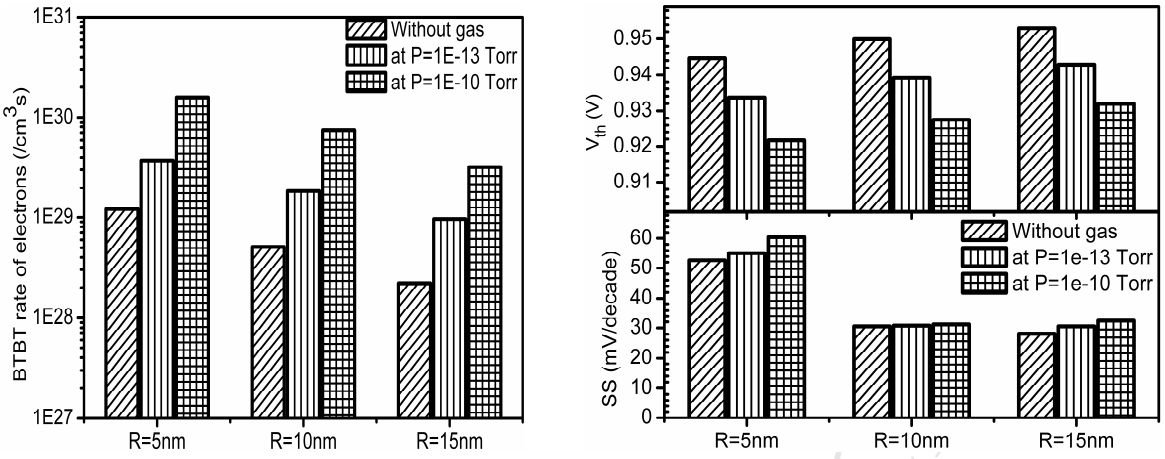


Fig. 6: Effect of radius variations on (a) band to band tunneling rate, (b) threshold voltage and subthreshold swing of HD-GAA-TFET gas sensor at T=300K and at constant gas pressures.

V. CONCLUSION

HD-GAA-TFET H_2 gas sensor unites the advantages of BTBT of electrons in case of tunnel FET along with hetero gate dielectric gate all around and provides substantially high sensitivity in comparison to conventional MOSFET, conventional TFET, GAA-TFET towards H_2 gas detection. Along with the high sensitivity, HD-GAA-TFET based H_2 gas sensor also has tolerable stability over wide temperature variations. Results have shown that for a radius of 10nm, the sensor can be optimized in terms of high sensitivity. The stability of sensor with respect to temperature affectability has also been studied, and it is found that the device is reasonably stable over the bearable temperature range. After analysing the stability and sensitivity of the sensor, the temperature affectability and impact of radius has been considered on static performance parameters of the sensor such as BTBT rate of electrons, subthreshold swing and threshold voltage. This highly sensitive HD GAA TFET based hydrogen gas sensor may fulfill the everlasting demand for automotive, environmental monitoring, petroleum refining process, and medical industries.

ACKNOWLEDGMENT

Authors would like to thank to Microelectronics Research Lab, Department of Engineering Physics Delhi Technological University to carry out this work. One of the authors (Jaya Madan) would like to thank University Grants Commission, Govt. of India, for providing the necessary financial assistance during the course of this research work.

REFERENCES

[1] T. Hübert, L. Boon-Brett, G. Black, and U. Banach, "Hydrogen sensors – A review," Sensors Actuators B Chem., vol. 157, no. 2, pp. 329–352, 2011.
[2] A. Cao, E. Sudhölter, and L. de Smet, "Silicon Nanowire-Based Devices for Gas-Phase Sensing," Sensors, vol. 14, no. 1, pp. 245–271, 2013.
[3] Y. Sun and H. H. Wang, "Electrodeposition of Pd nanoparticles on single-walled carbon nanotubes for flexible hydrogen sensors," Appl. Phys. Lett., vol. 90, no. 21, p. 213107, 2007.
[4] J. Kong, M. G. Chapline, and H. Dai, "Functionalized Carbon Nanotubes for Molecular Hydrogen Sensors," Adv. Mater., vol. 13, no. 18, pp. 1384–1386, 2001.
[5] S. Mubeen, T. Zhang, B. Yoo, M. a. Deshusses, and N. V. Myung, "Palladium Nanoparticles Decorated Single-Walled Carbon Nanotube Hydrogen Sensor," J. Phys. Chem. C, vol. 111, no. 17, pp. 6321–6327, 2007.
[6] A. D'Amico, A.Palma and E.Verona, "Surface acoustic wave hydrogen sensor," Sensors and Actuators, vol. 3, no. 1, pp. 31-39,1982.
[7] D.A. Papaconstantopoulos, B.M. Klein, E.N. Economou and L.L. Boyer, "Band structure and supercnductivity of PdDx and PdHx," Physical Review B, vol. 17, no. 1, pp. 141-150, 1978.
[8] L. Ekedahl, M. Eriksson and I. Lundstrom, "Hydrogen Sensing Mechanisms of Metal - Insulator Interfaces," Accounts of chemical research, vol. 31, no. 5, pp. 249–256, 1998.
[9] J. Fogelberg, M. Eriksson, H. Dannetun, and L. G. Petersson, "Kinetic modeling of hydrogen adsorption/absorption in thin

ACCEPTED MANUSCRIPT

films on hydrogen-sensitive field-effect devices: Observation of large hydrogen-induced dipoles at the Pd-SiO2 interface," J. Appl. Phys., vol. 78, no. 2, pp. 988–996, 1995.
[10] E. N. Dattoli, Q. Wan, W. Guo, Y. Chen, X. Pan, and W. Lu, "Fully transparent thin-film transistor devices based on SnO2 nanowires," *Nano Lett.*, vol. 7, no. 8, pp. 2463–2469, 2007.
[11] C. Li, D. Zhang, X. Liu, S. Han, T. Tang, J. Han, and C. Zhou, "In_2O_3 nanowires as chemical sensors," *Appl. Phys. Lett.*, vol. 82, no. 10, p. 1613-1615, 2003.
[12] Z. Fan, D. Wang, P.-C. Chang, W.-Y. Tseng, and J. G. Lu, "ZnO nanowire field-effect transistor and oxygen sensing property," *Appl. Phys. Lett.*, vol. 85, no. 24, p. 5923-5925, 2004.
[13] M. Liess, D. Chinn, D. Petelenz, and J. Janata, "Properties of insulated gate field-effect transistors with a polyaniline gate electrode," *Thin Solid Films*, vol. 286, no. 1, pp. 252–255, 1996.
[14] V. Meister, K. P.Kamloth, "Polymer-oxide-silicon-field-effect-transistor as sensor for gases and vapors," in Proc. Electrochemical society proceedings, vol. 97, no. 19, pp. 16-22, 1996.
[15] V. M. Fuenzalida, M. E. Pilleux, and I. Eisele, "Adsorbed water on hydrothermal BaTiO3 films: work function measurements," *Vacuum*, vol. 55, pp. 81–83, 1999.
[16] K. Scharnagl, a. Karthigeyan, M. Burgmair, M. Zimmer, T. Doll, and I. Eisele, "Low temperature hydrogen detection at high concentrations: comparison of platinum and iridium," *Sensors Actuators B Chem.*, vol. 80, no. 3, pp. 163–168, 2001.
[17] K. Scharnagl, M. Eriksson, a Karthigeyan, M. Burgmair, M. Zimmer, and I. Eisele, "Hydrogen Detection at High Concentrations with Stabilized Palladium," *Sensors Actuators B Chem.*, vol. 78, no. 1-3, pp. 138–143, 2001.
[18] M. Zimmer, M. Burgmair, K. Scharnagl, a Karthigeyan, T. Doll, and I. Eisele, "Gold and Platinum as Ozon Sensitive Layer in Work-Function Gas Sensors," *Sensors Actuators B Chem.*, vol. 80, no. 3, pp. 174-178, 2001.
[19] B. Choi, J. Ahn, J. Lee, J. Yoon, J. Lee, M. Jeon, D. M. Kim, D. H. Kim, I. Park, and S. Choi, "A bottom-gate silicon nanowire field-effect transistor with functionalized palladium nanoparticles for hydrogen gas sensors," *Solid-State Electronics* , vol. 114, pp. 76–79, 2015.
[20] A. M. Ionescu and H. Riel, "Tunnel field-effect transistors as energy-efficient electronic switches," *Nature*, vol. 479, no. 7373, pp. 329–337, 2011.
[21] J. Madan and R. Chaujar, "Interfacial Charge Analysis of Heterogeneous Gate Dielectric-Gate All Around-Tunnel FET for Improved Device Reliability," IEEE Trans. on Device and Materials Reliability, vol. 16, no. 2, pp. 227-234, June 2016.
[22] W. Y. Choi, B. G. Park, J. D. Lee, and T. J. K. Liu, "Tunneling field-effect transistors (TFETs) with subthreshold swing (SS) less than 60 mV/dec," *IEEE Electron Device Lett.*, vol. 28, no. 8, pp. 743–745, 2007.
[23] E.-H. Toh, G. H. Wang, L. Chan, G. Samudra, and Y.-C. Yeo, "Device physics and guiding principles for the design of double-gate tunneling field effect transistor with silicon-germanium source heterojunction," *Appl. Phys. Lett.*, vol. 91, no. 24, pp. 243505, 2007.
[24] A. Mallik and A. Chattopadhyay, "Drain-dependence of tunnel field-effect transistor characteristics: The role of the channel," *IEEE Trans. Electron Devices*, vol. 58, no. 12, pp. 4250–4257, 2011.
[25] R. Jhaveri, V. Nagavarapu, and J. C. S. Woo, "Effect of pocket doping and annealing schemes on the source-pocket tunnel field-effect Transistor," *IEEE Trans. Electron Devices*, vol. 58, no. 1, pp. 80–86, 2011.
[26] J. Madan, R. S. Gupta, and R. Chaujar, "Analytical drain current formulation for gate dielectric engineered dual material gate-gate all around-tunneling fi eld effect transistor," *Japanese Journal of Applied Physics*, vol. 54, no. 9, pp. 094202, 2015.
[27] J. Madan, R. S. Gupta, and R. Chaujar, "Mathematical modeling insight of hetero gate dielectric-dual material gate-GAA-tunnel FET for VLSI/analog applications," *Microsyst. Technol*., 2016. Available online:- DOI 10.1007/s00542-016-2872-9
[28] ATLAS User's Manual: 3-D Device Simulator, Version 5.14.0.R, SILVACO International, Santa Clara, CA, USA, Version 5.14.0.R, 2010.
[29] Z. X. Chen, H. Y. Yu, N. Singh, N. S. Shen, R. D. Sayanthan, G. Q. Lo, and D.-L. Kwong, "Demonstration of tunneling FETs based on highly scalable vertical silicon nanowires," *IEEE Electron Device Letters*, vol. 30, no. 7, pp. 754-756, July 2009.
[30] A. L. Vallett, S. Minassian, P. Kaszuba, S. Datta, J. M. Redwing, and T. S. Mayer, "Fabrication and Characterization of Axially Doped Silicon Nanowire Tunnel Field-Effect Transistors," *Nano Letters*,vol. 10, no. 12, pp. 4813–4818, 2010.
[31] S. Marjani and S. E. Hosseini, "Radio-frequency small-signal model of hetero-gate-dielectric p-n-p-n tunneling field-effect transistor including charge conservation capacitance and substrate parameters," *J. Appl. Phys.*, vol. 118, no. 9, pp. 095708, 2015.
[32] R. Gandhi, Z. Chen, N. Singh, K. Banerjee, and S. Lee, "CMOS-Compatible vertical-silicon-nanowire gate-all-around P-Type tunneling FETs with ≤ 50-mV/decade subthreshold swing," *IEEE Electron Device Lett.*, vol. 32, no. 11, pp. 1504–1506, 2011.
[33] R. Gandhi, Z. Chen, N. Singh, S. Member, K. Banerjee, and S. Lee, "Vertical Si-Nanowire n -Type Tunneling FETs With at Room Temperature," *IEEE Electron Device Lett.*, vol. 32, no. 4, pp. 437–439, 2011.
[34] D. Sarkar, H. Gossner, W.Hansch, and K. Banerjee, "Tunnel-field-effect-transistor based gas-sensor: Introducing gas detection with a quantum-mechanical transducer," *Applied Physics Letters*, vol. 102, no. 2, pp. 023110, 2013.

ACCEPTED MANUSCRIPT

HIGHLIGHTS

- Palladium based Hydrogen Gas sensor has been proposed using Tunnel FET.
- Sensitivity of the sensor has been enhanced using gate dielectric engineering and gate all around architecture.
- Sensitivity of the sensor has been studied for temperature affectability and radius variation.
- Impact of temperature and channel radius on static performance of proposed gas sensor has been obtained for improved performance.
- The response of the HD-GAA-TFET has been found superior in terms of sensitivity in comparison to its conventional counterparts, thus it could be considered as a promising candidate for Hydrogen sensing applications.

ACCEPTED MANUSCRIPT

Ramakant Rana, R.S. Walia, Qasim Murtaza, Mohit Tyagi / TORONTO'2016
AES-ATEMA 29th Int. Conference (Toronto, CANADA: July 04 - 08, 2016) pp. 151 - 162.

ISBN 978-1-927838-29-7 (CD-ROM) & ISBN 978-1-927838-28-0 (Book)

AES ATEMA'2016
Montreal, CANADA

TORONTO 2016 AES-ATEMA International Conference
Advances and Trends in Engineering Materials and their Applications
(Toronto, CANADA: July 04 08, 2016)

Parametric Optimization of Hybrid Electrode EDM Process

Ramakant Rana[1], R.S. Walia[2*], Qasim Murtaza[3], Mohit Tyagi[4]

[1]Research Scholar, Delhi Technological University, Mechanical Engineering, Delhi, India.
(email:7ramakant@gmail.com)
[2] *Associate Professor, Delhi Technological University, Mechanical Engineering, Delhi, India.
(email:waliaravinder@yahoo.com) (corresponding author)
[3] Associate Professor, Delhi Technological University, Mechanical Engineering, Delhi, India.
(email:qasimmurtaza@gmail.com)
[4] Assistant Professor, Delhi Technological University, Mechanical Engineering, Delhi, India.
(email:mohitmied@gmail.com)

Abstract

Hybrid Electric Discharge Machining Electrode (HEDME) process is developed by comprising the features of Electric Discharge Machining (EDM) and traditional grinding which occurs alternatively in place of their simultaneous effect as EDG process. This paper reports the experimental study of HEDME during machining of High Carbon Alloy Steel for material removal rate (MRR), tool wear rate (TWR) and surface roughness (SR). The experiments were carried out on a indigenously developed HEDME attachment on Sparkonix EDM. The effects of main machining parameters such as type of tool, current and machining time have been studied. The effect of the machining on the workpiece surface machined by HEDME has been optimized using Taguchi L_9 OA and results are reported. Experimental study shows that the TWR is found to be the least with third design of the electrode and it decrease with the decreasing value of current, also surface finish increases with decrease in current. Moreover, the third design of electrode gives the lowest SR and highest MRR.

Keywords.
EDM; Grinding; MRR; TWR; Surface Roughness.

© 2016, Advanced Engineering Solutions (AES.COM)
Ottawa, Canada.
All rights are reserved.

INTRODUCTION AND LITERATURE REVIEW

Continued improvements in the quality of the product have become a necessity rather than an ancillary. Subsequent improvements in the efficiency and productivity of the process electrode. The mechanism of material removal of the HEDME process is shown in the Figure 1 [Jain, (2004); Shan, (2005); Joshi and Pande, (2009); Kopac and Krajnik, (2006); Koshy et al., (1997)].

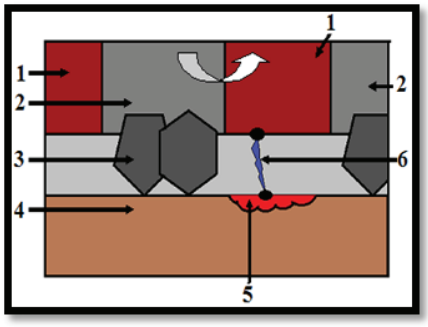


Figure 1. Mechanism of material removal of the HEDME process (1: Metallic part of electrode, 2: Abrasive Ceramic segment of electrode, 3: Abrasive Ceramic particles, 4: Workpiece, 5: Recast Layer, 6: Spark).

In this process, the material is removed in two

phases. Firstly, the spark is generated between workpiece and metallic portion of the HEDME during Pulse-on in the EDM machine. Due to the spark material is melted and softened below the melt zone. The molten material is removed during pulse off-time of EDM process. This phenomenon is repeated at entire metallic portion of the hybrid electrode. Secondly the material is removed due to the abrasive action of the abrasive ceramic particles [Abothula et al., (1996); Koshy et al., (1996)]. These two actions are repeated due to rotation of the electrode and material is removed due to the individual effect of spark erosion and abrasion processes. Many process parameters affect the performance of the HEDME process. These parameters are of either EDM, grinding or related to the both [Benedict, (1987); Bhandari, (1999)]. The Figure 4 shows the schematic diagram of the HEDME process.

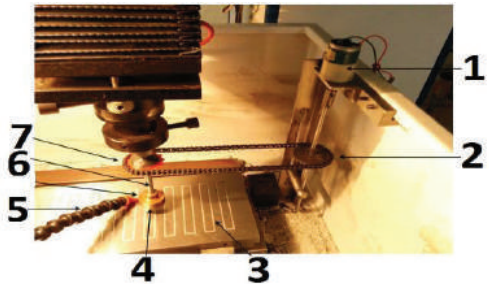


Figure 2. Shown the indigenously developed HEDME Process setup (1: DC Motor, 2: Chain Drive for the rotation motion, 3: Magnetic Chuck for Holding workpiece, 4: Hybrid EDM Electrode, 5: Flushing Pipe, 6: Electrode Holder, 7: Plastic Gear).

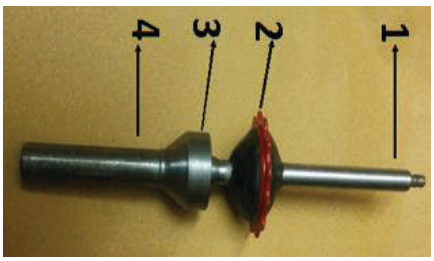


Figure 3. Developed Electrode Holder. (1: Lower part, 2: Plastic Gear, 3: Bearing, 4: Upper Part).

The workpiece is machined for a predetermined machining time. After the machining is over, the workpiece is taken out from the setup and cleaned with acetone. An electronic balance (Shimadzu, LC 0.1mg) was used for the measurement of material removal [Jain, (2004); Joshi and Pande, (2009); Kopac and Krajnik, (2006); Koshy et al., (1993)].

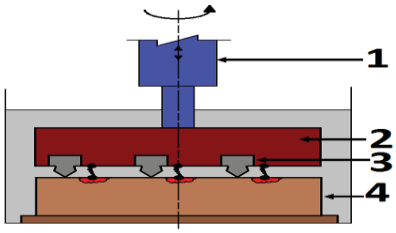


Figure 4. Schematic view of the HEDME process (1: EDM electrode holder, 2: Metallic part of Electrode, 3: Abrasive Ceramic Particles, 4: Workpiece).

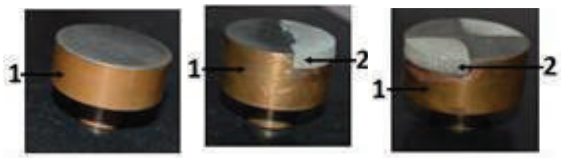


Figure 5. Shown the various design of developed Hybrid Electric Discharge Machining Electrode (1: Copper Part, 2: Abrasive Ceramic particles Slab).

The Mahr Federal (Model: Pocket Surf III) was used to measure surface roughness (SR) values of the workpiece. Several Ra values were taken at different locations on the surface of the workpieces.

PROCESS PARAMETERS OF HEDME PROCESS

The various process variables that may affect the material removal rate (MRR) tool wear rate (TWR) and surface roughness (SR) of the HEDME process are as follows:

1. Machine-based parameters: Current, Voltage, Pulse-on Time, Pulse-off Time, Polarity, Flushing method, machining time, Duty cycle.
2. Tool-based parameters: Type of Tool, abrasive material, and abrasive grain size and shape of tool.

© 2016, Advanced Engineering Solutions (AES.COM)
Ottawa, Canada.
All rights are reserved.

3. Workpiece-based parameters: material of workpiece, workpiece diameter, shape and geometry.

Out of these parameters the following were kept constant to limit the volume of work involved in the investigation: Work Material, Workpiece Diameter, Polarity, and Flushing Pressure. This article reports the optimization of the selected significant parameters that affect the material removal, tool wear and surface roughness. The workable range of the parameters was decided on the basis of the results of the pilot experiments conducted by varying one parameter at a time approach [Montgomery (2001)] and the limitations imposed by the experimental setup. In the present work, the three types of tool were selected (figure 5). The first type of tool was selected to compare the responses with the basic rotational EDM. From the various types of abrasive particles, such as silicon carbide, boron carbide, aluminum oxide, diamond, etc., the boron carbide abrasive was used in the present work because of its availability. The range of current used was 2, 6, and 10 A. The process parameters, their designated symbols and ranges are given in Table 1.

TAGUCHI'S PHILOSOPHY

One of the outstanding engineering accomplishments of the 20th century is Taguchi's comprehensive system of quality engineering.

Table 1. Definitions and trial levels factors in the Taguchi's L_9 OA experiment.

Process Parameters Designation	Process Parameters	Level 1	Level 2	Level 3
A	Type of Tool	S_1	S_2	S_3
B	Current (Ampere)	2	6	10
C	Time (minutes)	30	40	50

Work Material: EN-31 High Carbon Alloy Steel, Workpiece Diameter : 50 mm, Electrode (Tool): Copper and Abrasive particles (Diameter 36mm, Abrasive particle Height 5mm, Total Height 18mm), Polarity: Positive, Dielectric Fluid: EDM Oil (LL 21), Flushing Pressure: Normal Submerged ($1kg/cm^2$): Temperature: 32±2°C.

To remain cost-effective and reduce variability, small scale experiments are used by upstream methods efficiently and robust designs for large-scale production and the marketplace. Real-time, cost-based methods for preserving and monitoring the quality in production are provided by the shop- level techniques. An "off-line" strategy for quality improvement is proposed by the Taguchi's method as an alternative to an attempt to inspect quality into a product on the production line. Taguchi observed that the poor quality cannot be improved by the process of screening, salvaging and inspection. No amount of inspection can put quality back into the product. Taguchi recommended a three-stage process: System design, Parameter design, and Tolerance design [Ross (1988), Roy (1990)]. In the present work, we have used Taguchi's parameter design approach study the effect of process parameters on the MRR, TWR and SR of HEDME process.

SELECTION OF AN ORTHOGONAL ARRAY (OA)

The following two points must first be considered, before choosing a particular OA to be employed as a matrix for conducting the experiments [Ross (1988), Roy (1990)]: The number of parameters and interactions of interest and the number of levels for the parameters of interest.

If the nonlinear behavior exists, among the process parameters, then the process parameters can only be studied if more than two levels of the parameters are used. Thus, each parameter was analyzed at three levels. Table 1 shows the selected number of process parameters and their levels.

The second-order interactions among the parameters were not considered, for the sake of simplification. Each three-level parameter has two degrees of freedom (DOF) (number of levels -1), the total DOF required for three parameters each at three levels is 6 {=3 □ (3 – 1)}. The total DOF of selected OA must be larger than or equal to the total DOF required for the experiment, as per Taguchi's method. So an L_9 OA (a standard 3-level OA) having 8 {= 9 - 1} degree of freedom was selected for the present analysis (Table 2).

© 2016, Advanced Engineering Solutions (AES.COM)
Ottawa, Canada.
All rights are reserved.

EXPERIMENT, ANALYSIS, AND DISCUSSION

The HEDME experiments are performed at the trial conditions as for Taguchi L_9 (OA). Three workpieces for each trial condition was machined by using randomized technique, and the run numbers have been given in the second column of the Table 2. The response parameters measured in this work were material removal rate (MRR) tool wear rate (TWR) and surface roughness (SR). The difference between the workpiece weight before and after machining was calculated to measure the MRR. Similarly the difference between the electrode weight before and after machining was calculated to measure the TWR.

Table 2. Taguchi $L_9(3^4)$ OA (parameters assigned) with response.

Exp. No.	Run order	Parameters Trial Conditions				Responses (Raw Data)			S/N ratio (db)
		A	B	C	-				
		1	2	3	4	**R_1**	**R_2**	**R_3**	
1	3	1	1	1	1	Y_{11}	Y_{12}	Y_{13}	S/N (1)
2	7	1	2	2	2	Y_{21}	Y_{22}	Y_{23}	S/N (2)
3	5	1	3	3	3	Y_{31}	Y_{32}	Y_{33}	S/N (3)
4	1	2	1	3	3	Y_{41}	Y_{42}	Y_{43}	S/N (4)
5	4	2	2	1	1	Y_{51}	Y_{52}	Y_{53}	S/N (5)
6	6	2	3	2	2	Y_{61}	Y_{62}	Y_{63}	S/N (6)
7	9	3	1	2	2	Y_{71}	Y_{72}	Y_{73}	S/N (7)
8	2	3	2	1	3	Y_{81}	Y_{82}	Y_{83}	S/N (8)
9	8	3	3	3	1	Y_{91}	Y_{92}	Y_{93}	S/N (9)
Total						$\sum$	$\sum$	$\sum$	

R_1, R_2, R_3 represent responses values for three repetitions of each trial. The 1's, 2's, and 3's represent levels 1, 2, and 3 of the parameters, which appear at the top of the column. (–) represents no assignment in the column. Y_{ij} are the measured values of the response.

Several Ra values were taken at different locations on the surface of test specimens by using Mahr Federal (Model: Pocket Surf III), and the values of SR were noted. The values of MRR, TWR and SR for each trial condition and replications were recorded and are given in Table 3. The quality characteristic for MRR is of higher-the better type. The S/N ratio for the "higher-the-better" type of response given below by Eq. (1) was used:

$$(S/N)_{HB} = -10log\left[\frac{1}{n}\sum_{j=1}^{R}(1/Y_j{}^2)\right] \quad (1)$$

The quality characteristic for TWR and SR is of lower-the-better type. The S/N ratio for the "lower-the-better" type of response given below by Eq. (2) was used:

$$(S/N)_{LB} = -10log\left[\frac{1}{n}\sum_{j=1}^{R}(1/Y_j{}^2)\right] \quad (2)$$

Where Y_j, j = 1, 2,…, n are the response values for the trial conditions repeated "n" times. The S/N ratio was computed for MRR TWR and SR for each of the nine trial values. These values are also given in Table 3.

The mean response (raw data) refers to the average value of the performance characteristic for each parameter at different levels. The average values of MRR, TWR and SR for each parameter at levels 1, 2, and 3 are calculated and are given in Tables 4, 5 and 6, respectively. These values are plotted in Figs. 6, 7 and 8 respectively. The average values of S/N ratios of various process parameters at different levels are also given in Tables 4, 5 and 6.

It is clear from Figure6 that the MRR is highest at the third level of parameters A (A_3), third level of the parameter B (B_3), and the second level of parameter C(C_2). The S/N ratio analysis (Figure6) also suggests the same levels of the parameters (A_3, B_3, and C_2) as the best levels for maximum MRR of workpieces in HEDME process.The first graph of Figure 6shows the variation of MRR with the type of tool used for the machining process i.e. pure copper (S_1), half copper half abrasive particle (S_2) and third combination of copper and abrasive particle (S_3). As the tool is changed from pure copper to the combination of copper and abrasive Particle the MRR is increased as shown by both experimental and predicted values. The second graph of Figure 6 shows that MRR increases with the increase in current at constant speed duty, cycle, and polarity. It is observed that within the range of current investigated MRR increases with increase of current, this is due to the fact that the with an increase of current, the discharge energy increases i.e. increase in current, increases the energy supply between the tool and workpiece. Hence, more material becomes softer as more discharge energy blends in the workpiece.

© 2016, Advanced Engineering Solutions (AES.COM)
Ottawa, Canada.
All rights reserved.

Table 3. Experimental results of material removal, tool wear and surface roughness.

	Material removal rate (mg) MRR				Tool wear rate (mg) TWR				Surface finish (µm) SR			
Trial no.	R1	R2	R3	**S/N Ratio (dB)**	R1	R2	R3	**S/N Ratio (dB)**	R1	R2	R3	**S/N Ratio (dB)**
1	0.16	0.18	0.17	-15.42	0.02	0.021	0.02	33.83	3.22	3.19	3.18	-10.09
2	2.39	1.94	1.76	5.94	0.03	0.039	0.034	29.24	5.05	5.234	5.08	-14.18
3	3.35	3.9	4.54	11.69	0.038	0.037	0.039	28.40	6.06	6.75	6.05	-15.98
4	0.46	0.54	0.29	-8.25	0.07	0.07	0.08	22.67	2.90	2.91	2.98	-9.34
5	2.98	2.62	2.53	8.59	0.05	0.061	0.05	25.36	4.29	4.656	4.05	-12.75
6	1.37	1.81	1.48	3.65	0.075	0.073	0.069	22.81	5.31	5.27	5.31	-14.48
7	0.65	0.71	0.63	-3.59	0.01	0.013	0.014	38.09	2.87	2.87	2.71	-8.99
8	1.39	1.47	1.53	3.28	0.016	0.016	0.015	36.09	4.13	4.25	4.10	-12.38
9	5.01	6.57	6.97	15.55	0.038	0.039	0.032	28.76	5.98	4.3	5.12	-14.28
	$\bar{T}$= overall mean of				$\bar{T}$= overall mean of				$\bar{T}$= overall mean of			
	MRR = 2.12 mg				TWR = 0.0396				SR=4.36			

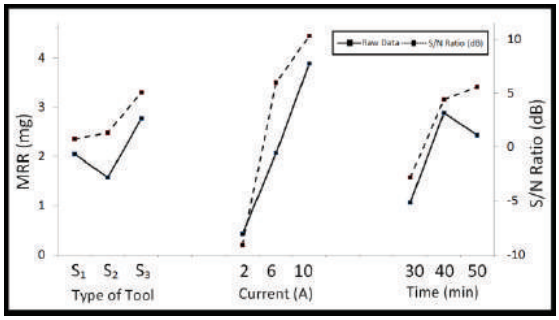


Figure 6. Effect of parameters on MRR.

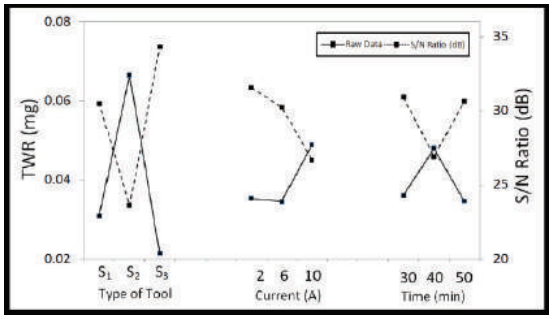


Figure 7. Effect of parameters on TWR.

The MRR increases since, the softer material is easily removed during grinding action (Yadav et al.,2013; Abhothula et al., 2010; Shih et al., 2008; Shu et al., 2003; Kozak, 2002). The third graph of Figure 6 shows the effect of machining time on MRR. It is also observed that with increase in machining time MRR increases and then it begins to decrease. A comparatively longer time is available for conduction of heat into the workpiece, which results in melting a more workpiece material i.e. enough time is available for the discharge energy to enter into workpiece due to increase in machining time. Hence, MRR is increased as, the material becomes softer to a larger extent and the softer material is easily removed during grinding action of abrasive particle. The increase in MRR can is very significant. It is also observed that there is increase in MRR within the time limits 30-40 min. for constant duty cycle, polarity, and then it decreases within the time limit of 40-50 minutes (Yadav et al., 2013; Abhothula et al., 2010; Shih et al., 2008; Shu et al., 2003).

It is also clear from Figure 7 that the TWR is lowest at the third level of parameter A (A_3), first level of the parameter B (B_1), and third level of parameter C(C_3).

Table 4. Main effects of MRR on raw data and S/N data

		Type of Tool		Current (A)		Time (Min.)	
	LEVEL	**Raw Data**	**S/N data**	**Raw data**	**S/N Data**	**Raw data**	**S/N data**
Average values	L1	2.04	0.74	0.42	-9.09	1.06	-2.83
	L2	1.56	1.33	2.07	5.94	2.89	4.41
	L3	2.77	5.08	3.89	10.29	2.43	5.56
Main effects Difference	L2-L1	-0.48	0.59	1.65	15.03	1.82	7.24
	L3-L2	1.21	3.75	1.82	4.35	-0.45	1.15

L1, L2, and L3 represent average values raw data at levels 1, 2, 3, respectively, of parameters. L2–L1 and L3–L2 are the average main effect when the corresponding parameter changes from level 1 to level 2 and level 2 to level 3, respectively.

© 2016, Advanced Engineering Solutions (AES.COM)
Ottawa, Canada.
All rights are reserved.

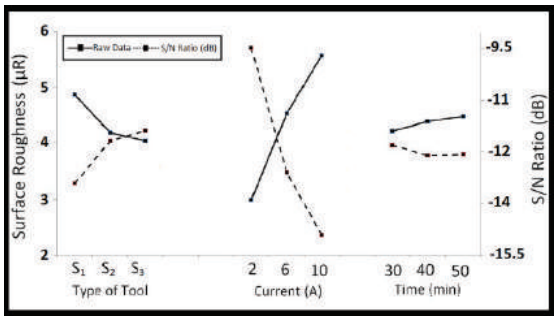


Figure 8. Effect of parameters on SR.

It can be further noticed that in the parameters A, B, and C, the lowest values of average response of TWR corresponds to highest values of S/N ratio. The S/N ratio analysis (Figure 7) also suggests the same levels of the parameters (A_3, B_1, and C_3) as the best levels for obtaining the favorable values TWR of workpieces in HEDME process. The first graph of Figure 7 shows the variation of TWR with the type of tool used for the machining process i.e. pure copper (S_1), half copper half abrasive particle (S_2) and third combination of copper and abrasive particle (S_3). For the highest S/N ratio the TWR is the lowest which corresponds to the third type of tool. This is due to the fact that two different materials wear out at different rate which cumulatively reduces the TWR for that combination of tool. The second graph of Figure 7 shows that TWR increases with the increase in current when the all other parameters are kept constant. It is observed that with increase of current TWR decreases up to a certain value of machining time and beyond that, it increases. The increase in electrode wear rate is always accompanied by an increase in current. This is due to the fact large amounts of heat is generated by the higher current densities, this causes electrode to wear by quickly overheating the electrode. From the Figure 8, we also discovered that, under some circumstances, the TWR decreased substantially [Choudhury et al., (1999); Chow et al, (1991); Hegeman et al., (2002)]. It might be because the dielectric fluid is mostly made of hydrocarbon compounds and in the machining process, the electric arc causes hydrocarbon compounds to decompose into carbons and other compounds by releasing great heat (Shih et al., 2008; Shu et al., 2003). The third graph of Figure 7 shows the effect of machining time on TWR.

Table 5. Main effects of TWR on raw data and S/N data.

	LEVEL	Type of Tool		Current (A)		Time (Min.)	
		Raw data	S/N data	Raw data	S/N data	Raw data	S/N data
Average values	L1	0.031	30.49	0.035	31.54	0.036	30.91
	L2	0.066	23.62	0.035	30.23	0.048	26.89
	L3	0.021	34.32	0.049	26.66	0.035	30.62
Main effects Difference	L2-L1	0.036	-6.87	-0.001	-1.30	0.012	-4.02
	L3-L2	-0.045	10.70	0.014	-3.58	-0.013	3.73

L1, L2, and L3 represent average values raw data at levels 1, 2, 3, respectively, of parameters. L2–L1 and L3–L2 are the average main effect when the corresponding parameter changes from level 1 to level 2 and level 2 to level 3, respectively.

Table 6: Main effects of SR on raw data and S/N data.

	LEVEL	Type of Tool		Current (A)		Time (Min.)	
		Raw data	S/N data	Raw data	S/N data	Raw data	S/N data
Average values	L1	4.87	-13.42	2.98	-9.48	4.22	-12.32
	L2	4.19	-12.19	4.54	-13.11	4.39	-12.61
	L3	4.04	-11.89	5.57	-14.92	4.48	-12.58
Main effects Difference	L2-L1	-0.69	1.23	1.56	-3.63	0.18	-0.28
	L3-L2	-0.15	0.30	1.04	-1.81	0.08	0.03

L1, L2, and L3 represent average values raw data at levels 1, 2, 3, respectively, of parameters. L2–L1 and L3–L2 are the average main effect when the corresponding parameter changes from level 1 to level 2 and level 2 to level 3, respectively.

It is also observed that with increase in

machining time, TWR increases up to a certain value of machining time and beyond that, it decreases. From the figure, we discovered that, under some circumstances, the TWR increased considerably. It is because the cutting debris gets assembled from the workpiece and inscribes onto the abrasive part of the electrodes removes the electrode's material (Shih et al., 2008; Shu et al., 2003). The S/N ratio analysis (Figure 7) suggests the A_3, B_1, and C_3 levels of the parameters as the best levels for obtaining the favorable values TWR of workpieces in HEDME process.
It is also clear from Figure 8 that the SR is lowest at the third level of parameter A (A_3) and first level of the parameter B (B_1). It can be further noticed that in the parameters A and B, the lowest values of average response of TWR corresponds to highest values of S/N ratio. The S/N ratio analysis (Figure8) also suggests the same levels of the parameters (A_3 and B_1) as the best levels for obtaining the favorable values SR of workpieces in HEDME process and the parameter C is found to be not significant. The first graph of Figure 8 shows the variation of SR with the type of tool used for the machining process i.e. pure copper (S_1), half copper half abrasive particle (S_2) and third combination of copper and abrasive particle (S_3). For the highest S/N ratio the SR is the lowest which corresponds to the third type of tool. This shows the surface roughness decreases if combination of materials is used in varying profiles. The second graph of Figure 8 shows that SR increases with the increase in current when the all other parameters are kept constant. It is observed that higher energy goes into the workpiece by the increase in current, resulting in formation of comparatively bigger size crater on the workpiece surface. In this situation, the abrasive abrasion is dominated by the spark erosion. Consequently, the SR increases due to increase of current. (Yadav et al., 2013; Abhothula et al., 2010; Shih et al., 2008; Shu et al., 2003). The third graph of Figure 8 shows the effect of pulse-on-time on SR. If the pulse-on-time is increased, then enough time is provided to heat to penetrate the tool and work surface. It is observed that with increase of machining time SR increases owing to formation of larger craters on the workpiece surface, after the riddance of the molten materials. Beyond a certain value of machining time, SR value decreases slightly with the increase of machining time. This is due to the fact that, for maintaining a constant temperature of molten material some of the discharge energy is spent, thus a smaller amount of material is melted. (Yadav et al., 2010; Abhothula et al., 2010; Shih et al., 2008; Shu et al., 2003). To study the significance of the process parameters toward the MRR, TWR and SR, analysis of variance (ANOVA) is performed. The pooled versions of ANOVA of the raw data and the S/N data for MRR, TWR and SR are given, respectively, in Tables 7, 8 and 9.From Table 7, it is clear that parameters A, B, and C significantly affect both the mean and the variation in the MRR values. Similarly from Table 8, it is clear that parameters A, B, and C significantly affect both the mean and the variation in the TWR values. Meanwhile from Table 9 it is clear that parameter C is insignificant, and parameters A and B significantly affect the SR values.

ESTIMATION OF OPTIMUM PERFORMANCE CHARACTERISTICS

Material Removal Rate

The optimum value of MRR is predicted at the selected levels of significant parameters A3, B3, and C2 (Table 4). The estimated mean of the response characteristic (MRR) can be determined (Kumar et al., 1996; Singh et al., 2002; Walia et al., 2006) as:

$$\text{MRR} = \overline{A}_3 + \overline{B}_3 + \overline{C}_2 - 2\overline{T} \qquad (3)$$

Where, $\overline{T}$ = Overall mean of MRR = 2.12 (Table 3),
$\overline{A}3$ = Average MRR at the third level of type of Tool = 2.77, $\overline{B}3$: Average MRR at the third level of Current = 3.89, $\overline{C}2$: Average MRR at the second level of Time = 2.89, Substituting the values of various terms in Eq. (3),
MRR = 2.77 + 3.89 + 2.89 – 2 x 2.12 = 5.28 mg
The 95% confidence interval of confirmation experiments (CI_{CE}) and of population (CI_{POP}) was calculated by using the following equations:

$$CI_{CE} = \sqrt{F_\alpha(1, f_e)V_e\left[\frac{1}{n_{eff}} + \frac{1}{R}\right]} \qquad (4)$$

and

$$CI_{POP} = \sqrt{\frac{F_\alpha(1, f_e)V_e}{n_{eff}}} \quad (5)$$

where $F_\alpha(1,f_e)$ = The F ratio at the confidence level of (1-α) against DOF 26 and error DOF f_e = 20, N = total number of results = 27 (treatment = 9, repetition = 3),

$$n_{eff} = \frac{N}{1+[\text{DOF associated in the estimate of mean response})} = 3.86$$

, R = sample size for confirmation experiments = 3, V_e = error variance (Table 7), f_e= error DOF = 20 (Table 7), $F_{0.05}(1,20)$ = 3.493 (tabuated F value), So, CI_{CE} = ±1.26, CI_{POP}= ±0.835.

The predicted optimal range (for a confirmation runs of three experiments) is "Mean MRR - CI_{CE} < MRR (mg) < Mean MRR + CI_{CE}"

4.02 < MRR (mg) < 6.54

The 95% conformation interval of the predicted mean is "Mean MRR - CI_{POP} < MRR (mg) < Mean MRR + CI_{POP}" : 4.44 < MRR (mg) < 6.11

Tool Wear Rate

The optimum value of TWR is predicted at the selected levels of significant parameters A3, B1, and C3 (Table 5). The estimated mean of the response characteristic (TWR) can be determined (Kumar et al., 1996; Singh et al., 2002; Walia et al., 2006) as:

$$TWR = \bar{A}_3 + \bar{B}_1 + \bar{C}_3 - 2\bar{T} \quad (6)$$

Where $\bar{T}$ = Overall mean of TWR = 0.039 (Table 3), $\bar{A}_3$ = Average TWR at the third level of type of Tool = 0.021, $\bar{B}_1$: Average TWR at the first level of Current = 0.035, $\bar{C}_3$: Average TWR at the third level of Time = 0.035, Substituting the values of various terms in Eq. (6),

TWR = 0.021 + 0.035 + 0.035 – 2 x 0.039 = 0.0118 mg

The 95% confidence interval of confirmation experiments (CI_{CE}) and of population (CI_{POP}) was calculated by using the equations number 4 and 5: CI_{CE}= ±0.00632, CI_{POP}= ±0.0042.

The predicted optimal range (for a confirmation runs of three experiments) is "Mean TWR - CI_{CE} < TWR (mg) < Mean TWR + CI_{CE}"

0.0055 < TWR (mg) < 0.0181

The 95% conformation interval of the predicted mean is "Mean TWR - CI_{POP} < TWR (mg) < Mean TWR + CI_{POP}"

0.0076 < TWR (mg) < 0.0159

Surface Roughness

The optimum value of SR is predicted at the selected levels of significant parameters A_3, and B_1 (Table 6). The estimated mean of the response characteristic (SR) can be determined (Kumar et al., 1996; Singh et al., 2002; Walia et al., 2006) as:

$$SR = \bar{A}_3 + \bar{B}_1 - \bar{T} \quad (7)$$

where $\bar{T}$ = Overall mean of SR = 4.364 (Table 3), $\bar{A}_3$ = Average SR at the third level of type of Tool = 4.037, $\bar{B}_1$: Average SR at the first level of Current = 2.982, Substituting the values of various terms in Eq. (7),

SR = 4.037 + 2.982 – 4.364 = 2.655

The 95% confidence interval of confirmation experiments (CI_{CE}) and of population (CI_{POP}) was calculated by using the equations numbered 4 and 5: CI_{CE}= ±0.484, CI_{POP}= ±0.319

The predicted optimal range (for a confirmation runs of three experiments) is "Mean SR - CI_{CE} < SR (μm) < Mean SR + CI_{CE}"

2.172 < SR (μm) < 3.139

The 95% conformation interval of the predicted mean is "Mean SR - CI_{POP} < SR (μm) < Mean SR + CI_{POP}" : 2.336 < SR (μm) < 2.975

CONFIRMATION EXPERIMENTS

Every experiment process is accomplished with the conduct of confirmation experiments. It aims at validating the results obtained by conducting the experiments. This confirmation experiment involves the combination of factors and levels previously determined to obtain the optimal responses. Three confirmation experiments were conducted at the optimum setting of the process parameters which yielded optimum MRR, TWR and SR. The type of tool was set at third level, Current at third level and time at second level for performing the confirmation experiment to obtain optimal MRR. Similarly the type of tool was set at third level, Current at first level and Time at third level for performing the confirmation experiment to obtain optimal TWR and for obtaining the optimal value of

© 2016, Advanced Engineering Solutions (AES.COM)
Ottawa, Canada.
All rights are reserved.

SR the type of tool was set at third level, Current at first level and Time at second level. The results obtained after conducting the confirmation experiments have been discussed.

Table 7. Pooled ANOVA MR raw data and S/N data.

SOURCE TYPE	SS		DOF		V		F-Ratio		SS'		P %	
	Raw data	S/N Data	Raw data	S/N Data	Raw data	S/N Data	Raw data	S/N Data	Raw data	S/N Data	Raw data	S/N Data
Type of Tool	6.63	33.25	2	2	3.32	16.63	4.31*	24.98*	5.09	31.92	5.51	4.09
Current	54.16	620.69	2	2	27.08	310.35	35.19*	466.19*	52.62	619.36	56.98	79.46
Time	16.17	124.16	2	2	8.09	62.08	10.51*	93.26*	14.63	122.83	15.84	15.76
E (Pooled)	15.39	1.33	20	2	0.77	0.66	---	---	20.01	5.32	21.66	0.68
Total	92.36	779.44	26	8	---	---	---	---	92.36	779.44	100	100

*Significant at 95% confidence level, SS = Sum of Squares, DOF= Degree of Freedom, V=Variance, F-ratio tabulated for raw data: 3.493, F-ratio tabulated for S/N Ratio: 19, P%- Percentage contribution.

Table 8. Pooled ANOVA TWR raw data and S/N data.

SOURCE TYPE	SS		DOF		V		F-Ratio		SS'		P %	
	Raw data	S/N Data	Raw data	S/N Data	Raw data	S/N Data	Raw data	S/N Data	Raw data	S/N Data	Raw data	S/N Data
Type of Tool	0.0101	176.44	2	2	0.0051	88.22	262.37*	112.113*	0.01	174.87	79.79	70.95
Current	0.0012	38.27	2	2	0.00058	19.14	30.272*	24.318*	0.001	36.69	8.94	14.89
Time	0.0009	30.17	2	2	0.00048	15.08	24.945*	19.169*	0.001	28.59	7.31	11.60
E (Pooled)	0.0004	1.57	20	2	0.00002	0.79	---	---	0.001	6.29	3.97	2.55
Total	0.0126	246.45	26	8	---	---	---	---	0.013	246.45	100	100

*Significant at 95% confidence level, SS = Sum of Squares, DOF= Degree of Freedom, V=Variance, F-ratio tabulated for raw data: 3.493, F-ratio tabulated for S/N Ratio: 19, P%- Percentage contribution.

Table 9. Pooled ANOVA SR raw data and S/N data.

SOURCE TYPE	SS		DOF		V		F-Ratio		SS'		P %	
	Raw data	S/N Data	Raw data	S/N Data	Raw data	S/N Data	Raw data	S/N Data	Raw data	S/N Data	Raw data	S/N Data
Type of Tool	3.53	3.95	2	2	1.76	1.97	15.60*	59.79*	3.30	3.89	8.99	7.75
Current	30.61	45.99	2	2	15.30	22.99	135.30*	695.78*	30.38	45.93	82.74	91.56
Time	0.32	0.15	2	2	0.16	0.07	1.41	2.24	---	---	---	---
E (Pooled)	2.26	0.07	20	2	0.11	0.03	---	---	3.03	0.35	8.26	0.69
Total	36.72	50.16	26	8	---	---	---	---	36.72	50.16	100	100

*Significant at 95% confidence level, SS = Sum of Squares, DOF= Degree of Freedom, V=Variance, F-ratio tabulated for raw data: 3.493, F-ratio tabulated for S/N Ratio: 19, P%- Percentage contribution.

© 2016, Advanced Engineering Solutions (AES.COM)
Ottawa, Canada.
All rights are reserved.

The average material removal rate, tool wear rate and surface roughness of the HEDME process are found to be 5.21 mg, 0.0105 mg and 2.89μm, respectively, which are within the confidence interval of the predicated optimal values of MRR, TWR and SR.

CONCLUSIONS

The following results reported in this article are for Hybrid Electric Discharge Machining Electrode (HEDME) process and which can be considered as one of the important processes for machining of rotating EDM.

Within the range of test conditions used, the following conclusions can be drawn:

1. The application of Abrasive material to EDM Electrode (Tool) in EDM enhances the amount of material removal in the given processing time. As a consequence, less machining time is required for removing the same amount of material from the work piece, if processed by HEMDE.
2. As compared to traditional electrode the Hybrid Electric Discharge Machining Electrode (HEDME) improves the MRR by causing better debris evacuation from the spark gap. Also the rotating Electrode leads to better surface finish of workpiece.
3. The Type of Tool, Current and Time significantly affect the material removal and tool removal rate. On the other hand, only Type of Tool and Current significantly affect the SR; the effect of time is insignificant on SR values.
4. The SR on the work surface remains nearly uniform if the workpiece is processed by HEMDE.
5. The predicted optimal range for MR is 4.02 < MR (mg) < 6.54, for TWR is 0.0055 < TWR (mg) < 0.0181 and SR is 2.172 < SR (μm) < 3.139.
6. The 95% confidence interval of the predicted mean for MR is 4.44 < MR (mg) < 6.11, for TWR is 0.0076 < TWR (mg) < 0.0159 and for SR is 2.336 < SR (μm) < 2.975.

REFERENCES

1. Abothula B. Chandrasekhar, Yadava Vinod and Singh Gyanendra Kumar (2010) "Development and Experimental Study of Electrodischarge Face Grinding", *Materials and Manufacturing Processes*, vol. 25, pp. 482–487.
2. Benedict G.F., (1987) "Non-traditional manufacturing processes", *Marcel Dekker*, New York.
3. Bhandari V.B. (1999) "Design of Machine Elements", *TMH Publishing Company Ltd.*, New Delhi, pp. 417–453.
4. S.K., Jain V.K. and Gupta M. (1999) "Electrical Discharge Diamond Grinding Of High Speed Steel", *Machining Science and Technology*, vol. 3, pp. 91-105.
5. Chow H.M., Yan B.H. and Huang F.Y. (1991) "Micro slit machining using electro-discharge machining with a modified rotary disk electrode (RDE)", *Journal of Materials Processing Technology*, vol. 91, pp. 161–166.
6. Hegeman J.B.J.W., Hosson J.T.M.G. and With G. (2002) "Grinding of WC–Co hardmetals", *Wear*, vol. 248, pp. 187-196.
7. Jain V.K. (2004) "Advanced machining processes", *Allied Publishers*, New Delhi.
8. Joshi S N and Pande S S. (2009) "Development of an intelligent process model for EDM", *International Journal of Advanced Manufacturing Technology*, vol. 45, pp. 300–317.

© 2016, Advanced Engineering Solutions (AES.COM)
Ottawa, Canada.
All rights are reserved.

9. Kopac J. and Krajnik P. (2006) "High-performance grinding-A review", *Journal of Materials Processing Technology*, vol. 175, pp. 278 - 284.
10. Koshy P, Jain V K. and Lal G K. (1997) "Grinding of cemented carbide with electrical spark assistance", *Journal of Materials Processing Technology*, vol. 72 pp. 61–68.
11. Koshy P., Jain V. K. and Lal G. K. (1996) "Mechanism of Material Removal in Electrical Discharge Diamond Grinding", *International Journal of Machine Tools & Manufacture*, 1996, Vol. 36, No. 10, pp. 1173-1185.
12. Koshy P., Jain V.K. and Lal G.K. (1993) "Experimental investigations into Electrical Discharge Machining with a rotating disk electrode", *Journal of Precision Engineering*, vol. 15, pp. 6–15.
13. Kozak J. (2002) "Abrasive Electro discharge Grinding (AEDG) of advanced materials", *Archives of Civil and Mechanical Engineering*, vol. 2, pp. 83-101.
14. Kumar P., Barua P.B. and Gaindher J.L. (1996) "Quality of V-process method through the Taguchi technique" *Quality and Reliability Engineering International*, vol. 12, pp. 421–427.
15. Montgomery D. (2001) "Design and Analysis of Experiments", *John Wiely and Sons*, New York.
16. Ross P.J. (1988) "Taguchi Techniques for Quality Engineering", *McGraw-Hill Book Company*, New York.
17. Roy R.K. (1990) "A Primer on Taguchi Method", *Van Nostrand Reinhold*, New York.
18. Shan H.S. (2005) "Advanced Manufacturing Methods" *Tata McGraw-Hill*, New Delhi, India.
19. Shih Hung Rung and Shu Kuen Ming (2008) "A study of electrical discharge grinding using a rotary disk electrode", *The International Journal of Advanced Manufacturing Technology*, vol. 38, pp. 59-67.
20. Shu K.M. and Tu G.C. (2003) "Study of electrical discharge grinding using metal matrix composite electrode", *International Journal of Machine Tools and Manufacture*, vol. 43, pp. 845–854.
21. Shu K.M. and Tu G.C. (2003) "Study of electrical discharge grinding using metal matrix composite electrodes", *International Journal of Machine Tools & Manufacture*, vol. 43, pp. 845–854.
22. Singh, S., Shan H.S. and Kumar P. (2002) "Parametric optimization of magnetic-field-assisted abrasive flow machining by the Taguchi method" *Quality and Reliability Engineering International*, vol. 18, pp. 273–283.
23. Walia R.S., Shan H.S. and Kumar Pradeep (2006) "Parametric Optimization of Centrifugal Force-Assisted Abrasive Flow Machining (CFAAFM) by the Taguchi Method", *Materials and Manufacturing Processes*, vol. 21, pp. 375–382.
24. Yadav Ravindra Nath, Yadava Vinod and Singh G.K. (2013) "Multi-objective optimization of process parameters in Electro-Discharge Diamond Face Grinding based on ANN-NSGA-II hybrid technique", *Frontiers of Mechanical Engineering*, vol. 8 pp. 319–332.
25. Yadav S K S and Yadava V. (2010) "Multi-objective optimization of electrical discharge diamond cutoff grinding (EDDCG) using Taguchi method", *International Journal of Manufacturing Technology and Industrial Engineering*, vol. 1 pp. 193-198.

© 2016, Advanced Engineering Solutions (AES.COM)
Ottawa, Canada.
All rights are reserved.

List of Symbols

Y_{ij}:	Measured values of the response
Y_j:	Response values for the trial conditions repeated '*n*' times.
j:	1,2,… *n*
$\bar{T}$:	Overall mean
$\bar{A}_j$:	Levels of type of Tool
$\bar{B}_j$:	Levels of Current
$\bar{C}_j$:	Levels of Time
CI_{POP}:	Confidence interval of population
CI_{CE}:	Confidence interval of confirmation experiments
$F_\alpha(1,f_e)$:	*F*-ratio at the confidence level of (1-α)
f_e:	Error DOF
N:	Total number of results
R:	Sample size for confirmation experiments
V_e:	Error variance
µm:	Micro meter
SS:	Sum of Squares,
DOF:	Degree of Freedom,
V:	Variance,
P%:	Percentage contribution.

© 2016, Advanced Engineering Solutions (AES.COM)
Ottawa, Canada.
All rights are reserved.

Microsyst Technol
DOI 10.1007/s00542-016-3143-5

TECHNICAL PAPER

Performance investigation of heterogeneous gate dielectric-gate metal engineered–gate all around-tunnel FET for RF applications

Jaya Madan[1] · **R. S. Gupta**[2] · **Rishu Chaujar**[1]

Received: 24 August 2015 / Accepted: 19 September 2016
© Springer-Verlag Berlin Heidelberg 2016

Abstract In this work, the effect of gate metal work function engineering (GME), gate bias and drain bias on the bias dependent parasitic capacitances has been studied. Further, RF Figure of merits (FOMs) such as power gains, cut-off frequency (f_T), maximum oscillation frequency (f_{Max}) and intrinsic delay of hetero-dielectric gate-metal-engineered gate-all-around tunnel FET (HD-GME-GAA-TFET) are studied and compared with HD-GAA-TFET. Simulation results show an appreciable improvement in RF FOMs with the application of GME architecture on GAA TFET. Further, it has been observed that GME exhibits 3.76 times enhancement and 0.017 times reduction in cut-off frequency and intrinsic delay respectively as we increase the work function difference, which makes it a promising candidate for low power switching applications. Moreover, the small signal Y-parameters have also been studied which indicates that HD-GME-GAA-TFET is a promising candidate for RF/microwave applications. All the simulations have been done using ATLAS device simulator.

✉ Rishu Chaujar
rishu.phy@dce.edu

Jaya Madan
jayamadan.2012@gmail.com

R. S. Gupta
rsgupta1943@gmail.com

[1] Microelectronics Research Lab, Department of Engineering Physics, Delhi Technological University, Bawana Road, Delhi 110042, India

[2] Maharaja Agrasen Institute of Technology, Rohini, Delhi 110086, India

1 Introduction

The escalating power crisis in the CMOS Technology due to aggressive device contraction has become an issue of concern for circuit designers. Along with enhanced static power dissipation, the conventional MOSFET faces arduous challenges such as numerous short channel effects (SCE) and leakage current. Extensive materials and novel device structures such as multi gate device architecture (Kavalieros et al. 2006), CNT/graphene based FET (Wang et al. 2008), alternate channel materials (Wu et al. 2009), were proposed to resolve these hitches. But due to the thermionic emission transport mechanism, the subthreshold swing of the MOSFET has a theoretical limitation of 60 mV/dec at room temperature. Therefore, one desires to design a device which uses other mode of carrier transport so that a lower subthreshold swing can be achieved. To overcome this, alternative device structures such as tunnel field-effect transistors (TFETs) are proposed. TFET uses a new current transport mechanism that does not involve Maxwell–Boltzmann statistics. Due to its built-in tunnel barrier, the TFET device does not suffer from SCEs, when compared to the conventional MOSFET devices. The basic architecture of TFET is a gated P-i-N diode with very high doping of P and N region working in reverse bias. Basic operation of TFET is based on Band to band tunneling of electrons from the valence band of the source to the conduction band of the channel, when a positive gate voltage greater than the threshold voltage is applied at gate such that it lower the bands in the channel and reduces the tunneling barrier width in case of n-TFET and allow electrons to tunnel through source to channel junction and then to drain (Madan and Chaujar 2016a). In the off-state for N-type TFET, the valence band of source is located below the conduction band of channel (Ionescu and Riel 2011). Due to the presence of large

Published online: 04 October 2016

tunneling barrier at the source-channel junction, the probability of the tunneling of electrons through this barrier is negligible. This results into very small off-state leakage current. This in turn lowers the value of off-state leakage current and results into better SCE immunity, and reduction in static power dissipation. Due to steeper SS and low OFF state current, TFET has been regarded as the most promising candidate for low standby power applications (Vandooren et al. 2013; Ghosh and Akram 2013; Guo et al. 2013; Lee et al. 2013) But the limited transmission through the large tunneling barrier present at the source channel junction and the higher effective carrier mass results into a low ON state current. To improve the major shortcoming of TFET (lower I_{ON}) without sacrificing I_{OFF} is the major engineering challenge for low power applications. This dilemma can be resolved by modifying the structure architectures such as thin silicon body (Toh et al. 2008), multi gate architecture (Zhang et al. 2012), dual material gate (Saurabh and Kumar 2011), low-k spacer (Anghel et al. 2010), heterogate dielectric (Choi and Lee 2010; Madan et al. 2015a) and gate source/drain overlap/underlap (Chattopadhyay and Mallik 2011; Verhulst et al. 2007) or by using altered materials other than silicon such as a channel material with lower bandgap (Yang et al. 2013), Ge in the source side (Kim et al. 2009) and delta layer of SiGe at the edge of the source (Bhuwalka et al. 2004). Another major problem with TFET is the ambipolar conduction (Wang et al. 2004) means conduction in two directions, both for positive and negative gate voltages. In this work we have incorporated the gate all around geometry, dual metal gate and heterogate dielectric for acquiring better performance of the device (Madan et al. 2015a).

The paper is organized as follows: Sect. 2 describes the device structure and simulation models, Sect. 3 describes the simulation methodology and the calibration of our model with the simulation results, Sect. 4 describes the effect of gate and drain bias along with effect of GME on parasitic capacitance and the effect of gate metal engineering is studied on unilateral power gain, current gain, maximum transducer power gain, intrinsic delay, maximum available power gain, cut-off frequency, maximum oscillation frequency and the Y-parameters. Finally the conclusions are drawn in Sect. 5.

2 Device analysis and simulation

The device structure i.e. HD-GME-GAA-TFET consisting of Gate metal engineered and heterogate dielectric is shown in Fig. 1. During the simulation, silicon is used as source, channel and drain material, gate all around structure with channel radius (R) = 10 nm, channel length L_g (=L_1 + L_2) = 50 nm (=20 + 30 nm) and gate oxide

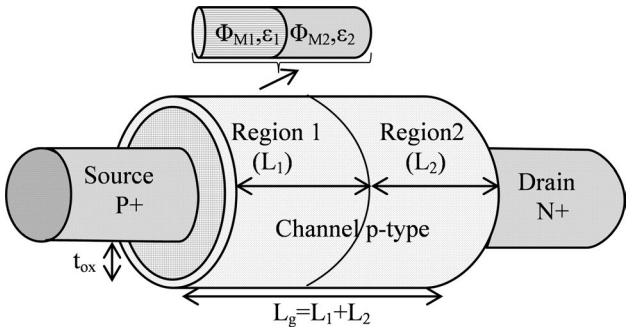


Fig. 1 Structure of n-type heterogeneous gate dielectric-gate metal engineered-GAA-TFET (HD-GME-GAA-TFET)

thickness (t_{ox}) = 3 nm is used. The source is p^+ type doped (10^{20} cm^{-3}), body is lightly p type doped (10^{16} cm^{-3}) and drain is n^+ doped (5×10^{18} cm^{-3}). To inhibit the ambipolarity effect, (tunneling at drain and channel junction) source and drain are doped asymmetrically.

Case 1. $\Phi_{M1} = 4.1$ eV (Al) and $\Phi_{M2} = 4.8$ eV (Au).
Case 2. $\Phi_{M1} = 4.3$ eV (Cr) and $\Phi_{M2} = 4.8$ eV.
Case 3. $\Phi_{M1} = 4.4$ eV (Ti) and $\Phi_{M2} = 4.8$ eV.
Case 4. $\Phi_{M} = 4.8$ eV.

Region 1 consists of dielectric constant $\varepsilon_1 = 21$ HfO_2 (near the source) and region 2 consists of $\varepsilon_2 = 3.9$ SiO_2 (near the drain) for all the cases. The source and drain junctions are abruptly doped for an effective band to band tunneling. In this work, the interface of high-k and SiO_2 is also abrupt with no interface defects. The interface defects however, had earlier been analyzed by (Madan and Chaujar 2016a). Various parasitic capacitances are extracted by small signal ac analysis at 1 GHz frequency. As the response time of the device is dependent on the gate to drain capacitance, so the drain capacitance is analyzed for the variation of both gate and drain bias. Further, the active power dissipation ($C_{gg}V_{dd}^2 f$) interdependence on the total gate capacitance C_{gg}, so the effect of gate and drain bias on total gate capacitance is also studied. Then to analyze the switching speed of the device f_T is studied. Moreover the effect of GME configurations on various high frequency gains and the admittance parameters has also been studied. To analyze the effect of gate metal work function, the dielectric constant of oxide for heterogeneous gate dielectric is kept constant throughout the simulation.

3 Model validation

3.1 Simulation methodology

All simulations have been performed using the ATLAS device simulator. The models invoked during simulation are described in Table 1. Both the numerical methods Gummel

Table 1 Simulations model

Physical models	Description
Mobility models	Concentration and field dependent mobility model is used
Recombination model	Shockley–Read–Hall (SRH) recombination also called trap assisted recombination is used to incorporate minority recombination effects with carrier lifetime (TAUP0 = 1×10^{-7} s). This process is the dominant generation and recombination process in silicon and other indirect bandgap materials
Statistics	Fermi–Dirac statistics, the use of Fermi–Dirac statistics are essential to account for certain properties of very highly doped (degenerate) materials. Such as reduced carrier concentrations in heavily doped regions (statistical approach)
Energy transport model	The simplest model of charge transport that is the drift–diffusion model is used. This model has the attractive feature that it does not introduce any independent variables in addition to ψ, n and p
Tunneling models	The most important model for Tunnel FET simulations is the band-to-band tunneling (BTBT) model. Non-local models have a more physical basis and do not depend on the electric field at the individual mesh points in the simulated device structure, but rather on band diagrams calculated along cross-sections through the device. According to BBT.NONLOCAL, the tunneling happens through 1D slice, at the tunnel junction, where each slice and the tunnel junction are perpendicular to each other. These slices are parallel to themselves
Bandgap narrowing model	For higher doping (>10^{18} cm^{-3}) experimental work has shown that the pn product in silicon becomes doping dependent. As the doping level increases, a decrease in the bandgap separation occurs

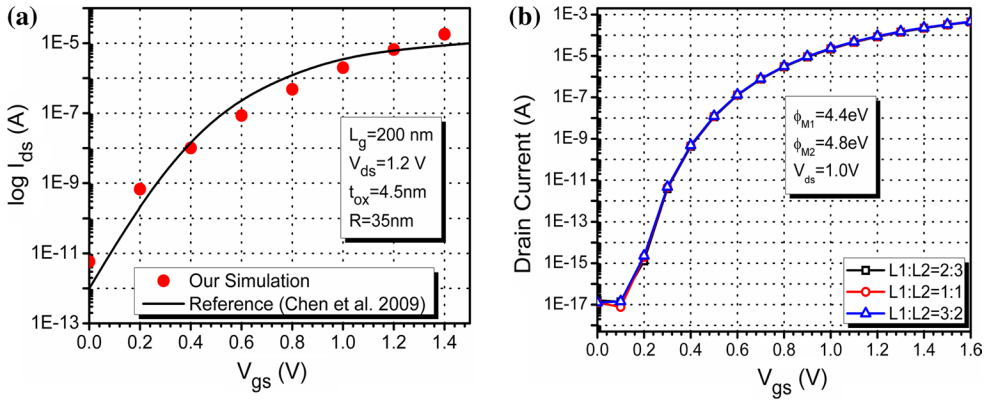


Fig. 2 **a** Calibration with the published result, I_{ds}–V_{gs} characteristics of 200 nm gate length SiNW-TFET (Chen et al. 2009). **b** Effect of tunneling gate length L_1 and auxiliary gate length L_2 on the transfer characteristics of HD-GME-GAA-TFET at constant $\Phi_{M1} = 4.4$ eV and $\Phi_{M2} = 4.8$ eV

(decoupled) together with Newton's (fully coupled) has been incorporated to mathematically solve the carrier transport equation (Atlas User's Manual 2014).

3.2 Calibration

Before simulating the device structure, the simulation models have been calibrated with the already published results (Chen et al. 2009). Figure 2a shows the transfer characteristics of the extracted data from the reference (Chen et al. 2009) and results obtained from the simulations. The results so obtained are in close proximity, thus validates the model parameters during the simulations. To analyze the impact of tunneling gate length and auxiliary gate length on the device performance, the effect of L_1 and L_2 has been studied on the transfer characteristics of HD-GME-GAA-TFET at a constant $\Phi_{M1} = 4.4$ eV and $\Phi_{M2} = 4.8$ eV. The plot of drain current with respect to gate voltage at a constant drain bias of 1.0 V for HD-GME-GAA-TFET at different combinations of L_1 and L_2 such as (20 + 30 nm), (25 + 25 nm) and (30 + 20 nm) is shown in Fig. 2b. It is clearly evident from the Fig. 2b that the drain current is immune to the variations of L_1 and L_2. This immunity against L_1 and L_2 is mainly attributed to the fact that TFET is a junction dependent device and its performance is mainly impacted by the tunneling junction and the drain channel junction. Thus, for the values of L_1 and L_2 lies in the range in between the channel length, will not affect the TFET performance. However, if L_1 is reduced to a value closer to the tunneling junction then the performance of TFET will be changed. However, in this work the impact of metal work functions of tunneling gate and auxiliary gate is studied on the capacitive and RF performance of the device keeping the length of tunneling gate and auxiliary gate as constant.

3.3 Fabrication process flow of HD-GME-GAA-TFET

The proposed summary of fabrication process flow for HD-GME-GAA-TFET is shown in Fig. 3. The fabrication

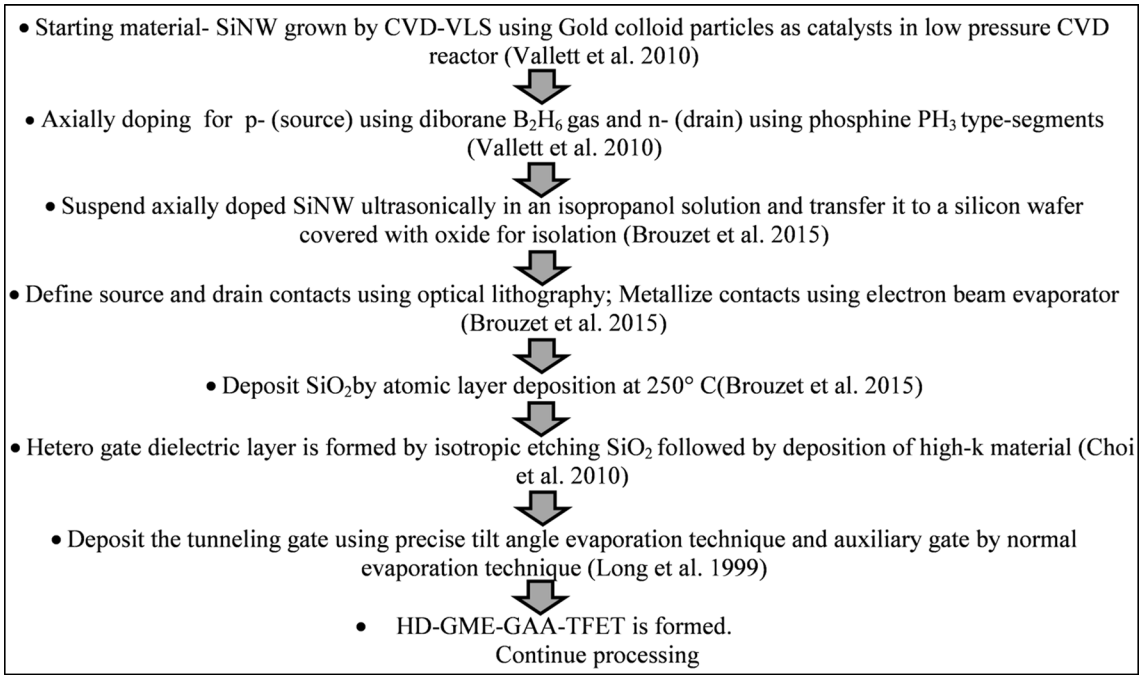


Fig. 3 Summary of fabrication process flow of HD-GME-GAA-TFET (Brouzet et al. 2015; Vallett et al. 2010)

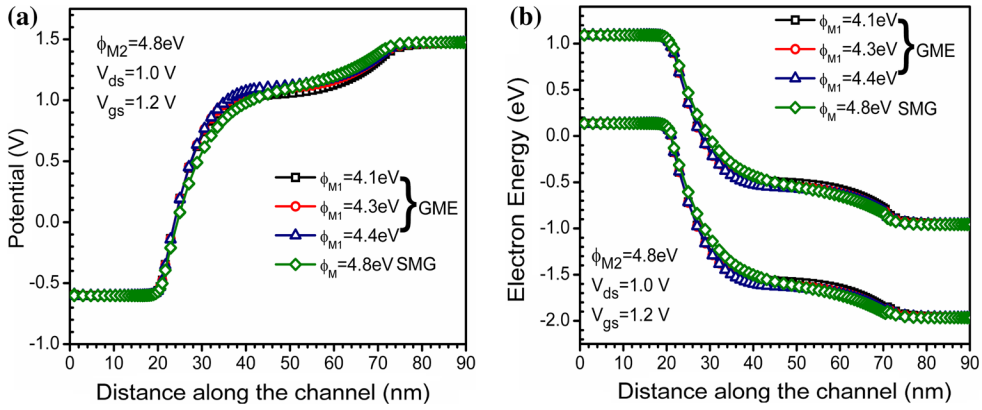


Fig. 4 **a** Surface potential profile. **b** Energy band profile along the channel of HD-GME-GAA-TFET and HD-GAA-TFET for various metal work function values at $V_{gs} = 1.2$ V and $V_{ds} = 1.0$ V

feasibility of GAA-TFET has already been reported in several literatures such as (Chen et al. 2009) fabricated vertical silicon nanowire TFET, (Gandhi et al. 2011a, b) fabricated both vertical Si-nanowire n-type and p-type TFET. Furthermore, for realization of GME architecture various schemes have been reported such as tilt angle evaporation technique (Long et al. 1999), metal interdiffusion process (Polishchuk et al. 2001). Thus, the HD-GME-GAA-TFET can be fabricated using the above device design schemes, in which the benefits of HD and GME engineering scheme have been combined with GAA TFET for accomplishing improved characteristics.

4 Results and discussion

Figure 4a, b represent the surface potential and energy band profile for HD-GME-GAA-TFET and HD-GAA-TFET respectively, in the ON-state of both the devices. Along with this, the impact of metal work functions of HD-GME-GAA-TFET has also been shown. For analyzing the effect of GME, three metals (of different work functions) are used near source side (tunneling gate) keeping metal near drain side (auxiliary gate) same. It is evident from the plot of surface potential that for a tunneling gate with lower metal work function, the surface potential is higher, that is needed

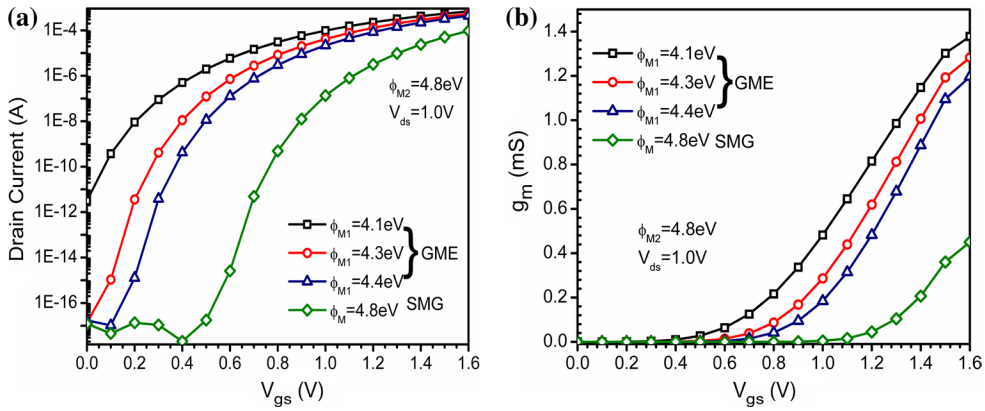


Fig. 5 **a** Transfer characteristics, **b** transconductance of HD-GME-GAA-TFET and HD-GAA-TFET for various metal work function values as a function of V_{gs}

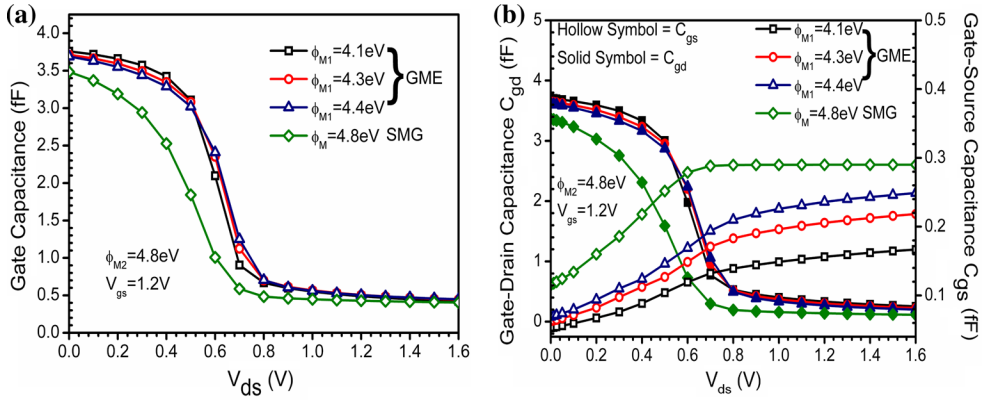


Fig. 6 **a** Gate capacitance. **b** gate-drain and gate-source capacitance of HD-GME-GAA-TFET and HD-GAA-TFET for various metal work function values as a function of V_{ds}

to enhance the band bending at the tunneling junction for achieving a high I_{ON}. In addition, the auxiliary metal with high metal work function used near drain side reduces the surface potential and thus improves the OFF-state characteristics and the ambipolar conduction. The energy band profile shown in Fig. 4b, reveals that for the presence of low metal work function near source side for the case of HD-GME-GAA-TFET, band bending at the tunneling junction increases that lowers the tunneling barrier width. This higher surface potential and lowered tunneling barrier width acquired by GME engineering scheme enhances the ON current, reduces the threshold voltage and the subthreshold swing of GAA-TFET.

Figure 5a compares the transfer characteristics of gate metal engineered TFET with single metal gate TFET of the same dimensions at a constant drain bias 1.0 V. It is evident from Fig. 5a, that I_{ON} of GME-TFET is many times greater than I_{ON} of SMG-TFET. It is clearly evident from Fig. 5a that the larger difference in metal work function (as in case 1 in comparison with case 3) leads to enhancement in I_{ON} by 2.68 times. Increase in I_{ON} is the main advantage of heterogate dielectric and gate metal engineering (Lee et al. 2012). The I_{ON} of case 4 which is the case of single metal gate (SMG) is much lower as compared to GME. The OFF-state current i.e. I_{OFF} is defined as the drain current at $V_{gs} = 0$ V and $V_{ds} = 1.0$ V. Variation of I_{OFF} for all the cases shows that I_{OFF} enhances from an order of 10^{-17}–10^{-11} A, as the metal work function difference of auxiliary and tunneling gate is increased to 0.7 eV. Thus we need to optimize the device for I_{ON}/I_{OFF} ratio for superior device performance.

An important device parameter that measures the device gain is the transconductance g_m, defined as the first order derivative of drain current w.r.t. gate voltage at a constant drain voltage. For a constant drain bias, g_m decides the current driving capability of the FET. Furthermore, higher g_m is desirable for acquiring higher gain. The transconductance g_m of HD-GME-GAA-TFET and HD-GAA-TFET are compared in Fig. 5b. It is found that g_m of HD-GME-GAA-TFET is superior in comparison with HD-GAA-TFET. The higher g_m of HD-GME-GAA-TFET is attributed to the improved driving current of HD-GME-GAA-TFET, obtained by GME architecture.

The switching speed in integrated circuits depends on the parasitic capacitances. For higher switching speed, parasitic capacitances should be as small as possible (Madan et al. 2015b). So, for the design of the circuits containing TFETs, the understanding of these capacitances is important. In this work, the reliance of parasitic capacitances of HD-GME-GAA-TFET on the drain bias, gate bias and the

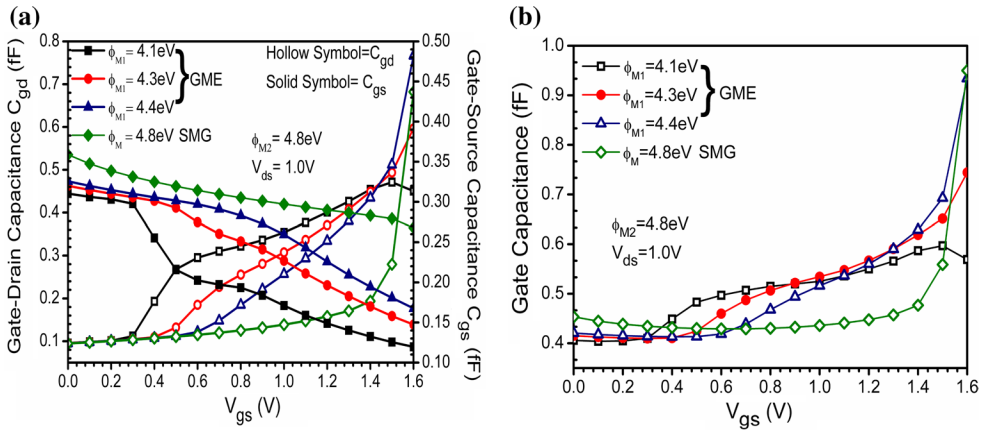


Fig. 7 **a** Gate drain and Gate-source capacitance. **b** Gate capacitance of HD-GME-GAA-TFET and HD-GAA-TFET for various metal work function values as a function of Vgs

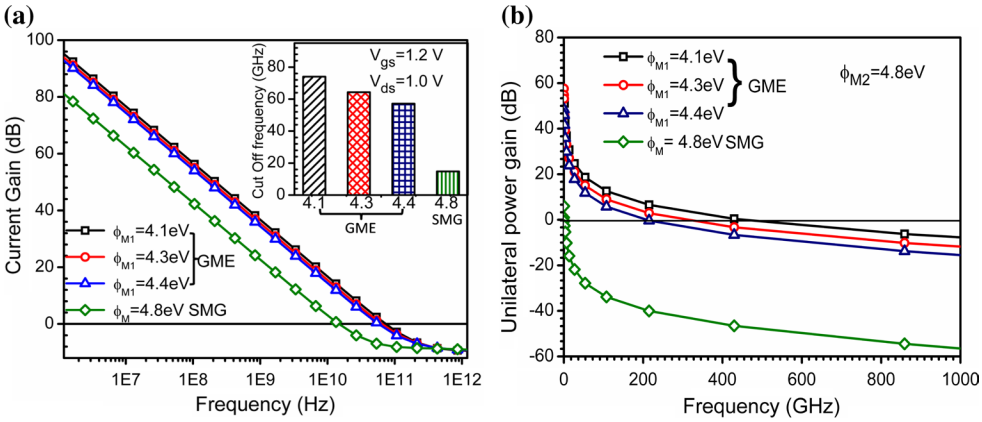


Fig. 8 **a** Current gain. **b** unilateral power gain of HD-GME-GAA-TFET and HD-GAA-TFET at $V_{gs} = 1.2$ V and $V_{ds} = 1.0$ V for various metal work function values as a function of frequency

metal work function variation is studied using the physics based technology-aided design (TCAD) simulator.

In case of MOSFET, in the linear region, the C_{gg} is symmetrically apportioned between both the source and drain regions as both source and drain regions are connected to the inversion region formed underneath the gate dielectric region. But in case of TFET, only the drain is connected to inversion layer due to different inversion charge distribution and results in larger C_{gd} as compared to C_{gs} in both linear and saturation regions. As $C_{gg} = C_{gd} + C_{gs}$ so, a large fraction of C_{gg} is contributed by C_{gd} as compared to C_{gs} (Yang et al. 2010). For a constant gate bias in ON state, the formation of inversion layer starts from the drain side and an increase in drain bias pinches the inversion layer towards the source side (unlike as in case of MOSFET where pinch off occurs towards the drain side).

Figure 6a depicts the variation of gate to drain capacitance and gate to source capacitance with drain bias at a constant gate bias ($V_{gs} = 1.2$ V). As it is clearly evident that in linear region i.e. for lower drain bias, (in which the device is in on- state) the gate drain capacitance is comparatively large. As the drain bias is increased, the inversion layer shifts towards source side and hence the reduction in gate drain capacitance is obtained. Again in the region before inversion layer formation, the gate drain capacitance is more in case of gate metal engineered TFET as compared to single metal gate TFET, but for a higher drain bias, the gate drain capacitance is almost same for GME and SMG. Before inversion occurs, the gate source capacitance is very small because for lower drain bias, all the inversion charges are near the drain. As drain bias is increased, the inversion layer shifts towards the source side which leads to enhanced gate to source capacitance as clear from Fig. 6a. For GME, the gate source capacitances are small as compared to SMG. From Fig. 6a it is clear that as the difference between metal work function of GME TFET is enhanced, the gate source capacitance is reduced. Further, the order of C_{gs} are very much less than that of C_{gd} as evident from Fig. 6a. So a higher I_{ON} is obtained for gate metal engineered (GME) TFET and simultaneously the parasitic capacitances are not adversely affected, making GME a better candidate for future demands. Total gate capacitance C_{gg} which is basically equal to the sum of gate-source and gate-drain capacitance is shown in Fig. 6b. As the gate-source capacitance is very small as compared to gate-drain capacitance, so the total gate capacitance is almost same as that of gate-drain capacitance or the gate drain capacitance contributes dominantly to C_{gg}.

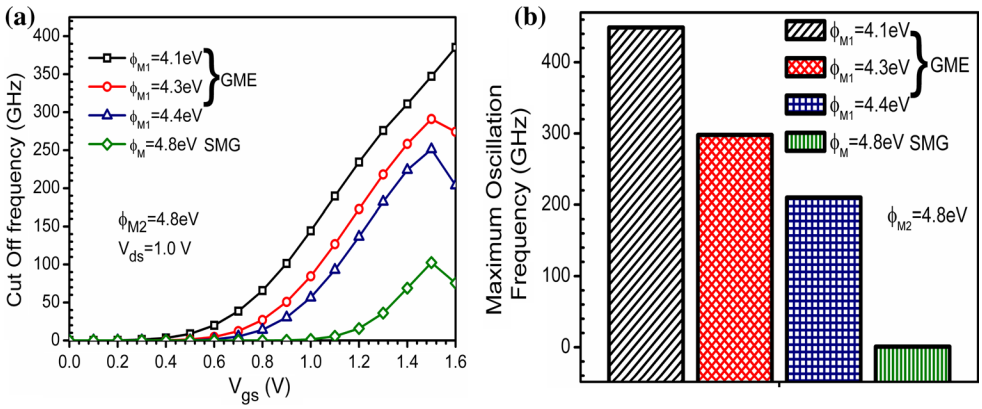


Fig. 9 **a** Cut off frequency as a function of gate bias. **b** Maximum oscillation frequency of HD-GME-GAA-TFET and HD-GAA-TFET at $V_{gs} = 1.2$ V and $V_{ds} = 1.0$ V for various metal work function values

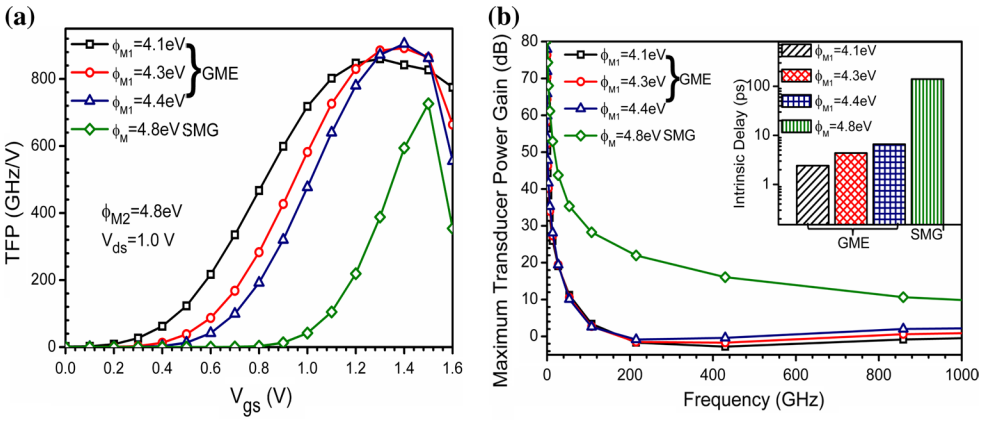


Fig. 10 **a** Transconductance frequency product at $V_{ds} = 1.0$ V as a function of gate bias. **b** Maximum transducer power gain of HD-GME-GAA-TFET and HD-GAA-TFET at $V_{gs} = 1.2$ V and $V_{ds} = 1.0$ V for various metal work function values as a function of frequency. *Inset* intrinsic delay at $V_{ds} = 1.0$ V

The plot of gate to drain capacitance and gate to source capacitance of both GME and single metal gate as a function of V_{gs} at $V_{ds} = 1.0$ V is shown in Fig. 7a. The inversion layer moves from the drain side towards the source side with an increase in gate bias so the gate drain capacitance increases with gate bias at a constant drain bias. The coupling between gate and source decreases with the extension of inversion layer towards the source side. This decoupling of the source and gate results in a monotonically decrease in gate source capacitance with increase in gate bias as shown in Fig. 7a. Total gate capacitance for GME and SMG with respect to gate bias is shown in Fig. 7b. As the gate source capacitance contributes a little, so the total gate capacitance is almost same as gate drain capacitance. For higher gate bias, the parasitic capacitances are comparatively low in case of GME.

In addition, for investigation of RF performance, the RF figures of merits (FOM) are analyzed in terms of cut off frequency f_T and maximum oscillation frequency f_{Max}. Current gain and unilateral power gain are extracted for determining the values of f_T and f_{Max} respectively. Figure 8a illustrates the impact of GME and SMG on the current gain. The increase in difference between metal work function of GME leads to enhanced current gain. The cut off frequency of the device is an important parameter for RF application. The inset of Fig. 8a shows the cut off frequency f_T of all the cases. The cut off frequency plotted in the inset of Fig. 8a is extracted from the plot of current gain and is the frequency at which the current gain falls to 0 dB. It is clearly evident that the f_T of HD-GME-GAA-TFET is higher than the f_T of HD-GAA-TFET. The f_T enhances by 3.86, 4.34, and 5 times for the case 3, 2 and 1 respectively, in comparison to case 4. To analyze the high frequency performance of the device, the unilateral power gain is of prime importance. It is the highest achievable power gain. It is the gain from a device at which no reverse transmission occurs or good reverse isolation. Figure 8b shows the unilateral power gain for GME and SMG TFETs. Again with incorporation of GME, the unilateral power gain is enhanced.

Figure 9a compares f_T of GME and SMG TFET at various gate biases. f_T is increasing with increase in gate bias. The switching speed of the device depends on the f_T. It is clearly evident from Fig. 9a that as the difference between gate metal work function increases in case of GME, the cut off frequency increases, which leads to higher switching speed. Maximum oscillation frequency is a more useful FOM for microwave applications because microwave designers are typically concerned with power gain under conjugately matched conditions (Razavi 1998). Figure 9b

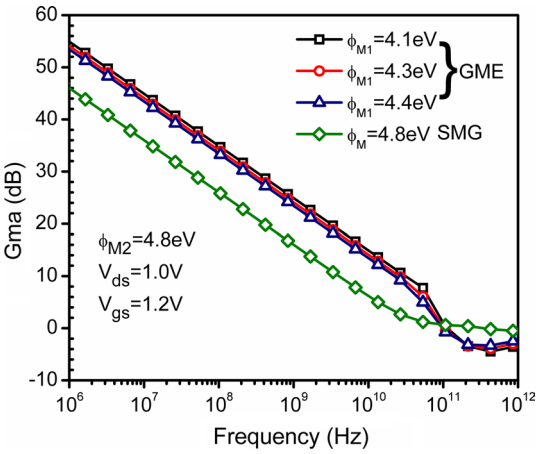


Fig. 11 Maximum available power gain of HD-GME-GAA-TFET and HD-SMG-GAA-TFET at $V_{gs} = 1.2$ V and $V_{ds} = 1.0$ V

depicts the maximum oscillation frequency which is extracted from the unilateral power gain. f_{Max} is the highest frequency at which the power gain is unity. It is clear from the Fig. 9b that in case of GME, in which the metal work function difference between the tunneling and the auxiliary gate is high (case 1), the maximum oscillation frequency is almost double as compared to case 3. The f_{Max} in case of SMG is much smaller than GME.

Transconductance frequency product TFP is an important high frequency circuit design parameter. TFP is defined as the product of device efficiency g_m/I_d and f_T. TFP is used to tradeoff between power and bandwidth. As is clear from Fig. 10a, TFP is enhanced in case of GME-GAA-TFET by 1.52 times as compared to SMG-GAA-TFET. This is because of the enhancement of f_T and device efficiency with the amalgamation of GME scheme on HD-GAA-TFET. Moreover the peak of TFP is further enhanced with an increase in difference of gate metal work function difference. Further, intrinsic delay is an important figure of merit for evaluating the transistors speed. It is the reciprocal of intrinsic switching frequency f_i and is expressed as:

$$\tau = \frac{C_{gg} \times V_{dd}}{I_{ON}}$$

Where; C_{gg} is the total gate capacitance, V_{dd} is the drain voltage and I_{ON} is the saturation drain current. It is clearly evident from the bar graph shown in the inset of Fig. 10b that there is an intensive reduction in intrinsic delay with the integrity of GME engineering scheme on HD-GME-GAA-TFET as compared to HD-GAA-TFET. This reduction is caused by enhanced on-current and reduced parasitic capacitance, thus considerable reduction in intrinsic delay of the device, which further results into higher switching speed of the device (as $f_i = 1/\tau$). Moreover with an increase in gate metal work function difference in GME scheme, intrinsic delay is further reduced. As we increase the metal work function difference by 0.4–0.7 eV, the intrinsic delay is reduced by 63.34 %.

Figure 11 shows the improvement of high frequency maximum available power gain (Gma) of HD-GME-GAA-TFET over HD-SMG-GAA-TFET. This enhancement is due to the lowering of tunneling barrier width which is further a resultant of GME engineering scheme (Madan et al. 2016b), resulting into higher on current and reduced parasitic capacitances as shown in Fig. 7. Moreover with alteration of metal work function in GME scheme, such as increased metal work function difference also results into enhanced Gma, due to enhancement in drain current and reduction in parasitic capacitance at higher metal work function difference.

Under small-signal conditions, the transistor can be described by a small-signal equivalent circuit. MOSFET can be replaced by its Y-parameters equivalent circuit consisting of the four Y-parameters Y_{11}, Y_{12}, Y_{21} and Y_{22}. The Y parameters are defined under ac short-circuit conditions (either at the input or at the output). Values of Y-parameters depend on the dc bias conditions as well as on the operating frequency. At low frequencies, ac voltages and ac currents can be easily measured, but at high frequency the measurement of these parameters becomes exceptionally complicated. Then, another set of parameters scattering or S-parameters can be measured at such high frequencies. But as Y-parameters are more closely related to device physics and design, so S parameters are again converted into Y parameters. So, study of Y-parameters becomes necessary.

Y_{11} is the short circuit input admittance, Y_{22} is the short circuit output admittance, Y_{12} is the short circuit forward transfer admittance and Y_{21} is the short circuit reverse transfer admittance. Figure 12a–d compares the real and imaginary component of Y-parameters of HD-GME-GAA-TFET and HD-SMG-GAA-TFET. It is clearly evident that Y_{11} and Y_{22} are lower at low frequency and increases gradually as frequency increases, while Y_{12} and Y_{21} are higher at low frequency and decreases gradually with increase in frequency thus, giving useful information to the RF engineers.

5 Conclusion

In this work, the small signal parameters and RF performance of HD-GME-GAA-TFET such as parasitic capacitances, power gains, cut off frequency, maximum oscillation frequency, intrinsic delay and admittance parameters has been analyzed using TCAD device simulations. With

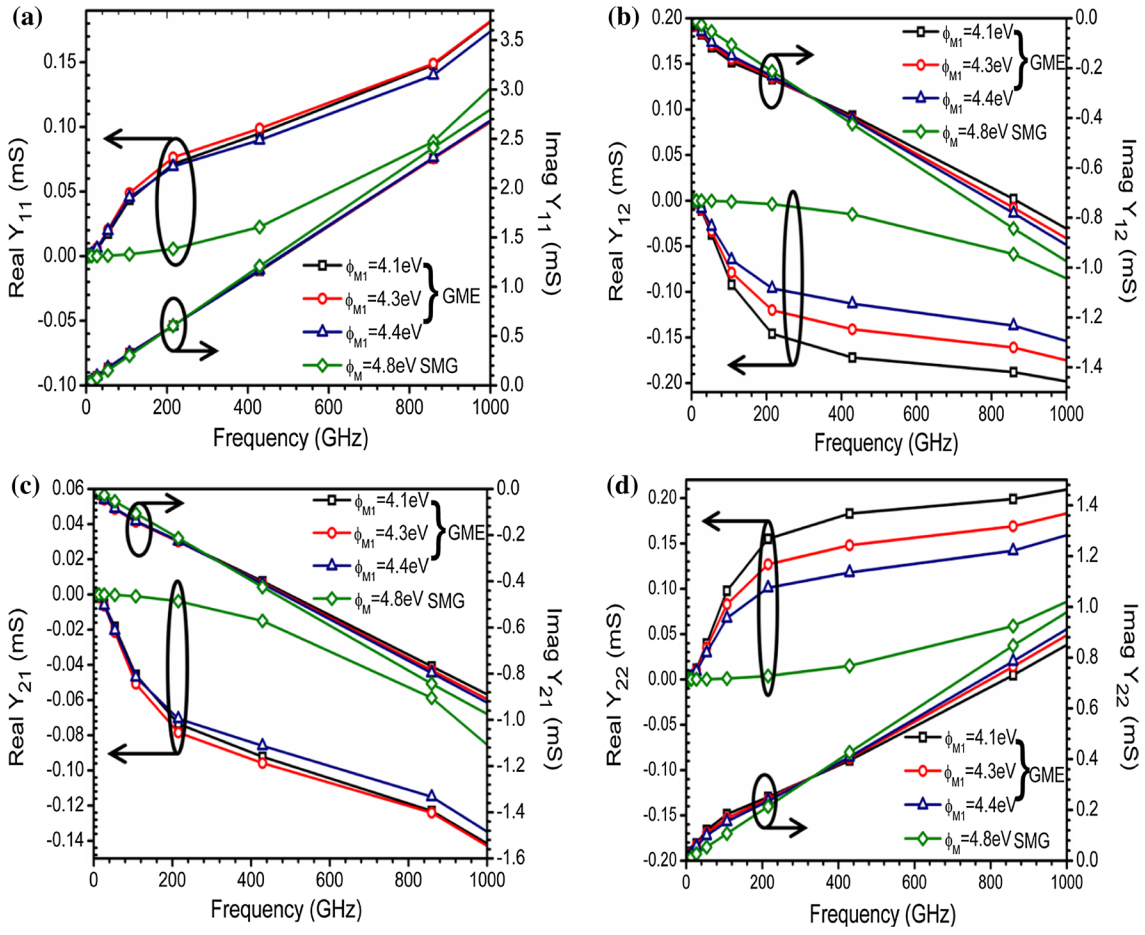


Fig. 12 Y-parameters of HD-GME-GAA-TFET and HD-GAA-TFET as a function of frequency at $V_{gs} = 1.2$ V and $V_{ds} = 1.0$ V. **a** Y_{11}, **b** Y_{12}, **c** Y_{21}, **d** Y_{22}

the implementation of GME, superior benefits of TFET are obtained. The parasitic capacitances are decreased, the cutoff frequency and the maximum oscillation frequency is manifold increased (better RF performance). Moreover it has been examined that with the amalgamation of GME scheme on HD-GAA-TFET on current is enhanced and parasitic capacitances are reduced, resulting into enhancement of numerous power gains thus makes it a suitable candidate for high frequency and microwave applications. Also the reduction in intrinsic delay and parasitic capacitances with GME architecture makes it applicable for analog and digital switching applications. In addition, the improvement in small signal Y parameters has been obtained with the GME architecture which is beneficial for the RF communication. So the HD-GME-GAA-TFET can find applications in high-switching-speed electronics.

Acknowledgments Authors would like to thank to Microelectronics Research Lab, Department of Engineering Physics Delhi Technological University to carry out this work. One of the authors (Jaya Madan) would like to thank University Grants Commission, Govt. of India, for providing the necessary financial assistance during the course of this research work.

References

Anghel C, Chilagani P, Amara A, Vladimirescu A (2010) Tunnel field effect transistor with increased on current, low-k spacer and high-k dielectric. Appl Phys Lett 96:122104. doi:10.1063/1.3367880

ATLAS user's manual (2014) Silvaco Int, Santa Clara

Bhuwalka KK, Schulze J, Eisele I (2004) Performance enhancement of vertical tunnel field-effect transistor with SiGe in the δp^+ layer. Jpn J Appl Phys 43:4073–4078. doi:10.1143/JJAP.43.4073

Brouzet V, Salem B, Periwal P, Rosaz G, Baron T, Bassani F, Gentile P, Ghibaudo G (2015) Fabrication and characterization of silicon nanowire p-i-n MOS gated diode for use as p-type tunnel FET. Appl Phys A 121(3):1285–1290. doi:10.1007/s00339-015-9507-3

Chattopadhyay A, Mallik A (2011) Impact of a spacer dielectric and a gate overlap/underlap on the device performance of a tunnel field-effect transistor. IEEE Trans Electron devices 58(3):677–683. doi:10.1109/TED.2010.2101603

Chen ZX, Yu HY, Singh N, Shen NS, Sayanthan RD, Lo GQ, Kwong DL (2009) Demonstration of tunneling FETs based on highly

scalable vertical silicon nanowires. IEEE Electron Device Lett 30(7):754–756. doi:10.1109/LED.2009.2021079

Choi WY, Lee W (2010) Hetero-gate-dielectric tunneling field-effect transistors. IEEE Trans Electron Devices 57(9):2317–2319. doi:10.1109/TED.2010.2052167

Gandhi R, Chen Z, Singh N, Banerjee K, Lee S (2011a) CMOS-compatible vertical-silicon-nanowire gate-all-around p-type tunneling FETs with ≤50-mV/decade subthreshold swing. IEEE Electron Device Lett 32(11):1504–1506. doi:10.1109/LED.2011.2165331

Gandhi R, Chen Z, Singh N, Banerjee K, Lee S (2011b) Vertical Si-nanowire n-type tunneling FETs with low subthreshold swing (≤50 mV/decade) at room temperature. IEEE Electron Device Lett 32(4):437–439. doi:10.1109/LED.2011.2106757

Ghosh B, Akram MW (2013) Junctionless tunnel field effect transistor. IEEE Electron Device Lett 34(5):584–586. doi:10.1109/LED.2013.2253752

Guo P, Yang Y, Cheng Y, Han G, Pan J, Zhang Z, Hu H, Shen ZX, Chia CK, Yeo YC (2013) Tunneling field-effect transistor with Ge/In0.53Ga 0.47As heterostructure as tunneling junction. J Appl Phys 113:094502. doi:10.1063/1.4794010

Ionescu AM, Riel H (2011) Tunnel field-effect transistors as energy-efficient electronic switches. Nature 479:329–337. doi:10.1038/nature10679

Kavalieros J, Doyle B, Datta S, Dewey G, Doczy M, Jin B, Lionberger D, Metz M, Rachmady W, Radosavljevic M, Shah U, Zelick N, Chau R (2006) Tri-gate transistor architecture with high-k gate dielectrics, metal gates and strain engineering. Symposium on VLSI Technology Digest of Technical Papers, pp 5–6. doi: 10.1109/VLSIT.2006.1705211

Kim SH, Kam H, Hu C, Liu TJK (2009) Germanium-source tunnel field effect transistors with record high I_{ON}/I_{OFF}. Symposium on VLSI Technology Digest of Technical papers, pp 178–179

Lee JS, Choi WY, Kang IM (2012) Characteristics of gate all around hetero gate dielectric tunneling field effect transistor. Jpn J Appl Phys 51:06FE03. doi:10.1143/JJAP.51.06FE03

Lee JS, Seo JH, Cho S, Lee JH, Kang SW, Bae JH, Cho ES, Kang IM (2013) Simulation study on effect of drain underlap in gate-all around tunneling field-effect transistors. Curr Appl Phys 13(6):1143–1149. doi:10.1016/j.cap.2013.03.012

Long W, Ou H, Kuo JM, Chin KK (1999) Dual-material gate (DMG) field effect transistor. IEEE Trans Electron Devices 46(5):865–870. doi:10.1109/16.760391

Madan J, Chaujar R (2016) Interfacial charge analysis of heterogeneous gate dielectric-gate all around-tunnel FET for improved device reliability. IEEE Trans Device Mater Reliab 16(2):227–234. doi:10.1109/TDMR.2016.2564448

Madan J, Gupta RS, Chaujar R (2015a) Analytical drain current formulation for gate dielectric engineered dual material gate-gate all around-tunneling field effect transistor. Jpn J Appl Phys 54:094202. doi:10.7567/JJAP.54.094202

Madan J, Gupta RS, Chaujar R (2015b) TCAD analysis of small signal parameters and RF performance of heterogeneous gate dielectric-Gate all around Tunnel FET. Adv Manuf Electron Microsyst Techconnect Briefs 2015:189–192

Madan J, Gupta RS, Chaujar R (2016) Mathematical modeling insight of hetero gate dielectric-dual material gate-GAA-tunnel FET for VLSI/analog applications. Microsyst Technol. doi:10.1007/s00542-016-2872-9

Polishchuk I, Ranade P, King TJ, Hu C (2001) Dual work function metal gate CMOS technology using metal interdiffusion. IEEE Electron Device Lett 22(9):444–446. doi:10.1109/55.944334

Razavi B (1998) RF microelectronics. Prentice Hall, Upper Saddle River, p 2

Saurabh S, Kumar MJ (2011) Novel attributes of a dual material gate nanoscale tunnel field-effect transistor. IEEE Trans Electron Devices 58(2):404–410. doi:10.1109/TED.2010.2093142

Toh EH, Wang GH, Samudra G, Yeo YC (2008) Device physics and design of germanium tunneling field-effect transistor with source and drain engineering for low power and high performance applications. J Appl Phys 103:104504. doi:10.1063/1.2924413

Vallett AL, Minassian S, Kaszuba P, Datta S, Redwing JM, Mayer TS (2010) Fabrication and characterization of axially doped silicon nanowire tunnel field-effect transistors. Nano Lett 10(12):4813–4818. doi:10.1021/nl102239q

Vandooren A, Leonelli D, Rooyackers R, Hikavyy A, Devriendt K, Demand M, Loo R, Groeseneken G, Huyghebaert C (2013) Analysis of trap-assisted tunneling in vertical Si homo-junction and SiGe hetero-junction tunnel-FETs. Solid State Electron 83:50–55. doi:10.1016/j.sse.2013.01.026

Verhulst AS, Vandenberghe WG, Maex K, Groeseneken G (2007) Tunnel field-effect transistor without gate-drain overlap. Appl Phys Lett 91:053102. doi:10.1063/1.2757593

Wang PF, Hilsenbeck K, Nirschl T, Oswald M, Stepper C, Weis M, Schmitt-Landsiedel D, Hansch W (2004) Complementary tunneling transistor for low power application. Solid State Electron 48(12):2281–2286. doi:10.1016/j.sse.2004.04.006

Wang X, Ouyang Y, Li X, Wang H, Guo J, Dai H (2008) Room-temperature all-semiconducting sub-10-nm graphene nanoribbon field-effect transistors. Phys Rev Lett 100(20):100–103. doi:10.1103/PhysRevLett.100.206803

Wu YQ, Xu M, Wang RS, Koybasi O, Ye PD (2009) High performance deep-submicron inversion-mode InGaAs MOSFETs with maximum G_m exceeding 1.1 mS/μm: new HBr pretreatment and channel engineering. IEEE International Electron Devices Meeting (IEDM), pp 1–4. doi: 10.1109/IEDM.2009.5424358

Yang Y, Tong X, Yang LT, Guo PF, Fan L, Yeo YC (2010) Tunneling field-effect transistor: capacitance components and modeling. IEEE Electron Device Lett 31(7):752–754. doi:10.1109/LED.2010.2047240

Yang Y, Han G, Guo P, Wang W, Gong X, Wang L, Low KL, Yeo YC (2013) Germanium-Tin P-channel tunneling field-effect transistor : device design and technology demonstration. IEEE Trans Electron Devices 60(12):4048–4056. doi:10.1109/TED.2013.2287031

Zhang L, Lin X, He J, Chan M (2012) An analytical charge model for double-gate tunnel FETs. IEEE Trans Electron Devices 59(12):3217–3223. doi:10.1109/TED.2012.2217145

Prominent photovoltaic response in multiferroic BFO/BTO heterostructures

Savita Sharma, Nitin K. Puri
Department of Applied Physics, Delhi Technological University, Delhi, INDIA

Vinay Gupta
Department of Physics and Astrophysics, University of Delhi, Delhi, INDIA

Monika Tomar*
Physics Department, Miranda House, University of Delhi, Delhi, INDIA
*Corresponding Author: monikatomar@gmail.com

Abstract-Present work focuses on the photovoltaic properties of the multilayered structure of Bismuth ferrite (BFO) and Barium titanate (BTO) thin films prepared by Pulsed Laser Deposition (PLD) technique on platinum coated silicon substrate. The five and six layered structures of BFO/BTO showed a remarkable increase in current density (J) (from 2.23×10^{-7} A/cm^2 to 3.18×10^{-4} A/cm^2 and from 4.50×10^{-8} A/cm^2 to 3.84×10^{-4} A/cm^2) upon illumination with laser light of wavelength 405 nm at an intensity of 160 mW/cm^2 . The values of short circuit photocurrent and open circuit voltage (V_{oc}) for five layered BFO/BTO PV cell were 0.3184 mA/cm^2 and -1.25 V respectively. The BFO/BTO six layer PV cell exhibits higher value of V_{oc} = -1.52 V and $J_{ON/OFF}$ = 8.53 x 10^3 due to improved ferroelectric properties related to significant interface coupling between 6 stacking layers of BFO and BTO. The BFO/BTO PV cell highlights its possible practical application in photovoltaics and multifunctional devices.

I. INTRODUCTION

In the past decades, BFO has attracted much attention due to its well known room temperature multiferroicity offering a series of possible applications in high density memory, spintronics and photovoltaics devices [1-4]. With the current trends of high integration and miniaturization in semiconductor industry, it becomes impulsive to emerge with next generation multiferroics with multifunctional applications. Ferroelectric photovoltaic effect (FPV) is a fascinating phenomenon with many unique features such as extremely large photo-voltage, where a photocurrent is proportional to the polarization magnitude. Designing of materials having enhanced multiferroic responses can be achieved using the principle of strain engineering employed for multilayer structures and superlattices (SLs). Recently, numerous studies on multilayer heterostructures containing alternating ferroelectric and multiferroic layers, such as $Pb(Zr,Ti)O_3/CoFe_2O_4$ [5-7], $(Pr_{0.88}Ca_{0.15}MnO_3)/(Ba_{0.6}Sr_{0.4}TiO_3)$ [8], $CoFe_2O_4/BaTiO_3$ [9], $BiFeO_3/BaTiO_3$ [10], $(Bi,Nd)FeO_3/(Ba,Sr)TiO_3$ [11], $BiFeO_3/BiMnO_3$ [12] have been performed but ferroelectric photovoltaic effect is seldom studied. Among the numerous ferroelectric oxides materials [13-15], BFO possessing narrow band gap (~2.2 eV) exhibit significant PV effect [13]. However being leaky in nature there are certain limitations to its applications. BTO being excellent ferroelectric material, provides high polarization value but has high band gap value. Thus, in order to improve the properties of both materials, in the present work, BFO/BTO multilayer structures with five and six individual layers were prepared using PLD technique towards the ferroelectric photovoltaic applications.

II. EXPERIMENTAL

BFO/BTO multilayered (five and six layered) structure was prepared by PLD technique. The single phase ceramic targets of BFO and BTO of one inch diameter were prepared using conventional solid state reaction method. The raw powders of Bi_2O_3, Fe_2O_3, $BaCO_3$ and TiO_2 (99.9% pure) were used for the preparation of BFO and BTO targets. The ceramic targets of BFO and BTO were ablated sequencially using the 4th harmonic of Nd:YAG pulsed laser (λ = 266 nm) and the multilayered structure of BFO/BTO were prepared on $Pt/Ti/SiO_2/Si$ substrates.

Total thickness of the multilayered structures was kept fixed at 350 nm. The multilayer structure was prepared at a substrate temperature of 750°C. The number of layers in multilayer structure was varied from five to six whilst keeping BTO as the bottom layer. The top circular electrodes (600 μm diameter, 40 nm thickness) of Au were deposited by thermal evaporation technique through a shadow mask on the surface of multilayered BFO/BTO structures. For comparison, thin films of both BFO and BTO of same thickness (350 nm) were also grown under the similar deposition conditions on $Pt/SiO_2/Si$ substrate.

978-1-5090-1871-0/16/$31.00 ©2016 IEEE

III. RESULTS AND DISCUSSION

Figure 1 shows the optical transmission spectra of five and six layer BFO/BTO structures deposited on quartz substrate over a wavelength range of 190 to 1100 nm. The transmission spectra of bare BFO and BTO thin films are also included in Figure 1 for comparison. It can be seen from Figure 1 that the bare BFO and BTO thin films were highly transparent (~70%) in the visible region demonstrating the growth of thin films (both BFO and BTO) with good optical quality and low absorption losses. However, transmittance in the case of multilayer structure dropped to about 60% (Figure 1) which may be due to scattering losses of light at the multiple interfaces. It is important to note from Figure 1 that BTO thin film has fundamental absorption edge at around 475 nm while BFO thin film and BFO/BTO multilayer structure show the fundamental absorption edges at comparatively lower wavelength (~ 431 nm). Hence, the multilayer structure was expected to absorb appreciable amount of light at a wavelength of 405 nm and can be used for harvesting the visible light.

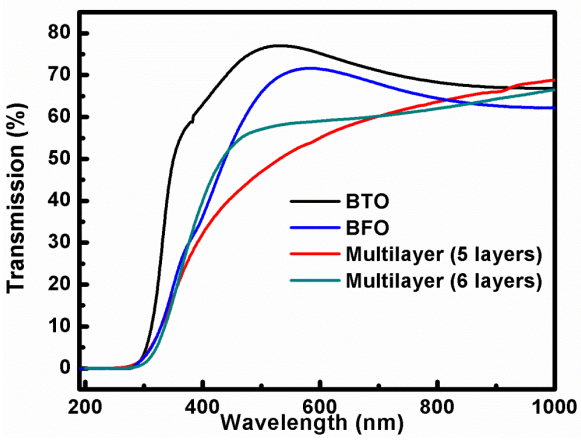


Figure 1: UV-Visible transmission spectra of bare BTO thin film, bare BFO thin film and BFO/BTO multilayer structure (five and six layers) deposited over quartz substrates.

Photovoltaic response studies

Figure 2(a) shows the current density–voltage (J–V) curve obtained for multilayer BFO/BTO structures (five and six layers) under both the dark and light illumination (λ = 405 nm) conditions. The J–V curve under light illumination (Figure 2(a)) showed a typical ferroelectric photovoltaic effect. The photovoltaic open-circuit voltage (V_{oc}) and short-circuit current density (J_{sc}) were found to be about -1.25 V and 0.318 mA/cm^2 respectively for five layers and -1.52 V and 0.384 mA/cm^2 respectively for six layers system as determined from the intercepts of the horizontal and the vertical axes (Figure 2(a)). It may also be noted from Figure 2(a) that the magnitude of J_{sc} increased from 318 to 384 μA/cm^2 with increase in number of stacking layers from 5 to 6 in the BFO/BTO multilayer structure. This is mainly attributed to the increase in magnitude of intrinsic polarization due to enhanced interfacial strain for six layer BFO/BTO structure. The low value of J_{sc} for five layer BFO/BTO structure in comparison to that of six layered structure was due to the comparatively reduced ferroelectric polarization and leakage current obtained for the five layer BFO/BTO system. The ON to OFF ratio was found to be more (~8.533 x 10^3) for six layer BFO/BTO multilayer structure as compared to the five layered structure. This may be attributed to the generation and separation of more photo-induced charge carriers under illumination for 6 layer BFO/BTO system.

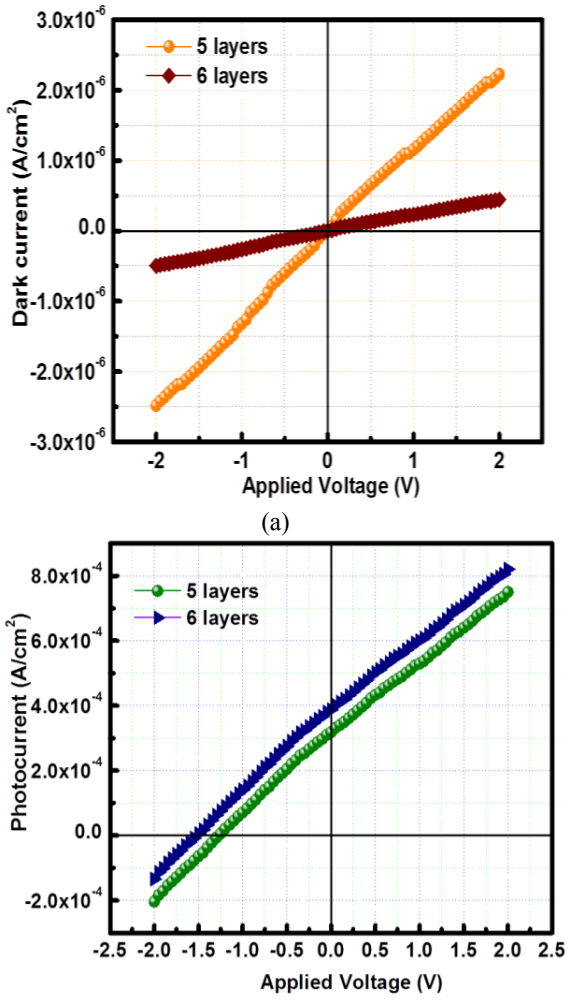


Figure 2: J-V curves for multilayer BFO/BTO structures having five and six layers under both (a) dark condition and (b) illumination of light ($\lambda = 405nm$ and intensity=160mW/cm^2).

The open circuit voltage (V_{oc}) obtained in the present case is considerably larger than that reported for the individual ferroelectric thin films by other researchers [15-17]. It is well known that the values of J_{SC} and V_{OC} of ferroelectric thin films under illumination depend on the internal electric field. The internal electric field in ferroelectric thin films is given as $E = E_{bi} + E_p$, where E_{bi} is the built-in field and E_p is the depolarization field. The built in field E_{bi} in ferroelectric thin films is driven by various factors [18-20]. The depolarization field Ep is directly proportional to the strength of polarization:

$$E_p = \frac{-p}{\varepsilon_o \varepsilon_F}\left(\frac{2\varepsilon_F / d}{2\varepsilon_F / d + \varepsilon_e / \lambda}\right) \quad (1)$$

Where ε_F is the relative dielectric constant of the ferroelectric thin film, ε_e is the relative dielectric constant of the electrode layer, λ is the screening length, P is the polarization value and d is the thickness of ferroelectric thin film [21]. Therefore, high photovoltaic output obtained for BFO/BTO six layer thin film structure is attributed to its higher internal field caused by the larger remnant polarization (as explained in our previous report). The large depolarization field can effectively separate the photogenerated electrons and holes and hence, result in an enhanced photovoltaic output for the BFO/BTO six layer structure.

IV. CONCLUSION

The five and six layer BFO/BTO multilayer structures showed a remarkable increase in current density (from 2.23×10^{-7} A/cm^2 to 3.18×10^{-4} A/cm^2 and from 4.50×10^{-8} A/cm^2 to 3.84×10^{-4} A/cm^2) upon illumination with laser light of wavelength 405 nm at an intensity of 160 mW/cm^2. The values of short circuit photocurrent and open circuit voltage for five layer multilayer PV cell were 0.3184 mA/cm^2 and -1.25 V respectively. The BFO/BTO six layer PV cell exhibits high value of V_{oc} = 1.52 V and $J_{ON/OFF}$ = 8.53 x 10^3 due to improved ferroelectric properties related to significant interface coupling between 6 stacking layers of BFO and BTO.

ACKNOWLEDGMENTS

The authors wish to thank the Department of science and technology (DST) and Delhi University for providing technical and financial support. Also one of the authors (SS) is thankful to Delhi Technological University (DTU) for teaching assistantship.

REFERENCES

[1] J. F. Ihlefeld, N. J. Podraza, Z. K. Liu, R. C. Rai, X. Xu, T. Heeg, Y. B. Chen, J. Li, R. W. Collins, J. L. Musfeldt, X. Q. Pan, J. Schubert, R. Ramesh and D. G. Schlom, "Optical band gap of $BiFeO_3$ grown by molecular-beam epitaxy," Appl. Phys. Letts., vol. 92, pp. 142908, 2008.

[2] S. Gupta, M. Tomar and V. Gupta, "Raman spectroscopy of nanocrystalline Mn-doped BiFeO3 thin films", J. Exp. Nanosci., vol. 8, pp. 261–266, 2013.

[3] H.W. Chang, F.T. Yuan, Y.C. Yu, P.C. Chen, C.R. Wang, C.S. Tu and S.U. Jen, "Photovoltaic property of sputtered $BiFeO_3$ thin films," J. Alloys Compd., vol. 574, pp. 402–406, 2013.

[4] Z. Lin, W. Cai, W. Jiang, C. Fu, C. Li and Y. Song, "Effects of annealing temperature on the microstructure, optical, ferroelectric and photovoltaic properties of $BiFeO_3$ thin films prepared by sol–gel method," Cera. Inter., vol. 39, pp. 8729–8736, 2013.

[5] N. Ortega, A. Kumar, R. S. Katiyar, and C. Rinaldi," Dynamic magneto-electric multiferroics PZT/CFO multilayered nanostructure, " J. Mater. Sci., vol. 44, pp. 5127-5142, 2009.

[6] N. Ortega, P. Bhattacharya, R. S. Katiyar, P. Dutta, A. Manivannan, M. S. Seehra, I. Takeuchi, and S. B. Majumder, "Multiferroic properties of Pb (Zr, Ti) O_3/ $CoFe_2O_4$ composite thin films," J. Appl. Phys., vol. 100, pp.126105, 2006.

[7] J. P. Zhou, H. Hongcai, Z. Shi, and C. W. Nan, "Magnetoelectric $CoFe_2O_4$/ Pb ($Zr_{0.52}Ti_{0.48}$) O_3 double-layer thin film prepared by pulsed-laser deposition," Appl. Phys. Letts., vol. 88, pp. 013111, 2006.

[8] P. Murugavel, M. P. Singh, W. Prellier, B. Mercey, C. Simon, and B. Raveau," The role of ferroelectric-ferromagnetic layers on the properties of superlattice-based multiferroics," J. Appl. Phys., vol. 97, pp.103914, 2006.

[9] H. Zheng, J. Wang, S. E. Lofland, Z. Ma, L. Mohaddes-Ardabili, T. Zhao, L. Salamanca-Riba, S. R. Shinde, S. B. Ogale, F. Bai, D. Viehland, Y. Jia, D. G. Schlom, M. Wuttig, A. Roytburd, R. Ramesh, "Multiferroic $BaTiO_3$-$CoFe_2O_4$ nanostructures, "Science, vol. 303, pp. 661-663, 2004.

[10] H. Toupet, V. V. Shvartsman, F. LeMarrec, P. Borisov, W. Kleemann, and M. Karkut, "Enhanced magnetization in $BiFeO_3$/$BaTiO_3$ multilayers: an interface effect," Integ. Ferro., vol. 100, pp.165-176, 2008.

[11] M. S. Ivanov, N. E. Sherstyuk, E. D. Mishina, A. S. Sigov, V. M. Mukhortov, and V. T. Moshnyaga, "Enhanced magnetization and ferroelectric switching in multiferroic BST/BNFO superstructures," Ferroelectrics, vol. 433, pp. 158-163, 2012.

[12] A. Chen, H. Zhou, Z. Bi, Y. Zhu, Z. Luo, A. Bayraktaroglu, and J. Phillips, "A New Class of Room-Temperature Multiferroic Thin Films with Bismuth-Based Supercell Structure," Adv. Mater., vol. 25, pp. 1028-1032, 2013.

[13] H. W. Chang, F. T. Yuan, Y. C. Yu, P. C. Chen, C. R. Wang, C. S. Tu, and S. U. Jen, "Photovoltaic property of sputtered $BiFeO_3$ thin films," J. Alloys Compd., vol. 574, pp. 402-406, 2013.

[14] M. Qin, K.Yao, and Y. C. Liang, "Photovoltaic mechanisms in ferroelectric thin films with the effects of the electrodes and interfaces," Appl. Phys. Letts., vol. 95, pp. 2, 2009.

[15] W. Jiang, W. Cai, Z. Lin, and C. Fu, "Effects of Nd-doping on optical and photovoltaic properties of barium titanate thin films prepared by sol–gel method," Mater. Res. Bull., vol. 48, pp. 3092-3097, 2013

[16] S. Gupta, M. Tomar, and V. Gupta, "Ferroelectric photovoltaic properties of Ce and Mn codoped $BiFeO_3$ thin film," J. Appl. Phys., vol. 115, pp. 014102, 2014.

[17] R. K. Katiyar, P. Misra, S. Sahoo, G. Morell, and R. S. Katiyar, "Enhanced photoresponse in $BiFeO_3/SrRuO_3$ heterostructure," J. Alloys Compd., vol. 609, pp. 168-172, 2014.

[18] A. Kazuhide, and S. Komatsu, "Ferroelectric properties in epitaxially grown $Ba_xSr_{1-x}TiO_3$ thin films," J. Appl. Phys., vol. 77, pp. 6461-6465, 1995.

[19] D. J. Kim, J. Y. Jo, Y. S. Kim, Y. J. Chang, J. S. Lee, J. G. Yoon, T. K. Song, and T. W. Noh, "Polarization relaxation induced by a depolarization field in ultrathin ferroelectric $BaTiO_3$ capacitors," Phys. Rev. Letts., vol. 95, pp. 237602, 2005.

[20] A. Gruverman, A. Kholkin, A. Kingon, and H. Tokumoto, "Asymmetric nanoscale switching in ferroelectric thin films by scanning force microscopy," Appl. Phys. Lett., vol. 78, pp. 2751-2753, 2001.

[21] B. Chen, M. Li, Y. Liu, Z. Zuo, F. Zhuge, Q. F. Zhan, R. W. Li, "Effect of top electrodes on photovoltaic properties of polycrystalline BiFeO3 based thin film capacitors," Nanotechnology, vol. 22, pp. 195201, 2011.

International Journal of Scientific Engineering and Applied Science (IJSEAS) – Volume-2, Issue-9, September 2016
ISSN: 2395-3470
www.ijseas.com

REDUCTION OF FREE FATTY ACID OF JATROPHA OIL USING TAGUCHI APPROACH

Suresh Kumar Saroj, Raghvendra Gautam, Nikhil Shubhendu

Delhi Technological University, Delhi

ABSTRACT

Taguchi approach is used to optimize the four important reaction variables for reduction of free fatty acid (FFA) content of the oil to around 1.5. Jatropha oil is esterified using acid catalyst (P-T-S-A) by esterification process and reduces the free fatty acid content of Jatropha oil. Important variables are studied that affect acid value during esterification such as temperature, catalyst concentration, oil to ethanol ratio and reaction time. Initial free fatty acid of Jatropha oil was found 8% and reduces below 2% in 2h under the conditions of Molar ratio 5:1, 1% P-T-S-A of oil at 65°C by using taguchi approach.

Keywords: Basic catalyst, Acid value, Jatropha oil, ethanol, Taguchi method, esterification.

INTRODUCTION

Economic development of any country in the world is depends on the optimum utilization of its natural resources. India is ranked fourth at the global level on the overall consumption of fossil fuel. Fossil fuel are non renewable in nature and India imports almost 85% of its crude oil consumption by spending billon of dollars and uncontrolled burning of fossil fuel contributes significantly to the environment pollution and global warming. All these lead to us to search for eco-friendly and sustainable alternative. Biodiesel as fuel is very essential for future energy sustainability. Feedstock selection is an important consideration for biodiesel preparation because of high amounts of free fatty acid content that hinders conversion [1]. Some oil has higher value of acidity, which need to minimize to produce biodiesel. It is possible to produce biodiesel from seeds of vary familiar tree species such as pongamia, neem, mahua, jatropha etc.

Jatropha is the one of the oil producing resource which can replace diesel oil [2]. Also jatropha is used for making biodiesel fuel without impact on food consumption. Many researches reveal that Jatropha is an oil bearing plant, which can be used directly with diesel engine without modifying the engine but has to reduce the viscosity [3]. This can be done by blending the diesel oil or without blending to it. Therefore the oil from Jatropha oil is one of the best alternatives to produce fuel and replace the oil imported from aboard. This is because Jatropha can be planted in almost any regions and give quick yield, which is very beneficial to the farmer for home usage or village usage. Especially agriculturists with low income can grow Jatropha and make diesel oil form Jatropha oil for small engine. This help agriculturist to reduce the fuel cost and become independent.

1. Esterification process:

Esterification process is the reaction of triglyceride (fat/oil) with an alcohol in the presence of acidic as a catalyst to reduce free fatty acid number of oil. The presence of strong acid accelerates the reaction [4]. The main purpose of esterification is to reduce FFA. In this study, FFA is reduced by reacting Jatropha oil with ethanol in the presence of acid catalyst (P-T-S-A). The Jatropha oil is first filtered to remove solid impurities then it is preheated at100°C for half an hour to remove moisture. A two stage process is used for producing biodiesel of Jatropha oil. The first stage is esterification to reduce free fatty acid content in Jatropha oil with ethanol (99% pure) and acid catalyst (98% pure) heated for two hour at 65oC in magnetic stirrer to reduce FFA below 2% [5]. After esterification, the esterified oil washed using water. The washing is carried out in a separating funnel. The hot water having temperature as that of esterified oil added in a separating funnel. Impurities like dust, carbon content; sulfur content is washed away with water. Four factor of three level which is used in experiment are given below.

Table I. Four parameter and three variables for design of experiment

Parameter	Level		
	1	2	3
Time(min)	60	90	120

Temp (°C)	55	60	65
Catalyst conc. (% wt.)	0.5	1.0	1.5
Molar ratio	4:1	5:1	6.67:1

2. Material:

Jatropha oil and chemical likes P-T-S-A, NaoH, Ethanol, isopropyl alcohol, Phenopthelene indicator is collected from the chowari bazaar. The esterification reaction used Para-toluene sulfuric acid (HPLC grade, 99.8%, Pharmco-AAPER) as the catalyst and ethanol (HPLC grade, 99.9%, Pharmco-AAPER) as the reactant.

3. Design Of Experiment:

Design of experiment consists of a set of experiments which is the setting of several products or process parameters to be studied that are changed from one experiment to another. Design of experiments is also called matrix experiment, parameters are also called factors and parameter settings are also called levels. Conducting matrix experiment using orthogonal array is an important technique. It gives more reliable estimates of factor effects with fewer numbers of experiments when compared with the traditional methods such as one factor at a time experiments [6]. The design of experiment via Taguchi method uses a set of orthogonal array for performing of the fewest experiments. Taguchi method involves the determination of large number of experimental situation, described as orthogonal array, to reduce errors and enhance the efficiency and reproducibility of experiments [7]. The columns of an orthogonal array are pair wise orthogonal that is for every pair of column, all combination of factor levels occur at an equal numbers of times. Although, in the taguchi software there is a different type of Array but I

have used L-9 Array that is suitable for four parameter and three level which is used in this paper.

The columns of an orthogonal array represent factors to be studied and the rows represent individual experiments. This study is associated with four factors with each at three levels. The orthogonal array used to find the effects of four parameters namely the molar ratio of oil to ethanol, time, and catalyst concentration and reaction temperature on the reduction of FFA. The four selected parameters at three levels i.e. L-9 experimentally studied are shown in this table I.

Table II shows the orthogonal array used to design experiments with four parameters at three levels. In this study, Taguchi approach is software for automatic design was used to analyze the results and optimize the experimental conditions for setting the control variables.

Signal to noise ratio

$$\frac{S}{N_{(Smaller)}} = -10 \log\left(\frac{\sum y_i^2}{n}\right)$$

If smaller is better then used this formula.

Where n is no. of experiment perform for one solution, in this case it is equel to 1 and y is the S/N ratio for the each set L-9 array [8].

Table II. L-9 Array for Design of Experiment

Exp no.	Column number and parameter assigned			
	Molar ratio	Catalyst conc.	Temp	Time
1	1	1	1	1
2	1	2	2	2
3	1	3	3	3
4	2	1	2	3
5	2	2	3	1
6	2	3	1	2
7	3	1	3	2

International Journal of Scientific Engineering and Applied Science (IJSEAS) – Volume-2, Issue-9, September 2016
ISSN: 2395-3470
www.ijseas.com

8	3	2	1	3
9	3	3	2	1

RESULT

1. S/N plot:

According to Taguchi approach smaller value of mean of S/N ratio corresponding each factor is the best value for maximum reduction in FFA. From the figure I it is observed that the optimum level of molar ratio, reaction time, and reaction temperature and catalyst concentration are 3, 2, 3, 1, i.e. 6.67:1, 90 min, 65°C, and 1.0% of oil. Hence we can conclude that it can give the lowest FFA of oil i.e.0.8

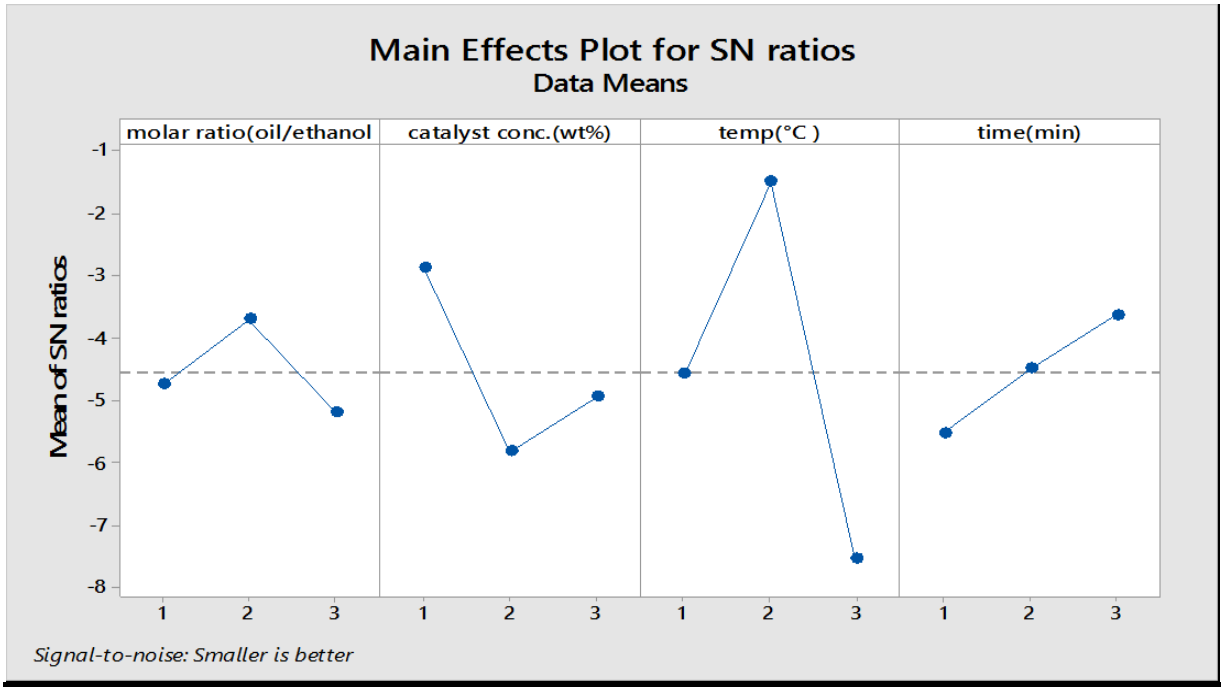


Figure I. Main effects plot of the control parameter

2. Anova table:

Different parameters affect the free fatty acid of oil to a different degree. The relative magnitude of the parameter effects are listed in table. A best feel for the relative effect of the different factors is obtained by the decomposition of variance, which is generally called as analysis of variance (ANOVA). This is obtained by the formula given below. Total sum of squares = Sum of square due to parameter A [(total number of experiments at level A1) x (mA1-m)] + [(total number of experiments at level A2) x (mA2-m)] + [(total number of experiments at level A3) x (mA3-m)].

Now all these sum of squares are listed in Table III. This is known as the ANOVA table.

Table III. Analysis of Variance

Source	DF	Adj. SS	Adj. MS	F-value	P-value
Molar ratio(oil/ethanol)	2	0.01556	0.00778	78.34	0.00012
Catalyst conc. (Wt. %)	2	0.42889	0.21444	7.33	0.042
Temp(°C)	2	2.06889	1.03444	21.33	0.022
Time(min)	2	0.16222	0.08111	0.06	0.18
Error	0	0	0		
Total	8	2.67556			

The larger the contribution of a particular parameter to the total sum of squares, the larger the ability is of that factor to affect the S/N ratio. More ever, the lower P- value, the larger will be the factor contribution in the reduction of FFA. For the molar ratio, catalyst conc. and reaction temperature P-value is very small; hence it has more contribution in the reduction of FFA.

CONCLUSION

The main effect plot for S/N ratio is shown in the Figure I. The average S/N ratio for maximum percentage yield of Jatropha oil ethyl ester is obtained at Molar ratio 5:1, catalyst% is 1%, reaction Temperature 65°C and reaction time 120min.That is the optimum parameter setting for high percentage reduction of FFA i.e. (0.8%) for highest yielding biodiesel.

REFERENCE

(1) Adebayo G. B., Ameen O.M and Abass L.T, "Physico – chemical properties of biodiesel produced from Jatropha curcas oil and fossil diesel", Journal of Microbiology and Biotechnology Research, 2011, pp 12 – 16.

(2) S.N. Bobade and V.B.Khyade, Preparation of Methyl Ester (Biodiesel) from Karanja (Pongamia pinnata) Oil, Research Journal of Chemical Sciences, Vol. 2(8), 43-50, August (2012).

(3) S.Antony Raja, D.S.Robinson smart, and C.Lindon Robert Lee, Research, Biodiesel production from Jatropha oil and its characterization, Journal of Chemical Sciences Vol. 1 (1), April (2011).

(4) SunTae Kim, Bongbeen Yim, Youngtaek Park, Application of Taguchi Experimental Design for the Optimization of Effective Parameters on the Rapeseed Methyl Ester Production, Environ. Eng. Res. 2010 September, 15(3), 129-134.

(5) Ramadhas AS, Jayaraj S, Muraleedharan C. Use of vegetable oils as I.C. engine fuel—a review. Renewable Energy-2004.

(6) Anya Uzo Anya, Nwobia Noelle Chioma and Ofoegbu Obinna (2012), "Optimized Reduction of Free Fatty Acid Content on Neem Seed Oil for Biodiesel Production", Journal of Basic and Applied Chemistry, Vol. 2, No. 4, pp. 21-28.

(7) Gautam R., Kumar N., (2013) Experimental investigation on use of jatropha oil ethyl ester and diesel blends in small capacity diesel engine. S.A.E. Technical paper 2013-24-0172; doi: 10.4271/2013-24-0172. (Publisher SAE International, Scopus Indexed).

(8)Gautam R., Kumar N.,(2013) Comparative Assessment of Performance, Emission and Combustion Characteristics of Blends of Methyl and Ethyl Ester of Jatropha Oil and

Diesel in Compression Ignition Engine 2013-01-2664; doi: 10.4271/2013-01-2664. (Publisher SAE International, Scopus Indexed).

Solar Energy 139 (2016) 47–57

Contents lists available at ScienceDirect

Solar Energy

journal homepage: www.elsevier.com/locate/solener

Resource assessment for hybrid solar-biomass power plant and its thermodynamic evaluation in India

U. Sahoo [a,b], R. Kumar [a,*], P.C. Pant [b], R. Chaudhary [a]

[a] Dept. of Mechanical Engineering, Delhi Technological University, Bawana Road, New Delhi 110042, India
[b] National Institute of Solar Energy, Ministry of New and Renewable Energy, Govt. of India, New Delhi 110003, India

ARTICLE INFO

Article history:
Received 17 April 2016
Received in revised form 11 September 2016
Accepted 21 September 2016

Keywords:
Solar
Biomass
Modeling
Hybrid
Efficiency
Energy
Exergy

ABSTRACT

Hybrid solar-biomass thermal power generation systems are important for continuous power generation installations which supplement each other seasonally in India. In this paper, several aspects associated with hybrid biomass-solar power generation installations such as state wise availability of biomass resources, solar direct normal irradiance (DNI) has been discussed. Month wise daily average DNI is considered as 20%, 40%, 60%, and 80% and remaining heat is taken from biomass resource in the proposed hybrid plant. The thermodynamic evaluation (i.e. Energy and Exergy) of hybrid solar-biomass power plant have also been investigated. The total input energy of the proposed hybrid system is taken from the heat transfer fluid through parabolic trough collector (PTC) as per availability of solar resource and remaining from biomass to maintain the steam at superheated state of 500 °C and 60 bar and supplied to turbine at steam mass flow rate of 5 kg/s. The energy and exergy analyses of 5 MW hybrid system with series mode was carried out to identify the effects of various operating parameters like DNI, condenser pressure, turbine inlet temperatures, boiler pressure on net power output energy and exergy efficiencies.
© 2016 Elsevier Ltd. All rights reserved.

1. Introduction

Biomass energy has provided sustenance to mankind through the ages and also attracting greater attention for power generation in India. Government of India recognized the potential role of biomass power in the Indian economy quite early and since then has been the vanguard of its promotion. If it is used as much as it is produced its benefits will include its renewable nature, wide availability, carbon neutrality and the potential to provide large productive employment in rural areas. As a further outcome of the carefully planned mix of policy and financial incentives introduced by the Government, capacity has been built up in the country for biomass power technologies, their operation and maintenance, management of biomass collection, manufacturing of equipment and resolving grid interfacing issues. The availability of crop residues like bagasse, rice husk, coconut shells and the wood processing wastes inherently limit the growth of the capacity of biomass power generation (Sahoo et al., 2015). One of the major barriers confronted by the biomass power plants is a secured supply of required quality and quantity at a competitive price for sustainable operation of the plant. Now the price of biomass resources has slowly increased due to non-availability of biomass at right price in recent years (Larson, 2001). On the other hand, solar thermal power plants (STPP) do not continuously generate power due to daily & seasonal variations and low level of direct normal irradiance (DNI; short transients) for at least 100–150 days in a year in most of places of this country. Although STPP with storage is one of the solution to maintain required amount of heat (Casati et al., 2015; Wittmann et al., 2011) due to DNI variations or short transients but difficult to store for the long duration of time for night cycle (Montes et al., 2009; Hoshi et al., 2005). Hybridization with STPP is most important for continuous generation of power for fulfilling the energy requirements. So, the choice of biomass resources is a judicious selection for hybridization with STPP for continuous power generation, which supplement with each other seasonally. Several authors investigated on hybrid solar biomass for power generation where water gets heated to saturated state through solar thermal technologies and superheated state through biomass boiler (Kaushika et al., 2005; Gordillo and Belghit, 2011; Ravaghi-Ardebili et al., 2015). Electricity production cost from hybrid solar thermal power plant is lower than that of stand-alone system (Spelling et al., 2013; Kotowicz et al., 2013) and reduction in the amount of CO_2 emitted to the atmosphere is also observed (Peterseim et al., 2013). The literature survey shows the limited focus in the area of resource assessments on solar and biomass for hybridization. The paper mainly focuses on the resource assess-

* Corresponding author.
E-mail address: dr.rajeshmits@gmail.com (R. Kumar).

http://dx.doi.org/10.1016/j.solener.2016.09.025
0038-092X/© 2016 Elsevier Ltd. All rights reserved.

Nomenclature

A_{ap}	aperture area of the parabolic trough collector field (m^2)
T	temperature (°C or K)
h	specific enthalpy (kJ/kg)
s	specific entropy (kJ/kg K)
η	efficiency of hybrid solar-biomass power plant (%)
W	rate of work transfer (kW)
Q	rate of heat transfer (kW)
E_x	exergy (kW)
E_{xD}	exergy destruction

Subscripts

b	biomass residue
C	condenser
E	energy
Ex	exergy
FWH	feed water heater
HE	heat exchanger
HSB	hybrid solar-biomass
i, e	exergy flowing stream at inlet and outlet
j	heat source of each state points of the system
opt	optical
$P1$ & $P2$	pump 1 and 2
PTC	parabolic trough collector
T	turbine
w	water
o	surrounding (or reference environment) condition
1 to 9, c, a, x, y and o	state points of HSB system

ment for hybrid solar-biomass, optimum use of solar and biomass resource for power generation and its Modeling for energy & exergy analysis.

2. Biomass resource availability and status of biomass power in India

In India over 500 million tons (MT) of biomass is produced every year in different states like; Andhra Pradesh, Bihar, Chhattisgarh, Gujarat, Haryana, Karnataka, Kerala, Maharashtra, Madhya Pradesh, Odisha, Punjab, Uttar Pradesh and West Bengal (Directorate of Economics and Statistics, 2012-13). Out of total resources, 350 MT of agricultural based major biomass resources are contributed by bagasse, rice husk, straw, cotton, coconut stalk, coconut shells and groundnut shells. Uttar Pradesh is one of the states, which produces the highest quantity of major biomass (56 MT) followed by Maharashtra (40 MT) and Punjab (37 MT) as shown in Fig. 1.

As per 12th five year plan, the proposed biomass power generation installation capacity of India is 1000 MW. The targeted power potential for 13th five year plan is estimated as 5730 MW (Road Map for Biomass Energy Report, 2011). Biomass based power generation capacity of 10,000 MW by the year of 2022 has been predicted for India (Renewable Energy Investment, 2015). A grid connected biomass gasifier based project of 1 MW capacity in Haryana has been installed for meeting the captive power needs of the industry. The installation of 50 biomass gasifier and combustion based system with cumulative installed capacity of 8.54 MW to meet the captive demand for electricity & thermal applications are under installation in different states (www.mnre.gov.in). World's largest coconut tree waste based power plant has been installed in Coimbatore district of Tamil Nadu with the generation capacity of the plant is 10 MW (Bio Power, India, 2014).

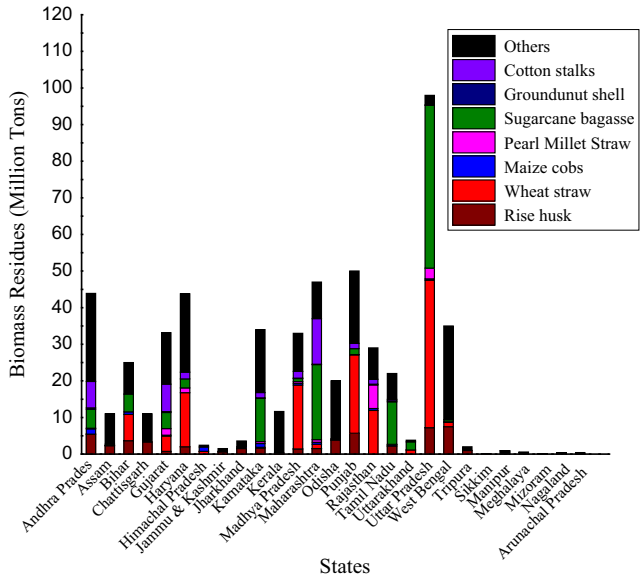


Fig. 1. State wise major agricultural based biomass residues.

3. Solar resource availability and status of solar thermal power in India

Most of the places in the country are having good sunshine, about 5000 trillion of kW h per year incident over India's land area with the most of the parts receiving Direct Normal Irradiance (DNI) of 4–5.5 kW h/m^2/day (Solar Radiation Energy over India, 2008). About 200–250 sunny days are available in a year in most parts of the country. Solar thermal for the generation of heat and electricity can be deployed during these sunny days. Fig. 2 shows the state wise annual average DNI available in India. This is based on daily average of DNI mapping resulted from the data available with National Renewable Energy Laboratory-National Institute of Solar Energy and Indian Meteorological Department (IMD) (Solar Resource Assessment based on satellite imagery, 2013; Solar Radiation Energy over India, 2008). State wise availability of DNI results indicated in Fig. 2 are reliable indication of the solar thermal potential.

The present installed capacity of total power generation in energy sector of India is 305×10^3 MW as on July 2016. This includes, 44.3×10^3 MW (14.52%) from renewable energy sources & 5.78×10^3 MW (1.89%) from nuclear. Out of 44.3×10^3 MW renewable energy, solar power is 7.8×10^3 MW (17.6%) (Ministry of Power, Govt. of India, 2016). To harness the solar energy potential for various applications including power generation, the Ministry of New and Renewable Energy (MNRE) launched Jawaharlal Nehru National Solar Mission (JNNSM) with a target of deploying 20,000 MW of grid connected solar power (i.e. both PV and Thermal) by 2022. The launching of the JNNSM symbolizes both and indeed encapsulates the vision and ambition for the future of solar energy. One of the aims of program is to reduce the cost of solar thermal technologies by deploying large solar thermal power generation capacity in various high potential areas of the country (IEA, 2014). The STPP grid connected power projects are being installed in India. In the country CSP based power plants of total 380 MW

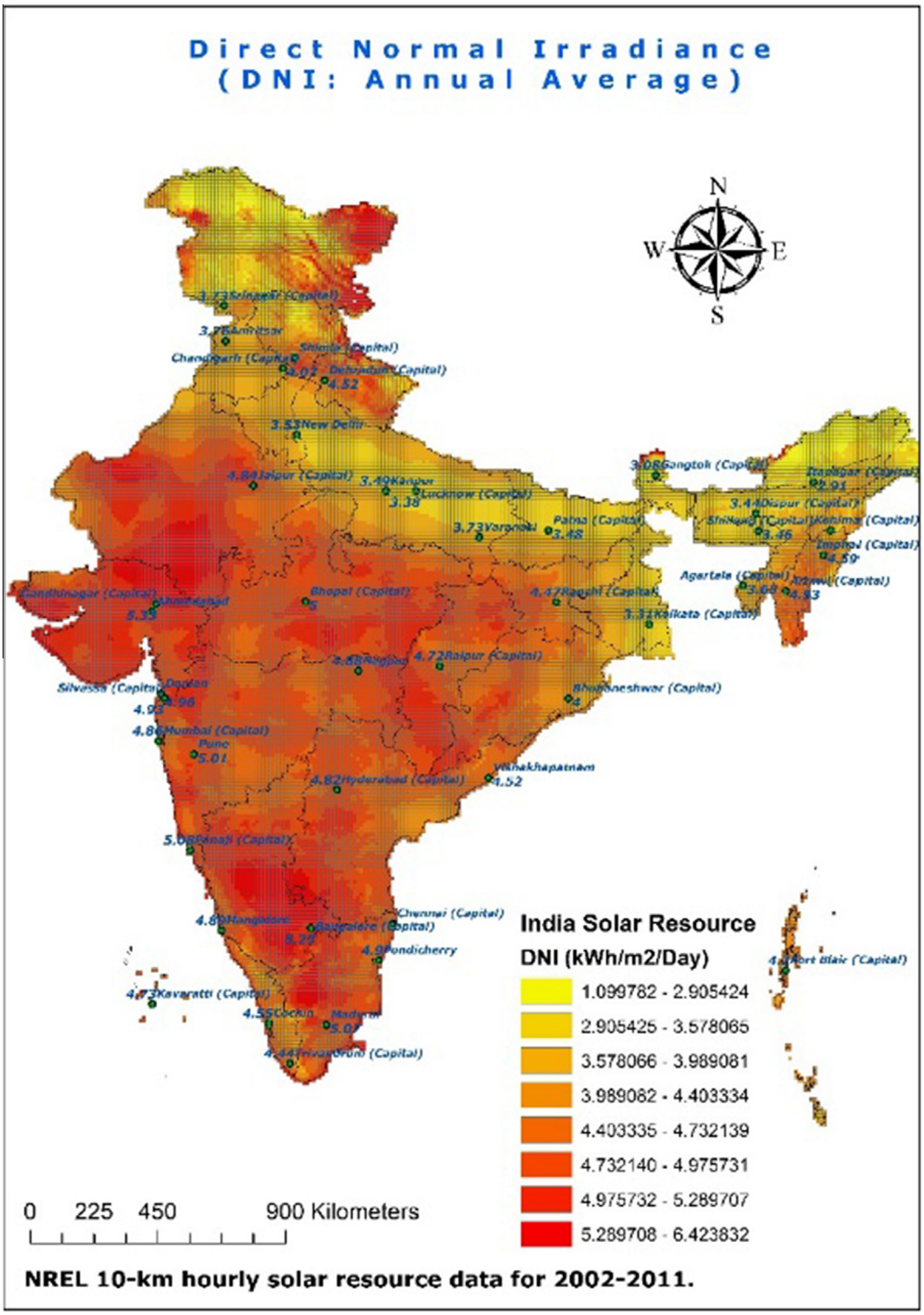


Fig. 2. State wise annual average DNI available in India.

capacity have been completed (Table 1) using different solar thermal technologies.

4. Scope of hybrid biomass-solar power generation

Hybrid biomass-solar power generation has been studied and investigated for several capacities between 5 MW and 110 MW (Novatec Solar GmbH, 2012; Department of Resources Energy and Tourism, 2013). These plants mainly focus on the integration of biomass combustion boiler with solar thermal power plant (Perez and Torres, 2010; Nixon et al., 2012). The solar field (PTC) heats the heat transfer fluid (oil) to a maximum temperature up to 290 °C which is directly supplied to the boiler for making saturated steam and then supplied to biomass combustion boiler for superheating of the steam. A hybrid power plant was investigated to provide electricity as well as process heat for running a cold

Table 1
Installed solar thermal power plants using different solar thermal technologies in India (A Compendium of Research, Development and Demonstration Projects 2014; NREL; Initiatives in Renewable Energy; AREVA Solar power Projects India; Desai et al., 2014; eSolar Solar Thermal Projects).

Sl.No.	Capacity of STPP (MW)	Technologies	Turbine pressure and temperature	Locations	References
1	50	PTC	40 bar/300 °C & 100 bar/550 °C	Nokh, Rajasthan	NREL
2	100	CLFR	90 bar/390 °C	Dhursar, Rajasthan	Initiatives in Renewable Energy and AREVA Solar power Projects India
3	1	PTC and CLFR	40 bar/350 °C	Gurgaon, Delhi	Desai et al. (2014)
4	2.75	Solar Tower	60 bar/440 °C	Bikaner, Rajasthan	eSolar Solar Thermal Projects
5	50	PTC	N.A.	Phalodi, Rajasthan	NREL
6	50	PTC	103 bar/380 °C	Anantpur, Andhra Pradesh	NREL
7	100	PTC	N.A.	Askandra, Rajasthan	NREL
8	28	PTC	N.A.	Kutch, Rajasthan	NREL
9	1	Scheffler	N.A.	Mount Abu, Rajasthan	A Compendium of Research, Development and Demonstration Projects (2014)

storage (Nixon et al., 2012). In another solar-biomass hybrid system, water gets converted into saturated steam at 40 bar and superheat at 520 °C through biomass combustion boiler (Morell, 2012a). A grid interactive hybrid solar power plant built by Thermosolar Borges having a capacity of 22.5 MW in Spain is using heat from solar DNI of 18 MJ/m^2/day and remaining from biomass residue to supplement each other (Protermosolar, 2012; Morell, 2012b). The month wise harvesting period of major biomass production are shown in Fig. 3 (Triathi Arun et al., 1998). It is seen that, the availability of biomass residue is high during the period from April to December. In this period greater amount of biomass resource can be used to generate power from hybrid system due to low solar DNI.

State-wise solar DNI and biomass potential are investigated for hybrid solar-biomass power generation which is shown in Fig. 4. For assessing the solar energy potential, only 10% of the total waste land area available has been considered in the major biomass energy contributing states like Punjab, Uttar Pradesh, Haryana, Maharashtra, Madhya Pradesh, Karnataka, Tamil Nadu, Gujarat, Rajasthan, Kerala, Bihar, Andhra Pradesh, West Bengal, Odisha & Assam.

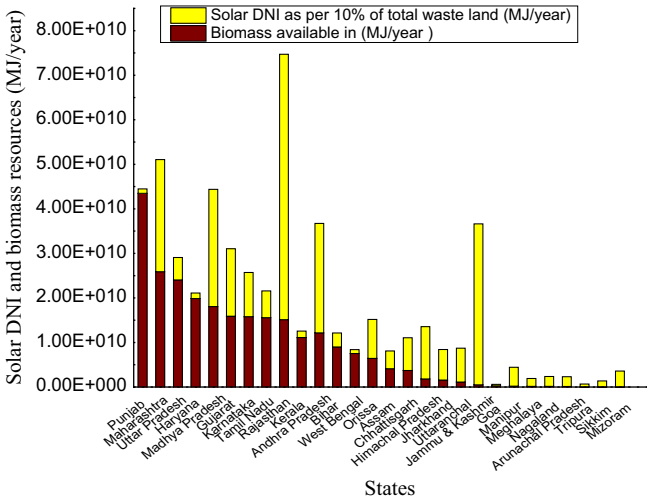


Fig. 4. State wise solar DNI and biomass potential.

5. Plant modeling approach of hybrid solar-biomass

The technical modeling of 5 MW hybrid solar-biomass power plant has been carried out in this study. In this hybrid power plant, biomass boiler arrangement is taken to operate on the biomass, whenever it needed at different load conditions. Solar field is utilized to heat the heat transfer fluid as per availability of DNI. Hot water from feed water heater gets heated through heat transfer fluid using heat exchanger (H.E) as shown in Fig. 5. Biomass boiler will run at lower capacity depending upon the condition of water



Fig. 3. Month-wise harvesting period of biomass resources.

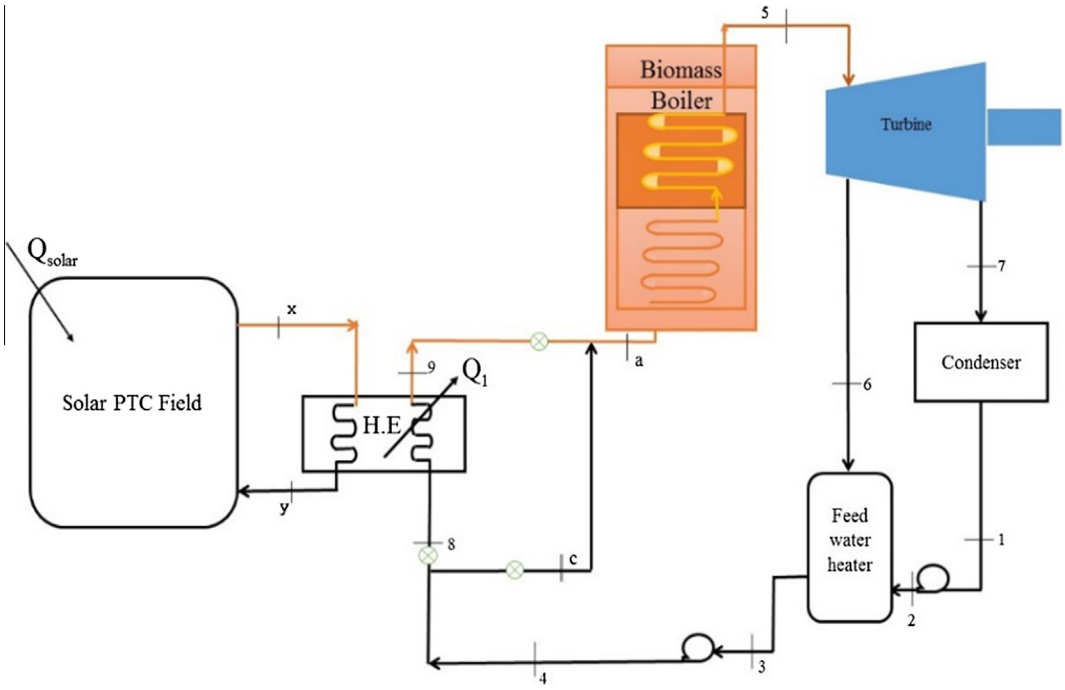


Fig. 5. Schematic diagram of the hybrid solar-biomass (HSB) power plant.

at state point 'a' through PTC field (4-8-9-a) and biomass boiler will operate at full load capacity in intermittency of day & night cycle (4-c-a). Steam gets superheated at pressure of 60 bar and temperature of 500 °C through biomass boiler and is supplied to turbine at mass flow rate of 5 kg/s steam. In this cases, steam is bled and expanded to an intermediate point '6'. And remaining steam is expanded at low pressure and medium temperature. The bled steam is mixed with condensed water to be preheated in feed water heater. At state point 1, condensed water is pumped to the feed water heater at pressure of 5 bar and mixed with bled steam in feed water heater. Hot water from feed water heater is pumped to the heat exchanger, 4-8 and/or directly pumped to the biomass boiler in intermittency of day/night time, 4-c-a.

5.1. Energy analysis

First law of thermodynamic is used to analyze the performance of hybrid power plant performed by several authors (Montes et al., 2009; Beerbaum and Weinrebe, 2000; Kosugi and Pak, 2003; Singh et al., 2000; Kaushik et al., 2001; Morin et al., 2012; Kalogirou, 2009). Parabolic trough collector transfers the solar DNI into useful heat (Q_1) at specific mass flow rate of heat transfer fluid (m_{oil}) i.e. Therminol VP-1. Specifications of major components of the hybrid system used in this analysis, are shown in Table 2.

The performance analysis of the parabolic trough collector are investigated by several authors (Kalogirou, 2004; Goswami et al., 2000; Tzivanidis et al., 2015; Duffie and Beckman, 1991; Sukhatme and Nayak, 2008).

The useful heat gain (Q_1) is defined as:

$$Q_1 = Q_{solar} \times \eta_{E,PTC} \tag{1}$$

where Q_{solar} is the solar energy falling on PTC field may be expressed as

$$Q_{solar} = A_{ap} \times DNI \tag{2}$$

The energy efficiency ($\eta_{E,PTC}$) of the parabolic trough collector is expressed as

Table 2
System specifications of major components of the hybrid system.

Equipment	Input parameters	Value	Units
Parabolic trough collector field	Aperture area, A_{ap}	45,080	m^2
	Optical efficiency, η_{opt}	65	%
	a_1	0.1	W/m^2 °C
	a_2	0.001	W/m^2 °C^2
	Mirror reflectance	94	%
	Mass flow rate of heat transfer fluid (Therminol VP-1)	28	kg/s
Turbine	Efficiency	96	%
Pump		88	%
Heat exchanger		100	%

$$\eta_{E,PTC} = \eta_{opt} - a_1 \frac{(T_m - T_o)}{DNI} - a_2 \left[\frac{(T_m - T_o)^2}{DNI} \right] \tag{3}$$

where η_{opt} is optical efficiency of the parabolic trough reflector, a_1 is the first order coefficient of the collector efficiency (W/m^2 °C), a_2 is the second order coefficient of the collector efficiency (W/m^2 °C^2), T_m is the mean temperature of the heat transfer fluid (oil) is defined as

$$T_m = \frac{T_y + T_x}{2} \tag{4}$$

The mass flow rate of heat transfer fluid (m_{oil}) is calculated as

$$m_{oil} = \frac{\eta_{E,PTC} \times A_{ap} \times DNI}{\Delta T \times C_p} \tag{5}$$

where C_p is the specific heat of heat transfer fluid, ΔT is the temperature difference of heat transfer fluid across the PTC field is expresses as

$$\Delta T = (T_x - T_y) \tag{6}$$

The energy balance equations of the major components of hybrid solar-biomass power plant are expressed as (Kalogirou, 2009; Kaushik et al., 2011)

For Turbine : $W_T = m_w[(h_5 - h_6) + (1-\alpha)(h_6 - h_7)]$ (7)

where 'α' is fraction of steam bled from turbine, m_w is the flow rate of water (kg/s).

Condenser : $Q_C = m_w(1-\alpha)(h_7 - h_1)$ (8)

Pump : $W_p = m_w[(h_3 - h_4) + (1-\alpha)(h_2 - h_1)]$ (9)

The energy efficiency of the hybrid solar-biomass ($\eta_{E,HSB}$) power plant is expressed as the ratio of output energy to input energy.

$$\eta_{E,HSB} = \frac{W_{net}}{Q_{solar} + Q_b} \quad (10)$$

where W_{net} is the net-work output of the plant and Q_b is the total heat produced from biomass expressed as

$$Q_b = m_b \times LHV_b \quad (11)$$

$$LHV_b = HHV_b - (226.04 \times H) - 25.82 \times \textit{moisture content of biomass} \quad (12)$$

$$HHV_b = 338.3 \times C + 1443 \times (H - O/8) - 94.2S \quad (13)$$

where m_b the flow rate of biomass residue, LHV_b is the lower heating value and HHV_b the higher heating values of biomass or can be calculated using Dulong's and Perit formula (Basu, 2006). C, H, O and S are the dry biomass weight (%) of carbon, hydrogen, oxygen and Sulphur.

On an average biomass consists of 40–50% Carbon, 4–7% Hydrogen and 30–45% Oxygen on moisture and ash free basis. Biomass contains negligible amounts of Nitrogen and Sulphur. The moisture content of rice husk has been taken 10%.

The net-work output (W_{net}) of the plant is defined as the difference of turbine work output and pump work input.

$$W_{net} = W_T - W_P \quad (14)$$

Heat transfer rate (Q_2) in the heat exchanger is expressed as

$$Q_2 = m_w(h_9 - h_4) = m_{oil}(h_x - h_y) \times \eta_{E,HE} \quad (15)$$

where $\eta_{E,HE}$ is energy efficiency of heat exchanger. The heat is taken from biomass boiler (Q_{boiler}) to maintain the quality of the steam at superheated condition may be expressed as

$$Q_{boiler} = m_w(h_5 - h_a) = Q_b \times \eta_{E,boiler} \quad (16)$$

where $\eta_{E,boiler}$ is the energy efficiency of the boiler.

The mathematical analysis of the energy losses of the major components of the hybrid power plant are as follows;

(a) Heat losses in PTC (L_{PTC}):

$$L_{PTC} = A_{ap} \times DNI \times (1 - \eta_{E,PTC}) \quad (17)$$

(b) Heat losses in biomass boiler (L_{boiler}) (Asthana, 2009; ASME, 1991; IS 13979:1994, 1999).

$$L_{boiler} = Q_b \times (1 - \eta_{\text{boiler}}) \quad (18)$$

where η_{boiler} is considered as 80%.

(c) Heat losses in turbine (L_T):

$$L_T = W_T - (W_T \times 0.96) = 0.04 \times W_T \quad (19)$$

(d) Heat loss in condenser (L_c):

$$L_c = m_w \times (1-\alpha) \times (h_7 - h_1) \quad (20)$$

(e) Heat losses in pump (L_P):

$$L_P = W_p - (W_p \times 0.88) = W_p \times 0.12 \quad (21)$$

5.2. Exergy analysis

Exergy analysis is a useful tool of the thermodynamic analysis to provide a detailed breakdown of the losses in terms of waste exergy emissions and exergy destruction for the overall system. However, limited researchers have analyzed on the exergy analysis of the thermal power plant (Bejan et al., 1981; Kaushik et al., 2000; Hepbasli, 2008; Dai et al., 2009; Lu et al., 2010; Dincer and Rosen, 2007; Gupta and Kaushik, 2010). The exergy analysis for the major components of hybrid solar-biomass power plant are analyzed in this study.

The steady-state process, respective balances for exergy can be written as (Petela, 2013)

$$\sum_i E_{xi} + \sum_j \left[1 - \frac{T_o}{T_j}\right] Q_j = \sum_e E_{xe} + W + E_{xD} \quad (22)$$

Exergy of the flowing stream at each state point (E_x) may be expressed as

$$E_x = [(h - h_o) - T_o(s - s_o)] \quad (23)$$

Exergy of solar radiation may be expressed as (E_{xSolar}) is expressed as (Kotas, 1995)

$$E_{xSolar} = Q_{solar} \times \left(1 - \left(\frac{4}{3}\right) \times \left(\frac{T_o}{T_{sun}}\right) + \left(\frac{1}{3}\right) \times \left(\frac{T_o}{T_{sun}}\right)^2\right) \quad (24)$$

where Q_{solar} is the useful heat gain from solar DNI and T_{sun} is apparent sun temperature.

Exergy heat gain of fluid (E_{x1}) from the Parabolic Trough Collector (PTC) field is expressed as

$$E_{x1} = \frac{Q_1}{T_x - T_y} \times \left((T_x - T_y) - T_o \cdot \ln\frac{T_x}{T_y}\right) \quad (25)$$

The exergy efficiency ($\eta_{Ex,PTC}$) of the parabolic trough collector is expressed as

$$\eta_{Ex,PTC} = \frac{E_{x1}}{E_{xsolar}} \quad (26)$$

For the biomass, the physical exergy is neglected as entering at restricted dead state. The chemical exergy of biomass $E_{x,b}$ is defined as

$$E_{x,b} = m_b \times \phi \times LHV_b \quad (27)$$

where ϕ is the multiplication factor and calculated as (Szargut, 2005)

$$\phi = 1.0401 + 0.1728\frac{H}{C} + 0.0432\frac{N}{C} + 0.2169\frac{O}{C} \times \left(1 - 0.2062\frac{H}{C}\right) \quad (28)$$

The exergy efficiency of the hybrid power cycle ($\eta_{Ex,HSB}$) can be expressed as the ratio of exergy on output to input.

Table 3
Geographical parameters for the Gurugram regions of Haryana, India.

DNI	5.35 kW h/m^2/day
Ambient temperature	35 °C
Latitude	28.425°
Longitude	77.155°
Elevation	259 m



Fig. 6. Month wise hourly percentage heat utilization from solar and biomass for hybrid system.

Table 4
State point properties of the proposed hybrid system.

State points	Fluid	Pressure (bar)	Temperature (°C)	Enthalpy (kJ/kg)	Entropy (kJ/kg K)	Mass flow rate (kg/s)	Energy (kW)	Exergy (kW)
1	Water	0.1	45.82	191.8	0.6493	4.269	959	34.685
2	Water	5	45.85	192.4	0.6495	4.269	962	38.195
3	Water	5	98.84	414.5	1.293	5.0	2072.5	80.45
4,c	Water	60	99.44	421.1	1.296	5.0	2105.5	109.90
5	Water	60	500	3422	6.881	5.0	17,110	6515
6	Water	5	204.60	2865	7.079	0.731	2094.315	500.29
7	Water	0.1	45.82	2330	7.352	4.269	9946.77	279.10
8	Water	60	99.22	420.2	1.293	5.0	2101	109.1
9,a	Water	60	275.6	2620	5.59	5.0	13,100	4492
x	Therminol VP-1	12	391.8	744.4	1.27	28.0	20,843	9890.72
y	Therminol VP-1	12	240	420.5	1.05	28.0	11,774	2718.8

These above data are generated by using Engineering Equations Solver (EES) software.

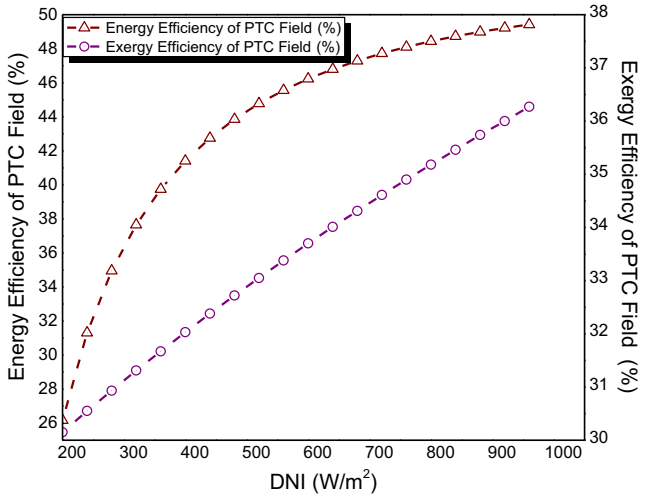


Fig. 7. Variation of energy efficiency and exergy efficiency of PTC field with change in DNI.

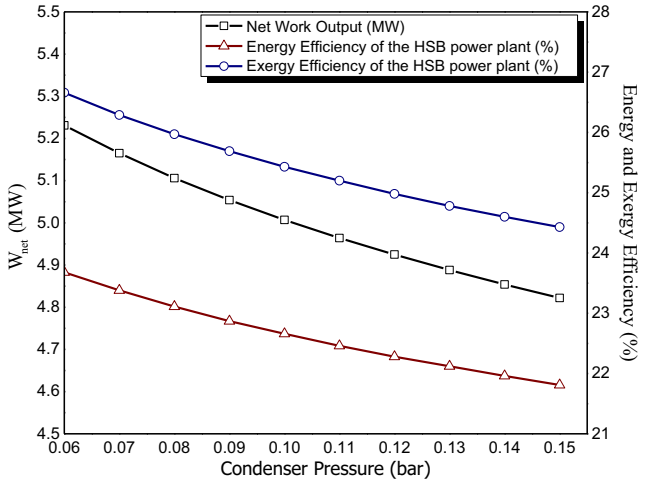


Fig. 8. Variation of energy efficiency, exergy efficiency and net work output of HSB power plant with change in condenser pressure.

$$\eta_{Ex,HSB} = \frac{W_{net}}{E_{xSolar} + E_{xb}} \tag{29}$$

Exergy destruction equations in major components of the hybrid system are given as:

$$\text{Boiler}: \quad E_{xD,Boiler} = E_{xb} - m_w[(h_5 - h_a) - T_o(s_5 - s_a)] \tag{30}$$

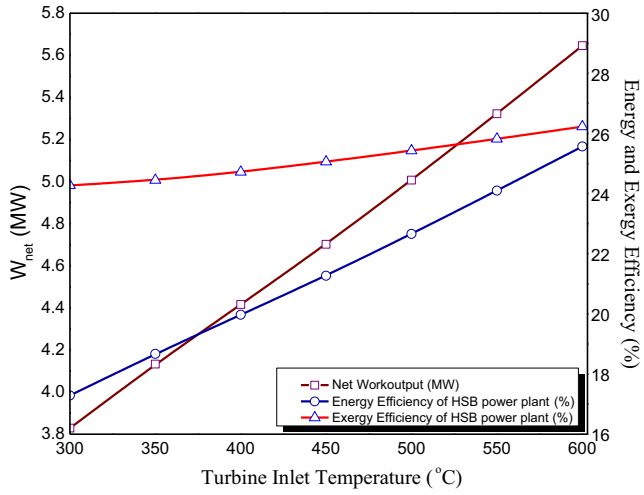


Fig. 9. Variation of energy efficiencies, exergy efficiencies and net work output of HSB power plant with change in turbine inlet temperature.

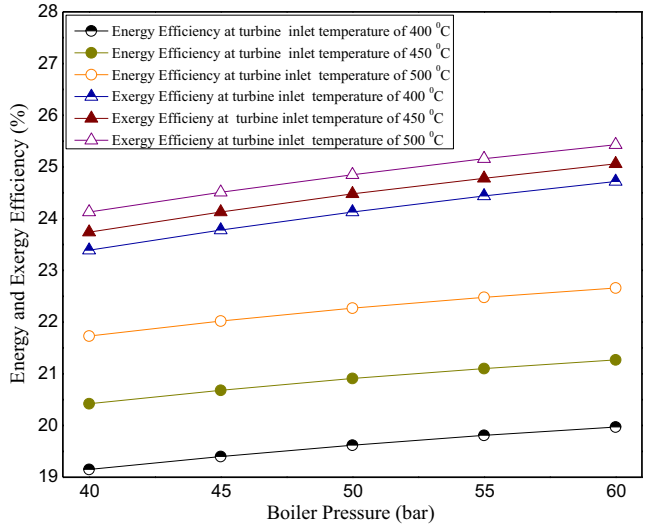


Fig. 10. Energy efficiencies and exergy efficiencies with change in boiler pressure at three turbine inlet temperature (i.e. 400 °C, 450 °C & 500 °C).

$$\text{Turbine}: \quad E_{xD,T} = m_w[\{h_5 - \alpha h_6 - (1-\alpha)h_7\} - T_o\{s_5 - \alpha s_6 - (1-\alpha)s_7\}] - W_T \tag{31}$$

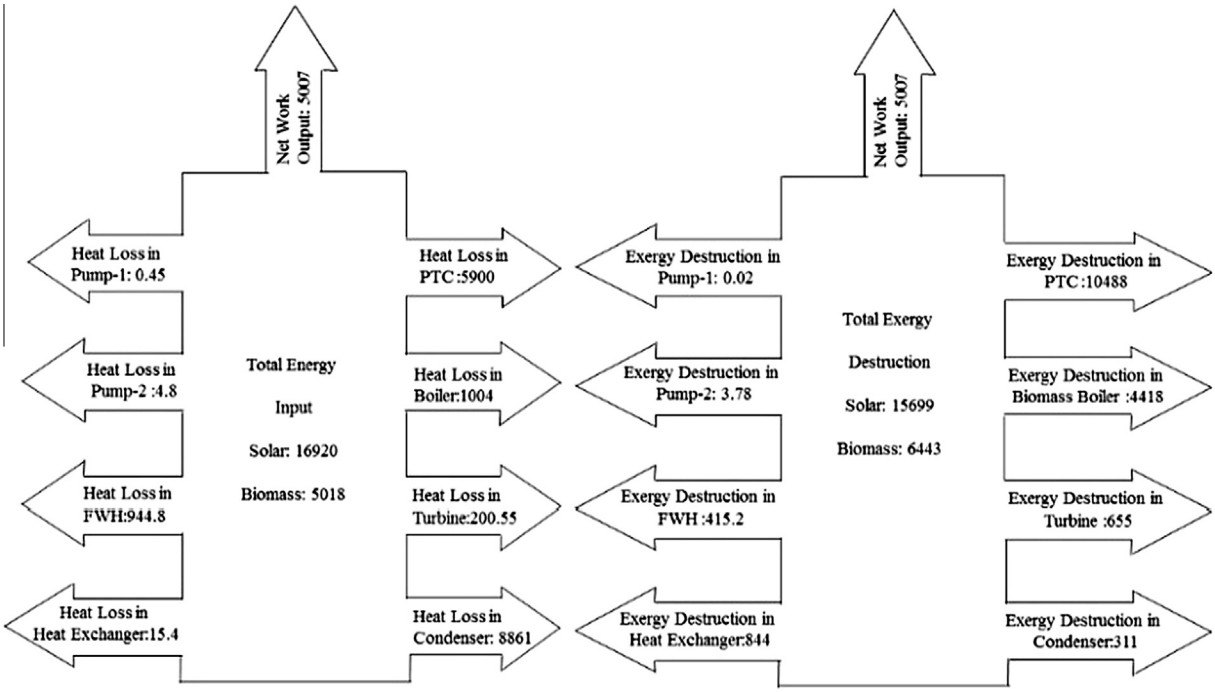


Fig. 11. Energy losses and exergy destruction (kW) of the major components of the hybrid system.

$$\text{Condenser}: \quad E_{xD,C} = (1-\alpha)m_w[(h_7 - h_1) - T_o(s_7 - s_1)] \tag{32}$$

$$\text{Pump-1}: \quad E_{xD,P1} = W_{p_1} - (1-\alpha)m_w[(h_2 - h_1) - T_o(s_2 - s_1)] \tag{33}$$

$$\text{Pump-2}: \quad E_{xD,P2} = W_{p_2} - \alpha m_w[(h_4 - h_3) - T_o(s_4 - s_3)] \tag{34}$$

$$\text{Feed water heater}: \quad E_{xD,FWH} = m_w[\alpha h_6 + (1-\alpha)h_2 - h_3 - T_o\{\alpha s_6 + (1-\alpha)s_2 - s_3\}] \tag{35}$$

$$\text{Heat exchanger}: \quad E_{xD,HE} = \frac{Q_1}{(T_x - T_y) \times \{(T_x - T_y) - T_o \times \ln\frac{T_x}{T_y}\}} - m_w\{(h_a - h_8) - T_o(s_a - s_8)\} \tag{36}$$

6. Results and discussions

A detailed study of availability of solar-biomass resources for hybrid power plant with energy analysis of hybrid power plant are carried out in this paper. A 5 MW hybrid solar-biomass power plant has been analyzed for Gurugram region of Delhi, India. The geographical parameters of this region is given in Table 3.

The low level of DNI in the month of January, July, August, September and December is observed. Fig. 6 represents monthly average utilization of heat gain from solar and biomass. It is seen that, in the month of November solar radiation decreases compared to May due to cosine effect (Desai et al., 2014). The PTC field will heat the heat transfer fluid and pump to the receiver depending upon the availability of DNI (i.e. 20%, 40%, 60% & 80%) and remaining heat will come from biomass boiler (i.e. 80%, 60%, 40% & 20%) for making steam at superheated condition. Condition of various state points of the system are given in Table 4.

The parametric study of the system has been carried out to simulate the network output, energy efficiency, exergy efficiency by varying various input parameters such as DNI, condenser pressure, boiler pressure and turbine inlet temperature. Fig. 7 shows the energy and exergy efficiency of the PTC field as a function of DNI. It is seen that, with increasing of DNI the energy efficiency increases from 26.1% to 49.2% and exergy efficiency increases from 30.15% to 36.2%. Fig. 8 shows that, when condenser pressure is raised from 0.06 bar to 0.15 bar, the energy efficiency decreases from 23.68% to 21.81%, exergy efficiency decreases from 26.66% to 24.43% and turbine work is also decreases from 5.23 MW to 4.82 MW. Turbine inlet temperature variation affects the energy efficiency, exergy efficiency and turbine work of the system as shown in Fig. 9. It is seen that as turbine inlet temperature increases from 300 °C to 600 °C energy efficiency increases linearly from 17.29% to 27.08%, exergy efficiency increases linearly from 24.27% to 26.64% and turbine work increases from 3.83 MW to 5.64 MW. This figure clearly indicates that, the energy & exergy efficiencies are tending to match each towards at 600 °C. Fig. 10 shows the energy and exergy efficiency with respect to boiler pressure at various boiler temperature (400, 450 and 500 °C). The energy efficiency increases slightly from 19.15% (40 bar, 400 °C) to 22.66% (60 bar, 500 °C) with pressure which is not appreciable as per added cost in equipment to increase the boiler pressure. The pressure 60 bar and temperature of 500 °C has been considered as the optimum of the given cycle under the design conditions for hybrid solar thermal power plant. The profile of exergy efficiency follow the same trend as energy efficiency against boiler pressure at these three turbine inlet temperature.

The energy losses and exergy destruction of the major components of the hybrid system is given in Fig. 11. It is seen that the heat energy (PTC and biomass boiler) input is highly efficient in energy losses whereas largest losses occur in the solar PTC and biomass boiler in the exergy destruction.

7. Conclusion

The state wise availability of solar-biomass resources for hybrid thermal power generation and its thermodynamic evaluation are analyzed to identify the effects of various parameters. The hybrid

solar-biomass power plant is an extremely promising energy system and is likely to provide a major share of renewable bulk electricity production. Taking in view, government of India is making biomass policy to minimize the biomass feed stock in the hybrid power plant for establishing the market. Apart from financial benefits to the promoters of these projects, the society will also be benefited due to intangible advantages such as employment generation in rural areas, environmental benefits, and distributed power generation. The potential estimated for power generation from the present surplus biomass could be further increased with development of technology and consequent increase in hybrid solar-biomass conversion efficiencies. Further, intensive cultivation of waste and marginal lands for energy crops, with use of advanced plantation techniques, could enable the country to increase its hybrid power potential even more. In the light of these possibilities that government of India has been promoting hybrid solar-biomass based power generation for enhancing indigenous capability in this area.

Acknowledgement

The Authors express their deep gratitude to Shri. S.K. Singh, Scientist 'G', Advisor, National Institute of Solar Energy, Ministry of New and Renewable Energy, Government of India for assisting in identifying and formulating the research problem. His valuable suggestion and advice gave us the confidence to overcome the challenges in formulation of this manuscript.

References

A Compendium of Research, Development and Demonstration Projects, 2014 <http://mnre.gov.in/file-manager/UserFiles/MNRE-Compendium-Book-of-R&D-2014>.
AREVA Solar Power Projects India. AREVA <http://www.reliancepower.co.in/business_areas/initiatives_in_renewable_energy.htm>.
ASME, Steam Generating Unit. ASME/ANSI Standard PTC 4.1:1974, Reaffirmed 1991, New York.
Asthana, Arvind Kumar, 2009. Biomass as a Fuel on Small Boiler. Asian Productivity Organization, Tokyo.
Basu, P., 2006. Combustion and Gasification in Fluidized Beds. CRC Press, USA.
Beerbaum, S., Weinrebe, G., 2000. Solar thermal power generation in Indiad – a techno–economic analysis. Renewable Energy 21 (2), 153–174.
Bejan, A., Kearney, D.W., Kreith, F., 1981. Second law analysis and synthesis of solar collector systems. J. Sol. Energy Eng. 103, 23–28.
Bio Power, India, 2014. MNRE-UNDP/GEF Biomass Power Project. 1(3):11–14.
Casati, E., Casella, F., Colonna, P., 2015. Design of CSP plants with optimally operated thermal storage. Sol. Energy 11, 371–387.
Dai, Y.P., Wang, J.F., Gao, L., 2009. Exergy analysis, parametric analysis and optimization for a novel combined power and ejector refrigeration cycle. Appl. Therm. Eng. 29, 1983–1990.
Department of Resources Energy and Tourism, 2013. Pathway to Solar Thermal for Coal-fired Collinsville. Canberra, 20-February-2013.
Desai, N.B., Bandyopadhyay, S., Nayak, J.K., Banerjee, R., Kedare, S.B., 2014. Simulation of 1 MW solar thermal power plant. Energy Procedia 57, 507–516.
Dincer, I., Rosen, M.A., 2007. Exergy: Energy, Environment and Sustainable Development. Elsevier, Oxford.
Directorate of Economics and Statistics, 2012-13. Department of Agriculture & Cooperation <http://agricoop.nic.in>.
Duffie, J.A., Beckman, W.A., 1991. Solar Engineering of Thermal Processes. John Wiley & Sons, New York, Brisbane, USA.
eSolar Solar Thermal Projects, Bikaner <http://www.esolar.com/projects/bikaner/>.
Gordillo, E.D., Belghit, A., 2011. A downdraft high temperature steam-only solar gasifier of biomass char: a modelling study. Biomass Bioenergy 35, 2034–2043.
Goswami, D.Y., Kreith, F., Kreider, J.F., Kreith, F., 2000. Principles of Solar Engineering. Taylor & Francis, Philadelphia, PA.
Gupta, M.K., Kaushik, S.C., 2010. Exergy analysis and investigation for various feed water heaters of direct steam generation solar-thermal power plant. Renewable Energy 35, 1228–1235.
Hepbasli, A., 2008. A key review on exergetic analysis and assessment of renewable energy resources for a sustainable future. Renew. Sustain. Energy Rev. 12, 593–661.
Hoshi, A., Mills, D.R., Bittar, A., Saitoh, T.S., 2005. Screening of high melting point phase change materials (PCM) in solar thermal concentrating technology based on CLFR. Sol. Energy 79 (3), 332–339.
International Energy Agency (IEA), 2014. World Energy Outlook 2014: WEO2014, Paris.
Initiatives in Renewable Energy. Reliance Power <http://www.reliancepower.co.in/business_areas/initiatives_in_renewable_energy.htm>.
IS 13979:1994, Reaffirmed 1999. Method of Calculation of Efficiency of Packaged Boilers. BIS, New Delhi.
Kalogirou, Soteris A., 2004. Solar thermal collectors and applications. Prog. Energy Combust. Sci. 30, 231–295.
Kalogirou, Soteris A., 2009. Solar Energy Engineering: Process and Systems. Elsevier.
Kaushik, S.C., Misra, R.D., Singh, N., 2000. Second law analysis of a solar thermal power system. Int. J. Solar Energy 20, 239–253.
Kaushik, S.C., Abhyankar, Y.P., Bose, S., Mohan, S., 2001. Exergoeconomic evaluation of a solar thermal power plant. Int. J. Solar Energy 21 (4), 293–314.
Kaushik, S.C., Siva Reddy, V., Tyagi, S.K., 2011. Energy and exergy analysis of thermal power plants: a review. Renew. Sustain. Energy Rev. 15, 1857–1872.
Kaushika, N., Mishra, A., Chakravarty, M., 2005. Thermal analysis of solar biomass hybrid co-generation plants. Int. J. Sustain. Energ. 24 (4), 175–186.
Kosugi, T., Pak, P.S., 2003. Economic evaluation of solar thermal hybrid H_2O turbine power generation systems. Energy 28 (3), 185–198.
Kotas, T.J., 1995. The Exergy Method of Thermal Plant Analysis. Krieger Publishing, New York.
Kotowicz, J., Sobolewski, A., Iluk, T., 2013. Energetic analysis of a system integrated with biomass gasification. Energy 52, 265–278.
Larson, E.D., 2001. A review of biomass integrated gasifier/gasturbine combined cycle technology and its application in sugarcane industries, with an analysis for Cuba. Energy Sustain. Dev. 5, 54–76.
Lu, J.F., Ding, J., Yang, J.P., 2010. Heat transfer performance and exergetic optimization for solar receiver pipe. Renewable Energy 35, 1477–1483.
Ministry of Power, Govt. of India, 2016. Central Electricity Authority: Monthly All India Installed Power Generation <http://www.cea.nic.in/reports/monthly/installedcapacity/2016/installed_capacity-07.pdf>.
Montes, M.J., Abánades, A., Martínez-Val, J.M., 2009. Performance of a direct steam generation solar thermal power plant for electricity production as a function of the solar multiple. Sol. Energy 83 (5), 679–689.
Morell, D., 2012. CSP BORGES. The World's First CSP plant hybridized with biomass. In: CSP Today USA 2012–6th Concentrated Solar Thermal Power Conference.
Morell, D., 2012. CSP BORGES the World's First CSP plant hybridized with biomass. In: CSP Today USA 2012–6th Concentrated Solar Thermal Power Conference.
Morin, G., Dersch, J., Platzer, W., Eck, M., Häberle, A., 2012. Comparison of linear Fresnel and parabolic trough collector power plants. Sol. Energy 86 (1), 1–12.
Nixon, J.D., Dey, P.K., Davies, P.A., 2012. The feasibility of hybrid solar–biomass power plants in India. Energy 46 (1), 541–554.
Novatec Solar GmbH, 2012 Novatec Solar's Australian Fuel-saver Commences Operation [Online]. Available <http://www.transfield.com.au/mediareleases/20121024_Novatec%20Solar%20Australian%20Fuel%20Saver%20Commences%20Operation.pdf>.
Concentrating Solar Power Project. NREL <http://www.nrel.gov/csp/solarpaces/by_countrydetail.cfm/country=IN>.
Perez, A., Torres N., 2010. Solar parabolic trough – biomass hybrid plants: a cost–efficient concept suitable for places in low irradiation conditions. In: Solar Paces Conference.
Petela, R., 2013. Exergy analysis of solar radiation, (Chapter 2). In: Enteria, N., Akbarzadeh, A. (Eds.), Solar Thermal Sciences and Engineering Applications. CRC Press, Taylor & Francis Group.
Peterseim, J.H., Tadros, A., White, S., Hellwig, U., Landler, J., Galang, K., 2013. Solar tower-biomass hybrid plants – maximizing plant performance. Energy Procedia 49, 1197–1206.
Protermosolar, 2012. Abantia and Comsa Emte Set up the First Facility in the World That Combines Solar Thermal and Biomass Energy <http://www.protermosolar.com/saladeprensa/?q1/4en/content/abantia-and-comsaemte-set-first-facility-world-combines-solar-thermal-and-biomass-energy>.
Ravaghi-Ardebili, Z., Manenti, F., Corbetta, M., Pirola, C., Ranzi, E., 2015. Biomass gasification using low-temperature solar-driven steam supply. Renewable Energy 74, 671–680.
Renewable Energy Investment, 2015. 1st Renewable Energy Global Investors Meet and Expo India <http://www.re-invest.in>.
Road Map for Biomass Energy Report: Scaling up Biomass Based Power Generation. MNRE, 2011, pp. 3–37.
Sahoo, U., Kumar, R., Pant, P.C., Chaudhury, R., 2015. Scope and sustainability of hybrid solar–biomass power plant with cooling, desalination in polygeneration process in India. Renew. Sustain. Energy Rev. 51, 304–316.
Singh, N., Kaushik, S.C., Misra, R.D., 2000. Exergetic analysis of a solar thermal power system. Renewable Energy 19, 135–143.
Solar Radiation Energy over India, 2008. Indian Meteorological Department and Ministry of New and Renewable Energy. Govt. of India.
Solar Radiation Energy over India, 2008. Indian Meteorological Department and Ministry of New and Renewable Energy. Govt. of India. <http://mnre.gov.in/file-manager/User Files/solar _radiant_energy_over_India.pdf>.
Solar Resource Assessment Based on Satellite Imagery (SEC-NREL Project), 2013 <http://www.nrel.gov/international/ra_india.html>.
Spelling, J., Laumert, B., Fransson, T., 2013. Advanced hybrid solar tower combined-cycle power plants. Energy Procedia 49, 1207–1217.
Sukhatme, S.P., Nayak, J.K., 2008. Solar Energy: Principles of Thermal Collection and Storage. Tata McGraw-Hill Education, New Delhi.
Szargut, J., 2005. Exergy Method: Technical and Ecological Applications. WIT Press, UK.

Triathi Arun, K., Iyer, P.V.R., Kandpal, T.C., Singh, K.K., 1998. Assessment of availability and cost of some agricultural residues used feedstock for biomass gasification and briquetting in India. Energy Convers. Manage. 39, 1611–1618.
Tzivanidis, C., Bellos, E., Korres, D., Antonopoulos, K.A., Mitsopoulos, G., 2015. Thermal and optical efficiency investigation of a parabolic trough collector. Case Stud. Therm. Eng. 6, 226–237.
Wittmann, M., Eck, M., Pitz-Paal, R., Müller-Steinhagen, H., 2011. Methodology for optimized operation strategies of solar thermal power plants with integrated heat storage. Sol. Energy 85, 653–659.
www.mnre.gov.in. Ministry of New and Renewable Energy, Govt. of India.

IOPscience iopscience.iop.org

Home Search Collections Journals About Contact us My IOPscience

Revised and extended calculations of level energies, M1 and E2 radiative rates for highly charged tungsten ions from W^{57+} to W^{60+}

This content has been downloaded from IOPscience. Please scroll down to see the full text.

2016 J. Phys. B: At. Mol. Opt. Phys. 49 205002

(http://iopscience.iop.org/0953-4075/49/20/205002)

View the table of contents for this issue, or go to the journal homepage for more

Download details:

IP Address: 14.139.251.107
This content was downloaded on 17/10/2016 at 05:34

Please note that terms and conditions apply.

You may also be interested in:

Extreme ultraviolet and soft x-ray spectral lines in Rb XXIX
Indu Khatri, Arun Goyal, Sunny Aggarwal et al.

M1 and E2 transitions in Ar II
B Saha and S Fritzsche

A theoretical survey of atomic structure and forbidden transitions in the 4pk and 4dk ground configurations of tungsten ions W29+ through W43+
Pascal Quinet

Review of highly charged tungsten spectroscopy research using low energy EBITs at the Shanghai EBIT laboratory
M L Qiu, W X Li, Z Z Zhao et al.

Energy levels and transition rates for Mg-like Kr XXV
R Si, X L Guo, J Yan et al.

Towards accurate transition data for E2 and M1 transitions
Charlotte Froese Fischer

IOP Publishing Journal of Physics B: Atomic, Molecular and Optical Physics
J. Phys. B: At. Mol. Opt. Phys. **49** (2016) 205002 (8pp) doi:10.1088/0953-4075/49/20/205002

Revised and extended calculations of level energies, M1 and E2 radiative rates for highly charged tungsten ions from W^{57+} to W^{60+}

Gajendra Singh and Nitin K Puri

Department of Applied Physics, Delhi Technological University, Bawana Road, Delhi-110042, India

E-mail: nitin.phy@dce.edu

Received 18 March 2016, revised 20 July 2016
Accepted for publication 9 August 2016
Published 5 October 2016



Abstract

We have applied systematically enlarged multiconfiguration Dirac–Fock wavefunctions using Grasp2K to calculate the transition energies, oscillator strengths and transition probabilities for fine structure M1 and E2 transitions between the low-lying levels of the $3s^23p^5$, $3s^23p^4$, $3s^23p^3$ and $3s^23p^2$ configurations of highly charged tungsten ions from W^{57+} to W^{60+}. Large wavefunction expansions are applied to calculate the transition probabilities, which are indispensable for calculating various plasma parameters accurately. In the present calculations, our theoretical data agrees well with that obtained in precise electron beam ion trap measurements, and is therefore important for the identification of weak forbidden lines for plasma diagnostic applications.

Keywords: atomic data, forbidden transitions, transition energies, plasma diagnostics

(Some figures may appear in colour only in the online journal)

1. Introduction

Existing tokamaks like the Joint European Torus (JET) are capable of surpassing solar temperatures, reaching 2.3×10^8 K, which is an order of magnitude hotter than the center of the Sun, i.e. 1.5×10^7 K [1]. The upcoming tokamak, ITER (a Latin word which means, 'the way') is the first of its kind that will be able to maintain such a fusion reaction for longer than the JET confinement time of 30 s. To withstand such extreme temperatures and pressures, tungsten is used to coat divertor region at ITER because it has better refractory characteristics than the previously used carbon fiber composites (CFCs) [2].

Tungsten is preferred because the ejected ions from the entrapped plasma also ablate materials from the protective tiles on the walls, polluting the plasma. Furthermore, the eroded tungsten atoms serve as impurity ions which are in turn used in the passive spectroscopy of the ITER plasma [3]. In passive spectroscopic studies, these tungsten impurity ions are the source of radiation in the x-ray [4], extreme ultraviolet (EUV) and ultraviolet (UV) region belonging to the various charge states, and this radiation is studied by placing a suitable spectrometer in the proper line of sight of the plasma [5, 6]. Experimental studies have detected the presence of many different charge states of impurity ions in the plasma. This in turn provides the motivation for the theoretical studies of the various charge states of tungsten ions necessary for the proper modeling of plasma, encompassing electron temperature, electron density, ion temperature, ion transport and diffusion as well as the bulk plasma motion [7–11]. The presence of highly charged tungsten in a fusion plasma is both advantageous and detrimental due to the heavy power loss caused by it in the form of radiation. Thus, in order to monitor the power losses due to these impurity ions in the plasma it is necessary to be aware of the abundance of all the charge states of tungsten. To do this, accurate atomic data of all the charge states of tungsten ions is required [12].

While performing spectroscopic studies of tungsten for diagnostic purposes, special focus is put on the identification of forbidden lines, because as compared to the allowed transitions these lines are very weak, and can thus be used for ion abundance calculations [33]. The forbidden lines observed in the Axially Symmetric Divertor Experimental reactor (ASDEX) tokamak plasma by Putterich *et al* [7], during their W spectra modeling studies for ITER, are

 © 2016 IOP Publishing Ltd Printed in the UK

severely blended for the $\triangle n = 0$ transitions in the W^{57+} to W^{60+} ions; thus, theoretical calculations by atomic structure code are important for these lines. Such theoretical studies are used to estimate the fractional abundance of the different charge states of W [13]. Such studies confirm that emission from Cr-like W^{50+} to C-like W^{68+} is capable of providing information about tungsten from the mid-radius to the centre of ITER. In carrying out similar vital studies, accurate atomic data in terms of the transition energies of low-lying levels and M1, and the E2 forbidden transition probability among the levels belonging to the ground configuration are of prime importance.

Considering the importance of these charge states, i.e. Cr-like W^{50+} to C-like W^{68+}, the present work intends to calculate this relevant atomic data for low-lying levels of the $3s^23p^5$, $3s^23p^4$, $3s^23p^3$ and $3s^23p^2$ configurations of highly charged tungsten ions from W^{57+} to W^{60+} by multi-configuration Dirac–Fock calculations using the latest 2013 updated version of the Grasp2K code [14–16]. In this paper, we extend the transition rate calculations undertaken in the past [17] on the lowest excited levels of tungsten, and special emphasis is put on the calculations of the forbidden transitions, i.e. M1 and E2. Some of these transitions have not been reported in work done in the past [31–46]. As more than 80 forbidden lines in tungsten ions from W^{28+} to W^{60+} are known from experimental measurements [18], our work intends to carry out the theoretical calculations from W^{57+} to W^{60+}. Another reason for studying the forbidden transition is that with an increase in ion charge, the probabilities of such transitions show a very strong increase, while the the collisional damping of the spectral lines becomes less effective due to a decrease of cross sections. As a result, forbidden lines are more prominent in multiply charged ion spectra, and this demands large-scale computational work—like the present one—to assist experimentalists in the proper identification of these forbidden lines. We hope that this data will primarily be useful for the diagnostic studies of ITER plasma as well as for EBIT and other experimental reactor experiments for the clearer and more confident identification of these forbidden lines in the future [19–22].

2. Theoretical approach

Tungsten is a high Z element and the ions under study are very highly charged, i.e. from W^{57+} to W^{60+}; so, to incorporate most of the correlation and relativistic effects [23, 24] in the calculations, the multiconfiguration Dirac–Fock (MCDF) method developed by Grant and co-workers [25, 26] is ideal for this purpose. Here, this approach is followed by using the latest version of the general purpose relativistic atomic structure package, Grasp2K [16]. We used the Grasp2k package because it implements a completely *ab initio* and fully relativistic method, applicable, in principle, to any atomic system ranging from negative to highly positively charged ions. This package implements the MCDF method in which an atomic state is approximated by the superposition of the configuration state functions (CSFs) of the same symmetry

$$\Psi_\alpha = \sum_{r=1}^{n_c} c_r(\alpha)|\gamma_r PJM\rangle. \quad (1)$$

In the above equation, the basis function is systematically enlarged by using the well-known active space method to capture most of the correlation and relativistic effects [27]. In the active space method, the configuration state functions of a particular parity and symmetry are generated by substitutions from a reference configuration to an active set of orbitals [28]. The major difference between the various relativistic computations concerns the number of CSFs. The size of the wavefunction expansions typically reflects the extent to which electron correlations are taken into account, but one still has to be very cautious while adding the correlation layers and trying to capture the maximum atomic structure properties—including relativistic effects with reasonable numbers of CSFs. In Grasp2k, the CSFs are the anti-symmetrized products of a common set of orthonormal orbitals which are optimized self-consistently on the basis of the Dirac–Coulomb Hamiltonian. Further relativistic corrections to the electron–electron interaction are added in a second step by diagonalizing the Dirac–Coulomb–Breit Hamiltonian matrix [28].

3. Computational details

In our calculations, the spectroscopic orbitals are generated by considering the ground state configurations $3s^23p^2$, $3s^23p^3$, $3s^23p^4$ and $3s^23p^5$ for W^{60+}, W^{59+}, W^{58+} and W^{57+} respectively. Thereafter, to include the correlation effects virtual orbitals were generated in four steps, and at each step the virtual set was extended by one layer of virtual orbitals. In the present paper, five layers of virtual orbitals each from the p, d, f, g, h symmetries were generated. At each step, while performing the configuration expansions, a first SDTQ (single, double, triple and quadrupole) excitation is carried out on the 3l shells, and then (single and double) SD substitutions from the valence shells to all the new orbitals and previously generated virtual layers are carried out. While applying such an SD and SDTQ approximation, all the newly generated orbitals are made orthogonal to others of the same symmetry. The initial shapes of the radial orbitals were obtained in the Thomas–Fermi potential, and for virtual orbitals screened hydrogenic potentials are used. Once all the radial orbitals are obtained they all are made to converge by keeping the self-consistency threshold set at 10^{-7} s^{-1}. All the radial orbitals were separately optimized for each of the four atomic states of interest.

After insuring the proper convergence with the subsequent addition of correlation layers i.e. 3l, 4l, 5l and 6l, we observed that our level energies were quite reliable—as shown in the convergence plot for W^{58+}—and a similar trend of convergence is also obtained for other ions. Here, we have plotted the level energy against the correlation layers, and as expected we obtained a straight line as the correlation layers

Table 1. The excitation level energies of $3p^2$, $3p^3$, $3p^4$ and $3p^5$ ground configurations.

Ions	J/P	This work (1000) cm^{-1}	NIST (1000) cm^{-1}	$\partial E(\%)$	Prev. work [29] (1000) cm^{-1}
$3p^2$	0+	0	0	0	0
	1+	2807.69	[2802]	0.20	2806.4
	2+	2883.07	2885.5	−0.08	2882.7
	2+	5747.68	[5736]	0.20	5746.7
	0+	5912.9	[5894]	0.32	5913.9
$3p^3$	3/2-	0	0	0.00	0
	3/2-	2755.42	[2750]	0.20	2754
	5/2-	2850.76	2848.3	0.09	2850
	1/2-	2975.04	[2965]	0.34	2976
	3/2-	5745.04	[5726]	0.33	5744
$3p^4$	2+	0	0	0.00	0
	0+	159.96	[153]	0.03	161.53
	1+	2801.6			2801.2
	2+	2879.13			2879.4
	0+	4077.87			5740.4
$3p^5$	3/2-	0	0	0.00	0
	1/2-	2806.44	[2796]	0.00	2806.4

were added one after another. Along with this, the uncertainty in the level energies has also been calculated as suggested by Charlotte Froese Fischer (2014) [47] using the following equation:

$$\partial E = \frac{E\,(\text{cal.}) - E\,(\text{obs.})}{E\,(\text{obs.})} \tag{2}$$

and the reliability of the transition energies or line strengths is checked by looking at the agreement of the velocity gauge and the length gauge. A simpler and more effective way of doing this is suggested by the same above author in [48] using the equation below:

$$\partial S = \frac{S\,(\text{length}) - S\,(\text{velocity})}{\max\,(S\,(\text{length}),\, S\,(\text{velocity}))}. \tag{3}$$

4. Results and discussion

4.1. Energy levels

Our results are listed in table 1, where we calculated the level energies of the $3p^2$, $3p^3$, $3p^4$ and $3p^5$ ground-level configurations. Here, we compared the results of the level energies with the existing computations [29] and NIST compilations [50], as shown in figure 1. We can see that the level energies overlap with the present work, the NIST levels and previous computations, except at one point in W^{58+}, where the most excited (0+) level in our computation is [4077.87 ×1000 cm^{-1}] against the previous computed value [5750.4 ×1000 cm^{-1}]. However, it is expected that for highly charged ions such as those considered here, the fully relativistic MCDF approach used in this work will be more appropriate, and consequently more accurate, than the pseudo-relativistic Hartree–Fock approximation used by Kramida and Shirai (2009). In the $3p^2$ ground configuration, we reported level energies which are close to the NIST values under 0.30 of ∂E (%). In the $3p^3$ ground configuration, all the computed ground levels match the NIST values under 0.35 of $\partial E(\%)$. It can also be observed in the $3p^3$ ground configurations that except the (5/2-) level, all the reported NIST values are extrapolated (values in square brackets), so our Grasp2k computed values can be used for further level energy studies. In the $3p^4$ ground configuration, NIST reported two (2) levels out of five (5) levels belonging to the ground configurations, while we report here that the computed values for all the levels belonging to the ground configuration, which match the previous computed values for the (0+), (1+) and (2+) levels—except for the most excited (0+) level where our value is [4077.87 ×1000 cm^{-1}] against the previous computed value [5750.4 ×1000 cm^{-1}]. To check the reliability of our level energy, we checked the convergence pattern with each added correlation layer, as shown in figure 2. In this plot we see that a good convergence for W^{58+} is achieved by the inclusion of an extra correlation layer of 6l orbitals, which is attributed to the achievement of better accuracy compared to the 5l correlation layers included in previous work [29].

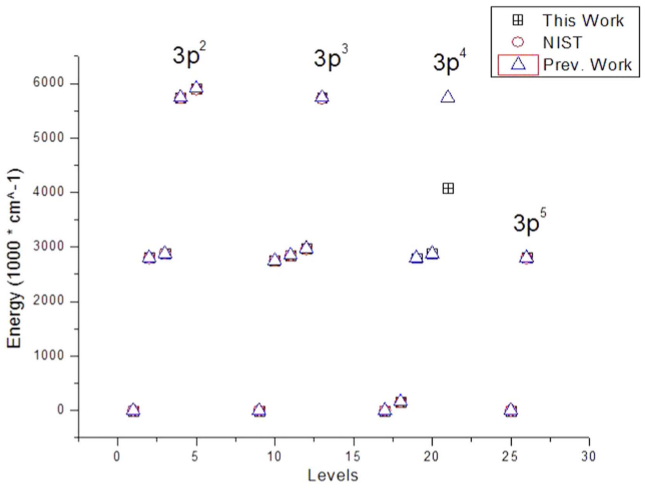


Figure 1. A comparison of the presently computed level energies with NIST and previous computations.

When a systematic procedure of the active space method is applied, like the one we used in these calculations, the size of the atomic state wavefunction becomes larger and larger. The results from such a procedure can be analyzed for convergence, as shown in figure 2 for W^{58+}, and similar trends obtained for other ions. Here, we have plotted the level energy against the correlation layers, and as expected we obtained a straight line as the correlation layers are added one after another. The calculated uncertainties $\partial E(\%)$ for these level energies are well within the limits being considered, which imparts confidence in the method of computation applied to get these values.

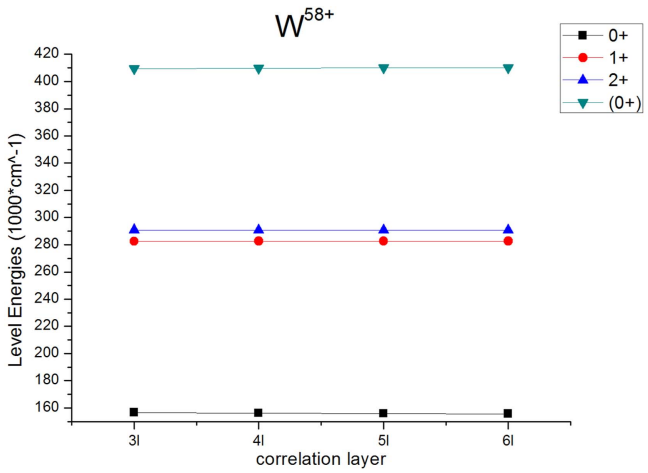


Figure 2. A plot of the obtained level energies of the W^{58+} ion with the subsequent addition of correlation layers.

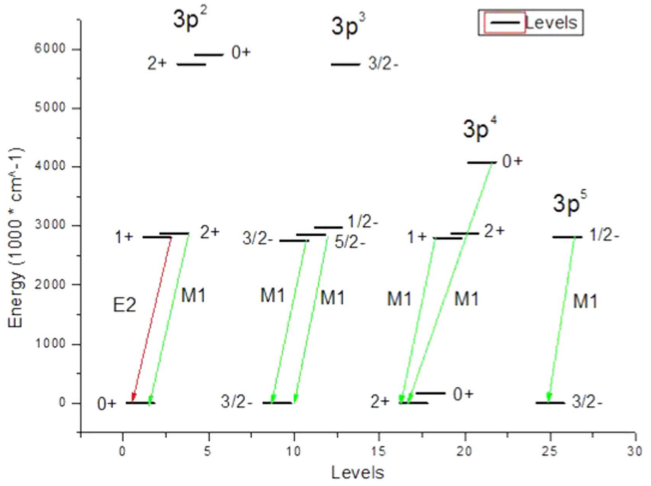


Figure 3. A GR-plot of the obtained level energies and E2 and M1 transitions between them.

4.2. M1 transition rates

In table 2, the transition probabilities and oscillator strength have been calculated for selected forbidden (M1) transitions between the above-mentioned levels of the ground configurations of tungsten. Here, we only report the fine structure forbidden (M1) transition between the ground states, because a similar transition between the first excited and ground state are observed to be very weak, resulting in shorter wavelengths beyond the spectral resolution limits of available spectroscopic instruments [30]. We compared our results with the similar previous calculations performed in [29], where the M1 and E2 transitions are reported simultaneously. So, we decided to report both types of transitions explicitly, as this is actually an important requirement for plasma modeling studies. However, it seems that both the values agree well—except at one place in W^{58+} from the $3p^4$ [0+] upper level to the $3p^4$ [1+] lower level. This difference may have been caused by a partially filled M-shell and an open shell structure, which are the primary source of such anomalies. As a result, further theoretical investigation on such M1 lines is needed. In table 4, using equation (4), we calculated some selected wavelengths which have also been previously reported in experiments by Thomas Lennartsson *et al* [34]. Our computed wavelengths matched those of the experimentally observed results under 0.30%, imparting confidence in our present computations. We have also shown these transitions in the Grotrian diagram in figure 3. The M1 line studies are important because the intensity ratios for lines from different ions can conveniently serve as the diagnostics of electron temperature and ionization balance calculations. Another advantage of M1 lines is that the spectral window for these lines is rather narrow, which reduces the dependence of

Table 2. The M1 forbidden transitions within the $3p^2$, $3p^3$, $3p^4$ and $3p^5$ ground configurations of tungsten.

Ions	Upper level	Lower level	$\triangle E$ (1000) cm^{-1}	A_{ij} (s^{-1})	gf	S	A_{ij} (prev.) [29] (s^{-1})
W^{60+}	$3p^2$ [0+]	$3p^2$ [1+]	3105.21	4.83(8)	7.51(−5)	5.98(−1)	4.84(8)
	$3p^2$ [2+]	$3p^2$ [1+]	2939.99	2.13(8)	1.85(−4)	1.55(0)	2.17(8)
	$3p^2$ [2+]	$3p^2$ [2+]	2864.61	2.09(8)	1.91(−4)	1.65(0)	2.17(8)
	$3p^2$ [1+]	$3p^2$ [0+]	2807.69	2.65(8)	1.51(−4)	1.33(0)	2.65(8)
W^{59+}	$3p^3$ [3/2−]	$3p^3$ [3/2−]	2989.62	4.39(8)	2.94(−4)	2.43(0)	4.43(8)
	$3p^3$ [1/2−]	$3p^3$ [3/2−]	2975.04	2.20(8)	7.47(−5)	6.21(−1)	2.28(8)
	$3p^3$ [3/2−]	$3p^3$ [5/2−]	2894.28	1.07(8)	7.66(−5)	6.54(−1)	1.20(8)
	$3p^3$ [5/2−]	$3p^3$ [3/2−]	2850.76	6.53(7)	7.23(−5)	6.27(−1)	7.30(7)
	$3p^3$ [3/2−]	$3p^3$ [1/2−]	2770.00	9.52(7)	7.44(−5)	6.64(−1)	9.74(7)
	$3p^3$ [3/2−]	$3p^3$ [3/2−]	2755.42	3.82(8)	3.01(−4)	2.70(0)	3.84(8)
W^{58+}	$3p^4$ [0+]	$3p^4$[1+]	1276.27	1.11(2)	1.02(−10)	1.98(−6)	8.43(8)
	$3p^4$[2+]	$3p^4$[2+]	2879.13	2.01(8)	1.81(−4)	1.56(+0)	2.09(8)
	$3p^4$[1+]	$3p^4$[2+]	2801.60	3.27(8)	1.87(−4)	1.65(+0)	3.33(8)
	$3p^4$[1+]	$3p^4$[0+]	2641.64	1.14(8)	7.39(−5)	6.92(−1)	1.14(8)
W^{57+}	$3p^5$ [1/2−]	$3p^5$ [3/2−]	2806.44	3.84(8)	1.46(−04)	1.28(0)	3.95(8)

Table 3. The E2 forbidden transitions within the $3p^2$, $3p^3$, $3p^4$ and $3p^5$ ground configurations of tungsten.

Ions	Upper level	Lower level	$\triangle E$ (1000) cm^{-1}	A_{ij} (s^{-1}) l form	gf l form	S v form	S l form	$\partial S(\%)$
W^{60+}	$3p^2$ [0+]	$3p^2$ [2+]	3029.83	1.49(7)	2.44(−6)	5.17(−4)	5.23(−4)	1.15
	$3p^2$ [2+]	$3p^2$ [0+]	2883.07	4.60(6)	4.14(−6)	1.02(−3)	1.03(−3)	0.97
W^{59+}	$3p^3$ [3/2−]	$3p^3$ [3/2−]	2989.62	2.69(6)	1.81(−6)	4.00(−4)	4.03(−4)	0.74
	$3p^3$ [1/2−]	$3p^3$ [3/2−]	2975.04	6.76(6)	2.29(−6)	5.12(−4)	5.18(−4)	1.16
	$3p^3$[3/2−]	$3p^3$ [5/2−]	2894.28	1.30(7)	9.32(−6)	2.26(−3)	2.28(−3)	0.88
	$3p^3$ [5/2−]	$3p^3$ [3/2−]	2850.76	7.67(6)	8.49(−6)	2.16(−3)	2.18(−3)	0.92
	$3p^3$ [3/2−]	$3p^3$ [1/2−]	2770.00	2.48(6)	1.93(−6)	5.40(−4)	5.43(−4)	0.55
	$3p^3$ [3/2−]	$3p^3$ [3/2−]	2755.42	2.00(6)	1.58(−6)	4.47(−4)	4.50(−4)	0.67
W^{58+}	$3p^4$ [2+]	$3p^3$[0+]	2719.17	1.80(6)	1.82(−6)	5.39(−4)	5.41(−4)	0.37
W^{57+}	$3p^5$ [1/2−]	$3p^5$ [3/2−]	2806.44	1.07(7)	4.07(−6)	1.09(−3)	1.09(−3)	0.00

Table 4. A comparison of our M1 and E2 excitation energies, the wavelengths for the selected transitions with the previous computations and the experiment.

Ions	Initial level	Final level	Type	$\triangle E$ (1000) cm^{-1}	Present (λ) calculation (A)	Expt. (λ) [34] (A)	Previous (λ) [34] calculation (A)
W^{60+}	$3p^2$ [0+]	$3p^2$ [2+]	E2	2883.07	34.671	34.720	34.76 34.69
	$3p^2$ [0+]	$3p^2$ [1+]	M1	2807.69	35.602	35.644	35.648
W^{59+}	$3p^3$ [3/2-]	$3p^3$ [5/2-]	M1	2850.76	35.079	35.109	35.13 35.08
	$3p^3$ [3/2-]	$3p^3$ [3/2-]	M1	2755.42	36.257	36.323	36.42 36.31
W^{58+}	$3p^4$[2+]	$3p^4$[2+]	M1	2879.13	34.724	34.779	34.735
	$3p^4$[2+]	$3p^4$[1+]	M1	2801.6	35.665		35.708
W^{57+}	$3p^5$[3/2-]	$3p^5$[1/2-]	M1	2806.44	35.557	35.668	35.635

spectrometer efficiency on wavelength [30].

$$A_{ji} = \frac{2.6974 \times 10^{13}}{\omega_j \lambda_{ji}^3} S \quad \text{and} \quad f_{ji} = \frac{4.044 \times 10^{-3}}{\omega_i \lambda_{ji}} S \quad (4)$$

It is also important to note that we can only interpret the results of higher order electric transitions (E1, E2) in length and velocity form and the same cannot be done for the higher order magnetic transition (M1, M2). The matrix element is calculated for the magnetic transition (M1) by the usual expansion in pure-coupling basis functions:

$$\langle \gamma J || J(1) + S(1) || \gamma' J' \rangle. \quad (5)$$

Because the basis functions are eigenfunctions of the operator $J(1)$ and $S(1)$, but in the case of $S(1)$ the eigenfunction does not involve radii, integration over the radial variables gives delta-factors in all the quantum numbers n and l; that is, the magnetic dipole matrix is diagonal in configuration. So, in principal, we cannot obtain the length and velocity form, which entirely depends on the radial function. Thus, here we have only calculated the length and velocity form for the E2 transitions and not for the M1 transition.

4.3. E2 transition rates

Some important E2 transition rates are calculated and reported in table 3. These E2 forbidden transitions are important for the ionization balance calculation as these transitions originate from long-lived metastable levels which then effectively act as ground levels from which the ion can reach its next charge state through electron collision [34]. These E2 forbidden transitions did not occur in dense plasma but they are present in low density sources like EBIT and tokamaks between the same levels among which the M1 transition usually occurs. Experimentalists usually report these forbidden transitions as M1+E2, as they are very difficult to resolve; but theoretically it must always be reported distinctly for plasma modeling studies, unlike what has been done in the past [29]. As these lines are used to calculate the diagnostic ratio of ions and electrons in density, so their relevance is essential [35]. Considering the importance of these E2

transition rates, we have optimized the wavefunctions for different J values independently while simultaneous optimization may lead to severe discrepancies. The E2 transition rate varies as $(\triangle E)^5$, so a small change in the transition energy results in a fairly large change in the transition rates. From our transition rate computed tables, we can figure out that the transition probability (A_{ij}) value for the E2 transitions is just two orders less compared to the M1 transition values. As there is a scarcity of experimental data for the E2 transitions, so proper identification work is required for both the M1 and E2 lines between the fine structure levels of the ground configurations. Here, keeping 10^5 s^{-1} as the lower threshold value for transition probability, all E2 transitions between the fine structure levels of the ground configuration are reported. We intend to include these E2 transitions because these lines fall in an important x-ray spectral range in the ITER plasma modeling studies from the mid-radius to the center of the ITER plasma, and they are hardly reported in previous computations [31–46]. Furthermore, to ensure the reliability of these E2 transition values, we also calculated the uncertainties $\partial S(\%)$ using equation (3), where we included the values from both the gauges, i.e. length and velocity form. The values in both the gauges closely match each other

$$A_{ji} = \frac{1.1199 \times 10^{18}}{\omega_j \lambda_{ji}^5} S \quad \text{and} \quad f_{ji} = \frac{167.89}{\omega_i \lambda_{ji}^3} S. \tag{6}$$

Regarding the interpretation of the length and velocity gauge, it is very important to understand that they are the sole parameters for checking the exactness of the obtained wavefunctions during these calculations, before computing the different transition rates, i.e. E1, E2 and M1, M2 etc. To elaborate on this let us consider the simplest electric transition, i.e. the electric dipole (E1) transition. In E1 transitions, the length form and velocity form are written as follows:

Length form: here the average value of r_i for the ion under study is calculated as follows:

$$\langle \gamma JM | \Sigma_i r_i | \gamma' J' M' \rangle. \tag{7}$$

Velocity form: the derivative of the same r_i for the ion is calculated as follows:

$$2(E' - E)^{-1} \langle \gamma JM | \Sigma_i \nabla_i | \gamma' J' M' \rangle. \tag{8}$$

So, in principal both the forms are equivalent when the exact wavefunctions are used, but they usually give rather different results when the approximate wavefunctions are used. In our calculations, adding co-relation layers actually means including an approximation theoretically and obtaining the approximate wavefunctions which are then used to calculate the transition rates. In our calculations, both the length and velocity forms agree well, which in turn imparts confidence in our calculated transition rates.

5. Conclusion

Using the fully relativistic multiconfiguration Dirac–Fock method, a new set of level energies, transition probabilities and oscillator strengths has been obtained for forbidden lines within the $3p^k$ ground configurations of highly charged tungsten ions from W^{57+} to W^{60+}. The presently computed atomic data agrees well with the previous computations along with the experimental values, which actually approves its reliability for further experimental identification in plasma diagnostic studies such as ion and electron temperature, transport properties and bulk plasma movement. The reported M1 and E2 transitions usually appear in the x-ray spectral range of 2 nm to 5 nm for $3p^k$ ground configurations, which is important in plasma study from the mid-radius to the center of the ITER plasma. Special emphasis has been put here on calculating the forbidden transitions, as they are the experimental indicators of the metastable states present in the plasma, which in turn helps the ion to achieve the next charge state. So, the study of these transitions is indispensable for the most important ionization balance calculations in plasma. With our systematically enlarged wavefunctions we are able to provide consistent and accurate data for the weak (M1, E2) forbidden transition in the $3p^2$, $3p^3$, $3p^4$ and $3p^5$ ground configurations of tungsten. The value of the M1 transition in the W^{58+} ion, taking place from the $3p^4$ [0+] upper level to the $3p^4$[1+] lower level, differs from the previous computations [29], which may be attributed to the partially filled M-shell and an open shell structure—these being the primary source of such anomalies. So, to overcome such ambiguity, further theoretical investigation is required to work on such M1 lines, and this will enhance our knowledge and understanding on open shell spectra. In conclusion, the presently revised and extended atomic data for W^{57+} to W^{60+} in this work, especially for forbidden lines, is expected to be useful for plasma diagnostics and modeling studies for future fusion reactors.

Acknowledgments

The work was carried out here under UFR-Project no. 52311, sponsored by the Inter University Accelerator Center (IUAC), New Delhi and Delhi Technological University, Delhi. Most of the computational work here was done at both places, and we are very thankful for the support of the scientific and academic communities of both institutions. The authors are also thankful to DAE-BRNS for providing the financial support in the form of a research project.

References

[1] 2015 Hot times for fusion plasmas *Phys. Today* **68** (10)
[2] Nunes I (on behalf of the JET Contributors) 2016 Plasma confinement at JET *Plasma Phys. Control. Fusion* **58** 014034
[3] Dux R, Peeters A G, Guide A, Kallenbach A, Neu R and Asdex Upgrade Team 1999 Z dependence of the core of impurity transport in ASDEX Upgrade H mode discharges *Nucl. Fusion* **39** 1509
[4] Sabkowska K, Rzadkiewicz J, Syrocki Ł, Szymańska E, Shumack A, Polasik M and Pereira N R JET contributors

2015 On the interpretation of high-resolution x-ray spectra from JET with an ITER-like wall *J. Phys. B: At. Mol. Opt. Phys.* **48** 144028
[5] Clementson J, Beiersdorfer P, Magee E W, McLean H S and Wood R D 2010 Tungsten spectroscopy relevant to the diagnostics of ITER divertor plasmas *J. Phys. B: At. Mol. Opt. Phys.* **43** 144009
[6] Ding X, Liu J, Koike F, Murakami I, Kato D, Sakauec H A, Nakamurad N and Donga C 2016 Collisional-radiative model for the visible spectrum of W^{26+} ions *Phys. Lett.* A **380** 874–7
[7] Putterich T *et al* the ASDEX Upgrade Team and JET EFDA Contributors 2013 Observation on the W-transport in the core plasma of JET and ASDEX upgrade *Plasma Phys. Control Fusion* **55** 124036
[8] Nakano T *et al* N J Conway JET contributors 2015 Determination of tungsten and molybdenum concentrations from an x-ray range spectrum in JET with the ITER-like wall configuration *J. Phys. B: At. Mol. Opt. Phys.* **48** 144023
[9] Słabkowska K, Polasik M, Szymanska E, Starosta J, Syrocki Ł, Rzadkiewicz J and Pereira N R 2014 Modeling of the L and M x-ray line structures for tungsten in high-temperature tokamak plasmas *Phys. Scr.* **T161** 014015
[10] Seely J F *et al* 2013 Tungsten L transition line shapes and energy shifts resulting from ionization in warm dense matter *High Energy Density Phys.* **9** 354–62
[11] Słabkowska K, Szymańska E, Starosta J, Polasik M, Pereira N R, Rzadkiewicz J, Kubkowska M and Czarnecka A 2014 Diagnostics of plasma based on K, L and M x-ray line positions *Phys. Scr.* **T161** 014033
[12] Beiersdorfer P 2015 Highly charged ions in magnetic fusion plasmas: research opportunities and diagnostic necessities *J. Phys. B: At. Mol. Opt. Phys.* **48** 144017
[13] Putterich T, Dux R, Neu R, Whiteford A D and O'Mullane M G the ASDEX Upgrade Team 2008 Modelling of measured tungsten spectra from ASDEX Upgrade and predictions for ITER *Plasma Phys. Control Fusion* **50** 085016
[14] Parpia F A, Fischer C F and Grant I P 2006 A package for large-scale relativistic atomic structure calculations *Comput. Phys. Commun.* **175** 745–7
[15] Jonsson P, Fischer C F and Grant I P 2007 The Grasp2K relativistic atomic structure package *Comput. Phys. Commun.* **177** 597–622
[16] Jonsson P, Gaigalas G, Bieroń J, Fischer C F and Grant I P 2013 New version: Grasp2K relativistic atomic structure package *Comput. Phys. Commun.* **184** 2197–203
[17] Aggarwal K M and Keenan F P 2014 Energy levels, radiative rates, and lifetimes for transitions in WLVIII *At. Data Nucl. Data Tables* **100** 1603–767
[18] Kramida A E, Ralchenko Yu, Reader J and NIST ASD Team 2015 *NIST Atomic Spectra Database* (version 5.3) (Gaithersburg, MD: National Institute of Standards and Technology) available at: http://physics.nist.gov/PhysRefData/ASD/Html/verhist.shtml
[19] Beiersdorfer P, Clementson J and Safronova U I 2015 *Tungsten Data for Current and Future Uses in Fusion and Plasma Science Atoms* **3** 260–72
[20] Biedermann C, Radtke R, Seidel R and Pütterich T 2009 Spectroscopy of highly charged tungsten ions relevant to fusion plasmas *Phys. Scr.* **T134** 014026
[21] Beiersdorfer P, May M J, Scofield J H and Hansen S B 2012 Atomic physics and ionization balance of high-Z Ions: critical ingredients for characterizing and understanding high-temperature plasmas *High Energy Density Phys.* **8** 271–83
[22] Beiersdorfer P, Lepson J K, Schneider M B and Bode M P 2012 L-shell x-ray emission from neon-like W^{64+} *Phys. Rev.* A **86** 012509
[23] Chen M H and Cheng K T 2010 A large-scale relativistic configuration-interaction approach: application to the 4s2-4s4p transition energies and E1 rates for Zn-like Ions *J. Phys. B: At. Mol. Opt. Phys.* **43** 074019
[24] Cheng K T, Chen M H, Johnson W R and Sapirstein J 2008 High-precision relativistic atomic structure calculations and the EBIT: tests of quantum electrodynamics in highly charged ions *Can. J. Phys.* **86** 33
[25] Grant I P, McKenzie B J, Norrington P H, Mayers D F and Pyper N C 1980 A program to calculate transverse Breit and QED corrections to level energies in a multiconfiguration Dirac–Fock environment *Comput. Phys. Commun.* **21** 207
[26] McKenzie B J, Grant I P and Norrington P H 1980 A program to calculate transverse Breit and QED corrections to level energies in a multiconfiguration Dirac–Fock environment *Comput. Phys. Commun.* **21** 233
[27] Grant I P 1988 *Methods in Computational Chemistry. Volume 2 Relativistic Effects in Atoms and Molecules* (New York: Plenum)
[28] Grant I P 2007 *Relativistic Quantum Theory of Atoms and Molecules: Theory and Computation* (*Springer Series on Atomic, Optical, and Plasma Physics* vol 40) (Berlin: Springer)
[29] Quinet P 2011 Dirac–Fock calculations of forbidden transitions within the 3pk and 3dk ground configurations of highly charged tungsten ions (W^{47+} to W^{61+}) *J. Phys. B: At. Mol. Opt. Phys.* **44** 195007
[30] Minoshima M *et al* 2013 Visible transitions of highly charged tungsten ions observed with a compact electron beam ion trap *Phys. Scr.* **T156** 014010
[31] Ralchenko Y, Tan J N, Gillaspy J D and Pomeroy J M 2006 Accurate modeling of benchmark x-ray spectra from highly charged ions of tungsten *Phys. Rev.* A **74** 042514
[32] Ralchenko Y, Draganic I N, Tan J N and Gillaspy J D 2008 EUV spectra of highly charged ions W^{54+} W^{63+} relevant to ITER diagnostics *J. Phys. B.* A **41** 021003
[33] Ralchenko Y, Draganic I N, Osin D, Gillaspy J D and Reader J 2011 Spectroscopy of diagnostically important magnetic-dipole lines in highly charged $3d^n$ ions of tungsten *Phys. Rev.* A **83** 032517
[34] Lennartsson T, Clementson J and Beiersdorfer P 2013 Experimental wavelengths for intrashell transitions in tungsten ions with partially filled 3p and 3d subshells *Phys. Rev.* A **87** 062505
[35] Clementson J, Beiersdorfer P and Gu M F 2010 X-ray spectroscopy of E2 and M3 transitions in Ni-like W *Phys. Rev.* A **81** 012505
[36] Huang K-N 1984 Energy-level scheme and transition probabilities of P-like ions *At. Data Nucl. Data Tables* **30** 313–421
[37] Huang K-N 1985 Energy-level scheme and transition probabilities of Si-like ions *At. Data Nucl. Data Tables* **32** 503
[38] Huang K-N 1986 Energy-level scheme and transition probabilities of Al-like ions *At. Data Nucl. Data Tables* **34** 1
[39] Saloman E B and Kim Y K 1989 Energy levels and transition probabilities in the ground state configuration of sulphur-like ions *At. Data Nucl. Data Tables.* **41** 339–56
[40] Feldman U, Indelicato P and Sugar P 1991 Magnetic dipole line from U LXXI ground-term levels predicted at 3200 Å *J. Opt. Soc. Am.* B **83** 3–5
[41] Feldman U, Doron R, Klapisch M and Bar-Shalom A 2001 Intensity versus electron density of the ultraviolet M1 transition in Xe32+, Gd42+, W52+, Bi61+, and U70+ (Ti-like ions) *Phys. Scr.* **63** 284
[42] Doron R and Feldman U 2001 Visible and near-UV M1 transitions within N-shell ground configurations of heavy ions predicted to be bright in low-density plasmas *Phys. Scr.* **64** 319

[43] Charro E, Curiel Z and Martin I 2002 Atomic data for M1 and E2 emission lines in the potassium isoelectronic sequence *Astron. Astrophys.* **387** 1146
[44] Charro E, Lopez-Ferrero S and Martin I 2003 Trends in E2 and M1 transition rates between $3p_{3/2}$ and $3p_{1/2}$ levels in $3s^2$ 3p k systems *Astron. Astrophys.* **406** 741
[45] Safronova U I, Sataka M, Albritton J R, Johnson W R and Safronova M S 2003 Relativistic many-body calculations of electric-dipole lifetimes, transition rates, and oscillator strengths for $n = 3$ states in Al-like ions *At. Data Nucl. Data Tables* **84** 1–83
[46] Safronova U I and Safronova A S 2010 *J. Phys. B: At. Mol. Opt. Phys.* **43** 074026
[47] Fischer C F 2009 Evaluating the accuracy of theoretical transition data *Phys. Scr.* **T134** 014019
[48] Fischer C F 2014 Evaluation and comparison of the configuration interaction calculations for complex atoms *Atoms* **2** 1–14
[49] Kramida A E 2011 Recent progress in spectroscopy of tungsten *Can. J. Phys.* **89** 551
[50] Kramida A E and Shirai T 2009 Energy levels and spectral lines of tungsten, W III through W LXXIV *At. Data Nucl. Data Tables* **95** 305

Applied Mathematical Modelling 000 (2016) 1–31

Contents lists available at ScienceDirect

Applied Mathematical Modelling

journal homepage: www.elsevier.com/locate/apm

Stability analysis of predator–prey system with migrating prey and disease infection in both species

Shashi Kant*, Vivek Kumar

Department of Applied Mathematics, Delhi Technological University, Formerly Delhi College of Engineering, Main Bawana Road, Shahbad Daulatpur, Delhi 110042, India

ARTICLE INFO

Article history:
Received 12 September 2014
Revised 23 June 2016
Accepted 10 October 2016
Available online xxx

Keywords:
Prey–predator system
Stability
Lotka–Volterra functional response

ABSTRACT

We formulated and studied a predator–prey system with migrating prey and disease infection in both species. We used Lotka–Volterra type functional response. Mathematically, we analyzed the dynamics of the system such as existence of non negative equilibria, their stability. The basic reproduction number R_0 for the proposed mathematical model is calculated. Disease is endemic if $R_0 > 1$. Model is simulated by assuming hypothetical initial values and parameters.

© 2016 Elsevier Inc. All rights reserved.

1. Introduction

After the seminal work of Lotka [1] and Volterra [2] predator–prey study become popular and important research area in applied sciences (population dynamics and mathematical ecology etc.). Similarly, the pioneer work of Kermack–Meckindric [3] opened new door to epidemiology. After the work of Lotka [1], Volterra [2] and Kermack and Meckindric [3] many papers published in literature (for example see [4–8] and references therein) In [4], Maiti et al. studied a ratio dependent prey–predator model and considered the stochastic and deterministic aspects of it. They also studied the effect of delay on the dynamics of the system. They studied four equilibrium points and their stability conditions. They also used bifurcation theory and discuss Hopf bifurcation for the model. Wang et al. [5] considered a delayed stage structured model with stages on prey. They considered delay as the duration of the immature stage of prey population. They analyzed the model in terms of global stability and conclude some important ecological results. Haque et al. [6] proposed and analyzed an eco-epidemiological model by considering standard incidence. They assumed that disease is spreading among prey population. They observed the behavior of the proposed system about all possible equilibria. They also studied the Hopf bifurcation. Haque and Venturino [7] studied a predator–prey model by considering Holling–Tanner functional response. The concepts of control and reconfigurable in reference to prey–predator model has been studied in [8].

Ecology and epidemiology are two different research areas and has its importance its own right. But both areas have many similarities. Keeping this in mind, in recent decades the combined study of ecology and epidemiology has been so important which is termed as eco-epidemiology. Few recent studies are cited here (see [9–12] etc. and references therein). Many authors in literature proposed eco-epidemiological models with disease in the prey only, for example (see [11,13–21] and references cited therein). In [13], Johri et al. studied a Lotka–Volterra type predator–prey model with disease in prey.

* Corresponding author.
E-mail address: onlineskmishra@gmail.com (S. Kant).

http://dx.doi.org/10.1016/j.apm.2016.10.003
0307-904X/© 2016 Elsevier Inc. All rights reserved.

Please cite this article as: S. Kant, V. Kumar, Stability analysis of predator–prey system with migrating prey and disease infection in both species, Applied Mathematical Modelling (2016), http://dx.doi.org/10.1016/j.apm.2016.10.003

They analyzed the model in terms of local and global stability. In [14], Mukhopadhyaya and Bhattacharyya considered a prey predator model with Holling type II functional response and observed the effect of diffusion and delay on the dynamics of the system. They also discussed the role of diffusivity on the stability and persistence of the model. In [15], Greenhalgh and Haque proposed and analyzed a predator prey model with disease in the prey population. Hu and Li proposed and analyzed a three dimensional prey predator delayed model with disease in prey in [16]. They also studied the direction and stability of Hopf bifurcation. Chattopadhyay and Orino [17] proposed a very basic two and three dimensional models and established local stability results and also investigated important relation between two and three dimensional models. Further they also presented the direction of Hopf bifurcation. Liu et al. [18] studied an impulsive system for prey–predator system with disease in prey. They studied semi trivial, infection free, predator free equilibria. Naji and Hasan [19] proposed an eco-epidemiological model with Crowley–Martin functional response and analyzed it with local and global aspects. Samanta [20] analyzed a delayed nonautonomous predator–prey system with infection in prey and observe the permanence and global stability. A predator–prey system with infection in prey under the effect of polluted environment is proposed and analyzed in [11]. Sinha [11] observed that in polluted environment infected prey are more venerable as compare to predator. Xiao and Chen [21] proposed a system of retarded functional differential equations to study the dynamics of prey predator system with the presence of the infection in prey. They found that if the coefficient of conversing prey to predator (k) is constant (i.e. independent of gestation period). If $k = k_0 e^{-d\overline{\tau}}$, where $d, \overline{\tau}$ are mortality and delay respectively, they proved that delay has both destabilizing and stabilizing effects. It means that positive equilibrium, if exists will be stable for larger values of time delay.

Similarly, some authors proposed and analyzed the eco-epidemiological models with disease in predators for reference (see [22–24] and references therein). Hilker and Schmitz [22] considered a resident predator–prey system with infection in predator population. They found that infection among predators counteracts the predator of enrichment. They also investigated that if parasites removes from the food webs, it could have catastrophic effects. They also included biological control and resource management in their study. In [23], Haque proposed that infection in predator population acts as biological control. He also proved that absence of prey is beneficial for predator in case of infection in predator. Pal et al. [24], studied a model with disease in predators and analyze in terms of stability. They also determined the direction of Hopf bifurcation. Besides this some papers are available in literature with disease in prey–predator both, at this juncture we may refer reader to ([25,26] and references cited therein). Han et al. [25] suggested four modifications to prey–predator model by incorporating SIS or SIR parasitic infection and thresholds have been investigated. They studied models with both type of incidences viz. standard and mass action. Hsieh and Hsiao [26] proposed a predator–prey model with infection in both species for the possibility of a contagious infection crossing populations obstacle from prey to predator. They obtained number of threshold parameters for local analysis of different equilibria of the proposed system and coupled conditions on the thresholds which determined the stability of equilibria. One of the coupled conditions, in the form of an ecological thresholds for the ecosystem, always determined the coexistence of species. The other condition, in the form of basic reproduction number, suggests whether the infection will become endemic in the prey predator model. Under the combination of coupled conditions, infectious disease could generates the predator species to the extinction when predators and prey can coexist without the infection. For other combination of the conditions, the predation of infected prey could cause the infection to be eliminated in the ecosystem. They proved that the presence of infection in both populations could promote or impair coexistence, and its exact impact needs to be discovered specifically in each particular condition. By considering infection in both populations, their model also generates more complex dynamics, and chance for bistability and periodic oscillation, in either infection-free or endemic states, in the system for which the results are obtained analytically and also with numerical simulations.

Further, migration is a very important demographic event which is universally found in all the species including human on the planet earth. But the reasons for migration may vary from species to species. In human beings the migration is usually due to education, employment, marriages etc. Similarly, migration among other species may be founded specially due to climate change, for habitat, searching for food etc. Thus species migration is an important ecological and demographic event. This takes place on seasonal basis. It has been founded in all the major animal groups including mammals, fish, birds, reptiles, amphibians, insects and crustaceans [27,28]. Most of the migrations occurred in an annual cycle. Some daily movements may also referred to the migration, for instance, many aquatic animals make a migration which is called vertical migration [28,29]. Similarly some jellyfish make daily movements which is called horizontal migration [28,30]. As an example of migratory birds, we can refer to [31]. It is noted that in the month of October, 2013 almost 300 thousands birds including Greylag Goose, Mallards, Teals, Shovelers and Pintails Junaid Kathju migrated to Kashmir (India) from different countries including Siberia, China, Central Asia and North Europe and these migrated birds stayed in wetlands of Kashmir (India) [31]. A list of animals that usually migrated can see in the web source [32]. Similarly for a consolidated list of migratory Indian birds could be found in [33]. From this discussion it is very much clear that to study the prey–predator system more scientifically, the effect of migration must be taken into consideration while formulating of mathematical model of the prey–predator systems. As far as the data on migration is concerned, there are a very few authentic sources are available in the literature. As pointed out earlier that migration of birds to Jammu and Kashmir (India) could be seen in [31], but the method how they enumerated, related methodology etc. are not well defined. However data of human migration may be found in census reports in any of the country. Available data on human migration is more accurate and authentic as compare to other species. The reason for this is quite simple that human population have documentary evidences for movements but other species do not have. To our knowledge, exact data on migration of other species is not available. It is also

Please cite this article as: S. Kant, V. Kumar, Stability analysis of predator–prey system with migrating prey and disease infection in both species, Applied Mathematical Modelling (2016), http://dx.doi.org/10.1016/j.apm.2016.10.003

important to be mentioned here that human–prey interaction are not usually modeled and no such literature is available. In the present study we considered the effect of migration on prey population only.

It is revealed from previous paragraph that migration is an important ecological and demographic event. In mathematical ecology the work on migration of species is also considered as a matter of great concern. Many mathematical models dealing with prey–predator system with migration have been published, for references we can refer reader to ([34–36] and references therein). Bhattacharyya and Mukhopadhyay [34], proposed prey–predator models with prey migration and predator switching. They found interesting dynamics regarding stability and bifurcation. Sun et al. [36] studied the dynamical complexity of a spatial predator–prey model with migration. They considered both diffusion and migration in their study. There may be many ecological situations when prey can out migrated. For example, suppose a disaster occurred then prey can migrated. In this study, we considered migration as stochastic process not deterministic.

Motivated by Hu and Li [16], Bhattacharyya and Mukhopadhyay [34] and Sun et al. [36] in the present study, we proposed and analyzed an eco-epidemiological model with migrating prey and disease infection in both species. It is a four-dimensional model governing the healthy prey, infected prey, healthy predator and infected predator populations. Local stability analysis has been performed. Detailed assumptions are listed in next section.

Remaining part of the paper is structured as follows: Next section is dealing with the model formulation. Section 3 provides the analysis of the model without migration and disease. Section 4 is related to analysis of the main model followed by Section 5 in which a numerical example is given. Paper is concluded by Section 6 with a detailed discussion on ecological aspects of each equilibrium point, remarks on migration and future scope.

2. Model formulation

In the present study, our model has two populations

(i) The prey, whose total density is denoted by $N(t)$.
(ii) The predator, whose population density is denoted by $Y(t)$.

For mathematical transformation of real situations, we make the following assumptions:

(H_1) In the absence of disease and predation, prey population grows according to logistic law with growth rate r ($r > 0$) and carrying capacity k ($k > 0$) [16].
(H_2) It is assumed that disease infection spreads among the prey and predator populations both. In the presence of disease, prey population is divided into two parts: Susceptible (S) and Infective (I), thus total biomass of the prey is $S(t) + I(t)$. Similarly, in the presence of disease, predator population is divided into two parts: Y_1 and Y_2, thus total biomass of the predator population is $Y_1(t) + Y_2(t)$. Thus, we are dealing with four populations viz. healthy prey, infected prey, healthy predator, infected predator.
(H_3) Only the susceptible prey is assumed to be reproducing offsprings with logistic law i.e. only S has growth rate.
(H_4) Prey may have one source of infection (external source) viz. viruses and other seasonal effects. After infection they converted to infected prey (I). However, the case in which, the infected prey is already present is also included, thus we have considered the initial value of infected prey of the form $I(0) \geq 0$. Further, it is also assumed that, infection in predator population occurs due to predation of infected prey only. The case of infection in predator population from any other vector, carrier etc. has been ignored. Hence, we have taken the initial value of infected predator as $Y_2(0) \equiv 0$. As considered in papers [15,18,35,37] that a mass-action incidence assumption is more appropriate than a proportional mixing one in describing dynamics of direct transmission. Therefore, it is assumed that the transmission of disease follow the simple law of mass action βSI where β is the force of infection. Similarly in case of predator, we have the term $\gamma Y_1 Y_2$. The detailed dynamics of infection and causes of infection along with control strategies have been omitted here.
(H_5) Prey (susceptible (S) and infective (I)) may have out migration i.e they can migrate to other geographical zone. Let m_1 and m_2 are the rate of migration of susceptible(S) and infective (I) populations, respectively. Also ecology suggested that $m_1 > m_2$. It is natural factor that susceptible (healthy/sound) prey are more strong as compared to infected one therefore the probability of migration of healthy prey is more than that of infected prey.
(H_6) It is also assumed that infected prey has high probability of being predated (eaten) by the predator (healthy prey has minimum probability of being captured by predator). Similarly infected predator has low capacity of capturing prey as compare to healthy one.
(H_7) It is also assumed that coefficient of conversing of both the prey to different predators are different. They are denoted by q_1, q_2, q_3, q_4 (Table 1).
(H_8) It is considered that all the four species have their natural death rates.
(H_9) It is also assumed that neither infected prey nor infected predator recover and immune.
(H_{10}) We considered Lotka–Volterra type linear functional response [16].

Please cite this article as: S. Kant, V. Kumar, Stability analysis of predator–prey system with migrating prey and disease infection in both species, Applied Mathematical Modelling (2016), http://dx.doi.org/10.1016/j.apm.2016.10.003

Table 1
Biological/ecological meaning of parameters.

Symbol	Biological/ecological meaning
r	Intrinsic growth rate of prey
β	Infection coefficient (force of infection) of healthy prey
γ	Infection coefficient (force of infection) of predator
k	Carrying capacity
p_1	Healthy prey–predation coefficient w.r.t. healthy predator
p_2	Infected prey–predation coefficient w.r.t. healthy predator
p_3	Healthy prey–predation coefficient w.r.t. infected predator
p_4	Infected prey–predation coefficient w.r.t. infected predator
q_1	Conversion coefficient from healthy prey to healthy predator
q_2	Conversion coefficient from infected prey to healthy predator
q_3	Conversion coefficient from healthy prey to infected predator
q_4	Conversion coefficient from infected prey to infected predator
m_1	Migration rate of healthy prey
m_2	Migration rate of infected prey
d_1	Natural death rate of healthy prey
d_2	Natural death rate of infected prey
d_3	Natural death rate of healthy predator
d_4	Natural death rate of infected predator
d_5	Death rate of infected predator due to infection
c	Death rate of infected prey due to infection

We give mathematical realization of all these assumptions into the mathematical model:

$$\begin{aligned}
\frac{dS}{dt} &= \underbrace{rS\left(1-\frac{S+I}{k}\right)}_{Growth} - \underbrace{SI\beta}_{Infection} - \underbrace{p_1SY_1 - p_3SY_2}_{Predation} - \underbrace{m_1S}_{Migration} - \underbrace{d_1S,}_{Mortality}\\
\frac{dI}{dt} &= \underbrace{SI\beta}_{Infection} - \underbrace{p_2IY_1 - p_4IY_2}_{Predation} - \underbrace{m_2I}_{Migration} - \underbrace{(c+d_2)I,}_{Mortality}\\
\frac{dY_1}{dt} &= \underbrace{q_1p_1SY_1 + q_2p_2IY_1}_{PreyConsumption} - \underbrace{\gamma Y_1Y_2}_{Infection} - \underbrace{d_3Y_1,}_{Mortality}\\
\frac{dY_2}{dt} &= \underbrace{q_3p_3SY_2 + q_4p_4IY_2}_{PreyConsumption} + \underbrace{\gamma Y_1Y_2}_{Infection} - \underbrace{(d_4+d_5)Y_2,}_{Mortality}
\end{aligned} \tag{2.1}$$

initial conditions are $S(0) > 0, I(0) \geq 0, Y_1(0) > 0, Y_2(0) = 0$. The biological and ecological meaning of the parameters are given in Table 1.

Remark 1. It is interested to note that migration terms in model (2.1) look like mortality terms, but in this paper, we have maintained distinction between mortality and migration. A detailed study about migration has been done in Section 6 (discussion) (refer especially Table 5).

Remark 2. It must be noted that m_1 and m_2 are migration rates (refer Table 1). More specifically they are the quantities which followed some probability distributions.

Remark 3. Critical/special discussion regarding mortality have done in discussion section (refer Eqs. (6.1)–(6.6)).

3. Model without migration and disease

In this section, model (2.1) is subjected to the two assumptions (i) infection does not occurred (ii) migration not allowed. The model (2.1) reduced to the basic two dimensional prey predator model dealing with two populations viz. sound prey and sound predator. Model (2.1) takes the form:

$$\begin{aligned}
\frac{dS}{dt} &= rS(1-\frac{S}{k}) - p_1SY_1 - d_1S,\\
\frac{dY_1}{dt} &= q_1p_1SY_1 - d_3Y_1,
\end{aligned} \tag{3.1}$$

initial conditions are $S(0) > 0$, $Y_1(0) > 0$. Model (3.1) is two dimensional prey–predator model. Similarly, if model (2.1) is subjected to the assumption that infection does not occurred in the ecosystem. Model (2.1) is again two dimensional prey

Please cite this article as: S. Kant, V. Kumar, Stability analysis of predator–prey system with migrating prey and disease infection in both species, Applied Mathematical Modelling (2016), http://dx.doi.org/10.1016/j.apm.2016.10.003

Table 2
The equilibria, their feasibility and stability conditions of model (3.1).

Equilibrium point	Existence condition (s)	Stability condition (s)
$E_1(0, 0)$	Always	$(r - d_1) < 0$
$E_2(\widetilde{S}, 0)$	$r > d_1$	$\left(\frac{q_1 p_1 k(r-d_1)}{r} - d_3\right) < 0$
$E_3(\widehat{S}, \widehat{Y})$	$(r - d_1) > \frac{rd_3}{q_1 p_1 k}$	$\left[(r - d_1) - \frac{rd_3}{kq_1 p_1}\right] > 0$

Table 3
Equilibria, their feasibility and stability conditions of model (3.2).

Equilibria	Existence condition (s)	Stability condition (s)
$E_1^*(0, 0)$	Always	$(r - d_1 - m_1) < 0$
$E_2^*(\widetilde{S}, 0)$	$r > (d_1 + m_1)$	$\left(\frac{q_1 p_1 k(r-d_1-m_1)}{r} - d_3\right) < 0$
$E_3^*(\widehat{S}, \widehat{Y_1})$	$(r - d_1 - m_1) > \frac{rd_3}{q_1 p_1 k}$	$\left[(r - d_1 - m_1) - \frac{rd_3}{kq_1 p_1}\right] > 0$

predator model dealing with two populations viz. sound prey and sound predator. Model (2.1) takes the form:

$$\begin{aligned}\frac{dS}{dt} &= rS\left(1 - \frac{S}{k}\right) - p_1 SY_1 - (d_1 + m_1)S,\\ \frac{dY_1}{dt} &= q_1 p_1 SY_1 - d_3 Y_1,\end{aligned} \tag{3.2}$$

initial conditions are $S(0) > 0$, $Y_1(0) > 0$. It is observed that models (3.1) and (3.2) are quite similar to Lotka–Volterra model [1,2]. Therefore, we state the results directly in Tables 2 and 3.

4. Dynamics of model (2.1)

In this section, we obtained number of threshold parameters for local analysis of different equilibria of the proposed system and coupled conditions on the thresholds which determined the stability of equilibria. One of the coupled conditions, in the form of an ecological thresholds for the ecosystem, always determined the coexistence of species. The other condition, in the form of basic reproduction number (generally denoted by (R_0) or R), suggests whether the infection will become endemic in the prey predator model. Under the combination of coupled conditions, infectious disease could generates the predator species to the extinction when predators and prey can coexist without the infection. For other combination of the conditions, the predation of infected prey could cause the infection to be eliminated in the ecosystem. The boundedness and positivity are trivial which may be proved easily and hence omitted.

We performed the next generation matrix method [38] for the calculation of basic reproduction number. Now we seen that I and Y_2 are the concerned classes for infection. We can write our model as follows:

$$\begin{aligned}\frac{dI}{dt} &= \underbrace{SI\beta}_{Infection} - \underbrace{p_2 IY_1 - p_4 IY_2}_{Predation} - \underbrace{m_2 I}_{Migration} - \underbrace{(c + d_2)I}_{Mortality},\\ \frac{dY_2}{dt} &= \underbrace{q_3 p_3 SY_2 + q_4 p_4 IY_2}_{PreyConsumption} + \underbrace{\gamma Y_1 Y_2}_{Infection} - \underbrace{(d_4 + d_5)Y_2}_{Mortality},\\ \frac{dS}{dt} &= \underbrace{rS\left(1 - \frac{S+I}{k}\right)}_{Growth} - \underbrace{SI\beta}_{Infection} - \underbrace{p_1 SY_1 - p_3 SY_2}_{Predation} - \underbrace{m_1 S}_{Migration} - \underbrace{d_1 S}_{Mortality},\\ \frac{dY_1}{dt} &= \underbrace{q_1 p_1 SY_1 + q_2 p_2 IY_1}_{PreyConsumption} - \underbrace{\gamma Y_1 Y_2}_{Infection} - \underbrace{d_3 Y_1}_{Mortality},\ .\end{aligned}$$

Therefore, we have the following components vectors, Gain components $= \begin{pmatrix}\beta SI\\ \gamma Y_1 Y_2\end{pmatrix}$ and Loss components $= \begin{pmatrix}(c+d_2+m_2)I\\ (d_4+d_5)Y_2\end{pmatrix}$.

Now we calculated two matrices $F = \begin{pmatrix}\beta S^{(7)} & 0\\ 0 & \gamma Y_1^{(7)}\end{pmatrix}$, $V = \begin{pmatrix}(c+d_2+m_2) & 0\\ 0 & (d_4+d_5)\end{pmatrix}$ which are the gain and loss matrices evaluated at the infection free equilibrium $E^{(7)}(S^{(7)}, 0, Y_1^{(7)}, 0)$ where $S^{(7)} = \frac{d_3}{q_1 p_1}$ and $Y_1^{(7)} = \frac{(r - m_1 - d_1 - \frac{rd_3}{kq_1 p_1})}{p_1}$. Now define the next generation matrix $G = FV^{-1}$. Dominant eigenvalue of the next generation matrix is the basic reproduction number. In this case basic reproduction number is given by $R_0 = \frac{\gamma \beta S^{(7)} Y_1^{(7)}}{(c+d_2+m_2)(d_4+d_5)}$. Therefore, disease will be endemic if $R_0 > 1$.

In the preceding sections, mathematically equilibrium points and their stability conditions have been investigated. The ecological explanations have been done in last section.

Please cite this article as: S. Kant, V. Kumar, Stability analysis of predator–prey system with migrating prey and disease infection in both species, Applied Mathematical Modelling (2016), http://dx.doi.org/10.1016/j.apm.2016.10.003

4.1. Equilibria

Mathematically, the model (2.1) may have the following equilibrium points:

(i) $E^{(1)}(0, 0, 0, 0)$.
(ii) $E^{(2)}(S^{(2)}, 0, 0, 0)$, where $S^{(2)} = k$.
(iii) $E^{(3)}(0, I^{(3)}, 0, 0), E^{(4)}(0, 0, Y_1^{(4)}, 0),\ E^{(5)}(0, 0, 0, Y_2^{(5)})$.
(iv) $E^{(6)}(S^{(6)}, I^{(6)}, 0, 0)$ where $S^{(6)} = \frac{c+d_2+m_2}{\beta}$ and $I^{(6)} = \frac{k\beta(r-m_1-d_1)-r(c+d_2+m_2)}{\beta(r+k\beta)}$.
(v) $E^{(7)}(S^{(7)}, 0, Y_1^{(7)}, 0)$ where $S^{(7)} = \frac{d_3}{q_1 p_1}$ and $Y_1^{(7)} = \frac{(r-m_1-d_1-\frac{rd_3}{kq_1p_1})}{p_1}$.
(vi) $E^{(8)}(S^{(8)}, 0, 0, Y_2^{(8)})$, where $S^{(8)} = \frac{d_4+d_5}{q_3 p_3}$ and $Y_2^{(8)} = \frac{[(r-m_1-d_1)-\frac{r(d_4+d_5)}{kq_3p_3}]}{p_3}$.
(vii) $E^{(9)}(0, 0, Y_1^{(9)}, Y_2^{(9)})$, where $Y_1^{(9)} = \frac{d_4+d_5}{\gamma}$ and $Y_2^{(9)} = \frac{d_3}{\gamma}$.
(viii) $E^{(10)}(0, I^{(10)}, Y_1^{(10)}, Y_2^{(10)})$, where:

$$I^{(10)} = \frac{\gamma(c+m_2+d_2) + p_2(d_4+d_5) - p_4 d_3}{p_4(p_2q_4 - q_2p_2)},$$
$$Y_1^{(10)} = \frac{d_4+d_5-q_4p_4I^{(10)}}{\gamma},$$
$$Y_2^{(10)} = \frac{q_2p_2I^{(10)} - d_3}{\gamma}.$$

(ix) $E^{(11)}(S^{(11)}, 0, Y_1^{(11)}, Y_2^{(11)})$, where:

$$Y_1^{(11)} = \frac{\left(r-m_1-d_1-\frac{rd_3}{kq_1p_1}+p_3\right)\left(\frac{(d_4+d_5)q_1p_1}{\gamma q_3p_3} - \frac{d_3}{\gamma}\right)}{p_1 - \left(\frac{r\gamma}{q_1p_1k}+p_3\right)\left(\frac{q_1p_1}{q_3p_3}\right)},$$
$$Y_2^{(11)} = \left(\frac{(d_4+d_5)q_1p_1}{q_3p_{3\gamma}} - \frac{d_3}{\gamma}\right) - \frac{q_1p_1}{q_3p_3}Y_1^{(11)},$$
$$S^{(11)} = \frac{d_4+d_5-\gamma Y_1^{(11)}}{q_3p_3}.$$

(x) $E^{(12)}(S^{(12)}, I^{(12)}, 0, Y_2^{(12)})$, where:

$$S^{(12)} = -\frac{X}{Y},$$
$$I^{(12)} = \frac{d_4+d_5-q_3p_3S^{(12)}}{q_4p_4},$$
$$Y_2^{(12)} = \frac{\beta S^{(12)} - c - d_2 - m_2}{p_4},$$
$$X = r - d_1 - m_1 - \left(\frac{r}{k}+\beta\right)\frac{d_4+d_5}{q_4p_4} + \frac{p_3(c+d_2+m_2)}{p_4},$$
$$Y = \frac{-r}{k} + \left(\frac{r}{k}+\beta\right)\frac{q_3p_3}{q_4p_4} - \frac{p_3\beta}{p_4}.$$

(xi) $E^{(13)}(S^{(13)}, I^{(13)}, Y_1^{(13)}, 0)$, where:

$$S^{(13)} = \frac{-B}{A},$$
$$I^{(13)} = \frac{d_3 - q_1p_1S^{(13)}}{q_2p_2},$$
$$Y_1^{(13)} = \frac{\beta S^{(13)} - c - d_2 - m_2}{p_2},$$
$$A = \frac{-r}{k} + \left(\frac{r}{k}+\beta\right)\frac{q_1p_1}{q_2p_2} - \frac{p_1\beta}{p_2},$$
$$B = r - d_1 - m_1 - \left(\frac{r}{k}+\beta\right)\frac{d_3}{q_2p_2} + \frac{p_1(c+d_2+m_2)}{p_2}.$$

Please cite this article as: S. Kant, V. Kumar, Stability analysis of predator–prey system with migrating prey and disease infection in both species, Applied Mathematical Modelling (2016), http://dx.doi.org/10.1016/j.apm.2016.10.003

(xii) $E^{(14)}(S^{(14)}, I^{(14)}, Y_1^{(14)}, Y_2^{(14)})$, where:

$$I^{(14)} = \frac{D}{E},$$

where:

$$D = \frac{\left[\left(\frac{\gamma\beta}{q_1p_1} - p_4\right) + \frac{p_2\left(p_3 + \frac{\gamma r}{q_1p_1k}\right)}{p_1}\right]\left[\frac{q_1p_1(d_4+d_5)}{q_3p_3} - d_3 - \frac{\gamma q_1}{q_3p_3}\left((r - d_1 - m_1) - \frac{\gamma d_3}{q_1p_1k}\right)\right]}{\left[\gamma - \frac{\gamma q_1\left(p_3 + \frac{\gamma r}{q_1p_1k}\right)}{q_3p_3}\right]} + \left[\frac{\beta d_3}{q_1p_1} - (c + m_2 + d_2) - \frac{p_2}{p_1}\left(r - m_1 - d_1 - \frac{\gamma d_3}{q_1p_1k}\right)\right],$$

$$E = \frac{\left[\left(\frac{\gamma\beta}{q_1p_1} - p_4\right) + \frac{p_2(p_3 + \frac{\gamma r}{q_1p_1k})}{p_1}\right]\left[\frac{\gamma q_1}{q_3p_3}\left(\frac{rq_2p_2}{q_1p_1k} - \left(\frac{r}{k} + \beta\right) + q_2p_2 + \frac{q_1p_1q_4p_4}{q_3p_3}\right)\right]}{\left[\gamma - \frac{\gamma q_1(p_3 + \frac{\gamma r}{q_1p_1k})}{q_3p_3}\right]} + \left[\frac{\beta q_2p_2}{q_1p_1} - \frac{p_2}{p_1}\left(\frac{rq_2p_2}{q_1p_1k} - \left(\frac{r}{k} + \beta\right)\right)\right].$$

$Y_2^{(14)}$ is governed by:

$$Y_2^{(14)}\left[\gamma - \frac{\gamma q_1}{q_3p_3}\left(p_3 + \frac{\gamma r}{q_1p_1k}\right)\right] + I^{(14)}\left[\frac{\gamma q_1}{q_3p_3}\left(\frac{rq_2p_2}{q_1p_1k} - \left(\frac{r}{k} + \beta\right)\right) + q_2p_2 + \frac{q_1p_1q_4p_4}{q_3p_3}\right] + \left[\frac{\gamma q_1}{q_3p_3}\left((r - m_1 - d_1) - \frac{rd_3}{q_1p_1k}\right) + \left(d_3 - \frac{q_1p_1(d_4+d_5)}{q_3p_3}\right)\right] = 0.$$

$Y_1^{(14)}$ is given by:

$$p_1Y_1^{(14)} + p_3Y_2^{(14)} = 0.$$

$S^{(14)}$ is governed by:

$$S^{(14)} = \frac{1}{q_1p_1}\left[d_3 + \gamma Y_2^{(14)} - q_2p_2I^{(14)}\right],$$

or,

$$S^{(14)} = \frac{1}{q_3p_3}\left[d_4 + d_5 - q_4p_4I^{(14)} - \gamma Y_1^{(14)}\right].$$

4.2. Existence conditions

The equilibrium points:

(i) $E^{(1)}(0, 0, 0, 0)$, $E^{(2)}(S^{(2)}, 0, 0, 0)$ and $E^{(9)}(0, 0, Y_1^{(9)}, Y_2^{(9)})$ do always exist.
(ii) $E^{(3)}(0, I^{(3)}, 0, 0)$, $E^{(4)}(0, 0, Y_1^{(4)}, 0)$, $E^{(5)}(0, 0, 0, Y_2^{(5)})$ do not exist.
(iii) $E^{(6)}(S^{(6)}, I^{(6)}, 0, 0)$ exists provided $(r - m_1 - d_1) - r(c + d_2 + m_2) > 0$.
(iv) The existence condition for $E^{(7)}(S^{(7)}, 0, Y_1^{(7)}, 0)$ is $(r - m_1 - d_1 - \frac{rd_3}{kq_1p_1}) > 0$.
(v) The existence condition for $E^{(8)}(S^{(8)}, 0, 0, Y_2^{(8)})$ is $[(r - m_1 - d_1) - \frac{r(d_4+d_5)}{kq_3p_3}] > 0$.
(vi) The conditions required for the existence for the equilibrium $E^{(10)}(0, I^{(10)}, Y_1^{(10)}, Y_2^{(10)})$ are:

$$[\gamma(c + m_2 + d_2) + p_2(d_4 + d_5) - p_4d_3] > 0,$$
$$(p_2q_4 - q_2p_2) > 0, (d_4 + d_5 - q_4p_4I^{(10)}) > 0,$$
$$(q_2p_2I^{(10)} - d_3) > 0.$$

(vii) The essential conditions for existence for the equilibrium $E^{(11)}(S^{(11)}, 0, Y_1^{(11)}, Y_2^{(11)})$ are:

$$\left(r - m_1 - d_1 - \frac{rd_3}{kq_1p_1} + p_3\right) > 0,$$
$$\left(\frac{(d_4 + d_5)q_1p_1}{\gamma q_3p_3} - \frac{d_3}{\gamma}\right) > 0,$$

Please cite this article as: S. Kant, V. Kumar, Stability analysis of predator–prey system with migrating prey and disease infection in both species, Applied Mathematical Modelling (2016), http://dx.doi.org/10.1016/j.apm.2016.10.003

$$(p_1 - \left(\frac{r\gamma}{q_1 p_1 k} + p_3\right)\left(\frac{q_1 p_1}{q_3 p_3}\right) > 0,$$
$$\left(\frac{(d_4 + d_5)q_1 p_1}{q_3 p_3} - d_3\right) - \frac{q_1 p_1}{q_3 p_3} Y_1^{(11)} > 0,$$
$$(d_4 + d_5 - \gamma Y_1^{(11)}) > 0.$$

(viii) $E^{(12)}(S^{(12)}, I^{(12)}, 0, Y_2^{(12)})$ exists provided:

$$(d_4 + d_5 - q_3 p_3 S^{(12)}) > 0,$$
$$(\beta S^{(12)} - c - d_2 - m_2) > 0,$$

and one of these two conditions are satisfied (not simultaneously):

$$\left(r - d_1 - m_1 - \left(\frac{r}{k} + \beta\right)\frac{d_4 + d_5}{q_4 p_4} + \frac{p_3(c + d_2 + m_2)}{p_4}\right) < 0,$$
$$\left(\frac{-r}{k} + \left(\frac{r}{k} + \beta\right)\frac{q_3 p_3}{q_4 p_4} - \frac{p_3 \beta}{p_4}\right) < 0.$$

(ix) $E^{(13)}(S^{(13)}, I^{(13)}, Y_1^{(13)}, 0)$ exists provided:

$$(d_3 - q_1 p_1 S^{(13)}) > 0,$$
$$(\beta S^{(13)} - c - d_2 - m_2) > 0,$$

and one of these two conditions are satisfied (not simultaneously):

$$A = \left(\frac{-r}{k} + \left(\frac{r}{k} + \beta\right)\frac{q_1 p_1}{q_2 p_2} - \frac{p_1 \beta}{p_2}\right) < 0,$$
$$B = \left(-d_1 - m_1 - \left(\frac{r}{k} + \beta\right)\frac{d_3}{q_2 p_2} + \frac{p_1(c + d_2 + m_2)}{p_2}\right) < 0.$$

(x) $E^{(14)}(S^{(14)}, I^{(14)}, Y_1^{(14)}, Y_2^{(14)})$ exists provided the following conditions are satisfied:

$$\left[\gamma - \frac{\gamma q_1\left(p_3 + \frac{\gamma r}{q_1 p_1 k}\right)}{q_3 p_3}\right] > 0,$$
$$\left[\frac{\beta d_3}{q_1 p_1} - (c + m_2 + d_2) - \frac{p_2}{p_1}\left(r - m_1 - d_1 - \frac{\gamma d_3}{q_1 p_1 k}\right)\right] > 0,$$
$$\left[\left(\frac{\gamma \beta}{q_1 p_1} - p_4\right) + \frac{p_2\left(p_3 + \frac{\gamma r}{q_1 p_1 k}\right)}{p_1}\right] > 0,$$
$$\left[\frac{q_1 p_1 (d_4 + d_5)}{q_3 p_3} - d_3 - \frac{\gamma q_1}{q_3 p_3}\left((r - d_1 - m_1) - \frac{\gamma d_3}{q_1 p_1 k}\right)\right] > 0,$$
$$\left[\left(\frac{\gamma \beta}{q_1 p_1} - p_4\right) + \frac{p_2\left(p_3 + \frac{\gamma r}{q_1 p_1 k}\right)}{p_1}\right] > 0,$$
$$\left[\frac{\gamma q_1}{q_3 p_3}\left(\frac{r q_2 p_2}{q_1 p_1 k} - \left(\frac{r}{k} + \beta\right) + q_2 p_2 + \frac{q_1 p_1 q_4 p_4}{q_3 p_3}\right)\right] > 0,$$
$$\left[\frac{\beta q_2 p_2}{q_1 p_1} - \frac{p_2}{p_1}\left(\frac{r q_2 p_2}{q_1 p_1 k} - \left(\frac{r}{k} + \beta\right)\right)\right] > 0,$$

the following equation

$$Y_2^{(14)}\left[\gamma - \frac{\gamma q_1}{q_3 p_3}\left(p_3 + \frac{\gamma r}{q_1 p_1 k}\right)\right] + I^{(14)}\left[\frac{\gamma q_1}{q_3 p_3}\left(\frac{r q_2 p_2}{q_1 p_1 k} - \left(\frac{r}{k} + \beta\right)\right) + q_2 p_2 + \frac{q_1 p_1 q_4 p_4}{q_3 p_3}\right]$$
$$+\left[\frac{\gamma q_1}{q_3 p_3}\left((r - m_1 - d_1) - \frac{r d_3}{q_1 p_1 k}\right) + \left(d_3 - \frac{q_1 p_1 (d_4 + d_5)}{q_3 p_3}\right)\right] = 0$$

generated the positive value of $Y_2^{(14)}$. The following equation:

$$p_1 Y_1^{(14)} + p_3 Y_2^{(14)} = 0,$$

Please cite this article as: S. Kant, V. Kumar, Stability analysis of predator–prey system with migrating prey and disease infection in both species, Applied Mathematical Modelling (2016), http://dx.doi.org/10.1016/j.apm.2016.10.003

generated the positive value of $Y_1^{(14)}$. The following equations:

$$S^{(14)} = \frac{1}{q_1 p_1}\left[d_3 + \gamma Y_2^{(14)} - q_2 p_2 I^{(14)}\right],$$

or

$$S^{(14)} = \frac{1}{q_3 p_3}\left[d_4 + d_5 - q_4 p_4 I^{(14)} - \gamma Y_1^{(14)}\right],$$

generated the positive value of $S^{(14)}$.

Remark 4. We seen that equilibrium points $E^{(3)}$, $E^{(4)}$, $E^{(5)}$ do not exist. It means that mathematically these equilibrium points are not feasible. It is also important to mention that all these equilibrium points are prey free. Ecologically, these are the cases when the ecosystem is free from prey population and only predator population is persisted. But without prey, it is too difficult for predator population to survive. Therefore, mathematical and ecological messages are same. However, for the ecosystems in which prey population is not available, there are studies in which the concept of additional food have been introduced for the survival of predator population (refer [39] and references therein).

4.3. Stability analysis

The Jacobian matrix of the model (2.1) is given by:

$$J = \begin{pmatrix} \left(r - m_1 - d_1 - \frac{2r}{k}S - \left(\frac{r}{k}+\beta\right) I - p_1 Y_1 - p_3 Y_2\right) & -\left(\frac{r}{k}+\beta\right)S & -p_1 S & -p_3 S \\ \beta I & (\beta S - p_2 Y_1 - p_4 Y_2 - (c + m_2 + d_2)) & -p_2 I & -p_4 I \\ q_1 p_1 Y_1 & q_2 p_2 Y_1 & (q_2 p_2 I + q_1 p_1 S - \gamma Y_2 - d_3) & -\gamma Y_1 \\ q_3 p_3 Y_2 & q_4 p_4 Y_2 & \gamma Y_2 & (q_3 p_3 S + q_4 p_4 I + \gamma Y_1 - (d_4 + d_5)) \end{pmatrix}, \tag{4.1}$$

with help of this matrix we will analyze our model.

4.3.1. Trivial equilibrium ($E^{(1)}(0, 0, 0, 0)$)

The Jacobian matrix at $E^{(1)}(0, 0, 0, 0)$ is:

$$J_{E^{(1)}(0,0,0,0)} = \begin{pmatrix} (r - m_1 - d_1) & 0 & 0 & 0 \\ 0 & (c + m_2 + d_2) & 0 & 0 \\ 0 & 0 & (-d_3) & 0 \\ 0 & 0 & 0 & -(d_4 + d_5) \end{pmatrix}.$$

The eigenvalues of this matrix are $(r - m_1 - d_1), (c + m_2 + d_2), -(d_4 + d_5), -(d_3)$. Hence $E^{(1)}(0, 0, 0, 0)$ is not a stable equilibrium point, in fact it is a saddle point.

4.3.2. Equilibrium ($E^{(2)}(S^{(2)}, 0, 0, 0)$)

We note that $S^{(2)} = k$, the Jacobian matrix at $E^{(2)}(S^{(2)}, 0, 0, 0)$ is:

$$J_{E^{(2)}(S^{(2)},0,0,0)} = \begin{pmatrix} (r - m_1 - d_1) - \frac{2r}{k}k & -\left(\frac{r}{k}+\beta\right)k & -p_1 k & -p_3 k \\ 0 & \beta k - (c + m_2 + d_2) & 0 & 0 \\ 0 & 0 & (q_1 p_1 k - d_3) & 0 \\ 0 & 0 & 0 & q_3 p_3 k - (d_4 + d_5) \end{pmatrix},$$

or

$$J_{E^{(2)}(S^{(2)},0,0,0)} = \begin{pmatrix} -(r - m_1 - d_1) & -\left(\frac{r}{k}+\beta\right)k & -p_1 k & -p_3 k \\ 0 & \beta k - (c + m_2 + d_2) & 0 & 0 \\ 0 & 0 & (q_1 p_1 k - d_3) & 0 \\ 0 & 0 & 0 & q_3 p_3 k - (d_4 + d_5) \end{pmatrix},$$

this is a upper triangular matrix and therefore this has the following eigenvalues:

$$\begin{cases} -(r - m_1 - d_1), \\ \beta k - (c + m_2 + d_2), \\ (q_1 p_1 k - d_3), \\ q_3 p_3 k - (d_4 + d_5). \end{cases}$$

Please cite this article as: S. Kant, V. Kumar, Stability analysis of predator–prey system with migrating prey and disease infection in both species, Applied Mathematical Modelling (2016), http://dx.doi.org/10.1016/j.apm.2016.10.003

Hence, $E^{(2)}$ is locally stable provided the following conditions are satisfied:

$$\begin{cases} \beta k - (c + m_2 + d_2) < 0, \\ (q_1 p_1 k - d_3) < 0, \\ q_3 p_3 k - (d_4 + d_5) < 0. \end{cases} \tag{4.2}$$

4.3.3. Equilibrium ($E^{(6)}(S^{(6)}, I^{(6)}, 0, 0)$)

The Jacobian matrix at $E^{(6)}(S^{(6)}, I^{(6)}, 0, 0)$ is:

$$J_{E^{(6)}(S^{(6)},I^{(6)},0,0)} = \begin{pmatrix} (r - m_1 - d_1 - \frac{2r}{k}S^{(6)} - \left(\frac{r}{k} + \beta\right)I^{(6)}) & -\left(\frac{r}{k} + \beta\right)S^{(6)} & -p_1 S^{(6)} & -p_3 S^{(6)} \\ \beta I^{(6)} & (\beta S^{(6)} - (c + m_2 + d_2)) & -p_2 S^{(6)} & -p_4 S^{(6)} \\ 0 & 0 & (q_2 p_2 I^{(6)} + q_1 p_1 S^{(6)} - d_3) & 0 \\ 0 & 0 & 0 & q_3 p_3 S^{(6)} + q_4 p_4 I^{(6)} \\ & & & -(d_4 + d_5) \end{pmatrix}.$$

Characteristics equation is given by:

$$\begin{aligned} &\left(\lambda - (q_3 p_3 S^{(6)} + q_4 p_4 I^{(6)} - (d_4 + d_5))\right)\left(\lambda - (q_2 p_2 I^{(6)} + q_1 p_1 S^{(6)} - d_3)\right) \\ &\times \begin{bmatrix} (r - m_1 - d_1 - \frac{2r}{k}S^{(6)} - \left(\frac{r}{k} + \beta\right)I^{(6)}) - \lambda & -\left(\frac{r}{k} + \beta\right)S^{(6)} \\ \beta I^{(6)} & (\beta S^{(6)} - (c + m_2 + d_2)) - \lambda \end{bmatrix} = 0 \\ &\Rightarrow \left(\lambda - (q_3 p_3 S^{(6)} + q_4 p_4 I^{(6)} - (d_4 + d_5))\right)\left(\lambda - (q_2 p_2 I^{(6)} + q_1 p_1 S^{(6)} - d_3)\right) \times \left[\lambda^2 + \left(\frac{r}{k\beta}(c + d_2 + m_2)\right)\lambda\right. \\ &\left. + \left((c + m_2 + d_2)(r - m - 1 - d_1) - \frac{r}{k\beta}(c + d_2 + m_2)^2\right)\right] = 0. \end{aligned}$$

Thus the equilibrium point $E^{(6)}(S^{(6)}, I^{(6)}, 0, 0)$ is locally stable provided the following conditions are satisfied:

$$\begin{cases} (q_3 p_3 S^{(6)} + q_4 p_4 I^{(6)} - (d_4 + d_5)) < 0, \\ (q_2 p_2 I^{(6)} + q_1 p_1 S^{(6)} - d_3) < 0, \\ \left((r - m - 1 - d_1) - \frac{r}{k\beta}(c + d_2 + m_2)\right) > 0. \end{cases} \tag{4.3}$$

4.3.4. Equilibrium ($E^{(7)}(S^{(7)}, 0, Y_1^{(7)}, 0)$)

The Jacobian matrix at $E^{(7)}(S^{(7)}, 0, Y_1^{(7)}, 0)$ is:

$$J_{E^{(7)}(S^{(7)},0,Y_1^{(7)},0)} = \begin{pmatrix} (r - m_1 - d_1 - \frac{2r}{k}S^{(7)-p_1 Y_1^{(7)}}) & -\left(\frac{r}{k} + \beta\right)S^{(7)} & -p_1 S^{(7)} & -p_3 S^{(7)} \\ 0 & (\beta S^{(7)} - p_2 Y_1^7 - (c + m_2 + d_2)) & 0 & 0 \\ q_1 p_1 Y_1^{(7)} & q_2 p_2 Y_1^{(7)} & (q_1 p_1 S^{(7)} - d_3) & -\gamma Y_1^{(7)} \\ 0 & 0 & 0 & q_3 p_3 S^{(7)} + \gamma Y_1^{(7)} - (d_4 + d_5) \end{pmatrix},$$

or

$$J_{E^{(7)}(S^{(7)},0,Y_1^{(7)},0)} = \begin{pmatrix} (r - m_1 - d_1 - \frac{2r}{k}S^{(7)-p_1 Y_1^{(7)}}) & -\left(\frac{r}{k} + \beta\right)S^{(7)} & -p_1 S^{(7)} & -p_3 S^{(7)} \\ q_1 p_1 Y_1^{(7)} & q_2 p_2 Y_1^{(7)} & (q_1 p_1 S^{(7)} - d_3) & -\gamma Y_1^{(7)} \\ 0 & (\beta S^{(7)} - p_2 Y_1^{(7)} - (c + m_2 + d_2)) & 0 & 0 \\ 0 & 0 & 0 & q_3 p_3 S^{(7)} + \gamma Y_1^{(7)} - (d_4 + d_5) \end{pmatrix}.$$

The two eigenvalues are:

$$q_3 p_3 S^{(7)} + \gamma Y_1^{(7)} - (d_4 + d_5),$$
$$(\beta S^{(7)} - p_2 Y_1^{(7)} - (c + m_2 + d_2)).$$

Please cite this article as: S. Kant, V. Kumar, Stability analysis of predator–prey system with migrating prey and disease infection in both species, Applied Mathematical Modelling (2016), http://dx.doi.org/10.1016/j.apm.2016.10.003

Remaining two eigenvalues are given by the eigen values of the matrix:

$$\begin{bmatrix} (r-m_1-d_1-\frac{2r}{k}S^{(7)-p_1Y_1^{(7)}}) & -\left(\frac{r}{k}+\beta\right)S^{(7)} \\ q_1p_1Y_1^{(7)} & (q_1p_1S^{(7)}-d_3) \\ e & \end{bmatrix}.$$

The characteristics equation of this matrix is:

$$\lambda^2+\left[\frac{rd_3}{kq_1p_1}\right]\lambda+d_3\left(r-m_1-d_1-\frac{rd_3}{kq_1p_1}\right)=0.$$

After simplification, we see that $E^{(7)}(S^{(7)},0,Y_1^{(7)},0)$ is locally stable provided the following conditions are satisfied:

$$\begin{cases} \left(\frac{q_3p_3d_3}{q_1p_1}+\frac{\gamma}{p_1}\left(r-m_1-d_1\frac{rd_3}{kq_1p_1}\right)-(d_4+d_5)\right)<0, \\ \left(\frac{\beta d_3}{q_1p_1}-\frac{p_2}{p_1}(r-m_1-d_1-\frac{rd_3}{kq_1p_1}-c_2-m_2-d_2\right)<0, \\ \left(r-m_1-d_1-\frac{rd_3}{kq_1p_1}\right)>0. \end{cases} \tag{4.4}$$

4.3.5. Equilibrium $(E^{(8)}(S^{(8)},0,0,Y_2^{(8)}))$

The Jacobian matrix at $E^{(8)}(S^{(8)},0,0,Y_2^{(8)})$ is:

$$J_{E^{(8)}(S^{(8)},0,0,Y_2^{(8)})} = \begin{pmatrix} \left(r-m_1-d_1-\frac{2r}{k} S^{(8)-p_3Y_2^{(8)}}\right) & -\left(\frac{r}{k}+\beta\right)S^{(8)} & -p_1S^{(8)} & -p_3S^{(8)} \\ 0 & (\beta S^{(8)}-p_4Y_2^{(8)}-(c+m_2+d_2)) & 0 & 0 \\ 0 & 0 & (q_1p_1S^{(8)}-\gamma Y_2^{(8)}-d_3) & 0 \\ q_3p_3Y_2^{(8)} & q_4p_4Y_2^{(8)} & \gamma Y_2^{(8)} & q_3p_3S^{(8)}-(d_4+d_5) \end{pmatrix},$$

or

$$J_{E^{(8)}(S^{(8)},0,0,Y_2^{(8)})} = \begin{pmatrix} \left(r-m_1-d_1-\frac{2r}{k} S^{(8)-p_3Y_2^{(8)}}\right) & -\left(\frac{r}{k}+\beta\right)S^{(8)} & -p_1S^{(8)} & -p_3S^{(8)} \\ q_3p_3Y_2^{(8)} & q_4p_4Y_2^{(8)} & \gamma Y_2^{(8)} & q_3p_3S^{(8)} \\ & & & -(d_4+d_5) \\ 0 & (\beta S^{(8)}-p_4Y_2^{(8)}-(c+m_2+d_2)) & 0 & 0 \\ 0 & 0 & (q_1p_1S^{(8)}-\gamma Y_2^{(8)}-d_3) & 0 \end{pmatrix}. \tag{4.5}$$

The two eigenvalues are:

$$(\beta S^{(8)}-p_4Y_2^{(8)}-(c+m_2+d_2)),$$
$$(q_1p_1S^{(8)}-\gamma Y_2^{(8)}-d_3).$$

Remaining two eigenvalues are given by the eigenvalues of the matrix:

$$\begin{bmatrix} \left(r-m_1-d_1-\frac{2r}{k}S^{(8)-p_3Y_2^{(8)}}\right) & -p_3S^{(8)} \\ q_3p_3Y_2^{(8)} & q_3p_3S^{(8)}-(d_4+d_5) \end{bmatrix}.$$

The characteristics equation of this matrix is:

$$\lambda^2+\left[\frac{r(d_4+d_5)}{kq_3p_3}\right]\lambda+(d_4+d_5)\left(r-m_1-d_1-\frac{r(d_4+d_5)}{kq_3p_3}\right)=0.$$

Please cite this article as: S. Kant, V. Kumar, Stability analysis of predator–prey system with migrating prey and disease infection in both species, Applied Mathematical Modelling (2016), http://dx.doi.org/10.1016/j.apm.2016.10.003

From the above discussion we conclude that the equilibrium $E^{(8)}(S^{(8)}, 0, 0, Y_2^{(8)})$ is locally stable provided the following conditions are satisfied:

$$\begin{cases} \left(\beta\frac{d_4+d_5}{q_3p_3} - p_4 - \left(\frac{[(r-m_1-d_1)-\frac{r(d_4+d_5)}{kq_3p_3}]}{p_3}\right)(c+m_2+d_2)\right) < 0, \\ \left(q_1p_1\frac{d_4+d_5}{q_3p_3} - \gamma\left(\frac{[(r-m_1-d_1)-\frac{r(d_4+d_5)}{kq_3p_3}]}{p_3}\right) - d_3\right) < 0, \\ \left(r-m_1-d_1-\frac{r(d_4+d_5)}{kq_3p_3}\right) > 0. \end{cases} \tag{4.6}$$

4.3.6. Equilibrium $(E^{(9)}(0, 0, Y_1^{(9)}, Y_2^{(9)}))$

The Jacobian matrix at $E^{(9)}(0, 0, Y_1^{(9)}, Y_2^{(9)})$ is:

$$J_{E^{(9)}(0,0,Y_1^{(9)},Y_2^{(9)})} = \begin{pmatrix} (r-m_1-d_1 & 0 & 0 & 0 \\ \quad -p_1Y_1^{(9)} - p_3Y_2^{(9)}) & & & \\ 0 & (-p_2Y_1^{(9)} - p_4Y_2^{(9)} & 0 & 0 \\ & \quad -(c+m_2+d_2)) & & \\ q_1p_1Y_1^{(9)} & q_2p_2Y_1^{(9)} & (-\gamma Y_2^{(9)} - d_3) & -\gamma Y_1^{(9)} \\ q_3p_3Y_2^{(9)} & q_4p_4Y_2^{(9)} & \gamma Y_2^{(9)} & (\gamma Y_1^{(9)} - (d_4+d_5)) \end{pmatrix}.$$

The two eigenvalues are:

$$(r-m_1-d_1-p_1Y_1^{(9)} - p_3Y_2^{(9)}),$$
$$(-p_2Y_1^{(9)} - p_4Y_2^{(9)} - (c+m_2+d_2)).$$

Remaining two eigenvalues are given by the eigenvalues of the matrix:

$$\begin{bmatrix} (-\gamma Y_2^{(9)} - d_3) & -\gamma Y_1^{(9)} \\ \gamma Y_2^{(9)} & (\gamma Y_1^{(9)} - (d_4+d_5)) \end{bmatrix}.$$

The characteristics equation of this matrix is:

$$\lambda^2 + [\gamma Y_2^{(9)} - \gamma Y_1^{(9)} + d_3 + d_4 + d_5]\lambda + (d_4+d_5)(\gamma+d_3) - \gamma d_3 Y_1^{(9)} = 0,$$

after simplification it becomes:

$$\lambda^2 + 2d_3\lambda + (d_4+d_5)\gamma = 0.$$

Now Routh–Hurvitz criteria guarantee that this equation has two roots with negative real parts from the above discussion we find that the equilibrium point $E^{(9)}(0, 0, Y_1^{(9)}, Y_2^{(9)})$ is locally stable provided the following two conditions are satisfied:

$$\begin{cases} \left(r-m_1-d_1-p_1\frac{(d_4+d_5)}{\gamma} - p_3\frac{d_3}{\gamma}\right) < 0, \\ \left(-p_2\frac{(d_4+d_5)}{\gamma} - p_4\frac{d_3}{\gamma} - (c+m_2+d_2)\right) < 0. \end{cases} \tag{4.7}$$

Further, we also note that second condition is also satisfied since parameters under consideration are positive, hence for local stability of the equilibrium $E^{(9)}(0, 0, Y_1^{(9)}, Y_2^{(9)})$ the only condition required is:

$$\left(r-m_1-d_1-p_1\frac{(d_4+d_5)}{\gamma} - p_3\frac{d_3}{\gamma}\right) < 0. \tag{4.8}$$

4.3.7. Equilibrium $(E^{(10)}(0, I^{(10)}, Y_1^{(10)}, Y_2^{(10)}))$

Jacobian matrix at $E^{(10)}(0, I^{(10)}, Y_1^{(10)}, Y_2^{(10)})$ is:

$$J_{E^{(10)}(0,I^{(10)},Y_1^{(10)},Y_2^{(10)})} = \begin{pmatrix} a_{11} & 0 & 0 & 0 \\ \beta I^{(10)} & a_{22} & -p_2I^{(10)} & -p_4I^{(10)} \\ q_1p_1Y_1^{(10)} & q_2p_2Y_1^{(10)} & a_{33} & -\gamma Y_1^{(10)} \\ q_3p_3Y_2^{(10)} & q_4p_4Y_2^{(10)} & \gamma Y_2^{(10)} & a_{44} \end{pmatrix},$$

where,

$$a_{11} = \left(r-m_1-d_1-\left(\frac{r}{k}+\beta\right)I^{(10)} - p_1Y_1^{(10)} - p_3Y_2^{(10)}\right),$$
$$a_{22} = \left(p_2Y_1^{(10)} - p_4Y_2^{(10)} - (c+m_2+d_2)\right),$$

Please cite this article as: S. Kant, V. Kumar, Stability analysis of predator–prey system with migrating prey and disease infection in both species, Applied Mathematical Modelling (2016), http://dx.doi.org/10.1016/j.apm.2016.10.003

$$a_{33} = (q_2 p_2 I^{(10)} - \gamma Y_2^{(10)} - d_3),$$
$$a_{44} = q_4 p_4 I^{(10)} + \gamma Y_1^{(10)} - (d_4 + d_5)).$$

One eigen value is:

$$a_{11} = (r - m_1 - d_1 - \left(\frac{r}{k} + \beta\right) I^{(10)} - p_1 Y_1^{(10)} - p_3 Y_2^{(10)}),$$

and remaining three eigenvalues are given by the eigenvalues of the matrix:

$$J'_{E^{(10)}(0,I^{(10)},Y_1^{(10)},Y_2^{(10)})} = \begin{pmatrix} (p_2 Y_1^{(10)} - p_4 Y_2^{(10)} & -p_2 I^{(10)} & -p_4 I^{(10)} \\ \quad -(c + m_2 + d_2)) & & \\ q_2 p_2 Y_1^{(10)} & (q_2 p_2 I^{(10)} - \gamma Y_2^{(10)} - d_3) & -\gamma Y_1^{(10)} \\ q_4 p_4 Y_2^{(10)} & \gamma Y_2^{(10)} & q_4 p_4 I^{(10)} + \gamma Y_1^{(10)} - (d_4 + d_5)) \end{pmatrix}.$$

The characteristics equation of the above matrix is given by:

$$\lambda^3 + A_1 \lambda^2 + A_2 \lambda + A_3 = 0. \tag{4.9}$$

The values of the coefficients viz.:

$$\begin{cases} A_1 = -tr.(J'_{E^{(10)}(0,I^{(10)},Y_1^{(10)},Y_2^{(10)})}), \\ A_2 = (A_{11}^{(10)} + A_{22}^{(10)} + A_{33}^{(10)}), \\ A_3 = -Det.(J'_{E^{(10)}(0,I^{(10)},Y_1^{(10)},Y_2^{(10)})}). \end{cases}$$

are listed at Appendix A.1. Thus, the equilibrium $E^{(10)}(0, I^{(10)}, Y_1^{(10)}, Y_2^{(10)})$ is locally stable provided the following conditions are satisfied:

$$\begin{cases} \left(r - m_1 - d_1 - \left(\frac{r}{k} + \beta\right) I^{(10)} - p_1 Y_1^{(10)} - p_3 Y_2^{(10)}\right) < 0, \\ A_1 A_2 > A_3, \\ Ai > 0, i = 1, 2, 3. \end{cases} \tag{4.10}$$

4.3.8. Equilibrium $(E^{(11)}(S^{(11)}, 0, Y_1^{(11)}, Y_2^{(11)}))$

The Jacobian matrix at $E^{(11)}(S^{(11)}, 0, Y_1^{(11)}, Y_2^{(11)})$ of the model is given by:

$$J_{E^{(11)}(S^{(11)},0,Y_1^{(11)},Y_2^{(11)})} = \begin{pmatrix} b_{11} & -\left(\frac{r}{k} + \beta\right) S^{(11)} & -p_1 S^{(11)} & -p_3 S^{(11)} \\ 0 & b_{22} & 0 & 0 \\ q_1 p_1 Y_1^{(11)} & q_2 p_2 Y_1^{(11)} & b_{33} & -\gamma Y_1^{(11)} \\ q_3 p_3 Y_2^{(11)} & q_4 p_4 Y_2^{(11)} & \gamma Y_2^{(11)} & b_{44} \end{pmatrix},$$

where,

$$b_{11} = (r - m_1 - d_1 - \frac{2r}{k} S^{(11)} - p_1 Y_1^{(11)} - p_3 Y_2^{(11)}),$$
$$b_{22} = (\beta S^{(11)} - p_2 Y_1^{(11)} - p_4 Y_2^{(11)} - (c + m_2 + d_2)),$$
$$b_{33} = (q_1 p_1 S^{(11)} - \gamma Y_2^{(11)} - d_3),$$
$$b_{44} = (q_3 p_3 S^{(11)} + \gamma Y_1^{(11)} - (d_4 + d_5)).$$

One eigen value of this matrix is:

$$b_{22} = (\beta S^{(11)} - p_2 Y_1^{(11)} - p_4 Y_2^{(11)} - (c + m_2 + d_2)).$$

Remaining three eigenvalues are given by the eigenvalues of the matrix:

$$J'_{E^{(11)}(S^{(11)},0,Y_1^{(11)},Y_2^{(11)})} = \begin{pmatrix} (r - m_1 - d_1 - \frac{2r}{k} S^{(11)} & -p_1 S^{(11)} & -p_3 S^{(11)} \\ \quad -p_1 Y_1^{(11)} - p_3 Y_2^{(11)}) & & \\ q_1 p_1 Y_1^{(11)} & (q_1 p_1 S^{(11)} - \gamma Y_2^{(11)} - d_3) & -\gamma Y_1^{(11)} \\ q_3 p_3 Y_2^{(11)} & \gamma Y_2^{(11)} & (q_3 p_3 S^{(11)} + \gamma Y_1^{(11)} - (d_4 + d_5)) \end{pmatrix}.$$

The eigenvalues are the roots of the characteristics equation:

$$\lambda^3 + B_1 \lambda^2 + B_2 \lambda + B_3 = 0. \tag{4.11}$$

Please cite this article as: S. Kant, V. Kumar, Stability analysis of predator–prey system with migrating prey and disease infection in both species, Applied Mathematical Modelling (2016), http://dx.doi.org/10.1016/j.apm.2016.10.003

The values of the coefficients of this equation viz.:

$$\begin{cases} B_1 = -tr.(J'_{E^{(11)}(S^{(11)},0,Y_1^{(11)},Y_2^{(11)})}), \\ B_2 = (A_{11}^{(11)} + A_{22}^{(11)} + A_{33}^{(11)}), \\ B_3 = -Det.(J'_{E^{(11)}(S^{(11)},0,Y_1^{(11)},Y_2^{(11)})}), \end{cases} \tag{4.12}$$

can see at Appendix A.2. Hence by Routh–Hurwitz criteria the equilibrium $E^{(11)}(S^{(11)}, 0, Y_1^{(11)}, Y_2^{(11)})$ is locally stable provided the following conditions are satisfied:

$$\begin{cases} (\beta S^{(11)} - p_2 Y_1^{(11)} - p_4 Y_2^{(11)} - (c + m_2 + d_2)) < 0, \\ B_1 B_2 > B_3, \\ Bi > 0, i = 1, 2, 3. \end{cases} \tag{4.13}$$

4.3.9. Equilibrium $(E^{(12)}(S^{(12)}, I^{(12)}, 0, Y_2^{(12)}))$

The Jacobian matrix at $E^{(12)}(S^{(12)}, I^{(12)}, 0, Y_2^{(12)})$ is:

$$J_{E^{(12)}(S^{(12)},I^{(12)},0,Y_2^{(12)})} = \begin{pmatrix} c_{11} & -\left(\frac{r}{k} + \beta\right)S^{(12)} & -p_1 S^{(12)} & -p_3 S^{(12)} \\ \beta I^{(12)} & c_{22} & -p_2 I^{(12)} & -p_4 I^{(12)} \\ 0 & 0 & c_{33} & 0 \\ q_3 p_3 Y_2^{(12)} & q_4 p_4 Y_2^{(12)} & \gamma Y_2^{(12)} & c_{44} \end{pmatrix},$$

where,

$$\begin{aligned} c_{11} &= (r - m_1 - d_1 - \frac{2r}{k} S^{(12)} - \left(\frac{r}{k} + \beta\right) I^{(12)} - p_3 Y_2^{(12)}), \\ c_{22} &= (\beta S^{(12)} - p_4 Y_2^{(12)} - (c + m_2 + d_2)), \\ c_{33} &= (q_2 p_2 I^{(12)} + q_1 p_1 S^{(12)} - \gamma Y_2^{(12)} - d_3), \\ c_{44} &= (q_3 p_3 S^{(12)} + q_4 p_4 I^{(12)} - (d_4 + d_5)). \end{aligned}$$

One eigen value of this matrix is:

$$c_{33} = (q_2 p_2 I^{(12)} + q_1 p_1 S^{(12)} - \gamma Y_2^{(12)} - d_3).$$

Remaining three eigenvalues are given by the eigenvalues of the matrix:

$$\begin{pmatrix} (r - m_1 - d_1 - \frac{2r}{k} S^{(12)} - \left(\frac{r}{k} + \beta\right) I^{(12)} - p_3 Y_2^{(12)}) & -\left(\frac{r}{k} + \beta\right) S^{(12)} & -p_3 S^{(12)} \\ \beta I^{(12)} & (\beta S^{(12)} - p_4 Y_2^{(12)} - (c + m_2 + d_2)) & -p_4 I^{(12)} \\ q_3 p_3 Y_2^{(12)} & q_4 p_4 Y_2^{(12)} & (q_3 p_3 S^{(12)} + q_4 p_4 I^{(12)} - (d_4 + d_5)) \end{pmatrix}.$$

The eigenvalues are the roots of the characteristics equation:

$$\lambda^3 + C_1 \lambda^2 + C_2 \lambda + C_3 = 0. \tag{4.14}$$

The values of the coefficients of this equation viz.:

$$\begin{cases} C_1 = -tr.(E^{(12)}(S^{(12)}, I^{(12)}, 0, Y_2^{(12)})), \\ C_2 = (A_{11}^{(12)} + A_{22}^{(12)} + A_{33}^{(12)}), \\ C_3 = -Det.(E^{(12)}(S^{(12)}, I^{(12)}, 0, Y_2^{(12)})), \end{cases} \tag{4.15}$$

can see at Appendix A.3. Hence by Routh–Hurwitz criteria the equilibrium $E^{(11)}(S^{(11)}, 0, Y_1^{(11)}, Y_2^{(11)})$ is locally stable provided the following conditions are satisfied:

$$\begin{cases} (q_2 p_2 I^{(12)} + q_1 p_1 S^{(12)} - \gamma Y_2^{(12)} - d_3) < 0 \\ C_1 C_2 > C_3 \\ Ci > 0, i = 1, 2, 3. \end{cases} \tag{4.16}$$

Please cite this article as: S. Kant, V. Kumar, Stability analysis of predator–prey system with migrating prey and disease infection in both species, Applied Mathematical Modelling (2016), http://dx.doi.org/10.1016/j.apm.2016.10.003

4.3.10. Equilibrium $(E^{(13)}(S^{(13)}, I^{(13)}, Y_1^{(13)}, 0))$

The Jacobian matrix of the model at $E^{(13)}(S^{(13)}, I^{(13)}, Y_1^{(13)}, 0)$ is given by:

$$J_{E^{(13)}(S^{(13)},I^{(13)},Y_1^{(13)},0)} = \begin{pmatrix} d_{11} & -\left(\frac{r}{k}+\beta\right)S^{(13)} & -p_1S^{(13)} & -p_3S^{(13)} \\ \beta I^{(13)} & d_{22} & -p_2I^{(13)} & -p_4S^{(13)} \\ q_1p_1Y_1^{(13)} & q_2p_2Y_1^{(13)} & d_{33} & -\gamma Y_1^{(13)} \\ 0 & 0 & 0 & d_{44} \end{pmatrix},$$

where,

$$d_{11} = \left(r - m_1 - d_1 - \frac{2r}{k}S^{(13)} - \left(\frac{r}{k}+\beta\right)I^{(13)} - p_1Y_1^{(13)}\right),$$
$$d_{22} = (\beta S^{(13)} - p_2Y_1^{(13)} - (c + m_2 + d_2)),$$
$$d_{33} = (q_2p_2S^{(13)} + q_1p_1S^{(13)} - d_3),$$
$$d_{44} = (q_3p_3S^{(13)} + q_4p_4I^{(13)} + \gamma Y_1^{(13)} - (d_4 + d_5)).$$

One eigen value is:

$$d_{44} = (q_3p_3S^{(13)} + q_4p_4I^{(13)} + \gamma Y_1^{(13)} - (d_4 + d_5)).$$

Remaining three eigenvalues are given by the eigenvalues of the matrix:

$$J'_{E^{(13)}(S^{(13)},I^{(13)},Y_1^{(13)},0)} = \begin{pmatrix} \left(r - m_1 - d_1 - \frac{2r}{k}S^{(13)} - \left(\frac{r}{k}+\beta\right)I^{(13)} - p_1Y_1^{(13)}\right) & -\left(\frac{r}{k}+\beta\right)S^{(13)} & -p_1S^{(13)} \\ \beta I^{(13)} & (\beta S^{(13)} - p_2Y_1^{(13)} - (c + m_2 + d_2)) & -p_2I^{(13)} \\ q_1p_1Y_1^{(13)} & q_2p_2Y_1^{(13)} & (q_2p_2I^{(13)} + q_1p_1S^{(13)} - d_3) \end{pmatrix}. \quad (4.17)$$

The characteristics equation is given by:

$$\lambda^3 + D_1\lambda^2 + D_2\lambda + D_3 = 0. \quad (4.18)$$

The values of the coefficients:

$$\begin{cases} D_1 = -tr.(J'_{E^{(13)}(S^{(13)},I^{(13)},Y_1^{(13)},0)}), \\ D_2 = (A_{11}^{(13)} + A_{22}^{(13)} + A_{33}^{(13)}), \\ D_3 = -Det.(J'_{E^{(13)}(S^{(13)},I^{(13)},Y_1^{(13)},0)}) \end{cases}$$

can see at Appendix A.4. From this we can say that the equilibrium $E^{(13)}(S^{(13)}, I^{(13)}, Y_1^{(13)}, 0)$ is locally stable provided the following conditions are satisfied:

$$\begin{cases} (q_3p_3S^{(13)} + q_4p_4I^{(13)} + \gamma Y_1^{(13)} - (d_4 + d_5)) < 0, \\ D_1D_2 > D_3, \\ Di > 0, i = 1, 2, 3. \end{cases} \quad (4.19)$$

4.3.11. Non zero equilibrium $(E^{(14)}(S^{(14)}, I^{(14)}, Y_1^{(14)}, Y_2^{(14)}))$

From ecological point of view this equilibrium is very important. The reason is quite obvious that in this case all four populations will exist simultaneously. This provides actual interaction and competition among all four different populations. The Jacobian matrix of the model is given by:

$$J_{E^{(14)}(S^{(14)},I^{(14)},Y_1^{(14)},Y_2^{(14)})} = \begin{pmatrix} e_{11} & e_{12} & e_{13} & e_{14} \\ e_{21} & e_{22} & e_{23} & e_{24} \\ e_{31} & e_{32} & e_{33} & e_{34} \\ e_{41} & e_{42} & e_{43} & e_{44} \end{pmatrix}, \quad (4.20)$$

where,

$$e_{11} = \left(r - m_1 - d_1 - \frac{2r}{k}S^{(14)} - \left(\frac{r}{k}+\beta\right)I^{(14)} - p_1Y_1^{(14)} - p_3Y_2^{(14)}\right),$$
$$e_{12} = -\left(\frac{r}{k}+\beta\right)S^{(14)},$$

Please cite this article as: S. Kant, V. Kumar, Stability analysis of predator–prey system with migrating prey and disease infection in both species, Applied Mathematical Modelling (2016), http://dx.doi.org/10.1016/j.apm.2016.10.003

$$
\begin{aligned}
e_{13} &= -p_1 S^{(14)},\\
e_{14} &= -p_3 S^{(14)},\\
e_{21} &= \beta I^{(14)},\\
e_{22} &= \left(\beta S^{(14)} - p_2 Y_1^{(14)} - p_4 Y_2^{(14)} - (c + m_2 + d_2)\right),\\
e_{23} &= -p_2 I^{(14)},\\
e_{24} &= -p_4 I^{(14)},\\
e_{31} &= q_1 p_1 Y_1^{(14)},\\
e_{32} &= q_2 p_2 Y_1^{(14)},\\
e_{33} &= \left(q_2 p_2 I^{(14)} + q_1 p_1 S^{(14)} - \gamma Y_2^{(14)} - d_3\right),\\
e_{34} &= -\gamma Y_1^{(14)},\\
e_{41} &= q_3 p_3 Y_2^{(14)},\\
e_{42} &= q_4 p_4 Y_2^{(14)},\\
e_{43} &= \gamma Y_2^{(14)},\\
e_{44} &= \left(q_3 p_3 S^{(14)} + q_4 p_4 I^{(14)} + \gamma Y_1^{(14)} - (d_4 + d_5)\right).
\end{aligned}
$$

The characteristics equation of this matrix may be written as:

$$\lambda^4 + E_1\lambda^3 + E_2\lambda^2 + E_3\lambda + E_4 = 0, \tag{4.21}$$

where,

$E_1 = -(a_{11} + a_{22} + a_{33} + a_{44})$,
$E_2 = \Sigma M_2$, M_2 = Sum of all possible principal minors of order 2.
$E_3 = -\Sigma M_3$, M_3 = Sum of all possible principal minors of order 3.
$E_4 = Det.(J_{E^{(14)}(S^{(14)}, I^{(14)}, Y_1^{(14)}, Y_2^{(14)})})$.

Simplified values of the coefficients of Eq. (4.21) are listed at Appendix (A.5). From Routh-Hurwitz criteria we can conclude that the $E^{(14)}(S^{(14)}, I^{(14)}, Y_1^{(14)}, Y_2^{(14)})$ is locally stable provided:

$$
\begin{cases}
E_i > 0, i = 1, 2, 3, 4,\\
E_1E_2 - E_3 > 0,\\
E_1(E_2E_3 - E_1E_4) - E_3^2 > 0.
\end{cases} \tag{4.22}
$$

5. Numerical examples

In this section, we performed some numerical simulations. Few parameters are taken from Hu and Li [16] and few are assumed (Table 4). It is assumed that all the parameters are constant except migration parameters m_1 and m_2. We varied the values of migration parameters m_1 and m_2 and observed the effect on the dynamics of system (2.1).

5.1. Example 1

If we assume $m_1 = m_2 = 0$ and $I = Y_2 = 0$, with parameters in Table 4, mathematical model (3.1) takes the form:

$$
\begin{aligned}
\frac{dS}{dt} &= \frac{1}{2}S\left(1 - \frac{S}{1000}\right) - \frac{1}{8}SY_1 - \frac{1}{8}S,\\
\frac{dY_1}{dt} &= \frac{1}{64}SY_1 - \frac{1}{8}Y_1.
\end{aligned} \tag{5.1}
$$

This is observed that system admits all the three equilibrium points (Table 2) they are: (i)$E_1(0, 0)$, (ii)$E_2(750, 0)$ and (iii)$E_3(8, \frac{371}{125})$. From Section 3 (Table 2), it is noticed that $E_1(0, 0)$ is unstable because $r - d_1 = \frac{3}{8} > 0$. Thus we needed to check the stability of remaining two equilibrium points viz. $E_2(750, 0)$ and $E_3(8, \frac{371}{125})$. Since $(\frac{(r-d_1)kq_1p_1}{r} - d_3) = \frac{371}{32} > 0$, hence by the result in Section 3 (Table 2), we concluded that $E_2(750, 0)$ is unstable. Further, $[(r - d_1) - \frac{rd_3}{kq_1p_1}] = \frac{742}{2000} > 0$ again from Section 3 (Table 2), it is concluded that $E_3(8, \frac{371}{125})$ is locally stable.

As mentioned in Remark 2, m_1 *and* m_2 followed the probability distributions but in this paper we considered them as constant rates only (see Fig. 1). More precisely these are considered as probabilities. Since probabilities lies between 0 and 1, so $m_1, m_2 \in [0, 1]$.

Please cite this article as: S. Kant, V. Kumar, Stability analysis of predator–prey system with migrating prey and disease infection in both species, Applied Mathematical Modelling (2016), http://dx.doi.org/10.1016/j.apm.2016.10.003

Table 4
Parameter values.

Symbol	Numerical value	Source
r	1/2	Hu and Li [16]
k	1000	Assumed
β	1/2	Assumed
γ	1/4	Assumed
p_1	1/8	Hu and Li [16]
p_2	1/8	Assumed
p_3	1/4	Assumed
p_4	1/16	Assumed
q_1	1/8	Assumed
q_2	1/16	Assumed
q_3	1/4	Assumed
q_4	1/16	Assumed
d_1	1/8	Assumed
d_2	1/4	Assumed
d_3	1/8	Assumed
d_4	1/16	Assumed
d_5	1/4	Assumed
c	1/4	Hu and Li [16]
$S(0)$	1000	Assumed
$I(0)$	10	Assumed
$Y_1(0)$	1000	Assumed
$Y_2(0)$	0	Assumed

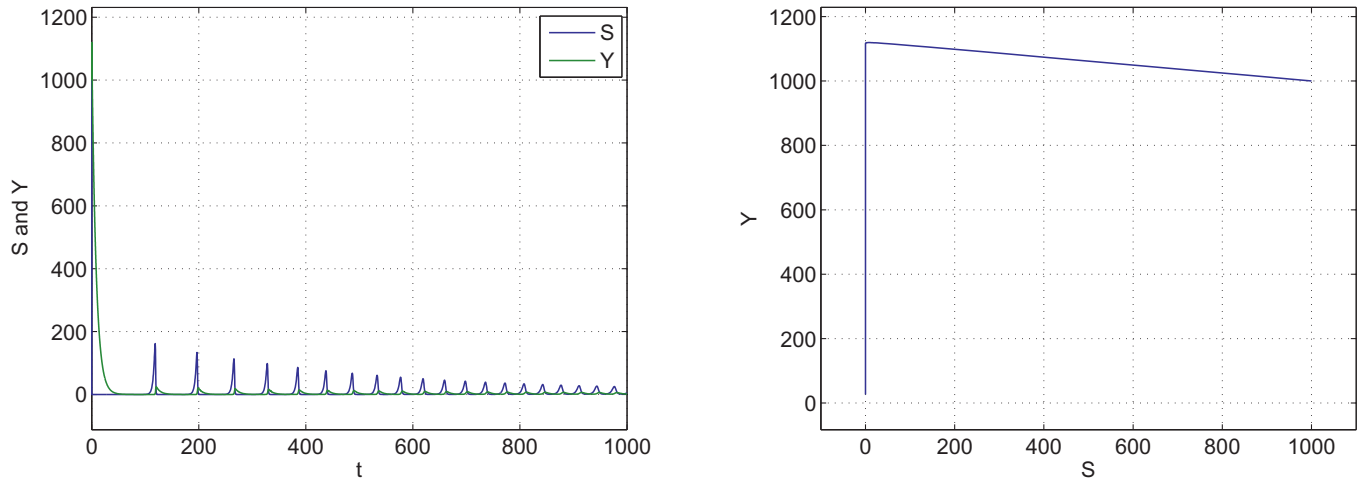


Fig. 1. Numerical solution with parameter set in Table 4 for the model without disease and migration.

We take $m_1 = \frac{1}{3}$ and $m_2 = \frac{1}{6}$. Model (3.2) is:

$$\frac{dS}{dt} = \frac{1}{2}S\left(1 - \frac{S}{1000}\right) - \frac{1}{8}SY_1 - \left(\frac{1}{8} + \frac{1}{3}\right)S,$$
$$\frac{dY_1}{dt} = \frac{1}{64}SY_1 - \frac{1}{8}Y_1. \tag{5.2}$$

This is observed that systems admits all the three equilibrium points they are: (i)$E_1^*(0,0)$, (ii)$E_2^*(\frac{250}{3}, 0)$ and (iii) $E_3^*(8, \frac{226}{750})$. From Section 3, it is noticed that $E_1^*(0,0)$ is always unstable. Thus we needed to check the stability of remaining two equilibrium points viz. $E_2^*(\frac{250}{3}, 0)$ and $E_3^*(8, \frac{226}{750})$. Since $(\frac{(r-d_1-m_1)kq_1p_1}{r} - d_3) = \frac{113}{96} > 0$, hence by the result in Section 3, we concluded that $E_2^*(\frac{250}{3}, 0)$ is unstable. Further, $[(r - d_1 - m_1) - \frac{rd_3}{kq_1p_1}] = \frac{742}{2000} > 0$ therefore by the result in Section 3, we seen that $E_3^*(8, \frac{226}{750})$ is locally stable (see Fig. 2).

If we put $m_1 = \frac{1}{3}$ and $m_2 = \frac{1}{6}$. Model (2.1) is:

$$\frac{dS}{dt} = \frac{1}{2}S\left(1 - \frac{S+I}{1000}\right) - \frac{1}{2}SI - \frac{1}{8}SY_1 - \frac{1}{4}SY_2 - \left(\frac{1}{8} + \frac{1}{3}\right)S,$$
$$\frac{dI}{dt} = \frac{1}{2}SI - \frac{1}{8}IY_1 - \frac{1}{16}IY_2 - \left(\frac{1}{8} + \frac{1}{6} + \frac{1}{4}\right),$$

Please cite this article as: S. Kant, V. Kumar, Stability analysis of predator–prey system with migrating prey and disease infection in both species, Applied Mathematical Modelling (2016), http://dx.doi.org/10.1016/j.apm.2016.10.003

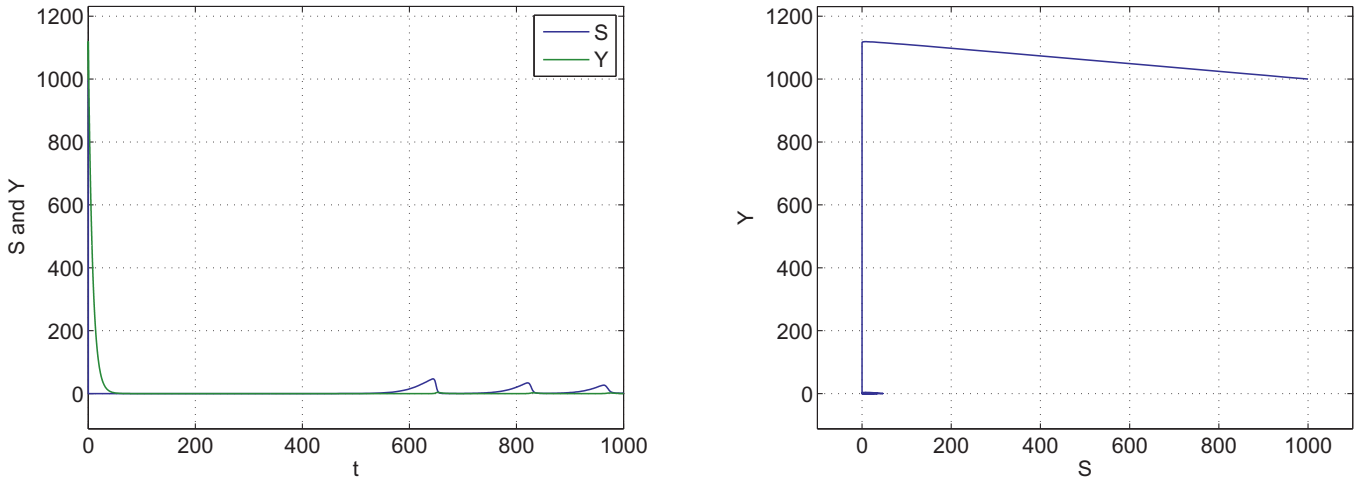


Fig. 2. Numerical solution with parameter set in Table 4 for the model without disease with $m_1 = 1/3, m_2 = 1/6$.

$$\frac{dY_1}{dt} = \frac{1}{64}SY_1 + \frac{1}{128}IY_1 - \frac{1}{4}Y_1Y_2 - \frac{1}{8}Y_1,$$
$$\frac{dY_2}{dt} = \frac{1}{16}SY_2 + \frac{1}{256}IY_2 + \frac{1}{4}Y_1Y_2 - \left(\frac{1}{16} + \frac{1}{4}\right)Y_2. \tag{5.3}$$

From Section 4, we noted that equilibria $E^{(1)}(0, 0, 0, 0)$, $E^{(2)}(1000, 0, 0, 0)$ and $E^{(9)}(0, 0, \frac{5}{4}, \frac{1}{2})$ do always exist. Also $E^{(3)}$, $E^{(4)}$ and $E^{(5)}$ do not exist. Since $k\beta(r - m_1 - d_1) - r(c + d_2 + m_2) > 0$ hence from Section 4, the equilibrium $E^{(6)}$ exists. Further $(r - m_1 - d_1) - \frac{rd_3}{kq_1p_1} = (\frac{1}{24} - \frac{1}{250}) = \frac{226}{6000} > 0$, hence by existence condition for $E^{(7)}$ this equilibrium exist. Next $(r - m_1 - d_1) - \frac{r(d_4+d_5)}{kq_1p_1} = \frac{1}{24} - \frac{1}{100} > 0$, hence by existence condition for $E^{(8)}$ this equilibrium exist as well. For existence of the equilibrium $E^{(10)}$ let us check the existence conditions $[\gamma(c + d_2 + m_2) + p_2(d_4 + d_5) - p_4d_3] = \frac{38}{192} > 0$, $p_2q_4 - q_2p_2 = 0$ hence $E^{(10)}$ does not exist. Similarly one of the existence conditions for the equilibrium $E^{(11)}$ $(r - m_1 - d_1) - \frac{rd_3}{kq_1p_1} + p_3 = -\frac{3}{16} < 0$ is not satisfied hence $E^{(11)}$ does not exist. To investigate the existence of the $E^{(12)}$, we have $S^{(12)} = \frac{-X}{Y}, X = -\frac{22399}{600} and Y = \frac{1751875}{250000} \Rightarrow S^{(12)} = \frac{55997500}{1751875} \equiv 31.96$, now $d_4 + d_5 - q_3p_3S^{(12)} = -\frac{26.96}{16} < 0$, hence by Section 4, $S^{(12)}$ does not exist. Similarly, $S^{(13)} = \frac{-B}{A}$, $B = -\frac{21899}{3000}$, $A = \frac{1001}{2000} \Rightarrow S^{(13)} \equiv 14.58$, now $d_3 - q_1p_1S^{(13)} = \frac{-6.58}{64} < 0$, hence by Section 4, $E^{(13)}$ does not exist. Let us proceed for the existence of $E^{(14)}$, we note that:

Condition 1: $\gamma - \frac{\gamma q_1(p_3 + \frac{r\gamma}{q_1p_1k})}{q_3p_3} = \frac{121}{1000} > 0$, hence this is satisfied.

Condition 2: $\frac{\beta d_3}{q_1p_1} - (c + m_2 + d_2) - \frac{p_2}{p_1}(r - m_1 - d_1 - \frac{d_3\gamma}{q_1p_1k}) = \frac{38572}{12000} > 0$, this is also satisfied.

Condition 3: $(\frac{\gamma\beta}{q_1p_1} - p_4) + \frac{p_2(p_3 + \frac{\gamma r}{q_1p_1k})}{p_1} = \frac{127}{16} + \frac{129}{500} > 0$, this condition is also satisfied.

Condition 4: $\left(\frac{q_1p_1(d_4+d_5)}{q_3p_3} - d_3 - \frac{\gamma q_1}{q_3p_3}(r - m_1 - d_1 - \frac{\gamma d_3}{q_1p_1k})\right) = \frac{10384}{96000} > 0.$

Condition 5: $\left[\frac{\gamma q_1}{q_3p_3}\left(\frac{rq_2p_2}{q_1p_1k} - (\frac{r}{k} + \beta) + q_2p_2 + \frac{q_1p_1q_4p_4}{q_3p_3}\right)\right] = \frac{-2013024}{4096000} < 0$ which is not satisfied since $\left[\frac{\gamma q_1}{q_3p_3}\left(\frac{rq_2p_2}{q_1p_1k} - (\frac{r}{k} + \beta) + q_2p_2 + \frac{q_1p_1q_4p_4}{q_3p_3}\right)\right]$ should be greater than zero. Therefore remaining conditions is not required to be checked. Thus non zero equilibrium $E^{(14)}$ does not exist (see Fig. 3).

5.2. Example 2

With parameters in Table 4 and $m_1 = \frac{1}{6}$, $m_2 = \frac{1}{8}$ $(m_1 > m_2)$. Model (3.2) takes the form:

$$\frac{dS}{dt} = \frac{1}{2}S(1 - \frac{S}{1000}) - \frac{1}{8}SY_1 - (\frac{1}{8} + \frac{1}{6})S,$$
$$\frac{dY_1}{dt} = \frac{1}{64}SY_1 - \frac{1}{8}Y_1. \tag{5.4}$$

Then (i) $E_1^*(0, 0)$ exists but not stable, (ii) $E_2^*(416.6, 0)$ exists but not stable and (iii) $E_3^*(8, .2043)$ exists and stable.

Please cite this article as: S. Kant, V. Kumar, Stability analysis of predator–prey system with migrating prey and disease infection in both species, Applied Mathematical Modelling (2016), http://dx.doi.org/10.1016/j.apm.2016.10.003

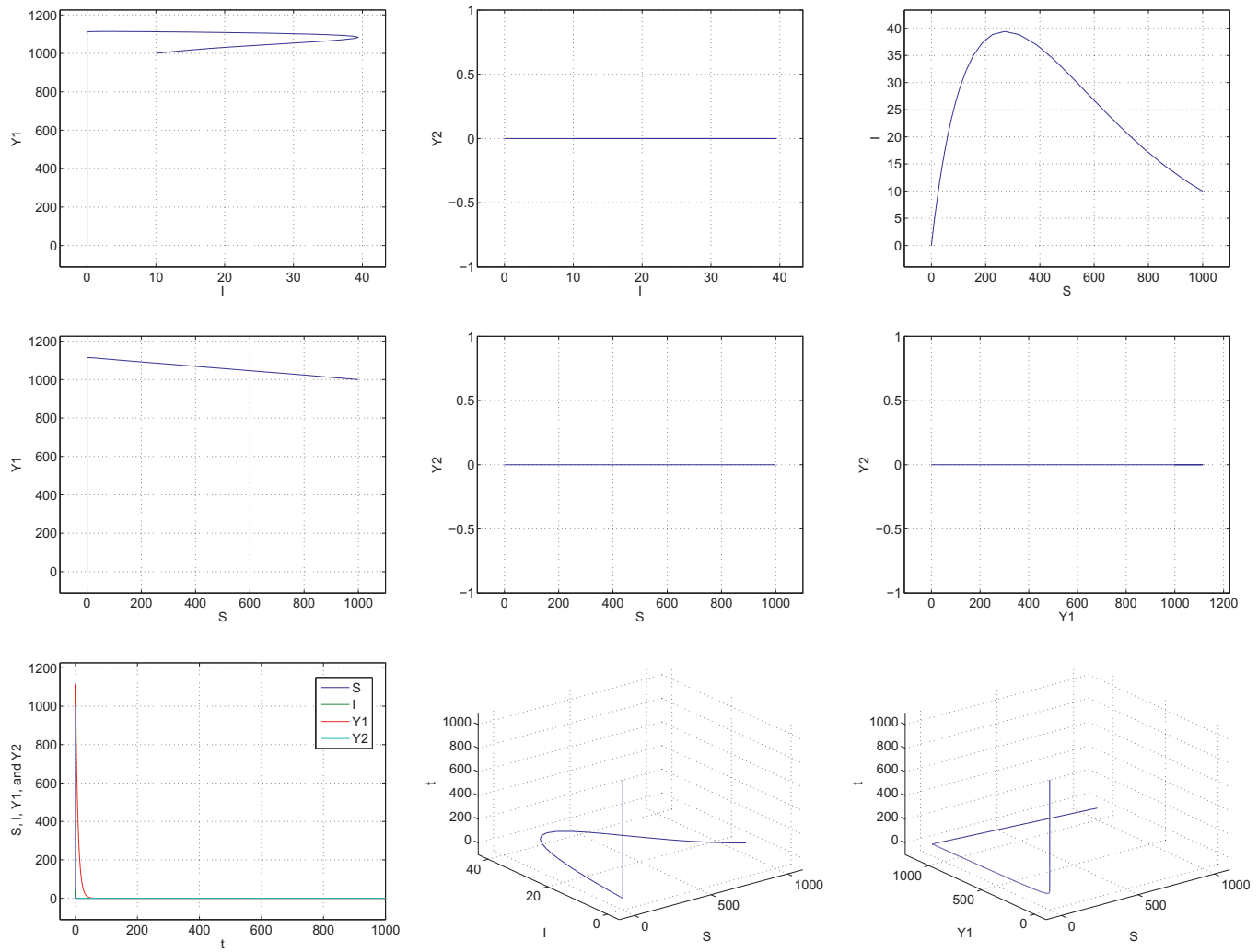


Fig. 3. Numerical solution with parameter set in Table 4 for the main model with $m_1 = 1/3, m_2 = 1/6$.

Model (2.1) takes the form:

$$\begin{aligned}
\frac{dS}{dt} &= \frac{1}{2}S\left(1 - \frac{S+I}{1000}\right) - \frac{1}{2}SI - \frac{1}{8}SY_1 - \frac{1}{4}SY_2 - \left(\frac{1}{8} + \frac{1}{6}\right)S,\\
\frac{dI}{dt} &= \frac{1}{2}SI - \frac{1}{8}IY_1 - \frac{1}{16}IY_2 - \left(\frac{1}{8} + \frac{1}{8} + \frac{1}{4}\right),\\
\frac{dY_1}{dt} &= \frac{1}{64}SY_1 + \frac{1}{128}IY_1 - \frac{1}{4}Y_1Y_2 - \frac{1}{8}Y_1,\\
\frac{dY_2}{dt} &= \frac{1}{16}SY_2 + \frac{1}{256}IY_2 + \frac{1}{4}Y_1Y_2 - \left(\frac{1}{16} + \frac{1}{4}\right)Y_2.
\end{aligned} \tag{5.5}$$

Equilibrium points $E^{(1)}(0, 0, 0, 0)$, $E^{(2)}(1000, 0, 0, 0)$ and $E^{(9)}(0, 0, \frac{5}{4}, \frac{1}{2})$ are independent of migration and always exist and $E^{(3)}$, $E^{(4)}$, $E^{(5)}$ never exist. The equilibrium point $E^{(6)}(.3125, .4149, 0, 0)$ exists and $q_3p_3S^{(6)} + q_4p_4I^{(6)} - (d_4 + d_5) = -.3060 < 0$, $q_2p_2I^{(6)} + q_1p_1S^{(6)} - (d_3) = -.1169 < 0$, $(r - m_1 - d_1) - \frac{r(c+m_2+d_2)}{k\beta} = .2081 > 0$, therefore $E^{(6)}(.3125, .4149, 0, 0)$ is locally stable. $E^{(7)}(8, 0, 1.6344, 0)$ exists and $\frac{q_3p_3d_3}{q_1p_1} + \frac{\gamma}{q_1}(r - m_1 - d_1 - \frac{d_3}{q_1p_1}) - (d_4 + d_5) = .5961 > 0$, hence $E^{(7)}(8, 0, 1.6344, 0)$ is not stable. $E^{(8)}(5, 0, 0, .8332)$ exists and $(\beta\frac{d_4+d_5}{q_3p_3} - p_4 - \left(\frac{[(r-m_1-d_1)-\frac{r(d_4+d_5)}{kq_3p_3}]}{p_3}\right)(c + m_2 + d_2)) = -.5735 < 0, (q_1p_1\frac{d_4+d_5}{q_3p_3} - \gamma\left(\frac{[(r-m_1-d_1)-\frac{r(d_4+d_5)}{kq_3p_3}]}{p_3}\right) - d_3) = -.3330 < 0$. Hence, $E^{(8)}(5, 0, 0, .8332)$ is stable. Since $(r - m_1 - d_1 - p_1\frac{(d_4+d_5)}{\gamma} - p_3\frac{d_3}{\gamma}) = .1907 < 0$, $E^{(9)}(0, 0, \frac{5}{4}, \frac{1}{2})$ is not stable. Equilibria $E^{(10)}$, $E^{(11)}$, $E^{(12)}$, $E^{(13)}$, $E^{(14)}$ do not exist (see Fig. 4).

The basic reproduction number in this case is calculated as $R_0 = 8.37 > 1$. Therefore disease in this case is endemic.

Please cite this article as: S. Kant, V. Kumar, Stability analysis of predator–prey system with migrating prey and disease infection in both species, Applied Mathematical Modelling (2016), http://dx.doi.org/10.1016/j.apm.2016.10.003

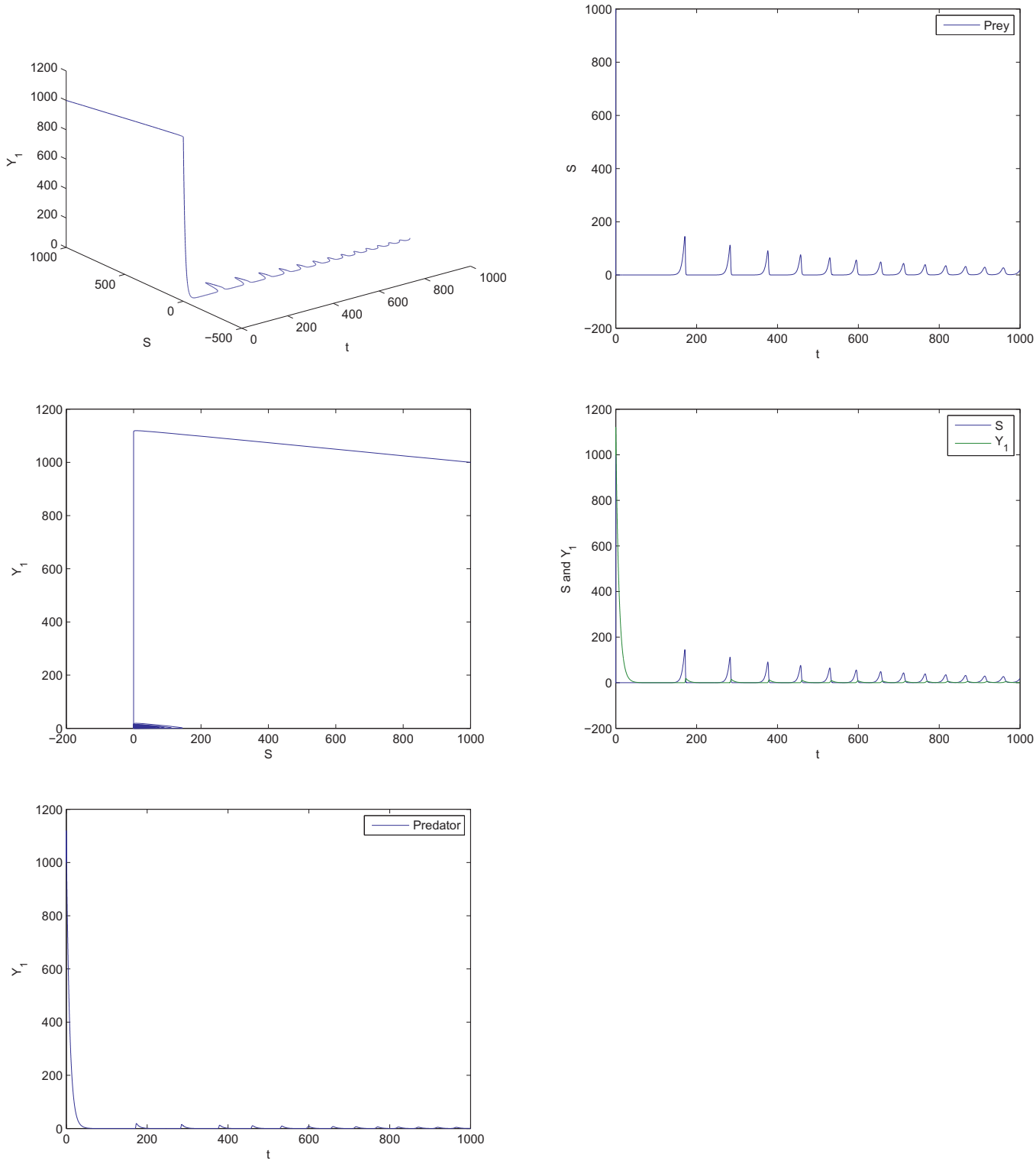


Fig. 4. Numerical solution of model without disease with parameter set in Table 4 with $m_1 = 1/6, m_2 = 1/8$.

5.3. Example 3

With parameters in Table 4 and $m_1 = \frac{1}{6}$, $m_2 = \frac{1}{6}$ $(m_1 = m_2)$. Model (2.1) takes the form:

$$\frac{dS}{dt} = \frac{1}{2}S\left(1 - \frac{S+I}{1000}\right) - \frac{1}{2}SI - \frac{1}{8}SY_1 - \frac{1}{4}SY_2 - \left(\frac{1}{8} + \frac{1}{6}\right)S,$$
$$\frac{dI}{dt} = \frac{1}{2}SI - \frac{1}{8}IY_1 - \frac{1}{16}IY_2 - \left(\frac{1}{8} + \frac{1}{6} + \frac{1}{4}\right)I,$$

Please cite this article as: S. Kant, V. Kumar, Stability analysis of predator–prey system with migrating prey and disease infection in both species, Applied Mathematical Modelling (2016), http://dx.doi.org/10.1016/j.apm.2016.10.003

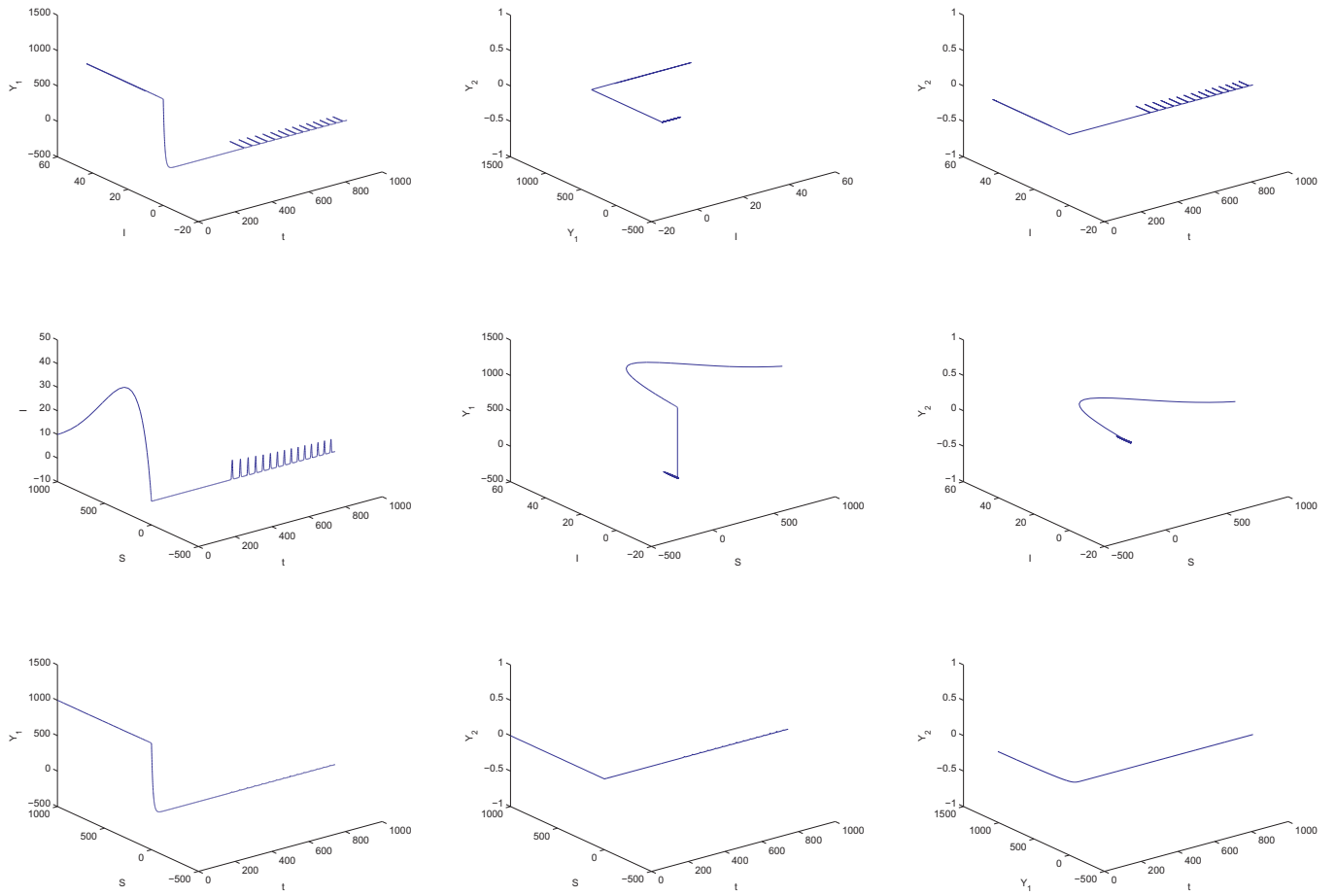


Fig. 5. Numerical solution of model with parameter set in Table 4 with $m_1 = 1/6, m_2 = 1/8$.

$$\begin{aligned}
\frac{dY_1}{dt} &= \frac{1}{64}SY_1 + \frac{1}{128}IY_1 - \frac{1}{4}Y_1Y_2 - \frac{1}{8}Y_1,\\
\frac{dY_2}{dt} &= \frac{1}{16}SY_2 + \frac{1}{256}IY_2 + \frac{1}{4}Y_1Y_2 - \left(\frac{1}{16} + \frac{1}{4}\right)Y_2.
\end{aligned} \tag{5.6}$$

The equilibrium point $E^{(6)}(1.3334, .1027, 0, 0)$ exists and $q_3p_3S^{(6)} + q_4p_4I^{(6)} - (d_4 + d_5) = -.2288 < 0$, $q_2p_2I^{(6)} + q_1p_1S^{(6)} - (d_3) = -.0409 < 0$, therefore $E^{(6)}(1.334, .1027, 0, 0)$ is locally stable. $E^{(7)}(8, 0, 1.6344, 0)$ exists and $\frac{q_3p_3d_3}{q_1p_1} + \frac{\gamma}{q_1}(r - m_1 - d_1 - \frac{d_3}{q_1p_1}) - (d_4 + d_5) = .5961 > 0$, hence $E^{(7)}(8, 0, 1.6344, 0)$ is not stable. $E^{(8)}(5, 0, 0, .8232)$ exists and $(\beta\frac{d_4+d_5}{q_3p_3} - p_4 - \left(\frac{[(r-m_1-d_1)-\frac{r(d_4+d_5)}{kq_3p_3}]}{p_3}\right)(c + m_2 + d_2)) = -0.6016 < 0$,. Hence, $E^{(8)}(5, 0, 0, .8332)$ is not stable. Since $(r - m_1 - d_1 - p_1\frac{(d_4+d_5)}{\gamma} - p_3\frac{d_3}{\gamma}) = -.0729 < 0$, $E^{(9)}(0, 0, \frac{5}{4}, \frac{1}{2})$ is stable. Equilibria $E^{(10)}$, $E^{(11)}$, $E^{(12)}$, $E^{(13)}$, $E^{(14)}$ do not exist (Figs. 5–8).

The basic reproduction number in this case is calculated as $R_0 = 7.84 > 1$. Therefore disease in this case is endemic.

5.4. Example 4

With parameters in Table 4 and $m_1 = \frac{1}{6}$, $m_2 = \frac{1}{3}$ ($m_1 < m_2$). Model (2.1) takes the form:

$$\begin{aligned}
\frac{dS}{dt} &= \frac{1}{2}S\left(1 - \frac{S+I}{1000}\right) - \frac{1}{2}SI - \frac{1}{8}SY_1 - \frac{1}{4}SY_2 - \left(\frac{1}{8} + \frac{1}{6}\right)S,\\
\frac{dI}{dt} &= \frac{1}{2}SI - \frac{1}{8}IY_1 - \frac{1}{16}IY_2 - \left(\frac{1}{8} + \frac{1}{3} + \frac{1}{4}\right)I,\\
\frac{dY_1}{dt} &= \frac{1}{64}SY_1 + \frac{1}{128}IY_1 - \frac{1}{4}Y_1Y_2 - \frac{1}{8}Y_1,\\
\frac{dY_2}{dt} &= \frac{1}{16}SY_2 + \frac{1}{256}IY_2 + \frac{1}{4}Y_1Y_2 - \left(\frac{1}{16} + \frac{1}{4}\right)Y_2.
\end{aligned} \tag{5.7}$$

Please cite this article as: S. Kant, V. Kumar, Stability analysis of predator–prey system with migrating prey and disease infection in both species, Applied Mathematical Modelling (2016), http://dx.doi.org/10.1016/j.apm.2016.10.003

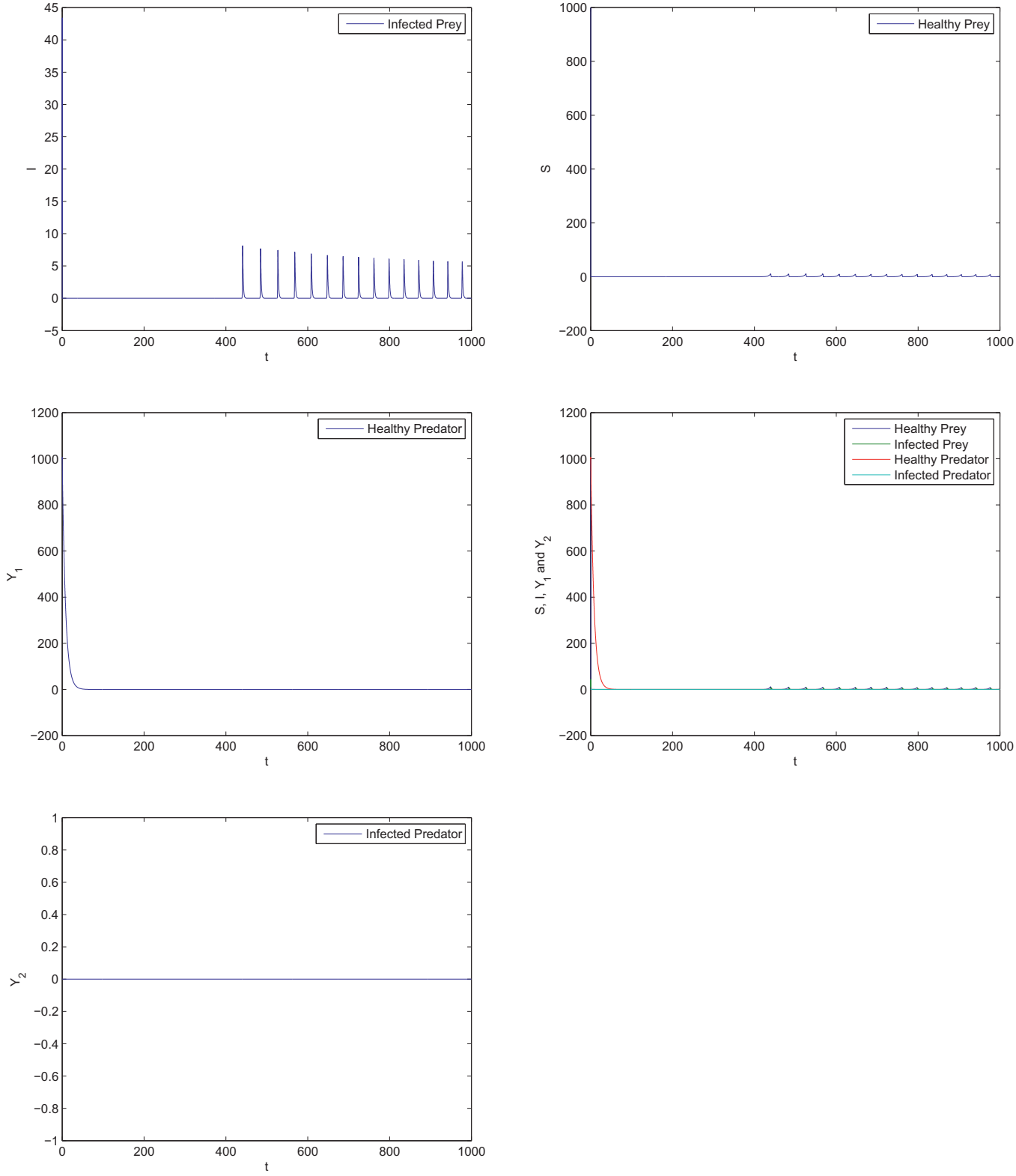


Fig. 6. Numerical solution of model with parameter set in Table 4 with $m_1 = 1/6, m_2 = 1/8$ (contd.).

The equilibrium point $E^{(6)}(.4167, .4145, 0, 0)$ exists and $q_3p_3S^{(6)} + q_4p_4I^{(6)} - (d_4 + d_5) = -.2848 < 0$, $q_2p_2I^{(6)} + q_1p_1S^{(6)} - (d_3) = -.0957 < 0$, therefore $E^{(6)}(1.3334, .1027, 0, 0)$ is locally stable. $E^{(7)}(8, 0, .8172, 0)$ exists and $\frac{q_3p_3d_3}{q_1p_1} + \frac{\gamma}{q_1}(r - m_1 - d_1 - \frac{d_3}{q_1p_1}) - (d_4 + d_5) = .5961 > 0$, hence $E^{(7)}(8, 0, 1.6344, 0)$ is not stable. $E^{(8)}(5, 0, 0, .0515)$ exists and $(\beta\frac{d_4+d_5}{q_3p_3} - p_4 -$

Please cite this article as: S. Kant, V. Kumar, Stability analysis of predator–prey system with migrating prey and disease infection in both species, Applied Mathematical Modelling (2016), http://dx.doi.org/10.1016/j.apm.2016.10.003

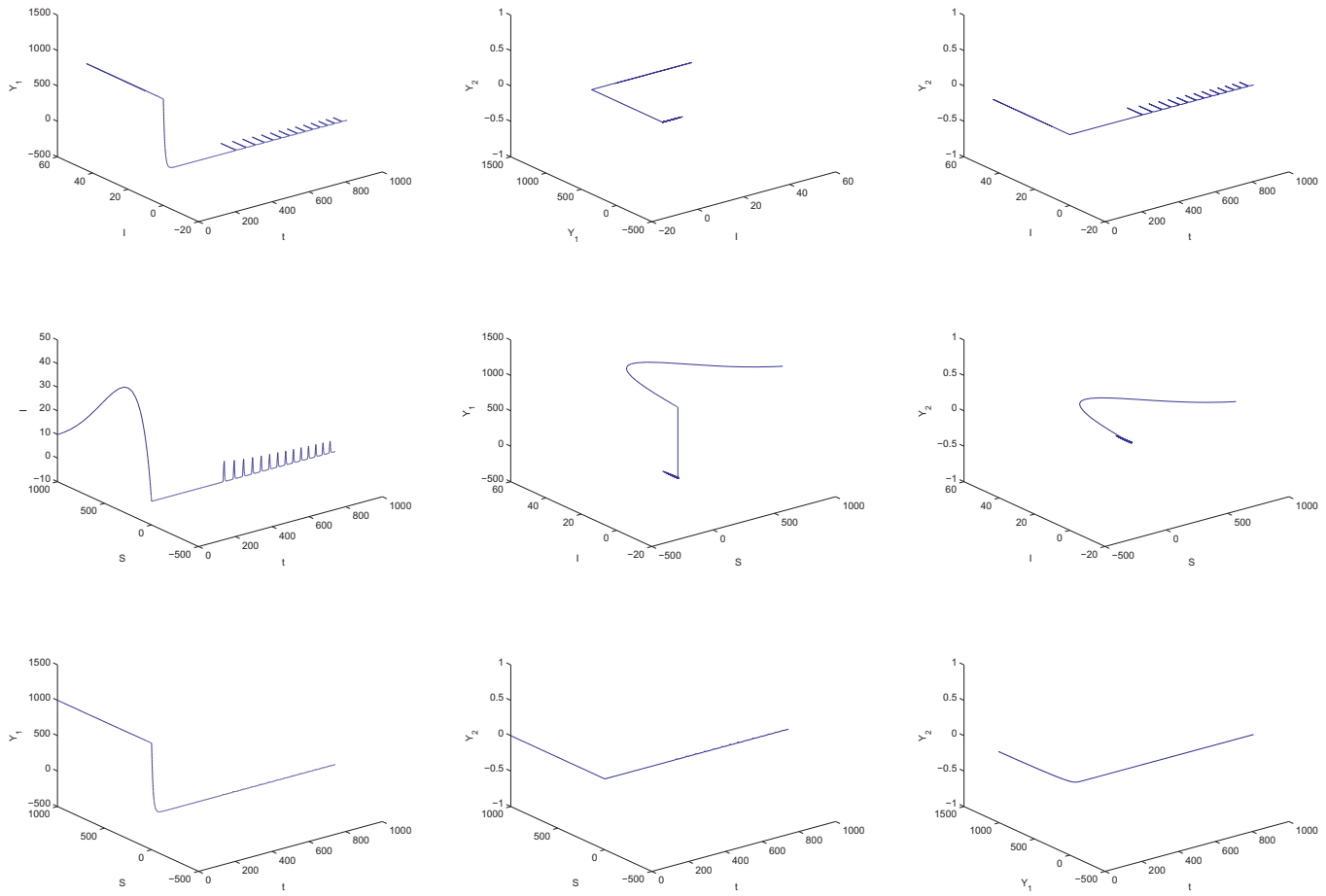


Fig. 7. Numerical solution of model with parameter set in Table 4 with $m_1 = 1/6, m_2 = 1/6$.

$\left(\frac{[(r-m_1-d_1)-\frac{r(d_4+d_5)}{kq_3p_3}]}{p_3}\right)(c+m_2+d_2)) = 1.7515 > 0$, $(q_1p_1\frac{d_4+d_5}{q_3p_3} - \gamma\left(\frac{[(r-m_1-d_1)-\frac{r(d_4+d_5)}{kq_3p_3}]}{p_3}\right) - d_3) = -.0980 < 0$ Hence, $E^{(8)}(5,$ 0, 0, .8332) is stable. Since $(r - m_1 - d_1 - p_1\frac{(d_4+d_5)}{\gamma} - p_3\frac{d_3}{\gamma}) = -.0729 < 0$, $E^{(9)}(0, 0, \frac{5}{4}, \frac{1}{2})$ is stable. Equilibria $E^{(10)}$, $E^{(11)}$, $E^{(12)}$, $E^{(13)}$, $E^{(14)}$ do not exist.

The basic reproduction number in this case is calculated as $R_0 = 6.27 > 1$. Therefore disease in this case is endemic (Figs. 9 and 10).

Remark 5. It is seen that migration parameters m_1 *and* m_2 have the range [0, 1]. Therefore there are two extreme cases (i) $m_1 = 0$ (ii) $m_1 = 1$. If we diagnose both the cases, we found that case (i) is corresponding to no migration and therefore in this case it is feasible to draw a conclusion that extinction of healthy prey is possible only due to mortality. Case (ii) is corresponding to 100 percent out migration of healthy prey. Therefore, extinction of healthy prey is possible only due to out migration. It means that in case (ii), healthy prey will be out migrated before death/predation. It must be noted that both the cases are ideal and practically not feasible. If it is possible to perform an empirical study of any ecosystem such cases may be validated. On the same way, conclusion for $m_2 = 0, m_2 = 1$ may be drawn.

6. Discussion

In this paper, we studied a diseased predator–prey system wherein migration of prey is allowed. Crucial step in the modeling process of the prey predator systems is to identify the predator's functional response. A number of functional responses have been proposed e.g.

- $g(x) = C(t)x$: Holling type I or linear function response [40–42].
- $g(x) = \frac{C(t)x}{m+x}$: Holling type II [40–43].
- $g(x) = \frac{C(t)x^p}{1+mx^p}, 0 < p \leq 1$: Generalized type II Holling functional response [44].
- $g(x) = \frac{C(t)x^2}{m+x^2}$: Holling type III [40–42].
- $g(x) = \frac{C(t)x}{a+x+\frac{x^2}{m}}$: Holling type IV [42,45–48].

Please cite this article as: S. Kant, V. Kumar, Stability analysis of predator–prey system with migrating prey and disease infection in both species, Applied Mathematical Modelling (2016), http://dx.doi.org/10.1016/j.apm.2016.10.003

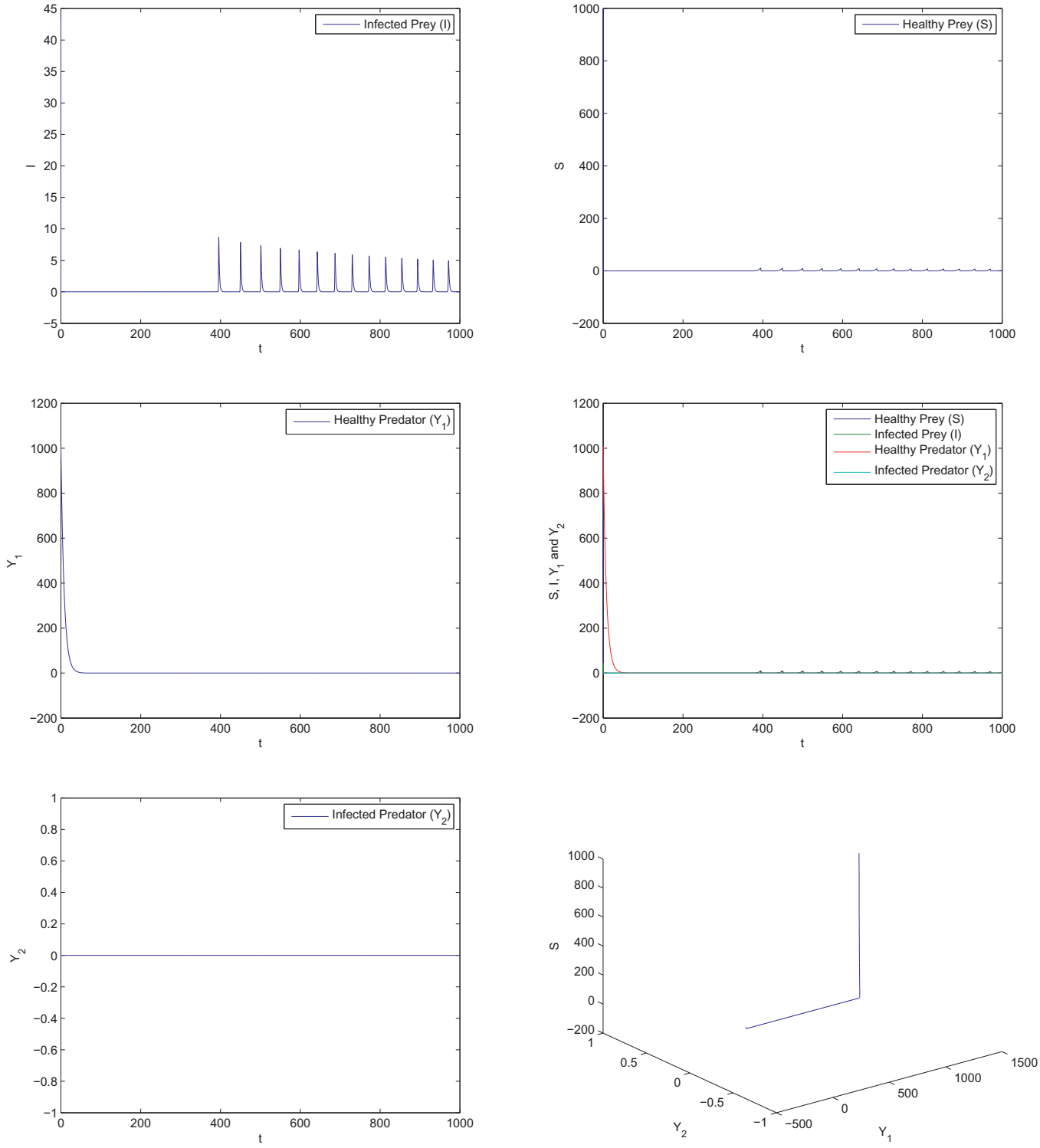


Fig. 8. Numerical solution of model with parameter set in Table 4 with $m_1 = 1/6, m_2 = 1/6$ (contd.).

- $g(x, y) = \frac{xy}{ay+x}$: Ratio dependent [49–51].
- $g(x, y) = \frac{Cxy}{(1+ax)(1+by)}$: Crowley–Martin type functional response [52,53].
- Hassell–Verley type functional response [53,54].
- $g(x, y) = \frac{Cx}{1+k_1x+k_2y}$: Beddington–De Anglis type [53,55,56].
- Function response of the type $g(x) = k(1 - e^{-Cx})$ (Ivlev [57]).

Many papers are available in literature for these functional responses. It is also remarkable that Holling type functional responses are more frequently used as compare to other functional responses. Recently a very good study of Dawes and

Please cite this article as: S. Kant, V. Kumar, Stability analysis of predator–prey system with migrating prey and disease infection in both species, Applied Mathematical Modelling (2016), http://dx.doi.org/10.1016/j.apm.2016.10.003

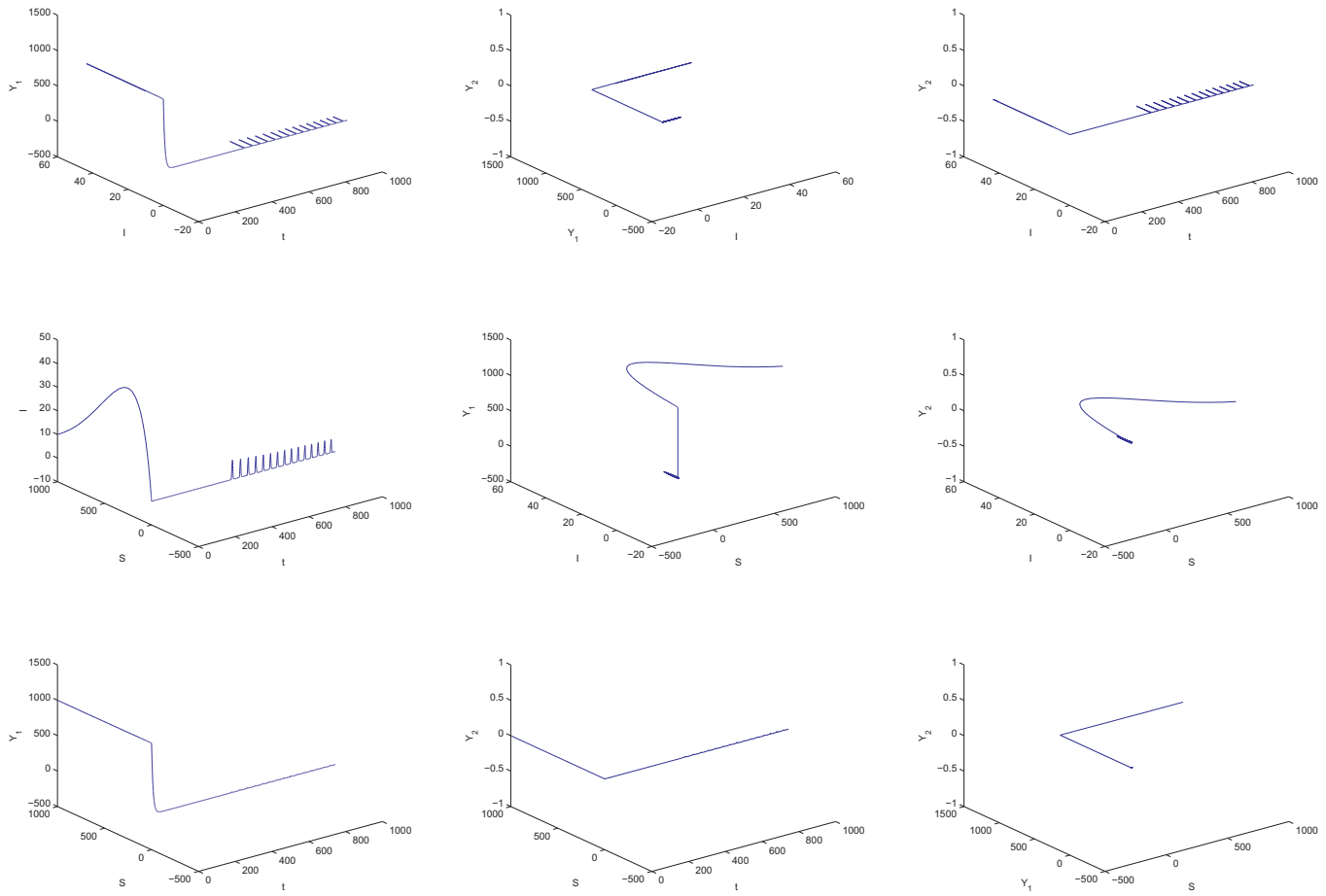


Fig. 9. Numerical solution of model with parameter set in Table 4 with $m_1 = 1/6, m_2 = 1/3$.

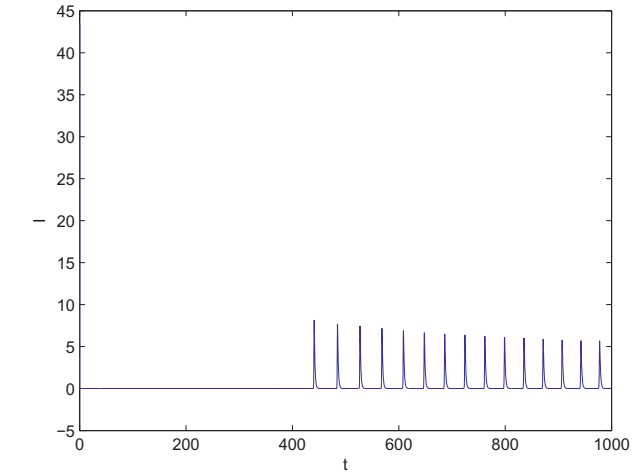
Table 5
Dependency of equilibria on migration for the model (2.1).

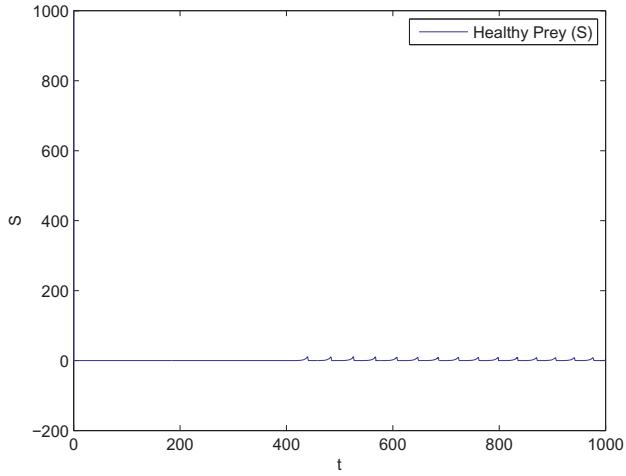
Equilibria	Existence	Stability
$E^{(1)}$	Independent	Independent
$E^{(2)}$	Independent	m_2
$E^{(9)}$	Independent	m_1
$E^{(6)}$	m_1, m_2	m_1, m_2
$E^{(7)}$	m_1	m_1, m_2
$E^{(8)}$	m_1	m_1, m_2
$E^{(10)}$	m_2	m_2
$E^{(11)}$	m_1	m_1, m_2
$E^{(12)}$	m_1, m_2	m_1, m_2
$E^{(13)}$	m_1, m_2	m_1, m_2
$E^{(14)}$	m_1, m_2	m_1, m_2

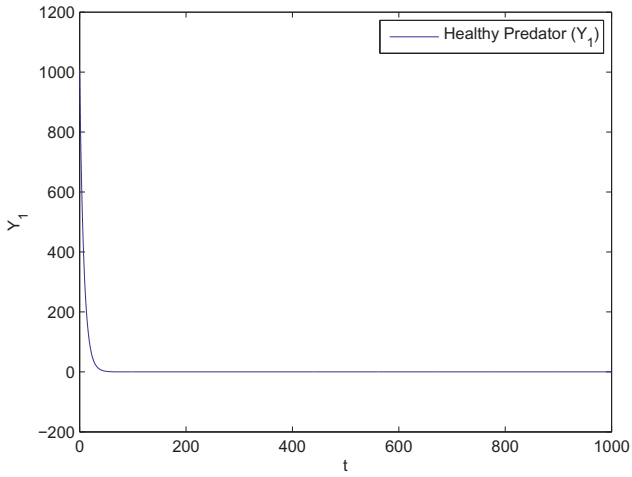
Souza [44] on Holling type functional responses is published. They derived Holling's type I, II, III responses and possible generalization of these responses. However, linear or Lotka–Volterra type functional response is also frequent (see Samanta [20], Hu. and Li [16] and references therein). By the above discussion, we can note that each of the functional responses are useful and have their specific importance in ecology. However, motivated by study of [16,20] in the present study we have considered linear functional response.

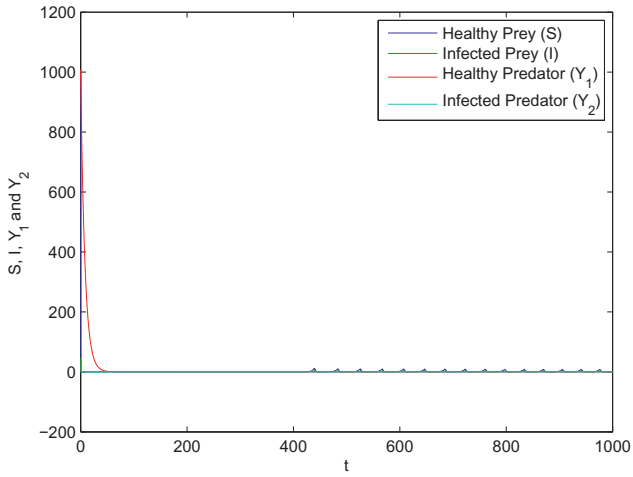
Keeping the ecological and biological point of view that real populations cannot assume negative values and they are bounded in some specific domains of the ecosystem, therefore by using the inequality given in [58–60], we usually proved the boundedness and positivity for wellposedness of proposed system. In this study, we analyzed the model regarding the local stability of the system and found ecological thresholds. In Section 3 we considered the model without migration and disease. We calculated the equilibrium points and their stability. Analysis of the main mathematical model is observed in Section 4. We observed fourteen equilibrium points for our model their existence conditions and stability is pointed out. If we revisit our model (2.1), then the logistic term in the first equation is $\frac{dS}{dt} = rS(1 - \frac{S+I}{k})$. If we imposed the assumption (H2) then, we have $\frac{dS}{dt} = rS(1 - \frac{N}{k})$. It is not difficult to scaled off by suitable rescaling this term can be written as $\frac{dS}{dt} = S(1 - N)$. Tables 4 and 5 show that migration of healthy prey (m_1) plays a lead role in the existence and stabilities of equilibria of

Please cite this article as: S. Kant, V. Kumar, Stability analysis of predator–prey system with migrating prey and disease infection in both species, Applied Mathematical Modelling (2016), http://dx.doi.org/10.1016/j.apm.2016.10.003









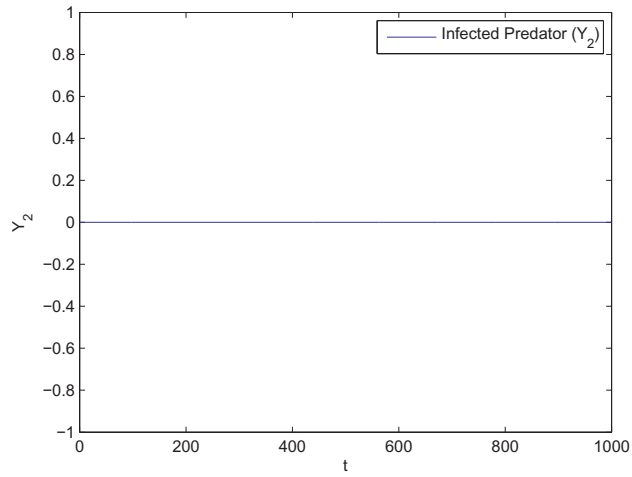


Fig. 10. Numerical solution of model with parameter set in Table 4 with $m_1 = 1/6, m_2 = 1/3$ (contd.).

systems (3.1) and (3.2). Existence of E_1^* is independent of m_1, but stability of it depends on m_1 and existence and stability of E_2^* and E_3^* depend on m_1. Similar dependency on migration for the model (2.1), we have the table.

The equilibrium points $E_3(\widehat{S}, \widehat{Y}_1)$, $E_3^*(\widehat{S}, \widehat{Y}_1)$ and $E^{(7)}(S^{(7)}, 0, Y_1^{(7)}, 0)$ conveyed the same message ecologically and biologically because all these equilibrium points are infection free conditions but at the same time mathematically look different because former two are two dimensional and third one is four dimensional study. But they studied the same ecological situation.

Similarly, the equilibrium points $E_2(\widetilde{S}, 0)$, $E_2^*(\widetilde{S}, 0)$ and $E^{(2)}(S^{(2)}, 0, 0, 0)$ are predator and infected prey free equilibrium points i.e. in this case the predator population and infected prey population will be wiped out. If these equilibrium points

Please cite this article as: S. Kant, V. Kumar, Stability analysis of predator–prey system with migrating prey and disease infection in both species, Applied Mathematical Modelling (2016), http://dx.doi.org/10.1016/j.apm.2016.10.003

are stable then prey population will be survived for a long time. Because the predator population will not consumed the prey population and no disease infection will be occurred this will help the prey population for its long time survival. As discussed in previous paragraph the equilibrium points $E_2(\widetilde{S}, 0)$, $E_2^*(\widetilde{S}, 0)$ and $E^{(2)}(S^{(2)}, 0, 0, 0)$ are ecologically same but mathematically they are different because $E_2(\widetilde{S}, 0)$, $E_2^*(\widetilde{S}, 0)$ is a two dimensional study but $E^{(2)}(S^{(2)}, 0, 0, 0)$ is four dimensional.

Trivial equilibrium points $E_1^*(0, 0)$, $E_1(0, 0)$ and $E^{(1)}(0, 0, 0, 0)$ are less important cases in ecological as well as mathematical point of view. Reason is quite simple because in this condition no population will be survived ecologically. Similarly, mathematically we seen that they all are unstable and this condition naturally is not a good sign for living species. If at any moment for any ecosystem trivial equilibrium point become stable it means that complete extinction of life in that ecosystem. Thus we seen that trivial equilibrium points always exist but never stable ecologically as well as mathematically.

Further, if we recall the Remark 4, it is found that equilibrium points $E^{(3)}$, $E^{(4)}$ and $E^{(5)}$ do not exist. We observed that all these equilibrium points are prey free. Non-existence of $E^{(3)}$, $E^{(4)}$ and $E^{(5)}$ ecologically suggested that without prey population in an eco-system, predator population cannot survive. It is also noted that $E^{(9)}$ always exist, this is also a prey free equilibrium. However, on the contrary, it is also remarkable that prey free equilibrium point in case of models (3.1) and (3.2) do not exist. Thus without prey population the predator population can survive but the additional food to the ecosystem is required. Few studies are available on the concept of additional food supply (see Prasad et al. [39] and references cited therein). Universal existence of $E^{(9)}$ also suggested that, if disease is spreading in both the populations, then disease in prey is beneficial for predator population.

Further, $E^{(10)}$ tells us that healthy prey will be removed from eco-system. Firstly, ecologically this is possible because healthy prey are more active as compared to infected one. To save our life the healthy prey will be out migrated to another eco-system before being predated or captured by the predator population. Mathematically we seen that this equilibrium exists provided certain conditions prescribed in Section 4.1 are satisfied. Secondly, it is also a possibility that predator consumed the whole prey population. Let x_1 number of healthy prey be captured by predator and x_2 be the number of healthy prey that migrated to other eco-system then for the extinction of healthy prey we have the following mathematical relation:

$$x_1 + x_2 = 0. \tag{6.1}$$

Further bifurcation of x_1 is also possible. If x_{i1} and x_{i2} be the number of healthy prey be captured by healthy and infected predators respectively, then:

$$x_1 = x_{i1} + x_{i2}, \tag{6.2}$$

thus we can write Eq. (6.1)as:

$$x_{i1} + x_{i2} + x_2 = 0. \tag{6.3}$$

Besides this other factors may be the mortality of healthy prey. Suppose at any time t, x_3 be the number of healthy prey that lost due to mortality, then we must extend Eq. (6.3) to:

$$x_{i1} + x_{i2} + x_2 + x_3 = 0. \tag{6.4}$$

More research is possible by assuming a real eco-system to find the exact values of x_{i1}, x_{i2}, x_2, x_3 etc. for reason of extinction of healthy prey.

Let us discuss about the equilibrium point $E^{(11)}$. This equilibrium provides the extinction of infected prey from the ecosystem. As discussed in the case of healthy prey in the previous paragraph the possible reasons are quite similar but in this case we observed the following points:

(i) Since infected prey are quite lazy and idle as compared to healthy one and so migration may not be so frequent.
(ii) Similarly, infected predator are not so active as healthy one and so it is also a possibility that predation by healthy predator may be high as compare to infected one.
(iii) Since death due to disease may also frequent as compare to natural death, thus corresponding equation for infected prey may be written as:

$$y_{i1} + y_{i2} + y_2 + y_3 = 0. \tag{6.5}$$

Now in this case mortality is due to disease and natural as well, therefore bifurcated again into y_{3n} and y_{3d}, thus equation can be written as:

$$y_{i1} + y_{i2} + y_2 + y_{3n} + y_{3d} = 0. \tag{6.6}$$

By field research y_{i1}, y_{i2}, y_2, y_{3n}, y_{3d} may be calculated then proper reason of extinction of the infected prey may be identified with actual proportions.

Equilibrium point $E^{(12)}$ means healthy predator will extinct from eco-system. Since migration of predator is not allowed in this paper. Only possible reasons may be (i) non-consumption of prey population i.e. due to lack of food (ii) death or mortality. For support of (i) the possible reason may be migration of prey. Second point (ii) is trivial since natural death is found in all the species as considered.

Please cite this article as: S. Kant, V. Kumar, Stability analysis of predator–prey system with migrating prey and disease infection in both species, Applied Mathematical Modelling (2016), http://dx.doi.org/10.1016/j.apm.2016.10.003

Equilibrium point $E^{(13)}$ is an infected predator free equilibrium. The possible reasons for extinction of infected predator may be (i) Non-availability of food for consumption. (ii) Mortality. (iii) Non-infection in predators. We noted that infected predator are less active as compare to healthy one hence they cannot catch prey as fast as healthy predator. Hence reason (i) is quite feasible for extinction of infected predator. Further, it is revealed from the governing equation of Y_2(infected predator), infected predator has two types of mortality. In this case death due to disease is quite more frequent as compare to natural mortality. Next, there are few chances that infection in predator does not occurred. If this reason is true then remaining two reasons are not arise. Thus either conditions (i) and (ii) or (iii) but not simultaneously will be satisfied.

$E^{(14)}$ is most important equilibrium point since it provides the coexistence of all the four species simultaneously. For ecological balance of an eco-system coexistence of all the species in respective proportions is very important. If $E^{(14)}$ is stable then it **indicates** the existence of all the species for a long time.

As pointed out in introduction part that data on migration for species other than human is not readily available. If it is available then it is not authentic. More emphasized should be given on collection of data on species migration. Further, real parameters are required for further numerical solutions of the mathematical models. For explanation of our theoretical framework so constructed we considered a hypothetical set of parameters. We seen that existence and stability of equilibrium points depend on the parameters so considered. Thus estimation of parameters from real data is an important aspect of applied mathematics and is an open problem.

As mentioned in Remarks 1 and 2, we seen that migration rates may follow different probability distributions viz. normal distribution, Poisson distribution etc. Identification of the suitable migration probability distribution is included in the future scope of the study.

Appendix A

A1. (Coefficients of Eq. (4.9))

$A_1 = -tr(J_{E^{(10)}(0,I^{(10)},Y_1^{(10)},Y_2^{(10)})}) = -(I^{(10)}(q_2p_2+q_4p_4)+Y_1^{(10)}(-p_2+\gamma)+Y_2^{(10)}(-\gamma-p_4)-(c+m_2+d_2+d_3+d_4+d_5))$.

Now:

$$A_{11}^{(10)} = \begin{pmatrix} (q_2p_2I^{(10)}-\gamma Y_2^{(10)}-d_3) & -\gamma Y_1^{(10)} \\ \gamma Y_2^{(10)} & q_4p_4I^{(10)}+\gamma Y_1^{(10)}-(d_4+d_5)) \end{pmatrix}$$

$\Rightarrow A_{11}^{(10)} = q_2p_2q_4p_4(I^{(10)})^2 + I^{(10)}(-(d_4+d_5)q_2p_2 - d_3q_4p_4) + q_2p_2\gamma Y_1^{(10)}I^{(10)} - q_4p_4\gamma Y_2^{(10)}I^{(10)} + \gamma(d_4+d_5)Y_2^{(10)} - \gamma d_3Y_1^{(10)} + d_3(d_4+d_5)$

$$A_{22}^{(10)} = \begin{pmatrix} (-p_2Y_1^{(10)}-p_4Y_2^{(10)}-(c+m_2+d_2)) & -p_4I^{(10)} \\ q_4p_4Y_2^{(10)} & q_4p_4I^{(10)}+\gamma Y_1^{(10)}-(d_4+d_5)) \end{pmatrix}$$

$\Rightarrow A_{22}^{(10)} = -\gamma p_2(Y_1^{(10)})^2 - q_4p_4p_2I^{(10)}Y_1^{(10)} - \gamma p_4Y_1^{(10)}Y_2^{(10)} + Y_1^{(10)}[p_2(d_4+d_5)-\gamma(c+m+d_2)] + Y_2^{(10)}[p_4(d_4+d_5)] + I^{(10)}[-(c+m+d_2)q_4p_4] + (c+m+d_2)(d_4+d_5)$

$$A_{33}^{(10)} = \begin{pmatrix} (-p_2Y_1^{(10)}-p_4Y_2^{(10)}-(c+m_2+d_2)) & -p_2I^{(10)} \\ q_2p_2Y_1^{(10)} & (q_2p_2I^{(10)}-\gamma Y_2^{(10)}-d_3) \end{pmatrix}$$

$\Rightarrow A_{33}^{(10)} = \gamma p_4(Y_2^{(10)})^2 + I^{(10)}Y_1^{(10)}[q_2p_2^2-q_2p_2^2] + Y_1^{(10)}Y_2^{(10)}[\gamma p_2] + Y_2^{(10)}I^{(10)}[-q_2p_2p_4] + Y_1^{(10)}[d_3p_2] + Y_2^{(10)}[p_4d_3+\gamma(c+m_2+d_2)] - (c+m_2+d_2)q_2p_2I^{(10)} + d_3(c+m_2+d_2)$.

Therefore,

$A_2 = A_{11}^{(10)} + A_{22}^{(10)} + A_{33}^{(10)} = q_2p_2q_4p_4(I^{(10)})^2 + I^{(10)}(-(d_4+d_5)q_2p_2 - d_3q_4p_4) + q_2p_2\gamma Y_1^{(10)}I^{(10)} - q_4p_4\gamma Y_2^{(10)}I^{(10)} + \gamma(d_4+d_5)Y_2^{(10)} - \gamma d_3Y_1^{(10)} + d_3(d_4+d_5) - \gamma p_2(Y_1^{(10)})^2 - q_4p_4p_2I^{(10)}Y_1^{(10)} - \gamma p_4Y_1^{(10)}Y_2^{(10)} + Y_1^{(10)}[p_2(d_4+d_5)-\gamma(c+m+d_2)] + Y_2^{(10)}[p_4(d_4+d_5)] + I^{(10)}[-(c+m+d_2)q_4p_4] + (c+m+d_2)(d_4+d_5) + \gamma p_4(Y_2^{(10)})^2 + I^{(10)}Y_1^{(10)}[q_2p_2^2-q_2p_2^2] + Y_1^{(10)}Y_2^{(10)}[\gamma p_2] + Y_2^{(10)}I^{(10)}[-q_2p_2p_4] + Y_1^{(10)}[d_3p_2] + Y_2^{(10)}[p_4d_3+\gamma(c+m_2+d_2)] - (c+m_2+d_2)q_2p_2I^{(10)} + d_3(c+m_2+d_2)$,

after simplification, we have:

$A_2 = q_2p_2q_4p_4(I^{(10)})^2 - \gamma p_2(Y_1^{(10)})^2 + \gamma p_4(Y_2^{(10)})^2 + Y_1^{(10)}I^{(10)}[\gamma q_2p_2 - q_4p_4p_2] + Y_2^{(10)}I^{(10)}[-\gamma q_4p_4 - q_2p_2p_4] + Y_1^{(10)}Y_2^{(10)}[-\gamma p_4+\gamma p_2] + I^{(10)}[-(d_4+d_5)q_2p_2 - d_3q_4p_4 - q_4p_4(c+m_2+d_2) + (c+m_2+d_2)(d_4+d_5) - (c+m_2+d_2)q_2p_2] + Y_1^{(10)}[-\gamma d_3 + p_2(d_4+d_5) - \gamma(c+m_2+d_2) + d_3p_2] + Y_2^{(10)}[p_4d_3+\gamma(c+m_2+d_2) + p_4(d_4+d_5) + \gamma(d_4+d_5)] + [d_3(d_4+d_5) + (d_4+d_5)(c+m_2+d_2) + (c+m_2+d_2)d_3]$

$A_3 = -(D_1^{10}+D_2^{10}+D_3^{10})$,

where: $D_1^{10} = -q_2p_2^2q_4p_4Y_1^{(10)}(I^{(10)})^2 + Y_1^{(10)}I^{(10)}[(d_4+d_5)q_2p_2^2 + q_4p_4p_2d_3] - q_2p_2^2\gamma(Y_1^{(10)})^2(I^{(10)}) + \gamma p_2q_4p_4Y_1^{(10)}I^{(10)}Y_2^{(10)} - \gamma p_2(d_4+d_5)Y_1^{(10)}Y_2^{(10)} + \gamma d_3p_2(Y_1^{(10)})^2 - d_3(d_4+d_5)p_2Y_1^{(10)} - q_2p_2q_4p_4^2Y_2^{(10)}(I^{(10)})^2 - Y_1^{(10)}(I^{(10)})[p_4q_2p_2(d_4+d_5) + d_3q_4p_4^2] - \gamma q_2p_2p_4Y_1^{(10)}I^{(10)}Y_2^{(10)} + I^{(10)}(Y_2^{(10)})^2[q_4p_4^2] - \gamma(d_4+d_5)p_4(Y_2^{(10)})^2 + \gamma p_4d_3Y_1^{(10)}Y_2^{(10)} - d_3(d_4+d_5)p_4Y_2^{(10)} - (c+m_2+d_2)q_2p_2p_4q_4(I^{(10)})^2 - I^{(10)}(c+m_2+d_2)[-(d_4+d_5)q_2p_2 - q_4p_4d_3] - \gamma(c+m_2+d_2)q_2p_2Y_1^{(10)}I^{(10)} + Y_2^{(10)}I^{(10)}\gamma q_4p_4(c+m_2+d_2) - \gamma(c+m_2+d_2)(d_4+d_5)Y_2^{(10)} + \gamma Y_1^{(10)}(c+m_2+d_2)d_3 - (c+m_2+d_2)d_3(d_4+d_5)$

$D_2^{10} = -q_2p_2^2q_4p_4Y_1^{(10)}(I^{(10)})^2 - q_2p_2^2\gamma(Y_1^{(10)})^2I^{(10)} + (d_4+d_5)q_2p_2^2\gamma(Y_1^{(10)})I^{(10)} - \gamma p_2q_4p_4Y_2^{(10)}I^{(10)}Y_1^{(10)}$

Please cite this article as: S. Kant, V. Kumar, Stability analysis of predator–prey system with migrating prey and disease infection in both species, Applied Mathematical Modelling (2016), http://dx.doi.org/10.1016/j.apm.2016.10.003

$D_3^{10} = -\gamma p_2 q_2 p_4 Y_2^{(10)} I^{(10)} Y_1^{(10)} + q_1 p_1 q_4 p_4^2 (Y_1^{(10)})(I^{(10)})^2 - q_4 p_4^2 \gamma I^{(10)} Y_2^2 + q_4 p_4^2 (Y_2^{(10)}) I^{(10)}$.

A2. (Coefficients of Eq. (4.11))

$B_1 = -tr.(J'_{E^{(11)}(S^{(11)},0,Y_1^{(11)},Y_2^{(11)})}) = -((r - m_1 - d_1 - d_4 - d_5) + S^{(11)}(-\frac{2r}{k} + q_1 p_1) + Y_1^{(11)}[-p_1 + \gamma] + Y_2^{(11)}[-p_3 - \gamma])$.

Now:

$A_{11}^{(11)} = \begin{pmatrix} (q_1 p_1 S^{(11)} - \gamma Y_2^{(11)} - d_3) & -\gamma Y_1^{(11)} \\ \gamma Y_2^{(11)} & (q_3 p_3 S^{(11)} + \gamma Y_1^{(11)} - (d_4 + d_5)) \end{pmatrix}$,or:

$A_{11}^{(11)} = q_1 p_1 p_3 (S^{(11)})^2 + S^{(11)}[q_1 p_1 (d_4 + d_5) - q_3 p_3 d_3] + Y_1^{(11)} S^{(11)}[\gamma q_1 p_1] + S^{(11)} Y_2^{(11)}[-\gamma q_3 p_3] + Y_2^{(11)}[\gamma (d_4 + d_5)] + Y_1^{(11)}[-\gamma d_3] + d_3 (d_3 + d_5)$

$A_{22}^{(11)} = \begin{pmatrix} (r - m_1 - d_1 - \frac{2r}{k} S^{(11)} - p_1 Y_1^{(11)} - p_3 Y_2^{(11)}) & -p_3 S^{(11)} \\ q_3 p_3 Y_2^{(11)} & (q_3 p_3 S^{(11)} + \gamma Y_1^{(11)} - (d_4 + d_5)) \end{pmatrix}$ or,

$A_{22}^{(11)} = -\frac{2rq_3 p_3}{k}(S^{(11)})^2 - p_1 \gamma (Y_1^{(11)})^2 + S^{(11)} Y_1^{(11)}[\frac{\gamma 2r}{k} - q_3 p_1 p_3] + Y_1^{(11)} Y_2^{(11)}[-\gamma p_3] + S^{(11)}[q_3 p_3 (r - m_1 - d_1) + \frac{2r}{k}(d_4 + d_5)] + Y_1^{(11)}[\gamma (r - m_1 - d_1) + p_1 (d_4 + d_5)] + Y_2^{(11)}[p_3 (d_4 + d_5)] + [-(d_4 + d_5)(r - m_1 - d_1)]$

$A_{33}^{(11)} = \begin{pmatrix} (r - m_1 - d_1 - \frac{2r}{k} S^{(11)} - p_1 Y_1^{(11)} - p_3 Y_2^{(11)}) & -p_1 S^{(11)} \\ q_1 p_1 Y_1^{(11)} & (q_1 p_1 S^{(11)} - \gamma Y_2^{(11)} - d_3) \end{pmatrix}$,or:

$A_{33}^{(11)} = -\frac{2rq_1 p_1}{k}(S^{(11)})^2 + p_3 \gamma (Y_1^{(11)})^2 + S^{(11)} Y_2^{(11)}[\frac{\gamma 2r}{k} - q_1 p_1 p_3] + Y_1^{(11)} Y_2^{(11)}[\gamma p_1] + S^{(11)}[q_1 p_1 (r - m_1 - d_1)] + Y_1^{(11)}[p_1 d_3] + Y_2^{(11)}[p_3 d_3 - \gamma (r - m_1 - d_1)] - d_3 (r - m_1 - d_1)$.

Therefore:

$B_2 = A_{11}^{(11)} + A_{22}^{(11)} + A_{33}^{(11)} = (S^{(11)})^2[-\frac{2rq_1 p_1}{k} - \frac{2rq_3 p_3}{k} + q_1 p_1 q_3 p_3] + (Y_1^{(11)})^2[-p_1 \gamma] + (Y_2^{(11)})^2[\gamma p_3] + S^{(11)} Y_1^{(11)}[\frac{\gamma 2r}{k} - q_1 p_1 p_3 + \gamma p_1 q_1] + S^{(11)} Y_2^{(11)}[\frac{\gamma 2r}{k} - q_1 p_1 p_3 - \gamma p_3 q_3] + Y_1^{(11)} Y_2^{(11)}[\gamma p_1 - \gamma p_3] + S^{(11)}[(r - m_1 - d_1) q_1 p_1 + \frac{2rd_3}{k} + q_3 p_3 (r - m_1 - d_1) + \frac{2r(d_4 + d_5)}{k} - (d_4 + d_5) q_1 p_1 - q_3 p_3 d_3] + Y_1^{(11)}[p_1 d_3 + \gamma (r - m_1 - d_1) + p_1 (d_4 + d_5) - \gamma d_3] + Y_2^{(11)}[-\gamma (r - m_1 - d_1) + p_3 d_3 + p_3 d_3 + p_3 (d_4 + d_5) + \gamma (d_4 + d_5)] + [d_3 (d_4 + d_5) - d_3 (r - m_1 - d_1) - (d_4 + d_5)(r - m_1 - d_1)]$.

Now B_3 is given by:

$B_3 = -Det.(J'_{E^{(11)}(S^{(11)},0,Y_1^{(11)},Y_2^{(11)})}) = -(D_1^{11} + D_2^{11} + D_3^{11})$,

where,

$D_1^{11} = (r - m_1 - d_1 - \frac{2r}{k} S^{(11)} - p_1 Y_1^{(11)} - p_3 Y_2^{(11)}) A_{11}^{11}$,

after putting the value of $A_{11}^{(11)}$ and simplifying we get:

$D_1^{11} = (r - m_1 - d_1) p_1 q_1 p_3 q_3 (S^{(11)})^2 + S^{(11)}(r - m_1 - d_1)[-q_1 p_1 (d_4 + d_5) - q_3 p_3 d_3] + Y_1^{(11)} S^{(11)}[\gamma (r - m_1 - d_1) q_1 p_1] + Y_2^{(11)} S^{(11)}[-\gamma (r - m_1 - d_1) q_3 p_3] + Y_2^{(11)}[\gamma (r - m_1 - d_1)(d_4 + d_5)] + Y_1^{(11)}[-\gamma (r - m_1 - d_1) d_3] + d_3 (r - m_1 - d_1)(d_4 + d_5) - (S^{(11)})^3[\frac{2rq_1 p_1 q_3 p_3}{k}] + (S^{(11)})^2 \frac{2r}{k}[q_1 p_1 (d_4 + d_5) + p_3 d_3 q_3] - (S^{(11)})^2 Y_1^{(11)}[-\frac{2r\gamma q_1 p_1}{k}] + (S^{(11)})^2 Y_2^{(11)}[\frac{2r\gamma q_3 p_3}{k}] - (S^{(11)}) Y_2^{(11)}[\frac{2r\gamma (d_4 + d_5)}{k}] + (S^{(11)}) Y_1^{(11)}[\frac{2r\gamma d_3}{k}] - S^{(11)}[\frac{2rd_3 (d_4 + d_5)}{k}] - q_1 p_1^2 q_3 p_3 (S^{(11)})^2 Y_1^{(11)} + S^{(11)} Y_1^{(11)}[q_1 p_1^2 (d_4 + d_5) + q_3 p_3 d_3 p_1] + S^{(11)}(Y_1^{(11)})^2[-\gamma q_1 p_1^2] + S^{(11)} Y_1^{(11)} Y_2^{(11)}[\gamma q_3 p_3 p_1] + Y_1^{(11)} Y_2^{(11)}[-\gamma (d_4 + d_5) p_1] + \gamma d_3 p_1 (Y_1^{(11)})^2 - [(d_4 + d_5) p_1 \gamma] Y_1^{(11)} - q_1 p_1 q_3 p_3^2 (S^{(11)})^2 Y_2^{(11)} + S^{(11)} Y_2^{(11)}[q_1 p_1 p_3 (d_4 + d_5) + q_3 p_3^2 d_3] - S^{(11)} Y_1^{(11)} Y_2^{(11)}[\gamma q_1 p_1 q_3 p_3] + S^{(11)}(Y_2^{(11)})^2[\gamma q_3 p_3^2] - \gamma p_3 (d_4 + d_5)(Y_2^{(11)})^2 + \gamma d_3 p_3 Y_1^{(11)} Y_2^{(11)} - d_3 p_3 (d_4 + d_5) Y_2^{(11)}$

$D_2^{11} = -p_1 S^{(11)} \begin{vmatrix} q_1 p_1 Y_1^{(11)} & -\gamma Y_1^{(11)} \\ q_3 p_3 Y_2^{(11)} & (q_3 p_3 S^{(11)} + \gamma Y_1^{(11)} - (d_4 + d_5)) \end{vmatrix}$ after simplification we get:

$D_2^{11} = -q_1 p_1^2 p_3 (S^{(11)})^2 Y_1^{(11)} - \gamma q_1 p_1^2 S^{(11)} (Y_1^{(11)})^2 + (d_4 + d_5) q_1 p_1^2 S^{(11)} Y_1^{(11)} - \gamma p_3 q_3 p_1 S^{(11)} Y_1^{(11)} Y_2^{(11)}$

$D_3^{11} = -p_3 S^{(11)} \begin{vmatrix} q_1 p_1 Y_1^{(11)} & q_1 p_1 S^{(11)} - \gamma Y_2^{(11)} - d_3 \\ q_3 p_3 Y_2^{(11)} & \gamma Y_2^{(11)}) \end{vmatrix}$,

after simplification we get:

$D_3^{11} = q_1 p_1 q_3 p_3^2 (S^{(11)})^2 Y_2^{(11)} - \gamma q_3 p_3^2 S^{(11)} (Y_2^{(11)})^2 + d_3 q_3 p_3^2 S^{(11)} Y_2^{(11)} - \gamma p_3 q_1 p_1 S^{(11)} Y_1^{(11)} Y_2^{(11)}$.

A3. (Coefficients of Eq. (4.14))

$D_1 = -tr.(J'_{E^{(12)}(S^{(12)},I^{(12)},0,Y_2^{(12)})}) = (r - m_1 - d_1 - c - m_2 - d_2 - d_3) + S^{(12)}(-\frac{2r}{k} + \beta + q_1 p_1) + I^{(12)}(-\frac{r}{k} - \beta + q_2 p_2) - (p_1 + p_2) Y_2^{(12)}$

$D_2 = (A_{11}^{13} + A_{22}^{13} + A_{33}^{13}) = (S^{(12)})^2[\beta q_1 p_1 - \frac{2rq_1 p_1}{k} - \frac{2r\beta}{k}] + (Y_2^{(12)})^2[p_1 p_2] + (I^{(12)})^2[(\frac{r}{k} + \beta) q_2 p_2] + S^{(12)} I^{(12)}[\beta q_2 p_2 - \frac{2rq_2 p_2}{k} - (\frac{r}{k} + \beta) q_1 p_1] = +S^{(12)} Y_2^{(12)}[-q_1 p_1 p_2 - q_1 p_1^2 + \frac{2rp_2}{k} - p_1 \beta] + I^{(12)} Y_2^{(12)}[-q_2 p_1 p_2 + (\frac{r}{K} + \beta) p_2] + S^{(12)}\Big[-\beta d_3 - (c + d_2 + m_2) q_1 p_1 + (r - d_1 - m_1) q_1 p_1 + \frac{2rd_3}{k} + (r - d_1 - m_1)\beta + \frac{2r(c + d_2 + m_2)}{k}\Big] + I^{(12)}\Big[-(c + d_2 + m_2) q_2 p_2 + (r - d_1 - m_1) q_2 p_2 + (\frac{r}{k} + \beta) d_3 + (\frac{r}{k} + \beta)(c + d_2 + m_2)\Big] + Y_2^{(12)}$
$[d_3 p_1 - (r - d_1 - m_1) p_2 + p_1 (c + d_2 + m_2)] + [d_3 (c + d_2 + m_2) - (r - d_1 - m_1) d_3 - (r - d_1 - m_1)(c + d_2 + m_2)]$

Please cite this article as: S. Kant, V. Kumar, Stability analysis of predator–prey system with migrating prey and disease infection in both species, Applied Mathematical Modelling (2016), http://dx.doi.org/10.1016/j.apm.2016.10.003

$$D_3 = -Det.(J'_{E^{(12)}(S^{(12)},I^{(12)},0,Y_2^{(12)})}) = S^{(12)}[-\tfrac{2rq_1p_1\beta}{k}] + S^{(12)}Y_2^{(12)}[\tfrac{2rq_1p_1p_2}{k}] + (S^{(12)})^2I^{(12)}[\tfrac{2rq_1p_1p_2}{k}] +$$
$$(I^{(12)})^2Y_2^{(12)}[(\tfrac{r}{k}+\beta)q_2p_2^2] + (Y_2^{(12)})^2I^{(12)}[q_2p_2^2p_1] + S^{(12)}I^{(12)}Y_2^{(12)}\Big[-\tfrac{2rq_2p_2^2\beta}{k} + 2(\tfrac{r}{K}+\beta)q_1p_1p_2 - 2\beta q_2p_1p_2\Big] +$$
$$(S^{(12)})^2\Big[\beta(r-d_1-m_1)q_1p_1 + \tfrac{2rd_3\beta}{K} + \tfrac{2rq_1p_1(c+d_2+m_2)}{k}\Big] + (I^{(12)})^2[(\tfrac{r}{K}+\beta)q_2p_2(c+d_2+m_2)] + (Y_1^{(12)})^2[d_3p_1p_2] +$$
$$S^{(12)}I^{(12)}\Big[\beta(r-d_1-m_1)q_2p_2 + \tfrac{2rq_2p_2(c+d_2+m_2)}{k} + (\tfrac{r}{k}+\beta)(c+d_2+m_2)q_1p_1\Big] + S^{(12)}Y_2^{(12)}[-(r-d_1-$$
$$m_1)q_1p_1p_2 + \tfrac{2rp_2d_3}{k} + d_3\beta p_1] + I^{(12)}Y_2^{(12)}\Big[-(r-d_1-m_1)q_2p_2^2 + (\tfrac{r}{K}+\beta)d_3p_2 + (c+d_2+m_2)q_2p_1p_2\Big] +$$
$$S^{(12)}\Big[-d_3(r-d_1-m_1)\beta - (r-d_1-m_1)(c+d_2+m_2)q_1p_1 - \tfrac{2r(c+d_2+m_2)d_3}{K}\Big]$$
$$+ I^{(12)}\Big[-(r-d_1-m_1)(c+d_2+m_2)q_2p_2 - (\tfrac{r}{k}+\beta)(c+d_2+m_2)d_3\Big] + Y_2^{(12)}[-d_3p_2(r-d_1-m_1) - (c+d_2+m_2)d_3p_1] + (r-$$
$$d_1-m_1)(c+d_2+m_2)d_3.$$

A4. (Coefficients of Eq. (4.18))

$$D_1 = -tr.(J'_{E^{(13)}(S^{(13)},I^{(13)},Y_1^{(13)},0)}) = (r-m_1-d_1-c-m_2-d_2-d_3) + S^{(13)}(-\tfrac{2r}{k}+\beta+q_1p_1) + I^{(13)}(-\tfrac{r}{k}-\beta+q_2p_2) - (p_1+$$
$$p_2)Y_1^{(13)}$$
$$D_2 = (A_{11}^{13}+A_{22}^{13}+A_{33}^{13}) = (S^{(13)})^2[\beta q_1p_1 - \tfrac{2rq_1p_1}{k} - \tfrac{2r\beta}{k}] + (Y_1^{(13)})^2[p_1p_2] + (I^{(13)})^2[(\tfrac{r}{k}+\beta)q_2p_2] +$$
$$S^{(13)}I^{(13)}[\beta q_2p_2 - \tfrac{2rq_2p_2}{k} - (\tfrac{r}{k}+\beta)q_1p_1] + S^{(13)}Y_1^{(13)}[-q_1p_1p_2 - q_1p_1^2 + \tfrac{2rp_2}{k} - p_1\beta] + I^{(13)}Y_1^{(13)}[-q_2p_1p_2 +$$
$$(\tfrac{r}{K}+\beta)p_2] + S^{(13)}\Big[-\beta d_3 - (c+d_2+m_2)q_1p_1 + (r-d_1-m_1)q_1p_1 + \tfrac{2rd_3}{k} + (r-d_1-m_1)\beta + \tfrac{2r(c+d_2+m_2)}{k}\Big] +$$
$$I^{(13)}\Big[-(c+d_2+m_2)q_2p_2 + (r-d_1-m_1)q_2p_2 + (\tfrac{r}{k}+\beta)d_3 + (\tfrac{r}{k}+\beta)(c+d_2+m_2)\Big]$$
$$+ Y_1^{(13)}[d_3p_1 - (r-d_1-m_1)p_2 + p_1(c+d_2+m_2)] + [d_3(c+d_2+m_2) - (r-d_1-m_1)d_3 - (r-d_1-m_1)(c+d_2+m_2)]$$
$$D_3 = -Det.(J'_{E^{(13)}(S^{(13)},I^{(13)},Y_1^{(13)},0)}) = S^{(13)}[-\tfrac{2rq_1p_1\beta}{k}] + S^{(13)}Y_1^{(13)}[\tfrac{2rq_1p_1p_2}{k}] + (S^{(13)})^2I^{(13)}[\tfrac{2rq_1p_1p_2}{k}] +$$
$$(I^{(13)})^2Y_1^{(13)}[(\tfrac{r}{k}+\beta)q_2p_2^2] + (Y_1^{(13)})^2I^{(13)}[q_2p_2^2p_1] + S^{(13)}I^{(13)}Y_1^{(13)}\Big[-\tfrac{2rq_2p_2^2\beta}{k} + 2(\tfrac{r}{K}+\beta)q_1p_1p_2 - 2\beta q_2p_1p_2\Big] +$$
$$(S^{(13)})^2\Big[\beta(r-d_1-m_1)q_1p_1 + \tfrac{2rd_3\beta}{K} + \tfrac{2rq_1p_1(c+d_2+m_2)}{k}\Big] + (I^{(13)})^2[(\tfrac{r}{K}+\beta)q_2p_2(c+d_2+m_2)] + (Y_1^{(13)})^2[d_3p_1p_2] +$$
$$S^{(13)}I^{(13)}\Big[\beta(r-d_1-m_1)q_2p_2 + \tfrac{2rq_2p_2(c+d_2+m_2)}{k} + (\tfrac{r}{k}+\beta)(c+d_2+m_2)q_1p_1\Big] + S^{(13)}Y_1^{(13)}[-(r-d_1-$$
$$m_1)q_1p_1p_2 + \tfrac{2rp_2d_3}{k} + d_3\beta p_1] + I^{(13)}Y_1^{(13)}\Big[-(r-d_1-m_1)q_2p_2^2 + (\tfrac{r}{K}+\beta)d_3p_2 + (c+d_2+m_2)q_2p_1p_2\Big] +$$
$$S^{(13)}\Big[-d_3(r-d_1-m_1)\beta - (r-d_1-m_1)(c+d_2+m_2)q_1p_1 - \tfrac{2r(c+d_2+m_2)d_3}{K}\Big]$$
$$+ I^{(13)}\Big[-(r-d_1-m_1)(c+d_2+m_2)q_2p_2 - (\tfrac{r}{k}+\beta)(c+d_2+m_2)d_3\Big] + Y_1^{(13)}[-d_3p_2(r-d_1-m_1) - (c+d_2+m_2)d_3p_1] + (r-$$
$$d_1-m_1)(c+d_2+m_2)d_3\ .$$

A5. (Coefficients of Eq. (4.21))

$$E_1 = -(e_{11}+e_{22}+e_{33}+e_{44})$$
$$E_2 = -e_{34}e_{43} + e_{11}e_{33} - e_{32}e_{23} - e_{21}e_{12} + e_{13}e_{31}$$
$$E_3 = (e_{32}e_{23}+e_{34}e_{43})e_{11} + e_{21}e_{12}e_{33} + e_{12}e_{23}e_{31} + e_{32}e_{21}e_{13}$$
$$E_4 = e_{12}e_{21}e_{34}e_{43}.$$

References

[1] V. Volterra, Variazioni e fluttauazionidel numero d individui in species animals conviventii, Mem. R. Accad. Naz. Linciei 2 (1926) 31–33.
[2] A. Lotka, Elements of Physical Biology, Williams and Wilkins, Baltimore, 1925.
[3] W.O. Kermack, A.G. Mckendrick, Contributions to the mathematical theory of epidemics, part 1, Proc. R. Soc. A 115 (5) (1927) 700–721.
[4] A. Maiti, et al., Deterministic and stochastic analysis of a ratio-dependent predator-prey system with delay, Nonlinear Anal. Model. Control 12 (3) (2010) 383–398. www.lana.lt/journal/26/Maiti.pdf.
[5] F. Wang, et al., Stability and bifurcation of a stage-structured predator-prey model with both discrete and distributed delays, Chaos Solitons Fractals 46 (2013) 19–27. http://dx.doi.org/10.1016/j.chaos.2012.10.003.
[6] M. Haque, et al., An eco-epidemiological predator-prey model with standard disease incidence, Math. Methods Appl. Sci. (2008). http://dx.doi.org/10.1002/mma.1071.
[7] M. Haque, E. Venturino, The role of transmissible diseases in Holling-Tanner predator-prey model, Theor. Popul. Biol. 70 (3) (2006) 273–288.
[8] L. Yi-min, Z. Yan, The control and the reconfigurable control for prey-predator ecosystem with time delay, Appl. Math. Model. 33 (1) (2009) 148–160. http://dx.doi.org/10.1016/j.apm.2007.10.024.
[9] R.K. Naji, A.N. Mustafa, The dynamics of an eco-epidemiological model with nonlinear incidence rate, J. Appl. Math. (2012). http://dx.doi.org./10.1155/2012/852631.
[10] S.R.J. Jang, J. Baglama, Continuous-time predator-prey models with parasites, J. Biol. Dyn. 3 (1) (2009) 87–98. http://dx.doi.org/10.1080/17513750802283253.
[11] S. Sinha, et al., Modelling a predator-prey system with infected prey in polluted environment, Appl. Math. Model. 34 (7) (2010) 1861–1872. http://dx.doi.org/10.1016/j.apm.2009.10.003.

Please cite this article as: S. Kant, V. Kumar, Stability analysis of predator–prey system with migrating prey and disease infection in both species, Applied Mathematical Modelling (2016), http://dx.doi.org/10.1016/j.apm.2016.10.003

[12] S. Jana, T.K. Kar, Modeling and analysis of a prey-predator system with disease in the prey, Chaos Solitons Fractals 47 (2013) 42–53. http://dx.doi.org/10.1016/j.chaos.2012.12.002.
[13] A. Johri, et al., Study of a prey-predator model with diseased prey, Int. J. Contemp. Math. Sci. 7 (10) (2012) 489–498.
[14] B. Mukhopadhyaya, B. Bhattacharyya, Dynamics of a delay-diffusion prey-predator model with disease in the prey, J. Appl. Math. Comput. 17 (12) (2005) 361–377. http://dx.doi.org/10.1007/BF02936062.
[15] D. Greenhalgh, M. Haque, A predator-prey model with disease in the prey species only, Math. Methods Appl. Sci. 30 (2007) 911–929. http://dx.doi.org/10.1002/mma.815.
[16] G.P. Hu, X.-L. Li, Stability and Hopf bifurcation for a delayed predator-prey model with disease in the prey, Chaos Solitons Fractals 45 (3) (2012) 229–237. http://dx.doi.org/10.1016/j.chaos.2011.11.011.
[17] J. Chattopadhyay, O. Arino, A predator-prey model with disease in prey, Nonlinear Anal. 36 (1999) 747–766. http://dx.doi.org/10.1016/S0362-546X(98)00126-6.
[18] L. Maoxing, et al., An impulsive predator-prey model with communicable disease in the prey species only, Nonlinear Anal. Real World Appl. 10 (5) (2009) 3098–3111. http://dx.doi.org/10.1016/j.nonrwa.2008.10.010.
[19] R.K. Naji, K.A. Hasan, the dynamics of prey-predator model with disease in the prey, J. Math. Comput. Sci. 2 (4) (2012) 1052–1072. http://scik.org
[20] G.P. Samanta, Analysis of a delay nonautonomous predator-prey system with disease in the prey, Nonlinear Anal. Model. Control 15 (1) (2010) 97–108. www.lana.lt/journal/36/Samanta.pdf
[21] Y. Xiao, L. Chen, Modeling and analysis of a predator-prey model with disease in the prey, Math. Biosci. 171 (2001) 59–82. http://dx.doi.org/10.1016/S0025-5564(01)00049-9.
[22] F.M. Hilker, K. Schmitz, Disease-induced stabilization of predator prey oscillations, J. Theor. Biol. 255 (2008) 299–306. http://dx.doi.org/10.1016/j.jtbi.2008.08.018.
[23] M. Haque, A predator-prey model with disease in the predator, Nonlinear Anal. Real World Appl. 11 (4) (2010) 2224–2236. http://dx.doi.org/10.1016/j.nonrwa.2009.06.012.
[24] P.J. Pal, et al. Dynamics of a predator prey model with disease in the predator, Math. Methods Appl. Sci. http://dx.doi.org./10.1002/mma.2988.
[25] L. Han, M.A. Zhien, Four predator prey models with infectious diseases, Math. Comput. Model. 34 (7–8) (2001) 849–858. http://dx.doi.org/S0895-7177(01)00104-2.
[26] Y.-H. Hsieh, C.-K. Hsiao, Predator-prey model with disease infection in both populations, Math. Med. Biol. 25 (2008) 247–266. http://dx.doi.org/10.1093/imammb/dqn017.
[27] H. Dingle, V.A. Drake, What is migration? BioScience 57 (2007) 113–121. http://dx.doi.org/10.1641/B570206.
[28] en.wikipedia.org/Wiki/Animal-migration.
[29] I.A. Mclaren, Demographic strategy of vertical migration by a marine copepod, Am. Nat. 108 (959) (1974) 91–102. JSTOR 2459738
[30] W.M. Hamner, I.R. Hauri, Long-distance horizontal migrations of zooplankton (scyphomedusae mastigias), Limnol. Oceanogr. 26 (3) (1981) 414–423.
[31] www.risingkashmir.com/record-3-lakh-migratory-birds-arrive-in-kashmir/.
[32] listofeverythimg.wordpress.com/2011/03/04/list-of-animals-that-migrate-animal-migration-list/.
[33] www.iLoveindia.com/wildlife/migratory-birds.html.
[34] R. Bhattacharyya, B. Mukhopadhyay, Spatial dynamics of nonlinear prey-predator models with prey migration and predator switching, Ecol. Complex. 3 (2006) 160–169. http://dx.doi.org/10.1016/j.ecocom.2006.01.001.
[35] K. Berthier, et al., Dynamics of a feline virus with two transmission models with exponentially growing host populations, Proc. R. Soc. Lond. 3267 (2000) 2049–2056.
[36] G.-Q. Sun, et al., Dynamical complexity of a spatial predator-prey model with migration, Ecol. Model. 219 (1–2) (2008) 248–255. http://dx.doi.org/10.1016/j.ecolmodel.2008.08.009.
[37] M.C.M. De Jong, How does infection depend on the population size?, in: D. Mollison (Ed.) Epidemic Models, Their Structure and Relation in Data, Cambridge University Press, 1994.
[38] http://web.stanford.edu/~jhj1/teachingdocs/Jones-on-R0.pdf.
[39] B.S.R.V. Prasad, et al., Dynamics of additional food provided predator-prey system with mutually interfering predators, Math. Biosci. 246 (2013) 176–190. http://dx.doi.org/10.1016/j.mbs.2013.08.013.
[40] C.S. Holling, The components of predation as revealed by a study of small mammal predation of the European pine sawfly, Can. Entomol. 91 (1959a) 293–320.
[41] C.S. Holling, Some characteristics of simple types of predation and parasitism, Can. Entomol. 91 (1959b) 385–395.
[42] Y. Xia, et al., Multiple periodic solutions of a delayed stage-structured predator-prey model with non-monotonic functional responses, Appl. Math. Model. 31 (9) (2007) 1947–1959. http://dx.doi.org/10.1016/j.apm.2006.08.012.
[43] X. Tian, R. Xu, Global dynamics of a predator-prey system with Holling type II functional response, Nonlinear Anal. Model. Control 16 (2) (2011) 242–253. www.lana.lt/journal/41/NA16210.pdf
[44] J.H. Dawes, M.O. Souza, A derivatization of Holling's type I,II and III functional responses in predator-prey system, J. Theor. Biol. 327 (2013) 11–22. http://dx.doi.org/10.1016/j.thbi.2013.02.017.
[45] J.F. Andrews, A mathematical model for the continuous culture of microorganisms utilizing inhibitory substrates, Biotechnol. Bioeng. 10 (1968) 707–723.
[46] H. Book, A food chain system with Holling type IV functional response and impulsive perturbations, Comput. Math. Appl. 60 (2010) 1152–1163.
[47] F. Lian, Y. Xu, Hopf-bifurcation analysis of a predator-prey system with Holling type IV functional response and time delay, Appl. Math. Comput. 215 (2009) 1484–1495.
[48] C. Shen, Permanence and global attractivity of the food chain system with Holling type IV functional response, Appl. Math. Comput. 194 (2007) 179–185.
[49] Y. Kuang, E. Beretta, Global qualitative analysis of a ratio-dependent predator-prey system, J. Math. Biol. 36 (4) (1998) 389–406. http://dx.doi.org/10.1007/s002850050105.
[50] R. Xu, et al., Persistence and global stability of a ratio dependent prey model with stage-structure, Appl. Math. Comput. 158 (3) (2004) 729–744. http://dx.doi.org/10.1016/j.amc.2003.10.012.
[51] R. Arditi, L.R. Ginzburg, Coupling in predator-prey dynamics: ratio-dependence, J. Theor. Biol. 139 (1989) 311–326.
[52] P.H. Crowley, E.K. Martin, Functional responses and interference within and between year classes of a dragonfly population, J. N. Am. Benthol. Soc. 8 (1989) 211–221.
[53] S. Liu, E. Beretta, A stage-structured predator-prey model of Beddington-DeAgelis type, SIAM J. Appl. Math. 66 (4) (2006) 1101–1129. http://dx.doi.org/10.1137/050630003.
[54] M.P. Hassell, C.C. Varley, New inductive population model for insect parasites and its bearing on biological control, Nature 223 (1969) 1133–1137.
[55] D.L. Deangenis, et al., A model for trophic interaction, Ecology 56 (1975) 881–892.
[56] J.R. Beddington, Mutual interference between parasites or predators and its effect on searching efficiency, J. Anim. Ecol. 44 (1975) 331–340.
[57] V.S. Ivlev, Experiment Ecology of the Feeding of Fishes, Yale University Press, New Haven, C.T., 1961.
[58] G. Birkoff, G.C. Rota, Ordinary Differential Equations, Ginn, Bostan, 1982.
[59] S.S. Sana, D. Purohit, K. Chaudhury, Joint project of fishery and poltury - a bioeconomic model, Appl. Math. Model. 36 (2012) 72–86. http://dx.doi.org/10.1016/j.apm.2011.04.031.
[60] T.K. Kar, S. Jana, A theoretical study on mathematical modelling of an infectious disease with application of optimal control, Biosystems 111 (2012) 37–50. http://dx.doi.org/10.1016/j.biosystems.2012.10.024.

Please cite this article as: S. Kant, V. Kumar, Stability analysis of predator–prey system with migrating prey and disease infection in both species, Applied Mathematical Modelling (2016), http://dx.doi.org/10.1016/j.apm.2016.10.003

International Journal of Electrical Electronics Computers & Mechanical Engineering (IJEECM)
ISSN: 2278-2808
www.ijeecm.org Volume 3 Issue8 ǁ Aug. 2016

IJEECM journal of Mechanical Engineering (ijeecm-jme)

Structural Analysis and Balancing Test for Impeller Before Conducting Over Speed Test

S.Rakesh [1], J.Govardhan [2]

[1,2] *Electrical & Electronics Department,*

[1,2] AVN Institute of Engineering and Technology, Koheda Road, Ibrahimpatnam, Ranga Reddy Dist., T.S(India)

***Abstract*— This project is process structural analysis and balancing test for impeller before conducting over speed test of manufacturing a component, it is essential to check various properties of the component that may get changed after the manufacturing process. The Centrifugal Compressor Impellers are manufactured from forgings, which is the basic raw material for impellers. During the process of producing the impeller from the forgings, the forgings have to undergo many machining operations and welding processes. These operations may change the mechanical properties and these changes should be accounted in order to have good performance and accuracy. Since the impeller is a high speed rotating component, some stresses may get induced in it and cause dimensional inaccuracies depending upon the mechanical properties of the component material.**

Hence each Impeller of the Compressor rotor is individually over speed in a vacuum chamber to a value of 115% of Maximum continuous speed to check the mechanical soundness of the impeller. After that dimensional and Dye checks are carried out on over-sped impellers for any permanent deformations and micro cracks at the welds. The whole process should be done before the impeller is made ready to be mounted on the rotor shaft. Before conducting the Over Speed Test (O.S.T.) on the impeller, first it has to be balanced. The reasons for balancing, procedure to be followed and the detailed description of the over speeding test are discussed below.

Keywords: **solidworks, ansys.**

I. INTRODUCTION

In the process of manufacturing a component, it is essential to check various properties of the component that may get changed after the manufacturing process. The Centrifugal Compressor Impellers are manufactured from forgings, which is the basic raw material for impellers. During the process of producing the impeller from the forgings, the forgings have to undergo many machining operations and welding processes. These operations may change the mechanical properties and these changes should be accounted in order to have good performance and accuracy. Since the impeller is a high speed rotating component, some stresses may get induced in it and cause dimensional inaccuracies depending upon the mechanical properties of the component material.

Hence each Impeller of the Compressor rotor is individually oversped in a vacuum chamber to a value of 115% of Maximum continuous speed to check the mechanical soundness of the impeller. After that dimensional and Dye checks are carried out on over-sped impellers for any permanent deformations and micro cracks at the welds. The whole process should be done before the impeller is made ready to be mounted on the rotor shaft. Before conducting the Over Speed Test (O.S.T.) on the impeller, first it has to be balanced. The reasons for

balancing, procedure to be followed and the detailed description of the over speeding test are discussed below.

2. DIESEL ENGINE

A diesel engine is an internal combustion engine. The cycle of the cylinders is the same in a diesel engine as it is in a gasoline engine, assuming it is a four-stroke engine Aside from the fuel type, the major difference between the two engines is the combustion itself. A gasoline engine uses a spark plug to initiate combustion. A diesel engine compresses the air then injects the fuel into the cylinder at the top of the stroke. The high temperature of the compressed air ignites the fuel. The hot gases expand, force the piston down, and create a torque on the crankshaft. The final stroke is the exhaust stroke, which releases the hot gases into the exhaust system.

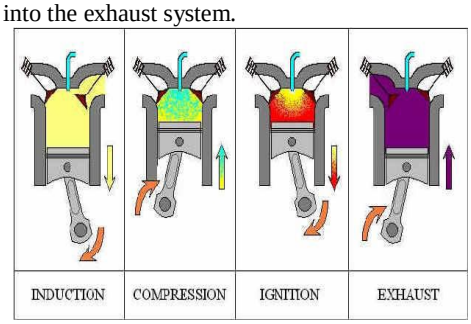


Figure 1 Diesel Engine Four-Stroke Cycle

DIESEL ENGINE FOUR-STROKE CYCLE

The torque created from the downward motion of the piston acting on the crankshaft is transmitted from the crankshaft to the flywheel and into the transmission. To increase power to the transmission, the power must be increased in the cylinder. There are several ways to increase the power of an engine. One of the more common ways of increasing engine power is to increase the airflow into the cylinder by increasing the density of the air entering the cylinder.1 A turbocharger uses waste energy from the exhaust system to compress air entering the cylinder, thus increasing engine power.

3. LITERATUTE REVIEW

Turbo – machines are devices in which energy is transferred either to or from, a continuously flowing fluid by the dynamic action of moving blades of the runner.

Leonardo Da Vinci (1452-1519) was probably the first to coin the idea of lifting water by centrifugal forces. He has described primitive models of turbomachines by making some sketches. From his original sketches, a French physicist Denis Papin was first to describe the centrifugal pump scientifically in 1687. He built first pump in 1705, which had impeller with blades and a volute. Thus, centrifugal pumps and blowers of today are made after more than 300 years' of revolution.

4. DESIGN OF IMPPLER



Figure 2 Impeller

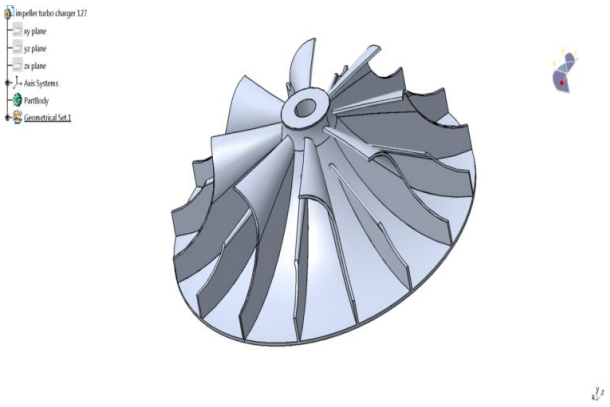


Figure 2 Impeller CATIA Model

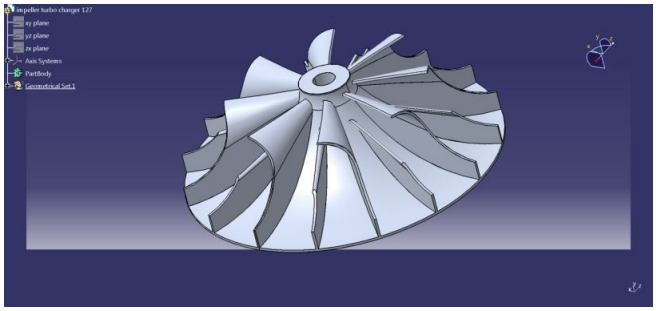


Figure 3 Impeller 3-D Model

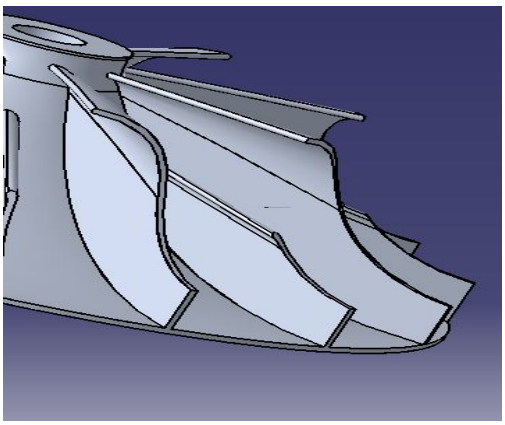


Figure 4 Impeller Blades Shapes

4. ANALYSIS

INTRODUCTION TO FEA

The Basic concept in FEA is that the body or structure may be divided into smaller elements of finite dimensions called “Finite Elements”. The original body or the structure is then considered as an assemblage of these elements connected at a finite number of joints called “Nodes” or “Nodal Points”. Simple functions are chosen to approximate the displacements over each finite element. Such assumed functions are called “shape functions”. This will represent the displacement with in the element in terms of the displacement at the nodes of the element.

5. ANALYSIS RESULTS

Imported model in to ansys

AISI 4063 Steel

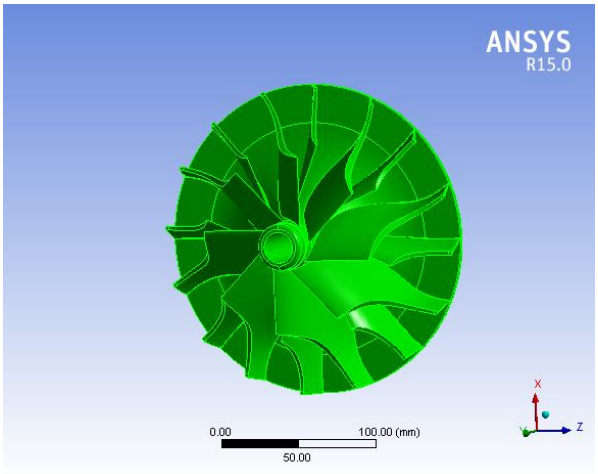


Figure 6 Imported models in to ansys

Element Type: solid 20 nodes 95
Material Properties:

Youngs Modulus (EX) : 209 GPA

Poisson’s Ratio (PRXY) : 0.29

Density : **7.75 g/cc**

Tensile strength ultimate: 1855 MPA

Tensile strength yield : 1593 MPA

MESHED MODEL

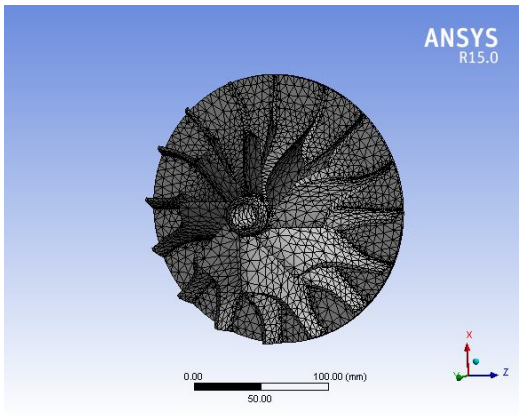


Figure 7 Meshed Model

Rotating speed: 13000 RPM

Displacement

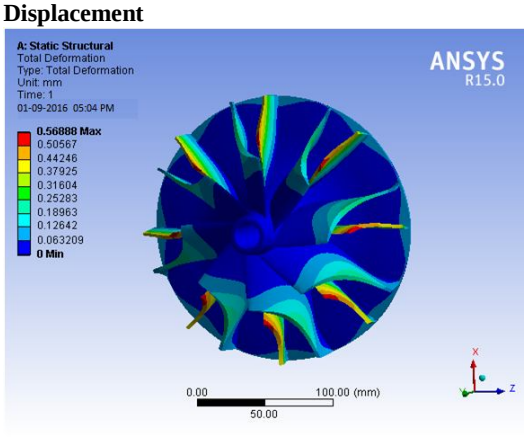


Figure 8 Displacement

STRESS

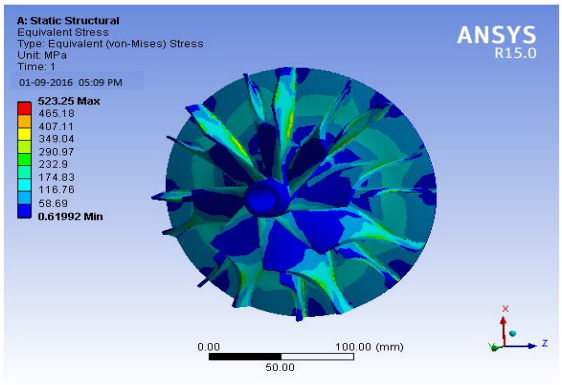


Figure 9 Stress

STRAIN

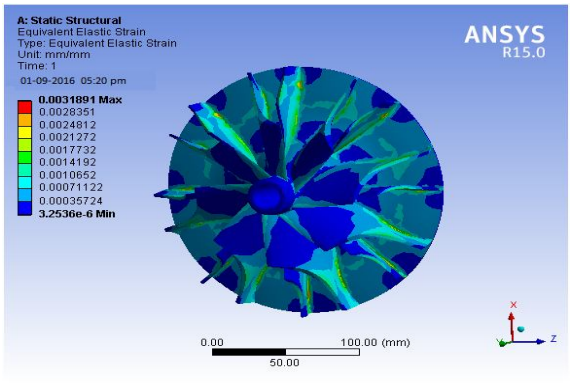


Figure 50 Stain

INCONEL 718

Element Type: Solid 20 node 95

Material Properties:

Youngs Modulus (EX) : **205** GPA

Poissons Ratio (PRXY) : **0.284**

Density : **8.19 g/cc**

Tensile strength ultimate: **1120** MPA

Tensile strength yield : **827** MPA

Rotating speed :13000 RPM

Displacement

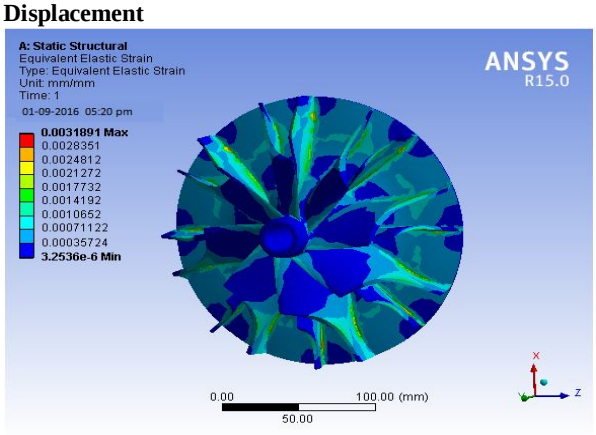


Figure 11 Displacement

STRESS

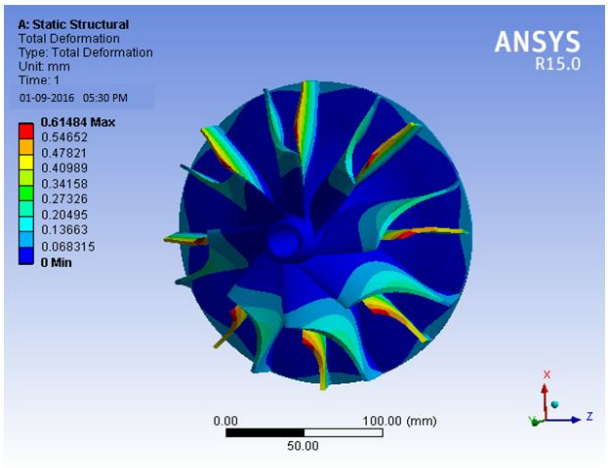


Figure 12 **Stress**

STRAIN

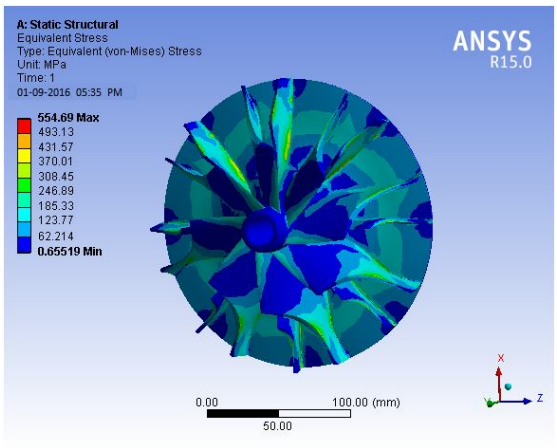


Figure 13 Stain

Titanium Ti6-2-4-6

Element Type: Solid 20 node 95

Material Properties: Youngs Modulus (EX) : **114** GPA

Poissons Ratio (PRXY) : **0.33**

Density : **4.65 g/cc**

Tensile strength ultimate: **1580** MPA

Tensile strength yield : **1410** MPA

Rotating speed :13000 RPM

Displacement

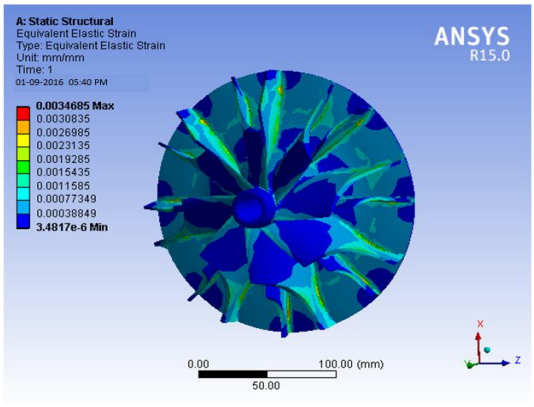


Figure 14 Displacement

STRESS

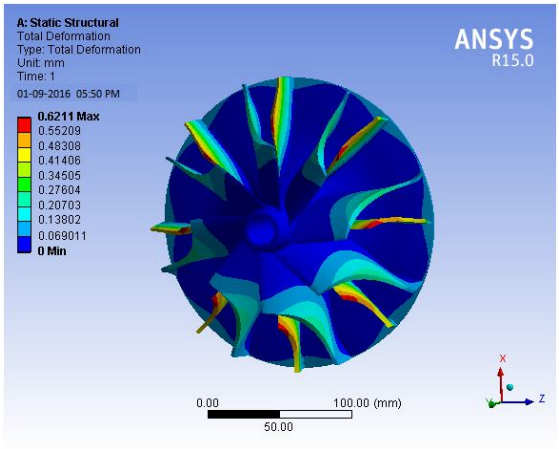


Figure 15 Stress

STRAIN

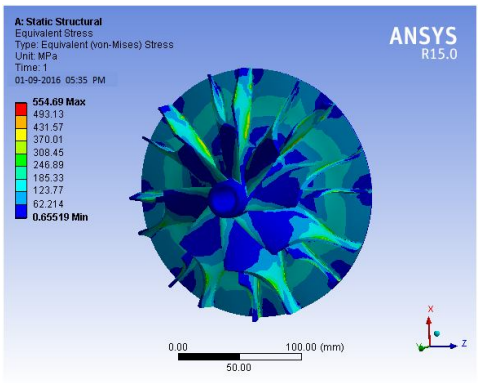


Figure 16 Strain

Technetium
Element Type: Solid 20 node 95
Material Properties: Youngs Modulus (EX) : **322** GPA
Poissons Ratio (PRXY) : **0.31**
Density : **11.5 g/cc**
Tensile strength ultimate: **1510** MPA
Tensile strength yield : **1290** MPA
Rotating speed :13000 RPM

Displacement

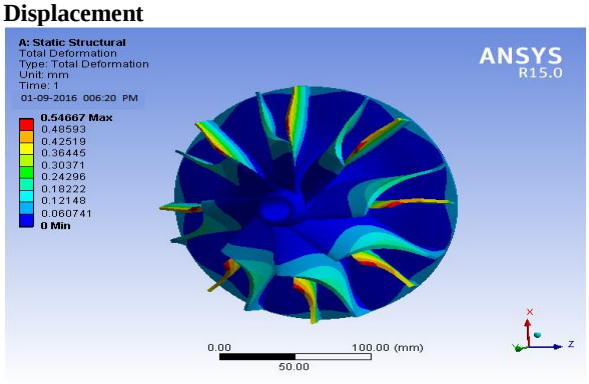


Figure 17 Displacement

STRESS

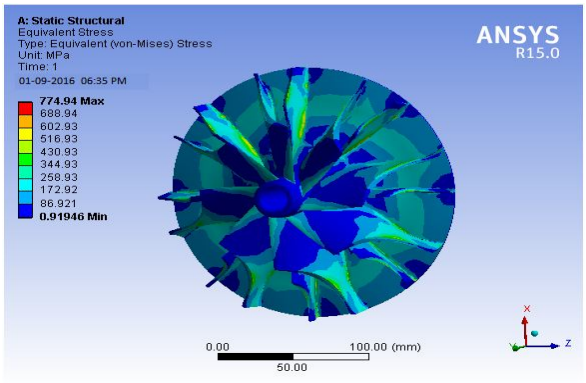


Figure 18 Stress

STRAIN

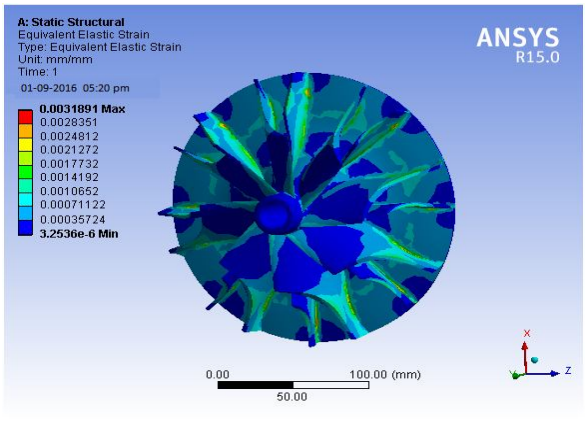


Figure 19 Stain

6. RESULTS OF FINITE ELEMENT ANALYSIS

Table 1 Result Tables

Name of the Material	**DISP mm**	**STRESS N/mm^2**	**STRAIN**
AISI 4063 Steel	0.5688	523.25	3.189E^{-6}
INCONEL 718	0.6148	554.69	3.468E^{-06}
Titanium Ti6-2-4-6	0.6211	312.13	3.445E^{-06}
Technetium	0.5467	774.94	3.053E-^{06}

FEA has become a solution to the task of predicting failure due to unknown stresses by showing problem areas in a material and allowing designers to see all of the theoretical stresses within. This method of product design and testing is far superior to the manufacturing costs which would accrue if each sample was actually built and tested. In practice, a finite element analysis usually consists of three principal steps:

1. **Preprocessing**: The user constructs a model of the part to be analyzed in which the geometry is divided into a number of discrete sub regions, or elements," connected at discrete points called nodes." Certain of these nodes

will have fixed displacements, and others will have prescribed loads. These models can be extremely time consuming to prepare, and commercial codes vie with one another to have the most user-friendly graphical "preprocessor" to assist in this rather tedious chore. Some of these preprocessors can overlay a mesh on a preexisting CAD file, so that finite element analysis can be done conveniently as part of the computerized drafting-and-design process.

2. **Analysis**: The dataset prepared by the preprocessor is used as input to the finite element code itself, which constructs and solves a system of linear or nonlinear algebraic equations

$$Kijuj = fi$$

where u and f are the displacements and externally applied forces at the nodal points. The formation of the K matrix is dependent on the type of problem being attacked, and this module will outline the approach for truss and linear elastic stress analyses. Commercial codes may have very large element libraries, with elements appropriate to a wide range of problem types. One of FEA's principal advantages is that many problem types can be addressed with the same code, merely by specifying the appropriate element types from the library.

3. **Post processing**: In the earlier days of finite element analysis, the user would pore through reams of numbers generated by the code, listing displacements and stresses at discrete positions within the model. It is easy to miss important trends and hot spots this way, and modern codes use graphical displays to assist in visualizing the results. A typical post processor display overlays colored contours representing stress levels on the model, showing a full field picture similar to that of photo elastic or moiré experimental results.

7. CONCLUSION

Hence we can conclude that Over-speed testing of large industrial and utility compressor rotors offers many benefits to the end user because the objectives of over-speed testing include

- Helping the end user feel more comfortable knowing that these huge rotors have been tested at speeds well in excess of the actual maximum operating speed.
- A second benefit is that inspection of the rotor welded joints before and after testing (using non-destructive inspection techniques) provides further proof that the rotor can tolerate such high stress levels without cracks developing.
- A third benefit is that subjecting the rotor to even one cycle at such high stress levels offers an advantage regarding the rotor's fatigue life.
- These factors provide comprehensive proof that the materials and workmanship . incorporated into the rotor have resulted in equipment that is safe to operate even at
- speeds above the expected operating range.

Hence Over-speed testing does more than just provide a warm and fuzzy feeling.

8. REFERENCES

1. J. Wang, Piechnajanusz, et al. A novel design of composite water turbine using CFD. Journal of Hydrodynamics, 2012, 24(1): 11–16.
2. R. Barrio, J. Parrondo, E. Blanco. Numerical analysis of the unsteady flow in the near-tongue region in a volute-type centrifugal pump for different operating points. Computers & Fluids, 2012, 39: 859–870.
3. J. Wang, B. gower, N. M¨uller. Numerical investigation on composite material marine current turbine using cfd. Central European Journal of Engineering, 2011, 1(4): 334–340.
4. J. Wang, J. Piechna, N. M¨uller. Numerical investigation of the power generation of a ducted composite material marine current turbine. Journal of Zhejiang University-SCIENCE A, 2013, 14(1): 25–30.
5. S. Anagnostopoulos. A fast numerical method for flow analysis and blade design in centrifugal pump impellers. Computers & Fluids, 2009, 38: 284–289.
6. C. Lam, K. Bremhorst. Modified form of model for predicting wall turbulence. ASME Journal of Fluids Engineering, 1981, 103: 456–460.

7. M. Nataraj, R. Ragothsingh. Analyzing pump impeller for performance evaluation using rsm and cfd. Desalination and Water Treatment, ahead of print, 2013, 1–10.

8. Technical paper. Advanced boundary cartesian meshing technology in solidworks flow simulation. in: Dassault- Systemes, SolidWorks corporation, 1–31.

9. Technical paper. Enhanced turbulence modeling in solidworks flow simulation. DassaultSystemes, SolidWorks corporation, 1–21.

10. R. Ragothsingh, M. Nataraj. Parametric study and optimization of pump impeller by varying the design parameter using computational fluid dynamics. International Review of Mechanical Engineering, 2012, 6: 1581–1585.

11. M. Shojaeefard, M. Tahani, et al. Numerical study of the effects of some geometric characteristics of a centrifugal pump impeller that pumps a viscous fluid. Computers & Fluids, 2012, 60: 61–70.
12. R. Singh, R. Nataraj, et al. Investigation of a centrifugal pump impeller vane profile using cfd,. International Review on Modelling and Simulations, 2013, 6(4): 1327–1333.

13. [K. Srinivasan. Rotodynamic pumps (centrifugal and axial). New age international, 2008.

14. W. Zhou, Z. Zhao, et al. Investigation of flow through centrifugal pump impellers using computational fluid dynamics. Journal of Rotating Machinery, 2003, 9(1): 49–61.



Dr. J. Govardhan holds Ph.D in Mechanical Engineering from Osmania University, Hyderabad. He obtained his Masters degree from Delhi College of Engineering, Delhi University and bachelors from Institute of Engineers (India).

He served defence for 20 years. Also has 16 years of teaching experience in various positions at Padmasri BV Raju Institute of Engineering and Technology, Narsapur, DVR College of Engineering and Technology, Kandi and PRRM College of Engineering and Technology, Shabad. He is presently Principal of AVN Institute of Engineering and Technology at Hyderabad.



Mr.S.Rakesh M.tech student, AVN Institute of Engineering and Technology, under Jawaharlal Nehru Technological University Hyderabad (JNTUH). Bachelor of engineering from AVN Institute of Engineering and Technology,I am Participated in many technical events and activities.My main project is completed on anti lock braking system(proto type)from santha shivam industry Pvt.Ltd,Coimbatore,tamilnadu.

Int J Interact Des Manuf
DOI 10.1007/s12008-016-0359-7

ORIGINAL PAPER

Taguchi and utility based concept for determining optimal process parameters of cold sprayed coatings for multiple responses

Tarun Goyal[1] · **R. S. Walia**[2] · **T. S. Sidhu**[3]

Received: 13 October 2016 / Accepted: 18 October 2016
© Springer-Verlag France 2016

Abstract Most of the existing multi-response optimization approaches focus on subjective and practical know how of the process. As a result some confusions and uncertainties are introduced in overall decision making process. In this investigation, an approach based on a Utility theory and Taguchi quality loss function has been applied to low-pressure cold spray process to deposit copper coatings, for simultaneous optimization of more than one response characteristics. In the present paper, three potential response parameters i.e. coating density, surface roughness and Micro hardness have been selected. Utility values based upon these response parameters have been analyzed for optimization by using Taguchi approach. The selected input parameters of powder feeding arrangement, substrate material, air stagnation pressure, air stagnation temperature and stand-off distance significantly improves the Utility function (raw data) comprising of quality characteristics (coating density, surface roughness and micro hardness). The percentage contribution of the parameters to achieve a higher value of utility function is: substrate material (64.59%), air stagnation pressure (16.35%), powder feeding arrangement (6.92%), air stagnation temperature (6.49%) and stand-off distance (1.84%) respectively.

Keywords Cold spray (CS) · Optimization · Taguchi method · Utility concept

✉ Tarun Goyal
goyaltarun1@gmail.com

[1] IKGPTU, Kapurthala, Punjab 144603, India

[2] Delhi Technological University, Delhi, India

[3] SBSSTC, Ferozepur, Punjab, India

1 Introduction

There are many coating deposition techniques available, and choosing the best process depends on the functional requirements, adaptability of the coating material to the technique intended, level of adhesion required, size, shape, and metallurgy of the substrate, and availability and cost of the equipment. Goyal et al. [3] enlisted the commonly employed coating deposition techniques in Fig. 1.

In the early nineteen hundreds, a young Swiss inventor named Dr. Max Schoop invented thermal spraying, after watching his son playing with his toy cannon. Dr. Schoop observed that the hot lead shots that were projected out of the cannon, stuck to almost any surface, the result of which gave him the idea that if metal could be melted and projected in a spray like manner, then a surface could be built up with that material.

Knotek [12] explained that the technology continued, but expanded in the 70s due to development of the thermal plasmas and the increasing demand of high-temperature and wear resistant materials and coating systems. Marceau et al. [15], Groshart [8] and Ishikawa et al. [11] found that Thermal spraying is one of the most versatile hard facing techniques available for the application of coating materials used to protect components from abrasive wear, adhesive wear, erosive wear or surface fatigue and corrosion (such as that caused by oxidation or seawater).

CS is a process of applying coatings by exposing a metallic or dielectric substrate to a high velocity (300–1200 m/s) jet of small (1–50 μm) particles accelerated by a supersonic jet of compressed gas. The two main clear cut distinctions of the Low Pressure Cold Gas Dynamic Spray (LPCGDS) system from the High Pressure Cold Gas Dynamic Spray (HPCGDS) system are: the utilization of low pressure gas (5–10 bars instead of 25–30 bars) and the radial injection of

Published online: 27 October 2016

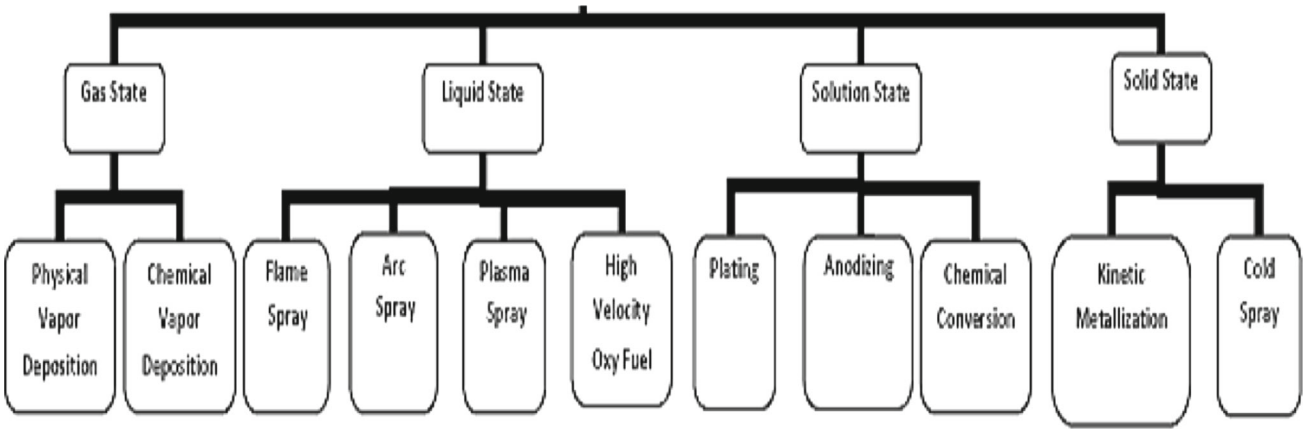


Fig. 1 Various coating deposition processes in commercial use

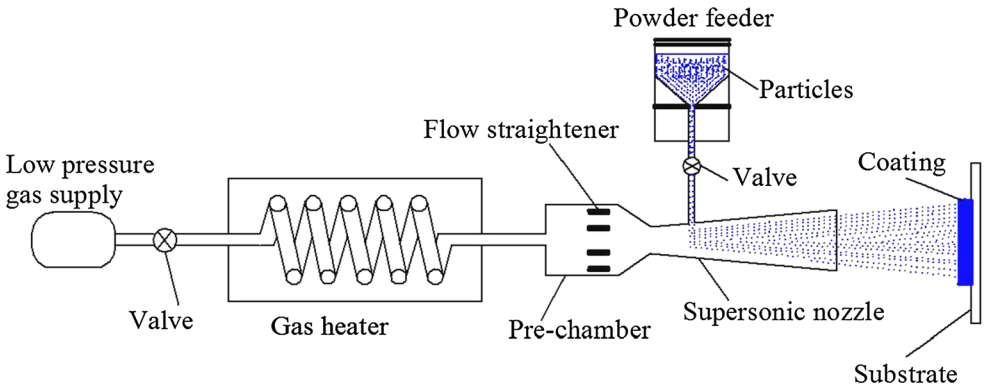


Fig. 2 A typical LPCGDS device

powder instead of axial injection. The accelerating gas (usually air or N_2) is injected at low pressure (5–10 bars) and preheated within the gas heater to temperatures up to about 400°C to optimize its aerodynamic properties. Solid powder particles are radially introduced downstream of the throat section of the supersonic nozzle thus eliminating the need for a high pressure delivery system, which increases system portability, operational safety and significantly reduces spraying costs. Maev and Leshchynsky [14] discovered that within the nozzle, static pressure is maintained below the atmospheric pressure ensuring that feedstock particles are effectively drawn in from the powder feeder by Venturi effect. Grujicic et al. [9] shows a schematic of the LPCGDS system in Fig. 2.

To obtain good quality coatings, these spray parameters should be selected carefully and then optimized. In the process of optimization of process parameters, it is seen that one particular setting of input parameters for a response characteristics may not be suitable for other characteristics of the process/product. In most of the manufacturing processes, more than one quality characteristics has to be considered for optimization of process parameters making it necessary that several response characteristics have to be simultaneously optimized. Based on the foregoing discussions, in this paper, Taguchi method is briefly reviewed for the multi-response optimization. The multi-response optimization of the response parameters of Low Pressure Cold Spray (LPCS) process is presented by using the experimental data. Optimization models have been developed by combination of Taguchi Method and the Utility concept. The multi-response optimization of quality characteristics i.e. coating density, surface roughness and micro hardness of LPCS has been carried.

2 Experimental procedure

2.1 Development of coatings

Substrate material

The substrate materials selected were Al (ASTM B221), Brass (ASTM B36) and Ni (ASTM B435) in the rolled sheet form. The substrate materials selected for the study finds application in the manufacture of electrical contact points, fuse element of electric mains plug, battery terminals,

Table 1 Nominal chemical composition of the substrate materials chosen

Nominal Chemical composition of ASTM B 221 (Al alloy)													
%Si	%Fe	%Cu	%Mn	%Mg	%Cr	%Zn	%Ti	%Others	%Al				
0.4–0.8	0.7	0.15–0.40	0.15	0.8–1.2	0.04–0.35	0.25	0.15	0.15	Rem.				
Nominal Chemical composition of ASTM B 36 (Brass)													
%Cu	%Pb	%Fe	%Zn										
64–68.5	0.15	0.05	Remainder										
Nominal Chemical composition of ASTM B 435 (Ni alloy)													
%Fe	%Ni	%Co	%Cr	%Mo	%W	%Mn	%Si	%Ta	%Al	%C	%N	%Zr	%La
31	20	18	22	3	2.5	1	0.4	0.6	0.2	0.1	0.2	0.02	0.02

Table 2 Process parameters and their range

Symbol	Process parameters	Range	Level 1	Level 2	Level 3
A	Feed type	Gravity, Argon	Gravity	Argon	–
B	Substrate material	Al alloy, Brass, Ni alloy	Al alloy	Brass	Ni alloy
C	Stagnation pressure	104–120 psi	104	112	120
D	Stagnation temperature	350–400 °C	350	375	400
E	Stand-off distance	2.5–7.5 mm	2.5	5.0	7.5

Nozzle type: Converging-diverging, Carrier gas: Air, Powder size: <45 μm

bimetallic joints, heat sinks, waste incinerators, gas turbines, brazing and soldering alloys and many more. The nominal chemical composition of the substrate material used in the study is mentioned in Table 1. The samples were cut from the alloy sheet to form approximately 25 mm × 15 mm × 5 mm sized specimens. The specimens were polished and grit blasted with alumina powders (grit 60) before being cold sprayed.

Coating formulation

The coating powder selected was commercially available Copper (less than 45 microns diameter; spherical morphology) obtained from Centreline (Windsor), Ltd (Windsor, ON, Canada) (material ID- 440-00251 and Catalogue Number-SST-C5001). The carrier gas used in the system was compressed air. The coating deposition was done at Surface and Coatings Laboratory, University of Alberta, Edmonton, Canada using Low-Pressure Cold Spray Equipment-SST LPCS Model # SSM-P3800-001, produced by Centreline Windsor, Canada. Table 2 show the process parameters that were identified as potential important in affecting the quality characteristics of the LPCS process under consideration. The process parameters, their designated symbols and ranges are also given in Table 2.

Taguchi's mixed level design was selected as it was decided to keep two levels of powder feeding arrangement. The rest four parameters were studied at three levels. The effect of selected process parameters was studied on the following response characteristics of LPCS process:

a. Coating density (CD)
b. Surface Roughness (SR)
c. Micro hardness (MH)

Coating density and micro hardness are "higher the better" whereas surface roughness is "lower the better" type of quality characteristics.

The coating density was calculated by measuring coating thickness for the samples using digital Micrometer, Mitutoyo, Japan make for an accuracy of 0.0254 mm (0.0001 inch) [4,5]. Goyal et al. [4,5] measured the surface roughness of the samples with the help of Surface Roughness Tester, Mitutoyo, Japan make, Model SJ 400 for a resolution of 0.000125 μm and maximum measuring range of 800 μm. Goyal et al. [6] measured the micro hardness of the coating by Metco's Micro-hardness Tester. A load of 300 g (2.94 N) was provided to the needle for penetration; the loading time was selected as 18 s, and hardness value was based on the relation $Hv = 1854.4\,(F)/d^2$ (where F is the load in grams and d is the mean penetrated diameter in μm).

Goyal et al. [7] used a simplified multi-criterion methodology based on Taguchi's approach and utility concept (given

below) to achieve the objective of this study. The observed values of response parameters are given in Table 3.

2.2 Utility concept

Utility can be defined as the usefulness of a product or a process in reference to the expectations of the users. The overall usefulness of a process/product can be represented by a unified index termed as *Utility* which is the sum of the individual utilities of various quality characteristics of the process/product. The methodological basis for Utility approach is to transform the estimated response of each quality characteristic into a common index.

Derek [2] explained that if X_i is the measure of effectiveness of an attribute (or quality characteristic) i and there are n attributes evaluating the outcome space, then the joint Utility function can be expressed as:

$$\mathrm{U}(\mathrm{X}_1, \mathrm{X}_2, \ldots \mathrm{X}_\mathrm{n}) = \mathrm{f}(\mathrm{U}_1(\mathrm{X}_1), \mathrm{U}_2(\mathrm{X}_2) \ldots . \mathrm{U}_\mathrm{n}(\mathrm{X}_\mathrm{n})) \quad (1)$$

where $\mathrm{U_i}(\mathrm{X_i})$ is the utility of the ith attribute.

The overall Utility function is the sum of individual utilities if the attributes are independent, and is given as follows:

$$\mathrm{U}(\mathrm{X}_1, \mathrm{X}_2, \ldots \mathrm{X}_\mathrm{n}) = \sum_{\mathrm{i}=1}^{\mathrm{n}} \mathrm{U_i}(\mathrm{X_i}) \quad (2)$$

The attributes may be assigned weights depending upon the relative importance or priorities of the characteristics. The overall utility function after assigning weights to the attributes can be expressed as:

$$\mathrm{U}(\mathrm{X}_1, \mathrm{X}_2, \ldots \mathrm{X}_\mathrm{n}) = \sum_{\mathrm{i}=1}^{\mathrm{n}} \mathrm{W_i U_i}(\mathrm{X_i}) \quad (3)$$

where $\mathrm{W_i}$ is the weight assigned to the attribute i, the sum of the weights for all the attributes must be equal to 1.

2.3 Determination of utility value

A preference scale for each quality characteristic is constructed for determining its utility value. Two arbitrary numerical values (preference number) 0 and 9 are assigned to the just acceptable and the best value of the quality characteristic respectively. Gupta and Murthy [10,13] proposed that the preference number ($\mathrm{P_i}$) can be expressed on a logarithmic scale as follows:

$$P_i = A \times \log\left(\frac{X_i}{X_i'}\right) \quad (4)$$

where $\mathrm{X_i}$ = value of any quality characteristic or attribute i

X_i' = just acceptable value of quality characteristic or attribute i

A = constant

The value of A can be found by the condition that if $\mathrm{X_i} = \mathrm{X}^*$ (where X^* is the optimal or best value), then $\mathrm{P_i} = 9$

Therefore, $A = \frac{9}{\log \frac{X^*}{X_i'}}$

The overall utility can be calculated as follows:

$$\mathrm{U} = \sum_{\mathrm{i}=1}^{\mathrm{n}} \mathrm{W_i P_i} \quad (5)$$

subject to the condition: $\sum_{\mathrm{i}=1}^{\mathrm{n}} \mathrm{W_i} = 1$

Among various quality characteristics type viz. smaller the better, higher the better, and nominal the better, suggested by Taguchi, the Utility function would be higher the better type. Therefore, if the Utility function is maximized, the quality characteristics considered for its evaluation will automatically be optimized (maximized or minimized as the case may be).

3 Analysis and discussions

Based upon the methodology developed in the previous section, following case have been considered to obtain the optimal settings of the process parameters of LPCS for predicting the optimal values of combined responses. Three quality characteristics i.e. Coating density, Surface Roughness and Micro hardness have been included in utility response.

Roy [16] explained Taguchi $\mathrm{L_{18}}$ orthogonal array (OA) which has been adopted for conducting the experiments. Powder feeding arrangement (A), Substrate material (B), air stagnation pressure (C), air stagnation temperature (D), and stand-off distance (E) were selected as input parameters. Response parameters (quality characteristics) were coating density, surface roughness and micro hardness, when they are optimized individually; the summary of results is produced in Table 4.

Following is the stepwise procedure for transforming experimental data into utility data.

3.1 Construction of preference scales

(a) Preference scale for CD (P_{CD}):

X^* = Optimal value of CD = 27,584.59 (refer Table 4)

X_i' = Just acceptable value of CD = 2700 (All the observed values of CD are greater than 2700)

Following equation is obtained from Eq. 4:

$$P_{CD} = 8.91 \times \log\left(\frac{X_{CD}}{2700}\right) \quad (6)$$

Table 3 Experimental results of various response characteristics

Exp. No.	Coating density (kg/m^3) CD			S/N ratio (dB)	Surface roughness (μm) SR			S/N ratio (dB)	Micro hardness ($H_{v0.3}$) MH			S/N ratio (dB)
	R1	R2	R3		R1	R2	R3		R1	R2	R3	
1	4654.4	4623.6	4593.2	73.29	13.56	13.71	13.83	−22.73	122	126	124	41.86
2	3128.5	3157.9	3116.9	69.92	10.87	10.91	10.36	−20.60	134	129	132	42.38
3	5012.1	5034.4	4997.4	74.00	8.05	7.81	7.73	−17.91	131	132	122	42.15
4	4638.1	4654.1	4614.4	73.32	9.2	10.04	10.68	−19.99	126	128	124	42.00
5	6229.5	6169.3	6125.0	75.81	8.17	8.02	10.23	−18.95	124	125	128	41.98
6	9016.9	8992.2	9021.0	79.09	8.7	7.5	8.6	−18.36	126	127	128	42.07
7	27354.5	27106.4	27500.7	88.72	11.17	11.22	11.56	−21.07	129	131	132	42.32
8	8948.0	8887.9	8877.1	78.99	6.69	6.68	7.35	−16.79	137	133	134	42.58
9	9440.4	9442.0	9474.6	79.51	6.89	6.97	7.02	−16.85	134	135	139	42.66
10	3075.1	3111.0	3084.0	69.79	8.31	8.26	9.59	−18.83	123	118	111	41.36
11	3259.0	3211.9	3245.9	70.20	9.24	9.6	9.52	−19.51	119	115	117	41.36
12	3422.3	3457.9	3437.5	70.72	8.42	8.29	8.92	−18.63	126	131	129	42.18
13	5273.6	5261.5	5225.3	74.40	9.04	9.78	9.62	−19.54	125	121	122	41.77
14	5206.4	5299.1	5216.8	74.38	7.19	7.79	7.82	−17.62	110	119	113	41.12
15	2741.4	2758.3	2749.8	68.78	6.18	6.97	6.39	−16.28	122	120	124	41.72
16	8615.5	8628.4	8671.6	78.72	7.94	8.13	8.15	−18.14	129	125	127	42.07
17	5796.5	5874.8	5818.7	75.31	7.19	8.62	7.34	−17.77	125	127	128	42.05
18	30161.0	30513.7	30244.6	89.63	7.94	7.11	7.84	−17.66	123	128	132	42.11
Total	145973.1	146184.4	146014.3	1364.67	154.75	157.41	162.55	−337.23	2265	2270	2266	755.80
	$\bar{T}D$ = overall mean of CD = 8114.29				$\overline{T}_{SR}$ = overall mean of SR = 8.79				$\overline{T}_{MH}$ = overall mean of MH = 125.94			

Table 4 Optimal setting and values of process parameters

Response characteristics	Optimal level of process parameters	Significant process parameters	Predicted optimal value of quality characteristics
CD	A1, B3, C3, D2, E1	A, B, C, D, E	27584.59 kg/m^3
SR	A2, B3, C3, D3, E3	A, B, C, D, E	4.92 μm
MH	A1, B3, C3, D2, E2	A, B, C, D, E	138.36 $H_{v0.3}$

(b) Preference scale for SR (P_{SR}):
X^* = Optimal value of SR = 4.92 (refer Table 4)
X_i' = Just acceptable value of SR = 14 (All the observed values of SR are lesser than 14)
Following equation is obtained from Eq. 4:

$$P_{SR} = -19.81 \times \log\left(\frac{X_{SR}}{14}\right) \tag{7}$$

(c) Preference scale for MH (P_{MH}):
X^* = Optimal value of MH = 138.36 (refer Table 4)
X_i' = Just acceptable value of MH = 110 (All the observed values of MH are greater than 110)
Following equation is obtained from Eq. 4:

$$P_{MH} = 90.34 \times \log\left(\frac{X_{MH}}{110}\right) \tag{8}$$

3.2 Calculation of utility value

Equal weights (1/3 each) have been assigned to the selected quality characteristics assuming all the quality characteristics, are equally important. However, these weights can be varied depending upon the case or user requirements, if any.

The following relation was used to calculate the utility function based upon the experimental trials:

$$U(n, r) = P_{CD}(n, r) \times W_{CD} + P_{SR}(n, r) \times W_{SR} + P_{MH}(n, r) \times W_{MH} \tag{9}$$

where $W_{CD} = \frac{1}{3}$; $W_{SR} = \frac{1}{3}$; $W_{MH} = \frac{1}{3}$
n is the trial number ($n = 1, 2, 3, \ldots, 18$) and r is the repetition number (r = 1,2,3). The calculated Utility values are shown in Table 5.

3.3 Analysis of utility data for optimal settings of process parameters

Roy [16] found that Taguchi suggests two different routes to carry out the complete analysis of the experiments. First the standard approach, where the results of a single run or the average of the repetitive runs are processed through main effect and ANOVA analysis (Raw data analysis). The second approach which Taguchi strongly recommends for multiple runs is to use signal-to-noise (S/N) ratio for the same steps in the analysis. The S/N ratio is a concurrent quality metric linked to the loss function. By maximizing the S/N ratio, the loss associated can be minimized. The S/N ratio determines the most robust set of operating conditions from variation within the results. The S/N ratio is treated as a response parameter (transform of raw data) of the experiment. Byrne and Taguchi [1] gave S/N ratio for a "higher the better" type of quality characteristic by:

$$(S/N)_{HB} = -10\log(MSD_{HB})$$

where $MSD_{HB} = \frac{1}{R}\sum_{j=1}^{R}(1/y_j^2)$
where, MSD denotes mean square deviation, which presents the average of squares of all deviations from the target value rather than around the average value.

The average and main response in terms of Utility values and S/N ratio (Tables 6, 7) are plotted in Fig. 3. It can be observed from Fig. 3(i)–(v) that the 1st level of powder feed

Table 5 Calculated utility data based on responses CD, SR and MH

Trial number	Utility values			S/N ratio (dB)
	R1	R2	R3	
1	2.15	2.53	2.29	9.26
2	3.50	3.00	3.43	10.34
3	4.67	4.86	3.85	12.85
4	3.68	3.64	3.04	10.66
5	4.19	4.34	3.94	12.35
6	4.70	5.22	4.94	13.87
7	5.72	5.90	5.93	15.34
8	6.54	6.14	5.97	15.85
9	6.23	6.30	6.66	16.11
10	3.13	2.61	2.38	8.48
11	1.96	1.89	2.05	5.86
12	3.54	4.11	3.69	11.50
13	3.79	3.14	3.28	10.56
14	2.76	3.58	2.87	9.58
15	3.72	3.17	3.84	10.97
16	4.21	4.73	4.94	13.24
17	4.57	4.27	4.83	13.14
18	6.20	7.06	7.17	16.60

R1, R2, R3 = repetitions of experiments against each of the trial conditions

Table 6 Average and main Effects (raw data: CD, SR and MH)

Process parameter designation	Average utility values			Main effects		Difference
	L1	L2	L3	L2–L1	L3–L2	(L3–L2) – (L2–L1)
A	4.57	3.83	–	−0.74	–	−0.74
B	3.09	3.77	5.74	0.68	1.97	1.29
C	3.73	3.88	5	0.15	1.12	0.97
D	3.71	4.55	4.34	0.84	−0.21	−1.05
E	4.16	4.16	4.28	0	0.12	0.12

L1, L2 and L3 represents average values of raw data of corresponding parameters at levels 1, 2 and 3 respectively. L2–L1 is the average main effect when the corresponding parameter changes from level 1 to level 2. L3-L2 is average main effect when the corresponding parameter changes from level 2 to level 3. A-Powder feed arrangement, B- Substrate material, C-air stagnation pressure, D-air stagnation temperature, E-stand-off distance

Table 7 Average S/N values and main effects (raw data: CD, SR and MH)

Process parameter designation	S/N Average values			Main effects (dB)		Difference
	L1	L2	L3	L2–L1	L3-L2	(L3-L2)-(L2-L1)
A	12.74	11.1	–	−1.63	–	−1.63
B	9.38	11.33	15.05	1.95	3.72	1.77
C	10.92	11.19	13.65	0.26	2.46	2.2
D	10.67	12.78	12.31	2.11	−0.47	−2.58
E	11.42	12.09	12.25	0.67	0.16	−0.51

L1, L2 and L3 represents average values of S/N data of corresponding parameters at levels 1, 2 and 3 respectively. L2–L1 is the average main effect when the corresponding parameter changes from level 1 to level 2. L3–L2 is average main effect when the corresponding parameter changes from level 2 to level 3. A-Powder feed arrangement, B- Substrate material, C-air stagnation pressure, D-air stagnation temperature, E-stand-off distance

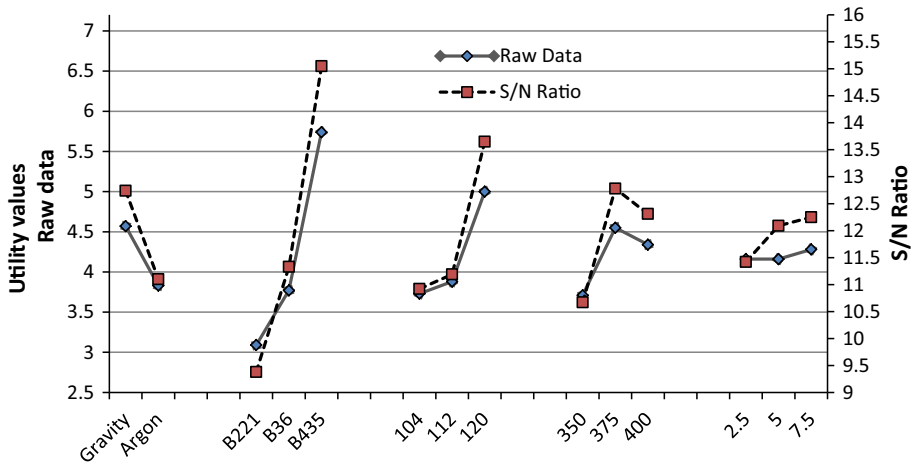


Fig. 3 Average and main response in terms of Utility values and S/N ratio

arrangement (A 1), 3rd level of substrate material (B 3), 3rd level of air stagnation pressure (C 3), 2nd level of air stagnation temperature (D 2) and 3rd level stand-off distance (E 3) are expected to yield a maximum values of the utility and S/N ratio within the experimental space.

The pooled version of ANOVA for utility data and S/N ratio are given in Tables 8 and 9 respectively. It can be noticed from Table 8 that all the input parameters have significant effect (at 95% confidence level) on the utility function. Similarly, it had been found from Table 9 that all the chosen parameters in study have significant effect on the S/N ratio of utility function.

3.4 Optimal values of quality characteristics (predicted means)

The average values of all the response characteristics at the optimum levels of significant parameters with respect to Utility function are recorded in Table 10.

Table 8 Pooled ANOVA (raw Data: CD, SR and MH)

Source	SS	DOF	V	F-Ratio	SS′	P %
A	7.31	1	7.31	79.81*	7.22	6.92
B	68.28	2	34.14	372.72*	68.10	64.59
C	17.28	2	8.64	64.27*	17.10	16.34
D	6.86	2	3.43	79.81*	6.68	6.49
E	1.95	2	0.97	10.64*	1.77	1.84
E (Pooled)	4.03	44	0.09	–	4.85	3.81
Total (T)	105.72	53	–	–	105.72	100

* Significant at 95% confidence level
SS sum of Squares, *DOF* degree of freedom, *V* variance, *SS*′ pure sum of squares

Table 9 S/N pooled ANOVA (raw data: CD, SR and MH)

Source	SS	DOF	V	F-Ratio	SS′	P %
A	11.99	1	11.99	54.40*	11.77	7.61
B	99.44	2	49.72	225.53*	99.00	63.13
C	27.19	2	13.59	61.66*	26.74	17.26
D	14.81	2	7.40	33.58*	14.37	9.40
E	2.32	2	1.16	5.27*	1.88	1.48
E (Pooled)	1.76	8	0.22	–	3.75	1.12
Total (T)	157.51	17	–	–	157.51	100

* Significant at 95% confidence level
SS sum of Squares, *DOF* degree of freedom, *V* variance, *SS*′ pure sum of squares

Table 10 Average values of various responses at optimal levels

Levels	Coating density, CD (kg/m^3)	Surface roughness, SR (μm)	Micro hardness, MH ($Hv_{0.3}$)
A1	8696.68	9.390	129.33
B3	15075.3	8.101	130.44
C3	9995.41	7.629	128.28
D2	12604.7	9.415	127.83
E3	5802.51	8.258	126.11

The above average values are taken from experimental data

The optimal values of the predicted means (μ) of different response characteristics can be obtained from the following equation:

$$\mu = A1 + B3 + C3 + D2 + E3 - 4T \tag{10}$$

where, A1-First level of powder feed arrangement, B3-Third level of substrate material, C3-Third level of air stagnation pressure, D2-Second level of air stagnation temperature and E3-Third level of stand-off distance.

Roy [16] described that the 95% confidence interval of confirmation experiments (CI_{CE}) can be computed by using the following equation:

$$CI_{CE} = \sqrt{F_{\alpha}(1,f_e)V_e\left[\frac{1}{n_{eff}} + \frac{1}{R}\right]} \tag{11}$$

where, $F_{\alpha}(1, f_e)$ = The F-ratio at the confidence level of (1- α) against DOF 1 and error degree of freedom f_e, R = Sample size for conformation experiments, V_e = Error variance, $n_{eff} = \frac{N}{1+DOF}$, N= total number of trials, and DOF= Total degrees of freedom associated in the estimate of mean response.

(a) For Coating density (CD)

$$\mu_{CD} = A1 + B3 + C3 + D2 + E3 - 4T_{CD} = 19717.44$$

where A1 = 8696.68, B3 = 15075.3, C3 = 9995.41, D2 = 12604.7, E3 = 5802.51 (Table 10):
T_{CD} = 8114.29 (Table 3)
The following values have been obtained by the ANOVA:
N = 54, f_e = 44; v_e = 4349657.9, n_{eff} = 5.4, R = 3, $F_{0.05}(1, 44) = 4.064$
From Eq. 11, $CI_{CE} = \pm 3027.52$
The predicted optimal range (for conformation runs of three experiments) for CD is given by
CI_{CE} : 16689.92 < μ_{CD} < 22744.96

(b) For Surface Roughness (SR)

$$\mu_{SR} = A1 + B3 + C3 + D2 + E3 - 4T_{SR} = 7.633$$

where A1 = 9.390, B3 = 8.101, C3 = 7.629, D2 = 9.415, E3 = 8.258, (Table 10):
T_{SR} = 8.79 (Table 3)
The following values have been obtained by the ANOVA:
N = 54, f_e = 44; v_e = .000387079, n_{eff} = 5.4, R = 3, $F_{0.05}(1, 44) = 4.064$
From Eq. 11, $CI_{CE} = \pm 0.02856$
The predicted optimal range (for conformation runs of three experiments) for SR is given by
CI_{CE} : 7.60444 < μ_{SR} < 7.66156

(c) For Micro hardness (MH)

$$\mu_{MH} = A1 + B3 + C3 + D2 + E3 - 4T_{MH} = 138.23$$

where A1 = 129.33, B3 = 130.44, C3 = 128.28, D2 = 127.83, E3 = 126.11, (Table 10):
T_{MH} = 125.94 (Table 3)
The following values have been obtained by the ANOVA:
N = 54, f_e = 44; v_e = 19.77, n_{eff} = 5.4, R = 3, $F_{0.05}(1, 44) = 4.064$
From Eq. 10, $CI_{CE} = \pm 6.45$
The predicted optimal range (for conformation runs of three experiments) for MH is given by
CI_{CE} : 131.77 < μ_{MH} < 144.68

Table 11 Observed values of quality characteristics (Confirmation experiment)

Exp. no.	CD (kg/m^3)			SR (μm)			MH ($Hv_{0.3}$)		
	r_1	r_2	r_3	r_1	r_2	r_3	r_1	r_2	r_3
1	18798.5	19765.6	20987.5	7.62	7.63	7.65	135	139	137
2	19682.8	21942.8	20736.4	7.64	7.65	7.62	134	137	138
3	18952.7	19428.9	21659.3	7.61	7.64	7.63	142	142	141
Overall average	20217.2			7.63			138.336		

3.5 Confirmation experiment

For confirmation of experimental results, three experiments were performed at optimal settings as suggested by Taguchi analysis of Utility data. The observed values of various response characteristics have been given in Table 11. It can be noticed that overall average of the observed values of the response characteristics fall well within the 95% CI_{CE} of the optimal range of the respective response characteristics.

4 Conclusions

A simplified model based on the Taguchi method and Utility concept was used to analyze the multi-response optimization of Low-pressure cold spray process. Following conclusions can be drawn from this study:

- All the input parameter significantly improves the Utility function comprising of three quality characteristics (coating density, surface roughness and micro hardness). All the chosen process parameters are found to have significant effect on the S/N ratio of Utility function.
- The optimal setting of the process parameters were predicted for optimization of coating density, surface roughness and micro hardness using the model. The optimal settings were A1- First level of powder feed arrangement, B3-Third level of substrate material, C3-Third level of air stagnation pressure, D2-Second level of air stagnation temperature and E2-Third level of stand-off distance.
- The decreasing order of percentage contribution of the parameters to achieve a higher value of utility function is: substrate material (64.59%), air stagnation pressure (16.34%), stand-off distance (6.92%), air stagnation temperature (6.49%) and powder feeding arrangement (1.84%) respectively.
- The overall average of quality characteristics was found to be 20, 217.2 kg/m^3 for coating density, 7.63 μm for surface roughness and 138.34 $H_{v0.3}$ for micro hardness which falls well within the 95% CI_{CE} of the optimal range of the respective response characteristics.

References

1. Byrne, D.M., Taguchi, G.: The Taguchi approach to parameter design. J. Qual. Progress **20**(12), 19–26 (1987)
2. Derek, W.B.: Analysis for optimal decisions. Wiley, New York (1982)
3. Tarun, Goyal, Sidhu, T.S., Walia, R.S.: An overview on Cold spray process over competitive technologies for electro-technical applications. Indian J. Eng. Sci. Technol. **4**(1), 41–45 (2010)
4. Goyal, Tarun, Walia, R.S., Sidhu, T.S.: Effect of parameters on coating density for cold spray process. Int. J. Mater. Manufact. Process. **27**(2), 193–200 (2012)
5. Goyal, Tarun, Walia, R.S., Sidhu, T.S.: Surface roughness optimization of cold sprayed coatings using Taguchi method. Int. J. Adv. Manufact. Technol. **60**(5–8), 611–623 (2012)
6. Goyal, Tarun., Walia, R.S., Sidhu, T.S.: Taguchi based optimization for micro hardness of cold spray coating process", Int. J. Surface Eng. Interdiscipl. Mater. Sci. **2**, Nos 2, July-Dec, 2014; pp. 23–33 (2015)
7. Goyal, Tarun, Walia, R.S., Sidhu, T.S.: Multi-response optimization of low- pressure cold sprayed coatings through Taguchi method and Utility concept. Int. J. Adv. Manufact. Technol. **64**(5–8), 903–914 (2013)
8. Groshart, E.C.: Military Aircraft and Aerospace, in ASTM, Corrosion Tests and Standards Manual: Application and Interpretation, American Society for Testing and Materials Society, pp. 579–581 (1995)
9. Grujicic, M., Zhao, C.L., Tong, C., DeRosset, W.S., Helfritch, D.: Analysis of the impact velocity of powder particles in the cold-gas dynamic-spray process. Mater. Sci. Eng. A **368**, 222–230 (2004)
10. Gupta, V., Murthy, P.N.: An introduction to engineering design methods. Tata McGraw Hill, New Delhi (1980)
11. Ishikawa, K., Seki, M., Tobe, S.: Application of Thermal Spray Coatings to Prevent Corrosion of Construction in Japan. Proc. of the 5th National Thermal Spraying Conference, Anaheim, CA, USA, pp. 679–684 (1993)
12. Knotek, O.: Chapter 3: Thermal Spraying and Detonation Spray Gun Processes, in *Handbook of Hard Coatings: Deposition Technologies, Properties and Applications*, Ed. Bunshah, R. F.; Noyes Pub. Park Ridge, New Jersey, U. S. A./William Andrew Publishing, LLC, Norwich, New York, U.S.A., pp. 77–107 (2001)
13. Kumar, P., Barua, P.B., Gaindhar, J.L.: Quality optimization (Multi-Characteristics) through Taguchi Technique and Utility Concept. J. Qual. Reliabil. Eng. Int. **16**, 475–485 (2000)
14. Maev, R.Gr., Leshchynsky, V.: Introduction to Low Pressure Gas Dynamic Spray Physics and Technology, Wiley2VCH, Weinheim (2008)
15. Marceau, J.A., Adjorlolo, A.A.: Commercial Aircraft, in ASTM, *Corrosion Tests and Standards: Application and Interpretation*, pp. 574–578 (1995)
16. Roy, R.K.: A primer on Taguchi method. Van Nostrand Reinhold, New York (1990)

This article has been accepted for publication in a future issue of this journal, but has not been fully edited. Content may change prior to final publication. Citation information: DOI 10.1109/JSEN.2016.2614748, IEEE Sensors Journal

T-MQM: Testbed based Multi-metric Quality Measurement of Sensor Deployment for Precision Agriculture-A Case Study

Omprakash Kaiwartya, *Member IEEE*, Abdul Hanan Abdullah, *Member IEEE*, Yue Cao, *Member IEEE*, Ram Shringar Raw, Sushil Kumar, D.K. Lobiyal, Ismail Fauzi Isnin, Xiulei Liu, Rajiv Ratn Shah, *Student Member IEEE*

***Abstract*— Efficient sensor deployment is one of primary requirements of precision agriculture use case of Wireless Sensor Networks (WSNs) to provide qualitative and optimal coverage and connectivity. The application-based performance variations of the geometrical-model-based sensor deployment patterns restricts the generalization of a specific deployment pattern for all applications. Further, single or double metrics based evaluation of the deployment patterns focusing on theoretical or simulation aspects can be attributed to the difference in performance of real applications and the reported performance in literature. In this context, this paper proposes a Testbed based Multi-metric Quality Measurement (T-MQM) of sensor deployment for precision agriculture use case of WSNs. Specifically, seven metrics are derived for qualitative measurement of sensor deployment patterns for precision agriculture. The seven metrics are quantified for four sensor deployment patterns to measure the quality of coverage and connectivity. Analytical and simulation based evaluations of the measurements are validated through testbed experiment based evaluations which are carried out in 'INDRIYA' WSNs testbed. Towards realistic research impact, the investigative evaluation of the geometrical-model-based deployment patterns presented in this article could be useful for practitioners and researchers in developing performance guaranteed applications for precision agriculture and novel coverage and connectivity models for deployment patterns.**

***Index Terms*— Precision agriculture, Testbed, WSNs, Deployment**

I. Introduction

Application of Wireless Sensor Networks (WSNs) is expanding enormously due to the inclusion of new areas day by day. Few examples of the application area include environmental monitoring, agricultural monitoring, on-road traffic monitoring, vehicular communication, healthcare, home automation and indoor energy conservation, and warfare [1-3].

The research is supported by Ministry of Higher Education Malaysia in collaboration with Research Management Center at Universiti Teknologi Malaysia (vote: Q.J130000.2528.14H81).

O. Kaiwartya, A.H. Abdullah, Ismail Fauzi Isnin are with the Faculty of Computing, Universiti Teknologi Malaysia (UTM), Johor Bahru, 81310, Malaysia. Email: omprakash@utm.my; hanan@utm.my; ismailfauzi@utm.my

Y. Cao (Corresponding Author) is with the Department of Computer Science and Digital Technologies, Northumbria University, Newcastle upon Tyne, NE1 8ST, UK. Email: yue.cao@northumbria.ac.uk

R. S. Raw is with the Department of Computer Science, Indira Gandhi National Tribal University, M.P., India, 484886, Email: rsrao08@yahoo.in

S. Kumar, D.K. Lobiyal are with the SC&SS, Jawaharlal Nehru University, New Delhi, India, 110067. Email: skdohare; dkl@mail.jnu.ac.in

Xiulei Liu is with the Computer School, Beijing Information Science and Technology University, Beijing, 10010, China. Email: xiuleiliu@hotmail.com

R. R. Shah is with the School of Computing, National University of Singapore (NUS), Singapore, 117417. Email: rajiv@comp.nus.edu.sg

In any application of WSNs, sensor deployment is one of the most important and critical issue since it is directly related to the cost and performance of the applications. A better sensor deployment strategy not only reduces the redundancy of sensors subsequently minimizing the cost of the network, but also extends the lifetime of the network [4].

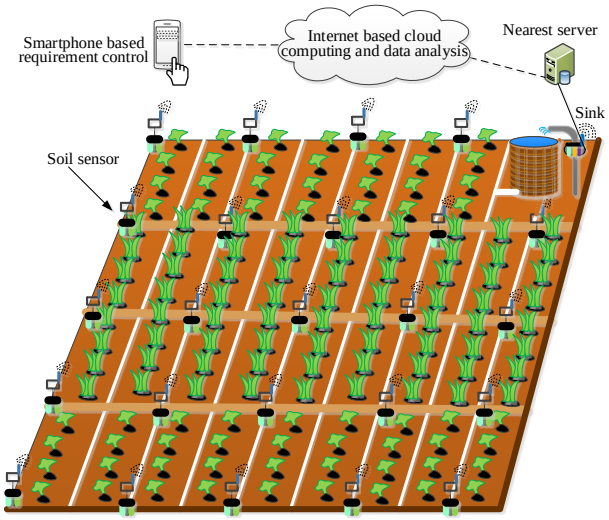


Fig. 1. Precision agriculture use case of WSNs

The deployment patterns followed in planned sensor deployment have significant impact on the performance of wireless sensor networks [5]. Therefore, these patterns are considerably important for the applications of sensors in regular terrain non-hostile environment where planned sensor deployment is followed. Precision agriculture is one of the promising use case of planed sensor deployment of WSNs in regular terrain non-hostile environment [6]. Recently, precision agriculture using WSNs has witnessed significant attention from industries as well as academia due to the huge potential to increase per hectare production in agriculture by efficient and automated nutrition requirement control in forming [7]. Various patterns for planned sensor deployment have been suggested for the applications in regular terrain non-hostile environment; e.g., precision agriculture, which are based on geometrical models including square, rhombus, pentagon and hexagon [8]. An application of square deployment pattern in precision agriculture is depicted in Fig. 1 in which soil sensors are utilized to remotely monitor and control the nutrition requirements of plants in forming.

The geometrical model based deployment patterns followed in planned sensor deployment have significant impact on the

1530-437X (c) 2016 IEEE. Personal use is permitted, but republication/redistribution requires IEEE permission. See http://www.ieee.org/publications_standards/publications/rights/index.html for more information.

This article has been accepted for publication in a future issue of this journal, but has not been fully edited. Content may change prior to final publication. Citation information: DOI 10.1109/JSEN.2016.2614748, IEEE Sensors Journal

overall performance of the applications of wireless sensor networks [9]. Due to the different physical characteristics of these geometrical models, considerable variations have been observed on performance of the deployment patterns based on these geometrical models in different kinds of applications [10]. The application-based performance variations restricts the generalization of the performance of a particular deployment pattern for all kinds of applications [11]. Therefore, qualitative measurements of these geometrical model based deployment patterns for precision agriculture use case of WSNs need to be investigated considering the early stage development in precision agriculture use case of WSNs [9, 12]. Further, most of these geometrical model-based deployment patterns have been evaluated using single [13-16] or double [17-20] metrics of coverage and connectivity. In real applications, performance of these geometrical model-based deployment patterns are quite different and far away from the reported performance in literature which are based on evaluations considering single or double metrics of coverage and connectivity [21]. Insufficient number of metrics for measuring coverage and connectivity is a cause of concern in terms of monitoring quality [22]. The inter-dependency of metrics have not been investigated which is also one of the main reasons for the quite deviation in the performance of applications from the reported performance [23]. It is also highlighted that majority of the previous works on quality measurement in WSNs pay attention on theoretical or simulation based evaluation, whereas this paper focuses on testbed experiment based evaluation.

In this context, this paper proposes Testbed-based Multi-metric Quality Measurement (T-MQM) to evaluate sensor deployment patterns in terms of offered quality of coverage and connectivity for precision agriculture use case of WSNs. The key contributions of the paper are as follows.

1) The derivation of seven metrics for measuring quality of coverage and connectivity which are correlated with each other for effectively analyzing the impact of inter-dependency of metrics on the performance of deployment patterns.
2) The quantification of seven metrics for four sensor deployment patterns of precision agriculture use case to measure the quality of coverage and connectivity.
3) The analytical and simulation evaluations of the quality of coverage and connectivity measurements using mathematical analysis and Network Simulator (NS-2); respectively.
4) The testbed experiment based assessment using 'INDRIYA' wireless sensor network testbed at School of Computing, National University of Singapore (NUS) [24] to validate the analytical and simulation evaluations.

The rest of the paper is organized in following sections. Section II qualitatively reviews coverage and connectivity measurements in wireless sensor networks by categorizing the theme into single, double and multiple metrics based measurements and points out the research gap in deployment measurement for precision agriculture. Section III presents derivation of the seven metrics and measurement of quality of coverage and connectivity for four deployment patterns by quantifying the seven metrics. Section IV discusses the analytical, simulation and testbed based evaluations of the measurement of deployment patterns. Section V concludes this paper with some future directions of research in the theme.

II. Related Work

In this section, a qualitative review on coverage and connectivity measurements of sensor deployment in wireless sensor networks is presented, by classifying the theme into three categories including single, double and multi-metric based measurement. The contribution area of the paper; i.e., precision agriculture using WSNs, is revisited to precisely point out the research gap in deployment measurement for precision agriculture use case.

A. Single Metric based Measurement

Analysis of quality of deployment in Surveillance Wireless Sensor Networks (SWSNs) has been performed using probabilistic models with detection ratio as a single metric for measurement [13]. Authors have suggested the usage of image segmentation algorithm for reducing the impact of obstacles in deployment strategies. The number of sensor requirement has been studied and analyzed experimentally considering the probability of detecting intrusion and time taken for detection. Mathematical model for measuring deployment quality and analytical analysis of the iso-sensing graph based approach has not been provided in this surveillance analysis. Various deployment patterns have been explored to obtain Optimal Deployment Patterns (ODP) for providing full coverage and k-connectivity ($k \leq 6$) using percentage coverage metric [14]. Authors have presented a universal elementary deployment pattern to generate the other optimal deployment patterns considered. The universal deployment pattern is based on hexagon geometry. They have also suggested an approach to prove an optimal pattern for the situation where Voronoi diagram based approach is not suitable. In spite of analyzing regular deployment pattern, overlapped coverage area has not been taken into consideration. Un-even deployment of sensors in the sensing region or error in deployment planning may result into interference in wireless sensor networks.

Impact of Interference in Wireless Communication has been investigated in Fading Environment (IWC-FE) using outage probability metric [15]. Authors have analyzed co-channel interference and derived mathematical functions; i.e. probability density function and cumulative density function for signal-to-noise interference ratio. Although intensity of interference is closely related with physical deployment of sensors yet, the impact of deployment patterns on interference has not been taken into consideration. Regular and Random Deployment patterns have been evaluated in terms of Throughput (RRD-T) metric which is significantly dependent on connectivity metric [16]. Authors have utilized 'slotted ALOHA' as Medium Access Control (MAC) protocol and Rayleigh distribution as fading channel. In particular, authors have mathematically derived average link throughput for three regular deployment patterns; namely square, triangular and hexagonal and compared the performance of these deployment patterns in terms of throughput, transmission efficiency and delivery capacity. Although the analysis has been validated

1530-437X (c) 2016 IEEE. Personal use is permitted, but republication/redistribution requires IEEE permission. See http://www.ieee.org/publications_standards/publications/rights/index.html for more information.

This article has been accepted for publication in a future issue of this journal, but has not been fully edited. Content may change prior to final publication. Citation information: DOI 10.1109/JSEN.2016.2614748, IEEE Sensors Journal

through numerical simulations yet, verification of the results using network simulator platform is missing.

B. Double Metrics based Measurement

Quality of Connectivity of Regular Topologies (QC-RT) has been evaluated using two metrics; namely, isolation probability and end-to-end connectivity for geometrical deployment patterns [17]. Authors have used probabilistic models to analyze connectivity considering reliability of sensors and fading of channels due to the interferers and multiple channel access. Three different fading models; namely, Rayleigh, Nakagami and Log normal have been used to analyze probabilistic connectivity in terms of node isolation probability and end-to-end network connectivity. The analysis did not consider coverage in spite of the fact that coverage and connectivity should be studied together due to their companion nature. Minimum number of sensors required for retaining a sensor network functioning with desired level of coverage and connectivity has been estimated using distance and degree metrics of graph theory in Connectivity Coverage and Power Consumption (CCPC) [18]. Authors have suggested a network management protocol for equalizing the remaining energy among all the sensors by switching off appropriate sensors in time slots while maintaining the desired coverage and connectivity. Presence of obstacles has not been taken into consideration in spite of analyzing random wireless sensor networks which are mostly deployed in hostile environment where presence of obstacles is un-avoidable.

Two deployment strategies; namely, Expected-area Coverage Deployment (ECD) and Boundary Assistant Deployment (BOAD) have been suggested and evaluated using deployment quality and deployment error metrics for providing guaranteed coverage in wireless sensor networks [19]. Authors have addressed the problem of overestimation of coverage through their deployment strategies. Although random deployment has been considered yet, the presence of obstacles in the field of interest has not been realized. Uncertainty Aware Deployment Technique (UADT) has been evaluated using detection probability and connectivity percentage in mixed wireless sensor networks [20]. In particular, authors have suggested a deployment approach which discovers coverage holes by computing joint detection probability and moves the appropriate mobile sensors into coverage holes using bipartite graph based approach. Uncertainty aware deployment approach assumes that only static sensors are unreliable but the reliability of movable sensors has not been taken into account.

C. Multi-Metrics based Measurement

The multi-metric measurement of coverage and connectivity in WSNs have not been explored accountably for the applications of WSNs in regular terrain non-hostile environment. Some of the following investigations are restricted to either for a specific application which could not be generalized, or for particular type of WSNs with theoretical or simulation perspective. Coverage and connectivity have been evaluated using three metrics; namely, probability of instantaneous event detection, probability of delayed event capture and probability of communication in Duty-Cycled partitioned synchronous Wireless Sensor Networks (DC-WSNs) [25]. The probabilistic models of these metrics have been derived for both synchronous and asynchronous networks. The impact of ratio of duty time and time interval on the performance of these metrics have been explored using mathematical and analytical analysis. Although the optimization of network performance in partitioned synchronous network is a challenging task considering the cooperation requirements among sensors yet, the applicability of the network is minimal due to the synchronization constraints. For bridge monitoring applications, sensor deployment has been evaluated using the metrics including model strain energy index, modal assurance criterion and modal participant factor [26]. Specifically, an optimal sensors placement method has been presented by optimizing multiple performance metrics and resources. There are two major operational steps in the method. Firstly, modal energy index of randomly deployed sensor's locations are enhanced using Modal Strain Energy (MSE) as initial assignment of sensors on the bridge. Secondly, Adapted Genetic Algorithm (AGA) is developed using root mean square based fitness function for optimizing both number of sensors and their locations. No pattern is followed in the evaluation therefore, generalization of the measurement is not possible.

D. The Contribution Area-Precision Agriculture

The applicability of the findings of measurement of the deployment strategies in which any geometrical patterns are not followed, is lesser in other applications in regular terrain non-hostile environment; e.g., precision agriculture. Readers are advised to go through the article [27] to explore more about application-based deployment strategies and related issues. These deployment measurements could not be generalized for other applications of wireless sensor networks in regular terrain non-hostile environment. Precision agriculture is one of the fine use case of WSNs in regular terrain non-hostile environment. Recently, the early stage studies in precision agriculture use case of WSNs has focused on addressing the implementation issues of precision agriculture system. Cluster based WSNs has been considered to optimize IEEE 802.15.4 MAC parameters for precision agriculture [28]. Star topology has been utilized within clusters with a cluster head in each cluster working as getaway for the cluster. The impact of topology change on the performance of the network has not been explored in the MAC parameter optimization. Automated actions based on the intelligence acquired from the perceived, processed and analysed data by sensors is one of the fundamental objectives of precision agriculture which has been investigated as data logger for precision agriculture [29].

A complete system implementation for precision agriculture using WSNs is presented considering two types of sensors; namely, management and normal sensors [30]. Random deployment of normal sensors within monitoring area has been considered therefore, the system lacks the cost and performance optimization using sensor deployment patterns. To address the battery power limitation, and thus replacement or recharging, attached with normal sensor, pluggable Radio Frequency Identification (RFID) based wireless sensor network system for precision agriculture is suggested [31].

1530-437X (c) 2016 IEEE. Personal use is permitted, but republication/redistribution requires IEEE permission. See http://www.ieee.org/publications_standards/publications/rights/index.html for more information.

This article has been accepted for publication in a future issue of this journal, but has not been fully edited. Content may change prior to final publication. Citation information: DOI 10.1109/JSEN.2016.2614748, IEEE Sensors Journal

The aforementioned recent and early stage investigations on precision agriculture use case of WSNs have considered the design and development of data acquisition system for precision agriculture and claimed that the system is adaptable to different requirements of precision agriculture. From the best of our knowledge, qualitative evaluation of sensor deployment patterns and the impact of deployment patterns on the quality of coverage and connectivity for precision agriculture use case have not been taken into consideration yet [28-31]. It is also observed that majority the works in related literature pay attention on theoretical or simulation based study, whereas this paper focuses on testbed based study.

In this context, Testbed based Multi-metric Quality Measurement (T-MQM) is presented to evaluate geometrical model based sensor deployment patterns for precision agriculture using wireless sensor networks in regular terrain non-hostile environment. Efficient sensor deployment is one of the primary functional module in precision agriculture use case of WSNs. Some of the key requirements of a sensor deployment technique for large scale sensor-based applications; e.g., precision agriculture, include covering the complete sensing field with minimum overlapping coverage area among sensors [32], maintaining quality of connectivity among sensors throughout the networks [33] and reducing network operation cost [34]. To optimize these requirements, the quality of sensor deployment patterns need to be verified through multiple metrics and testbed based measurements rather than relying on single or double metrics and theoretical or simulation based measurements.

III. Testbed based Multi-metric Quality Measurement

In this section, T-MQM is presented for measuring the quality of coverage and connectivity as a real research impact. Firstly, seven metrics are derived to measure the quality of coverage and connectivity of sensor deployment patterns. The metrics include total coverage area, effective coverage area, net effective coverage area, net effective coverage area ratio, total overlapped coverage area, total non-overlapped coverage area, and quality of connectivity. Secondly, the seven metrics are quantified for four sensor deployment patterns including square, rhombus, pentagon and hexagon patterns to measure the quality of coverage and connectivity. The nomenclature used in the design of T-MQM are precisely introduced in Table 1.

Table 1. Nomenclature

Notation	Description
$\mathrm{C_a^T}$	Total coverage area
$\mathrm{C_a^{TO}}$	Total overlapped coverage area
$\mathrm{C_a^{TNO}}$	Total non-overlapped coverage area
$\mathrm{C_a^E}$	Effective coverage area
C_a^1	Coverage area of a sensor
N	Number of sensors
$\mathrm{C_a^{NE}}$	Net effective coverage area
$\mathrm{C_a^{IO}}$	Individual overlapped coverage area within a sensor
C_a^{NER}	Net effective coverage area ratio
$\mathrm{C_a^{TNO}}$	Total non-overlapped coverage area
$\mathrm{C_a^{TO}}$	Total overlapped coverage area
Q_c	Quality of connectivity
K	Conversion constant
S_i	i^{th}sensor in a sensor deployment pattern
r	Sensing range
t	Transmission range
π	Constant
P	Length of a side of a deployment pattern
d	Distance between two sensors
h	Height of the arcs of the intersection area between two sensors
θ	An angle in a deployment pattern geometry

A. The Metrics

The seven metrics are derived to measure quality of coverage and connectivity of sensor deployment pattern for precision agriculture. The metrics are also applicable for other applications of WSNs in regular terrain non-hostile environment. However, the Squared Error (SE) metric is more relevant for the applications where the requirement of quality of coverage varies on the different sub-regions of a region of interest [35]. This can be attributed to the fact that the SE metric considers the difference between achieved and required detection/miss probabilities on each sub-region before deploying a sensor on any sub-region of a region of interest. In these applications, the constraints in terms of quality of coverage requirement on the different sub-regions, are significant. However, in the context of precision agriculture, different quality of coverage on the sub-regions of a farming region is not considered. The constraints are not attached in case of precision agriculture, and thus, the following metrics are suitable.

1) Total Coverage Area

The total coverage area $\mathrm{C_a^T}$ of a sensor deployment pattern in a sensing field is the total area covered by all the sensors. It is the sum of the total overlapped coverage area $\mathrm{C_a^{TO}}$ and total non-overlapped coverage area $\mathrm{C_a^{TNO}}$ among sensing range of the sensors deployed in a sensing field. In terms of precision agriculture, it defines the area of the part of the form where actual forming is practiced. It can be measured as expressed by Eq. (1).

$$C_a^T = \mathrm{C_a^{TO}} + \mathrm{C_a^{TNO}} \quad (1)$$

2) Effective Coverage Area

In a sensing field where N number of sensors are deployed, the effective coverage area $\mathrm{C_a^E}$ of a deployment pattern is the ratio of total coverage area and the sum of coverage area of all the individual sensors. In terms of precision agriculture, it defines the area referring to cost effectiveness of deployment pattern. It can be measured as expressed by Eq. (2).

$$C_a^E = \frac{C_a^T}{NC_a^1} = \frac{\mathrm{C_a^{TO}} + \mathrm{C_a^{TNO}}}{N\pi r^2} \quad (2)$$

where, C_a^1 is the coverage area of an individual sensor and r is the sensing range, $C_a^T \leq NC_a^1$ and $\frac{1}{N} \leq C_a^E \leq 1$.

3) Net Effective Coverage Area

In a sensor deployment pattern, the net effective coverage area $\mathrm{C_a^{NE}}$ is the area covered by an individual sensor only. It is the difference between the area $\mathrm{C_a^1}$ covered by an individual sensor and the overlapped coverage area $\mathrm{C_a^{IO}}$ within an individual sensor's coverage area in the deployment pattern. In terms of precision agriculture, it defines the area referring to the unit of coverage in terms of a sensor. It can be measured as expressed by Eq. (3).

$$C_a^{NE} = C_a^1 - \mathrm{C_a^{IO}} = \pi r^2 \left(1 - \frac{\mathrm{C_a^{IO}}}{\pi r^2}\right), \; 0 < \mathrm{C_a^{NE}} \leq \pi r^2 \quad (3)$$

4) Net Effective Coverage Area Ratio

In a sensing field where N number of sensors are deployed, the net effective coverage area ratio C_a^{NER} of a deployment

1530-437X (c) 2016 IEEE. Personal use is permitted, but republication/redistribution requires IEEE permission. See http://www.ieee.org/publications_standards/publications/rights/index.html for more information.

This article has been accepted for publication in a future issue of this journal, but has not been fully edited. Content may change prior to final publication. Citation information: DOI 10.1109/JSEN.2016.2614748, IEEE Sensors Journal

pattern is the ratio of net effective coverage area and an individual sensor's coverage area. In terms of precision agriculture, it defines the unit of qualitative coverage area offered in the return of an asset in terms of an individual sensor's coverage area in a particular deployment patterns. It can be measured as expressed by Eq. (4).

$$C_a^{NER} = \frac{C_a^{NE}}{C_a^1} = \frac{\pi r^2\left(1-\frac{C_a^{IO}}{\pi r^2}\right)}{\pi r^2} = 1 - \frac{C_a^{IO}}{\pi r^2},\ 0 < C_a^{NER} \leq 1 \quad (4)$$

5) Total Non-overlapped Coverage Area

The total non-overlapped coverage area C_a^{TNO} of a deployment pattern is the total coverage area covered by individual sensors only in the sensing field. In terms of precision agriculture, it defines the overall area within the form which is qualitatively monitored by geometrically deployed sensors following a particular deployment pattern. It can be measured as expressed by Eq. (5).

$$C_a^{TNO} = NC_a^{NE} = N(\pi r^2 - C_a^{IO}) = N\pi r^2\left(1 - \frac{C_a^{IO}}{\pi r^2}\right) \quad (5)$$

6) Total Overlapped Coverage Area

The total overlapped coverage area C_a^{TO} of a deployment pattern is the total area covered by more than one sensors. In terms of precision agriculture, it defines the overall coverage interference area within the form consequently resulting in coverage capability depletion and coverage quality degradation by redundant sensors. It can be measured as expressed by Eq. (6).

$$C_a^{TO} = C_a^T - C_a^{TNO} = C_a^T - \left\{N\pi r^2\left(1 - \frac{C_a^{IO}}{\pi r^2}\right)\right\} \quad (6)$$

7) Quality of Connectivity

The quality of connectivity Q_c of a deployment pattern defines the communication quality among the geometrically sensors. Apart from the impact of the geometrical pattern followed in a particular deployment, quality of communication medium or environment also significantly affects the quality of connectivity of a deployment pattern. In terms of precision agriculture, it defines the overall quality of the system employed to enhance and ease agriculture process. It can be measured as expressed by Eq. (7).

$$Q_c = \frac{K\,C_a^{TO}}{C_a^E} = \frac{K\left[C_a^T - \left\{N\pi r^2\left(1-\frac{C_a^{IO}}{\pi r^2}\right)\right\}\right]}{\frac{C_a^{TO} + C_a^{TNO}}{N\pi r^2}} = \frac{KN\pi r^2\{C_a^T - N\pi r^2 + N\,C_a^{IO}\}}{C_a^T}$$

$$= KN\pi r^2\left\{1 - \frac{N\pi r^2}{C_a^T} + \frac{N\,C_a^{IO}}{C_a^T}\right\} \quad (7)$$

where, K is the quality of connectivity conversion constant. For ideal case K = 1 has been considered. The quality of connectivity has been normalized to obtain the value of quality of connectivity in the defined range.

8) Multi-objective Optimization

The aforementioned seven metrics are considered as objective functions of the Multi-objective Optimization (MOO) formulation. The formulation can be expressed as given by Eq. (8).

$$Max(f_1, f_2, f_3, f_4, f_5, f_6^{-1}, f_7) \quad (8)$$

where $f_1 = C_a^T$ represents total coverage area, $f_2 = C_a^E$ represents effective coverage area, $f_3 = C_a^{NE}$ represents net effective coverage area, $f_4 = C_a^{NER}$ represents net effective coverage area ratio, $f_5 = C_a^{TNO}$represents total no-overlapped coverage area, $f_6^{-1} = (C_a^{TO})^{-1}$ represents total overlapped coverage area, and $f_7 = Q_c$represents quality of connectivity. The constraints of each metric denotes the constraints of the MOO formulation. The constraints include $C_a^T \leq NC_a^1$, $\frac{1}{N} \leq C_a^E \leq 1$, $0 < C_a^{NE} \leq \pi r^2$, $0 < C_a^{NER} \leq 1$.

The cost of deployment has significant impact on the overall cost of WSNs in case of heterogeneous sensors or hostile environments [36]. Thus, it could be considered as a metric. However, uniform quality of coverage requirement and ease of access of farming regions reduce the relevance of cost of deployment in precision agriculture using WSNs.

B. The Measurements

The aforementioned metrics for measuring quality of coverage and connectivity are utilized to evaluate four geometrical model based deployment patterns. The exact mathematical derivation of all the metrics are obtained for each deployment pattern exploiting their geometrical characteristics. Using the mathematical derivations, each of the metric has been quantified which can be used to compare the quality of coverage and connectivity of deployment patterns.

1) Metric Quantification in Square Pattern based forming

Square deployment pattern is one of simplest deployment approach in WSNs. Two cases of square deployment pattern are explored. In the first case, nine sensors are deployed at the vertices of four adjoining squares (see Fig. 2(a)). In the second case, sixteen sensors are deployed at the vertices of nine adjoining squares (see Fig. 2(b)). The length of side of squares is considered equal to the sensing range of sensors in both the cases of measurement.

- *Total Coverage Area*

$$C_a^T = 4(\diamond AS_1H) + 4(\diamond AS_2B) + 8(\Delta AS_1S_2) + \square S_1S_3S_9S_7$$

$$= 4\left(\frac{150}{360}\pi r^2\right) + 4\left(\frac{\pi}{6}r^2\right) + 8\left(\frac{\sqrt{3}}{4}r^2\right) + 4r^2 = \left(\frac{7\pi}{3} + 2\sqrt{3} + 4\right)r^2 \quad (9)$$

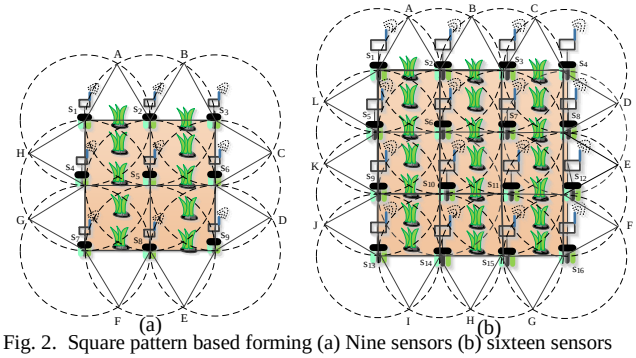


Fig. 2. Square pattern based forming (a) Nine sensors (b) sixteen sensors

- *Effective Coverage Area*

$$C_a^E = \frac{C_a^{TO} + C_a^{TNO}}{N\pi r^2} = \frac{\left(\frac{7\pi}{3}+2\sqrt{3}+4\right)r^2}{9\pi r^2} = \frac{7}{27} + \frac{2\sqrt{3}}{9\pi} + \frac{4}{9\pi} = 0.52 \quad (10)$$

- *Net Effective Coverage Area*

$$C_a^{NE} = \pi r^2 - C_a^{IO} = \pi r^2 - \left\{\frac{\pi}{4}r^2 + 2\left(\frac{\pi}{6}r^2\right) + 2\left(\frac{\pi}{6}r^2 - \frac{\sqrt{3}}{4}r^2\right)\right\}$$

$$= \pi r^2 - \left\{\frac{\pi}{4}r^2 + \frac{2\pi}{3}r^2 - \frac{\sqrt{3}}{4}r^2\right\} = \frac{\pi+6\sqrt{3}}{12}r^2 \quad (11)$$

- *Net Effective Coverage Area Ratio*

$$C_a^{NER} = 1 - \frac{C_a^{IO}}{\pi r^2} = 1 - \frac{\left\{\frac{\pi}{4}r^2 + \frac{2\pi}{3}r^2 - \frac{\sqrt{3}}{4}r^2\right\}}{\pi r^2} = 0.35 \quad (12)$$

1530-437X (c) 2016 IEEE. Personal use is permitted, but republication/redistribution requires IEEE permission. See http://www.ieee.org/publications_standards/publications/rights/index.html for more information.

This article has been accepted for publication in a future issue of this journal, but has not been fully edited. Content may change prior to final publication. Citation information: DOI 10.1109/JSEN.2016.2614748, IEEE Sensors Journal

• *Total Non-overlapped Coverage Area*

$$C_a^{TNO} = N\pi r^2\left(1-\frac{C_a^{IO}}{\pi r^2}\right) = 9\pi r^2\left(1-\frac{\left\{\frac{\pi}{4}r^2+\frac{2\pi}{3}r^2-\frac{\sqrt{3}}{4}r^2\right\}}{\pi r^2}\right)$$

$$= 3\left(\frac{\pi+6\sqrt{3}}{4}\right)r^2 \quad (13)$$

• *Total Overlapped Coverage Area*

$$C_a^{TO} = C_a^T - \left\{N\pi r^2\left(1-\frac{C_a^{IO}}{\pi r^2}\right)\right\} = \left(\frac{7\pi}{3}+2\sqrt{3}+4\right)r^2 - 3\left(\frac{\pi+6\sqrt{3}}{4}r^2\right) = \left(\frac{19\pi}{12}-\frac{5\sqrt{3}}{2}+4\right)r^2 \quad (14)$$

• *Quality of Connectivity*

$$Q_c = KN\pi r^2\left\{1-\frac{N\pi r^2}{C_a^T}+\frac{N\,C_a^{IO}}{C_a^T}\right\} = 9\pi r^2\left\{1-\frac{9\pi r^2}{\left(\frac{7\pi}{3}+2\sqrt{3}+4\right)r^2}+\frac{9\left\{\frac{\pi}{4}r^2+\frac{2\pi}{3}r^2-\frac{\sqrt{3}}{4}r^2\right\}}{\left(\frac{7\pi}{3}+2\sqrt{3}+4\right)r^2}\right\} = \frac{\left(\frac{19\pi}{12}-\frac{5\sqrt{3}}{2}+4\right)r^2}{0.52} \quad (15)$$

In the second case, sixteen sensors are deployed at the vertices of nine adjoining squares (see Fig 2(b)). All the sensors S_1 to S_{16} have equal sensing range and the length of the side of square is equal to the sensing range. The quality of the sixteen sensor square deployment pattern is measured below.

• *Total Coverage Area*

$$C_a^T = 4(\diamond AS_1L) + 8(\diamond AS_2B) + 12(\Delta AS_1S_2) + S_1S_4S_{16}S_{13} = 4\left(\frac{150}{360}\pi r^2\right) + 8\left(\frac{\pi}{6}r^2\right) + 12\left(\frac{\sqrt{3}}{4}r^2\right) + 9r^2 = \left(3\pi+3\sqrt{3}+9\right)r^2 \quad (16)$$

• *Effective Coverage Area*

$$C_a^E = \frac{C_a^{TO}+C_a^{TNO}}{N\pi r^2} = \frac{(3\pi+3\sqrt{3}+9)r^2}{16\pi r^2} = \frac{3}{16}+\frac{3\sqrt{3}}{16\pi}+\frac{9}{16\pi} = 0.47 \quad (17)$$

• *Net Effective Coverage Area*

$$C_a^{NE} = \pi r^2 - C_a^{IO} = \pi r^2 - \left\{\frac{\pi}{4}r^2+2\left(\frac{\pi}{6}r^2\right)+2\left(\frac{\pi}{6}r^2-\frac{\sqrt{3}}{4}r^2\right)\right\} = \pi r^2 - \left\{\frac{\pi}{4}r^2+\frac{2\pi}{3}r^2-\frac{\sqrt{3}}{4}r^2\right\} = \frac{\pi+6\sqrt{3}}{12}r^2 \quad (18)$$

• *Net Effective Coverage Area Ratio*

$$C_a^{NER} = 1-\frac{C_a^{IO}}{\pi r^2} = 1-\frac{\left\{\frac{\pi}{4}r^2+\frac{2\pi}{3}r^2-\frac{\sqrt{3}}{4}r^2\right\}}{\pi r^2} = 0.35 \quad (19)$$

• *Total Non-overlapped Coverage Area*

$$C_a^{TNO} = N\pi r^2\left(1-\frac{C_a^{IO}}{\pi r^2}\right) = 16\pi r^2\left(1-\frac{\left\{\frac{\pi}{4}r^2+\frac{2\pi}{3}r^2-\frac{\sqrt{3}}{4}r^2\right\}}{\pi r^2}\right) = 4\left(\frac{\pi+6\sqrt{3}}{3}\right)r^2 \quad (20)$$

• *Total Overlapped Coverage Area*

$$C_a^{TO} = C_a^T - \left\{N\pi r^2\left(1-\frac{C_a^{IO}}{\pi r^2}\right)\right\} = \left(3\pi+3\sqrt{3}+9\right)r^2 - 4\left(\frac{\pi+6\sqrt{3}}{3}r^2\right) = \left(\frac{5\pi}{3}+5\sqrt{3}+9\right)r^2 \quad (21)$$

• *Quality of Connectivity*

$$Q_c = KN\pi r^2\left\{1-\frac{N\pi r^2}{C_a^T}+\frac{N\,C_a^{IO}}{C_a^T}\right\} = 16\pi r^2\left\{1-\frac{16\pi r^2}{(3\pi+3\sqrt{3}+9)r^2}+\frac{16\left\{\frac{\pi}{4}r^2+\frac{2\pi}{3}r^2-\frac{\sqrt{3}}{4}r^2\right\}}{(3\pi+3\sqrt{3}+9)r^2}\right\} = \frac{\left(\frac{5\pi}{3}+5\sqrt{3}+9\right)r^2}{0.47} \quad (22)$$

2) *Metric Quantification in Pentagon Pattern based forming*

The pentagon deployment pattern is a modified consideration of triangular deployment patter in which five sensors are deployed at the vertices of a pentagon and one sensor at the center of pentagon (see Fig. 3). The sensing range of the sensors has been considered as r and the side of the pentagon has been considered as P. The value $P = 2r\tan(36^o)$ can be calculated using simple geometrical calculations. Considering radius AS_1 as tangent to the circle having center at S_5, the radius S_5A will be perpendicular to the AS_1. In other words, the angle $< S_5AS_1 = 90^o$ and thus, $< AS_5S_1 =< AS_1S_5 = 45^o$. The quality of coverage and connectivity of pentagon deployment pattern are measured below.

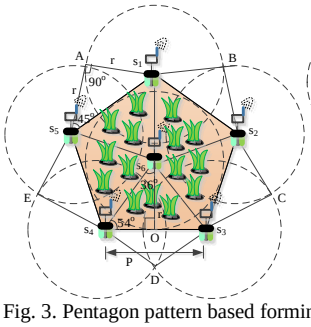


Fig. 3. Pentagon pattern based forming

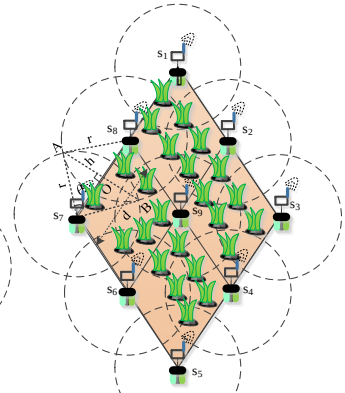


Fig. 4. Rhombus pattern based forming

• *Total Coverage Area*

$$C_a^T = 5\{\diamond AS_1B + \Delta AS_1S_5 + \Delta S_3S_4S_6\} = 5\left\{\left(\frac{162\pi}{360}r^2\right)+\left(\frac{r^2}{2}\right)+r^2\tan(36^o)\right\} = \left(\frac{9\pi}{4}+6.13\right)r^2 \quad (23)$$

• *Effective Coverage Area*

$$C_a^E = \frac{C_a^{TO}+C_a^{TNO}}{N\pi r^2} = \frac{\left(\frac{9\pi}{4}+6.13\right)r^2}{6\pi r^2} = 0.88 \quad (24)$$

• *Net Effective Coverage Area*

$$C_a^{NE} = \pi r^2 - C_a^{IO} = \pi r^2 - \left\{\frac{108\mu}{360}r^2+2\left(\frac{45\pi}{360}r^2\right)\right\} = \pi r^2 - \left\{\frac{11\pi}{20}r^2\right\} = \frac{9\pi}{20}r^2 \quad (25)$$

• *Net Effective Coverage Area Ratio*

$$C_a^{NER} = 1-\frac{C_a^{IO}}{\pi r^2} = 1-\frac{\left\{\frac{11\pi}{20}r^2\right\}}{\pi r^2} = 0.80 \quad (26)$$

• *Total Non-overlapped Coverage Area*

$$C_a^{TNO} = N\pi r^2\left(1-\frac{C_a^{IO}}{\pi r^2}\right) = 6\pi r^2\left(1-\frac{\left\{\frac{11\pi}{20}r^2\right\}}{\pi r^2}\right) = \frac{27}{10}r^2 \quad (27)$$

• *Total Overlapped Coverage Area*

$$C_a^{TO} = C_a^T - \left\{N\pi r^2\left(1-\frac{C_a^{IO}}{\pi r^2}\right)\right\} = \left(\frac{9\pi}{4}+6.13\right)r^2 - \frac{27}{10}r^2 = \left(\frac{9\pi}{4}+3.43\right)r^2 \quad (28)$$

• *Quality of Connectivity*

$$Q_c = KN\pi r^2\left\{1-\frac{N\pi r^2}{C_a^T}+\frac{N\,C_a^{IO}}{C_a^T}\right\} = 6\pi r^2\left\{1-\frac{6\pi r^2}{C_a^T}+\frac{6\left\{\frac{11\pi}{20}r^2\right\}}{C_a^T}\right\} = \frac{\left(\frac{9\pi}{4}+3.43\right)r^2}{0.88} \quad (29)$$

3) *Metric Quantification in Rhombus Pattern based forming*

In rhombus deployment pattern, sensors are deployed at the vertices of adjoining rhombus. Following the pattern, nine sensors are deployed at the vertices of rhombus (see Fig. 4). In this deployment pattern, the intersection coverage area between any two sensors is always equal. To determine the intersection coverage area, the distance between the sensors is considered as d. The angle $\theta = \cos^{-1}(d/2r)$ is derived using

1530-437X (c) 2016 IEEE. Personal use is permitted, but republication/redistribution requires IEEE permission. See http://www.ieee.org/publications_standards/publications/rights/index.html for more information.

This article has been accepted for publication in a future issue of this journal, but has not been fully edited. Content may change prior to final publication. Citation information: DOI 10.1109/JSEN.2016.2614748, IEEE Sensors Journal

trigonometry rules. The value $h = \sqrt{r^2 - (d/2)^2}$ is derived using triangle rules and it is used to calculate the area of $\Delta AS_7B = d\left(\sqrt{r^2 - (d/2)^2}\right)/2$. The intersection coverage area between the two sensors s_7 and s_8 can be derived subtracting the area of the triangle ΔAS_7B from the area of the sector $AS_7B = \theta r^2$. Thus, the intersection coverage area is $2\left\{\theta r^2 - \left(d\left(\sqrt{r^2 - (d/2)^2}\right)/2\right)\right\}$. The quality of coverage and connectivity of rhombus deployment pattern is measured through following derivations.

- *Total Coverage Area*

$$C_a^T = 9(\pi r^2) - 16\left(2\left\{\theta r^2 - \left(d\left(\sqrt{r^2 - (d/2)^2}\right)/2\right)\right\}\right)$$

To simplify the calculation, $d = r$ is considered. In other words, the sensing range of two neoghboring sensors passes through the centers. Thus, the value of $\theta = 60^o$ can be derived using simple geometrical calculations. The the value of C_a^T can be calculated as expressed by Eq. (30).

$$C_a^T = 9(\pi r^2) - 16\left\{\frac{(2\pi - 3\sqrt{3})r^2}{6}\right\} = \left(\frac{11\pi}{3} + 8\sqrt{3}\right)r^2 \quad (30)$$

- *Effective Coverage Area*

$$C_a^E = \frac{C_a^{TO} + C_a^{TNO}}{N\pi r^2} = \frac{\left(\frac{11\pi}{3} + 8\sqrt{3}\right)r^2}{9\pi r^2} = 0.7 \quad (31)$$

- *Net Effective Coverage Area*

$$C_a^{NE} = \pi r^2 - C_a^{IO} = \pi r^2 - 2\left\{\frac{(2\pi - 3\sqrt{3})r^2}{6}\right\} = \left(\frac{\pi + 3\sqrt{3}}{3}\right)r^2 \quad (32)$$

- *Net Effective Coverage Area Ratio*

$$C_a^{NER} = 1 - \frac{C_a^{IO}}{\pi r^2} = 1 - \frac{2\left\{\frac{(2\pi - 3\sqrt{3})r^2}{6}\right\}}{\pi r^2} = 0.45 \quad (33)$$

- *Total Non-overlapped Coverage Area*

$$C_a^{TNO} = N\pi r^2\left(1 - \frac{C_a^{IO}}{\pi r^2}\right) = 9\pi r^2\left(1 - \frac{2\left\{\frac{(2\pi - 3\sqrt{3})r^2}{6}\right\}}{\pi r^2}\right)$$
$$= 3\left(\pi + 3\sqrt{3}\right)r^2 \quad (34)$$

- *Total Overlapped Coverage Area*

$$C_a^{TO} = C_a^T - \left\{N\pi r^2\left(1 - \frac{C_a^{IO}}{\pi r^2}\right)\right\} = \left(\frac{11\pi}{3} + 8\sqrt{3}\right)r^2 - 3\left(\pi + 3\sqrt{3}\right)r^2 = \left(\frac{2\pi}{3} - \sqrt{3}\right)r^2 \quad (35)$$

- *Quality of Connectivity*

$$Q_c = KN\pi r^2\left\{1 - \frac{N\pi r^2}{C_a^T} + \frac{N\,C_a^{IO}}{C_a^T}\right\} = 9\pi r^2\left\{1 - \frac{9\pi r^2}{\left(\frac{11\pi}{3} + 8\sqrt{3}\right)r^2} + \frac{92\left\{\frac{(2\pi - 3\sqrt{3})r^2}{6}\right\}}{\left(\frac{11\pi}{3} + 8\sqrt{3}\right)r^2}\right\} = \frac{\left(\frac{2\pi}{3} - \sqrt{3}\right)r^2}{0.7} \quad (36)$$

4) *Metric Quantification in Hexagon Pattern based forming*

In hexagon deployment pattern, six sensors are deployed at the vertices of hexagon and one sensor is deployed at the center of the hexagon (see Fig.5). In this deployment pattern also, the intersection coverage area between the sensing range of any two sensors is always equal. The calculation of intersection coverage area in hexagon deployment is similar to what is performed to calculate intersection area in rhombus deployment pattern. Following the steps, the intersection coverage area in hexagon deployment can be calculated as $2\left\{\theta r^2 - \left(d\left(\sqrt{r^2 - (d/2)^2}\right)/2\right)\right\}$. The quality of coverage and connectivity of hexagon deployment pattern is measured below.

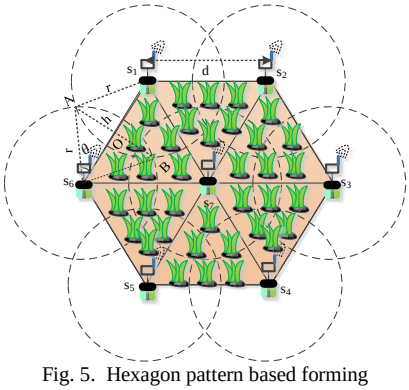


Fig. 5. Hexagon pattern based forming

- *Total Coverage Area*

$$C_a^T = 7(\pi r^2) - 12\left(2\left\{\theta r^2 - \left(d\left(\sqrt{r^2 - (d/2)^2}\right)/2\right)\right\}\right)$$

Here in this section also, the case has been simplified with same assumption as considered in case of rhombus deployment; i.e., $d = r$. With this assumption, total coverage area C_a^T can be calculated as expressed by Eq. (37).

$$C_a^T = 7(\pi r^2) - 12\left\{\frac{(2\pi - 3\sqrt{3})r^2}{6}\right\} = \left(3\pi + 6\sqrt{3}\right)r^2 \quad (37)$$

- *Effective Coverage Area*

$$C_a^E = \frac{C_a^{TO} + C_a^{TNO}}{N\pi r^2} = \frac{(3\pi + 6\sqrt{3})r^2}{7\pi r^2} = \frac{3}{7} + \frac{6\sqrt{3}}{7\pi} = 0.90 \quad (38)$$

- *Net Effective Coverage Area*

$$C_a^{NE} = \pi r^2 - C_a^{IO} = \pi r^2 - 3\left\{\frac{(2\pi - 3\sqrt{3})r^2}{6}\right\} = \frac{3\sqrt{3}}{2}r^2 \quad (39)$$

- *Net Effective Coverage Area Ratio*

$$C_a^{NER} = 1 - \frac{C_a^{IO}}{\pi r^2} = 1 - \frac{3\left\{\frac{(2\pi - 3\sqrt{3})r^2}{6}\right\}}{\pi r^2} = \frac{\frac{3\sqrt{3}}{2}r^2}{\pi r^2} = 0.82 \quad (40)$$

- *Total Non-overlapped Coverage Area*

$$C_a^{TNO} = N\pi r^2\left(1 - \frac{C_a^{IO}}{\pi r^2}\right) = 7\pi r^2\left(1 - \frac{3\left\{\frac{(2\pi - 3\sqrt{3})r^2}{6}\right\}}{\pi r^2}\right)$$
$$= \left(\frac{21\sqrt{3}}{2}\right)r^2 \quad (41)$$

- *Total Overlapped Coverage Area*

$$C_a^{TO} = C_a^T - \left\{N\pi r^2\left(1 - \frac{C_a^{IO}}{\pi r^2}\right)\right\} = \left(3\pi + 6\sqrt{3}\right)r^2 - \left(\frac{21\sqrt{3}}{2}\right)r^2 = \left(3\pi - \frac{9\sqrt{3}}{2}\right)r^2 \quad (42)$$

- *Quality of Connectivity*

$$Q_c = KN\pi r^2\left\{1 - \frac{N\pi r^2}{C_a^T} + \frac{N\,C_a^{IO}}{C_a^T}\right\} = 7\pi r^2\left\{1 - \frac{7\pi r^2}{(3\pi + 6\sqrt{3})r^2} + \frac{21\left\{\frac{(2\pi - 3\sqrt{3})r^2}{6}\right\}}{(3\pi + 6\sqrt{3})r^2}\right\} = \frac{\left(3\pi - \frac{9\sqrt{3}}{2}\right)r^2}{0.90} \quad (43)$$

IV. Empirical Results

In this section, analytical, simulation and testbed results are discussed for measuring the quality of coverage and connectivity of deployment patterns in terms of the considered metrics. This section is broadly divided into three parts. In the first part, the analytical results are discussed whereas in the second and third parts simulation and testbed results are discussed; respectively.

1530-437X (c) 2016 IEEE. Personal use is permitted, but republication/redistribution requires IEEE permission. See http://www.ieee.org/publications_standards/publications/rights/index.html for more information.

This article has been accepted for publication in a future issue of this journal, but has not been fully edited. Content may change prior to final publication. Citation information: DOI 10.1109/JSEN.2016.2614748, IEEE Sensors Journal

A. *Analytical Results*

In this section, the derivations obtained in terms of coverage and connectivity metrics for each of the considered deployment pattern are analytically evaluated using mathematical tool. The sensing range $r = 15$ m and transmission range $t = 25$ m are considered while measuring coverage to focus on coverage metrics whereas both sensing range and transmission range are considered equal; i.e., $r = t = 15$ m for measuring connectivity to focus on connectivity metric.

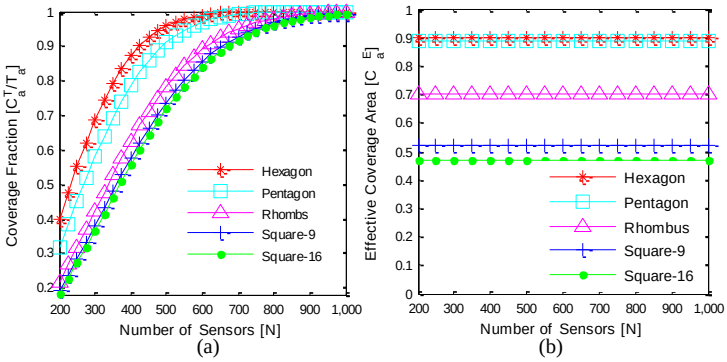


Fig. 6. Analytical results: (a) coverage fraction, (b) effective coverage area

Fig.6 (a) shows the impact of sensor density on coverage fraction of deployment patterns. The coverage fraction is defined as ratio of total covered sensing area and total area of sensing field considered for the experiment. It can be clearly observed that hexagon deployment pattern provides 100% coverage with least number of sensors; i.e., approximately with 620 sensors. All the other considered deployment patterns require more number of sensors for providing 100% coverage as compared to hexagon deployment. Specifically, the number of sensors required for providing 100% coverage is approximately 720 for pentagon and it is above 900 for all the other considered deployment patterns. Therefore, hexagonal deployment pattern is far better than other deployment patterns in providing coverage fraction. The results in Fig.6 (b) show the impact of sensor density on effective coverage area C_a^E of deployment pattern. The results reveal that sensor density has negligible impact on effective coverage area of the considered deployment patterns. The results confirm the constant values of effective coverage area obtained in the derivations in previous section for each of the considered deployment pattern. In particular, the effective coverage area for hexagonal and pentagon deployment patterns are approximately equal to 0.9 whereas it is 0.7 for rhombus and near 0.5 for both the considered square deployment patterns.

Fig. 7(a) shows the impact of sensor density on net effective coverage area C_a^{NE} of deployment patters. It can be clearly observed from the results that hexagon deployment pattern offers higher net effective coverage area as compared to those of the other considered deployment patterns. This can be attributed to the fact that the overlapping of coverage area is lower in hexagon as compared to the other deployment patterns. Pentagon deployment pattern offers lesser net effective coverage area as compared to hexagon deployment but the net effective coverage area offered by pentagon deployment is closer to what is offered by hexagon deployment for each of the considered density of sensors. The net effective coverage area offered by the other deployment patterns which includes rhombus, square-9 and square-16 are far less than what is offered by hexagon or pentagon deployment patterns due to the higher coverage overlapping.

The results in Fig. 7(b) show the impact of sensor density on net effective coverage area ratio C_a^{NER} of the deployment patterns. The results reveal that sensor density has negligible impact on net effective coverage area ration of the considered deployment patterns. The results attest the constant values obtained for net effective coverage area ratio metric in the derivations of the metric in previous section for each of the considered deployment patterns. In particular, the net effective coverage area ratio of hexagon deployment pattern is noted as 0.82 which is the maximum value of net effective coverage area among the considered deployment patterns. The value of C_a^{NER} of pentagon deployment pattern is 0.8 which is close to the value offered by hexagon. The value of C_a^{NER} for the other considered deployment patterns is far below than 0.5. Two different deployment strategies considered under square deployment pattern show equal value of net effective coverage area ratio due to the similar geometrical shape resulting in equal coverage overlapping within an individual sensor's coverage area.

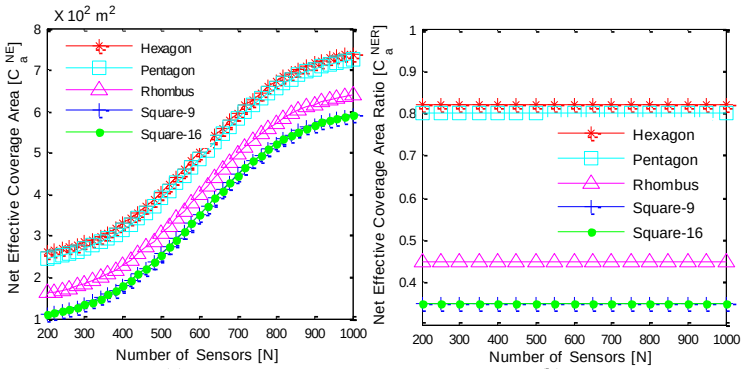


Fig.7. Analytical results: (a) net effective coverage area, (b) net effective coverage area ratio

Fig.8 (a) demonstrate the impact of sensor density on total overlapped coverage area C_a^{TO} of the deployment patterns. The rapid increment in total overlapped coverage area for all the deployment patterns can be clearly observed from the results. The total overlapped coverage area in hexagon deployment pattern is smaller than that of other deployment patterns for each of the sensor density taken into consideration. In case of pentagon, C_a^{TO} is definitely bigger than that of hexagon but it is closer to the hexagon's C_a^{TO} as compared to the rhombus and square deployment patterns. . This is because of geometrical shape similarity between pentagon and hexagon. The results in Fig.8 (b) show the impact of sensor density on quality of connectivity of the network. Square deployment patterns offer higher quality of connectivity among the considered deployment patterns which confirms the derivation of quality of connectivity carried out in previous section. For all the deployment patterns considered, quality of connectivity of the network is approximately constant up to 500 sensors and it increases linearly when number of sensors are more than 500. This can

1530-437X (c) 2016 IEEE. Personal use is permitted, but republication/redistribution requires IEEE permission. See http://www.ieee.org/publications_standards/publications/rights/index.html for more information.

This article has been accepted for publication in a future issue of this journal, but has not been fully edited. Content may change prior to final publication. Citation information: DOI 10.1109/JSEN.2016.2614748, IEEE Sensors Journal

be attributed to the fact that till 500 sensors coverage overlapping is lesser as evident from Fig. 8(a). Once the closeness of sensors increase with more than 500 sensors, the better quality of connectivity is noted for the deployment patterns.

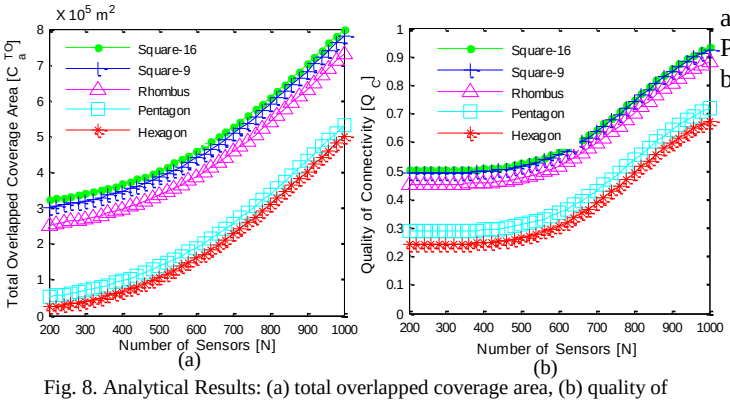
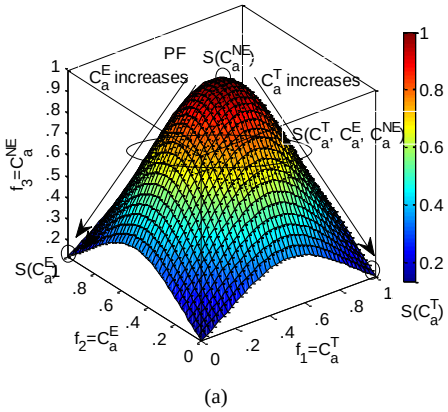


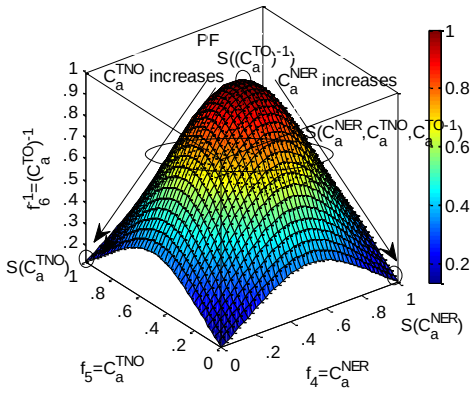
Fig. 8. Analytical Results: (a) total overlapped coverage area, (b) quality of connectivity

1) Analysis of the Multi-objective Optimization

In MOO, a better solution or Pareto optimal solution $S(*)$ in comparison with another solution $S(A)$ is defined as $\forall\, i \in \{1,2,\dots,7\}, S(*)_i \prec S(A)_i \wedge \exists\, i \in \{1,2,\dots,7\}, S(*)_i > S(A)_i$. The set of all Pareto solutions in the objective space is mapped to Pareto optimal Front (PF) [37]. Due to the number of metrics considered, a solution which optimizes all the metrics with maximum values at the same time, rarely exists. Therefore, Pareto optimal solutions are aimed. This analysis would provide some insights of the properties and features of the solutions in the PF of the MOO. Three different set of objectives are considered for analysis due to the number of direction representation in space. In Fig. 9(a), the objectives including $f_1 = C_a^T, f_2 = C_a^E$ and $f_3 = C_a^{NE}$ are considered. The optimal solution is designed analytically considering each objective. The optimal solution considering objective f_1 is represented by $S(C_a^T)$ which has maximum C_a^T but minimum C_a^E and C_a^{NE} . The maximum value of C_a^T and minimum value of C_a^E and C_a^{NE} represented by the solution $S(C_a^T)$, i.e., $C_a^T\left(S(C_a^T)\right) = \max(C_a^T), C_a^E\left(S(C_a^T)\right) = min(C_a^E)$ and $C_a^{NE}\left(S(C_a^T)\right) = min(C_a^{NE})$ can be defined and normalized with the help of the constraints of the corresponding metrics. The optimal solution considering objective f_2 is represented by $S(C_a^E)$ which has maximum C_a^E but minimum C_a^T and C_a^{NE}. The optimal values of the metrics defined by the solution $S(C_a^E)$, i.e., $C_a^E\left(S(C_a^E)\right) = \max(C_a^T), C_a^T\left(S(C_a^E)\right) = min(C_a^T)$ and $C_a^{NE}\left(S(C_a^E)\right) = min(C_a^{NE})$ can be generated and normalized considering the related constraints. The optimal solution considering objective f_3 is represented by $S(C_a^{NE})$ which has maximum C_a^{NE} but minimum C_a^T and C_a^E. The maximum value of C_a^{NE} and minimum value C_a^T and C_a^E, i.e., $C_a^{NE}\left(S(C_a^{NE})\right) = max(C_a^{NE}), C_a^T\left(S(C_a^{NE})\right) = min(C_a^T)$ and $C_a^E\left(S(C_a^{NE})\right) = min(C_a^E)$ can be obtained and normalized based on the corresponding constraints of the metrics. However, the Pareto optimal solutions $PF - \{S(C_a^T), S(C_a^E), S(C_a^{NE})\}$ are more significant, because some of these solutions optimize all the three objectives at the same time. These solutions are represented by $S(C_a^T, C_a^E, C_a^{NE})$. Similar observations can be made in Fig. 9(b) where the other three objectives including $f_4 = C_a^{NER}, f_5 = C_a^{TNO}$ and $f_6^{-1} = (C_a^{TO})^{-1}$ are considered. The optimal solutions considering objectives f_4, f_5 and f_6^{-1} are represented by $S(C_a^{NER}), S(C_a^{TNO})$ and $S((C_a^{TO})^{-1})$, respectively. However, the more significant Pareto optimal solution is represented by $S(C_a^{NER}, C_a^{TNO}, (C_a^{TO})^{-1})$.



(a)



(b)

Fig. 9. The solution characteristics of the MOO: (a) with $\boldsymbol{f_1 = C_a^T, f_2 = C_a^E}$ and $\boldsymbol{f_3 = C_a^{NE}}$, (b) with $\boldsymbol{f_4 = C_a^{NER}, f_5 = C_a^{TNO}}$ and $\boldsymbol{f_6^{-1} = \left(C_a^{TO}\right)^{-1}}$

B. Simulation Results

In this section, simulations are performed in Network Simulator (NS-2) to measure the performance of deployment patterns in terms of quality of coverage and connectivity in realistic environment for verifying the analytical results obtained in the previous section. The simulation experiments are conducted for each of the deployment patterns considered one-by-one. For each experiments, simulation area of $1500 \times 1500\ \text{m}^2$ is considered and sensors are deployed in the range $200 - 1000$ following a particular deployment patterns. After following a particular pattern, the impact of exceeded sensors is not considered for simplicity in comparative evaluation. For example, with 200 sensors in the network, 2 sensors exceeded in square-9, rhombus and pentagon, 4 sensors exceeded in hexagon, and 8 sensors exceeded in square-16 deployment patterns. Two percent sensors are randomly selected as active senders for communication in each experiment. Each sensor generates data following Poisson process of rate μ, where $1/\mu = 0.1/s$. In each

1530-437X (c) 2016 IEEE. Personal use is permitted, but republication/redistribution requires IEEE permission. See http://www.ieee.org/publications_standards/publications/rights/index.html for more information.

This article has been accepted for publication in a future issue of this journal, but has not been fully edited. Content may change prior to final publication. Citation information: DOI 10.1109/JSEN.2016.2614748, IEEE Sensors Journal

experiment, the destination sensor is changed following exponential distribution of rate $\delta = {}^{1}/_{20}\, ms$. During the simulation of coverage metric, sensing range r = 15 m and transmission range t = 25 m are considered for focusing on coverage measurement. For quality of connectivity measurement, both sensing range and transmission range are considered equal; i.e., r = t = 15 m. The data rate considered in the simulation for communication among sensor nodes is 40 kbps. Propagation delay during transmission has been considered negligible taking into account the specified simulation area. The basic parameter values used in the simulations are summarized in Table-2. Each experiment has been repeated 30 times over different seeds and average has been taken for data record utilized in the results with 95% confidence interval.

Table 2. Basic parameter setting for simulations

Parameter	Value	Parameter	Value
Simulation area	$1500 \times 1500\ m^2$	Packet Type	UDP
Simulation time	$600s$	Ifqlen	50
No of sensors	$200 - 1000$	Channel Type	$Wireless$
Bandwidth	40 Kbps	Propagation model	$Shadowing$
t	$15m\ and\ 25\ m$	Antenna Model	$Omni\ dir.$
r	$15m$	MAC protocol	$IEEE$ 802.11
Data senders	$2\%\ sensors$	Query period	$3s$
$1/\mu$	$0.1/s$	Hello timeout	$1s$
δ	$1/20\ ms$	Packet Type	UDP

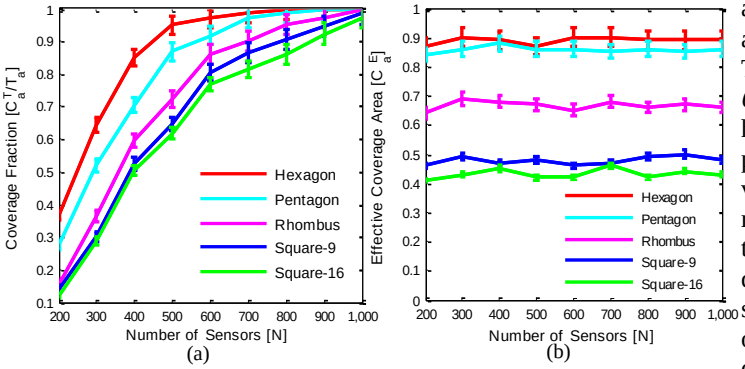


Fig. 10. Simulation Results: (a) coverage fraction, (b) effective coverage area

Simulation results shown in Fig. 10(a) corroborate the analytical results of coverage fraction. It can be clearly observed that hexagon deployment pattern provides higher coverage fraction with lesser number of sensors as compared to the other regular deployment patterns considered. Although the coverage fractions obtained through simulations is lesser from the estimated coverage fraction in analytical results for each of sensor density considered but they are very close the analytically estimated coverage fractions. For example, N = 500 sensors, the coverage fraction offered by hexagon deployment is 0.93 in simulation whereas it is 0.98 in analytical results as depicted in Fig. 6(a). Simulation results shown in Fig. 10(b) confirm the corresponding analytical results for effective coverage area. In simulation results, effective coverage area provided by the considered deployment patterns are not exactly constant as estimated in analytical results but they are slightly varying around constant values observed in analytical results. Hexagon deployment pattern which provide bigger effective coverage area among the considered deployment patterns in analytical results is validated by simulation results. For example, for $N = 600 - 1000$ sensors, the constant value of effective coverage area for hexagon deployment pattern is approximately 0.89 which is close to what is noted in analytical results; i.e., 0.9.

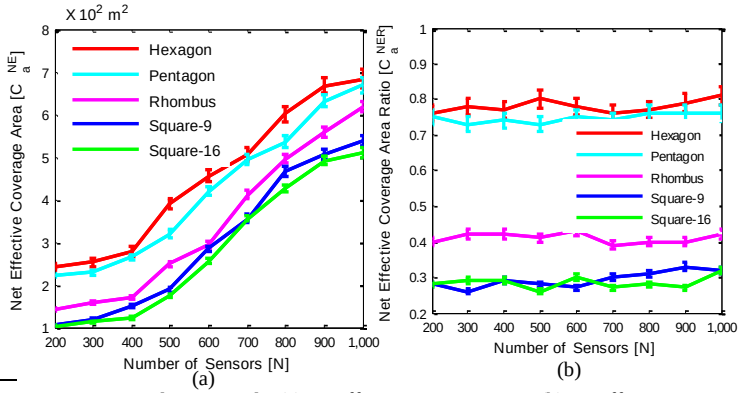


Fig. 11. Simulation Results (a) net effective coverage area, (b) net effective coverage area ratio

Simulation results depicted in Fig. 11(a) verifies the analytical results for net effective coverage area metric. The increment in C_a^{NE} with the increase in number of sensors is similar to what is observed in analytical results. For example, $N = 200, 600$ and 1000, hexagon deployment offers approximately $230,440$ and $690\ m^2$ net effective coverage area; respectively, whereas it offers approximately $260,480$ and $706\ m^2$ net effective coverage area in analytical results. The other deployment patterns also offer similar increment in C_a^{NE} to what is offered in analytical results. Therefore, the higher net effective coverage area offered by hexagon and pentagon deployments due to lower coverage overlapping is verified by simulation results. Fig. 11(b) shows simulation results for net effective coverage area ratio metric and attest the observed constant values in analytical results for each deployment pattern. Although C_a^{NER} is not exactly constant in simulation results yet, it is varying near the constant values observed in analytical results. Specifically, net effective coverage area ratio of hexagon deployment varies in the range $0.78 - 0.81$ in simulation results which close to the constant value of 0.81 observed in analytical results. Similarly, the ratio of pentagon deployment varies in the range $0.75 - 0.78$ in simulation results which is also close to the constant value of 0.8 observed in analytical results. It is also noteworthy that there is slight fluctuation in the net effective coverage area ratio of square-9 and square-16 deployment patterns due to the difference of number of exceeded sensors after following these two deployment patterns in the network with specified number of sensors. Thus, the higher and constant net effective coverage area ratio provided by both hexagon and pentagon deployments in analytical results are attested by simulation results.

Total overlapped coverage area of deployment patterns measured through simulation is shown in Fig.12 (a). Simulation results attest the lower coverage overlapping provided by hexagon and pentagon deployment patters in analytical results. The results also verify the higher coverage overlapping of square deployment patterns. For example, $N = 200$, the total overlapped coverage area of hexagon and pentagon deployments are 1275 and $2575\ m^2$; respectively,

1530-437X (c) 2016 IEEE. Personal use is permitted, but republication/redistribution requires IEEE permission. See http://www.ieee.org/publications_standards/publications/rights/index.html for more information.

This article has been accepted for publication in a future issue of this journal, but has not been fully edited. Content may change prior to final publication. Citation information: DOI 10.1109/JSEN.2016.2614748, IEEE Sensors Journal

which are lower as compared to that of other deployment patters. For $N = 1000$, the total overlapped coverage area of square-16 and square-9 deployments are 71000 and 66000 m^2; respectively, which are higher as compared to that of other deployment patters. Simulation results of quality of connectivity of deployment patterns is shown in Fig. 12(b) which contradict with what is observed in analytical results due to the no consideration of interference in the derivation of the metric. Specifically, quality of connectivity of hexagon deployment pattern is higher due to the lower coverage overlapping resulting in lower interference. Quality of connectivity is lower for square deployment patterns due to the higher interference resulting from higher coverage overlapping. Therefore, in realistic simulation scenario, the quality of connectivity is considerably affected by interference of the network resulting from coverage overlapping.

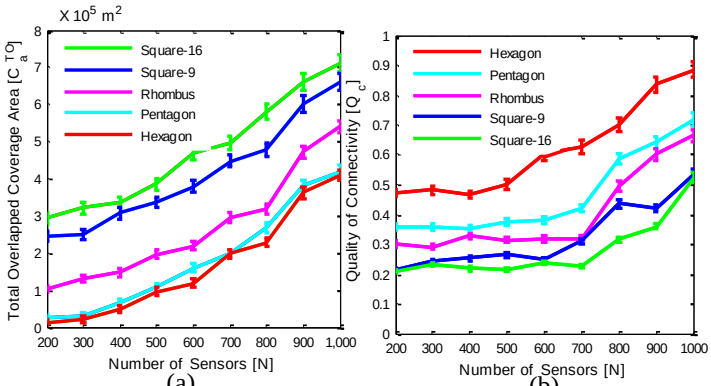


Fig.12. Simulation Results: (a) total overlapped coverage area, (b) quality of connectivity

C. Testbed Results

In this section, sensor deployment patters are evaluated in 'INDRIYA' wireless sensor network testbed of the School of Computing, National University of Singapore (NUS) [22]. Total 139 number of wireless sensor network nodes which are commonly known as motes N_m are available in the testbed for experiment. Most of the motes are in good condition and available to researchers for experiment through online and offline ways. There are four types of sensors utilized in these motes; namely, WiEye, SBT30, SBT80 and TelosB. The different kinds of motes are used for monitoring different activities required for precision agriculture use case.

As an example experiment, the deployment of motes is depicted in Fig. 13 where different deployment patterns are implemented in different sets of motes of 'INDRIYA'. Different set of motes are selected for implementing the considered deployment patterns. The set of nodes are selected in such a way that the patterns can be implemented with minimum possible error in terms of geometrical model. Some of the example of patterns are as follows. For square deployment pattern the set of motes that can be selected from the 1st set are 13, 11, 21, 8, 12, 19, 1, 16 and 22. Pentagon and rhombus deployment patterns can be implemented in 2nd set using the motes 70, 72, 77, 71, 84, 76 and 52, 74, 67, 75, 69, 62, 68, 60, 63; respectively. Hexagonal deployment patterns can be implemented in 3rd set with the motes 90, 103, 124, 137, 139, 104 and 97. The probability of connectivity of most of links among the motes is 1.0 and very few links are connected with probability in between 0.8 and 1.0, 0.6 and 0.8, and less than 0.6. The connectivity is measured at the default maximum transmission power $0dBM$. Some physical characteristics of the devices used in the motes are shown in Table-3. For measuring coverage area, monitoring of activities related to precision agriculture is carried out and the measured sensory data of the motes are analyzed. Thirty measurements are performed for each different types of deployment patterns. Flowchart of the workflow of the testbed implementation is provided in Fig. 14.

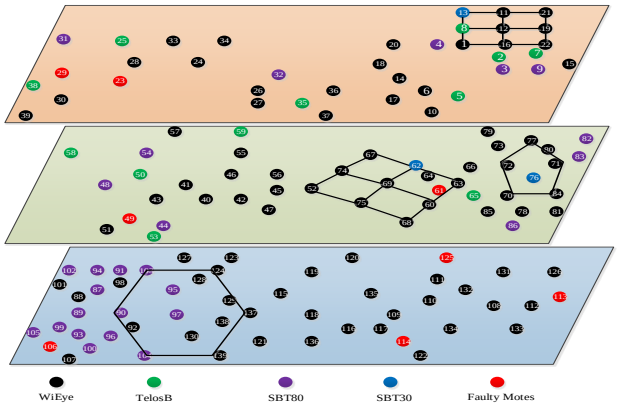


Fig. 13. Implementation of the patterns using the motes of 'INDRIYA'

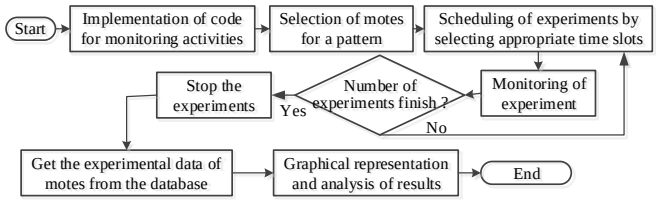


Fig.14. Workflow diagram for Testbed experiment

Table 3. Physical characteristics of the motes

Characteristics	Value	Characteristics	Value
Processor	16 bit and 8 MHz	Internal Flash	48 KB
ADC	12 bit	Sensitivity	-95dBm
RAM	10 KB	Transceiver	250 Kbps
RF chip	TI-2420	Microcontroller	TI-MSP430

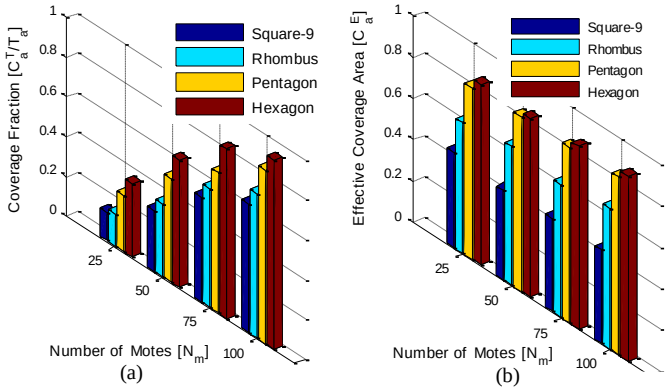


Fig.15. Testbed Results; (a) coverage fraction, (b) effective coverage area

Testbed results shown in Fig. 15(a) validates the simulation and analytical results for coverage fraction metric of deployment patterns. It can be clearly observed that the coverage fraction obtained of hexagon and pentagon deployment patterns are higher as compared to the rhombus

1530-437X (c) 2016 IEEE. Personal use is permitted, but republication/redistribution requires IEEE permission. See http://www.ieee.org/publications_standards/publications/rights/index.html for more information.

This article has been accepted for publication in a future issue of this journal, but has not been fully edited. Content may change prior to final publication. Citation information: DOI 10.1109/JSEN.2016.2614748, IEEE Sensors Journal

and square deployment patterns. This is because of the geometrical shape property of hexagon which results in lower coverage overlapping. The lower coverage overlapping significantly enhances coverage fraction of hexagon and pentagon deployment patterns. The higher effective coverage area in hexagonal deployment pattern is noted in testbed results shown in Fig. 15 (b) which attest the simulation and analytical results of effective coverage area metric. The impact of number of motes on effective coverage area is negligible and the values are constants. Specifically, net effective coverage area noted for hexagon and pentagon deployment patterns are above 0.8 which is quite similar to what is observed in simulation and analytical results. The effective coverage area observed for rhombus and square deployment are above 0.4 and 0.6; respectively, which are also similar to the noted values in simulation and analytical results.

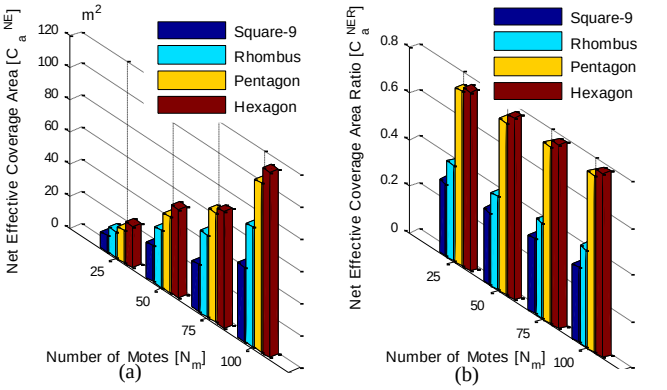


Fig.16. Testbed Results; (a) net effective coverage area, (b) net effective coverage area ratio

Testbed results shown in Fig. 16(a) validates the simulation and analytical results for net effective coverage area metric of deployment patterns. The continuous increment of net effective coverage area with the increase in number of motes is clearly the same observation what it is noted in simulation and analytical results. The size of net effective coverage area noted in testbed results is smaller than what it is observed in simulation and analytical results due to the lesser number of motes available for experiment in the testbed. Specifically, the maximum net effective coverage area noted in testbed results is less than $120\ m^2$ whereas it is $700\ m^2$ in simulation and testbed results. The constant values of net effective coverage area ratio metrics of deployment patterns observed in testbed results are depicted in Fig 16(b) which strongly validate the constant values observed in analytical and simulation results for the metric. The values of the metric for hexagon and pentagon deployment patters are higher as compared to those of other deployment patters. The constant values for hexagon and pentagon deployment patterns are also close to each other. The higher and closer constant values of the metric for hexagon and pentagon deployment is similar to what is observed in simulation and analytical results.

Testbed results in Fig. 17(a) attest the higher coverage overlapping in square deployment pattern as compared to the hexagon and pentagon deployment patterns which is observed in simulation and analytical results as well. Although the size of the total overlapped coverage area noted in testbed results is smaller than what it is observed in simulation and analytical results yet, the increment pattern with the increase of number of motes is quite similar to the simulation and analytical results. The difference in total overlapped coverage area is due to the lesser number of motes available for experiment in testbed as compared the number of sensors considered in simulation and analytical results. The better quality of connectivity in hexagon deployment pattern is observed in testbed results depicted in Fig. 17 (b) which confirms the simulation and analytical results regarding quality of connectivity. This can be attributed to the fact that the lower total overlapped coverage area is noted in hexagonal deployment pattern resulting in lower interference and better quality of connectivity as compared to the other deployment patterns. Due to the deployment of motes in precisely calculated locations at the three floors of NUS, the quality of connectivity is stable in testbed results which can be noticed as constant values for deployment patterns.

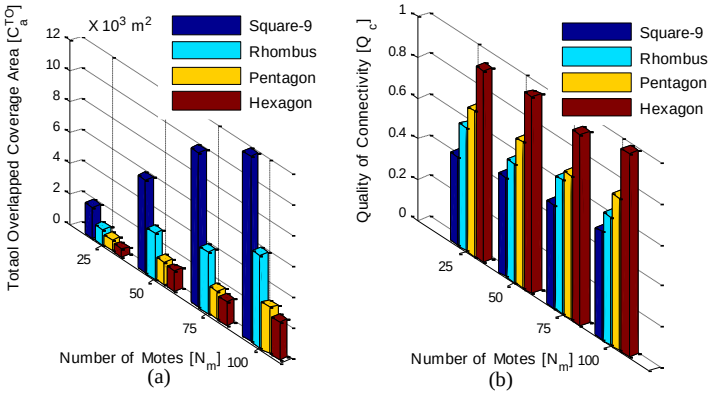


Fig.17. Testbed Results; (a) total overlapped coverage area, (b) quality of connectivity

D. Summary of Observations

From the derivation, implementation and analysis of experimental results, following is the summary of observations. The metrics for measurement of quality of coverage and connectivity are closely inter-related and have considerable impact on each other. The coverage overlapping resulting in interference substantially impacts the quality of connectivity of deployment patterns. Due to the geometrical shape property, lower coverage overlapping is observed in case of hexagon deployment pattern. The performance of hexagon and pentagon deployment is better as compared to rhombus and square deployment in case of most of the considered metrics. The larger total overlapped coverage area is observed for square deployment patterns. Analytical results shows the performance of deployment patterns in ideal environment whereas simulation results shows the performance of deployment patterns in realistically modelled environment. The testbed results shows the performance of deployment patterns in real environment.

V. Conclusion and Future Work

In this paper, a Testbed based Multi-metric Quality Measurement (T-MQM) of sensor deployment patterns for precision agriculture using WSNs is presented. The seven metrics are derived and quantified for four sensor deployment patterns in precision agriculture to measure the quality of

1530-437X (c) 2016 IEEE. Personal use is permitted, but republication/redistribution requires IEEE permission. See http://www.ieee.org/publications_standards/publications/rights/index.html for more information.

This article has been accepted for publication in a future issue of this journal, but has not been fully edited. Content may change prior to final publication. Citation information: DOI 10.1109/JSEN.2016.2614748, IEEE Sensors Journal

coverage and connectivity. The measurement practically evaluates the quality of coverage and connectivity of deployment patterns in precision agriculture through testbed implementation. The measurements and evaluations through analytical and simulation based studies which are validated using testbed experiments, are accurate and helpful for realistic implementations. The measurement should be useful for practitioners in developing performance guaranteed applications for precision agriculture whereas it should be useful for researchers in developing novel coverage and connectivity models for deployment patterns. In future research work, authors will explore three dimensional deployment patterns for precision agriculture. The impact of external interferers on quality of coverage and connectivity and development of hybrid deployment pattern exploiting mathematical geometry will also be the quest.

REFERENCES

[1] L.M. Borges, F.J. Velez, and A.S. Lebres, "Survey on the characterization and classification of wireless sensor network applications," IEEE Commun. Surveys & Tutorials, vol. 16, no. 4, pp.1860-1890, 2014.

[2] Y. Cao, N. Wang, Z. Sun, and H. Cruickshank, "A reliable and efficient encounter-based routing framework for delay/disruption tolerant networks," IEEE Sensors Journal, vol. 15, no. 7, pp.4004-4018, 2015.

[3] O. Kaiwartya, A.H. Abdullah, Y. Cao, A. Altameem, M. Prasad, C.T. Lin and X. Liu, "Internet of Vehicles: Motivation, Layered Architecture, Network Model, Challenges and Future Aspects," IEEE Access, vol. PP, no.99,pp.1-1, 2016. doi: 10.1109/ACCESS.2016.2603219

[4] S. Halder and S. DasBit, "Design of a Probability Density Function Targeting Energy-Efficient Node Deployment in Wireless Sensor Networks," IEEE Transaction on Network and Service Management, vol. 11, no. 2, pp. 204-219, 2014.

[5] D.S. Deif and Y. Gadallah, "Classification of wireless sensor networks deployment techniques," IEEE Communications Surveys & Tutorials, IEEE, vol. 16, no. 2, pp.834-855, 2014.

[6] A.J. Phillips, N.K. Newlands, S. Liang, and B.H. Ellert, "Integrated sensing of soil moisture at the field-scale: Measuring, modeling and sharing for improved agricultural decision support," Computers and Electronics in Agriculture, vol. 107, no. 1, pp.73-88, 2014.

[7] M. Srbinovska, C. Gavrovski, V. Dimcev, A. Krkoleva, A. and V. Borozan, "Environmental parameters monitoring in precision agriculture using wireless sensor networks," Journal of Cleaner Production, vol. 88, no. 1, pp.297-307, 2015.

[8] H.P. Gupta, P.K. Tyagi, and M.P. Singh, "Regular node deployment for coverage in connected wireless networks," IEEE Sensors Journal, vo. 15, no. 12, pp.7126-7134, 2015.

[9] W. Li, C. Zhu, V.C. Leung, L.T. Yang, and Y. Ma, "Performance Comparison of Cognitive Radio Sensor Networks for Industrial IoT with Different Deployment Patterns," IEEE Systems Journal, vol. PP, no, 99, pp. 1-11, 2015.

[10] K. Sakai, M.T. Sun, W.S. Ku,T.H. Lai, and A.V. Vasilakos, "A Framework for the Optimal-Coverage Deployment Patterns of Wireless Sensors," IEEE Sensors Journal, vol. 15, no. 12, pp.7273-7283, 2015.

[11] K. Mukherjee, S. Gupta, A. Ray, and T.A. Wettergren, "Statistical-mechanics-inspired optimization of sensor field configuration for detection of mobile targets," IEEE Transactions on Systems, Man, and Cybernetics, Part B, vol. 41, no. 3, pp.783-791, 2011.

[12] S. Ivanov, K. Bhargava, and W. Donnelly, "Precision Farming: Sensor Analytics," IEEE Intelligent Systems, vol. 30, no. 4, pp.76-80, 2015.

[13] E. Onur, C. Ersoy, H. Deliç and L. Akarun, "Surveillance Wireless Sensor Networks: Deployment Quality Analysis," IEEE Network, vol. 21, no. 6, pp. 48-53, 2007.

[14] Z. Yun, X. Bai, D. Xuan, T. Lai & W. Jia, "Optimal Deployment Patterns for Full Coverage and K-Connectivity Wireless Sensor Networks," IEEE Transactions on Networking, vol. 18, no. 3, pp. 934-947, 2010.

[15] G. Stamenovic, S.R. Panic, D. Ranci, C. Stefanovi and M. Stefanovic "Performance analysis of wireless communication system in general fading environment subjected to shadowing and interference," EURASIP Journal on Wireless Communications, vol. 124, no. 1, pp. 1-8, 2014.

[16] X. Liu & M. Haenggi, "Throughput Analysis of Fading Sensor Networks with Regular and Random Topologies," EURASIP Journal on Wireless Communications and Networking, vol. 4, no. 1, pp. 554-564, 2005.

[17] R. Rajagopalan and P. K. Varshney, "Connectivity analysis of wireless sensor networks with regular topologies in the presence of fading," IEEE Trans. on Wireless Communications, vol. 8, no. 7, pp. 3475-3483, 2009.

[18] H. Wang, H. E. Roman, L. Yuan, Y. Huang and R. Wang, "Connectivity, coverage and power consumption in large-scale wireless sensor networks," Computer Networks, vol. 75, pp. 212-225, 2014.

[19] G. Fan, R. Wang, H. Huang, L. Sun and C. Sha, "Coverage-Guaranteed Sensor Node Deployment Strategies for Wireless Sensor Networks," Sensors, vol. 10, no. 3, pp. 2064-2087, 2010.

[20] Y. Chang, S. Zhang, Y. Zhang, J. Fan and J. Wang, "Uncertainty-Aware Sensor Deployment Strategy in Mixed Wireless Sensor Networks," International Journal of Distributed Sensor Networks, vol. 2013, no. 1, pp. 1-9, 2013.

[21] C. Zhu, C. Zheng and L. Shu, "A survey on coverage and connectivity issues in wireless sensor networks," Journal of Network and Computer Applications, vol. 35, no. 2, pp.619-632, 2012.

[22] M. Khalesian, and M.R. Delavar, "Wireless sensors deployment optimization using a constrained Pareto-based multi-objective evolutionary approach," Engineering Applications of Artificial Intelligence, vol. 53, no. 1, pp.126-139, 2016

[23] J. Chen, L. Zhang and Y. Kuo, "Coverage-Enhancing Algorithm Based on Overlap-Sense Ratio in Wireless Multimedia Sensor Networks," IEEE Sensors Journal, vol. 13, no. 6, pp. 2077-2083, 2013.

[24] 'INDRIYA': "Wireless Sensor Network Testbed, School of Computing, National University of Singapore", http://indriya.comp.nus.edu.sg/ Accessed on: 09/06/2016.

[25] S. He, J. Chen and Y. Sun, "Coverage and Connectivity in Duty-Cycled Wireless Sensor Networks for Event Monitoring," IEEE Transactions on Parallel and Distributed Systems, vol. 23, no. 3, pp. 475-482, 2012.

[26] C. He, J. Xing, J. Li, Q. Yang, R. Wang and X. Zhang, "A Combined Optimal Sensor Placement Strategy for the Structural Health Monitoring of Bridge Structures," International Journal of Distributed Sensor Networks, vol. 2013, no. 1, pp. 1-9, 2013.

[27] K. Ovsthus, and L. Kristensen, "An industrial perspective on wireless sensor networks a survey of requirements, protocols, and challenges," IEEE communications surveys & tutorials, vol. 16, no. 3, pp.1391-1412, 2014.

[28] C. T. Kone, A. Hafid and M. Boushaba, "Performance Management of IEEE 802.15.4 Wireless Sensor Network for Precision Agriculture," in IEEE Sensors Journal, vol. 15, no. 10, pp. 5734-5747, Oct. 2015.

[29] C. Lozoya, A. Aguilar and C. Mendoza, "Service Oriented Design Approach for a Precision Agriculture Datalogger," in IEEE Latin America Transactions, vol. 14, no. 4, pp. 1683-1688, April 2016.

[30] T.D. Le, and D.H. Tan, "Design and deploy a wireless sensor network for precision agriculture," In Proceedings on NICS, IEEE, pp. 294-299, Ho Chi Minh, Vietnam, September, 2015.

[31] C. Wang, D. George, and P.R. Green, P.R., "Development of plough-able RFID sensor network systems for precision agriculture," In Proceedings on WiSNET, IEEE, pp. 64-66, Newport Beach, CA USA, January 2014.

[32] J.H. Seok, J.Y. Lee, W. Kim, and J.J. Lee, "A bi-population-based evolutionary algorithm for solving full area coverage problems," IEEE Sensors Journal, vol. 13, no. 12, pp.4796-4807, 2013.

[33] A. S. Ibrahim, K. G. Seddik and K. R. Liu, "Connectivity-aware network maintenance and repair via relays deployment," IEEE Transactions on Wireless Communications, vol. 8, no. 1, pp. 356-366, 2009.

[34] K. He, M. Jia, and Q. Xu, "Optimal Sensor Deployment for Manufacturing Process Monitoring Based on Quantitative Cause-Effect Graph," IEEE Transactions on Automation Science and Engineering, vol. 13, no. 2, pp.963-975, 2016.

[35] A. Ababnah, and B. Natarajan, "Optimal control-based strategy for sensor deployment," IEEE Transactions on Systems, Man, and Cybernetics-Part A: Systems and Humans, vol. 41, no. 1, pp.97-104, 2011.

[36] J. Guo, and H. Jafarkhani, "Sensor Deployment with Limited Communication Range in Homogeneous and Heterogeneous Wireless Sensor Networks," IEEE Transactions on Wireless Communication, 2016 DOI 10.1109/TWC.2016.2590541

[37] O. Kaiwartya, S. Kumar, D.K. Lobiyal, P.K. Tiwari, A.H. Abdullah, and A.N. Hassan, "Multiobjective dynamic vehicle routing problem and time seed based solution using particle swarm optimization," Journal of Sensors, vol. 15, no.1, pp. 1-14, 2015.

1530-437X (c) 2016 IEEE. Personal use is permitted, but republication/redistribution requires IEEE permission. See http://www.ieee.org/publications_standards/publications/rights/index.html for more information.

This article has been accepted for publication in a future issue of this journal, but has not been fully edited. Content may change prior to final publication. Citation information: DOI 10.1109/JSEN.2016.2614748, IEEE Sensors Journal



Omprakash Kaiwartya received his Ph.D., degree in Computer Science from School of Computer and Systems Sciences, Jawaharlal Nehru University, New Delhi, India in 2015. He is currently a Postdoctoral Research Fellow at Faculty of Computing, Universiti Teknologi Malaysia (UTM), Johor Bahru, Malaysia. His research interests focus on Vehicular Ad-hoc Networks, Mobile Ad-hoc Networks and Wireless Sensor Networks.



Abdul Hanan Abdullah received his Ph.D. degree from Aston University in Birmingham, United Kingdom in 1995. He is currently working as a Professor and heading Pervasive Computing Research Group at Faculty of Computing, Universiti Teknologi Malaysia, Johor Bahru, Malaysia. His research interests include Wireless Sensor Networks, Vehicular Adhoc Networks, Internet of Things, Network Security and Next Generation Networks.



Yue Cao received his PhD degree from the Institute for Communication Systems (ICS) formerly known as Centre for Communication Systems Research, at University of Surrey, Guildford, UK in 2013. Further to his PhD study, he was a Research Fellow at the ICS. Since October 2016, he has been the Lecturer in Department of Computer Science and Digital Technologies, at Northumbria University, Newcastle upon Tyne, UK. His research interests focus on Delay/Disruption Tolerant Networks, Electric Vehicle (EV) charging management, Information Centric Networking (ICN), Device-to-Device (D2D) communication and Mobile Edge Computing (MEC).



Ram Shringar Raw received his Ph.D. degree in Computer Science from School of Computer and Systems Sciences, Jawaharlal Nehru University, New Delhi, India in 2011. He is currently working as Associate Professor at Department of Computer Science, Indira Gandhi National Tribal University, Amarkantak, India. His research interest includes Vehicular Ad-hoc Networks, Mobile Ad-hoc Networks and Wireless Sensor Networks.



Sushil Kumar received his Ph.D. degree in Computer Science from School of Computer and Systems Sciences, Jawaharlal Nehru University, New Delhi, India in 2014. He is currently working as Assistant Professor at School of Computer and Systems Sciences, Jawaharlal Nehru University, New Delhi, India. His research interest includes Vehicular Ad-hoc Networks, Mobile Ad-hoc Networks and Wireless Sensor Networks.



D. K. Lobiyal received his Ph.D. degree in Computer Science from School of Computer and Systems Sciences, Jawaharlal Nehru University, New Delhi, India in 1996. He is currently working as Professor at School of Computer and Systems Sciences, Jawaharlal Nehru University, New Delhi, India. His research interest includes Mobile Ad hoc Networks, VoD, Bioinformatics and Natural Language Processing.



Ismail Fauzi Isnin received his Ph.D. degree in Computer Science from University of Plymouth, United Kingdom in 2011. He is currently a Senior Lecturer at Faculty of Computing, Universiti Teknologi Malaysia (UTM), Johor Bahru, Malaysia. His research interests focus on Network Security, Communication Networks and Wireless Communications.



Xiulei Liu received the PhD degree in computer science from Beijing University of Posts and Telecommunications, P.R. China in March 2013. Since May 2013, he has been a Lecturer in Computer School, Beijing Information Science and Technology University, P.R. China. From October 2008 to October 2010, he was a visiting PhD student in Centre for Communication System Research (CCSR), University of Surrey, UK. His research interests include semantic sensor, semantic web, knowledge graph, semantic information retrieval.



Rajiv Ratn Shah received his M. Tech. from Delhi Technological University, New Delhi, India in 2012. He is currently a PhD candidate in School of Computing, National University of Singapore (NUS), Singapore. His main research interests focus on multimodal analysis of user-generated content in support of social media applications, location-based services in support of social media applications, multimedia analysis and retrieval.

1530-437X (c) 2016 IEEE. Personal use is permitted, but republication/redistribution requires IEEE permission. See http://www.ieee.org/publications_standards/publications/rights/index.html for more information.

Vibrational Spectroscopy 87 (2016) 207–214

Contents lists available at ScienceDirect

Vibrational Spectroscopy

journal homepage: www.elsevier.com/locate/vibspec

Trace detection of explosive and their derivatives in stand-off mode using time gated Raman spectroscopy

Sanjay Gulia[a,b,*], Kamal K. Gulati[a], Vijayeta Gambhir[a], Rinku Sharma[b], M.N. Reddy[a]

[a] Laser Science and Technology Centre, Delhi, 110054, India
[b] Delhi Technological University, Delhi, 110042, India

ARTICLE INFO

Article history:
Received 24 June 2016
Received in revised form 16 October 2016
Accepted 23 October 2016
Available online 24 October 2016

Keywords:
Gated Raman spectroscopy
Stand-off detection
Explosives
Laser spectroscopy
Trace detection

ABSTRACT

Trace detection is utmost important for detection of concealed explosive materials in form of IEDs. Surfaces of suspicious objects may be scanned for contamination of explosives. Sensitivity and selectivity are two main concerns in field of explosive detection. Raman spectroscopy provides remarkable selectivity. Time-gated Raman spectroscopy also has potential of providing sensitivity for trace detection. In present study, time-gated Raman spectroscopy investigated for detection of ppm level concentration of explosives. To achieve better sensitivity, various parameters of the experimental set-up like gain of intensifier, number of pulse accumulated and pulse energy of laser were optimised. The trend of change in intensity of Raman scattering (background subtracted) was observed by varying values of these above mentioned parameters. Followed by optimization of these parameters for better sensitivity, Raman spectra of RDX samples at lower concentrations (prepared by mixing RDX with KBr) were recorded. The corrected intensity increased in linear fashion with increase in gain of intensifier, number of pulses accumulated and pulse energy. After that, Raman spectra of RDX were recorded from a stand-off distance of 5 m in backscattered mode with concentrations down to 100 ppm.

© 2016 Elsevier B.V. All rights reserved.

1. Introduction

Since last two decades, terrorism has evolved as the most challenging menace against humanity. Most of the terrorist attacks have been noticed for use of explosives materials stored in some concealed form like metal container etc. Such types of bombs are known as improvised explosive devices (IEDs).Till today the methods used require approaching the suspicious object in order to perform the analysis with a great risk to the operator. Therefore, a new technique, need to be developed to detect and identify target object with acceptable level of confidence maintaining safe distance for the operator [1–4].

Standoff explosive detection involves methods for sensing the presence of explosive devices when vital assets and those individuals monitoring, operating, and responding to the means of detection are physically separated from the explosive device. The zone of severe damage varies with scenario and bomb type, it may vary from 10 m for a pedestrian suicide bomber and 100 m for a vehicle-based bomb [5]. Standoff detection and identification of such explosive materials is one of the most unavoidable but greatest challenging tasks for researchers and engineers.

The detection at large distances involves physical difficulties like i. the intensity of the return light decreases inversely with the distance squared and ii. absorption & scattering losses in air lead to significant compromise in sensitivity.

Laser-based spectroscopic techniques such as laser-induced breakdown spectroscopy (LIBS), Raman spectroscopy (RS), resonant Raman spectroscopy (RRS), photo-dissociated/laser-induced fluorescence (PD/LIF) and laser-based photo-acoustic spectroscopy (LPAS) have the potential to detect minute amount of explosive materials on contaminated surfaces left by handling etc. [6–9].

LIBS technique involves power density of the order of GW/cm^2 to generate plasma of the target sample [10–12]. This level of power density is achievable with short, high peak power laser pulses and tight focusing of the laser beam by transmitting optics (usually spot size of the order of few microns). LIBS signal comprises elemental information i.e. spectral lines in LIBS spectra gives information of elements presents in the test sample whereas explosive detection requires molecular information [13,14]. It is destructive technique and hence not suitable to examine people and vehicles. Since laser beamis tightly focused into a small spot, it is difficult and time-taking to scan large objects in real conditions

* Corresponding author: Laser Science and Technology Centre, Delhi, 110054, India.
E-mail address: sanjay-gulia@lastec.drdo.in (S. Gulia).

http://dx.doi.org/10.1016/j.vibspec.2016.10.009
0924-2031/© 2016 Elsevier B.V. All rights reserved.

[15]. Photo-dissociation Laser-induced fluorescence (PD-LIF) involvesdecomposition (dissociation) of polyatomic molecules into characteristic fragments [16–18]. PF-LIF method can be used to detect only nitrogen-containing explosives. In addition, the dissociation of different molecules may require different level of energy and wavelengths. In addition, absorption characteristics of species generated in dissociation process of different molecules shall be different. Thus, PD-LIF requires a tunable laser source. In addition, it involves excitation with UV wavelength and hence thermal degradation of the sample may occur [19,20]. Laser-photo acoustic spectroscopy (LPAS) involves the vibrational absorption and hence requires the tunable laser source in mid IR range i.e. 5–12 μm which corresponds to 830–2000 cm^{-1}. Quantum-cascade lasers are the main contestant for LPAS due to their compactness and light weight [21–25]. The main concerns with QCLs are their requirement of cooled environment and limited tenability [26]. In addition, detection of suspicious materials through even transparent glass and plastic containers is not possible. The sensitivity is adversely affected by humidity.

Raman spectroscopy is one of the effective techniques for detection and identification of explosive materials [27–30]. This technique is suitable for detecting both organic and inorganic explosive materials in form of solid, liquid and powder. A single-wavelength laser is sufficient to generate Raman scattering of all the molecules of interest. Raman spectroscopy is a molecular spectroscopy that provides direct information about the molecular structure and composition of the material. The potential of this technique lies in its ability to locate and identify unequivocally many different compounds at a time. The process is non-destructive, sensitive, fast, and repeatable. The vibrational spectrum provided by Raman spectroscopy is a unique molecular 'fingerprint', that is capable of differentiating very similarly structured molecules from one another with great level of specificity in real-scenario [31–34]. Conventional Raman spectroscopy in back-scattered mode, resonance-Raman spectroscopy (RRS) [35,36], surface-enhanced Raman spectroscopy (SERS) [37–39], spatially-offset Raman spectroscopy (SORS) [40–42], time-gated Raman spectroscopy [21,27,29] are being explored for detection of explosives. Time-gated Raman spectroscopy is the most suitable technique for stand-off detection of explosive materials. It involves pulse laser source and intensifier-charge coupled device (ICCD). ICCD is being synchronized with optical laser pulse with appropriate delay depending upon mainly stand-off distance [21,36,43].

In stand-off Raman spectroscopy, a pulsed laser source of nanosecond or shorter pulse is preferred as excitation source as it provides high peak power (few MW). In addition, pulse laser enables gated-detection which in turn ensures the rejection of ambient light between consecutive laser pulses and collection of Raman photons (photons generated in inelastic scattering) only during laser pulse. In this way, high power pulse with gated detection results in better signal-to-noise ratio (SNR). Raman photons are collected with a receiving optics, and then coupled to dispersive spectrograph directly or using optical fiber. Intensified CCD coupled with spectrograph is used to detect and produce Raman spectrum of the sample under study [28,44,45]. Dry sand samples having explosive concentrations 4–8% have been investigated using 532 nm as excitation laser wavelength [29]. Visibly excited stand-off detection may face fluorescence of samples and impurity. However, using pulse laser as excitation source and gated detection can be utilized to reduce contribution fluorescence and ambient light [9]. Random Raman lasing using 532 nm as excitation is being reported for stand-off explosive detection. The occurrence of Random Raman laser depends on beam-quality which is difficult to maintain at large stand-off distances [46].

Raman spectroscopy promises better sensitivity with visible wavelength as excitation compared to that in near infrared range as the Raman scattering cross-section depends inversely on the fourth power of the wavelength [31]. So far, stand-off UV Raman systems reported in the literature have been applied mainly to detection of explosives and chemicals (chemical and biological contaminants) [27,47–51]. Though, UV range excitation theoretically offers further better sensitivity, high energy UV photons exhibit potential risk of sample degradation and burning [31,52–54]. UV excitation in absorption bands of explosives causes photolysis which decreases concentration of the explosive molecules (51). Explosives exhibit problem of sample burning remarkably due to their absorption in deep UV range [55,56]. Photo-degradation of sample with UV excitation may be reduced remarkably by following two methods: (a) either sample should be in motion like open-stream flow or magnetic stirring [47] so that point of interaction of laser with samples may be varied during investigating target material (not possible in real scenario) or (b) use of pulse energy of level of micro-joule (not sufficient for stand-off detection).UV excitation based methods do not promise the detection of explosives through normal transparent glass and plastic containers. Though UV excitation promises higher maximum permissible energy (MEP) for eye safety, it may generate other irreversible biological effects in operator body [57,58]. Hence, UV excitation is not practical in stand-off where high pulse energy has to be transmitted.

Despite of several advancements in Raman spectroscopy has been achieved in the area of explosive detection, however Raman spectroscopy in the visible range remained to be investigated for trace detection of explosives. Trace detection targets surfaces of suspicious objects where there is probability of contamination like door handle of vehicles, handles of brief-case etc. The level of contamination may vary from few ng/cm^2 to $\mu g/cm^2$(i.e. ppm to ppb level) depending on the way of handling the explosives in making IED etc and adhesive nature of explosives. In addition, the effect of various parameters of the set-up of time-gated Raman spectroscopy on the sensitivity remains to be explored. Here, the effect of various parameters like gain of intensifier of intensified charge-coupled device (ICCD), number of pulses used in accumulation and pulse energy of laser on sensitivity was investigated thoroughly. After optimization of these parameters in terms of sensitivity, RDX was detected at lower concentrations. Stand-off detection of 1,3,5-trinitroperhydro-1,3,5-triazine(RDX) up to 100 ppm level using visible Raman spectroscopy i.e. 532 nm as excitation laser beam was demonstrated.

2. Experimentation

An experimental set-up used in the present study was developed according to the schematic depicted in Fig. 1. This prototype mainly involves a pulse laser excitation source, ICCD-coupled spectrograph and a compact receiving optics. The pulse laser was a 2nd harmonic of Flash lamp-pumped Nd:YAG laser (Make: Quantel, France, model: Brilliant). It has maximum pulse energy of about 160 mJ at 532 nm, pulse duration of the order of 6 ns and beam divergence of about 1mrad. It has variable pulse repetition rate of 1–10 Hz. In these measurements, pulse repetition rate of 10 Hz was used.

The collection optics was very compact having diameter of 1 inch and consisted of collimating optics (C), long pass filter (LPF) and finally focusing optics (F). The revived backscattered Raman signal was collected and collimated with collimating optics (C). Long pass filter (LPF) at 532 nm with very steep transition width ~225 cm^{-1} and high optical density (O.D.) of the order of 6 (Make: Semrock, USA) was used to reject Rayleigh scattered photons. Finally focusing optics (F) was used to focus the remaining signal

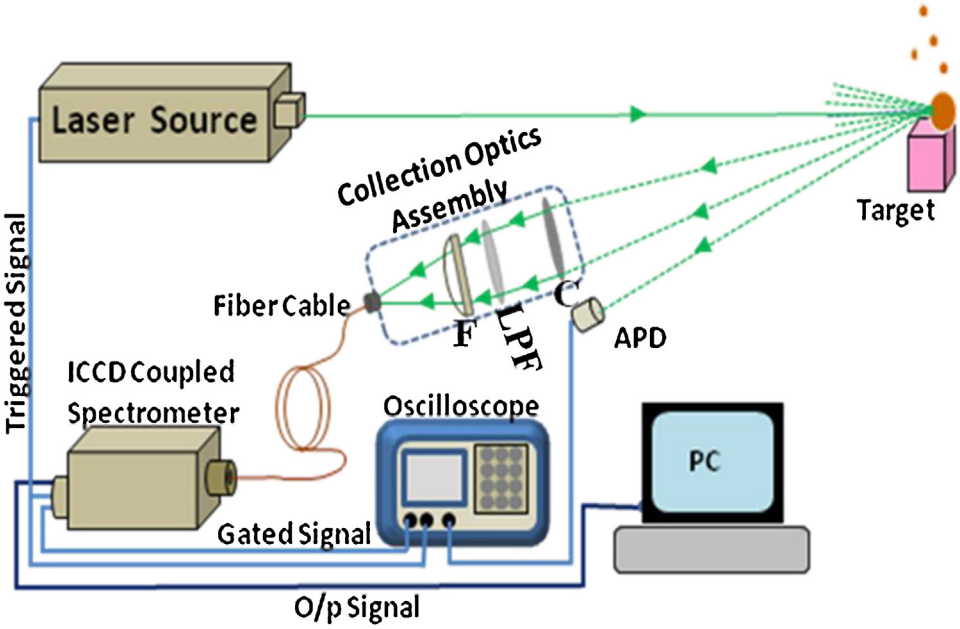


Fig. 1. Schematic of ICCD based pulse Raman Stand-off detection system. C: Collimating optics, LPF: Longpass Filter, F: Focusing optics, ICCD: Intensified Charge Coupled Device, APD: Avalanche photodiode.

i.e. Raman signal at fiber-tip of an optical fiber bundle of core diameter of 200 μm (make: M/s ANDOR, USA & model: SR-OPT-8024. This bundle has 19 fibers arranged in circular manner at one end where Raman signal was focused, and in linear way at other end coupled to spectrograph. The optical fiber bundle was used to couple the Raman signal to spectrograph (Make: ANDOR, USA, model: SR303i) attached with the intensified charge coupled Device (ICCD). The spectrograph has motorized entrance slit with a variable width varying from 10 μm–2.5 mm. In present study, silt width of 20 μm was used. This spectrograph has 303 mm focal length and f/4 aperture ratio. It consists of grating having 300 lines/mm blazed in visible range having efficiency greater than 65%. Its resulting spectral resolution is $\sim$20 cm^{-1}.

Intensified charge-coupled device (ICCD) (make: ANDOR, USA and model: iStar720-25-U) coupled with spectrograph (SR303) was used to record Raman spectra. The ICCD has thermo-electrically cooling (TEC) mechanism and array of 1024×256 pixels. The operational temperature of ICCD was set at $-20\,^{\circ}C$ in these experiments. The ICCD may be gated 3 ns to 25 s with resolution of 25 ps. Vertical binning was performed in the measurements. Its various parameters like intensifier gain, gate width, number of pulses to be accumulated were varied to observe their effects on intensity of Raman peaks. Present study was carried out in ambient conditions i.e. day-light conditions.

There are various sources of noise including solar-noise, thermal noise of CCD and fluorescence of the samples as well as substrates. The samples like p-nitrobenzoic acid (PNBA), dinitro-benzene (TNB) and RDX mixed with KBr do not exhibit remarkable fluorescence. In addition, samples were prepared in form of pellets and hence no fluorescence from the substrate. Though, the effect of other noise sources as mentioned above may be observed separately, the idea behind current study was to simulate the experiment in real scenario where all the noise sources may exist together.

2.1. Synchronizing of optical pulse with gate width

Matching the timings for optical pulse and gate width is one of critical aspects in experiments of time-gated Raman spectroscopy. As Raman scattering takes place without any delay, detector should be switched ON as soon as the optical pulse reaches at the detector. But still some delay has to be introduced to cater the travelling time of incident photons from laser to sample and Raman photons from sample to detection end. The difference between travelling time of photons from molecule to molecule or layer to layer (in order of sub ns) may be neglected as compared to longer laser pulses (6 ns) and gate widths ($\geq$10 ns) used in this work.

The triggering TTL signal of laser system was fed to the ICCD detector. The laser pulse detected using APD, which was kept near the receiver. The synchronization achieved by monitoring gate output of ICCD and APD signal on oscilloscope for accurate overlapping of both signals in time-domain by inserting proper delay. ICCD has inbuilt electronic card that controls gate width, gate delay and gain of the intensifier of ICCD. These parameters may be varied by the user by inserting the required values in software of ICCD.

3. Sample preparation

In current study, 1,3,5-trinitrobenzene (TNB), p-nitro benzoic acid (PNBA) and 1,3,5-trinitroperhydro-1,3,5-triazine (RDX) were used. Samples of p-nitro benzoic acid and RDX were prepared by mixing with potassium bromide (KBr) at different ratio (w/w) in the form of pallets. Aqueous solution of diluted concentration of 1,3,5-trinitrobenzene (TNB) deposited uniformly on aluminum sheet (100 mg of TNB in 1 l of water). Then mass of TNB per unit area estimated and found approximately 100 $\mu g/cm^2$.

4. Results and discussion

Initial experiments were started with benzene and 1,3,5-trinitrobenzene which share common benzene ring with many explosives like 2,4,6-trinitrotoluene (TNT), 2,4-dinitrotoluene (DNT), 2,4,6-triamino-1,3,5-trinitrobenzene (TATB), picric acid, 2,4,6-trinitrophenylmethylnitroamine (commonly known as tetryl) etc. [59,60]. Further Raman spectra of RDX and p-nitrobenzoic acid were recorded in stand-off mode from a distance of 5 m and effect of various parameters was investigated to optimize

Table 1
Assignment of the most intense peak of Raman spectra of TNB, PNBA & RDX.

Molecule	Transition (most-intense)	Assignment	Intrinsic Raman scattering cross-section
TNB	1354 cm^{-1}	NO_2 symmetric stretching + NO_2i.p. deformation + CN stretching [61]	3.7×10^{-28} [65]
PNBA	1368 cm^{-1}	NO_2 symmetric stretching [62]	–
RDX	887 cm^{-1}	Ring-breathing mode [63,64]	1.8×10^{-29} [66]

experimental set-up for better sensitivity. Finally, Raman spectra of RDX were recorded in lower concentrations at 1000 ppm, 500 ppm and 100 ppm level in stand-off mode from 5 m using optimised experimental parameters. The peak assignments corresponding to the most intense peak in Raman spectra of 1,3,5-trinitrobenzene (TNB), p-nitrobenzoic acid (PNBA) and 1,3,5-trinitroperhydro-1,3,5-triazine (RDX) are summarized in Table 1.

Raman scattering Raman cross-section is wavelength dependent used as excitation. For example, Raman scattering cross-section of RDX is 1.8×10^{-29}, 5.8×10^{-30} and 2.1×10^{-30} with excitation wavelength at 532 nm, 633 nm and 785 nm respectively for the peak at 887 cm^{-1} [66].

4.1. Gated-Raman signal and normal Raman signal

In case of standoff detection, scattered Raman signal is accompanied by strong background noise available from other sources. This unwanted background noise can be solar or from any other light source near to targeted materials. Depending on conditions, this noise may be much strong and does not provide any information about targeted materials. Raman signal, having molecular information of targeted materials, may be easily obscured by this unwanted strong background noise. Gated detection opens the path to detect suspicious materials from stand-off distances in daytime by reducing effect of ambient light and fluorescence. This technique provides increased the signal-to-noise ratio of the Raman signal. A gated detector also improves the Raman signal by decreasing the fluorescence background [27].

Gated-Raman spectroscopy where detector synchronized with pulse laser, was used in the current study and therefore weak Raman signal of 1,3,5-trinitrobenzene at low concentration (μg/cm^2) was measured from the stand-off distance of 5 m as shown in Fig. 2. Raman signal of 1,3,5-trinitrobenzene was recorded in stand-off backscattered mode from a distance of 5 m by using ICCD in CW mode as well as in synchronized mode. The aqueous sample of diluted concentration (100 mg of TNB in 1 l of water) of 1,3,5-trinitrobenzene (TNB) deposited uniformly on aluminum sheet. The quantity of the chemical was approximately 100 μg/cm^2. In case of CW mode, intensifier of ICCD was kept continuously ON. Whereas it was synchronized with optical pulse of laser in synchronized mode. In both measurements pulse energy of laser, gain (G) of intensifier and gate width were kept at 15 mJ, 100 and 20 ns respectively. In CW mode, weak Raman signal (due to quantity at trace level ~100 μg/cm^2) was completely obscured by background noise which also gets amplified by intensifier continuously and hence molecular information cannot be extracted from scattered light collected at receiver (Fig. 2). However, in synchronized mode, weak Raman signal easily detected and molecular information in terms of Raman stokes lines was clearly observed as shown in Fig. 2.

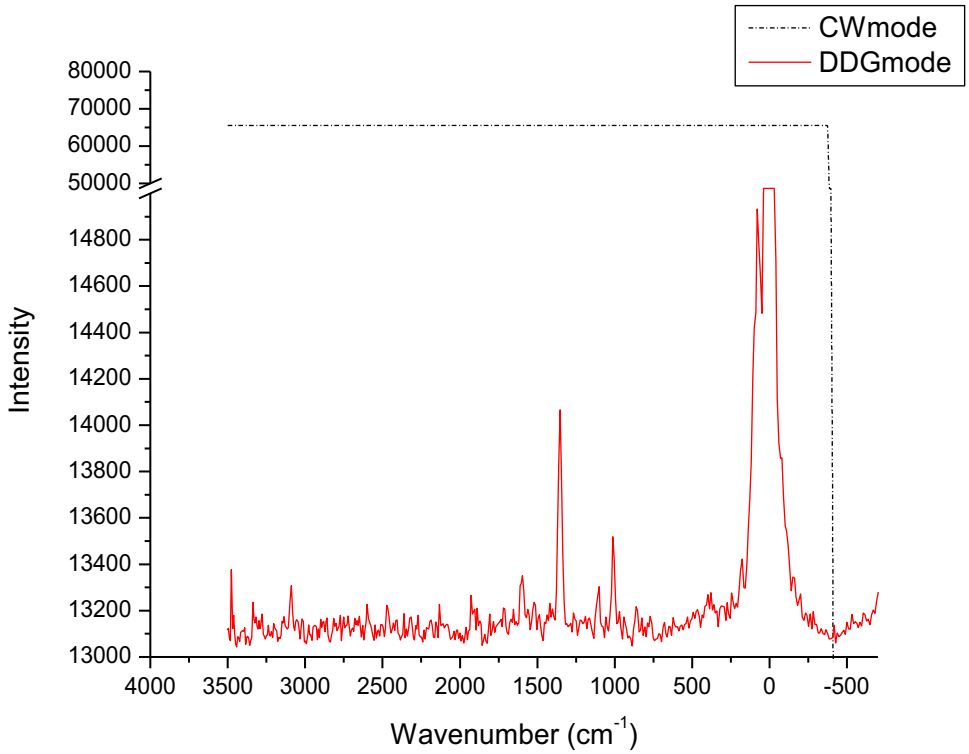


Fig. 2. Raman spectra of 1,3,5 – trinitrobenzene at low concentration (100 μg/cm^2)recorded using ICCD in CW mode and gate mode. Pulse energy of laser, gain (G) of intensifier and gate width kept at 15 mJ, 100 and 20 ns respectively.

4.2. ICCD gain effect on Raman spectra

Photons entering to an ICCD strike a photocathode plate where they are converted to electrons which are directed towards micro-channel plate (MCP). At MCP, electrons are multiplied by applying a high voltage. Gain of the ICCD depends on this multiplication and hence the applied voltage to MCP. Therefore, by controlling the voltage at MCP, gain of ICCD can be controlled.

To analyze the effect of gain of intensifier on intensity of Raman scattering, Raman spectra of 1,3,5-trinitrobenzene in stand-off mode from a distance of 5 m was recorded by varying the gain 0 to 200. Pulse energy of laser and gate width were kept at 15 mJ and 20 ns respectively. These Raman spectra were recorded with accumulation over 100 number of laser pulses.

Results of the study revealed a significant improvement in SNR of Raman peaks with increasing gain of intensifier as shown in Fig. 3. Raman spectra of 1,3,5-trinitrobenzene at gain of 0, 50, 100 and 200 are shown in Fig. 3A.The improvement in SNR of Raman peak at 1354 cm^{-1} (NO_2 symmetric stretching) can be easily visualized. In addition, due to increase in sensitivity with increasing gain, less intense peaks e.g. peaks at 1007 cm^{-1} and 3076 cm^{-1} which did not exist with lower gain, start appearing in Raman spectra. It was observed that the intensity of Raman peak at 1354 cm^{-1} increased with increase in gain as shown in Fig. 3B. The background subtracted intensity of Raman scattering at 1354 cm^{-1} increased gradually with gain upto 80 and beyond it increased rapidly. The signal-to-noise ratio (SNR) of Raman peak at 1354 cm^{-1} was 30 and 85 in case of gain of intensifier at 50 and 200 respectively.

Raman signal and noise both go under process of amplification. Raman signal appears in phase wise manner and keeps adding on during accumulation of pulses. Whereas, noise is a random process and therefore can be averaged out when accumulated over a number of pulses and thus improved SNR was observed in present study.

4.3. Pulse accumulation effect on Raman spectra

To study the effect of pulse accumulation on Raman spectra, pulse energy, gain (G) of intensifier and gate width were kept at 30 mJ, 100 and 20 ns respectively. The test sample i.e. p-nitrobenzoic acid mixed with KBr at 1000 ppm (w/w) was in pellet form. Raman spectra of p-nitrobenzene were recorded in stand-off mode from a distance of 5 m by accumulating number of pulses in range 10–2000. Raman spectra of p-nitrobenzoic acid mixed with KBr (at 1000 ppm) recorded using accumulation of 10, 100, 1000 and 2000 pulses in Fig. 4A. A significant increase in intensity of Raman signal was observed with increasing number of pulses accumulated. Experimental results indicated that less intense peaks i.e. 1368 cm^{-1} (NO_2 symmetric stretching) that was almost invisible with 10 numbers of pulses started appearing at 100 numbers of pulses. Further, improvement in SNR of Raman peaks was observed visually as the pulses increased. Fig. 4B shows the trend of change in background subtracted intensity of Raman peak at 1368 cm^{-1} with increase in accumulated pulse number. It was further observed that the intensity improves in a linear fashion with increase in number of pulses accumulated. The signal-to-noise ratio (SNR) of Raman peak at 1368 cm^{-1} was 17 and 40 in case of number of pulses accumulated is 100 and 1000 respectively. These results reveal that better sensitivity achievable by accumulating Raman spectra corresponding to more and more optical pulses of laser. However, at the same time, it is not possible to keep adding large number of pulses as this process is time consuming. In real time scenario, explosive detection and identification should be completed within a few seconds. This imposes a limit on the number of pulses to be accumulated. For

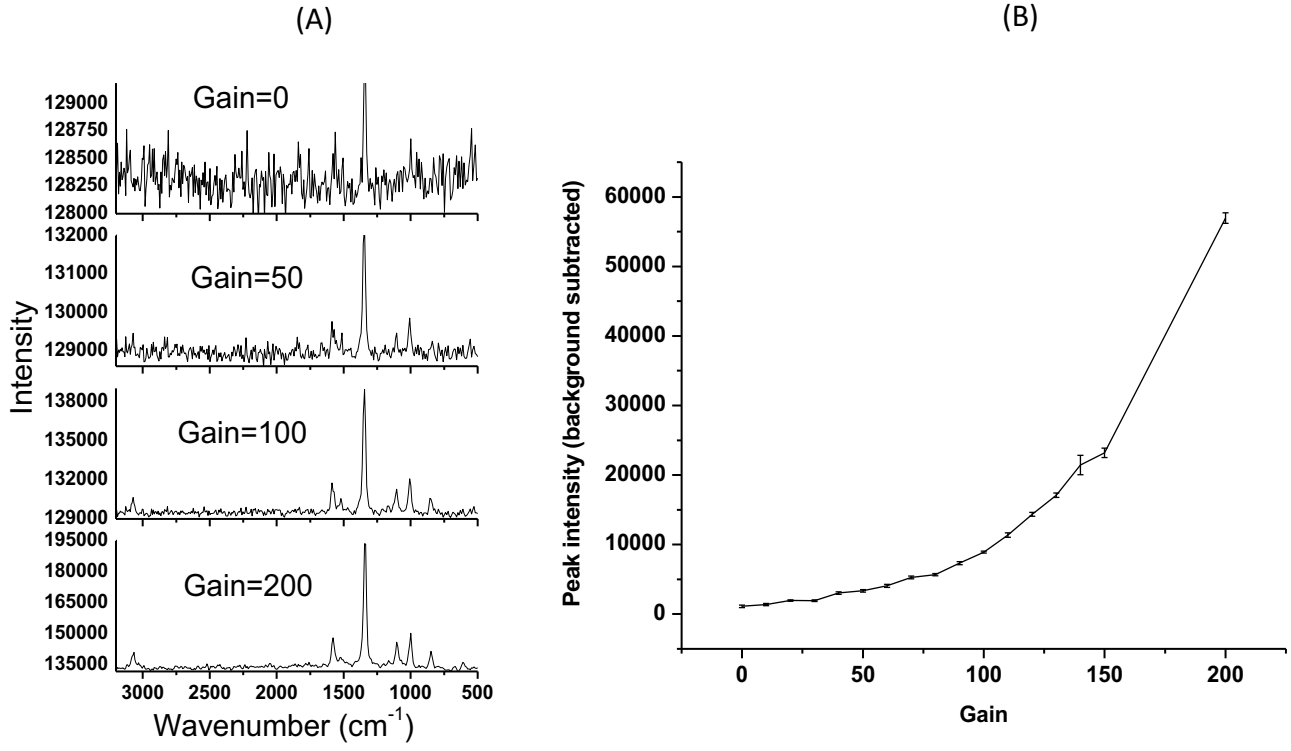


Fig. 3. A: Raman spectra of 1,3,5 – trinitrobenzene recorded using gain of intensifier of ICCD detector at 0, 50, 100 and 200. In both measurements pulse energy of laser, gain (G) of intensifier and gate width were kept at 15 mJ, 100 and 20 ns respectively and B: Variation in peak intensity (background subtracted) of Raman peak at 1354 cm^{-1} w.r.t. gain of intensifier when gain value is varied 0 to 200. The error bars represent the standard deviation (SD) of three time measurement.

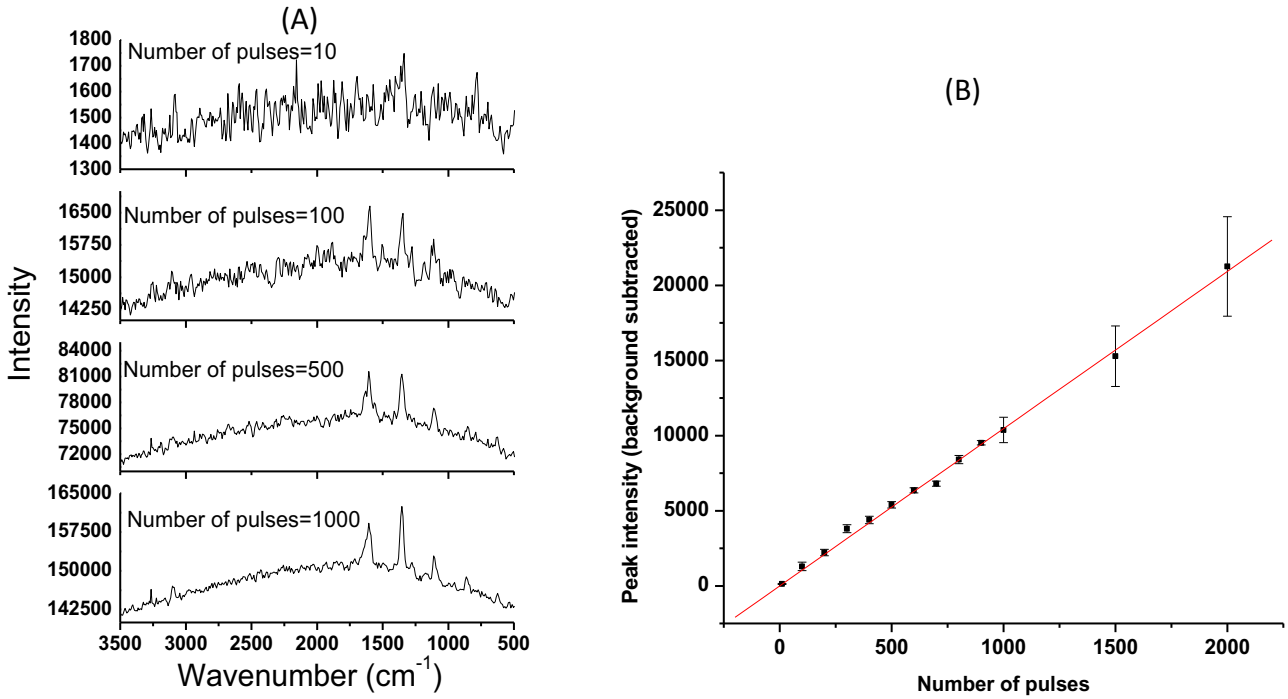


Fig. 4. A: Raman spectra of p-nitrobenzoic acid recorded with accumulation of 10, 100, 1000 and 2000 pulses. Pulse energy of laser, gain (G) of intensifier and gate width at 30 mJ, 100 and 20 ns respectively and B: Variation of SNR of peak at 1368 cm^{-1} w.r.t. number of pulses accumulated. The error bars represent the standard deviation (SD) of three time measurement.

example it takes 100 s for accumulation of 1000 number of pulses in case of repetition rate of 10 Hz. The detection process can be made faster by using laser of high repetition rate. However, it may induce thermal effects and damage the target material. So, there has to be a trade-off between number of pulses accumulated, detection-analysis time and pulse repetition rate.

4.4. Pulse energy effect

Pulse energy of laser is one of the critical parameters which decide the maximum achievable sensitivity. The effect of pulse energy on intensity of Raman peaks i.e. on sensitivity was carried out. Gain of intensifier, gate width and number of pulses

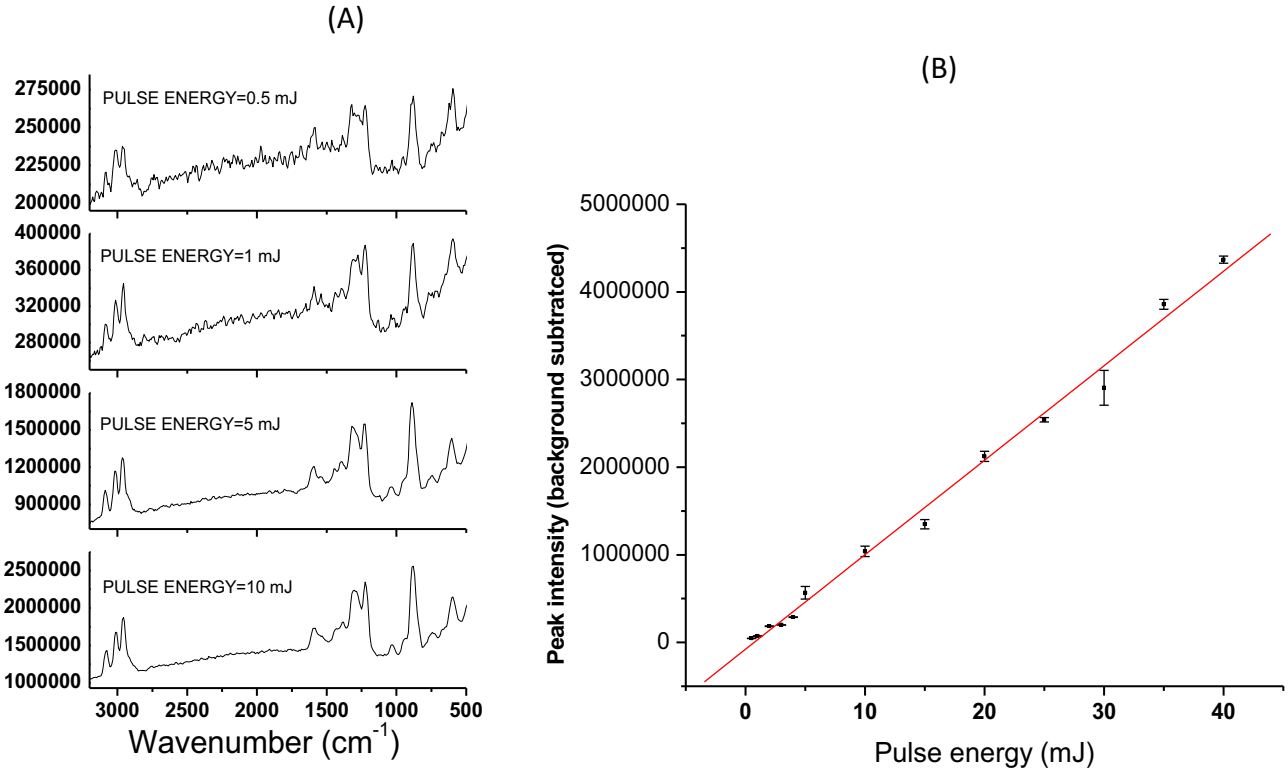


Fig. 5. A: Raman spectra of RDX with pulse energy of 0.5 mJ, 1 mJ, 5 mJ and 10 mJ. Intensifier, gate width, pulses accumulated are kept at 100, 20 ns and 1000 respectively and B: Variation of SNR of peak at 887 cm^{-1} w.r.t. pulse energy. The error bars represent the standard deviation (SD) of three time measurement.

accumulated were kept at 100, 20 ns and 1000 respectively. The sample was a pellet of RDX mixed with KBr at 1000 ppm (w/w). Fig. 5A shows recorded Raman spectra of RDX mixed with KBr (at 1000 ppm) were recorded with pulse energy varying in range 0.5–45 mJ. Raman spectra of RDX (at 1000 ppm) with pulse energy at 0.5 mJ, 1.0 mJ, 5.0 mJ and 10 mJ were shown in Fig. 5A. Significant improvement in SNR of Raman peaks was easily observed when pulse energy increased. The background subtracted intensity of Raman peak at 887 cm^{-1} (ring breathing mode) was found to be increased linearly with increase in pulse energy of laser as shown in Fig. 5B. The signal-to-noise ratio (SNR) of Raman peak at 887 cm^{-1} was observed to be increases from 35 at pulse energy of 1 mJ to 211 at pulse energy of 10 mJ respectively.

4.5. Raman spectra of explosives at ppm concentrations in stand-off mode

The effects of experimental parameters like gain of intensifier, number of pulses used in accumulation and pulses energy on the sensitivity were studied. Raman spectra of RDX mixed in KBr at concentrations 1000 ppm, 500 ppm and 100 ppm were recorded in stand-off mode from distance of 5 m as shown in Fig. 6.For achieving good sensitivity and recording of Raman spectra at these low concentrations, experimental parameters were set at optimised values. In recording of these Raman spectra, pulse energy of 20 mJ, repetition rate of 10 Hz, ICCD gain at 200, gate width of 100 ns were used and 1000 nos. of scans accumulated. Pulse energy of 20 mJ was found sufficient for detection of RDX at concentration of 100 ppm and hence higher pulse energy was not used.Raman spectra of RDX were successfully recorded at lowest tested concentration level i.e. 100 ppm in stand-off mode from distance of 5 m (Fig. 6). The intensity of Raman peaks decreased almost linearly as the concentration of sample came down from 1000 ppm to 500 ppm and then 100 ppm. Further the limit of detection (LoD) was estimated using Raman spectrum of RDX (peak at 887 cm^{-1}) of 100 ppm. In estimation of the detection limit, the intensity has to be atleast three times the standard deviation (STD) of the background [29]. By determining the standard deviation and applying a scaling factor to reduce the background-subtracted Raman signal to three times the calculated background STD, we estimated that the detection limit of RDX is approximately 10 parts-per-million. As the background-subtracted Raman intensity is linear to pulse energy and number of pulses used in accumulations, the limit of detection reaches at 1000 ppb using pulse energy of 100 mJ and accumulation of 2000 pulses.

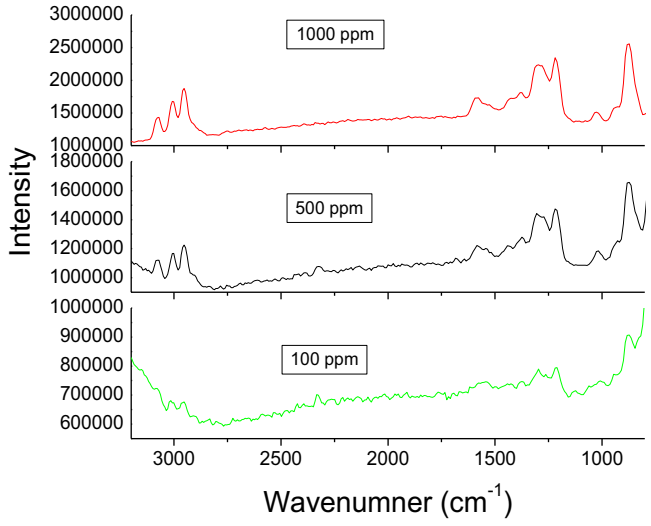


Fig. 6. Raman spectra of RDX at concentrations 1000 ppm, 500 ppm and 100 ppm. Pulse energy of 20 mJ, repetition rate of 10 Hz, ICCD gain at 200, gate width of 100 ns and accumulation of 1000 nos. of pulses.

5. Conclusion

This study illustrates that time-gated Raman spectroscopy has great potential in detecting explosives in trace mode i.e. on contaminated surfaces. The effect of various parameters i.e. pulse energy, repetition rate, ICCD gain and number of pulses on sensitivity was observed. Further the system was optimised for sensitivity at lower concentrations in terms of laser pulse energy, repetition rate, ICCD gain as well as number of pulses. Raman spectra of explosives and their derivatives were recorded in stand-off mode at a distance of 5 m. Raman spectra of RDX recorded with different concentrations down to 100 ppm with optimised experimental parameters and estimated limit of detection is 1000 ppb which is the requirement in trace detection. This study also gives a fare idea of optimised value of different specifications of laser, ICCDs, optics etc. and envisages design of time-gated Raman spectroscopy based compact and portable explosive detector for trace detection of explosive materials.

Acknowledgement

We are thankful to Sh. Hari Babu Srivastava, Director, LASTEC for his guidance and support in pursuing this work. I also express my sincere thanks towards Delhi Technological University for providing good environment of research.

References

[1] J.S. Caygill, F. Davis, S.P.J. Higson, Talanta 88 (2012) 14–29.
[2] Z. Bielecki, J. Janucki, A. Kawalec, J. Mikołajczyk, N. Pałka, M. Pasternak, T. Pustelny, T. Stacewicz, J. Wojtas, Metrol. Meas. Syst. 19 (1) (2012) 3–28.
[3] D.J. Brenner, Radiology 259 (1) (2011) 6–10.
[4] M. Tourne, J. Forensic Res. S12 (2013) S12–002, doi:http://dx.doi.org/10.4172/2157-7145.
[5] S. Wallin, A. Pettersson, H. Ostmark, A. Hobro, Anal. Bioanal. Chem. 395 (1) (2009) 259–274.
[6] L.A. Skvortsov, Laser methods for detecting explosive residues on surfaces of distant objects, Quantum Electron. 42 (1) (2012) 1–11.
[7] K.E. Brown, M.T. Greenfield, S.D. McGrane, D.S. Morre, Advances in explosives analysis- part II: photon and neutron methods, Anal. Bioanal. Chem. 408 (2016) 49–65.
[8] E.L. Izake, Forensic and homeland security applications of modern portable Raman spectroscopy, Forensic Sci. Int. 202 (2010) 1–8.
[9] K.L. Gares, K.T. Hufziger, S.V. Bykov, S.A. Asher, Review of explosive detection methodologies and the emergence of standoff deep UV resonance Raman, J. Raman Spectrosc. 47 (2016) 124–141.
[10] J.L. Gottfried, F.C. De Lucia, Anal. Bioanal. Chem. 395 (2) (2009) 283–300.
[11] D.A. Cremers, L.J. Radziemski, Handbook of Laser-Induced Breakdown Spectroscopy, J. Wiley & Sons, Berlin, 2006.
[12] A.M. Popov, T.A. Labutin, N.B. Zorov, Moscow Univ. Chem. Bull. 64 (6) (2009) 366–377.
[13] D.W. Hahn, N. Omenetto, Appl. Spectrosc. 64 (12) (2010) 335–366.
[14] D.W. Hahn, N. Omenetto, Appl. Spectrosc. 66 (4) (2012) 347–419.
[15] J.L. Gottfried, F.C. De Lucia, C.A. Munson, A.W. Miziolek, J. Anal. At. Spectrom. 23 (2008) 205–216.
[16] C.M. Wynn, S. Palmacci, R.R. Kunz, M. Aernecke, Optical Express 19 (19) (2011) 18671–18677.
[17] J.D. White, F.A. Akin, H. Oser, D.R. Crosley, Appl. Opt. 50 (1) (2011) 74–81.
[18] C.M. Wynn, S. Palmacci, K. Clow R.R. Kunz, M. Rothshild, Proc. SPIE Int. Soc. Opt. Eng. 6954 (2008) 695407.
[19] C.M. Wynn, S. Palmacci, R.R. Kunz, K. Clow, M. Rothschild, Appl. Opt. 47 (31) (2008) 5767–5776.
[20] C. Wynn, S. Palmacci, R.R. Kunz, M. Rothschild, Opt. Express 18 (6) (2010) 5399–5406.
[21] X. Chen, L. Cheng, D. Guo, Y. Kostov, F.S. Choa, Opt. Express 19 (2011) 20251–20257.
[22] S. Gulia, DRDO Sci. Spectr. 86 (2015).
[23] J.B. Johnson, S.D. Allen, J. Merten, L. Johnson, D. Pinkham, S.W. Reeve, J. Spectrosc. (2014) 1–13.
[24] N. Petra, J. Zweck, A.A. Kosterev, S.E. Minkoff, D. Thomazy, Appl. Phys. B 94 (4) (2009) 673–680.

[25] X. Chen, L. Cheng, D. Guo, Y. Kostov, F. Choa, Opt. Express 19 (21) (2011) 20251–20257.
[26] J.P. Waclawek, R. Lewicki, H. Moser, M. Brandstetter, F.K. Tittel, B. Lendl, Appl. Phys. B Lasers Opt. (2014), doi:http://dx.doi.org/10.1007/s00340-014-5809-y.
[27] M. Gaft, L. Nagli, Opt. Mater. 30 (11) (2008) 1739–1746.
[28] A.K. Misra, S.K. Sharma, C.H. Chio, P.G. Lucey, B. Lienert, Spectrochim. Acta A 61 (2005) 2281–2287.
[29] J.C. Carter, S.M. Angel, M.L. Snyder, J. Scaffidi, R.E. Whipple, J.G. Reynolds, Appl. Spectrosc. 59 (6) (2005) 769–775.
[30] S.A. Oladepo, K. Xiong, Z. Hong, S.A. Asher, J. Handen, I.K. Lednev, Chem. Rev. 112 (5) (2012) 2604–2628.
[31] E. Smith, G. Dent, Modern Spectroscopy -A Raman Practical Approach, John Wiley & Ltd. Sons, 2005.
[32] J.R. Ferraro, K. Nakamoto, C.W. Brown, Introductory Raman Spectroscopy, Academic Press, London, 2003.
[33] D.A. Long, The Raman Effect −A Unified Treatment of the Theory of Raman Scattering by Molecules, John Wiley & Sons, 2002.
[34] S.A. Asher, Handbook of Vibrational Spectroscopy, J. Wiley & Sons, 2002.
[35] W.A. Al-Saidi, S.A. Asher, P. Norman, J. Phys. Chem. 116 (2012) 7862–7872.
[36] A. Ehlerding, I. Johansson, S. Wallin, H. Ostmark, Int. J. Spectrosc. 2012 (2012) Article ID 158715.
[37] Z. Gong, H. Du, F. Cheng, C. Wang, C. Wang, M. Fan, ACS Appl. Mater. Interfaces 6 (24) (2014) 21931–21937.
[38] P.M. Mercado, S.P. Rivera, Int. J. Spectrosc. 2012 (2012) Article ID 716527.
[39] H. Syed, G.K. Podagatlapalli, M.A. Mohiddon, V.R. Soma, Adv. Mater. Lett. 6 (12) (2015) 1073–1080.
[40] P. Matousek, I.P. Clark, E.R. Draper, M.D. Morris, A.E. Goodship, N. Everall, M. Towrie, W.F. Finney, A.W. Parker, Appl. Spectrosc. 59 (4) (2005) 393–400.
[41] J. Guicheteau, R. Hopkins, Proc. SPIE 9824, Chemical, Biological, Radiological, Nuclear, and Explosives (CBRNE) Sensing XVII, 98240G (May 12, 2016); 10.1117/12.2229157.
[42] B. Zachhuber, H. Ostmark, T. Carlsson, Spatially offset hyperspectral stand-off Raman imaging for explosive detection inside containers, Proc. SPIE 9073 (2014), doi:http://dx.doi.org/10.1117/12.2053251.
[43] J.H. Chung, S.G. Cho, Bull. Korean Chem. Soc. 35 (12) (2014) 3547–3552.
[44] S.K. Sharma, S.M. Angel, M. Ghosh, H.W. Hubble, P.G. Lucey, Appl. Spectrosc. 56 (6) (2002) 699–705.
[45] J.H. Chung, S.G. Cho, Bull. Korean Chem. Soc. 34 (6) (2013) 1668–1672.
[46] B.H. Hokr, J.N. Bixler, G.D. Noojin, R.J. Thomas, B.A. Rockwell, V.V. Yakovlev, M. O. Scully, Proc. Natl. Acad. Sci. 111 (34) (2014) 12320–12324.
[47] D.D. Tuschel, A.V. Mikhonin, B.E. Lemoff, S.A. Asher, Appl. Spectrosc. 64 (4) (2010) 425–432.
[48] A. Pettersson, S. Wallin, H. Östmark, A. Ehlerding, I. Johansson, M. Nordberg, H. Ellis, A. Khalili, Proc. SPIE. 7664 (2010) (76641K).
[49] R. Forest, F. Babin, D. Gay, N. Ho, O. Pancrati, S. Deblois, S. Desilets, J. Maheux, Proc. SPIE 8358 (2012) (83580M.).
[50] T.A. Reichardt, S.E. Bisson, T.J. Kulp, Sandia National Labs (2011) SAND2011-7955.
[51] S.V. Bykov, M. Mao, K.L. Gares, S.A. Asher, Appl. Spectrosc. 69 (8) (2015) 895–901.
[52] R.L. McCreery, Raman Spectroscopy for Chemical Analysis, John Wiley & Sons Inc., New York, 2005.
[53] T.L. Andrew, T.M. Swager, J. Org. Chem. 76 (9) (2011) 2976–2993.
[54] R.R. Kunz, K.E. Gregory, M.J. Aernecke, M.L. Clark, A. Ostrinskaya, A.W. Fountain 3rd, J. Phys. Chem. A 116 (14) (2012) 3611–3624.
[55] K.L. Gares, S.V. Bykov, B. Godugu, S.A. Asher, Appl. Spectrosc. 68 (1) (2014) 49–56.
[56] K.L. Gares, S.V. Bykov, B. Godugu, S.A. Asher, Appl. Spectrosc 69 (5) (2015) 545–554.
[57] A.V. Parisi, M.G. Kimlin, J.C.F. Wong, R.A. Fleming, Photodermatol. Photoimmunol. Photomed. 12 (2) (1996) 57–65.
[58] M.F. Holick, Anticancer Res. 36 (3) (2016) 1397–1401.
[59] S. Gulia, V. Gambhir, M.N. Reddy, High Energy Materials Conference and Exhibit (HEMCE), High Energy Materials Research Laboratory, DRDO, 2009.
[60] S. Gulia, M.N. Reddy, V. Gambhir, R. Sharma, National Laser Symposium (NLS-23), Sri Venkateswara University, India, 2014.
[61] P.S. Santos, N.S. Goncalves, J. Raman Spectrosc. 20 (1989) 551–554.
[62] X.M. Yang, D.A. Tryk, K. Hashimoto, A. Fujishima, J. Phys. Chem. B 102 (1998) 4933–4943.
[63] W.A. Al-Saidi, S.A. Asher, P. Norman, J. Phys. Chem. A 116 (2012) 7862–7872.
[64] Nahla A, Hatab b, GyulaEres, Paul Hatzinger and BaohuaGu, J. Raman Spectrosc. 41 (2010) 1131–1136.
[65] K. Sakamoto, G. Mizutani, S. Ushioda, Phys. Rev. B Condens. Matter 48 (12) (1993) 8993–9005.
[66] E.D. Emmons, J.A. Guicheteau, A.W. Fountain III, S.D. Christesen, Appl. Spectrosc. 66 (6) (2012) 628–635.